DÜZCE ÜNİVERSİTESİ

DÜZCE ÜNİVERSİTESİ BİLİM ve TEKNOLOJİ DERGİSİ

Düzce University Journal of Science & Technology

e-ISSN: 2148-2446

Cilt Volume 13 Sayı Issue 1 Ocak/January 2025

Düzce Üniversitesi
BİLİM ve TEKNOLOJİ DERGİSİ
DÜBİTED

http://dergipark.org.tr/dubited

Düzce University
JOURNAL of SCIENCE & TECHNOLOGY
DUBITED

http://dergipark.org.tr/dubited

Fatih TAŞPINAR, Düzce Üniversitesi, Türkiye
Fatih YILMAZ, Bayburt Üniversitesi, Türkiye
Fikret POLAT, Düzce Üniversitesi, Türkiye
Alev ÖZKÖK, Hacettepe Üniversitesi, Türkiye
Gökhan YILDIZ, Düzce Üniversitesi, Türkiye
Hakan ARSLAN, Düzce Üniversitesi, Türkiye
Harun BAYRAKDAR, Düzce Üniversitesi, Türkiye
Hüseyin BUDAK, Düzce Üniversitesi, Türkiye
Hüseyin BAKIR, Doğuş Üniversitesi, Türkiye
İrem DÜZDAR ARGUN, Düzce Üniversitesi, Türkiye
Koray ŞARKAYA, Pamukkale Üniversitesi, Türkiye
Mecit AKSU, Düzce Üniversitesi, Türkiye
Mehmet SÖNMEZ, Osmaniye Korkut Ata Üniversitesi, Türkiye
Melahat Sevgül BAKAY AĞBULUT, Düzce Üniversitesi, Türkiye
Melike ERDOĞAN, Düzce Üniversitesi, Türkiye
Mert YILDIRIM, Düzce Üniversitesi, Türkiye
Metin TOZ, Karamanoğlu Mehmetbey Üniversitesi, Türkiye
Mevlüt ERSOY, Süleyman Demirel Üniversitesi, Türkiye
Muhanmmet Emin ŞAHİN, Yozgat Bozok Üniversitesi, Türkiye
Muhammet GÜL, Munzur Üniversitesi, Türkiye
Mustafa KARAGÖZ, Karabük Üniversitesi, Türkiye
Murat AYDEMİR, Erzurum Teknik Üniversitesi, Türkiye
Murat Kadir YEŞİLYURT, Bozok Üniversitesi, Türkiye
Murat EYVAZ, Gebze Teknik Üniversitesi, Türkiye
Mustafa DAYI, Düzce Üniversitesi, Türkiye
Musa Çadırcı, Düzce Üniversitesi, Türkiye
Nuray Benli YILDIZ, Düzce Üniversitesi, Türkiye
Nİhat Hakan AKYOL, Kocaeli Üniversitesi, Türkiye
Nuri ŞEN, Düzce Üniversitesi, Türkiye
Osman DİKMEN, Düzce Üniversitesi, Türkiye
Osman KANDARA, Southern University,
Özge Tüzün ÖZMEN, İzmir Bakırçay Üniversitesi, Türkiye
Özlem ÖZKAN ÖNÜR, İstanbul Nişantaşı Üniversitesi, Türkiye
Pınar GÜLTEKİN, Düzce Üniversitesi, Türkiye
Revna ACAR VURAL, Yıldız Teknik Üniversitesi, Türkiye
Salih Tunç KAYA, Düzce Üniversitesi, Türkiye
Semih ÖZDEN, Milli Savunma Üniversitesi, Türkiye
Sercan SERİN, Osmaniye Korkut Ata Üniversitesi, Türkiye
Serdar BİROĞUL, Düzce Üniversitesi, Türkiye
Serhat DUMAN, Bandırma Onyedi Eylül Üniversitesi, Türkiye

Ulusal Danışma Kurulu
National Advisory Board

Cilt ***Volume*** **13** **Sayı** ***Issue*** **1** **Ocak/ january** **2025**

Ürün Bilgisi
Product Information

Yayıncı
Publisher
Düzce Üniversitesi Lisansüstü Eğitim Enstitüsü
Düzce University Institute of Graduate Programs

Sahibi
Owner
Nedim SÖZBİR (Düzce Üniversitesi Rektörü)
(D. Ü. Lisansüstü Eğitim Enstitüsü adına)
(On behalf of D. U. Institute of Graduate Programs)

Sorumlu Yazı İşleri Müdürü
Publishing Manager
Pınar GÜLTEKİN

Web Sayfası
Web Page
http://dergipark.org.tr/dubited

Basım Tarihi *Date of Publication*	Ocak 2025 *January 2025*
Yayın Dili *Language*	İngilizce *English*
Yayın Aralığı *Frequency*	Yılda dört kez yayınlanır *Published four times in a year*
Yayın Türü *Type of Publication*	Süreli yayın *Periodical*
e-ISSN Numarası *e-ISSN Number*	2148-2446

Yazışma Adresi

Düzce Üniversitesi Lisansüstü Eğitim Enstitüsü Rektörlük Binası 3. Kat 81620 Düzce/TÜRKİYE

Telefon: +90 380 542 12 08

Fax: +90 380 542 12 38

E-posta: dubitedyayin@duzce.edu.tr

http://dergipark.org.tr/dubited adresinden dergiye ilişkin bilgilere ve makalelerin tam metnine ulaşılabilir.

Correspondence Address

Düzce University Institute of Graduate Programs Rectorship Building 3rf Floor 81620 Düzce/TURKEY

Phone: +90 380 542 12 08

Fax: +90 380 542 12 38

E-mail: dubitedyayin@duzce.edu.tr

Instructions for authors and all articles in this journal can be reached at http://dergipark.org.tr/dubited

İÇİNDEKİLER

Sayfa **Makale**

ÇEVRE / ZİRAAT / JEOLOJİ MÜHENDİSLİĞİ

Araştırma Makalesi/ *Research Article*

Derleme Makale / *Review Article*

ELEKTRİK/ELEKTRONİK / ELEKTRİK ELEKTRONİK/ MEKATRONİK/ENERJİ MÜHENDİSLİĞİ

Araştırma Makalesi/ *Research Article*

İNŞAAT / MİMARLIK / PEYZAJ MİMARLIĞI / METALURJİ ve MALZEME / ÇEVRE MÜHENDİSLİĞİ

Araştırma Makalesi/ *Research Article*

MAKİNE / MEKATRONİK /MALZEME / ENDÜSTRİ / BİYOMEDİKAL/ İMALAT / OTOMOTİV MÜHENDİSLİĞİ

Araştırma Makalesi/ *Research Article*

Düzce Üniversitesi Bilim ve Teknoloji Dergisi

Araştırma Makalesi

Aynı Anda Buharlaştırma Yöntemiyle Üretilen CIGS İnce Filmlerin Yapısal Özelliklerinin İncelenmesi ve Kutup Figürlerinin Belirlenmesi

Celal Alp YAVRU [a*], Murat KALELİ [b, c], İsmail Serkan ÜNCÜ [d]

[a] *Elektrik Elektronik Mühendisliği Bölümü, Lisansüstü Eğitim Enstitüsü, Isparta Uygulamalı Bilimler Üniversitesi, Isparta, TÜRKİYE*

[b] *Fizik Bölümü, Fen Edebiyat Fakültesi, Süleyman Demirel Üniversitesi, Isparta, TÜRKİYE*

[c] *Yenilikçi Teknolojiler Uygulama ve Araştırma Merkezi (YETEM), Süleyman Demirel Üniversitesi, Isparta, TÜRKİYE*

[d] *Elektrik Elektronik Mühendisliği Bölümü, Teknoloji Fakültesi, Isparta Uygulamalı Bilimler Üniversitesi, Isparta, TÜRKİYE*

** Sorumlu yazarın e-posta adresi: c.alpyavru@gmail.com*

DOI: 10.29130/dubited.1121646

Öz

Bu çalışmada dörtlü element kompozisyonundan oluşan ve elektro-optik uygulamalarda sıkça kullanılan CIGS ince filmler, aynı anda termal buharlaştırma yöntemiyle üretilmiş, yapısal ve elektriksel özellikleri incelenmiştir. SEM ve AFM sistemleri ile yüzey ve kalınlık analizleri, XRD sistemi ile detaylı yapı ve doku analizleri gerçekleştirilmiştir. SEM ve AFM görüntüleri incelenerek histogram eğrileri ve bunlara bağlı Gaussian teğetleri elde edilmiştir. SEM görüntülerinde film yüzeyinde farklı boyutlarda kümelenmelerin olduğu görülmüş ve histogram grafiği incelenerek bu kümelenmelerin homojen şekilde dağıldığı belirlenmiştir. AFM görüntülerinden ortalama yüzey pürüzlülüğünün 4,94 nm olduğu görülmüştür. AFM görüntülerinden elde edilen histogram grafikleri incelendiğinde de pürüzlülüğe sebep olan yapılanmaların yüzeyde homojen dağıldıkları tespit edilmiştir. Üretilen filmlerin 20˚- 60˚ 2θ aralığında XRD ölçümleri alınmış, filmlerin tetragonal $Cu(In_{0.5}Ga_{0.5})Se_2$ yapısında ve (112), (204/220) ve (312/116) yönelimlerine sahip olduğu belirlenmiştir. Doku analizleri sonucunda elde edilen kutup figürleri çıkarılmış ve deneysel kutup figürleri ile tekrar hesaplanan teorik kutup figürleri karşılaştırılmıştır. Çalışmanın sonucunda deneysel kutup figürleri ile tekrar hesaplanan teorik kutup figürleri arasındaki benzerlik oranlarının, XRD ölçümlerindeki pik şiddetleri ile orantılı olarak değiştiği tespit edilmiştir. Üretilen CIGS filmine ait kristal yönelimlerinin şiddeti ve film düzlemi boyunca dağılımlarının homojenliği kutup figürlerinin analizi ile çalışılmıştır. Literatürde yüksek verimler elde edilmiş çalışmalardaki kristal yapılar ile kıyaslanarak verimli güneş gözelerini üretmede kullanılabilirliği tespit edilmeye çalışılmıştır. Filmlerin Hall etkisi ölçümleri oda sıcaklığında, 1,1 Tesla manyetik alan altında ve 3 µA akım seviyesinde alınmıştır. Üretilen CIGS ince filmin p tipinde olduğu görülmüş ve sırasıyla öz direnci ve taşıyıcı yoğunluğunun $3{,}33\times10^{2}\,\Omega.cm$ ve $1{,}36\times10^{11}\ cm^{-3}$ olduğu hesaplanmıştır.

Anahtar Kelimeler: *CIGS, İnce Film, Kutup Figürleri, Doku Analizi, Hall Etkisi, Histogram, Gaussian*

Investigation of Structural Properties and Determination of Pole Figures of CIGS Thin Films Produced by Co-Evaporation Method

ABSTRACT

In this study, CIGS thin films, which consist of quaternary element composition and are frequently used in electro-optical applications, were produced by the thermal co-evaporation method, and their structural and electrical properties were investigated. Surface and thickness analyze were performed with SEM and AFM systems, and

Geliş: 26/05/2022, Düzeltme: 05/06/2022, Kabul: 04/12/2022

detailed structure and texture analyzes were performed with the XRD system. By examining SEM and AFM images, histogram curves and their associated Gaussian fits were obtained. In SEM images, it was observed that there were clusters of different sizes on the film surface, and by examining the histogram graph, it was determined that these clusters were homogeneously distributed. The average surface roughness was 4.94 nm from the AFM images. When the histogram graphics obtained from AFM images were examined, it was determined that the structures causing the roughness were homogeneously distributed on the surface. XRD measurements of the produced films were taken in the 20˚-60˚ 2θ range, and it was determined that the films had tetragonal $Cu(In_{0.5}Ga_{0.5})Se_2$ structure and (112), (204/220) and (312/116) orientations. The pole figures obtained as a result of the texture analysis were gained and the experimental pole figures were compared with the recalculated theoretical pole figures. As a result of the study, it was determined that the similarity ratios between the experimental pole figures and the recalculated theoretical pole figures changed in proportion to the peak intensities in the XRD measurements. "The intensity of the crystal orientations of the produced CIGS film and the homogeneity of their distribution along the film plane were studied by the analysis of the polar figures. It has been tried to determine its usability in producing efficient solar cells by comparing it with the crystal structures in the studies in which high yields have been obtained in the literature. Hall effect measurements were taken at room temperature, under a magnetic field of 1.1 Tesla, and at a current level of 3 μA. It was determined that the produced CIGS thin film was of p-type and the resistivity and carrier density were calculated as 3.33×102 Ω.cm and 1.36×1011 cm-3, respectively.

Keywords: *CIGS, Thin Film, Pole Figures, Hall Effect, Histogram, Gaussian*

I. GİRİŞ

$Cu(In_xGa_{1-x})Se_2$ (CIGS) dörtlü p-tipi yarıiletken bir malzemedir. Optoelektronik aygıt üretimde, özellikle güneş hücresi çalışmalarında çokça kullanılan, araştırılan ve gelişmeye açık malzemelerdendir [1], [2]. Yapısındaki Ga/(Ga+In) oranı değiştirilerek yasak bant aralığı 1,02-1,68 eV aralığında ayarlanabilmektedir [3], [4]. CIGS birleşik yapısına tellür (Te), sülfür (S) eklenerek CIGSeS veya CIGSTe beşli bileşikleri de elde edilebilmekte ayrıca Ga ve In yerine çinko (Zn) ve tellür (Te) katkılanarak CZTS gibi farklı yarı iletken malzemeler üretilebilmektedir [5]–[8]. CIGS ince filmler, güneş hücresi çalışmalarında üretim kolaylığı ve etkin maliyetleri ile sıklıkla kullanılan n-CdS ve ITO gibi malzemeler ile elektron ilgileri uyuşmaktadır. Tüm bu öne çıkan özellikleri nedeniyle CIGS malzemesi heteroeklem yapılarda sıkça tercih edilmektedir [2], [9]. CIGS filmler; sprey proliz, kimyasal sprey proliz, elektro kaplama, saçtırma ve termal buharlaştırma gibi farklı ince film biriktirme yöntemleri ile cam, silikon, esnek polimer gibi alttaşlar üzerine kaplanabilmektedir[10]–[15] CIGS yarıiletken malzemesi kullanılarak üretilen güneş hücreleri, %23,35 ile en yüksek verime sahip polikristal güneş hücrelerindendir [16]. Özellikle son yıllarda güneş hücresi teknolojisinde popüler araştırma konularından olan çok eklemli hücre (tandem cell) çalışmalarında da sıkça kullanılmaktadır [17]–[21]. Güneş hücresi çalışmaları dışında CIGS yarıiletkeninin literatürde foto sensör, foto detektör ve Schottky diyot gibi uygulamaları da bulunmaktadır [22]–[25].

CIGS ince filmlerin yapısal ve yüzey özelliklerinin ~~incelenmesi~~ iyileştirilmesi filmin kalitesi ve dolayısıyla aygıt uygulamaları üzerinde büyük önem taşımaktadır. Filmin kristal yöneliminin değişiminin takip edilerek istenilen yönelimlerde ve kalitede filmlerin üretilmesi mümkündür [26], [27]. Yapısındaki elementlerin oranına bağlı olarak CIGS ince filmler farklı kristal yönelimlere sahip olmakta veya yönelim tercihleri birbirlerine göre görece artıp azalmaktadır [14]. CIGS ince filmler üzerine kaplandığı alt katman malzemeye (altlık -alttaş- substrat) bağlı olarak da farklı kristal yönelimleri tercih edebilmektedir [28]. Ayrıca üretim parametrelerine bağlı olarak CIGS ince filmlerin yüzeyinde farklı boyutlarda (0,3-2μm) ve yönelimlerde kümelenmeler meydana gelmektedir [29], [30]. İnce filmlerin kristal yapıları ve yapı oluşurken malzemenin tercih ettiği kristal yönelimleri, filmlerin yüzey enerjisi üzerine etki etmektedir. Yüzey enerjisine bağlı olarak katmanlar arası temas dirençleri değişmektedir [31], [32]. Üretilen malzemelerin kristallenme özellikleri incelenerek doku analizleri yapılabilir ve ilgili kutup figürleri belirlenebilir. Kutup figürleri kristal yapı içerisindeki yönelimlerin hangi pozisyonlarda olduğunu göstermektedir. İnce filmlerin yüzey, topoğrafya ve doku analizlerinin beraber değerlendirilmesi sonucu yapının tercih ettiği yönelimler detaylı bir şekilde tespit edilebilmektedir.

Bu çalışmada, aynı anda termal buharlaştırma yöntemi ile üretilen CIGS ince filmlerin taramalı elektron mikroskobu (SEM) ile yüzey, atomik kuvvet mikroskobu (AFM) ile topoğrafya analizleri yapılmıştır. Elde edilen SEM görüntülerinin histogram grafikleri ile bu grafiklerin Gaussian Teğetleri uydurulmuş ve yüzey homojenliği görüntü analizleri ile belirlenmeye çalışmıştır. Aynı şekilde 2 boyutlu AFM görüntüsünün de histogram grafiği ve Gaussian teğeti elde edilmiş, böylece pürüzlülüğün yüzeyde ne kadar homojen dağıldığı tespit edilmeye çalışmıştır. Filmlerin X-ışını kırınımı (XRD) sistemi ile 20˚ - 60˚ 2θ aralığında yapısal analizi yapılmıştır. Bu aralıkta görülen pik yönelimleri için doku analizleri (Texture) gerçekleştirilerek kutup figürleri (Pole Figure) elde edilmiştir. Elektriksel karakterizasyon sistemi ile 1,1 Tesla (T) manyetik alan altında Hall etkisi ölçümleri yapılmıştır. SEM, AFM, XRD ve elektriksel karakterizasyon sonuçları beraber değerlendirilmiş ve literatürde var olan çalışmalar incelenerek üretilen CIGS ince filmlerin tercih ettiği yönelimler ile karşılaştırılmıştır. Sonuç olarak yüksek verimli güneş hücreleri için uygun yönelime sahip CIGS malzemelerinin üretim parametreleri belirlenmeye çalışılmıştır.

II. DENEYSEL PROSEDÜR

CIGS ince filmler VAKSİS Midas 4T1M sisteminde aynı anda termal buharlaştırma yöntemiyle üretilmiştir. Üretim öncesi vakum seviyesi $8{,}5\times10^{-6}$ Pa seviyesine kadar düşürülmüştür. Kaynak element pelletler efüzyon fırınları içerisine sırasıyla Cu (%99,999 Kurt J. Lesker Company, ABD), In (%99,99 Kurt J. Lesker Company, ABD), Ga (%99,9999 Alfa Aesar,) ve Se (%99,999 Kurt J. Lesker Company, ABD), yerleştirilmiştir. Efüzyon fırınları ısıtıldığında ise vakum seviyesinin $5{,}0\times10^{-3}$ Pa' a kadar yükseldiği görülmüştür. Üretim kazanı içerisindeki vakum seviyesi 3×10^{-3} Pa seviyesine geldiğinde efüzyon fırınlarının üzerindeki kapaklar aynı anda açılmış ve cam alttaşlar üzerine üretim işlemi başlamıştır. Selenizasyon işlemine kadar alttaş sıcaklığı 250 °C' de sabit tutulmuştur. Selenizasyon işlemine başlandığında Cu, In, Ga elementlerinin bulunduğu efüzyon fırınlarının kapakları kapatılarak Se gönderilmeye devam edilmiş ve bu işlem süresince alttaş sıcaklığı 400 °C' ye yükseltilmiştir. Üretim boyunca gönderilen malzemelerin buharlaşma miktarları Cu, In, Ga ve Se için sırasıyla 0,9 Å/s, 1,1 Å/s, 1,2 Å/s ve 8,5 Å/s olarak kaydedilmiştir. Üretim işlemi; 50 dakika "eş buharlaştırma" ve takiben 50 dakika selenizasyon ile toplamda 100 dakika sürede tamamlanmıştır. Üretim sonrası filmler oda sıcaklığına gelene kadar sistem içerisinde bekletilmiştir. CIGS ince filmlerin üretim işleminin ardından, AFM, SEM ve XRD ölçümleri gerçekleşmiştir. XRD sisteminde CIGS ince filmlerin doku analizi yapılmış ve doku analizi sonucu kutup figürleri elde edilmiştir. Elde edilen kutup figürü sonuçları ile teorik hesaplamalar sonucu olması gereken kutup figürleri karşılaştırılmıştır. Kutup figürleri elde edilirken kullanılan ince film doku analizi yönteminde numune ölçüm boyunca kendi çevresinde (ϕ=360˚) etrafında ve χ kadar yatay eksen etrafında döndürülür**.** Örnek ölçüm şeması Şekil 1' de gösterilmiştir.

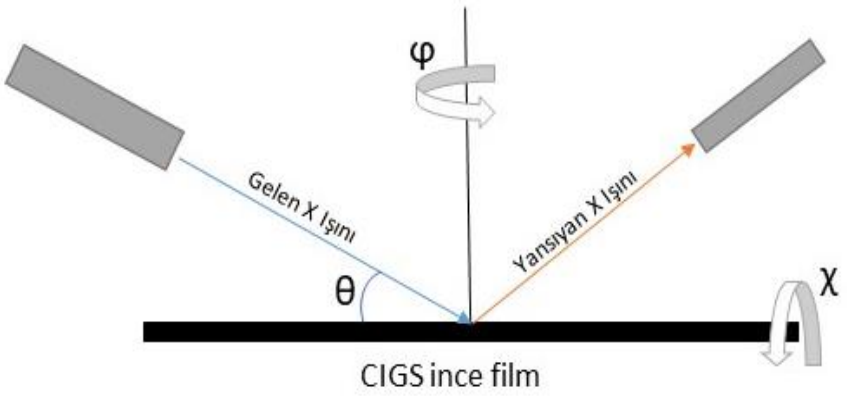

Şekil 1. *XRD sisteminde yapılan doku analizinde (texture) kullanılan ölçüm düzeneğinin şematik gösterimi*

Yüzey ve yapı analizleri yapılan CIGS ince filmin elektriksel özelliklerini belirlemek için Hall Etkisi ölçümleri de alınmıştır. Böylece üretilen filmlerin yüzey, yapı ve elektriksel özellikleri daha önce yapılmış ve yüksek verim elde edilmiş çalışmalar ile kıyaslanmış ve bu çalışmada detayları verilen üretim parametrelerinin, yüksek verimli güneş hücrelerinde olası kullanımı için uygunluğu belirlenmeye çalışılmıştır.

III. BULGULAR ve TARTIŞMA

CIGS ince filmlerin SEM sistemi ile yüzey ve kesit görüntüleri şekil 2 (a) ve (b)' de sırasıyla gösterilmiştir. Yüzey SEM görüntüleri incelendiğinde, film yüzeyinde kümelenmelerin olduğu görülmektedir. Bu kümelenmelerin boyutları yaklaşık olarak 67 nm ile 375 nm aralığında değişmektedir. SEM yüzey görüntülerinde tespit edilen kümelenmelerin 50 nm ve üzeri olduğu takdirde CIGS filmlerin kristallenmelerinin yüksek olacağı ve aygır uygulamaları için iyi bir örnek olarak kabul edilebileceği bilinmektedir [11], [33].

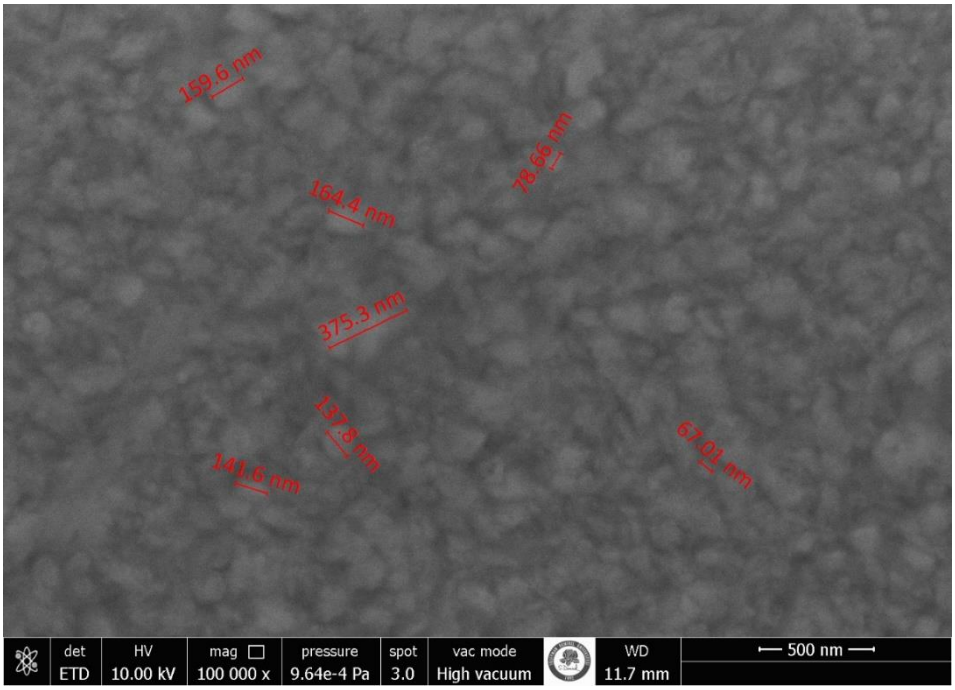

(a)

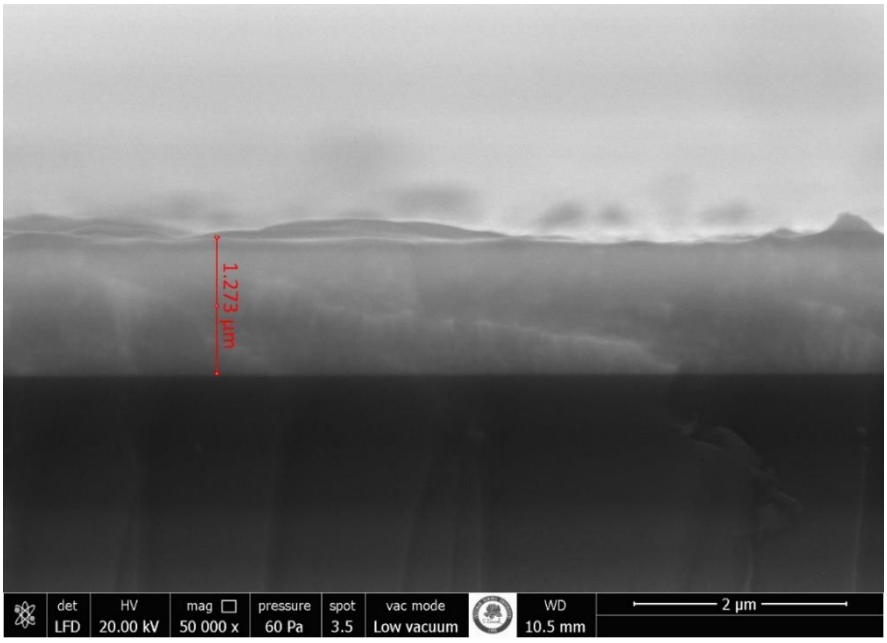

(b)

Şekil 2. a) *CIGS ince filmlerin SEM sisteminde alınmış yüzey görüntüsü,* ***b)*** *Kesit görüntüsü*

Ayrıca kümelenmelerin yüzey üzerine ne kadar iyi dağıldığının bir niceliği olarak yüzey görüntüsünün görüntü işleme metoduyla gir skala da histogram eğrisi çıkarılmıştır. Histogram eğrisine Gaussian teğeti uydurulmuş ve yüzey homojenliği değerlendirilmiştir. Elde edilen histogram eğrisi ve Gaussian Teğeti, Şekil 3' de gösterilmiştir.

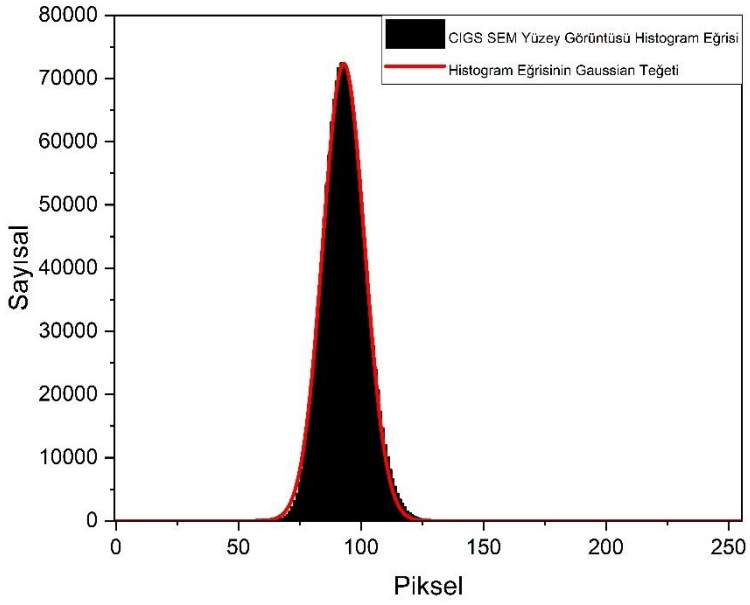

Şekil 3. *CIGS ince filmlerin SEM yüzey görüntüsünün gri skala histogram eğrisi ve Gaussian teğeti*

Histogram grafiğinin, Gaussian teğeti ile benzerlik oranı r^2=0,998 olarak bulunmuştur. Böylece SEM yüzey görüntülerinde görülen kümelenmelerin boyutları farklı olsa da kabul edilebilir seviyede yüzeyde homojen şekilde dağıldığı söylenebilir. Şekil 2 (b)' de verilen SEM kesit görüntülerinde ise film kalınlığının yaklaşık 1,273 µm olduğu görülmektedir. Ayrıca SEM kesit görüntüsünden filmin farklı kalınlıklarında kontrast farkının oluştuğu açıkça görülmektedir. Bu kontrast farklılığının film büyürken yüzeye doğru oluşan sütunlu yapılardan kaynaklandığı düşünülmektedir.

Filmlerin AFM görüntüleri 5 µm × 5 µm' lik alandan 3µm/s tarama hızı ile alınmıştır. 2 ve 3 boyutlu AFM görüntüleri sırasıyla, şekil 4 (a) ve 4(b)' de verilmiştir.

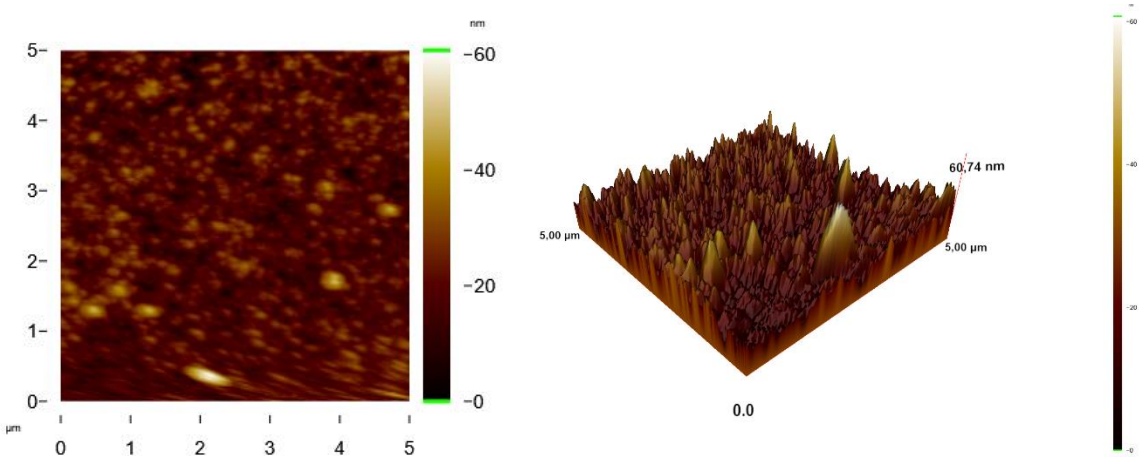

Şekil 4. a) *CIGS ince filmlerin 2 boyutlu AFM görüntüsü,* ***b)*** *3boyutlu AFM görüntüsü*

Şekil 4 (a)' da gösterilen 2 boyutlu AFM görüntüsünün analiz sistemine ait "Image Analyzer" programı kullanılarak tepe ve çukur noktaları için 0 ile 60 nm aralığında pürüzlülük histogram grafiği çıkarılmış ve Gaussian teğeti gösterilerek Şekil 5' de verilmiştir. Pürüzlülük için histogram grafiğinin, Gaussian teğeti ile benzerlik oranı r^2=0,999 olarak bulunmuştur. Böylece 2 ve 3 boyutlu AFM görüntülerinde görülen tepe ve çukur noktaların yüzeyde ne kadar homojen dağıldığı hakkında grafiksel bir değer elde edilmeye çalışılmıştır. AFM analizlerinde CIGS ince filmlerin ortalama yüzey pürüzlülüğünün (R_{ort}) 4,97 nm olduğu tespit edilmiştir. Elde edilen SEM ve AFM görüntüleri ile histogram eğrileri ve Gaussian teğetleri birlikte değerlendirilirse film yüzeylerinin homojen oldukları söylenebilir.

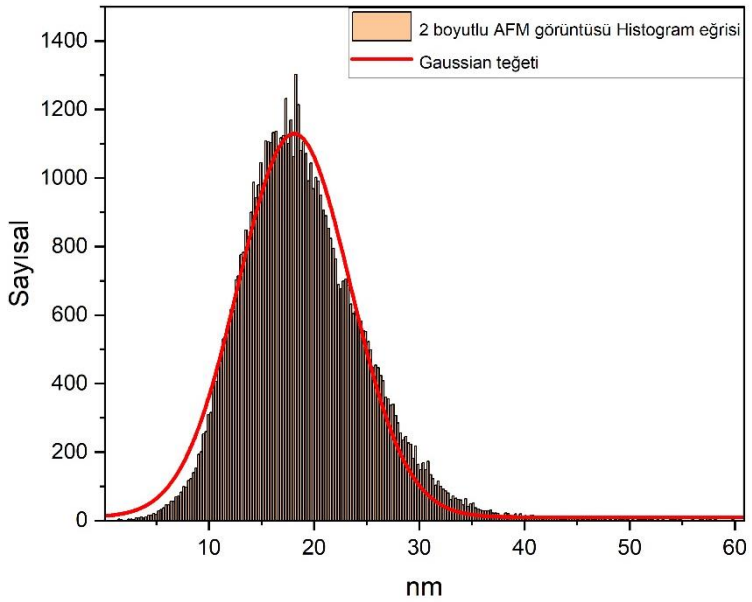

Şekil 5. *CIGS ince filmlerin 2 boyutlu AFM görüntüsünden elde edilen pürüzlülük değerleri için histogram eğrisi ve uydurulan Gaussian teğeti*

Bu çalışmada üretilen CIGS ince filmlerin XRD deseni Şekil 6' da gösterilmektedir. Elde edilen XRD deseni, CIGS ince filmler için standart PDF 00-040-1488 veri kartıyla eşleşmiş ve böylece üretilen filmlerin tetragonal $Cu(In_{0.5}Ga_{0.5})Se_2$ yapısında olduğu belirlenmiştir. XRD deseni incelendiğinde CIGS malzemesine ait 3 farklı pikin yapıda varlığı görülmektedir. Bu piklerin açıları, açılara ait olan yönelimler ve her bir pik için elde edilmiş olan kristal boyutları tablo 1' de gösterilmektedir. Buna göre 27,2°' de görülen pik (112) kristal yönelimi, 45,1°' de görülen pik (204)/(220) yönelimlerini ve 53,4°'

de görülen pik (312)/(116) yönelimlerine karşılık gelmektedir. Ayrıca bu açılarda elde edilen her bir pik için Debye-Scherrer metodu kullanılarak kristal boyutları hesaplanmış ve sırasıyla 19,9, 11,2 ve 10,1 nm olarak elde edilmiştir.

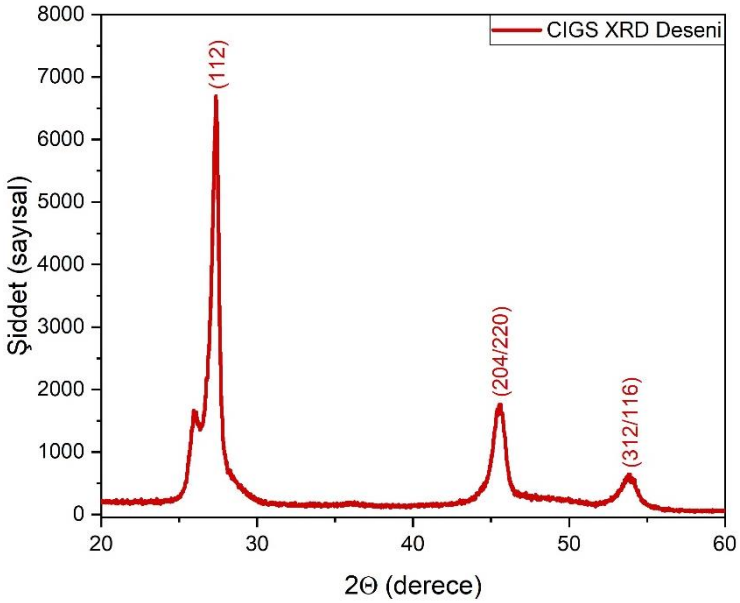

Şekil 6. *CIGS ince filmlerin XRD deseni*

Tablo 1. *XRD piklerinin açısı, açılara ait yönelimler ve kristal boyutları*

Açı (2θ°)	Yönelim (h,k,l)	Kristal Boyutu (nm)
27,2	(112)	19,9
45,1	(204) / (220)	11,2
53,4	(312) / (116)	10,1

Üretilen CIGS filmlerin XRD analizi sonucu elde edilen her bir yönelimi için doku analizleri gerçekleştirilmiş ve kutup figürleri elde edilmiştir. Şekil 7(a), (b) ve (c)' de, üretilen CIGS ince filmlerinin (112) yönelimi için deneysel, tekrar hesaplanmış doku analizleri ve deneysel ile tekrar hesaplanan analizlerin farkı sırasıyla verilmektedir. (204/220) ve (312/116) yönelimleri için yapılan doku analizleri ve elde edilen kutup figürleri sırasıyla Şekil 8 ve Şekil 9' da gösterilmektedir.

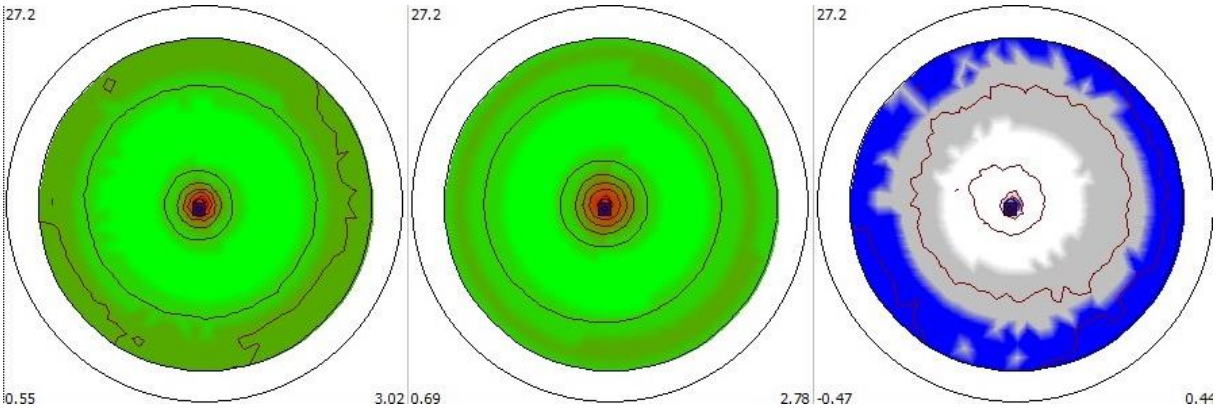

Şekil 7. *(112) yönelimi için* ***a)*** *Deneysel kutup figürleri,* ***b)*** *Tekrar hesaplanan kutup figürleri,* ***c)*** *Deneysel ve tekrar hesaplanan kutup figürü sonuçlarının farkı*

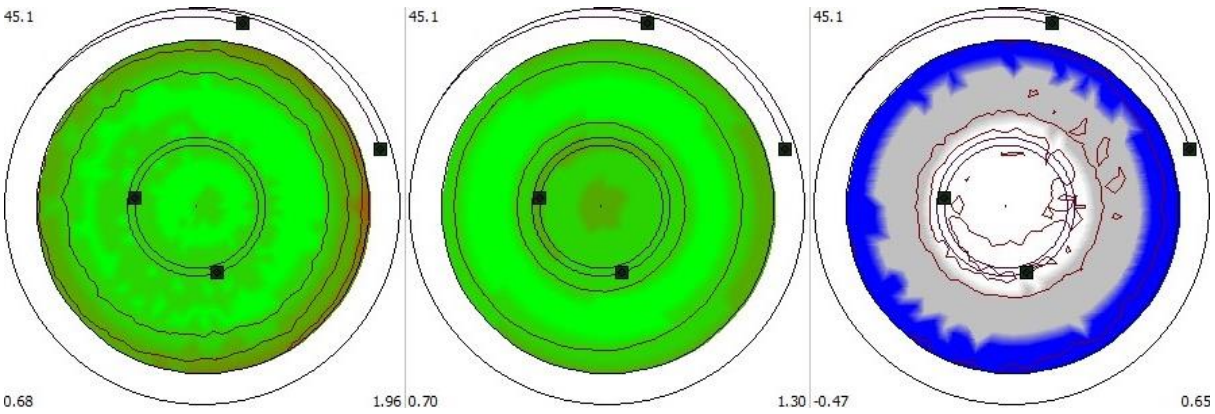

Şekil 8. *(204/220) yönelimi için* ***a)*** *Deneysel kutup figürleri,* ***b)*** *Tekrar hesaplanan kutup figürleri,* ***c)*** *Deneysel ve tekrar hesaplanan kutup figürü sonuçlarının farkı*

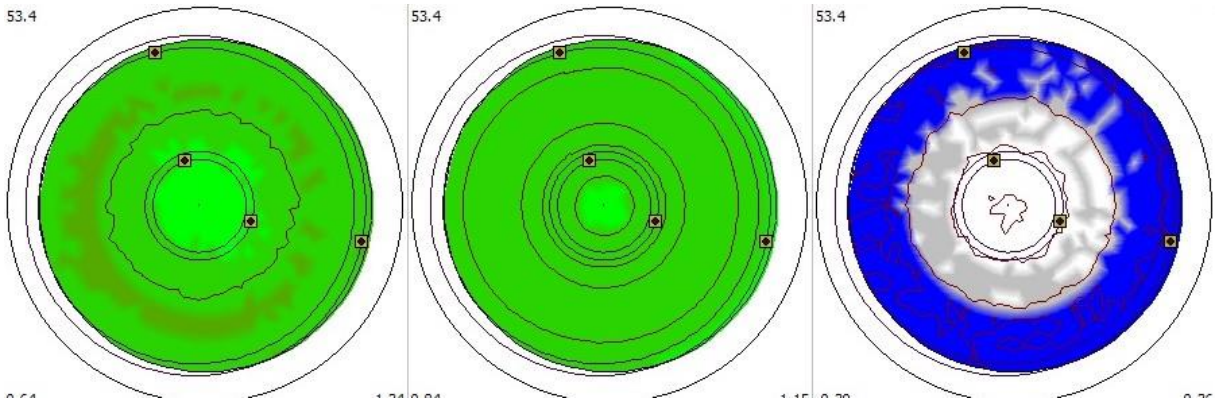

Şekil 9. *(312/116) yönelimi için* ***a)*** *Deneysel kutup figürleri,* ***b)*** *Tekrar hesaplanan kutup figürleri,* ***c)*** *Deneysel ve tekrar hesaplanan kutup figürü sonuçlarının farkı*

Yapılan analizlerden görüldüğü üzere; deneysel olarak elde edilen kutup figürleri ile tekrar hesaplanan kutup figürleri yüksek oranda benzerlik göstermektedir. Özellikle ana pik olan (112) yönelimine ait kutup figürlerinin, diğer piklere göre benzerliğinin daha fazla olduğu açıktır. Kutup figürlerindeki görece benzerliğin artması ile kristal boyutlarının ve pik şiddetlerinin de birbirlerine göre orantılı olarak arttığı tespit edilmiştir. Literatürde (204/220) ve (312/116) farklı yönelimleri için tam oryantasyonun belirlenmesi çalışmaları yapılmış ve bu yönelimlerin herhangi bir kristal düzleminin en düşük polaritesini sergilediği, yani eşit sayıda katyon ve anyona sahip olduğu bildirilmiştir [34]. Bu sebeple bu piklere ait yönelimlerin (hkl) indisleri net olarak verilememektedir.

Tablo 2. *Üretilen CIGS ince filmlerin Hall etkisi ölçümleri*

Sıcaklık (K)	**Manyetik Alan (T)**	**Akım(µA)**	**Öz Direnç (Ω.cm)**	**Hall Gerilimi (V)**	**Taşıyıcı Yoğunluğu (cm^{-3})**	**Tip**
300	1,1	3	$3{,}33\times10^{2}$	$1{,}51\times10^{-2}$	$1{,}36\times10^{11}$	P

Üretilen filmlerin Hall etkisi ve direnç ölçümleri van der Pauw geometrisinde, 1,1 Tesla (T) manyetik alan altında, oda sıcaklığında ve 3 µA akım seviyesinde alınmıştır. Filmlerin Hall etkisi ölçüm sonuçları tablo 2' de gösterilmektedir. Literatürde CIGS ince filmleri için malzemenin yapısı ve elektriksel özellikleri arasındaki bağlantıyı inceleyen pek çok yayın mevcuttur. Bu çalışmalarda üretim parametrelerinin, kullanılan alttaşın, katkılama miktarlarının kristal yönelimleri ve elektriksel özelikleri üzerine etkileri pek çok çalışmada detaylıca incelenmiştir [35]–[40] Üretilen CIGS ince filmlerin elektriksel özelliklerinin literatür ile uyumlu olduğu tespit edilmiştir [41].

IV. SONUÇ

Aynı anda buharlaştırma yöntemi ile üretilen CIGS ince filmlerin SEM sistemi ile yüzey ve kalınlık analizleri yapılmıştır. Yüzey SEM görüntüsünde farklı boyutlarda homojen dağılmış kümelenmelerin olduğu ve yüksek kristalizasyon sayesinde bu kümelenmelerinin 67- 375 nm aralığındaki boyutlara ulaştığı görülmüştür. Ayrıca film yüzeyine ait SEM görüntülerinin, görüntü işleme ile analizlerinden elde edilen histogram eğrisi incelendiğinde, görüntünün homojen bir dağılıma sahip olduğu tespit edilmiştir. Bu sebeple yüzeydeki kümelenmelerin de film yüzeyi boyunca homojen şekilde dağıldığı sonucu çıkarılmıştır. AFM görüntüleri incelendiği takdirde, ortalama yüzey pürüzlülük değeri 4,97 nm olarak tespit edilmiştir. Benzer şekilde 2 boyutlu AFM görüntüsünün histogram eğrisi incelenirse, ortalama pürüzlülük değerinin yine bütün yüzey boyunca homojen şekilde dağıldığı görülmektedir. XRD analizleri, üretilen filmlerin CIGS'e ait 3 farklı kristal yönelimine sahip olduğunu göstermektedir. Bu yönelimlere ait doku analizleri yapılarak elde edilen kutup figürleri incelendiğinde deneysel sonuçlar ile yeniden hesaplanan teorik sonuçların birbirlerine yakın oldukları görülmüştür. Üretilen CIGS ince filminin kristal yapısındaki bu yönelimlere ait kutup figürlerinin analizi; kristalleşme mertebesini gösteren pik şiddetinin yanında, kristal düzlemlerinin film düzlemine göre ne kadar homojen dağıldığının da bir göstergesidir. Filmlerin elektriksel analizleri değerlendirildiğinde özdirenç ve taşıyıcı yoğunluğu değerlerinin daha önce yapılmış literatür çalışmaları ile mertebe olarak uyumlu olduğu tespit edilmiştir. Bu çalışmada üretim parametreleri verilen CIGS ince filmlerin detaylı yapısal analiz ve elektriksel karakterizasyon sonuçları beraber değerlendirildiğinde ve literatürde var olan çalışmalar ile karşılaştırıldığında, yüksek verime sahip CIGS güneş hücrelerinde kullanımı için uygun olduğu söylenebilir.

TEŞEKKÜR**:** Makalenin yazarlarından Celal Alp YAVRU' ya 100/2000 Doktora Programı kapsamında destek veren Yükseköğretim Kurulu (YÖK)' na ve 4905-YL1-17 numaralı proje desteği için SDÜ BAP'a teşekkür ederiz.

V. KAYNAKLAR

[1] S. H. Kang, Y. K. Kim, D. S. Choi, and Y. E. Sung, "Characterization of electrodeposited CuInSe2 (CIS) film," Electrochimica Acta, vol. 51, no. 21, pp. 4433–4438, 2006.

[2] M. Al-Hattab, L. Moudou, M. Khenfouch, O. Bajjou, Y. Chrafih, and K. Rahmani, "Numerical simulation of a new heterostructure CIGS/GaSe solar cell system using SCAPS-1D software," Solar Energy, vol. 227, Elsevier Ltd, pp. 13–22, 2021.

[3] H. H. Sheu, Y. T. Hsu, S.Y. Jian, and S.C. Liang, "The effect of Cu concentration in the photovoltaic efficiency of CIGS solar cells prepared by co-evaporation technique," Vacuum, vol. 131, pp. 278–284, 2016.

[4] W. Liu, H. Li, B. Qiao, S. Zhao, Z. Xu, and D. Song, "Highly efficient CIGS solar cells based on a new CIGS bandgap gradient design characterized by numerical simulation," Solar Energy, vol. 233, pp. 337–344, 2022.

[5] M. P. Suryawanshi, G. L. Agawane, S. M. Bhosale, S. W. Shin, P. S. Patil, J. H. Kim, and A. V. Moholkar, "CZTS based thin film solar cells: a status review," Materials Technology, vol. 28, no. 1–2, pp. 98–109, 2013.

[6] W. Daranfed, M. S. Aida, N. Attaf, J. Bougdira, and H. Rinnert, "Cu 2ZnSnS 4 thin films deposition by ultrasonic spray pyrolysis," J Alloys Compd, vol. 542, pp. 22–27, 2012.

[7] Y. Atasoy, B. M. Başol, I. Polat, M. Tomakin, M. Parlak, and E. Bacaksiz, “Cu(In,Ga)(Se,Te)2 pentenary thin films formed by reaction of precursor layers,” Thin Solid Films, vol. 592, no. 2, pp. 189–194, 2015.

[8] Y. Atasoy, “Düşük tellür katkılı CuInGaSe2 ince filmlerin yapısal özelliklerinin incelenmesi”, Journal of the Institute of Science and Technology, vol. 9, no. 4, pp. 2088–2096, 2019.

[9] U. Rau, D. Braunger, R. Herberholz, and W. Schock, “Oxygenation and air-annealing effects on the electronic properties of Cu(In,Ga)Se2 films and devices,” J Appl Phys, vol. 86, no. 1, pp. 497–505, 1999.

[10] M. Katerski, A. Mere, V. Kazlauskiene, J. Miskinis, A. Saar, L. Matisen, A. Kikas, M. Krunks, “Surface analysis of spray deposited copper indium disulfide films,” Thin Solid Films, vol. 516, no. 20, pp. 7110–7115, 2008.

[11] D. Lee, S. Park, and J. Kim, “Structural analysis of CIGS fi lm prepared by chemical spray deposition,” Current Applied Physics, vol. 11, no. 1, pp. S88–S92, 2011.

[12] F. Long, W. Wang, J. Du, and Z. Zou, “CIS(CIGS) thin films prepared for solar cells by one-step electrodeposition in alcohol solution,” Journal of Physics: Conference Series, vol. 152, p. 012074, 2009.

[13] I. L. Repins, D. Fisher, W. K. Batchelor, L. Woods, and M. E. Beck, “A non-contact low-cost sensor for improved repeatability in co-evaporated CIGS,” Progress in Photovoltaics: Research and Applications, vol. 13, no. 4, pp. 311–323, 2005.

[14] M. Kaleli and C. Alp Yavru, “Depth profile crystal orientation determination of Cu(In1−xGax)Se2 thin films by GIXRD method applying skin depth theory,” Journal of Materials Science: Materials in Electronics, vol. 30, no. 22, pp. 20154–20159, 2019.

[15] J. Piekoszewski, J. J. Loferski, R. Beaulieu, J. Beall, B. Roessler and J. Shewchun, “RF-Sputtered CulnSe2 thin films”, Solar Energy Materials, vol. 2, no. 3, pp. 363–372, 1980.

[16] M. Nakamura, K. Yamaguchi, Y. Kimoto, Y. Yasaki, T. Kato, and H. Sugimoto, “Cd-Free Cu(In,Ga)(Se,S)2 thin-film solar cell with record efficiency of 23.35%,” IEEE Journal of Photovoltaics, vol. 9, no. 6, pp. 1863–1867, 2019.

[17] A. Guchhait, H. A. Dewi, S. W. Leow, H. Wang, G. Han, F. B. Suhaimi, S. Mhaisalkar, H. L. Wong, and N. Mathews, “Over 20% Efficient CIGS-Perovskite Tandem Solar Cells,” ACS Energy Lett, vol. 2, no. 4, pp. 807–812, 2017.

[18] T. J. Jacobsson, A. Hultqvist, S. Svanstrom, L. Riekehr, U. B. Cappel, E. Unger, H. Rensmo, E. M. J. Johansson, M. Edoff, G. Boschloo, “2-Terminal CIGS-perovskite tandem cells: A layer by layer exploration,” Solar Energy, vol. 207, vol. 207 no. 1, pp. 270–288, 2020.

[19] C. D. Bailie, M. G. Christoforo, J. P. Mailoa, A. R. Bowring, E. L. Unger, W. H. Nguyen, J. Burschka, N. Pellet, J. Z. Lee, M. Gratzel, R. Noufi, T. Buonassisi, A. Salleo, and M. D. McGehee, “Semi-transparent perovskite solar cells for tandems with silicon and CIGS,” Energy Environ Sci, vol. 8, no. 3, pp. 956–963, 2015.

[20] S. U. Nanayakkara, K. Horowitz, A. Kanevce, M. Woodhouse, and P. Basore, “Evaluating the economic viability of CdTe / CIS and CIGS / CIS tandem photovoltaic modules,” Progress in Photovoltaics, vol. 25, no.4, 2017.

[21] S. Gharibzadeh, I. M. Hossain, P. Fassl, B. A. Nejand, T. Abzieher, M. Schultes, E. Ahlswede, P. Jackson, M. Powalla, S. Schafer, M. Rienacker, T. Wietler, R. Peibst, U. Lemmer, B. S. Richards, U. W. Paetzold, “2D/3D Heterostructure for Semitransparent Perovskite Solar Cells with Engineered Bandgap Enables Efficiencies Exceeding 25% in Four-Terminal Tandems with Silicon and CIGS,” Adv Funct Mater, vol. 30, no. 19, 2020.

[22] D. A. Aldemir, M. Kaleli, and A. C. Yavru, “Electrical and photoelectric properties of Yb/CIGS thin film Schottky photodiode,” Sens Actuators A Phys, vol. 311, pp. 112091, 2020.

[23] C. A. Yavru, M. Kaleli, İ. S. Üncü, M. Koç, and D. A. Aldemir, “Solar and infrared light sensing comparison of Yb/CIGS photodiode,” Sens Actuators A Phys, pp. 113973, 2022.

[24] B. Theys, T. Klinkert, F. Mollica, E. Leite, F. Donsanti, M. Jubault, D. Lincot, “Revisiting Schottky barriers for CIGS solar cells: Electrical characterization of the Al/Cu(InGa)Se2 contact,” Physica Status Solidi (A) Applications and Materials Science, vol. 213, no. 9, pp. 2425–2430, 2016.

[25] S. Fiat, I. Polat, E. Bacaksiz, M. Kompitsas, and G. Çankaya, “The influence of annealing temperature and tellurium (Te) on electrical and dielectrical properties of Al/p-CIGSeTe/Mo Schottky diodes,” Current Applied Physics, vol. 13, no. 6, pp. 1112–1118, 2013.

[26] M. Kaleli, C. A. Yavru, M. Koç, S. Akyürekli, A. B. Bayram, “Termal Buharlaştırma Yöntemiyle Hazırlanan Ga Katkılı CuInSe 2 İnce Filmlerin Yapısal Özelliklerinin İncelenmesi,” Süleyman Demirel Üniversitesi Fen Edebiyat Fakültesi Fen Dergisi, vol. 12, no. 2, pp. 19–32, 2017.

[27] C. A. Yavru, İ. S. Üncü, M. Kaleli, and S. Akyürekli, “CIGS İnce Film Yüzeyindeki Morfolojik Farklılıkların GLCM Görüntü İşleme Yöntemi ile İncelenmesi,” Süleyman Demirel Üniversitesi Fen Edebiyat Fakültesi Fen Dergisi, vol. 17, no. 2, pp. 460–477, 2022.

[28] J. H. Yoon, K. H. Yoon, J. K. Kim, J. K. Park, T. S. Lee, Y. J. Baik, T. Y. Seong, and J. H. Jeong, “Effect of the Mo back contact microstructure on the preferred orientation of CIGS thin films,” in Conference Record of the IEEE Photovoltaic Specialists Conference, pp. 2443–2447, 2010.

[29] S. Rozeveld, C. Reinhardt, E. Bykov, and A. Wall, “ Measurement of Grain Boundary Properties in Cu(ln,Ga)Se 2 Thin Films ,” Micros Today, vol. 26, no. 3, pp. 32–39, 2018.

[30] G. Hanna, T. Glatzel, S. Sadewasser, N. Ott, H. P. Strunk, U. Rau, and J. H. Werner, “Texture and electronic activity of grain boundaries in Cu(In,Ga)Se 2 thin films,” Appl Phys A Mater Sci Process, vol. 82, no. 1, pp. 1–7, 2006.

[31] R. Krishnan, M. Riley, S. Lee, and T. M. Lu, “Formation of biaxially textured molybdenum thin films under the influence of recrystallization conditions,” Thin Solid Films, vol. 519, no. 16, pp. 5429–5432, 2011.

[32] M. L. Lobanov, S. V. Danilov, V. I. Pastukhov, S. A. Averin, Y. Y. Khrunyk, and A. A. Popov, “The crystallographic relationship of molybdenum textures after hot rolling and recrystallization,” Materials and Design, vol. 109, no. July, pp. 251–255, 2016.

[33] A. B. Jain, Y. R. Toda, and D. N. Gujarathi, “Structural and Electrical properties of Thermally Evaporated Nanostructured CuInSe Thin Films,” vol. 9, no. 2, pp. 19–26, 2017.

[34] M. A. Contreras, B. Egaas, K. Raöanathan, J. Hiltner, A. Swartzlander, F. Hasoon, and R. Noufi, “Progress Toward 20% Efficiency in Cu(In,Ga)Se2 Polycrystalline Thin-film Solar Cells,” Progress in Photovoltaics: Research and Applications, vol. 7, no.4, pp. 311–316, 1999.

[35] A. Slobodskyy, T. Slobodskyy, T. Ulyanenkova, S. Doyle, M. Powalla, T. Baumbach, and U. Lemmer, “In-depth analysis of the CuIn1-x Gax Se2 film for solar cells, structural and optical characterization,” Applied Physics Letters, vol. 97, no. 25, Dec. 2010.

[36] Y. M. Xue, B. H. Yang, C. Q. Qu, L. Zhang, C. M. Xu, and Y. Sun, “Structural and electrical properties of co-evaporated In, Ga rich CIGS thin films,” Optoelectronics Letters, vol. 4, no. 6, pp. 0437–0439, Nov. 2008.

[37] R. Caballero, C. A. Kaufmann, T. Eisenbarth, T. Unold, S. Schorr, R. Hesse, R. Klenk, and H. W. Schock “The effect of NaF precursors on low temperature growth of CIGS thin film solar cells on polyimide substrates,” Physica Status Solidi (A) Applications and Materials Science, vol. 206, no. 5, pp. 1049–1053, May 2009.

[38] D.H. Cho, Y.-D. Chung, K.-S. Lee, J.-H. Kim, S.-J. Park, and J. Kim, “Control of Na diffusion from soda-lime glass and NaF film into Cu(In,Ga)Se2 for thin-film solar cells,”, pp. 1–4, 2014.

[39] H. Wang, Z. Yang, X. L. Kou, Y. A. Cai, W. Liu, T. Yu, J. B. Pang, C. J. Li, and Y. Sun “Effect of substrate temperature on the structural and electrical properties of CIGS films based on the one-stage co-evaporation process,” Semiconductor Science and Technology, vol. 25, no. 5, 2010.

[40] D. Abou-Ras, D. Rudmann, G. Kostorz, S. Spiering, M. Powalla, and A. N. Tiwari, “Microstructural and chemical studies of interfaces between Cu(In,Ga) Se 2 and In 2 S 3 layers,” J Appl Phys, vol. 97, no. 8, pp. 084908, 2005.

[41] B. K. H. Al-Maiyaly, I. H. Khudayer, A. H. A. Alrazak, “Effect of Thickness on the Electrical Conductivity and Hall Effect Measurements of (CIGS) Films” Ibn Al- Haitham jour. For pure and Appl. Science, vol.27, no.3, pp. 300-308, 2014.

Düzce University
Journal of Science & Technology

Research Article

The effect of Centrifuged Hot-Dip Galvanisation (CHDG) Process on the Corrosion on Nuts

Hüsnü GERENGİ [a], Muhammed MARAŞLI [b], Mesut YILDIZ [a,*], Kader COŞKUN [b], Yusuf GÜNER [c], Beyza AŞIKOĞLU [b]

[a] *Corrosion Research Laboratory, Department of Mechanical Engineering, Faculty of Engineering, Düzce University, 81620 Düzce, TÜRKİYE*
[b] *Fibrobeton Company R&D Center, Düzce, TÜRKİYE*
[c] *Standard Profile Corporation, Research and Development Center, Düzce, TÜRKİYE*
** Corresponding author's e-mail address: mesutyildiz@duzce.edu.tr*
DOI: 10.29130/dubited.1460076

ABSTRACT

The bolted fasteners, widely used in various industries, are the fundamental structural components most commonly used in the assembly of steel structures. Bolted fasteners offer advantages such as versatility, reliability, minimal maintenance and inspection costs, easy and fast assembly, and good strength under variable loads. However, fastener failures occur due to complex loading conditions, hydrogen embrittlement during fabrication or service, fatigue failures due to alternative stress, and combined effects of corrosion and stress. Therefore, the study of fastener failure is critical for safety in both every day and industrial applications. Zinc plating has long been a preferred method of protecting fasteners from corrosive environments. One of the most commonly used methods for coating fasteners today is the centrifugal hot dip galvanising (CHDG) process. CHDG is suitable for outdoor applications on small metal parts (bolts, nuts, washers) that cannot be hot dip galvanised. Centrifugation removes all excess zinc from the threads of bolts. Oversized nuts fit perfectly on very small parts. In this study, nut samples coated with CHDG were exposed to corrosion in a corrosive environment according to ASTM B117 standards. At the end of thirteen (13) days, the outer surface of the nut attached to the screw was cut and the screw steps were examined using scanning electron microscopy (SEM) and energy dispersive X-ray spectrometry (EDS). The results show that the zinc coating on the surface produced by the CHDG process is effective in protecting the metal nuts against corrosion. The zinc patina begins its development with exposure to oxygen in the atmosphere, forming a layer of zinc oxide on the surface. Moisture from rain or humid air reacts with the zinc oxide to form zinc hydroxide which then reacts with carbon dioxide present in the air to form the tightly adherent, insoluble zinc patina.

Keywords: *Corrosion, Nut, Centrifugal Hot Dip Galvanising*

Santrifüjlü Sıcak Daldırma Galvaniz (SHDG) İşleminin Somunlar Üzerindeki Korozyona Etkisi

ÖZ

Çeşitli endüstrilerde yaygın olarak kullanılan cıvatalı bağlantı elemanları, çelik yapıların montajında en yaygın olarak kullanılan temel yapısal bileşenlerdir. Cıvatalı bağlantı elemanları çok yönlülük, güvenilirlik, minimum bakım ve denetim maliyeti, kolay ve hızlı montaj ve değişken yükler altında iyi mukavemet gibi avantajlar sunmaktadır. Bununla birlikte, bağlantı elemanı arızaları karmaşık yükleme koşulları, imalat veya servis sırasında hidrojen gevrekleşmesi, alternatif stres nedeniyle yorulma arızaları ve korozyon ve stresin birleşik etkileri

Received: 29/03/2024, Revised: 05/04/2024, Accepted: 25/07/2024

nedeniyle meydana gelmektedir. Bu nedenle, bağlantı elemanı arızalarının incelenmesi hem günlük hem de endüstriyel uygulamalarda güvenlik açısından kritik öneme sahiptir. Çinko kaplama, bağlantı elemanlarını korozif ortamlardan korumak için uzun zamandır tercih edilen bir yöntemdir. Günümüzde bağlantı elemanlarının kaplanmasında en yaygın kullanılan yöntemlerden biri santrifüj sıcak daldırma galvanizleme (SHDG) işlemidir. SHDG, sıcak daldırma ile galvanizlenemeyen küçük metal parçalar (cıvatalar, somunlar, pullar) üzerindeki dış mekan uygulamaları için uygundur. Santrifüjleme, cıvataların dişlerindeki tüm fazla çinkoyu giderir. Büyük boyutlu somunlar çok küçük parçalara mükemmel uyum sağlar. Bu çalışmada, SHDG ile kaplanmış somun numuneleri ASTM B117 standartlarına göre korozif bir ortamda korozyona maruz bırakılmıştır. On üç (13) günün sonunda vidaya bağlı somunun dış yüzeyi kesilmiş ve vida basamakları taramalı elektron mikroskobu (SEM) ve enerji dağılımlı X-ışını spektrometresi (EDS) kullanılarak incelenmiştir. Sonuçlar, SHDG işlemiyle üretilen yüzeydeki çinko kaplamanın metal somunları korozyona karşı korumada etkili olduğunu göstermektedir. Çinko patina, atmosferdeki oksijene maruz kaldığında gelişmeye başlar ve yüzeyde bir çinko oksit tabakası oluşturur. Yağmurdan veya nemli havadan gelen nem çinko oksit ile reaksiyona girerek çinko hidroksit oluşturur ve bu da havada bulunan karbondioksit ile reaksiyona girerek sıkıca yapışan, çözünmeyen çinko patinayı oluşturur.

Anahtar Kelimeler: *Korozyon, Somun, Santrifüj Sıcak Daldırma Galvaniz*

I. INTRODUCTION

Corrosion is defined as the deterioration of a material, usually a metal, due to its reaction with the environment [1]. The destructive effects of corrosion have a direct impact on the durability and safety. Corrosion is an extremely important economic problem. Economic losses are directly related to the necessity of replacing damaged structures, machinery, equipment, or their components. These losses result from the use of costly corrosion-resistant materials, expenses associated with corrosion protection, and are also indirectly influenced by production stoppages due to the need to replace parts or repair damage [2], [3].

There are five primary methods of corrosion control that play a vital role in mitigating the detrimental effects of corrosion: material selection, coatings, inhibitors, cathodic protection and design. Material selection involves selecting materials that are inherently resistant to corrosion or that can be treated to increase their resistance. Coatings, such as paints and metallic coatings, create barriers between the metal surface and the corrosive environment, preventing direct contact and corrosion initiation. Inhibitors are chemicals that can be added to the environment or applied directly to the metal surface to inhibit corrosion reactions. Cathodic protection involves the application of an external electrical current or sacrificial anode to shift the corrosion potential of the metal to a more passive state. Finally, design considerations such as proper drainage, ventilation and avoidance of crevices can minimize corrosion by reducing the accumulation of moisture and corrosive agents. Each of these methods is critical to effective corrosion management and will be further explored in subsequent chapters to provide a comprehensive understanding of corrosion control strategies (Figure 1).

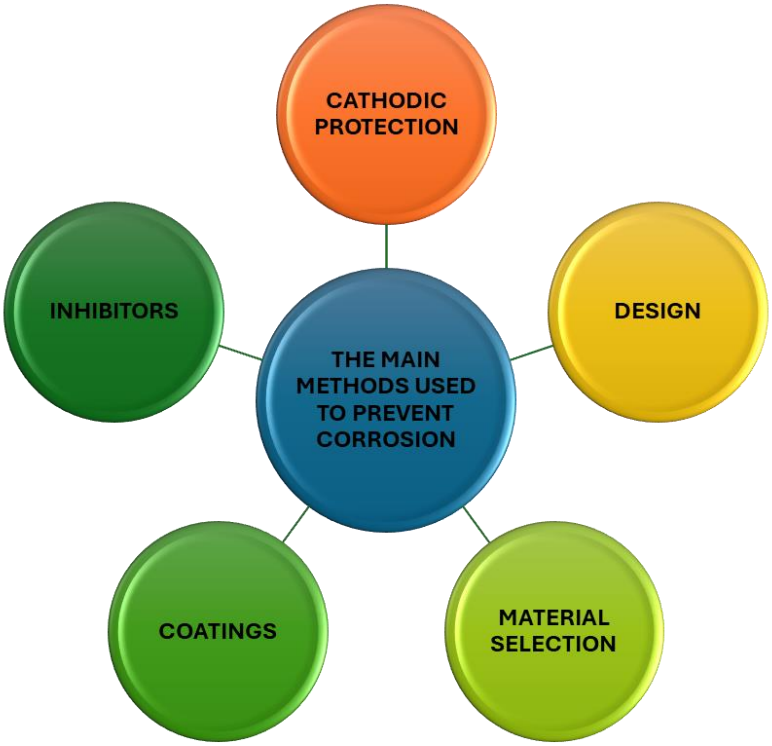

Figure 1. *The main methods used to prevent corrosion*

The world population has been growing at a significant rate in recent decades. Naturally, the consumption of all type of metals increases accordingly. Steel is the most widely used material in the world due to its versatility, low cost and good strength properties [4]. Carbon steel products are widely used in the automotive, infrastructure and construction industries. It is a material that determines the development of industry and society as a whole, and its production is constantly growing [5]. It is therefore important to be able to preserve this metal cheaply and effectively for a long period of time.

Zinc has been widely used in the surface treatment of various steel structures to improve the service life of the structure, due to its good corrosion resistance. Zinc forms galvanized steel after solidification on the surface of the steel [6].

The hot-dip galvanizing process offers a unique combination of superior properties such as high strength, formability, light weight, corrosion resistance, low cost and recyclability. In the hot dip galvanizing process, a steel sample is cleaned, fluxed and then immersed in a molten zinc bath at a temperature of approximately 450 °C [7]. Hot dip galvanized steels have been extensively used in industrial sectors such as automobiles, household appliances or construction due to their excellent corrosion resistance properties [8], [9]. While the hot-dip galvanizing process is successfully applied to large metal parts, the centrifugal hot-dip galvanizing process (CHDG) is applied to small metal parts. Centrifugation is employed to achieve a homogeneous coating by removing excess zinc from the surface. In this process, the steel product is rotated in a crucible to facilitate the removal of excess zinc through centrifugal force. Consequently, a more uniform and thinner zinc coating is achieved, enhancing the quality of the coating and providing more durable protection (Figure 2).

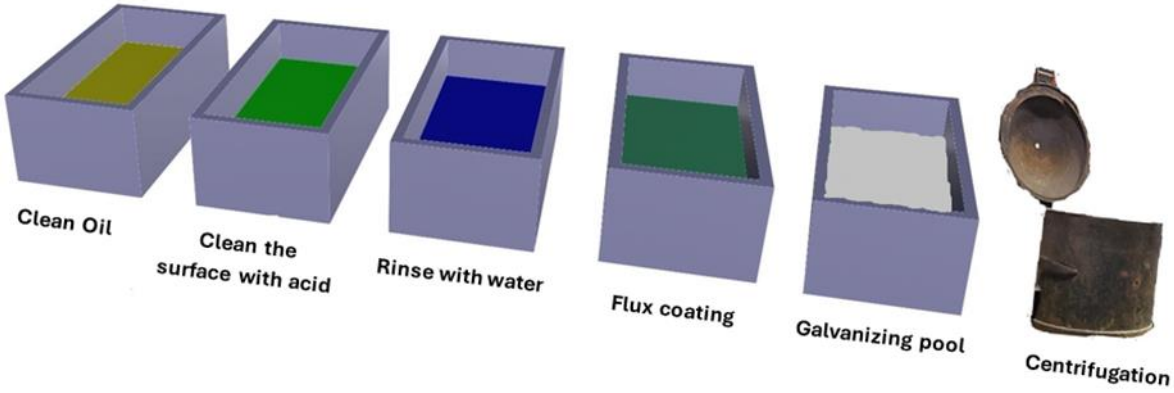

Figure 2. *The CHDG process*

In this study, the morphological changes of the nuts tested according to ASTM B117 standards for 13 days before and after the experiment were compared by SEM and EDS analysis and the results were discussed.

II. MATERIAL AND METHOD

The nuts used in this study are M8 nuts manufactured to ISO 4032 standard. It is used as a fastener in the connection of carcass elements and pad hooks in the construction industry [10]. Fasteners (nuts and bolts) were plated with 114 μm zinc using the CHDG method. The fasteners were well cleaned prior to the corrosion experiments (Figure 3). The galvanised steel bolts and nuts were exposed to the corrosive medium for 1, 5, 9 and 13 days according to ASTM B117 standards [11]. To examine the corrosion occurring in the bolt steps at the end of 13 days, the nut exposed to corrosive environment were mechanically cut. The surface morphologies of the galvanised nuts were observed using a scanning electron microscope (SEM, FEI Quanta FEG 250) and elemental composition analysis was carried out using an energy dispersive X-ray spectrometer (EDS) before and after the experiment. Galvanised nuts were mounted on an aluminium stub using double-sided carbon tape and an accelerating voltage of 20 KeV was applied for the SEM analyses.

III. RESULTS AND DISCUSSION

A. SALT SPRAY TEST RESULTS

A salt spray test (ASTM B117) provided relative corrosion resistance values for CHDG coated nuts in a standardised corrosive environment. The experimental results presented in this study were obtained using 5% NaCl at 35 °C with 50% humidity for 13 days. Figure 3 shows images of bolts and nuts coated by the CHDG process prior to salt spray testing. Before the salt spray test, the surfaces of the bolts and nuts appear to be bright and intact appearance.

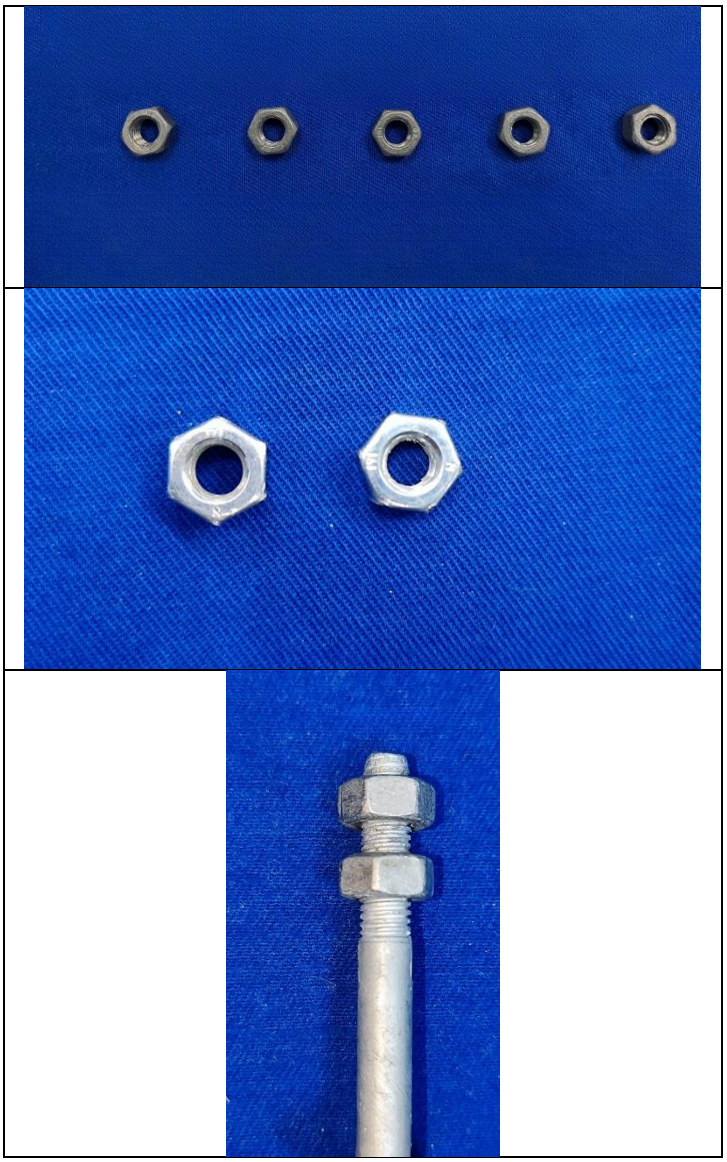

Figure 3. *Visual inspection before the salt spray test*

The specimens placed in the salt cabinet were removed at the end of the 1st, 5th, 9th and 13th days respectively and examined visually (Figure 4). After 1 day of salt spray testing, it was observed that the lustre of the coating had diminished and the zinc coating had begun to corrode, resulting in the appearance of white patches. It can be seen that the degree of corrosion increases with the duration of exposure. At the end of the 13th day, white corrosion products were observed prominently covering the surfaces of both the bolt and nut samples. This observation indicates that the zinc coating applied to these components has undergone uniform corrosion. No brown colour formation was observed on the surface of the bolt and nut at the end of the specified periods. The continued presence of the protective zinc coating, indicated by the absence of brown rust, demonstrates that the underlying matrix material remains protected from corrosive elements and potential degradation. The coating thickness of the nut removed from the test chamber on the 13th day of the salt spray test was 224 μm. The increase in coating thickness may be due to the formation of possible oxide layers such as ZnO, $Zn_5(OH)_8Cl_2 \cdot H_2O$ or $Zn_5(CO_3)_2(OH)_6$ formed on the surface of the nut [12].

After 1 day

After 5 days

After 9 days

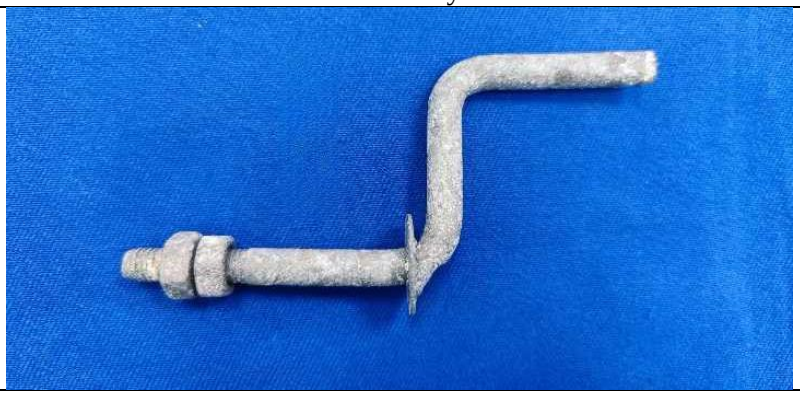

After 13 days

Figure 4. *Visual inspection after the salt spray test*

B. SURFACE MORPHOLOGY ANALYSİS

SEM-EDS analysis was performed to investigate the surface morphologies of galvanized nuts cut in half before corrosion and exposed to a corrosive environment for 13 days. Figure 5 shows SEM images taken from the thread area of galvanized nuts before exposure to corrosion.

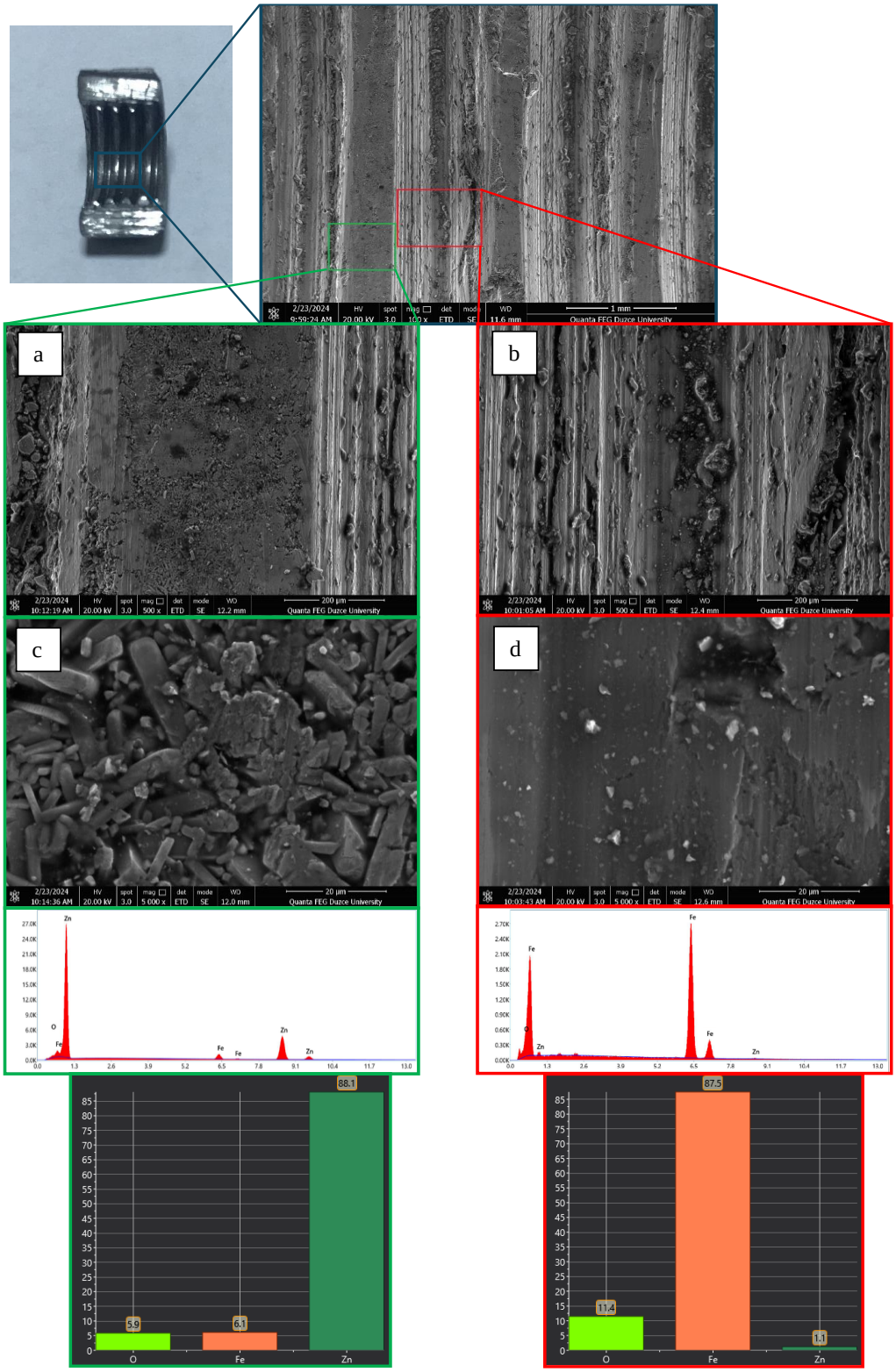

Figure 5. *SEM images of galvanized nuts before corrosion (a and c: 500x and 5000x of top regions; b and d: 500x and 5000x of hollow regions)*

In Figure 5, the red area shows the hollow area and the green area shows the top area in the galvanized nut sample. It can be seen that the surface is rough as a result of coating the nut with Zn. As a result of EDS analysis, Zn, Fe and O were detected on the surface of the nut. Zn, used as the main coating element, functions in two capacities, both as a barrier against corrosion and as a matrix element protector [13]. As a result of EDS taken from the tops in the thread area, 88% Zn was detected, while 1% Zn (87.5% Fe) was detected in the hollow areas. This indicates that the top areas are better covered with Zn, while the hollow areas are less covered. Similarly, in the EDS element mapping results, it can be seen in Figure 6 that the Zn element is concentrated in the top regions and Fe is dominant in the hollow regions.

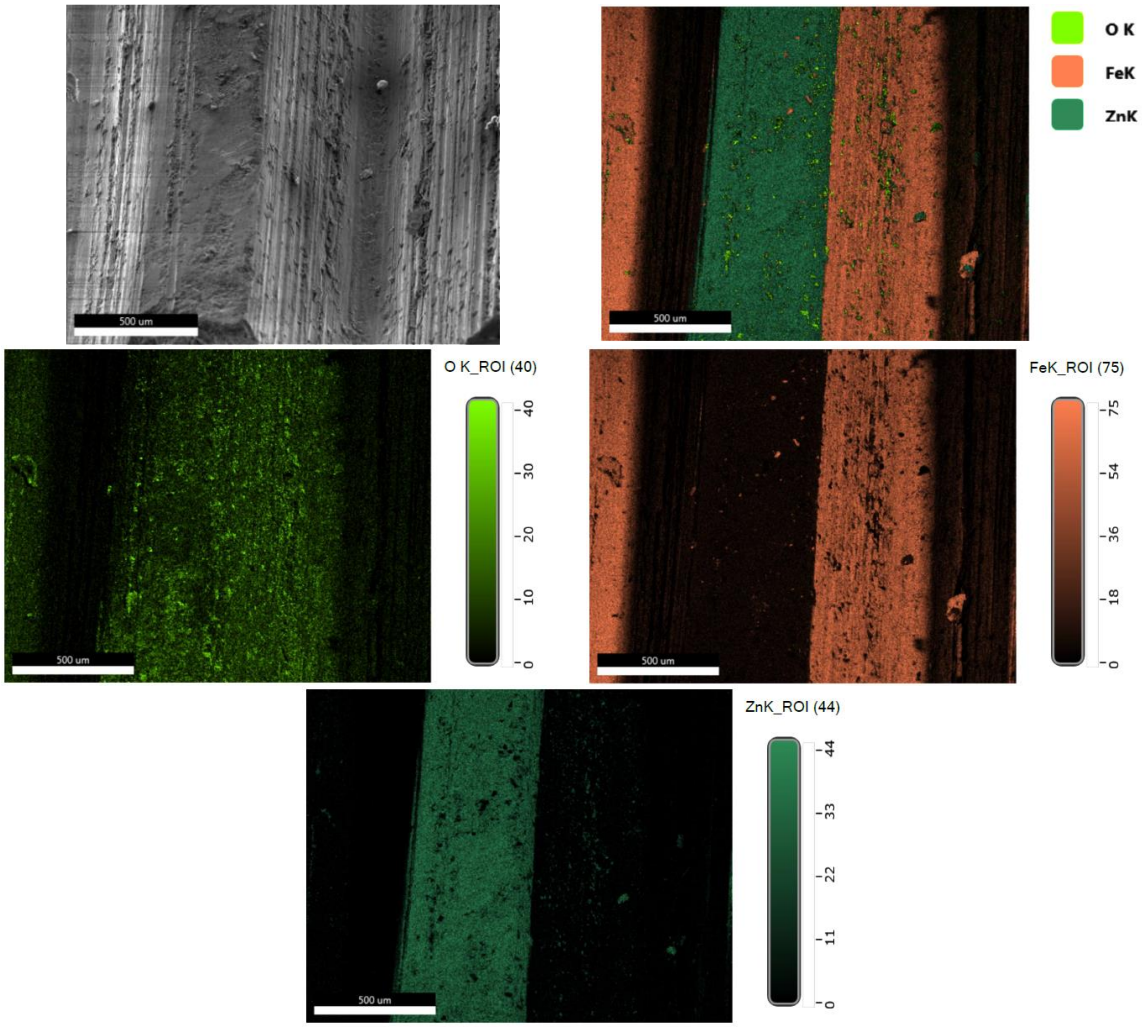

Figure 6. *EDS element mapping images of galvanized nuts before corrosion*

Figure 7 shows SEM images and EDS results of galvanized nuts exposed to a corrosive environment for 13 days.

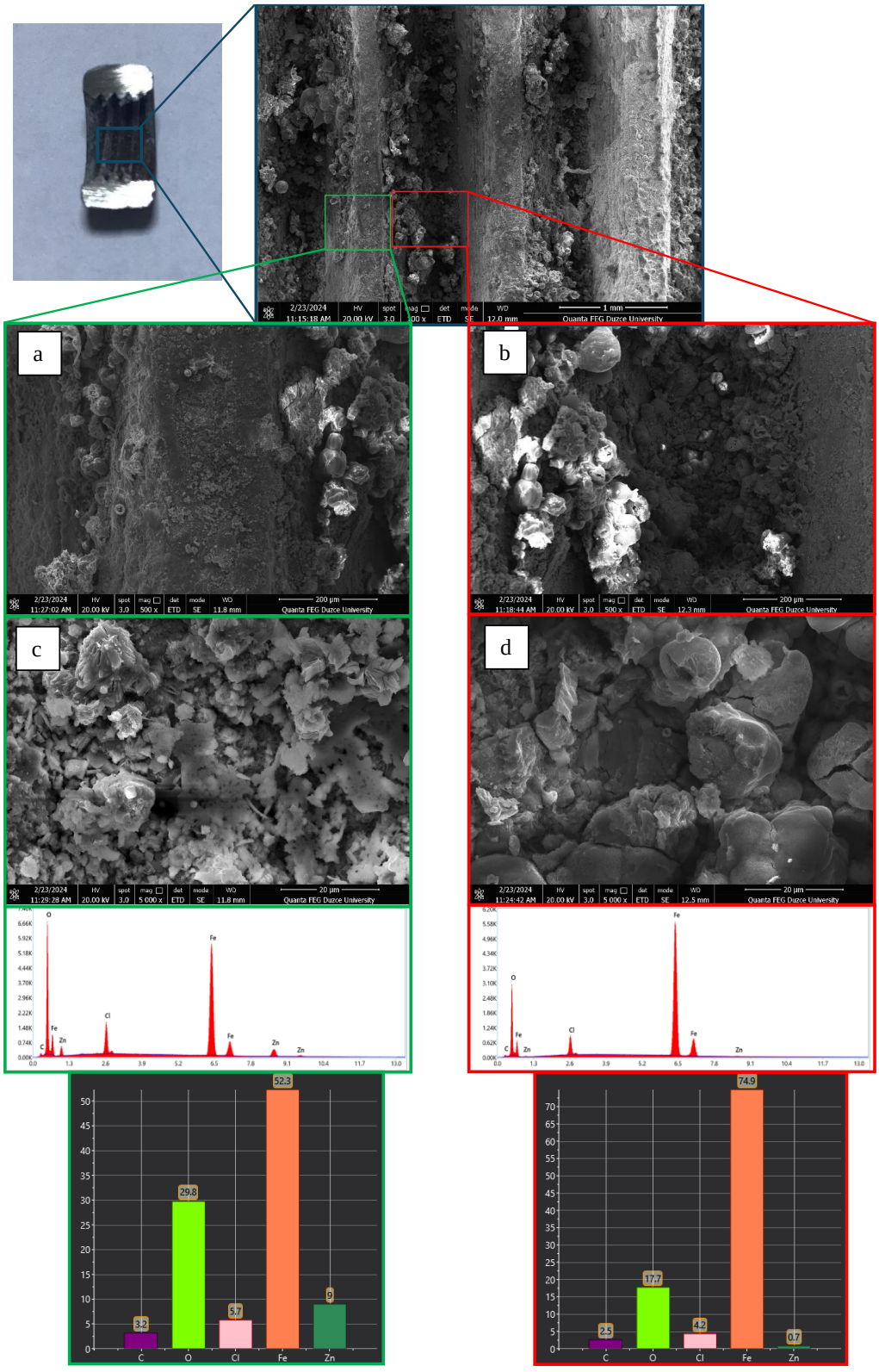

Figure 7. *SEM images of galvanized nuts exposed to corrosive environment after 13 days (a and c: 500x and 5000x of top regions; b and d: 500x and 5000x of hollow regions)*

In the SEM images of the galvanized nut after corrosion, it is seen that corrosion products occur in both hollow and top regions (Figure 7). After 13 days, it is seen that different corrosion products are formed in different parts of the surface. EDS data show that Zn, Fe and O are the main components of corrosion products. The presence of Cl ions on the surface was observed upon exposure to the salt test. Zn, the

main component in the coating layer, decreased with the intensification of corrosion after 13 days of exposure. It was determined that the Zn rate was lower in the hollow regions compared to the top regions. While the Fe content was 52.3% in the top region, it was found to be 75% in the hollow region. Since it is difficult for the electrolyte to reach the thread area during the first exposure period in bolt-nut samples, the area is dry and corrosion is less. However, when it enters the electrolyte over time, it keeps the thread area wet and the deterioration of zinc accelerates the formation of Fe-based corrosion products on the surface [13]. Figure 8 shows the EDS element mapping images of galvanized nut samples after corrosion. According to the EDS mapping result, the presence of corrosion products in the thread area of the galvanized nut was detected. It has been determined that corrosion products are associated with regions richer in Fe.

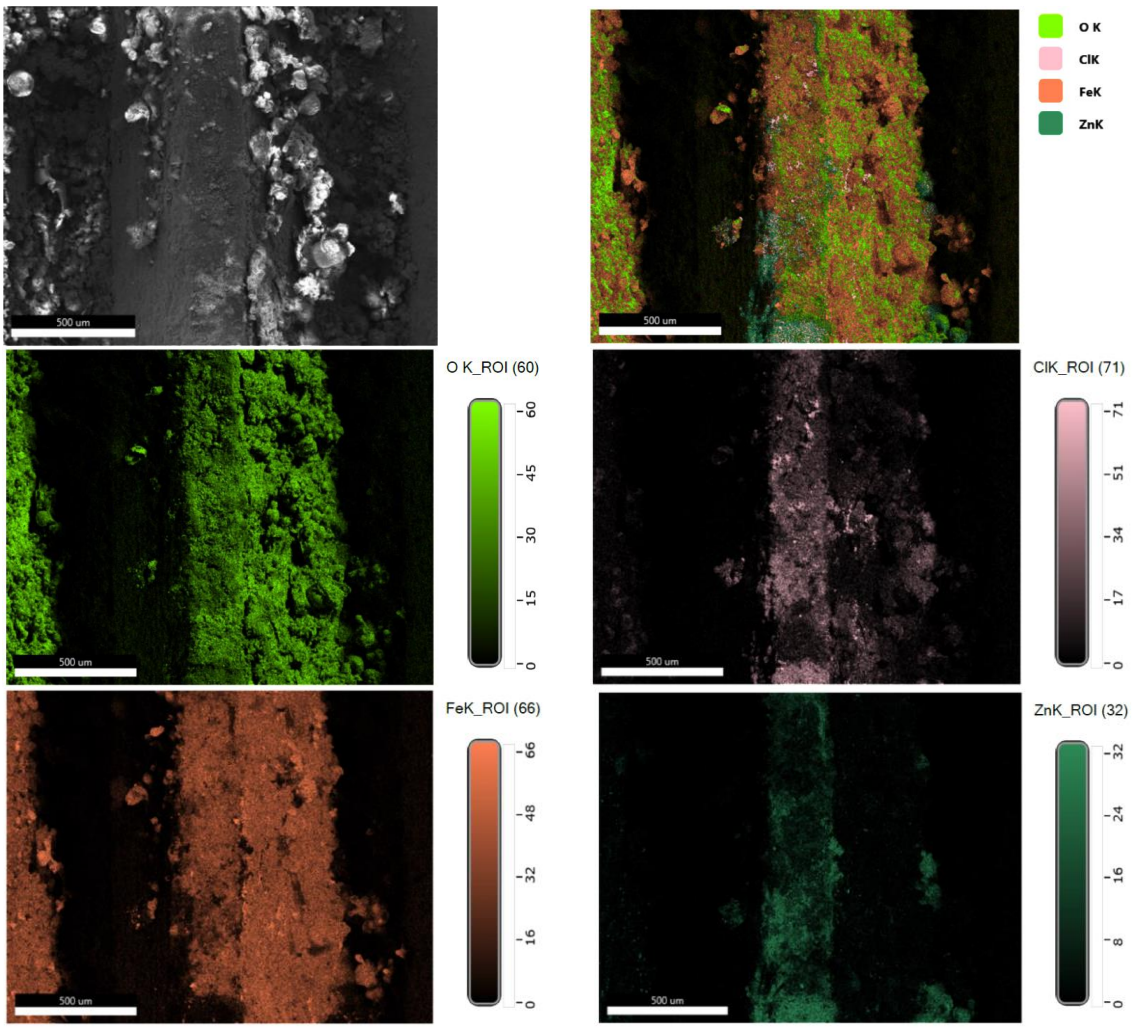

Figure 8. *EDS element mapping images of galvanized nut samples after 13 days*

The cross-sectional images of galvanized nut specimens before and after 13 days of exposure to the salt spray test were observed using SEM-EDS, as shown in Figure 9.

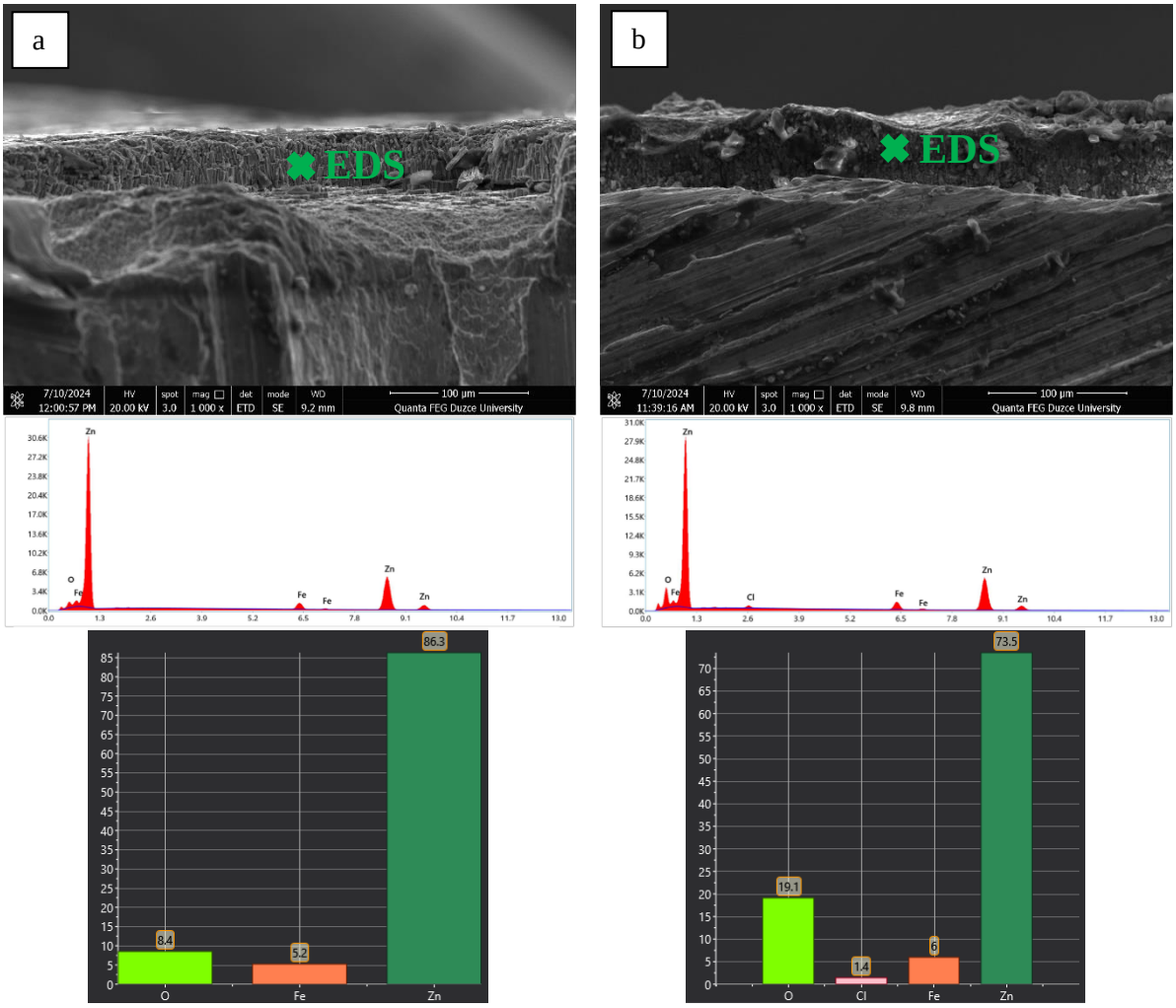

Figure 9. The cross-sectional images and EDS spectrum of the nut: (a) Before corrosion and (b) After the salt spray test.

It can be seen from the cross-sectional morphologies shown in Figure 9 that the layer thickness on the surface increases when galvanised nuts are exposed to corrosion. As mentioned in the salt spray test results section, the increase in thickness of the Zn layer after 13 days is due to the formation of oxide layers on the surface. The EDS results for the elements O, Fe and Zn in the coating layer before the corrosion tests were 8.4%, 5.2% and 86.3% respectively. After being subjected to the salt spray test for 13 days, the EDS results showed that the O and Fe ratio increased to 19.1% and 6%, respectively, while the Zn ratio exhibited a decrease to 73.5%. Additionally, the presence of 1.4% Cl from the environment was also observed.

IV. CONCLUSION

The corrosion evolution of CHDG coated steel nuts exposed to a corrosive environment for 13 days according to ASTM B117 standards was investigated and the results were as follows.

1. Steel nuts coated with Zn by the CHDG method were found to be corrosion resistant. At the end of the 13th day, the coating thickness was found to have increased to 224 µm. It is believed that this increase is due to the formation of oxide layers on the surface.
2. As a result of the data obtained by SEM-EDS analysis, it was observed that corrosion products start to form in the nut thread area after 13 days. However, after 13 days of aggressive testing, this result shows that the CHDG coating continues to protect the threads of the nut. This is

evidenced by the fact that the Zn element is still present on the surface of the threads in the EDS mapping analysis.

3. According to the EDS results, it was determined that the Zn ratio was lower in the hollow regions compared to the top regions, and therefore corrosion was observed to be more intense in the hollow regions.
4. The cross-sectional SEM images showed that the thickness of the coating layer deposited on the nuts by the CHDG process increased after the salt spray test for 13 days. The EDS results of the coating layer showed an increase in the O and Fe ratios, a decrease in the Zn ratio and the presence of the Cl element on the surface.
5. Electrochemical corrosion detection methods such as Dynamic Electrochemical Impedance Spectroscopy (DEIS) can be used to further investigate the corrosion mechanisms of CHDG coated steel nuts over the time. In addition, the structures of Zn and Fe based corrosion products formed on the surface should be investigated by using characterisation techniques in further research.

ACKNOWLEDGEMENTS: This scientific study was conducted as a result of cooperation between Düzce University, Fibrobeton Company, and Standard Profile Corporation Research and Development Centers. The authors extend their gratitude to Volkan Özdal, Volkan Akmaz, Sedat Enveş, Yasemin Hatipoğlu, and Faik Ali Birinci from the Fibrobeton Company R&D Center for their valuable assistance during this research.

V. REFERENCES

[1] H. Gerengi, "Anticorrosive Properties of Date Palm (Phoenix dactylifera L.) Fruit Juice on 7075 Type Aluminum Alloy in 3.5% NaCl Solution," *Industrial & Engineering Chemistry Research*, vol. 51, no. 39, pp. 12835–12843, 2012.

[2] H. Gerengi and H. İ. Uğraş, "Patent Studies on Using Cationic Boron Doped Ionic Liquids as Corrosion Inhibitor," *NWSA Academic Journals*, vol. 12, no. 2, pp. 53–65, 2017.

[3] H. Kania, "Corrosion and Anticorrosion of Alloys/Metals: The Important Global Issue," *Coatings*, vol. 13, no. 2, p. 216, 2023.

[4] M. M. Solomon, H. Gerengi, T. Kaya, and S. A. Umoren, "Performance Evaluation of a Chitosan/Silver Nanoparticles Composite on St37 Steel Corrosion in a 15% HCl Solution," *ACS Sustainable Chemistry & Engineering*, vol. 5, no. 1, pp. 809–820, 2017.

[5] D. Dwivedi, K. Lepková, and T. Becker, "Carbon Steel Corrosion: A Review of Key Surface Properties and Characterization Methods," *RSC Advances*, vol. 7, no. 8, pp. 4580–4610, 2017.

[6] Y. Liu, H. Gao, H. Wang, X. Tao, and W. Zhou, "Study on The Corrosion Behavior of Hot-dip Galvanized Steel in Simulated Industrial Atmospheric Environments," *International Journal of Electrochemical Science*, vol. 19, no. 1, p. 100445, 2024.

[7] R. Sa-nguanmoo, E. Nisaratanaporn, and Y. Boonyongmaneerat, "Hot-dip Galvanization with Pulse-electrodeposited Nickel Pre-coatings," *Corrosion Science*, vol. 53, no. 1, pp. 122–126, 2011.

[8] M. Maraşlı, K. Dikmen, V. Özdal, V. Akmaz, and H. Gerengi, "Investigation of The Corrosion Behavior of Hot Dip Galvanized (HDG) St37 Steel in 3.5% NaCl Solution," in *8th International Congress On Engineering, Architecture And Design*, Istanbul, 2021, pp. 681–690.

[9] S. M. A. Shibli, B. N. Meena, and R. Remya, “A Review on Recent Approaches in the field of Hot Dip Zinc Galvanizing Process,” *Surface and Coatings Technology*, vol. 262, pp. 210–215, 2015.

[10] H. Gerengi, M. M. Solomon, M. Maraslı, and B. B. Kohen, “A comparative analysis of The Corrosion Characteristics of Electro-galvanized Steel Coated with Epoxy Zinc-free and Zinc-rich Coatings in 5% NaCl,” *Journal of Adhesion Science and Technology*, vol. 37, no. 20, pp. 2795–2806, 2023.

[11] H. Gerengi, M. Maraşlı, M. Rizvi, B. Kohen, and I. Taşkıran, “Protection of Steel Hooks Embedded in Glass-Fiber-Reinforced Concrete against Macrocell Corrosion,” *Petroleum Research*, vol. 9, no. 2, pp. 317–326, 2024.

[12] K. Zhang, R. Song, and Y. Gao, “Corrosion Behavior of Hot-dip Galvanized Advanced High Strength Steel Sheet in a Simulated Marine Atmospheric Environment,” *International Journal of Electrochemical Science*, vol. 14, no. 2, pp. 1488–1499, 2019.

[13] E. F. Daniel, C. Wang, C. Li, J. Dong, I. I. Udoh, D. Zhang, W. Zhong, and S. Zhong, “Evolution of Corrosion Degradation in Galvanised Steel Bolts Exposed to a Tropical Marine Environment,” *Journal of Materials Research and Technology*, vol. 27, pp. 5177–5190, 2023.

Düzce University
Journal of Science & Technology

Research Article

Characterization of Luffa-reinforced Polyaniline Films

Özge AKAY SEFER [a,*]
[a]*Department of Mechatronic Engineering, Marmara University, Istanbul 34854, Turkey*
** Corresponding author's e-mail address: ozge.akay@marmara.edu.tr*
DOI: 10.29130/dubited.1469198

ABSTRACT

Herein, Polyaniline (PANI)/polyethylene oxide (PEO) - luffa cylindrica bio-composite films of various mass fractions (%) have been prepared via casting solution of emeraldine base polyaniline and cellulose extracted from luffa. The biopolymer films were structurally and thermally characterized using X-ray diffraction (XRD), Fourier Transform-InfraRed (FT-IR) spectroscopy, and differential scanning calorimetry analysis (DSC). Moreover, the electrical properties of conductive biopolymer solutions were measured by using the conductivity meter. According to the obtained results, treated luffa increases the conductivity of biopolymers. XRD results reveal that luffa increases the crystallinity of bio-composite films in comparison to PANI/PEO films. FTIR analysis proved the presence of functional groups of PANI, PEO, and luffa in the film structure. Also, an increase in the weight of luffa in the bio-composite film brings about an increase in the peak intensities of the O-H group. It is determined that luffa enhances the thermal stability of composites via the results of DSC analysis.

Keywords: *Luffa, PANI, Bio-composite, film*

Luffa Takviyeli Polianilin Filmlerin Karakterizasyonu

Öz

Burada, emeraldin bazlı polianilin ve lif kabağından ekstrakte edilen selülozun döküm çözeltisi kullanılarak çeşitli kütle fraksiyonlarına (%) polianilin (PANİ)/polietilen oksit (PEO) - lif kabağı cylindrica biyo-kompozit filmler hazırlanmıştır. Biyopolimer filmler, X-ışını kırınımı (XRD), Fourier Dönüşüm-Kızılötesi (FT-IR) spektroskopisi ve diferansiyel taramalı kalorimetri analizi (DSC) kullanılarak yapısal ve termal olarak karakterize edilmiştir. Ayrıca, iletkenlik ölçer kullanılarak iletken biyopolimer çözeltilerinin elektriksel özellikleri ölçülmüştür. Elde edilen sonuçlara göre, işlenmiş lif kabağı biyopolimerlerin iletkenliğini artırmaktadır. XRD sonuçları, lif kabağının PANI/PEO filmlerine kıyasla biyo-kompozit filmlerin kristalliğini artırdığını ortaya koymaktadır. FTIR analizi, film yapısında PANI, PEO ve lif kabağı fonksiyonel gruplarının varlığını kanıtlamıştır. Ayrıca, biyo-kompozit ince filmdeki lif kabağı ağırlığındaki artış, O-H grubunun pik yoğunluklarında artışa neden olur. Lif kabağının DSC analizinin sonuçlarına göre kompozitlerin termal kararlılığını artırdığı belirlenmiştir.

Anahtar Kelimeler: *Luffa, PANI, Biyokompozit, film*

Received: 16/04/2024, Revised: 10/05/2024, Accepted: 23/08/2024

I. INTRODUCTION

Due to environmental problems, the rate of use of biomaterials in industry is increasing considerably. Among them, fiber-reinforced composites (FRC) have gained great attention due to substantial mechanical properties such as flexibility, good strength, and low density, and environmental properties such as biocompatibility, biodegradability, and availability[1,2] . Owing to these properties, FRC has found a wide application in the automotive[3], marine[4], aerospace construction[5], and textile industries [6]. FRCs may contain synthetic fibers like carbon, glass, and Kevlar or natural fibers such as jute, kenaf, sisal, cotton and luffa. However, natural fibers are preferred over synthetic fibers due to easier recycling and lower environmental impact. Since it is difficult to dissociate non-natural fibers from composites, it brings about industrial waste.

Luffa cylindrica (Luffa) is one of the natural plant fibers composed of cellulose, hemicellulose, lignin, and waxy materials. It is classified in the cucurbitaceous family. It is common in Asia, Africa, and South America. Luffa, also known as a vegetable sponge, used in this study, was obtained in the southern part of Turkey. Luffa cylindrica (LC) has been used in a variety of investigations. LC has used printed circuit board (PCB) instead of glass fibers to eliminate recycling problems [7]. Sahli, M. et al. did a photocatalytic study with luffa cylindrical to investigate the structural properties of new composite [8]. Moreover, diverse bio-composites reinforced by luffa cylindrica have been fabricated in order to improve the physical, chemical, and electrical properties of materials [9-11]. For sensor applications, luffa cylindrica has been utilized as a sensing layer to investigate the sensing properties of devices[12]. Polyaniline (PANI) is one of the applicable conductive materials in the literature, such as gas sensors [13], humidity sensors [14], and biomedical devices [15] due to its easy synthesis, low cost, and easy transition from the conductor (emeraldine-salt) type to the insulator (emeraldine-based) type [16]. Generally, PANI is used with polyvinyl alcohol (PVA), polyethylene oxide (PEO), Poly (Vinyl Chloride) (PVL), etc. [17,18] since it has been difficult to obtain PANI as a self-contained film. For film or hydrogel film synthesis, the desired properties are solubility and bio-compatibility, and when compared to the others, PEO has been preferred more due to its excellent solubility in water, bio-compatibility, and non-toxicity [19]. For developing composite film, several methods are used to obtain smooth and homogeneous film, such as spin coating [20], dip coating [21], and solvent casting [22]. The most used method is the solvent casting method, which does not require any special apparatus to conduct an experiment [23]. To synthesize conductive polymers, several methods are used, such as solution mixing and impregnation method, in situ polymerization method, melt mixing method, and so on. Each method is applicable according to the study's purposes. For instance, to investigate the mechanical properties of the material, the in-situ polymerization method can be used [24] , or to modify the surface properties of the composite, the solution mixing method is more convenient [25]. Also, for thermoplastic materials, the melt mixing method may be used[26].

In this work, PANI/PEO/LC bio-composite films were fabricated in different weight ratios of luffa in PANI/PEO copolymer by using the melt mixing method. This study aims to investigate the effect of luffa on conductive copolymer PANI/PEO composites on their structural, chemical, and thermal characteristics, which have not been extensively studied before by adding different weight ratios of it. Initially, cellulose of luffa cylindrica was extracted by means of an alkali treatment method. Then, PANI was polymerized with PEO, which was added to the solution to obtain a film. Finally, the treated luffa was added and stirred with PANI/PEO copolymer with different weight ratios in order to investigate the structural effects on the biopolymer film. To investigate the structural, chemical, and thermal properties of films, FTIR, XRD, and DSC analyses were conducted, respectively.

II. MATERIALS AND METHODS

A.1 Materials

The Luffa Cylindrica utilized in this work are from Hatay, Turkey. Ethanol, xylene, sodium hydroxide (NaOH), hydrochloric acid (HCl) were used for luffa treatment process. PANI-emeraldin base (Mw = 50,000), PEO (Mv = 900,000), camphor sulfonic acid (CSA) were used for PANI/PEO solution. PANI, PEO, CSA were purchased from Sigma-Aldrich and other chemicals were acquired as guaranteed-grade reagents from Merck and other commercial suppliers and utilized without additional purification.

A. 2. Methods

A.2.1. Luffa Treatment

The alkali treatment methods were utilized in the luffa cylindrica to eliminate hemicellulose, lignin and other waxy and gummy substances[27]. Before this procedure, luffa cylindrica slices were dried in a vacuum oven at 50 C for 8 hours. As illustrated in Figure 1, luffa cylindrica were cut into small pieces to place in the vibratory disc mill and powdered at 1000 rpm for a minute. At each chemical treatment steps, luffa was rinsed with distilled water and ethanol and then filtered with a vacuum motor. Firstly, 5g grounded luffa in a flask was stirred in xylene/ethanol (2:1, v/v) for 6 hours. After that, 2 M hydrochloric acid (HCL) was added into flask at 85 C for 8 h. After filtration, luffa was treated with NaOH for 2 h at 85 C and as a final step, hydrogen peroxide was put into flask for 6 h to remove all constituents and impurities from Luffa cylindrica. Then, after filtering treated luffa powder with distilled water at least twice to ensure the elimination of chemical substances and dried, the brownish treated luffa was attained as shown in Figure 1.

A.2.2. Preparation of PANI/PEO/Luffa Films

The PANI/PEO composite solution was synthesized via the melt mixing method. The polyoniline were dispersed in an aqueous solution mixture with CSA (1:1.5) in chloroform/DMF (1:1) and stirred for 24h in the flask. Then, 2% PEO was added to the PANI/Luffa solutions as a carrier polymer, and they were stirred 24 hours at room temperature. As a final step, the luffa cellulose powder (treated luffa powders) was added and mixed in PANI/PEO solution for 24 h to obtain the bio-composite solution. All the stirring process has done in room temperature and humidity (25 ^{o}C, % 35). For the bio-composite film structure; 4 samples were prepared as PANI/PEO (here in after referred to as PANI or P), 1PANI:1Luffa (1P:1L), 1PANI:2Luffa (1P:2L), 2PANI:1Luffa (2P:1L) with casting solution method. The Table 1 contains the ratios used in the samples.

Table 1. *Weight ratio of luffa and PANI/PEO bio-composites.*

Sample	PANI/PEO (%)	Luffa (%)	Chloroform/DMF (ml)
PANI/PEO	3	-	12
1P:1L	3	3	12
1P:2L	3	6	12
2P:1L	6	3	12

A. 2.3. *Instrumentation*

Endress + Hauser conductivity meter was used to measure electrical properties of biopolymer films**.** Fourier transform infrared (FT-IR) and X-ray diffraction (XRD) spectroscopies were performed to

analyse vibrational and structural properties of PANI/PEO/LF bio-composite films. Perkin Elmer Spectrum 100 series FT-IR spectrometer was used to obtain functional groups of films. For XRD analyses, Bruker AXS D8 Advance system was utilized in the 2θ range of 5°–50° at room temperature. DSC measurements were conducted on a Perkin Elmer Jade DSC.

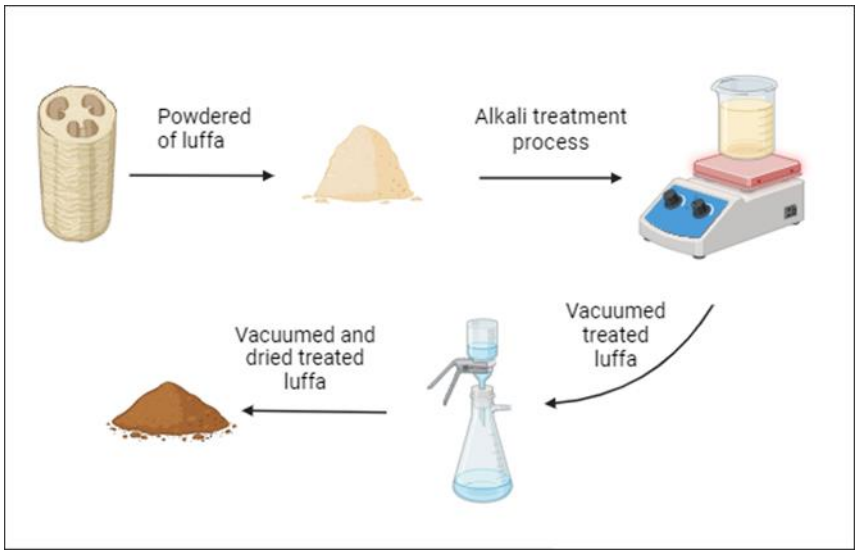

Figure 1. *Schematic of extracting cellulose from luffa cylindrica.*

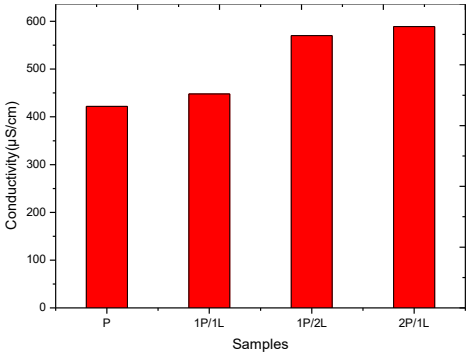

Figure 2. *The conductivity value of bio-composite films with different luffa concentration*

III. RESULTS AND DISCUSSIONS

The conductivity of the prepared bio-composite films was shown in Figure 2. According to the results, the conductivity values increase with the increasing ratio of PANI in the bio-composite as expected. However, the luffa ratio also improves the conductivity of bio-composite films. As shown in Figure 2, the conductivity value of 1P/2L is bigger than the conductivity of 1P/1L. This ascent may occur due to the plasticizing effect of blending polymers with macro molecules, bringing about an increase in conductivity at room temperature [9]. This increment may also be because of the chemicals that are used in the alkali treatment of luffa cylindrica.

Regarding structural analysis, firstly XRD was carried out with 35 kV power and a 30-mA current at room temperature in the angle range between 5° to 50°. The XRD spectroscopy results of PANI/PEO, 1P/1L, 2P/1L, 1P/2L and luffa are illustrated in Figure 3(a) and Figure (3b), respectively. For XRD pattern of PANI/PEO, the intense peaks were observed in 2θ ≅ 15.34° (PANI), 2θ ≅ 20. 32°(PANI) and 2θ ≅ 26.66°(PEO) as also reported in literature [28-30]. When adding luffa cellulose at different ratios

to the PANI/PEO copolymer, the peak intensities increase, and the peak widths decrease with the increasing the amount of luffa as shown in Figure 3(b). This behaviour means that luffa enhance the crystalline structure of PANI/PEO film [31]. As reported by Prabowo et al, treated ijuk fibers also increase the crystallinity of polypropylene composite[32]. The XRD results are also consistent with the conductivity of the bio-composite films, as seen in Table 1, the increasing of conductivity by adding luffa also increased the crystallinity of the films[33]. Our XRD results are also compatible with the study conducted by Awatef Dali et al. who fabricated PANI-coated luffa thin film by in-situ polymerization of anilin and obtained more ordered structure than PANI [34].

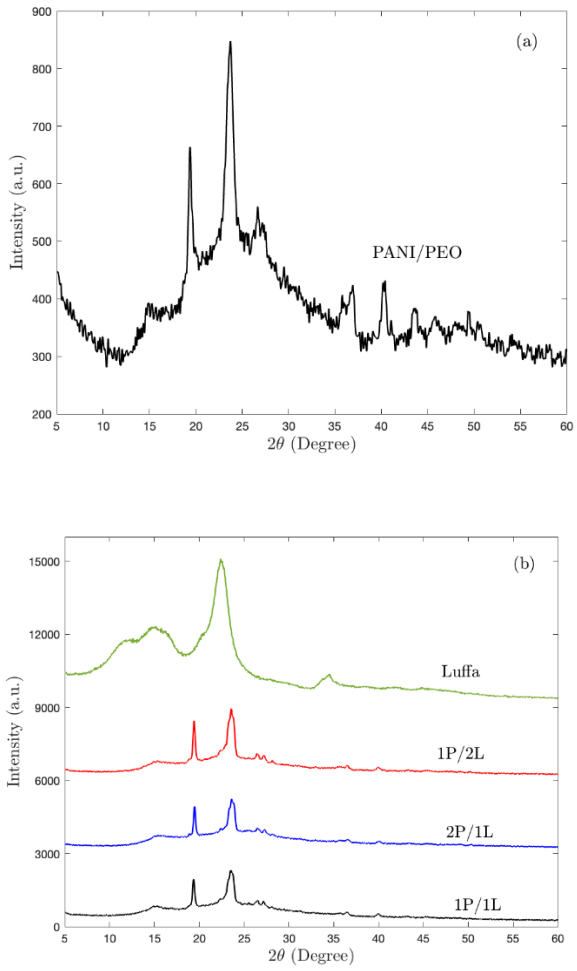

***Figure 3**. X-ray diffraction patterns of (a) PANI/PEO, (b) Luffa ,1P/2L , 2P/1L and 1P/1L films.*

The surface composition of bio-composite films was investigated via FT-IR spectroscopy. Figure 4(a) illustrates the changing of the chemical structure of treated luffa (TL) with untreated luffa (UTL). The strongest intensity peaks were observed in the region 3340 cm^{-1} in relation to the -OH group for cellulose and hemicellulose and 2900 cm^{-1} in relation to C-H groups due to the aliphatic fragments of the cellulose and hemicellulose components[35]. The absorption at 1429 cm-1 indicates the presence of C=C double bonds in aromatic stretching in lignin. A band at 1029 cm-1 corresponds to the vibration of the C–O stretching bond carbon of cellulose and hemicellulose [36]. After treatment of luffa, decreasing peak intensities occur, meaning the reduction of the corresponding functional groups. For instance, the intensities of 3340 cm-1 and 2900 cm-1 peaks decrease fairly, as shown in Figure 4(a). Hence, Lignin and hemicellulose were successfully eliminated from UTL as also studied by Yong et al. [37].

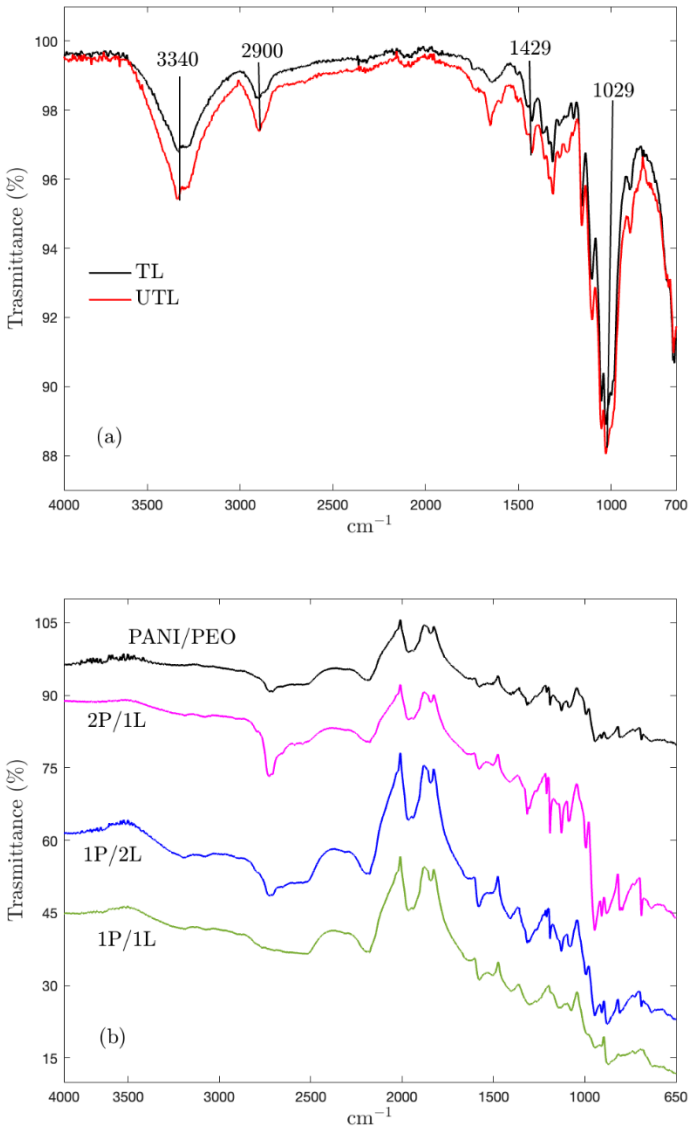

Figure 4. *FT-IR spectroscopies of treated luffa (TL) and untreated luffa (UTL) (a) PANI/PEO copolymer, 2P/1L, 1P/2L, and 1P/1L bio-composite(b) films.*

The comparison of functional groups of PANI/PEO, 2P/1L, 1P/1L, and 1P/2L biocomposite films was given in Figure 4(b). The composite film spectra are similar to the PANI/PEO film spectra. As shown in spectra (Figure 4b), the intensity of peaks increases when adding luffa to the PANI/PEO film. In addition, the peaks were shifted also a little from 2890 cm^{-1} to 2920 cm-1 and from 3382 cm^{-1} to 3347 cm^{-1} due to the chemical interaction of PANI/PEO with the luffa cellulose in Figure 3(b). Around 1700 cm^{-1} and 800 cm^{-1} regions, the transfer peaks occur on 1P/2L, 1P/1L, and 2P/1L owing to forming strong hydrogen bond between the luffa cellulose and the PANI/PEO co-polymer [38].

The thermal behavior of bio-composite samples was investigated with DSC measurements to determine the glass transition temperature (Tg) of film composites. Figure 5 illustrates the heating DSC curves with the glass transition of 2P/1L, 1P/1L, and 1P/2L films. In this figure, the highest Tg (202,31 ^{o}C) belongs to 1P/2L film, and when compared to the other films, the Tg value decreases with the decreasing luffa ratio in films. In other words, it can easily be said that luffa increases the crystallinity of the film, as reported by P.V. Joseph et al.[39] and decreases the free volume of the composites, which means the elongation of copolymer chains and, at the same time, strengthens the intermolecular force between the

polymer chains[40,41]. Another important result of glass transition temperature is that composites with higher glass transition temperature (Tg) values typically exhibit higher melting temperatures[42]. Hence, the 1P/2L bio-composite film has greater thermal stability due to higher Tg (202.31 ºC) and is the most applicable specimen, especially for sensor technologies. Moreover, the first large endothermic peaks occur (around 60-70 ºC) in the DSC analyses of each composite because of the evaporation of water/solvent molecules during the heat process, and the peak temperatures are compatible when compared to the literature that is about 50-80 ºC [43].

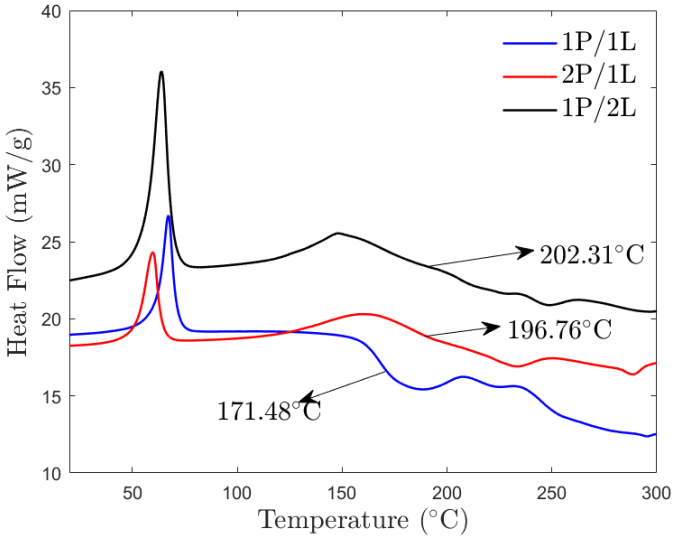

Figure 5. *DSC thermograms of 2P/1L, 1P/2L, and 1P/1L bio-composite films.*

IV. CONCLUSION

In brief, the structural, vibrational and thermal properties of bio-composites consisting of PANI, PEO, and Luffa cellulose with different weight ratios was investigated. It was confirmed by XRD spectroscopy that luffa-based cellulose can enhance the crystalline structure of PANI/PEO co-polymer by observing more intense peaks on 1P/2L bio-composite film. FTIR analysis proves the presence of functional groups of PANI, PEO, and cellulose in film structures. The alkali treatment successfully eliminated hemicellulose and lignin from the raw luffa. The DSC results show that cellulose extracted from luffa cylindrical increases the structure order of PANI/PEO film copolymer and makes films more crystallized, obtaining coherent outcomes with the XRD. Among synthesized bio-composite films, the 1P/2L is a good candidate that might potentially be used, especially in sensor technologies and other innovative functional materials, due to expressing better electrical properties as shown in Table 1 and thermal properties that has higher glass transition temperature (T_g=202.31ºC). The next step in this work will be to fabricate the PANI/PEO/Luffa bio-composite thin film using the spin coating method, characterize this new bio-composite in terms of its uniformity, homogeneity, and morphological properties using profilometry, SEM, or AFM, and test it for mechanical properties using mechanical test techniques.

V. REFERENCES

[1] S. K. Ramamoorthy, M. Skrifvars, and A. Persson, ‘A Review of Natural Fibers Used in Biocomposites: Plant, Animal and Regenerated Cellulose Fibers’, Polym. Rev., vol. 55, no. 1, pp. 107–162, Jan. 2015, doi: 10.1080/15583724.2014.971124.

[2] I. L. Kalnin, ‘Glass fiber reinforced composite article exhibiting enhanced longitudinal tensile and compressive moduli’, US3691000A, Sep. 12, 1972 Accessed: Jun. 20, 2023. [Online]. Available: https://patents.google.com/patent/US3691000A/en

[3] O. Akampumuza, Paul. M. Wambua, A. Ahmed, W. Li, and X.-H. Qin, ‘Review of the applications of biocomposites in the automotive industry’, Polym. Compos., vol. 38, no. 11, pp. 2553–2569, 2017, doi: 10.1002/pc.23847.

[4] P. Balakrishnan, M. John, L. Pothan, M. S. Sreekala, and S. Thomas, ‘Natural fibre and polymer matrix composites and their applications in aerospace engineering’, 2016, pp. 365–383. doi: 10.1016/B978-0-08-100037-3.00012-2.

[5] M. P. Ansell, ‘14 - Natural fibre composites in a marine environment’, in Natural Fibre Composites, A. Hodzic and R. Shanks, Eds., Woodhead Publishing, 2014, pp. 365–374. doi: 10.1533/9780857099228.3.365.

[6] D. U. Shah, D. Porter, and F. Vollrath, ‘Opportunities for silk textiles in reinforced biocomposites: Studying through-thickness compaction behaviour’, Compos. Part Appl. Sci. Manuf., vol. 62, pp. 1–10, Jul. 2014, doi: 10.1016/j.compositesa.2014.03.008.

[7] G. Genc, A. Sarikas, U. Kesen, and S. Aydin, ‘Luffa/Epoxy Composites: Electrical Properties for PCB Application’, IEEE Trans. Compon. Packag. Manuf. Technol., vol. 10, no. 6, pp. 933–940, Jun. 2020, doi: 10.1109/TCPMT.2020.2988456.

[8] M. Sahli, S. Rudz, K. Chetehouna, R. Bensaha, and M. Korichi, ‘Development, characterization and photocatalytic study of biocomposites based on PTFE, TiO2 and luffa cylindrica fibers’, Mater. Chem. Phys., p. 127635, 2023, doi: 10.1016/j.matchemphys.2023.127635.

[9] G. K. Ege, H. Yuce, O. Akay, H. Oner, and G. Genc, ‘A fabrication and characterization of luffa/PANI/PEO biocomposite nanofibers by means of electrospinning’, Pigment Resin Technol., vol. 52, no. 1, pp. 151–159, Jan. 2023, doi: 10.1108/PRT-09-2021-0105.

[10] O. Akay, C. Altinkok, G. Acik, H. Yuce, G. K. Ege, and G. Genc, ‘Preparation of a sustainable bio-copolymer based on Luffa cylindrica cellulose and poly(ε-caprolactone) for bioplastic applications’, Int. J. Biol. Macromol., vol. 196, no. October 2021, pp. 98–106, 2022, doi: 10.1016/j.ijbiomac.2021.12.051.

[11] B. V. Porras, ‘Characterization of Poly-hydroxybutyrate / Luffa Fibers Composite Material’, no. July, 2020.

[12] G. Konuk Ege, Ö. Akay, and H. Yüce, ‘A chemosensitive based ammonia gas sensor with PANI/PEO- ZnO nanofiber composites sensing layer’, Microelectron. Int., Mar. 2023, doi: 10.1108/MI-09-2022-0161.

[13] P. P. Sengupta, S. Barik, and B. Adhikari, ‘Polyaniline as a Gas-Sensor Material’, Mater. Manuf. Process., vol. 21, no. 3, pp. 263–270, May 2006, doi: 10.1080/10426910500464602.

[14] F.-W. Zeng, X.-X. Liu, D. Diamond, and K. T. Lau, ‘Humidity sensors based on polyaniline nanofibres’, Sens. Actuators B Chem., vol. 143, no. 2, pp. 530–534, Jan. 2010, doi: 10.1016/j.snb.2009.09.050.

[15] E. N. Zare, P. Makvandi, B. Ashtari, F. Rossi, A. Motahari, and G. Perale, 'Progress in Conductive Polyaniline-Based Nanocomposites for Biomedical Applications: A Review', J. Med. Chem., vol. 63, no. 1, pp. 1–22, Jan. 2020, doi: 10.1021/acs.jmedchem.9b00803.

[16] C. Bavatharani et al., 'Electrospinning technique for production of polyaniline nanocomposites/nanofibres for multi-functional applications: A review', Synth. Met., vol. 271, p. 116609, Jan. 2021, doi: 10.1016/j.synthmet.2020.116609.

[17] N. Z. Al-Hazeem and N. M. Ahmed, 'Effect of Addition of Polyaniline on Polyethylene Oxide and Polyvinyl Alcohol for the Fabrication of Nanorods', ACS Omega, vol. 5, no. 35, pp. 22389–22394, Sep. 2020, doi: 10.1021/acsomega.0c02802.

[18] M. Yazid, S. A. Ghani, S. J. Tan, A. F. Osman, and S. Hajar, 'Utilization of Polyaniline (PAni) as Conductive Filler on Poly (Ethylene Oxide) / Poly (Vinyl Chloride) Films: Effects of Naphthalene as Surface Modifier on Electrical Conductivity', J. Phys. Conf. Ser., vol. 908, p. 012006, Oct. 2017, doi: 10.1088/1742-6596/908/1/012006.

[19] M. S. Thompson, T. P. Vadala, M. L. Vadala, Y. Lin, and J. S. Riffle, 'Synthesis and applications of heterobifunctional poly(ethylene oxide) oligomers', Polymer, vol. 49, no. 2, pp. 345–373, Jan. 2008, doi: 10.1016/j.polymer.2007.10.029.

[20] D. B. Hall, P. Underhill, and J. M. Torkelson, 'Spin coating of thin and ultrathin polymer films', Polym. Eng. Sci., vol. 38, no. 12, pp. 2039–2045, 1998, doi: 10.1002/pen.10373.

[21] D. Dastan, S. L. Panahi, and N. B. Chaure, 'Characterization of titania thin films grown by dip-coating technique', J. Mater. Sci. Mater. Electron., vol. 27, no. 12, pp. 12291–12296, Dec. 2016, doi: 10.1007/s10854-016-4985-4.

[22] U. Siemann, 'Solvent cast technology – a versatile tool for thin film production', in Scattering Methods and the Properties of Polymer Materials, N. Stribeck and B. Smarsly, Eds., Berlin, Heidelberg: Springer, 2005, pp. 1–14. doi: 10.1007/b107336.

[23] S. Zhong et al., 'Recent progress in thin separators for upgraded lithium ion batteries', Energy Storage Mater., vol. 41, pp. 805–841, Oct. 2021, doi: 10.1016/j.ensm.2021.07.028.

[24] Y. Xia and Yun Lu, 'Fabrication and properties of conductive conjugated polymers/silk fibroin composite fibers', Compos. Sci. Technol., vol. 68, no. 6, pp. 1471–1479, May 2008, doi: 10.1016/j.compscitech.2007.10.044.

[25] S. Choi, S. I. Han, D. Kim, T. Hyeon, and D.-H. Kim, 'High-performance stretchable conductive nanocomposites: materials, processes, and device applications', Chem. Soc. Rev., vol. 48, no. 6, pp. 1566–1595, Mar. 2019, doi: 10.1039/C8CS00706C.

[26] P. Pötschke et al., 'Melt Mixing as Method to Disperse Carbon Nanotubes into Thermoplastic Polymers', Fuller. Nanotub. Carbon Nanostructures, Apr. 2005, doi: 10.1081/FST-200039267.

[27] L. Ghali, S. Msahli, M. Zidi, and F. Sakli, 'Effect of pre-treatment of Luffa fibres on the structural properties', Mater. Lett., vol. 63, no. 1, pp. 61–63, Jan. 2009, doi: 10.1016/j.matlet.2008.09.008.

[28] M. Doni, D. Sreeramulu, and N. Ramesh, ‘Synthesis, Characterization, and Properties of Epoxy Filled Luffa cylindrica reinforced composites’, Mater. Today Proc., vol. 5, pp. 6518–6524, Jan. 2018, doi: 10.1016/j.matpr.2018.01.140.

[29] I. A. Alhagri et al., ‘Enhanced Structural, Optical Properties and Antibacterial Activity of PEO/CMC Doped TiO2 NPs for Food Packaging Applications’, Polymers, vol. 15, no. 2, Art. no. 2, Jan. 2023, doi: 10.3390/polym15020384.

[30] R. Sonker, B. Yadav, and G. Dzhardimalieva, ‘Preparation and Properties of Nanostructured PANI Thin Film and Its Application as Low Temperature NO2 Sensor’, J. Inorg. Organomet. Polym. Mater., vol. 26, Nov. 2016, doi: 10.1007/s10904-016-0439-y.

[31] M. Á. Robles-García et al., ‘Nanofibers of cellulose bagasse from Agave tequilana Weber var. azul by electrospinning: preparation and characterization’, Carbohydr. Polym., vol. 192, pp. 69–74, Jul. 2018, doi: 10.1016/j.carbpol.2018.03.058.

[32] I. Prabowo, J. N. Pratama, and M. Chalid, ‘The effect of modified ijuk fibers to crystallinity of polypropylene composite’, IOP Conf. Ser. Mater. Sci. Eng., vol. 223, no. 1, p. 012020, Jul. 2017, doi: 10.1088/1757-899X/223/1/012020.

[33] A. Villa, J. C. Verduzco, J. A. Libera, and E. E. Marinero, ‘Ionic conductivity optimization of composite polymer electrolytes through filler particle chemical modification’, Ionics, vol. 27, no. 6, pp. 2483–2493, Jun. 2021, doi: 10.1007/s11581-021-04042-9.

[34] A. Dali, I. E. Boulguemh, F. Louafi, and C. Mouats, ‘Synthesis, characterization and environmental application of an original adsorbent: polyaniline-coated luffa cylindrica’, J. Polym. Res., vol. 28, no. 2, p. 33, Jan. 2021, doi: 10.1007/s10965-020-02365-1.

[35] A. Kesraoui, A. Moussa, G. B. Ali, and M. Seffen, ‘Biosorption of alpacide blue from aqueous solution by lignocellulosic biomass: Luffa cylindrica fibers’, Environ. Sci. Pollut. Res. Int., vol. 23, no. 16, pp. 15832–15840, Aug. 2016, doi: 10.1007/s11356-015-5262-4.

[36] H. N. Tran, H.-P. Chao, and S.-J. You, ‘Activated carbons from golden shower upon different chemical activation methods: Synthesis and characterizations’, Adsorpt. Sci. Technol., vol. 36, no. 1–2, pp. 95–113, Feb. 2018, doi: 10.1177/0263617416684837.

[37] Y. Guo, L. Wang, Y. Chen, P. Luo, and T. Chen, ‘Properties of Luffa Fiber Reinforced PHBV Biodegradable Composites’, Polymers, vol. 11, p. 1765, Oct. 2019, doi: 10.3390/polym11111765.

[38] D. A. Gopakumar et al., ‘Cellulose Nanofiber-Based Polyaniline Flexible Papers as Sustainable Microwave Absorbers in the X-Band’, ACS Appl. Mater. Interfaces, vol. 10, no. 23, pp. 20032–20043, Jun. 2018, doi: 10.1021/acsami.8b04549.

[39] P. V. Joseph et al., ‘The thermal and crystallisation studies of short sisal fibre reinforced polypropylene composites’, Compos. Part Appl. Sci. Manuf., vol. 34, no. 3, pp. 253–266, Mar. 2003, doi: 10.1016/S1359-835X(02)00185-9.

[40] S. Percec, ‘Chemical modification of poly(2,6-dimethyl-1,4-phenylene oxide) via phase transfer catalysis’, J. Appl. Polym. Sci., vol. 36, no. 2, pp. 415–427, 1988, doi: 10.1002/app.1988.070360213.

[41] B. O. Sen, S. Cetin, U. Yahşi, and U. Soykan, ‘Role of free volume in mechanical behaviors of side chain lcp grafted products of high density polyethylene’, J. Polym. Res., vol. 28, no. 8, p. 313, Jul. 2021, doi: 10.1007/s10965-021-02646-3.

[42] R. O. Ebewele, Polymer Science and Technology. Boca Raton: CRC Press, 2015. doi: 10.1201/9781420057805.

[43] G. R. Shetty, B. L. Rao, S. Asha, Y. Wang, and Y. Sangappa, ‘Preparation and characterization of silk fibroin/hydroxypropyl methyl cellulose (HPMC) blend films’, Fibers Polym., vol. 16, no. 8, pp. 1734–1741, Aug. 2015, doi: 10.1007/s12221-015-5223-z.

Düzce University
Journal of Science & Technology

Research Article

A Physical Properties-Focused Analysis for the Selection of Impregnated Wood in Architecture

Habibe ÖZTÜRK [a], Doç. Dr. Z. Sevgen PERKER [b*]

[a] *M.Arch, Bursa, TÜRKİYE*
[b] *Department of Architecture, Faculty of Architecture, Bursa Uludağ University, Bursa, TÜRKİYE*
** Corresponding author's e-mail address: zsperker@uludag.edu.tr*
DOI: 10.29130/dubited.1431384

ABSTRACT

Wood, one of the building material of the architectural tradition and the future, is subject to deterioration due to various factors. The most commonly used process for the protection of wooden materials is impregnation. The diversity of wood species and impregnation materials and methods complicates building material selection processes for architects. The diversity of building elements requires focusing on the different performances of the material in the building material selection process. In this context, this research aims to provide a guiding framework that focuses on the effect of impregnation on the physical properties of wooden materials. Within the scope of the research, 35 Turkey-based, experimental research articles on the subject in the Dergipark database were analyzed in terms of wood type, impregnation material, impregnation method, and the effect of impregnation on the physical properties of the wood material. As a result of the research, a physical property-oriented framework has been reached that will rationalize the impregnated wood building material selection processes for architects who are decision-makers in the architectural design and building repair stages.

Keywords: *Architecture, Wood, Impregnation, Material, Physical Properties*

Mimaride Emprenyeli Ahşap Seçimi İçin Fiziksel Özellik Odaklı Bir Analiz

Öz

Mimarlık geleneğinin ve geleceğin başlıca yapı malzemelerinden biri olan ahşap, çeşitli etkenler karşısında bozulmaya uğramaktadır. Ahşap malzemenin korunması konusunda yaygın olarak uygulanan işlem emprenyedir. Ağaç türlerinin yanı sıra emprenye madde ve yöntemlerinin çeşitliliği, mimarlar için yapı malzemesi seçim süreçlerini karmaşık hale getirmektedir. Ahşap yapı elemanlarının çeşitliliği ise yapı malzemesi seçim sürecinde malzemenin farklı performanslarına odaklanılmasını gerektirmektedir. Bu bağlamda bu araştırmanın amacı; emprenyenin ahşap malzemenin fiziksel özelliklerine etkisine odaklanan, rehber niteliğinde bir çerçeve sunmaktır. Araştırma kapsamında, Dergipark veritabanında yer alan, konuyla ilgili 35 adet Türkiye merkezli, deneysel içerikli araştırma makalesi ağaç türü, emprenye maddesi, emprenye yöntemi ve emprenyenin ahşap malzemenin fiziksel özelliklerine etkisi bakımından analiz edilmiştir. Araştırma sonucunda, mimari tasarım ve yapı onarım aşamalarında karar verici konumda olan mimarlar için, emprenyeli ahşap yapı malzemesi seçim süreçlerini rasyonel hale getirecek, fiziksel özellik odaklı bir çerçeveye ulaşılmıştır.

Anahtar Kelimeler: *Mimarlık, Ahşap, Emprenye, Malzeme, Fiziksel Özellikler*

Received: 04/02/2024, Revised: 10/03/2024, Accepted: 24/08/2024

I. INTRODUCTION

Material is fundamental to realizing the architectural design and maintaining an existing structure. Material selection processes are carried out by architects as decision-makers, both during the design of a new building and the maintenance, repair, or renovation of an existing building. They are multi-dimensional, multi-parameter, complex processes. Aesthetic concerns, technical performances, environment-product interactions, costs, and socio-cultural requirements are considered in the architect's selection of building materials. There may be many parameters [1]. It is of great importance for architects to systematize and rationalize the complex material selection process.

In today's architectural environment, many material alternatives come to the fore for the architect. However, the responsible architecture approach, especially regarding the environment and human health, necessitates the selection of environmentally friendly materials. Wooden material, which has provided important examples of traditional architecture throughout history and is considered one of the primary materials of today's sustainable architecture, stands out among material alternatives due to its superior aspects, especially its positive environmental interaction.

Despite its superior properties, wooden material can also deteriorate due to physical, chemical, biological, and human-induced reasons [2-3]. The preservation of the universal architectural heritage produced with wooden materials and the widespread use of wood as an ecological building material choice in contemporary buildings are closely related to minimizing material problems. The most commonly used process for the protection of wooden materials is impregnation. There are various studies on the impregnation process in the literature. However, the mentioned studies are: It is seen that it varies in terms of wood species, impregnation materials, impregnation methods, and the properties desired to be imparted by impregnation. The diversity of building elements produced with wooden materials, and on the other hand, the variety of impregnation processes, which is a wood material protection application, cause the architect's choice of building element design, maintenance, repair, and renewal to become more complicated. Therefore, it is significant to create rational selection aids that can be useful for the architect in choosing impregnated wood materials. In addition, the diversity of building elements in which wooden materials can be used requires focusing on the different performances of the material in the material selection process.

There are various experimental studies on the impregnation of wood materials in Turkey-based literature. However, in the relevant literature, holistic research that focuses on the specific performance of the impregnated wood material to be used in building element design and provides a guide that can help architects in material selection in this sense has yet to be found. In this context, this research aims to analyze Turkey-based experimental research focusing on the effect of impregnation on the physical properties of wooden materials; the aim is to present a guiding scheme that will help the architect rationally choose the impregnated wooden material to be used in the design, maintenance, repair or renewal of building elements.

II. PHYSICAL PROPERTIES OF WOOD

Wood's Physical properties are examined under the headings of moisture, density, thermal properties, electrical properties, acoustic properties, visual properties, and permeability.

A. MOISTURE

Wood is a material that can absorb and release moisture in its environment thanks to its hygroscopic feature [4]. The moisture content of wood material varies depending on the type of tree, its age, growing environment, the part of the wood from which it was taken, and the cutting season. Water is present in tree cells in three different forms:

- Structural water is included in wood's chemical structure and is not affected by drying processes.
- The absorption of water occurs due to the tendency of the cellulose in the cells to attract water. This type of water can cause the wood to swell.
- It is water that is found free between and within cells.

The physical properties of wood change depending on the moisture level. When dry wood is placed in a humid environment, it absorbs moisture, expands in size, and increases volume [5-6].

The moisture content in the wood is a factor that determines the quality of impregnation. Therefore, the wood material must be dried to a suitable moisture before impregnation. Effective impregnation penetration cannot be achieved in newly cut trees due to their high humidity and low void volume.

B. DENSITY

The specific gravity of wood varies depending on the type of tree, which part of the tree it is taken from, and the moisture content it contains. While the water content in freshly cut wood is generally between 35-50%, this rate drops to 10-20% in dried wood. Therefore, the specific gravity of freshly cut wood has a different value than dried wood. Additionally, there is a directly proportional relationship between the specific gravity of the wooden material and the mechanical properties of the material. The mechanical properties of wood material with high specific gravity are also expected to be strong [2].

C. THERMAL PROPERTIES

Wood has low heat permeability because it contains air due to the heat impermeability of its essential component, cellulose, and its porous structure. However, the thermal conductivity of wood may vary depending on the moisture in the wood, its type, and fiber direction. Wood expands when exposed to heat and contracts when cooled. However, these expansion and contraction rates are small [5, 7].

D. ELECTRICAL PROPERTIES

The dried wood material cannot conduct electricity. However, as the moisture level of the wood increases, its electrical conductivity also increases, and a change in electrical conductivity occurs depending on the fiber direction of the wood [6]. Wooden can be an effective insulation material when impregnated or glued with paraffin or synthetic resins and when it does not contain moisture [7-8].

E. ACOUSTIC PROPERTIES

Air gaps in the internal structure of wood provide wood with the ability to absorb sound. Thus, it can provide good insulation against sound. The propagation speed of sound waves in wood varies depending on the tree type, fiber orientation, annual ring structure, void ratio, surface roughness, humidity, temperature, density, and frequency of sound waves. As the moisture content in wood material increases, the material shows a heterogeneous feature, which reduces the speed of sound propagation [7].

F. VISUAL PROPERTIES

Elements such as color, texture, shine, and smell reflect the physical properties of wood. Wooden material can have various color tones due to the extractive substances it contains. Even in wooden materials from the same tree species, different color tones can be observed. This is due to the different densities within the same tree and the different reflections of light. Whether the wooden material has a glossy or matte appearance is related to the material's ability to reflect light. In addition, extractive substances found in the structure of wood material, especially substances such as essential oils, resin, and tannin, can contribute to the identification of the tree species by creating the unique smell of the material [2].

G. PERMEABILITY

Permeability is an important factor determining the degree of impregnability of wood. It is a term that generally describes the rate at which liquids pass through a porous surface under pressure [9]. If a material allows liquid flow easily under pressure, it is understood to have high permeability. The type of wood material, sapwood or heartwood, causes significant differences in permeability [10].

III. METHOD

The research material consists of academic articles with experimental content based in Turkey and published in Turkish. In order to obtain the material to be studied within the scope of the research, in the first stage, a search was done on the "Dergipark" database with the keyword "impregnation." The articles encountered as a result of the scanning were examined in detail, and 35 articles focusing on the effect of impregnation on the physical properties of wooden materials were identified. The mentioned articles constituted the study material of this research.

The contents of the articles covered within the scope of the research: The tree/wood type, impregnation material, and impregnation method were analyzed and evaluated in terms of impregnation's effect on the wood's physical properties.

IV. RESULTS

In this section, the effects of the impregnation process on the physical properties of wood were examined in the studies covered within the scope of the research, and various parameters were discussed to evaluate these effects. The mentioned parameters include the type of tree/wood being impregnated, impregnation materials, impregnation methods, and the effects of impregnation on the physical properties of the wooden material.

In this context, samples of two different types of wood were used in the studies examined. Among the natural and engineered wooden materials used, applications of different wood species have also been identified. As seen in Table 1, examples of softwood species in the studies include spruce, Picea Orientalis, Scots pine, black pine, red pine, fir, Uludağ fir, cedar, and hybrid. Among the hardwood species, beech, oriental beech, alder, heaven tree, black poplar, poplar, eucalyptus, iroko, oak, Quercus Petraea, Anatolian walnut, and ash were used.

Table 1. *Wood species used in the articles*

WOOD SPECIES			ARTICLES																																
			1	2	3	4	5	6	7	8	9	10	11	12	13	14	15	16	17	18	19	20	21	22	23	24	25	26	27	28	29	30	31	32	33	34	35
NATURAL WOOD	SOFTWOOD	Scotch Pine		■	■	■			■				■				■	■			■	■				■			■		■					■	
		Black Pine									■						■		■	■			■	■													
		Red Pine	■									■							■	■			■					■							■		
		Uludağ Fir											■									■									■						
		Spruce		■	■	■																										■					
		Picea Orientalis										■						■														■					
		Hybrid															■																				
	HARDWOOD	Oriental Beech										■	■					■			■										■	■					
		Oak (Quercus Robur)																								■				■							
		Quercus Petraea																				■									■						■
		Ash																									■										
		Walnut																																			■
		Poplar															■																				
		Eucalyptus					■								■																						
		Beech		■	■	■																				■				■			■				
		Alder		■	■	■																															
		Heaven Tree						■																													
		Iroko															■																				
ENGINEERED WOOD	SOFTWOOD	Red Pine												■		■																					
		Scotch Pine								■																								■			
		Anatolian Black Pine												■		■																					
		Cedar of Lebanon												■		■																					
	HARDWOOD	Alder																																■			
		Poplar														■																					
		Black Poplar												■																							
		Oriental Beech								■																											

Studies have shown that various impregnation substances that affect the physical properties of wood are used. The impregnation materials used in studies on this effect are classified into four categories: natural, oil-borne, water-borne, and organic solvent preservatives.

Accordingly, colophon (pine resin), linseed oil, tea plant extract, pine tannin, acorn, and waste sunflower oil were identified as examples of natural impregnation materials (Table 2). Boron oil, base oil, paraffin and alkyd resin were among the oil-impregnation materials used in a few studies (Table 3). In the water-soluble impregnation materials category, boric acid (BA), borax (Bx), sodium perborate, polyethylene glycol (PEG-400), Vacsol, Vacsol-Aqua, Immersol-WR, copper-chrom-boron (Tanalith-CBC), Phosphoric acid (FA), ammonium sulfate (AS), diammonium phosphate (DAP), zinc chloride, copper-chrom-boron (Wolmanit-CB), sodium borate, Alkaline Copper Quat (Celcure AC500), Micronized Copper Quat (MCQ), geothermal water (Afyonkarahisar, Ömer-Gecek- Gazlıgöl), (Kütahya, Eynal-Çitgöl-Naşa), (Aydın, Alangüllü-Çamköy-Germencik), (Konya, Ilgın), (Afyonkarahisar-Denizli-Kütahya), Imersol aqua, Timber care aqua, copper azole (Tanalith-E), monoammonium phosphate (MAP), nano titanium dioxide, nano boron nitride, zinc borate and alkyl ketene dimer (AKD) were used (Table 4). As organic solvent impregnation agent, styrene (St), methylmethacrylate (MMA), isocyanate (ISO), ProtimWR230, barite (Baso4), and organosilicon compounds (Dow Corning 1-6184; Z-6341, 2-9034, IE 6683, Z70) (Table 5).

Table 2. *Natural preservatives used in articles*

NATURAL PRESERVATIVES	ARTICLES																																		
	1	2	3	4	5	6	7	8	9	10	11	12	13	14	15	16	17	18	19	20	21	22	23	24	25	26	27	28	29	30	31	32	33	34	35
Acorns																							■												
Colophon (Pine Resin)		■												■																					
Linseed Oil			■																																
Pine Tannin																							■												
Tea Plant Extract															■																				
Waste Sunflower Oil																															■				

Table 3. *Oil-borne preservatives used in articles*

OIL-BORNE PRESERVATIVES	ARTICLES																																		
	1	2	3	4	5	6	7	8	9	10	11	12	13	14	15	16	17	18	19	20	21	22	23	24	25	26	27	28	29	30	31	32	33	34	35
Alkyd Resin														■																					
Paraffin	■			■			■																	■											
Paraffin Wax			■																																
Vaseline																								■											
Base Oil																								■											
Boron Oil											■																								

Table 4. *Water-borne preservatives used in articles*

WATER-BORNE PRESERVATIVES	ARTICLES																																		
	1	2	3	4	5	6	7	8	9	10	11	12	13	14	15	16	17	18	19	20	21	22	23	24	25	26	27	28	29	30	31	32	33	34	35
Alkyl Ketene Dimer																																		■	
Alkaline Copper Quaternary																■																			
Ammonium Sulfate							■	■					■	■													■					■				
Borax					■	■	■					■	■	■													■									
Boric Acid	■				■	■	■					■	■	■													■								■	
Copper Azole																									■				■						
Copper-Chrome-Borate						■	■		■			■	■	■																					
Diammonium Phosphate							■																												
Geothermal Water																	■	■				■				■								■	
Immersol Aqua																							■												
Immersol-WR 2000						■							■																						
Micronized Copper Quaternary																■																			
Monoammonium Phosphate																																■			
Nano Boron Nitride																												■							
Nano Titanium Dioxide																												■							
Phosphoric Acid						■																													
Polyethylene Glycol	■				■	■	■						■																						
Sodium Borate									■																										
Sodium Perborate	■				■																														
Timber Care Aqua																							■												
Vacsol						■	■																												
Vacsol-Aqua																				■															
Vacsol-WR													■																						
Zinc Borate																																■			
Zinc Chloride								■																			■								

Table 5*. Organic solvent preservatives used in articles*

ORGANIC SOLVENT PRESERVATIVES	ARTICLES																																		
	1	2	3	4	5	6	7	8	9	10	11	12	13	14	15	16	17	18	19	20	21	22	23	24	25	26	27	28	29	30	31	32	33	34	35
Isocyanate	■				■	■	■																												
Methyl Methacrylate	■				■	■	■						■																						
Organosilicon Compounds																														■					
ProtimWR230									■																										
Styrene	■				■	■	■						■																						■
White Spirit			■																																
Barite																			■																

In these studies, it was determined that two impregnation methods were used to determine the effect of impregnation on the physical properties of wood. These are methods where non-pressure is applied and methods where pressure is applied. Table 6 shows that brushing/spraying, dipping, soaking, and hot-cold bath methods were used among the methods that do non-pressure. It has been observed that the filled cell and vacuum methods are used among the methods where pressure is applied.

Table 6. *Impregnation methods used in articles*

IMPREGNATION METHODS		ARTICLES																																
		1	2	3	4	5	6	7	8	9	10	11	12	13	14	15	16	17	18	19	20	21	22	23	24	25	26	27	28	29	30	31	32	33	34	35
NON-PRESSURE	Brushing or Spraying												■		■																	■				
	Dipping		■	■	■					■		■						■	■		■		■	■	■			■		■		■	■			■
	Hot-Cold Bath																										■					■				
	Soaking																					■												■		
PRESSURE	Full Cell Process											■					■												■		■				■	
	Vacuum process	■				■	■	■	■		■			■		■				■						■		■								

Accordingly, the effects of the wood species, impregnation material, and method used in these studies, where impregnation affects the physical properties of wood, are given in Table 7.

Table 7. *Matrix showing the effect of impregnation on the physical properties of wood*

PHYSICAL PROPERTIES	ARTICLES																																	
	1	2	3	4	5	6	7	8	9	10	11	12	13	14	15	16	17	18	19	20	21	22	23	24	25	26	27	28	29	30	31	32	33	34	35
Moisture	■		■		■	■	■					■	■	■			■				■		■	■				■			■		■	■	■
Density						■					■	■		■				■	■			■	■		■	■			■	■	■				
Thermal Properties								■																			■						■			
Electrical Properties																																			
Acoustic Properties																																			
Visual Properties		■		■					■	■						■				■									■							
Permeability							■					■		■		■	■	■				■			■											

Effects that cause wood to change due to moisture are the effects of wood's resistance to water intake and swelling and contraction values. In the studies examined, it was determined that boric acid and borax, which are water-borne impregnation materials, showed good resistance to water [11-13]. In addition, it is seen that water resistance is increased by mixing boric acid with alkyl ketene dimer (AKD), which has poor water resistance properties when used alone [14]. It has been determined that paraffin and petroleum jelly, which are oil-borne impregnation materials, have good water resistance [15]. Linseed oil and colophon, which are natural impregnation materials, have properties that increase water resistance in wooden materials [16-17]. It has been determined that organic solvent impregnation materials defined as "water repellents" increase the water resistance of wood materials [18]. It has been determined that the substances that increase the water resistance of wood by affecting its swelling and shrinkage movements are boron nitride and geothermal water taken from Kütahya-Eynal and Denizli [19-21]. On the other hand, styrene material negatively affects the swelling and shrinkage values of wood, reducing the material's dimensional stability and causing a decrease in water resistance [22].

As the amount of boron-containing substances used in the impregnation process increases, the density of the wood material also increases [23]. Since the mechanical properties of wood material with high density are expected to be strong, the mentioned increase is positive for wood material.

Ammonium sulfate has a positive change in the thermal properties of artificial wood material obtained from Scots pine and oriental beech, and impregnation substances such as monoammonium phosphate, zinc borate, and boric acid in artificial wood material obtained from Scots pine appears to cause [24-25].

When the color change and surface roughness values from the visual characteristics of the wooden material were examined, it was determined that paraffin had an improved effect on the visual properties of the material despite the odor, and Wolmanit-CB and MCQ substances increased the color change resistance [26-28]. It has been found that sodium borate and Vacsol negatively affect the visual properties by increasing the surface roughness [29-30].

In some of the studies examined, it is seen that some mechanical properties of the wood material and its physical properties are discussed due to the multiple parameters in the impregnation. Among the

mechanical properties considered, Features such as modulus of elasticity, compressive strength, bending strength, and dynamic bending strength are included.

As a result of analyzing the experimental studies included in the research, a scheme was created that holistically reveals the positive contribution of impregnation to the physical properties of wood material (Figure 1). The diagram includes research results that positively contribute to the physical properties of wooden materials [31].

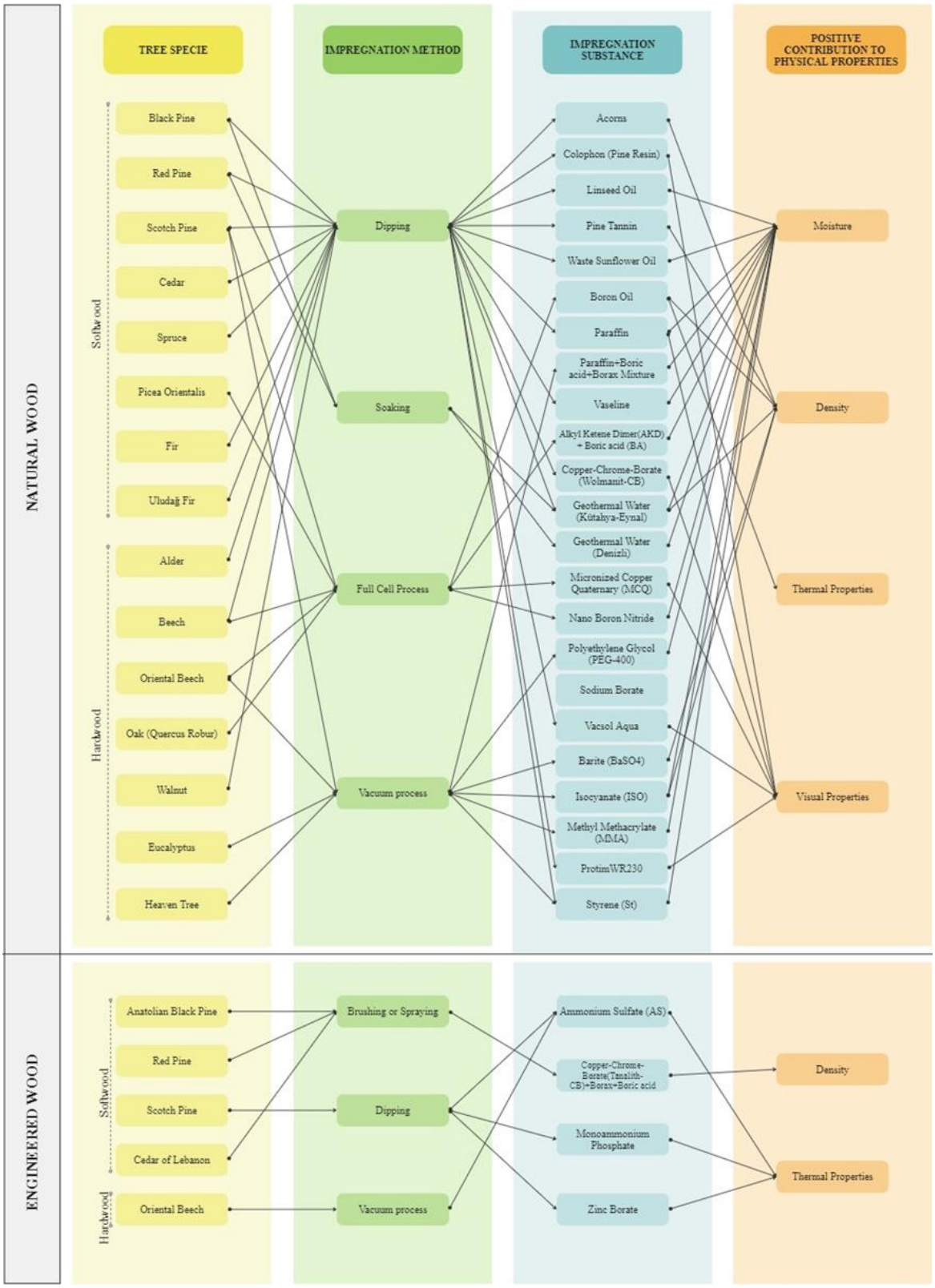

Figure 1. *Scheme for the positive contribution of impregnation to the physical properties of wooden materials*

V. CONCLUSION

Today's architectural environment has to bear the responsibility of producing ecological solutions with high energy efficiency that reduce environmental pollution and carbon footprint in the face of various environmental problems, especially climate change. Wood, one of the primary materials of the architectural tradition in world history, has a significant potential for producing responsible architectural products in the face of today's environmental problems. The popularization of wood as a building material that offers ecological solutions depends on the efficient use of existing raw material resources and the long life of the wood used. For this reason, it is significant to improve the behavior of wooden materials against various factors.

Within the scope of the research, thirty-five articles written in Turkish were obtained from the Dergipark database, which includes academic articles in Turkey and focuses on the effect of impregnation on the physical properties of wooden materials. The tree/wood type, impregnation material, impregnation method, and the impregnation process's effect on the wooden material's physical properties were systematically analyzed.

In studies focusing on the effect of impregnation on the physical properties of wooden materials, Both natural and engineered samples as tree/wood type, It has been observed that natural, oil-borne, water-borne, and organic solvent preservatives are used as impregnation materials, and both non-pressure and pressure applied methods are used as impregnation methods. Within the scope of the research, it is understood that linseed oil and colophon (pine resin), which are natural preservatives, paraffin and vaseline, which are oil-borne preservatives, and boric acid and borax, which are water-borne preservatives, come to the fore in increasing the water resistance of the material. It has been noted that boron-containing impregnation materials have a positive effect on the density of wood, ammonium sulfate, mono ammonium phosphate, zinc borate, and boric acid have a positive effect on the thermal properties of wood, and preservatives such as Wolmanit-CB and micronized copper quat have a positive effect on color change resistance.

As a result of the research, a scheme was created that holistically reveals the positive contribution of impregnation to the physical properties of wooden materials. It is believed that the created scheme is a guide that will contribute to the architect going through a systematic process focused on physical performance in selecting impregnated wood materials.

VI. REFERENCES

[1] F. Sezgin and G. Çelebi, "Bina Tasarımında Malzeme Seçimi için Model Çalışması," *Politeknik Dergisi*, vol. 14, no. 3, pp. 215-222, 2011.

[2] Z. S. Perker, "Geleneksel ahşap yapılarımızda kullanım sürecinde oluşan yapı elemanı bozulmalarının Cumalıkızık örneğinde incelenmesi," Yüksek Lisans Tezi, Fen Bilimleri Enstitüsü, Mimarlık Anabilim Dalı, Uludağ Üniversitesi, Bursa, 2004.

[3] Z. S. Perker and N. Akıncıtürk, "Cumalıkızık'da Ahşap Yapı Elemanı Bozulmaları," *Uludağ Üniversitesi Mühendislik Fakültesi Dergisi*, vol. 11, no. 2, 2006. [Online]. Available: https://doi.org/10.17482/uujfe.61527

[4] H. E. Desch and J. M. Dinwoodie, Timber: Structure, Properties, Conversion and Use, 7th Edition. MacMillan, New York, 1996.

[5] Anonim, The encyclopedia of wood. New York: Sterling Publishing Co Inc, 1980.

[6] R. Günay, Geleneksel ahşap yapılar sorunları ve çözüm yolları. İstanbul: Birsen Yayınevi, 2002.
[7] Y. Örs and H. Keskin, Ağaç malzeme bilgisi. Ankara: Atlas Yayınevi, 2001.

[8] İ. Hacı Aktar, "Yapıda kaplama malzemesi olarak ahşap ve ahşap esaslı ürün kullanımının araştırılması," Yüksek Lisans Tezi, Fen Bilimleri Enstitüsü, Mimarlık Anabilim Dalı, Bursa Uludağ Üniversitesi, Bursa, 2017.

[9] Naval Facilities Engineering Command, "Wood protection. Chapter 2. Wood as a construction material," 2-1/ 28, 1990. [Online]. Available: https://www.wbdg.org/FFC/NAVFAC/OPER/mo312.pdf

[10] A. Y. Bozkurt, Y. Göker, and N. Erdin, Emprenye Tekniği. İstanbul Üniversitesi Orman Fakültesi, Yayın No: 3779, 425s. İstanbul, 1993.

[11] M. K. Yalınkılıç, E. Baysal, and Z. Demirci, "Bazı Borlu Bileşiklerin Ve Su İtici Maddelerin Kızılçam Odununun Higroskopisitesi Üzerine Etkileri," *Pamukkale Üniversitesi Mühendislik Bilimleri Dergisi*, vol. 1, no. 3, pp. 161-168, 1995.

[12] E. Baysal, H. Peker, and M. Çolak, "Borlu Bileşikler ve Su İtici Maddelerin Cennet Ağacı Odununun Fiziksel Özellikleri Üzerine Etkileri," *Erciyes Üniversitesi Fen Bilimleri Enstitüsü Fen Bilimleri Dergisi*, vol. 20, no. 1, pp. 55-65, 2004.

[13] E. Baysal, H. Peker, and M. Çolak, "Çeşitli Emprenye Maddeleri ile Muamele Edilen Sarıçam (Pinus sylvestris L.) Odununda Retensiyon ve Higroskopisite Miktarları," *Erciyes Üniversitesi Fen Bilimleri Enstitüsü Fen Bilimleri Dergisi*, vol. 21, no. 1, pp. 166-179, 2005.

[14] G. Köse Demirel and A. Temiz, "Alkil keten dimer / borik asit kombinasyonları ile emprenye edilen sarıçam (Pinus sylvestris L.) örneklerinin boyutsal kararlılığı ve mekanik özellikleri," *Ormancılık Araştırma Dergisi*, vol. 9, Özel Sayı, pp. 142-147, 2022. [Online]. Available: https://doi.org/10.17568/ogmoad.1094444

[15] H. Pelit, M. Korkmaz, and M. Budakçı, "Farklı Ahşap Malzemelerin Bazı Fiziksel Özelliklerine Su İtici Maddelerin Etkileri," *İleri Teknoloji Bilimleri Dergisi*, vol. 6, no. 3, pp. 1027-1036, 2017.

[16] A. Var, E. Öktem, and Ü. Yıldız, "Kuru Sıcaklığın Kolofan İle Emprenye Edilmiş Ahşap Malzemenin Makroskopik Özellikleri Üzerine Etkisi," *Turkish Journal of Forestry*, vol. 1, no. 1, pp. 75-86, 2000. [Online]. Available: https://doi.org/10.18182/tjf.07646

[17] A. Var, "Ahşap Malzemede Su Alımının Parafin Vaks / Bezir Yağı Karışımıyla Azaltılması," *Turkish Journal of Forestry*, vol. 2, no. 1, pp. 97-110, 2001. [Online]. Available: https://doi.org/10.18182/tjf.30704

[18] H. Tan, M. Özbayram, H. Peker, and Ü. C. Yıldız, "Effects of Some Boron Compounds on the Leachabılıty of Eucalyptus (Eucalyptus camaldulensis Dehn.) WOOD," *Artvin Çoruh Üniversitesi Orman Fakültesi Dergisi*, vol. 4, no. 1, pp. 127-136, 2003.

[19] S. Kızılırmak and D. Aydemir, "Çeşitli Nano Partiküllerle Emprenyelenmiş Isıl İşlemli Ahşap Malzemelerin Bazı Özellikleri," *Bartın Orman Fakültesi Dergisi*, vol. 21, no. 3, pp. 722-730, 2019.

[20] A. A. Var and A. Yalçındağ, "Jeotermal kaynak sularının ahşabın hacimsel daralma ve genişleme özelliklerine karşı önleyici etkinliği," *Turkish Journal of Forestry*, vol. 22, no. 4, pp. 444-448, 2021. [Online]. Available: https://doi.org/10.18182/tjf.962675

[21] A. A. Var and İ. Kardaş, "Kütahya-Simav jeotermal sularıyla emprenyeli çam odunlarının çekme ve şişme özellikleri ile kullanım yeri stabilitesi," *Turkish Journal of Forestry*, vol. 18, no. 1, pp. 57-62, 2017. [Online]. Available: https://doi.org/10.18182/tjf.308993

[22] B. Öztürk and M. Atar, "Ahşap Lavabo ve Küvetlerde Boyutsal Kararlılık Tasarımına Emprenye İşleminin Etkisi," *Politeknik Dergisi*, vol. 26, no. 1, pp. 477-485, 2023. [Online]. Available: https://doi.org/10.2339/politeknik.1256422

[23] A. Var, "Borlu Madde Katılım Oranının Yongalevhanın Fiziksel Özelliklerine Etkileri," *Süleyman Demirel Üniversitesi Fen Bilimleri Enstitüsü Dergisi*, vol. 14, no. 3, pp. 235-245, 2010. [Online]. Available: https://doi.org/10.19113/sdufbed.71138

[24] H. Ş. Kol, A. Özçifçi, and S. Altun, "Üre Formaldehit ve Fenol Formaldehit Tutkalı ile Üretilen Lamine Ağaç Malzemelerin Isı İletkenliği Katsayısı Üzerine Emprenye Maddelerinin Etkileri," *Kastamonu University Journal of Forestry Faculty*, vol. 8, no. 2, pp. 125-130, 2008.

[25] A. Demir and İ. Aydın, "Yangın geciktirici kimyasallarla emprenye edilmiş kontrplakların en iyi ısı iletim özellikleri için optimum çözelti konsantrasyonunun yapay sinir ağları ile belirlenmesi," *Artvin Çoruh Üniversitesi Orman Fakültesi Dergisi*, vol. 22, no. 2, pp. 161-169, 2021. [Online]. Available: https://doi.org/10.17474/artvinofd.896585

[26] A. Var, "Parafinle Emprenye Edilen Ahşabın Makroskopik Özellikleri Üzerine Kuru Sıcaklığın Etkisi," *Turkish Journal of Forestry*, vol. 4, no. 2, pp. 61-68, 2003. [Online]. Available: https://doi.org/10.18182/tjf.60356

[27] M. Özalp and H. Hafızoğlu, "Su Soğutma Kulelerinde Kullanılan Karaçam Örneklerinde Fiziksel ve Mekanik Özelliklerde Meydana Gelen Değişimin İncelenmesi," *Dumlupınar Üniversitesi Fen Bilimleri Enstitüsü Dergisi*, no. 017, pp. 129-138, 2008.

[28] O. Özgenç, Ü. Yıldız, and S. YILDIZ, "Odun Yüzeylerinin Bazı Yeni Nesil Emprenye Maddeleri ve Üst Yüzey İşlemler ile Açık Hava Etkilerine Karşı Korunması," *Artvin Çoruh Üniversitesi Orman Fakültesi Dergisi*, vol. 14, no. 2, pp. 203-215, 2013.

[29] C. Söğütlü and N. Döngel, "Emprenye İşleminin Ağaç Malzeme Yüzey Pürüzlülüğü ve Renk Değişimine Etkisi," *Politeknik Dergisi*, vol. 12, no. 3, pp. 179-184, 2009.

[30] H. İ. Kesik, H. Keskin, F. Temel, and Y. Öztürk, "Vacsol Aqua ile Emprenye Edilmiş Bazı Ağaç Malzemelerin Yüzey Pürüzlülüğü ve Yapışma Direnç Özellikleri," *Kastamonu University Journal of Forestry Faculty*, vol. 16, no. 1, 2016. [Online]. Available: https://doi.org/10.17475/kujff.75845

[31] H. Öztürk, "Ahşap Emprenyesi Üzerine Yapılan Çalışmaların Analizi," Yüksek Lisans Tezi, Fen Bilimleri Enstitüsü, Mimarlık Anabilim Dalı, Bursa Uludağ Üniversitesi, Bursa, 2024.

Düzce University Journal of Science & Technology

Research Article

Adding Value to Outdoor Space with Modular Bird Houses Approach

Hüseyin Samet AŞIKKUTLU [a,*], Latif Gürkan KAYA [a], Betül Halime UZUNAY [b]

[a] *Department of Landscape Architecture, Faculty of Engineering and Architecture, Burdur Mehmet Akif Ersoy University, Burdur, TÜRKİYE*

[b] *Interior Design Program, Department of Design, Technical Sciences Vocational School, Burdur Mehmet Akif Ersoy University, Burdur, TÜRKİYE*

** Corresponding author's e-mail address: sasikkutlu@mehmetakif.edu.tr*

DOI: 10.29130/dubited.1508605

ABSTRACT

The aim of the study is to reveal the cultural values of bird houses used on the facades of buildings as a traditional approach and current design approaches for their use today. For this purpose, modular bird house designs that can be used in outdoor spaces were developed and the visual situation in the areas where they can be used was analyzed with the visuals prepared. As a result, with the use of modular bird house designs developed within the scope of the study, it will be possible to develop ecosystems for bird species in residential areas and open-green areas.

Keywords: *Bird house, Modular bird house, Outdoor, Space*

Modüler Kuş Evleri Yaklaşımı ile Dış Mekâna Değer Katılması

Öz

Çalışmanın amacı, geleneksel bir yaklaşım olarak yapıların dış cephelerinde kullanılan kuş evlerinin kültürel değerlerinin ve günümüzde kullanımına yönelik güncel tasarım yaklaşımlarının ortaya konulmasıdır. Bu amaç doğrultusunda dış mekânlarda kullanılabilecek modüler kuş evi tasarımları geliştirilmiş ve hazırlanan görseller ile kullanılabileceği alanlardaki görsel durum analiz edilmiştir. Sonuç olarak, çalışma kapsamında geliştirilen modüler kuş evi tasarımlarının kullanılması ile dış mekânların kimlik kazanması sağlanmakla birlikte yapılaşma alanları ve açık-yeşil alanlarda kuş türleri için ekosistemlerin geliştirilmesi mümkün olabilecektir.

Anahtar Kelimeler: *Kuş evi, Modüler kuş evi, Dış mekân, Mekân*

Received: 01/07/2024, Revised: 10/08/2024, Accepted: 28/08/2024

I. INTRODUCTION

The word tradition is defined as deep-rooted habits that can be passed from one generation to another and that turn into a pattern of behavior as a result of this hand-over-hand situation that lasts for generations. The origin of the word tradition comes from the Latin word "tradere" and its English equivalent is "tradition" and its Arabic equivalent is "an'ane" [1]. The concept of tradition, which includes a wide range of human behaviors, can only be maintained due to habits [2] and is a current issue due to the attitude of the modern age [3]. Traditions express a temporality based on iterations. One way of organizing the future is through the past, and the orientation towards the past is inherent to tradition. Traditions are a routine because of their slow pace of change. However, this gives the tradition a comfortable and reassuring quality [4]. It is almost impossible to know the founding dates or founders of traditions. Each of them emerged at some stage of the historical process, served mankind in different fields, and continues to serve today. In the current period, there are traditions in many fields, the first examples that come to mind are the tradition of art, the tradition of religion, the tradition of politics (state tradition), the tradition of literature and the tradition of science. The lifespan of these examples represents thousands of years of history [1].

Tradition is not customs and traditions as understood by almost everyone, but a historical-cultural heritage in its entirety, including customs and traditions [5]. In this context, it is possible to state that it is natural for traditions that constitute culture to be formed as a result of interactions with other areas of life and to be transferred from the past to the present by transforming and changing [6].

When we look at the historical process, animals have left their mark on people's lives, sometimes because they are aesthetically evaluated and sometimes because they enjoy their care. In this context, birds, one of the most important creatures from the past to the present, have been used in the art branches of different cultures. For example, the bird theme has taken place in many fields such as architecture, painting, sculpture, literature, fashion, music and cinema. In the historical process, birds were given importance in Turkish societies because they were believed to bring good luck. Especially because they can fly, they were perceived as having a special power and therefore they were considered sacred [7].

Birds are known as creatures that can build their nests when left to their own nature. However, not only birds but all living creatures and their habitats can be harmed in the environment we use in common. Birds, which were one of the expressions of the sense of nature for people before the industrialization period, could not find a place for themselves in modern cities after the industrialization period. Therefore, it is possible to state that people's relationship with nature was more sincere before the industrialization period. In this sense, looking at Ottoman society as an example, it is possible to find hospitals, houses and similar structures built with many living creatures in mind. In particular, although it became a duty to protect birds with a hollow or hole to shelter them, over time this became a passion in the Ottoman Empire. Thus, bird holes turned into bird houses [8].

A. HISTORY OF BIRD HOUSES

In Turkish architectural art, bird houses are considered as a masterpiece of art. The approach of decorating the facades of buildings with bird houses started in the 16th century with the Ottoman architecture of the classical period, developed towards the end of the 19th century and became a very important detail element of national architecture [9]. When we look at the Ottoman period, it is seen that it was very rich in terms of such structures and they were built on the exterior surfaces of buildings such as mosques, barracks, madrasahs, inns, libraries, tombs, bridges, schools and residences built after 1375. These architectural elements were not only a nest for birds, but also an ornament for their location. In terms of their architectural compositions and construction styles, bird houses can be categorized into two groups: nests carved into stone or masonry or small-sized architectural designs made with different techniques and materials in the form of high relief mounted on masonry. The first group of bird houses are cells formed with bricks placed in different directions or eyes carved into the

surface of the stone wall, the entrance to which is provided by small arches. The second group of bird houses, on the other hand, were created as architectural models that were placed on a console positioned between the wall flesh or connected to iron rods coming from inside the wall [10]. Regarding the first group of bird houses, an image of the bird house in the outbuildings of the Tur-i Sina Church (Figure 1) and an image of the bird house in the Selimiye Mosque (Figure 2) were presented for the second group of bird houses.

Figure 1. *Image of the bird house in the outbuildings of the Tur-i Sina Church, İstanbul [11].*

Figure 2. *Image of the bird house in Selimiye Mosque, İstanbul [12].*

It is possible to encounter bird houses, which are given names such as sparrow palace, bird pavilion, bird house, bird exchange by researchers, in many settlements in Anatolia and Rumelia, especially in İstanbul [13]. Figure 3 presents image of the bird house on the Büyükçekmece Bridge in İstanbul.

Figure 3. *Image of the bird house at Büyükçekmece Bridge, İstanbul [14].*

There is a bird house carved out of stone on the north-facing part of the buttress supporting the eastern wall of the Second Bayezid Mosque in Amasya. The central part of the bird house has a bay window and is projected out with two consoles, and an entrance opening was created to the east and west. On the facades of the protruding part, there are two windows at the bottom and two pointed arched deaf windows at the top [15]. Figure 4 and Figure 5 presents images of the bird house in the Second Bayezid Mosque.

Figure 4. *Image of the bird house in the Second Bayezid Mosque, Amasya [15].*

Figure 5. *Another image of the bird house in the Second Bayezid Mosque, Amasya [16].*

The Ayazma Mosque is considered one of the richest collections of bird houses in İstanbul. Some of the seventeen bird houses in the Ayazma mosque, which can be called a bird house museum, are in partially good condition, while others are quite dilapidated. Especially, the bird house located on the west facade is distinguished from the others with its monumentality [10]. Figure 6 and Figure 7 presents images of the bird houses in Ayazma Mosque.

Figure 6. *Image of the bird house on the west facade of Ayazma Mosque, İstanbul [10].*

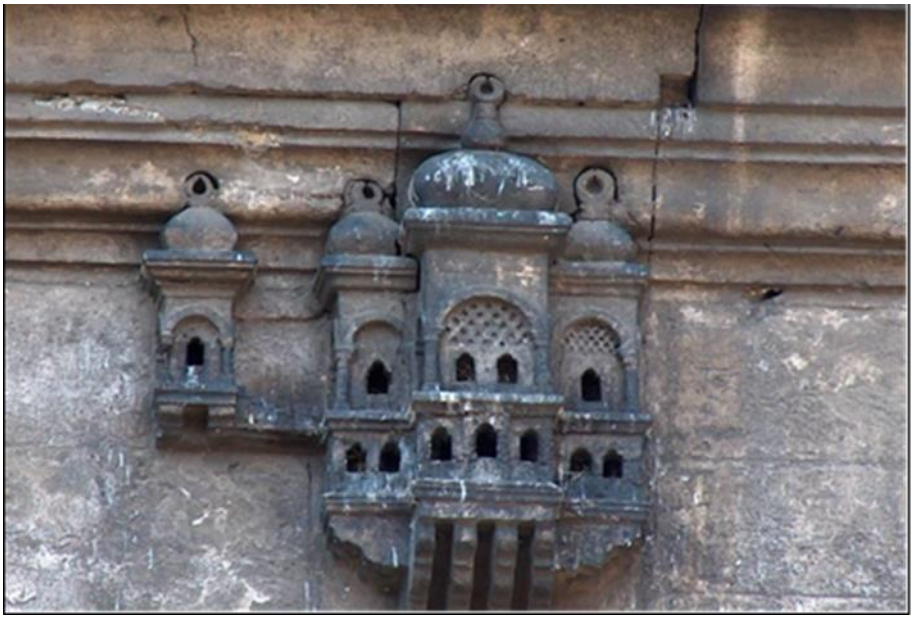

Figure 7. *Image of the bird house on the south facade of the Ayazma Mosque, İstanbul [10].*

Sulu Inn in Tokat is a building with a bird house. Built of brick, the bird house is arranged on a cantilever with two floors. However, the upper cover and part of the front part have not survived to the present day [13]. Figure 8 presents image of the bird house on the entrance facade of Sulu Inn.

Figure 8. *Image of the bird house on the entrance facade of Sulu Inn, Tokat [13].*

B. BIRD HOUSE APPROACHES TODAY

With the technology developed in recent years, bird houses can be made of concrete, wood, stone (marble, molded stone), plastic and ceramic materials. However, metal material is not a suitable material for use because it conducts heat and creates danger for birds in cold or hot weather [7]. Bird houses may face breakage and crumbling due to carelessness and lack of maintenance. For example, some wooden bird houses applied on the facades of wooden villas have not survived to the present day due to fire, weather conditions and lack of maintenance. From this point of view, it is possible to state

that the use of ceramics in bird houses is appropriate due to its ease of shaping and gaining strength by firing [17].

Examples of bird houses built today show that "S Brick" is suitable for swifts and other cavity-nesting birds without compromising the integrity or appearance of the building. The "S Brick", which takes up as much space as a single brick, is installed as part of the standard construction process. A plywood nest form is placed on its floor [18]. Figure 9 presents image of the bird houses called "S Brick".

Figure 9. *Image of the bird houses called "S Brick" [18].*

The box-shaped "Schwegler Lightweight Swift Box Type 1A" is an ideal bird house for incorporation into thermal insulation systems in external walls. The entrance of the bird house is circular and can be mounted flush with the wall surface. However, this bird house should be located on the sheltered facade of the building, at least 5 meters above the ground and under or near the roof. The dimensions of the product, made of wood and concrete, are 340mm (Width) x 135mm (Height) x 150mm (Depth) and weighs approximately 2.7 kilograms [19]. Figure 10 presents image of the bird house called "Schwegler Lightweight Swift Box Type 1A".

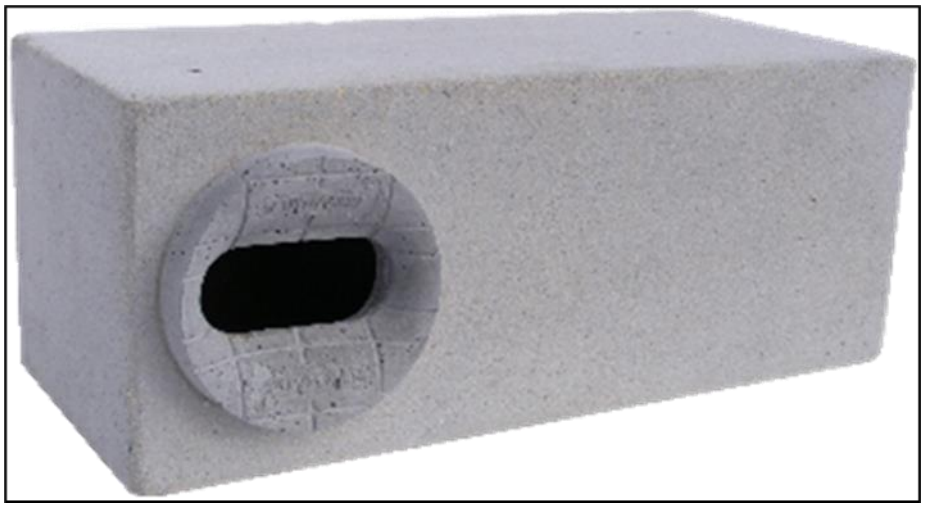

Figure 10. *Image of the bird house called "Schwegler Lightweight Swift Box Type Type 1A" [19].*

Another design, "Bird Bricks", is a bird house approach developed in response to the fact that birds living in cities are dependent on the buildings where people live and seek places to build their nests. "Bird Bricks" can be applied to any kind of brick building starting from 2 meters in height [20]. Figure 11 presents image of the bird house called "Bird Bricks".

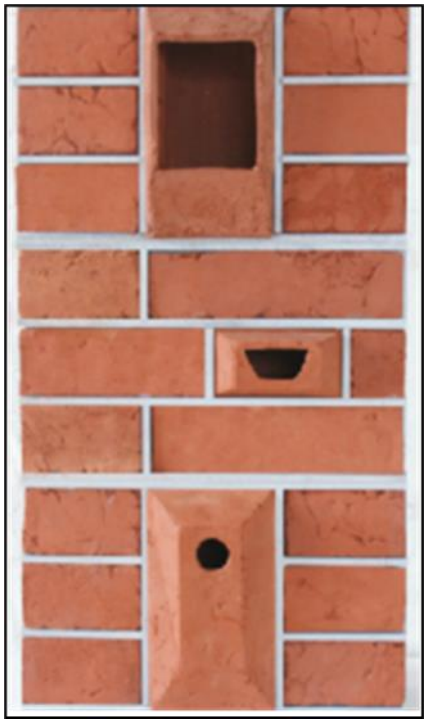

Figure 11. *Image of the bird house called "Bird Bricks" [20].*

"Brick Habitats" is a bird house design based on the placement on the walls of houses. In this design, an approach that aims to host wildlife in urban and residential areas is adopted [21]. Figure 12 presents image of the bird house called "Brick Habitats".

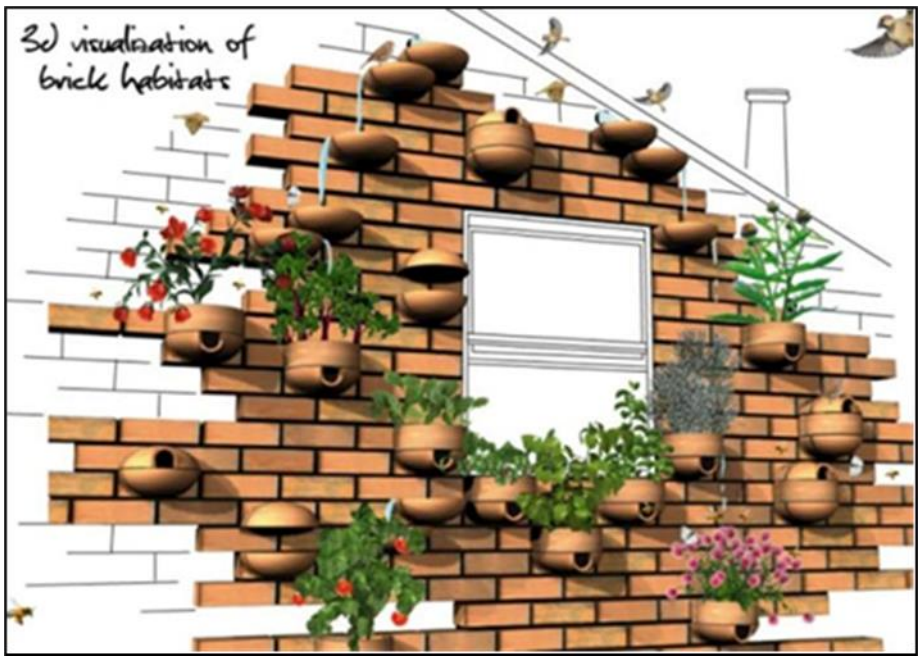

Figure 12. *Image of the bird house called "Brick Habitats" [21].*

The "Brick Habitats" design consists of three different types of special bricks. Growing areas, habitats and forage areas can be used individually or in combination for the flora and fauna to be supported. The bowl-shaped pieces can be placed upright or upside down. A brick with a ring-shaped hole on it can be used as a planter [21]. Figure 13 presents image of the bird house called "Brick Habitats".

Figure 13. *Image of special bricks developed for bird houses called "Brick Habitats" [21].*

"Dziupla", a bird house design for songbirds that can be mounted on walls and trees in the city, can provide various spaces on the walls of buildings with the approach offered by its shape. "Dziupla", which can be made of plywood and pine boards, can be considered as an alternative approach compared to typical bird houses [22]. Figure 14 presents image of the bird house called "Dziupla".

Figure 14. *Image of the bird house called "Dziupla" [22].*

The aim of this study is to draw attention to bird houses, which have been lost in the historical process and have a traditional value, and also to reveal modular bird house designs that will add meaning to outdoor designs today.

II. MATERIALS AND METHODS

The material of the study consists of studies published in national and international literature on bird houses, internet resources, AutoCAD, 3ds Max and Adobe PhotoShop programs.

Within the scope of the study, studies published in national and international literature and internet resources were examined. In line with these examinations, technical drawings of bird house designs were made in AutoCAD program, and then their 3D models were created through 3ds Max program. Finally, the 3D modeled bird houses were placed on the architectural structures and trees using Adobe PhotoShop program and photomontage method. The method flow chart presented in Figure 15 shows the stages followed in the preparation of the study.

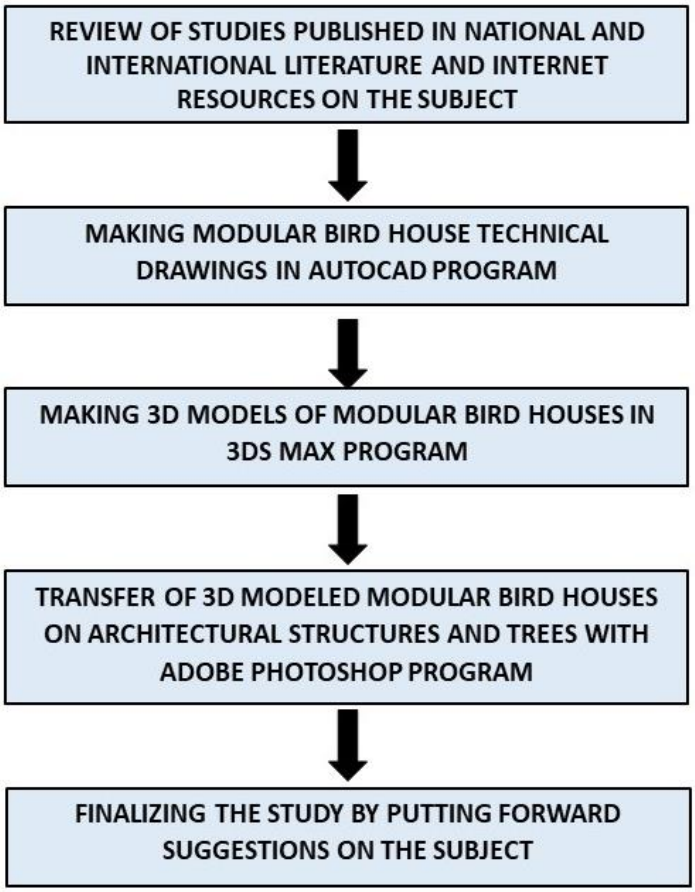

Figure 15. *Method flow chart.*

III. RESULTS AND DISCUSSION

"Schwegler Lightweight Swift Box Type 1A" bird house dimensions (340mm (Width) x 135mm (Height) x 150mm (Depth)) specified in URL-2 [19] were taken as reference in order to create a modular bird house design that can be used in many places in accordance with today. Figure 16

presents the technical drawing details of the modular bird houses created in line with the relevant source.

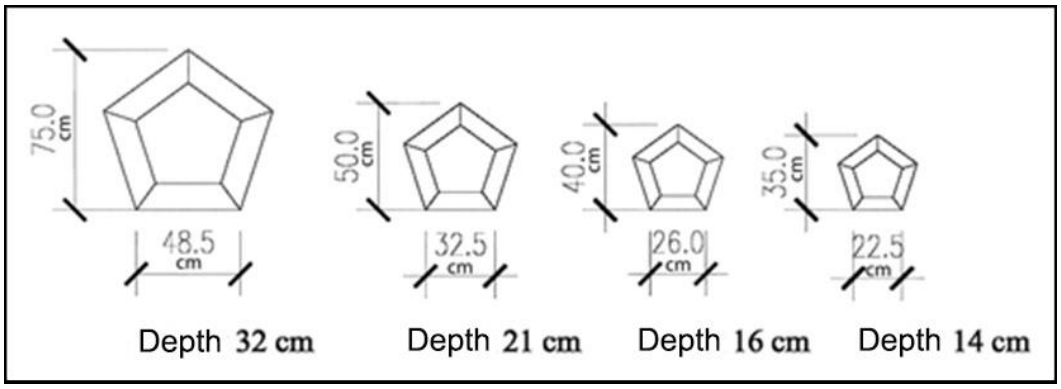

Figure 16. *Technical drawing details of the modular bird house design.*

It is possible to use pentagonal modular bird houses of four different sizes as flower pots by creating pentagonal modules between them (Figure 17).

Figure 17. *3D visualization of pentagonal modular bird houses.*

It is possible to create various combinations by assembling the pentagonal modular bird houses in a straight line (Figure 18) or in a staggered shape (Figure 19).

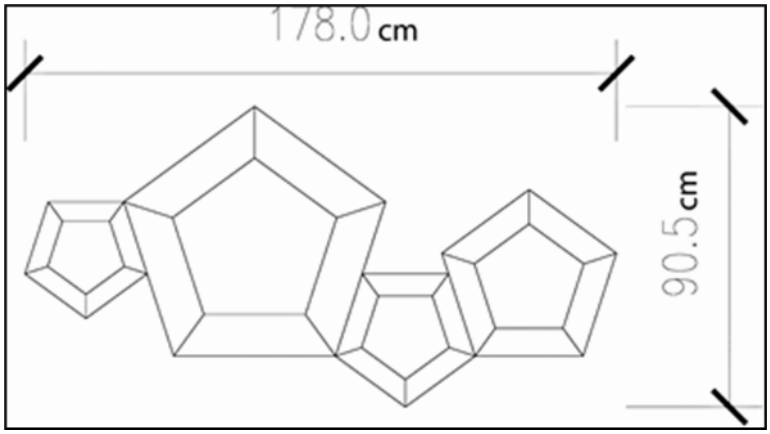

Figure 18. *Image of the use of pentagonal modular bird houses in flat form.*

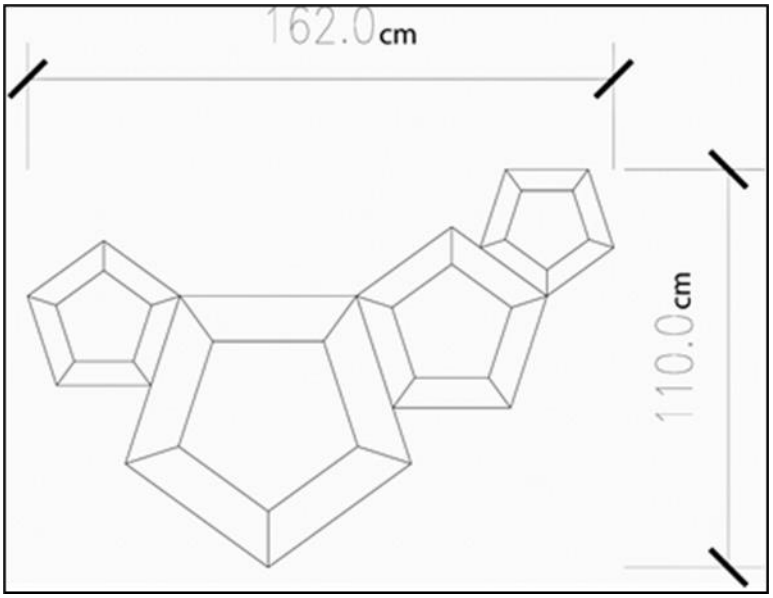

Figure 19. *Image of the use of pentagonal modular bird houses in a staggered form.*

Depending on the creativity and imagination of the users, modular bird houses can be designed in different combinations by using the desired number of modules and positioning these modules independently from each other. Figure 20 presents image of modular bird houses that can be used on the facade of a historical building.

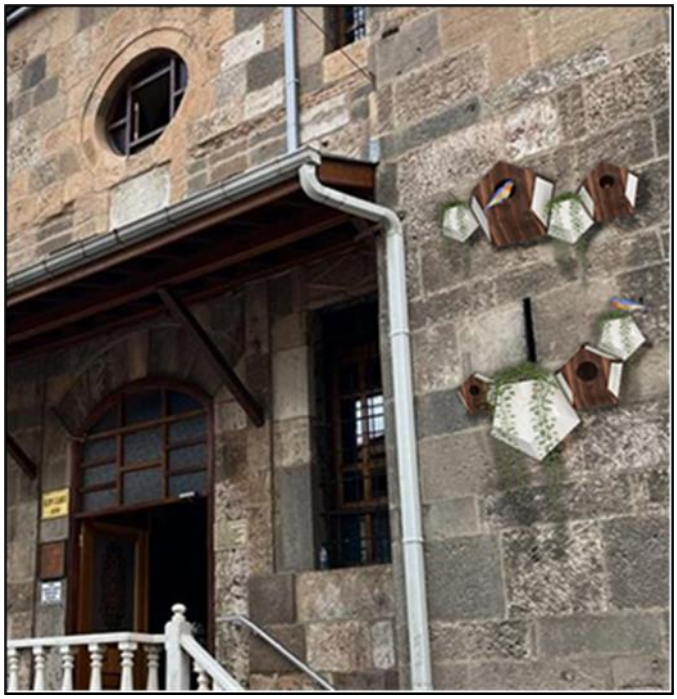

Figure 20. *Image of modular bird houses that can be used on the facade of a historic building.*

Since modular bird houses can be placed in different sizes and individually, they can also be used on cylindrical surfaces such as tree trunks (Figure 21).

Figure 21. *Image of modular bird houses used in tree trunks.*

The sample bird house modules presented in Figure 20 and Figure 21 can be used on exterior facades of modern and historical buildings, vertical gardens, tree trunks, retaining and garden walls, etc. in the form and size desired by the users.

IV. CONCLUSION

This study focuses on revealing the traditional bird house culture and developing modular bird house designs that can be used outdoors today. Suggestions regarding the benefits that the modular bird house designs put forward within the scope of the study will provide with their use in outdoor spaces are given below:

- In urban areas, it is possible to create spaces where different and more bird species can live by supporting natural life. This can be considered as a factor that will bring natural quality to the forefront with the enrichment of fauna in cities.
- A more aesthetic visual effect will be achieved on the facades of historical and modern buildings, and the buildings will be integrated with nature.
- It will be possible to increase the natural effect by enriching the fauna not only in built-up areas but also in parks and gardens. Therefore, this will be a motivational factor for many users by providing a natural effect in parks and gardens, which are an important value for urban and non-urban recreational activities.
- Structurally, a traditional approach will be maintained and promoted. This is an approach that supports the preservation and development of the historical fabric in the areas where the buildings are located, and may be an approach that will positively affect tourism.
- As an artistic approach, it will be possible to contribute to the outdoor space. Thus, an imaginary effect can be created in spaces such as residential areas, parks and gardens.

As a result, it can be stated that modular bird houses designed to be used in outdoor spaces within the scope of the study will be an effective element in gaining identity for outdoor spaces as well as maintaining a traditional approach. In addition, with the use of these bird houses, it will not only be possible to create spaces for bird species to live, but also to develop ecosystems for bird species in both built-up areas and open-green areas. Therefore, it is important to encourage the use of bird houses by adopting new design approaches.

V. REFERENCES

[1] S. Uğurlu, "Gelenek ve kimlik ilişkisi," Doktora tezi, Sosyal Bilimler Enstitüsü, Sakarya Üniversitesi, Sakarya, Türkiye, 2010.

[2] R. Sweterlitsch, "Gelenek," (Çev.: Aslı Büyükokutan Töret), *Milli Folklor,* c. 28, s. 110, ss. 121-124, 2016.

[3] M. Vural, "Gelenek ve dinlerin aşkın birliği," *Doğu Batı*, c. 25, ss. 161-175, 2003.

[4] E. Güney, "Mimarlık gerçekleri ve mimarlık zamanın kavrayışı," Doktora tezi, Fen Bilimleri Enstitüsü, İstanbul Teknik Üniversitesi, İstanbul, Türkiye, 2003.

[5] T. Tatar, "Gelenek ve gelecek," *İstanbul Journal of Sociological Studies*, c. 26, ss. 199-215, 2011.

[6] N. Özdemir, "Geleneksel bilgi ve kültür ekonomisi," *Türk Dünyası İncelemeleri Dergisi*, c. 18, s. 1, ss. 1-28, 2018.

[7] M. Özçakı, "Türk kültüründe güvercinlik ve kuş evleri ve günümüze yansımaları," *Sanat ve Tasarım Dergisi*, c. 10, s. 2, ss. 238-261. 2020. http://dx.doi.org/10.20488/sanattasarim.876545

[8] H.N. Kuruçay ve E. Kuruçay, "Doğa ve insan ilişkisinde kuş evleri," *Sanat ve Tasarım Dergisi*, c. 28, ss. 317-333, 2021. http://dx.doi.org/10.18603/sanatvetasarim.1048704

[9] Ş. Edeer, "Tarihsel gelişimi içinde kuş figürünün plastik sanatlardaki yeri," Yüksek lisans tezi, Sosyal Bilimler Enstitüsü, Anadolu Üniversitesi, Eskişehir, Türkiye, 1992.

[10] D. İlkhan Söylemez, "Two samples of bird houses in the late Ottoman architecture: Ayazma and Selimiye Mosque," *Journal of Current Research on Social Sciences*, vol. 9 no. 4, pp. 41-58, 2019. http://dx.doi.org/10.26579/jocress.335

[11] F.Y. Köroğlu, (2022, 20 Eylül). *Tur-i Sina Kilisesi Müştemilatı Kuş Evleri* [Çevrimiçi]. Erişim:https://kulturenvanteri.com/en/yer/turisinakilisesimustemilatikusevleri/#17.1/41.033188/28.947428.

[12] N. Tak, (2019, 8 Mayıs). *Selimiye Camisi Kuş Evi* [Çevrimiçi]. Erişim: https://haberuskudar.com/tarihi-kus-evlerinin-pesinde-bir-gun

[13] E. Atak, "Tokat tarihi yapılarındaki kuşevleri," *The Journal of Academic Social Science Studies*, c. 59, ss. 323-342, 2017. http://dx.doi.org/10.9761/JASSS7238

[14] İ. Kıran. (2023, 23 Mart). *Büyükçekmece Köprüsü Kuş Evi* [Çevrimiçi]. Erişim: https://kulturenvanteri.com/tr/yer/buyukcekmece-koprusu kusevi/#17.1/41.021523/28.568447

[15] S. Atakan, "II. Bayezid dönemi cami ve mescidlerinde (Tokat-Amasya-Edirne-İstanbul) mimari süsleme programı," Yüksek lisans tezi, Sosyal Bilimler Enstitüsü, Mimar Sinan Güzel Sanatlar Üniversitesi, İstanbul, Türkiye, 2019.

[16] F. Tunç, "Amasya Osmanlı camilerinde bulunan taş bezemeler," Yüksek lisans tezi, Güzel Sanatlar Fakültesi, Geleneksel Türk El Sanatları Anasanat Dalı, Atatürk Üniversitesi, Erzurum, Türkiye, 2013.

[17] D. Onur Erman, Bird houses in Turkish culture and contemporary applications," *Procedia - Social and Behavioral Sciences*, vol. 122, pp. 306 – 311, 2014. http://dx.doi.org/10.1016/j.sbspro.2014.01.1345

[18] URL-1 (2024, 14 May). *"S Brick" bird house* [Online]. Available: https://www.actionforswifts.com

[19] URL-2 (2024, 14 May). *"Schwegler Lightweight Swift Box Type 1A" bird house* [Online]. Available: https://www.nhbs.com/schwegler-lightweight-swift-box-type-1a

[20] URL-3 (2024, 14 May). *"Bird Bricks" bird house* [Online]. Available: https://www.moreinspiration.com/article/5384/birdbricks?f=improve%20storage%20

[21] URL-4 (2024, 16 May). *"Brick Habitats" bird house* [Online]. Available: https://dornob.com/nature-loving-bricks-bring-wildlife-straight-to-your-walls/

[22] URL-5 (2024, 16 May). *"Dziupla" bird house* [Online]. Available: https://lodzdesign.com/makeme/katalog/dziupla/

Düzce University
Journal of Science & Technology

Research Article

Theoretical Investigation of the Molecular Properties of the Fluoroaniline and Fluoroanisole Isomers

Yavuz EKİNCİOĞLU [a,*], Abdullah KEPCEOĞLU [b]

[a] *Bayburt University, Department of Opticianry, Bayburt, TÜRKİYE*
[b] *Koç University Surface Science and Technology Center (KUYTAM), İstanbul, TÜRKİYE*
* *Corresponding author's e-mail address: yekincioglu@bayburt.edu.tr*
DOI: 10.29130/dubited.1396459

ABSTRACT

This research paper aims to analyse the molecular properties of fluoroaniline and fluoroanisole isomers through a range of theoretical methods. These methods include optimization of molecular structures, conformational analysis, and calculation of nonlinear optics (NLO) properties, frontier molecular orbital (HOMO-1, HOMO/SOMO, LUMO, LUMO+1) energies, chemical reactivity descriptors (ionization potentials - vertical and adiabatic, electron affinity, chemical hardness, softness, and electronegativity), molecular electrostatic potential (MEP), natural bonding orbital (NBO), and UV-Vis spectra. To achieve this, the density functional theory method with B3LYP functional and 6-311++G (d, p) basis set were used for the calculations. Additionally, the research examines the vertical and adiabatic ionization energy parameters of the molecules by constructing singly charged cation radicals. The outcome of this study provides valuable insights into the molecular properties of fluoroaniline and fluoroanisole isomers, which can be useful in the production of pharmaceuticals and agrochemicals.

Keywords: *Isomers, FMOs, NLO, MEP, TD-DFT, Ionization energy.*

Floroanilin ve Floroanizol İzomerlerin Moleküler Özelliklerinin Teorik İncelenmesi

Öz

Bu çalışmada, floranilin ve fluoroanisol izomerlerinin moleküler özelliklerini çeşitli teorik yöntemlerle analiz edilmesi amaçlamaktadır. Bu yöntemler arasında moleküler yapıların optimizasyonu, konformasyon analizi ve doğrusal olmayan optik (NLO) özelliklerin, sınır moleküler orbital (HOMO-1, HOMO/SOMO, LUMO, LUMO+1) enerjilerinin, kimyasal reaktivite tanımlayıcılarının (iyonlaşma potansiyelleri - dikey ve adyabatik, elektron afinitesi, kimyasal sertlik, yumuşaklık ve elektronegatiflik), moleküler elektrostatik potansiyel (MEP), doğal bağ orbital (NBO) ve UV-Vis spektrumlarının hesaplanması bulunmaktadır. Bu hesaplamaları gerçekleştirmek için, yoğunluk fonksiyonel teorisi (YFT) yöntemi B3LYP fonksiyonu ve 6-311++G (d, p) baz seti kullanılmıştır. Ayrıca, araştırmada, moleküllerin dikey ve adyabatik iyonizasyon enerji parametrelerini tek yüklü katyon radikalleri oluşturarak incelemektedir. Bu çalışmanın sonuçları, floroanilin ve floroanizol izomerlerinin moleküler özelliklerine dair değerli bilgiler sağlamaktadır ve bu bilgiler, ilaç ve tarım kimyasalları üretiminde faydalı olabilir.

Anahtar Kelimeler: *İzomerler, FMOs, NLO, MEP, TD-DFT, İyonlaşma Enerjisi*

Received: 27/11/2023, Revised: 05/12/2023, Accepted: 28/08/2024

I. INTRODUCTION

Fluoroanilines, namely 2-, 3-, and 4-fluoroaniline, or o-, m-, p-fluoroaniline, are commonly employed in synthesizing pesticides, plant growth regulators, and larger molecules. These chemicals may pose a risk to agricultural workers and other living organisms, prompting researchers to investigate their effects on the microsomal system. The 19F-NMR method was employed to explore the effects as mentioned earlier [1].

The impact of halogen atoms, such as F, Cl, and Br, bonded to the aniline molecule was examined in relation to the molecule's geometric structure and vibrational frequencies. The π-electrons of the aniline ring to which the halogens are attached were observed to be displaced, with the halogens contributing to this displacement. Moreover, it was determined that para-halogen-aniline molecules contributed less to these electron displacements compared to ortho- and meta-halogen aniline molecules [2].
In addition, the ground state vibrations of the p-fluoroaniline molecule in the IR region and far-IR regions were studied [3, 4].

UV absorption spectra (S1← S0 transitions) have also been studied for fluoraniline isomers, and it is reported that no results were observed for the change of molecular geometry between the ground state and the excited state [5]. In contrast, in another study investigating similar properties, the base (S0) and first excited singlet (S1) energy levels of the p-fluoraniline (4-fluoraniline) molecule were investigated both experimentally and ab-initio. The S0←S1 transitions and the related vibrational bands have been investigated both experimentally by UV-fluorescence excitation and comparatively by DFT methods. It was observed that the minimum potential of the amino group attached to the benzene ring varies between -20 and 20 for the S1 level depending on the pyramidal structure and dihedral angle [6]. Similarly, the photoelectron spectra of fluoronitrobenzene isomers were analyzed using He(I) and He(II) photoelectron spectroscopy and ab initio methods [7].

Resonance two-photon ionization studies (R2PI) determined that the 0-0 band transition for p-fluoraniline is at 306.25nm [8]. Similarly, the 0-0 transition for p-fluoraniline was experimentally observed at 306.20 nm. Additionally, all levels spanning from 306.20 nm down to 287.34 nm were discerned [9].

Adiabatic ionization energy values for the cationic ground state of the p-fluoraniline molecule were experimentally determined using mass-analyzed threshold ionization (MATI) and two-color resonant two-photon ionization (2CR2PI) methods, and ionization energies and vibrational frequencies of the ground state and cationic state were also calculated using the DFT method. They were measured experimentally at 62543 cm^{-1} (7.754 eV) with MATI and 62550 cm-1 (7.755 nm) with 2CR2PI. In calculations using the DFT method and B3LYP/6-311+G** basis sets, this value was calculated as 61084 cm^{-1} (7.573 eV), a difference of 2.3% [10]. A similar study was performed for o-fluoraniline and the ionization energy was found to be 63644±5 cm^{-1} (7.8904±0.0006eV) [11]. For the o-fluoraniline molecule, this value was found to be 64159±5 cm^{-1} (7.9542±0.0006 eV) [12].

Proton affinities of various MALDI matrices were determined by electrospray ionization (EI) employing the kinetic method. P-fluoraniline and aniline-derived chemicals served as a reference compounds for this purpose [13].

Ionization of fluoraniline isomers utilizing the atmospheric-pressure photoionization-ion mobility spectrometry-mass spectrometry (APPI-IMS-MS) method (ionization was performed with a krypton lamp) revealed the presence of product ions M●+ (100%), (M+18)●+ (79%). Additionally peaks indicative of (water molecule + parent molecule) were predominantly observed in the mass spectrum [14].

Due to advancements in computer technology and quantum chemistry, molecular modeling is becoming more prevalent. Parallel to these improvements, ab initio methods play an important role in explaining

experimental and theoretical findings [15]. One of the most prominent of these methods is density functional theory (DFT), which uses a quantum mechanical modeling methodology to investigate the electronic structure of molecules, their spectroscopic properties, and energy values, all at a low cost [16, 17]. Furthermore, DFT has proven to be an effective research tool for validating or characterizing experimental results [18].

In this investigation, Floraniline, a chemical compound manifesting three distinct isomeric configurations, constitutes the subject under scrutiny. The molecular composition and associated physical and chemical attributes of the respective Floraniline isomers are delineated in Table 1, retrieved from the NIST database.

Table 1. *Structure and properties of fluoroaniline isomers*

Isomer	**o-Fluoroaniline (2-Fluoroaniline)**	**m-Fluoroaniline (3-Fluoroaniline)**	**p-Fluoroaniline (4-Fluoroaniline)**
Structure	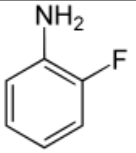	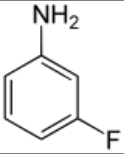	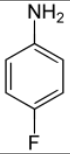
CAS	348-54-9	372-19-0	371-40-4
Mp °C	-35 °C	-5 °C	-35 °C
Bp °C	182–183 °C	186.3±13.0 °C	182–183 °C
Density g/mL	1.151	1.156	1.173
Refractive Index	1.544	1.542	1.539
Ionization Energy (eV)	8.50 [19] 8.18 [20, 21]	8.32 [21] 8.33 [20]	7.9 [22] 8.18 [20, 21]

Table 1 delineates the physical properties of fluoraniline isomers, present in a liquid state under ambient conditions, with boiling points approximately at 180°C. The ionization energies of ortho- and meta-isomers are close in proximity, whereas the para-fluoraniline molecule exhibits a diminished value. Anisole, with the molecular formula C_7H_8O, is a versatile molecule utilized in the production of various compounds, including pesticides, medicines, flavourings, and perfumes. The preparation of synthetic anethole, for instance, involves the use of anisole. In terms of reactivity, anisoles exhibit a greater electrophilic aromatic substitution rate than benzene. Furthermore, fluoroanisoles have found extensive application in the production of pharmaceuticals, agricultural tools, and fluorinated medical compounds. Of note, the 4-fluoroanisole isomer has been utilized in the synthesis of a thermally and chemically stable polymer that shows potential for use in optoelectronics, batteries, and sensors [23].

Isomers of molecules play a crucial role in delineating the physical properties associated with the molecular system. Fluoroanisole exhibits three distinct isomers, namely 2-, 3-, and 4-fluoroanisole, designated as o-, m-, and p-fluoroanisole (or ortho-, meta-, para-fluoroanisole). The conformer characteristics of fluoroanisoles have been studied many times in experimental and theoretical studies. Several research groups have studied the conformational properties of anisole molecules by using electron diffraction [24], microwave spectroscopy [25], and high-resolution spectroscopy [26] method experimentally, and ab-initio and DFT [27] computational approaches. The molecular geometry of 2-fluoroanisole has been specifically investigated using FT-IR spectroscopy and quantum chemical methods [25, 27].

The mass analysis threshold ionization spectra of anisole were performed by ionizing four vibrational states and as a result, the adiabatic ionization energies of these species were determined to be 8.23243± 0.00062 eV [28]. Similarly, the molecular properties of anisole in the ground state and the first excited state have been investigated using various spectroscopic techniques. As a result, the ionization energy of anisole is presented as 8.20 ± 0.05 eV.

Infrared absorption, Raman scattering, optical absorption, and thermal analysis were studied experimentally and with the DFT (3-21g*) basis set to assess the vibrations and optical properties. Time-resolved photoluminescence (TR-PL) spectroscopy was used to evaluate both chloroform solutions and film states. The faster PL decays in the thin film are shown to result from both conformer structures and π-π stacking interactions among molecules [29].

The vibrational structure of 4-fluoroanisole in its first excited state was investigated by mass-selected resonance-enhanced two-photon ionization spectroscopy and the S1← S0 transition of 4-fluoroanisole was found to occur at 4.35792 eV. The vibrational frequencies and optimized molecular geometries of the ground state and cation ground state were determined by DFT calculations. The molecular structures and conformer properties of 2- and 4- fluoroanisole in the gas phase were investigated by electron diffraction techniques alongside quantum chemical calculations [30].

The cation spectra of 2-fluoroanisole and 4-fluoroanisole isomers were obtained using two-colour resonance two-photon mass analysis threshold ionization spectroscopic techniques. The adiabatic ionization energies of these structures were found to be 8.35083 ± 0.00062 eV and 8.23714 ± 0.00062 eV, respectively. Consequently, the positions of the F atom and the OCH_3 group are significantly impact the transition energies and molecular vibrations. The adiabatic ionization energies for the cis and trans states of the 3-fluoroanisole molecule were found to be 8.41444 ± 0.00062 eV and 8.46862 ± 0.00062 eV for the cis and trans states, respectively, using the same spectroscopic techniques. As a result, the localization of the F atom and the OCH_3 group plays a crucial role in influencing both transition energies and molecular vibrations [31].

The proton affinities of 2-, 3- and 4-fluoroanisole molecules were determined via Fourier transform ion cyclotron resonance (FT-ICR) mass spectra. The values obtained were 808 kJ mol^{-1} (2-fluoroanisole), 825 kJ mol^{-1} (3-fluoroanisole) and 795 kJ mol^{-1} (4-fluoroanisole). The experimental data were compared with the proton affinities calculated using ab-initio methods employing the G3, G3(MP2) and MP2(fc)/6-11G(2d,p)//HF/6-31G(d,p) basis sets. As a result of these comparisons, calculations with the G3(MP2) basis set gave the best evaluation in experimental and ab-initio calculations [32]. Comparisons of ionization and appearance potentials of m- and p-X doped anisoles [M - CH_3] and [M - CH_3O] revealed that their difference did not exceed approximately 0.20 eV [33].

The standard enthalpies of formation of the three isomers of the fluoroanisole molecule in the liquid phase were compared with experimental and theoretical calculations. As a result, they are ordered at positions 3 > 4 > 2 [34].

Molecular structure and conformer studies of 4-fluoroanisole and 3,4-difluoroanisole molecules were conducted employing diverse quantum chemical computation methods. It was determined that 4-fluoroanisole possesses solely a singular conformer [35].

The molecular structure and conformer analyses of 2-fluoroanisole were studied using diverse quantum chemical calculation methods. The impact of the fluorine atom introduction to anisole on its conformer and molecular structure were studied. In addition, stereochemical, specifically orbital interaction energies, were analyzed by natural bonding orbital (NBO) analysis [36].

Also, in the literature, jet-cooled laser-induced fluorescence (LIF) excitation, UV-UV cavity combustion and single vibrational level fluorescence (SVLF) spectra of 2-fluoroanisole were measured. The most intense lowest frequency band at 4.53931 eV was determined to mark the onset of the most stable trans conformer. The vibrational band analysis using B3LYP/cc-pVTZ and CIS/6-311G(d,p) levels was conducted via quantum chemical calculations [37].

The chemical under examination in this study is fluoroanisole, which comprises three distinct isomers. The molecular structure along with select physical and chemical properties of fluoroanisole isomers are detailed in Table.2, sourced from the NIST database.

Table 2. *Structure and properties of fluoroanisole isomers*

Isomer	**o-Fluoroanisole (2-Fluoroanisole)**	**m-Fluoroanisole (3-Fluoroanisole)**	**p-Fluoroanisole (4-Fluoroanisole)**
Structure	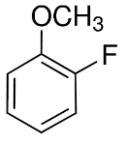	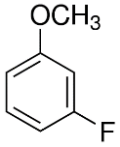	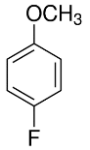
CAS	321-28-8	456-49-5	459-60-9
Mw (amu)	126.13	126.13	126.13
Mp °C	−39	-35	−45
Bp °C	154-155	158	157
Density g/mL	1.124	1.104	1.114
Ionization Energy (eV)	8.91 [38] 8.92 [39]	8.41 [40] 8.7 [33]	8.6 [33] 8.79 [38]

As seen in Table.2, fluoroanisole isomers are liquid at room temperature, and their boiling temperatures are approximately ~155 °C. The ionization energies of the o- and p- isomers are close to each other, with a lower value observed in the m-fluoroanisole molecule.

II. MATERIAL AND METHODS

The conformer analysis and theoretical calculations of various properties of Fluoroaniline and Fluoroanisole isomers were performed in this study. The Merck molecular force field (MMFF) in the molecular mechanic method was used to carry out the conformer analysis by the Spartan 08 package program [41]. Subsequently, the ground state geometries of each isomer were optimized in the gas phase using the functional hybrid Becke three-parameter [42] Lee–Yang–Parr exchange-correlation functional [43, 44] (B3LYP) and the 6- 311++G(d,p) basis set with the Gaussian09 program [45]. The B3LYP functional density functional theory method with the basis set 6-311++G(d,p) was chosen since it has previously demonstrated accuracy and dependability in investigations involving aniline and aniline derivatives [46-50]. The HOMO and LUMO energy levels, chemical reactivity descriptors, non-linear optical properties, molecular electrostatic potentials map (MEP-map), natural bond orbital analysis (NBO), thermodynamic properties, and UV-Vis spectra were calculated using the same level of theory. The GaussView 5.0 program was used to visualize the results, while the GaussSum program [51] was utilized to plot the UV-Vis spectra. The adiabatic and vertical ionization parameters were calculated by optimizing the most stable molecular conformational geometry and using the same molecular geometry as the neutrals, respectively.

III. RESULTS AND DISCUSSION

Conformational analysis constitutes a pivotal stage in determining the most energetically favorable configuration of a molecule. In this study, the Spartan 08 package program utilizing MMFF within molecular mechanic methods was employed for conducting conformational analysis [41]. The findings delineated singular conformer structures for each of the o-fluoroaniline, m-fluoroaniline, and p-fluoroaniline isomers (Figure 1), underscoring the robust stability of each isomer. The geometric configurations of these isomers are depicted in Figure 1, while the conformer energies and optimized energies are detailed in Table 3. Furthermore, the selected geometric parameters of the o-fluoroaniline, m-fluoroaniline, and p-fluoroaniline isomers are presented in Table 4.

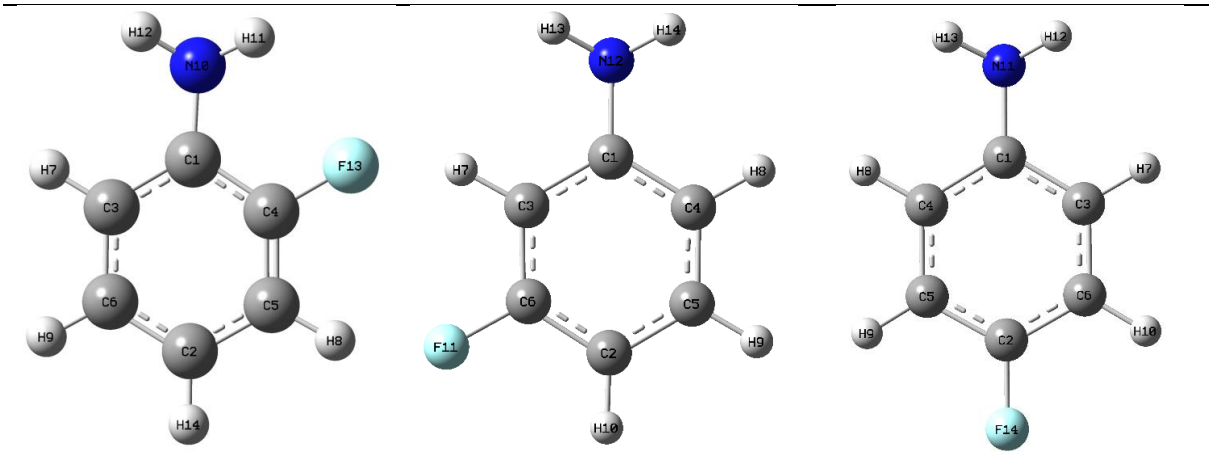

o-Fluoroaniline	m-Fluoroaniline	p-Fluoroaniline

Figure 1. *Possible conformers and the most stable structures of o-fluoroaniline, m-fluoroaniline, and p-fluoroaniline isomers*

Table 3. *The conformer energies and energies of optimized structures of o-fluoroaniline, m-fluoroaniline, and p-fluoroaniline isomers*

Fluoroaniline isomers	Conformer Energies (kJ/mol)	Optimized energies (Hartree)
***o*Fluoroaniline**	905.4682	-386.956300
***m*Fluoroaniline**	15.9827	-386.957352
***p*Fluoroaniline**	11.2923	-386.954731

Table 4. *The selected geometric parameters of o-fluoroaniline, m-fluoroaniline, and p-fluoroaniline isomers*

Parameters	*o*-Fluoroaniline	*m*-Fluoroaniline	*p*-Fluoroaniline	***Ref*** [52]
Bond lengths (Å)				
C1-C3	1.4019	1.4028	1.4024	
C1-C4	1.3987	1.4046	1.4024	
C1-N10	1.391	-	-	
C1-N12	-	1.3937		
C1-N11	-	-	1.4009	
C2-C5	1.3957	1.3951	1.3849	
C2-C6	1.3938	1.3855	1.3849	
C2-H14	1.0828	-	-	1.08
C2-H10	-	1.0817	-	
C3-H7	-	-	1.085	0.94
C2-F14	-	-	1.3616	
C6-F11	-	1.3586	-	
C4-F13	1.3662	-	-	
N10-H11	1.0092	-	-	0.86
N12-H13	-	1.0089	-	
N11-H13	-	-	1.0096	
N10-F13	2.72	-	-	2.68
H11-F13	2.45	-	-	2.36
C2-F13	3.64	-	-	3.22
H14-F13	4.52	-	-	2.52
C4-H8	-	-	1.08	0.98
C4-H8	-	-	3.634	3.570
C4-F14	-	-	4.50	2.70

C3-F14	-	-	3.634	3.605
H7-F14	-	-	4.50	2.73
C5-H9	-	-	1.08	0.93
C5-N11	-	-	3.711	3.559
H9-N11	-	-	4.59	2.68
Bond angle (◦)				
C1-N10-H11	115.5877	-	-	
C1-N12-H13	-	116.2156	-	
C1-N11-H13	-	-	115.326	
C1-N10-H12	115.8906	-	-	
C1-N12-H14	-	115.9535	-	
C1-N11-H12	-	-	115.3263	
C1-N10-C4	120.4733	-	-	
C1-N12-C3	-	120.3119	-	
C1-N11-C4	-	-	120.7199	
C1-C4-F13	117.1358	-	-	
C1-C3-H7	-	121.5045	-	
C1-C4-H8	-	-	119.6762	
C4-C5-F13	119.5111	-	-	
C3-C6-H7	-	119.5753	-	
C4-C5-H8	119.0692	-	119.4145	
C3-C6-F11	-	117.8707	-	
C4-C5-H9	-	-	121.1185	
C2-C5-H8	121.9277	-	-	
C2-C6-F11	-	118.787	-	
C2-C5-H9	-	-	119.8334	
C2-C5-H14	120.0012	-	-	
C2-C6-H10	-	120.4146	-	
C2-C5-F14	-	-	119.2012	
C2-C6-H14	120.7225	-	-	
C2-C5-H10	-	122.452	-	
C2-C6-F14	-	-	119.2019	
N10-H11-F13	100	-	-	96
C2-H14-F13	139	-	-	126
C4-H8-F14	-	-	138	150
C3-H7-F14	-	-	138	156
C5-H9-N11	-	-	140	157
Dihedral angle (◦)				
H11-N10-C1-C3	162.7948	-	-	
H13-N12-C1-C4	-	-158.8276	-	
H13-N11-C1-C3	-	-	-157.8406	
H11-N10-C1-C4	-20.162	-	-	
H13-N12-C1-C3	-	24.0235	-	
H13-N11-C1-C4	-	-	25.2674	
H12-N10-C1-C3	26.7605	-	-	
H14-N12-C1-C4	-	-23.0641	-	
H12-N11-C1-C3	-	-	-25.2758	
H12-N10-C1-C4	-156.1963	-	-	
H14-N12-C1-C3	-	159.787	-	
H12-N11-C1-C4	-	-	157.8322	
F13-C4-C1-N10	3.36	-	-	
F11-C6-C3-H7	-	-0.4627	-	
F14-C2-C5-H9	-	-	-0.0537	
F13-C4-C5-H8	-0.3328	-	-	
F11-C6-C3-C1	-	179.8568	-	

F14-C2-C6-H10	-	-	0.0537
F13-C4-C5-C2	179.4556	-	-
F11-C6-C2-C5	-	-179.9597	-
F14-C2-C6-C3	-	-	-179.9217

In this study, we contrasted the low-temperature crystal structures of p-fluoroaniline and o-fluoroaniline, as reported by Chopra, D. et al., outcomes derived from our research, detailed in Table 4. The obtained results showed a general agreement between the experimental and theoretical datasets. Nevertheless, the crystallographic scrutiny of m-fluoroaniline remains outstanding, owing to the absence of pertinent experimental data in the extant literature, to our best understanding.

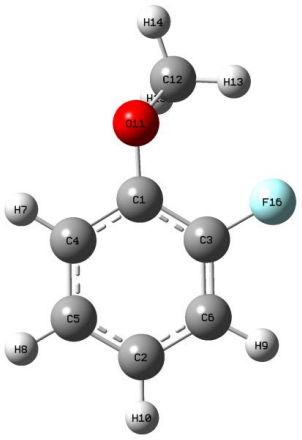

Conf 1 = *o*-Fluoroanisole

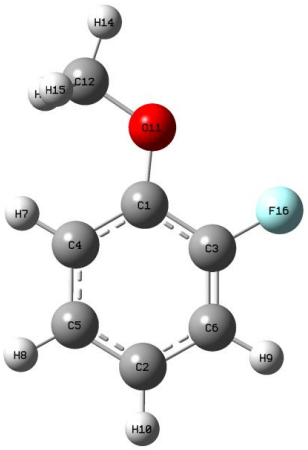

Conf 2 = *o*-Fluoroanisole

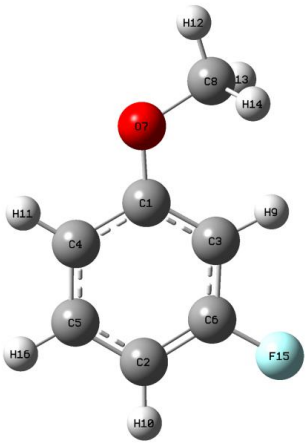

Conf 1 = *m*-Fluoroanisole

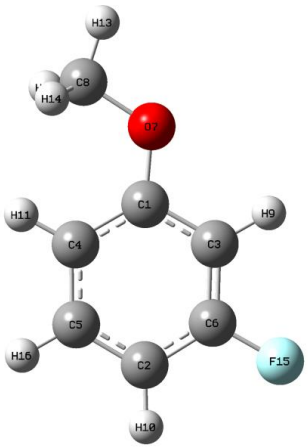

Conf 2 = *m*-Fluoroanisole

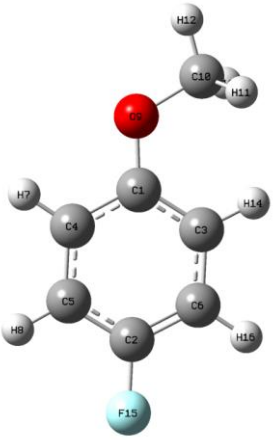

Conf 1 = *p*-Fluoroanisole

Figure 2. *Possible conformers and the most stable structures of o-fluoroanisole, m-fluoroanisole, and p-fluoroanisole isomers*

Table 5. *Conformer energies and energies of optimized structures of o-fluoroanisole, m-fluoroanisole, and p-fluoroanisole isomers*

Fluoroanisole isomers	Conformer Energies (kJ/mol)	Optimization energies (Hartree)
Conf 1 = *o*-Fluoroanisole	129.5518	-446.129075
Conf 2 = *o*-Fluoroanisole	**139.9477**	**-446.131300**
Conf 1 = *m*-Fluoroanisole	**60.0276**	**-446.136811**
Conf 2 = *m*-Fluoroanisole	60.9810	-446.136612
Conf 1 = *p*-Fluoroanisole	**70.2210**	**-446.134766**

A conformational analysis of each fluoroanisole isomer was conducted using the Spartan program. The results revealed the presence of two conformers, denoted as **Conf 1** and **Conf 2**, in the ortho and meta isomers (Figure 2). Conversely, only one conformer was identified in the para isomer. Table.5 presents the optimized structure and energy values of all conformers. Based on the minimum energy values for each isomer, the most stable structures were determined to be **Conf 2** for the ortho isomer, **Conf 1** for the meta isomer, and **Conf 1** for the para isomer.

Table 6. *The selected geometric parameters of o-fluoroanisole, m-fluoroanisole, and p-fluoroanisole isomers*

Parameters	***o*-Fluoroanisole**	***m*-Fluoroanisole**	***p*-Fluoroanisole**
Bond lengths (Å)			
C1-C3	1.4030	1.3978	1.3971
C1-C4	1.3968	1.4018	1.4007
C1-O11	1.3578	-	-
C1-O7	-	1.3613	-
C12-O11	1.4220	-	-
C8-O7	-	1.4223	-
C10-O9	-	-	1.4205
C12-H14	1.0882	-	-
C8-H12	-	1.0884	-
C10-H13	-	-	1.0957
C3-F16	1.3510	-	-
C6-F15	-	1.3576	-
C2-F15	-	-	1.3593
C2-C6	1.3971	1.3816	-
C2-C5	-	-	1.3888
C3-C6	1.3800	1.3893	-
C4-C5	-	-	1.3878
Bond angle (◦)			
O11-C12-H13	111.3754	-	-
O11-C12-H14	105.6402	-	-
O11-C12-H15	111.3746	-	-
O7-C8-H12	-	105.7863	-
O7-C8-H13	-	111.3591	-
O7-C8-H14	-	111.3589	-
O9-C10-H11	-	-	111.4521
O9-C10-H12	-	-	105.8163
O9-C10-H13	-	-	111.4512
O11-C1-C4	125.6922	-	-
C12-O11-C1	118.2856	-	-
C8-O7-C1	-	118.7370	-
O7-C1-C3	-	123.9381	-
C10-O9-C1	-	-	118.5631

O9-C1-C4	-	-	115.7157
C1-C3-F16	118.4131	-	-
C1-C3-C6	122.1193	-	-
C3-C6-F15	-	117.5447	-
C3-C6-C2	-	123.4696	-
O9-C1-C3	-	-	124.5807
C5-C2-C6	-	-	121.7921
F16-C3-C6	119.4674	-	-
F16-C3-C1	118.4131	-	-
F15-C6-C2	-	118.9856	-
F15-C6-C3	-	117.5447	-
F15-C2-C5	-	-	118.9647
F15-C2-C6	-	-	119.2431
Dihedral angle (◦)			
C1-O11-C12-H13	-61.3113	-	-
C1-O11-C12-H14	179.9780	-	-
C1-O11-C12-H15	61.2677	-	-
C1-O7-C8-H12	-	-180	-
C1-O7-C8-H13	-	61.2963	-
C1-O7-C8-H14	-	-61.2968	-
C1-O9-C10-H11	-	-	-61.2634
C1-O9-C10-H12	-	-	-179.9851
C1-O9-C10-H13	-	-	61.2933
C12-O11-C1-C3	-179.9754	-	-
C12-O11-C1-C4	0.0283	-	-
C8-O7-C1-C3	-	-	-
C8-O7-C1-C4	-	-	-
O11-C1-C3-F16	0.0069	-	-
O7-C1-C3-C6	-	-180	-
O9-C1-C4-C5	-	-	-179.9986
F16-C3-C6-H9	-0.0040	-	-
F16-C3-C6-C2	179.9954	-	-
F15-C6-C3-H9	-	-0.0005	-
F15-C6-C3-C1	-	-179.9995	-
F15-C2-C5-H8	-	-	0.0041
F15-C2-C5-C4			-179.9969

3.1. Frontier Molecular Orbital (FMO) and chemical reactivity descriptors

Frontier molecular orbitals (FMOs) are critical in understanding the electronic properties and chemical reactivity of molecules. The HOMO governs the molecule's tendency to lose electrons, while the LUMO indicates the molecule's inclination to gain electrons. The isosurfaces of the molecule, where red and green colours depict positive and negative phases, offer a visual representation of the electronic distribution. The energy gap between the HOMO and LUMO dictates the stability of the chemical framework. Smaller energy gaps result in heightened chemical reactivity, elevated polarizability, and increased softness, which is a unique characteristic of the molecule. Conversely, hardness, the inverse of the softness, defines the rigidity of the molecule.

***o*-Fluoroaniline**	***m*-Fluoroaniline**	***p*-Fluoroaniline**
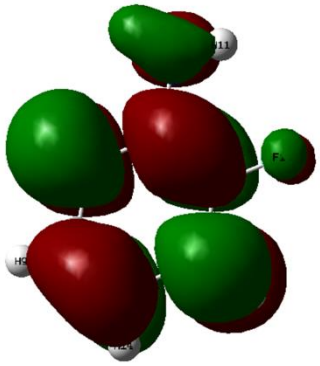	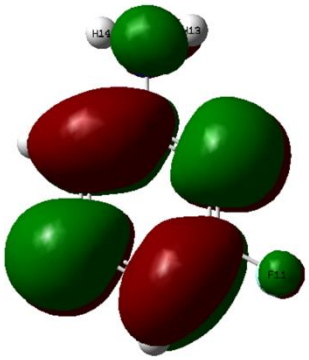	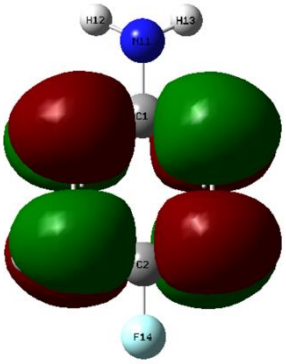
$E_{LUMO} = -4.80\ eV$	$E_{LUMO} = -4.87 eV$	$E_{LUMO} = -5.13\ eV$
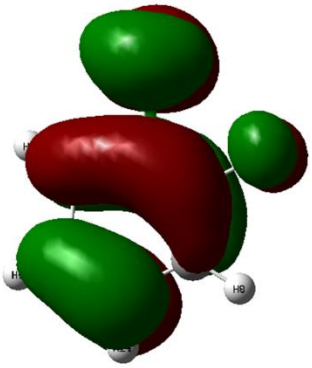	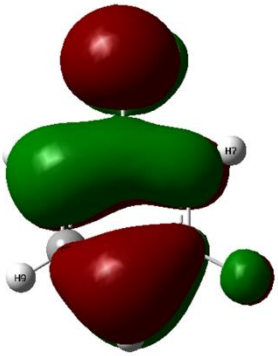	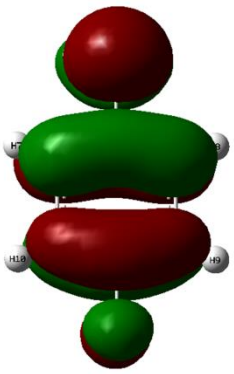
$E_{HOMO} = -8.77 eV$	$E_{HOMO} = -9.03\ eV$	$E_{HOMO} = -8.65\ eV$

Figure 3. *HOMO and LUMO for the o-fluoroaniline, m-fluoroaniline, and p-fluoroaniline isomers*

Chemical reactivity descriptors were computed using Koopman's theorem [53]. The electron affinity (EA), ionization potential (IP), chemical potential (μ), chemical hardness (η), softness (s), electronegativity (χ), and electrophilicity index (ω) were calculated by utilizing the HOMO and LUMO energy values [54, 55]. The resulting values are presented in Table 7.

$$IP = -E_{HOMO} \quad (1)$$

$$EA = -E_{LUMO} \quad (2)$$

$$\mu = \frac{1}{2}[E_{LUMO} + E_{HOMO}] \quad (3)$$

$$\eta = \frac{1}{2}[E_{LUMO} - E_{HOMO}] \quad (4)$$

$$S = \frac{1}{2\eta} \quad (5)$$

$$\omega = \frac{\mu^2}{2\eta} \quad (6)$$

$$\chi = -\frac{1}{2}[E_{HOMO} + E_{LUMO}] \quad (7)$$

Table 7. *Chemical reactivity descriptors of o-fluoroaniline, m-fluoroaniline, and p-fluoroaniline isomers*

Isomers	E_{gap} (eV)	IP (eV)	EA (eV)	μ (eV)	η (eV)	S (eV)	ω (eV)	χ (eV)
***o*Fluoroaniline**	3.97	8.77	4.80	-6.78	1.98	0.25	11.60	6.78
***m*Fluoroaniline**	4.16	9.03	4.87	-6.95	2.08	0.24	11.61	6.95
***p*Fluoroaniline**	3.52	8.65	5.13	-6.89	1.76	0.28	13.48	6.89

The results of the study indicate that the chemical reactivity values for the fluoroaniline isomers follow the order of p-fluoroaniline > o-fluoroaniline > m-fluoroaniline. Similarly, the softness values were found to be in the order of m-fluoroaniline > o-fluoroaniline > p-fluoroaniline, which indicates that the m-isomer is the most polarizable. The hardness values were found to be in the order of p-fluoroaniline > o-fluoroaniline > m-fluoroaniline, indicating that the p-isomer is the hardest. The ionization potentials of the isomers follow the order of o-fluoroaniline (8.77 eV) < p-fluoroaniline (8.65 eV) < m-fluoroaniline (9.03 eV), while the electron affinities are in the order of p-fluoroaniline (5.13 eV) > m-fluoroaniline (4.87 eV) > o-fluoroaniline (4.80 eV). Furthermore, the electrophilicity values of the isomers follow the order of p-fluoroaniline > p-fluoroaniline ≈ m-fluoroaniline, while the electronegativity values are ranked as m-fluoroaniline > p-fluoroaniline > o-fluoroaniline. These findings provide valuable insights into the chemical reactivity and electronic properties of the fluoroaniline isomers.

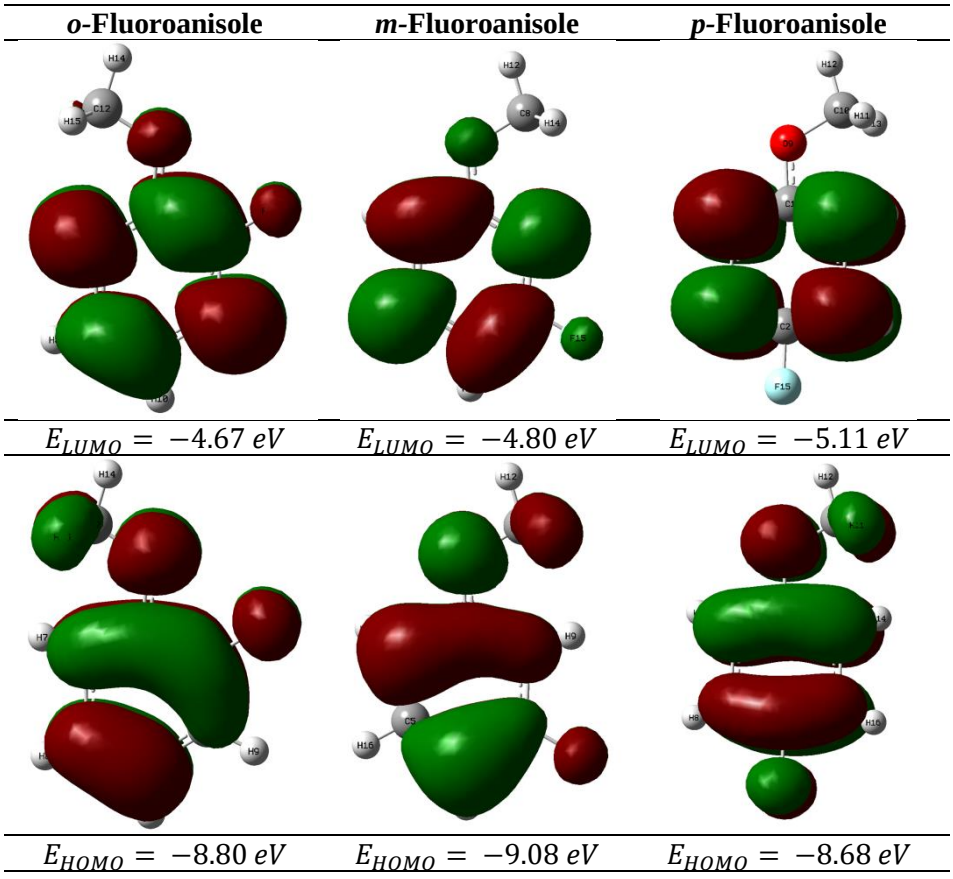

Figure 4. *HOMO and LUMO for o-fluoroanisole, m-fluoroanisole, and p-fluoroanisole isomers*

The highest occupied molecular orbital (HOMO) and lowest unoccupied molecular orbital (LUMO) of each fluoroanisole isomer are presented in Figure 4. The HOMO-LUMO analysis of the o- and m-fluoroanisole isomers revealed that the fluorine atoms have positive phases, while in the p-fluoroanisole isomer, the phases are negative. The o-fluoroanisole isomer has a HOMO energy of -8.80 eV and a

LUMO energy of -4.67 eV. The corresponding HOMO-LUMO gap energy for this isomer is 4.13 eV. The m-fluoroanisole isomer has the highest HOMO-LUMO gap energy of 4.28 eV, with a HOMO energy of -9.08 eV and a LUMO energy of -4.80 eV. On the other hand, the p-fluoroanisole isomer has the lowest HOMO-LUMO gap energy of 3.57 eV, with a HOMO energy of -8.68 eV and a LUMO energy of -5.11 eV. The detailed results are provided in Table 8.

Table 8. *Chemical reactivity descriptors of o-fluoroanisole, m-fluoroanisole, and p-fluoroanisole isomers*

Isomers	E_{gap} (eV)	IP (eV)	EA (eV)	μ (eV)	η (eV)	S (eV)	ω (eV)	χ (eV)
***o*-Fluoroanisole**	4.13	8.80	4.67	-6.73	2.06	0.24	10.99	6.73
***m*-Fluoroanisole**	4.28	9.08	4.80	-6.91	2.14	0.23	11.15	6.91
***p*-Fluoroanisole**	3.57	8.68	5.11	-6.89	1.78	0.28	13.33	6.89

The results of the study reveal the order of chemical reactivity values for fluoroaniline isomers to be in the sequence of m-fluoroanisole > o-fluoroanisole > p-fluoroanisole. Additionally, the softness values for fluoroanisole isomers have been determined to be in the sequence of p-fluoroanisole > o-fluoroanisole > m-fluoroanisole. Based on these values, the hardness of the isomers can be ordered as m-fluoroanisole > o-fluoroanisole > p-fluoroanisole.

3.2. Non-linear optical (NLO) properties

Nonlinear optical (NLO) properties play a crucial role in the design of advanced technologies, including signal processing, optical devices, and communication systems [56]. Theoretical investigations of the NLO properties of molecules are vital in advancing such technologies. To probe the nonlinear optical behaviour, we calculated the dipole moment, polarizability, and first hyperpolarizability using the B3LYP functional with the 6-311++G(d,p) basis set. The values of dipole moment (μ), polarizability (α), and first-order hyperpolarizability (β) were determined through the relevant equations and are presented in Table 9.
Total dipole moment (μ_{tot}) for a molecule is defined as in Equation 8

$$\mu_{tot} = \left(\mu_x + \mu_y + \mu_z\right)^{\frac{1}{2}} \quad (8)$$

Total polarizability (α_{tot}) for a molecule can be evaluated by Equation 9

$$\alpha_{tot} = \frac{1}{3}\left(\alpha_{xx} + \alpha_{yy} + \alpha_{zz}\right) \quad (9)$$

The total first-order hyperpolarizability (β_{tot}) can be calculated by Equation 10

$$\beta_{tot} = \left(\beta_x^2 + \beta_y^2 + \beta_z^2\right)^{\frac{1}{2}} \quad (10)$$

where β_x, β_y and β_z are defined to be

$$\beta_x = \left(\beta_{xxx} + \beta_{xyy} + \beta_{xzz}\right) \quad (11)$$

$$\beta_y = \left(\beta_{yyy} + \beta_{yzz} + \beta_{yxx}\right) \quad (12)$$

$$\beta_z = \left(\beta_{zzz} + \beta_{zxx} + \beta_{zyy}\right) \quad (13)$$

Total first-order hyperpolarizability from Gaussian09 output is given in Equation 14.

$$\beta_{tot} = \left[\left(\beta_{xxx} + \beta_{xyy} + \beta_{xzz}\right)^2 + \left(\beta_{yyy} + \beta_{yzz} + \beta_{yxx}\right)^2 + \left(\beta_{zzz} + \beta_{zxx} + \beta_{zyy}\right)^2\right]^{\frac{1}{2}} \quad (14)$$

Table 9. *The values of calculated dipole moment (μ), polarizability (α), and first-order hyperpolarizability (β) components of o-fluoroaniline, m-fluoroaniline, and p-fluoroaniline isomers*

Parameters	***o*-Fluoroaniline**	***m*-Fluoroaniline**	***p*-Fluoroaniline**
Dipole moment (Debye)			
μ_x	-0.1114	-2.7342	-2.9829
μ_y	1.4985	0.3232	-0.0001
μ_z	0.9204	0.9195	0.9878
μ_{tot}	1.7621	2.9028	3.1422
Polarizability (a.u)			
α_{xx}	99.574	99.823	101.922
α_{yy}	87.529	87.972	84.278
α_{zz}	46.926	46.769	46.478
α_{tot} (a.u)	78.010	78.188	77.559
α_{tot} (esu)	11.561 x10^{-24}	11.587 x10^{-24}	11.494 x10^{-24}
Hyperpolarizability (a.u)			
β_{xxx}	327.725	118.188	83.332
β_{xxy}	-64.699	215.700	0.0007
β_{xyy}	-77.891	8.781	-15.603
β_{yyy}	37.772	3.101	0.0003
β_{xxz}	10.851	10.994	8.642
β_{xyz}	1.799	1.557	0.0013
β_{yyz}	5.528	6.497	7.327
β_{xzz}	-52.144	-17.855	-34.654
β_{yzz}	17.846	36.774	-0.0006
β_{zzz}	12.612	14.336	13.853
β_{tot} (a.u)	458.751	279.711	44.534
β_{tot} (esu)	3963.28 x10^{-33}	2416.50 x10^{-33}	384.74 x10^{-33}

In Table.9, the total dipole moment, polarizabilities, and first-order hyperpolarizabilities of the fluoroaniline molecule isomers have been listed. Values in atomic units (a.u) obtained were converted to Statcoulomb (esu) units following using the conversion factors: for μ, 1 a.u. = 2.5412 Debye; for α, 1 a.u. = 0.1482 × 10^{-24} esu; and for β, 1a.u. = 8.6393 × 10^{-33} esu [23, 57-59]. The dipole moment values of all isomers were calculated in the order *p*-fluoroaniline > *m*-fluoroaniline > *o*-fluoroaniline. The polarisability of all isomers was obtained in the order *m*-fluoroaniline > *o*-fluoroaniline > *p*-fluoroaniline. The results obtained indicate that all isomers do have not a strong response to the external electric field. In addition, results show minor changes in the polarizability values among the isomers. The first-order hyperpolarizability values of all isomers were calculated in the order *o*-fluoroaniline > *m*-fluoroaniline > *p*-fluoroaniline. o-fluoroaniline has the highest hyperpolarizability value (3963.28 × 10^{-33} esu). This may be because the fluorine atom is closer to the -NH_2.

Table 10. *The values of calculated dipole moment (μ), polarizability (α), first-order hyperpolarizability (β) components of o-fluoroanisole, m-fluoroanisole, and p-fluoroanisole isomers*

Parameters	***o*-Fluoroanisole**	***m*-Fluoroanisole**	***p*-Fluoroanisole**
Dipole moment (Debye)			
μ_x	-0.5125	-1.5309	2.4626
μ_y	-2.7022	0.0810	-0.9387
μ_z	0.0006	0	0.0004
μ_{tot}	2.7504	1.5330	2.6355
Polarizability (a.u)			
α_{xx}	111.193	109.785	111.954
α_{yy}	91.169	92.541	89.538
α_{zz}	52.967	52.731	52.576

α_{tot} (a.u)	85.110	85.019	84.689
α_{tot} (esu)	12.613 x10^{-24}	12.599 x10^{-24}	12.551 x10^{-24}
Hyperpolarizability (a.u)			
β_{xxx}	222.784	241.683	-12.285
β_{xxy}	-89.835	61.011	-33.706
β_{xyy}	30.452	-105.156	18.102
β_{yyy}	-164.099	40.236	-20.04
β_{xxz}	0.004	0.001	0.010
β_{xyz}	-0.008	-0.0009	0.005
β_{yyz}	-0.007	-0.0008	-0.011
β_{xzz}	36.878	15.727	23.651
β_{yzz}	-93.081	-2.152	-46.208
β_{zzz}	0.038	0.001	0.029
β_{tot} (a.u)	452.313	181.662	104.208
β_{tot} (esu)	3907.66 x10^{-33}	1569.43 x10^{-33}	900.28 x10^{-33}

The total dipole moment, polarizabilities, and the first-order hyper-polarizabilities of the fluoroanisole molecule isomers have been listed in Table.10. The dipole moment is the most frequently used data to define the polarity of molecule systems. It is the polarity indicator of the separation of negative and positive charges between the atoms and the distance between the two bonded atoms. The dipole moment values of all isomers were calculated in the order *o*-fluoroanisole > *p*-fluoroanisole > *m*-fluoroanisole. The values of polarizability and the first-order hyper-polarizabilities are necessary to examine the NLO properties of materials. The polarizability of all isomers was obtained in the order *o*-fluoroanisole > *m*-fluoroanisole > *p*-fluoroanisole. Additionally, the first-order hyper-polarizability values of all isomers were calculated in the order *o*-fluoroaniline > *m*-fluoroanisole > *p*-fluoroanisole. *o*-fluoroanisole has the highest hyperpolarizability value (3907.66 x10^{-33} esu).

3.3. Molecular Electrostatic Potential (MEP) map

The molecular electrostatic potential (MEP) map provides a graphical representation of the electrostatic forces exerted on a unit positive charge placed at different points on a molecule. It allows for the identification of electron-rich or electron-poor regions on the surface of a molecule, which can be visualized using different colors. The MEP map is an important tool for understanding the electrophilic and nucleophilic reactivity of a molecule. Regions of the molecule with the most negative electrostatic potential are typically displayed as red, and these areas can be classified as electrophilic. Conversely, regions with the most positive electrostatic potential are generally displayed as blue, and these regions are typically nucleophilic [58, 60-62].

Based on the molecular electrostatic potential (MEP) map, the MEPs for all isomers exhibit comparable patterns. The negative region of each isomer is located on the fluorine atom, whereas the positive region is positioned on the amine group. The colour code of *o*-Fluoroaniline, *m*-fluoroaniline and *p*-fluoroaniline molecular range from -4.765×10^{-2} a.u — 4.765×10^{-2} a.u, -4.867 ×10^{-2} a.u — 4.867 ×10^{-2} a.u and -4.706×x10^{-2} a.u — 4.706×10^{-2} a.u, respectively, as illustrated in Figure 5. Furthermore, 2D contour map of electrostatic potential of the total density of fluoroaniline isomers are shown in Figure 6.

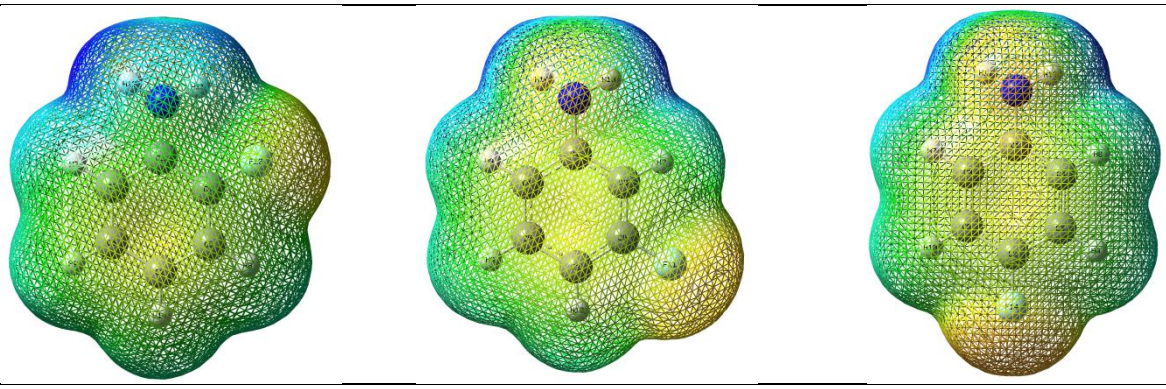

***o*-Fluoroaniline**	***m*-Fluoroaniline**	***p*-Fluoroaniline**
-4.765×10^{-2} a.u — 4.765×10^{-2} a.u	-4.867×10^{-2} a.u — 4.867×10^{-2} a.u	$-4.706\times x10^{-2}$ a.u — $4.706\times x10^{-2}$ a.u

Figure 5. *Molecular electrostatic potential maps of o-fluoroaniline, m-fluoroaniline, and p-fluoroaniline isomers*

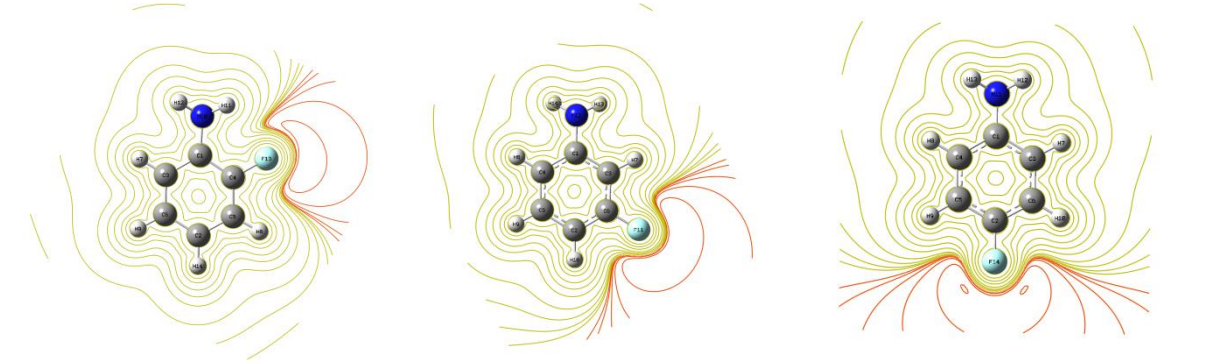

***o*-Fluoroaniline**	***m*-Fluoroaniline**	***p*-Fluoroaniline**

Figure 6. *Contour maps of o-fluoroaniline, m-fluoroaniline, and p-fluoroaniline isomers*

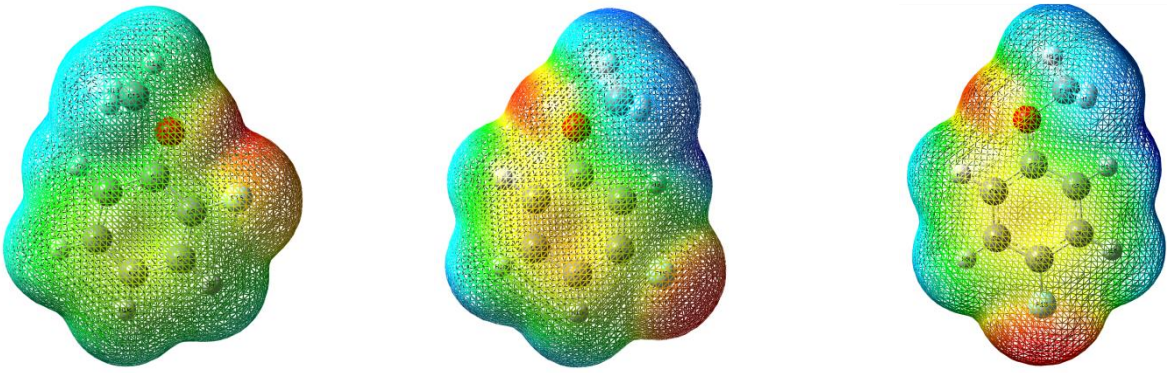

***o*-Fluoroanisole**	***m*-Fluoroanisole**	***p*-Fluoroanisole**
-4.682×10^{-2} a.u — 4.682×10^{-2} a.u	-2.823×10^{-2} a.u — 2.823×10^{-2} a.u	$-2.968\times x10^{-2}$ a.u — $2.968\times x10^{-2}$ a.u

Figure 7. *Molecular electrostatic potential maps of o-fluoroanisole, m-fluoroanisole, and p-fluoroanisole isomers*

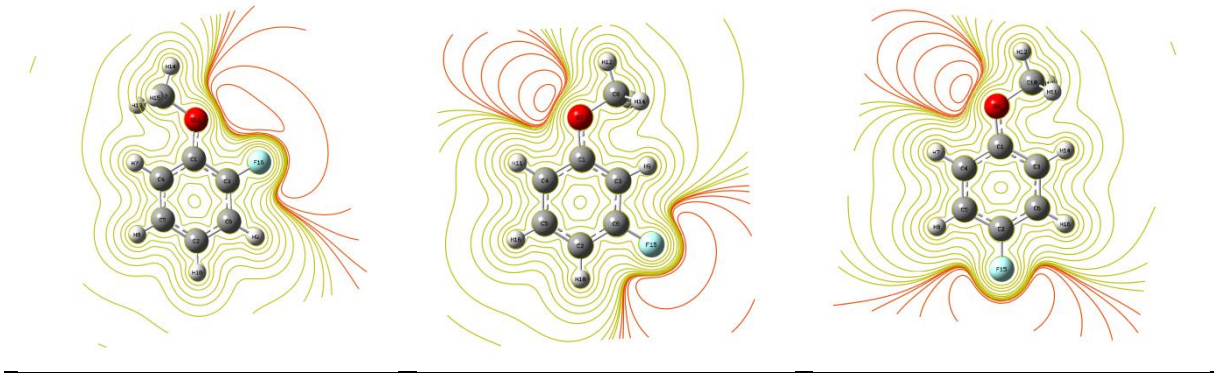

***o*-Fluoroanisole**	***m*-Fluoroanisole**	***p*-Fluoroanisole**

Figure 8. *Contour maps of o-fluoroanisole, m-fluoroanisole, and p-fluoroanisole isomers*

The molecular electrostatic potential (MEP) map provides information about the electrophilic and nucleophilic regions of molecules. The MEP maps of o-, m-, and p-fluoroanisole isomers are shown in Figure 7. Furthermore, 2D contour map of the electrostatic potential of the total density of fluoroanisole isomers is shown in Figure 8. The electrophilic regions, where electrophilic attacks are likely to occur, are highlighted in red, while the nucleophilic regions, where nucleophilic attacks are likely to occur, are highlighted in blue. The MEP maps demonstrate that the electrophilic regions of all isomers are primarily located on the fluorine and oxygen atoms, whereas the nucleophilic regions are primarily located on the -CH3 and hydrogen atoms. The color code *o*-fluoroanisole, *m*-fluoroanisole, and *p*-fluoroanisole isomers range from -4.682×10^{-2} a.u — 4.682×10^{-2} a.u -2.823 ×10^{-2} a.u — 2.823 ×10^{-2} a.u and -2.968×x10^{-2} a.u — 2.968×x10^{-2} a.u respectively.

3.4. Natural bond orbital (NBO) analysis

The natural bond orbital analysis is a well-established and valuable technique used to study various aspects of molecular interactions, such as charge transfer and conjugative interactions. It also allows for a detailed evaluation of Lewis and non-Lewis orbitals, which contribute to intramolecular hydrogen bonding and intermolecular bonding interactions [63, 64]. This analysis provides a comprehensive description of the interaction between donor and acceptor orbitals, which is essential for understanding the underlying molecular properties. To investigate the donor and acceptor orbitals, the second-order Fock matrix was calculated for all isomers using the NBO analysis. The delocalization donor (i) → acceptor (j) stabilization energy (E2) can be determined using equation 15 [65].

$$E_2 = \Delta E_{ij} = q_i \frac{F(i,j)^2}{\epsilon_j - \epsilon_i} \quad (15)$$

Where q_i is the donor orbital occupancy, ϵ_j and ϵ_i are diagonal elements and $F(i,j)^2$ is the off-diagonal NBO Fock matrix element.

Table 11 presents the nine most important values of stabilization energy (E2), orbital energies for donor and acceptor Natural Bond Orbital (NBOs), and Fock matrix for each isomer of the molecule. The NBO results, determined using second-order perturbation values of the Fock matrix, indicate that the intramolecular hydrogen bonding strength follows the order o-fluoroaniline > m-fluoroaniline > p-fluoroaniline.

The strongest delocalization for the o-fluoroaniline isomer is observed between the C4-C5 donor orbital and C2-C6 acceptor orbital, which exhibits the largest stabilizing energy. Charge transfer in this molecule is expected to occur between these bonds. The m-fluoroaniline isomer shows the strongest delocalization between the N12 donor orbital and C1-C3 acceptor orbital, resulting in the largest stabilizing energy. The p-fluoroaniline isomer, on the other hand, exhibits the strongest delocalization between the N11 donor orbital and C1-C4 acceptor orbital, again with the largest stabilizing energy.

Furthermore, if charge transfer occurs in any of these isomers, it is anticipated to occur between the bonds mentioned above.

Table 11. *The Second order Perbution of Fock Matrix of NBO of o-fluoroaniline, m-fluoroaniline, and p-fluoroaniline isomers*

Isomers	Donor (i)	ED (i)	Acceptor (j)	ED (j)	E (2) (kcal/mol)	E (j) - E (i) (a.u)	F (i,j) (a.u)
***o*-Fluoroaniline**	C4-C5	0.38022	C2-C6	0.36238	303.51	0.01	0.082
	N10	1.84499	C1-C3	0.4138	27.28	0.32	0.09
	C1-C3	1.64887	C2-C6	0.36238	22.32	0.29	0.072
	C2-C6	1.97902	C4-C5	0.38022	21.61	0.27	0.069
	C4-C5	1.70878	C1-C3	0.41383	20.08	0.29	0.071
	C1-C3	1.64887	C4-C5	0.38022	19.23	0.28	0.066
	C2-C6	1.97902	C1-C3	0.41383	18.3	0.27	0.065
	C4-C5	1.70878	C2-C6	0.36238	16.68	0.3	0.065
	F13	1.93724	C4-C5	0.38022	15.81	0.44	0.081
***m*-Fluoroaniline**	N12	1.84420	C1-C3	0.41570	28.09	0.32	0.091
	C1-C3	1.65314	C2-C6	0.39855	27.26	0.28	0.079
	C2-C6	1.67417	C4-C5	0.34979	23.68	0.29	0.075
	C4-C5	1.71790	C1-C3	0.41570	23.43	0.28	0.074
	F11	1.92858	C2-C6	0.39855	18.06	0.43	0.086
	C2-C6	1.67417	C1-C3	0.41570	15.72	0.28	0.061
	C1-C3	1.65314	C4-C5	0.34979	15.19	0.29	0.059
	C4-C5	1.71790	C2-C6	0.39855	15.08	0.28	0.059
	F11	1.98950	C6	0.00835	8.03	2.18	0.118
***p*-Fluoroaniline**	N11	1.86027	C1-C4	0.40348	25	0.33	0.087
	C1-C4	1.63949	C2-C5	0.39104	22.68	0.28	0.071
	C2-C5	1.67178	C3-C6	0.36507	21.42	0.29	0.071
	C3-C6	1.71636	C1-C4	0.40348	20.32	0.28	0.07
	C3-C6	1.71636	C2-C5	0.39104	19.03	0.28	0.067
	C1-C4	1.63949	C3-C6	0.36507	18.53	0.28	0.064
	C2-C5	1.67178	C1-C4	0.40348	17.79	0.29	0.065
	F14	1.93562	C2-C5	0.39104	16.57	0.43	0.082
	F14	1.93562	C2	0.00801	7.76	2.2	0.117

E (2): Stabilization energy.
E (j) – E (I): Energy difference of donor and acceptor orbitals.
F (i,j): Fock matrix of delocalization.

The NBO analysis provides a comprehensive account of the interaction between Lewis and non-Lewis orbitals, specifically the donor and acceptor orbitals. As depicted in Table 12, the nine most significant second-order perturbations of the Fock matrix for all isomers have been identified. Among the isomers, o-fluoroanisole, m-fluoroanisole, and p-fluoroanisole display strong intramolecular hyper-conjugative interactions, specifically between C1-C4 and C2-C5, C1-C3 and C4-C5, and O9 and C1-C3, respectively. These interactions are responsible for the stabilization energy, a critical parameter that determines the stability and intra-molecular charge transfer of all isomers [66]. Remarkably, the stabilization energy follows the order of o-fluoroanisole > m-fluoroanisole > p-fluoroanisole.

Table 12. *The Second order Perturbation of Fock Matrix of NBO for o-fluoroanisole, m-fluoroanisole, and p-fluoroanisole isomers*

Isomers	Donor (i)	ED (i)	Acceptor (j)	ED (j)	E (2) (kcal/mol)	E (j) – E (i) (a.u)	F (i,j) (a.u)

	C1-C4	0.39864	C2-C5	0.39864	225.3	0.01	0.08
	O11	1.84061	C1-C4	0.39864	30.26	0.34	0.096
	C2-C5	1.69697	C3-C6	0.35983	20.42	0.27	0.068
	C1-C4	1.68180	C2-C5	1.69697	20.23	0.3	0.07
***o*-Fluoroanisole**	C3-C6	1.98036	C1-C4	0.39864	19.52	0.29	0.069
	C2-C5	1.69697	C1-C4	0.39864	18.49	0.27	0.065
	C1-C4	1.68180	C3-C6	0.35983	18.28	0.29	0.066
	F16	1.92822	C3-C6	0.35983	17.86	0.43	0.085
	C3-C6	1.98036	C2-C5	1.69697	17.85	0.3	0.066
	C1-C3	0.40039	C4-C5	0.32450	218.88	0.01	0.083
	O7	1.83948	C1-C3	0.40039	31.25	0.34	0.097
	C1-C3	1.68201	C2-C6	0.37548	24.84	0.29	0.077
	C4-C5	1.71250	C1-C3	0.40039	23.27	0.27	0.073
***m*-Fluoroanisole**	C2-C6	1.68820	C4-C5	0.32450	22.09	0.3	0.073
	F15	1.92847	C2-C6	0.37548	18.18	0.43	0.086
	C4-C5	1.71250	C2-C6	0.37548	16.16	0.28	0.061
	C2-C6	1.68820	C1-C3	0.40039	15.72	0.28	0.061
	C1-C3	1.68201	C4-C5	0.32450	15.1	0.3	0.06
	O9	1.84805	C1-C3	0.39064	29.32	0.34	0.095
	C1-C3	1.67187	C2-C6	0.37018	20.7	0.29	0.07
	C4-C5	1.71457	C1-C3	0.39064	20.05	0.28	0.069
	C4-C5	1.71457	C2-C6	0.37018	19.99	0.28	0.068
***p*-Fluoroanisole**	C2-C6	1.68750	C4-C5	0.33372	19.96	0.3	0.069
	C1-C3	1.67187	C4-C5	0.33372	18.11	0.29	0.065
	C2-C6	1.68750	C1-C3	0.39064	17.59	0.29	0.065
	F15	1.93371	C2-C6	0.37018	17.19	0.43	0.083
	F15	1.98984	C2	0.00800	7.86	2.2	0.117

E (2): Stabilization energy.
E (j) - E(I): Energy difference of donor and acceptor orbitals.
F (i,j): Fock matrix of delocalization.

3.5. Thermodynamic Properties

The examination of chemical reactions necessitates an in-depth analysis of the thermodynamic parameters [67]. Table.13. presents the thermodynamic parameters of each isomer, which are of utmost importance in the scientific community. These theoretical outcomes are considered a valuable source of preliminary data for experimental work on fluoroaniline isomers. Moreover, they are instrumental in studying the intermolecular interactions between fluoroaniline isomers and other molecules.

The thermodynamic analysis of fluoroaniline isomers has yielded insightful results. It has been observed that the total energy of the o-fluoroaniline isomer is greater than that of the m-fluoroaniline isomer, which in turn is greater than that of the p-fluoroaniline isomer. The heat capacity of the p-fluoroaniline isomer is greater than that of the m-fluoroaniline isomer, which in turn is greater than that of the o-fluoroaniline isomer. Similarly, the entropy values of the isomers follow the same order. The zero-point vibrational energy, sum of electronic and zero-point energies, sum of electronic and thermal free energies, and rotational constants of the isomers have also been tabulated in Table.13.

Table 13. *The thermodynamic parameters for o-fluoroaniline, m-fluoroaniline, and p-fluoroaniline isomers*

Parameters	***o*-Fluoroaniline**	***m*-Fluoroaniline**	***p*-Fluoroaniline**
Total energy (thermal), E_{total} (kcal.mol^{-1})			
TOTAL	72.258	72.149	72.128
Electronic	0.000	0.000	0.000
Translational	0.889	0.889	0.889

Rotational	0.889	0.889	0.889
Vibrational	70.481	70.372	70.351
Heat capacity at const. volume, C_v (cal.mol^{-1}.K^{-1})			
TOTAL	26.266	26.398	26.411
Electronic	0.000	0.000	0.000
Translational	2.981	2.981	2.981
Rotational	2.981	2.981	2.981
Vibrational	20.304	20.436	20.449
Entropy, S (cal.mol^{-1}.K^{-1})			
TOTAL	79.892	80.128	80.425
Electronic	0.000	0.000	0.000
Translational	40.030	40.030	40.030
Rotational	27.894	28.083	27.937
Vibrational	11.967	12.014	12.458
Zero-point vibrational energy, E_0 (kcal.mol^{-1})	68.11104	67.98526	67.92509
Sum of electronic and zero-point energies (Hartree/Particle)	-386.847758	-386.849010	-386.846486
Sum of electronic and thermal free energies (Hartree/Particle)	-386.878164	-386.879501	386.877056
Rotational constants (GHz)			
A	3.30655	3.72296	5.61105
B	2.21364	1.78657	1.44345
C	1.32729	1.20832	1.14923

The relative reactivity and stability of isomers can be elucidated by their thermodynamic properties. A calculated thermodynamic values table (Table 6) was used to determine the thermodynamic characteristics of fluoroanisole isomers. The results revealed that the total energy of o-fluoroanisole was greater than m-fluoroanisole and p-fluoroanisole. Heat capacity was highest in p-fluoroanisole, followed by m-fluoroanisole and then o-fluoroanisole. Entropy values followed a similar trend, with p-fluoroanisole having the highest value and m-fluoroanisole the lowest. Additionally, Table.14. presented the zero-point vibrational energy, sum of electronic and zero-point energies, sum of electronic and thermal free energies, and rotational constants values of the isomers.

Table 14. *The thermodynamic parameters for o-fluoroanisole, m-fluoroanisole, and p-fluoroanisole isomers*

Parameters	***o*-Fluoroanisole**	***m*-Fluoroanisole**	***p*-Fluoroanisole**
Total energy (thermal), E_{total} (kcal.mol^{-1})			
TOTAL	82.810	82.729	82.680
Electronic	0.000	0.000	0.000
Translational	0.889	0.889	0.889
Rotational	0.889	0.889	0.889
Vibrational	81.032	80.951	80.903
Heat capacity at const. volume, C_v (cal.mol^{-1} K^{-1})			
TOTAL	29.508	29.564	29.614
Electronic	0.000	0.000	0.000
Translational	2.981	2.981	2.981
Rotational	2.981	2.981	2.981
Vibrational	23.546	23.603	23.653

Entropy, S (cal. Mol^{-1} K^{-1})			
TOTAL	86.564	86.530	86.914
Electronic	0.000	0.000	0.000
Translational	40.408	40.408	40.408
Rotational	28.829	29.009	28.815
Vibrational	17.326	17.113	17.691
Zero-point vibrational energy, E_0 (kcal.mol^{-1})	77.93658	77.86811	77.78749
Sum of electronic and zero-point energies (Hartree/Particle)	-446.007100	-446.012721	-446.010804
Sum of electronic and thermal free energies (Hartree/Particle)	-446.039519	-446.045144	-446.043358
Rotational constants (GHz)			
A	2.52225	2.81762	4.91197
B	1.55401	1.27305	0.96536
C	0.96751	0.88180	0.81097

3.6. TD-DFT Results: UV-Vis Spectra and Ionization Energies

The ultraviolet-visible (UV-Vis) spectra of fluoroaniline isomers were determined using the time-dependent density functional theory (TD-DFT) approach, employing the B3LYP/6-311++G(d,p) functional and basis set. The computed spectra are depicted in Figure 9, revealing a robust absorption band around 190 nm and a comparatively weaker absorption band around 230 nm. The significant components of the UV-Vis spectra, along with their associated transitions, are tabulated in Tables 15 to 17.

The UV-Vis spectrum of the o-fluoroaniline isomer can be attributed to several leading contributions. Specifically, the transitions HOMO-1→LUMO+1, HOMO-1→LUMO+2, HOMO→LUMO+2 account for 31%, 22%, and 12% of the spectrum, respectively, with a wavelength of 193.565 nm. Furthermore, the HOMO-1→LUMO, HOMO→LUMO+2 transitions contribute 18% and 61% to the spectrum, respectively, with a wavelength of 225.061 nm. Finally, the HOMO→LUMO transition is the most prominent, accounting for 79% of the spectrum with a wavelength of 262.428 nm.

In the case of the m-fluoroaniline isomer, the leading contributions to the UV-Vis spectrum are attributed to various transitions. Notably, the HOMO-1→LUMO+3 transition accounts for 83% of the spectrum with a wavelength of 194.744 nm and energy of 6.367 eV. Additionally, the HOMO-1→LUMO, HOMO-1→LUMO+2, HOMO-1→LUMO+3, HOMO→LUMO+2, HOMO→LUMO+3, HOMO→LUMO, and HOMO→LUMO+1 transitions contribute 29%, 27%, 14%, 63%, 11%, 25%, and 63% to the spectrum, respectively, with corresponding wavelengths and energies.

For the p-fluoroaniline isomer, the leading contributions to the UV-Vis spectrum arise from the following transitions: HOMO-2→LUMO, HOMO-1→LUMO+2, HOMO-1→LUMO, HOMO→LUMO+2, HOMO→LUMO+4, and HOMO→LUMO, with corresponding percentages and wavelengths/energies. Notably, the HOMO-1→LUMO+2 transition accounts for 66% of the spectrum with a wavelength of 188.217 nm and energy of 6.588 eV, while the HOMO→LUMO transition contributes 93% of the spectrum with a wavelength of 276.207 nm and energy of 4.489 eV.

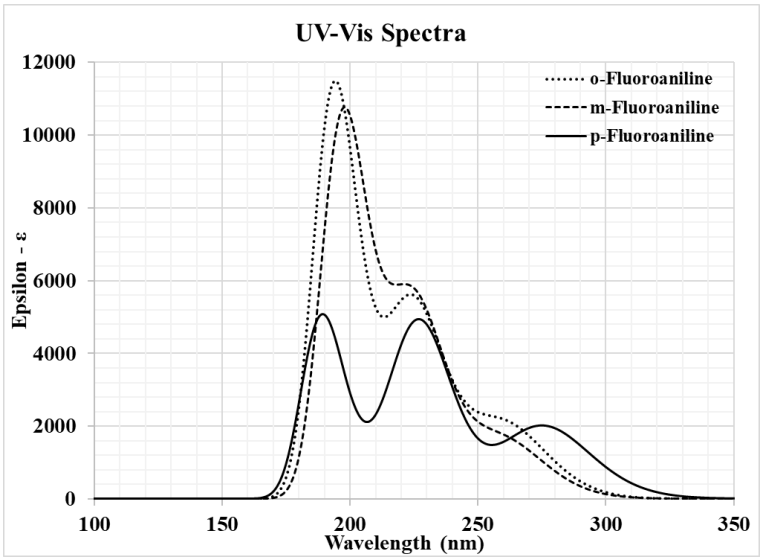

Figure 9. *Calculated UV-Vis spectra of the fluoroaniline isomers (GaussSum program [51] was used to plot spectra)*

Table 15. *TD-DFT results for the excited states of the neutral o-fluoroaniline isomer (f is the oscillator strength)*

Excited State	Energy (eV)	ΔE (nm)	f	Major Contributions to the Transitions (percentage)
1	4.725	262.428	0.0355	HOMO→LUMO (79%)
2	4.837	256.335	0.0151	HOMO→L+1 (86%)
3	5.238	236.710	0.0019	HOMO→L+2 (11%), HOMO→L+3 (86%)
4	5.509	225.061	0.1144	H-1→LUMO (18%), HOMO→L+2 (61%)
5	5.550	223.394	0.0145	HOMO→L+4 (87%)
6	5.969	207.713	0.0138	H-1→LUMO (14%), H-1→L+1 (75%)
7	6.076	204.069	0.0014	HOMO→L+5 (69%), HOMO→L+6 (21%)
8	6.152	201.547	0.0078	HOMO→L+5 (24%), HOMO→L+6 (71%)
9	6.247	198.492	0.0122	H-1→L+2 (10%), H-1→L+3 (83%)
10	6.406	193.565	0.2615	H-1→L (31%), H-1→L+2 (22%), H→L+2 (12%)

Table 16. *TD-DFT results for the excited states of the neutral m-fluoroaniline isomer (f is the oscillator strength)*

Excited State	Energy (eV)	ΔE (nm)	f	Major Contributions to the Transitions (percentage)
1	4.749	261.063	0.0148	HOMO→LUMO (60%), HOMO→L+1 (33%)
2	4.781	259.316	0.0241	HOMO→LUMO (25%), HOMO→L+1 (63%)
3	5.363	231.180	0.0058	HOMO→L+2 (12%), HOMO→L+3 (85%)
4	5.502	225.372	0.1177	H-1→L (11%), H→L+2 (63%), H→L+3 (11%)
5	5.619	220.675	0.0073	HOMO→L+4 (90%)
6	5.860	211.598	0.0104	H-1→LUMO (22%), H-1→L+1 (71%)
7	6.059	204.638	0.0025	HOMO→L+5 (63%), HOMO→L+6 (30%)
8	6.123	202.502	0.0133	HOMO→L+5 (31%), HOMO→L+6 (65%)
9	6.267	197.833	0.1914	H-1→L (29%), H-1→L+2 (27%), H-1→L+3 (14%)
10	6.367	194.744	0.0573	H-1→L+3 (83%)

Table 17. *TD-DFT results for the excited states of the neutral p-fluoroaniline isomer (f is the oscillator strength)*

Excited State	Energy (eV)	ΔE (nm)	f	Major Contributions to the Transitions (percentage)
1	4.489	276.207	0.0446	HOMO→LUMO (93%)
2	4.588	270.253	0.0048	HOMO→L+1 (97%)
3	5.265	235.483	0.0001	HOMO→L+3 (98%)

4	5.300	233.945	0.0148	HOMO→L+2 (30%), HOMO→L+4 (68%)
5	5.473	226.533	0.1067	H-1→L (11%), H→L+2 (56%), H→L+4 (30%)
6	5.906	209.925	0.0067	HOMO→L+5 (95%)
7	5.990	207.009	0.0	HOMO→L+6 (96%)
8	6.150	201.593	0.0086	H-1→L+1 (95%)
9	6.424	192.998	0.0207	HOMO→L+7 (89%)
10	6.588	188.217	0.1037	H-2→LUMO (20%), H-1→L+2 (66%)

The UV-Vis spectra of fluoroaniline isomers were computed using the TD-DFT method, with the B3LYP/6-311++G(d,p) functional and basis set. The resulting spectra are depicted in Figure 10, showing a strong absorption band at approximately 190 nm and a relatively weak absorption band at around 220 nm. The p-fluoroanisole isomer, however, exhibits a distinct absorption peak at 255 nm.

To better understand the contributions to the UV-Vis spectra, the major transitions and corresponding wavelengths and energy gaps were analyzed and are presented in Tables 18 to 20. For the o-fluoroanisole isomer, the dominant contributions originated from HOMO-1→LUMO (31%), HOMO-1→LUMO+2 (22%), and HOMO→LUMO+2 (12%) transitions, with a wavelength of 193.565 nm and an energy gap of 6.406 eV. Additionally, HOMO-1→LUMO (18%), HOMO→LUMO+2 (61%) transitions were observed at 225.061 nm with an energy gap of 5.509 eV, and HOMO-1→LUMO+3 (58%), HOMO→LUMO (79%) transitions were observed at 262.428 nm with an energy gap of 4.725 eV.

In the case of the m-fluoroanisole isomer, the leading contributions to the UV-Vis spectrum were from HOMO-1→LUMO+3 (83%) transitions, with a wavelength of 194.744 nm and an energy gap of 6.367 eV. Other significant contributions included HOMO-1→LUMO (29%), HOMO-1→LUMO+2 (27%), and HOMO-1→LUMO+3 (14%) transitions at 197.833 nm with an energy gap of 6.267 eV, as well as HOMO-1→LUMO (11%), HOMO→LUMO+2 (63%), and HOMO→LUMO+3 (11%) transitions at 225.061 nm with an energy gap of 5.509 eV. A final significant transition was HOMO→LUMO (25%), HOMO→LUMO+1 (63%) at 259.316 nm with an energy gap of 4.781 eV.

Finally, for the p-fluoroanisole isomer, the dominant contributions to the UV-Vis spectrum originated from HOMO-2→LUMO (20%), HOMO-1→LUMO+2 (66%) transitions at a wavelength of 188.217 nm with an energy gap of 6.588 eV. Other significant transitions were observed at 226.533 nm with an energy gap of 5.473 eV, including HOMO-1→LUMO (11%), HOMO→LUMO+2 (56%), and HOMO→LUMO+4 (30%) transitions, as well as HOMO→LUMO (93%) transitions at 276.207 nm with an energy gap of 4.489 eV.

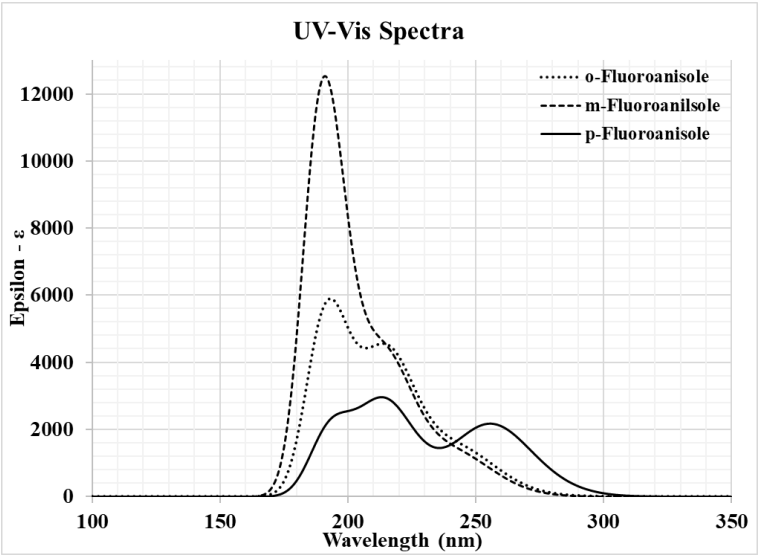

Figure 10. *Calculated UV-Vis spectra of the fluoroanisole isomers (GaussSum program [51] was used to plot spectra)*

Table 18. *TD-DFT results for the excited states of the neutral o-fluoroanisole isomer (f is the oscillator strength)*

Excited State	Energy (eV)	ΔE (nm)	f	Major Contributions to the Transitions (percentage)
1	4.725	262.428	0.0355	HOMO→LUMO (79%)
2	4.837	256.335	0.0151	HOMO→L+1 (86%)
3	5.238	236.710	0.0019	HOMO→L+2 (11%), HOMO→L+3 (86%)
4	5.509	225.061	0.1144	H-1→LUMO (18%), HOMO→L+2 (61%)
5	5.550	223.394	0.0145	HOMO→L+4 (87%)
6	5.969	207.713	0.0138	H-1→LUMO (14%), H-1→L+1 (75%)
7	6.076	204.069	0.0014	HOMO→L+5 (69%), HOMO→L+6 (21%)
8	6.152	201.547	0.0078	HOMO→L+5 (24%), HOMO→L+6 (71%)
9	6.247	198.492	0.0122	H-1→L+2 (10%), H-1→L+3 (83%)
10	6.406	193.565	0.2615	H-1→L (31%), H-1→L+2 (22%), H→L+2 (12%)

Table 19. *TD-DFT results for the excited states of the neutral m-fluoroanisole isomer (f is the oscillator strength)*

Excited State	Energy (eV)	ΔE (nm)	f	Major Contributions to the Transitions (percentage)
1	4.749	261.063	0.0148	HOMO→LUMO (60%), HOMO→L+1 (33%)
2	4.781	259.316	0.0241	HOMO→LUMO (25%), HOMO→L+1 (63%)
3	5.363	231.180	0.0058	HOMO→L+2 (12%), HOMO→L+3 (85%)
4	5.502	225.372	0.1177	H-1→L (11%), H→L+2 (63%), H→L+3 (11%)
5	5.619	220.675	0.0073	HOMO→L+4 (90%)
6	5.860	211.598	0.0104	H-1→LUMO (22%), H-1→L+1 (71%)
7	6.059	204.638	0.0025	HOMO→L+5 (63%), HOMO->L+6 (30%)
8	6.123	202.502	0.0133	HOMO→L+5 (31%), HOMO->L+6 (65%)
9	6.267	197.833	0.1914	H-1→L (29%), H-1→L+2 (27%), H-1→L+3 (14%)
10	6.367	194.744	0.0573	H-1->L+3 (83%)

Table 20. *TD-DFT results for the excited states of the neutral p-fluoroanisole isomer (f is the oscillator strength)*

Excited State	Energy (eV)	ΔE (nm)	f	Major Contributions to the Transitions (percentage)
1	4.489	276.207	0.0446	HOMO→LUMO (93%)
2	4.588	270.253	0.0048	HOMO→L+1 (97%)
3	5.265	235.483	0.0001	HOMO→L+3 (98%)
4	5.300	233.945	0.0148	HOMO→L+2 (30%), HOMO→L+4 (68%)
5	5.473	226.533	0.1067	H-1→L (11%), H→L+2 (56%), H→L+4 (30%)
6	5.906	209.925	0.0067	HOMO→L+5 (95%)
7	5.990	207.009	0.0	HOMO→L+6 (96%)
8	6.150	201.593	0.0086	H-1→L+1 (95%)
9	6.424	192.998	0.0207	HOMO→L+7 (89%)
10	6.588	188.217	0.1037	H-2→LUMO (20%), H-1→L+2 (66%)

The ionization of o-, m-, and p-fluoroaniline isomers was studied through adiabatic and vertical methods. The resulting minimum energies were found to be -386.672, -386.671, and -386.676 Hartree for the o-, m-, and p-isomers, respectively. These energies correspond to 0.284, 0.287, and 0.278 Hartree relative to their respective neutrals. The minimum energies for the vertically ionized isomers were -386.533, -386.657, and -386.662 Hartree, with respective energy reductions of 0.423, 0.301, and 0.293 Hartree compared to their neutrals. The dipole moment values for both adiabatically and vertically ionized molecules followed the order para>meta>ortho, similar to their respective neutrals.

Similarly, the ionization of o-, m-, and p-fluoroanisole isomers was studied, and the resulting minimum energies were -445.831, -445.834, and -445.839 Hartree, corresponding to 0.300, 0.303, and 0.296

Hartree relative to their respective neutrals. The minimum energies for the vertically ionized isomers were -445.822, -445.825, and -445.829 Hartree, with respective energy reductions of 0.309, 0.312, and 0.306 Hartree compared to their neutrals. The dipole moment values for both adiabatically and vertically ionized molecules followed the order ortho>para>meta, similar to their respective neutrals.

Koopman's theorem was employed to calculate the chemical reactivity descriptors of fluoroaniline and fluoroanisole isomers, as presented in Table 7 and Table 8. This was done by utilizing the HOMO and LUMO energy values. To further examine these findings, vertical and adiabatic ionization energy parameters were also determined by creating singly charged cation radicals. Previous studies have employed comparable techniques to investigate the isomers of xylene [68] and xylenol [69].

The ionization potentials for the isomers of o-fluoroaniline, m-fluoroaniline, and p-fluoroaniline were computed to be 8.77, 9.03, and 8.65 eV, respectively. The adiabatic and vertical ionization values were tabulated in Table.21. The adiabatic ionization energies were determined to be 7.726, 7.798, and 7.573 eV for o-, m-, and p-fluoroaniline, respectively. These findings are in close agreement with experimental data [10-12]. Furthermore, the vertical ionization energies were calculated to be 11.506, 8.187, and 7.961 eV for o-, m-, and p-fluoroaniline, respectively.

The ionization potentials of the isomeric forms of o-fluoroanisole, m-fluoroanisole, and p-fluoroanisole have been calculated and are presented in Table 8. The values obtained for o-fluoroanisole, m-fluoroanisole, and p-fluoroanisole are 8.80, 9.08, and 8.68 eV, respectively. Adiabatic ionization energies of these compounds were also determined and found to be 8.169, 8.253, and 8.058 eV for o-, m-, and p-fluoroanisole, respectively. The values obtained from these calculations are in good agreement with experimental results [28, 31]. Additionally, the vertical ionization energies were determined and found to be 8.411, 8.477, and 8.319 eV for o-, m-, and p-fluoroanisole, respectively.

Table 21. *Molecular energies (relative to its neutrals) and dipole moments of the fluoroaniline and fluoroanisole isomers (AI: Adiabatic Ionization, VI: Vertical Ionization)*

Isomers	Energy (Hartree)	Relative Energy (Hartree)	Relative Energy (kcal/mol)	Relative Energy (cm^{-1})	Relative Energy (eV)	Dipole Moment (D)
o-fluoroaniline (AI)	-386.672	0.284	178.162	62311.703	7.726	3.007
m-fluoroaniline (AI)	-386.671	0.287	179.821	62891.762	7.798	5.499
p-fluoroaniline (AI)	-386.676	0.278	174.623	61073.892	7.573	5.905
o-fluoroaniline (VI)	-386.533	0.423	265.319	92794.769	11.506	4.174
m-fluoroaniline (VI)	-386.657	0.301	188.784	66026.672	8.187	5.087
p-fluoroaniline (VI)	-386.662	0.293	183.572	64203.754	7.961	5.531
o-fluoroanisole (AI)	-445.831	0.300	188.380	65885.333	8.169	3.680
m-fluoroanisole (AI)	-445.834	0.303	190.321	66564.373	8.253	2.073
p-fluoroanisole (AI)	-445.839	0.296	185.818	64989.237	8.058	3.119
o-fluoroanisole (VI)	-445.822	0.309	193.953	67834.665	8.411	4.098
m-fluoroanisole (VI)	-445.825	0.312	195.473	68366.002	8.477	2.055

p-fluoroanisole (VI)	-445,829	0,306	191.832	67092.637	8.319	3.147

IV. CONCLUSION

The present study investigated two significant aromatic compounds, fluoroaniline and fluoroanisole isomers, through theoretical methods. Firstly, molecular structure optimization was carried out, followed by conformational analysis to identify the most stable isomer structure. Furthermore, nonlinear optics properties (NLO), frontier molecular orbital energies (HOMO-1, HOMO/SOMO, LUMO, LUMO+1), and chemical reactivity descriptors, including ionization potentials (vertical and adiabatic), electron affinity, chemical hardness, softness, and electronegativity, were calculated using density functional theory method with B3LYP functional and 6-311++G (d, p) basis set. The molecular electrostatic potential (MEP), natural bonding orbital (NBO), and UV-Vis spectra were also obtained, along with the first ten excited states energies and oscillator strengths. Additionally, the vertical and adiabatic ionization energy parameters were investigated through the construction of the singly charged cation radicals. The results obtained through this method were found to be more reliable for calculating the ionization energies of the titled molecules compared to Koopman's theorem.

ACKNOWLEDGEMENTS**:** This work was supported by the Scientific and Technical Research Council of Turkey (TUBITAK) under Grant No. 118C476 and Grant No. 122F301. However, the entire responsibility of the publication belongs to the authors of the publication. The financial support received from TÜBİTAK does not mean that the content of the publication is approved in a scientific sense by TÜBİTAK.

V. REFERENCES

[1] I. M. Rietjens and J. Vervoort, "Microsomal metabolism of fluoroanilines," *Xenobiotica*, vol. 19, no. 11, pp. 1297-1305, 1989.

[2] K. Haruna, A. A. Alenaizan, and A. A. Al-Saadi, "Density functional theory study of the substituent effect on the structure, conformation and vibrational spectra in halosubstituted anilines," *RSC Advances*, vol. 6, no. 72, pp. 67794-67804, 2016.

[3] M. Shashidhar, K. S. Rao, and E. Jayadevappa, "Vibrational spectra of ortho-, meta and para-fluoroanilines," *Spectrochimica Acta Part A: Molecular Spectroscopy*, vol. 26, no. 12, pp. 2373-2377, 1970.

[4] R. Kydd and P. Krueger, "The far-infrared vapor phase spectra of some halosubstituted anilines," *The Journal of Chemical Physics*, vol. 69, no. 2, pp. 827-832, 1978.

[5] R. D. Gordon, D. Clark, J. Crawley, and R. Mitchell, "Excited state amino inversion potentials in aniline derivatives: Fluoroanilines and aminopyridines," *Spectrochimica Acta Part A: Molecular Spectroscopy*, vol. 40, no. 7, pp. 657-668, 1984.

[6] M. Becucci, E. Castellucci, I. Lopez-Tocon, G. Pietraperzia, P. Salvi, and W. Caminati, "Inversion Motion and S1 Equilibrium Geometry of 4-Fluoroaniline: Molecular Beam High-Resolution Spectroscopy and ab Initio Calculations," *The Journal of Physical Chemistry* A, vol. 103, no. 45, pp. 8946-8951, 1999.

[7] M. H. Palmer, W. Moyes, M. Speirs, and J. N. A. Ridyard, "The electronic structure of substituted benzenes; ab initio calculations and photoelectron spectra for phenol, the methyl-and fluoro-derivatives, and the dihydroxybenzenes," *Journal of Molecular Structure*, vol. 52, pp. 293-307, 1979.

[8] C. H. Sin, R. Tembreull, and D. M. Lubman, "Resonant two-photon ionization spectroscopy in supersonic beams for discrimination of disubstituted benzenes in mass spectrometry," *Analytical Chemistry*, vol. 56, no. 14, pp. 2776-2781, 1984.

[9] R. Tembreull, T. M. Dunn, and D. M. Lubman, "Excited state spectroscopy of para di-substituted benzenes in a supersonic beam using resonant two photon ionization," *Spectrochimica Acta Part A: Molecular Spectroscopy*, vol. 42, no. 8, pp. 899-906, 1986.

[10] W. Tzeng and J. Lin, "Ionization energy of p-fluoroaniline and vibrational levels of p-fluoroaniline cation determined by mass-analyzed threshold ionization spectroscopy," *The Journal of Physical Chemistr*y A, vol. 103, no. 43, pp. 8612-8619, 1999.

[11] J. L. Lin and W. B. Tzeng, "Ionization energy of o-fluoroaniline and vibrational levels of o-fluoroaniline cation determined by mass-analyzed threshold ionization spectroscopy," *Physical Chemistry Chemical Physics*, vol. 2, no. 17, pp. 3759-3763, 2000.

[12] J. L. Lin, K. C. Lin, and W. B. Tzeng, "Species-selected mass-analyzed threshold ionization spectra of m-fluoroaniline cation," (in English), *Applied Spectroscopy*, vol. 55, no. 2, pp. 120-124, Feb 2001.

[13] S. P. Mirza, N. P. Raju, and M. Vairamani, "Estimation of the proton affinity values of fifteen matrix-assisted laser desorption/ionization matrices under electrospray ionization conditions using the kinetic method," *Journal of the American Society for Mass Spectrometry*, vol. 15, no. 3, pp. 431-435, 2004.

[14] H. Borsdorf, E. Nazarov, and R. Miller, "Time-of-flight ion mobility spectrometry and differential mobility spectrometry: A comparative study of their efficiency in the analysis of halogenated compounds," *Talanta*, vol. 71, no. 4, pp. 1804-1812, 2007.

[15] G. Chałasiński and M. M. Szczęśniak, "State of the art and challenges of the ab initio theory of intermolecular interactions," Chemical reviews, vol. 100, no. 11, pp. 4227-4252, 2000.

[16] A. Abdou, H. M. Mostafa, and A.-M. M. Abdel-Mawgoud, "Seven metal-based bi-dentate NO azocoumarine complexes: Synthesis, physicochemical properties, DFT calculations, drug-likeness, in vitro antimicrobial screening and molecular docking analysis," I*norganica Chimica Acta*, vol. 539, p. 121043, 2022.

[17] S. Bahçeli, E. K. Sarıkaya, and Ö. Dereli, "5-Bromosalicylaldehyde: Theoretical, Experimental and Spectroscopic (FT-IR, Raman, H1 and C13-NMR, UV-Vis) Studies and Their Photovoltaic Parameters," *ChemistrySelect*, vol. 9, no. 12, p. e202400054, 2024.

[18] E.-W. Huang et al., "Machine-learning and high-throughput studies for high-entropy materials," *Materials Science and Engineering: R: Report*s, vol. 147, p. 100645, 2022.

[19] M. A. Baldwin, A. G. Loudon, A. Maccoll, and K. S. Webb, "The nature and fragmentation pathways of the molecular ions of some arylureas, arylthioureas, acetanilides, thioacetanilides and related compounds," *Journal of Mass Spectrometry*, vol. 11, no. 11, pp. 1181-1193, 1976.

[20] G. G. Furin, A. S. Sultanov, and I. I. Furlei, "Photoelectronic spectra of fluorine-containing aromatic amines," (in English), Bulletin of the Academy of Sciences of the USSR Division of Chemical Science, vol. 36, no. 3, pp. 530-534, Mar 1987.

[21] M. H. Palmer, W. Moyes, and M. Spiers, "The electronic structure of substituted benzenes: ab initio calculations and photoelectron spectra for benzonitrile, the tolunitriles, fluorobenzonitriles, dicyanobenzenes and ethynylbenzene," (in English), *Journal of Molecular Structure*, vol. 62, no. Feb, pp. 165-187, 1980.

[22] P. Farrell and J. Newton, "Ionization potentials of primary aromatic amines and aza-hydrocarbons," *Tetrahedron Letters*, vol. 7, no. 45, pp. 5517-5523, 1966.

[23] I. C. de Silva, R. M. de Silva, and K. N. De Silva, "Investigations of nonlinear optical (NLO) properties of Fe, Ru and Os organometallic complexes using high accuracy density functional theory (DFT) calculations," vol. 728, no. 1-3, pp. 141-145, 2005.

[24] H. Seip and R. Seip, "On the Structure of Gaseous Anisole," *Acta Chem. Scand*, vol. 27, pp. 4024-4027, 1973.

[25] O. Desyatnyk, L. Pszczółkowski, S. Thorwirth, T. Krygowski, and Z. Kisiel, "The rotational spectra, electric dipole moments and molecular structures of anisole and benzaldehyde," *Physical Chemistry Chemical Physics*, vol. 7, no. 8, pp. 1708-1715, 2005.

[26] C. Eisenhardt, G. Pietraperzia, and M. Becucci, "The high resolution spectrum of the S 1← S 0 transition of anisole," *Physical Chemistry Chemical Physics*, vol. 3, no. 8, pp. 1407-1410, 2001.

[27] M. Bossa, S. Morpurgo, and S. Stranges, "The use of ab initio and DFT calculations in the interpretation of ultraviolet photoelectron spectra: the rotational isomerism of anisole and thioanisole as a case study," Journal of Molecular Structure: THEOCHEM, vol. 618, no. 1, pp. 155-164, 2002.

[28] M. Pradhan, C. Li, J. L. Lin, and W. B. Tzeng, "Mass analyzed threshold ionization spectroscopy of anisole cation and the OCH 3 substitution effect," *Chemical physics letters*, vol. 407, no. 1, pp. 100-104, 2005.

[29] I. B. Khalifa et al., "About some properties of electro-synthesized short Oligo (Para-Fluoro-Anisole)(OPFA): A combined experimental and theoretical study," *Journal of Molecular Structure*, vol. 997, no. 1, pp. 37-45, 2011.

[30] D. Xiao et al., "Vibrational spectrum of p-fluoroanisole in the first excited state (S 1) and ab initio calculations," *Journal of Molecular Structure*, vol. 882, no. 1, pp. 56-62, 2008.

[31] K. S. Shiung, D. Yu, H. C. Huang, and W. B. Tzeng, "Rotamers of m-fluoroanisole studied by two-color resonant two-photon mass-analyzed threshold ionization spectroscopy," *Journal of Molecular Spectroscopy*, vol. 274, pp. 43-47, 2012.

[32] B. Bogdanov, D. van Duijn, S. Ingemann, and S. Hammerum, "Protonation of fluorophenols and fluoroanisoles in the gas phase: experiment and theory," *Physical Chemistry Chemical Physics*, vol. 4, no. 13, pp. 2904-2910, 2002.

[33] P. Brown, "Kinetic studies in mass spectrometry—VIII: Competing [M□ CH3] and [M□ CH2O] reactions in substituted anisoles. Approximate activation energies from ioniziation and appearance potentals," *Organic Mass Spectrometry*, vol. 4, no. S1, pp. 519-532, 1970.

[34] M. A. R. da Silva and A. I. L. Ferreira, "Experimental and computational study on the molecular energetics of the three monofluoroanisole isomers," *The Journal of Chemical Thermodynamics*, vol. 41, no. 3, pp. 361-366, 2009.

[35] N. I. Giricheva, G. V. Girichev, J. S. Levina, and H. Oberhammer, "Molecular structures and conformations of 4-fluoranisole and 3, 4-difluoranisole: gas electron diffraction and quantum chemical calculations," *Journal of molecular structure*, vol. 703, no. 1, pp. 55-62, 2004.

[36] V. P. Novikov, L. V. Vilkov, and H. Oberhammer, "Conformational properties of 2-fluoroanisole in the gas phase," The Journal of Physical Chemistry A, vol. 107, no. 6, pp. 908-913, 2003.

[37] T. Isozaki, K. Sakeda, T. Suzuki, and T. Ichimura, "Fluorescence spectroscopy of jet-cooled o-fluoroanisole: Mixing through Duschinsky effect and Fermi resonance," The Journal of chemical physics, vol. 132, no. 21, p. 214308, 2010.

[38] S. G. Lias and P. Ausloos, "Ionization energies of organic compounds by equilibrium measurements," Journal of the American Chemical Society, vol. 100, no. 19, pp. 6027-6034, 1978.

[39] K. Watanabe, T. Nakayama, and J. Mottl, "Ionization potentials of some molecules," Journal of Quantitative Spectroscopy and Radiative Transfer, vol. 2, no. 4, pp. 369-382, 1962.

[40] A. Oikawa, H. Abe, N. Mikami, and M. Ito, "Electronic spectra and ionization potentials of rotational isomers of several disubstituted benzenes," Chemical physics letters, vol. 116, no. 1, pp. 50-54, 1985.

[41] Y. Shao et al., "Spartan'08, Wavefunction, Inc. Irvine, CA," vol. 8, pp. 3172-3191, 2006.

[42] A. D. Becke, "Density-functional exchange-energy approximation with correct asymptotic behavior," Physical Review A, vol. 38, no. 6, pp. 3098-3100, 09/01/ 1988.

[43] C. Lee, W. Yang, and R. G. Parr, "Development of the Colle-Salvetti correlation-energy formula into a functional of the electron density," Physical review B, vol. 37, no. 2, p. 785, 1988.

[44] B. Miehlich, A. Savin, H. Stoll, and H. Preuss, "Results obtained with the correlation energy density functionals of Becke and Lee, Yang and Parr," Chemical Physics Letters, vol. 157, no. 3, pp. 200-206, 1989.

[45] M. Frisch et al., "Gaussian 09, revision D. 01," ed: Gaussian, Inc., Wallingford CT, 2009.

[46] V. Balachandran, G. Santhi, V. Karpagam, and A. Lakshmi, "DFT computation and spectroscopic analysis of N-(p-methoxybenzylidene) aniline, a potentially useful NLO material," Journal of Molecular Structure, vol. 1047, pp. 249-261, 2013.

[47] E. Enbaraj et al., "Novel Synthesis of NE, N′ E-4, 4′-sulfonylbis (N-(substituted-dichlorobenzylidene) anilines derivative their application biological and DFT studies," in Journal of Physics: Conference Series, 2021, vol. 1724, no. 1, p. 012046: IOP Publishing.

[48] N. Kang, Z.-X. Zhao, and H.-X. Zhang, "Mechanistic Study on CpRh (III)-Catalyzed [3+ 2] Annulation of Aniline Derivatives with Vinylsilanes: A DFT Study," The Journal of Organic Chemistry, vol. 88, no. 11, pp. 7320-7327, 2023.

[49] H. T. Le, R. Flammang, M. Barbieux-Flammang, P. Gerbaux, and M. T. Nguyen, "Ionized aniline and its distonic radical cation isomers," International Journal of Mass Spectrometry, vol. 217, no. 1-3, pp. 45-54, 2002.

[50] A. R. Kumar et al., "Comparison of spectroscopic, structural, and molecular docking studies of 5-nitro-2-fluoroaniline and 2-nitro-5-fluoroaniline: An attempt on fluoroaniline isomers," Journal of Fluorine Chemistry, vol. 270, p. 110167, 2023.

[51] N. M. O'boyle, A. L. Tenderholt, and K. M. Langner, "Cclib: a library for package-independent computational chemistry algorithms," Journal of computational chemistry, vol. 29, no. 5, pp. 839-845, 2008.

[52] D. Chopra, V. Thiruvenkatam, T. N. G. J. C. g. Row, and design, "In situ cryo-crystallization of fluorinated amines: A comparative study of cooperative intermolecular interactions involving ordered and disordered fluorine," vol. 6, no. 4, pp. 843-845, 2006.

[53] T. Koopmans, "Über die Zuordnung von Wellenfunktionen und Eigenwerten zu den einzelnen Elektronen eines Atoms," vol. 1, no. 1-6, pp. 104-113, 1934.

[54] L. Pauling, The Nature of the Chemical Bond. Cornell university press Ithaca, NY, 1960.

[55] R. G. Parr, L. v. Szentpaly, and S. Liu, "Electrophilicity index," vol. 121, no. 9, pp. 1922-1924, 1999.

[56] P. S. Liyanage, R. M. de Silva, and K. N. de Silva, "Nonlinear optical (NLO) properties of novel organometallic complexes: high accuracy density functional theory (DFT) calculations," vol. 639, no. 1-3, pp. 195-201, 2003.

[57] P. N. Prasad and D. J. Williams, Introduction to nonlinear optical effects in molecules and polymers. Wiley New York, 1991.

[58] Y. Ekincioğlu, H. Ş. Kılıç, and Ö. Dereli, "DFT Study of Conformational Analysis, Molecular Structure and Properties of para-, meta-and ortho 4-Methoxyphenyl Piperazine Isomers," pp. 1-11, 2021.

[59] A. Zawadzka et al., "Optical and structural characterization of thin films containing metallophthalocyanine chlorides," Dyes and Pigments, vol. 112, pp. 116-126, 2015.

[60] I. Alkorta and J. J. Perez, "Molecular polarization potential maps of the nucleic acid bases," vol. 57, no. 1, pp. 123-135, 1996.

[61] B. Lengsfield and D. R. Yarkony, "Nonadiabatic interactions between potential energy surfaces: Theory and applications," vol. 82, no. 2, pp. 1-71, 1992.

[62] P. Politzer and J. S. Murray, "The fundamental nature and role of the electrostatic potential in atoms and molecules," vol. 108, no. 3, pp. 134-142, 2002.

[63] F. Weinhold, C. Landis, and E. Glendening, "What is NBO analysis and how is it useful?," vol. 35, no. 3, pp. 399-440, 2016.

[64] Y. Ekincioğlu, H. Ş. Kılıç, and Ö. Dereli, "Structural Parameters, Electronic, Spectroscopic and Nonlinear Optical Theoretical Research of 1-(m-Chlorophenyl) piperazine (mCPP) Molecule," vol. 4, no. 2, pp. 88-97.

[65] K. Andersson, P. A. Malmqvist, B. O. Roos, A. J. Sadlej, and K. Wolinski, "Second-order perturbation theory with a CASSCF reference function," vol. 94, no. 14, pp. 5483-5488, 1990.

[66] J. A. Agwupuye, H. Louis, T. O. Unimuke, P. David, E. I. Ubana, and Y. L. Moshood, "Electronic structure investigation of the stability, reactivity, NBO analysis, thermodynamics, and the nature of the interactions in methyl-substituted imidazolium-based ionic liquids," vol. 337, p. 116458, 2021.

[67] M. Lillo-Ródenas, D. Cazorla-Amorós, and A. Linares-Solano, "Understanding chemical reactions between carbons and NaOH and KOH: an insight into the chemical activation mechanism," vol. 41, no. 2, pp. 267-275, 2003.

[68] A. Kepceoglu, Y. Gundogdu, O. Dereli, and H. S. Kilic, "Molecular Structure and TD-DFT Study of the Xylene Isomers," *Gazi University Journal of Science*, vol. 32, no. 1, pp. 300-308, 2019.

[69] A. Kepceoğlu, N. Köklü, Y. Gündoğdu, Ö. Dereli, and H. Kilic, "Analysis of the xylenol isomers by femtosecond laser time of flight mass spectrometry," *Canadian Journal of Physics*, vol. 96, no. 7, pp. 711-715, 2018.

Düzce University
Journal of Science & Technology

Research Article

Energy and Economical Analysis of Drying Process of Domestic Wastewater Treatment Sludge with Heat Pump

Selman CAGMAN [a,*], Ozan EFE[b], Ümit Ünver [c]

[a] *Department of Energy Systems Engineering, Faculty of Technology, Kocaeli University, Kocaeli, TURKEY*
[b] *Department of Mechanical Engineering, Faculty of Engineering, Yalova University, Yalova, TURKEY*
[c] *Department of Energy Technologies, Institute of Science and Technology, Yıldız Teknik University, Istanbul, TURKEY*
** Corresponding author's e-mail address: selmancagman@gmail.com*
DOI: 10.29130/dubited.1472611

ABSTRACT

In this study, a heat pump was designed to dry the sludge produced by a wastewater treatment plant. The purpose of drying the sludge is to convert it into raw material as fuel pellets, which can provide some or all of the energy needed by the treatment plant. The design of the heat pump considered the plant's production capacity and sludge generation rate. All thermal analyses were carried out according to the First Law of Thermodynamics. The heat pump system performances are investigated by using Danfoss Coolselector 2.0 program. The capacities of the heat pump components were calculated for different refrigerants and performance coefficients. The highest coefficient of performance (CoP) was found to be 5.99 for R1234zeE in summer, while the lowest was 2.33 for R134a. If the sludge is burned as biofuel, theoretically it was estimated that the energy production could range from 723,000 kWh/month to 744,000 kWh/month for the R407c and R1234zeE refrigerants respectively. The economic analysis showed that the system's payback period could range from 1.9 to 6.5 years.

Keywords: *Sludge, drying, heat pump, refrigerant, energy calculation*

Evsel Atıksu Arıtma Çamurunun Isı Pompası Yardımıyla Kurutulması Prosesinin Enerji ve Ekonomik Analizi

Öz

Bu çalışmada, bir atık su arıtma tesisi tarafından üretilen çamuru kurutmak için bir ısı pompası tasarlanmıştır. Çamurun kurutulmasının amacı, arıtma tesisin ihtiyaç duyduğu enerjinin bir kısmını veya tamamını sağlayabilecek yakıt peletleri olarak hammaddeye dönüştürmektir. Isı pompasının tasarımında tesisin üretim kapasitesi ve çamur üretim oranı dikkate alınmıştır. Tüm termal analizler Termodinamiğin Birinci Yasasına göre gerçekleştirilmiştir. Isı pompası sistem performansları Danfoss Coolselector 2.0 programı kullanılarak incelenmiştir. Isı pompası bileşenlerinin kapasiteleri farklı soğutucu akışkanlar ve performans katsayıları için hesaplanmıştır. En yüksek performans katsayısı (CoP) yaz aylarında R1234zeE için 5,99 olarak bulunurken, en düşük performans katsayısı R134a için 2,33 olarak bulunmuştur. Çamurun biyoyakıt olarak yakılması halinde, teorik olarak enerji üretiminin R407c ve R1234zeE soğutucu akışkanları için sırasıyla 723.000 kWh/ay ile 744.000 kWh/ay arasında değişebileceği tahmin edilmiştir. Ekonomik analiz, sistemin geri ödeme süresinin 1,9 ila 6,5 yıl arasında değişebileceğini göstermiştir.

Anahtar Kelimeler: *Arıtma çamuru, kurutma, ısı pompası, soğutucu akışkan, enerji hesabı*

Received: 23/04/2024, Revised: 05/05/2024, Accepted: 08/09/2024

I. INTRODUCTION

The misuse of existing water resources due to technological innovations, industrialization, and increased population causes various environmental problems. Wastewater treatment plants are the facilities where both domestic and industrial wastewater are collected and treated to solve this problem. After the wastewater is treated, it leaves the site in two forms: solid and liquid. While the liquid part is discharged to the receiving environment, the solid part, i.e. treatment sludge, is accumulated in the facility or stored in a suitable area. Since sludge cannot be released into the environment without any treatment, there is a search for a sustainable solution for the sludge generated in wastewater treatment plants [1]. There are some methods for converting sludge into a useful input. Biological methods such as anaerobic fermentation, composting, thermal methods such as incineration, pyrolysis, and gasification, as well as energy production, soil applications, use as an auxiliary by-product in other sectors or as a building material are among the current existing applications [2-4]. On the other hand, according to subparagraph "k" of Article 13 of the Regulation on Soil Pollution and Control of the Ministry of Environment and Urbanization and Climate Change, the sludge generated in facilities with a capacity of over one million equivalent population must be dried to at least 90% dry matter (DM) value [5].

Since the moisture content of the sludge is high when it exits the process at the end of the process, the moisture must be removed from the sludge. Moisture removal requires energy, so sludge drying is an energy-intensive and therefore a costly process. The use of sludge as a by-product or input depends on solving the energy source required for drying at a low cost. Incineration of sewage sludge in the incineration process is not technically feasible due to the high moisture content of the sludge. Additional fuel supplementation is required as the calorific value of sewage sludge is low. The high moisture content sludge will have a longer ignition time compared to other fuels (coal, sawdust, wood, natural gas, etc.) during incineration. The sewage sludge should enter the drying process so that the moisture content is reduced, and the calorific value is increased just before entering the incineration process [2]. The amount of the sludge production rate is 10-15 kg (27-41 g DM/person/day) as dry matter (DM) in EU countries while it is 36 g DM/person/day in Turkey [2, 5]. According to 2018 TURKSTAT data, 3.8 billion m^3 of the 4.5 billion m^3 of urban wastewater collected by municipalities through the sewerage network was treated in urban wastewater treatment plants, resulting in approximately 319,000 tons of sludge on a dry matter basis [4].

It will be easier to store, transport, or use the low moisture content sludge compared to high moisture content one. In addition, the calorific value of the sludge will increase after drying, so it can be used alone as an input in the energy production process. Conveying dryers, where hot air is directly applied to the sludge for drying, are available in the market as rotary or drum, fluidized bed, or belt dryers. These systems transfer the heat with conduction so the heat transfer of the sludge with the hot fluid takes place indirectly without contacting each other. Heating efficiency is lower than direct/conductive systems. There are different methods such as conveyor belt, drum dryer, thin film type, disk type, and fluidized bed drying systems [6-7]. The cost of the selected drying method is also important for the operation of the system and its sustainability. When looking at the costs, the investment cost for thermal drying is 350 Euro/ton.DM, while the operating cost is 50 Euro/ton.DM. On the other hand, the solar energy drying system is 400 Euro/ton.DM and 45 Euro/ton.DM respectively [3, 8]. The investment cost for the treatment of sludge in a wastewater treatment plant is between 20-30% of the wastewater treatment plant cost. The operating cost of the sludge treatment plant is 50-70% of the operating cost of the wastewater treatment plant [9, 10].

Sıkı [6] dried sewage sludge to reduce the moisture content from 82% to 9% and the total amount of wet sludge entering the system decreased by 19% at the outlet with a paddle type dryer. Salihoğlu [1], on the other hand, loaded 1,600 kg of sewage sludge containing 14-19% DM into solar drying system with a flow rate of 400 kg per day for 4 days and reached 93-98% DM at the end of the 4^{th} day. Sapmaz [11] determined that 13 m^3 of natural gas per ton can be saved if the sludge is burned auto thermally at 50% DM by applying partial drying. Sayılgan et al. [12] dewatered the sludge with a closed solar system and determined that the sludge reached 90% dry matter value within 15-20 days in the winter season

and 5 days in the summer season. In addition, Ameri [13] tried to dry sludge with 85% moisture content with solar energy through natural convection. They recommended this method for plants where the capacity of the wastewater treatment plant is lower (20-30 tons/day) in regions with high solar radiation by focusing on the thermodynamic parameters of the system. There is an indoor area needed for this process that can directly receive the sun for drying.

Kocbek et al. [10] studied sludge drying using microwaves. They performed an energy analysis of the sludge drying process by generating microwaves at different energy levels and found that this method requires more energy than conventional drying methods. Finally, Schmitt et al. [14] stated that when the wastewater treatment sludge was dried with thermal drying, the moisture content reached 80%, its calorific value (1,800-2,500 kcal/kg) was close to half the value of lignite. Tunckal and Doymaz [15] studied the effect of the incoming air temperature of the banana slices drying with a heat pump system. They suggested that the drying rate exhibited an upward tendency with increasing temperature of the incoming air temperature of the drying cabinet, while both the coefficient of performance (CoP) and specific moisture extraction rate gradually rose. Zheng et al. [16] investigated the change and distribution laws of circulating air in sludge heat pump drying equipment. The results showed that the adverse effect of increasing sludge thickness was greater than the beneficial effect of extending drying time. Liu et al. [17] studied the effects of temperature, relative humidity, and sludge thickness on sludge drying characteristics to provide an energy-saving working condition for heat pump drying. They stated that under the conditions of 2–6 mm thickness, 40–60 ºC temperature, and 30–60% relative humidity, drying time decreased by 15–25% for a 10 ºC increase in temperature when thickness and relative humidity were fixed. Additionally, relative humidity decreased from 60% to 30% and drying time decreased by about 50%. Hu et al. [18] established a model for a closed low-temperature heat pump sludge drying system. The effects of incoming air temperatures of the drying cabinet, circulating air volume, and ambient temperature on both drying rate and system performance were investigated. The findings revealed that the drying rate and specific moisture extraction rate rose with higher incoming air temperatures of the drying cabinet and circulating air volume, while the coefficient of performance (CoP) exhibited a contrasting trend. In addition, the CoP increased as the ambient temperature rose, while the drying rate decreased gradually.

Sludge drying and subsequent treatment require energy with low investment and operating costs. Therefore, renewable energy sources can be a solution for sludge drying. There are many studies on solar-powered systems. However, the disadvantages of solar sludge drying are the need for either large areas or long waiting times and the short period of solar availability [19]. On the other hand, sludge drying by heat pumps is also another renewable energy source. Moreover, when compared to other renewable sources, the availability of a heat pump system is much higher than, for example, a solar system. While conveyor belts are used for transportation purposes, it has been determined that they also provide benefits for sludge drying depending on the ambient temperature. In the study, it was determined that when hot air or gas is given to the sludge from an appropriate distance, it provides drying. The conveyor system is also used in pyrolysis, gasification, coal-fired thermal power plants, and waste incineration plants, but they also drew attention to the fact that the sludge can easily move on the conveyor belt without sticking and easily leave the conveyor at the point of end use [20].

There are many methods and studies on sludge drying in the literature. It is observed that each method has its limitations. In this study, a sustainable and low operating cost system, that can be a good alternative to similar drying applications in the literature, is proposed for wastewater treatment plants. This study aims to increase the dry matter content of the domestic wastewater treatment sludge. A heat pump system is analytically designed to supply the necessary heat in reducing the water content of the sludge. When compared with other studies in the literature, it can be stated that the proposed system provides advantages to waste water treatment plants in terms of lower operating cost, availability, and energy consumption. This study aims to transform sludge, which is a residual product for domestic wastewater treatment plants, into a useful product with a sustainable method. The treatment sludge (44% moisture + 56% dry matter) from the decanter is transported out of the plant by conveyor belt. While being transported by a conveyor belt, the belt is covered, and the amount of moisture is reduced by drying with hot air. The hot air is supplied from an air source heat pump. The system consists of a

compressor and a fan. The performance of the refrigerants used in the compressor, the amount of energy required for the system, and energy costs were examined within the scope of this study.

II. MATERIAL AND METHODS

A. SYSTEM DESCRIPTION

In this study, an air source heat pump drying system is designed to convert the sludge of a treatment plant operating in the Marmara region and utilized as pellets for biomass fuel. In this way, the 90% DM target required by the Ministry of Environment and Urbanization and Climate Change will be achieved [5].

The facility considered in this study is the largest wastewater treatment plant in Yalova. Domestic sewage from pumping stations in Yalova and surrounding areas is treated using biological methods. At the end of the treatment process, sludge cakes are produced. The disposal of these dewatered solid sludge cakes represents a significant cost and workload for the facility due to the need for storage and transportation. Therefore, this study analytically investigates the drying of the sludge and its conversion into fuel pellets to create a value-added product.

The wet sludge process subject to the study is stored in ponds at the wastewater treatment plant. This stored sludge is directed to the dewatering unit. The sludge is conveyed to decanter units as illustrated in Figure 1, where it is separated into two phases: solid and liquid.

Figure 1. *The decanter unit considered in this study*
1&2 Decanter units (main and spare one), 3&4 Sludge feeding, 5 Decanter electric motor 6-Separated liquid output 7-Separated solid output

There is a conveyor belt 4.9 meters long and 0.5 meters wide that takes the sludge to the storage area located at the outside of the building like the one shown in Figure 2. Afterward, the sludge is transported to the landfill or suitable dumping areas.

Figure 2. *Sample sludge conveyor unit*
1-Conveyor belt feeding from decanter, 2-Conveyor belt sludge transfer, 3-Sludge sampling point

Sludge samples were taken from the conveyor belt and analyzed within the on-site laboratory and the results are given in Figure 2.

Table 1. *Sampling results of the sludge*

Sludge dry matter content (DM) *(%)*	56
Sludge moisture content *(%)*	44
Sludge density *(kg/m^3)*	567.6

The sludge production rate was measured and found that the volumetric flow rate was 5 m^3/hour (this was calculated while the sludge was poured onto an open trailer), and the mass flow rate was 2,837.9 kg/hour (0.79 kg/second) (The gravimetric method was used to calculate the dry matter and water content of sludge within the on-site laboratory). These values are given in Table 2.

Table 2. *Output flow data*

Volumetric Flow *(m^3/hour)*	5
Mass Flow Rate *(kg/hour)*	2.837,9
Mass Flow Rate *(kg/second)*	0.79
Mass Moisture Flow Rate *(kg/moisture.s)*	0.27
Inlet Moisture *(%)*	44
Final Moisture *(%)*	10

The drying characteristics in Table 2 represent the characteristics of the sludge flowing on the conveyor belt after the decanter unit in Figure 2. Therefore, the system is designed to remove 0.27 kg/second of moisture from the sludge at a flow rate of 5 m^3/hour after the decanter, thus reducing the moisture content of the sludge from 44% to 10%.

B. SLUDGE DRYING SYSTEM DESIGN

It is planned to cover the conveyor belt and blow the hot air that comes from the air source heat pump to the sludge with the help of a fan while the dewatered sludge flows over the belt after the decanter. The designed heat pump air dryer system is illustrated in Figure 3.

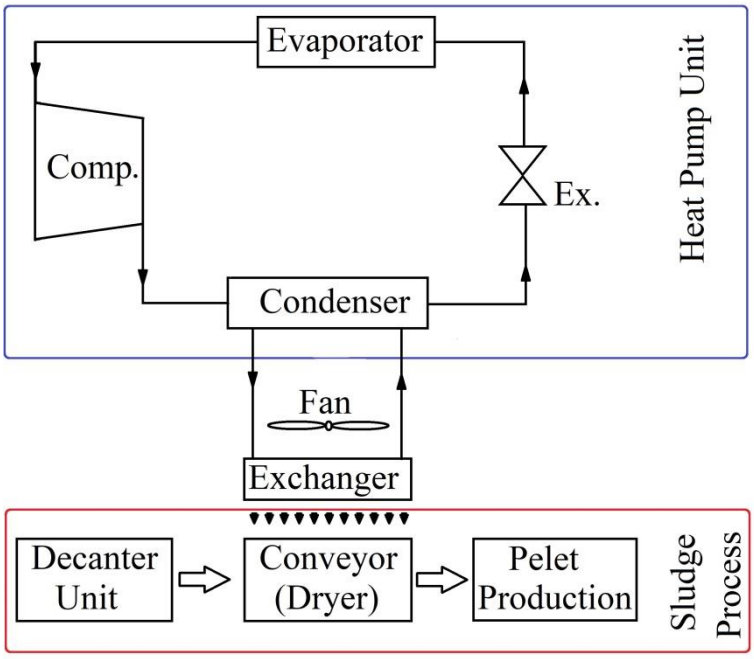

Figure 3. *Sludge drying system*

The sludge is sent away from the plant by a conveyor belt after the decanter unit (Figure 3). The hot air blowing system is installed on the conveyor belt. It is shown as a heat exchanger. In this hot air-blowing system, a heat exchanger is designed to be placed on top of the conveyor belt. The hot air will be blown to the conveyor line using a fan and the moisture of the sludge will dry. The heat exchanger is positioned perpendicularly over the conveyor belt, and it is designed to transfer the entire effect of the blown air to the sludge on the belt by splitting to the right and left. At this stage, the calculations related to the system design are given respectively.
The mass flow rate of the sludge is calculated as follows.

$$\dot{m}_t = m \times \rho \tag{1}$$

The following calculation was used to remove a 34% moisture difference (44% initial moisture content and 10% target value) from the sludge to reduce the moisture content of the sludge.

$$M = (y_{in} - y_{out}) \times m_t \tag{2}$$

The thermal power required to evaporate the targeted moisture from the sludge ($\dot{E}$) was obtained by the following calculation.

$$\dot{E} = M \times (h_g - h_f) \tag{3}$$

The amount of heat needed is determined by the following equation with the assumption of η = 95% heat exchanger efficiency.

$$\dot{Q}_{net} = \frac{\dot{E}}{\eta} \tag{4}$$

The results are presented in Table 3.

***Table 3**. Calculation results*

Parameter	Abbreviation	Value	Unit
Active Operating Period	t_m	8	*h/day*
Number of Working Days	d	30	*day/month*
Hourly Sludge Flow	m	5.0	m^3/h
Sludge Density	ρ	567.6	kg/m^3
Sludge Mass Flow	$\dot{m}$	2,837.9	*kg/h*
		0.79	*kg/s*
Moisture Percentage in Sludge	y_{in}	0.44	*%*
Target Moisture Percentage of Sludge	y_{out}	0.10	*%*
Moisture to be Evaporated	M	0.27	*kg.moisture/h*
		268.0	*g.moisture/h*
Hf Value for Water @35 ºC	h_f	146.6	*kj/kg*
Hg Value for Water @35 ºC	h_g	2,564.5	*kj/kg*
Enthalpy Difference	Δh	2,417.9	*kj/kg*
Required Energy	$\dot{E}$	648.0	*kj/s*
Heat Exchanger Efficiency	η	0.95	*%*
Net Heat	$\dot{Q}_{net\,\text{net}}$	682.1	*kWt*

The electricity consumption of the compressor is determined by the following calculation.

$$E_{comp} = \frac{\dot{Q}_{net}}{CoP} x\ t\ x30 \tag{5}$$

here CoP is the coefficient of performance The capacity calculation of the fan that blows the hot air below is calculated by Eq. (6).

$$\dot{Q}_{fan} = \frac{\dot{E}x3.600}{4{,}184} \tag{6}$$

60 ºC maximum condenser outlet temperature was taken for each refrigerant. Monthly average temperature values were used on the evaporator side. The CoP is calculated with Equation 7 by using monthly outdoor temperatures and 60 ºC constant outlet temperature data.

***Table 4.** Average monthly atmospheric temperatures of Yalova*

Month	**Jan**	**Feb**	**March**	**April**	**May**	**June**	**July**	**August**	**Sep**	**Oct**	**Nov**	**Dec**
Temperature *(ºC)*	6.5	7	8.4	12.2	16.8	21.1	23.4	23.5	20.1	16.1	12.1	8.7

The electricity consumption according to the nominal power of the fan was calculated considering the monthly average temperature data of the city where the plant is located (Table 4). The theoretical fan power is calculated by;

$$\dot{E}_{fan} = \frac{\dot{Q}_{net}}{Cp \times (T_{cond} - T_{ambient})} \times \Delta P \quad (7)$$

The following equation is used for the fan nominal power.

$$N_m = \frac{\dot{E}_{fan}}{t_m} \quad (8)$$

If the system operates for 30 days and 8 hours/day, the fan nominal power is calculated as 51.3 kWe (Table 5). However, the fan capacity was selected as 55 kWe, which is slightly above the calculated value. Fan efficiency was assumed to be 80% in the calculations.

Table 5. *Specifications of the hot air fan in the system*

Parameter	Abbreviation	Value	Unit
Amount of heat to be fed	$\dot{Q}_{\text{fan}}$	557,308	*kcal/h*
Specific heat of air	Cp	0.31	*kcal/m^3.C*
Pressure difference	ΔP	30	*mbar*
Fan rated power	N_m	51.3	*kWe*
Selected fan-rated power		55	*kWe*

The CoP of the system by using different refrigerants that can be used within the compressor determined per each design according to the monthly temperature variation was calculated separately. CoP's of the refrigerants are compared. Refrigerants, R290, R1234zeE, R513a, R134a, R134a, and R407c, are the preferred fluids that can be used within the compressors available in the market. Since these fluids are available within the market, they are preferred within the scope of the study. Electricity consumption for the compressor and fan was calculated monthly and the sum of these two was accepted as the total monthly electricity consumption of the system. A semi-hermetic type of compressor was selected to pressurize these fluids.

Finally, the Monthly Net Energy Gain (MNEG) that can be obtained basis monthly is the difference between the energy obtained from burning the pellets derived from the sludge and the energy consumed to operate the heat pump, calculated using the following equation.

$$MNEG = \sum E_p - \sum E_c \quad (9)$$

Here Ep is the energy production (kWh) and Ec (kWh) is the energy consumption that accounts for the energy consumed by fans and the energy consumed by compressor.

III. RESULTS AND DISCUSSION

It is planned to use the condenser of the heat pump for heating purposes. The drying system is planned to take the drying air from both the atmosphere and the heat from the condenser of the heat pump and send it to the sludge. Five different refrigerants were included in the calculations in this study. The Danfoss Coolselector 2.0 program was utilized to determine the CoP of the designed heat pump. This program has a compressor selection interface and simulates the performance of the compressors according to the chosen refrigerant, heating capacity, evaporator input temperature, and condenser output temperature. The performance simulation was carried out to enter the following values for each refrigerant evaluated in the study, and these outputs were referenced to seasonal CoP.

- Refrigerant fluid type: R290, R1234zeE, R513a, R134a, R407c
- Heating capacity of the heat pump: 682 kWt
- Condenser output temperature: 60 °C
- Evaporator input temperature: Monthly outdoor air temperatures taken from meteorology

During the hot summer months, the same CoP is observed in the systems. This is due to the maximum evaporator input temperature limits of the preferred compressors suitable for the refrigerator. All the results from the Danfoss Coolselector 2.0 software are presented in Figure 4.
The CoP value of the system varies between 3.20 and 6.00. The refrigerant with the highest CoP value is R1234zeE. The lowest CoP belongs to R407c. While the CoP value of R407c is around 3.50, the CoP value of R1234zeE rises to 3.80 in winter and 6.00 in summer. In contrast, R134a refrigerant is the most frequently and easily available refrigerant and has the lowest performance in winter. However, it has the highest CoP value after R1234zeE in summer.

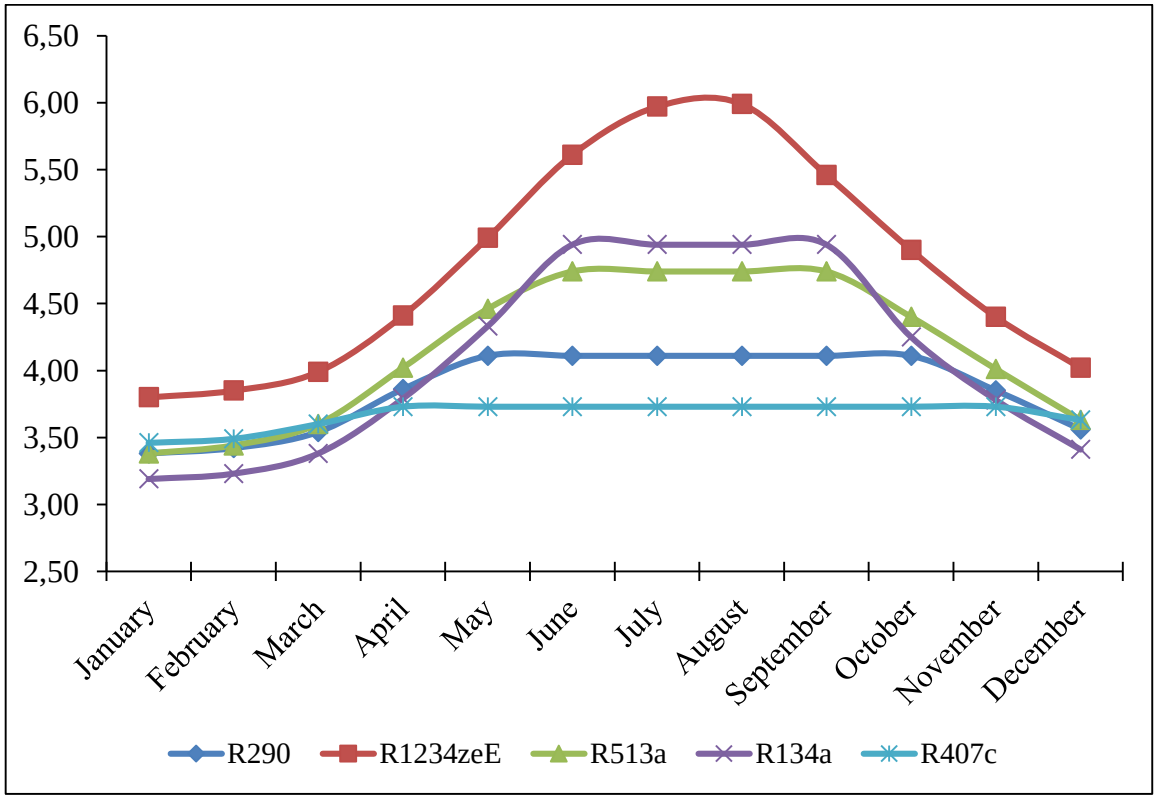

Figure 4. *Variation of CoP of the system vs. different refrigerants*

CoP is an important indicator when selecting a heat pump drying system. However, other indicators should also be considered before making an investment decision. In this study, the MNEG, another important indicator, was calculated. Figure 5 shows the MNEG calculated for different refrigerants. To calculate MNEG, the approximate energy that can be obtained from burning the sludge was theoretically calculated. In this calculation, the average calorific value of the sludge was assumed to be 4,500 kcal/kg, and the efficiency of the energy conversion system was assumed to be 30%. Thus, the thermal power that can be obtained from burning the sludge was calculated to be 3,267 kW. To calculate MNEG, the consumption of the heat pump compressor and fan, which consume electricity in the system, was subtracted from the total production.

If R1234zeE is used as the refrigerant in the heat pump, the electricity production could range between 727,000 kWh and 733,000 kWh per month. If R290 refrigerant is chosen, the monthly MNEG ranges between 724,500 kWh and 739,500 kWh. This amount is sufficient to meet the energy consumption of approximately 2,500 households.

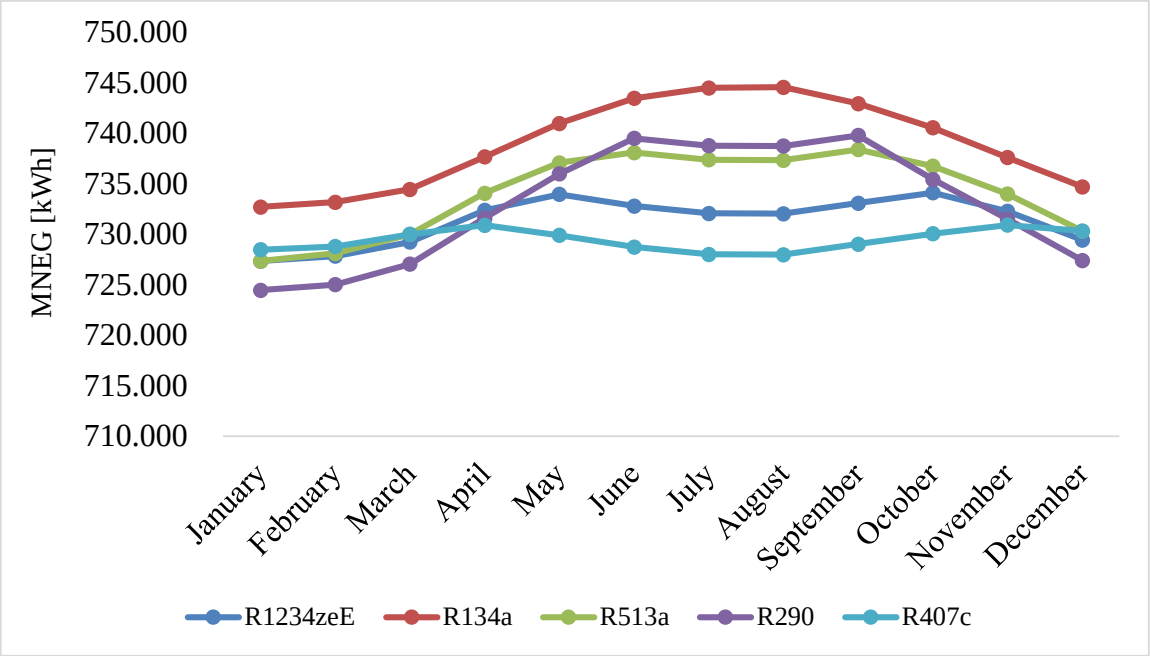

***Figure 5**. Monthly net energy gain of the system according to refrigerants*

Energy conversion from pellets produced from dried sludge can be conducted at locations other than the treatment facility. In such cases, the treatment plant will only consume energy to operate the heat pump system. To analyze the scenario where the treatment plant does not gain energy or generate revenue from energy sales, the energy costs of the system using different refrigerants were calculated. In case no electricity is generated from the produced pellets, the cost of the energy for operating system is given in Figure 6.

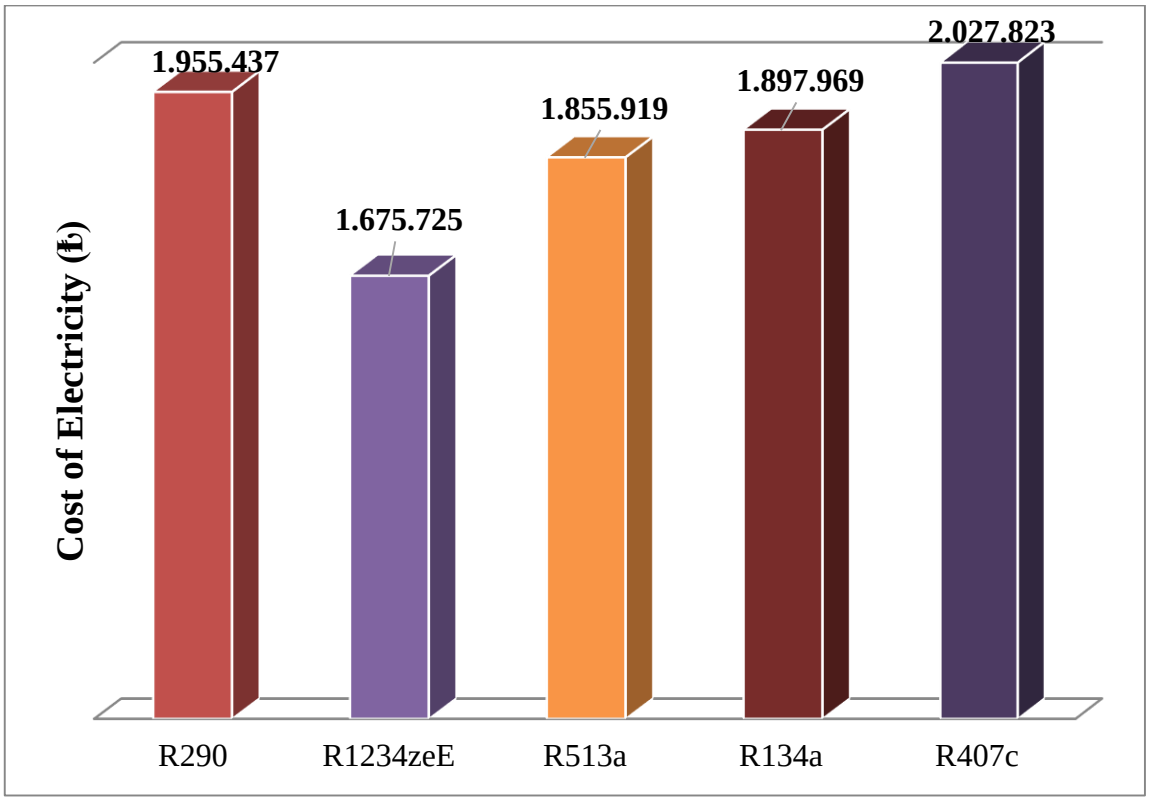

***Figure 6.** Monthly electricity cost of the heat pump system*

The energy cost of the R1234zeE fluid, which is the most efficient among the analyzed refrigerants, is the lowest with 1.68 million ₺. If the R407c fluid is used, the monthly energy cost exceeds 2 million ₺. In the analysis, the unit price of electricity is taken as 3.09 ₺/kWh. All analysis is being done as the produced energy is not utilized within the plant. The cost of the sludge heating system is presented in this study. However, if the electricity is produced with 30% efficiency, then there is no energy cost for the plant.

IV. CONCLUSION

This study investigated reducing the moisture content of domestic wastewater treatment plant sludge by drying it with hot air coming from an air source heat pump. The sludge was from a domestic wastewater treatment plant and the moisture content was 44%. The moisture content was reduced to 10% with this drying system. 5 different refrigerants were analyzed and compared for the heat pump. According to the calculations, the CoP of the system varies between 3.20 and 6.00. The refrigerant with the highest CoP is R1234zeE. The lowest CoP belongs to R407c. While the CoP value of R407c is around 3.5, the CoP value of R1234zeE rises to 3.80 in winter and 6.00 in summer. In contrast, R134a refrigerant is the most frequently and easily available refrigerant and has the lowest performance in winter. However, it has the highest CoP value after R1234zeE in summer. It is calculated that the net amount of electrical energy obtained because of installing a heat pump system using R407c fluid and drying and burning the sludge will be around 730,000 kWh/month. This figure is sufficient to meet the energy consumption of 2,500 households consuming an average of 300 kWh of energy per month. Finally, in the absence of energy production, the most efficient system is the one with R1234zeE fluid, and the electricity cost of this system is 1.675 million ₺. In the case of the R407c refrigerant, the electricity cost is more than 2 million ₺. Sludge drying so that the sludge can be utilized in energy production with the help of a heat pump has been analyzed within the scope of this study. The investment cost of the system is not included in this study. Therefore, it is possible to carry out studies on topics such as investment cost analysis of the system, utilization of sludge in a better efficient energy production process, use of sludge as an input in the pyrolysis process, or research on drying with other renewable energy sources.

Nomenclature

CoP	Coefficient of Performance
Cp	Specific heat of supply air (kCal/m^3 C)
DM	Dry Matter
E_{comp}	Electricity consumption of the compressor (kWh)
$\dot{E}_{fan}$	Theoretical fan power (kW)
$\dot{E}$	Required thermal power (kW)
h_g	Enthalpy of saturated water at gas phase (kj/kg)
hf	Enthalpy of saturated water at fluid phase (kj/kg)
m	Volumetric Flow (m^3/hour)
$\dot{m}_t$	Mass flow rate of the sludge (kg/s)
M	Mass Moisture Flow Rate
MNEG	Monthly Net Energy Gain
Nm	Nominal Power
$\dot{Q}_{fan}$	Fan power (kW)
$\dot{Q}_{net}$	Net thermal power (kW)
t_m	Operation period (h/day)
y_{in}, y_{out}	Inlet and final moisture (%)
ΔP	Pressure difference supplied by fan (bar)
ρ	Density of the Sludge (kg/m^3)
η	Exchanger efficiency

V. REFERENCES

[1] N. K. Salihoğlu,., "Yenilenebilir enerji ile arıtma çamuru kurutma sistemi," Uludağ University Journal of The Faculty of Engineering, c. 23, ss. 41–50, 2018. https://doi.org/10.17482/uumfd.315164.

[2] F. O. Topaç ve S. Uçaroğlu, "Atıksu arıtma çamurlarının sürdürülebilir kullanım alternatifleri: öncelikli yaklaşımlar," Avrupa Bilim ve Teknoloji Dergisi, c. 20, ss. 728-739, 2020.

[3] A. Filibeli, A. Ayol, ve N. Büyükkamacı, "Arıtma Çamurlarının Yönetimi ve Maliyeti: Gediz Havzası Arıtma Çamuru Yönetimi Projesi," Çevre, İklim ve Sürdürülebilirlik, c. 23, ss. 79–90, 2022.

[4] A. Özdemir, A. Özkan, Z. Günkaya ve M. Banar, "Kentsel katı atıkların ve kentsel atıksu arıtma çamurlarının birlikte pirolizi ve sıvı ürün karakterizasyonu," *Pamukkale Univ. Muh. Bilim Dergisi*, c. 28, ss. 920-928, 2022.

[5] T. Bay, E. Kara, S. Bayseç, M. Söylemez ve R. Yumrutaş, "Arıtma çamuru bertarafında kullanılan yakma yönteminin Dünya ve Türkiye'de kullanımı," Akademik Bilim Fen Bilimleri Dergisi (ABFED), ISSN (print): 2149-5122, 2016.

[6] R. Sıkı, "Arıtma çamurunun kurutulmasının termodinamik analizi," Yüksek Lisans Tezi, Makina Mühendisligi Bölümü, Kocaeli Universitesi, Kocaeli, Turkiye, 2017.

[7] Q. Zheng, Z. Hu, P. Li, L. Ni, G. Huang, Y. Yao, and L. Zhou, "Effects of air parameters on sewage sludge drying characteristics and regression analyses of drying model coefficients," *Applied Thermal Engineering*, vol. 198, pp. 117501, 2021.

[8] J. Michalska, J. Turek-Szytow, A. Dudło, and J. Surmacz-Górska, "Characterization of humic substances recovered from the sewage sludge and validity of their removal from this waste'" *EFB Bioeconomy Journal*, vol. 2, pp. 100026, 2022.

[9] M. Yüksekdağ, S. Gökpınar ve B. Yelmen, "Atıksu arıtma tesislerinde arıtma çamurları ve bertaraf uygulamaları." *Avrupa Bilim ve Teknoloji Dergisi*, c. 18, ss. 895-904, 2020.

[10] E. Kocbek, H. A. Garcia, C. M., Hooijmans, I. Mijatović, B. Lah, and D. Brdjanovic, "Microwave treatment of Municipal Sewage Sludge: Evaluation of the drying performance and energy demand of a pilot-scale microwave drying system," *Science of The Total Environment*, vol. 742, pp. 140541, 2020, https://doi.org/10.1016/j.scitotenv.2020.140541

[11] S. Sapmaz, "Arıtma çamurlarının bertarafında kullanılan kurutma sistemlerinin enerji verimliliğinin değerlendirilmesi," Doktora Tezi, Enerji Sistemleri Mühendisliği Bölümü, Kocaeli Üniversitesi, Kocaeli, Turkiye, 2022.

[12] E. Sayılgan, ve H.I. Ünlü, "Evsel Arıtma çamurunun kapalı solar kurutulmasında mevsim faktörünün değerlendirilmesi," *Fırat Üniversitesi Mühendislik Bilimleri Dergisi,* c. 33, ss. 251–261, 2020. https://doi.org/10.35234/fumbd.791158

[13] B. Ameri, S. Hanini, and M. Boumahdi, "Influence of drying methods on the thermodynamic parameters, effective moisture diffusion and drying rate of wastewater sewage sludge," *Renewable Energy*, vol. 147, pp. 1107–1119, 2020, https://doi.org/10.1016/j.renene.2019.09.072.

[14] N. Schmitt, A. Apfelbacher, N. Jager, R. Daschner, F. Stenzel, and A. Hornung, "Thermo-chemical conversion of biomass and upgrading to biofuel: the Thermo-Catalytic Reforming process – a review," *Biofuels, Bioproducts and Biorefining*, vol. 13, pp. 822–837, 2019, https://doi.org/10.1002/bbb.1980.Schneider.

[15] C. Tunckal, and I. Doymaz, “Performance analysis and mathematical modeling of banana slices in a heat pump drying system,” *Renew. Energy*, vol. 150, pp. 918–923, 2020.

[16] Q.S. Zheng, L. Cao, L. Ni, and G.Y. Huang, “Operating characteristics of sludge heat pump dryer and influencing factors of performance: a field experiment in an electroplating factory,” *Appl. Therm. Eng.* vol. 212, pp. 118602, 2022.

[17] Liu, D., Wang, Q., Hu, A., Wang, Z., Zhang, Q., & Wang, L., “Optimized model of sludge drying characteristics based on an experimental study of thickness, temperature, and humidity,” *Journal of Cleaner Production*, vol. 429, pp. 139540, 2023, https://doi.org/10.1016/j.jclepro.2023.139540

[18] Hu A., Ma L., Liu D., Jiang L., Wang Z., Wang L., “Study on drying characteristics of sludge under different conditions based on the low-temperature sludge heat pump drying model,” *Journal of Cleaner Production*, vol. 450, pp. 142035, 2024, https://doi.org/10.1016/j.jclepro.2024.142035.

[19] Afshari, F., Khanlari, A., Tuncer, A. D., Sözen, A., Şahinkesen, I. and Nicola, G. Di, “Dehumidification of sewage sludge using Quonset Solar Tunnel Dryer: An experimental and numerical approach,” *Renewable Energy*, vol. 171, pp. 784–798, 2021, https://doi.org/10.1016/j.renene.2021.02.158

[20] Schnell, M. J., Horst, T., and Quicker, P., “Thermal treatment of sewage sludge in Germany: A review,” *Journal of Environmental Management*, vol. 263, pp. 110367, 2020, https://doi.org/10.1016/j.jenvman.2020.110367

Düzce University
Journal of Science & Technology

Research Article

Determination of Structural Parameters and Design of Experiments Approach-Based Optimisation of Steel Track Undercarriage Link

Kübra POLAT [a,*], Mehmet Murat TOPAÇ [a], Onur ÇOLAK [a], Ali Özgür GÜNAY [b]

[a] *Department of Mechanical Engineering, Faculty of Engineering, Dokuz Eylül University, İzmir, TÜRKİYE*
[b] *Smart İş Makinaları San. Tic. A.Ş., Manisa, TÜRKİYE*
** Corresponding author's e-mail address: k.polat@ogr.deu.edu.tr*
DOI: 10.29130/dubited.1472942

ABSTRACT

In this study, the design and optimisation processes of the link to be used in the steel track undercarriage system of a tracked vehicle are summarised. In the first stage, a preliminary model was created by considering existing design examples and constraints. Two different Finite Element (FE) models were built using the maximum driving torque and track - ground contact forces. According to the results obtain from the analyses, three critical regions where stress concentration occurs, were identified. Seven structural design parameters were chosen to minimise stress concentrations in these regions. A Design of Experiments-based optimisation study was performed using these parameters. After obtaining new dimensional values, a new link design was created. The FE analyses conducted for maximum torque case showed that approximately decrease of 61%, 55%, and 20% was obtained in terms of stress concentration at the first, second, and third critical regions, respectively. Under the effect of vertical and lateral forces, the improvement percentages are 63%, 26%, and 31%, in the same order. It was observed that the stress values obtained at the critical regions of the new design under the failure loads, were below the permissible values.

Keywords: *Design of Experiment (DoE), Steel track undercarriage, Tracked Vehicles*

Çelik Paletli Yürüyüş Sistemi Baklasının Yapısal Parametrelerinin Belirlenmesi ve Deney Tasarımı Yaklaşımıyla Optimizasyonu

ÖZ

Bu çalışma kapsamında, bir paletli taşıtın çelik paletli yürüyüş sisteminde kullanılan baklanın tasarım ve optimizasyon süreçleri özetlenmiştir. İlk aşamada, uygulanmış tasarım örnekleri ve tasarım kısıtları dikkate alınarak bir ön model oluşturulmuştur. Baklaya etkimesi beklenen maksimum tahrik torku ve temas kuvvetleri yardımıyla iki farklı Sonlu Elemanlar (SE) modeli kurulmuştur. Bu model yardımıyla parça üzerinde gerilme açısından üç kritik bölge belirlenmiştir. Gerilme yığılmalarının azaltılması için bakla üzerinde yedi adet yapısal tasarım parametresi seçilmiştir. Bu parametreler kullanılarak gerçekleştirilen Deney Tasarımı tabanlı bir optimizasyon çalışması sonucunda elde edilen boyutsal değerler yardımıyla, yeni bakla tasarımı oluşturulmuştur. Motordan sisteme maksimum tork uygulanması durumu için yapılan SE analizleri, birinci, ikinci ve üçüncü kritik bölgelerde gerilme yığılması açısından sırasıyla, yaklaşık %61, %55 ve %20 oranlarında iyileşme elde edildiğini göstermiştir. Düşey ve yanal kuvvet etkisi altında ise iyileşme yüzdeleri, aynı sıralamayla, %63, %26 ve %31'dir. Sonuç olarak, elde edilen parametrelerle gerçekleştirilen yeni bakla tasarımında, kritik bölgelerde elde edilen gerilme değerlerinin, hasar oluşumuna neden olan değerlerin altında kaldığı görülmüştür.

Anahtar Kelimeler: *Deney Tasarımı (DT), Paletli yürüyüş sistemi, Paletli Taşıtlar*

Received: 24/04/2024, Revised: 21/08/2024, Accepted: 09/09/2024

I. INTRODUCTION

Tracked walking systems have a wide range of applications in many different disciplines such as defence, construction, mining, agriculture and mobile robotics. These vehicles were initially designed as a "portable railway" which are laid in front of the road wheels and mounted on the vehicle during the motion [1]. With the advancement of technology, these vehicles have become more durable and manoeuvrable. Tracked vehicles are advantageous compared to wheeled vehicles especially in off-road conditions such as soil, mud and snow. The main reasons for this advantage are the larger contact area and longer tyre contact length of tracked vehicles compared to wheeled vehicles [1,2]. At the same time, the larger total contact area of tracked vehicles allows them to contact a larger amount of the ground surface. This is one of the main reasons why the traction of tracked vehicles is higher than that of wheeled vehicles. Because it is known from the literature that increasing the tyre contact length and area increases the traction of a wheeled vehicle on the terrain [1]. Figure 1 shows the crawler excavator used in this study.

Figure 1. *General view of the steel track undercarriage system (Courtesy of Smart İş Makinaları San. Tic. A.Ş.).*

Failures can occur on the undercarriage system of tracked vehicles under overload and harsh operating conditions. This can result from various reasons such as design and/or manufacturing defects, inconvenient working conditions and environmental factors. In open literature, failure investigation studies have been reported for these systems [3-8]. Zhi-wei et al. [4], investigated the failure of two crawler links of a tracked vehicle used for dredging. Characterisation studies show that, undesired residues in the track link material caused the component to become brittle. In the study by Bošnjak et al. [5], the chain link failure was investigated by metallographic examination and the Finite Element Method (FEM) for a specified lifetime of a tracked vehicle. As a result of the analysis and tests, it was found that the mechanical properties of the material significantly deviated from the specifications. In addition, the micro and macro cracks were detected in the material structure and it was shown that the failure was caused by manufacturing defects. In another study by Bošnjak et al [6], various methods were used to determine the cause of failure of track links. As a result of the analyses, it was determined that the increase in sulphur content in the link material caused the failure. Zhao et al [7] investigated the stresses on the link under different steering conditions of the excavator at low speeds. In the FE analyses, it was observed that the maximum stress value in the chain links was lower than the yield strength, but there was a crack in the corner where the bolt holes of the chain link on the lateral force bearing side were located. Literature studies show that the failures in the track links are generally caused by manufacturing defects and fatigue.

Tracked excavators consist of parts such as track (1), track shoe (2), link (3), bushing connection pin (4), idler (5), sprocket (6) and track tensioning system shown in Figure 2. The links are connected by pins and bushes to hold the chain together. The drive wheel transfers the drive torque from the engine to the track chain via the links and thus enables the chassis (7) to move on the ground. The track rollers (8), which are rotatable mounted on the chassis, roll on the links. The chassis' vertical load is transmitted

via the rollers to the links and the track shoes connected to them. In this way, a uniform pressure distribution is provided on the ground contact surface and the movement. This enables the vehicle to have better traction characteristics in difficult ground conditions [9,10]. The failure of the track undercarriage system during operation in various surface conditions causes material and temporal losses [4,7].

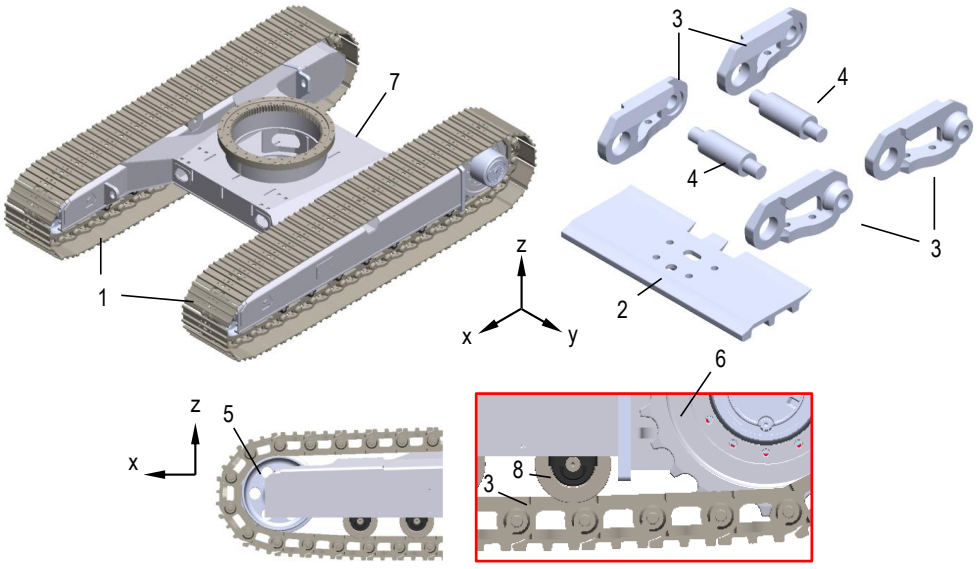

Figure 2. *General view of the steel crawler system used in an excavator and layout of structural elements [9]*

In this study, the design and optimisation processes of the link to be used in the steel track system of a tracked vehicle shown in Figure 3 are summarised. In the first step, a preliminary model was constructed by considering the applicable design examples and constraints. Two different Finite Element (FE) models were also built with the help of the maximum drive torque and link contact forces. These models used to identify three critical regions on the part in terms of stress concentrations. Seven structural design parameters were selected to minimise stress concentrations in these regions. Using these parameters, a new link design was generated using the dimensional values obtained from a Design of Experiments-based optimisation study. It was observed that the new design obtained as an optimization result did not exceed the fatigue stress value obtained from the literature [7].

As mentioned, there are studies in the open literature based on investigating the cause of link failure; however, to the best of the authors' knowledge, studies which summarise a complete design process of a steel crawler excavator link using DoE-based optimisation is not available in the open literature.

II. MATERIAL AND METHOD

A. LOAD MODEL AND FINITE ELEMENT MODEL

The solid models were imported into ANSYS® Workbench 2020R2 commercial FE software for stress analysis. The load scenario in which the chassis operates at low speed where the right and left tracks moving in opposite directions relative to each other, i.e. a pivot steering around the vertical axis, was selected as the load scenario.

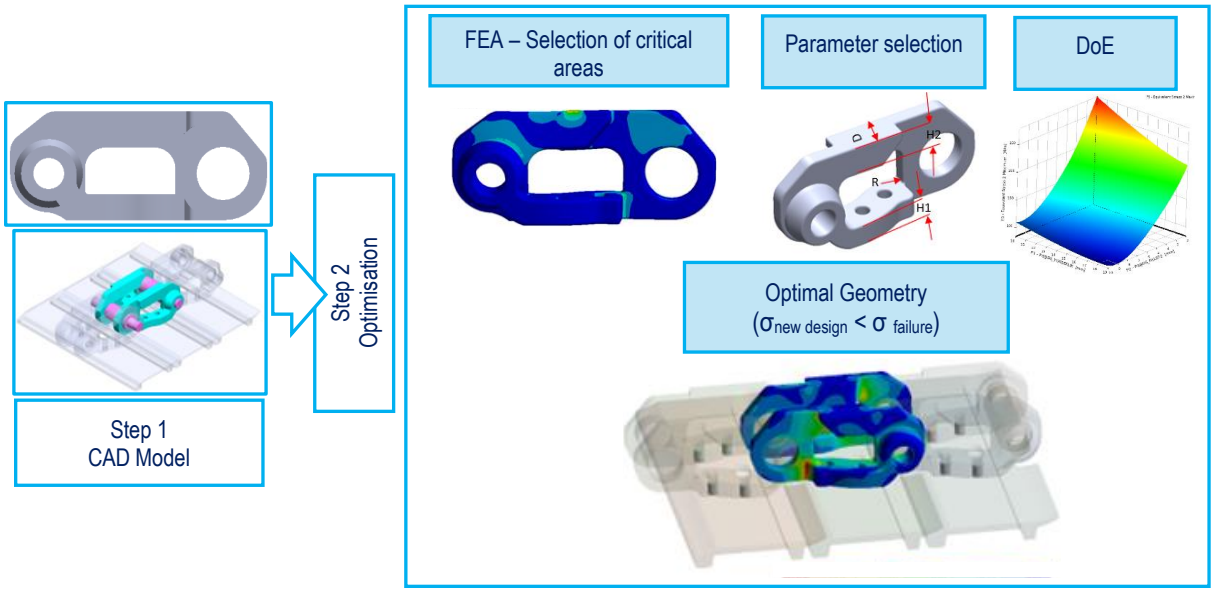

Figure 3. *Study Summary*

According to this load model, two different FE models including the maximum drive torque and contact forces were built. For low speeds the load was assumed to be uniformly distributed. The idealised loads acting on the crawler are as shown in Figure 4 [11,12].

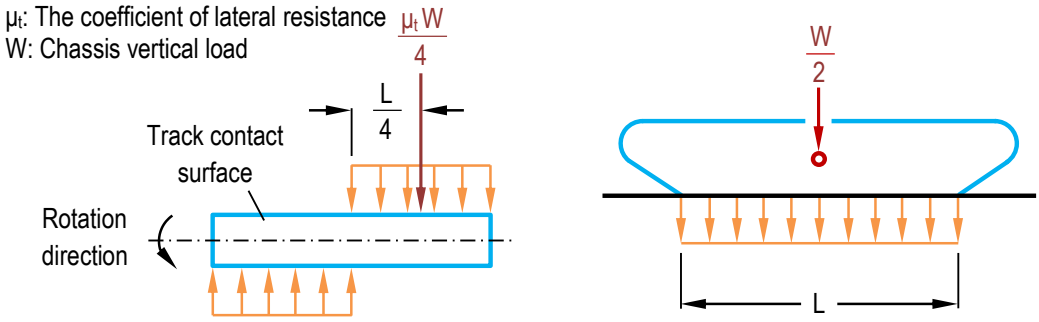

Figure 4. *Lateral resistance acting on the track during low-speed rotation (according to [12])*

For the maximum drive torque model, the maximum tensile force was calculated via maximum engine torque and the drive sprocket diameter provided by the manufacturer. For the second load model, the vertical and lateral forces between the roller and link utilised for the fatigue analysis of a track chain link used in a similar weight excavator were obtained from the literature [7]. The two different loading models summarised in Figure 5. In the first case, named as case "a", the link begins to wrap on the drive wheel sprocket and operates under maximum tensile force. In the second case (or case "b"), the link is in contact with both the ground and the roller.

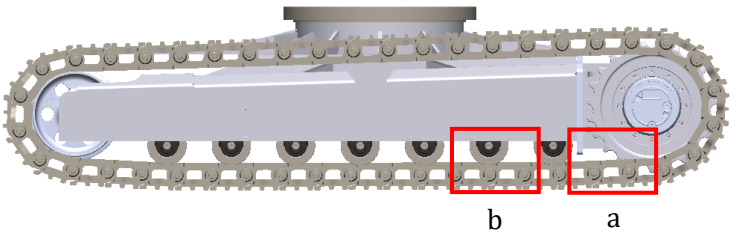

Figure 5. (a) *Maximum traction case and* ***(b)*** *both in contact with the ground and contact force by the roller*

These two selected load models were applied to both the single link model and the sub-model. By this way, the stress distributions for both models were obtained. In the first model, the tensile force acting on the single link was applied as half of the total tensile force (F_x) through pin A in the -x axis direction. Here, load distribution was assumed symmetric as shown in Figure 6.a. The translational movement of the pin A in the force direction was allowed, while the translational and rotational movements in other directions were constrained. In the latter model, the rotational movement around the drive sprocket and the horizontal movement of the link are unconstrained. Here, pin D is fixed. In order to model the contact forces that occur when the rollers pass over the link, the contact points of the rollers on the link were determined first. These regions were separated on the part. Then, vertical and lateral forces were applied to the separated contact area in addition to the tensile force. Due to the distance between the centres of the two rollers mounted on the chassis, during the movement of the track, only a single roller can be in contact with a link at any given time, during the interval when the roller contacts and then leaves the link. In the sub-model shown in Figure 6.c, the tensile force Fx acting on the link is applied through pin A in the -x axis direction. The rotational freedom of pin D is constrained and the friction between links, rollers and pins is not considered in the model. Due to the surface contact resistance acting on the track shoe, the idealised longitudinal and lateral forces (R and S), which are assumed to act on the chassis from the road, are modelled as uniformly distributed surface pressure on the track shoe.

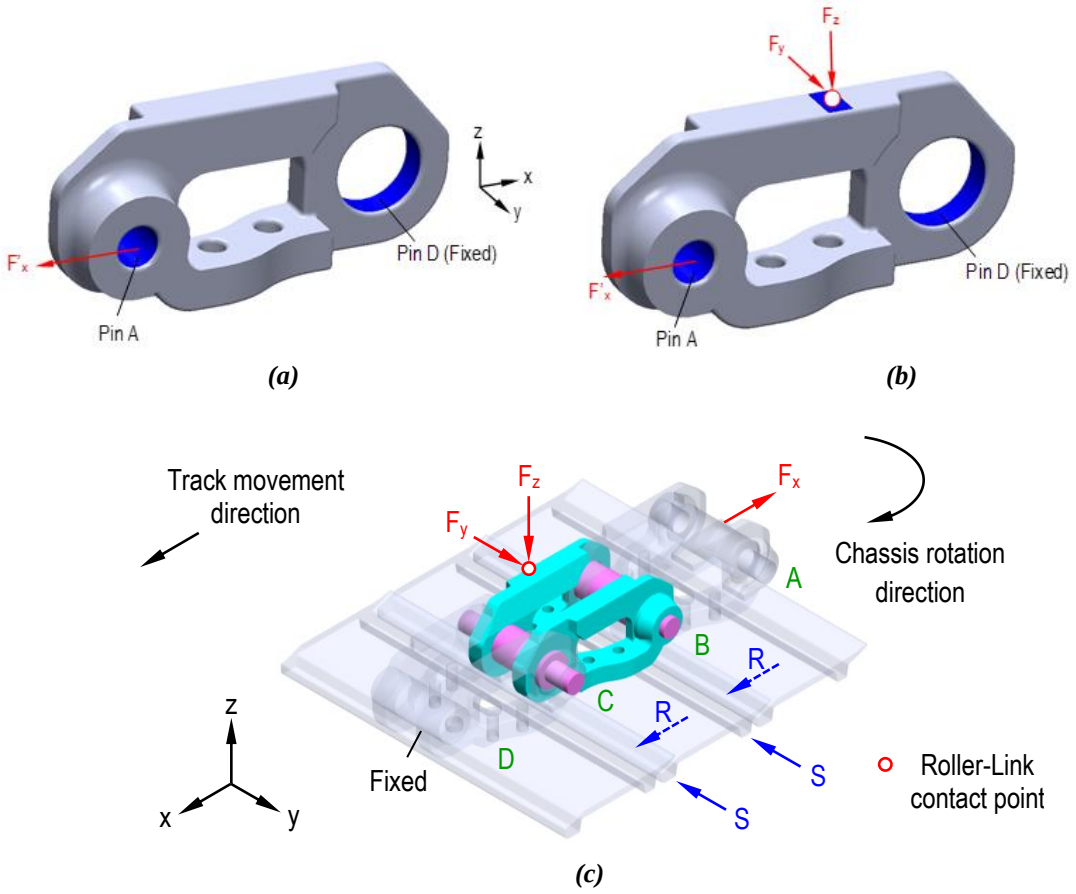

Figure 6. (a) *Maximum tension model,* ***(b)*** *Model subjected to crushing by rollers and* ***(c)*** *Sub-model [9]*

B. DESIGN OF EXPERIMENTS -RESPONSE SURFACE METHOD

Design of Experiments (DoE) and Response Surface Methodology (RSM) are methods often used in engineering to optimise the performance of a system or process. These methods are used together to study the relationship between input parameters, known as design variables, and the response of the system, known as output parameters. This method helps to determine the effects of variables on the system and their optimal levels. In other words, in order to systematically investigate the effect of

multiple variables in the system on the response, DoE is generally used. To build a model describing the relationship between the design variables and the system response, response surface experiments with specific rules are required. The results obtained from these experiments allow us to determine the effects of the design variables on the system response and using this information we can build a mathematical model. The regression model for a second order RS can be defined as follows [13];

$$y = \beta_0 + \sum_{i=1}^{k} \beta_i x_i + \sum_{i \leq j}^{k} \beta_{ij} x_i x_j + \varepsilon \quad (1)$$

if written in matrix form:

$$y = X\beta + \varepsilon \quad (2)$$

where, y is the observation vector, X is the model matrix, β is the vector containing partial regression constants and ε is the error vector [13]. In this study, a table was created by the software using the DoE method for the allowable values of the input parameters using design examples. The optimisation was performed using ANSYS Workbench® software. Central Composite Design (CCD) was used to determine the optimum parameter values. CCD is an option available in the DoE module design table and a detailed description of this procedure is available in the literature [14-16].

III. RESULTS AND DISCUSSION

C. DESIGN CONSTRAINTS AND PRELIMINARY DESIGN

In the first stage, a preliminary solid model was designed considering the existing design examples [17,18] and constraints. The link geometries were firstly designed in two groups: In the first group pin slot structure was altered where upper and lower height values remain constant. In the second group, both height values were changed additionally. While constructing these models, the penetration of the parts in the range of the link rotation angle when it is wrapped on the drive wheel and the distances between the drive wheel and the links were taken into account, as shown in Figure 7. Then, a preliminary model was selected among these two groups. Figure 8 shows the FEA results of the link geometries.

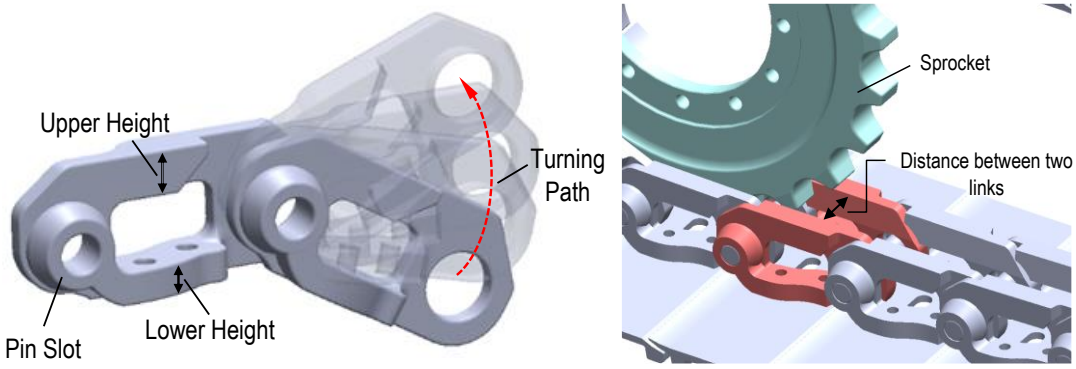

Figure 7. *Working envelope of the chain link*

ANSYS® Workbench 2020R2 commercial FE software was used for the stress analysis of the link. SOLID187 element type consisting of a total of ten nodes, each with three linear degrees of freedom, was used in the FE model. The analysis model consists of 256,810 elements and 368,334 nodes.

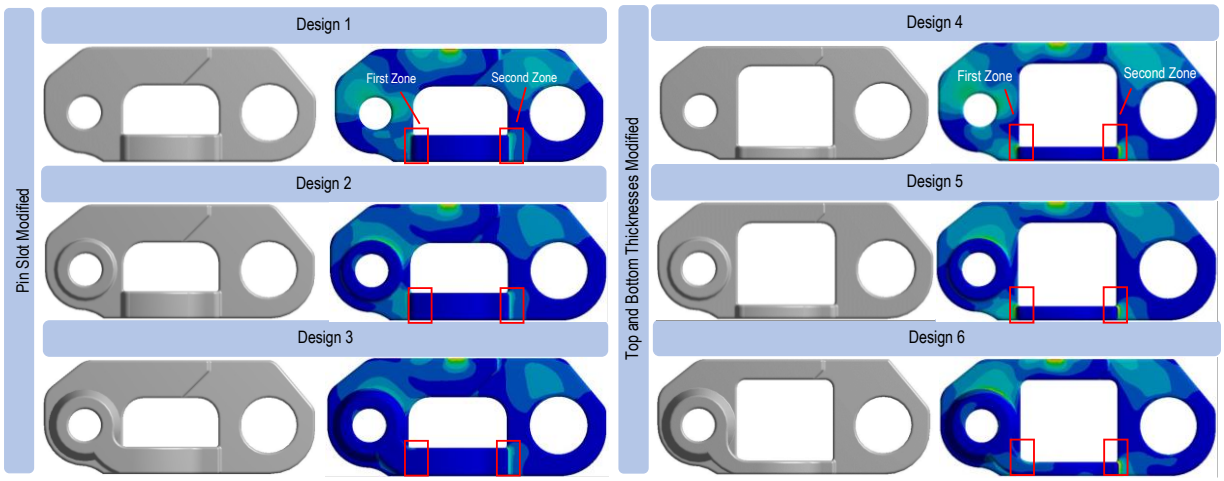

Figure 8. *Link designs with different geometries created for preliminary model selection*

According to the FEA results, the stress concentration values at the first and second regions of Design 4, 5 and 6 approximately twice compared to Designs 1, 2 and 3. Therefore, the preliminary model was selected from the group in which the pin slot was replaced. The maximum stress values of Design 1 and Design 2 is three times greater than Design 3 in the first region, while this value increases up to five times in the second region. For this reason, Design 3 was chosen as the most suitable preliminary design for both regions. Hence, critical regions were identified through this model. Figure 9 shows a comparison of the stress concentrations for both regions of whole designs. Here, the stress values of the preliminary model shown as PM assumed as a reference. Other stress values normalised to these values.

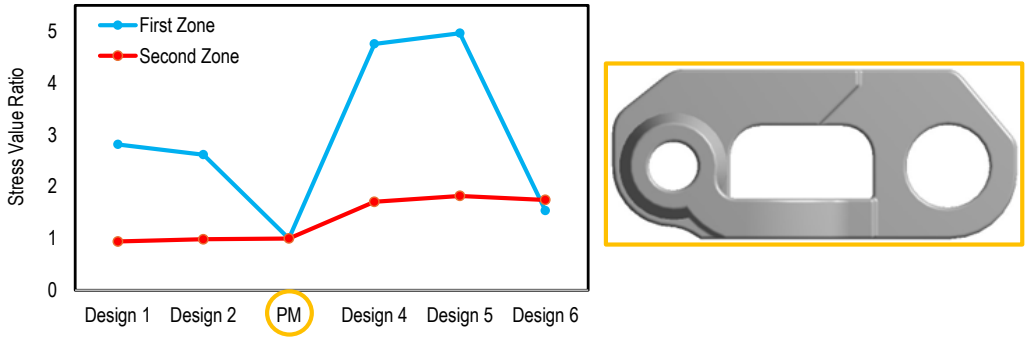

Figure 9. *Comparison of first and second zone stresses of links with different geometries according to the selected preliminary model*

D. PARAMETRIC OPTIMISATION

According to the FEA results of the preliminary model, three critical stress regions were identified for the DoE. In the selection of these regions, the principal stress distribution on the link was analysed and it was found that the selected regions operate mainly under tensile stress. The area selected as the first critical region is a zone where failure has been observed [7]. The second and third critical regions were selected for the optimisation study as the stress concentration occurring in these regions is higher than the stress value at which failure occurs [7]. Figure 10 shows the stress distributions in the critical regions determined on the link.

To minimise stress concentrations in these critical regions, seven structural design parameters were selected. Then, a DoE based optimisation study was performed using these parameters and a new link design was built using the obtained values. Figure 11 show the critical regions and selected design parameters.

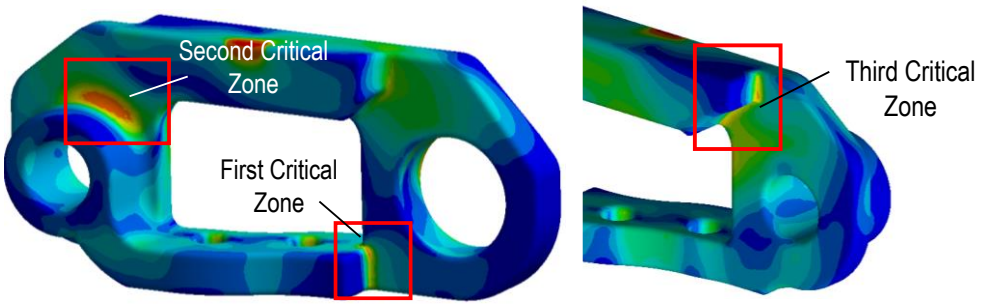

Figure 10. *Selected critical areas on the link*

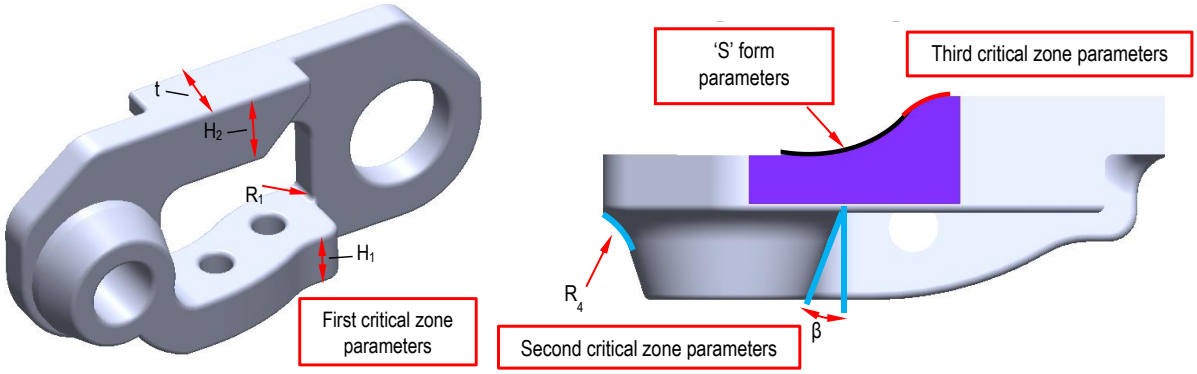

Figure 11. *Parameters of the link*

Firstly, the effect of design parameters such as fillet radius (R_1), part thickness (t), lower part height (H_1) and upper part height (H_2) on the stress concentration at the first critical region was analysed and the optimum design values were determined. The RS graphs were generated by using the maximum stress (σ_{max}) values calculated for the design points. The parameter's variation ranges determined by considering Figure 7. To reduce the stress concentration at the first critical region, design improvements were also done. The RS graphs obtained according to the maximum stress as a result of DoE are shown in Figure 12.

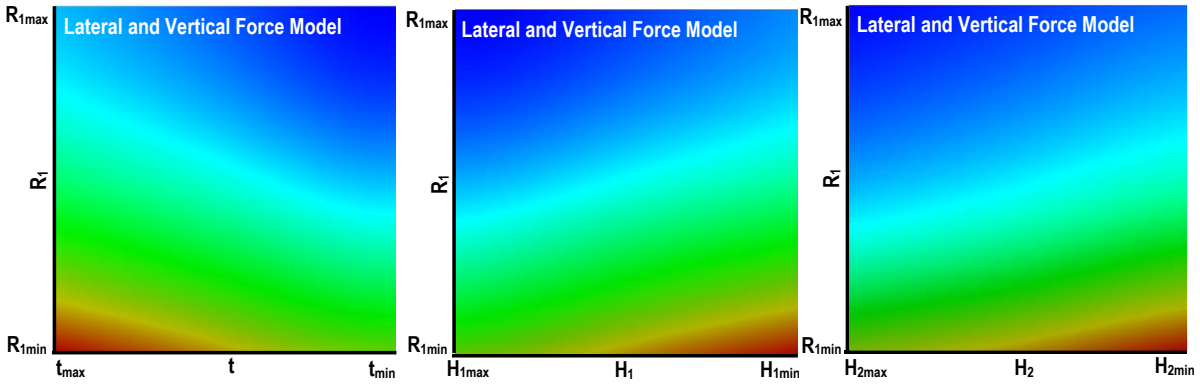

Figure 12. *Response Surface plots obtained according to the maximum stress at the first critical zone*

In the first critical region, the effect of the fillet radius (R_1), which is approximately determined as 62 %, is higher than the other parameter effects. In the maximum torque model, its effect is greater than the lateral and vertical force model. At the first critical region, the effect of the upper height was found to be approximately 12% for the maximum torque model. In the other load model, this value is 15%. Figure 13 shows the effect percentages of the parameters.

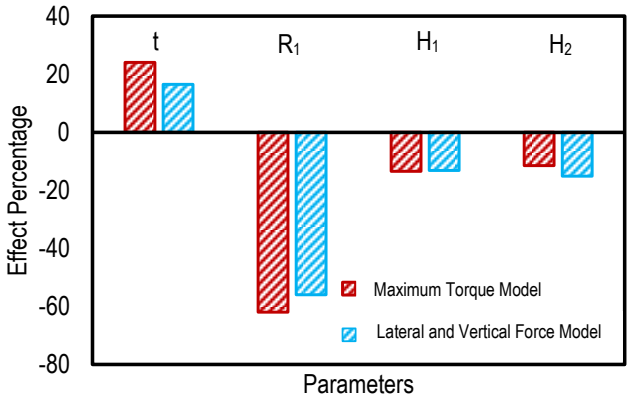

Figure 13. *Effect percentages of parameters in the first critical region*

In the DoE study of the third critical region, the structure of the upper part was given an 'S' form to ensure a smooth transition. Two radii were defined as shown in Figure 14.a. The R_2 parameter was found to have the highest effect on stress concentration. When the model for specific R_2 and R_3 values was analysed for two different load cases, a 57% increase in stress concentrations was observed in the second load model compared to the first model. This result shows that, a specific load model may not be sufficient for parameter selection. The effect of these parameters on the stress values over the third critical region is shown in Figure 14.b.

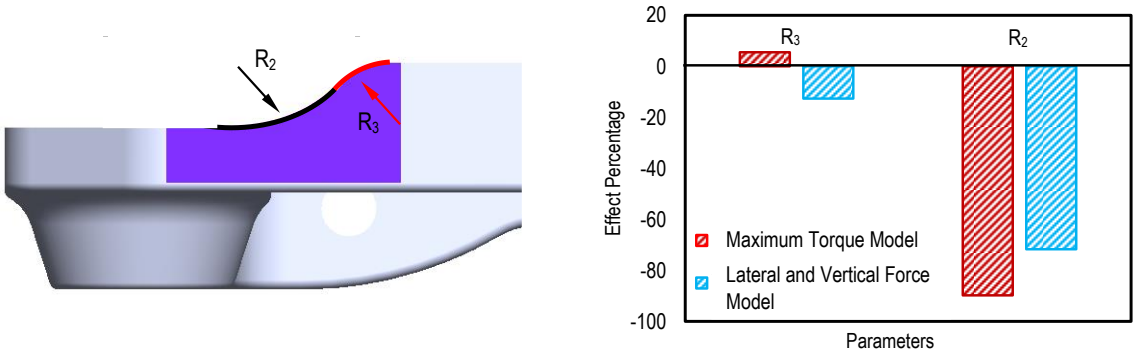

Figure 14. *Effect percentages of parameters in the third critical region*

After determining the optimal values of the first and third critical region parameters, the second DoE study was carried out for the pin slot region (second critical region) optimisation. For this purpose, the optimal geometrical values for the fillet radius (R_4) and the taper angle (β) of the second region shown in Figure 15 were determined as a result of the DoE - RMS. The variation ranges of the parameters were determined according to the operating volume of the links (Figure 7), model structure and production conditions.

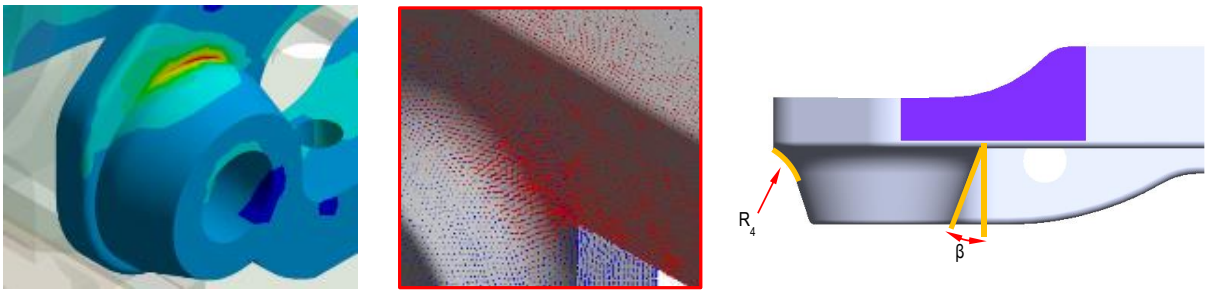

Figure 15. *FEA result of pin slot and selected parameters*

As a result of the analyses performed for the second region, the parameter with the highest effect was determined as the taper angle (β) in the maximum torque model and the fillet radius (R_4) in the lateral force model. In the maximum tensile model, it was observed that the increase in the taper angle increased the stress values. In addition, in the lateral and vertical force model, it was determined that the stress decreases as the fillet radius R_4 increases. Figure 16 shows the response surfaces obtained from these parameters.

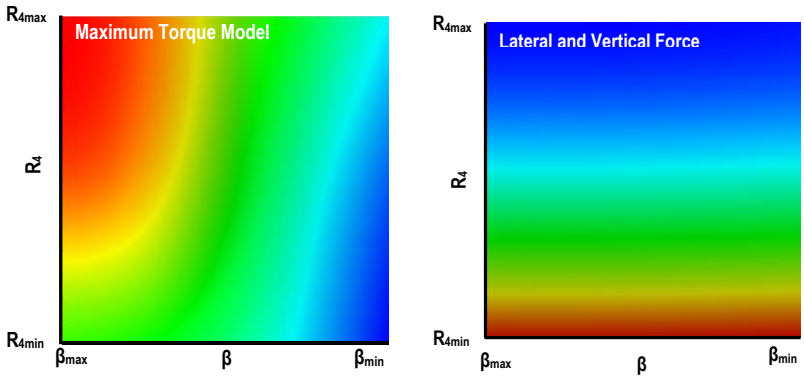

Figure 16. *Response surface plots of the second critical zone parameters*

In order to investigate the stress distribution around the pin slot, the stress values of twelve regions taken at 15° intervals are given in Figure 17 for both force models. As a result of the analyses performed using the optimal values of the parameters, 20% stress reduction was achieved for the first load case and 31% for the second load case.

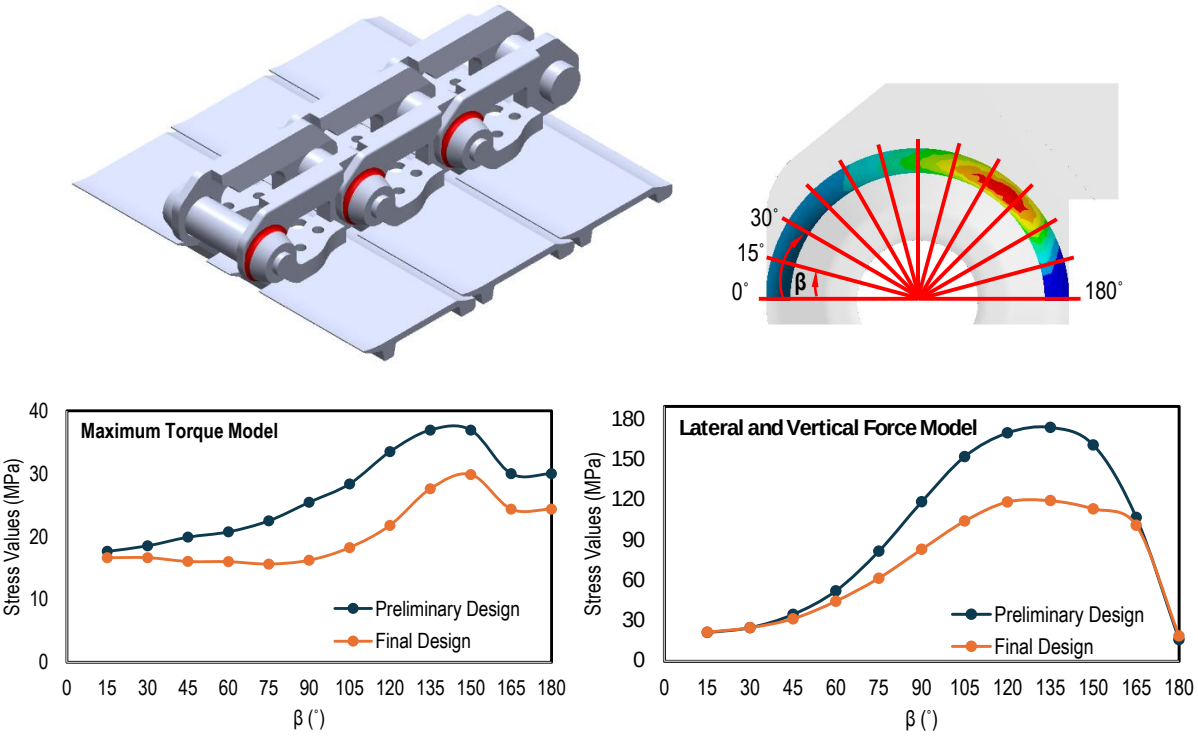

Figure 17. Stress variation at the at the second critical region

The FEA results of the sub-model simulating the operation of the links with each other are shown in Figure 18. In this sub-model, it is seen that the stress concentrations obtained in the critical regions are lower than the failure limits given in the literature as shown in Figure 18.a.

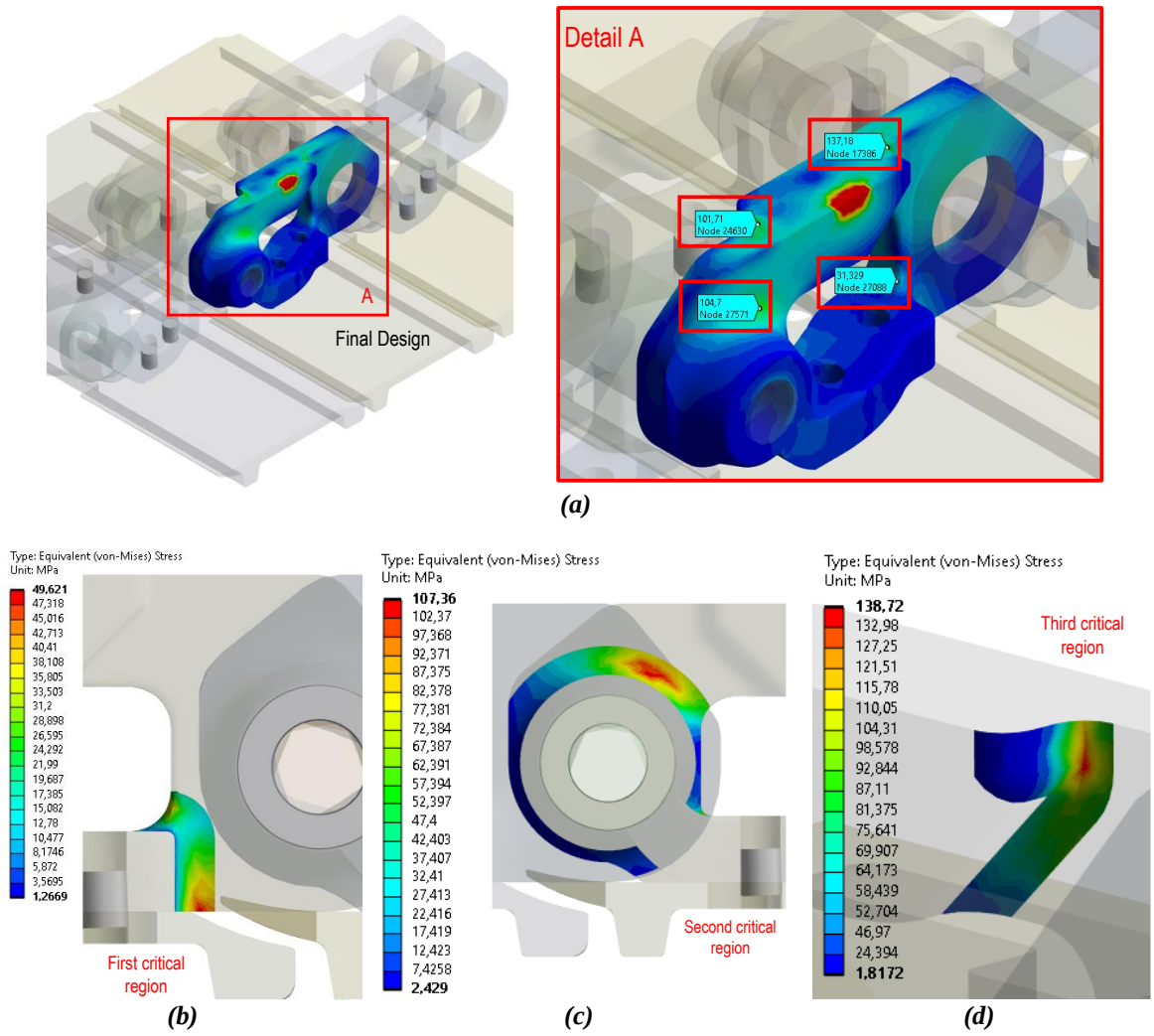

Figure 18. (a) *Sub-model,* ***(b)*** *First critical region,* ***(c)*** *Second critical region and* ***(d)*** *Third critical region*

IV. CONCLUSION

In this study, the design and optimisation processes of the link to be used in the steel track walking system of a tracked vehicle are summarised. Firstly, a preliminary model was created by considering various applied design examples and design constraints determined according to the operating envelope of the link. In this envelope, the penetration of the links in the whole relative rotation angle range is considered. The distances between the drive wheel and the links were also taken into account. Two different Finite Element (FE) models were built: the maximum tension force resulting from the maximum drive torque, and the contact forces caused by the roller contacts in addition to the tension force. With the help of these models, three critical regions in terms of stress concentration were determined on the link. To reduce the stress concentrations in these regions, seven structural design parameters were selected on the component. Using these parameters, a new link design was built using dimensional values obtained from a DoE-based study. The FE analyses for the first case showed that it is possible to reduce the stress concentration approximately 61%, 55% and 20% at the first, second and third critical regions, respectively. For the second load model, the improvement percentages are 63%, 26% and 31% in the same order. An FEA of the sub-model including the new link geometry was also carried out under the same loading conditions. As a result, the stress values at the critical regions of the new link design were found to be below the failure limits reported in the literature.

This paper summarises the design methodology of a track link using simplified ground contact models. It is possible to obtain different designs by using more complex track contact force models.

ACKNOWLEDGEMENTS: The authors are grateful to Smart İş Makinaları San. Tic. A.Ş. and Mr. Sercan Okan for technical support. The technical material presented in this study is published with the permission of Smart İş Makinaları San. Tic. A.Ş. Some technical details of the system are not given in the study due to the confidentiality policy of Smart İş Makinaları San. Tic. A.Ş.

V. REFERENCES

[1] J. Y. Wong and W. Huang, "Wheels vs. tracks – A fundamental evaluation from the traction perspective," *Journal of Terramechanics*, vol. 43, no. 1, pp. 27-42, 2006.

[2] J. Y. Wong, "Dynamics of tracked vehicles," *Vehicle System Dynamics*, vol. 28, no. 2-3, pp. 197-219, 1997.

[3] S. M. Bošnjak, M. A. Arsic, N. D. Zrnic, Z. D. Odanovic, and M. D. Dordevic, "Failure analysis of the stacker crawler chain link," *Procedia Engineering*, vol. 10, pp. 2244-2249, 2011.

[4] Z. W. Yu, X. L. Xu, and X. Mu, "Failure investigation on the cracked crawler pad link," *Engineering Failure Analysis*, vol. 17, no. 5, pp. 1102-1109, 2010.

[5] S. M. Bošnjak, D. B. Momčilović, Z. D. Petković, M. P. Pantelić, and N. B. Gnjatović, "Failure investigation of the bucket wheel excavator crawler chain link," *Engineering Failure Analysis*, vol. 35, pp. 462-469, 2013.

[6] Y. Li, D. He, Q. Si, and X. Meng, "Effect of track shoes structural parameters on traction performance of unmanned underwater tracked bulldozer," *Ocean Engineering*, vol. 237, p. 109655, 2021.

[7] H. Zhao, G. Wang, H. Wang, Q. Bi, and X. Li, "Fatigue life analysis of crawler chain link of excavator," *Engineering Failure Analysis*, vol. 79, pp. 737-748, 2017.

[8] M. A. Arsić, S. M. Bošnjak, Z. D. Odanović, M. M. Dunjić, and A. M. Simonović, "Analysis of the spreader track wheels premature damages," *Engineering Failure Analysis*, vol. 20, pp. 118-136, 2012.

[9] M. M. Topaç, K. Polat, ve O. Çolak, "Çelik paletli yürüyüş sisteminde yapısal emniyetin bakla-makara temas konumuna bağlı değişiminin sayısal incelemesi," INCOHIS 2023: Int. Cong. of New Horizons in Sciences, İstanbul, 2023.

[10] D. Dudek, S. Frydman, W. Huss, and G. Pękalski, "The L35GSM cast steel—Possibilities of structure and properties shaping at the example of crawler links," *Archives of Civil and Mechanical Engineering*, vol. 11, no. 1, pp. 19-32, 2011.

[11] M. G. Bekker, *Theory of Land Locomotion*, Michigan, USA: University of Michigan Press, 1956, pp. 232-282.

[12] J. Y. Wong, *Theory of Ground Vehicles*, 3rd ed., New York, USA: John Wiley & Sons, 2001, pp. 388-431.

[13] T. Amago, “Sizing optimization using response surface method in FOA,” *R&D Review of Toyota CRDL*, vol. 37, no. 1, pp. 1-7, 2002.

[14] M. Aydın and Y. S. Ünlüsoy, “Optimization of suspension parameters to improve impact harshness of road vehicles,” *The International Journal of Advanced Manufacturing Technology*, vol. 60, pp. 743-754, 2012.

[15] D. C. Montgomery, *Design and Analysis of Experiments*, 5th ed., New Jersey, USA : John Wiley & Sons, 2000, pp. 489-569.

[16] R. H. Myers, D. C. Montgomery, and C. M. Anderson-Cook, *Response Surface Methodology, Process and Product Optimization Using Design of Experiments*, 3rd ed., New Jersey, USA: John Wiley & Sons, 2009, pp. 1-349.

[17] B. Gelman and M. Moskvin, *Farm Tractors*, Moscow, : Mir Publishers, 1975, pp. 100-150.

[18] *Komatsu D80A-12, D85A-12 Bulldozers Shop Manual*, Tokyo, Japan : Komatsu, Ltd., pp. 12/05-12/07.

Düzce University
Journal of Science & Technology

Research Article

Overcut Optimization in Machining of DIN 1.2767 Tool Steel with Electro Erosion Technique

Abubaker Yousef FATATIT [a], Ali KALYON [b,*]

[a] *Karabük University, Natural and Applied Sciences, Manufacturing Eng. 078050 Karabük, Turkey*
[b] *Yalova University, Engineering Faculty, Mechanical Eng. Dep. 077200 Yalova, Turkey*
** Corresponding author's e-mail address: ali.kalyon@yalova.edu.tr*
DOI: 10.29130/dubited.1422393

ABSTRACT

Electro discharge machining is an energy based method that can cause fast electrode wear and dimensional errors. This study aimed to identify the optimum process parameters for processing 1.2767 steel using copper-based electrodes. The Taguchi optimization approach was used, and 18 pieces of 1.2767 steel were prepared for the experiments. The electrodes used were CuCoNiBe and $CuNi_2SiCr$, and the electrode surfaces were sanded and polished before processing. The results showed that the $CuNi_2SiCr$ electrode produced the lowest overcut value of 0.07 mm, while the CuCoNiBe electrode had the highest observed overcut value of 0.320 mm. The discharge level had the most significant impact on overcut, while the type of electrode had the least. The optimal parameters for the $CuNi_2SiCr$ electrode were 12 A discharge current, 50 µs pulse duration, and 800 µs pulse off time. The processing under ideal conditions resulted in an overcut measurement value of 0.05 mm.

Keywords: *EDM, Overcut, Copper, Taguchi, Optimization*

DIN 1.2767 Takım Çeliğinin Elektro Erozyon Tekniği ile İşlenmesinde Yanal Açıklık Optimizasyonu

ÖZ

Elektro erozyon ile işleme, hızlı elektrot aşınmasına ve boyutsal hatalara neden olabilecek enerji tabanlı bir işleme yöntemidir. Bu çalışma, bakır bazlı elektrotlar kullanarak 1.2767 çeliğini işlemek için optimum işlem parametrelerini belirlemeyi amaçlamıştır. Taguchi optimizasyon tekniği kullanılarak deneyler için 18 adet 1.2767 çeliğinden işparçası hazırlanmıştır. İşleme deneylerinde CuCoNiBe ve $CuNi_2SiCr$ elektrot kullanılmıştır ve elektrot yüzeyleri işlemeden önce zımparalanarak parlatılmıştır. Çalışma sonucunda $CuNi_2SiCr$ elektrot ile en düşük yanal açıklık değeri olan 0.07 mm, CuCoNiBe elektrod ile en yüksek yanal açıklık değeri olan 0.320 mm elde edilmiştir. Boşalım akımı, yanal açıklık üzerinde en önemli etkiye sahipken, elektrot tipi en az etkiye sahip parametre olmuştur. $CuNi_2SiCr$ elektrot için optimum işlem parametreleri 12 A boşalım akımı, 50 µs vurum süresi ve 800 µs bekleme süresi olarak belirlenmiştir. Optimum işleme şartında, yanal açıklık değeri 0.05 mm olarak elde edilmiştir.

Anahtar Kelimeler: *EEİ, Yanal açıklık, Bakır, Taguchi, Optimizasyon*

Received: 24/01/2024, Revised: 05/02/2024, Accepted: 15/09/2024

I. INTRODUCTION

Complex and highly precise parts are processed using the electrical discharge machining (EDM) technique. Furthermore, it is particularly suggested for precision machining and the processing of hard materials. It is evident from the benefits that the EDM process is among the best manufacturing techniques for molding. The two most crucial output parameters in the processing of industrial molds are surface quality and measurement accuracy. Surface quality affects the service life of molding components and varies significantly based on processing Parameters [1-3]. In order to avoid production-related errors, dimensional integrity is a critical consideration when producing molding products for mass production. Desired dimensional and shape errors in the EDM process are caused by machining parameters. Vibrations that arise during the machining process, particularly in machining methods, have an impact on both measurement accuracy and surface quality [4-5]. For this reason, it is a subject that needs to be studied to determine the effect of machining parameters on the EDM method. It is important to determine the optimum processing parameters in advance to shorten the processing time and ensure the accuracy of the measurement and surface quality [6-7].

The machinability of electro-discharge machining is dependent on numerous factors. The discharge current, pulse length, pulse on time, electrode type, workpiece material, fluid type of the dielectric medium, and application technique are these. Achieving high-performance processing requires careful selection of these parameters. If not, processing costs rise and processed parts develop dimensional errors. Processing time is decreased by selecting high processing parameters. In terms of cost, this arrangement appears advantageous, but in terms of electrode wear and measurement accuracy, it is not. In a study on Ti-6Al-4V machining, Ahmed et al. used four electrode materials with two different polarities: graphite, aluminum, copper, and brass. In an effort to reduce overcutting and tool wear, they looked into overcutting and tool wear rate. They met the requirements of minimum tool wear and minimum overcut (OC) by choosing the best tool with common tool polarity [8]. Patil and Jadhav came to the conclusion that material removal rate (MRR) is most affected by discharge current (Ip), but also significantly influenced by pulse on time (Ton) and Gap voltage (V). Ip and Ton have the biggest effects on tool wear rate (TWR); duty cycle and V have less of an impact. While surface finishes are improved by higher values of Ton, SR increases as Ip and Toff increase. The largest effect on OC is caused by Ip. Ton and the duty cycle both significantly affect OC. Gap voltage has little effect on open circuit voltage [9]. Kumar, Dewangan, and Pandey's study focuses on how the parameters of the EDM process affect the overcut and surface integrity of machined surfaces. They use the RSM approach to optimize performance metrics, with P91 steel serving as the workpiece and copper serving as the electrode tool. The results show that peak current is the most important factor, followed by duty cycle and pulse-on time [10]. In the EDM process, Chiang and Wang looked into variations in the side and bottom overcuts, electrode dimensions, spark hole dimensions, and machine positioning accuracy. The experiment's findings demonstrate that a key element in determining how the side overcut varies during the EDM process is the coupling effect between the electrode and spark hole diameters [11]. The reduction of side overcut through distortion of the electrical field between the tool and workpiece's side was the subject of Moghanizadeh's investigation. The findings show that using an external voltage around the side of the tools reduces side overcut, and that increasing the external voltage causes the value of overcut to decrease [12]. In Ti-6Al-4V EDM, Ishfaq et al. performed experiments with nano-graphene mixed with kerosene dielectric. They discovered that dimensional errors in axial and radial machining orientations are highly influenced by spark voltage and pulse-time ratio. While a large pulse-time ratio minimizes machining errors in both cutting directions [13]. In order to enhance surface integrity aspects following EDM of AISI P20 tool steel, Dewangan et al. suggested the best possible EDM process parameter settings. The impact of different EDM process parameters on different facets of surface integrity was examined, including Ip, pulse-on Ton, tool work time (Tw), and tool lift time (Tup). They came to the conclusion that dimensional accuracy is negatively impacted by greater pulse duration and current [14]. Using a response surface methodology (RSM) experimental design, Das et al. studied the effects of process variables on overcut. The findings demonstrated that overcut was highly influenced by discharge current, with higher current producing more overcut. The gap, pulse on, and pulse off times were additional factors influencing overcut. Increasing the gap led to the lowest overcut, which was also the

result of having the highest pulse on and the lowest pulse time [15]. During the EDM of Ti-6Al-4V, a reversal trend was seen between OC and discharge current (i.e., low intensity of discharge current provided poor dimensional accuracy) [16]. According to a different study, the most important factors in determining the OC magnitude are the tool material and pulse on time [17]. Grey relational analysis and analysis of variance were used in another study on Ti-6Al-4V EDM. It was determined that the key input parameter influencing the OC value is spark voltage [18].

Cold work tool steels have gathered significant interest for critical roles in a variety of industrial domains, including blanking and forming dies, gauges, and collets. They are commonly used in a variety of applications, including dies for cutting and shaping, coining, punching, shear blades, fullers, thermosetting resin forming, cold forming, thread rolling, fine blanking, stripper plates, profiling rollers, press tools, brick molds, chisels, and pneumatic tools [19,20]. Cakir and Ceritbinmez conducted a study to investigate the performance enhancement of brass EDM electrodes using cryogenic treatment while machining cold work steel AISI D2.The results show that cryogenic treatment improves material removal rate, tool wear, and surface quality, which can be attributed to increased electrical conductivity and changes in the internal structure of the brass electrode [21]. A study on cryogenically treated mold steel electrodes demonstrates the potential of machine learning algorithms to predict electro-erosion wear during EDM processes. The models showed exceptional accuracy, identifying factors affecting wear patterns and improving productivity and production quality [22]. Ramesh et al conducted an experimental study of powder-mixed electric discharge machining of AISI P20 steel with various powders and tool materials. Experiments are conducted using Taguchi's L_{27} orthogonal array. The results show that the copper tool combined with Al powder achieves the highest material removal rate, while the Al_2O_3 powder combined with tungsten tool produces the least radial overcut [23]. Dewangan et al investigated the optimization of input parameters in EDM of AISI 1020 steel with 0.2% carbon content. Five samples were chosen, each with distinct physical characteristics. The samples' hardness varied after heat treatment, taking into account current, pulse-on-time, and pulse-off-time variables. The study discovered that water and oil-quenched specimens could be machined with less current, indicating that heat treatment had successfully improved the material's properties [24]. Nas investigated the machinability of AISI H13 hot work tool steel that had undergone deep cryogenic treatment with electro-erosion machining. The parameters used in the study included current, pulse time, and three electrodes (copper, graphite, and tuncop). The experimental design was based on the Taguchi L_{27} model, and machinability tests were carried out to evaluate the results. The study discovered that surface roughness, hole diameter, material wear, and crater diameter increased with ampere and impact time [25]. Electro discharge machining is a sort of energy-based machining. A disadvantage of this electrodischarge machining approach is the inability to control the energy used in uncommon production processes. Choosing high processing settings, especially to reduce processing times, results in fast electrode wear and the formation of dimensional errors. An optimization analysis was carried out in this study to identify optimum process parameters in the processing of 1.2767 steel using various copper-based electrodes for this purpose. Graphics are used to interpret the impact of process parameters. Using the Taguchi optimization approach, ideal machining settings were found in order to produce the optimum dimensional values.

II. MATERIAL & METHODS

The Taguchi L_{18} orthogonal experiment set was used for electro-discharge machining experiments. 18 pieces of 1.2767 steel with dimensions of 50 mm x 25 mm x 12 mm were prepared for the experimental studies. The chemical composition of 1.2767 steel is shown in Table 1. As electrodes in the experiment, 16 mm CuCoNiBe, and $CuNi_2SiCr$ were used. A holder connects the electrodes to the bench. Each experimental condition required its own set of electrodes. The chemical composition of the electrodes is shown in Table 2.

Table 1. *DIN 1.2767 steel chemical composition (weight percentage)*

Element	C	Si	Mn	Cr	Mo	Ni	Fe
Weight (%)	0.45	0.25	0.35	1.35	0.25	4.05	Balance

Table 2. *Copper electrode chemical composition (weight percentage)*

	Cu	Cr	Si	Be	Co+Ni	Mn	Ni	Pb	Fe	Others
CuCoNiBe	Base	-	-	1	2	-	-	-	-	0.5
$CuNi_2SiCr$	Base	0.35	0.65	-	-	0.10	2.5	0.02	0.15	-

The Furkan M25A sink erosion machine was used for the experiments. The experiments were conducted on the FURKAN M25A sinker electrical discharge machine. The maximum peak current is 25 Amps and the maximum pulse on-time and pulse off-time are 1600 µs. The sinking EDM machine tool consists of the power supply, control unit, tool holder, worktable, servo control system and dielectric fluid delivery system. Three different electrodes, three different discharge currents, pulse on time, and pulse off time were used in the processability experiments. During the processing, a negative pole was chosen for the workpieces and a positive pole for the electrode. The dielectric medium fluid was kerosene. Laterally, dielectric medium fluid was applied to the processing zone. Each workpiece was processed for 1 hour for processing experiments. A stereomicroscope was used to measure the processed areas after they had been processed. Figure 1 represents the schematic diagram of the experimental study.

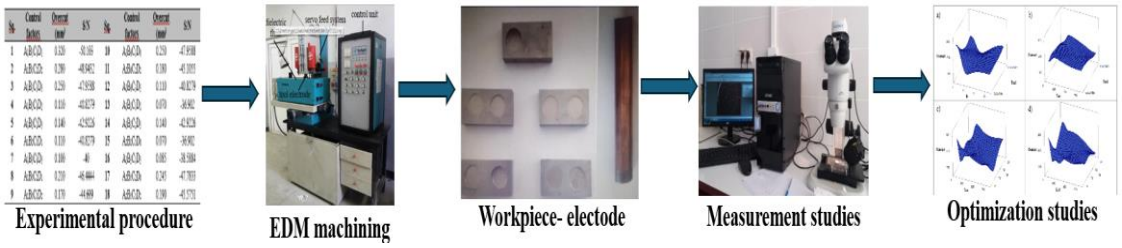

Figure 1. *Schematic diagram of the experimental study*

In industrial settings, traditional experimental design techniques are expensive and time-consuming, which increases experimentation and challenges. The Taguchi method (TM) of fractional factorial design provides a simpler and more effective solution by minimizing the number of experiments needed and enabling independent factor evaluation. By creating equal samples for various levels of factors under each tested condition, the TM maintains equilibrium in the experimental design. Reducing variability around the target value is the TM's primary goal [26,27].

A signal-to-noise (S/N) ratio, which compares the actual value required from the system to a factor not taken into account during design, is used to evaluate the measurement results. A product with a higher S/N ratio is of higher quality, and as signal values rise, noise levels should also fall. The three most popular methods for calculating the S/N ratio are "nominal is best," "smaller is better," and "larger is better." In this study, the maxim "smaller is better" was applied to minimize overcut, as determined by Equation (1), in which n is the number of experiments and yi is the experiment's data [28,29]. The Taguchi experimental design determined for the experimental study is shown in Table 3.

$$S/N = -10log\left[\frac{1}{n}\sum_{i=1}^{n} y_i^2\right] \quad (1)$$

Table 3. *Erosion Parameters and levels*

Inputs	Unit	Level 1	Level 2	Level 3
Electrode		CuCoNiBe	CuNi2SiCr	
Ip	A	6	12	25
Ton	µs	50	200	800
Toff	µs	50	200	800

III. RESULTS AND DISCUSSION

The overcut values obtained from the experimental investigation utilizing CuCoNiBe and $CuNi_2SiCr$ electrodes are displayed in Table 4. Three different discharge current levels 6, 12, and 25 Amperes as discharge current, as pulse on and pulse off times 50, 200, and 800 µs were employed in the experimental investigation. The experimental study resulted in the lowest overcut value of 0.07 mm when the $CuNi_2SiCr$ electrode was used in the circumcantes of $A_2B_2C_1D_2$ and $A_2B_2C_3D_1$ experimental conditions. Under experimental conditions of 6 A, 50 µs, and 50 µs, the CuCoNiBe electrode resulted in the highest measured overcut value of 0.320.

Table 4. *Experimental results and S/N ratios*

Sq.	Control factors	Overcut (mm)	S/N	Sq.	Control factors	Overcut (mm)	S/N
1	$A_1B_1C_1D_1$	0.320	-50.103	**10**	$A_2B_1C_1D_1$	0.250	-47.9588
2	$A_1B_1C_2D_2$	0.280	-48.9432	**11**	$A_2B_1C_2D_2$	0.180	-45.1055
3	$A_1B_1C_3D_3$	0.250	-47.9588	**12**	$A_2B_1C_3D_3$	0.110	-40.8279
4	$A_1B_2C_1D_2$	0.110	-40.8279	**13**	$A_2B_2C_1D_2$	0.070	-36.902
5	$A_1B_2C_2D_3$	0.140	-42.9226	**14**	$A_2B_2C_2D_3$	0.140	-42.9226
6	$A_1B_2C_3D_1$	0.110	-40.8279	**15**	$A_2B_2C_3D_1$	0.070	-36.902
7	$A_1B_3C_1D_3$	0.100	-40	**16**	$A_2B_3C_1D_3$	0.085	-38.5884
8	$A_1B_3C_2D_1$	0.210	-46.4444	**17**	$A_2B_3C_2D_1$	0.245	-47.7833
9	$A_1B_3C_3D_2$	0.170	-44.609	**18**	$A_2B_3C_3D_2$	0.190	-45.5751

The graphs generated from the overcut values measured resulting from electro erosion processing using two different electrodes are shown in Figure 2. The application of the $CuNi_2SiCr$ electrode has a negative, though slight, impact on the overcut value, as Figure 2.a illustrates. It appears that the CuCoNiBe electrode can lead to improved measurement accuracy. It can be observed that the overcut value rises as the discharge current value accomplishes. In particular, high discharge current values had a positive impact on the overcut value, whereas low discharge current values increased the overcut value. The impact of electrode type and pulse duration on overcut can be seen in Figure 2.b. It can be observed that as pulse time increases, the overcut value rises as well [30-31]. Compared to the $CuNi_2SiCr$ electrode, it appears that the CuCoNiBe electrode has a more detrimental effect on overcut.

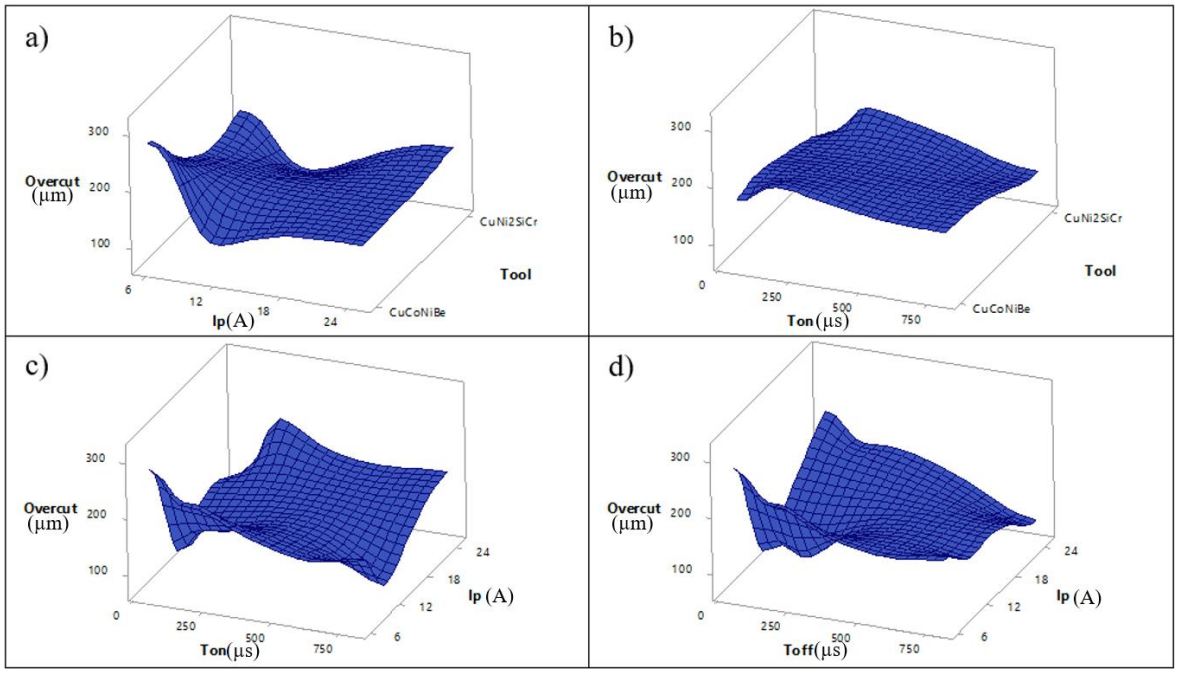

Figure 2. *Effect of erosion parameters on overcut*

Figure 2.c shows that the effect of pulse duration and discharge current on overcut varies according to parameter levels. It seems that increasing the pulse duration has a negative effect on overcut. However, while low discharge and high discharge levels increased the overcut value, better results were obtained at medium discharge current values. Figure 2.d shows that increasing the pulse off time has a positive effect on the overcut value. It is known that increasing the pulse off time results in better cleaning of the processing area and the creation of a better processing environment [32]. It is seen that using high discharge current at high erosion levels reduces the overcut value [33,34]. This shows that cleaning the processing area from particles formed after processing is an important issue for the measurement accuracy of the processing operation.

The S/N ratios of the parameter effect on the overcut are displayed in Figure 3. Examining the graph reveals that overcut is significantly influenced by the discharge level. It is evident that the electrode type has the lowest effect level. Overcut values are observed to rise with the CuCoNiBe electrode and at low current levels. Overcut values are also adversely affected by medium pulse duration and low pulse off times [35,36].

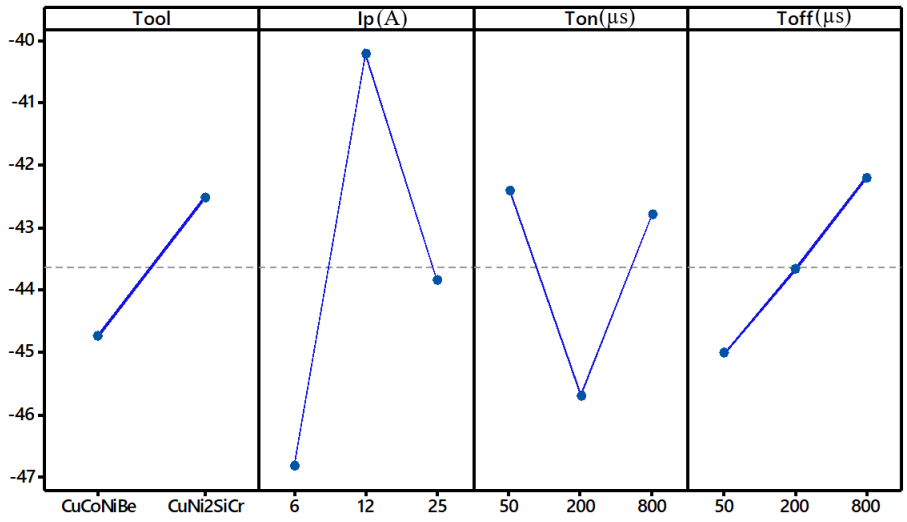

Figure 3. *S/N ratios*

The S/N ratios in Figure 3 can be better understood by examining at the tabulated values in Table 5. The optimal values for the processing Parameters electrode type, discharge current, pulse on time, and pulse off time can be observed by studying Table 5. It was determined that the $CuNi_2SiCr$ electrode, discharge current of 12 A, pulse on time of 50 µs, and pulse off time of 800 µs were the ideal parameter levels for the electrode type.

Table 5. *Optimum machining levels for the overcut*

Level	Tool	Ip	Ton	Toff
1	-44.74	-46.82	-42.40	-45.00
2	-42.51	-40.22	-45.69	-43.66
3		-43.83	-42.78	-42.20
Delta	2.23	6.60	3.29	2.80

The workpiece processed using the $CuNi_2SiCr$ electrode under the $A_2B_2C_1D_2$ experimental condition characterized by a 12 A discharge current, 50 µs pulse on time, and 200 µs pulse off time yielded an overcut value of 0.07 mm, as depicted in Figure 4.a. Through Taguchi optimization, the $A_2B_2C_1D_3$ experimental condition was identified as the optimal set of parameters. The predicted overcut value for this condition, according to Taguchi analysis, was 0.0438 mm. Upon validating this prediction, the overcut measurement under the optimized conditions (using the $CuNi_2SiCr$ electrode with a 12 A

discharge current, 50 µs pulse on time, and an extended 800 µs pulse off time) resulted in a measured overcut of 0.05 mm, as shown in Figure 4.b.

This finding highlights the effectiveness of using Taguchi optimization to fine-tune the EDM process parameters for achieving minimal overcut. The reduction in overcut from the initial 0.07 mm to 0.05 mm demonstrates that adjusting the pulse off time plays a critical role in enhancing machining precision. Consequently, by systematically experimenting with different electrodes and processing conditions, it is possible to accurately determine the ideal overcut value for machining DIN 1.2767 steel, thereby improving the overall accuracy and quality of the final product.

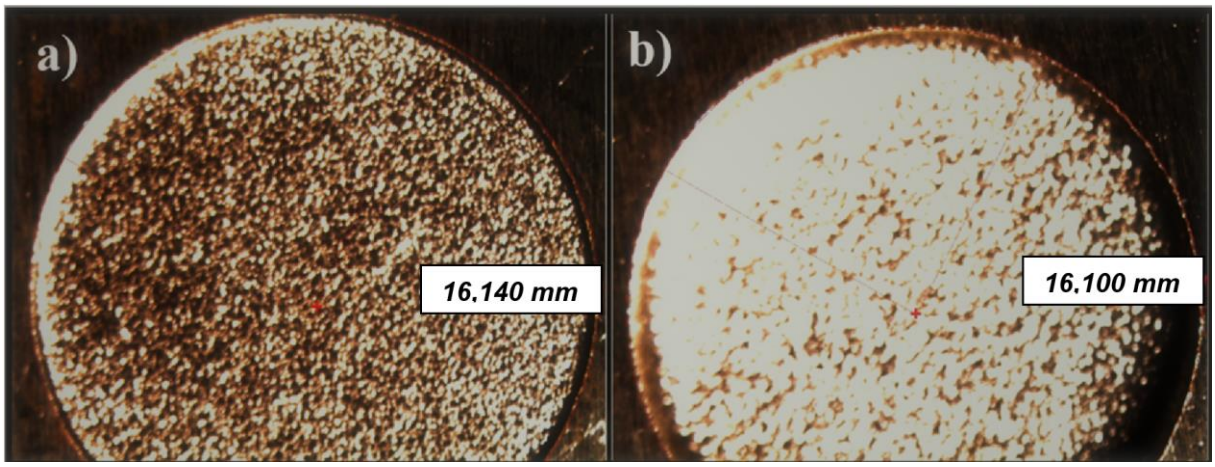

Figure 4. *Overcut measurement results a) $A_2B_2C_1D_2$ b) $A_2B_2C_1D_3$*

IV. CONCLUSION

Taguchi optimization aids in establishing the ideal combination of input parameters such as voltage, current, pulse duration, and electrode material, resulting in improved machining efficiency. By systematically adjusting these parameters using Taguchi methodologies, the process could be adjusted to get the required machining results with little trial and error. CuCoNiBe and $CuNi_2SiCr$ electrodes were used in this work to process DIN 1.2767 steel under various processing conditions. The impacts of the process parameters on the overcut value were examined by measuring the machining area. As the $CuNi_2SiCr$ electrode was employed in the circumcantes of the $A_2B_2C_1D_2$ and $A_2B_2C_3D_1$ experimental settings, the experimental investigation produced the lowest overcut value of 0.07 mm. The CuCoNiBe electrode exhibited the highest observed overcut value of 0.320 mm while investigated at 6 A, 50 µs, and 50 µs. The discharge level has a major impact on overcut. The least impact on overcut is caused by the type of electrode. At low current levels, it is observed that overcut values increase when using the CuCoNiBe electrode. Medium pulse on time and low pulse off times also have a negative impact on overcut values. The optimal parameter levels for the electrode type were found to be the CuNi2SiCr electrode, discharge current of 12 A, pulse on time of 50 µs, and pulse off time of 800 µs. Processing under ideal experimental circumstances led to a measurement of the overcut measurement value of 0.05 mm. By identifying the optimal combination of parameters, Taguchi methods help to achieve precise control over the machining process, reducing overcut and improving dimensional accuracy.

V. REFERENCES

[1] A. Kalyon, “Optimization of the machinability of aluminum 6082 alloy by brass electrode” *El-Cezeri*, vol. 6, no. 1, pp. 118–130, 2019.

[2] N. Mohd Abbas, D. G. Solomon, and M. Fuad Bahari, “A review on current research trends in electrical discharge machining (EDM),” *International Journal of Machine Tools and Manufacture*, vol. 47, no. 7–8, pp. 1214–1228, 2007.

[3] K. H. Ho and S. T. Newman, “State of the art electrical discharge machining (EDM),” *International Journal of Machine Tools and Manufacture*, vol. 43, no. 13, pp. 1287–1300, 2003.

[4] M. Dastagiri and A. Hemantha Kumar, “Experimental investigation of EDM parameters on stainless steel & En41b,” *Procedia Engineering*, vol. 97, pp. 1551-1564, 2014.

[5] K. Jarosz, P. Nieslony, and P. Löschner, “Investigation of the effect of process parameters on surface roughness in EDM machining of ORVAR® supreme die steel,” *Lecture Notes in Mechanical Engineering*, pp. 333–340, 2019.

[6] S. Sharif, W. Safiei, A. F. Mansor, M. H. M. Isa, and R. M. Saad, “Experimental study of electrical discharge machine (die sinking) on stainless steel 316L using design of experiment,” *Procedia Manufacturing*, vol. 2, pp. 147–152, 2015.

[7] A. Kalyon, “Experimental investigation of the machinability of AISI D2 cold work tool steel with electro discharge technique,” *Mehmet Akif Ersoy Üniversitesi Uygulamalı Bilimler Dergisi*, vol. 3, no. 1, pp. 75–86, 2019.

[8] N. Ahmed, K. Ishfaq, M. Rafaqat, S. Pervaiz, S. Anwar, and B. Salah, “EDM of Ti-6Al-4V: electrode and polarity selection for minimum tool wear rate and overcut,” *Materials and Manufacturing Processes*, vol. 34, no. 7, pp. 769–778 2019.

[9] V. D. Patil, K. K., & Jadhav, “Study of machining parameters in EDM,” *International Journal of Engineering Applied Sciences and Technology*, vol. 4, no. 1, pp. 72–78, 2016.

[10] P. Kumar, S. Dewangan, and C. Pandey, “Analysis of surface integrity and dimensional accuracy in EDM of P91 steels,” *Materials Today: Proceedings*, vol. 33, pp. 5378–5383, 2020.

[11] H. N. Chiang and J. J. J. Wang, “An analysis of overcut variation and coupling effects of dimensional variable in EDM process,” *The International Journal of Advanced Manufacturing Technology*, vol. 55, no. 9, pp. 935–943, 2011.

[12] A. Moghanizadeh, “Reducing side overcut in EDM process by changing electrical field between tool and work piece,” *The International Journal of Advanced Manufacturing Technology*, vol. 90, no. 1, pp. 1035–1042, 2016.

[13] K. Ishfaq, M. Asad, M. Harris, A. Alfaify, S. Anwar, L. Lamberti, M.L. Scutaru, “EDM of Ti-6Al-4V under nano-graphene mixed dielectric: A detailed investigation on axial and radial dimensional overcuts,” *Nanomaterials*, vol. 12, pp. 432, 2022.

[14] S. Dewangan, S. Gangopadhyay, and C. K. Biswas, “Study of surface integrity and dimensional accuracy in edm using fuzzy topsis and sensitivity analysis,” *Measurement*, vol. 63, pp. 364–376, 2015.

[15] A. Das, S. Padhan, and S. Ranjan Das, “Analysis on hole overcut during micro-edm of inconel 718,” *Materials Today: Proceedings*, vol. 56, pp. 29-35, 2021.

[16] M. Y. Lin, C. C. Tsao, H. H. Huang, C. Y. Wu, and C. Y. Hsu, “Use of the grey-taguchi method to optimise the micro-electrical discharge machining (micro-EDM) of Ti-6Al-4V alloy,” *International Journal of Computer Integrated Manufacturing*, vol. 28, no. 6, pp. 569–576, 2015.

[17] V. J. Mathai, H. K. Dave, and K. P. Desai, "Analysis of dimensional inaccuracies in square cavities generated on Ti-6Al-4V using planetary edm," *International Journal of Materials and Product Technology*, vol. 56, no. 1/2, pp. 108, 2018.

[18] V. K. Meena and M. S. Azad, "Grey relational analysis of micro-edm machining of ti-6Al-4V alloy," *Materials and Manufacturing Processes*, vol. 27, no. 9, pp. 973–977, 2012.

[19] M. Akgün, B. Özlü, and F. Kara, "Effect of PVD-TiN and CVD-Al2O3 coatings on cutting force, surface roughness, cutting power, and temperature in hard turning of AISI H13 steel," *Journal of Materials Engineering and Performance*, vol. 32, no. 3, pp. 1390–1401, 2023.

[20] B. Reddy Gunamgari, G. N. Kumar, and M. Kharub, "Cryogenic processing of AISI P20 tool steel: evaluation of mechanical properties and microstructure," *Materials Today*, 2023.

[21] F. H. Cakir and F. Ceritbinmez, "Performance enhancement of brass edm electrodes with cryogenic treatment while machining the cold work steel AISI D2," *Surface Review and Letters*, 2023.

[22] A. Cetin, G. Atali, C. Erden, and S. S. Ozkan, "Assessing the performance of state-of-the-art machine learning algorithms for predicting electro-erosion wear in cryogenic treated electrodes of mold steels," *Advanced Engineering Informatics*, vol. 61, no. 102468, p. 102468, 2024.

[23] Ramesh, M. P. Jenarthanan, and B. Kanna, "Experimental investigation of powder-mixed electric discharge machining of AISI P20 steel using different powders and tool materials," *Multidiscipline Modeling in Materials and Structures*, vol. 14, no. 3, pp. 549–566, 2018.

[24] S. Dewangan, G. Sukhwal, S. Naidu, L. Maheshwari, H. Surana, and A. R. Kulkarni, "Optimization of input parameters used for machining heat-treated 0.2%-C steel under the edm method," *Journal of The Institution of Engineers (India): Series D*, pp. 1-17,2024.

[25] E. Nas, "Experimental and statistical investigation of electro-erosion machining performance of cryogenic treated hardened AISI H13 hot work tool steel," *Tribology International*, vol. 193, no. 109453, p. 109453, 2024.

[26] B. Erman and A. Kalyon, "Multi objective optimization of parameters in EDM of Mirrax steel," *Materials and Manufacturing Processes*, vol. 38, no. 7, pp. 848–858, 2023.

[27] A. Kalyon, "Taguchi method for optimizing tool wear rate and overcut in electro discharge machining" *Adıyaman Üniversitesi Mühendislik Bilimleri Dergisi*, vol. 9, no. 18, pp. 471–480, 2022.

[28] A. Kalyon, "Optimization of surface roughness and material removal Rate for aluminum alloy by Taguchi technique in electro discharge machining" *Dokuz Eylül Üniversitesi Mühendislik Fakültesi Fen ve Mühendislik Dergisi*, vol. 21, no. 62, pp. 595–605, 2019.

[29] G. Bedir and E. Nas, "Investigation of electro-discharge driling performance of 32CRMOV12-10 steel" *Düzce Üniversitesi Bilim ve Teknoloji Dergisi*, vol. 10, no. 5, pp. 1–9, 2022.

[30] R. Mahajan, H. Krishna, A. K. Singh, and R. K. Ghadai, "A review on copper and its alloys used as electrode in EDM," *IOP Conference Series: Materials Science and Engineering*, vol. 377, p. 012183, 2018.

[31] D. Marelli, S. K. Singh, S. Nagari, and R. Subbiah, "Optimisation of machining parameters of wire-cut EDM on super alloy materials–A review," *Materials Today*, vol. 26, pp. 1021–1027, 2020.

[32] A. Kalyon, "Optimization of machining parameters in sinking electrical discharge machine of caldie plastic mold tool steel," *Sadhana*, vol. 45, no. 1, 2020.

[33] D. Sharma and S. S. Hiremath, “Review on tools and tool wear in edm,” *Machining Science and Technology*, vol. 25, no. 5, pp. 802–873, 2021.

[34] J. E. A. Qudeiri, A. Zaiout, A.-H. I. Mourad, M. H. Abidi, and A. Elkaseer, “Principles and characteristics of different edm processes in machining tool and die steels,” *Applied Sciences*, vol. 10, no. 6, p. 2082, 2020.

[35] M. N. Alam, A. N. Siddiquee, Z. A. Khan, and N. Z. Khan, “A comprehensive review on wire edm performance evaluation,” *Proceedings of the Institution of Mechanical Engineers, Part E: Journal of Process Mechanical Engineering*, vol. 236, no. 4, pp. 1724–1746, 2022.

[36] R. Singh, R. P. Singh, and R. Trehan, “State of the art in processing of shape memory alloys with electrical discharge machining: A review,” *Proceedings of the Institution of Mechanical Engineers, Part B: Journal of Engineering Manufacture*, vol. 235, no. 3, pp. 333–366, 2021.

Düzce University
Journal of Science & Technology

Review Article

Coumarins: Chemical Synthesis, Properties and Applications

Safa ELMUSA [a,*], Muna ELMUSA [a,b], Benan ELMUSA [c], Rahmi KASIMOĞULLARI [a]

[a] *Department of Chemistry, Faculty of Arts and Sciences, Dumlupinar University, Kutahya, Turkey*
[b] *Elfurat Engineering Research and Development Limited Company, Ankara, Turkey*
[c] *Department of Material Science and Engineering, Faculty of Engineering Eskisehir Technical University, Eskisehir, Turkey*
* *Corresponding author's e-mail address: safa.elmusa@gmail.com*
DOI: 10.29130/dubited.1441144

ABSTRACT

Coumarins are compounds characterized by a benzopyrone structure resulting from the condensation of pyrone and a benzene ring. They are commonly found as secondary metabolites in various plants, microorganisms, and sponges. These metabolites play a crucial role in defence mechanisms, and extensive research has revealed numerous biological activities associated with these compounds. Coumarin and its derivatives show significant potential as candidates for new drugs due to their exceptional biocompatibility and a wide range of biological activities, including antimicrobial, anticancer, antimitotic, antioxidant, anti-inflammatory, and anticoagulant properties. Beyond medicinal applications, the simple and versatile scaffold structures of coumarins have found use in fields such as food production, agriculture, cosmetics, and textiles. This review covers the classification of coumarin and its derivatives, as well as various chemical synthesis methods. Furthermore, it delves into the properties, biological activities, and diverse application areas of coumarins.

Keywords: *Coumarin, Coumarin Derivatives, Classification, Chemical Synthesis, Biological Activity, Applications*

Kumarinler: Kimyasal Sentez, Özellikler ve Uygulamalar

Öz

Kumarinler, piron ve bir benzen halkası arasında meydana gelen kondenzasyon sonucu oluşan benzopiron yapısı ile karakterize edilen bileşiklerdir. Bu metabolitler çeşitli bitkilerde, mikroorganizmalarda ve süngerlerde ikincil metabolitler olarak yaygın olarak bulunurlar. Bu metabolitler, savunma mekanizmalarında önemli bir rol oynarlar ve geniş çapta yapılan araştırmalar bu bileşiklerle ilişkilendirilen çok sayıda biyolojik aktiviteyi ortaya koymuştur. Kumarin ve türevleri, antimikrobiyal, antikanser, antimitotik, antioksidan, antiinflamatuar ve antikoagülan özellikler dahil olmak üzere geniş bir biyolojik aktivite yelpazesine sahip olmaları nedeniyle yeni ilaç adayları olarak önemli potansiyele sahiptirler. Tıbbi uygulamaların ötesinde, kumarinlerin basit ve çok yönlü iskelet yapıları, gıda üretimi, tarım, kozmetik ve tekstil gibi alanlarda kullanım bulmuştur. Bu derleme, kumarin ve türevlerinin sınıflandırılmasını, çeşitli kimyasal sentez yöntemlerini kapsamaktadır. Ayrıca, kumarinlerin özellikleri, biyolojik aktiviteleri ve çeşitli uygulama alanlarına da değinmektedir.

Anahtar Kelimeler*: Kumarin, Kumarin Türevleri, Sınıflandırma, Kimyasal Sentez, Biyolojik Aktivite, Uygulamalar*

Received: 21/02/2024, Revised: 10/03/2024, Accepted: 17/09/2024

I. INTRODUCTION

Coumarins (coumarin and its derivatives) are compounds that are formed as a result of the joining of benzene and α-pyrone rings and have a core structure defined as chromen-2-one or benzopyran-2-one [1]. Coumarins, an important member of the polyphenolic compounds class, are characterized by their benzopyrone structure [2]. According to the substituents next to this heterocyclic structure, coumarins; It is divided into 6 different classes: simple coumarins, pyranocoumarins, furanocoumarins, dihydrofuranocoumarin, phenylcoumarin and bicoumarin [3]. Found in the seeds, roots and leaves of many plants, coumarin was first found in high concentration in tonka beans. For this reason, it is named after the French word "Coumarou" meaning tonka bean [4].

More than 1800 coumarin derivatives have been found so far [5]. It has been reported that these coumarins can be found in free form in nature as well as in conjugated form with other compounds such as methyl and sugar [5], [6]. There are studies reporting that coumarins belonging to the benzopyrone family have potential activity against many diseases such as cancer [6]. In addition, coumarins, which are secondary metabolites related to the defence mechanism in living things, have been reported in many articles to have a number of pharmacological properties such as anti-inflammatory, antioxidant, antimicrobial, antidepressant, neuroprotective or antitumoral effects [7].

The heterocyclic systems present in coumarins have led to their widespread adoption as scaffolds in various applications. Moreover, owing to their remarkable biological activities, coumarins have assumed a pivotal role in the development of novel candidate drugs [8]. In the following sections of this paper, we will delve into the classification of coumarin and its derivatives, explore various chemical synthesis methods, and discuss their properties, biological activities, and manifold areas of application.

II. CLASSES OF COUMARINS

Coumarins can be classified in different ways according to their chemical structure, source and synthesis methods.

A. CLASSIFICATION OF COUMARINS BY CHEMICAL STRUCTURE

This classification based on the most common chemical (core) structure of coumarins with 1,2-benzopyrone structure [6], [7].

A. 1. Simple Coumarins

It contains unsubstituted, mono-substituted, di-substituted, tri-substituted, tetra-substituted coumarins (Figure 1). Simple coumarins are divided into the following 5 classes:

a) Isocoumarins: It is an isomer of coumarin formed by the replacement of the carbonyl group and oxygen in the coumarin structure. For example: isocoumarin.
b) Glycosid coumarins: The coumarin ring is formed by bonding with a sugar. For example: esculin, daphnin, skimmin.
c) Pyrone-substituted coumarins: It is a type of coumarin formed by binding different substituents to the pyron ring. For example: warfarin.
d) Benzene-substituted coumarins: They are structures formed by attaching a phenyl group to the coumarin ring. For example: limettin, umbelliferone, osthole.
e) Complex coumarins: It is formed by the bonding of different substituents in both the benzene ring and the pyron ring. For example: novobiocin, alternariol.

Simple coumarins form a new product family called Seskiterpene coumarins by forming C-C bonds [9].

A. 2. Furanocoumarins

It is formed by the bonding of coumarin and furan ring, and there are two types as linear and angular. For example: psoralen, marmelosin, angelicin, isobergapten (Figure 2).

A. 3. Dihydrofuranocoumarins

It is a coumarin derivative formed by the bonding of coumarin and dihydrofuran ring. For example: marmesin, felamidin (Figure 2).

A. 4. Pyranocoumarins

They are compounds that have two types, linear type and angular type, and are formed as a result of the bonding of coumarin and pyran ring. For example: xanthyletin, seselin, visnadin (Figure 2).

A. 5. Phenylcoumarins

It is formed by attaching a phenyl group to the pyron ring in the coumarin ring. For example: isodispar B, mammea A/AB (Figure 2).

A. 6. Bicoumarins

It is formed as a result of the bonding of two coumarin rings. For example: dicoumarol (Figure 2).

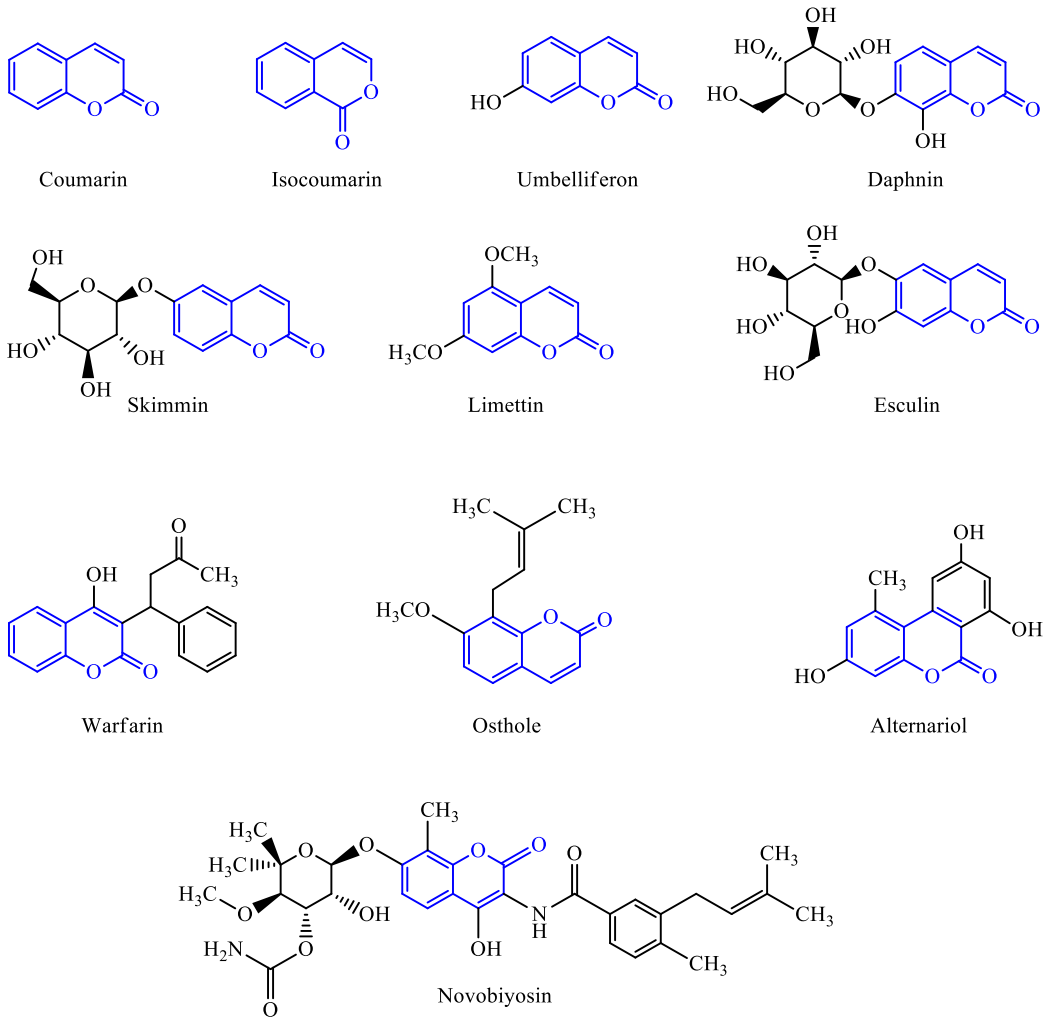

Figure 1. *Chemical Structure of Simple Coumarins.*

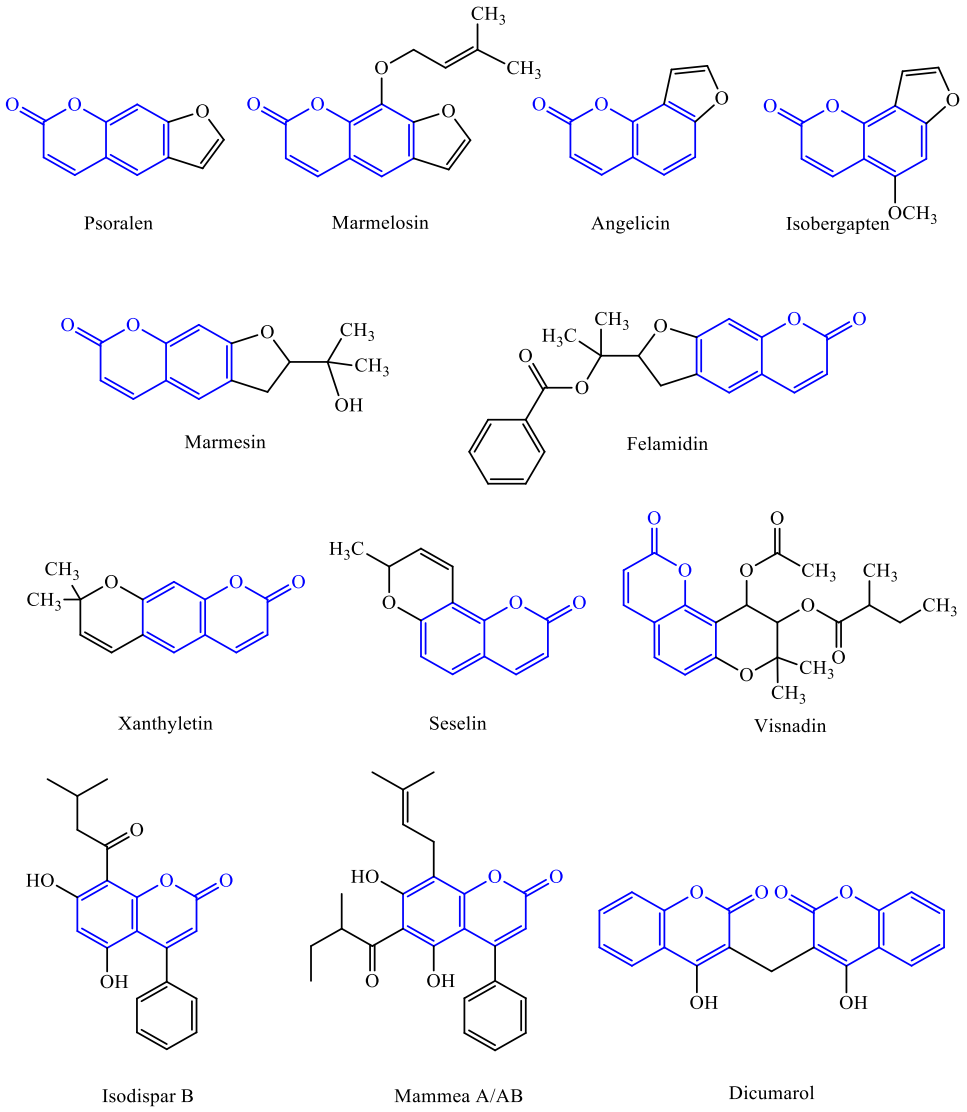

Figure 2. *Chemical Structure of Other Coumarins.*

B. CLASSIFICATION OF COUMARINS BY THEIR LOCATIONS

B. 1. Plant-Derived Coumarins

Secondary metabolites, which enable plants to adapt to adverse environmental conditions, are produced through various pathways. Most of the secondary metabolites produced by the phenylpropanoid pathway are related to the defence mechanisms of plants. The secondary metabolite known as coumarins, synthesized by plants via the Phenylpropanoid pathway, can be classified as plant-derived coumarins [7], [10]. These coumarins, isolated from hundreds of plant species belonging to more than 40 different families, can be found in different parts of plants such as roots, leaves, flowers and fruits. They can also be found in the free form or in the form of glycosides. Plants belonging to the *Apiaceae* family are considered the main source of coumarins and have been reported to contain five different coumarin species [6]. Coumarins contained in plants are accepted as chemotaxonomic markers that will provide information about the evolution level of plants [6], [11]. Coumarins produced by plants protect plants against pathogens and also act as iron chelators [12].

B. 2. Microorganism-Derived Coumarins

Although coumarins are mostly synthesized in plants, they have been detected in some microorganisms. Examples include the new coumarin derivative isolated from two fungal species by J. Wang et al. in 2015 [13],

3 coumarin compounds obtained from *Alternaria* fungus by Umashankar et al. [14], and the new coumarin derivative isolated from *Aspergillus versicolor* fungus strain in 2020 [15].

B. 3. Animal-Derived Coumarins

Apart from plants and microorganisms, coumarins are also found in a small number of animal species [6]. In 2007, Simone et al. succeeded in isolating two coumarin derivatives, esculetin-4-carboxylic acid methyl ester and esculetin-4-carboxylic acid ethyl ester, from sea sponge of *Axinella corrugate* species for the first time [16]. Although research on this subject is limited, coumarin derivatives that may be found of animal origin in ongoing studies may be included in this class.

C. CLASSIFICATION OF COUMARINS BY SYNTHESIS METHODS

Perkin, Pechmann or Knoevenagel methods are mostly preferred for the synthesis of coumarins. However, the low yields of coumarin formed as a result of the Perkin reaction and the formation of by-products are the disadvantages of this method [17]. The Pechmann reaction has disadvantages such as the need for large amounts of acid, high temperatures and long reaction times [18]. The Knoevenagel reaction is an easy and highly efficient reaction. In addition, it provides high purity final products compared to other reactions. However, this reaction is limited as it can only be used for the synthesis of 3-substituted coumarins [19], [20]. Therefore, apart from these methods, researchers have also developed methods such as Wittig reaction, Reformatsky reaction, Kostanecki reaction, Claisen rearrangement for the synthesis of various coumarin derivatives with high efficiency. Chemical synthesis methods commonly used in the synthesis of coumarins are briefly explained below.

C. 1. Perkin Reaction

The Perkin reaction involves the formation of coumarin from aromatic 2-hydroxybenzaldehyde and acetic anhydride in a basic medium. Typically, this method yields 3- or 4-substituted coumarins (Figure 3) [21].

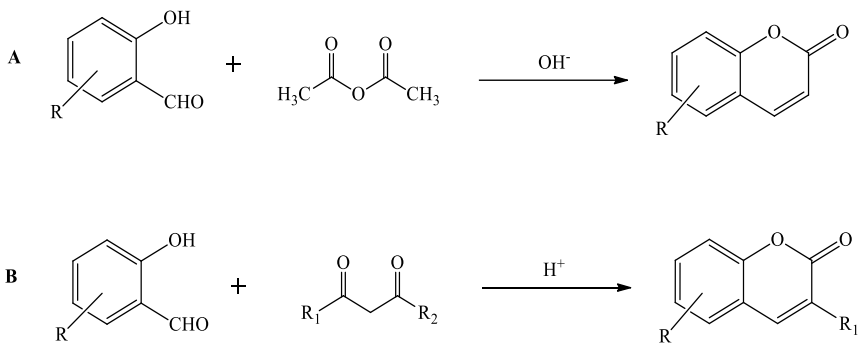

Figure 3. *(A) Perkin Reaction (B) Knoevenagel Reaction of Coumarins Synthesis.*

C. 2. Knoevenagel Reaction

Coumarin synthesis occurs through the interaction of salicylaldehyde derivatives and α, β-diketones in an acidic environment during the Knoevenagel reaction. This reaction method is commonly used to synthesize 3- or 4-substituted coumarins (Figure 3) [22].

C. 3. Pechmann Reaction

Phenol derivatives transform into coumarins when they react with β-ketoesters in an acidic environment in the Pechmann reaction. This method is preferred for the synthesis of 3- or 4-substituted coumarins (Figure 4) [20], [22]. Researchers have employed various catalysts to synthesize coumarins from substituted phenols and β-ketoester compounds. The Pechmann reaction has been successfully executed in the presence of various catalytic systems, including but not limited to Fe_3O_4@Boehmite-NH_2-CoII NP [23], Amberlyst-15 [24], $FeCl_3 \cdot 6H2O$ [24], $InCl_3$ [25], H_2SO_4 [26],

and SnO_2 nanoparticles [27]. These catalytic methodologies have demonstrated efficacy in facilitating the formation of coumarin derivatives under different reaction conditions.

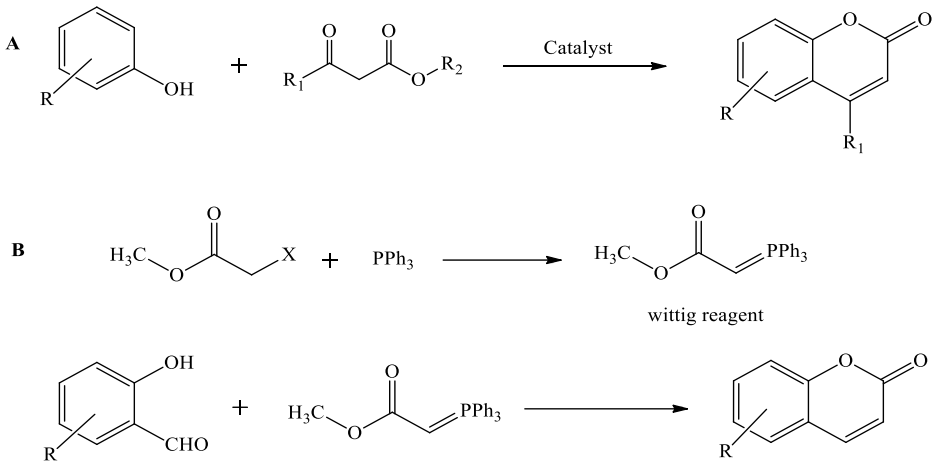

Figure 4. *(A) Pechmann Reaction (B) Wittig Reaction of Coumarins Synthesis.*

C. 4. Wittig Reaction

The Wittig reaction involves the synthesis of coumarins by the interaction of salicylaldehyde, methyl haloacetate, and phosphonium ylide. This method is commonly used to produce 3- or 4-substituted coumarins (Figure 4) [28], [29].

C. 5. Reformatsky Reaction

For the synthesis of coumarins, the Reformatsky reaction employs aldehyde or ketone derivatives with ethyl-α-haloacetate under Zn catalysis. This method is used primarily for the synthesis of 3,4-dialkylsubstituted coumarins (Figure 5) [22], [30].

C. 6. Kostanecki (acylation) Reaction

Known as the Kostanecki acylation, Kostanecki-Robinson or Allan-Robinson reaction involves the reaction of 2-hydroxyphenylalkylketone and its derivatives with aliphatic acetic anhydride in a basic medium to synthesize coumarin and chromone (Figure 5) [22]. The transformation of 2-hydroxyphenylalkylketone derivatives to chromone is represented by Allan-Robinson reaction, while the conversion to coumarin is reerred to as Kostanecki (acylation) reaction.

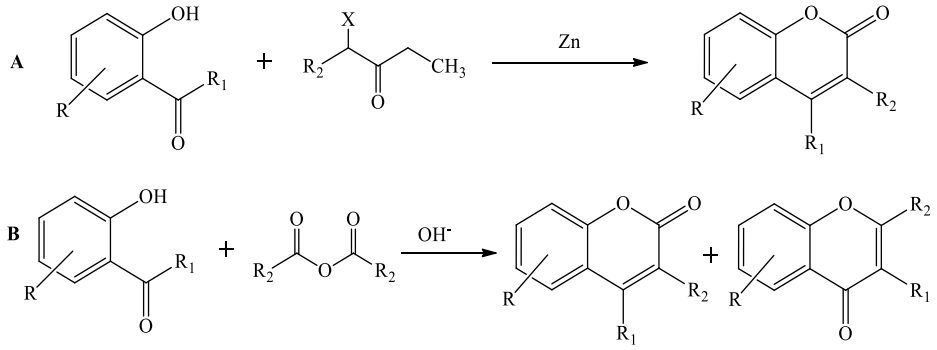

Figure 5. *(A) Reformatsky Reaction (B) Kostanecki Reaction of Coumarins Synthesis.*

C. 7. Claisen Rearrangement

Coumarin derivatives are obtained through the Claisen rearrangement by subjecting the claisen product, formed by heating the mixture of Methyl-2-((2-formylphenoxy) methyl)-3-phenylacrylate and 2,2'-disulfanediyldianiline, to an acidic environment (

Figure **6**) [31].

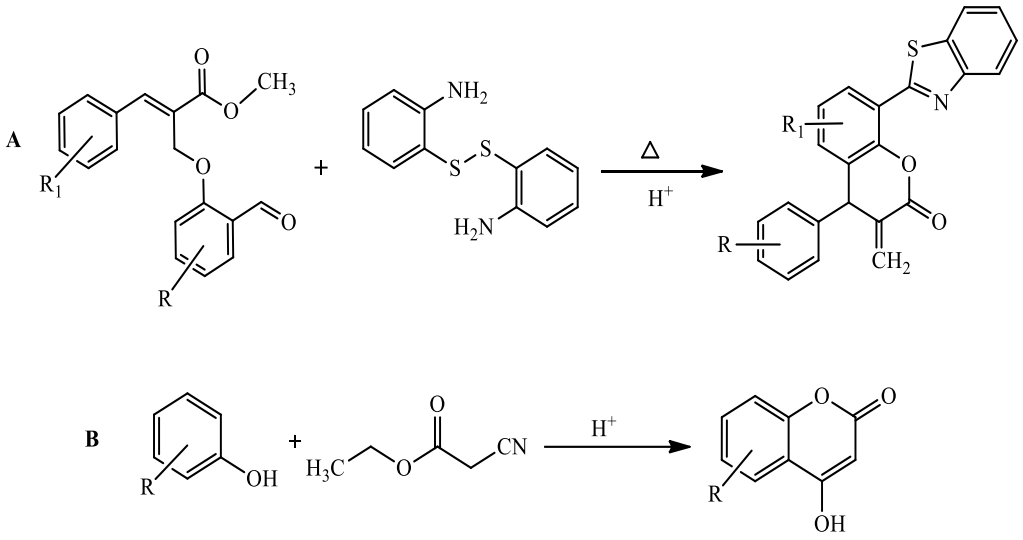

Figure 6. *(A) Claisen Rearrangement (B) Sonn Reaction of Coumarins Synthesis.*

C. 8. Sonn Reaction (Heuben-Hoesch Reaction)

Phenol derivatives react with ethyl cyanoacetate in an acidic medium to obtain coumarins during the Sonn Reaction (

Figure **6**) [20].

C. 9. Weiss-Merksammer Reaction

The Weiss-Merksammer Reaction involves the synthesis of coumarins resulting from the reaction of 2-hydroxyacetophenone with ethyl ethoxy methylene acetoacetate catalysed by NaOEt (Figure 7) [20].

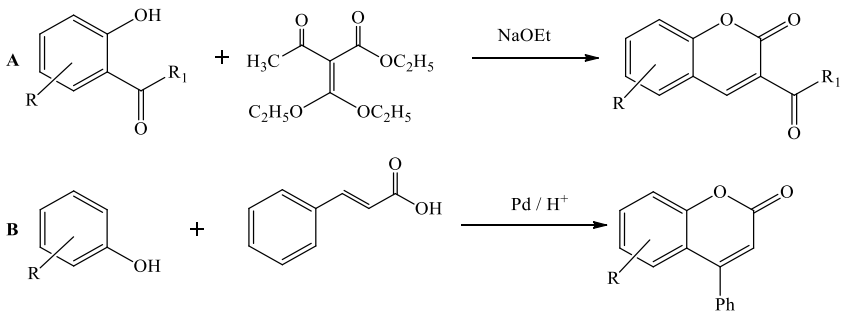

Figure 7. *(A) Weiss-Merksammer Reaction (B) Tsugio Kitamura Reaction of Coumarins Synthesis.*

C. 10. Tsugio Kitamura Reaction

Phenols react with cinnamic acid and trifluoroacetic acid, catalyzed by Pd and Pt, to form coumarin during the Tsugio Kitamura Reaction (Figure 7) [20], [32].

C. 11. Baker Reaction

3-phenylcoumarins are synthesized in the Baker Reaction through the reaction of phenols with 2-formylphenylacetonitrile in $POCl_3$ or HCl (Figure 8) [20].

C. 12. Smith-Dobrovolny Reaction

The Smith-Dobrovolny Reaction results in the synthesis of 3-carbethoxycoumarin derivatives by reacting Duroquinone and ethyl sodiummalonate (Figure 8) [20].

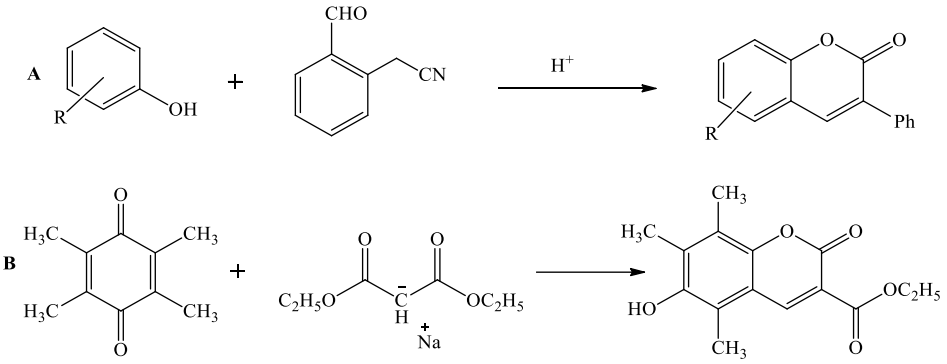

Figure 8. *(A) Baker Reaction (B) Smith-Dobrovolny Reaction of Coumarins Synthesis.*

C. 13. Chakravarti-Majumdar Reaction

The Chakravarti-Majumdar Reaction involves the synthesis of coumarins from 2-methoxyaryl alkyl ketone under Reformatsky reaction conditions (Figure 9) [20].

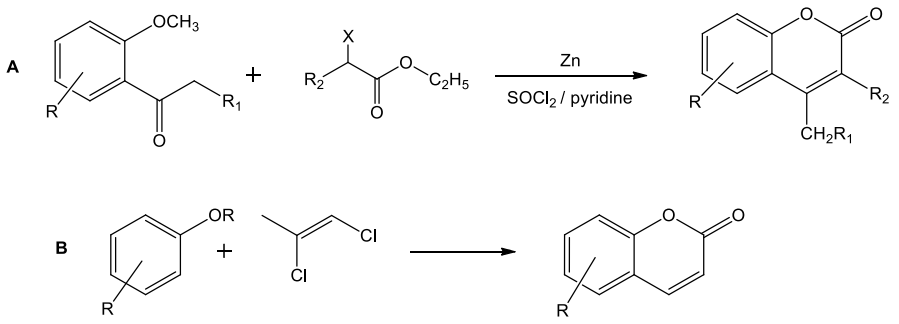

Figure 9. *(A) Chakravarti-Majumdar Reaction (B) Bert Reaction of Coumarins Synthesis.*

C. 14. Bert Reaction

The Bert Reaction converts phenolic ether and 1,2-dichloroprop-1-ene into coumarin in the presence of Zn or by the Friedel-Crafts reaction (Figure 9) [20].

C. 15. Baylis-Hillman Reaction

Salicylaldehyde reacts with methylacrylate in the presence of 1,4-diazabicyclo[2,2,2]octane (DABCO) to obtain coumarin and coumarone during the Baylis-Hillman Reaction (Figure 10) [33].

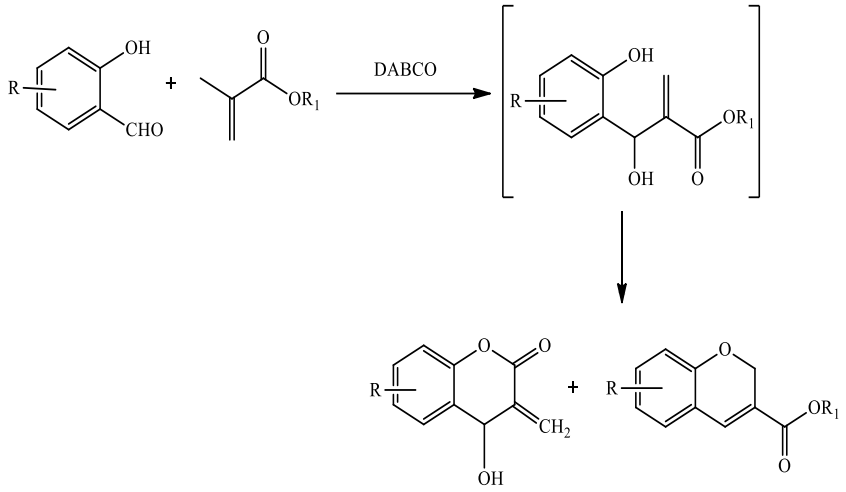

Figure 10. *Baylis-Hillman Reaction of Coumarins Synthesis.*

C. 16. Michael Addition Reaction

3-benzoylcoumarin derivatives can be synthesized with good yield using salicylaldehyde derivatives and 3,3-bis(methylsulfanyl)-1-phenylpropenone dithioacetate in the presence of piperidine during the Michael Addition Reaction (Figure 11) [33].

C. 17. Other Methods

In addition to the synthesis methods of coumarin and its derivatives above, some researchers have developed chemical synthesis methods based on different reactions. For example, Wang D. et al. synthesized a high-yield series of biscoumarins from $PhSO_3H$-catalyzed Bis(2-hydroxyphenyl) methanone derivatives and Meldrum's acid's reaction (Figure 11) [34].

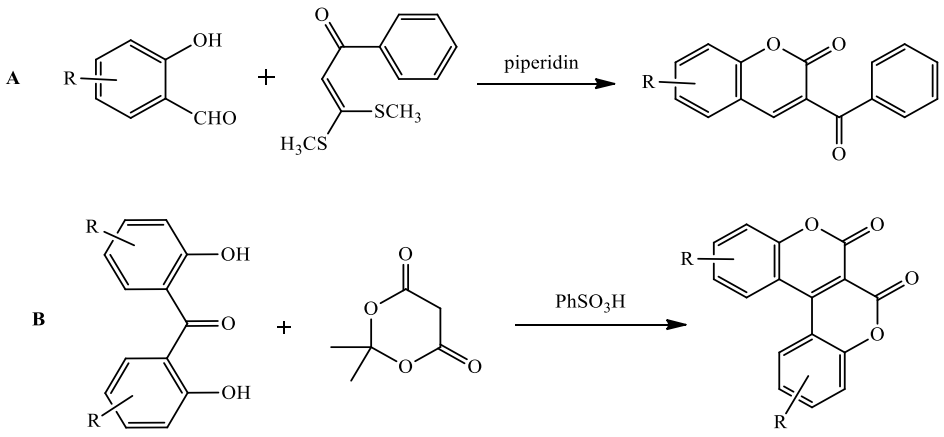

Figure 11. *(A) Michael Addition Reaction (B) Synthesis of Biscoumarins by Using Meldrum's Acid.*

Trost B. M. et al. used phenol derivatives and ethyl propiolates compounds in the presence of different catalysts in an acidic environment for the synthesis of substituted coumarins (Figure 12). In this study, as a result of the use of $Pd(OAc)_2$ or $Pd_2(dba)_3$ catalysts, an efficiency between 42-69% was obtained [35]. Kutubi S. et al., who made a similar study, obtained 60-93% efficiency by using the $FeCl_3$/AgOTf catalyst mixture [36]. Co_2Rh_2, which was used as a catalyst by Park K. H. et al., provided 79-89% efficiency [37]. Finally, $ZnCl_2$, which was used by Leao R. A. C. et al., achieved the best result with a yield of 70-95% [38].

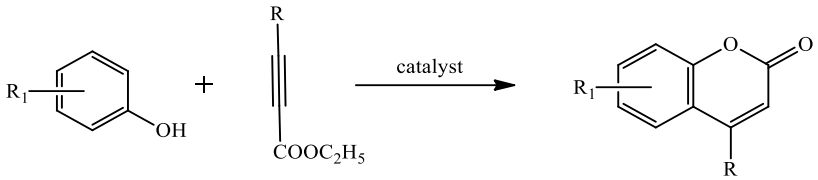

Figure 12. *Synthesis of Coumarin by Coupling of Phenol and Alkyne Derivatives.*

III. CHEMICAL SYNTHESIS OF COUMARINS

Coumarin was first synthesized in 1868 as a pharmaceutical agent (Dikumarol) [6]. Continued research on coumarin and its derivatives has given coumarin-based compounds a wide range of uses from medicine to industry [33]. Researchers have developed many strategies to find the most efficient and practical method for the synthesis of coumarin and its derivatives [39]. For the synthesis of coumarin and its derivatives; reflux, microwave and ultrasonic based methods have been developed. In these developed methods the research on increasing the yield of coumarin by changing the reaction conditions has made great progress [33].

In 2022, Sharma V. et al. synthesized compound 5-Amino-6-cyano-3-hydroxybenzo[c]coumarin by refluxing a homogeneous mixture of salicylaldehyde, ethyl acetoacetate and malononitrile in ethanol/water with Ni-Cu-Al-CO_3 hydrotalcite catalysis at 80 °C for 90 minutes. The obtained coumarin derivatives showed antimicrobial activity against human pathogenic bacteria such as *S. aureus*, *P. aeruginosa* and *P. bulgaria*. In this study, the effect of temperature, catalyst and solvent change was investigated. As a result, it was observed that increasing the reaction temperature up to 80 °C, increasing the amount of catalyst and using ethanol instead of acetone and acetonitrile increased the yield of coumarin [40]. In a study conducted by Rahayu et al. in 2022, 7-hydroxy-4-methyl coumarin was synthesized by microwave (800W) using resorcinol and ethyl acetoacetate under the catalysis of $SnCl_2.2H_2O$. It has been found that reducing or increasing the reaction time during synthesis does not increase the yield. A decrease in yield was reported when the ratio of reagents (resorcinol: ethyl acetoacetate) was changed from 1:1 mol to 1:1.25 mol. Performing the reactions without solvents resulted in better yields than performing them in the presence of ethanol (polar protic) and acetonitrile (polar aprotic) solvents. Finally, it has been reported that the highest efficiency was achieved when the $SnCl_2.H_2O$ catalyst used in this study was used as 10% mol [41].

Özdemir M. et al. (2022) synthesized the polymer containing sulfo-coumarin group in 4 steps. In the first step, 2,4-dihydroxybenzaldehyde, 4-methylsulfonyl) phenyl acetic acid and sodium acetate were dissolved in dry acetic anhydride. 7-acetyl-3-[4-(methylsulfonyl) phenyl] coumarin was then refluxed for 22 hours at 160 °C and under a nitrogen atmosphere. The product obtained in the second step was dissolved in methanol/THF and 7-Hydroxy-3-[4-(methylsulfonyl) phenyl] coumarin was synthesized by adding aqueous LiOH solution and refluxing for 3 hours. In the 3rd step, triethylamine and methacryloyl chloride were added to the product dissolved in THF, and sulfo-coumarin monomer was obtained by stirring for 12 hours. In the last step, the monomer was converted into polymer using the Radical Polymerization method [42]. Some studies based on chemical synthesis methods are summarized in Table 1.

Table 1. *Studies on Chemical Synthesis of Coumarins.*

Method	Reaction Conditions	Reagent	Catalyst	Solvent	Time *(h)*	Yield *(%)*	Number of compounds	Ref.
Microwave	800 W	resorcinol, ethyl acetoacetate	$SnCl_2.2H_2O$	-	0.07	55.25	1	[41]
	100 – 170 °C	salicylaldehyde derivatives, phenylacetic acid derivative	acetic anhydride, TEA	-	0.17 – 0.2	46 - 77	8	[43]
	Room temperature (RT) under argon atmosphere	2,3,4-Trimethoxybenzaldehyde, 4-methylphenylacetonitrile	NaOH	EtOH	0.5	88	1	[44]
	320 W	2-(2,3,4-trimethoxyphenyl)-1-(4-methyl phenyl)acrylonitrile, silicagel, pyridinium hydrochloride	-	-	0.42	74	1	
	250 °C	4-substitue salicylaldehyde, ethyl-2-(triphenylphosphoranylidene)acetate	-	N,N-dimethylanilin e	0.17 - 1	20 - 91	15	[45], [46]
	100 - 170 °C 100 - 200 W	salicylaldehyde derivatives, phenyl acetic acid derivatives	acetic anhydride, TEA	-	0.17 – 0.2	34 - 85	24	[47]
	-	2-hydroxy-4-propynyloxybenzaldehyde, 3-bromopropyne	K_2CO_3	DMF/H_2O	0.08 – 0.12	86 - 90	4	[48]
Reflux	80 °C	salicylaldehyde, ethylacetoacetateand malononitrile	Ni−Cu−Al−CO_3 hydrotalcite	EtOH/su	0.5 + 1	85	1	[40]
	160 °C under N_2 atmosphere	2,4-dihydroxy benzaldehyde, 4-methylsulfonyl)phenylacetic acid	sodium acetate	dry acetic anhydride	22	82	-	[42]

RT	hydroxycoumarin, alkyl halide	potassium carbonate	DMF	24	32 - 77	7	[49]
	4-hydroxycoumarin, acid chloride	TEA	THF	5	27	1	
	coumarin-3-carboxylic acid, Aromatic alcohol, dicyclohexylcarbodiimide (DCC)	4-(dimethylamino)pyridine	DCM	24	14 - 38	4	
	organic acid, amine, benzotriazol-1-yl oxytripyrrolidinophosphonium hexafluorophosphate (pyBOP)	TEA	DMF	24	41 - 73	7	
	2-hydroxy acetophenone, aldehyde	NaOH	MeOH	48	22.8	1	
	4-chromanon, aldehyde	pyrrolidine	MeOH	24	16 - 76	4	
60 °C	salicylaldehydes, β-keto ester	sulfated tungstate	-	TLC	81 - 98	20	[50]
110 °C	2-hydroxy benzaldehyde, phenyl/thiophenylacetic acid	N,N′-dicyclohexyl carbodiimide	dimethyl sulfoxide (DMSO)	24	-	20	[51]
Reflux	methoxy-3-arylcoumarin, acetic anhydride	hydriodic acid	Acetic acid	3	-	8	
55 °C	fluorescein, benzo-15-crown-5	NaOH	MeOH+ $CHCl_3$	6	-	3	[52]
Reflux	aldehyde, diethyl malonate	-	EtOH	6			
100 °C	ester derivatives	NaOH	MeOH	4			

Reflux	7-hydroxy-2*H*-chromen-2-one, benzyl chloride	K_2CO_3	acetonitrile	TLC	69 - 84	22	[53]
Reflux	benzylchlorides, 4-hydroxy benzylalcohol	K_2CO_3	ACN	TLC	-	1	
N_2 25 - 30 °C	4-(benzyloxy)phenyl)methanol, methane sulphonyl chloride	TEA	DCM	TLC	-	1	
Reflux	4-(benzyloxy)benzyl methanesulfonate, 7-hydroxy-2*H*-chromen-2-one	K_2CO_3	ACN	TLC	62 - 84	23	
Reflux or using backflow condenser	cyclopropane derivatives	glacial acetic acid	toluene	4 – 18	49 - 76	7	[54]
Reflux	cyclopropane derivatives	glacial acetic acid	chlorobenzene	16	67	1	
RT	cyclopropane derivatives	$DMF/POCl_3$	DMF	2	92	1	
RT	cyclopropane derivatives	$NaBH_4$	$MeOH/CHCl_3$	5	82	1	
boiling with backflow condenser	cyclopropane derivatives	glacial acetic acid	Toluene	6	48	1	
Reflux	cyclopropane derivatives	Zn powder, AcOH	MeOH	1	-	1	
Reflux; RT	7-diethylamino-3-formylcoumarin, sulfonamide; methyl trimethylsilyl dimethylketene acetal	pyridinium p-tolunesulfonate (PPTS); Y(OTf)	Toluene, DCM, THF	0.3 - 24	47 - 53	3	[55]
RT	8-formyl-7-hydroxy-4-Methylcoumarin, malononitrile	TEA	DCM	8	79.2	1	[56]

50 - 60 °C	4,4-dimethylpiperidine-2,6-dione, 4-bromomethyl coumarin	anhydrous K_2CO_3	dry acetone	10	73 - 84	10	[57]
RT °C	guanosine-6,8-dithione türevi + coumarin türevi	ammonium hydroxide	Water+ACN	1	70 - 86	18	[58]
RT	2-(2-(2-chloroethoxy)ethoxy) Ethanol, 4-toluenesulfonyl chloride	Et_3N, 4-dimethylaminopyridine (DMAP)	DCM	5	95	3	[59]
RT under argon atmosphere	2-(2-(2-chloroethoxy)ethoxy)ethyl 4-benzene sulfonate, 7-hydroxycoumarin	K_2CO_3, 18-crown-6	acetone	96	99		
70 °C	7-(2-(2-(2-chloroethoxy) ethoxy)ethoxy)-2H-cromen-2-one, NaI	-	acetone	120	87		
RT	N, N-diethylamino-3-acetyl coumarin, 2-hydrazino benzothiazole	H_2SO_4	EtOH	TLC	85	14	[60]
100 °C	5-isopropyl-2-methylphenol, $SnCl_4$, paraform aldehyde	Et_3N	toluene	8	63	2	[61]
110 °C	2-hydroxy-6-isopropyl-3-methyl benzaldehyde, acetic anhydride, 2-(3-methoxyphenyl)acetic acid	Et_3N	-	TLC	-		
Reflux	3-(bis(pyridin-2-ylmethyl)amino)phenols, ethyl acetoacetate	H_2SO_4	-	3	90 - 94	2	[62]
	7-(bis(pyridin-2-ylmethyl)amino)-4-methyl-coumarin, $Cu(NO_3)_2$	-	MeOH/H_2O	0.5	90 - 94	2	
Reflux	*o*-hydroxybenzaldehydes, pyridazinone ester	piperidine	2-propanol	5	73 - 87	6	[63]

	70 °C	phenol derivatives, malonic acid, $POCl_3$	$ZnCl_2$	-	20	-	4	[64]
	Reflux	naphthyl hydroxybenzaldehyde, methyl-2-(1,3,5-triazin-2-yl)acetate	Piperidin	EtOH	12 – 48	79 - 87	4	[65]
	112 °C MW, 80 °C reflux	2-phenylacetic acid derivatives, salicylaldehyde derivatives, HCl	TEA, acetic anhydride	EtOH	1.17 + 3	22 - 96	43	[66]
	80 °C MW 0 °C	salicylaldehyde derivatives, meldrum's acid, H_2SO_4	-	-	2 + 1,5	90	1	[48]
	Reflux under inert atmosphere	2-hydroxy-4-propynyloxybenzaldehyde, 3-bromopropyne	K_2CO_3	dry acetone	4 – 5,5	75 - 79	4	[67]
	0 - 5 °C	phenol derivatives, ethyl-4-bromo-3-oxobutanoate	H_2SO_4	-	-	-	2	[68]
Ultrasound	RT, 250 W, 40 kHz	aromatic aldehyde, malononitrile, phenylhidrazine, β-dicarbonyl compounds	L-proline	EtOH	0.83	78 - 90	20	[69]
	60 - 65 °C, 200 W, 35 kHz	aromatic aldehyde, aromatik amine, dimedone, 4-hydroxycoumarin	CTAB	H_2O	0.25	79 - 89	25	[70]
	130 W, 20 kHz	aromatic aldehyde, 4-hydroxycoumarin, 6-aminourasil or 6-aminothiourasil	sulfamic acid	EtOH/ H_2O	0.17 – 0.5	66 -98	26	[71]
	130 W, 20 kHz	aromatic aldehyde, 4-hydroxycoumarin, 2-aminopiridins	sulfamic acid	EtOH/ H_2O	0.07 – 0.63	70 - 97	30	[72]
	60 °C, 140 W, 50 - 60 Hz	isatin, malononitrile, dimedone or 4-hydroxycoumarin	S-alkyl O-hydrogen sulfothioate	EtOH/ H_2O or H_2O	1.75 – 4	76 - 94	12	[73]

		functionalized silica-coated magnetic nanoparticles (AHST-MNPs)					
45 °C	peracetylated glucose azide, coumarin alkyne	GO-Fe_3O_4@CuO	H_2O	1.33	85 - 96	6	[74]
80 °C	phenol derivatives, ethyl acetoacetate derivatives	Fe_3O_4@C@PrS-SO_3H NPs	-	0.25 – 0.67	58 - 98	14	[75]
70 °C	phenols, β-keto ester derivatives	$HFe(SO_4)_2$.4 H_2O-Ch NCs	-	0.17 – 6	59 - 99	28	[76]
50 – 60 °C, 100W, 36 kHz	2-(1-(2-oxo-2*H*-chromen-3-yl)ethylidene) thiosemicarbazide, hydrazonoyl halide derivatives	Et_3N	dioxan	0.5	72 - 76	8	[77]
80 °C, 37 kHz	phenylhydrazone, vilsmeier reagent	-	-	0.33	91	1	[78]

IV. PROPERTIES OF COUMARINS

Coumarin (2*H*-chromen-2-one), which has a vanilla-like odor, has a volatile, colorless or yellow crystal structure. The molecular weight of coumarin is 146.15 g/mol and it sublimes at 100 °C. It melts between 68 - 70 °C and boils at 303 °C. While coumarin is soluble in diethyl ether, ethanol and chloroform, it is slightly soluble in water [79], [80].

Coumarins are compounds with fluorescent properties. These coumarins in solution or polymer form are generally located in the blue-green wavelength region. Synthesis of these fluorescent coumarin compounds is relatively easy. Therefore, various models have been reported and their photo-physical and spectroscopic properties have been extensively investigated. Recently, solid fluorescent dyes based on coumarin have received much attention [81]. Cocco A. et al. investigated the fluorescence properties of phenyl coumarins, which are coumarin derivatives. It was found that while the addition of Fe^{+3} to 6-(6-methoxynaphthalen-2-yl)-coumarin-3-carbonitrile (4e) and 6-(6-methoxynaphthalen-2-yl)-3-(methylsulfonyl)-coumarin (4f) compounds caused them to lose their fluorescent properties, the addition of Al^{+3} to the same compounds increased their fluorescent properties. It has been reported that ethyl 6-(6-methoxynaphthalen-2-yl)-coumarin-3-carboxylate (4c), 4e and 4f compounds, which were found to have low toxicity, may be candidates for bioimaging [82]. Sarih N. M. et al. synthesized a series of furocoumarin derivatives. Compound 2-(cyclohexyl amino)-3-phenyl-4*H*-furo[3,2-c] chromen-4-one (FH), which showed the strongest fluorescence of these compounds, was complexed with various metals. It was found that the fluorescence property of the obtained complexes was less compared to the FH compound and the complexes with Fe^{+3} lost their fluorescence property. Later, the FH-Fe^{+3} complex was formed into different complexes with 13 other metals, but it was observed that the FH-Fe^{+3}-metal compounds lost their fluorescence properties in general [83]. Hua C. J. et al. determined that coumarin-dihydropyridine derivatives have fluorescent properties. Among these compounds, 7-(p-tolyl)-9,10,11,12-tetrahydro-6*H*-chromeno[4,3-b] quinoline-6,8(7*H*)-dione (4e) showed the best fluorescence properties. Synthesized coumarin-dihydropyridine derivatives showed different fluorescence in acetic and basic environments, and it was noticed that the fluorescence color of these compounds changed from blue to yellow and then green when the pH value of these compounds was changed from acidic to basic [84]. Jarraya N. A. et al. compared 3-cyano-7-diethylamino-2-iminocoumarin with coumarin to search for compounds with the best fluorescence properties. It has been reported that the investigated compounds have very close fluorescence properties in solution, while in solid state, iminocoumarins are much more fluorescent than coumarins. As a result, it was found that coumarin derivatives behave very differently in liquid and solid state [81].

V. BIOLOGICAL ACTIVITY OF COUMARINS

Coumarin and its derivatives exhibit remarkable pharmacological properties. These compounds offer advantages such as high bioavailability, potent pharmacological activity, low potential for drug resistance, minimal side effect profiles, and optimized therapeutic efficacy. Numerous studies in the literature reveal the broad-spectrum bioactivity of coumarins. These studies report that coumarin derivatives possess antimicrobial, anti-tuberculosis, neuroprotective, anti-inflammatory, anticoagulant, antihypertensive, anti-hyperglycemic, antidiabetic, antioxidant, and antineoplastic properties [6], [12]. In light of this comprehensive bioactivity profile, the current review will focus specifically on the anticoagulant, antithrombotic, anti-neurodegenerative, and anticancer effects of coumarins. Analyzing the molecular mechanisms and potential therapeutic applications of these activities will contribute to a better understanding of the role of coumarins in drug discovery and development.

A. ANTICOAGULANT ACTIVITY

Coumarins are a class of heterocyclic compounds characterized by their anticoagulant properties. Anticoagulants are agents that modulate the hemostasis process and inhibit thrombus formation. This

pharmacological profile makes them valuable therapeutic tools in the prophylaxis and treatment of thromboembolic diseases. From a historical perspective, dicoumarol, the first synthesized coumarin derivative, played a critical role as a precursor compound in the development of anticoagulant drugs. Subsequent research has led to the synthesis and widespread clinical application of coumarin-based anticoagulants with various structural modifications [85].

The anticoagulant activity of coumarins is particularly evident in prototype molecules such as dicoumarol and warfarin, whose mechanism of action involves the inhibition of the enzyme vitamin K epoxide reductase. This enzymatic inhibition disrupts the biosynthesis of vitamin K-dependent coagulation factors, leading to the modulation of hemostasis and a consequent reduction in blood clotting capacity [86].

Coumarin derivatives hold a significant position in drug discovery and development due to their broad spectrum of biological activities. Coumarin analogs with anticoagulant efficacy are especially utilized as therapeutic agents in patients with a high risk of thrombosis during the perioperative period and in the primary and secondary prophylaxis of cardiovascular diseases. The optimization of these compounds' pharmacokinetics, pharmacodynamics, and safety profiles is a focal point of ongoing research aimed at enhancing the efficacy of anticoagulant therapy and minimizing potential side effects [85].

In a 2020 study by Bang et al., the synthesis of 7-hydroxycoumarin-salicylic acid derivatives was conducted. Among the compounds obtained, 1a-b derivatives were found to exhibit high anticoagulant activity. The chemical structures of these compounds are shown in figure 13. The analysis revealed that these derivatives were 1.5 times more active than warfarin [87].

B. ANTITHROMBOTIC ACTIVITY

Thrombosis poses a significant threat to human health worldwide as a major cause of mortality. Antithrombotic drugs play a critical role in the treatment of thrombotic diseases by preventing the onset and progression of these conditions. The need for new and safer antithrombotic drugs arises from the serious side effects and inadequate efficacy of existing medications. Coumarin derivatives have been demonstrated to exhibit antithrombotic properties, as well as anticoagulant and antiplatelet aggregation activities [88].

Coumarins prevent thrombosis due to their capacity to inhibit platelet aggregation, thus making them potential therapeutic agents in the treatment of cardiovascular diseases. This mechanism of action of coumarins is primarily attributed to their inhibition of the synthesis of coagulation factors through vitamin K antagonism, thereby regulating blood clotting. Additionally, some coumarin derivatives provide an extra benefit in reducing thrombosis risk by directly inhibiting platelet aggregation [89].

Recent studies on the antithrombotic effects of coumarin derivatives sheds light on their potential therapeutic applications. In a study conducted by Quezada et al. (2010), coumarin-resveratrol hybrid compounds were synthesized and their anti-platelet aggregatory activities were investigated. The researchers reported that compounds designated as 2a-c (Figure 13) exhibited higher anti-platelet aggregation activity than trans-resveratrol (t-RESV). Notably, compound 2b was found to demonstrate antiplatelet aggregatory activity thirty times more potent than t-RESV [90].

A study conducted by Lu et al. (2022) elucidated the mechanisms by which coumarin derivatives inhibit platelet aggregation. The research findings revealed that these compounds prevent platelet aggregation by inhibiting the glycoprotein GPIIb/IIIa complex on the platelet surface and adenosine diphosphate (ADP) receptor signaling pathways. Furthermore, intracellular mechanisms such as calcium release and regulation of platelet intracellular cyclic AMP (cAMP) were also found to play a role in this process [91].

In the same year, Mazreku et al. (2022) synthesized 4-hydroxycoumarin-pyridine derivatives and evaluated their *in vivo* anticoagulant effects in mouse models. The results demonstrated that compounds coded as 3a-b (Figure 13) exhibited higher Prothrombin Time values compared to the standard anticoagulant drug Warfarin. This finding indicates that these compounds more effectively modulate the blood coagulation process [92].

The study conducted by Hrubša et al. in 2022 provides significant contributions in terms of the synthesis of coumarin-indole hybrid compounds and the assessment of their antithrombotic potential. The researchers designed and synthesized a series of novel hybrid molecules by combining coumarin and indole structures using an innovative approach. The platelet antiaggregatory activities of these new compounds were systematically investigated through *in vitro* experiments. Among the obtained results, the high antiplatelet activity exhibited by compound 4 (Figure 13) is particularly noteworthy. This compound demonstrated stronger platelet aggregation inhibition when compared to the commonly used antithrombotic agent aspirin. This result suggests that compound 4 should be considered as a potential therapeutic candidate [93].

C. ANTI-NEURODEGENERATIVE ACTIVITY

Neurodegenerative diseases (ND) are a heterogeneous group of pathologies that affect the nervous system and are characterized by the progressive loss of neurons. Alzheimer's disease (AD) and Parkinson's disease (PD) are the most common types of these disorders, with increasing prevalence among the aging population. The etiology of NDs is complex and multifactorial, involving the interplay of aging, environmental, genetic, and epigenetic factors [63]. Protein aggregation and accumulation play a critical role in the pathogenesis, with cholinergic and dopaminergic system dysfunction being characteristic features of AD and PD, respectively. Current treatment strategies often focus on multi-target-directed ligands (MTDLs). In this context, the inhibition of enzymes such as monoamine oxidase (MAO), acetylcholinesterase (AChE), butyrylcholinesterase (BuChE), and carbonic anhydrase (CA) isoforms has gained importance [94].

Coumarin derivatives have emerged as potential therapeutic agents in the treatment of neurodegenerative diseases (ND) due to their broad-spectrum biological activities and substitution potential at various positions in their molecular structure. Particularly, 3-aryl coumarin compounds exhibit high affinity and selectivity towards enzymes involved in neurodegeneration. The neuroprotective properties demonstrated by these compounds offer a promising approach for developing new therapeutic strategies in the treatment of NDs [95].

Berrino and colleagues (2023) synthesized coumarins with alkyl groups substituted at different positions to reduce oxidative stress and inflammation observed in neurodegenerative diseases (ND). These compounds were tested against enzymes like carbonic anhydrases (CA), monoamine oxidases (MAO), and cholinesterases (ChE), which play a role in neurodegeneration. The compounds 5a-b, shown in figure 13, stood out as the most promising due to their ability to inhibit multiple enzymes and exhibit *in vitro* neuroprotective activities. They demonstrated the capability to reduce oxidative stress-related neuroinflammation and inhibit the secretion of interleukin-6 [94].

The neuroprotective effects and mechanisms of action of coumarins have been better understood through recent studies. Specifically, coumarin derivatives like Osthole act by activating the Nrf2 signaling pathway and inhibiting the NF-κB pathway. Activation of the Nrf2 signaling pathway strengthens cellular defense mechanisms against oxidative stress by increasing the production of endogenous antioxidants such as HO-1 and NQO1. This effect has been demonstrated in both *in vitro* and *in vivo* studies, including in HT22 mouse hippocampal neuron cells and in mouse models of Alzheimer's disease [96], [97].

Inhibition of the NF-κB pathway reduces the production of pro-inflammatory cytokines (IL-6, TNF-α, IL-1β). This effect has been observed in the reduction of LPS-induced inflammation in Caco-2 cells

and Caco-2/THP-1 macrophage co-cultures [98]. Additionally, simple coumarin derivatives like umbelliferon have been reported to exhibit similar effects through the Nrf2/ARE pathway [99].

The positive effects of coumarins on mitochondrial functions are primarily based on their ability to reduce oxidative stress and activate the Nrf2 signaling pathway. These mechanisms form the basis of the neuroprotective and anti-inflammatory effects of coumarins, making them potential therapeutic agents in the treatment of neurodegenerative diseases [100].

Despite the potential of coumarins in the treatment of NDs, there are some limitations. For instance, some coumarin derivatives have been reported to have limited ability to cross the blood-brain barrier (BBB), which could potentially limit their therapeutic efficacy. Additionally, some coumarin derivatives have been reported to cause hepatotoxicity at high doses [101]. These studies support the potential of coumarins in the treatment of NDs, while also highlighting the need for further research and optimization.

C.1. Alzheimer's Disease

Alzheimer's disease (AD) is a neurodegenerative disorder characterized by the progressive loss of brain cells and is the most common form of dementia in the elderly population. Clinical symptoms include general and persistent memory loss, impairment of cognitive functions, emotional and behavioral changes, and loss of independent living skills [95]. While the pathogenesis of AD is not fully understood, the "cholinergic hypothesis" and "beta-amyloid cascade hypothesis" are among the most widely accepted theories. The cholinergic hypothesis suggests that the disease is caused by a reduction in acetylcholine synthesis, while the beta-amyloid cascade hypothesis emphasizes that the accumulation of β-amyloid peptide (Aβ) and the formation of neurofibrillary tangles (NFTs) from hyperphosphorylated tau protein are the hallmark pathological features of AD [95]. Mitochondrial dysfunction and dysregulation of the glycogen synthase kinase-3β (GSK-3β) enzyme play significant roles in the pathogenesis of AD. Increased GSK-3β activity has been observed in the brains of AD patients, and it has been suggested that this enzyme has a molecular relationship with Aβ and tau proteins. Experimental studies have shown that overexpression of GSK-3β leads to hyperphosphorylation of tau and its accumulation in hippocampal neurons [102].

Acetylcholinesterase (AChE) inhibitors and monoamine oxidase-B (MAO-B) inhibitors play a crucial role in the treatment of AD. These drugs are used to slow the progression of the disease and improve the cognitive functions of patients [95]. Coumarin derivatives hold promise as AChE and BuChE inhibitors. These compounds potentially improve cholinergic signaling and exhibit neuroprotective effects, offering potential in the treatment of AD [103]. Recent studies support the potential of coumarin derivatives in the treatment of AD. Hu et al. (2019) investigated the AChE and BuChE inhibitory activity of 3-substituted coumarin derivatives *in vitro* and *in vivo*. Compound 6c showed high AChE inhibitory activity, while compound 6a was found to be five times more potent than donepezil in inhibiting BuChE [104].

In another study, Huang et al. (2014) observed that derivatives synthesized by combining clioquinol and coumarin exhibited AChE/MAO-B inhibitory activity and inhibited beta-amyloid (Aβ1-24) aggregation. Particularly, compound 7 showed the highest effect in both MAO-B inhibition and inhibition of Aβ1–42 aggregation [105]. A study by Chiu et al. (2021) reported that new coumarin-chalcone hybrid compounds inhibited amyloid-β aggregation, reduced tau hyperphosphorylation, and improved cholinergic neurotransmission [106]. Finally, Babaei et al. (2022) investigated the anti-Alzheimer potential of a series of coumarin-pyridine hybrid compounds. Compound 8a was found to be seven times more effective against AChE than the standard drug, while compound 8b exhibited 305 times more inhibitory effect against BuChE [107].

C.2. Parkinson's Disease

Parkinson's disease (PD) is a neurodegenerative disorder characterized by progressive neurodegeneration and impaired motor control. The main pathological features of PD include the loss of dopaminergic neurons in the substantia nigra pars compacta and the aggregation of α-synuclein protein [108].

Monoamine oxidase (MAO) enzyme inhibitors play a crucial role in the treatment of central nervous system disorders such as depression and Parkinson's disease. Specifically, MAO-B inhibitors contribute to the control of motor symptoms by reducing the breakdown of dopamine. In this context, coumarin derivatives stand out as promising compounds in the treatment of PD due to their neuroprotective effects [109], [110].

The studies have shown that coumarin derivatives can influence PD pathogenesis through various mechanisms. These compounds inhibit MAO-B enzyme, reduce dopamine degradation, reduce oxidative stress with their strong antioxidant properties, inhibit α-synuclein protein aggregation, improve mitochondrial dysfunction, and suppress neuroinflammatory processes. These multifaceted mechanisms increase the potential of coumarins to be used as multi-target-directed ligands (MTDL) in the treatment of PD [110].

Various studies have investigated the potential therapeutic effects of different coumarin derivatives on PD. For instance, Sashidhara et al. (2014) synthesized a series of 3-aryl coumarin-tacrine derivatives, considering the complex etiology of PD. This study found that compounds 9a-b inhibited α-synuclein protein aggregation, increased dopamine levels, and exhibited strong antioxidant properties [111]. In another study by Kumar et al. (2018), scopoletin, found in the fruit of *Morinda citrifolia*, was investigated for its potential therapeutic effects on PD. Research has shown that scopoletin possesses strong neuroprotective properties. Specifically, scopoletin significantly reduced cell death by protecting SH-SY5Y cells from rotenone-induced apoptosis. The underlying mechanism of this protective effect was associated with the activation of the Nrf2/ARE pathway. Scopoletin enhanced the antioxidant response by increasing the phosphorylation and nuclear translocation of Nrf2 protein. Additionally, scopoletin supported the stabilization and activation of Nrf2 by raising DJ-1 protein levels. This effect played an important role in enhancing cellular defense against oxidative stress. As a result, scopoletin appears to have the potential to ameliorate the pathophysiological processes such as oxidative stress and protein aggregation underlying PD. These findings suggest that scopoletin could be used as a new therapeutic agent in the treatment of PD [112].

Tao et al. (2019) comprehensively evaluated the therapeutic potential of coumarin Mannich base (β-amino ketone) derivatives as a novel approach to PD treatment. Among the synthesized coumarin Mannich derivatives, compound 10 (Figure 13) showed particularly notable results. This compound demonstrated high selectivity in inhibiting the MAO-B enzyme and reducing neuroinflammatory processes in both *in vitro* and *in vivo* experiments. Additionally, compound 10 was observed to improve motor dysfunction, prevent dopaminergic neuron loss, and increase the number of tyrosine hydroxylase-positive neurons. It was also found to reduce neuroinflammatory response by inhibiting COX-2 and iNOS expression [113].

In another study, Ham et al. (2019) explored the therapeutic potential of a coumarin derivative called Peucedanocoumarin III in a PD model. Peucedanocoumarin III showed the ability to dissolve α-synuclein fibrils and prevent dopaminergic neuron loss [114]. Studies by Hannan et al. (2022) and Predhan et al. (2020) investigated the neuroprotective effects of a coumarin derivative named scopoletin in a PD model. Scopoletin was shown to reduce dopaminergic neuron loss associated with oxidative stress, improve mitochondrial function, and enhance dopamine efficacy [115], [116].
In a comprehensive study conducted by Sayed et al. (2022), the multifaceted effects of the furanocoumarin derivative xanthotoxin on PD have been examined. Researchers have revealed xanthotoxin's neuroprotective properties and its positive effects on various mechanisms involved in PD

pathogenesis. The findings indicate that xanthotoxin protects dopaminergic neurons, restores tyrosine hydroxylase-positive cells, reduces α-synuclein accumulation, and improves striatal dopamine levels. These effects have been clinically validated by the reduction of motor dysfunction in experimental animal models. Additionally, xanthotoxin has been found to reduce oxidative stress, strengthen antioxidant defenses, and suppress neuroinflammation. At the cellular level, it has been shown to act by preserving the MAPK signaling pathway and inhibiting apoptotic processes. These multifaceted effects have led to the consideration of xanthotoxin as a potential therapeutic agent in the treatment of Parkinson's disease [117].

Finally, Wang and colleagues (2024) synthesized coumarin-phenolic acid hybrid compounds targeting α-synuclein aggregation. Compounds 11a-c (Figure 13) demonstrated strong inhibitory effects. The candidate compounds showed the ability to prevent the formation of β-sheet aggregates by maintaining the proteostasis conformation of α-synuclein and to disassemble preformed α-synuclein oligomers and fibrils. In addition, the candidate compounds demonstrated impressive efficacy in inhibiting α-synuclein aggregation within neural cells, reducing the likelihood of inclusion formation [118].

D. ANTICANCER ACTIVITY

Coumarin and its derivatives are biologically active against various cancer cell lines and are considered potential anticancer agents in cancer treatment. These compounds can be effective against cancer cells through mechanisms such as cell cycle arrest, induction of apoptosis, inhibition of angiogenesis, prevention of metastasis, and inhibition of telomerase and kinases. The anticancer effects of coumarins are primarily based on their ability to scavenge free radicals, which forms the basis of many of their biological activities. However, they may be associated with hepatotoxicity at high doses [118].

As antitumor agents, coumarins stand out for their ability to inhibit DNA-associated enzymes, trigger cell apoptosis, modulate estrogen receptors, and block the cell cycle. Additionally, they exhibit anticancer effects by inhibiting multi-drug resistance, human carbonic anhydrase, the PI3K/AKT/mTOR signaling pathway, microtubule polymerization, tumor angiogenesis, and proteins associated with apoptosis, as well as regulating reactive oxygen species. Due to this broad spectrum of biological activities and minimal side effects, coumarin derivatives are considered promising compounds in cancer therapy [119].

Shen and colleagues (2017) synthesized and evaluated new pyrazole-coumarin hybrid compounds as dual inhibitors of cyclooxygenase-2 (COX-2) and 5-lipoxygenase (5-LOX). The compound coded 1 (Figure 14) in the study showed strong inhibition against COX-2 and 5-LOX. It also exhibited antiproliferative effects and dose-dependent apoptosis induction against the lung cancer (A549) cell line. These findings suggest that compound 1 could be a potential lead molecule for the development of anticancer therapies [120].

In another study on coumarins, Muhamed et al. (2019) synthesized new pyrazole-thiazole-coumarin hybrid compounds (2a-d) (Figure 14). Their potential against five different cancer cell lines was examined. Specifically, compound 2d, shown in figure 14, exhibited significant VEGFR-2 inhibition and high cytotoxic effects against breast cancer MCF-7 cells. The mechanism of action of compound 2d was investigated in detail, revealing that it induced cell cycle arrest at the G2/M phase, increased apoptotic cell death, regulated p53 gene expression, and activated the apoptotic pathway by increasing the Bax/Bcl-2 ratio. Furthermore, it was found to enhance apoptotic induction by increasing caspase-7 and caspase-9 activation. These findings suggested that compound 2d could be considered an effective apoptosis modulator and a promising lead molecule for the development of future anti-breast cancer agents [121].

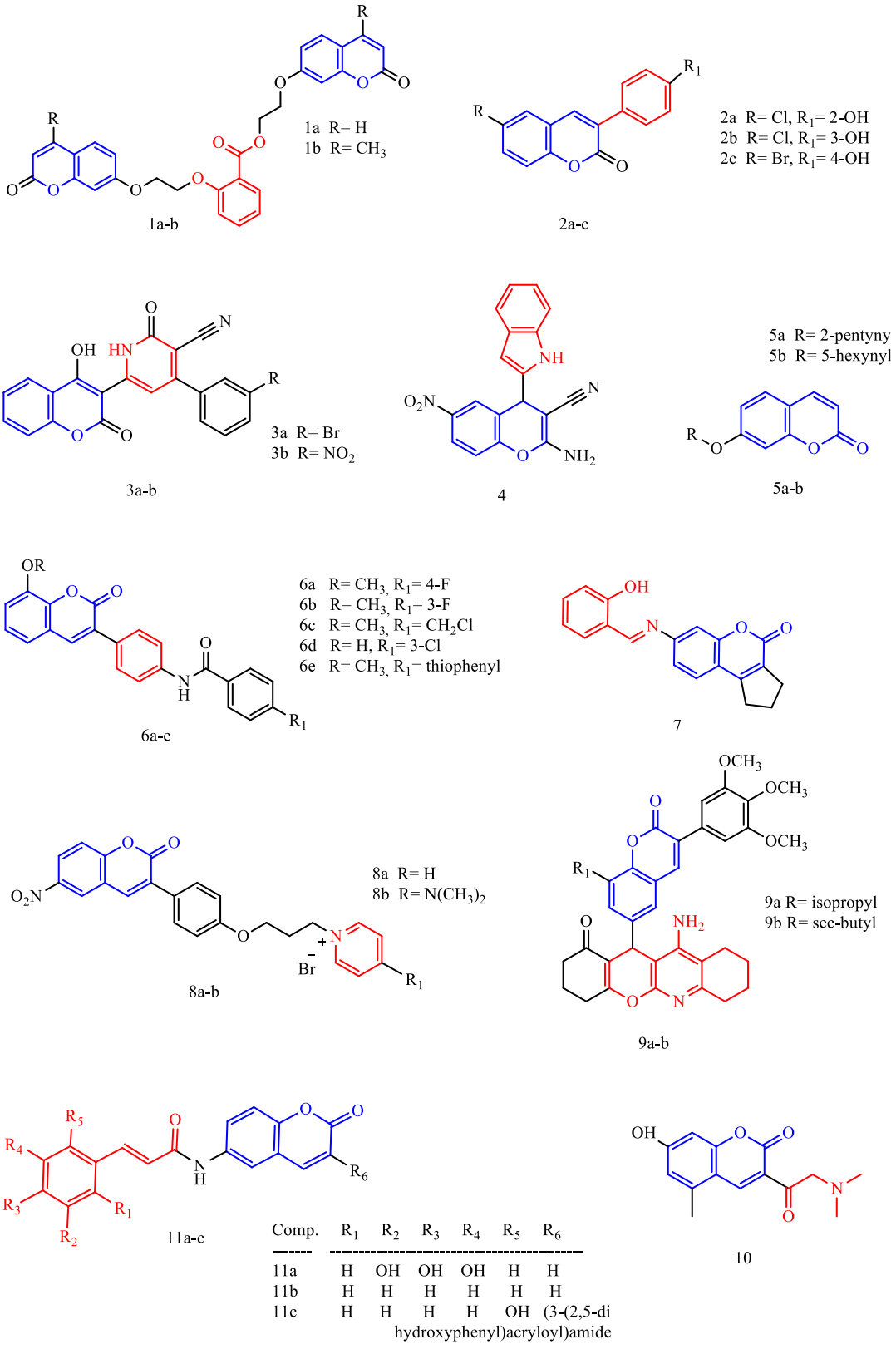

Figure 13. *Chemical Structures of Coumarin Hybrid Compounds with Diverse Biological Activities.*

In this study, Durgapal and Soman (2019) synthesized coumarin-proline sulfonamide hybrid derivatives, which show promise for cancer treatment. The anticancer activities of all synthesized compounds were examined *in vitro* against lung cancer (A549) and breast cancer (MCF7) cell lines.

While all compounds exhibited moderate activity in the A549 cell line, they showed distinctly good activity in the MCF7 cancer cell line. Notably, compound 3 (Figure 14) demonstrated excellent activity against the MCF7 cell line [122].

Wang et al. (2020) developed new coumarin-chalcone hybrid compounds as thioredoxin reductase (TrxR) inhibitors and evaluated their anticancer potential. Compound 4 (Figure 14) showed strong antitumor activity against HCT-116 colorectal cancer cells. Due to its red fluorescent property, compound 4 allowed for intracellular imaging. It was observed to reduce TrxR expression, increase reactive oxygen species (ROS) accumulation, induce apoptosis, and inhibit the metastasis of cancer cells. These findings suggest that compound 4 could be a promising theranostic TrxR inhibitor for human cancer treatment [123].

Heris et al. (2020) conducted a study on the anticancer potential of aminothiazole-coumarin derivatives. The researchers identified a new class of aminothiazoles that function as energy-restricting mimetic agents (ERMA). These compounds exhibited strong anticancer activity, particularly against colorectal cancer (CRC) cell lines. Compounds 5a and 5b (Figure 14) showed the most promising results. Their mechanism of action involved inhibiting glucose uptake in cancer cells, increasing the production of reactive oxygen species (ROS), and decreasing the NADPH/NADP+ ratio. Additionally, these compounds demonstrated a synergistic effect with cisplatin. The study highlighted that thiazole-coumarin derivatives could be used as potential anticancer agents by targeting cellular energy mechanisms and showed promise in combination therapy with traditional chemotherapeutic agents. However, it was noted that further research is needed to evaluate their efficacy in different cancer types and in combination with other chemotherapeutic agents [124].

Ahmed and colleagues (2020) synthesized twenty-five new coumarin derivatives and evaluated their *in vitro* anticancer activities against breast cancer (MCF-7) and prostate cancer (PC-3) cell lines. Most of the synthesized compounds exhibited high anticancer activity against the MCF-7 cell line. In particular, compounds 6a and 6b (Figure 14) showed superior activity compared to the positive control, staurosporine. Additionally, compound 6a demonstrated VEGFR-2 kinase inhibitor activity, induced preG1 apoptosis, arrested cell growth in the G2/M phase, and activated caspase-9 [125].

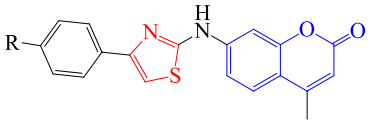

1a-b

1a R= Br
1b R= NO_2

($IC_{50\ M}M$)

Compounds	HT-29	HCT-116
1a	0.38 ± 0.004	0.53 ± 0.077
1b	3.96 ± 0506	2.56 ± 0.553
OSU-OG5	10.14 + 0.373	2.85 + 0.111
OSU-OG12	10.82 + 1.259	3.4 + 0.581
4-Hydroxycoumarin	200>	200>

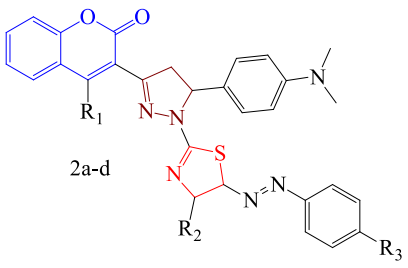

2a-d

($IC_{50\ M}M$)

Compounds	MCF-7	R_1	R_2	R_3
2a	8.61	H	CH_3	Cl
2b	6.56	OH	Ph	CH_3
2c	6.51	H	Ph	Cl
2d	5.41	OH	Ph	Cl
Doxorubicin	6.73	--	--	--

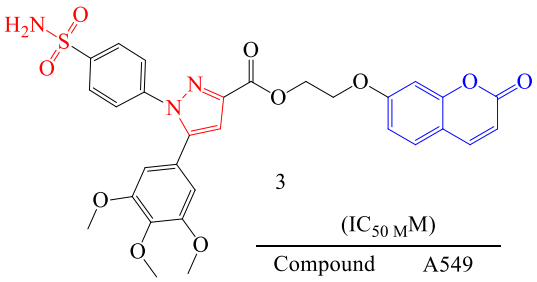

3

($IC_{50\ M}M$)

Compound	A549
3	4.48 ± 0.57
Celecoxib	7.68 ± 0.55

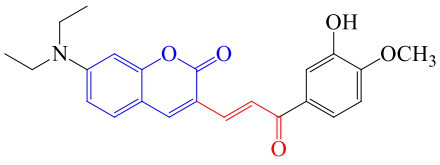

4

($IC_{50\ M}M$)

Compound	HCT-116
4	3.60 ± 0.06
Xanthohumol	27.60 ± 1.50

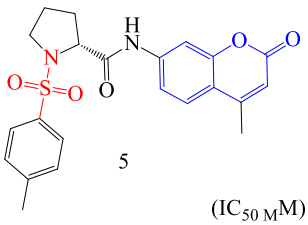

5

($IC_{50\ M}M$)

Compound	MCF-7
5	1.07
5-Fluorouracil	45.04

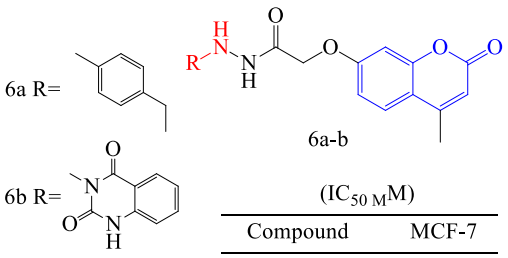

6a-b

($IC_{50\ M}M$)

Compound	MCF-7
6a	1.24 ±0.06
6b	1.65 ±0.07
Staurospiorine	8.81 ± 0.39

Figure 14. *Chemical Structures of Some Coumarin Hybrid Compounds with Anticancer Activity.*

Beyond their notable anticancer properties, coumarins have been explored for a range of other pharmacological activities. Some of these studies are compiled in in

Table **2** and

Table **3**, highlighting their antimicrobial, antioxidant, and other anti-inflammatory potentials. Furthermore, Table 4 summarizes the enzymatic activities of various coumarin derivatives, detailing the type of coumarin, concentration, and observed results.

Table 2. *Microbial Activity of Coumarins.*

Type of Coumarin	Compound Type	Concentration *(mg/mL)*	Microorganism Type	Microorganism	Test Method	Result *(mm)*	Ref.
Synthetic	Triazol	10 20	Bacteria	*S. Aureus* *B. Subtilis*	Disk diffusion	09- 26 17- 36 09- 27 18- 42	[48]
		10 20	Bacteria	*E. Coli* *K. Pneumonia*	Disk diffusion	08- 21 11- 29 04- 14 09- 22	
		50	Fungus	*Aspergillus niger* *Aspergillus flavus* *Fusariumoxy sporum*	Disk diffusion	08.2-18.8 06.4- 17.6 06.6- 19	
Synthetic	Coumarin-tethered (benz)imidazolium salts and their silver(I) N-heterocyclic carbene complexes	800	Bacteria	*S. Aureus* *B. Subtilis* *E. Coli* *P. Aeruginosa*	Disk diffusion	6-12 7-19 19-28 8-20	[126]
Synthetic	Coumarin-pyrazole hybrid	25000, 50000, 100000	Bacteria	*B. Subtilis* *S. Aureus* *E. Coli* *P. Aeruginosa*	Agar-Well Diffusion	6.25- 100 µg/mL 0.78- 50 µg/mL 3.125-100 µg/L 6.25- 100 µg/mL	[127]

Synthetic	Catechol-3-arylcoumarins	100 μM	Parasite	*Trypanosoma cruzi* *Vero cells*	MTT	7.4- 39.4 % 0.3- 30.4 %	[128]

Table 3. *Pharmacological Activity of Coumarins.*

Type of Coumarin	**Compound Type**	**Activity Type**	**Test Method**	**Result** *(μM/mL)*	**Ref.**
Synthetic	Triazol	Antioxidant	DPPH radical scavenging assay	0.061- 343.33	[48]
			H_2O_2 scavenging assay	0.061- 343.33	
		Anti-inflammatory	Egg-albumin	15.78- 238.13	
			Heat-induced hemolytic	12.06- 138.13	
Synthetic	3-arylcoumarin	Antioxidant	DPPH OH	1.33- 756.42 μM 244.02- 996.24 μM	[129, p. 3]
Synthetic	Trihybridized coumarin -1,3,4-oxadiazole derivatives	Antioxidant	DPPH	48.3- 113.89 μg/mL	[130]
Synthetic	Catechol- 3-arylcoumarins	Antioxidant	ORAC-FL	0.4-5.6 μM	[128]

Synthetic	Coumarin-pyrazole hybrid	Anti-inflammatory	Egg-albumin	3.78- 67.27 µg/mL	[127]

(DPPH): 1,1-diphenyl-2-picryl hydrazyl radical assay.
(ORAC-FL): Oxygen radical antioxidant Capacity-fluorescein

Table 4. *Biochemical (Enzymatic) Activity of Coumarins.*

Type of Coumarin	**Compound Type**	**Concentration** *(µM)*	**Enzyme**	**Result** *(µM)*	**Ref.**
Synthetic	3-arylcoumarin	100	α-glucosidase inhibitory	0.050- 280.38	[129]
		Less than 10.00	AGEs inhibitory	1.42- 298.83	
Synthetic	3-phenylcoumarin	100	monoamine oxidase A (MAO-A)	0- 24.57	[47]
		10	monoamine oxidase B (MAO-B)	75.75- 111.93	
		10	ER inhibition	0- 91.34	
		1	HSD1 inhibition	0- 54	
Synthetic	Trihybridized coumarin -1,3,4-oxadiazole derivatives	100, 50, 40, 30, 20, 10	Anticholinesterase AchE	28.68- 159.74	[130]
			Butyrylcholinesterase BuChE	23.97- 105.93	

VI. USAGES/APPLICATIONS

Coumaric compounds have a wide range of applications thanks to their electron-rich conjugate systems and their versatile and simple scaffold structure [6]. Coumarin and its derivatives, which can be used as fluorescent probe, ion-based receptor and biological dyes; It offers comprehensive application possibilities such as illuminating complex biological processes, monitoring enzyme activity and monitoring pharmacokinetic properties instantly [6].

Studies on coumarin and its derivatives have proven that the presence of different substituents in the coumarin ring gives it different biological properties [131]. It has become the focus of scientific research due to the antibacterial, antifungal, antiviral, anticoagulant, antimitotic, anticancer, anti-inflammatory, anti-allergic, antioxidant, antithrombotic anticonvulsant (antiepileptic) properties that coumarins offer [33], [132], [133], [134], [135], [136]. Coumarin-based compounds have been used in the pharmaceutical industry, especially due to their pharmacological properties such as antimicrobial (antibacterial, antiviral, antifungal and anti-parasitic), anticoagulant, anti-inflammatory, antioxidant and anticarcinogenic [137]. Studies have also reported that some coumarin derivatives have analgesic and hypothermic activity [138]. Some coumarin derivatives have been reported to increase the amount of acetylcholine in the brain by inhibiting acetylcholinesterase. These coumarinic compounds may be drug candidates for the treatment of Alzheimer's associated with learning and understanding memory functions [139].

Coumaric compounds are compounds with low toxicity, high fluorescence quantum yields and stokes shifts, giving absorption and emission spectra in the visible region. In addition, since coumarins can absorb UV light and are very sensitive to natural light, they offer the opportunity to be used in photochemotherapy and chemical sensors [6]. Due to the extraordinary properties of coumarins such as real-time detection, high selectivity and high efficiency, they can be used as fluorescent probes for intracellular bioimaging and can also be used to detect certain cancers. Today, medical imaging has made great advances in locating and distinguishing tumor lesions. Research continues to expand the use of coumarinic compounds as fluorescent probes [140].

Apart from the pharmaceutical industry, coumarin and its derivatives are also used in agriculture. It has been preferred in pesticides due to the herbicide properties of some coumarinic compounds [47]. It has been reported that coumarin derivatives are used as sweeteners and food additives in the food industry. Some coumarins have been used as flavor enhancers in alcoholic beverages and tobacco. It has also been used in perfumes since 1882 due to the nice smell of coumarins [6]. Coumarins are also used in the manufacture of soaps and cleaning products [141].

VII. CONCLUSION

Coumarins constitute a significant portion of the secondary metabolites produced by plants [142], [143]. While the complete synthesis pathway of natural coumarins remains not entirely elucidated, ongoing research has made substantial progress [144]. Studies have unveiled a myriad of pharmacological and biochemical activities associated with both natural and synthetic coumarins. Their exceptional properties have not only found applications in the pharmaceutical industry but have also extended to their use as additives in food, pesticides in agriculture, and fragrances in cosmetics. Notably, research has indicated that coumarin and its derivatives, which have undergone photophysical investigations, hold promise as biological probes owing to their fluorescence characteristics [145], [146]. In this review, we provided insights into the classification of coumarins, summarized various chemical synthesis methods, and elucidated the chemical-physical properties and biological activities of coumarin and its derivatives. Furthermore, we compiled their diverse application areas.

CONFLICT OF INTERESTS: The author has no competing interests to declare that are relevant to the content of this article.

ACKNOWLEDGEMENTS: The authors thank Research Assistant Dr. Ayhan Yilmaz (Dumlupinar University, Department of Biology) and Fatıma ELMUSA (Eskisehir Technical University, Department of Biology) for proofreading the article.

AUTHOR CONTRIBUTIONS: The idea for the article was performed by Safa ELMUSA and Muna ELMUSA. The literature search and data collection were performed by Safa ELMUSA, Muna ELMUSA, and Benan ELMUSA. Figure and table were performed by Muna ELMUSA. The first draft of the manuscript was written by Safa ELMUSA and Muna ELMUSA. Resources were performed by Safa ELMUSA and Muna ELMUSA. Writing review and editing were performed by Rahmi KASIMOĞULLARI. All authors read and approved the final manuscript.

ETHICAL DISCLOSURES: Since this study is a data collection study (review), it does not have experimental data. Therefore, ethics committee approval was not obtained because it does not require ethics committee approval.

VIII. REFERENCES

[1] Ł. Balewski, S. Szulta, A. Jalińska, and A. Kornicka, "A Mini-Review: Recent Advances in Coumarin-Metal Complexes With Biological Properties," Front. Chem., vol. 9, p. 781779, Dec. 2021, doi: 10.3389/fchem.2021.781779.

[2] Y. Wu, J. Xu, Y. Liu, Y. Zeng, and G. Wu, "A Review on Anti-Tumor Mechanisms of Coumarins," Front. Oncol., vol. 10, p. 592853, Dec. 2020, doi: 10.3389/fonc.2020.592853.

[3] C. S. Kılıç, "Herbal coumarins in healthcare," in Herbal Biomolecules in Healthcare Applications, S. C. Mandal, A. K. Nayak, and A. K. Dhara, Eds., Elsevier, 2022, pp. 363–380. doi: 10.1016/B978-0-323-85852-6.00003-2.

[4] M. Musa, J. Cooperwood, and M. O. Khan, "A Review of Coumarin Derivatives in Pharmacotherapy of Breast Cancer," Curr. Med. Chem., vol. 15, no. 26, pp. 2664–2679, 2008, doi: 10.2174/092986708786242877.

[5] S. C. Heghes, O. Vostinaru, C. Mogosan, D. Miere, C. A. Iuga, and L. Filip, "Safety Profile of Nutraceuticals Rich in Coumarins: An Update," Front. Pharmacol., vol. 13, p. 803338, Jan. 2022, doi: 10.3389/fphar.2022.803338.

[6] M. J. Matos, L. Santana, E. Uriarte, O. A. Abreu, E. Molina, and E. G. Yordi, "Coumarins — An Important Class of Phytochemicals," in Phytochemicals - Isolation, Characterisation and Role in Human Health, A. V. Rao and L. G. Rao, Eds., InTech, 2015. doi: 10.5772/59982.

[7] I. A. Stringlis, R. De Jonge, and C. M. J. Pieterse, "The Age of Coumarins in Plant–Microbe Interactions," Plant Cell Physiol., vol. 60, no. 7, pp. 1405–1419, Jul. 2019, doi: 10.1093/pcp/pcz076.

[8] V. M. Adimule, S. S. Nandi, S. S. Kerur, S. A. Khadapure, and S. Chinnam, "Recent Advances in the One-Pot Synthesis of Coumarin Derivatives from Different Starting Materials Using Nanoparticles: A Review," Top. Catal., Jan. 2022, doi: 10.1007/s11244-022-01571-z.

[9] A. Gliszczyńska and P. E. Brodelius, “Sesquiterpene coumarins,” Phytochem. Rev., vol. 11, pp. 77–96, Nov. 2011, doi: 10.1007/s11101-011-9220-6.

[10] F. Bourgaud et al., “Biosynthesis of coumarins in plants: a major pathway still to be unravelled for cytochrome P450 enzymes,” Phytochem. Rev., vol. 5, no. 2–3, pp. 293–308, Nov. 2006, doi: 10.1007/s11101-006-9040-2.

[11] A. Forycka and W. Buchwald, “Variability of composition of essential oil and coumarin compounds of Angelica archangelica L.,” Herba Pol., vol. 65, no. 4, pp. 62–75, Dec. 2019, doi: 10.2478/hepo-2019-0027.

[12] S.-M. Yang, G. Y. Shim, B.-G. Kim, and J.-H. Ahn, “Biological synthesis of coumarins in Escherichia coli,” Microb. Cell Factories, vol. 14, no. 1, p. 65, May 2015, doi: 10.1186/s12934-015-0248-y.

[13] J. Wang, S. Huang, C. Li, W. Ding, Z. She, and C. Li, “A New Coumarin Produced by Mixed Fermentation of Two Marine Fungi,” Chem. Nat. Compd., vol. 51, pp. 239–241, Mar. 2015, doi: 10.1007/s10600-015-1252-5.

[14] T. Umashankar, M. Govindappa, Y. Ramachandra, C. Chandrappa, S. R. Padmalatha, and R. Channabasava, “Isolation, purification and in vitro cytotoxicity activities of coumarin isolated from endophytic fungi, alternariaspecies of crotalaria pallida,” Indo Am. J. Pharm. Res., vol. 5, no. 2, pp. 926–936, 2015.

[15] T.-X. Li et al., “Antioxidant coumarin and pyrone derivatives from the insect-associated fungus Aspergillus Versicolor,” Nat. Prod. Res., vol. 34, no. 10, pp. 1360–1365, Nov. 2020, doi: 10.1080/14786419.2018.1509334.

[16] S. P. D. Lira et al., “A SARS-coronovirus 3CL protease inhibitor isolated from the marine sponge Axinella cf. corrugata: structure elucidation and synthesis,” J. Braz. Chem. Soc., vol. 18, no. 2, pp. 440–443, Apr. 2007, doi: 10.1590/S0103-50532007000200030.

[17] A. Parikh, H. Parikh, and K. Parikh, “Perkin Reaction,” in Name Reactions in Organic Synthesis, 1st ed., Foundation Books, 2012, pp. 338–341. doi: 10.1017/UPO9788175968295.093.

[18] T. Symeonidis, M. Chamilos, D. J. Hadjipavlou-Litina, M. Kallitsakis, and K. E. Litinas, “Synthesis of hydroxycoumarins and hydroxybenzo[f]- or [h]coumarins as lipid peroxidation inhibitors,” Bioorg. Med. Chem. Lett., vol. 19, no. 4, pp. 1139–1142, Feb. 2009, doi: 10.1016/j.bmcl.2008.12.098.

[19] A. Song, X. Wang, and K. S. Lam, “A convenient synthesis of coumarin-3-carboxylic acids via Knoevenagel condensation of Meldrum’s acid with ortho-hydroxyaryl aldehydes or ketones,” Tetrahedron Lett., vol. 44, no. 9, pp. 1755–1758, Feb. 2003, doi: 10.1016/S0040-4039(03)00108-4.

[20] S. M. Sethna and N. M. Shah, “The Chemistry of Coumarins.,” Chem. Rev., vol. 36, no. 1, pp. 1–62, Feb. 1945, doi: 10.1021/cr60113a001.

[21] G. Rabbani, “A Concise Introduction of Perkin Reaction,” Org. Chem. Curr. Res., vol. 07, no. 02, May 2018, doi: 10.4172/2161-0401.1000191.

[22] D. Sharma, V. Dhayalan, C. Manikandan, and R. Dandela, “Recent Methods for Synthesis of Coumarin Derivatives and Their New Applications,” in Strategies for the Synthesis of Heterocycles and Their Applications, P. Kumari and A. B. Patel, Eds., IntechOpen, 2022. doi: 10.5772/intechopen.108563.

[23] S. Pakdel, B. Akhlaghinia, and A. Mohammadinezhad, “Fe3O4@Boehmite-NH2-CoII NPs: An Environment Friendly Nanocatalyst for Solvent Free Synthesis of Coumarin Derivatives Through

Pechmann Condensation Reaction," Chem. Afr., vol. 3, no. 2, pp. 367–376, Jan. 2019, doi: 10.1007/s42250-019-00042-5.

[24] M. Lončarić, D. Gašo-Sokač, S. Jokić, and M. Molnar, "Recent Advances in the Synthesis of Coumarin Derivatives from Different Starting Materials," Biomolecules, vol. 10, no. 1, p. 151, Jan. 2020, doi: 10.3390/biom10010151.

[25] S. Gulati, R. Singh, and S. Sangwan, "A review on convenient synthesis of substituted coumarins using reuseable solid acid catalysts," RSC Adv., vol. 11, no. 47, pp. 29130–29155, Sep. 2021, doi: 10.1039/D1RA04887B.

[26] A. Y. Mohammed and L. S. Ahamed, "Synthesis and Characterization of New Substituted Coumarin Derivatives and Study Their Biological Activity," Chem. Methodol., no. Online First, Aug. 2022, doi: 10.22034/CHEMM.2022.349124.1569.

[27] Y. Rangraz, S. M. Vadat, and S. Khaksar, "SnO2 nanoparticles: A recyclable and heterogeneous catalyst for Pechmann condensation of coumarins and Knoevenagel condensation-Michael addition of biscoumarins." Accessed: Jul. 30, 2024. [Online]. Available: https://pubmed.ncbi.nlm.nih.gov/37123921/

[28] S. S. Vagh, B.-J. Hou, A. Edukondalu, P.-C. Wang, and W. Lin, "Phosphine-Mediated MBH-Type/Acyl Transfer/Wittig Sequence for Construction of Functionalized Furo[3,2-c]coumarins," Org. Lett., vol. 23, no. 3, pp. 842–846, Jan. 2021, doi: 10.1021/acs.orglett.0c04082.

[29] S. Yang et al., "Diversity-Oriented Synthesis of Furo[3,2-c]coumarins and Benzofuranyl Chromenones through Chemoselective Acylation/Wittig Reaction," Angew. Chem., vol. 130, no. 6, pp. 1684–1688, Dec. 2017, doi: 10.1002/ange.201711524.

[30] B. Zhao et al., "Reformatsky Reaction Promoted by an Ionic Liquid ([Bmim]Cl) in the Synthesis of β-Hydroxyl Ketone Derivatives Bearing a Coumarin Unit," J. Chem. Res., vol. 36, no. 7, pp. 393–395, Jul. 2012, doi: 10.3184/174751912X13371652436057.

[31] M. Bakthadoss and R. Selvakumar, "One-Pot Synthesis of Benzothiazole-Tethered Chromanones/Coumarins via Claisen Rearrangement Using the Solid State Melt Reaction," J. Org. Chem., vol. 81, no. 8, pp. 3391–3399, Mar. 2016, doi: 10.1021/acs.joc.5b02920.

[32] S. Aoki, C. Amamoto, J. Oyamada, and T. Kitamura, "A convenient synthesis of dihydrocoumarins from phenols and cinnamic acid derivatives," Tetrahedron, vol. 61, no. 39, pp. 9291–9297, Sep. 2005, doi: 10.1016/j.tet.2005.07.062.

[33] I. Ansary and A. Taher, "One-Pot Synthesis of Coumarin Derivatives," in Phytochemicals in Human Health, V. Rao, D. Mans, and L. Rao, Eds., IntechOpen, 2019, p. 298. doi: 10.5772/intechopen.89013.

[34] D. Wang et al., "Synthesis of V-Shaped Bis-coumarins through Aldol Reaction/Double Lactonization Cascade Reaction from Bis(2-hydroxyphenyl)methanone and Meldrum's Acid," Eur. J. Org. Chem., vol. 2022, no. 13, Mar. 2022, doi: 10.1002/ejoc.202101489.

[35] B. M. Trost, F. D. Toste, and K. Greenman, "Atom Economy Palladium-Catalyzed Formation of Coumarins by Addition of Phenols and Alkynoates via a Net C−H Insertion," J. Am. Chem. Soc., vol. 125, no. 15, pp. 4518–4526, Mar. 2003, doi: 10.1021/ja0286573.

[36] Md. Kutubi, T. Hashimoto, and T. Kitamura, "Improved Synthesis of Coumarins by Iron(III)-Catalyzed Cascade Reaction of Propiolic Acids and Phenols," Synthesis, vol. 2011, no. 08, pp. 1283–1289, Mar. 2011, doi: 10.1055/s-0030-1258473.

[37] K. Park, I. Jung, and Y. Chung, "Synthesis of Coumarins Catalyzed by Heterobimetallic Co/Rh Nanoparticles," Synlett, vol. 2004, no. 14, pp. 2541–2544, Oct. 2004, doi: 10.1055/s-2004-834826.

[38] R. Leão, P. de F. de Moraes, M. Pedro, and P. Costa, “Synthesis of Coumarins and Neoflavones through Zinc Chloride Catalyzed Hydroarylation of Acetylenic Esters with Phenols,” Synthesis, vol. 2011, no. 22, pp. 3692–3696, Oct. 2011, doi: 10.1055/s-0031-1289576.

[39] A. Thakur, R. Singla, and V. Jaitak, “Coumarins as anticancer agents: A review on synthetic strategies, mechanism of action and SAR studies,” Eur. J. Med. Chem., vol. 101, pp. 476–495, Aug. 2015, doi: 10.1016/j.ejmech.2015.07.010.

[40] V. Sharma et al., “Synthesis, Electrochemical Studies, Molecular Docking, and Biological Evaluation as an Antimicrobial Agent of 5-Amino-6-cyano-3-hydroxybenzo[c]coumarin Using Ni–Cu–Al–CO3 Hydrotalcite as a Catalyst,” ACS Omega, vol. 7, no. 18, pp. 15718–15727, Apr. 2022, doi: 10.1021/acsomega.2c00666.

[41] D. U. C. Rahayu et al., “Microwave-Assisted Synthesis Of 4-Methyl Coumarins, Their Antioxidant and Antibacterial Activities,” RASAYAN J. Chem., vol. 15, no. 2, pp. 1053–1062, 2022, doi: 10.31788/RJC.2022.1526780.

[42] M. Özdemir, F. Biryan, K. Koran, B. Yalçın, and A. O. Görgülü, “Synthesis, structural characterization, therotical and electrical properties of novel sulpho-coumarin based methacrylate polymer,” J. Polym. Res., vol. 29, no. 190, Apr. 2022, doi: 10.1007/s10965-022-03034-1.

[43] R. O. Juvonen, M. Ahinko, J. Huuskonen, H. Raunio, and O. T. Pentikäinen, “Development of new Coumarin-based profluorescent substrates for human cytochrome P450 enzymes,” Xenobiotica, vol. 49, no. 9, pp. 1015–1024, Sep. 2019, doi: 10.1080/00498254.2018.1530399.

[44] Ş. N. Karuk Elmas et al., “Selective and sensitive fluorescent and colorimetric chemosensor for detection of CO32- anions in aqueous solution and living cells,” Talanta, vol. 188, pp. 614–622, Oct. 2018, doi: 10.1016/j.talanta.2018.06.036.

[45] C. Schultze and B. Schmidt, “Prenylcoumarins in One or Two Steps by a Microwave-Promoted Tandem Claisen Rearrangement/Wittig Olefination/Cyclization Sequence,” J. Org. Chem., vol. 83, no. 9, pp. 5210–5224, May 2018, doi: 10.1021/acs.joc.8b00667.

[46] C. Schultze and B. Schmidt, “Ring-closing-metathesis-based synthesis of annellated coumarins from 8-allylcoumarins,” Beilstein J. Org. Chem., vol. 14, pp. 2991–2998, Dec. 2018, doi: 10.3762/bjoc.14.278.

[47] S. Rauhamäki et al., “Structure-Activity Relationship Analysis of 3-Phenylcoumarin-Based Monoamine Oxidase B Inhibitors,” Front. Chem., vol. 6, no. 41, Mar. 2018, doi: 10.3389/fchem.2018.00041.

[48] R. Dharavath et al., “Microwave-assisted synthesis, biological evaluation and molecular docking studies of new coumarin-based 1,2,3-triazoles,” RSC Adv., vol. 10, no. 20, pp. 11615–11623, Mar. 2020, doi: 10.1039/D0RA01052A.

[49] A. R. Ferreira, D. D. N. Alves, R. D. De Castro, Y. Perez-Castillo, and D. P. De Sousa, “Synthesis of Coumarin and Homoisoflavonoid Derivatives and Analogs: The Search for New Antifungal Agents,” Pharmaceuticals, vol. 15, no. 6, p. 712, Jun. 2022, doi: 10.3390/ph15060712.

[50] K. D. Dhawale, A. P. Ingale, M. S. Pansare, S. S. Gaikwad, N. M. Thorat, and L. R. Patil, “Sulfated Tungstate as a Heterogeneous Catalyst for Synthesis of 3-Functionalized Coumarins under Solvent-Free Conditions,” Polycycl. Aromat. Compd., vol. 43, no. 4, pp. 3588–3600, Apr. 2023, doi: 10.1080/10406638.2022.2074477.

[51] A. Fais et al., “Coumarin derivatives as promising xanthine oxidase inhibitors,” Int. J. Biol. Macromol., vol. 120(Pt A), pp. 1286–1293, Dec. 2018, doi: 10.1016/j.ijbiomac.2018.09.001.

[52] S. Qi et al., “Coumarin/fluorescein-fused fluorescent dyes for rapidly monitoring mitochondrial pH changes in living cells,” Spectrochim. Acta. A. Mol. Biomol. Spectrosc., vol. 204, pp. 590–597, Nov. 2018, doi: 10.1016/j.saa.2018.06.095.

[53] H. M. Mali et al., “Rational design of coumarin derivatives as antituberculosis agents,” Future Med. Chem., vol. 10, no. 20, pp. 2431–2444, Oct. 2018, doi: 10.4155/fmc-2018-0015.

[54] O. Ivanova, V. Andronov, I. Levina, A. Chagarovskiy, L. Voskressensky, and I. Trushkov, “Convenient Synthesis of Functionalized Cyclopropa[c]coumarin-1a-carboxylates,” Molecules, vol. 24, no. 1, p. 57, Dec. 2018, doi: 10.3390/molecules24010057.

[55] C. S. Wijesooriya, M. Nieszala, A. Stafford, J. R. Zimmerman, and E. A. Smith, “Coumarin-based Fluorescent Probes for Selectively Targeting and Imaging the Endoplasmic Reticulum in Mammalian Cells,” Photochem. Photobiol., vol. 95, no. 2, pp. 556–562, Mar. 2019, doi: 10.1111/php.12985.

[56] M. Shangguan et al., “A coumarin-based fluorescent probe for hypochlorite ion detection in environmental water samples and living cells,” Talanta, vol. 202, pp. 303–307, Sep. 2019, doi: 10.1016/j.talanta.2019.04.074.

[57] D. S. Reddy et al., “Coumarin tethered cyclic imides as efficacious glucose uptake agents and investigation of hit candidate to probe its binding mechanism with human serum albumin,” Bioorganic Chem., vol. 92, p. 103212, Nov. 2019, doi: 10.1016/j.bioorg.2019.103212.

[58] J. R. Hwu et al., “Chikungunya virus inhibition by synthetic coumarin–guanosine conjugates,” Eur. J. Med. Chem., vol. 166, pp. 136–143, Mar. 2019, doi: 10.1016/j.ejmech.2019.01.037.

[59] R. Beninatto et al., “Photocrosslinked hydrogels from coumarin derivatives of hyaluronic acid for tissue engineering applications,” Mater. Sci. Eng. C, vol. 96, pp. 625–634, Mar. 2019, doi: 10.1016/j.msec.2018.11.052.

[60] K. S. Mani et al., “Coumarin based hydrazone as an ICT-based fluorescence chemosensor for the detection of Cu2+ ions and the application in HeLa cells,” Spectrochim. Acta. A. Mol. Biomol. Spectrosc., vol. 214, pp. 170–176, May 2019, doi: 10.1016/j.saa.2019.02.020.

[61] B. Zhang, L. Xu, Y. Zhou, W. Zhang, Y. Wang, and Y. Zhu, “Synthesis and activity of a coumarin-based fluorescent probe for hydroxyl radical detection,” Luminescence, vol. 35, no. 2, pp. 305–311, Mar. 2020, doi: 10.1002/bio.3728.

[62] W.-L. Lee, T.-W. Hsu, W.-C. Hung, and J.-M. Fang, “A copper(ii)–dipicolylamine–coumarin sensor for maltosyltransferase assay,” Dalton Trans., vol. 48, no. 23, pp. 8026–8029, Jun. 2019, doi: 10.1039/C9DT01339C.

[63] F. Rodríguez-Enríquez et al., “Novel coumarin-pyridazine hybrids as selective MAO-B inhibitors for the Parkinson’s disease therapy,” Bioorganic Chem., vol. 104, p. 104203, Nov. 2020, doi: 10.1016/j.bioorg.2020.104203.

[64] S. K. Konidala, V. Kotra, R. C. S. R. Danduga, and P. K. Kola, “Coumarin-chalcone hybrids targeting insulin receptor: Design, synthesis, anti-diabetic activity, and molecular docking,” Bioorganic Chem., vol. 104, p. 104207, Nov. 2020, doi: 10.1016/j.bioorg.2020.104207.

[65] D. Iacopini, A. Moscardini, F. Lessi, V. Di Bussolo, S. Di Pietro, and G. Signore, “Coumarin-based fluorescent biosensor with large linear range for ratiometric measurement of intracellular pH,” Bioorganic Chem., vol. 105, p. 104372, Dec. 2020, doi: 10.1016/j.bioorg.2020.104372.

[66] M. B. Majnooni, S. Fakhri, Y. Shokoohinia, M. Mojarrab, S. Kazemi-Afrakoti, and M. H. Farzaei, “Isofraxidin: Synthesis, Biosynthesis, Isolation, Pharmacokinetic and Pharmacological Properties,” Molecules, vol. 25, no. 9, p. 2040, Apr. 2020, doi: 10.3390/molecules25092040.

[67] A. R. Nesaragi et al., “Green synthesis of therapeutically active 1,3,4-oxadiazoles as antioxidants, selective COX-2 inhibitors and their in silico studies,” Bioorg. Med. Chem. Lett., vol. 43, p. 128112, Jul. 2021, doi: 10.1016/j.bmcl.2021.128112.

[68] M. Seydimemet, K. Ablajan, M. Hamdulla, W. Li, A. Omar, and M. Obul, “l -Proline catalyzed four-component one-pot synthesis of coumarin-containing dihydropyrano[2,3-c]pyrazoles under ultrasonic irradiation,” Tetrahedron, vol. 72, no. 47, pp. 7599–7605, Nov. 2016, doi: 10.1016/j.tet.2016.10.016.

[69] M. R. Bhosle, S. A. Joshi, and G. M. Bondle, “An efficient contemporary multicomponent synthesis for the facile access to coumarin-fused new thiazolyl chromeno[4,3-b]quinolones in aqueous micellar medium,” J. Heterocycl. Chem., vol. 57, no. 1, pp. 456–468, Oct. 2019, doi: 10.1002/jhet.3802.

[70] G. Brahmachari, M. Mandal, I. Karmakar, K. Nurjamal, and B. Mandal, “Ultrasound-Promoted Expedient and Green Synthesis of Diversely Functionalized 6-Amino-5-((4-hydroxy-2-oxo-2H-chromen-3-yl)(aryl)methyl)pyrimidine-2,4(1H,3H)-diones via One-Pot Multicomponent Reaction under Sulfamic Acid Catalysis at Ambient Conditions,” ACS Sustain. Chem. Eng., vol. 7, no. 6, pp. 6369–6380, Feb. 2019, doi: 10.1021/acssuschemeng.9b00133.

[71] G. Brahmachari, I. Karmakar, and K. Nurjamal, “Ultrasound-Assisted Expedient and Green Synthesis of a New Series of Diversely Functionalized 7-Aryl/heteroarylchromeno[4,3-d]pyrido[1,2-a]pyrimidin-6(7H)-ones via One-Pot Multicomponent Reaction under Sulfamic Acid Catalysis at Ambient Conditions,” ACS Sustain. Chem. Eng., vol. 6, no. 8, pp. 11018–11028, Jun. 2018, doi: 10.1021/acssuschemeng.8b02448.

[72] S. Kanchithalaivan, R. V. Sumesh, and R. R. Kumar, “Ultrasound-Assisted Sequential Multicomponent Strategy for the Combinatorial Synthesis of Novel Coumarin Hybrids,” ACS Comb. Sci., vol. 16, no. 10, pp. 566–572, Oct. 2014, doi: 10.1021/co500092b.

[73] A. R. Karimi, R. Davood Abadi, and Z. Dalirnasab, “Synthesis of mono- and bis-spiro-2-amino-4H-pyrans catalyzed by S-alkyl O-hydrogen sulfothioate functionalized silica-coated magnetic nanoparticles under ultrasound irradiation,” Res. Chem. Intermed., vol. 41, pp. 7427–7435, Oct. 2014, doi: 10.1007/s11164-014-1834-z.

[74] Y. Jain, M. Kumari, R. P. Singh, D. Kumar, and R. Gupta, “Sonochemical Decoration of Graphene Oxide with Magnetic Fe3O4@CuO Nanocomposite for Efficient Click Synthesis of Coumarin-Sugar Based Bioconjugates and Their Cytotoxic Activity,” Catal. Lett., vol. 150, pp. 1142–1154, Oct. 2019, doi: 10.1007/s10562-019-02982-6.

[75] M. Feizpour Bonab, S. Soleimani-Amiri, and B. Mirza, “Fe3O4@C@PrS-SO3H: A Novel Efficient Magnetically Recoverable Heterogeneous Catalyst in the Ultrasound-Assisted Synthesis of Coumarin Derivatives,” Polycycl. Aromat. Compd., vol. 43, no. 2, pp. 1628–1643, Jan. 2022, doi: 10.1080/10406638.2022.2032768.

[76] F. Zarei, S. Soleimani-Amiri, and Z. Azizi, “Heterogeneously Catalyzed Pechmann Condensation Employing the HFe(SO 4) 2 .4H 2 O-Chitosan Nano-Composite: Ultrasound-Accelerated Green Synthesis of Coumarins,” Polycycl. Aromat. Compd., vol. 42, no. 9, pp. 6072–6089, Sep. 2021, doi: 10.1080/10406638.2021.1973520.

[77] S. M. Gomha and K. D. Khalil, “A Convenient Ultrasound-Promoted Synthesis of Some New Thiazole Derivatives Bearing a Coumarin Nucleus and Their Cytotoxic Activity,” Molecules, vol. 17, no. 8, pp. 9335–9347, Aug. 2012, doi: 10.3390/molecules17089335.

[78] A. Jain, R. Gupta, and M. Agarwal, “Instantaneous and Selective Bare Eye Detection of Inorganic Fluoride Ion by Coumarin–Pyrazole-Based Receptors,” J. Heterocycl. Chem., vol. 54, no. 5, pp. 2808–2816, Sep. 2017, doi: 10.1002/jhet.2884.

[79] K. Skalicka-Woźniak and K. Głowniak, “Coumarins: Analytical and Preparative Techniques,” in Handbook of Chemical and Biological Plant Analytical Methods, 1st ed., vol. 3, K. Hostettmann, Ed., UK: John Wiley & Sons Ltd, 2014, pp. 569–594. doi: 10.1002/9780470027318.a9925.

[80] D. Egan, R. O’kennedy, E. Moran, D. Cox, E. Prosser, and R. D. Thornes, “The Pharmacology, Metabolism, Analysis, and Applications of Coumarin and Coumarin-Related Compounds,” Drug Metab. Rev., vol. 22, no. 5, pp. 503–529, 1990, doi: 10.3109/03602539008991449.

[81] N. Abid-Jarraya, K. Khemakhem, H. Turki-Guermazi, S. Abid, N. Saffon, and S. Fery-Forgues, “Solid-state fluorescence properties of small iminocoumarin derivatives and their analogues in the coumarin series,” Dyes Pigments, vol. 132, pp. 177–184, Apr. 2016, doi: 10.1016/j.dyepig.2016.04.039.

[82] A. Cocco et al., “Synthesis and Photophysical Properties of Fluorescent 6-Aryl-D-π-A Coumarin Derivatives,” ACS Omega, vol. 6, no. 49, pp. 33708–33716, Nov. 2021, doi: 10.1021/acsomega.1c04810.

[83] N. M. Sarih et al., “Furo[3,2-c]coumarin-derived Fe3+ Selective Fluorescence Sensor: Synthesis, Fluorescence Study and Application to Water Analysis,” Sci. Rep., vol. 10, no. 1, p. 7421, May 2020, doi: 10.1038/s41598-020-63262-7.

[84] C. Hua et al., “High quantum yield and pH sensitive fluorescence dyes based on coumarin derivatives: fluorescence characteristics and theoretical study,” RSC Adv., vol. 6, no. 54, pp. 49221–49227, May 2016, doi: 10.1039/C6RA05996A.

[85] F. Annunziata, C. Pinna, S. Dallavalle, L. Tamborini, and A. Pinto, “An Overview of Coumarin as a Versatile and Readily Accessible Scaffold with Broad-Ranging Biological Activities,” Int. J. Mol. Sci., vol. 21, no. 13, Art. no. 13, Jan. 2020, doi: 10.3390/ijms21134618.

[86] R. H. Olie, K. Winckers, B. Rocca, and H. ten Cate, “Oral Anticoagulants Beyond Warfarin,” Annu. Rev. Pharmacol. Toxicol., vol. 64, no. 2024, pp. 551–575, Sep. 2023, doi: https://doi.org/10.1146/annurev-pharmtox-032823- 122811.

[87] N. C. Bang, A. Z. Abyshev, and D. Yu. Ivkin, “Synthesis and In Vivo Evaluation of New Coumarin Conjugates as Potential Indirect-Action Anticoagulants,” Pharm. Chem. J., vol. 53, no. 5, pp. 419–422, Aug. 2019, doi: 10.1007/s11094-019-02013-z.

[88] T. M. Ramsis, M. A. Ebrahim, and E. A. Fayed, “Synthetic coumarin derivatives with anticoagulation and antiplatelet aggregation inhibitory effects,” Med. Chem. Res., vol. 32, no. 11, pp. 2269–2278, Nov. 2023, doi: 10.1007/s00044-023-03148-1.

[89] L. Gao, F. Wang, Y. Chen, F. Li, B. Han, and D. Liu, “The antithrombotic activity of natural and synthetic coumarins,” Fitoterapia, vol. 154, p. 104947, Oct. 2021, doi: 10.1016/j.fitote.2021.104947.

[90] E. Quezada et al., “Synthesis and Vasorelaxant and Platelet Antiaggregatory Activities of a New Series of 6-Halo-3-phenylcoumarins,” Molecules, vol. 15, no. 1, Art. no. 1, Jan. 2010, doi: 10.3390/molecules15010270.

[91] P.-H. Lu et al., “Coumarin Derivatives Inhibit ADP-Induced Platelet Activation and Aggregation,” Molecules, vol. 27, no. 13, p. 4054, Jun. 2022, doi: https://doi.org/10.3390/molecules27134054.

[92] Ii. Mazreku, I. Rudhani, L. Lajqi, M. H. Ibrahimi, and A. Haziri, “Some Experimental Studies on the Anticoagulant Activity of the Synthetic Coumarin Derivatives,” Jordan J. Biol. Sci., vol. 15, no. 04, pp. 643–647, Dec. 2022, doi: 10.54319/jjbs/150413.

[93] M. Hrubša et al., “Screening of Synthetic Heterocyclic Compounds as Antiplatelet Drugs,” Med. Chem. Shariqah United Arab Emir., vol. 18, no. 5, pp. 536–543, 2022, doi: 10.2174/1573406417666211026150658.

[94] E. Berrino et al., “A Multitarget Approach against Neuroinflammation: Alkyl Substituted Coumarins as Inhibitors of Enzymes Involved in Neurodegeneration,” Antioxidants, vol. 12, no. 12, Art. no. 12, Dec. 2023, doi: 10.3390/antiox12122044.

[95] Q. Zhang et al., “Natural source, bioactivity and synthesis of 3-Arylcoumarin derivatives,” J. Enzyme Inhib. Med. Chem., vol. 37, no. 1, pp. 1023–1042, Dec. 2022, doi: 10.1080/14756366.2022.2058499.

[96] E. H. M. Hassanein, A. M. Sayed, O. E. Hussein, and A. M. Mahmoud, “Coumarins as Modulators of the Keap1/Nrf2/ARE Signaling Pathway,” Oxid. Med. Cell. Longev., vol. 2020, no. 1, p. 1675957, Apr. 2020, doi: https://doi.org/10.1155/2020/1675957.

[97] Q. Chu et al., “Studies on the Neuroprotection of Osthole on Glutamate-Induced Apoptotic Cells and an Alzheimer’s Disease Mouse Model via Modulation Oxidative Stress,” Appl. Biochem. Biotechnol., vol. 190, no. 2, pp. 634–644, Feb. 2020, doi: 10.1007/s12010-019-03101-2.

[98] N. K. Kordulewska et al., “Modulatory Effects of Osthole on Lipopolysaccharides-Induced Inflammation in Caco-2 Cell Monolayer and Co-Cultures with THP-1 and THP-1-Derived Macrophages,” Nutrients, vol. 13, no. 1, p. 123, Dec. 2020, doi: 10.3390/nu13010123.

[99] M. O. Hindam, R. H. Sayed, K. Skalicka-Woźniak, B. Budzyńska, and N. S. E. Sayed, “Xanthotoxin and umbelliferone attenuate cognitive dysfunction in a streptozotocin-induced rat model of sporadic Alzheimer’s disease: The role of JAK2/STAT3 and Nrf2/HO-1 signalling pathway modulation,” Phytother. Res., vol. 34, no. 9, 2020, doi: 10.1002/ptr.6686.

[100] D. Stasi and L. C, “Natural Coumarin Derivatives Activating Nrf2 Signaling Pathway as Lead Compounds for the Design and Synthesis of Intestinal Anti-Inflammatory Drugs,” Pharmaceuticals, vol. 16, no. 4, Art. no. 4, Apr. 2023, doi: 10.3390/ph16040511.

[101] M. Abomosallam, B. M. Hendam, A. A. Abdallah, R. Refaat, and H. N. G. EL-Hak, “Neuroprotective effect of Withania somnifera leaves extract nanoemulsion against penconazole-induced neurotoxicity in albino rats via modulating TGF-β1/Smad2 signaling pathway,” Inflammopharmacology, vol. 32, no. 3, pp. 1903–1928, Jun. 2024, doi: 10.1007/s10787-024-01461-8.

[102] F. Villavicencio Tejo and R. A. Quintanilla, “Contribution of the Nrf2 Pathway on Oxidative Damage and Mitochondrial Failure in Parkinson and Alzheimer’s Disease,” Antioxidants, vol. 10, no. 7, Art. no. 7, Jul. 2021, doi: 10.3390/antiox10071069.

[103] A. Benazzouz-Touami et al., “New Coumarin-Pyrazole hybrids: Synthesis, Docking studies and Biological evaluation as potential cholinesterase inhibitors,” J. Mol. Struct., vol. 1249, p. 131591, Feb. 2022, doi: 10.1016/j.molstruc.2021.131591.

[104] Y.-H. Hu et al., “Synthesis and biological evaluation of 3–(4-aminophenyl)-coumarin derivatives as potential anti-Alzheimer’s disease agents,” J. Enzyme Inhib. Med. Chem., vol. 34, no. 1, pp. 1083–1092, Jan. 2019, doi: 10.1080/14756366.2019.1615484.

[105] M. Huang, S.-S. Xie, N. Jiang, J.-S. Lan, L.-Y. Kong, and X.-B. Wang, “Multifunctional coumarin derivatives: Monoamine oxidase B (MAO-B) inhibition, anti-β-amyloid (Aβ) aggregation and metal chelation properties against Alzheimer’s disease,” Bioorg. Med. Chem. Lett., vol. 25, no. 3, pp. 508–513, Feb. 2015, doi: 10.1016/j.bmcl.2014.12.034.

[106] Y.-J. Chiu et al., “Novel Synthetic Coumarin-Chalcone Derivative (E)-3-(3-(4-(Dimethylamino)Phenyl)Acryloyl)-4-Hydroxy-2H-Chromen-2-One Activates CREB-Mediated

Neuroprotection in Aβ and Tau Cell Models of Alzheimer's Disease," Oxid. Med. Cell. Longev., vol. 2021, no. 1, p. 3058861, 2021, doi: 10.1155/2021/3058861.

[107] E. Babaei et al., "Novel Coumarin–Pyridine Hybrids as Potent Multi-Target Directed Ligands Aiming at Symptoms of Alzheimer's Disease," Front. Chem., vol. 10, Jun. 2022, doi: 10.3389/fchem.2022.895483.

[108] M. F. Urmeneta-Ortíz, A. R. Tejeda-Martínez, O. González-Reynoso, and M. E. Flores-Soto, "Potential Neuroprotective Effect of the Endocannabinoid System on Parkinson's Disease," Park. Dis., vol. 2024, no. 1, p. 5519396, 2024, doi: 10.1155/2024/5519396.

[109] E. Bester, A. Petzer, and J. P. Petzer, "Coumarin derivatives as inhibitors of d-amino acid oxidase and monoamine oxidase," Bioorganic Chem., vol. 123, p. 105791, Jun. 2022, doi: 10.1016/j.bioorg.2022.105791.

[110] A. K. El-Damasy et al., "Novel coumarin benzamides as potent and reversible monoamine oxidase-B inhibitors: Design, synthesis, and neuroprotective effects," Bioorganic Chem., vol. 142, p. 106939, Jan. 2024, doi: 10.1016/j.bioorg.2023.106939.

[111] K. V. Sashidhara et al., "Discovery of 3-Arylcoumarin-tetracyclic Tacrine Hybrids as Multifunctional Agents against Parkinson's Disease," ACS Med. Chem. Lett., vol. 5, no. 10, pp. 1099–1103, Oct. 2014, doi: 10.1021/ml500222g.

[112] S. N. K. Kumar et al., "Scopoletin Augments DJ1/Nrf2 Signalling and Prevents Protein Aggregation in Parkinson's disease," Feb. 05, 2018, bioRxiv. doi: 10.1101/260521.

[113] D. Tao et al., "Discovery of coumarin Mannich base derivatives as multifunctional agents against monoamine oxidase B and neuroinflammation for the treatment of Parkinson's disease," Eur. J. Med. Chem., vol. 173, pp. 203–212, Jul. 2019, doi: 10.1016/j.ejmech.2019.04.016.

[114] S. Ham et al., "Therapeutic Evaluation of Synthetic Peucedanocoumarin III in an Animal Model of Parkinson's Disease," Int. J. Mol. Sci., vol. 20, no. 21, Art. no. 21, Jan. 2019, doi: 10.3390/ijms20215481.

[115] Md. A. Hannan et al., "Protective Mechanisms of Nootropic Herb Shankhpushpi (Convolvulus pluricaulis) against Dementia: Network Pharmacology and Computational Approach," Evid. Based Complement. Alternat. Med., vol. 2022, no. 1, p. 1015310, 2022, doi: 10.1155/2022/1015310.

[116] P. Pradhan, O. Majhi, A. Biswas, V. K. Joshi, and D. Sinha, "Enhanced accumulation of reduced glutathione by Scopoletin improves survivability of dopaminergic neurons in Parkinson's model," Cell Death Dis., vol. 11, no. 9, pp. 1–11, Sep. 2020, doi: 10.1038/s41419-020-02942-8.

[117] A. S. Sayed, N. S. El Sayed, B. Budzyńska, K. Skalicka-Woźniak, M. K. Ahmed, and E. A. Kandil, "Xanthotoxin modulates oxidative stress, inflammation, and MAPK signaling in a rotenone-induced Parkinson's disease model," Life Sci., vol. 310, p. 121129, Dec. 2022, doi: 10.1016/j.lfs.2022.121129.

[118] A. Rawat and A. V. B. Reddy, "Recent advances on anticancer activity of coumarin derivatives," Eur. J. Med. Chem. Rep., vol. 5, p. 100038, Aug. 2022, doi: 10.1016/j.ejmcr.2022.100038.

[119] A. K. Yadav, R. Maharjan Shrestha, and P. N. Yadav, "Anticancer mechanism of coumarin-based derivatives," Eur. J. Med. Chem., vol. 267, p. 116179, Mar. 2024, doi: 10.1016/j.ejmech.2024.116179.

[120] F.-Q. Shen et al., "Synthesis of novel hybrids of pyrazole and coumarin as dual inhibitors of COX-2 and 5-LOX," Bioorg. Med. Chem. Lett., vol. 27, no. 16, pp. 3653–3660, Aug. 2017, doi: 10.1016/j.bmcl.2017.07.020.

[121] T. K. Mohamed, R. Z. Batran, S. A. Elseginy, M. M. Ali, and A. E. Mahmoud, "Synthesis, anticancer effect and molecular modeling of new thiazolylpyrazolyl coumarin derivatives targeting VEGFR-2 kinase and inducing cell cycle arrest and apoptosis," Bioorganic Chem., vol. 85, pp. 253–273, Apr. 2019, doi: 10.1016/j.bioorg.2018.12.040.

[122] S. D. Durgapal and S. S. Soman, "Evaluation of novel coumarin-proline sulfonamide hybrids as anticancer and antidiabetic agents," Synth. Commun., vol. 49, no. 21, pp. 2869–2883, Nov. 2019, doi: 10.1080/00397911.2019.1647439.

[123] Y. Wang, W. Zhang, J. Dong, and J. Gao, "Design, synthesis and bioactivity evaluation of coumarin-chalcone hybrids as potential anticancer agents," Bioorganic Chem., vol. 95, p. 103530, Jan. 2020, doi: 10.1016/j.bioorg.2019.103530.

[124] F. Hersi et al., "Design and synthesis of new energy restriction mimetic agents: Potent anti-tumor activities of hybrid motifs of aminothiazoles and coumarins," Sci. Rep., vol. 10, no. 1, p. 2893, Feb. 2020, doi: 10.1038/s41598-020-59685-x.

[125] E. Y. Ahmed, N. A. Abdel Latif, M. F. El-Mansy, W. S. Elserwy, and O. M. Abdelhafez, "VEGFR-2 inhibiting effect and molecular modeling of newly synthesized coumarin derivatives as anti-breast cancer agents," Bioorg. Med. Chem., vol. 28, no. 5, p. 115328, Mar. 2020, doi: 10.1016/j.bmc.2020.115328.

[126] G. Achar, R. V. C., U. K., and S. Budagumpi, "Coumarin-tethered (benz)imidazolium salts and their silver(I) N-heterocyclic carbene complexes: Synthesis, characterization, crystal structure and antibacterial studies," Appl. Organomet. Chem., vol. 31, no. 11, p. e3770, Mar. 2017, doi: 10.1002/aoc.3770.

[127] R. R. Chavan and K. M. Hosamani, "Microwave-assisted synthesis, computational studies and antibacterial/ anti-inflammatory activities of compounds based on coumarin-pyrazole hybrid," R. Soc. Open Sci., vol. 5, May 2018, doi: 10.1098/rsos.172435.

[128] J. Pozo-Martínez et al., "Synthesis and study of the trypanocidal activity of catechol-containing 3-arylcoumarins, inclusion in β-cyclodextrin complexes and combination with benznidazole," Arab. J. Chem., vol. 15, no. 3, p. 103641, Mar. 2022, doi: 10.1016/j.arabjc.2021.103641.

[129] Y. Hu, B. Wang, J. Yang, T. Liu, J. Sun, and X. Wang, "Synthesis and biological evaluation of 3-arylcoumarin derivatives as potential anti-diabetic agents," J. Enzyme Inhib. Med. Chem., vol. 34, no. 1, pp. 15–30, Dec. 2019, doi: 10.1080/14756366.2018.1518958.

[130] N. George, B. A. Sabahi, M. AbuKhader, K. A. Balushi, Md. J. Akhtar, and S. A. Khan, "Design, synthesis and in vitro biological activities of coumarin linked 1,3,4-oxadiazole hybrids as potential multi-target directed anti-Alzheimer agents," J. King Saud Univ. - Sci., vol. 34, no. 4, Jun. 2022, doi: 10.1016/j.jksus.2022.101977.

[131] A. R. Bhat, "Biological Activity of Pyrimidine Derivativies: A Review," Org. Med. Chem., vol. 2, no. 2, p. 555581, Apr. 2017, doi: DOI:10.19080/omcij.2017.02.555581.

[132] A. Srivastava, V. Mishra, P. Singh, and R. Kumar, "Coumarin-based polymer and its silver nanocomposite as advanced antibacterial agents: Synthetic path, kinetics of polymerization, and applications," J. Appl. Polym. Sci., vol. 126, no. 2, pp. 395–407, Apr. 2012, doi: 10.1002/app.36999.

[133] Z. Nofal, M. El-Zahar, and S. Abd El-Karim, "Novel Coumarin Derivatives with Expected Biological Activity," Molecules, vol. 5, no. 2, pp. 99–113, Feb. 2000, doi: 10.3390/50200099.

[134] A. A. Emmanuel-Giota, K. C. Fylaktakidou, K. E. Litinas, D. N. Nicolaides, and D. J. Hadjipavlou-Litina, "Synthesis and biological evaluation of several 3-(coumarin-4-

yl)tetrahydroisoxazole and 3-(coumarin-4-yl)dihydropyrazole derivatives," J. Heterocycl. Chem., vol. 38, no. 3, pp. 717–722, Mar. 2001, doi: 10.1002/jhet.5570380329.

[135] R. M. Shaker, "Synthesis and reactions of some new 4H-pyrano[3,2-c]benzopyran-5-one derivatives and their potential biological activities," Pharmazie, vol. 51, no. 3, pp. 148–151, Mar. 1996.

[136] T. Patonay, G. Litkei, R. Bognár, J. Erdei, and C. Miszti, "Synthesis, antibacterial and antifungal activity of 4-hydroxycoumarin derivatives, analogues of novobiocin," Pharmazie, vol. 39, no. 2, pp. 84–91, Feb. 1984.

[137] M. Erşatır and E. S. Giray, "Synthesis of Various Chalcone-Coumarin Hybrid Compounds," Çukurova Univ. Grad. Sch. Nat. Appl. Sci., vol. 35, no. 6, pp. 111–120, 2018.

[138] M. Asif, "Overview of Diverse Pharmacological Activities of Substituted Coumarins: Compounds with Therapeutic Potentials," Med. Chem., Jan. 2015, [Online]. Available: https://api.semanticscholar.org/CorpusID:94501826}

[139] X. Zhou, M. Li, X.-B. Wang, T. Wang, and L.-Y. Kong, "Synthesis of Benzofuran Derivatives via Rearrangement and Their Inhibitory Activity on Acetylcholinesterase," Molecules, vol. 15, no. 12, pp. 8593–601, Nov. 2010, doi: 10.3390/molecules15128593.

[140] A. M. Saleh, M. M. Y. Madany, and L. González, "The Effect of Coumarin Application on Early Growth and Some Physiological Parameters in Faba Bean (Vicia faba L.)," J. Plant Growth Regul., vol. 34, no. 2, pp. 233–241, Nov. 2014, doi: 10.1007/s00344-014-9459-4.

[141] N. V. Soucy, "Acetophenone," in Encyclopedia of Toxicology, Academic Press: Elsevier, 2014, pp. 43–45. doi: 10.1016/B978-0-12-386454-3.01157-X.

[142] K. Robe, E. Izquierdo, F. Vignols, H. Rouached, and C. Dubos, "The Coumarins: Secondary Metabolites Playing a Primary Role in Plant Nutrition and Health," Trends Plant Sci., vol. 26, no. 3, pp. 248–259, Mar. 2021, doi: 10.1016/j.tplants.2020.10.008.

[143] S. Malla, M. A. G. Koffas, R. J. Kazlauskas, and B.-G. Kim, "Production of 7-O-Methyl Aromadendrin, a Medicinally Valuable Flavonoid, in Escherichia coli," Appl. Environ. Microbiol., vol. 78, no. 3, pp. 684–694, Feb. 2012, doi: 10.1128/AEM.06274-11.

[144] K. Kai, B. Shimizu, M. Mizutani, K. Watanabe, and K. Sakata, "Accumulation of coumarins in Arabidopsis thaliana," Phytochemistry, vol. 67, no. 4, pp. 379–386, Feb. 2006, doi: 10.1016/j.phytochem.2005.11.006.

[145] K. N. Venugopala, V. Rashmi, and B. Odhav, "Review on Natural Coumarin Lead Compounds for Their Pharmacological Activity," BioMed Res. Int., vol. 2013, no. 963248, pp. 1–14, Mar. 2013, doi: 10.1155/2013/963248.

[146] A. Stefanachi, F. Leonetti, L. Pisani, M. Catto, and A. Carotti, "Coumarin: A Natural, Privileged and Versatile Scaffold for Bioactive Compounds," Molecules, vol. 23, no. 2, p. 250, Jan. 2018, doi: 10.3390/molecules23020250.

Düzce University
Journal of Science & Technology

Research Article

Numerical Investigation of Firing Characteristic of Stochastic Hodgkin-Huxley Neuron under Different Forcing Regimes

Ali ÇALIM [a*]

[a] Department of Computer Engineering, Bolu Abant Izzet Baysal University, 14030 Bolu, TURKIYE
*Corresponding author's e-mail address: ali.calim@hotmail.com
DOI: 10.29130/dubited.1525920

ABSTRACT

This paper investigates the influence of the ion channel noise on the response of a Hodgkin-Huxley neuron in different stimulus regimes. Our results reveal that type of stimuli can induce emergence of various phenomena with the help of such an internal noise. In the case of DC current introduction, number of firings monotonically increase with high noise intensity, and firing behaviour is also irregular. Intermediate noise levels give rise to reduction of neural firings in spiking neuron, which is known as inverse stochastic resonance phenomenon. Moreover, firing behaviour of such neuron interestingly becomes highly irregular even up to higher noise intensities. On the other hand, we examine the influence of channel noise on the neural response to a periodic signal. We show that frequency of subthreshold signal has a significant effect on the response sensitivity whereas firing probability and regularity are in a close relationship depending on increasing noise intensity. Finally, firing behaviour in the case of suprathreshold periodic forcing is analysed. Up to a certain level of channel noise, it does not seriously affect number of firings which has a nonlinear relationship with increasing signal frequencies. It is also possible to see inverse stochastic resonance effect at the high frequency regions. Another interesting finding is that increasing channel noise cannot enhance the regularity at certain frequencies, yielding the presence of irregular response region at suprathreshold periodic inputs. This work contributes to a better understanding of the role of internal noise in the relation between incoming stimuli and neural response.

Keywords: *Channel noise, spiking regularity, firing rate, DC stimulus, periodic input*

Farklı Uyartım Rejimlerinde Stokastik Hodgkin-Huxley Nöronunun Ateşleme Karakteristiğinin Sayısal İncelemesi

ÖZ

Bu makale, iyon kanal gürültüsünün farklı uyartım rejimlerinde Hodgkin-Huxley nöronunun tepkisi üzerindeki etkisini araştırmaktadır. Sonuçlarımız, uyartım tipinin içsel gürültü yardımıyla çeşitli olguların ortaya çıkmasına neden olabileceğini göstermektedir. DC akım uygulanması durumunda ateşleme sayısı yüksek gürültü yoğunluğuyla monoton bir şekilde artmakta ve ateşleme davranışı da düzensiz olmaktadır. Orta düzeydeki gürültü seviyeleri, ateşleyen nöronlardaki ateşleme sayılarının azalmasına, yani ters stokastik rezonans olayına yol açmaktadır. Üstelik bu nöronun ateşleme davranışı ilginç bir şekilde yüksek gürültü yoğunluklarında bile oldukça düzensiz olmaktadır. Öte yandan, kanal gürültüsünün periyodik bir sinyale verilen nöral cevap üzerindeki etkisini inceledik. Eşikaltı sinyal frekansının cevap hassasiyeti üzerinde önemli bir etkiye sahip iken, artan gürültü yoğunluğuna bağlı olarak ateşleme olasılığı ve düzenliliğin yakın bir ilişkide olduğunu

Received: 31/07/2024, Revised: 12/09/2024, Accepted: 20/09/2024

gösteriyoruz. Son olarak, eşik üstü periyodik uyartım durumunda ateşleme davranışı analiz edilmiştir. Belirli bir kanal gürültüsü seviyesine kadar, gürültü artan sinyal frekanslarıyla doğrusal olmayan bir ilişkiye sahip olan ateşleme sayısını ciddi şekilde etkilememektedir. Yüksek frekans bölgelerinde de ters stokastik rezonans etkisini görmek mümkündür. Bir diğer ilginç bulgu ise artan kanal gürültüsünün belirli frekanslarda düzenliliği arttıramamasıdır, ki bu eşik üstü periyodik sinyal uygulandığında düzensiz tepki bölgesinin varlığını ortaya çıkarmaktadır. Bu çalışma, gelen uyaranlar ile nöral cevap arasındaki ilişkide içsel gürültünün rolünün daha iyi anlaşılmasına katkıda bulunmaktadır.

Anahtar Kelimeler: *Kanal gürültüsü, ateşleme düzenliliği, ateşleme oranı, DC uyartım, periyodik girdi*

I. INTRODUCTION

The nervous system is the most complicated system in humans, and how it maintains flawless functionality with high efficiency remain a mystery. This system undertakes essential functions like regulating internal processes, carrying out communication, and processing information. It is widely accepted that these tasks are accomplished through certain electrical signals known as action potentials, generated by neurons that are the fundamental units of the system. This also indicates that neurons are the vital biological components that receive and respond to environmental stimuli [1-2]. The collective behaviours of neurons, especially their firing patterns in various brain regions, are linked to critical functions such as central pattern generation and working memory. Numerous studies have demonstrated that neural activities exhibit regular, irregular, and chaotic spiking regimes while performing vital functions [3-7].

In the cortex, neurons can respond to a variety of stimulus types, such as sensory stimuli (e.g. visual, auditory) [8], integrative stimuli from decision-making processes [9] and direct electrical currents [10]. Each type of stimulus produces different responses in cortical neurons. The nature of stimulus types that a neuron can respond to generally depends on its position, function, and connectivity within the brain [11-13]. However, regardless of its type, stimulus has a significant effect on the excitability of neurons. Any type of stimuli can profoundly impact the excitability of neurons by modulating membrane potential through depolarization or hyperpolarization, excitatory or inhibitory synaptic inputs, and through long-term plasticity mechanisms, thereby affecting how neurons process and respond to information signals [14-16].

As a part of neural information processing task, there are two fundamental encoding mechanisms in the nervous system: temporal and rate coding. These are two important information processing strategies by which the nervous system encodes and transmits information. Rate coding refers to the agreement that the frequency of action potentials or firing rate within a neuron encodes information about a stimulus [17-18]. In this strategy, a higher firing rate generally means a stronger stimulus, while a lower rate indicates a weaker one. This type of coding is relatively straightforward and has been extensively studied, particularly in sensory systems like vision and audition, where the intensity of a stimulus can be said to be directly correlated with the firing rate of specific neurons [19-21]. Temporal coding, however, is believed to be performed with the precise timing of action potentials. In this strategy, the timing of each spike, relative to other spikes, carries definite information [22]. Temporal coding can capture more complex information than rate coding, such as the fine temporal structure of an auditory input or the synchronization of spikes across different neurons in the same cortical or brain area [23-25]. This mechanism is particularly important in neural circuits where timing is crucial, such as in the auditory system for sound localization or in the hippocampus for encoding sequences of vital body functions. Both coding strategies often work together to enhance the brain's ability to process and interpret complex stimuli [26-29].

Extensive experimental and theoretical works manifest that neurons are continuously subjected to noise throughout all stages of information processing. In recent decades, significant progress has been made in understanding the effects of noise on neuron dynamics. A great number of neuroscience research has revealed that noise can induce a variety of complex behavioural patterns, including

stochastic resonance [30-32], coherence resonance [33-34], synchronization [35-36], bursting [37] and chaos [38]. These findings suggest that noise plays a crucial role in regular functioning of the brain, such as cognitive and perceptual mechanisms [39-40].

One of the main sources of noise in the nervous system is the ion channel noise. Channel noise refers to the variability and randomness that are inherent in the opening and closing processes of ion channels within neural membranes. This type of noise arises due to the stochastic nature of ion channel behaviour, where a single channel switches between open and closed states in an unpredictable manner [41]. Despite being a source of variability, channel noise can significantly influence neural functions, e.g. signal processing and information transmission [42-46]. It can impact the reliability and precision of action potential generation, affect synaptic transmission, and even contribute to the overall excitability of neurons. Interestingly, while channel noise might seem destructive, it can also play constructive roles, such as enhancing signal detection through mechanisms like stochastic resonance, where the presence of a proper noise level actually improves the ability of neurons to respond to weak inputs [47-48]. A deep understanding of channel noise is crucial for a comprehension of neural dynamics and the robustness of neural computations in the brain.

In the present work, we investigate neural behaviour related to rate and temporal coding using spatiotemporal dynamics, i.e. spike number and firing regularity. With a holistic approach which considers different stimuli projections, we obtain a general view on firing behaviour of a single neuron. To do this, we use class II Hodgkin-Huxley neuron of which variability stems from the presence of internal noise, i.e. ion channel noise. We perform comprehensive simulations applying different stimulus types to the neuron (e.g. direct current stimulus, subthreshold and suprathreshold sinusoidal forcing). The rest of the paper is organized as follows: In the next section, we introduce the model, that is, a stochastic Hodgkin- Huxley neuron, and the methods used for the clarification of neural response to applied stimuli projections in terms of firing rate and regularity. In section III, we present the bifurcation diagram of deterministic Hodgkin-Huxley neuron model and give a brief analysis on its firing behaviour and excitability. Then, we demonstrate our main results regarding direct electric current, subthreshold weak signal input and suprathreshold periodic forcing cases. Finally, we summarize the main conclusions in section IV.

II. MODEL AND METHOD

In our study, stochastic Hodgkin-Huxley (H-H) neuron with ion channel noise dynamics is considered. The time variation of the membrane potential of stochastic H-H neuron is described by the following equations [49]:

$$C\frac{dV}{dt} = I_{ex} - g_{Na}m^3h(V - E_{Na}) - g_K n^4(V - E_K) - g_L(V - E_L) \quad (1)$$

Here, V is the membrane potential in millivolts. $C = 1\ uF/cm^2$ represents the membrane capacitance of considered neuron. Maximum channel conductances are given as $g_{Na} = 120\ mS/cm^2$ for sodium, $g_K = 36\ mS/cm^2$ for potassium, and $g_L = 0.3\ mS/cm^2$ for leakage currents. Correspondingly, the equilibrium potentials for these ion currents are determined as $E_{Na} = 115\ mV$, $E_K = -12\ mV$, and $E_L = 10.6\ mV$, respectively. Activation and inactivation of sodium gates are controlled by probability functions m and h, whereas activation of potassium gates is controlled by probability function n. The random motion of each ion gates creates stochastic effects on neuron dynamics. The change in gate probability functions over time with the presence of stochastic dynamics is modeled according to the Fox algorithm [50]:

$$\frac{dx}{dt} = \alpha_x(V)(1 - x) - \beta_x(V)x + \xi_x(t), x = m; n; h \quad (2)$$

The α_x and β_x given in Equation (2) are rate functions showing the opening and closing of ion gates that vary depending on the membrane potential, and are calculated for each gate variable as follows:

$$\alpha_m = 0.1\ \frac{(25 - V)}{exp[(25 - V)/10] - 1} \tag{3}$$

$$\beta_m = 4\ exp[-V/10] \tag{4}$$

$$\alpha_n = 0.01\ \frac{(10 - V)}{exp[(10 - V)/10] - 1} \tag{5}$$

$$\beta_n = 0.125\ exp[-V/80] \tag{6}$$

$$\alpha_h = 0.07\ exp[-V/20] \tag{7}$$

$$\beta_h = \frac{1}{exp[(30 - V)/10] + 1} \tag{8}$$

The randomness in the sodium and potassium gates is described by white Gaussian noise whose autocorrelation function is as follows:

$$\langle \xi_m(t)\xi_m(t')\rangle = \frac{2\alpha_m\beta_m}{N_{Na}(\alpha_m + \beta_m)}\delta(t - t') \tag{9}$$

$$\langle \xi_h(t)\xi_h(t')\rangle = \frac{2\alpha_h\beta_h}{N_{Na}(\alpha_h + \beta_h)}\delta(t - t') \tag{10}$$

$$\langle \xi_n(t)\xi_n(t')\rangle = \frac{2\alpha_n\beta_n}{N_K(\alpha_n + \beta_n)}\delta(t - t') \tag{11}$$

Here, the parameters N_{Na} and N_K represent the total sodium and potassium channel numbers on the membrane surface, respectively. The total channel numbers are calculated for a membrane area of A with the equations $N_{Na} = \rho_{Na}A$ and $N_K = \rho_K A$. In these equations, the values given as $\rho_{Na} = 60\ \mu m^{-2}$ and $\rho_K = 18\ \mu m^{-2}$ indicate related channel densities. Thus, A becomes a parameter that determines the level of noise originated from ion channels. Literally, the membrane area and the effective ion channel noise amplitude are inversely proportional. Accordingly, since many ion channels are involved in the system dynamics for a large membrane area, it can be said that the stochastic contribution of individual ion channels becomes negligible. Lastly, $I_{ex} = I_b + S\sin(2\pi f t)$ is the total input applied to the neuron externally. I_b is the bias current that also determines the excitability of the neuron. $S\sin(2\pi f t)$ is the sinusoidal input current, which is used for different forcing regimes, i.e. subthreshold or suprathreshold stimulus state.

One of the characteristic features of cortical neurons is that the spike trains they emit are irregular at a certain level and different neuron types at distinct brain layers exhibit regularity at different degrees. We examine the firing regularity via the coefficient of variation (CV). This method is defined as the ratio of the standard deviation of the interspike intervals (ISI) in the entire spike train to the mean ISI and is calculated at trial i as follows [51]:

$$CV_i = \frac{\sigma_{ISI}}{\langle ISI\rangle} \tag{12}$$

$$\sigma_{ISI} = \sqrt{\langle ISI^2\rangle - \langle ISI\rangle^2} \tag{13}$$

$$\langle ISI\rangle = \sum_{s=1}^{p-1} \frac{t_{s+1} - t_s}{p} \tag{14}$$

$$\langle ISI^2 \rangle = \sum_{s=1}^{p-1} \frac{(t_{s+1} - t_s)^2}{p} \tag{15}$$

where p indicates total number of spikes in a single simulation and t_s denotes occurrence time of s^{th} spike. As CV value approaches zero, it represents regularity, and as it takes values close to one and even larger values, it serves as irregularity. In completely irregular firing sequences, CV can be greater than one [52].

To further characterize spiking behaviour quantitatively, we calculate the mean firing rate that is averaged over trials for a given parameter set. We first randomly select initial conditions for the neuron with uniform probability within the range from -10 to $80\,mV$ for the membrane voltage variable V, and within the range from 0 to 1 for the gating variables m, n, and h. After a transient time for $1\,s$, we count the number of spikes FR_i generated by the neuron and calculate the regularity measure CV_i at trial i within the following examination time $\tau = 30\,s$. To obtain statistical accuracy, these procedures are repeated $L = 50$ times for any parameter set, and the mean firing rate and the mean CV are calculated as follows:

$$FR = \frac{1}{\tau L} \sum_{i=1}^{L} FR_i \tag{16}$$

$$CV = \frac{1}{L} \sum_{i=1}^{L} CV_i \tag{17}$$

Numerical simulation of the system is integrated using the forward Euler algorithm with a time step $10\,\mu s$.

III. RESULTS AND DISCUSSION

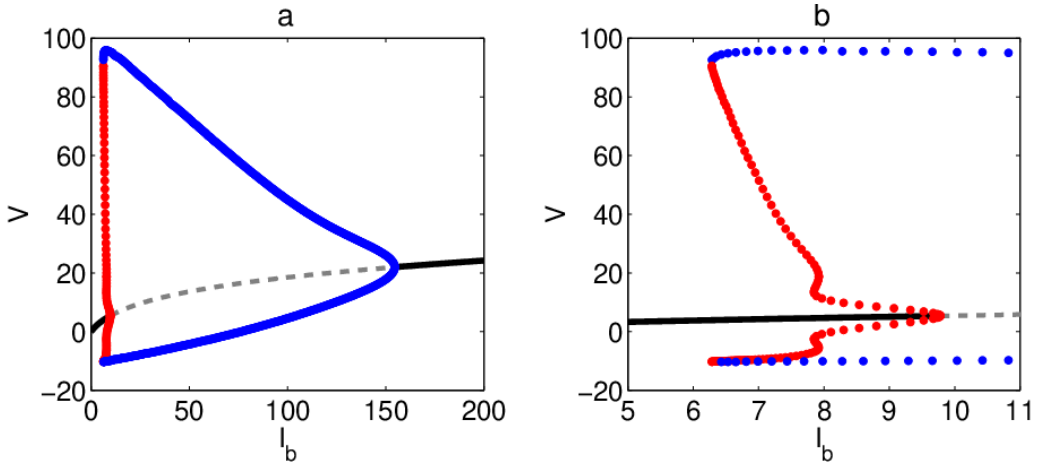

Figure 1. *Bifurcation diagram of deterministic Hodgkin-Huxley neuron. Black solid (dashed) line represents stable (unstable) fixed point that the neuron exhibits resting behaviour. Blue (red) solid circles show stable (unstable) limit cycle which the neuron is at spiking mode. The limit cycles are born at I_b=6.26 with saddle-node bifurcation. As I_b increases, unstable limit cycle shrinks and collapses to an unstable fixed point at I_b=9.78 with subcritical Andronov–Hopf bifurcation. The interval between these two points defines the range of bistability where there is an unstable limit cycle that separates coexisting stable limit cycles and fixed points.*

In this study, we investigate firing behaviour of stochastic H-H neuron through the analysis of firing frequency and regularity under effect of channel noise modulations and different stimuli projections. To obtain a theoretical understanding for underlying process of emitting spikes, we first look at the

system behaviour of a deterministic H-H neuron. For this aim, we present two parameter bifurcation of H-H neuron model in figure 1 where panel a and panel b show long and zoomed-in version of the diagram. As a response to applied DC bias current, H-H neuron exhibits subcritical Andronov-Hopf bifurcation, which is a clear indication of class II excitability and a non-zero firing frequency. H-H neuron shows bistability between $I_b = 6.26$ and $I_b = 9.78$, implying that there are both stable limit cycle and stable fixed point at the same time in this interval, and it has an unstable limit cycle separating the two stable focuses. Fluctuations in neuron dynamics, such as noisy input currents, can force the neuron to oscillate or become silent by pushing towards the two attractors. Neurons is excitable, where there exists only stable fixed point, before the bistability interval. On the contrary, H-H is a pacemaker neuron that continuously fires at a constant frequency after above-mentioned interval where there are stable limit cycle and unstable fixed point.

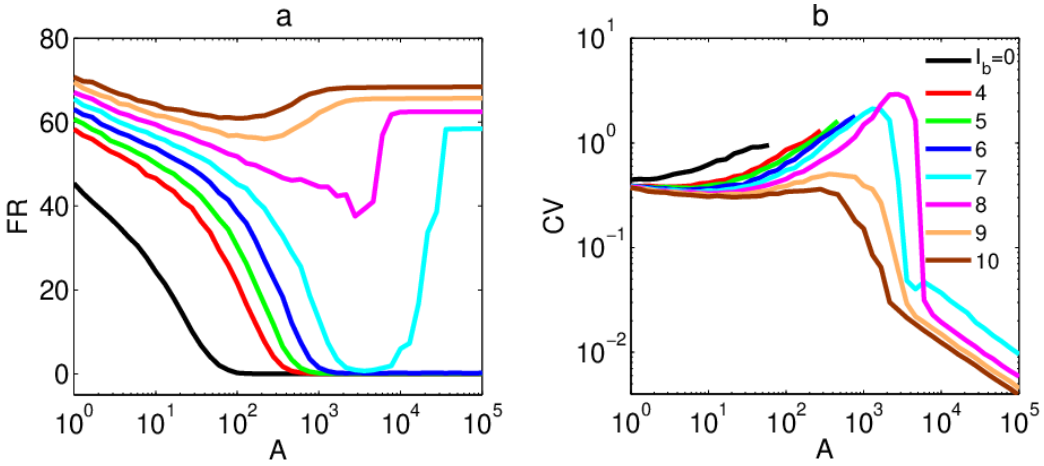

Figure 2. *Firing behaviour of class II H-H neuron depending on ion channel noise variations at different bias current levels. Panels show both (a) firing rate and (b) CV measure for corresponding bias current cases with same-coloured lines. It is seen that excitable neuron exhibits only spontaneous irregular spiking activity. However, when the neuron is bistable, it shows regular spiking behaviour in lower noise regions, and while noise intensity increases, inverse stochastic resonance effect emerges with a high irregularity.*

The level of DC input applied to the neuron can be considered as a bias current which determines the subthreshold and suprathreshold regimes. When $I_b > 6.26$, the neuron may exhibit firing behaviour depending on the initial conditions and environmental factors. We now examine the effects of internal noise on firing behaviour and regularity of neural firing patterns in subthreshold and suprathreshold regimes. The noise governed by the Fox algorithm is modulated with the membrane surface area in order to control the internal noise level occurring in the ion channels. Accordingly, when the membrane area is small, random ion movements cause too much noise in the total membrane potential. Otherwise, the randomness in ion movements spreads over a much larger membrane area and fluctuations in membrane potential becomes minimal. Connected with these assumptions, the average firing numbers as a function of membrane area and the regularity in the firing patterns were calculated in the presence of increasing bias current. The obtained results are given in the figure 2.

Figure 2a shows that the excitable neuron ($I_b < 6.26$) can fire spontaneously if channel noise with a high intensity is present. On the other hand, according to CV measure in figure 2b, an irregular firing pattern emerges in the size of the area where the neural firings first begin to occur, and as the size of surface area decreases, relatively more regular firings occur due to the increasing noise intensity. When the bias current applied to the neuron is taken as $I_b = 7$, the neuron exhibits channel noise-induced inverse stochastic resonance phenomenon, and this continues to occur at the suprathreshold excitation regions. When the stimulation is enough for the neuron to emit spikes (i.e. $I_b > 6.26$), low channel noise has a limited effect on firing regularity and H-H neuron exhibits a regular firing activity with a constant firing rate. However, due to the stronger channel noise arising from membrane size in intervals where the ISR effect occurs, although the neuron is exposed to a stimulation current sufficient to fire, such a level of noise can prevent the neuron from firing or even push it to the silent

state. The main reason behind this fashion of spiking is that the neuron exhibits bistable behaviour in the range of $6.26 < I_b < 9.78$, and the unstable attractor separating these two stable states narrows as I_b increases. Thus, it makes easier to explain the behavior of regular firings with constant rates over a wider range due to increasing channel noise for the cases in this bias current interval.

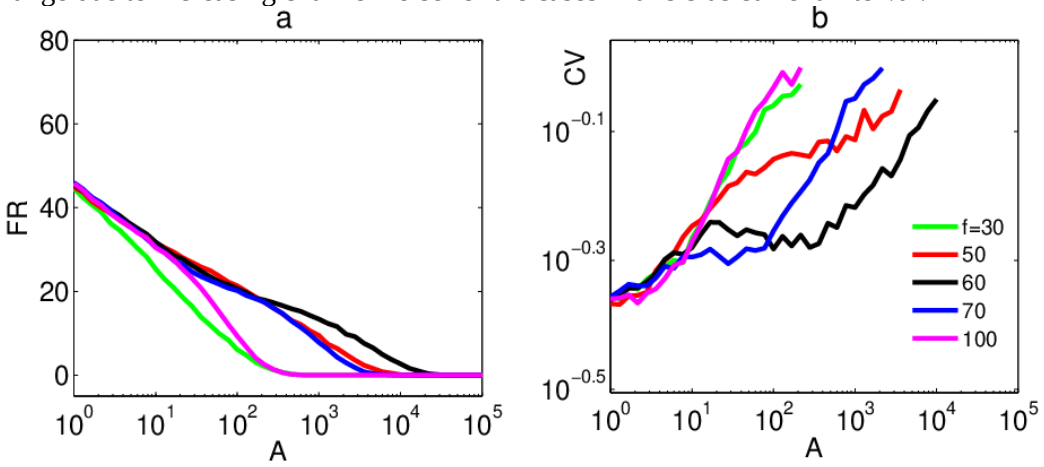

Figure 3. *Firing behaviour of H-H neuron as a response to subthreshold periodic input signal. Panel a and panel b show firing rate (spike probability) and variation of CV as a function of ion channel noise for different signal frequencies. Legends in panel b are also valid for panel a. To obtain subthreshold regime, signal amplitude is fixed as S=1.4.*

Neurons constantly receive various stimuli in distinct nature from inner neural medium and environmental sources. Regarding this fact, we now investigate firing behaviour of stochastic H-H neuron exposed to sinusoidal inputs. We first explore how increasing channel noise shapes the neural response to the sinusoidal forcing signal that is subthreshold for deterministic H-H neuron. To do this, we measured number of firings and calculated regularity due to CV as a function of membrane area for different weak signal frequencies. Obtained results are depicted in figure 3. Basically, if internal channel noise arises from very narrow and large membrane patch areas, it has a similar effect on firing probability of neuron. This can be clearly seen from figure 3a. In these cases, regardless of varying weak signal frequencies, all sinusoidal inputs are subthreshold for deterministic H-H neuron to emit a spike and large area roughly makes membrane potential insensitive to ion fluctuations. On the other hand, very small membrane area produces highly intense ion channel noise, and this forces the neuron to fire spontaneously with a certain average frequency level. Apart from these extreme points, intermediate channel noise levels obtained through relative membrane areas induce different firing behaviours for varying weak signal frequencies. According to [53], threshold for spike generation shows the presence of a nonlinear relation between amplitude and frequency of sinusoidal forcing. Under the light of this evidence, the neuron receiving signal with a fixed amplitude $S = 1.4$ at a given frequency $f = 30$ and even $f = 100$ needs more excitation to switch to firing mode than the cases of frequencies in between, such as $f = 60$. Our results confirm that with inherent stochastic dynamics strong enough, sensitivity to subthreshold signal frequency for entering firing regime follows the same distance with the previous findings in presence of relative channel noise intensity.

Furthermore, we explore how the regularity of neural firings is affected by internal noise if subthreshold signal oscillates at given different frequencies. In figure 3b, by comparing with figure 3a, it can be obviously inferred that behaviours of firing rate and regularity is in a close relationship. Notice that CV values are calculated only if there is a spiking activity. Since a sinusoidal input with $f = 60$ Hz makes the neuron more excitable to respond with an action potential, and lower or higher frequencies such as $f = 30$ Hz or $f = 100$ Hz make it harder, corresponding channel noise levels initially give rise to emergent irregular firing activity. The figure shows that if input signal is set with $f = 60$ Hz, i.e. frequency value which make it easier for neuron to respond, increasing channel noise intensity helps to more easily get through more regular spiking behaviour. The figure also

demonstrates that channel noise with high intensity coalesces the values of spiking regularity induced by different signal frequencies at a fairly decent CV level.

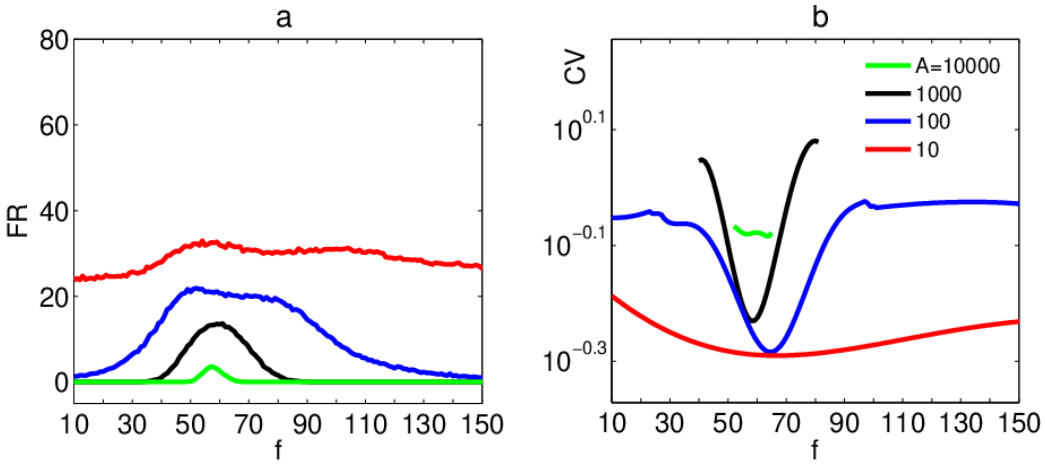

Figure 4. *Variation of (a) firing rate and (b) CV values as a function of weak signal frequencies for different ion channel noise intensities. Signal amplitude is subthreshold with S=1.4. Notice that legends in panel b are also valid for panel a.*

Our results show that a certain level of ion channel noise can trigger spiking events as a neural response to the subthreshold signal, and the frequency of the weak sinusoidal signal can modulate this level and precision of firing behaviour. To further illustrate the effect of frequency, we now present illustrations of firing rate and CV as functions of signal frequency at different noise levels. The results are shown in figure 4. Here we consider that no bias DC current is applied to the neuron and sinusoidal forcing is subthreshold. Under these conditions, figure 4a and 4b show that our class II neuron exhibits spiking behaviour with a relatively high firing rate at all frequencies in the presence of high channel noise ($A = 10$), and in this case, the emergent firing patterns are fairly regular. On the other hand, it is seen that when there is a medium level of channel noise (see $A = 100$), the neuron can still fire at all frequencies, but especially in the range of approximately $f = 30$ Hz to $f = 100$ Hz, the firing rate forms a bell-shaped curve with the help of this noise intensity. Furthermore, it is seen that when much lower noise levels are adjusted, it is possible for the neuron to fire in a much narrower frequency range and this effect becomes evident around $f = 60$ Hz, and as the noise weakens, the number of firings also decreases. Firing regularity appears as an inverse resonance curve around $f = 60$ Hz in the range of $40 < f < 80$ Hz for $A = 1000$. This can also indicate that the firing regularity increases considerably especially in this frequency range and the weak signal encoding becomes easier. Similar dynamical behavior was reported in [54-57], where signal detection performance for a subthreshold external stimulus with a varying frequency exhibited resonance behaviours with the help of different stochastic or chaotic signal fluctuations at an appropriate intensity, and it was shown that the optimum range of weak signal frequencies for high efficiency lay between approximately $f = 40$ and $f = 80$ Hz. Lastly, limited and irregular firing behaviour is observed with only very sparse firings for $A = 10000$.

Brain operates in an inevitably noisy environment by generating action potentials which is the fundamental units of neural communication. One of main players in the nervous system are spiking neurons which are exposed to suprathreshold signals to emit a spike. These action potentials encode information not only in spike rate but also in their precise timing and pattern. Accordingly, through temporal and rate coding processes, neurons convey the strength and type of stimuli to target neurons or neural circuits. This ensures that sensory information is accurately represented and processed, and enables the nervous system to perceive and respond to stimuli with appropriate sensitivity and specificity [58-59]. Thus, suprathreshold signal encoding has a vital role in neural information processing and even perceptual decisions.

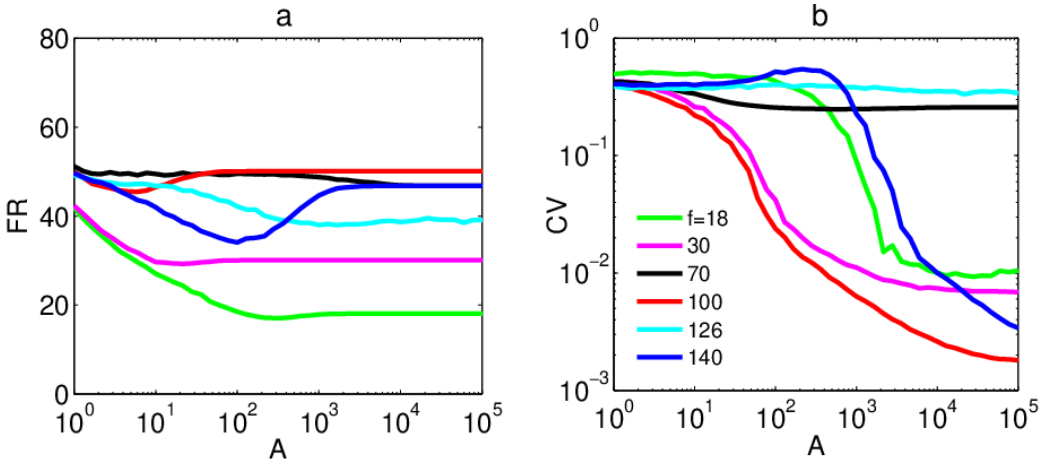

Figure 5. *Firing behaviour of H-H neuron as a response to suprathreshold periodic forcing. Figure demonstrates firing rate in panel a and variation of CV in panel b as a function of ion channel noise for different frequencies (see same-coloured lines for the same frequency values). To obtain suprathreshold input, we set signal amplitude as S=4.*

Let us hereafter examine firing behaviour of stochastic H-H neuron exposed to suprathreshold signal under the effect of channel noise. We analysed firing rate with spiking numbers of neuron and regularity of spiking patterns via CV measure as functions of membrane area for different frequencies of suprathreshold signal whose amplitude is fixed as $S = 4$. We selected our essential sample frequencies for suprathreshold regime from the interval that lays between 16.5 and 144 Hz for the given amplitude [60]. We demonstrate the results considering spike counts in figure 5a. When we look at firing rates for increasing frequency levels, all cases show us that each sinusoidal forcing is readily enough for the stochastic neuron to fire a spike. But firing rates do not increase completely parallel with varying signal frequency. In the firing rate scheme, it is possible to mention about two noise regions regarding spike counts in response to suprathreshold inputs: right and left side of $A \approx 1000$ to separate low and high channel noise intensities, respectively. When we analyse weak noise region, channel noise does not have any significant effect on the firing probability and the neuron exhibits nonlinear firing behaviour due to increasing signal frequency in here, such that firing mode emerges with a relatively low rate with 18 Hz and this continues to increase up to 100 Hz, then it non-monotonically drops with a further increase of signal frequency. On the other hand, we see more intriguing firing behaviours in strong noise region. For instance, for $f = 100$ and $f = 140$ Hz, there appears inverse stochastic resonance effect whereby average firing activity of a neuron exhibits a depression with respect to noise. For $f = 70$ Hz, it is seen that increasing channel noise still have no significant effect on firing probability of the neuron. Moreover, similar effect can be observed in the case of $f = 126$ Hz only with a slight increase in firing rate. Furthermore, low values of selected suprathreshold signal frequencies show more stable firing behaviour in response to increasing noise intensity.

To further investigate neural response behaviour in suprathreshold regime, stochastic H-H neuron is also analysed with regularity as a function of channel noise intensity. Figure 5b illustrates corresponding CV curves. It is apparent that while stochastic ion channel dynamics can change regularity at most cases, it remains very ineffective for suprathreshold signal with $f = 70$ Hz and $f = 126$ Hz. This can also imply that these frequency values cause principally irregular response of the neuron since also very low channel noise give rise to higher CV levels. On the other hand, extreme choices of suprathreshold signal frequency, i.e. lower and upper limit values $f = 18$ Hz and $f = 140$ Hz, exhibit similar CV function due to channel noise modification. This is also valid for other remaining moderate values ($f = 30$ Hz and $f = 100$ Hz). But regularity in the boundary circumstances changes faster than intermediate choices of suprathreshold signal frequency by increasing noise intensity. Furthermore, the last cases look like more advantageous in terms of regular spiking behaviour although high noise intensity cause irregular firing activity for all cases.

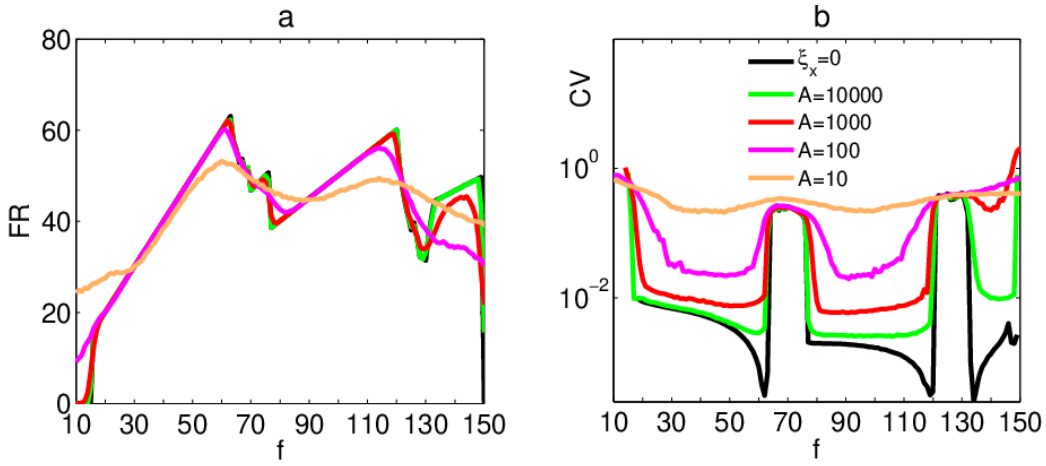

Figure 6. *Variation of firing rate and CV depending on suprathreshold signal frequencies for deterministic and stochastic H-H neuron with different membrane areas (see same-coloured lines for the same noise levels). Signal amplitude is set as S=4.*

To get a broader picture, we illustrate in figure 6 firing rate and regularity functions of deterministic and stochastic H-H neurons depending on suprathreshold driving frequency for different levels of channel noise intensities. When we analyse very intense noise conditions (see brown lines, case of $A = 10$) in both figure 6a and 6b, it gives rise to very variable spiking behaviour regardless of signal frequency as seen from variations of firing probability and regularity. Lower channel noise due to higher membrane area seems to be ineffective for firing rate of the neuron at most of the signal frequency range. On the other hand, one can infer that predominantly there is a linear relationship between input frequency and firing rate of deterministic and stochastic H-H neurons (except the previous case). But, by looking deterministic H-H neuron, it is reasonable to speculate that there is some inconstancy within the intervals of roughly $63 < f < 77$ Hz and $120 < f < 133$ Hz. It happens for the noiseless and low noise cases. Thus, this can imply the presence of some deterioration events in the condition of the neural system. When we examine the regularity via CV functions, it can be obviously seen that neuron exhibit considerably irregular firing behaviors in these situations. This irregular neural response also exists for stochastic H-H neuron due to random spikes arising from adequate noise fluctuations at the borders of suprathreshold frequency range.

To detail these behaviours, we next present ISI bifurcation of H-H neuron for deterministic and different levels of noise cases. To do this, we computed ISI values and normalized to the driving signal period as a function of weak signal frequency. Figure 7 shows obtained results for deterministic (a) and stochastic H-H neuron with $A = 10000$ (b), $A = 1000$ (c) and $A = 100$ (d). Figure 7a shows that our H-H neuron reproduce and essentially exhibits five different behaviours defined in [53] with respect to normalized ISI distribution depending on the suprathreshold signal frequency. By introducing channel noise dynamics into the system equations, in figure 7b, H-H neuron begins to show irregularity at the spiking regime borders, i.e. around $f = 16$ Hz and after $f = 130$ Hz. Due to sensitivity of the neuron to fluctuations, this change in spiking behaviour becomes more apparent with the introduction of higher level of stochasticity with $A = 1000$, as seen in figure 7c. In this case, irregularity in the neighbourhoods of limit frequency values and even in the irregular response regions is increased considerably. It is evident that channel noise has a prevailing effect on spiking behaviour of the neuron. This effect becomes even more obvious when the neuron has a narrower membrane area. When $A = 100$, as shown in figure 7d, ion channel noise make irregularity within the regions mentioned in figure 7c increased and, furthermore, destroys regular spiking trends in the regions between them. Nevertheless, it is possible to indicate that response of stochastic H-H neuron is more sensitive to ion channel noise at the limits of suprathreshold signal frequency values and apparently irregular response region.

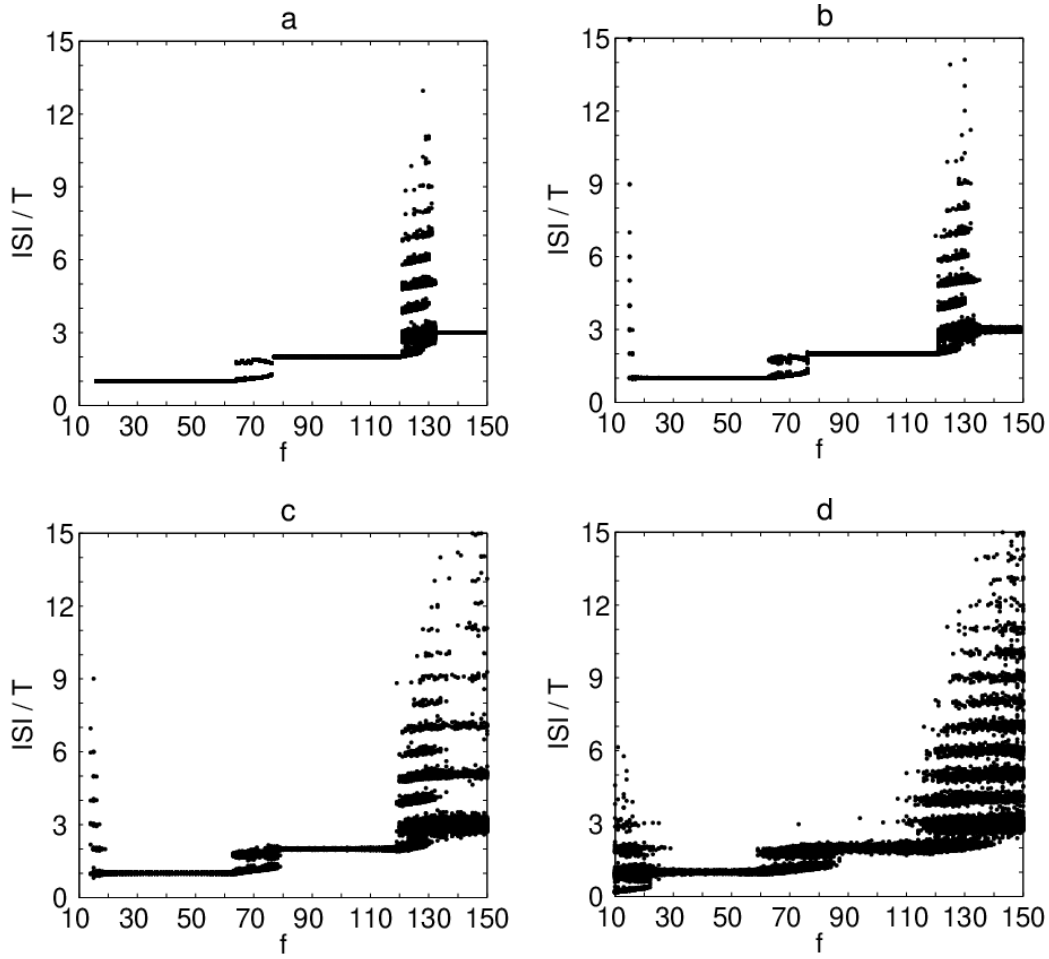

Figure 7. *Bifurcation of normalized ISI distribution over suprathreshold signal frequencies for deterministic (a) and stochastic H-H neuron with various membrane areas as the values of A=10000 (b), A=1000 (c), A=100 (d).*

IV. CONCLUSION

We investigated the influence of ion channel noise on the firing characteristics of class II H-H neuron for different stimuli projections. We observed that for bias current input, neural firings in excitable neuron are only spontaneous and irregular due to channel noise fluctuations. However, the neuron within bistability range exhibits inverse stochastic resonance that emerge with spike skipping or termination. Moreover, we examined neural firing behaviour as a response to subthreshold weak signal under the influence of channel noise. We observed that in this case, frequency has a meaningful impact on the neural response depending on channel noise, and there is a close relationship between spike rate and regularity. Finally, we analysed the firing behaviour of stochastic H-H neuron in the case of suprathreshold signal input. We show that ion channel noise does not have significant effect on spiking rate up to a certain level, and that channel noise does not influence the regularity at certain ranges of signal frequencies where emergent firing behaviour is always irregular, implying the existence of irregular neural response region to suprathreshold periodic signals. Emerging neural response due to applied inputs has gained a more realistic scenario via introduction of channel noise into neuron dynamics. Therefore, for future direction, it is possible that this study can be carried out at network level with different synapse types and biologically meaningful topologies.

V. REFERENCES

[1] E. Schneidman, I. Segev and N. Tishby, “Information capacity and robustness of stochastic neuron models,” in Advances in Neural Information Processing Systems 12, S. Solla, T. Leen and K. Müller, Eds., MIT Press, 1999, pp. 178–84.

[2] B. P. Bean, “The action potential in mammalian central neurons,” Nat. Rev. Neurosci., vol. 8, no. 6, pp. 451–65, 2007.

[3] Y. Zhang, Y. Xu, Z. Yao and J. Ma, “A feasible neuron for estimating the magnetic field effect,” Nonlinear Dyn., vol. 102, pp. 1849–67, 2020.

[4] K. M. Stiefel, B. Englitz and T. J. Sejnowski, “Origin of intrinsic irregular firing in cortical interneurons,” Proc. Natl. Acad. Sci., vol. 110, no. 19, pp. 7886–91, 2013.

[5] A. Bahramian, F. Parastesh, V.-T. Pham, T. Kapitaniak, S. Jafari and M. Perc, “Collective behavior in a two-layer neural network with time-varying chemical connections that are controlled by a Petri net,” Chaos, vol. 31, no. 3, pp. 033138, 2021.

[6] S. Majhi, B. K. Bera, D. Ghosh and M. Perc, “Chimera states in neural networks: a review,” Phys. Life Rev., vol. 28, pp. 100–21, 2019.

[7] A. Calim, J. J. Torres, M. Ozer and M. Uzuntarla, “Chimera states in hybrid coupled neuron populations,” Neural Netw., vol. 126, pp. 108–17, 2020.

[8] Y. Gallero-Salas et al., “Sensory and behavioral components of neocortical signal flow in discrimination tasks with short-term memory,” Neuron, vol. 109, no. 1, pp. 135-148, 2021.

[9] S. W. Kennerley and M. E. Walton, “Decision making and reward in frontal cortex: complementary evidence from neurophysiological and neuropsychological studies,” Behav. Neurosci., vol. 125, no. 3, pp. 297-317, 2011.

[10] A. Csemer et al., “Astrocyte- and NMDA receptor-dependent slow inward currents differently contribute to synaptic plasticity in an age-dependent manner in mouse and human neocortex,” Aging Cell, vol. 22, no. 9, pp. e13939, 2023.

[11] D. A. Ruff and M. R. Cohen, “Stimulus dependence of correlated variability across cortical areas,” J. Neurosci., vol. 36, no. 28, pp. 7546-7556, 2016.

[12] A. F. Meyer, R. S. Williamson, J. F. Linden and M. Sahani, “Models of neural stimulus-response functions: elaboration, estimation, and evaluation,” Front. Syst. Neurosci., vol. 10, pp. 109, 2017.

[13] D. Tang, J. Zylberberg, X. Jia and H. Choi, “Stimulus type shapes the topology of cellular functional networks in mouse visual cortex,” Nat. Commun., vol. 15, no. 1, pp. 5753, 2024.

[14] T. O’Leary, M. C. van Rossum and D. J. Wyllie, “Homeostasis of intrinsic excitability in hippocampal neurones: dynamics and mechanism of the response to chronic depolarization,” J. Physiol., vol. 588, no. 1, pp. 157-170, 2010.

[15] S. A. Alpizar, I. H. Cho and M. B. Hoppa, “Subcellular control of membrane excitability in the axon,” Curr. Opin. Neurobiol., vol. 57, pp. 117-125, 2019.

[16] J. A. Rosenkranz and D. Johnston, “Dopaminergic regulation of neural excitability through modulation of Ih in layer V entorhinal cortex,” J. Neurosci., vol. 26, no. 12, pp. 3229-3244, 2006.

[17] W. Gerstner, A. K. Kreiter, H. Markram and A. V. Herz, “Neural codes: firing rates and beyond,” Proc. Natl. Acad. Sci., vol. 94, no. 24, pp. 12740-12741, 1997.

[18] S. Panzeri, J. H. Macke, J. Gross and C. Kayser, “Neural population coding: combining insights from microscopic and mass signals,” Trends Cogn. Sci., vol. 19, no. 3, pp. 162-172, 2015.

[19] M. N. Shadlen and W. T. Newsome, “The variable discharge of cortical neurons: implications for connectivity, computation, and information coding,” J. Neurosci., vol. 18, no. 10, pp. 3870-3896, 1998.

[20] F. Li et al., “An artificial visual neuron with multiplexed rate and time-to-first-spike coding,” Nat. Commun., vol. 15, no. 1, pp. 3689, 2024.

[21] L. Gao, K. Kostlan, Y. Wang and X. Wang, “Distinct subthreshold mechanisms underlying rate-coding principles in primate auditory cortex,” Neuron, vol. 91, no. 4, pp. 905-919, 2016.

[22] C. P. Billimoria, R. A. DiCaprio, J. T. Birmingham, L. F. Abbott and E. Marder, “Neuromodulation of spike-timing precision in sensory neurons,” J. Neurosci., vol. 26, pp. 5910-5919, 2006.

[23] M. Bieler, K. Sieben, N. Cichon, S. Schildt, B. Röder and I. L. Hanganu-Opatz, “Rate and temporal coding convey multisensory information in primary sensory cortices,” eNeuro, vol. 4, no. 2, pp. e0037-17.2017, 2017.

[24] X. Wang, T. Lu, D. Bendor and E. Bartlett, “Neural coding of temporal information in auditory thalamus and cortex,” Neuroscience, vol. 154, no. 1, pp. 294-303, 2008.

[25] C. A. Navntoft and V. Adenis, “Does auditory cortex code temporal information from acoustic and cochlear implant stimulation in a similar way?,” J. Neurosci., vol. 38, no. 2, pp. 260-262, 2018.

[26] Y. Zuo, H. Safaai, G. Notaro, A. Mazzoni, S. Panzeri and M. E. Diamond, “Complementary contributions of spike timing and spike rate to perceptual decisions in rat S1 and S2 cortex,” Curr. Biol., vol. 25, no. 3, pp. 357-363, 2015.

[27] M. Ainsworth, S. Lee, M. O. Cunningham, R. D. Traub, N. J. Kopell and M. A. Whittington, “Rates and rhythms: a synergistic view of frequency and temporal coding in neural networks,” Neuron, vol. 75, no. 4, pp. 572-583, 2012.

[28] J. O'keefe and N. Burgess, “Dual phase and rate coding in hippocampal place cells: theoretical significance and relationship to entorhinal grid cells,” Hippocampus, vol. 15, no. 7, pp. 853-866, 2005.

[29] S. K. Sudhakar, B. Torben-Nielsen and E. De Schutter, “Cerebellar nuclear neurons use time and rate coding to transmit Purkinje neuron pauses,” PLoS Comput. Biol., vol. 11, no. 12, pp. e1004641, 2015.

[30] L. Gammaitoni, P. Hänggi, P. Jung and F. Marchesoni, “Stochastic resonance,” Rev. Mod. Phys., vol. 70, no. 1, pp. 223, 1998.

[31] F. Moss, L. M. Ward and W. G. Sannita, “Stochastic resonance and sensory information processing: a tutorial and review of application,” Clin. Neurophysiol., vol. 115, no. 2, pp. 267-281, 2004.

[32] J. F. Mejias and J. J. Torres, “Emergence of resonances in neural systems: the interplay between adaptive threshold and short-term synaptic plasticity,” PLOS ONE, vol. 6, no. 3, pp. e17255, 2011.

[33] A. Torcini, S. Luccioli and T. Kreuz, “Coherent response of the Hodgkin–Huxley neuron in the high-input regime,” Neurocomputing, vol. 70, no. 10-12, pp. 1943-1948, 2007.

[34] D. Guo and C. Li, “Stochastic and coherence resonance in feed-forward-loop neural network motifs,” Phys. Rev. E, vol. 79, no. 5, pp. 051921, 2009.

[35] Q. Wang, M. Perc, Z. Duan and G. Chen, “Synchronization transitions on scale-free neural networks due to finite information transmission delays,” Phys. Rev. E, vol. 80, no. 2, pp. 026206, 2009.

[36] Q. Wang, G. Chen and M. Perc, “Synchronous bursts on scale-free neural networks with attractive and repulsive coupling,” PLOS ONE, vol. 6, no. 1, pp. e15851, 2011.

[37] A. B. Neiman, T. A. Yakusheva and D. F. Russell, “Noise-induced transition to bursting in responses of paddlefish electroreceptor afferents,” J. Neurophysiol., vol. 98, no. 5, pp. 2795-2806, 2007.

[38] D. Hansel and H. Sompolinsky, “Synchronization and computation in a chaotic neural network,” Phys. Rev. Lett., vol. 68, no. 5, pp. 718, 1992.

[39] B. A. Dosher and Z. L. Lu, “Perceptual learning reflects external noise filtering and internal noise reduction through channel reweighting,” Proc. Natl. Acad. Sci., vol. 95, no. 23, pp. 13988-93, 1998.

[40] J. Grenzebach and E. Romanus, “Quantifying the effect of noise on cognitive processes: a review of psychophysiological correlates of workload,” Noise Health, vol. 24, no. 115, pp. 199-214, 2022.

[41] H. Yu, R. R. Dhingra, T. E. Dick and R. F. Galán, “Effects of ion channel noise on neural circuits: an application to the respiratory pattern generator to investigate breathing variability,” J. Neurophysiol., vol. 117, no. 1, pp. 230-242, 2017.

[42] A. Manwani and C. Koch, “Detecting and estimating signals in noisy cable structures, I: Neural noise sources,” Neural Comput., vol. 11, no. 8, pp. 1797-1829, 1999.

[42] D. Guo, M. Perc, T. Liu and D. Yao, “Functional importance of noise in neural information processing,” EPL, vol. 124, no. 5, pp. 50001, 2018.

[44] J. A. White, R. Klink, A. Alonso and A. R. Kay, “Noise from voltage-gated ion channels may influence neural dynamics in the entorhinal cortex,” J. Neurophysiol., vol. 80, no. 1, pp. 262-269, 1998.

[45] Z. Jiang, D. Wang, H. Shang and Y. Chen, “Effect of potassium channel noise on nerve discharge based on the Chay model,” Technology and Health Care, vol. 28, no. S1, pp. 371-381, 2020.

[46] B. Moezzi, N. Iannella and M. D. McDonnell, “Ion channel noise can explain firing correlation in auditory nerves,” J. Comput. Neurosci., vol. 41, pp. 193-206, 2016.

[47] H. Yu, R. F. Galán, J. Wang, Y. Cao and J. Liu, “Stochastic resonance, coherence resonance, and spike timing reliability of Hodgkin–Huxley neurons with ion-channel noise,” Phys. A: Stat. Mech. Appl., vol. 471, pp. 263-275, 2017.

[48] M. Ozer, M. Perc and M. Uzuntarla, “Stochastic resonance on Newman–Watts networks of Hodgkin–Huxley neurons with local periodic driving,” Phys. Lett. A, vol. 373, no. 10, pp. 964-968, 2009.

[49] A. L. Hodgkin and A. F. Huxley, “A quantitative description of membrane current and its application to conduction and excitation in nerve,” J. Physiol., vol. 117, no. 4, pp. 500-544, 1952.

[50] R. F. Fox, “Stochastic versions of the Hodgkin-Huxley equations,” Biophys. J., vol. 72, no. 5, pp. 2068-2074, 1997.

[51] M. Ozer, M. Perc and M. Uzuntarla, “Controlling the spontaneous spiking regularity via channel blocking on Newman-Watts networks of Hodgkin-Huxley neurons,” EPL, vol. 86, no. 4, pp. 40008, 2009.

[52] K. M. Stiefel, B. Englitz and T. J. Sejnowski, “Origin of intrinsic irregular firing in cortical interneurons,” Proc. Natl. Acad. Sci., vol. 110, no. 19, pp. 7886-7891, 2013.

[53] E. V. Pankratova, A. V. Polovinkin and E. Mosekilde, “Resonant activation in a stochastic Hodgkin-Huxley model: interplay between noise and suprathreshold driving effects,” EPJ B, vol. 45, pp. 391-397, 2005.

[54] V. Baysal, Z. Saraç and E. Yilmaz, “Chaotic resonance in Hodgkin–Huxley neuron,” Nonlinear Dyn., vol. 97, pp. 1275-1285, 2019.

[55] A. Calim and V. Baysal, “Chaotic resonance in an astrocyte-coupled excitable neuron,” Chaos Soliton Fract., vol. 176, pp. 114105, 2023.

[56] H. Yang, G. Xu and H. Wang, “Effects of magnetic fields on stochastic resonance in Hodgkin-Huxley neural network driven by Gaussian noise and non-Gaussian noise,” Cogn. Neurodyn., vol. 16, no. 3, pp. 707-717, 2022.

[57] K. Wu and J. Li, “Effects of high-low frequency electromagnetic radiation on vibrational resonance in Hodgkin–Huxley neural system,” J. Phys. A, vol. 57, no. 14, pp. 145702, 2024.

[58] V. Koren, G. Bondanelli and S. Panzeri, “Computational methods to study information processing in neural circuits,” Comput. Struct. Biotechnol. J., vol. 21, pp. 910-922, 2023.

[59] M. Perc and M. Marhl, “Amplification of information transfer in excitable systems that reside in a steady state near a bifurcation point to complex oscillatory behavior,” Phys. Rev. E, vol. 71, no. 2, pp. 026229, 2005.

[60] E. V. Pankratova, V. N. Belykh and E. Mosekilde, “Role of the driving frequency in a randomly perturbed Hodgkin-Huxley neuron with suprathreshold forcing,” EPJ B, vol. 53, pp. 529-536, 2006.

Düzce University Journal of Science & Technology

Research Article

An Investigation on the Evaluation and Improvement of Existing Features of Foot Exercise Apparatus Designed for Use in Evertor and Invertor Muscle Dysfunction

Ufuk ATESOGLU[a, b], Serap YESİLKİR BAYDAR [b, c, *], Osman Nuri OZYALVAC [d, e]

[a] *Department of Mechatronic Engineering, Faculty of Engineering and Architecture, Istanbul Gelisim University, Istanbul, TURKIYE*
[b] *Life Sciences and Biomedical Engineering Research and Application Center, Istanbul Gelisim University, Istanbul, TURKIYE*
[c] *Department of Biomedical Engineering, Faculty of Engineering and Architecture, Istanbul Gelisim University, Istanbul, TURKIYE*
[d] *Department of Orthopaedics Surgery and Traumatology, Health Science University, Istanbul, TURKIYE*
[e] *Baltalimani Bone Diseases Education and Research Hospital, Istanbul, TURKIYE*
* *Corresponding author's e-mail address: syesilkir@gelisim.edu.tr*
DOI: 10.29130/dubited.1398015

ABSTRACT

Clubfoot deformity is one of the most important congenital anomalies of paediatric orthopaedics and characterised by equinus, supination and inversion of the foot muscles. Although treatment of this pathology, which presents as a gait disorder in the early stages of development, is currently attempted with exercise, physiotherapy and/or surgical approaches, the success rates of these treatments are low and/or lateral compression recurs. This situation confronts many children and their families with the difficulties and costs of the treatment process. The aim of this study is to produce and develop an apparatus for the treatment of this dysfunction with today's engineering approaches. For this purpose, in this study, a prototype was designed and manufactured using three-dimensional (3D) printing method with tough polylactic acid (PLA). The prototype can support both the right and left foot and enables to exercise up to angles of 31.8° for both evertor and invertor muscle.

Keywords: *Clubfoot deformity, Evertor muscle, Design and fabrication, 3D printer*

Evertör ve Invertör Kas Disfonksiyonları için Ayak Egzersiz Aletinin Kavramsal Tasarımı ve 3D Yazıcı ile Üretimi

ÖZET

Çarpık ayak deformitesi pediatrik ortopedinin en önemli konjenital anomalilerinden biridir ve ayak kaslarının ekinus, supinasyon ve inversiyonu ile karakterizedir. Gelişimin erken dönemlerinde yürüme bozukluğu olarak ortaya çıkan bu patolojinin tedavisi için günümüzde egzersiz, fizyoterapi ve/veya cerrahi yaklaşımlarla yapılmaya çalışılsa da bu tedavilerin başarı oranları düşüktür ve/veya yan basma sorunu yeniden tekrarlamaktadır. Bu durum birçok çocuk ve ailesini tedavi sürecinin zorlukları ve maliyetleri ile karşı karşıya bırakmaktadır. Bu çalışmanın amacı, günümüz mühendislik yaklaşımları ile bu fonksiyon bozukluğunun tedavisine yönelik bir aparat üretmek ve geliştirmektir. Bu amaçla, bu

Received: 03/12/2023, Revised: 10/09/2013, Accepted: 21/09/2024

çalışmada sert polilaktik asit (PLA) ile üç boyutlu (3D) baskı yöntemi kullanılarak bir prototip tasarlanmış ve üretilmiştir. Prototip hem sağ hem de sol ayağı destekleyebilmekte ve hem evertor hem de invertor kasları için 31,8°'lik açılara kadar egzersiz yapmaya olanak sağlamaktadır.

Anahtar Kelimeler: *Çarpık ayak deformitesi, Evertor kası, Tasarım ve fabrikasyon, 3D yazıcı*

I. INTRODUCTION

Clubfoot is one of the major and common congenital anomalies in paediatric orthopaedics in the world and it is characterized by equinus, supination, and inversion of the foot. This defect is a dysfunction of the evertor and inverter muscles that causes impairments, limitations, and disabilities in the gait of children and adults besides painful and uncomfortable situations for the patient (Figure 1) [1, 2]. Treatment of this case includes serial casting and, rarely, surgery [1-5]. Children are also followed through their growing years and frequently require secondary procedures. Long-term follow-up is crucial for evaluating different treatments such as surgery vs. casting [2, 3]. The goal in the correction of congenital clubfoot is to obtain a painless, straight, plantigrade, mobile foot with reestablishment of anatomic bony relationships, normal radiographic appearance, and which allows the development of a normal gait pattern [5].

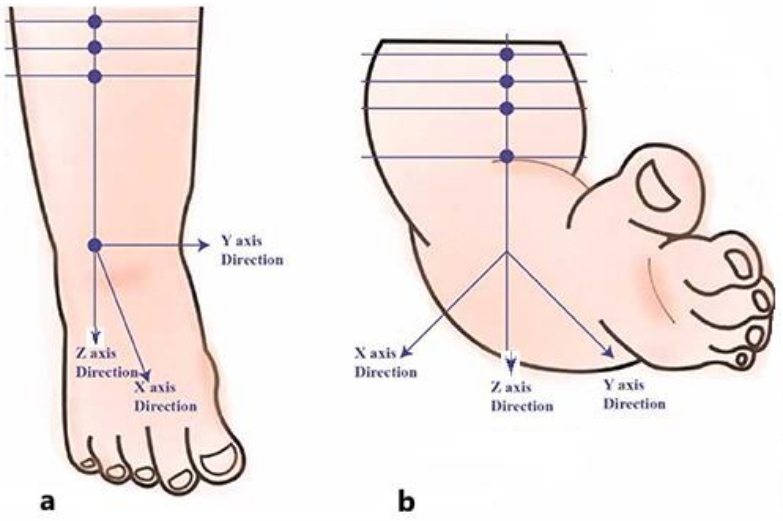

Figure 1. (a) *Normal foot and* ***(b)*** *Clubfoot anomaly appearance according to X, Y and Z directions [6]*

It is known that the treatment of clubfoot has been known since ancient times and various approaches have been applied for treatment since these times [1, 7, 8]. Today, it is tried to be treated with exercises, physical therapy and/or surgical approaches and to facilitate the daily life of individuals; however, these treatments have low success rates and/or relapse of side pressure. Today, it is tried to be treated with exercises, physical therapy and/or surgical approaches and to facilitate the daily life of individuals; however, these treatments have low success rates and/or relapse of side pressure. Ponseti Method is the gold standard protocol for the treatment of clubfoot and enables successive serial manipulations and plastering to achieve successful results. But although it is the gold standard, recurrences can be seen in clubfoot treatment up to 50%, regardless of the successful initial treatment process and the satisfactory results obtained. This is a situation encountered with non-compliance with the Ponseti brace protocol. Repeated manual applications or surgical interventions may be required in curing the pathology for recurrence of the deformity [9-11]. Each patient may need a personalized but also a cheaper treatment because this lifelong treatment has high costs for the families [11, 12]. On the other hand, consisting of

treatments, especially for patients older than 4-5 years old, are boring, time wasting and sometimes torture for them and hard to control for parents. More research is needed to determine whether a specific treatment approach is beneficial for children [13] and there is a great expectation for new different approaches. At this very moment, designing technological developments for the health sector has been a key element in biomedical engineering education. As Petroski [14, 15] has stated, design is the "soul of engineering". The incredible contributions of today's technology and engineering approaches in medicine have laid the groundwork for the production and development of an apparatus for curing this dysfunction. Today, personalised designs are customized to various parts of the human body in accordance with the geometric specifications with an increasing attention. Three-dimensional design technologies take attention and are utilised for the needs of human body which is an organic object and show free-form properties [16]. In our study, for children, we re-designed and fabricated a foot exercise apparatus, using the principles of basic biomechatronics and biomedical devices, and printed an apparatus using a 3D printer for use in evertor and inverter muscle dysfunction. There is a lack of personalised devices clubfoot deformity especially for children older than 24 months and for the first time in this study, a novel and functional device is presented.

II. MATERIALS AND METHODS

In this study we evaluated a prototype apparatus called as *Pedped$_1$* that was conceptualised as a mobile application mediated exercise device for children who were diagnosed with clubfoot. Although this device was useful, it was a *prototype* and has some limitations. To overcome the limitations such as movement restrictions and limited usability for both right and left foot, we re-designed and then fabricated the new version of *Pedped$_2$*, the device. The design, 3D printer-supported studies were carried out within the scope of this study and the tough PLA used in this study were carried out by using the facilities of Mechatronics Engineering Department and Life Sciences and Biomedical Engineering Application and Research Centre at Istanbul Gelişim University. Electronic components were obtained from Dr. Özyalvaç.

A. DIGITAL EVALUATION

Pedped$_1$ was digitized using a computer aided design (CAD) software SolidWorks© which is a 3D solid modeling program for designing and assembling parts [17, 18]. 3D properties of the apparatus were transferred to the solid modeling program to generate schemes and tailored via its tools. Technical and clinical expectations were discussed by our team and re-digitized according to orthopedic treatment requirements and biomedical device design fundamentals [14].

B. DESIGN PROCESS

The design process is an important period of biomedical device development and needs sufficient attention to be given as it affects the long-term outcome of the devices. In this study, design fundamentals and engineering cares were both handled to content the basic expectations for users (doctors, nurses, practitioners, patients etc.) [19]. For these purposes, the finite element analysis (FEA) can be appropriate. In biomechatronics, FEA is applied to living systems, especially the human body, is an important tool for simulating human body studies and conducting comparative studies [20]. The FEA has become increasingly popular among researchers in the field of computational biomechanics as it allows us to understand the detailed biomechanical responses of load-bearing biological systems [20]. In order to perform FEA, ANSYS software was used to provide numerical analyses of structural affects to the pedal directly [21]. Considering the apparatus and the lower part of the leg (crus) where the apparatus will be mounted and the amount of force that will be applied to the pedal part of the apparatus with a child's foot was analysed. During the force loading analyses, it was assumed that no other force would be applied to any part of the apparatus other than the pedal part. On the other hand, tough PLA material, which we will print with a 3D printer, was considered in the analysis studies and the forces to

be applied to the pedal part of the apparatus produced with this material were evaluated. The maximum angle that can occur during the maximum stress was calculated. Several different schemes that have a lightweight, space-saving and pleasing to the eye models were designed using SolidWorks© 2022 software for rendering and assembling three-dimensional models (Figure 2).

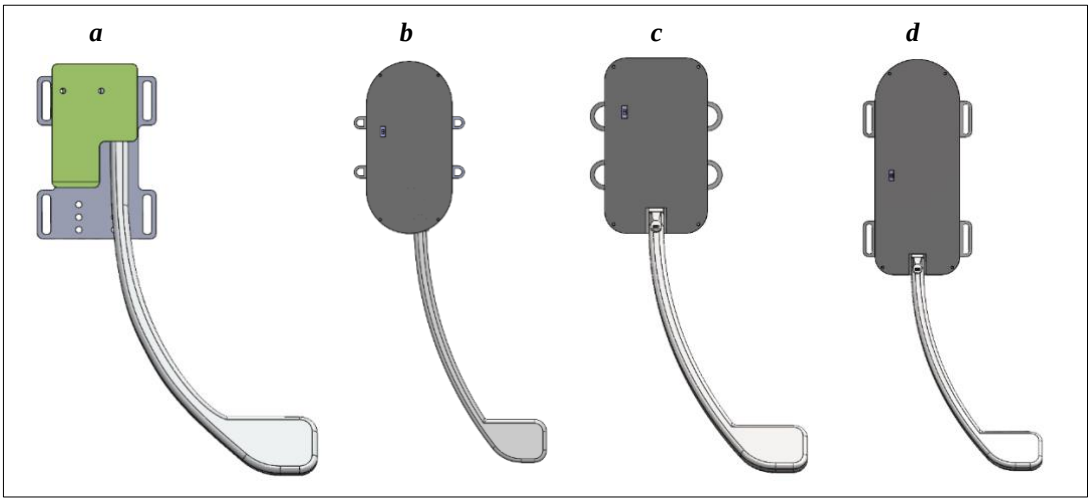

Figure 2. (a) *The first (Pedped1) and* ***(b, c, d)*** *the other new ideas of samples designs [22].*

C. MATERIAL SELECTION AND FABRICATION (3D PRINTING)

Another important step for biomedical device design is material selection. Choice of materials will impact virtually all aspects of the device's use: the dimensions, lifespan, and capabilities of the device; the cost and complexity of validation, manufacture, and application [23]. In other words, *design process* is linked to the material choice and *material selection process* is linked to *the fabrication process*. Thus a well-known material needs to be evaluated considering both the design and fabrication. According to physical features of the designed apparatus we searched the literature and decided to fabricate it via 3D printing. *Tough PLA* was appeared as a reasonable material for our 3D printing procedures. Tough PLA is a design material that combines the stiffness of PLA with the impact resistance and strength of ABS, has high surface quality and can be printed very easily [24, 25]. Properties by manufacturer of tough PLA (BCN3D, Barcelona, Spain) are like as 1,21 g/mL specific gravity with a tensile strength at yield and break 46 and 19 MPa, respectively. Also, the elongation strain at yield is 2% while elongation at break is 27%. Vicat Softening point is 57 ºC.

Fabrication of the apparatus was provided with 3D printing method that is an additive manufacturing. This method enables the cost-effective, sensitive and faster synthesis of complex 3D structures such as human body parts and is increasingly replacing many traditional methods [26]. In this process, a tough PLA filament with a tolerance of ± 0.10 mm Ø and ≥ 95% roundness and a size of 2.85 mm was used for the Epsilon W50 (BCN3D, Barcelona, Spain) 3D printer. The printing parameters were layer thickness 0.05 - 0.5 mm, nozzle diameter 0.4 mm, layer height 0.1 mm, fill 80%, fill overlap 15% and wall thickness 0.8 mm. The specimens were produced horizontally.

On the other hand, the analysis of *Pedped*$_2$ was carried out with the finite element model method using ANSYS program. The SOLID187 element was used in the finite element model. SOLID187 is a 3D element with 10 nodes and has quadratic displacement behavior and is suitable for modeling irregular structures (e.g. those produced by CAD/CAM systems). On the other hand, the SOLID187 element defines 10 nodes (Figure 3) with 3 degrees of freedom at each node. This element, with its plasticity, hyperelasticity, creep, strain hardening, strain hardening, high deformation and high tensile capacity [27, 28], was used for the analysis of *Pedped*$_2$.

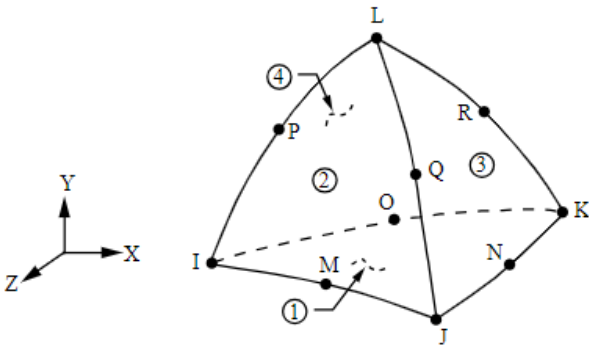

Figure 3. *Solid187 element of 10 nodes with X, Y and Z axis (ANSYS Manual) [28].*

III. RESULTS AND DISCUSSION

A. RESULTS

The final design and fabricated prototype of device (*Pedped*$_2$) is shown in Figure 2. Different from the first version, *Pedped*$_2$ includes two parts: the *main body* and the *pedal* part that are connected to each other with female and male joints (Figure 4). The main body of the design is used to fix the apparatus to the tibia of the children with the help of a bandage. The pedal, which is connected to the main body, forms the moving mechanism of the apparatus with its golf club-shaped design. The pedal part is ergonomic and provides convenience for both right and left feet to perform both evertor and inverter muscle movements.

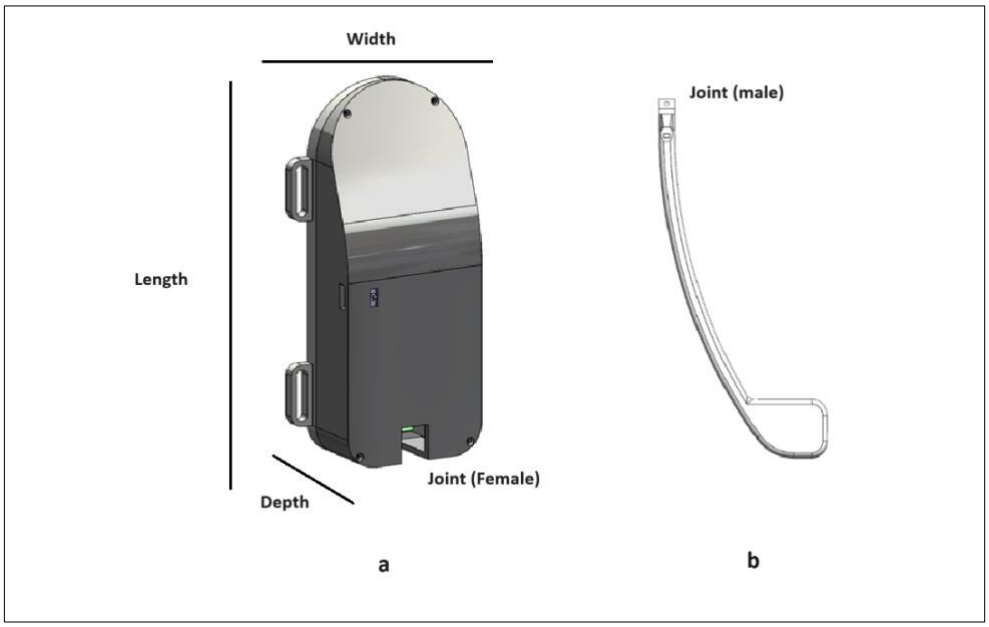

Figure 4. *The parts of 3D printed prototype of Pedped*$_2$ ***(a)*** *The main body; and* ***(b)*** *pedal [22].*

First version could be used just for one foot and just left or right movement. That was the major limitation of *Pedped*$_1$. On the other hand, as seen on Table 1, *Pedped*$_1$ has 3 separate parts and total weight of these parts were heavier, and release degree of the pedal was lower. *Pedped*$_2$ had advantages with its lighter, free movement support and two-sided feet that helps to work out both right and left feet for evertor and invertor muscles' movements. This version of the apparatus' pedal enables to exercise up to angles of 31.8° for both evertor and invertor muscle. Total length of *Pedped*$_2$ is longer that helps to allows the weight of the device to be distributed over the surface of the tibia.

Table 1. *Comparison of the measurements of Pedped$_1$ and Pedped$_2$. Measurements were obtained from Atesoglu, 2023 [22].*

	Part of the device	**Width** (mm)	**Length** (mm)	**Dept** (mm)	**Weight** (g)	**Release degree**
Pedped$_1$	*Main body*	47.3	68.5	42	179	-
	Pedal	155.5	273	Top 48 Buttom 52	239	27.4
	Joint	66	90	6 - 10	31	-
Pedped$_2$	*Main body*	90	180	Top 8 Buttom 39	197	-
	Pedal	10	199	10	21	31.8

The apparatus in consideration is designed for the treatment of clubfoot as a completely different product that has no counterpart, especially for children to make their exercises enjoyable without difficulty (Figure 5).

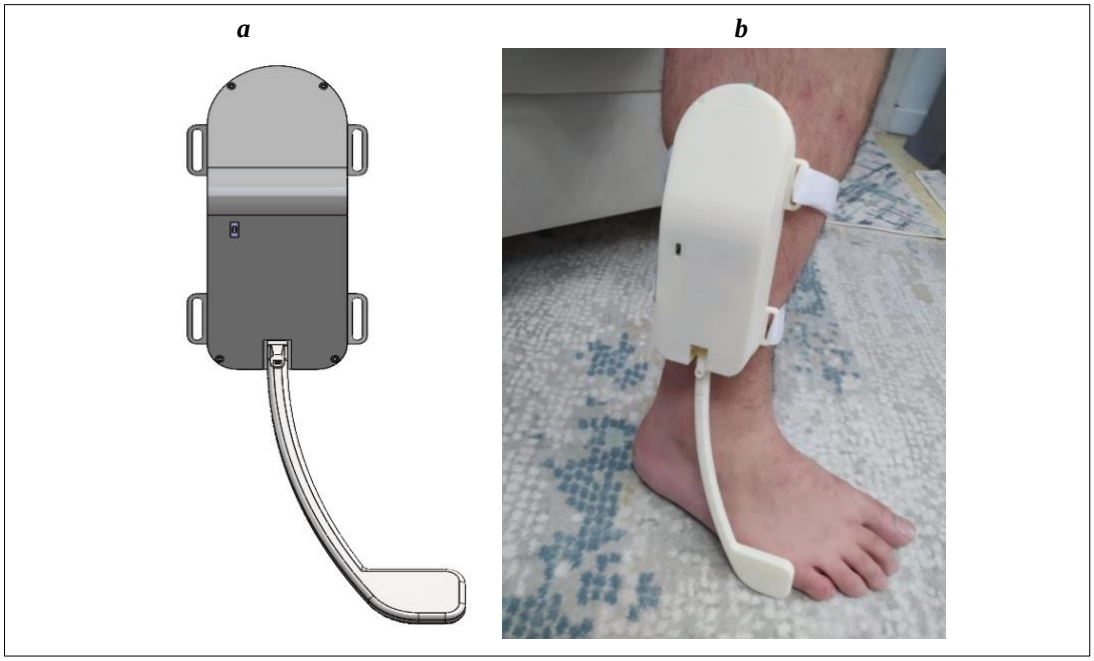

Figure 4. *Final design of Pedped$_2$* ***(a)*** *illustration,* ***(b)*** *fabricated prototype on the foot [22].*

We also evaluated the meshing process of the apparatus and obtained the two-sided isometric view (Figure 6a and 6b). Figure 7a and 7b shows the boundary conditions of *Pedped$_2$*. After the boundary conditions were determined, total deformation (Figure 7c and 7d), stress and strain analyses were performed for F=0.5 N and F=1 N according to our experiments (Data not shown).

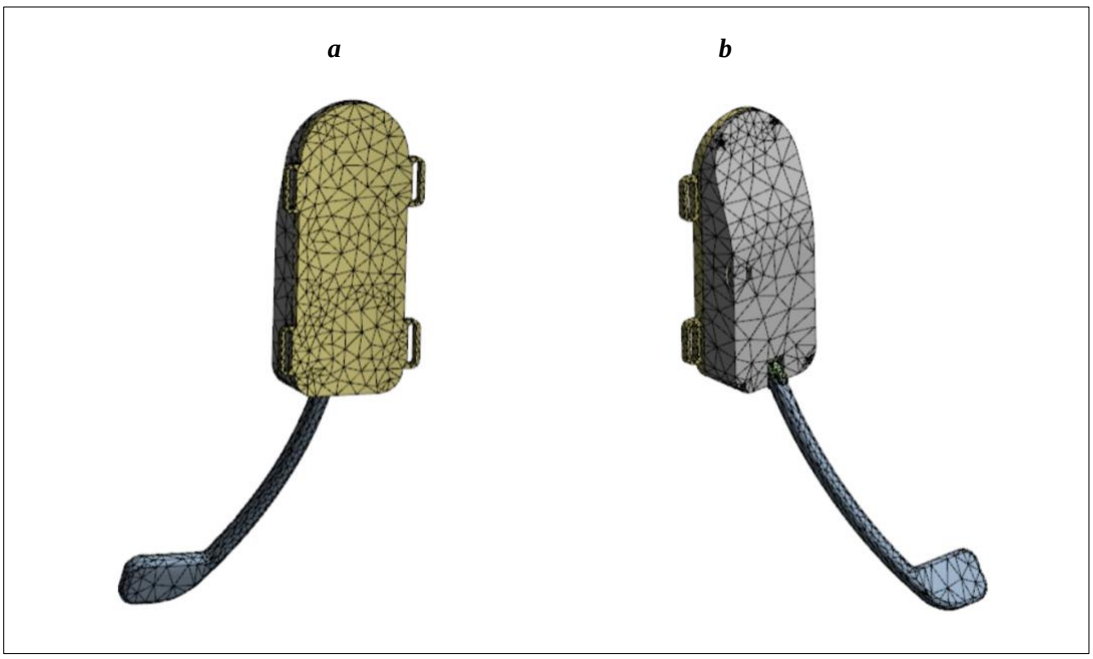

Figure 6. *Isometric view of the mesh of Pedped$_2$* ***(a)*** *back side* ***(b)*** *front side*

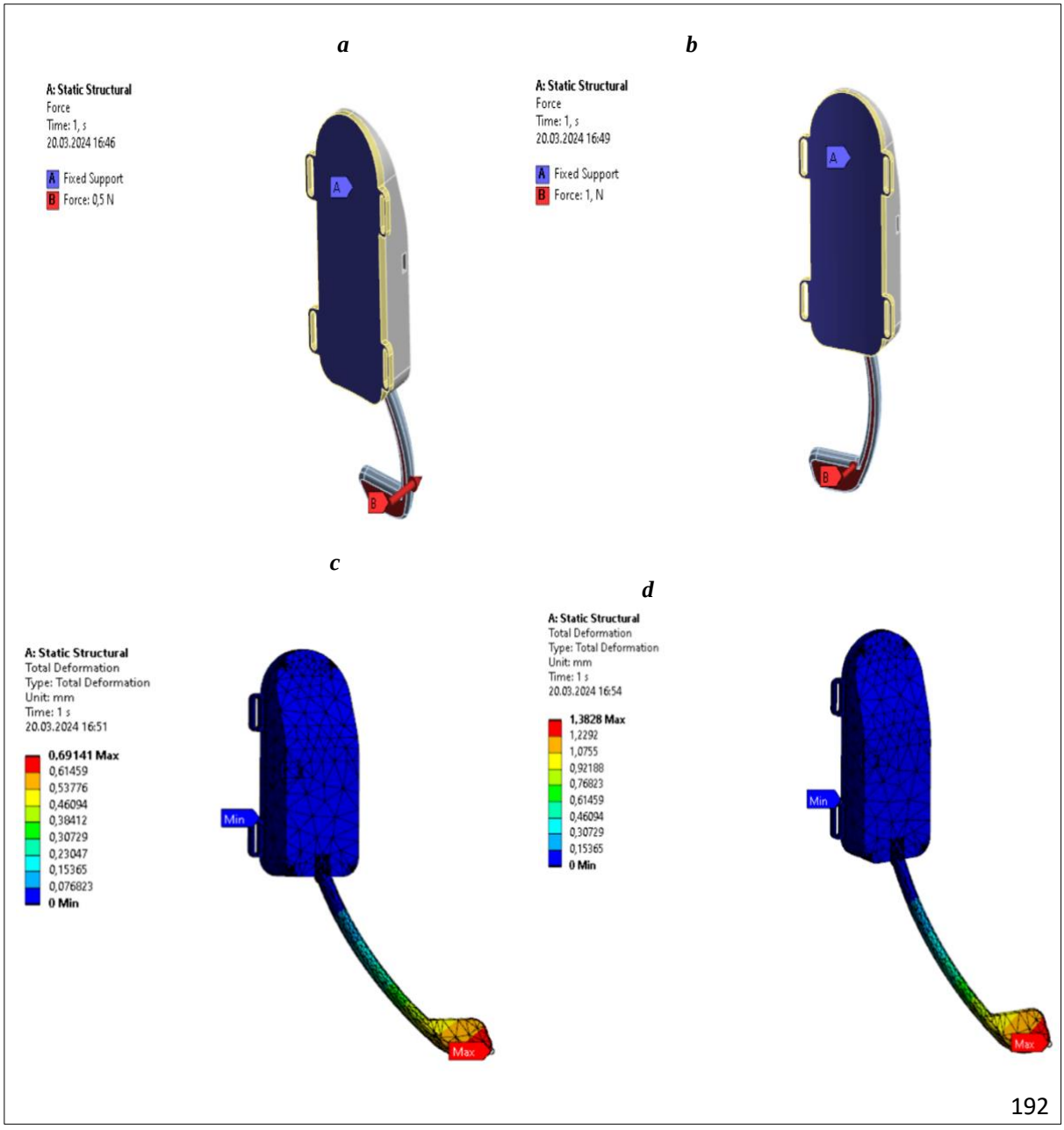

Figure 7. *Boundary conditions for Pedped$_2$ simulations when* ***(a)*** *F=0,5 N* ***(b)*** *F=1 N; and total deformation when* ***(c)*** *F=0,5 N* ***(d)*** *F=1 N*

The aim of the new version is to be user-friendly in design, to be advantageous in terms of price/performance in production, to have a post-modern design and to fully serve its orthopaedic clinical purpose. Total deformation, stress and strain analyses results showed that *Pedped$_2$* is a suitable apparatus to handle the exercises for evertor and invertor muscles. The apparatus also has the necessary mechanical and electronic parts to ensure its operation. These mechanical parts are discs and springs; the electronic parts are potentiometer; PCB card and battery A potentiometer is basically a type of adjustable resistor. However, since it has a rotatable structure, it can also be used for position detection. It was also used for our purpose in this study. Finally, there is an application interface that allows the device to be connected to the phone. The electrical parts of the device were not evaluated in this study; thus, they were placed into the main body. The whole mechanic and electric systems worked correctly.

B. DISCUSSION

In recent years, engineering studies in the field of health have developed rapidly and thousands of products that can be used for diagnosis and treatment have begun to be offered to humanity. It is expected that the number of medical devices to be made in this area will increase even more. On the other hand, for low- and middle-income countries, the design of medical devices is of vital importance. Both the development of the country and the opportunity to access technology at a more affordable price should be provided [29].

There is a very important need in the field of orthopaedics for engineering supported devices. Based on these purposes and needs, we used mechatronics engineering approaches together with biomedical device designs, and with the studies carried out, its effectiveness was increased, and it became a user-friendly apparatus. It helps to work out both right and left feet for evertor and invertor muscles' movements. The pedal helps to exercise up to angles of 31.8° for both evertor and invertor muscle. The apparatus in question can be used to effectively improve congenital clubfoot deformity, and a similar product is not available in the field of health. While many rehabilitation interventions involve the foot and ankle, the contributions of the foot and ankle to normal gait are not well understood. More specifically, understanding the effects of congenital defects, injuries, or other alterations in the lower limb and particularly the foot and ankle on mobility is a continuing challenge to medical rehabilitation researchers. Especially mobility in children is a very important title of the field, and there is limited apparatus and studies in literature. For this purpose, Savonen et al (2020) reported a study about a 3D printed brace (*RepRaps*) that can be used for babies using open-source CAD software (FreeCAD) for design, polylactic acid (PLA) as the material for 3D printing. Similar to our study they used printing fabrication method and but different from our study, *RepRaps* is for children, and it needs re-arrangements on the brace while the child grows. On the other hand, it has multiple exercises advantages for the rotations of the movements such as angle brackets with angles of 90°, 95°, 100°, 105°, and 110°[12]. Recent years, apart from traditional techniques, engineering technologies are stated such as developing new procedures for older children according to their needs [30-32].

IV. CONCLUSION

The aim of this study was to design a mobile application game-supported device that can be used by children with clubfoot aged 4-5 years and older. The prototype was fabricated using a 3D printer and the main material used is Tough PLA, a common textile product as a belt, electronic part inserted into the main body. As conclusion, in this study, it is aimed to make the exercises in the treatment process fun, affordable and not exhausting for children with clubfoot deformity who have undergone surgical intervention. In addition, an innovative approach that may delay or may not require no more surgical intervention in the treatment process is presented. However, further mechanical and electronically

improvements and clinical investigation need to be conducted since the device has not been tested with real patients.

ACKNOWLEDGEMENTS:

The authors declare that there is no conflict of interest regarding the publication of this article.

AUTHOR'S CONTRUBUTION:

In this study, we evaluated an apparatus ($Pedped_1$) that was conceptualised by O.N.Ö., S.Y.B. has conceptualised the re-design of the study, wrote the article. U.A. has used the software for designing *PedPed*$_2$ and printed it using 3D printer.

V. REFERENCES

[1] P. Hernigou, M. Huys, J. Pariat, and S. Jammal, "History of clubfoot treatment, part I: From manipulation in antiquity to splint and plaster in Renaissance before tenotomy," *Int Orthop,* vol. 41, pp. 1693-1704, Aug 2017.

[2] E. Ippolito, F. Mancini, M. Di Mario, and P. Farsetti, "A comparison of resultant subtalar joint pathology with functional results in two groups of clubfoot patients treated with two different protocols," *J Pediatr Orthop B,* vol. 14, pp. 358-61, Sep 2005.

[3] C. Roche, B. Mattingly, V. T. Md, C. Tylkowski, D. B. Stevens, P. A. Hardy, *et al.*, "Three-dimensional hindfoot motion in adolescents with surgically treated unilateral clubfoot," *J Pediatr Orthop,* vol. 25, pp. 630-4, Sep-Oct 2005.

[4] O. N. Ozyalvac and E. Akpinar, "Foot abduction increases after achilles tenotomy in clubfoot patients," *Journal of Orthopaedic Science,* vol. 26, pp. 1081-1084, 2021/11/01/ 2021.

[5] G. F. Harris, Smith, P.A. , *Foot and Ankle Motion Analysis: Clinical Treatment and Technology*, 1 ed.: CRC Press., 2007.

[6] B. Ganesan, A. Luximon, A. A. Al-Jumaily, J. Yip, P. J. Gibbons, and A. Chivers, "Developing a Three-Dimensional (3D) Assessment Method for Clubfoot—A Study Protocol," *Frontiers in Physiology*, vol. 8, 2018-January-04 2018.

[7] P. Hernigou, "History of clubfoot treatment; part III (twentieth century): back to the future," *Int Orthop,* vol. 41, pp. 2407-2414, Nov 2017.

[8] P. Hernigou, N. Gravina, D. Potage, and A. Dubory, "History of club-foot treatment; part II: tenotomy in the nineteenth century," *Int Orthop,* vol. 41, pp. 2205-2212, Oct 2017.

[9] b. özkul, Y. M. DİNÇEl, O. N. Ozyalvac, I. Bayhan, A. Kirat, and E. Akpinar, "The Effect of Tibialis Anterior Tendon Transfer on Metatarsus Adductus Deformity in Children with Clubfoot," *İstanbul Medical Journal,* vol. 20, pp. 35-38, 2019.

[10] C. Radler, "The Ponseti method for the treatment of congenital club foot: review of the current literature and treatment recommendations," *Int Orthop,* vol. 37, pp. 1747-53, Sep 2013.

[11] M. M. Thacker, D. M. Scher, D. A. Sala, H. J. van Bosse, D. S. Feldman, and W. B. Lehman, "Use of the foot abduction orthosis following Ponseti casts: is it essential?," *J Pediatr Orthop,* vol. 25, pp. 225-8, Mar-Apr 2005.

[12] B. Savonen, J. Gershenson, J. K. Bow, and J. M. Pearce, "Open-Source Three-Dimensional Printable Infant Clubfoot Brace," *JPO: Journal of Prosthetics and Orthotics*, vol. 32, 2020.

[13] Z. Little, A. Yeo, and Y. Gelfer, "Poor Evertor Muscle Activity Is a Predictor of Recurrence in Idiopathic Clubfoot Treated by the Ponseti Method: A Prospective Longitudinal Study With a 5-Year Follow-up," *Journal of Pediatric Orthopaedics*, vol. 39, pp. e467-e471, 2019.

[14] C. Miranda, J. Goñi, and N. Labruto, "Five Qualitative Research Concepts Grounded in Anthropological Methods for Teaching Design in Healthcare," *Healthcare (Basel)*, vol. 10, Feb 12 2022.

[15] H. Petroski, "An Engineer's Alphabet: Gleanings from the Softer Side of a Profession," *Civil Engineering Magazine*, vol. 81, pp. 70-77, 2011.

[16] H. K. Sürmen and T. GÜVen, "Tersine Mühendislik ve Eklemeli İmalat ile Kişiye Özel Nazal Dilatör Tasarımı ve Üretimi," *Afyon Kocatepe Üniversitesi Fen Ve Mühendislik Bilimleri Dergisi*, vol. 24, pp. 197-206, February 2024.

[17] J. Zhang, R. Zhang, G. Ren, and X. Zhang, "A method for using solid modeling CAD software to create an implant library for the fabrication of a custom abutment," *The Journal of Prosthetic Dentistry*, vol. 117, pp. 209-213, 2017/02/01/ 2017.

[18] M. George, K. R. Aroom, H. G. Hawes, B. S. Gill, and J. Love, "3D Printed Surgical Instruments: The Design and Fabrication Process," *World J Surg*, vol. 41, pp. 314-319, Jan 2017.

[19] T. A. Stolarski, "Mechanical engineering design (fifth edition): J.E. Shigley and C.R. Mischke," *Tribology International*, vol. 25, p. 295, 1992/01/01/ 1992.

[20] A. Merdji, B. Taharou, R. Hillstrom, A. Benaissa, S. Roy, P. L. Chong, *et al.*, "Finite-Element Study of Biomechanical Explanations for Bone Loss around Dental Implants," *J Long Term Eff Med Implants*, vol. 30, pp. 21-30, 2020.

[21] C. M. Sabliov, D. A. Salvi, and D. Boldor, "High Frequency Electromagnetism, Heat Transfer and Fluid Flow Coupling in ANSYS Multiphysics," *Journal of Microwave Power and Electromagnetic Energy*, vol. 41, pp. 5-17, 2006/01/01 2006.

[22] U. Ateşoğlu, "Evaluation and improvement of existing features of foot excersize apparatus designed for use in evertor and invertor muscle dysfunction," Master of Science, Mechatronics Engineering, Istanbul Gelisim University, Istanbul, 2023.

[23] A. Biesiekierski, K. Munir, Y. Li, and C. Wen, "2 - Material selection for medical devices," in *Metallic Biomaterials Processing and Medical Device Manufacturing*, C. Wen, Ed., ed: Woodhead Publishing, 2020, pp. 31-94.

[24] N. Naveed, "Investigating the Material Properties and Microstructural Changes of Fused Filament Fabricated PLA and Tough-PLA Parts," *Polymers (Basel)*, vol. 13, May 6 2021.

[25] A. Pandzic and D. Hodzic, "Mechanical properties comparison of PLA, tough PLA and PC 3D printed materials with infill structure – Influence of infill pattern on tensile mechanical properties," *IOP Conference Series: Materials Science and Engineering*, vol. 1208, p. 012019, 2021/11/01 2021.

[26] M. S. Jia, R. R. Rao, and M. Elsaadany, "Early introduction of 3D modeling modules promotes the development of simulation skills in downstream biomedical engineering curricula," *J Biol Eng*, vol. 17, p. 26, Mar 30 2023.

[27] A. M. Ali, S. R. Al-Taai, E. K. Jaafar, A.-M. Hadi Naser Ghadhban, H. M. Madhloom, and N. Al-Ansari, "NONLINEAR SIMULATION ANALYSIS OF MECHANICAL BEHAVIOUR OF RUBBERIZED CONCRETE," *GEOMATE Journal*, vol. 22, pp. 125-137, 04/04 2022.

[28] Inc. ANSYS. (12 September). *ANSYS Fluent User's Guide (Release 18.2 ed.)*. Available: https://www.mm.bme.hu/~gyebro/files/ans_help_v182/ans_elem/Hlp_E_SOLID187.html

[29] T. Saidi and T. S. Douglas, "Critical elements in the design, development and use of medical devices. A systemic perspective of orthopedic devices landscape in low- and middle-income countries," *Health Policy and Technology*, vol. 11, p. 100593, 2022/03/01/ 2022.

[30] R. Rizza, X. Liu, J. Thometz, R. Lyon, and C. Tassone, "A New Method in the Design of a Dynamic Pedorthosis for Children With Residual Clubfoot," *Journal of Medical Devices*, vol. 4, 2010.

[31] R. B. Giesberts, V. I. Sluiter, and G. J. Verkerke, "Design and Test of a New Inductive Force Sensor," *Sensors*, vol. 18, p. 2079, 2018.

[32] K. M. Kruger, P. A. Smith, and J. J. Krzak, "Biomechanical Implications of Congenital Conditions of the Foot/Ankle," *Foot and Ankle Clinics*, vol. 28, pp. 27-43, 2023/03/01/ 2023.

Düzce University
Journal of Science & Technology

Research Article

A Model Proposal for Estimate the Approximate Costs and Contract Fees of Public Education Buildings

Servet KESİM [a,*], Latif Onur UĞUR [b]

[a] *Department of Civil Engineering, Institute of Science, Düzce University, Düzce, TURKEY*
[b] *Department of Civil Engineering, Fakulty of Engineering, Düzce University, Düzce, TURKEY*
* *Corresponding author's e-mail address: servetkesim@gmail.com*
DOI: 10.29130/dubited.1529898

ABSTRACT

In this study, a method is proposed for the preliminary estimation of school building costs. For this purpose, the projects of 96 school buildings, which were put out to tender by public institutions and the result announcement was published, were provided from the Electronic Public Procurement Platform. These projects are divided into 81 training data and 15 test data. The construction cost of educational buildings through projects may affect the output vectors; "Number of Classrooms, Construction Duration, Total Number of Floors, Floor Height, Building Height, Building Height Class, Basement Height, Earthquake Design Class, Floor Class, Ground Safety Stress, Bed Coefficient, Concrete Class, Number of Elevators, Wet Area, Raft Foundation Height, Floor Area, Basement Area, Total Area" parameters were determined and used in modeling and analysis. Analyzes were carried out with "SPSS Statistics 26" software. Using these parameters, Regression Analyzes (RA) were performed and equations were developed to estimate the costs of educational structures. Approximate Costs and Contract Prices were tried to be estimated with the developed models. The model in which all parameters were used with the created equations was the model with the best correlation level, with the determination coefficient R^2=0.900 for the Approximate Cost Price and R^2=0.927 for the Contract Price. An error rate of 17,5% was found between the approximate cost estimates obtained using the model and the actual costs. It was determined that there was an 18,2% error between the estimated contract prices and the actual contract prices. The Durbin-Watson criterion was used to check the consistency between predicted results and actual results. As a result, an approach that can estimate the approximate costs and contract prices of school buildings of different types and coefficients with error rates lower than 20% has been created. Both public institutions and contracting construction companies will be able to make realistic cost estimates by benefiting from these modeling, providing time savings. Conducting similar studies by increasing the number of data may be a solution to minimize the error rate in subsequent modeling.

Keywords: *Building Cost Model, Multiple Linear Regression Model, School Buildings, Building Cost Estimation*

Kamu Eğitim Yapılarının (Okul Binalarının) Yaklaşık Maliyetleri ve Sözleşme Bedellerinin Tahmini için Bir Model Önerisi

ÖZ

Bu çalışmada, okul binası maliyetlerinin ön tahmini için bir yöntem önerisinde bulunulmuştur. Bu amaçla, Kamu Kurumları tarafından ihaleye çıkılmış ve sonuç ilanı yayınlanmış 96 adet okul binasına ait projeler Elektronik Kamu Alımları Platformu (EKAP)'tan sağlanmıştır. Bu projeler 81 adet eğitim, 15 adet test verisi olacak şekilde ayrılmıştır. Projeler üzerinden eğitim yapılarının inşaat maliyeti çıktı vektörlerini etkileyebilecek; "Derslik Sayısı, Yapım Süresi, Toplam Kat Sayısı, Kat Yüksekliği, Bina Yüksekliği, Bina Yükseklik Sınıfı (BYS), Bodrum Yüksekliği, Deprem Tasarım Sınıfı (DTS), Zemin Sınıfı, Zemin Emniyet Gerilmesi, Yatak Katsayısı, Beton Sınıfı, Asansör Sayısı, Islak Alan, Radye Temel Yüksekliği, Kat Alanı, Bodrum Alanı, Toplam Alan" parametreleri

Received: 08/08/2024, Revised: 11/09/2024, Accepted: 24/09/2024

belirlenerek modelleme ve analizlerde kullanılmıştır. Analizler "SPSS Statistics 26" yazılımı ile gerçekleştirilmiştir. Bu parametreler kullanılarak Regresyon Analizleri (RA) yapılmış ve eğitim yapılarının maliyetlerini tahmin etmek için denklemler geliştirilmiştir. Geliştirilen modellerle Yaklaşık Maliyetleri ve Sözleşme Bedelleri tahmin edilmeye çalışılmıştır. Oluşturulan denklemlerle tüm parametrelerin kullanıldığı model Yaklaşık Maliyet Bedeli için determinasyon katsayısı R^2=0.900, Sözleşme Bedeli için ise R^2=0.927 ile en iyi ilişki düzeyine sahip model olmuştur. Modelin kullanılması ile elde edilen yaklaşık maliyet tahminleri ve gerçek maliyetler arasında %17,5 düzeyinde hata oranı saptanmıştır. Tahmin edilen sözleşme bedelleri ile gerçek sözleşme bedelleri arasında ise %18,2 hata olduğu belirlenmiştir. Tahmin edilen sonuçlar ile gerçek sonuçlar arasındaki tutarlılığı kontrol etmek amacıyla Durbin-Watson kriteri kullanılmıştır. Sonuç olarak, farklı tip ve katsayılarına sahip okul yapılarının yaklaşık maliyetlerini ve sözleşme bedellerini %20'den düşük hata oranları ile tahmin edebilen bir yaklaşım oluşturulmuştur. Gerek kamu kuruluşları gerekse taahhütçü yapım firmaları bu modellemelerden istifade ederek zamansal tasarruflar sağlayarak gerçekçi maliyet tahminlerinde bulunabileceklerdir. Benzer çalışmaların veri adetleri arttırılarak yapılması, daha sonraki modellemelerde hata oranı minimizasyonu için bir çözüm olabilir.

Anahtar Kelimeler: *Yapı Maliyeti Modeli, Çoklu Doğrusal Regresyon Modeli, Okul Binaları, Yapı Maliyeti Tahmini*

I. INTRODUCTION

Cost is defined as the total expenses incurred to produce a product. Building cost, on the other hand, is evaluated as the total expenses from the formation of the building need to the construction process [1].

The primary objective of cost estimation is to determine the cost required to provide a desired quality of service or product by using scarce resources as effectively as possible. To achieve maximum production and complete the project at the anticipated quality, it is necessary to accurately predict the expenses that will be incurred and, at the same time, monitor these expenses with an effective cost control system within the specified cost limits [2]. Given the limited investment resources, it is essential to determine, plan, and control cost accounting with great precision. An incomplete or excessive cost estimate can lead to the failure of a construction project in terms of cost [3]. With well-prepared cost estimation, necessities such as materials for application, equipment and other resources can be specified. In order to make effective planning and actual budget preparation, all projects require cost estimation[4]. In the construction industry, it is quite important to create the financial model correctly during the idea phase of the project, in order to prevent cash flow problems and national wealth losses. This is only possible by estimating the cost correctly in predesign period [5].

A tender is the process of awarding a service or goods to the most suitable bidder among multiple applicants. In situations where the market price of the components of the job is not fully known or is uncertain, the tender process plays a significant role in price formation [6]. Public procurement refers to the purchase of goods, services, and construction works to meet the demands of administrative institutions of the state and the needs of the public. These tenders are crucial for national economies, and thus hold significant importance for the future of countries [7]. In Turkey, the Public Procurement Law No. 4734, enacted in 2002, has established the principles and procedures for tenders conducted by public institutions and organizations subject to public law or under public control or using public resources [8].

Since the 1970s, regression-based estimation models have been developed for construction cost estimation. These are based on statistical and mathematical tools, and regression techniques have been found to be successful in interpreting of the cost and the variables relationships[4].

II. BUILDING COST ESTIMATION METHODS

Cost models used for cost estimation at every stage of the construction process can be classified according to their intended use. The concept of cost modeling, which initially emerged as a simple planning method for residential and public buildings in Europe in the 1950s, began to be classified following research conducted in the 1970s and 1980s. These include traditional models, descriptive models, realistic models, and information system approach models [1].

A. TRADITIONAL MODELS

Traditional models can be categorized into Analytical models, Functional element-based models, Resource-based models, and Production unit-based models [1].

A.1. Analytical Models

These are models used from the initial stages of preliminary design when the scope of available information is very limited. The goal is to provide the most accurate cost estimate as quickly as possible and present it to users [1].

A.2. Functional Element-Based Models

Cost accounting based on elements is a type of cost accounting used during the design phase of the building production process to allow for cost planning and control [3].

A.3. Resource-Based Cost Models

These models, used during the construction phase of building production, help organize the site and perform effective site management by defining the lists of labor, materials, and equipment for each task and determining their costs [3].

A.4. Production Unit-Based Models

In the production phase of building construction, the production units and processes required to create the building constitute the production units. The production unit-based cost model is based on multiplying the previously determined unit prices for each unit by the quantities measured on the application project and summing these results to calculate the total cost of the building [3].

B. REALISTIC MODELS

Realistic models have lower estimation accuracy compared to quantity-based models. Despite this, while quantity-based models have nearly completed their development, it is suggested that realistic models have a much higher potential for development [1].

C. EXPERT SYSTEMS

These models use databases and computers for cost estimation. For successful cost estimation, these systems must be directed by experts [1].

D. DESCRIPTIVE MODELS

This approach is based on linking costs to the descriptive features of the design rather than quantities. Descriptive models are developed using regression analysis. The idea of using regression analysis was developed to determine the cost of the building both during the design phase and to allow the contractor to estimate the approximate cost [3].

D.1. Regression Analysis

Regression is the expression of the relationship between two or more variables with a cause-and-effect relationship using an equation. The direction or magnitude of the relationship between any two or more variables is determined by regression analysis. In regression analysis, the parameters of the variables in the model are estimated by making predictions based on the regression equation, thus mathematically revealing the relationships between dependent and independent variables. While there is only one dependent variable, the number of independent variables can vary. Models with one dependent and one independent variable are called simple regression models, while those with one dependent and multiple independent variables are called multiple regression models.

In regression analysis, the coefficients related to the variables forming the model are estimated. These coefficients indicate the direction and magnitude of the relationships between the dependent variable and independent variables. In short, regression analysis is a method that reveals the mathematical relationships between two or more variables with a cause-and-effect relationship [9].

D.1.1. Linear Regression Model

Regression analysis fundamentally relies on the assumption that one variable is explained by other variables. Here, a variable is mathematically modeled with other variables that have a cause-and-effect relationship, and this model is called the regression model. The regression model can be expressed in functional form as follows:

$$Y = \beta 0 + \beta 1X \quad (1)$$

Equation (1.1) shows the functional form of the relationship between two variables. These variables are Y and X. Here, Y is referred to as the explained or dependent variable, while X is called the explanatory or independent variable. β0 represents the constant coefficient, and β1 denotes the coefficient that indicates the direction and magnitude of the relationship between the Y and X variables [9].

In the production phase of building construction, the production units and processes required to create the building constitute the production units. The production unit-based cost model is based on multiplying the previously determined unit prices for each unit by the quantities measured on the application project and summing these results to calculate the total cost of the building [3].

D.1.1.1. Dependent and Independent Variables

The dependent variable is, in brief, the variable that changes depending on the independent variables, which explains it. The independent variable is the variable that explains the dependent variable and is not influenced by any other variable. In Equation (1), Y and X represent the dependent and independent variables, respectively. Thus, the dependent variable Y is explained by the independent variable X [9].

D.1.1.2. β0 and β1 Coefficients

The coefficient β0 in the model represents the constant coefficient. Essentially, the constant coefficient indicates the value that the dependent variable would take when the independent variable is zero. The β0 coefficient is commonly found in linear regression models unless strong theoretical reasons suggest otherwise. On the other hand, the β1 coefficient in the model is the coefficient of the independent variable, showing how changes in the independent variable affect the direction and magnitude of the dependent variable [9].

D.1.2. Multiple Linear Regression Model

Linear regression analysis involves dependent and independent variables. When there is only one independent variable, it is referred to as simple linear regression, while if there are two or more independent variables, it is called multiple linear regression. The goal of regression analysis is to functionally understand and model the relationship between variables [10]. It is based on the principle of keeping one of the variables or the category of the variable at predetermined levels and examining how the other variable changes according to that level. Regression can also be interpreted as finding unknown values using known values in modern statistics[11]. In the multiple regression equation, y represents the dependent variable, a is the constant coefficient, $x1 \ldots xn$ are the independent variables, and $\beta 1 \ldots \beta n$ are the coefficients for each independent variable.

$$y = a + \beta 1x1 + \beta 2x2 + \cdots + \beta nxn \quad (2)$$

III. RESEARCH AND FINDINGS

A. OBJECTIVE AND METHOD

This study will also contribute to the literature on accurately predicting approximate costs and contract amounts and alleviating the burden of lengthy measurement processes. In this context, the method of this study consists of two steps, outlined as follows:

1. Obtaining numerous similar projects through the Electronic Public Procurement Platform.

2. Conducting measurement studies and updating the approximate costs and contract amounts:
    a. Performing measurement studies on 96 public education projects.
    b. Updating the approximate cost and contract amounts of the projects according to Turkish Statistical Institute (TÜİK) data.

3. Finding the estimation equation for approximate cost and contract amount using multiple linear regression:
    a. Analyzing the correlations between independent variables and determining the regression datasets.
    b. Estimating approximate cost and contract amounts using regression analysis with the datasets obtained from correlation analysis.
    c. Examining the error rate in cost prediction for approximate cost and contract amount predictions with different variable selections based on correlation analysis.

B. FINDINGS

A total of 96 education buildings tendered and contracted by public institutions between 2020 and 2022 were examined, sourced through the Electronic Public Procurement Platform (EKAP) from various provinces in Turkey. In the regression analysis, 81 projects were designated as the training series, while 15 projects were reserved for testing purposes.

Due to annual unit price fluctuations, there is a time-dependent cost variation among the projects that have been tendered. To eliminate the time-dependent difference, the building construction cost index and change rate table published annually by TÜİK, as shown in Table 1, were used.

According to Table 1, coefficients for each month between 2020 and 2022 were determined based on the average cost rate for January 2023. All projects in the dataset were updated using these coefficients according to the year and month they were tendered. The figures for the approximate cost and contract amount for the years of tendering and the updated values are shown in Table 2 and Table 3.

Table 1. *Building construction cost index and change rates [12]*

Year	January	February	March	April	May	June	July	August	September	October	November	December
							Index					
2015	97,13	97,65	98,27	99,14	100,17	100,03	100,83	101,35	102,25	101,56	101,01	100,60
2016	108,19	108,12	109,39	110,26	112,11	111,60	111,52	111,90	112,19	113,06	115,83	118,90
2017	124,69	125,09	126,43	126,84	127,26	127,06	128,16	129,51	130,94	132,76	136,09	138,14
2018	144,92	146,60	149,08	152,10	156,58	160,17	162,78	172,71	182,87	182,57	176,85	173,57
2019	184,83	186,51	189,25	192,27	195,51	193,97	192,76	191,35	190,23	190,36	190,32	192,25
2020	202,04	202,34	202,34	204,08	206,85	208,46	210,43	216,30	220,87	227,47	234,07	240,35
2021	258,24	258,16	267,03	276,48	288,67	297,02	304,61	307,43	308,20	322,84	348,46	403,16
2022	464,60	491,20	538,26	571,22	593,87	614,46	654,13	667,06	677,52	700,80	709,02	719,25
2023	829,42	846,70	864,96	873,91	878,63	917,53	1061,35	1110,41				

Table 2. *Training Set*

Number	Project Name	EKAP Number	Approximate Cost (TL)	Contract Price (TL)	Updated Approximate Cost (2023 January)	Updated Contract Price (2023 January)
1	Selim Bozkuş 2 Derslikli Okul Yapım işi	2020/ 329035	₺1,021,314.10	₺729,700.00	₺4.025.558,81	₺2.876.147,76
2	Mersin Tarsus Günyurdu Ortaokulu 16 Derslikli Bina İnşaatı	2020/ 342776	₺6,322,113.59	₺4,103,796.00	₺24.918.915,81	₺16.175.309,98
3	Bozkır 8 Derslikli Okul Binası	2020/ 383719	₺3,774,808.69	₺2,869,000.00	₺14.474.811,94	₺11.001.414,61
4	İstanbul İli Küçükçekmece İlçesi 12 Derslikli Halk Eğitim Merkezi Yapım İşi	2020/ 399854	₺11,092,394.94	₺7,862,000.00	₺41.654.612,27	₺29.523.701,91
5	Altınekin İlçesi 16 Derslik Anadolu Lisesi Yapım İşi	2020/ 472257	₺4,957,008.20	₺4,093,000.00	₺18.074.654,86	₺14.924.236,43
6	Nevşehir Merkez 16 Derslikli Mesleki Teknik Anadolu Lisesi Yapım İşi	2020/ 681344	₺11,337,320.39	₺9,139,000.00	₺36.413.414,95	₺29.352.808,94
7	Manisa Saruhanlı Azimli (B+Z+1) İlkokulu Yapım İşi	2021/ 651850	₺9,636,299.46	₺7,177,000.00	₺22.936.748,83	₺17.083.014,81
8	Sorgun 12 Derslikli Bilim Sanat Merkezi Binası Yapım İşi	2021/ 662228	₺7,275,061.61	₺6,448,000.00	₺17.316.425,42	₺15.347.816,56
9	Ilgın Atatürk 24 Derslik İlkokul Yapım İşi	2021/ 672352	₺10,370,741.86	₺10,488,000.00	₺24.684.901,32	₺24.964.004,36

10	Kavak Anadolu Lisesi Yapımı	2021/ 697755	₺14,248,394.86	₺10,397,000.00	₺29.313.185,00	₺21.389.720,56
11	Selçuklu Öğretmen Fethiye Onsun 32 Derslik İlkokul Yapım İşi	2021/ 718485	₺14,200,647.79	₺15,480,000.00	₺29.214.955,08	₺31.846.962,99
12	Tuzlukçu 8 Derslik Ortaokul Yapım İşi	2021/ 739104	₺5,512,081.77	₺6,150,000.00	₺11.339.991,22	₺12.652.378,71

Table 2 (cont). *Training Set*

13	Aydın İli Didim İlçesi 24 Derslikli Atatürk İlkokulu Ek Bina Yapım İşi	2021/ 744558	₺13,064,889.41	₺12,913,000.00	₺26.878.362,37	₺26.565.880,69
14	Sinop Türkeli İmam Hatip Ortaokulu(16 Derslik) Yapım İşi	2021/ 781382	₺10,833,936.25	₺12,656,936.25	₺22.288.628,35	₺26.039.081,42
15	Artvin Kemalpaşa İlçesi İlkokul ve Ortaokul Yapım İnşaatı	2021/ 900450	₺34,750,666.37	₺31,500,000.00	₺62.038.092,34	₺56.234.890,23
16	Manisa Köprübaşı 8 Derslikli Halk Eğitim Merkezi Yapım İşi	2022/ 74214	₺17,762,641.35	₺15,549,000.00	₺27.370.954,54	₺23.959.892,21
17	Ağrı İli Eleşkirt İlçesi Yanıkdere Köyü 4 Derslikli İlkokul Yapım İşi	2022/ 76912	₺2,956,400.85	₺2,311,000.00	₺4.555.601,37	₺3.561.085,01
18	Ağrı Merkez Taştekne Köyü 4 Derslikli İlkokul Yapım İşi	2022/ 77623	₺2,733,603.94	₺2,076,760.00	₺4.615.850,53	₺3.506.731,02
19	İlkadım İstasyon Ortaokulu Yapım İşi	2022/ 85979	₺21,227,950.37	₺16,870,000.00	₺32.710.746,84	₺25.995.458,33
20	Antalya Kepez Esentepe 24 Derslikli İlkokul Yapım İşi	2022/ 90520	₺28,850,368.32	₺28,230,000.00	₺44.456.345,43	₺43.500.402,41
21	Dazkırı İlçesi Kızılören Köyü 4 Derslikli Ortaokul Yapım İşi	2022/ 104707	₺2,609,234.35	₺2,175,000.00	₺4.405.845,18	₺3.672.615,02
22	Hamur İlçesi Karakozan Köyü 8 Derslikli İlkokul Yapım İşi	2022/ 139925	₺7,917,781.10	₺7,815,000.00	₺12.200.731,99	₺12.042.353,70
23	Amasya Merkez 12 Derslikli Tuğgeneral Hikmet Akıncı İlkokulu Yapım İşi	2022/ 510058	₺14,075,742.45	₺17,000,000.00	₺18.999.938,65	₺22.947.205,68
24	Yomra Merkez İlkokul İnşaatı Yapımı	2022/ 552400	₺28,043,333.11	₺31,416,000.00	₺43.212.762,14	₺48.409.799,58
25	Malatya Doğanşehir Karşıyaka Merkez 12 Derslikli Ortaokulu Yapım İşi	2022/ 555268	₺21,248,716.02	₺18,444,000.00	₺32.742.745,22	₺28.420.879,28
26	Ağrı İli Patnos İlçesi Alparslan Mahallesi 12 Derslikli İmamhatip Ortaokulu Yapım İşi	2022/ 573373	₺19,271,467.82	₺18,790,000.00	₺29.695.947,76	₺28.954.040,43
27	Isparta Gönen Güneykent Yunus Emre 8 Derslikli İlkokul İnşaatı Yapım işi	2022/ 578065	₺13,625,023.08	₺12,723,777.00	₺20.995.181,96	₺19.606.426,48
28	Ağrı İli Patnos İlçesi İnönü Mahallesi 16 Derslikli 75. Yıl Ortaokulu Yapım İşi	2022/ 580323	₺23,284,974.69	₺21,289,000.00	₺35.880.473,58	₺32.804.819,94
29	Afyonkarahisar Sandıklı Miralay Reşat Bey 16 Derslikli İlkokul Yapım İşi	2022/ 599172	₺16,592,094.02	₺16,283,000.00	₺25.567.225,17	₺25.090.933,49
30	Antalya Konyaaltı Çakırlar 16 Derslik İlkokul Yapım İşi	2022/ 623726	₺24,732,702.37	₺23,749,000.00	₺38.111.317,95	₺36.595.503,25
31	Antalya Kepez General Şadi ÇETİNKAYA İlkokulu Yapım İşi	2022/ 625536	₺ 45,588,409.64	₺ 45,487,000.00	₺57.804.929,79	₺57.676.344,98
32	Antalya Kepez Yeni Mahalle 32 Derslik İlkokul Yapım İşi	2022/ 635162	₺ 47,466,964.79	₺ 46,919,660.00	₺60.186.889,36	₺59.492.920,97

33	Gaziantep İli Şahinbey İlçesi Dayı Ahmet Ağa İlkokulu Ek Bina Şahintepe Mah. 349 ada 1 parsele 24 Derslik İlkokul Yapım İşi	2022/ 636291	₺ 21,903,191.66	₺ 19,456,000.00	₺27.772.683,15	₺24.669.707,12
34	İlimiz Merkez Atatürk Anadolu Lisesi Binası Yapım İşi	2022/ 638323	₺ 31,748,903.66	₺ 27,378,378.78	₺48.922.780,21	₺42.188.115,27

Table 2 (cont). *Training Set*

35	Malatya Doğanşehir Gedikağzı 8 Derslikli Mustafa Kemal İmam Hatip Ortaokulu Yapım İşi	2022/ 643647	₺ 18,791,425.85	₺ 16,717,000.00	₺28.956.237,56	₺25.759.696,32
36	Diyarbakır İli Kulp İlçesi Uzunova Mahallesi 212 Ada 21 Nolu Parselde 8 Derslikli Ortaokul yapım İşi	2022/ 658379	₺ 16,040,560.04	₺ 12,253,000.00	₺20.339.017,18	₺15.536.488,56
37	Elazığ Merkez 24 Derslikli İmam Hatip Lisesi Yapım İşi	2022/ 685257	₺ 20,158,630.32	₺ 18,545,000.00	₺25.065.168,29	₺23.058.786,17
38	Hafik 12 Derslikli Okul Yapım İşi	2022/ 691992	₺ 17,599,626.62	₺ 16,225,700.00	₺21.883.312,31	₺20.174.976,90
39	Altıeylül İlçesine 24 Derslikli İlkokul Yapım İşi	2022/ 693431	₺ 19,579,105.78	₺ 19,579,105.78	₺24.344.589,57	₺23.624.531,53
40	Sivas Merkez Kurtlapa 12 Derslikli Okul Yapım işi	2022/ 695001	₺ 20,054,438.30	₺ 19,400,000.00	₺24.935.616,31	₺24.121.890,08
41	Bandırma İlçesine 24 Derslikli İlkokul Yapım İşi	2022/ 712397	₺ 35,019,324.53	₺ 33,033,000.00	₺43.542.901,92	₺41.073.113,15
42	İzmir İli Bergama İlçesi 643 Ada 7 Parsel 24 Derslik Ortaokul Yapım İşi	2022/ 724543	₺ 38,419,956.94	₺ 32,545,000.00	₺47.771.236,00	₺40.466.335,10
43	Şırnak İli Silopi İlçesi 111 Ada 49 Parsel 24 Derslikli Ortaokul Yapım İşi	2022/ 752039	₺ 19,289,958.49	₺ 15,730,000.00	₺23.985.064,87	₺19.558.625,31
44	Yenimahalle İlçesi, (Yenibatı Mh 13384 Ada 28 Parsel) Ortaokul (32 Derslik) Yapım İşi	2022/ 761112	₺ 55,637,918.72	₺ 47,407,000.00	₺69.179.987,62	₺58.945.692,95
45	Bilecik Merkez 24 Derslikli İlkokul Bina Yapım İşi	2022/ 777106	₺ 30,502,947.97	₺ 28,433,000.00	₺37.341.709,63	₺34.807.679,27
46	Gaziantep İli Nizip İlçesi Fatih Sultan Mah Ortaokulu Fatih Sultan MAH 1538 ada 94 parsel 32 derslik ortaokul Yapım İşi	2022/ 800074	₺ 39,172,466.01	₺ 32,700,000.00	₺47.954.933,81	₺40.031.340,77
47	Çaykara Karaçam İlkokul ve Ortaokul İnşaatı Yapım İşi	2022/ 1112069	₺11,696,327.44	₺11,619,000.00	₺13.682.502,48	₺13.592.043,92
48	Akyazı Kuzuluk İlkokulu 16 Derslik Yeni Bina Yapım İşi	2022/ 1129907	₺22,843,656.56	₺22,344,600.00	₺26.722.780,21	₺26.138.977,93
49	Sinop Durağan İlçesi 4 Derslikli İlkokul Binası Yapım İşi	2022/ 1145373	₺14,731,171.57	₺12,355,000.00	₺17.232.699,11	₺14.453.025,44
50	Altıeylül 12 Derslikli Edip Gürcün İlkokulu Yapım İşi	2022/ 1147319	₺18,623,901.98	₺16,713,000.00	₺21.786.461,28	₺19.551.065,50
51	Elazığ Merkez 24 Derslikli Fatih Anadolu Lisesi Yapım İşi	2022/ 1150115	₺36,198,279.01	₺26,417,000.00	₺42.345.175,84	₺30.902.919,72
52	Malatya Üçbağlar Hacı İbrahim Işık 32 Derslikli İlkokul Yapım İşi	2022/ 1151197	₺41,288,031.82	₺38,418,999.00	₺47.612.261,87	₺44.303.769,41
53	Karatay Fevzi Çakmak 32 Derslikli İlkokul Yapım İşi	2022/ 1159441	₺35,434,674.06	₺34,400,000.00	₺41.451.901,72	₺40.241.527,74
54	Meram Kalfalar 32 Derslik Ortaokulu Yapım İşi	2022/ 1159448	₺35,532,274.56	₺32,305,000.00	₺40.974.875,45	₺37.253.268,13

55	Diyarbakır İli Kayapınar İlçesi Taban Mahallesi 154 Ada 4 Parselde 12 Derslikli İlkokul Yapım İşi	2022/ 1163306	₺21,120,484.73	₺15,421,000.00	₺24.355.582,13	₺17.783.087,69
56	Diyarbakır İli Kayapınar İlçesi Kaldırım Mahallesi 101 Ada 431 Parselde 8 Derslikli İlkokul Yapım İşi	2022/ 1163671	₺16,088,016.29	₺11,058,000.00	₺18.819.952,15	₺12.935.779,47

Table 2 (cont). *Training Set*

57	Susurluk 12 Derslikli Şerafettin Tunalı İlkokulu Yapım İşi	2022/ 1182770	₺17,828,680.69	₺16,813,000.00	₺20.559.561,12	₺19.388.305,12
58	Sındırgı 12 Derslikli Kurtuluş İlkokulu Yapım İşi	2022/ 1182883	₺19,062,193.70	₺16,667,000.00	₺21.982.015,57	₺19.219.941,80
59	Bursa İli Osmangazi İlçesi Yunuseli Mahallesi 8849 Ada 19 Parsel 32 Derslikli İlkokul Yapım İşi	2022/ 1199194	₺47,702,294.86	₺45,813,061.00	₺55.009.019,68	₺52.830.405,36
60	Bursa İli Yıldırım İlçesi Millet Mahallesi 3086 Ada 1 Parsel 32 Derslikli Ortaokul Yapım İşi	2022/ 1200774	₺52,764,920.28	₺46,912,000.00	₺60.847.104,87	₺54.097.672,63
61	Bursa İli Osmangazi İlçesi Emek Mahallesi 518 Ada 1 Parsel 32 Derslik İlkokul Yapım İşi	2022/ 1201929	₺36,704,767.18	₺32,363,000.00	₺42.326.962,80	₺37.320.152,19
62	Bursa İli Yıldırım İlçesi Şirinevler 32 Derslikli Ortaokul Yapım İşi	2022/ 1202204	₺32,993,060.65	₺30,887,000.00	₺38.046.721,40	₺35.618.068,18
63	Bursa İli Yıldırım İlçesi Millet Mahallesi 3065 Ada 5 Parsel 32 Derslikli Ortaokul Yapım İşi	2022/ 1202463	₺37,702,698.91	₺33,000,000.00	₺43.477.751,17	₺38.054.723,67
64	Bingöl Altınçağ 16 Derslikli Ortaokul Yapım İşi	2022/ 1206460	₺23,038,739.40	₺22,366,000.00	₺26.567.662,47	₺25.791.877,26
65	Hanönü 8 Derslikli Ortaokulu Binası Yapım İşi	2022/ 1208747	₺20,727,363.51	₺20,621,000.00	₺23.902.245,18	₺23.779.589,60
66	Başçiftlik Çok Programlı Anadolu Lisesi Yapım İşi	2022/ 1219402	₺17,322,391.55	₺16,360,660.00	₺19.975.721,93	₺18.866.678,65
67	Karatay Hacısadık Ortaokulu 32 Derslik Yapım İşi	2022/ 1230517	₺37,042,028.46	₺38,732,000.00	₺42.715.883,55	₺44.664.713,85
68	Tarsus 100 Yıl İlkokulu Yapım İşi	2022/ 1247968	₺30,306,745.60	₺28,880,000.00	₺34.948.934,22	₺33.303.649,08
69	Mersin Akdeniz Fevzi Çakmak 32 Derslik Okul İnşaatı Yapım	2022/ 1248332	₺46,044,311.83	₺37,370,049.00	₺53.097.077,68	₺43.094.148,13
70	Gönen 16 Derslikli Mehmet Çanakçı İlkokulu Yapım İşi	2022/ 1250375	₺19,270,325.27	₺17,733,000.00	₺22.222.027,37	₺20.449.224,69
71	Erdek 12 Derslikli Kapıdağ MTAL Yapım İşi	2022/ 1264907	₺19,062,178.42	₺18,213,000.00	₺21.981.997,95	₺21.002.747,95
72	Siirt İli Kurtalan İlçesi Aksöğüt Köyü 8 Derslik İlk-Orta Okulu Yapım İşi	2022/ 1284341	₺9,349,630.19	₺7,273,000.00	₺10.781.745,25	₺8.387.030,46
73	Mersin Toroslar Arpaçsakarlar 32 Derslik Ortaokul İnşaatı	2022/ 1295596	₺50,507,014.25	₺41,821,000.00	₺58.243.347,60	₺48.226.866,62
74	Mersin Yenişehir Cumhuriyet İlkokulu Bina	2022/ 1296202	₺46,257,833.94	₺36,940,000.00	₺53.343.305,70	₺42.598.227,04
75	Ereğli Aziziye 24 Derslik İlkokulu Yapım İşi	2022/ 1298030	₺24,245,858.84	₺23,260,000.00	₺27.959.680,55	₺26.822.814,32
76	Karesi 24 Derslikli Atatürk MTAL Lise Yapım İşi	2022/ 1298485	₺32,722,272.37	₺29,940,000.00	₺37.734.455,54	₺34.526.012,93

77	Bandırma 24 Derslikli İmam Hatip Lisesi Yapım İşi	2022/ 1298510	₺32,969,222.65	₺29,250,000.00	₺38.019.232,05	₺33.730.323,25
78	Çorum İskilip İlçesi Ebussud Efendi İlkokulu Yapımı İnşaatı	2022/ 1299346	₺18,029,054.38	₺19,376,000.00	₺20.790.626,74	₺22.343.888,66

Table 2 (cont). *Training Set*

79	Mersin Tarsus 100. Yıl Ortaokulu Yapım İşi	2022/ 1336676	₺30,001,902.75	₺29,990,000.00	₺34.597.397,54	₺34.583.671,60
80	Ordu İli Kumru İlçesi Şehit Neşe Eryetim İmam Hatip Ortaokulu Yapım İşi	2022/ 1339580	₺17,441,476.32	₺17,647,000.00	₺17.441.476,32	₺17.647.000,00
81	Mersin Yenişehir Dr.Kamil TARHAN Orta Okulu Yapım İşi	2022/ 1352397	₺30,240,371.36	₺25,921,000.00	₺34.872.393,21	₺29.891.408,86

Table 3. *Test Set*

Number	**Project Name**	**EKAP Number**	**Approximate Cost (TL)**	**Contract Price (TL)**	**Updated Approximate Cost (2023 January)**	**Updated Contract Price (2023 January)**
1	Yalova Teşfikiye 8 Derslikli İlköğretim Okulu Yapım İşi	2020/ 652247	₺5,144,773.67	₺4,145,000.00	₺17.754.017,80	₺14.303.914,71
2	Seyhan İlçesi Fatih Mehmet 24 Derslikli İlkokul Yapım İşi	2021/ 678349	₺11,549,480.83	₺9,645,600.00	₺27.490.588,27	₺22.958.886,39
3	Tunceli Merkez 12 Derslikli Ortaokulu Yapımı	2021/ 788903	₺14,732,311.59	₺12,289,000.00	₺30.308.745,61	₺25.282.127,15
4	Akyazı Alaağaç İlkokulu-Ortaokulu 8 Derslikli Yeni Bina	2021/ 872200	₺5,732,314.68	₺6,329,000.00	₺10.233.526,56	₺11.298.749,85
5	Dazkırı İlçesi Şerife Memiş UÇAR 4 Derslikli İlkokul Yapım İşi	2022/ 103527	₺2,753,214.86	₺2,594,800.00	₺4.648.964,72	₺4.381.471,94
6	Ağrı Merkez Cumhuriyet Mahallesi 12 Derslikli İlkokul Yapım İşi	2022/ 571617	₺20,821,311.83	₺18,485,000.00	₺32.084.146,06	₺28.484.057,33
7	Mersin İli Akdeniz İlçesi Ulubatlı Hasan 24 Derslikli Ortaokul Bina İnşaatı	2022/ 1123063	₺29,920,269.76	₺25,965,000.00	₺34.503.260,54	₺29.942.148,49
8	Malatya İli Battalgazi İlçesi Hatunsuyu Saray 4 Derslikli İlkokul Yapım İşi	2022/ 1151194	₺14,882,398.57	₺12,144,444.00	₺17.409.606,25	₺14.206.714,54
9	Bursa İli İnegöl İlçesi 1767 Ada 1 Parsel 32 Derslik Ortaokul Yapım İşi	2022/ 1191537	₺39,678,634.50	₺36,780,000.00	₺45.756.347,62	₺42.413.719,29
10	Bursa İli Gürsu İlçesi 217 Ada 5 Parsel 32 Derslik Ortaokul Yapım İşi	2022/ 1201569	₺40,502,163.31	₺34,850,000.00	₺46.706.019,18	₺40.188.094,54
11	Gürpınar İlçesi Atatürk İlkokulu 8 Derslik Yapımı ve Çevre Düzenleme İşi	2022/ 1211745	₺21,570,694.37	₺15,365,000.00	₺24.874.751,93	₺17.718.509,98
12	Burhaniye 12 Derslikli Şehit Yılmaz Kobak İlkokulu Yapım İşi	2022/ 1259556	₺20,764,093.35	₺18,649,000.00	₺23.944.601,05	₺21.505.531,57
13	Ereğli Mehmet Akif Mahallesi 24 Derslik İlkokulu Yapım İşi	2022/ 1297609	₺22,539,471.31	₺22,342,000.00	₺25.991.919,77	₺25.764.201,10
14	Bandırma 24 Derslikli Haydar Çavuş MTAL Lise Yapım İşi	2022/ 1298507	₺32,454,585.73	₺30,942,000.00	₺37.425.766,42	₺35.681.492,72

15	Ayvalık Altınova 12 Derslikli İlkokulu Yapım İşi	2022/ 1333690	₺20,099,949.64	₺17,182,000.00	₺23.178.728,16	₺19.813.826,12

C. DATA SET CREATION

This section provides information about the construction projects for educational buildings tendered under Law No. 4734 on Public Procurement.

C.1. Characteristics of Projects Used in the Analysis

In this study, 96 construction projects for educational buildings, tendered and contracted by institutions subject to Law No. 4734 between 2020 and 2022, were utilized.

C.2. Measurement Calculation

Measurement calculation is the process of determining quantities by measuring each work item from the construction drawings. The measurement work performed to determine the cost of the building is a detailed and time-consuming phase carried out by both the public institution tendering the work and the bidders.

This section describes the measurement work conducted to create the dataset used in the study. Measurement items deemed suitable for educational building cost modeling were selected. For this study, 18 main measurement items known to affect building costs were chosen, and these items form the independent variables of the dataset. The characteristics of these independent variables are described below:

C.2.1. Number of Classrooms

This refers to the number of classrooms in the educational buildings to be constructed. The dataset includes buildings with a minimum of 2 classrooms and a maximum of 32 classrooms.

C.2.2. Construction Duration

This is the duration proposed by the contracting institution for the completion of construction, as stated in the tender documents. The minimum project duration in the dataset is 100 days, and the maximum is 750 days.

C.2.3. Total Number of Floors

Buildings consisting of a single block were preferred in the projects. Among the projects in the dataset, the minimum number of floors, including the basement, is 1, and the maximum is 5.

C.2.4. Floor Height

This independent variable refers to the floor height specified for the normal floors of a building in the project. The measurement of height is from the top of one floor slab to the top of the next floor slab. The minimum floor height in the dataset is 3.20 meters, and the maximum is 4.00 meters.

C.2.5. Building Height

This independent variable represents the difference between the building's +0.00 elevation and the top of the uppermost floor slab (excluding roof height). The minimum building height in the dataset is 3.20 meters, and the maximum is 20.50 meters.

C.2.6. Building Height Class

This independent variable refers to the Building Height Classes defined by the 2018 Earthquake Regulation. Buildings are categorized into eight Building Height Classes (BHC) based on their heights. The height ranges defined for these classes are determined according to the Earthquake Design Classes. In the dataset, the Building Height Class is named according to its number. The minimum value in the dataset is 5, and the maximum value is 8.

Table 4. *Building Height Ranges Defined According to Building Height Classes and Earthquake Design Classes [13]*

Building Height Class	**Building Height Ranges Defined According to Building Height Classes and Earthquake Design Classes [m]**		
	DTS = 1, 1a, 2, 2a	**DTS = 3, 3a**	**DTS = 4, 4a**
BYS=1	$H_N > 70$	$H_N > 91$	$H_N > 70$
BYS=2	$56 > H_N \geq 70$	$70 > H_N \geq 91$	$H_N > 70$
BYS=3	$42 > H_N \geq 56$	$56 > H_N \geq 70$	$H_N > 70$
BYS=4	$28 > H_N \geq 42$	$42 > H_N \geq 56$	
BYS=5	$17.5 > H_N \geq 28$	$28 > H_N \geq 42$	
BYS=6	$10.5 > H_N \geq 17.5$	$17.5 > H_N \geq 28$	
BYS=7	$7 > H_N \geq 10.5$	$10.5 > H_N \geq 17.5$	
BYS=8	$H_N \leq 7$	$H_N \leq 10.5$	

C.2.7. Basement Floor Height

This independent variable represents the number of floors located below the natural ground level (zero elevation) in the projects. A total of 16 buildings do not have a basement. There are basements in 80 buildings. In the dataset, the minimum basement floor height is 0.00 meters, and the maximum basement height is 5.15 meters.

C.2.8. Earthquake Design Class

This independent variable is determined based on the Building Use Classes defined by the 2018 Earthquake Regulation and the Short Period Design Spectral Acceleration Coefficient for the DD-2 earthquake ground motion level. The Earthquake Design Classes to be considered in design under earthquake effects are specified according to this Regulation.

Table 5. *Short Period Design Spectral Acceleration Coefficient at DD-2 Earthquake Ground Motion Level [13]*

Short Period Design Spectral Acceleration Coefficient (S_{DS}) at DD-2 Earthquake Ground Motion Level	**Building Usage Class**	
	BKS = 1	**BKS = 2, 3**
$S_{DS} < 0.33$	DTS = 4a	DTS = 4
$0.33 \leq S_{DS} < 0.50$	DTS = 3a	DTS = 3
$0.50 \leq S_{DS} < 0.75$	DTS = 2a	DTS = 2
$0.75 \leq S_{DS}$	DTS = 1a	DTS = 1

Table 6. *Values defined according to Earthquake Design Class in the Data Set*

DTS	Defined Value
1a	**1**
2a	**2**
3a	**3**
4a	**4**
1	**5**
2	**6**
3	**7**
4	**8**

The minimum value in the dataset is 1, and the maximum value is 5.

C.2.9. Soil Class

This independent variable represents the soil classification based on particle size and consistency, ranging between ZA and ZF. The soil classes for the projects in this study have been determined based on information from structural projects or geotechnical reports. The dataset includes projects representing all soil classes ranging from ZB to ZE.

Table 7. *Ground Class Values [13]*

Local Ground Class	Soil Type	Average in the upper 30 meters		
		$(Vs)_{30}$ [m/s]	**$(N_{60})_{30}$ [darbe/30 cm]**	**$(Cu)_{30}$ [kPa]**
ZA	Solid, hard rocks	> 1500	-	-
ZB	Slightly weathered, medium-solid rocks	760 - 1500	-	-
ZC	Very dense layers of sand, gravel and hard clay or weathered, weak rocks with many cracks	360 - 760	> 50	> 250
ZD	Medium-tight sand, gravel or very solid clay layers	180 - 360	15 - 50	70 - 250
ZE	Loose sand, gravel or soft-solid clay layers Profiles with a total thickness of more than 3 meters of soft clay layer (cu < 25 kPa) that meet the conditions of PI > 20 and w> 40%.	< 180	< 15	< 70
ZF	ZF Grounds requiring site-specific research and evaluation: 1) Soils at risk of collapse and potential collapse under the influence of earthquake (liquefiable soils, highly sensitive clays, collapsible weakly cemented soils, etc.), 2) Peat and/or clays with high organic content, with a total thickness of more than 3 meters, 3) High plasticity (PI > 50) clays with a total thickness of more than 8 meters, 4) Very thick (> 35 m) soft or medium solid clays.			

Table 8. *Values defined according to Soil Class in the Data Set*

Graund Class	Defined Value
ZA	1
ZB	2
ZC	3
ZD	4
ZE	5
ZF	6

C.2.10. Soil Bearing Capacity

This independent variable, like the soil class variable, varies according to the structure of the soil on which the projects will be built. It represents the maximum stress that the soil can safely bear. In this study, soil bearing capacity values were determined based on information found in static projects or geotechnical reports. The dataset includes projects with a maximum soil bearing capacity of 116 t/m² and a minimum of 8.50 t/m².

C.2.11. Soil Bedding Coefficient

Another independent variable calculated to determine the structure of the soil on which the projects will be built is the bedding coefficient. This variable represents the volumetric change in the soil due to the weight that will affect the soil as a result of the building's construction. In this study, the bedding coefficient was determined based on information found in static projects or geotechnical reports. The dataset shows that the bedding coefficient ranges from a maximum of 15,000 t/m³ to a minimum of 1,100 t/m³.

C.2.12. Concrete Class

This independent variable represents the concrete class value found in static calculations and projects. The concrete class is determined by the results of tests performed on cube and cylinder samples used in static calculations and expresses the compressive strength of the concrete. The dataset includes projects with concrete classes of C25, C30, C35, and C40. In the analyses, a value of 25 represents C25, 30 represents C30, 35 represents C35, and 40 represents C40.

C.2.13. Number of Elevators

This independent variable indicates the number of elevators in the project. There are 7 buildings with no elevators, 70 buildings with 1 elevator, and 19 buildings with 2 elevators in the dataset.

C.2.14. Wet Area

The bathroom and WC areas in architectural projects are referred to as "Wet Areas." This independent variable is determined by the total of the wet areas on each floor in the project. The projects in the dataset have a minimum wet area of 22.62 m² and a maximum wet area of 387.91 m².

C.2.15. Height of Raft Foundation Type

This independent variable is determined based on the foundation drawings and details in the static projects. The dataset shows that the minimum value is 0.30 m and the maximum value is 1.20 m.

C.2.16. Floor Area

This independent variable represents the area of a typical floor in the projects that make up the dataset. If a building has different typical floor areas, the value of the most common typical floor is taken. The projects in the dataset have a minimum floor area of 413.29 m² and a maximum floor area of 1,270.32 m².

C.2.17. Basement Area

This independent variable represents the area of the floors below the ground level, which is defined as the zero level, determined by the architectural and static calculations of the projects. The dataset includes projects with a minimum basement area of 0 m² and a maximum of 1,427.60 m².

C.2.18. Total Construction Area

This independent variable represents the total construction area of the floors in the project. The dataset shows that the floor area ranges from a minimum of 325.00 m² to a maximum of 9,113.12 m².

Using the 18 calculated variables above, an analysis was conducted to estimate the Contract Amount and Approximate Cost.

D. MODEL DEVELOPMENT USİNG MULTİPLE LİNEAR REGRESSİON

In the modeling study, variables such as Number of Classrooms, Construction Duration (days), Total Number of Floors, Floor Height (meters), Building Height (from +0.00 level, meters), Building Height Class (BYS), Basement Height (meters), Earthquake Design Class (DTS), Soil Class, Soil Bearing Capacity (t/m²), Bedding Coefficient (t/m³), Concrete Class, Number of Elevators, Wet Area (m²), Height of Raft Foundation (meters), Floor Area (m²), Basement Area (m²), and Total Area (m²) were taken as independent variables. The aim was to explain the project's Contract Amount and approximate cost values using these variables. The SPSS software package was used to develop a multiple regression model. The regression analysis of 81 school projects yielded the following results:

D.1. Contract Amount Regression Model

Contract Amount = − 2349012.559 + 46452.464 × **(Number of Classrooms)** − 277.169 × **(Construction Duration)** + 496947.262 × **(Total Number of Floors)** + 2021313.907 × **(Floor Height)** − 445038.095 × **(Building Height)** − 2020336.669 × **(Building Height Class)** − 2413730.060 × **(Basement Height)** + 21079.829 × **(Earthquake Design Class)** + 196257.334 × **(Soil Class)** − 34217.334 × **(Soil Bearing Capacity)** + 207.823 × **(Bedding Coefficient)** + 427461.327 × **(Concrete Class)** + 5537494.092 × **(Number of Elevators)** + 16687.841 × **(Wet Area)** + 9752894.338 × **(Height of Raft Foundation)** − 2534.565 × **(Floor Area)** + 12246.067 × **(Basement Area)** + 3711.671 × **(Total Area)**

Table 9. *Regression model prediction results of educational structures*

Number	Project Name	Updated Contract Price (2023 January)	Contract Price Estimated by Regression Equation	Error rate
1	Yalova Teşfikiye 8 Derslikli İlköğretim Okulu Yapım İşi	₺14.303.914,71	₺19.749.333.37	38.1%
2	Seyhan İlçesi Fatih Mehmet 24 Derslikli İlkokul Yapım İşi	₺22.958.886,39	₺30.063.223.09	30.9%
3	Tunceli Merkez 12 Derslikli Ortaokulu Yapımı	₺25.282.127,15	₺22.520.388.60	10.9%
4	Akyazı Alaağaç İlkokulu-Ortaokulu 8 Derslikli Yeni Bina	₺11.298.749,85	₺16.064.295.08	42.2%
5	Dazkırı İlçesi Şerife Memiş UÇAR 4 Derslikli İlkokul Yapım İşi	₺4.381.471,94	₺2.569.036.56	41.4%
6	Ağrı Merkez Cumhuriyet Mahallesi 12 Derslikli İlkokul Yapım İşi	₺28.484.057,33	₺30.083.289.02	5.6%
7	Mersin İli Akdeniz İlçesi Ulubatlı Hasan 24 Derslikli Ortaokul Bina İnşaatı	₺29.942.148,49	₺28.215.690.19	5.8%
8	Malatya İli Battalgazi İlçesi Hatunsuyu Saray 4 Derslikli İlkokul Yapım İşi	₺14.206.714,54	₺15.463.565.98	8.8%

Table 9. (cont.) *Regression model prediction results of educational structures*

9	Bursa İli İnegöl İlçesi 1767 Ada 1 Parsel 32 Derslik Ortaokul Yapım İşi	₺42.413.719,29	₺47.098.209.85	11.0%
10	Bursa İli Gürsu İlçesi 217 Ada 5 Parsel 32 Derslik Ortaokul Yapım İşi	₺40.188.094,54	₺44.822.007.71	11.5%
11	Gürpınar İlçesi Atatürk İlkokulu 8 Derslik Yapımı ve Çevre Düzenleme İşi	₺17.718.509,98	₺18.507.047.52	4.5%
12	Burhaniye 12 Derslikli Şehit Yılmaz Kobak İlkokulu Yapım İşi	₺21.505.531,57	₺24.547.419.40	14.1%
13	Ereğli Mehmet Akif Mahallesi 24 Derslik İlkokulu Yapım İşi	₺25.764.201,10	₺23.973.879.22	6.9%
14	Bandırma 24 Derslikli Haydar Çavuş MTAL Lise Yapım İşi	₺35.681.492,72	₺29.420.229.43	17.5%
15	Ayvalık Altınova 12 Derslikli İlkokulu Yapım İşi	₺19.813.826,12	₺24.386.985.98	23.1%
	AVERAGE ERROR VALUE			18,20%

Table 10. *Statistical data on Educational Buildings*

Model	Sum of Squares	Df	Mean Squares	F	p
Regression Sum of Squares	1340831142188650 0,000	18	744906190104806,000	43,620	,000[b]
Residual Sum of Squares	1058793525979290,000	62	17077314935149,900		
Grand Sum of Squares	14467104947865800,000	80			

Based on the calculations, the F-statistic value was determined to be 43.620. Using the F-table, it was found that the p-value is p<0.05, indicating that the model is statistically significant.

Table 11. *Statistical data on educational structures (Relationships Between Independent Variables)*

		Updated Contract Price (TL)	Number of Classrooms	Construction Time (Days)	Total Number of Floors	Floor Height (m)	Building Height (m)	Building Height Class	Basement Height (m)	Earthquake Design Class	Ground Class	Ground safety tension	Ground Bed Coefficient	Concrete Grade	Number of Elevators	Wet Area (m²)	Raft Foundation Height (m)	Floor Area (m²)	Basement Area (m²)	Total Area (m²)
Updated Contract Price (TL)	r	1,00	0,84	0,46	0,67	0,40	0,66	-0,49	0,49	0,12	-0,04	-0,03	-0,02	0,28	0,75	0,86	0,71	0,81	0,81	0,93
	p		0,00	0,00	0,00	0,00	0,00	0,00	0,00	0,15	0,37	0,38	0,45	0,01	0,00	0,00	0,00	0,00	0,00	0,00
Number of Classrooms	r	0,84	1,00	0,39	0,75	0,25	0,71	-0,42	0,51	0,15	0,00	-0,09	-0,08	0,31	0,64	0,77	0,63	0,68	0,76	0,89
	p	0,00		0,00	0,00	0,01	0,00	0,00	0,00	0,09	0,48	0,21	0,25	0,00	0,00	0,00	0,00	0,00	0,00	0,00
Construction Time (Days)	r	0,46	0,39	1,00	0,52	0,29	0,47	-0,41	0,45	-0,01	0,09	-0,05	0,20	0,06	0,45	0,34	0,25	0,27	0,42	0,43
	p	0,00	0,00		0,00	0,00	0,00	0,00	0,00	0,48	0,22	0,34	0,04	0,30	0,00	0,00	0,01	0,01	0,00	0,00
Total Number of Floors	r	0,67	0,75	0,52	1,00	0,37	0,93	-0,68	0,77	0,18	0,01	-0,13	-0,12	0,25	0,60	0,64	0,59	0,35	0,68	0,72
	p	0,00	0,00	0,00		0,00	0,00	0,00	0,00	0,05	0,45	0,12	0,15	0,01	0,00	0,00	0,00	0,00	0,00	0,00
Floor Height (m)	r	0,40	0,25	0,29	0,37	1,00	0,48	-0,45	0,38	0,12	-0,16	-0,11	-0,04	0,24	0,46	0,30	0,27	0,34	0,37	0,34
	p	0,00	0,01	0,00	0,00		0,00	0,00	0,00	0,14	0,08	0,17	0,38	0,01	0,00	0,00	0,01	0,00	0,00	0,00
Building Height (m)	r	0,66	0,71	0,47	0,93	0,48	1,00	-0,71	0,67	0,11	-0,05	-0,09	-0,12	0,28	0,62	0,62	0,56	0,38	0,63	0,70
	p	0,00	0,00	0,00	0,00	0,00		0,00	0,00	0,17	0,33	0,21	0,14	0,01	0,00	0,00	0,00	0,00	0,00	0,00
Building Height Class	r	-0,49	-0,42	-0,41	-0,68	-0,45	-0,71	1,00	-0,49	0,09	-0,02	0,19	0,18	-0,41	-0,34	-0,49	-0,43	-0,15	-0,39	-0,42
	p	0,00	0,00	0,00	0,00	0,00	0,00		0,00	0,22	0,44	0,04	0,05	0,00	0,00	0,00	0,00	0,09	0,00	0,00

Table 11.(cont.) *Statistical data on educational structures (Relationships Between Independent Variables)*

Basement Height (m)	r	0,49	0,51	0,45	0,77	0,38	0,67	-0,49	1,00	0,19	-0,07	-0,05	-0,06	0,29	0,47	0,53	0,47	0,30	0,79	0,55
	p	0,00	0,00	0,00	0,00	0,00	0,00	0,00		0,04	0,26	0,32	0,28	0,00	0,00	0,00	0,00	0,00	0,00	0,00
Earthquake Design Class	r	0,12	0,15	-0,01	0,18	0,12	0,11	0,09	0,19	1,00	-0,39	0,07	0,27	-0,17	0,17	0,08	0,10	0,19	0,22	0,18
	p	0,15	0,09	0,48	0,05	0,14	0,17	0,22	0,04		0,00	0,27	0,01	0,06	0,06	0,24	0,18	0,05	0,03	0,05
Ground Class	r	-0,04	0,00	0,09	0,01	-0,16	-0,05	-0,02	-0,07	-0,39	1,00	-0,33	-0,48	0,07	-0,17	-0,09	-0,08	-0,12	-0,07	-0,05
	p	0,37	0,48	0,22	0,45	0,08	0,33	0,44	0,26	0,00		0,00	0,00	0,26	0,07	0,21	0,25	0,14	0,26	0,34
Ground safety tension	r	-0,03	-0,09	-0,05	-0,13	-0,11	-0,09	0,19	-0,05	0,07	-0,33	1,00	0,45	-0,01	-0,01	0,02	0,04	0,02	-0,01	-0,06
	p	0,38	0,21	0,34	0,12	0,17	0,21	0,04	0,32	0,27	0,00		0,00	0,45	0,46	0,42	0,37	0,42	0,46	0,29
Ground Bed Coefficient	r	-0,02	-0,08	0,20	-0,12	-0,04	-0,12	0,18	-0,06	0,27	-0,48	0,45	1,00	-0,31	0,09	-0,13	-0,12	0,03	-0,04	-0,05
	p	0,45	0,25	0,04	0,15	0,38	0,14	0,05	0,28	0,01	0,00	0,00		0,00	0,21	0,12	0,13	0,38	0,37	0,34
Concrete Grade	r	0,28	0,31	0,06	0,25	0,24	0,28	-0,41	0,29	-0,17	0,07	-0,01	-0,31	1,00	0,01	0,31	0,38	0,11	0,29	0,23
	p	0,01	0,00	0,30	0,01	0,01	0,01	0,00	0,00	0,06	0,26	0,45	0,00		0,45	0,00	0,00	0,15	0,00	0,02
Number of Elevators	r	0,75	0,64	0,45	0,60	0,46	0,62	-0,34	0,47	0,17	-0,17	-0,01	0,09	0,01	1,00	0,63	0,47	0,73	0,66	0,78
	p	0,00	0,00	0,00	0,00	0,00	0,00	0,00	0,00	0,06	0,07	0,46	0,21	0,45		0,00	0,00	0,00	0,00	0,00
Wet Area (m²)	r	0,86	0,77	0,34	0,64	0,30	0,62	-0,49	0,53	0,08	-0,09	0,02	-0,13	0,31	0,63	1,00	0,69	0,72	0,76	0,87
	p	0,00	0,00	0,00	0,00	0,00	0,00	0,00	0,00	0,24	0,21	0,42	0,12	0,00	0,00		0,00	0,00	0,00	0,00
Raft Foundation Height (m)	r	0,71	0,63	0,25	0,59	0,27	0,56	-0,43	0,47	0,10	-0,08	0,04	-0,12	0,38	0,47	0,69	1,00	0,47	0,65	0,65
	p	0,00	0,00	0,01	0,00	0,01	0,00	0,00	0,00	0,18	0,25	0,37	0,13	0,00	0,00	0,00		0,00	0,00	0,00
Floor Area (m²)	r	0,81	0,68	0,27	0,35	0,34	0,38	-0,15	0,30	0,19	-0,12	0,02	0,03	0,11	0,73	0,72	0,47	1,00	0,71	0,88
	p	0,00	0,00	0,01	0,00	0,00	0,00	0,09	0,00	0,05	0,14	0,42	0,38	0,15	0,00	0,00	0,00		0,00	0,00
Basement Area (m²)	r	0,81	0,76	0,42	0,68	0,37	0,63	-0,39	0,79	0,22	-0,07	-0,01	-0,04	0,29	0,66	0,76	0,65	0,71	1,00	0,85
	p	0,00	0,00	0,00	0,00	0,00	0,00	0,00	0,00	0,03	0,26	0,46	0,37	0,00	0,00	0,00	0,00	0,00		0,00
Total Area (m²)	r	0,93	0,89	0,43	0,72	0,34	0,70	-0,42	0,55	0,18	-0,05	-0,06	-0,05	0,23	0,78	0,87	0,65	0,88	0,85	1,00
	p	0,00	0,00	0,00	0,00	0,00	0,00	0,00	0,00	0,05	0,34	0,29	0,34	0,02	0,00	0,00	0,00	0,00	0,00	

According to the table, there are strong correlations between some variables. Including these variables in the model simultaneously could lead to multicollinearity issues. Therefore, multicollinearity checks will need to be performed in the developed model.

Table 12. *Statistical data of educational structures (Autocorrelation and Multicollinearity Assumptions Controls)*

Durbin-Watson	**1,523**
Collinearity (VIF)	
Number of Classrooms	7.524
Construction Time (Days)	1.889
Total Number of Floors	32.216
Floor Height (m)	2.179
Building Height (m)	10.897
Building Height Class	3.301
Basement Height (m)	10.720
Earthquake Design Class	1.632
Ground Class	1.981
Ground safety tension	1.698
Ground Bed Coefficient	2.340
Concrete Grade	1.913
Number of Elevators	3.905
Wet Area (m²)	6.505
Raft Foundation Height (m)	2.551
Floor Area (m²)	24.326
Basement Area (m²)	14.567
Total Area (m²)	73.277

Autocorrelation is the condition where there is a correlation between the errors in the created model. There should be no autocorrelation in a regression model, and the errors in the created model should be random. This is checked with the Durbin-Watson test. A result around 2 indicates that there is no autocorrelation problem in the model. After analysis, the Durbin-Watson test result was found to be 1.523, indicating that there is no autocorrelation problem in our model.

To check for multicollinearity in the model, we look at the Variance Inflation Factor (VIF) values for the variables. The VIF value should not exceed 10. Among the 18 independent variables included in the model, it was found that the VIF value for 12 variables is below 10. This suggests that there is no multicollinearity problem for these 12 variables. However, there is evidence of multicollinearity for the variables Total Number of Floors, Building Height, Basement Height, Floor Area, Basement Area, and Total Area.

Table 13. *Statistical data of educational structures (Autocorrelation and Multicollinearity Assumptions*

Adjusted R^2	F	p
0.927	43,620	,000[b]

.000b: means p<0.05.

The model created to explain the Contract Amount variable is seen to be a significant model (F: 43.620, p<0.05). In this significant model, the independent variables can explain 92.7% of the variation in the dependent variable.

D.2. Regression Model for Approximate Cost

Approximate Cost = − 2349012.559 + 46452.464 × **(Number of Classrooms)** − 277.169 × **(Construction Duration)** + 496947.262 × **(Total Number of Floors)** + 2021313.907 × **(Floor Height)** − 445038.095 × **(Building Height)** − 2020336.669 × **(Building Height Class)** − 2413730.060 × **(Basement Height)** + 21079.829 × **(Earthquake Design Class)** + 196257.334 × **(Soil Class)** − 34217.334 × **(Soil Bearing Capacity)** + 207.823 × **(Bedding Coefficient)** + 427461.327 × **(Concrete Class)** + 5537494.092 × **(Number of Elevators)** + 16687.841 × **(Wet Area)** + 9752894.338 × **(Height of Raft Foundation)** − 2534.565 × **(Floor Area)** + 12246.067 × **(Basement Area)** + 3711.671 × **(Total Area)**

Table 14. *Regression model prediction results of educational structures*

Number	Project Name	Updated Approximate Cost (2023 January)	Approximate Cost Estimated by Regression Equation	Error rate
1	Yalova Teşfikiye 8 Derslikli İlköğretim Okulu Yapım İşi	₺17.754.017,80	₺21.922.242.40	23.5%
2	Seyhan İlçesi Fatih Mehmet 24 Derslikli İlkokul Yapım İşi	₺27.490.588,27	₺32.098.337.10	16.8%
3	Tunceli Merkez 12 Derslikli Ortaokulu Yapımı	₺30.308.745,61	₺25.447.991.92	16.0%
4	Akyazı Alaağaç İlkokulu-Ortaokulu 8 Derslikli Yeni Bina	₺10.233.526,56	₺18.925.837.07	84.9%
5	Dazkırı İlçesi Şerife Memiş UÇAR 4 Derslikli İlkokul Yapım İşi	₺4.648.964,72	₺3.599.820.94	22.6%
6	Ağrı Merkez Cumhuriyet Mahallesi 12 Derslikli İlkokul Yapım İşi	₺32.084.146,06	₺31.063.351.51	3.2%
7	Mersin İli Akdeniz İlçesi Ulubatlı Hasan 24 Derslikli Ortaokul Bina İnşaatı	₺34.503.260,54	₺31.371.867.31	9.1%
8	Malatya İli Battalgazi İlçesi Hatunsuyu Saray 4 Derslikli İlkokul Yapım İşi	₺17.409.606,25	₺19.396.878.43	11.4%
9	Bursa İli İnegöl İlçesi 1767 Ada 1 Parsel 32 Derslik Ortaokul Yapım İşi	₺45.756.347,62	₺50.840.134.38	11.1%

Table 14. (cont.) *Regression model prediction results of educational structures*

10	Bursa İli Gürsu İlçesi 217 Ada 5 Parsel 32 Derslik Ortaokul Yapım İşi	₺46.706.019,18	₺48.573.590.66	4.0%
11	Gürpınar İlçesi Atatürk İlkokulu 8 Derslik Yapımı ve Çevre Düzenleme İşi	₺24.874.751,93	₺20.487.483.32	17.6%
12	Burhaniye 12 Derslikli Şehit Yılmaz Kobak İlkokulu Yapım İşi	₺23.944.601,05	₺26.439.331.02	10.4%
13	Ereğli Mehmet Akif Mahallesi 24 Derslik İlkokulu Yapım İşi	₺25.991.919,77	₺26.703.014.36	2.7%
14	Bandırma 24 Derslikli Haydar Çavuş MTAL Lise Yapım İşi	₺37.425.766,42	₺31.760.801.94	15.1%
15	Ayvalık Altınova 12 Derslikli İlkokulu Yapım İşi	₺23.178.728,16	₺26.294.332.91	13.4%
	AVERAGE ERROR VALUE			17,50%

Table 15. *Statistical data on Educational Buildings*

Model	Sum of Squares	Df	Mean Squares	F	p
Regression Sum of Squares	15804502379673800,00	18	878027909981875,00	39,47	,000[b]
Residual Sum of Squares	1379190948240060,00	62	22245015294194,60		
Grand Sum of Squares	17183693327913800,00	80			

Based on the calculations, the F-statistic value was determined to be 39.47. Using the F-table, it was found that the p-value is p<0.05, indicating that the created model is statistically significant.

Table 16. *Statistical data on educational structures (Relationships between Independent Variables)*

		Updated Approximate Cost (TL)	Number of Classrooms	Construction Time (Days)	Total Number of Floors	Floor Height (m)	Building Height (m)	Building Height Class	Basement Height (m)	Earthquake Design Class	Ground Class	Ground safety tension	Ground Bed Coefficient	Concrete Grade	Number of Elevators	Wet Area (m²)	Raft Foundation Height (m)	Floor Area (m²)	Basement Area (m²)	Total Area (m²)
Updated Approximate Cost (TL)	r	1,00	0,83	0,41	0,66	0,39	0,65	-0,47	0,50	0,14	-0,06	-0,06	-0,05	0,31	0,77	0,84	0,72	0,81	0,82	0,93
	p		0,00	0,00	0,00	0,00	0,00	0,00	0,00	0,11	0,30	0,29	0,32	0,00	0,00	0,00	0,00	0,00	0,00	0,00
Number of Classrooms	r	0,83	1,00	0,39	0,75	0,25	0,71	-0,42	0,51	0,15	0,00	-0,09	-0,08	0,31	0,64	0,77	0,63	0,68	0,76	0,89
	p	0,00		0,00	0,00	0,01	0,00	0,00	0,00	0,09	0,48	0,21	0,25	0,00	0,00	0,00	0,00	0,00	0,00	0,00
Construction Time (Days)	r	0,41	0,39	1,00	0,52	0,29	0,47	-0,41	0,45	-0,01	0,09	-0,05	0,20	0,06	0,45	0,34	0,25	0,27	0,42	0,43
	p	0,00	0,00		0,00	0,00	0,00	0,00	0,00	0,48	0,22	0,34	0,04	0,30	0,00	0,00	0,01	0,01	0,00	0,00
Total Number of Floors	r	0,66	0,75	0,52	1,00	0,37	0,93	-0,68	0,77	0,18	0,01	-0,13	-0,12	0,25	0,60	0,64	0,59	0,35	0,68	0,72
	p	0,00	0,00	0,00		0,00	0,00	0,00	0,00	0,05	0,45	0,12	0,15	0,01	0,00	0,00	0,00	0,00	0,00	0,00
Floor Height (m)	r	0,39	0,25	0,29	0,37	1,00	0,48	-0,45	0,38	0,12	-0,16	-0,11	-0,04	0,24	0,46	0,30	0,27	0,34	0,37	0,34
	p	0,00	0,01	0,00	0,00		0,00	0,00	0,00	0,14	0,08	0,17	0,38	0,01	0,00	0,00	0,01	0,00	0,00	0,00
Building Height (m)	r	0,65	0,71	0,47	0,93	0,48	1,00	-0,71	0,67	0,11	-0,05	-0,09	-0,12	0,28	0,62	0,62	0,56	0,38	0,63	0,70
	p	0,00	0,00	0,00	0,00	0,00		0,00	0,00	0,17	0,33	0,21	0,14	0,01	0,00	0,00	0,00	0,00	0,00	0,00
Building Height Class	r	-0,47	-0,42	-0,41	-0,68	-0,45	-0,71	1,00	-0,49	0,09	-0,02	0,19	0,18	-0,41	-0,34	-0,49	-0,43	-0,15	-0,39	-0,42
	p	0,00	0,00	0,00	0,00	0,00	0,00		0,00	0,22	0,44	0,04	0,05	0,00	0,00	0,00	0,00	0,09	0,00	0,00
Basement Height (m)	r	0,50	0,51	0,45	0,77	0,38	0,67	-0,49	1,00	0,19	-0,07	-0,05	-0,06	0,29	0,47	0,53	0,47	0,30	0,79	0,55
	p	0,00	0,00	0,00	0,00	0,00	0,00	0,00		0,04	0,26	0,32	0,28	0,00	0,00	0,00	0,00	0,00	0,00	0,00
Earthquake Design Class	r	0,14	0,15	-0,01	0,18	0,12	0,11	0,09	0,19	1,00	-0,39	0,07	0,27	-0,17	0,17	0,08	0,10	0,19	0,22	0,18
	p	0,11	0,09	0,48	0,05	0,14	0,17	0,22	0,04		0,00	0,27	0,01	0,06	0,06	0,24	0,18	0,05	0,03	0,05

Table 16.(cont.) *Statistical data on educational structures (Relationships between Independent Variables)*

Ground Class	r	-0,06	0,00	0,09	0,01	-0,16	-0,05	-0,02	-0,07	-0,39	1,00	-0,33	-0,48	0,07	-0,17	-0,09	-0,08	-0,12	-0,07	-0,05
	p	0,30	0,48	0,22	0,45	0,08	0,33	0,44	0,26	0,00		0,00	0,00	0,26	0,07	0,21	0,25	0,14	0,26	0,34
Ground safety tension	r	-0,06	-0,09	-0,05	-0,13	-0,11	-0,09	0,19	-0,05	0,07	-0,33	1,00	0,45	-0,01	-0,01	0,02	0,04	0,02	-0,01	-0,06
	p	0,29	0,21	0,34	0,12	0,17	0,21	0,04	0,32	0,27	0,00		0,00	0,45	0,46	0,42	0,37	0,42	0,46	0,29
Ground Bed Coefficient	r	-0,05	-0,08	0,20	-0,12	-0,04	-0,12	0,18	-0,06	0,27	-0,48	0,45	1,00	-0,31	0,09	-0,13	-0,12	0,03	-0,04	-0,05
	p	0,32	0,25	0,04	0,15	0,38	0,14	0,05	0,28	0,01	0,00	0,00		0,00	0,21	0,12	0,13	0,38	0,37	0,34
Concrete Grade	r	0,31	0,31	0,06	0,25	0,24	0,28	-0,41	0,29	-0,17	0,07	-0,01	-0,31	1,00	0,01	0,31	0,38	0,11	0,29	0,23
	p	0,00	0,00	0,30	0,01	0,01	0,01	0,00	0,00	0,06	0,26	0,45	0,00		0,45	0,00	0,00	0,15	0,00	0,02
Number of Elevators	r	0,77	0,64	0,45	0,60	0,46	0,62	-0,34	0,47	0,17	-0,17	-0,01	0,09	0,01	1,00	0,63	0,47	0,73	0,66	0,78
	p	0,00	0,00	0,00	0,00	0,00	0,00	0,00	0,00	0,06	0,07	0,46	0,21	0,45		0,00	0,00	0,00	0,00	0,00
Wet Area (m^2)	r	0,84	0,77	0,34	0,64	0,30	0,62	-0,49	0,53	0,08	-0,09	0,02	-0,13	0,31	0,63	1,00	0,69	0,72	0,76	0,87
	p	0,00	0,00	0,00	0,00	0,00	0,00	0,00	0,00	0,24	0,21	0,42	0,12	0,00	0,00		0,00	0,00	0,00	0,00
Raft Foundation Height (m)	r	0,72	0,63	0,25	0,59	0,27	0,56	-0,43	0,47	0,10	-0,08	0,04	-0,12	0,38	0,47	0,69	1,00	0,47	0,65	0,65
	p	0,00	0,00	0,01	0,00	0,01	0,00	0,00	0,00	0,18	0,25	0,37	0,13	0,00	0,00	0,00		0,00	0,00	0,00
Floor Area (m^2)	r	0,81	0,68	0,27	0,35	0,34	0,38	-0,15	0,30	0,19	-0,12	0,02	0,03	0,11	0,73	0,72	0,47	1,00	0,71	0,88
	p	0,00	0,00	0,01	0,00	0,00	0,00	0,09	0,00	0,05	0,14	0,42	0,38	0,15	0,00	0,00	0,00		0,00	0,00
Basement Area (m^2)	r	0,82	0,76	0,42	0,68	0,37	0,63	-0,39	0,79	0,22	-0,07	-0,01	-0,04	0,29	0,66	0,76	0,65	0,71	1,00	0,85
	p	0,00	0,00	0,00	0,00	0,00	0,00	0,00	0,00	0,03	0,26	0,46	0,37	0,00	0,00	0,00	0,00	0,00		0,00
Total Area (m^2)	r	0,93	0,89	0,43	0,72	0,34	0,70	-0,42	0,55	0,18	-0,05	-0,06	-0,05	0,23	0,78	0,87	0,65	0,88	0,85	1,00
	p	0,00	0,00	0,00	0,00	0,00	0,00	0,00	0,00	0,05	0,34	0,29	0,34	0,02	0,00	0,00	0,00	0,00	0,00	

According to the table, there are strong correlations between some variables. Including these variables in the model simultaneously could lead to multicollinearity issues. Therefore, multicollinearity checks will need to be performed in the developed model.

Table 17. *Statistical data of educational structures (Autocorrelation and Multicollinearity Assumptions Controls)*

Durbin-Watson	**1,950**
Collinearity (VIF)	
Number of Classrooms	7.524
Construction Time (Days)	1.889
Total Number of Floors	32.216
Floor Height (m)	2.179
Building Height (m)	10.897
Building Height Class	3.301
Basement Height (m)	10.720
Earthquake Design Class	1.632
Ground Class	1.981
Ground safety tension	1.698
Ground Bed Coefficient	2.340
Concrete Grade	1.913
Number of Elevators	3.905
Wet Area (m^2)	6.505
Raft Foundation Height (m)	2.551
Floor Area (m^2)	24.326
Basement Area (m^2)	14.567
Total Area (m^2)	73.277

Autocorrelation occurs when there is a correlation between the errors in the created model. In a regression model, autocorrelation should not be present; the errors should be random. This is checked using the Durbin-Watson test. A Durbin-Watson result close to 2 indicates that there is no autocorrelation problem in the model. The analysis revealed a Durbin-Watson result of 1.950, indicating that there is no autocorrelation problem in the model.

To assess multicollinearity in the model, we examine the Variance Inflation Factor (VIF) values for the variables. The VIF value should not exceed 10. Among the 18 independent variables included in the model, 12 variables have VIF values below 10. This suggests that there is no multicollinearity

problem for these 12 variables. However, multicollinearity issues are present in the variables Total Number of Floors, Building Height, Basement Height, Floor Area, Basement Area, and Total Area.

Table 18. *Statistical data of educational structures (Autocorrelation and Multicollinearity Assumptions*

Adjusted R^2	F	p
0.900	39,470	,000[b]

.000b: means p<0.05.

The model created to explain the Contract Amount variable is found to be significant (F: 39.470, p<0.05). In this significant model, the independent variables can explain 90% of the variation in the dependent variable.

Table 19. *Statistical result data of educational structures*

	Approximate Cost	Contract Price
Error rate	%17,50	%18,20
Adjusted R^2	0,900	0,927
Durbin-Watson	1,950	1,523

IV. CONCLUSION

In this study, 96 school building projects that were tendered by public institutions and had published results were downloaded from the Electronic Public Procurement Platform. The projects were divided into 81 training data and 15 test data sets. The construction cost indices and change rates obtained from the Turkish Statistical Institute were used to adjust the approximate cost and contract amount to January 2023.

Parameters known to affect the construction cost of educational buildings were identified, including Number of Classrooms, Construction Duration, Total Number of Floors, Floor Height, Building Height, Building Height Class (BYS), Basement Height, Earthquake Design Class (DTS), Soil Class, Soil Bearing Capacity, Bedding Coefficient, Concrete Class, Number of Elevators, Wet Area, Height of Raft Foundation, Floor Area, Basement Area, and Total Area. These parameters were used in regression analysis performed with "SPSS Statistics 26" software. Regression analyses were conducted, and formulas were developed to estimate the costs of educational buildings.

The developed formulas were used to predict the Contract Amount and Approximate Cost. The error rates for the 15 test projects selected as test data were determined using the developed formulas. Among the models, the one using all parameters provided the best fit, with $R^2 = 0.927$ for the Contract Amount and $R^2 = 0.900$ for the Approximate Cost. The Durbin-Watson criterion was used to check the consistency between predicted and actual results.

The normal distribution condition for multiple regression analysis was met, and no multicollinearity or autocorrelation problems were detected (p<0.05). The average error rate for the Approximate Cost prediction model was found to be 17.50%, while the error rate for the Contract Amount prediction model was 18.20%. However, more accurate results could be achieved with a sufficient number of samples representing different variations.

In conclusion, an approach was developed that can predict the approximate costs and contract amounts of school buildings with different types and coefficients with error rates below 20%. Both public

institutions and contracting construction firms can benefit from these models to achieve time savings and more realistic cost estimates. Increasing the data size in similar studies could be a solution for minimizing error rates in future models.

V. REFERENCES

[1] M. Akınbingöl, & A. T. Gültekin, "Bina üretimi evresinde maliyet planlama ve denetimine yönelik bir maliyet yönetim modeli önerisi", Gazi Üniversitesi, Mühendislik ve Mimarlık Fakültesi Dergisi, ss. 449-505, 2005.

[2] M. Kuruoğlu, E., Yönez, E. Topkaya, & L. Y. Çelik, "İnşaat Sektöründe Kullanılan Ön Maliyet Tahmin Yöntemlerinin Karşılaştırılması", e-Journal of New World Sciences Academy, ss. 263-272, 2012.

[3] L. O. Uğur, "Yapı Maliyetinin Yapay Sinir Ağı ile Analizi", Doktora Tezi, Yapı Eğitimi Bölümü, Gazi Üniversitesi, Fen Bilimleri Enstitüsü, Ankara, 2007.

[4] Uğur, L.O., Kanıt, R., Erdal, H., Namlı, E., Erdal, H.İ., Baykan, U.N., Erdal, M., "Enhanced predictive models for construction costs: A case study of Turkish mass housing sector", Computational Economics, 53(4): 3336-3344, (2019).

[5] Sueri, M., & Erdal, M., (2022). Early Estimation of Sewerage Line Costs with Regression Analysis. Gazi University Journal of Science, vol.35, no.3, 822-832.

[6] U. Emek, "Kamu ihalelerinde rekabetin sağlanması ve korunması", T.C. Devlet Planlama Teşkilatı, 2002, ss.1-69.

[7] G. Kömürcü, "4734 sayılı kamu ihale kanunun uygulanmasında karşılaşılan sorunlar", Yüksek Lisans Tezi, Mimarlık Bölümü, İstanbul Teknik Üniversitesi, Fen Bilimleri Enstitüsü, İstanbul, 2006.

[8] Kamu İhale Kanunu, T.C. Resmi Gazete, Sayı: 24848, 22 Ocak 2002.

[9] Ü. Yıldız, & M. S. Temurlenk, Ekonometrinin Temelleri, 1. baskı, Eskişehir, Türkiye: Anadolu Üniversitesi Yayınları, 2020.

[10] Narin, S., Doğan, O., Bande, N., Genç, Y., "Keçiören/Ankara Özelinde Konut Rayiç Değerlerinin Tahmininde Çoklu Regresyon Analizi ve Yapay Sinir Ağları Yöntemlerinin Karşılaştırılması" Uluslararası Mühendislik Araştırma ve Geliştirme Dergisi, 15, (2), 828-839, (2023).

[11] B. Akış, "İstatistiki yöntemlerle değer belirleme ve değer haritası üretimi - Selçuklu örneği", Yüksek Lisans Tezi, Harita Mühendisliği Bölümü, Selçuk Üniversitesi, Fen Bilimleri Enstitüsü, Konya, 2013.

[12] Türkiye İstatistik Kurumu, (2023, 10 Mart), İnşaat Maliyet Endeksi, [Online]. Türkiye İstatistik Kurumu. Erişim: https://data.tuik.gov.tr/Bulten/Index?p=Insaat-Maliyet-Endeksi-Ocak-2023-49491#:~:text=%C4%B0n%C5%9Faat%20maliyet%20endeksi%20y%C4%B1ll%C4%B1k%20%78,endeksi%20%47%2C79%20artt%C4%B1.

[13] Türkiye Bina Deprem Yönetmeliği, T.C. Resmi Gazete, Sayı: 30364, 18 Mart 2018.

Düzce University
Journal of Science & Technology

Research Article

Classification of the Condition of Cancer Patients Receiving Home Health Care with Machine Learning Methods

Mürsel Kahveci [a,*]

[a] *Department of Anesthesia and Reanimation, Sabuncuoğlu Şerefeddin Research and Training Hospital, Amasya University, Amasya, Turkey*
** Corresponding author's e-mail address: drmurselkahveci@yahoo.com*
DOI: 10.29130/dubited.1501760

ABSTRACT

Determining the health status of cancer patients is of vital importance in the cancer treatment process. This process plays a critical role in assessing patients' quality of life and supporting the treatment process. We thought that the use of machine learning in the field of cancer treatment and patient care could contribute to better patient outcomes and increased quality of life. Evaluation results of cancer patients who received home health care from Amasya University and Research Hospital between January 2013 and August 2017 were discussed and 1000 patient files in home health service patient records were prospectively examined. In this article, cancer types were classified with machine learning methods using the Visual Analog Scale (VAS), Karnofsky performance scale, ECOG, Katz and Bartel scores to determine the quality of life of cancer patients receiving home health care. This study includes the evaluation results of 132 patients, 69 women (mean age 60.31±9.61) and 63 men (mean age 62.36±9.58). The DT classifier was noted to exhibit 83.3% accuracy and had the highest sensitivity in the lung cancer type, with a sensitivity of 88.9%. SVM classifier reached the highest accuracy compared to other classifiers with 90.2% accuracy. SVM has the highest sensitivity in lung cancers, with a sensitivity of 97.8%. The ANN classifier achieved 88.6% accuracy for all cancer types.The use of machine learning algorithms may provide a more sensitive and objective way to evaluate patients' response to treatment. Machine learning enables the classification of cancer types by analyzing feature spaces derived from VAS, Karnofsky performance scale, ECOG, Katz, and Bartel scores. This situation can also be constructed as an indicator in early diagnosis or risk group determination, and thus can contribute to improving home health services and increasing the quality of life of cancer patients. The results of this study may contribute to studies aimed at developing more effective strategies for the care and treatment of cancer patients.

Keywords: *Cancer, Deep learning, Machine learning, ANN, SVM, Decision process*

Evde Sağlık Hizmeti Alan Kanser Hastalarının Durumunun Makine Öğrenmesi Yöntemleri ile Sınıflandırılması

ÖZET

Kanser hastalarının sağlık durumlarının belirlenmesi, kanser tedavisi sürecinde hayati bir öneme sahiptir. Bu süreç, hastaların yaşam kalitesini değerlendirmek ve tedavi sürecini desteklemek için kritik bir rol oynamaktadır. Biz de makine öğrenmesinin kanser tedavisi ve hasta bakımı alanında kullanılmasının, daha iyi hasta sonuçlarına ve yaşam kalitesinin artırılmasına katkı sağlayabileceğini

Received: 15/06/2024, Revised: 12/09/2013, Accepted: 27/09/2024

düşündük. Ocak 2013-Ağustos 2017 tarihleri arasında XXX Hastanesi'nden evde sağlık hizmeti alan kanser hastalarının değerlendirme sonuçları ele alındı ve Evde sağlık hizmeti alan hasta kayıtlarındaki 1000 hasta dosyası prospektif olarak incelendi. Bu makalede, evde sağlık hizmeti alan, kanser hastalarının yaşam kalitesini belirlemek için Visual Analog Scale (VAS), Karnofsky performans ölçeği, ECOG, Katz ve Bartel skorlarını kullanarak makine öğrenmesi yöntemleriyle kanser türleri sınıflandırıldı. Bu çalışma, 69'u kadın (ortalama yaş 60,31±9,61) ve 63 erkek (ortalama yaş 62,36±9,58) olmak üzere 132 hastanın değerlendirme sonuçlarını içermektedir. DT sınıflandırıcı %83,3 doğruluk sergilediği ve akciğer kanser türünde %88,9 duyarlılıkla en yüksek duyarlılığa sahip olduğu kaydedilmiştir. SVM sınıflandırıcı %90.2 doğruluk ile diğer sınıflandırıcılara göre en yüksek doğruluğa ulaşmıştır. SVM en fazla %97.8 duyarlılıkla akciğer kanserlerinde duyarlılığa sahiptir. ANN sınıflandırıcısı tüm kanser türleri için %88.6 doğruluk elde etmiştir. Makine öğrenmesi algoritmalarının kullanımı, hastaların tedaviye yanıtının değerlendirilmesinde daha hassas ve objektif bir yol sağlayabilir. Makine öğrenmesi modeli, VAS, Karnofsky performans ölçeği, ECOG, Katz ve Bartel skorlarına dayalı özellik uzayını kullanarak kanser türünün belirlenmesine olanak sağlamaktadır. Bu durum erken tanıda ya da risk grubu belirlemede bir gösterge olarak da kurgulanabilir ve böylelikle evde sağlık hizmetlerinin iyileştirilmesine ve kanser hastalarının yaşam kalitesinin artırılmasına katkıda bulunabilir. Bu çalışmanın sonuçları, kanser hastalarının bakımı ve tedavisi için daha etkili stratejiler geliştirmeye yönelik yürütülen çalışmalara katkı sağlayabilir.

Anahtar Kelimeler: *Kanser; Derin öğrenme; Makine öğrenimi;YSA; DVM; Karar süreci*

I. INTRODUCTION

Cancer is one of the most complex and pervasive problems in medicine today. Affecting the lives of millions of people each year, it is a burden on health systems and societies. [1, 2]. The complex nature of cancer, combined with often debilitating treatments such as chemotherapy and radiation, presents a complex set of physical and psychosocial challenges for patients [3, 4]. In particular, people with advanced cancer experience problems with daily activities caused by diagnosis-specific symptoms and/or treatment-related side effects [5]. It is estimated that most of these individuals require palliative care [6, 7].

However, thanks to advances in screening and treatments, people are living longer and longer with the consequences of cancer and its treatment. Patients with cancer often report a constant symptom burden, exercise intolerance and loss of physical fitness, all of which can threaten a patient's daily independence [8]. Activities of daily living (ADLs) refer to essential tasks individuals must perform to maintain independent living in society [9]. In other words, the term GYA describes the practical daily tasks that need to be done at home in order to lead a manageable and worthwhile life [10].

Various tools developed to evaluate ADL problems have an important role in determining the quality of life of cancer patients. Among these tools, the Visual Analog Scale (VAS), Karnofsky performance scale, ECOG, Katz and Bartel scales stand out. While the Visual Analog Scale (VAS) allows patients to subjectively evaluate the symptoms they are experiencing or their quality of life, the Karnofsky performance scale and ECOG scales are used to objectively evaluate the patient's overall performance level and monitor the effectiveness of the treatment process. On the other hand, Katz and Bartel scales have an important role in evaluating independence and functional status in daily living activities. These evaluation criteria provide a solid basis for determining the quality of life of cancer patients, managing the treatment process, and creating personalized care plans. In this way, it is aimed to increase the quality of life of the patients and improve the treatment results by providing support in accordance with their needs.

Cancer treatment and patient care are increasingly complex processes and require a personalized approach for each patient. In this field, machine learning stands out as an important tool. By analyzing large amounts of patient data, machine learning algorithms make it possible to obtain valuable information about patients' diagnoses, response to treatment, and prognosis. Additionally, thanks to its

ability to detect complex relationships and patterns, machine learning can help personalize patients' treatment plans and determine the most effective treatment options. However, machine learning can also be used to analyze clinical assessment tools, such as scales used to determine patients' quality of life and monitor the treatment process. In this way, it may be possible to evaluate patients' conditions more accurately and direct treatment plans more effectively. Therefore, the use of machine learning in cancer treatment and patient care can contribute to better patient outcomes and improved quality of life.

Machine learning (ML) techniques have gained significant traction in healthcare over the past decade, particularly for disease diagnosis, prognosis, and treatment planning. Numerous studies have explored the effectiveness of ML models in classifying patient conditions across various medical domains, including oncology, cardiology, and neurology [11]. For instance, Esteva et al. (2017) demonstrated the success of deep learning in dermatology for the classification of skin lesions, achieving dermatologist-level accuracy [12]. Similarly, Che et al. (2017) applied recurrent neural networks (RNNs) to electronic health record data, showing the potential of ML in predicting patient outcomes across multiple chronic diseases, such as heart failure and chronic kidney disease [13]. These studies underscore the versatility and generalizability of ML models across different patient populations and medical conditions, which parallels the approach used in the current study for cancer classification.

This study contributes to the growing body of literature on the application of machine learning (ML) models in healthcare, with a specific focus on improving cancer care for home healthcare patients. While the effectiveness of ML models has been demonstrated extensively in clinical settings, their application in home healthcare remains relatively underexplored. By evaluating the classification performance of multiple ML techniques, including Support Vector Machines (SVM), Artificial Neural Networks (ANN), and Decision Trees (DT), we provide valuable insights into the strengths and limitations of these models for classifying cancer patients based on quality-of-life measures. The relationship between the Visual Analog Scale (VAS), Karnofsky Performance Scale, ECOG, Katz, and Bartel scores, and cancer type is rigorously analyzed, allowing for a more nuanced understanding of patient outcomes. Through this comparative analysis, our study not only highlights the utility of these classifiers in personalized healthcare but also underscores their potential in enhancing patient monitoring and care delivery in non-clinical environments. Future research could extend this approach to other chronic diseases and healthcare contexts, thereby further contributing to the generalizability of ML in medical applications and aiding in the development of more effective health service planning and quality-of-life improvements for diverse patient populations.

II. MATERYAL METOD

Dataset:

This study was conducted between January 2013 and August 2017 by Amasya University Sabuncuoğlu Şerefeddin Education and Research Res. It includes the evaluation results of cancer patients who receive home health care from the hospital. Clarify that 1000 files were reviewed, but the final analysis focused on 132 patients Patient groups diagnosed with colorectal cancer, breast cancer and lung cancer were included in the study. Other cancer types were not included in the study because sufficient numbers could not be reached. Additionally, other patient groups receiving home health care were excluded from the study. The standard patient groups included in the study are patients between the ages of 18-90. This study includes the evaluation results of 132 patients, 69 women (mean age 60.31±9.61) and 63 men (mean age 62.36±9.58). Ethics committee approval for the study was received from Tokat Gaziosmanpaşa University Ethics Committee (2016/07). The demographic characteristics of the patients are given in Table 1.

Table 1. *Demographic characteristics of the patients.*

		Colorectal Cancer	Breast Cancer	Lung Cancer	Total
Gender	**Female**	18	40	34	92
	Male	24	5	11	40
Age	**Female**	65,57 ±14,25	54,22±5,43	61,15±9,15	60,31±9,61
	Male	64,50±12,30	63,90±4,75	58,70±11,70	62,36±9,58

There are many scales used to evaluate patients in palliative care. These scales are aimed at learning the patient's needs, identifying their severity and the difficulties they face. During the evaluation phase, data were collected from the patients via a survey. More than one scale was used to evaluate daily living activities in the patient groups included in the study. These scales used:

Visual Analog Scale (VAS)

Among the data collected, VAS scoring in the range of 0-10 was used to measure the pain intensity of the patients. VAS, which is an extremely simple, effective, repeatable measurement tool that requires minimal tools, is a one-dimensional scale frequently used in the measurement of subjective parameters. The scale consists of a 10 cm long line drawn vertically or horizontally. At either end of this line are the two extreme descriptive words of the subjective category (0 = “no pain at all”, 10 = worst/unbearable pain”). The patient is told to make a mark on this line, appropriate to the intensity of pain, to intersect this line. The distance from the lowest VAS level to the patient's mark is measured with a ruler to obtain the numerical value of the patient's pain intensity in centimeters (cm) or millimeters (mm). [14, 15]. It has been shown that there is a good correlation between the horizontal and vertical plots of VAS, and it has been widely accepted in the world literature as a valid and reliable measurement tool in the evaluation of postoperative acute pain intensity. Most of the studies conducted to date indicate that VAS is a reliable tool that can be used to evaluate pain severity. The VAS score obtained from the collected data is shown in Figure 1.

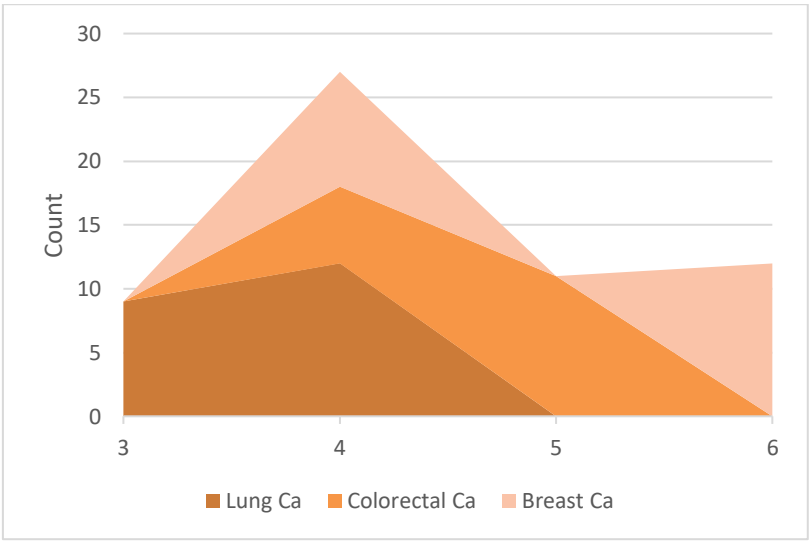

Figure 1. *VAS Score results*

Karnofsky Performance Scale

The scale was developed by Dr. Karnofsky in 1948 and was developed by Dr. Karnofsky in 1949. Burchenal and Dr. Remastered by Karnofsky [16]. The scale questions the patient's symptoms, ability to perform daily activities, addiction status, and need for medical care. While 100 points indicate

normal health status, functions gradually deteriorate with ten-point decreases, and 0 points correspond to death. Patients are divided into 3 groups according to the evaluation results: Individuals in category A (80-100%) do not require special care, they can continue their normal activities and work; Individuals in category B (50-70%) can do personal care with assistance but cannot work; Individuals in category C (0-40%) cannot take care of themselves and the disease rapidly progresses towards death. The Karnofsky performance scale is shown in Table 1 [16]. The Karnofsky performance scale results obtained in the study are shown in Figure 2.

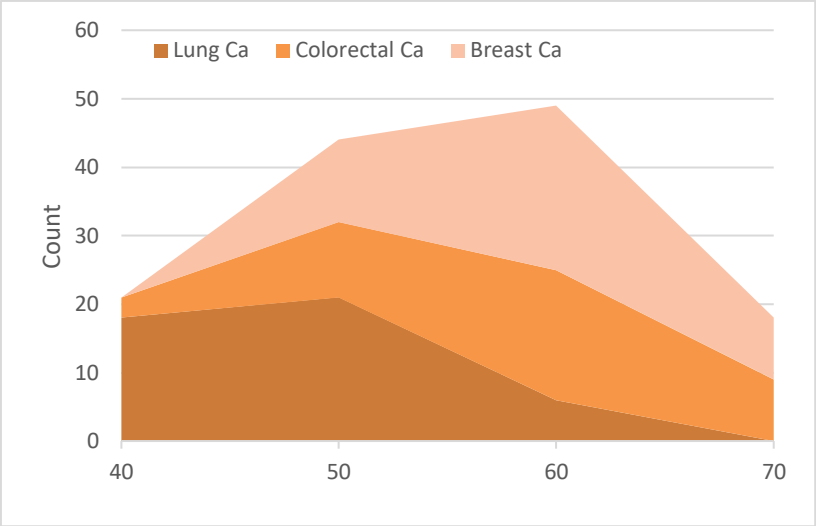

Figure 2. *Karnofsky performance scale results*

ECOG Performance Score

It consists of the initials of Eastern Cooperative Oncology Group. This performance score was developed and published in 1982 by the Eastern Cooperative Oncology Group (ECOG), part of the ECOG-ACRIN Cancer Research Group. The ECOG Performance Score is widely used to determine the functional status of cancer patients. The scale, also known as the WHO or Zubrod performance score, was developed in 1960. In the ECOG Performance Score: 0 indicates normal health and 5 indicates death. While low scores indicate good general condition, high scores indicate poor prognosis. ECOG Performance Score is shown in Table 2 [17]. The ECOG Performance Score results obtained in the study are shown in Figure 3.

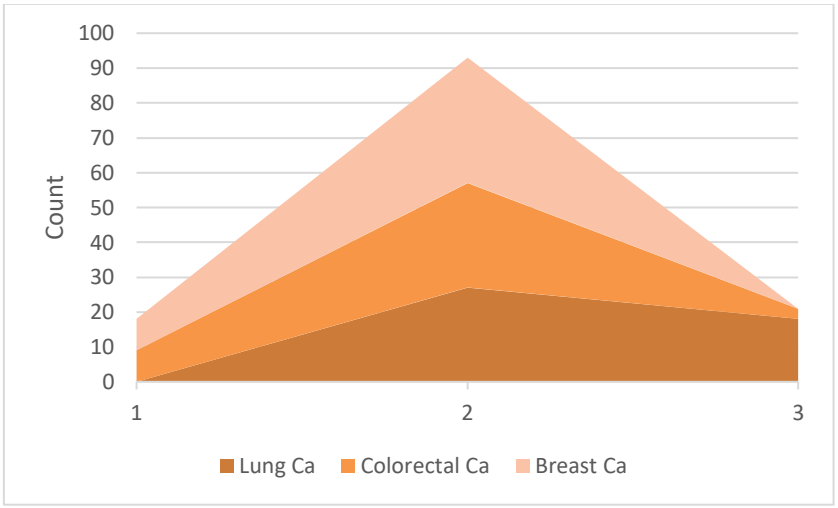

Figure 3. *ECOG Performance Score results*

Katz's Activities of Daily Living Index

It is a scale developed by Katz et al. in 1963. It consists of 6 questions regarding movement, nutrition, excretion, dressing, bathing and toilet functions, which evaluate whether the individual is dependent on other people to perform his daily life activities. If the individual can do each of these activities independently, 1 point is given, and if he cannot do it at all, 0 point is given. Functions performed with assistance receive 0 points, while functions performed independently receive 1 full point. A score of 6 indicates full function, a score of 4 indicates moderate function, and a score of 2 indicates less severe impairment. [18-21]. Katz's Activities of Daily Living results obtained in the study are shown in Figure 4.

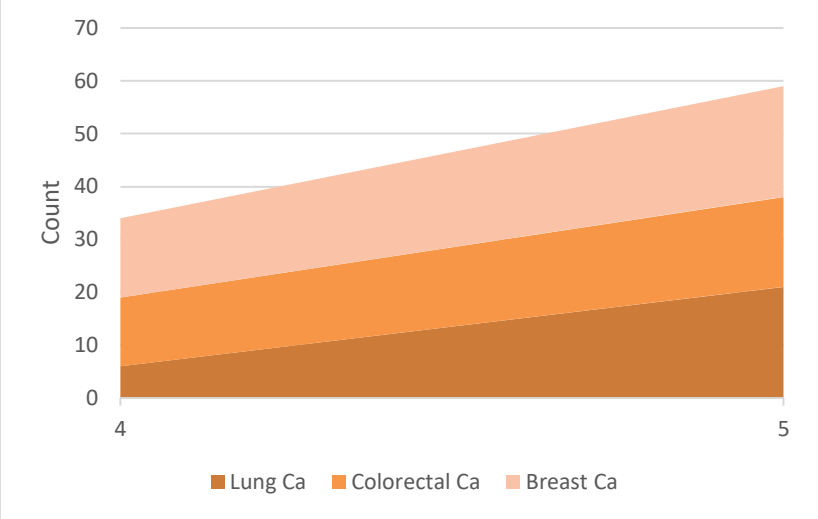

Figure 4. *Katz's Activities of Daily Living Score results*

Barthel Index-BI:

The index developed by Mahoney and Barthel in 1965 was modified by Shah et al. (1992). The Turkish version of the index was edited by Küçükdeveci et al. (2000) [22]. This scale evaluates mobility status and stair climbing functions such as feeding, washing, self-care, dressing, defecation control, urinary control, going to the toilet, ability to move from bed to wheelchair, walking or being dependent on a wheelchair, and stair climbing on a scale of 5-15 points (depending on the question). It consists of a total of 10 items that grade each other (0-15 points in 5-point increments). The main purpose of the evaluation made with this scale is to determine to what extent the patient performs these actions independently, without any physical or verbal assistance. It is not necessary to test the patient directly, but evaluation can be made in the light of direct observation, information obtained from the patient, the patient's relatives, or the caregiver or nurse involved in his/her care. In this scale, where the possible score ranges from 0 to 100, a higher score means that the patient is independent of other people and can run his own business. As a result of the scoring, 0-20 points are evaluated as fully dependent, 21-61 points as highly dependent, 62-90 points as moderately dependent, 91-99 points as mildly dependent, and 100 points as fully independent. [22]. The Bartel Index results obtained with the collected data are shown in Figure 5.

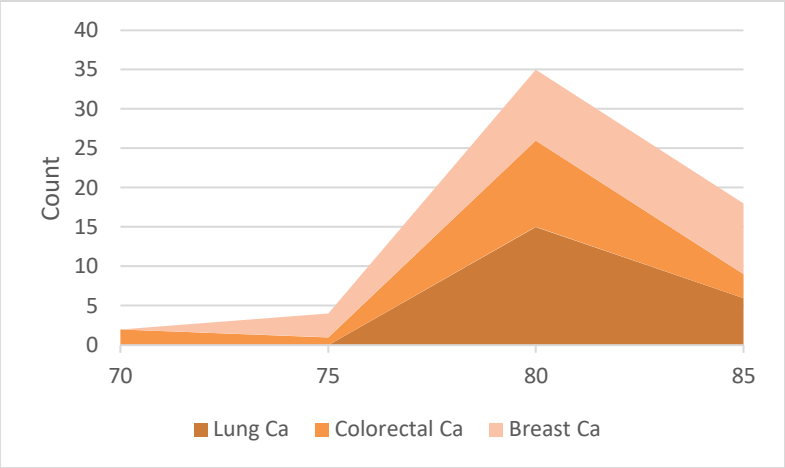

Figure 5. *Barthel Index results*

Classification model

Classification in data mining is commonly performed to discover hidden patterns in large-scale data sets. A pattern represents information that is observable, measurable, and repeatable. Classification algorithms are designed to separate data into specific groups (classes) to obtain specific target information. At this stage, feature extraction plays an important role. Feature extraction is the most suitable Torre in the classification process. This method is used for classification and pattern recognition problems in many different fields, such as medicine and signal processing. [23]. While support vector machines (SVM) are preferred for their classification performance and accuracy in predictions, they are also effective for classifying non-linear data sets. They offer a versatile solution when used in conjunction with other algorithms such as decision trees. Therefore, support vector machines are considered an important tool for extracting and classifying patterns in complex data sets. Figure 6 shows the general structure of SVM.

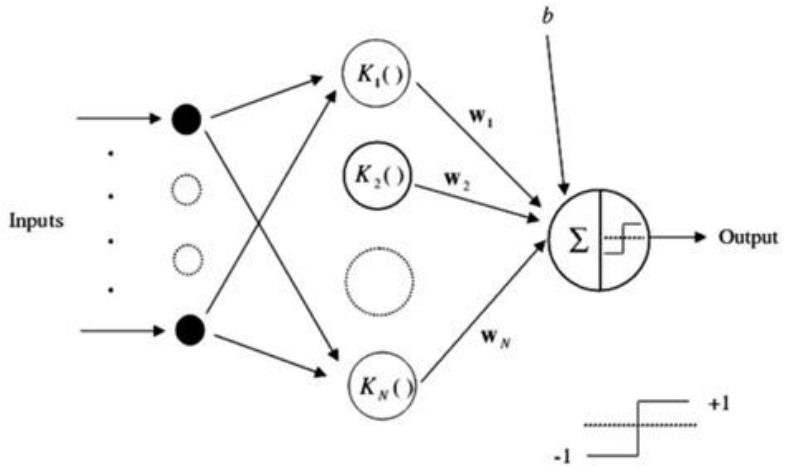

Figure 6. *Support vector machines network structure*

Artificial Neural Network (ANN)

ANN is a complex and multi-layered artificial learning model inspired by the functioning of the human brain. [24]. ANNs consist of neurons arranged in a manner similar to biological neural networks and use connections between these neurons to process information. [25]. ANNs generally have a double-layer and feed-forward structure, which allows data to be transferred in a single direction from input to output. Additionally, ANNs have the flexibility to work with numerical and categorical data and can solve a variety of complex problems. The learning process of ANNs is based on recognizing patterns in the data set and creating models through learning. In real-life applications, ANN is used in many different fields such as medicine, finance, industry and image recognition. [26,

27]. In particular, they provide successful results in tasks such as classification, regression and pattern recognition on complex data sets. ANNs are now considered an important machine learning tool because they have high processing power and a wide range of applications. The structure of the ANN is shown below in Figure 7 [25],

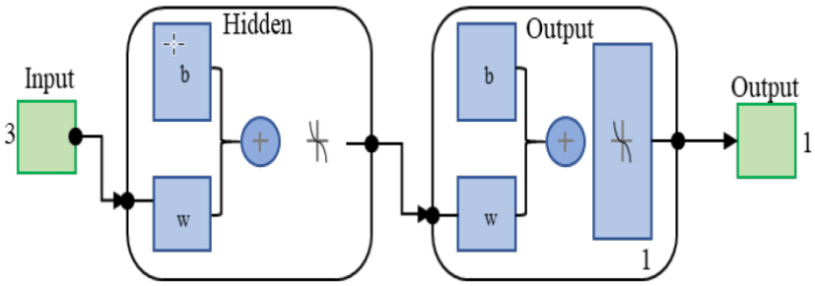

Figure 7. *Schematic ANN diagram [25]*

Decision Tree (DT)

A Decision Tree is a simple yet powerful classification and regression model that splits the dataset into branches based on certain decision criteria. Each internal node in a decision tree represents a feature (or attribute), each branch represents a decision rule, and each leaf node represents the outcome or class label. DTs are particularly valued for their interpretability, as they allow the user to easily understand and visualize the decision-making process. They work well on both numerical and categorical data and are capable of handling datasets with missing values. However, decision trees are prone to overfitting, especially with small datasets or when the tree becomes too deep, leading to high variance. To mitigate this, techniques like pruning or using ensemble methods (such as Random Forest or Gradient Boosting) are often applied to improve generalization. Despite these limitations, DTs are widely used in medical decision-making due to their ease of implementation and transparency in how they classify data.

The main purpose of choosing SVM, ANN and DT in this study is that each algorithm offers different advantages when considering the size and complexity of the data. While SVM shows strong performance especially in nonlinear relationships; ANN offers the capacity to learn deeper patterns in large data sets. DT is valuable in terms of fast decision making and model explainability. Therefore, the combination of these algorithms provided the most suitable solutions for this study, which evaluates and classifies the quality of life of cancer patients.

III. RESULTS

Confusion matrices of the classification results for the 5-dimensional feature space obtained as a result of the survey are given in Tables 3, 4 and 5. The Decision Tree (DT) model (Table 2) appears to have a strong performance, especially in classifying Lung Cancer with remarkable precision.

Table 2 DT Classification result.

DT		**Predicted Class**		
		Lung cancer	Lung cancer	Lung cancer
True Class	Lung cancer	40	2	3
	Colorectal Cancer	4	30	8
	Breast Cancer		5	40

The SVM model (Table 3) exhibited higher accuracy performance in all cancer types. Additionally, this model has been shown to show lower misclassification rates compared to the DT model in distinguishing Colorectal Cancer from breast cancer.

Table 3 *SVM classification result.*

SVM		**Predicted Class**		
		Lung cancer	**Lung cancer**	**Lung cancer**
True Class	**Lung cancer**	44	1	
	Colorectal Cancer	4	35	3
	Breast Cancer	2	3	40

The ANN model (Table 4) showed similar high performance to the SVM model, with better discrimination between Lung Cancer and other types of cancer. However, the ANN model noted some misclassifications between Colorectal Cancer and Breast Cancer, although to a lesser extent than the DT model.

Table 4 *ANN classification result.*

ANN		**Predicted Class**		
		Lung cancer	**Lung cancer**	**Lung cancer**
True Class	**Lung cancer**	**42**	**3**	
	Colorectal Cancer	**1**	**36**	**5**
	Breast Cancer		**6**	**39**

Figure 8 shows the ROC curves of the health scores of cancer patients receiving home healthcare services obtained by DT, SVM and ANN models. Examining the ROC curves, the high AUC values in all models indicate that machine learning can serve as a powerful adjunct to traditional statistical methods and provide clinicians with more detailed and data-driven tools to inform their decisions.

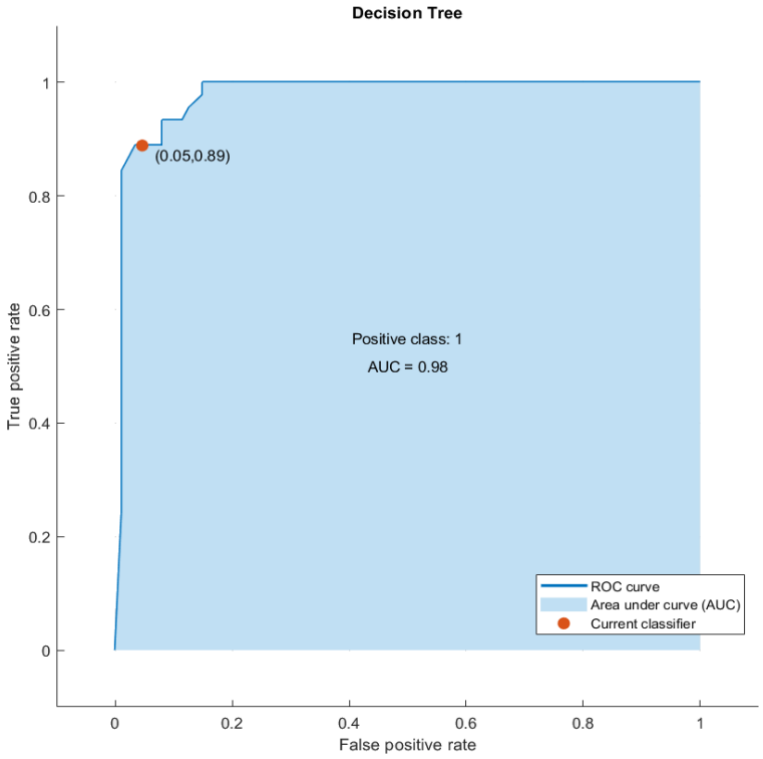
Decision Tree
(0.05,0.89)
Positive class: 1
AUC = 0.98
ROC curve
Area under curve (AUC)
Current classifier
True positive rate
False positive rate
0
0.2
0.4
0.6
0.8
1

a)

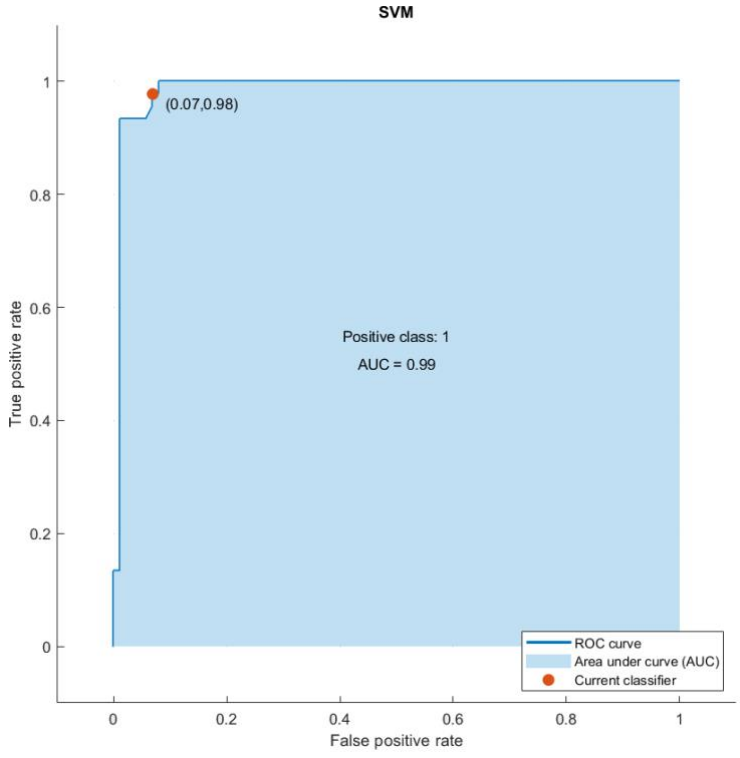
SVM
(0.07,0.98)
Positive class: 1
AUC = 0.99
ROC curve
Area under curve (AUC)
Current classifier
True positive rate
False positive rate
0
0.2
0.4
0.6
0.8
1

b)

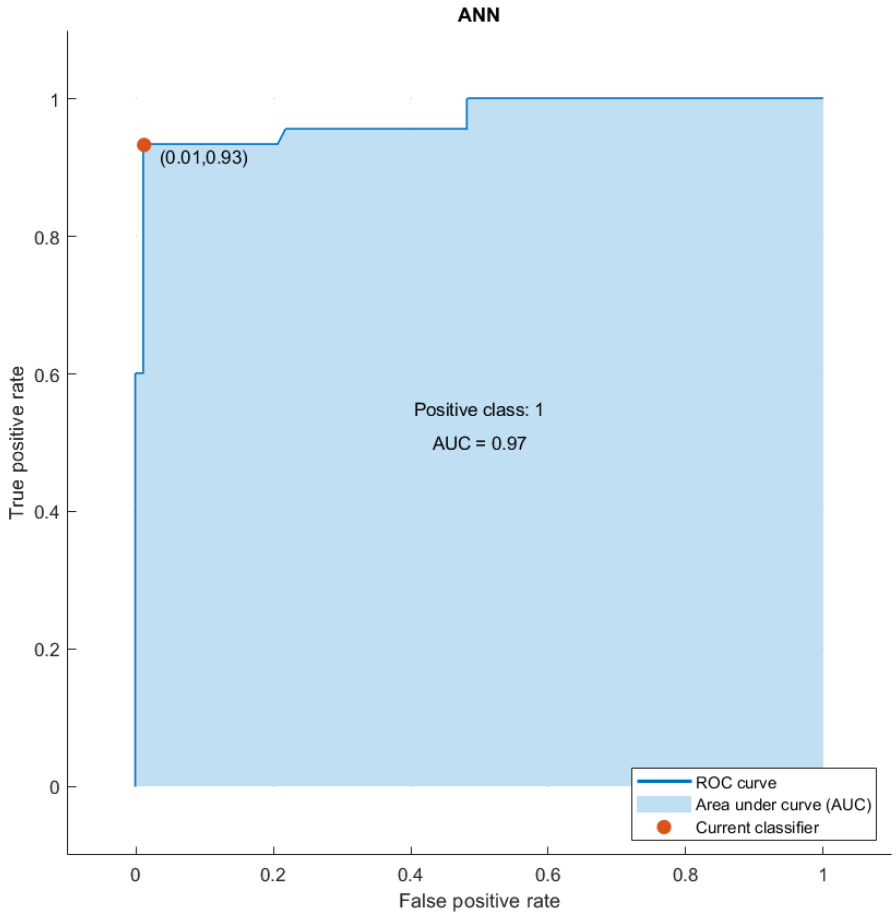

c)

Figure 8: *ROC Curves* ***a)*** *DT* ***b)*** *SVM* ***c)*** *ANN*

The accuracies and sensitivities obtained during the classification process are given in Table 5. When the table was examined, it was noted that the DT classifier exhibited 83.3% accuracy and had the highest sensitivity in the lung cancer type with 88.9% sensitivity. SVM classifier reached the highest accuracy compared to other classifiers with 90.2% accuracy. SVM has the highest sensitivity in lung cancers, with a sensitivity of 97.8%. The ANN classifier achieved an overall accuracy of 88.6%, with varying performance across different cancer types.

Table 5: *Precision and Accuracy for Each Classifier.*

		Precision (%)			Accuracies (%)
		Lung cancer	Lung cancer	Lung cancer	
Classifier	**DT**	88,9	71,4	88,9	83,3
	SVM	97,8	83,3	88,9	90,2
	ANN	93,3	85,7	86,7	88,6

When examining Table 5, DT model, while offering the lowest overall accuracy (83.3%), stood out for its interpretability, making it particularly valuable in clinical settings where transparent decision-making is essential. Although the ANN demonstrated slightly lower accuracy, it excelled in identifying complex patterns, especially in distinguishing cancer types with overlapping symptoms. ANN's ability to capture deep, non-linear relationships in the data makes it well-suited for more intricate and larger datasets. On the other hand, SVM showed the highest performance across all cancer types, particularly excelling in non-linear classification tasks such as lung cancer differentiation. SVM's strength lies in its ability to handle high-dimensional data and complex

patterns, making it a robust choice for datasets with significant variability, including those with multiple medical variables.

IV. DISCUSSION

In this study, Visual Analog Scale (VAS), Karnofsky performance scale, ECOG, Katz and Barthel Index scores were used to classify cancer patients receiving home health care. The machine learning methods used provided an effective way to classify patients into quality of life categories. The results of our study show that the classification performance of machine learning models, especially Decision Trees (DT), Support Vector Machines (SVM) and Artificial Neural Networks (ANN), make an important contribution to the detection of cancer patients.

The use of Decision Trees, Support Vector Machines and Artificial Neural Networks is a common approach in the literature for the management of cancer patients and quality of life assessment. [24, 29]. The findings of this study demonstrate the capacity of these algorithms to handle complex patient data and effectively classify various types of cancer. In particular, the SVM model exhibited highly accurate classification performance for all cancer types, confirming the strong classification ability of SVM observed in previous studies. [23, 30].

The Artificial Neural Network model showed similarly high performance and provided particularly good discrimination between 'Lung Cancer' and other cancer types. This finding shows that ANN is effective in complex classification problems and has a wide range of applications in real-world applications. [26, 27].

From a clinical perspective, the implementation of machine learning models like SVM and ANN can offer significant improvements in the management of cancer patients receiving home health care. These models could assist clinicians by providing data-driven predictions regarding patient outcomes and helping identify patients who may benefit from early intervention or specialized treatment plans [31]. The integration of such models into healthcare systems could also facilitate the early detection of cancer progression and improve the quality of life of patients by enabling more personalized and timely interventions [32].

The results of this study show that as an alternative to traditional statistical methods, machine learning can provide clinicians with more detailed and data-driven decision-making tools. In particular, the high AUC values observed in the ROC curves emphasize the usability of machine learning models in classifying cancer patients. These results are in line with the findings of Torre et al. (2016) and Coleman et al. (2008) and support the potential of machine learning in improving the management and treatment of cancer patients. [1, 2].

The study has limitations. The small sample size and limited cancer types (lung, colorectal, and breast) analyzed may restrict the generalizability of the findings. In addition, the lack of cross-validation raises concerns about model overfitting. Incorporating advanced validation techniques in future work would enhance the robustness and reliability of the results.

IV. CONCLUSİON

In this study, Visual Analog Scale (VAS), Karnofsky performance scale, ECOG, Katz and Barthel Index-BI scores were used to classify cancer patients receiving home health care services. The scores obtained were found to be an effective feature to accurately classify cancer types, with each of the Decision Tree (DT), Support Vector Machine (SVM) and Artificial Neural Network (ANN) classifiers, along with some models exhibiting higher efficiency for specific cancers. In conclusion, this study shows that machine learning models have the potential to provide benefits in identifying

cancer risk and early diagnosis of elderly people receiving home health care services. This will enable the design of systems that can assist clinicians.

The analysis shows that the SVM classifier is the best performing classifier with the highest accuracy of 90.2%. In particular, it showed a sensitivity of 97.8% for lung cancer, suggesting that it is highly reliable in detecting and differentiating lung cancer cases. The ANN classifier showed high accuracy for all cancer types. It was noted that the DT and SVM classifier achieved a sensitivity of 88.9% in the diagnosis of lung cancers.

These results suggest that different machine learning models may be superior in different areas. For lung cancer, both SVM and DT classifiers stand out and have high sensitivity rates that can be used in clinical settings for early detection.

V. REFERENCES

[1] L. A. Torre, R. L. Siegel, E. M. Ward, and A. Jemal, "Global cancer incidence and mortality rates and trends—an update," *Cancer epidemiology, biomarkers & prevention,* vol. 25, no. 1, pp. 16-27, 2016.

[2] M. P. Coleman *et al.*, "Cancer survival in five continents: a worldwide population-based study (CONCORD)," *The lancet oncology,* vol. 9, no. 8, pp. 730-756, 2008.

[3] D. L. Lovelace, L. R. McDaniel, and D. Golden, "Long-term effects of breast cancer surgery, treatment, and survivor care," *Journal of midwifery & women's health,* vol. 64, no. 6, pp. 713-724, 2019.

[4] D. P. Gopal, B. H. de Rooij, N. P. Ezendam, and S. J. Taylor, "Delivering long-term cancer care in primary care," vol. 70, ed: British Journal of General Practice, 2020, pp. 226-227.

[5] A. L. Cheville, A. B. Troxel, J. R. Basford, and A. B. Kornblith, "Prevalence and treatment patterns of physical impairments in patients with metastatic breast cancer," *Journal of clinical oncology: official journal of the American Society of Clinical Oncology,* vol. 26, no. 16, p. 2621, 2008.

[6] A. T. Johnsen, M. A. Petersen, L. Pedersen, L. J. Houmann, and M. Groenvold, "Do advanced cancer patients in Denmark receive the help they need? A nationally representative survey of the need related to 12 frequent symptoms/problems," *Psycho-Oncology,* vol. 22, no. 8, pp. 1724-1730, 2013.

[7] J. Thuesen and H. Timm, "Palliation og rehabilitering; begrebslige og praktiske forskelle og ligheder," *Omsorg. Nordisk tidsskrift for palliativ medisin,* vol. 31, no. 3, pp. 30-35, 2014.

[8] J. K. Silver, J. Baima, and R. S. Mayer, "Impairment-driven cancer rehabilitation: an essential component of quality care and survivorship," *CA: a cancer journal for clinicians,* vol. 63, no. 5, pp. 295-317, 2013.

[9] K. Covinsky, "Aging, arthritis, and disability," *Arthritis Care & Research: Official Journal of the American College of Rheumatology,* vol. 55, no. 2, pp. 175-176, 2006.

[10] E. K. Grov, S. D. Fosså, and A. A. Dahl, "Activity of daily living problems in older cancer survivors: A population-based controlled study," *Health & social care in the community,* vol. 18, no. 4, pp. 396-406, 2010.

[11] Shilo, S., Rossman, H., & Segal, E. "Axes of a revolution: challenges and promises of big data in healthcare". *Nature Medicine*, 26(1), 29-38, 2020.

[12] Esteva, A., Kuprel, B., Novoa, R. A., Ko, J., Swetter, S. M., Blau, H. M., & Thrun, S. " Dermatologist-level classification of skin cancer with deep neural networks." *Nature,* 542(7639), 115-118, 2017.

[13] Che, Z., Purushotham, S., Cho, K., Sontag, D., & Liu, Y. "Recurrent neural networks for multivariate time series with missing values." *Scientific reports*, 8(1), 6085,2017.

[14] R. Chou *et al.*, "Guidelines on the management of postoperative pain," *J Pain,* vol. 17, no. 2, pp. 131-157, 2016.

[15] H. B. Kjeldsen, T. W. Klausen, and J. Rosenberg, "Preferred presentation of the visual analog scale for measurement of postoperative pain," *Pain practice,* vol. 16, no. 8, pp. 980-984, 2016.

[16] D. Péus, N. Newcomb, and S. Hofer, "Appraisal of the Karnofsky Performance Status and proposal of a simple algorithmic system for its evaluation," *BMC medical informatics and decision making,* vol. 13, pp. 1-7, 2013.

[17] S.-Y. Suh, T. W. LeBlanc, R. A. Shelby, G. P. Samsa, and A. P. Abernethy, "Longitudinal patient-reported performance status assessment in the cancer clinic is feasible and prognostic," *Journal of oncology practice,* vol. 7, no. 6, pp. 374-381, 2011.

[18] S. Katz, A. B. Ford, R. W. Moskowitz, B. A. Jackson, and M. W. Jaffe, "Studies of illness in the aged: the index of ADL: a standardized measure of biological and psychosocial function," *jama,* vol. 185, no. 12, pp. 914-919, 1963.

[19] M. Şahbaz And H. Tel Aydin, "Evde yaşayan 65 yaş ve üzeri bireylerin günlük yaşam aktivitelerindeki bağımlılık durumu ile ev kazaları arasındaki işilkinin incelenmesi," *Türk Geriatri Dergisi,* vol. 9, no. 2, pp. 85-93, 2006.

[20] E. F. Ö. Pehlivanoğlu, M. U. Özkan, H. Balcioğlu, U. Bilge, and İ. Ünlüoğlu, "Adjustment and reliability of katz daily life activity measures for elderly in Turkish," *Ankara Medical Journal,* vol. 18, no. 2, pp. 219-223, 2018.

[21] S. Katz, T. D. Downs, H. R. Cash, and R. C. Grotz, "Progress in development of the index of ADL," *The gerontologist,* vol. 10, no. 1_Part_1, pp. 20-30, 1970.

[22] A. A. Küçükdeveci, G. Yavuzer, A. Tennant, N. Süldür, B. Sonel, and T. Arasil, "Adaptation of the modified Barthel Index for use in physical medicine and rehabilitation in Turkey," *Scandinavian journal of rehabilitation medicine,* vol. 32, no. 2, pp. 87-92, 2000.

[23] O. Olanloye, O. Olasunkanmi, And O. Oduntan, "Comparison of Support Vector Machine Models in the Classification of Susceptibility to Schistosomiasis," *Balkan Journal of Electrical and Computer Engineering,* vol. 8, no. 3, pp. 266-271, 2020.

[24] T. Wu and K. Lei, "Prediction of surface roughness in milling process using vibration signal analysis and artificial neural network," *The International Journal of Advanced Manufacturing Technology,* vol. 102, no. 1-4, pp. 305-314, 2019.

[25] M. D. Sadanand, "Basic of Artificial Neural Network."

[26] Ş. Bayraktar and C. Alparslan, "Artificial Neural Networks for Machining," in *Advances in Sustainable Machining and Manufacturing Processes*: CRC Press, 2022, pp. 189-204.

[27] R. Weiss, S. Karimijafarbigloo, D. Roggenbuck, and S. Rödiger, "Applications of Neural Networks in Biomedical Data Analysis," *Biomedicines,* vol. 10, no. 7, p. 1469, 2022.

[28] M. Ramezani and A. Afsari, "Surface roughness and cutting force estimation in the CNC turning using artificial neural networks," *Management Science Letters,* vol. 5, no. 4, pp. 357-362, 2015.

[29] V. Vapnik, "Statistical Learning Theory. New York: John Willey & Sons," *Inc,* 1998.

[30] S. R. Gunn, "Support vector machines for classification and regression," *ISIS technical report,* vol. 14, no. 1, pp. 5-16, 1998.

[31] Silver, J. K., Baima, J., and Mayer, R. S."Impairment-driven cancer rehabilitation: an essential component of quality care and survivorship." *CA: a cancer journal for clinicians*, 63(5), 295-317, 2013.

[32] Wu, T. Y., and K. W. Lei. "Prediction of surface roughness in milling process using vibration signal analysis and artificial neural network." *The International Journal of Advanced Manufacturing Technology* 102.1: 305-314, 2019.

Düzce University
Journal of Science & Technology

Research Article

Maintenance of corroded silos: A case study

Husnu GERENGI [a], Muhammed MARASLI [b], Kader COSKUN [*b],
Volkan ÖZDAL [b], İlyas UYGUR [c], Mecit AKSU [d]

[a] *Corrosion Research Laboratory, Department of Mechanical Engineering, Faculty of Engineering, Duzce University, 81620 DUZCE, TURKİYE.*
[b] *Fibrobeton Company R&D Center, DUZCE, TURKİYE.*
[c] *Department of Mechanical Engineering, Duzce University, 81620 DUZCE, TURKİYE.*
[d] *Faculty of Arts and Sciences, Department of Chemistry, Duzce University, 81620 DUZCE, TURKİYE.*
* *Corresponding author's e-mail address: kader.dikmen@fibrobeton.com.tr*
DOI: 10.29130/dubited.1505994

ABSTRACT

Silos used for storing fuels, foods, and chemicals are specialized structures designed to safely contain and dispense various types of chemicals commonly used in the construction industry, such as cement, aggregates, and additives. Most of the materials required for glass fiber reinforced concrete (GFRC) panel production are stored in silos. The required materials are taken from the silos with the help of pumps equipped with an automatic dosage system. Steel is prone to corrosion when exposed to moisture and oxygen in the air, resulting in the formation of rust. In the open air, especially in places with excessive humidity and rainfall, silos corrode faster over time. Therefore, punctured silos due to corrosion can lead to production stoppages and severe financial losses. Painting is one of the primary methods for protecting steel from corrosion as it creates a barrier between the metal surface and the environment, preventing direct contact with corrosive agents and extending the life of the steel structure. In this study, the maintenance work of two heavily corroded silos, which had been in use for 20 years by Fibrobeton GFRC company, was carried out step by step according to ASTM D3276, ISO 8501 and ISO 12944:2018 standards. Wet sandblasting was used to remove the paint from the surface, followed by cleaning of the oxide layer with a patented acid solution (TPE Patent Application No: 2017/11354) containing corrosion inhibitors, followed by the application of two coats of surface tolerant ($Zn_3(PO_4)_2$ based) epoxy paint and then acrylic paint with high UV resistance. During this maintenance process, attention was also drawn to the problems caused by not preparing the metal surface in accordance with the standards before painting.

Keywords: *Corrosion, silo, paint, maintenance, atmospheric corrosion*

Korozyona Uğramış Siloların Bakımı: Bir Vaka Çalışması

ÖZET

Yakıt, gıda ve kimyasalların depolanması için kullanılan silolar, inşaat sektöründe de yaygın olarak kullanılan çimento, agrega ve katkı maddeleri gibi çeşitli kimyasalları güvenli bir şekilde depolamak ve dağıtmak için tasarlanmış özel yapılardır. Cam elyaf takviyeli beton (GFRC) panel üretimi için gerekli malzemelerin çoğu silolarda depolanır. Gerekli malzemeler, otomatik dozaj sistemi ile donatılmış

Received: 27/06/2024, Revised: 13/09/2024, Accepted: 28/09/2024

pompalar yardımıyla silolardan alınır. Havadaki nem ve oksijene maruz kalan siloların korozyona uğrayıp pas oluşturması yüksek ihtimaldir. Açık havada, özellikle aşırı nem ve yağış alan yerlerde silolar zamanla daha hızlı korozyona uğrar. Dolayısıyla korozyon nedeniyle delinen silolar üretimin durmasına ve ciddi mali kayıplara yol açabilir. Boyama, metal yüzey ile çevre arasında bir bariyer oluşturarak korozif maddelerle doğrudan teması önlediği ve çelik yapının ömrünü uzattığı için çeliği korozyondan korumanın başlıca yöntemlerinden biridir. Bu çalışmada, Fibrobeton GFRC şirketi tarafından 20 yıldır kullanılan ve ağır korozyona uğramış iki silonun bakım çalışmaları ASTM D3276, ISO 8501 ve ISO 12944:2018 standartlarına göre adım adım gerçekleştirilmiştir. Eski boyanın silo yüzeyinden uzaklaştırılması için sulu kumlama kullanılmış, ardından korozyon inhibitörleri içeren patentli bir asit çözeltisi (TPE Patent Başvuru No: 2017/11354) ile oksit tabakası temizlenmiş, ardından iki kat yüzey toleranslı ($Zn_3(PO_4)_2$ bazlı) epoksi boya ve ardından UV dayanımı yüksek akrilik boya uygulanmıştır. Bu çalışmada bakım işlemi sırasında metal yüzeyin boya öncesi standartlara uygun olarak hazırlanmamasından kaynaklanan sorunlara da dikkat çekilmiştir.

Anahtar Kelimeler: *Korozyon, silo, boya, bakım, atmosferik korozyon*

I. INTRODUCTION

Corrosion is the process by which a material loses its physical and mechanical properties over time by reacting with its environment through chemical or electrochemical processes. Corrosion causes serious economic losses in the construction industry as well as in many other industries [1].
Atmospheric corrosion was one of the first types of corrosion to be observed. This type of corrosion is commonly observed on metals in both indoor and outdoor environments. Steel silos are generally used in an open atmosphere. Steel silos used in different atmospheric conditions in different parts of the world are corroded by the effects of humidity / moisture, temperature, salt ions and industrial gases formed due to air pollution [2]. Due to industrialisation, there are many toxic, acidic and alkaline solids, liquids and gases in the environment and atmosphere [3]. Unless there is a specific reason (e.g. food and health), silos are made from plain carbon steels because they are easy to form and weld and are readily available and cheap. It is important to protect these metals, which are less resistant to corrosion than other metal alloys, especially from atmospheric corrosion [4].

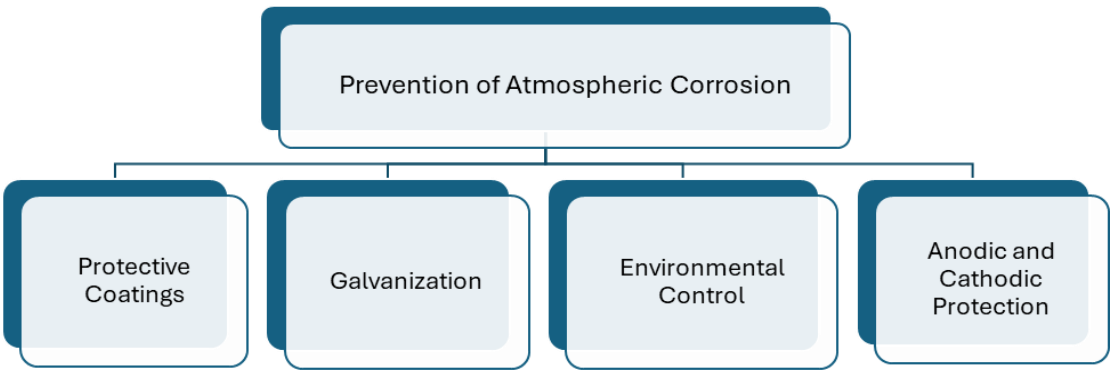

Figure 1. *Preventing atmospheric corrosion*

By applying the preventive measures shown in Figure 1, it is possible to effectively reduce the potential damage from atmospheric corrosion and thus extend the life of metallic materials exposed to the external environment. Steel silos have many auxiliary parts and equipment. Welding is a commonly used process in the manufacture of these parts. The welding process significantly affects not only the mechanical properties but also the corrosion properties of various types of metallic materials due to microstructural changes [5-8]. The weld areas are the most exposed and damaged areas to corrosion. Coatings are the

basic methods of protecting metals from corrosion. Metallic materials are successfully protected against corrosion for a long time thanks to coating methods based on the logic of creating a barrier by preventing the diffusion of water, oxygen and other factors [9,10].
Zinc is a typical metal coating widely used in anti-corrosion coatings. Zinc provides both cathodic protection and barrier protection [11,12]. Zinc-rich paints are used in various harsh environments [13]. Depending on the type of paint, zinc-rich coatings are divided into organic and inorganic coatings [14]. The most common organic binders are epoxy/polyamine-amide, vinyl resins, chlorinated rubbers, unsaturated polymers, etc. [15]. Paints containing corrosion inhibitors [16] have also become widely used.

In this study, two cement silos were cleaned of old paint and corrosion products by wet blasting. After sandblasting, the silos were washed with a patented corrosion inhibitor and prepared for painting. After two coats of a resin-based primer, the process was completed with a polyurethane-based topcoat. The problems experienced during all these processes and the experiences gained are presented in this study as a case study to shed light on future applications.

II. MATERIAL and METHOD

A. Surface Preparation Before Painting

Although the two 70 tonne silos, which have been in service for around 20 years, had undergone general maintenance on several occasions, it was found that the protective properties of the paint had been compromised due to under-shell corrosion (Figures 2 and 3).

Figure 2. *First state of silos*

Figure 3. *Condition of silos before painting*

Since the roof of the Fibrobeton Yapı Elemanları San.İnş.Tic.A.Ş. [17] factory is covered with solar panels to ensure energy and resource efficiency and reduce carbon emissions, wet blasting was preferred to remove the existing blistered old paint on the surface of the silos (Figure 4).

Figure 4. *Wet blasting process*

Aqueous blasting was carried out at a pressure of 300 bar using silica sand with a grain diameter of 0.125 mm-1.0 mm. Immediately after aqueous blasting, an oxide film was formed on the surface of the silos due to corrosion (Figure 5).

Figure 5. *General view of silos after wet blasting*

The removal of this oxide layer before painting is as important as the quality of the paint [18]. According to the Association for Material Protection and Performance (AMPP) [19] and ISO 8501 standards, chemical solutions can be used to clean the oxide film shown in Figure 5 [20].

This oxide film on the surface of the silos was cleaned with a patented solution (TPE Patent Application No: 2017/11354) previously tested by Coskun et al. [21]. As the solution has a density that can be applied with a high-pressure cleaner, the oxide film on the surface of the silos was removed by washing 3 times in a very short time (Figure 6).

Figure 6. *Washing process with chemical solution*

Figure 7. *After washing with chemical solution*

Figure 8. *After washing with chemical solution and wiping the silos with a car brush*

After washing with the chemical solution, a light grey layer was formed on the metal (Figure 7). In order not to leave dust on the surface, the silos were wiped with a brush and made ready for painting (Figure 8).

B. Preparation and Application of Paint

After the application of the chemical solution, two coats of primer and one coat of topcoat were applied respectively. After each paint application, paint thicknesses were measured with Elcometer thickness gauge device.

The primer paint used in the study was obtained from Kanat Boya company (15550 KANEPOX MASTICOAT). The primer paint used in the study is a resin-based two-component product cured with polyamine hardener, containing anticorrosive zinc phosphate pigments and low organic volatile matter, as specified in the product description form in Table 1.

Table 1. *Technical specifications of the primer*

Density (gr/ml)	1.50±0.10
Colour	Oxide Red
Theoretical spread rate (m^2/lt)	8.40
Flash point	43 °C
Volatile organic compounds (gr/lt)	132
Mixing ratio (by volume)	16 units "A" component + 4 units "B" component
Solid matter in the mixture (%)	84±2

The topcoat used was also supplied by Kanat Boya (37850 KANPOLY ACR ENAMEL DTM). It consists of a high solid, anti-corrosive, glossy acrylic polyurethane resin topcoat with zinc phosphate pigments. It has high adhesion, colour and gloss resistance, elasticity and mechanical resistance. The UV resistance has been tested by COT according to ISO 16474-3. Technical specifications of the topcoat are given in Table 2.

Table 2. *Technical specifications of the topcoat*

Density (gr/ml)	1.62±0.10
Colour	Grey
Theoretical spread rate (m^2/lt)	11.67
Flash point	39 °C
Volatile organic compounds (gr/lt)	270
Mixing ratio (by volume)	16 units "A" component + 2 units "B" component
Solid matter in the mixture (%)	70±2

The recommended dry paint film thickness for atmospheric corrosion categories in accordance with ISO 12944:2018 is shown in Table 3.

Table 3. *Guide values of coating thickness required in silos*

First coat of primer paint (µm)	Second coat of primer paint (µm)	Top coat paint (µm)
120	120	60

Thickness measurements were taken after the application of the first and second coats of primer and the top coat (Figures 9, 10, 11 and 12).

Figure 9. *First coat primer application*

Figure 10. *Measurement of primer paint thickness of silos*

Figure 11*. Second coat primer paint application of silos*

Figure 12. *Topcoat paint application of silos*

III. RESULTS and DISCUSSION

Research shows that most paint failures are caused by application errors. According to the ASTM D3276 standard, the relative humidity of the environment in which the paint is applied, the temperature of the metal surface and the proper preparation of the metal surface are extremely important. Unfortunately, the days chosen for painting were the days with the highest relative humidity. As the cranes were not allocated on time, the painting process took quite a long time. The thicknesses of silos numbered one and two were measured 3 (three) times from 8 points which were determined to be always on the same line and the average thickness values are shown in Table 4. As can be seen, higher thickness values were read where the first coat of primer should be 120µm. For example, at the fourth point the thickness doubled to 240 microns.

As can be seen in Table 4, the thickness of the first primer coating in silo number one was measured to be 70-90 µm higher. In high thickness paint applications, especially in the substrate, expansion and contraction may occur with temperature changes, which may lead to cracking and peeling of the paint over time. Excessively thick coatings can also cause sagging and dripping problems when applied to vertical surfaces. This situation will undoubtedly make it difficult to achieve a uniform appearance on the painted surface and will also increase the cost of protection.

Table 4. *Thickness measurements of paint applied to silo number one*

Measurement Point	1st primer paint (µm)		2nd primer paint (µm) + Topcoat paint (µm)		Total deviation compared to method
	Measurements	Average	Measurements	Average	
1	245, 178, 205	209	272, 326, 334	310	10 µm more
2	270, 196, 230	232	334, 313, 353	333	33 µm more
3	202, 270, 236	236	380, 414, 363	385	85 µm more
4	248, 242, 230	240	387, 401, 380	389	89 µm more
5	236, 220, 204	220	413, 368, 398	393	93 µm more
6	198, 176, 200	192	395, 321, 390	368	68 µm more
7	156, 118, 133	135	321, 314, 261	298	2 µm less
8	200, 193, 205	199	373, 328, 358	353	53 µm more

In silo number two, on the contrary, Table 5 shows that the first coat of primer is approximately 5-55 µm less. The curvature of the silos, due to their geometrical structure, prevented a homogeneous distribution of the paint thicknesses. As it was more difficult to work on the parts of the silos facing the factory wall due to the lack of space, the paint thicknesses in these areas were sometimes less than the first primer coat value as planned in Table 3. As it was not clear how much solvent was being used, the possibility of the technical staff using more solvent than necessary during the paint preparation process, particularly when preparing the paint required for silo number two, was also not considered. In addition, the average paint thickness after the second coat and the main coat varied between 215-393 µm in both silos for the reasons mentioned above.

Table 5. *Thickness measurements of paint applied to silo number two*

Measurement Point	1st primer paint (µm)		2nd primer paint (µm) + Topcoat paint (µm)		Total deviation compared to method
	Measurements	Average	Measurements	Average	
1	57, 78, 85	74	226, 244, 236	235	65 µm less
2	115, 82, 118	105	244, 270, 282	265	35 µm less
3	118, 73, 76	89	278, 241, 285	268	32 µm less
4	142, 83, 117	114	287, 192, 257	245	55 µm less
5	76, 72, 82	77	232, 225, 265	240	60 µm less
6	66, 60, 70	65	303, 282, 235	273	27 µm less
7	62, 70, 74	69	232, 218, 228	226	74 µm less
8	68, 107, 70	82	216, 227, 204	215	85 µm less

In the ISO 12944:2018 standard, the atmospheric corrosion classification is classified as C1 and C2 for atmospheres with high and low corrosion rates, respectively. In this context, it can be seen that the average total paint thickness of the silo (Silo 2) given in Table 5 is 108 µm less than the average total thickness of Silo 1. Therefore, it is 120 µm more than the recommended paint thickness for both silos for Class C1 and C2 atmospheres for corrosion protection. In this context, both silos have been coated according to the relevant standard to provide protection for more than 25 years [22, 23].

IV. CONCLUSIONS

This study summarises the experience and results obtained during the maintenance of two silos subjected to severe atmospheric corrosion.

1) The method used to remove old paint is important. The water molecules pulverised during the wet blasting process reacted with the metal and caused corrosion.
2) Homogeneous corrosion products formed on the metal surface can be successfully removed from the metal surface using chemical solutions. Care should be taken to ensure that the product selected for this process does not contain chemicals that are harmful to the environment and human health.
3) Weather conditions must be taken into account in the pre-coating design. A successful finish can only be achieved in favourable weather conditions.
4) Surface preparation is at least as important as the quality of the paint. Surfaces should be prepared in accordance with standards.
5) Applying excessive paint thickness to the metal surface does not mean better protection. Excess paint will only increase the cost.
6) Applying less primer than necessary to the metal surface will cause rust attack and rust spots (peak corrosion) on the surface of the painted material, depending on the conditions.
7) The primer and topcoat applied must be of compatible components. Otherwise, delamination will occur.
8) The solvent used in the preparation of the paint must be suitable for the paint and must be used in the required quantity.
9) It is expected that the painting process carried out in the atmospheric conditions of the two silos subject to this study will provide protection for more than 25 years according to the relevant standard.
10) This study has once again shown that the technical personnel involved in the process of preparing and painting the silo surface should receive all the necessary training. Technical personnel who do not have the necessary training and awareness may refuse to comply with the standards because they have difficulty understanding the importance of the work. In this context, the importance of institutions and organisations that provide vocational training has been confirmed by this study.

Acknowledgements: This scientific study was carried out in cooperation between Düzce University and Fibrobeton Research and Development Centre. The authors would like to thank Hasan Bilgin, Volkan Akmaz, Sedat Enveş, Yasemin Hatipoğlu and Faik Ali Birinci from Fibrobeton Company R&D Centre for their valuable assistance during this research.

V. REFERENCES

[1] G. Bereket, H. Gerengi, "How truly electrochemical measurements are evaluated in corrosion researches?", Journal of Corrosion, ISSN 1306-3588; 21(1), 33-44 pp., 2015.

[2] Y. Ma, Y. Li, F. Wang, "The atmospheric corrosion kinetics of low carbon steel in a tropical marine environment", Corrosion Science, vol.52, no.5, pp.1796-1800, 2010, https://doi.org/10.1016/j.corsci.2010.01.022.

[3] M. Marasli, K. Dikmen, V. Akmaz, M. Kam, H. Gerengi, "Investigation of the effect of acid rain on the corrosion mechanism of the anchorage element used in glass fiber reinforced concrete",

7th International Congress on Engineering, Architecture and Design, Oral presentation/ Oral presentation book: 103-112, ISBN 978-625-7367-12-7, Istanbul, 2021.

[4] M. Morcillo, D. de la Fuente, I. Díaz, H. Cano, "Atmospheric corrosion of mild steel", Rev. metal. 47 (5), issn: 0034-8570, 2011, https://doi.org/10.3989/revmetalm.1125.

[5] I. Uygur, B. Gulenc, "The effect of shielding gas compositions for MIG welding process on mechanical behavior of low carbon steel", Metalurgija 43 (1), pp 35-40, 2004.

[6] I. Uygur, "Influence of Shoulder Diameter on Mechanical Response And Microstructure of FSW Welded 1050 Al-Alloy", Archives of Metallurgy and Materials, 57 (1), 53-60, 2012, doi: 10.2478/v10172-011-0152-3.

[7] H. Gerengi, N. Sen, I. Uygur, E. Kaya, "Corrosion behavior of dual phase 600 and 800 steels in 3.5 wt.% NaCl environment", Journal of Adhesion Science and Technology, pp. 1-13, 2020.

[8] A. Kurt, I. Uygur, H. Ates, "Effect of Porosity Content on the Weldability of Powder Metal Parts Produced by Friction Stir Welding", Materials science forum 534, pp. 789-792, 2007.

[9] I. Danaee, E. Darmiani, G.R. Rashed, D. Zaarei, " Self-healing and anticorrosive properties of Ce(III)/Ce(IV) in nanoclay–epoxy coatings", Iran Polym. J. 23 pp. 891–898, 2014, https://doi.org/10.1007/s13726-014-0288-x.

[10] H. Shi, F. Liu, L. Yang, E. Han, "Characterization of protective performance of epoxy reinforced with nanometer-sized TiO2 and SiO2", Prog. Org. Coat. 6, pp. 359–368, 2008, https://doi.org/10.1016/j.porgcoat.2007.11.003.

[11] S. Shreepathi, P. Bajaj, B.P. Mallik, "Electrochemical impedance spectroscopy investigations of epoxy zinc rich coatings: Role of Zn content on corrosion protection mechanism", Electrochim. Acta 55, pp. 5129–5134, 2010, https://doi.org/10.1016/j.electacta.2010.04.018.

[12] N. Arianpouya, M. Shishesaz, M. Arianpouya, M. Nematollahi, "Evaluation of synergistic effect of nanozinc/nanoclay additives on the corrosion performance of zinc-rich polyurethane nanocomposite coatings using electrochemical properties and salt spray testing", Surf. Coat. Technol. 216, pp.199–206, 2013, https://doi.org/10.1016/j.surfcoat.2012.11.036.

[13] H. Marchebois, S. Joiret, C. Savall, J. Bernard, S. Touzain, "Characterization of zinc-rich powder coatings by EIS and Raman spectroscopy", Surf. Coat. Technol. 157, pp. 151–161, 2002, https://doi.org/10.1016/S0257-8972(02)00147-0.

[14] L. Zhang, A. Ma, J. Jiang, D. Song, "Anti-corrosion performance of waterborne Zn rich coating with modified silicon-based vehicle and lamellar Zn (Al) pigments", Prog. Natur. Sci: Mater. Int. 22, pp. 326–333, 2012, https://doi.org/10.1016/j.pnsc.2012.07.001.

[15] M.N. Kakaei, I. Danaee, D. Zaarei, "Evaluation of cathodic protection behavior of waterborne inorganic zinc-rich silicates containing various contents of MIO pigments", Anti-Corros. Methods Mater. 60, pp. 37–44, 2013, http://dx.doi.org/10.1108/00035591311287438.

[16] M. Rizvi, H. Gerengi, S. Kaya, I. Uygur, M. Yıldız, I. Sarıoglu, Z. Cingiz, "Sodium nitrite as a corrosion inhibitor of copper in simulated cooling water", Scientific reports 11 (1), 8353, 2021, doi:10.1038/s41598-021-87858-9.

[17] https://fibrobeton.com.tr/Anasayfa (Date of access:12.06.2024)

[18] S. Guo et al., "A critical review of corrosion development and rust removal techniques on the structural/environmental performance of corroded steel bridges", Journal of Cleaner Production 233, pp. 126-146, 2019, https://doi.org/10.1016/j.jclepro.2019.06.023.

[19] https://blogs.ampp.org/surface-prep-standards-a-quick-summary (Date of access: 22.05.2024)

[20] TS EN ISO 8501 (2008). Çelik taban malzeme yüzeylerin hazırlanması - Boya ve ilgili malzemelerin uygulanmasından önce - Yüzey temizliğinin gözle muayenesi, Türk Standartları Enstitüsü, Ankara.

[21] K. Coskun, K., H. Gerengi, M. Maraslı, F.A., Birinci, V. Özdal, "Use of Corrosion Inhibitors in Stainless Steel Anchors Used in Glass Fiber Reinforced Concrete (GRC) Precast Façade Elements", The European Journal of Research and Development, Vol.3 No.1, 2023. https://doi.org/10.56038/ejrnd.v3i1.220

[22] https://boyacozumleri.com.tr/tmweb/upload/B%C3%87%20ISO%2012944%202018.pdf (Date of access:20.04.2024)

[23] H. Gerengi, Mosses M. Solomon, M. Marasli, B. Kohen, "A comparative analysis of the corrosion characteristics of electro-galvanized steel coated with epoxy zinc-free and zinc-rich coatings in 5% NaCl", Journal of Adhesion Science and Technology, vol. 37, Issue 20, 2023, https://doi.org/10.1080/01694243.2022.2123603.

Düzce University Journal of Science & Technology

Research Article

Detection of Eye Pressure Disease Using ViT-Based Hybrid Learning Methods

Mahmut KAYA [a,*], Yusuf BİLGEN [b]

[a,*] *Department of Artificial Intelligence and Data Engineering, Faculty of Engineering, Elazığ, TURKEY*
[b] *Department of Computer Engineering, Faculty of Engineering, Siirt University, Siirt, TURKEY*
** Corresponding author's e-mail address: mahmutkaya@firat.edu.tr*
DOI: 10.29130/dubited.1494138

ABSTRACT

Glaucoma is a disease that occurs after a certain age due to damage to the optic nerves. Today, machine learning methods can be successfully applied to detect such diseases. Instead of using the image data directly, the classification process is carried to a new representation space, positively affecting the classification performance. In this study, principal component analysis (PCA), linear discriminant analysis (LDA), and vision transformation (ViT) methods are used for feature extraction. In addition, the CLAHE filtering technique before ViT B16 was used in one of the proposed models. The classification process was performed with six different models using these methods alone or in combination, and the results are presented comparatively. Fine Tuned ViT-PCA-SVM and Fine Tuned ViT-LDA-SVM models achieved 92% classification success. As a result, the combination of ViT, which is a deep learning method, and PCA or LDA, which are machine learning methods, as feature extraction methods increased the classification success.

Keywords: *Glaucoma, Classification, Vision transformer, Principal Component Analysis, Linear discriminant analysis*

ViT Tabanlı Hibrit Öğrenme Yöntemleri ile Göz Tansiyonu Hastalığının Tespiti

ÖZET

Glokom, belirli bir yaştan sonra görme sinirleri üzerinde oluşan bir hasardan dolayı ortaya çıkan bir rahatsızlıktır. Bu tür hastalıkların tespitini yapmada günümüzde makine öğrenmesi yöntemleri başarıyla uygulanabilmektedir. Görüntü verilerinin doğrudan kullanımı yerine yeni bir temsili uzaya taşınarak sınıflandırma işleminin gerçekleştirilmesi sınıflandırma performansını olumlu etkilemektedir. Bu çalışmada öznitelik çıkartmada temel bileşen analizi (PCA), doğrusal ayırım analizi (LDA) ve görü dönüştürücü (ViT) yönteminden yararlanılmıştır. Ayrıca önerilen modellerden birinde ViT B16 öncesi CLAHE filtremele tekniği kullanılmıştır. Bu yöntemlerin tek başına veya bir araya getirildiği altı farklı model ile sınıflandırma işlemi gerçekleştirilmiş olup sonuçlar karşılaştırmalı olarak verilmiştir. Fine Tuned ViT-PCA-SVM ve Fine Tuned ViT-LDA-SVM modelleri %92 oranında sınıflandırma başarısı elde etmiştir. Sonuç olarak derin öğrenme yöntemi olan ViT ve makine öğrenmesi yöntemlerinden olan PCA veya LDA'nın öznitelik çıkartma olarak bir arada kullanıldığı yöntemler sınıflandırma başarısını arttırmıştır.

Received: 07/06/2024, Revised: 20/09/2024, Accepted: 02/10/2024

Anahtar Kelimeler: *Glokom, Sınıflandırma, Görü dönüştürücü, Temel bileşen analizi, Doğrusal ayırma analizi*

I. INTRODUCTION

Glaucoma is a disorder caused by damage to the main visual nerve (optic nerve), which has a significant proportion among the causes of vision loss in middle age [1]. The main factor in glaucoma is long-term increased intraocular pressure [2]. However, there are also factors, such as lack of blood supply to the optic nerve head, that cause this condition [3, 4, 5]. When the diagnosis and treatment of glaucoma are delayed, it can result in blindness [1]. In this respect, Glaucoma is an important condition that should be taken seriously. According to estimates in the literature, approximately 64.3 million people in the 40-80 age group were diagnosed with glaucoma worldwide in 2013, and this number is expected to reach 112 million by 2040 [14].

Fundus is a term used in ophthalmology and refers to the posterior region of the inner part of the eye. This area includes the retina, optic disc (the beginning of the optic nerve), and blood vessels on the posterior wall of the eye. The first fundus imaging was performed with devices available in the 1960s. Fundus examination is used for disorders related to eye vessel structures, neurological problems, and retinal-optic nerve problems that cause vision loss. Fundus imaging provides images of structures such as the optic nerve, retina, and eye vessels [6].

Using machine learning and deep learning methods in medical imaging and disease diagnosis is becoming increasingly important [7, 8]. Deep learning segmentation applications for muscle pathology image analysis [9], tumor growth prediction using convolutional neural networks [10], automatic classification and reporting of multiple common thoracic diseases using chest radiographs [11], and early detection of epidemics are just a few of the applications.

Many successful machine learning methods exist for both classification and clustering problems in obtaining meaningful results from medical data [12]. However, various data transformation methods can be applied to these data before using classification and clustering methods. Data transformation can significantly improve classification performance by extracting more meaningful information from the data [13]. In this sense, various machine learning methods have proven their success in the literature. These transformations include principal component analysis (PCA) and linear discriminant analysis (LDA). Recently, deep learning methods have been used on large datasets, going beyond the disease diagnosis experiments of computer technologies and providing results with high accuracy rates. Vision transformer models also achieve very successful results for image data in the literature.

In this study, vision transformer b16 model (ViT), principal component analysis (PCA), and linear discriminant analysis (LDA) methods were used together and separately to obtain new features for the detection of glaucoma disease using a large dataset consisting of 17,292 fundus images from different hospitals. SoftMax or SVM was used in the proposed models to perform the classification process after feature extraction.
In our study, we used a hybrid model that we believe has not adequately detected glaucoma disease from model fundus images. The hybrid model combines the strengths of classical image processing techniques and deep learning algorithms, allowing us to analyze glaucoma findings in fundus images more successfully.

II. LITERATURE REVIEW

A summary of the studies in the literature is given below, including different approaches to detect Glaucoma. Some studies classified fundus images using transfer learning methods in convolutional neural networks. In the second group of studies, other clinical data were used instead of fundus

images, and classification studies were performed using machine learning models such as SVM. In the third group of studies, the authors developed deep learning models and trained them with fundus images. In the fourth group of studies, segmentation data alone or with fundus images were used for classification.

In their study, Şatır et al. performed data reduction with the rough sets method using the data of 168 individuals, followed by classification using decision trees and artificial neural networks. The study used parameters such as intraocular pressure, central corneal thickness, disc area, and age. When decision trees were used in the study, a success rate of 93.45% was achieved. In the classification using artificial neural networks, a success rate of 91.67% was achieved [1].

Yıldırım and Ozbay worked with AlexNet, ResNet-18, VGG16, SqueezeNet, and GoogleNet convolutional neural network models using 1000 images of people obtained from the open-source Origa (-light) dataset. In the study, the results were compared with many metrics. In terms of accuracy metric, the best value was obtained from GoogleNet with 97.98%, and the lowest value was obtained from the SqueezeNet model with 93.43% [14].

Uçar used a dataset of 4854 fundus images in his study. He used a transfer learning method with VGG16, Inception-V3, EfficientNet, DenseNet, ResNet50, and MobileNet architectures. He compared model performance with different validation metrics and cross-validation. As a result of the study, the models gave similar results. The highest accuracy value was obtained from the DenseNet architecture, with 96.19%. The lowest value was obtained from the MobileNet architecture, with 92.79% [15].

Dey et al. first applied some preprocessing to 100 fundus images, and feature extraction was performed using principal component analysis (PCA). The outputs were subjected to binary classification using support vector machine (SVM). The RBF kernel was used when applying SVM, and the gamma parameter was set to 1.5. The study, 10-fold cross-validation was used, and success was evaluated using different metrics. As a result of the study, 86% accuracy was achieved [16].

Karrothu et al. preprocessed the fundus images obtained from the Rim-One-R2 dataset, consisting of 248 images, by applying a CLAHE filter and then trained the VIT model to detect disease. Depending on whether the fundus images are left-eye or right-eye images, cropping was applied from the appropriate position and left the parts with the optic disc. As a result of the study, the success rate of 95.7% was obtained in CLAHE-applied images and 91.4% in unapplied images [17].

In the Wu et al. study, an SVM model was trained with 10-fold cross-validation using 114 OCT features and three clinical features (age, gender, and refraction) divided into nine groups in which values such as average thickness of the retina and nerve fiber layer were determined region by region from 752 Spectralis optical coherence tomography (OCT) data obtained from a hospital in Taiwan and performance evaluation was performed with various metrics. In this study, each OCT feature and three clinical features (age, gender, refraction) were evaluated for their association with glaucoma using the mutual information method. From these features, the top 20 features with the highest performance according to their mutual information values were selected and trained with the SVM model. The best-performing features were continuously added, and this process continued iteratively until ten features were selected. Only features that improved the model's performance compared to the previous steps were considered for the final subset. As a result of the study, with 96% accuracy in the advanced disease group and 92% in the intermediate disease group, the highest success rate was obtained, while a 73% success score was obtained in the early stage. [18].

In Phasuk et al.'s study, the network considers disease image information at two levels: the global image and the local disk region. In this paper, the DenseNet-121 model was used to learn the global image, and then a second part was used to segment the disc and cupping region using a residual deconvolution neural network. The ResNet-50 architecture was utilized in the second part. Horizontal translation and rotation were used for data augmentation to ensure generalization. In some neural networks, a maximum filter was applied to remove the blood vessel image. In addition, the contrast-

limited adaptive histogram equalization (CLAHE) method was also used to increase the contrast in the fundus image and prevent over-amplification noise. The results show that the data augmentation used affects the training time. Two streams were used to train the network in the optical disk region. After the local disk region is cropped, the local disk and cup region are labeled using segmentation. These data, which have the same structure as the network in the global image, were then imported into the Densenet-121 model. The second flow focuses on the polar coordinates of the optical and cup structures. Data augmentation was achieved with polar center shift and polar radius parameters in this part. The final classification was performed with a classical artificial neural network. As a result of the study, a 94.0% success rate was obtained [19].

Li et al. used 39,745 image data for classification in their study. After dividing the dataset into training and test data, the data was normalized and resized to 299x299, and local area averaged color subtraction was applied to ensure color stability. Horizontal shifting and random rotation operations were performed for data augmentation. Inception-v3 architecture was utilized in the study. The images misclassified as a result of the training were also examined by experts, and it was found that many of the patients had different eye problems. A high AUC value of 0.986 was obtained in the study [20].

Fu et al. derived their M-Net model from the U-Net architecture. In this architecture, an image is taken, and a polar transformation is applied to the optical disk region. The output is sent to a series of convolution layers. The model outputs maps segmenting the optic disc and optic cup. M-Net is a network designed explicitly for multi-label segmentation in fundus disease images. An automated method is used to localize the optic disc region. Then, the original fundus image is transformed into a polar coordinate system based on the detected disc center. The M-Net model has side outputs, and combining these outputs provides the final result. The study was performed using ORIGA and SCES datasets containing 2326 images, including 214 glaucoma-positive images, and an AUC value of 0.89 was achieved [21].

The DENet model, designed in Fu et al.'s study, performs classification by considering the fundus image's global and local disk region. This architecture includes four streams. These are the global image stream that produces the result based on the whole fundus image, the segmentation guidance network that detects the optic disc region and provides the disc-segmentation representation by estimating a probability, the disc region stream that works on the disc region cropped by the disc-segmentation map obtained from the segmentation guidance network, and the disc polar stream that transfers the disc region image to the polar coordinate system. The outputs of these four streams are then combined into the final glaucoma screening result. ResNet and U-Net architectures were used to realize these streams. The study used three datasets, ORIGA, SCES, and SINDI, containing 8109 images, 327 of which were glaucoma-positive, resulting in an AUC of 0.91 [22].

When the studies in the literature are examined, it is seen that very successful models have been obtained. However, the success rates of these models have not yet reached the success and stability that can be used in medical applications. This shows the necessity of artificial intelligence studies on glaucoma disease. In our study, we have made significant contributions to the subject based on this need identified in the literature and the health sector, and a successful model has been put forward with a hybrid model we have developed with a different approach to solving the problem. The multi-layered data analysis in fundus images of our hybrid artificial intelligence model brings an important innovation to the knowledge in the field by using the hybrid artificial intelligence model approach, which has not been sufficiently studied in the literature in diagnosing glaucoma.

III. MACHINE LEARNING AND DEEP LEARNING METHODS

A. VISION TRANSFORMER (VIT)

Vision Transformer is one of the deep learning architectures used in image processing. While the Transformer architecture was originally developed for natural language processing (NLP) tasks, ViT is one of the first major works to apply this architecture to image processing tasks [23]. Figure 1 shows the basic structure of a vision transformer model.

Vision Transformer divides images into small patches and processes these patches as an array. Each patch is treated like words in natural language processing. The attention mechanisms of the Transformer architecture then process the patches. The attention mechanisms allow it to focus on the relationships between different image regions, allowing the model to understand which regions are more important. While CNNs focus on local features, ViT can model the overall connections between all image regions. When trained on large amounts of data, ViT goes beyond the limitations of Convolutional Neural Networks (CNNs), which focus on local features, by breaking images into small chunks, processing these chunks as a sequence, and modeling the overall connections between regions through attentional mechanisms; therefore, ViT can achieve more impressive results on large datasets.

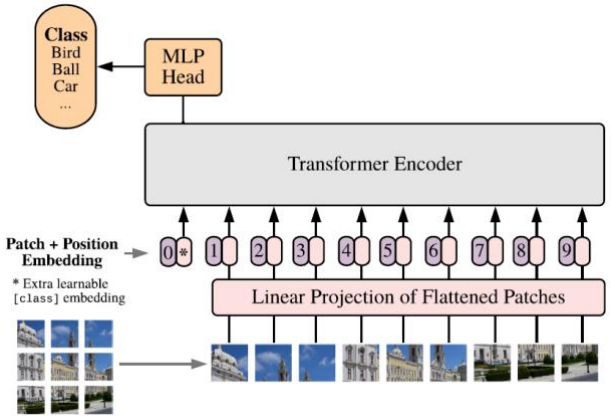

Figure 1. *Model Overview of Vision Transformer [23]*

B. PRINCIPAL COMPONENT ANALYSIS (PCA)

PCA is a statistical method that simplifies data by identifying the most important features in data sets [24]. Its main purpose is to find the principal components that maximize the variance in the data set and reduce its size by multiplying the data by a matrix of these components. The resulting new data set is usually smaller than the original dataset, discarding redundant information and noise while retaining the most important features. The implementation of PCA involves first centering the data around the mean value, then calculating the covariance matrix, finding the eigenvalues and eigenvectors of this matrix, and finally projecting the data onto these eigenvectors. This method reveals hidden structures and relationships, especially in large data sets, to facilitate visualization and make the data more understandable. PCA has been applied in many fields, such as face recognition, image processing, genetics, and financial analysis. In the PCA method, the calculation steps are done in 5 steps as follows;

First, the data is centralized by extracting the mean of each feature. If our data matrix X is of size n×p, where n is the number of samples and p is the number of features, we calculate the mean $\tilde{x}$ for each feature and subtract this mean from the data matrix

$$\bar{x} = \frac{1}{n}\sum_{i=1}^{n} x_i$$

$$X' = X - 1_n\bar{x}$$

Here, (1_n) is a unit vector of length n, and Xl denotes the centralized data matrix. In the second step, we calculate the covariance matrix of the centralized data matrix. Denote the covariance matrix by it is calculated as:

$$\Sigma = \frac{1}{n-1}(X')^T X'$$

In the third step, we need to find the eigenvalues and eigenvectors of the covariance matrix. With eigenvalues λ and eigenvectors v and Σ being the covariance matrix:

$$\Sigma v = \lambda v$$

To find the eigenvalues and corresponding eigenvectors of the covariance matrix. The fourth step is to select the Principal Components. We sort the eigenvalues from largest to smallest and select the eigenvectors usually associated with the largest eigenvalues. These selected eigenvectors transform the data into a less dimensional space.

In the final stage, we transform the data by multiplying it by the selected eigenvectors. Denote the transformed data matrix by X_{new}:

$$X_{new} = X'W$$

W is a size p x k matrix formed by the selected eigenvectors, and k is the number of principal components selected.

C. LINEAR DISCRIMINANT ANALYSIS (LDA)

LDA is a dimensionality reduction and classification technique used to classify samples from a dataset into classes [25]. Its main goal is to find a transformation that maximizes the separation between different classes. This process aims to maximize the distance between classes while minimizing the distance between instances belonging to the same class. LDA is beneficial for classification and data analysis. This is because it emphasizes the separation between classes, helping to achieve more accurate classification results. Unlike PCA, it is a supervised method and uses class labels. LDA analyzes how the data is distributed to distinguish specific classes. Therefore, it is more suitable for classification processes.

In LDA, the intra-class and inter-class scatter matrices are first calculated. The intra-class scatter matrix shows how the samples of the same class are distributed concerning the class average, while the inter-class scatter matrix shows how different classes differ from the overall average. These matrices are then used to find the discriminant axes that maximize class separation. Dimensionality reduction is performed by projecting the data onto these axes. LDA is used in supervised learning scenarios and has applications in fields as diverse as face recognition, biological data analysis, and finance.
The computation in the LDA method can be divided into several stages. Let X represent the features in a dataset. Let each sample contain an array denoted by x_i divided into c classes.

Let x_i be the sequence of each sample and, c be the classes, μ_k be the mean vector of each class is calculated as;

$$\mu_k = \frac{1}{N_k}\sum_{i \in C_k} x_i$$

N_k denotes the number of samples in the kth class, and C_k is the set of all data samples belonging to the kth class.

The mean vector μ for all data is calculated as follows.

$$\mu = \frac{1}{N}\sum_{i=1}^{N} x_i$$

Where N is the total number of samples, the within-class variance matrix S_W is calculated as follows.

$$S_W = \sum_{k=1}^{c}\sum_{i\in C_k}(x_i - \mu_k)(x_i - \mu_k)^T$$

In this way, the variance of the samples within each class is found. The between-class variance matrix S_B is calculated as follows.

$$S_B = \sum_{k=1}^{c} N_k(\mu_k - \mu)(\mu_k - \mu)^T$$

Thus, it finds the separation between classes. LDA finds the best linear projection to separate classes.

$$J(w) = \frac{w^T S_B w}{w^T S_W w}$$

This ratio represents the ratio of between-class variance to within-class variance. The w that maximizes this ratio represents the best linear discriminator. To solve this problem, we solve the eigenvalue problem, usually expressed as follows.

$$S_W^{-1} S_B w = \lambda w$$

Here λ is the eigenvalue, and w is the corresponding eigenvector. These eigenvectors are used as separating lines for the linear projection of the data. After this step, the eigenvectors corresponding to the m largest eigenvalues are selected. A projection matrix $W = [u_1, u_2, \dots, u_m]$ is created with the selected eigenvectors. The input vectors are projected into a lower dimensional space by applying $X' = XW$ to this projection matrix. The projection reduces the dataset size while increasing the separation between classes. X is the original data matrix, and X' is the projected data matrix.

D. SUPPORT VECTOR MACHINES (SVM)

Support Vector Machines (SVM) is a powerful and flexible machine learning algorithm that is one of the supervised learning models used for classification tasks. It performs particularly well in high-dimensional data spaces and marginally separable data sets. The basic principle of SVM is to find the best decision boundary (hyperplane) to classify the examples in the dataset into classes. This decision boundary is chosen to maximize the marginal distance between instances belonging to different classes. The examples that are closest to the boundary and determine the position of this boundary are called “support vectors.” Figure 2 shows a simple SVM implementation in two dimensions. The figure shows the optimal

hyperplane, the optimal margin, and the data points in red and blue. The red and blue data points represent different classes, and the optimal hyperplane is positioned to maximize the separation between these two classes.

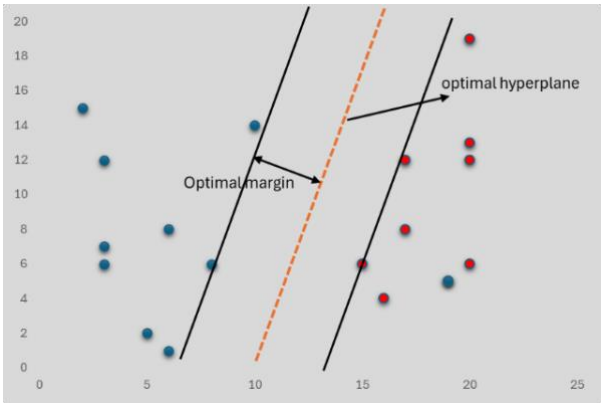

Figure 2. *A simple two-dimensional SVM example.*

SVM uses the kernel trick technique to process data sets that cannot be linearly separated. This technique transforms the data points from the original feature space into a higher-dimensional space, allowing linear separation in the new space. Standard kernel functions include polynomial, radial basis function (RBF), and sigmoid functions. The SVM algorithm is known for its high accuracy in many situations and its ability to create highly generalizable models. Therefore, it is successfully used in many fields.

E. CONTRAST LIMITED ADAPTIVE HISTOGRAM EQUALIZATION (CLAHE)

CLAHE is a method for improving contrast in images. It is particularly effective in low-contrast images and is widely used in medical imaging, satellite imagery, and photography.

CLAHE is based on the Histogram Equalization method. Histogram Equalization increases the contrast of an image by expanding its histogram, i.e., its color distribution, over the entire image. However, in some cases, it can result in excessive contrast enhancement and the appearance of noise. To solve this problem, CLAHE operates in a contrast-limited and adaptive way. CLAHE limits contrast increases above a certain threshold to prevent too high contrast enhancement. This prevents excessive increase of noise in the image. In addition, the image is divided into small regions to enable adaptive processing. Histogram equalization is applied separately for each region. Thus, a more balanced contrast enhancement is applied by considering the regional contrast differences of the image. Figure 3 shows an original fundus image from the dataset after the CLAHE application. Figure 3 clearly shows the positive effect of CLAHE application on contrast.

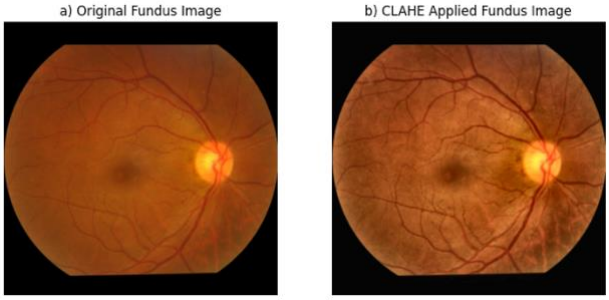

Figure 3. *CLAHE filter applied to RGB fundus image. a) Original image, b) CLAHE applied fundus image*

IV. MATERIAL AND PROPOSED MODELS

In this study, glaucoma disease was detected by classification with hybrid models. For this purpose, ViT, PCA, LDA, CLAHE, and SVM methods were utilized.

A. DATASET

SMDG-19 open-source dataset was used in our study. Information about this dataset is shown in Table 1.

Tablo 1. *SMDG-19 dataset*

Data	Number of Glaucoma Positive Images	Number of Glaucoma Negative Images	Total
Number of training samples	3328	5293	8621
Number of validation samples	2208	3539	5747
Number of test samples	1120	1754	2874
Total	6656	10586	17242

Depending on the dataset's size, the model's requirements, and the results of the preliminary studies, the dataset was divided into 50% training, 33% validation, and 17% test data. The original images in the dataset are at a standardized scale of 512x512. The images were obtained by merging and standardizing 19 different open-source datasets. Figure 5 shows a sample of glaucoma-positive and glaucoma-negative images from the dataset.

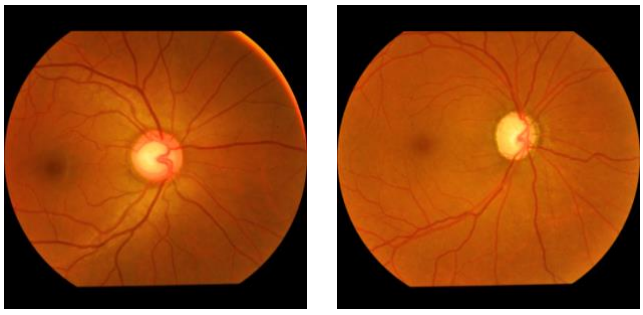

Figure 5. *Sample Glaucoma negative (left) and Glaucoma positive (right) images from the SMDG-19 dataset.*

B. DATA PREPROCESSING

One of the most important steps to increasing the success of deep neural network methods is to train the models with as much data as possible. Increasing data provides better learning and increases the model's reliability. For this reason, data augmentation was performed on the dataset before training the data. The data augmentation process can have different perspectives depending on the models applied, and each model, and the data augmentation techniques used in these models are given in Table 2.

Table 2. *Preprocessing and data augmentation for models.*

Model	Image size	Preprocessing and Data Augmentation
Fine Tuned ViT	224x224	Random horizontal and vertical flip
CLAHE-Fine Tuned Vit	224x224	CLAHE filter on the green channel, Random horizontal and vertical flip
Fine Tuned ViT-PCA-SVM	224x224	Random horizontal and vertical flip
Fine Tuned ViT-LDA-SVM	224x224	Random horizontal and vertical flip
ViT-PCA-SVM	224x224	Random horizontal and vertical flip
Incremental PCA - SVM	224x224	-

The SMDG-19 dataset used in the study increases the generalizability of the model. It is expected to provide a high degree of relevance to clinical applications thanks to its high number of images and the application of various preprocessing techniques. The large scope and standardization of the dataset increases the likelihood of adequately representing variations in real-world conditions, which aims to strengthen the expectation of supporting the clinical validity of the model.

C. VIT B16 MODEL

In our study, transfer learning was mainly performed on the pre-trained weights of the ViT B16 model using the fundus images in our dataset. To see the difference, we directly used the pre-training weights of the ViT B16 model without transfer learning in our ViT-PCA-SVM model. In our classification and transfer learning studies, the final layer of the model was set to have a softmax activation function, and a dense layer with two outputs was utilized. The images were first preprocessed and then trained with the specified parameters. A summary of our ViT model is given in Table 3.

Table 3. *ViT Model Summary*

Layer (type)	Output Shape	Parameter Count
Input Layer	(224, 224, 3)	0
Vit-b16 (Functional)	768	85798656
Flatten	768	0
***Dense (Feature)**	64	49216
Dense	32	2080
Dense	2	66

D. PROPOSED MODELS

In this study, we first focus on feature extraction and then classification of fundus images. Feature transformation methods have provided outstanding solutions for moving the data to a better

representation space. After feature extraction, SoftMax or SVM methods were used to predict the data category.

This study tried six different hybrid models, with the aim of obtaining the best result by combining different models. Figure 4 shows the structure of the hybrid models used.

In the first model, Fine-Tuned ViT and PCA methods were used for feature extraction, while SVM was used for classification. In the second model, Fine-Tuned ViT was first used for feature extraction. Then, a new transformation was made with LDA, and in the last stage, SVM was used for classification. In the third model, the CLAHE approach was first used on fundus images, and then the Fine-Tuned ViT model was preferred.

The data was trained and classified in the fourth model with Fine Tuned Vit B16. In the fifth model, data transformation was performed with Incremental PCA, and then SVM was used for classification. Finally, in the sixth model, feature extraction was performed on the fundus images first with ViT, then with PCA, and then with SVM classification.

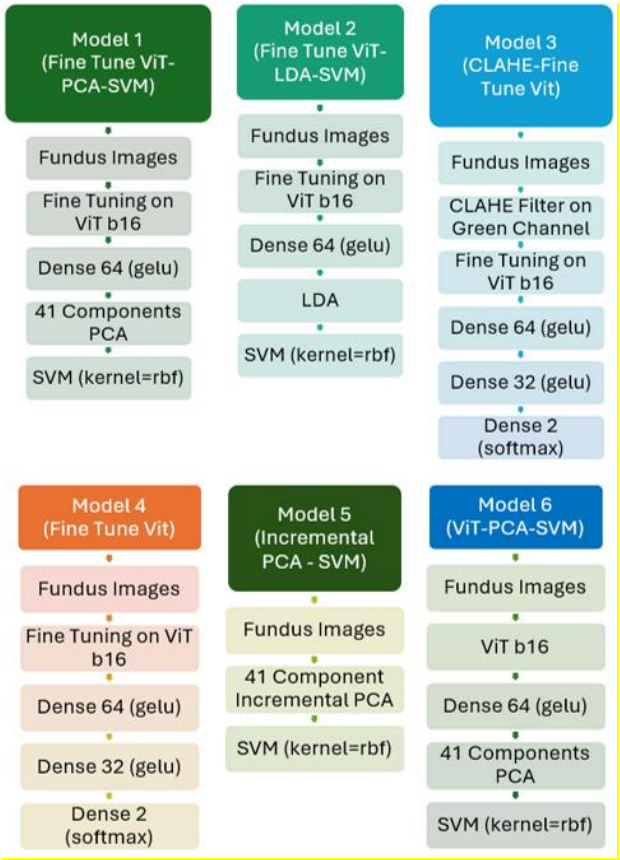

Figure 4. *Used model structures.*

E. PARAMETER SETTINGS

Parameters suitable for the structure of the model were selected for the models we used in our study. In the training of ViT models, Sparse Categorical Crossentropy was used as the loss function, and Adam with Weight Decay (AdamW) was used as the optimization algorithm. In the classification layer of ViT models, softmax was used as the activation function. The ViT models' batch size was 16, and the models were trained in 5 epochs. In the model with Incremental PCA, 256 was used as a batch size. Since the PCA method is based on statistical calculations, large batch sizes are preferred to analyze high-dimensional data together and increase efficiency. In contrast, smaller batch sizes are used because ViT models provide better generalization and computational efficiency with smaller

batches. Radial Basis Function Kernel (RBF) was used as Kernel in all SVM classifier models. The RBF kernel was chosen because it can learn efficient separation boundaries in high-dimensional data space and provides flexibility and robust performance for modeling complex relationships between data points. The number of components was chosen as 41. In cases where LDA was used as a classifier model, the number of components was set to "1" since the number of classes was 2.

F. PERFORMANCE EVALUATION METRICS

Our study used accuracy, precision, recall, and F1-score metrics to evaluate the classification performance. In addition, model performance was evaluated with the complexity matrix. Accuracy refers to the overall performance of the classification model. It shows how much of the total predictions are made correctly. It is usually used when the class distribution is balanced, and all classes are equally important. Mathematically, it is calculated as the ratio of correct predictions to total predictions, as in Equation 1.

Precision measures how many of the positively predicted samples are positive. In other words, it shows how "accurate" the model is. It is preferred when false positives (FP) are significant. Precision is preferred when correct positive predictions are more important than errors in the negative class. Its mathematical expression is as in Equation 2.

Recall measures how much of the samples that are actually positive are correctly predicted to be positive. It shows how well the model "remembers" positive cases. It is calculated using the expression in Equation 3.

The F1-Score is a metric that balances precision and sensitivity. It is calculated as the harmonic mean of both values and indicates the overall balance of the model. It is used when a trade-off between precision and sensitivity needs to be considered and is calculated using the expression in Equation 4.

The confusion matrix shows the performance of a classification model in detail. It presents the model's correct and incorrect predictions for each class in matrix form. It is used to examine the model's performance for each class in detail. Usually, the matrix rows represent the actual classes, and the columns represent the predicted classes. Four basic terms are usually used in the matrix.

True Positive (TP, True Positive): Situations that are positive and correctly predicted as positive.

False Positive (FP, False Positive): Situations that are actually negative but incorrectly predicted as positive.

True Negative (TN, True Negative): Situations that are negative and correctly predicted as negative.

False Negative (FN, False Negative): Cases that are actually positive but incorrectly predicted as negative. The representation of the complexity matrix is as in Table 4.

Table 4. *Confusion matrix.*

		Actual	
Predicted		TP	FP
		FN	TN

$$Accuracy = \frac{TP + TN}{TP + TN + FP + FN} \quad (1)$$

$$Precision = \frac{TP}{TP + FP} \quad (2)$$

$$Recall = \frac{TP}{TP + FN} \quad (3)$$

$$F1 - Score = \frac{2 * Precision * Recall}{Precision + Recall} \quad (4)$$

V. EXPERIMENTAL RESULTS AND DISCUSSION

The plots of the accuracy and loss graphs at each epoch for the train and validation data of the 6 different models applied in our study are shown in Figure 6.

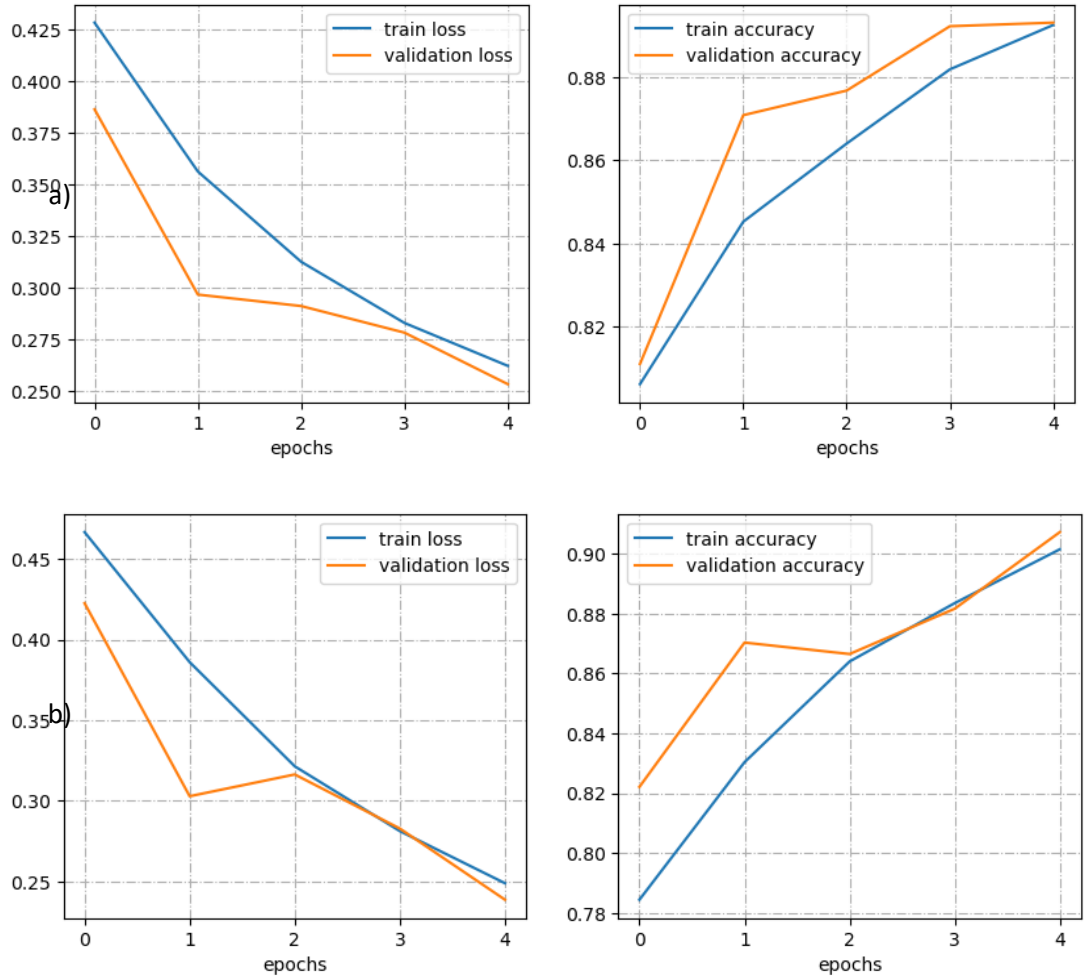

Figure 6. *Accuracy-epochs, Loss-epoch graphs of train and validation data. a) ViT fine tuning, b) ViT fine tuning after CLAHE filter.*

When the loss and accuracy graphs are analyzed, it is seen that the loss value decreases significantly for the train data and the accuracy value increases as expected as the epoch increases. However, this situation is not as clear for validation data. Since we train on pre-trained weights, the accuracy value rises above 84% after the first epoch. When Accuracy starts with a high value from the beginning, the changes in the subsequent iterations are not very significant. Still, there is a decrease in loss and an

increase in accuracy between the initial and final values, as desired. The confusion matrixes of our models are given in Figure 7.

Fine Tuned Vit Model

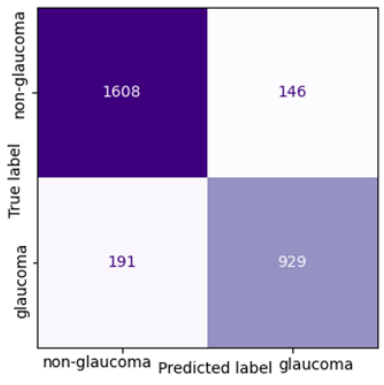

CLAHE-Fine Tuned Vit Model

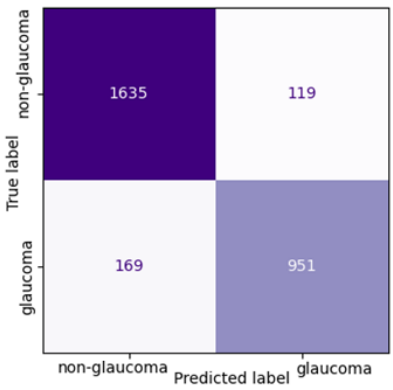

Fine-Tuned ViT-PCA-SVM Model

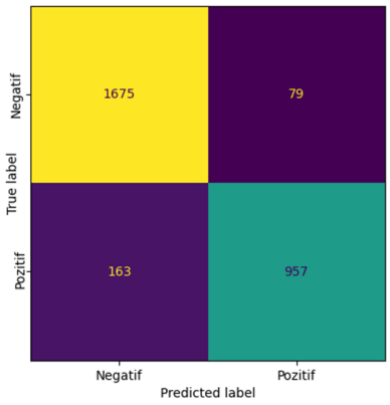

Fine-Tuned ViT-LDA-SVM Model

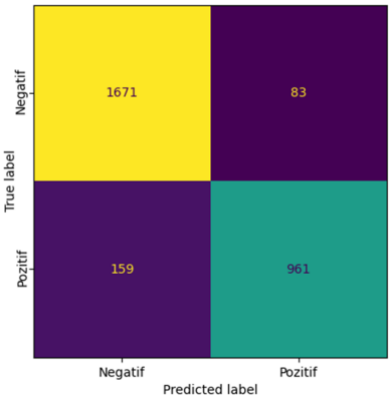

ViT-PCA-SVM Model

Incremental PCA - SVM Model

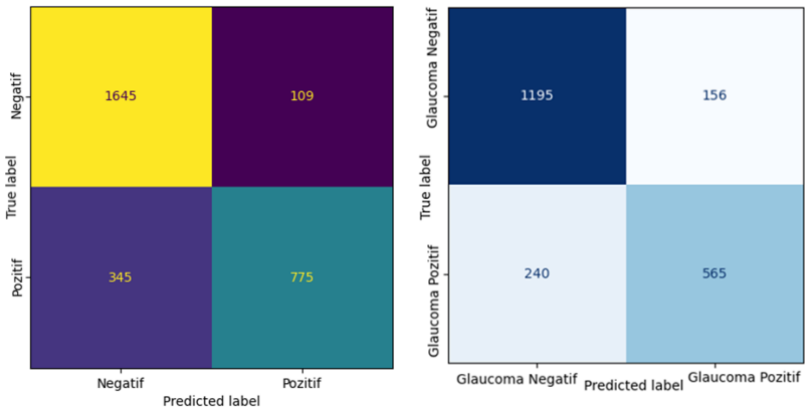

Figure 7. *Confusion matrices of the models used.*

The performance metrics calculated using the confusion matrixes are given in Table 5.

Table 5. C*lassification performance of models.*

Method	**Accuracy**	**Precision**	**Recall**	**F1- Score**
Fine Tuned Vit	0.88	0.88	0.88	0.88
CLAHE-Fine Tuned Vit	0.90	0.90	0.90	0.90
Fine Tuned ViT-PCA-SVM	0.92	0.92	0.92	0.92
Fine Tuned ViT-LDA-SVM	0.92	0.92	0.92	0.92
ViT-PCA-SVM	0.84	0.85	0.84	0.84
Incremental PCA - SVM	0.81	0.83	0.88	0.86

When the results are examined, it is seen that the best score of 0.92 is obtained in the models that follow the process steps of feature extraction from ViT models trained with the transfer learning method, reduction of these features with LDA or PCA, and then classification with SVM. In the “Fine Tuned Vit” and “CLAHE-Fine Tuned Vit” models, where classification is performed with dense layers after transfer learning is applied, the scores increase when we apply the CLAHE filter. In the ViT-PCA-SVM model, where we classify directly with the results of the pre-trained model without applying the transfer learning stage, the scores are lower than the other ViT models, as expected. It is important to see the benefit of transfer learning.

In the case where the images are directly classified with SVM after data reduction with PCA without using deep learning methods, although the results are lower than the other methods, it is seen that it is close to the values in the case where transfer learning is not applied and even surpasses this model in sensitivity and F1 score. This indicates that using deep learning without transfer learning is not very beneficial. In the Incremental PCA SVM model, direct PCA could not be applied due to memory problems. Incremental PCA, where the data is processed piece by piece, had to be applied.

When other studies in the literature are examined, it is seen that most of the studies have worked with smaller data sets. In addition, it is seen that many studies use data from patients in a specific hospital [16], [17], [18], [19]. This will negatively affect the generalizability of the results obtained. In the dataset we used, images from different hospitals in different countries were used. In this respect, it can be said that the models we obtained are more generalizable. Our study obtained an 81.0% accuracy when we applied Incremental PCA and SVM without ViT. Dey et al. [16] applied a similar method in their study and achieved 86% accuracy on a smaller dataset.

In our study, the success scores increase slightly when the CLAHE filter is applied, which is in line with Karrothu et al.'s study [17], which shows the study's reliability. With a large dataset, this study achieved a high success rate of 92% in detecting glaucoma disease, providing strong potential for earlier and more accurate patient diagnosis in clinical applications. Future studies with larger data sets are expected to pave the way for the direct use of the model in clinical studies.

VI. CONCLUSION

This study used six models to detect glaucoma disease using the SMDG-16 dataset of 17242 fundus images. Different approaches were applied to our models, and the results were analyzed. These approaches show the effects of transfer learning and using the CLAHE filter in ViT models. We also show the effects of classification with a dense layer or using combinations of PCA/LDA-SVM on the performance. Finally, it is shown how success scores would change in the absence of deep learning.

The study's results showed that the highest scores were 92% for the Fine Tuned ViT-PCA-SVM and Fine Tuned ViT-LDA-SVM models. The lowest scores were seen in the Incremental PCA-SVM model without deep learning and the ViT-PCA-SVM model without pre-trained weights.

REFERENCES

[1] E. ŞATIR, F. AZBOY, A. AYDIN, H. ARSLAN, and Ş. HACIEFENDİOĞLU, “Veri İndirgeme ve Sınıflandırma Teknikleri ile Glokom Hastalığı Teşhisi,” El-Cezeri Fen ve Mühendislik Dergisi, vol. 3, no. 3, pp. 485–497, Sep. 2016, doi: 10.31202/ecjse.258576.

[2] Y. Yılmaz, A. Koytak, K. Erol, Y. Çınar, and Y. Özertürk, “Primer Açık Açılı Glokomda Fundus Floresein Anjiyografi,” Kartal Eğitim ve Araştırma Hastanesi Tıp Dergisi, vol. 17, no. 1, pp. 1–5, 2006.

[3] S. S. Hayreh, “Evaluation of Optic Nerve Head Circulation: Review of the Methods Used,” J Glaucoma, vol. 6, no. 5, pp. 319–330, 1997.

[4] J. E. Grunwald, J. Piltz, S. M. Hariprasad, J. Dupont, and M. G. Maguire, “Optic nerve blood flow in glaucoma: effect of systemic hypertension,” Am J Ophthalmol, vol. 127, no. 5, pp. 516–522, May 1999, doi: 10.1016/S0002-9394(99)00028-8.

[5] J. E. Grunwald, J. Piltz, S. M. Hariprasad, and J. DuPont, “Optic nerve and choroidal circulation in glaucoma.,” Invest Ophthalmol Vis Sci, vol. 39, no. 12, pp. 2329–2336, Nov. 1998.

[6] L. A. Yannuzzi et al., “Ophthalmic fundus imaging: today and beyond,” Am J Ophthalmol, vol. 137, no. 3, pp. 511–524, Mar. 2004, doi: 10.1016/j.ajo.2003.12.035.

[7] Kaya, Y., Yiner, Z., Kaya, M., & Kuncan, F. (2022). A new approach to COVID-19 detection from X-ray images using angle transformation with GoogleNet and LSTM. Measurement Science and Technology, 33(12), 124011.

[8] Şenol, A., & Kaya, M. (2024). An Investigation on the Use of Clustering Algorithms for Data Preprocessing in Breast Cancer Diagnosis. Türk Doğa ve Fen Dergisi, 13(1), 70-77.

[9] Z. Wang and M. Lemmon, "Stability analysis of weak rural electrification microgrids with droop-controlled rotational and electronic distributed generators," in 2015 IEEE Power & Energy Society General Meeting, IEEE, Jul. 2015, pp. 1–5. doi: 10.1109/PESGM.2015.7286507.

[10] T. M. Lehmann, C. Gonner, and K. Spitzer, "Survey: interpolation methods in medical image processing," IEEE Trans Med Imaging, vol. 18, no. 11, pp. 1049–1075, 1999, doi: 10.1109/42.816070.

[11] G. J. Grevera and J. K. Udupa, "An objective comparison of 3-D image interpolation methods," IEEE Trans Med Imaging, vol. 17, no. 4, pp. 642–652, 1998, doi: 10.1109/42.730408.

[12] Şenol, A., Canbay, Y., & Kaya, M. (2021). Makine Öğrenmesi Yaklaşımlarını Kullanarak Salgınları Erken Evrede Tespit Etme Alanındaki Eğilimler. Bilişim Teknolojileri Dergisi, 14(4), 355-366.

[13] Utku, A., & Akcayol, M. A. (2024). Spread patterns of COVID-19 in European countries: hybrid deep learning model for prediction and transmission analysis. Neural Computing and Applications, 1-17.

[14] Ö. YILDIRIM and F. ALTUNBEY ÖZBAY, "Fundus Görüntülerinden Derin Öğrenme Teknikleri ile Glokom Hastalığının Tespiti," European Journal of Science and Technology, vol. 44, pp. 1–6, Dec. 2022, doi: 10.31590/ejosat.1216404.

[15] M. UÇAR, "Glokom Hastalığının Evrişimli Sinir Ağı Mimarileri ile Tespiti," Deu Muhendislik Fakultesi Fen ve Muhendislik, vol. 23, no. 68, pp. 521–529, May 2021, doi: 10.21205/deufmd.2021236815.

[16] A. Dey and S. Bandyopadhyay, "Automated Glaucoma Detection Using Support Vector Machine Classification Method," Br J Med Med Res, vol. 11, no. 12, pp. 1–12, Jan. 2016, doi: 10.9734/BJMMR/2016/19617.

[17] A. Karrothu and A. Chunduru, "Glaucoma Detection Using Computer Vision and Vision Transformers," International Journal of Computing and Digital Systems, vol. 14, no. 1, pp. 1–13, 2023.

[18] C.-W. Wu, H.-Y. Chen, J.-Y. Chen, and C.-H. Lee, "Glaucoma Detection Using Support Vector Machine Method Based on Spectralis OCT," Diagnostics, vol. 12, no. 2, pp. 391–406, Feb. 2022, doi: 10.3390/diagnostics12020391.

[19] S. Phasuk et al., "Automated Glaucoma Screening from Retinal Fundus Image Using Deep Learning," in 2019 41st Annual International Conference of the IEEE Engineering in Medicine and Biology Society (EMBC), IEEE, Jul. 2019, pp. 904–907. doi: 10.1109/EMBC.2019.8857136.

[20] Z. Li, Y. He, S. Keel, W. Meng, R. T. Chang, and M. He, "Efficacy of a Deep Learning System for Detecting Glaucomatous Optic Neuropathy Based on Color Fundus Photographs," Ophthalmology, vol. 125, no. 8, pp. 1199–1206, Aug. 2018, doi: 10.1016/j.ophtha.2018.01.023.

[21] H. Fu, J. Cheng, Y. Xu, D. W. K. Wong, J. Liu, and X. Cao, "Joint Optic Disc and Cup Segmentation Based on Multi-Label Deep Network and Polar Transformation," IEEE Trans Med Imaging, vol. 37, no. 7, pp. 1597–1605, Jul. 2018, doi: 10.1109/TMI.2018.2791488.

[22] H. Fu et al., “Disc-Aware Ensemble Network for Glaucoma Screening From Fundus Image,” IEEE Trans Med Imaging, vol. 37, no. 11, pp. 2493–2501, Nov. 2018, doi: 10.1109/TMI.2018.2837012.

[23] A. Dosovitskiy et al., “An Image is Worth 16x16 Words: Transformers for Image Recognition at Scale,” arXiv preprint arXiv, vol. 11929, Oct. 2020.

[24] M. Turk and A. Pentland, “Eigenfaces for Recognition,” J Cogn Neurosci, vol. 3, no. 1, pp. 71–86, Jan. 1991, doi: 10.1162/jocn.1991.3.1.71.

[25] K. Etemad and R. Chellappa, “Discriminant analysis for recognition of human face images,” Journal of the Optical Society of America A, vol. 14, no. 8, p. 1724, Aug. 1997, doi: 10.1364/JOSAA.14.001724.

Düzce University
Journal of Science & Technology

Research Article

Linearization of Photovoltaic Cell Single Diode Equivalent Circuit Model Using Piecewise Linear Parallel Branches Model and Finding Fill Factor

Süleyman ADAK [a,*]

[a] *Department of Electricity and Energy, MYO, Mardin Artuklu University, Mardin, TURKEY*
** Corresponding author's e-mail address: suleymanadak@artuklu.edu.tr*
DOI: 10.29130/dubited.1502554

ABSTRACT

In this article, the linearization and analysis of the Photovoltaic (PV) cell single-diode equivalent circuit model have been performed. The diode element in the PV cell equivalent circuit model is a nonlinear component. The nonlinear PV cell single diode model has been linearized using the piecewise linear parallel branches model (PLPBM). In addition, the maximum power and fill factor (FF) of the PV cell have been determined based on the equivalent circuit parameters. Thevenin theorem was used in this analysis process. For this theorem to apply, the circuit must have a linear characteristic. In practice, the aim is to transfer the maximum power (Pmax) from the PV cell. Another important parameter of the PV solar cell is the FF. The FF describes the general behavior of a solar PV cell. This factor is used to determine the quality of the solar PV cell. The FF provides information about the quality and efficiency of the solar cell. In a low FF scenario, the value of the series resistance is high, while the value of the parallel resistance is low. The FF of typical PV cells ranges between 50% and 82%. In the analysis conducted in the article, the FF of the PV solar cell was found to be 74%.

Keywords: Fill factor, Maximum power transfer, PV cell single diode equivalent circuit, Piecewise linear parallel branches model, Thevenin equivalent circuit

Fotovoltaik Hücre Tek Diyot Eşdeğer Devre Modelinin Parçalı Doğrusal Paralel Dal Modeli Kullanılarak Doğrusallaştırılması ve Dolum Faktörünün Bulunması

ÖZET

Bu makalede Fotovoltaik (PV) hücre tek diyot eşdeğer devre modelinin doğrusallaştırılması ve analizi yapılmıştır. PV hücresi eşdeğer devre modelindeki diyot elemanı doğrusal olmayan bir bileşendir. Doğrusal olmayan PV hücresi tek diyot modeli, parçalı doğrusal paralel dallar modeli kullanılarak doğrusallaştırılmıştır (PLPBM). Ayrıca PV hücresinin maksimum gücü ve doldurma faktörü (FF)

Received: 19/06/2024, Revised: 29/09/2024, Accepted: 06/10/2024

eşdeğer devre parametrelerine göre belirlenmiştir. Bu analiz sürecinde Thevenin teoremi kullanıldı. Bu teoremin uygulanabilmesi için devrenin doğrusal bir karakteristiğe sahip olması gerekir.
Uygulamada amaç, PV hücresinden maksimum gücü (Pmax) aktarmaktır. PV hücresinin bir diğer önemli parametresi FF'dir. FF, bir güneş PV hücresinin genel davranışını tanımlamak için kullanılır. Bu faktör solar PV hücresinin kalitesini belirlemek için kullanılır. FF, güneş pilinin kalitesi ve verimliliği hakkında bilgi sağlar. Düşük FF durumunda seri direncin değeri yüksek, paralel direncin değeri ise düşüktür. Tipik PV hücresinin FF'rü %50 ile %82 arasında değişir. Makalede yapılan analizde PV güneş pilinin FF %74 olarak bulunmuştur.

Anahtar Kelimeler: *Dolum faktörü, Maksimum güç aktarımı, PV hücresi tek diyot eşdeğer devresi, Parçalı doğrusal paralel dallanma modeli, Thevenin eşdeğer devresi*

I. INTRODUCTION

Renewable energy sources are increasingly being used day by day due to their inexhaustibility, lack of harm to the environment, and significantly lower cost compared to fossil fuels [1- 2]. The PV solar source holds significant importance among renewable energy sources. Solar energy is abundant and freely available in many regions of the world. Understanding the behavior of PV cells is crucial for optimizing their performance and increasing their efficiency. Photovoltaic cells, often called solar cells, are devices made from semiconductor materials such as silicon. When sunlight strikes the semiconductor material, it excites electrons, creating a flow of electricity. This phenomenon is known as the photovoltaic effect. The basic structure of a photovoltaic cell typically includes layers of semiconductor materials with different electronic properties. When photons from sunlight are absorbed by the semiconductor material, they transfer their energy to electrons, allowing them to flow through an external circuit as electric current. This flow of electrons is what we harness as electricity from solar panels. Solar PV cells come in various types, each with unique materials and mechanisms, influencing their efficiency and suitability for different applications. These cells are made from single-crystal silicon. Solar PV cell types and their efficiencies are given below:

A. MONOCRYSTALLİNE SİLİCON SOLAR CELLS

These are made from single-crystal silicon. They have high efficiency due to the purity of the silicon, typically ranging from 15% to 22% [3]. Monocrystalline silicon cells are widely used in residential and commercial installations.

B. POLYCRYSTALLİNE SİLİCON SOLAR CELLS

These are made from silicon crystals that are melted together. They are less expensive to produce compared to monocrystalline cells but have slightly lower efficiency, typically ranging from 13% to 18% [4].

C. THİN-FİLM SOLAR CELLS

Thin-film solar cells use thin layers of semiconductor materials deposited on a substrate. There are several types. Depending on the production type, efficiency varies between 5% and 13% [5].

D. PEROVSKİTE SOLAR CELLS

Perovskite cells have gained significant attention in recent years due to their rapid efficiency improvements and potential for low-cost production. Efficiency levels have quickly risen from below 10% to over 25% in laboratory settings, but commercialization is still underway, and long-term stability remains a challenge [6].

E. ORGANİC PHOTOVOLTAİC CELLS (OPVS)

OPVs are made from organic (carbon-based) materials and can be produced using low-cost printing techniques. Efficiencies for OPVs have been steadily improving, with recent achievements reaching around 15% [7].

It's worth noting that these efficiency figures are approximate and can vary depending on factors such as manufacturing techniques, materials' quality, and environmental conditions. Additionally, enhancing the durability and reliability of solar cells is crucial for long-term performance and reducing maintenance costs. This includes developing materials and coatings that can withstand harsh environmental conditions and degradation over time. While the efficiency of silicon solar cells and the effect of ambient temperature on solar modules were examined in ref. [8- 9], photovoltaic cell open circuit voltage and fill factor were examined in ref. [10].

When photovoltaic cells are connected in series, their voltages add up while the current remains same. In ref. [11], series-connected photovoltaic cell modeling and analysis were carried out. This configuration increases the overall voltage output of the system. It's similar to stacking batteries end-to-end in a flashlight to increase the total voltage. However, it's essential to note that the current. Remains the same throughout the series circuit, so if one cell is shaded or underperforming, it can significantly affect the performance of the entire string. Connecting cells in parallel increases the total current output while maintaining the same voltage as a single cell. This can be advantageous in situations where higher current is required, such as in low-light conditions or when powering devices with higher current demands. Additionally, in parallel connection of solar cells, the performance of other cells is less affected if one cell is shaded or malfunctions. When solar cells are connected in series, the current flowing through the cells remains the same, while the voltages of the cells are summed. As seen in Figure 1, the solar PV module consists of series-connected solar cells [12] .

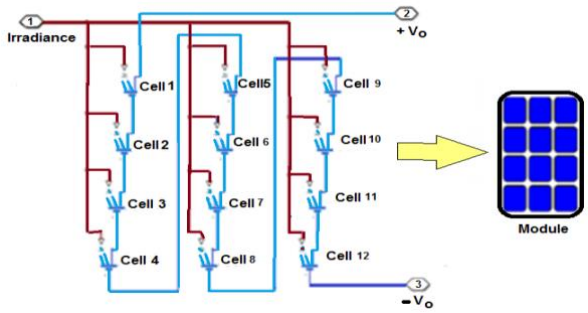

Figure 1. *A typical module has 12 cells connected in series*

In Figure 1, the total output voltage increases in this configuration group due to the series connection of solar cells. When solar cells are connected in parallel, the currents are added up and the voltage value remains the same as the voltage of a single cell group. This configuration increases the overall current output of the system. This setup allows for the optimization of both voltage and current levels, which is crucial for various applications, including solar panel systems. In this article, we explore the process of linearizing the PV cell single diode equivalent circuit model using the PLPB model. Validate the piecewise model by comparing it against the full nonlinear model, ensuring that the linearization captures the key behaviors of the PV cell, especially around critical points like the maximum power point (MPP).

In ref. [13], a new piecewise linear simulation algorithm using key-level model dynamics was studied. The I-V curve of the diode is typically divided into segments that correspond to different operating conditions, such as forward bias, reverse bias, and breakdown. For each segment, the slope (conductance) and intercept (bias voltage) are determined based on the local characteristics of the

diode at that operating point. By linearizing the diode's output characteristics with the PLPBM, the overall behavior of a PV system can be modeled more accurately, enabling designers and engineers to analyze and optimize system performance under various operating conditions. In ref. [14], modeling of solar cells and modules was performed using a piecewise linear parallel branch model. Using PLPBM for linearizing the single diode PV cell model simplifies the complex nonlinear equations while maintaining sufficient accuracy for most practical purposes. This approach is especially useful in applications where computational resources are limited, but accurate real-time modeling is necessary, such as in MPPT (Maximum Power Point Tracking) algorithms or power electronics simulations .

We examine the theoretical basis in depth of the PLPB model and its application in characterizing PV cell behavior. Furthermore, we investigate the implications of linearization on the calculation of maximum power and FF, essential parameters for assessing the performance of PV systems [15]. To overcome this limitation, researchers have developed various techniques to linearize the model and facilitate mathematical analysis.
The Thevenin equivalent model is a powerful tool for simplifying complex circuits, and it can be applied to model PV solar cells. In ref. [16], Thevenin Equivalent of Solar PV Cell Model and Maximum Power Transfer has been studied.The Thevenin equivalent model is useful for understanding how the PV cell interacts with external loads, especially when trying to match the maximum power point (MPP) of the cell to an external circuit. At the MPP, the Thevenin equivalent circuit provides an intuitive understanding of how the internal characteristics of the PV cell (such as the series resistance and diode behavior) impact the overall performance [17- 19]. The effective Thevenin resistance (Rth) influences how much voltage is dropped internally within the cell, and Thevenin voltage (Vth) defines the potential power that can be delivered.To analyze the MPP of a photovoltaic (PV) cell using the Thevenin equivalent model, we need to focus on the point at which the PV cell delivers maximum power to a load [18- 20].

II. MODELİNG AND ANALYSİS OF PV CELL SİNGLE DİODE EQUİVALENT MODEL

A. SİNGLE-DİODE EQUİVALENT CİRCUİT MODEL

The single-diode equivalent circuit model is a commonly used method to represent the behavior of a PV cell. It simplifies the complex physical processes occurring within the cell into a more manageable form, allowing for easier analysis and design of PV systems [21, 22]. The single-diode equivalent circuit model provides a valuable tool for modeling and analyzing the behavior of PV cells. It simplifies the complex physics of solar cells into a more manageable form, allowing engineers and researchers to design and optimize PV systems effectively. However, it's essential to recognize that the model has limitations and may not capture all aspects of the cell's behavior under various conditions.
Modeling and analysis of solar PV cells using the single diode equivalent model is widely used in analyzing and understanding the performance of solar cells. This model simplifies the complex physical processes within a solar cell into a single equivalent circuit, making it easier to analyze and design PV systems [23, 24]. The analysis involves solving the circuit equations derived from the fundamental equations governing the behavior of the solar cell, such as the Shockley diode equation and Kirchhoff's laws. Techniques such as numerical simulation and analytical methods are often employed to study the behavior of the PV cell and optimize its performance. The single-diode equivalent circuit for a solar PV cell is shown in Figure 2.

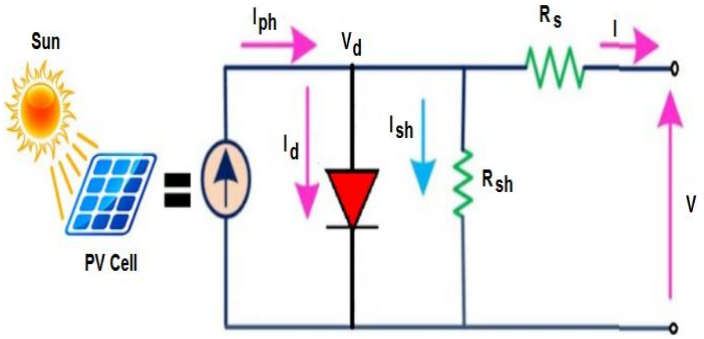

Figure 2. *PV cell single diode equivalent circuit model*

The single-diode model provides a good balance between simplicity and accuracy in describing the current-voltage (I-V) characteristics of a solar cell. It captures the essential physics of the cell without excessive complexity, making it suitable for practical simulations and analyses. Additionally, It serves as the foundation for designing and optimizing PV systems, including module and system-level analysis. The model helps in predicting the performance of solar cells under different conditions, such as varying irradiance and temperature, which are crucial for system design.

The single-diode equivalent circuit model given in Figure 2 is the general static equivalent circuit of the PV solar cell. This causes the circuit to have a nonlinear characteristic. The PV cell model given in Figure 2 is also referred to as a five unknown parameters model. These five parameters are Iph, Io, Rs, Rsh, and n. The variables you've mentioned are key parameters in the equivalent circuit model of a PV cell, often used to describe its behavior. PV cell equivalent circuit parameters are given below:

- Iph: This represents the photocurrent generated by the PV cell due to incident light. It is the current that flows through the external circuit connected to the solar cell when illuminated.
- Io: The reverse saturation current of the diode in the PV cell. This parameter characterizes the diode-like behavior of the solar cell, indicating the current that would flow through the cell in the absence of illumination.
- Rs: Series resistance of the PV cell. This resistance accounts for losses due to the internal resistance of the semiconductor materials and the interconnections within the cell.
- Rsh: Shunt resistance of the PV cell. This resistance represents leakage paths across the solar cell, which can reduce the efficiency of the cell if too low.
- n: The ideality factor (also known as the diode factor) of the PV cell. It is a dimensionless factor that represents deviations from ideal diode behavior due to recombination losses and other non-idealities within the semiconductor material.

These parameters are typically used in models such as the single-diode model or the double-diode model, which describe the current-voltage (I-V) characteristics of a solar cell under different operating conditions (illumination levels, temperature, etc.). These models help in understanding and predicting the performance of PV systems and optimizing their design for maximum efficiency.

B. ANALYSİS OF SINGLE DIODE EQUİVALENT CİRCUİTS

The single-diode model simplifies the complex behavior of a PV cell into a single-diode equation, which is relatively straightforward compared to the physical intricacies of the actual cell. Additionally, it allows for easier mathematical analysis and simulation compared to more detailed models. This makes it useful for quick calculations and initial design considerations.

The nonlinearity of the photovoltaic cell equivalent circuit presents several disadvantages, such as increased complexity in tracking the Maximum Power Point, sensitivity to environmental conditions, and partial shading issues. These challenges require sophisticated power electronics, complex control algorithms, and advanced design strategies to ensure optimal performance, leading to higher costs and

system complexity. However, with effective management, the impact of nonlinearity can be minimized to improve overall system efficiency and reliability. Nonlinear characteristics make it difficult to maintain the MPP, especially in changing conditions like cloudy weather or shading.

The model provides a clear relationship between the output current and voltage of the PV cell, making it easier to estimate key parameters such as the fill factor, maximum power point, and efficiency. Researchers can use the model to optimize the design of PV systems by predicting how changes in environmental conditions (like sunlight intensity and temperature) affect the electrical characteristics of the PV module. The unknown parameters in this model depend on the intensity of the irradiation and the temperature. Therefore, the irradiation and temperature levels must be known for each output value to be calculated. The single-diode equivalent circuit model offers a balance between accuracy and simplicity, making it a practical choice for various stages of PV system design, analysis, and education. Its advantages lie in ease of use, parameter estimation, design optimization, and its widespread acceptance and compatibility within the field of photovoltaics. The output current to be produced by the photovoltaic cell is found in Equation (1).

$$I_{sc} = I_{ph} - I_D - I_{sh} \quad (1)$$

The formula to calculate diode current it is as below:

$$I_D = I_0 \left[\exp\left(\frac{q(V+IR_s)}{nkT_c}\right) - 1\right] \quad (2)$$

The equation of the current flowing through the parallel resistor is as given below.

$$I_{sh} = \frac{V+IR_s}{R_{sh}} \quad (3)$$

The output current of the Kyocera KC200GT module PV cell depends on various factors such as the amount of sunlight (irradiance), temperature, and the load connected to the module. The output current of the photovoltaic cell is found as follows.

$$I = I_{ph} - I_0 \left[exp\left(\frac{q(V+IR_s)}{nkT_c}\right) - 1\right] - \frac{(V+IR_s)}{R_{sh}} \quad (4)$$

Where:
k - The Boltzmann constant (J/K)
Iph- Photocurrent (A).
q - The elementary electron charge (C)
I_0 - Diode reverse saturation current.
n -Ideality factor of diode.
Rs - Equivalent series resistance (Ω)
Rsh - Equivalent shunt resistance (Ω)
Tc - Cell temperature (K)

The I-V (current-voltage) curve of a PV module, such as the Kyocera KC200GT, represents the relationship between the current and voltage output of the module under varying conditions. Analyzing the I-V curve helps designers understand the performance of PV modules under different conditions and design optimal systems for various applications, whether it's for grid-tied solar installations, off-grid systems, or other solar-powered devices. The I-V curve is affected by

environmental factors such as temperature and solar irradiance. Higher temperatures generally reduce the voltage output of the panel, while increased irradiance (sunlight intensity) increases both the current and voltage outputs. The I-V curve of the Kyocera KC200GT module is given in Figure 3.

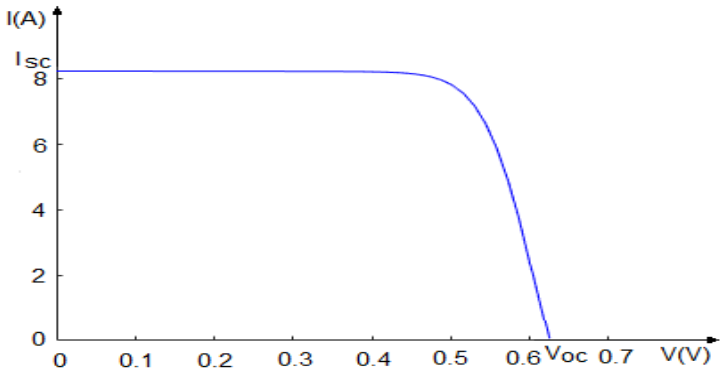

Figure 3. *I-V curve of the PV cell (at 25 °C, 1000 (W/m²)*

The I-V curve of a PV cell plays a crucial role in the design, analysis, optimization, and operation of PV systems. It provides valuable insights into the electrical characteristics of the cell, enabling efficient energy production, system monitoring, and maintenance. The short-circuit current (I_{SC}) of a PV cell refers to the current that flows through the cell when the circuit is short-circuited, meaning there is no external load connected to the cell. The formula to calculate the short circuit current of the PV cell is as below:

$$I_{sc} = I_{ph} - I_0\left[\exp\left(\frac{I_{sc}R_s}{nV_t}\right) - 1\right] - \frac{I_{sc}R_s}{R_{sh}} \tag{5}$$

This occurs when the voltage across the terminals of the cell is zero, causing the maximum current to flow through the circuit. PV cells convert absorbed solar irradiation into electrical energy through the photovoltaic effect. Standard Test Conditions (STC). These are measured under lab conditions of 1000W per sq meter of "sunlight" with a standard spectrum etc. The photocurrent generated by the cells is highest under optimal sunlight conditions (such as in sunny weather and under STC) and decreases under reduced irradiance levels (such as in cloudy or overcast weather). Understanding these dynamics helps in predicting and optimizing the performance of solar energy systems under different environmental conditions [25, 26]. The formula to calculate PV cell photocurrent is as below:

$$I_{ph} = [I_{sc} + K_i(T - T_n)]\frac{G}{G_n} \tag{6}$$

Where, Iph is photocurrent, G is irradiation value, Gn is the irradiation value accepted under STC, T is PV cell temperature, Tn is nominal temperature, Ki is temperature coefficient of current. The PV cell photo-current depends on the solar irradiation and temperature. The current at the Maximum Power Point (MPP) defined by Equation (7).

$$I_{mp} = I_{pf} - I_0\left[\exp\left(\frac{q(V_{mp} + I_{mp}R_s)}{nkT_c}\right) - 1\right] - \left(\frac{V_{mp} + I_{mp}R_s}{R_{sh}}\right) \tag{7}$$

This is the current that the PV cell produces when it is operating at its MPP. The diode reverse saturation current is a fundamental parameter that characterizes the behavior of semiconductor diodes, including those used in photovoltaic cells. It plays a significant role in determining the efficiency and performance characteristics of PV modules in converting solar energy into electrical power. The diode reverse saturation current is found by the following equation (8).

$$I_0 = I_{0ref}\left(\frac{T}{T_{ref}}\right)^3 \exp\left[\frac{qE_q}{nk}\left(\frac{1}{T_{ref}} - \frac{1}{T}\right)\right] \quad (8)$$

Where Ioref is diode saturation reverse current in the referred cell temperature condition. Eg is the band gap energy of the diode and T is the absolute temperature. During the design phase of a PV system, optimizing FF is critical to ensuring the system delivers maximum power output under varying environmental conditions. FF is influenced by the internal resistances of the solar cell, both series resistance (which lowers FF) and shunt resistance (which increases FF). High FF values generally indicate lower power losses due to resistance. The FF would slightly increase or decrease depending on the density of the irradiance and the influence of parasitic resistance [25, 26]. The FF is essentially a measure of the quality of the solar cell. The formula to calculate FF is as below:

$$FF = \frac{P_{max}}{I_{sc}V_{oc}} = \frac{V_{mp}I_{mp}}{I_{sc}V_{oc}} \quad (9)$$

The FF is calculated by dividing the maximum power obtained from the solar cell by the theoretical power obtained by multiplying the open circuit voltage by the short circuit current. PV cell efficiency is a critical parameter that determines how effectively solar energy can be converted into electrical power. Advances in materials, manufacturing processes, and design continue to drive improvements in PV cell efficiency, making solar energy an increasingly competitive and viable renewable energy option worldwide. PV cell efficiency is the ratio of electrical output power P(out) to solar input power P(in). The formula to calculate the efficiency of the solar PV cell is as below:

$$\eta = \frac{P_{out}}{P_{in}} = \frac{FF * I_{sc}V_{oc}}{G * A} \quad (10)$$

Where, FF is the fill factor, A is the area of the solar cell and G is solar irradiance. From the equation (10), as the FF value increases, the efficiency of the PV cell increases. Increasing the efficiency of photovoltaic (PV) cells is a key goal in solar energy research and development. High-Quality Semiconductor Materials: Using materials with optimal band gaps for absorbing sunlight can increase efficiency. Traditional silicon-based cells have limitations, so researchers are exploring materials like perovskites, multi-junction solar cells, and thin-film technologies. Tandem or multi-junction cells can achieve efficiencies higher than single-junction cells by capturing a wider range of wavelengths. Additionally, using perovskite solar cells. Perovskites offer high absorption efficiency and tunable bandgaps, and they have gained attention for their potential to outperform traditional silicon cells. The formula to calculate the open circuit current of the PV cell it is as below:

$$V_{oc} = \frac{nkT_c}{q} Ln\left(\frac{I_{ph}}{I_0} + 1\right) \quad (11)$$

Where, Iph is photocurrent, and Tc is cell temperature. By examining the above equation, it is seen that the open circuit voltage does not increase linearly with temperature. The open-circuit voltage shown on the I-V curve below is obtained when the current flowing through the cell is zero. Variation in PV cell temperature occurs due to changes in the ambient temperature as well as changes in the intensity of solar irradiation. The PV cell temperature is defined as:

Where, Iph is photocurrent, and Tc is cell temperature. By examining the above equation, it is seen that the open circuit voltage does not increase linearly with temperature. The open-circuit voltage shown on the I-V curve below is obtained when the current flowing through the cell is zero. Variation in PV cell temperature occurs due to changes in the ambient temperature as well as changes in the intensity of solar irradiation. The PV cell temperature is defined as:

$$T = T_{amb} + \left(\frac{NOCT - 20^0 C}{0.8}\right) G \quad (12)$$

Where Tamb is ambient temperature, NOCT is nominal operating cell temperature, and G is solar irradiation. An increase in solar cell temperature of about 1°C results in an efficiency decrease of about 0.45%. The specifications of PV modules provide the foundational information necessary for the successful design, installation, operation, and maintenance of solar power systems. The specifications of the PV Module (KC200GT) are given in Table 1.

Table 1. *The specification of the PV module used in study (PV Module KC200GT)*

Parameters	Value
Maximum Power (Pmax)	200W (＋10%／－5%)
Maximum Power Voltage (Vmp)	26.3 (V)
Maximum Power Current (Imp)	7.61 (A)
Open Circuit Voltage (Voc)	32.9 (V)
Short Circuit Current (Isc)	8.21 (A)
Temperature Coefficient of Voc	－1.23×10-1 (V/C)
Temperature Coefficient of Isc	3.18×10-3 (A/C)
Number of cells in series (Ns)	54

The PV module KC200GT refers to a specific model of photovoltaic module typically used in solar energy systems. PV modules like the KC200GT are used in various applications, including residential, commercial, and utility-scale solar installations, contributing to renewable energy generation worldwide.

III. LİNEARİZATİON OF PV CELL SİNGLE DİODE EQUİVALENT CİRCUİT MODEL USİNG PLPBM

The PV cell single-diode equivalent circuit model helps explain the electrical behavior of PV cells. However, due to the diode element in this model, the circuit has a nonlinear characteristic. The nonlinear characteristic makes it difficult to accurately model and analyze the single equivalent circuit of the PV cell. Traditional analytical methods are insufficient to directly solve the nonlinear equations of the single diode model, and require the development of special numerical techniques. Despite its complexity, the single-diode model is still the most widely used model for characterizing PV cell behavior and predicting performance under varying operating conditions. The Piecewise Linear Parallel Branch Model linearizes the diode characteristic in a photovoltaic cell by breaking it into several linear regions, each represented by a resistor in parallel. This approximation allows for easier analysis and simulation, particularly in modeling the behavior of the PV cell's equivalent circuit. In circuit simulation tools, the piecewise linear model is implemented by adding parallel resistor branches corresponding to different operating regions of the diode. This approach simplifies the nonlinear diode behavior into a more manageable form for analysis.

The linearization of the PV cell single-diode equivalent circuit model using the PLPBM represents a significant advance in the field of PV technology. The piecewise linear parallel branches model is based on the principle of linearization by dividing the nonlinear curve of the diode into linear sections. This simplification enables mathematical analysis and supports the development of efficient numerical algorithms for simulation and optimization. By dividing the nonlinear diode equation into multiple linear parts, the PLPBM significantly simplifies the computational complexity. Moreover, the piecewise linear parallel branches model provides a more intuitive understanding of how changes in operating conditions such as irradiance and temperature affect PV cell performance.

Based on the outlined criteria, the advocated approach appears to be technically correct and scientifically sound, provided it is rigorously formulated and validated through simulations and, ideally, experimental data. As with any scientific work, thorough documentation of assumptions, methodologies, and validations is essential for establishing credibility. If these aspects are adequately addressed in your paper, it would significantly contribute to the understanding and modeling of photovoltaic systems. Ensure that the mathematical equations used to describe the linear segments are correctly derived from the Shockley diode equation. The linearization should accurately reflect the slopes of the I-V curve in each segment. The equivalent of the diode circuit is given in Figure 4.

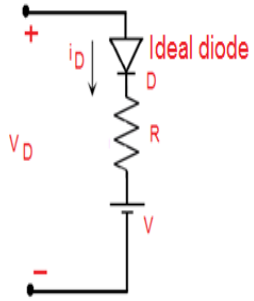

Figure 4. *The equivalent circuit of diode*

The equivalent circuit of a diode typically includes an ideal diode and a series resistance. The ideal diode represents the diode's one-way conduction behavior, conducting current when forward-biased and blocking current when reverse-biased. The series resistance accounts for the non-ideal behavior of real diodes, causing a voltage drop across the diode when it conducts in the forward direction. This simplified circuit model is commonly used in electronic circuit analysis to approximate the behavior of diodes. Higher irradiance levels result in higher current and power output from the solar cell, whereas lower irradiance levels result in lower outputs. These changes are reflected in both the I-V and P-V curves. The changes in the I-V and P-V curves at different irradiance values are given in Figure 5.

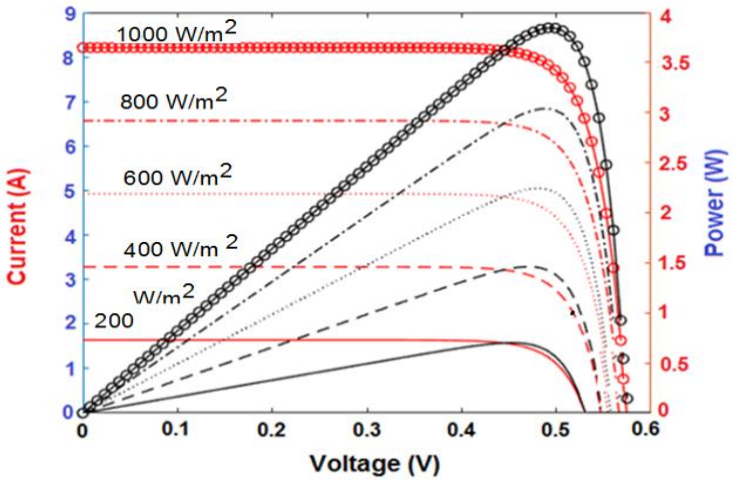

Figure 5. *The I-V and P-V solar cell curves at (200, 400, 600, 800 and 1000 (W/m^2)) irradiation values*

The piecewise linear parallel branches model of a diode is a simplification used in circuit analysis to approximate the behavior of a real diode. In this model, the diode characteristic curve (which relates the voltage across the diode to the current flowing through it) is approximated using multiple linear segments. The linearization of the diode with the PLPBM method is given in Figure 6.

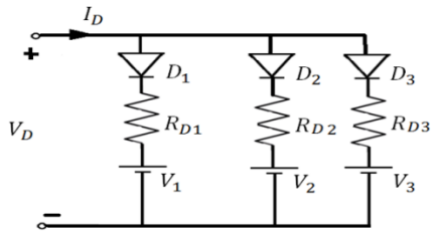

Figure 6. *Piecewise linear parallel branches model of diode*

The principle diagram of the piecewise linearization of non-linear characteristic of diode is given In Figure 7. In this method, the current-voltage curve of the diode is divided into several regions [27] .

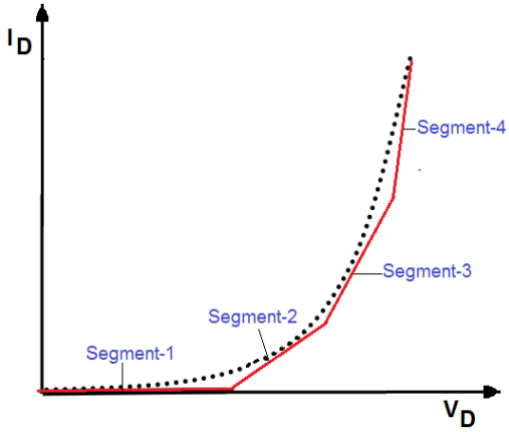

Figure 7. *Four segment piecewise diode model*

The PV cell equivalent circuit has a nonlinear characteristic due to the diode element. Using the PLPBM, the PV cell equivalent circuit can be linearized. This linearized model simplifies analysis and enables larger circuit simulations. The linearization of the PV cell with the PLPBM method is given in Figure 8.

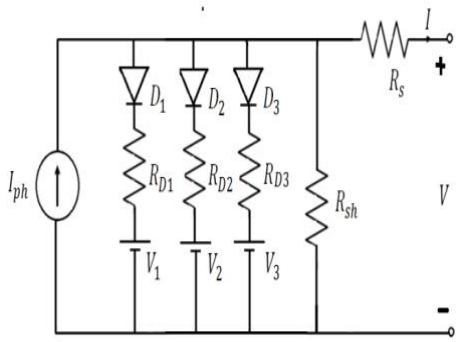

Figure 8. *Linearization of the PV cell equivalent circuit with the PLPBM method*

PV cell piecewise linearized model vertex points are located at:

$$0.9 * V_{MPP} \leq V_{amb} \leq 1.1 * V_{MPP} \quad (13)$$

Segment 1: ($V_D < V_1$) (V_1 = 0.9* MPP = 23.67 V). All diodes are in the off position. For this reason, almost all of the light current produced from the PV cell flows through the load and a small part flows through the shunt resistor.

Segment 2: ($V_1 < V_D < V_2$). D_1 diode is in the on position. In this range, the PV cell current decreases from 8.21 A to 7.61 A. In this case, 0.6 A current flows through D_1 diode. The value of R_{D1} resistance is found from Eq. (14) given below.

$$R_{D1} = \frac{V_{max} - 0.9V_{max}}{I_{D1}} \quad (14)$$

It is found as given below.

$$R_{D1} = 4.3833\ \Omega$$

Segment 3: ($V_2 < V_D < V_3$). In this range, D_1 diode and D_2 diode are in the on position. The current passing through D_1 diode is found with the Equation (15).

$$I_{D1} = \frac{1.1V_{max} - 0.9V_{max}}{R_{D1}} \quad (15)$$

The PV output current is 6.65 A, the current through D_2 diode:

$$I_{D2} = I_{ph} - I_{D1} - 1 \quad (16)$$

$$I_{D2} = 0.35\ A$$

ıs found. Resistance R_{D2} is calculated from Equation (17):

$$R_{D1} = \frac{1.1V_{max} - 0.9V_{max}}{I_{D2}} \quad (17)$$

$$R_{D2} = 7.514\ \Omega$$

ıs found.

Segment 4: ($V_3 < V_D < V_{OC}$). In this range, all diodes are in the on position. PV cell load current is zero. The open circuit voltage is 21.8 V. The current passing through D1 diode is found from equation (18).

$$I_{D1} = \frac{V_{oc} - 1.1V_{max}}{R_{D1}} \quad (18)$$

$$I_{D1} = 0.9057\ \text{A}$$

Is found. The current through D_2 diode is computed from Equation (19)

$$I_{D2} = \frac{V_{oc} - 1.1V_{max}}{R_{D2}} \quad (19)$$

($V_3 < V_D < V_{OC}$). In this range, since the PV output current (I) is zero, the current passing through D_3 diode is calculated from equation**:**

$$I_{D3} = I_{ph} - I_{D1} - I_{D2} - \quad (20)$$

$$\mathrm{I_{D3}} = 6.766\ \mathrm{A}$$

is found. R_{D3} resistance is calculated from Equation (21):

$$\mathrm{R_{D3}} = \frac{\mathrm{V_{oc}} - 1.1\mathrm{V_{max}}}{\mathrm{I_{D3}}} \quad (21)$$

$$\mathrm{R_{D3}} = 0.5867\ \Omega$$

is found. The maximum cell voltage at the MPP point is found from Equation (22)

$$\mathrm{V_{mpcell}} = \frac{\mathrm{V_{mp}}}{\mathrm{N_s}} \quad (22)$$

$$V_{mpcell} = \frac{26.3}{54} = 0.478\ V$$

is found. The equivalent of the voltages in Fig. 9 is calculated from Equation (23).

$$0.9 * \mathrm{V_{MPP}} < \mathrm{V_{MPP}} < 1.1 * \mathrm{V_{MPP}} \quad (23)$$

The voltage values of V1, V2, and V3 are found in Equation (22). As a result, V1, V2, and V3 are 0. 4302 V, 0.478 V, and 0,5258 V are calculated as. Since all PV cells are connected in series, the same current flows through all PV solar cells. The equivalent circuit parameters of the diode are given in Table 2.

***Table 2**. Equivalent circuit parameters of the diode*

Parameters	Values	Parameters	Values
I_{D1}	0.9057 (A)	R_{D1}	4.3833 (Ω)
I_{D2}	0.35 (A)	R_{D2}	7.514 (Ω)
I_{D3}	6.766 (A)	R_{D3}	0.5867 (Ω)
Vmpcell	0.478 (V)	V_1	0.4302 (V)
I	6.65 (A)	V_2	0.478 (V)
		V_3	0.5258 (V)

In the piecewise linear parallel branches model, the diode within the equivalent circuit of a PV cell is often linearized around its operating point to simplify analysis. By linearizing the diode model in this way, the equivalent circuit becomes easier to analyze using linear circuit analysis techniques, facilitating the design and optimization of PV systems. However it's essential to remember that this linearization is only valid around the operating point and may introduce inaccuracies outside this region.

The contributions of the paper can significantly advance the understanding and application of photovoltaic technology. By introducing a more accessible and efficient modeling approach, it has the potential to impact research, education, and practical implementations in the renewable energy sector, ultimately leading to more efficient energy systems and better integration of solar power into the energy grid.

A. DETERMİNİNG THE MAXİMUM POWER OF THE SOLAR PV CELL

To determine the maximum power output of a PV cell, we usually need to find the operating point at which the product of voltage and current is maximized. This point is called the Maximum Power Point (MPP). Locate the point on the IV curve where the product of current and voltage is maximized. Mathematically, this point corresponds to the maximum power output (Pmax) of the PV cell. It's important to note that the operating conditions, such as solar irradiance and temperature, can significantly affect the maximum power output of the PV cell. Additionally, the maximum power point may shift due to changes in these conditions. Therefore, it's often necessary to consider the real-world operating environment when determining the maximum power output of a PV cell. According to Thevenin's theorem, any linear electrical network with voltage and current sources and resistances can be replaced by a single voltage source (Thevenin voltage) in series with a single resistor (Thevenin resistance). This equivalent circuit represents the original circuit as seen from two terminals. To transfer the maximum power from a PV cell to the load, it is necessary to determine the Thevenin equivalent of the PV cell. Thevenin equivalent. Voltage sources are short-circuited and current sources are open-circuited to find Thevenin equivalent resistance. The aim here is to simplify the complex circuit, allowing the circuit to be analyzed more easily. Thevenin voltage and resistance values are given below.

$$V_{Thi} = V_i + R_{Di}\left(\frac{I_{ph}R_{sh} - V_i}{R_{sh} + R_{Di}}\right) \tag{24}$$

$$R_{Thi} = R_s + \left(\frac{R_{sh}R_{Di}}{R_{sh} + R_{Di}}\right) \tag{25}$$

V_{Thi} is the open circuit voltage between two points. The R_{Thi} resistor is the input or equivalent circuit resistor when independent sources are disabled. Thevenin's equivalent circuit is shown in Figure 9.

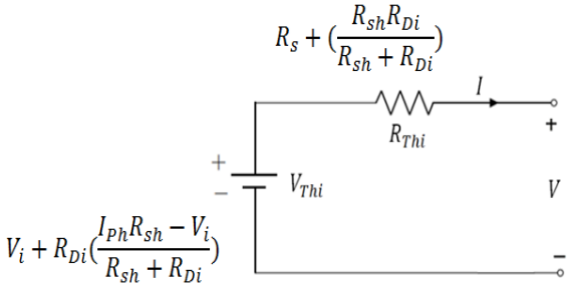

Figure 9. *Derivation of Thevenin equivalent model of solar PV cell*

Where V_{Thi} and R_{Thi} are Thevenin's equivalent voltage and resistance of the model of Figure 9 at region i (i = 1, 2, 3....number of regions). Thévenin's theorem states that any linear electrical network can be replaced by an equivalent circuit consisting of a single voltage source Vth in series with a single resistor Rth, where Vth is the open-circuit voltage at the terminals of the network, and Rth is the equivalent resistance seen from those terminals when all independent sources are turned off (replaced by their internal resistances). Thévenin's theorem provides a useful theoretical framework for understanding and optimizing the power output of PV modules by identifying the conditions under which maximum power transfer occurs. This theorem is fundamental in PV system design and operation, facilitating efficient energy conversion from sunlight to electrical power. The equivalent of this circuit is given in Figure 10.

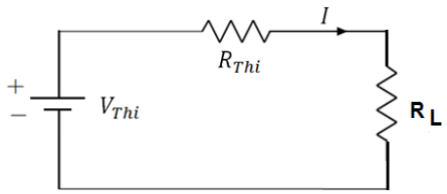

Figure 10. *Development of Thevenin equivalent model PV cell with RL loaded*

The current through the load for any value of load resistance is

$$I_L = \frac{V_{Thi}}{R_{Thi} + R_L} \tag{26}$$

The power transferred to the load is

$$\mathrm{P} = \mathrm{I_L^2} * \mathrm{R_L} \tag{27}$$

When we take the derivative of equation (26), the following expression is obtained.

$$\frac{dP}{dR_L} = V_{Th}^2 \left[\frac{(R_{Thi} + R_L)^2 - 2R_L + (R_{Thi} + R_L)}{(R_{Thi} + R_L)^2}\right] = 0 \tag{28}$$

The result of equation (28) is found as follows.

$$R_L = R_{Thi} \tag{29}$$

This principle ensures that the maximum amount of power is transferred from the source to the load. When the load resistance matches the source resistance in the Thevenin equivalent circuit, the circuit operates most efficiently, maximizing power transfer. The maximum power transferred to the load is found using the following formula.

$$\mathrm{P_{max}} = \left(\frac{\mathrm{V_{Thi}}}{\mathrm{R_{Thi} + R_L}}\right)^2 * \mathrm{R_L} \tag{30}$$

The change of cell output power depending on the load resistance is given in Figure 11.

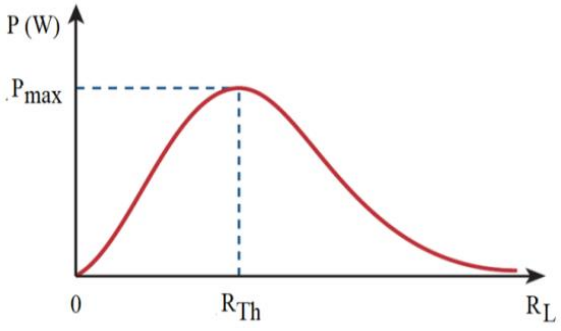

Figure 11. *Output power dependent on load resistor*

As a result, the maximum power value is obtained as:

$$\mathrm{P_{max}} = \frac{\mathrm{V_{Thi}^2}}{4\mathrm{R_{Thi}}} \tag{31}$$

The value of the Thevenin voltage given in equation (32).

$$V_{Thi} = V_i + R_{Di}\left(\frac{I_{ph}R_{sh} - V_i}{R_{sh} + R_{Di}}\right) \tag{32}$$

The formula to calculate the Theremin resistance of the PV cell it is as below:

$$R_{Thi} = R_s + \left(\frac{R_{sh}R_{Di}}{R_{sh} + R_{Di}}\right) \tag{33}$$

Maximum power to be transferred from the PV cell to the load from equation (31).

$$P_{max} = \frac{\left[V_i(R_{sh} + R_{Di}) + R_{Di}\left(I_{ph}R_{sh} - V_i\right)\right]^2}{4(R_{sh} + R_{Di})[R_s(R_{sh} + R_{Di}) + R_{sh}R_{Di}]} \tag{34}$$

Maximum power transfer is the finding of the load value that provides the greatest power transfer from a PV cell to the connected load. The goal of a photovoltaic (PV) system is to convert sunlight into electrical energy as efficiently as possible. Ensuring maximum power transfer from the PV cell to the load is crucial.Maximizing power transfer from a photovoltaic cell is essential for ensuring the efficiency, reliability, and economic viability of solar energy systems. The Maximum Power Point Tracking **(MPPT)** technique is the most effective method to ensure maximum power transfer, along with proper system design, impedance matching, and load management. These strategies allow PV systems to capture and utilize the highest possible amount of energy from the sun, improving the overall performance and efficiency of solar power systems.

IV. DEVELOPMENT OF THE ANALYTICAL EXPRESSION OF THE MAXIMUM POWER AND FILL FACTOR BASED ON EQUIVALENT CIRCUIT PARAMETERS

The value of the fill factor gives information about the ideality of the PV cell. In an ideal PV cell, the fill factor is equal to one. Therefore, the fill factor should be close to one in any PV cell. The parameters shown in Table 1. are used in the simulation and are given by the manufacturer's PV module..

$$P_{max} = \frac{\left[V_1(R_{sh} + R_{D1}) + R_{D1}\left(I_{ph}R_{sh} - V_1\right)\right]^2}{4(R_{sh} + R_{D1})[R_s(R_{sh} + R_{D1}) + R_{sh}R_{D1}]} + \frac{\left[V_2(R_{sh} + R_{D2}) + R_{D2}\left(I_{ph}R_{sh} - V_2\right)\right]^2}{4(R_{sh} + R_{D2})[R_s(R_{sh} + R_{D2}) + R_{sh}R_{D2}]} + \frac{\left[V_3(R_{sh} + R_{D3}) + R_{D3}\left(I_{ph}R_{sh} - V_3\right)\right]^2}{4(R_{sh} + R_{D3})[R_s(R_{sh} + R_{D3}) + R_{sh}R_{D3}]} \tag{36}$$

Solar PV cells are exposed to non-uniform solar irradiation throughout the day. Shadowing in PV panels can significantly reduce energy production and efficiency. Proper design, including the use of bypass diodes and careful system layout, along with ongoing monitoring and maintenance, is essential to mitigate the impact of shading and maximize the performance of photovoltaic systems over their operational lifetime. The P-V characteristic curve of the PV module is given in Figure 12.

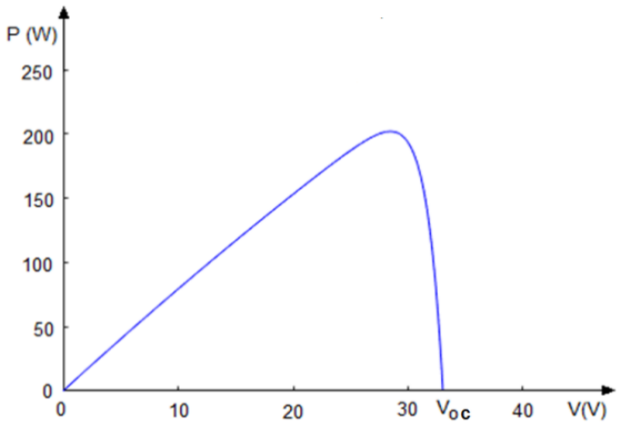

Figure 12. *P-V curve of the PV module (at 25 °C, 1000 W/m²)*

The measurement of the maximum power value produced by photovoltaic cells under different irradiation intensities and operating conditions is important as it reflects the system's performance. Because the power output of photovoltaic panels depends on radiation intensity, operating temperature, and other climatic parameters. In this study, a piecewise linear diode model has been developed to obtain a characteristic close to the nonlinear characteristic of a single diode of the PV cell. From equation (9), the fill factor of the solar system is as given in Equation (36).

$$FF = \frac{\frac{\left[V_1(R_{sh}+R_{D1})+R_{D1}\left(I_{ph}R_{sh}-V_1\right)\right]^2}{4(R_{sh}+R_{D1})[R_s(R_{sh}+R_{D1})+R_{sh}R_{D1}]}+\frac{\left[V_2(R_{sh}+R_{D2})+R_{D2}\left(I_{ph}R_{sh}-V_2\right)\right]^2}{4(R_{sh}+R_{D2})[R_s(R_{sh}+R_{D2})+R_{sh}R_{D2}]}+\frac{\left[V_3(R_{sh}+R_{D3})+R_{D3}\left(I_{ph}R_{sh}-V_3\right)\right]^2}{4(R_{sh}+R_{D3})[R_s(R_{sh}+R_{D3})+R_{sh}R_{D3}]}}{I_{sc}V_{oc}} \quad (36)$$

The value of the Fill Factor is found as follows from the results of the Equation (36).

FF=74 %

is found. The value of the FF gives information about the ideality of the PV cell. In an ideal PV cell, the fill factor is equal to one. Therefore, the fill factor should be close to one in any PV cell. For the fill factor to be large, the series resistance (Rs), the ideality factor of the diode (n), the reverse saturation current density (Io), and the temperature (T) in the PV cell equivalent circuit should be small. However, the band gap energy (Eq) and the shunt resistance (Rsh) must be large.

IV. CONCLUSION

Since there is a diode element in the PV cell equivalent circuit, this model is not linear and Thevenin's theorem cannot be applied to this equivalent circuit. However, the Thevenin equivalent was found after linearizing the nonlinear PV cell equivalent circuit with the piecewise linear parallel branches model. The proposed new PV cell model is widely used in the analysis and simulation of PV systems. In this study, we focused on modeling and simulation of PV cell single diode equivalent circuits, taking into account linearized equivalent circuit parameters.

Maximizing power transfer from PV modules is essential for achieving high energy conversion efficiency, optimizing system performance, and ensuring the economic viability and longevity of solar energy installations. Advanced technologies and careful system design play crucial roles in achieving these goals in solar power applications. Proper system design, including module orientation, tilt angle,

shading analysis, and optimal wiring configuration, contributes to maximizing power transfer efficiency.

The fill factor is directly affected by the series and shunt resistors and diode losses in the equivalent circuit of the PV cell. The fill factor is a critical parameter in assessing the efficiency, performance, and quality of photovoltaic devices. It plays a vital role in maximizing the energy conversion efficiency of solar cells and modules, thereby contributing to the overall success and adoption of solar energy technologies. As a result, the efficiency of the PV cell increases, and the output power approaches its maximum value.

V. REFERENCES

[1] M. Niu *et al*., "Reliability Importance of Renewable Energy Sources to Overall Generating Systems," in *IEEE Access*, vol. 9, pp. 20450-20459, 2021, doi: 10.1109/ACCESS.2021.3055354

[2] J. Lee, Y.T. Yoon, and Lee, G.J. "Renewable Energy Sources: From Non-Dispatchable to Dispatchable, and Their Application for Power System Carbon Neutrality Considering System Reliability." *J. Electr. Eng. Technol.* vol.19, no. 1, pp. 2015–2028, 2014, doi:10.1007/s42835-023-01669-8

[3] K. A. Munzer, K. T. Holdermann, R. E. Schlosser and S. Sterk, "Thin monocrystalline silicon solar cells," *in IEEE Transactions on Electron Devices*, vol. 46, no. 10, pp. 2055-2061, 1999, doi: 10.1109/16.791996.

[4] P. Sana, J. Salami and A. Rohatgi, "Fabrication and analysis of high-efficiency polycrystalline silicon solar cells," *in IEEE Transactions on Electron Devices*, vol. 40, no. 8, pp. 1461-1468, 1993, doi: 10.1109/16.223706

[5] N.N. Feng *et al*., "Design of Highly Efficient Light-Trapping Structures for Thin-Film Crystalline Silicon Solar Cells," *in IEEE Transactions on Electron Devices*, vol. 54, no. 8, pp. 1926-1933, 2007, doi: 10.1109/TED.2007.900976

[6] S. A. Moiz, A. N. M. Alahmadi and A. J. Aljohani, "Design of a Novel Lead-Free Perovskite Solar Cell for 17.83% Efficiency," *in IEEE Access*, vol. 9, pp. 54254-54263, 2021, doi: 10.1109/ACCESS.2021.3070112

[7] D. Liu *et al*., "Improved Efficiency of Organic Photovoltaic Cells by Incorporation of AuAg-Alloyed Nanoprisms," *in IEEE Journal of Photovoltaics*, vol. 7, no. 4, pp. 1036-1041, July 2017, doi: 10.1109/JPHOTOV.2017.2688578

[8] R.M. Swanson, "Approaching the 29% limit efficiency of silicon solar cells," *Conference Record of the Thirty-first IEEE Photovoltaic Specialists Conference*, Lake Buena Vista, FL, USA, 2005, pp. 889-894, doi:10.1109/PVSC.2005.1488274

[9] I.M. Kirpichnikofva and I.B. Makhsumov, "The Influence of Ambient Temperature on the Energy Characteristics of Solar Modules," *2020 International Conference on Industrial Engineering, Applications and Manufacturing (ICIEAM)*, Sochi, Russia, 2020, pp. 1-5 doi:10.1109/ICIEAM48468.2020.9112064

[10] S. Adak and H. Cangi, “Development software program for finding photovoltaic cell open-circuit voltage and fill factor based on the photovoltaic cell one-diode equivalent circuit model.” *Electr Eng*. vol. 106, pp. 1251–1264 , 2024, doi:10.1007/s00202-023-02082-0

[11] A. Al Tarabsheh, M. Akmal, and M. Ghazal, “Series Connected Photovoltaic Cells—Modelling and Analysis,” *MPDI Sustainability*, vol. 9. no. 3, pp.371-391, 2017, https://doi.org/10.3390/su9030371

[12] https://pv-manufacturing.org/solar-cell-manufacturing/pv-module-manufacturing/

[13] Z. Navabi et al “Modeling Timing Behavior of Logic Circuits Using Piecewise Linear Models,” *International Conference on Computer Hardware Description Languages and their Applications–Chdl'93,* Ottawa, Ontario, Canada, 1993, pp. 569-586, doi:10.1016/B978-0-444-81641-2.50046-0.

[14] Y.J. Wang and P.C. Hsu, “Modelling of solar cells and modules using piecewis linear parallel branches.” IET Renewable Power Generation, vol.5, no. 3, 2012, doi:10.1049/iet-rpg.2010.0134

[15] N. Dong and J. Roychowdhury, "Piecewise polynomial nonlinear model reduction," *Proceedings 2003. Design Automation Conference (IEEE Cat. No.03CH37451),* Anaheim, CA, USA, 2003, pp. 484-489, doi: 10.1145/775832.775957

[16] S. Adak, H. Cangi and A. S. Yilmaz, "Thevenin Equivalent of Solar PV Cell Model and Maximum Power Transfer," *2021 International Conference on Electrical, Communication, and Computer Engineering (ICECCE)*, Kuala Lumpur, Malaysia, 2021, pp. 1-5, doi:10.1109/ICECCE52056.2021.9514221

[17] A. Chatterjee and A. Keyhani, "Thevenin's equivalent of photovoltaic source models for MPPT and power grid studies," *2011 IEEE Power and Energy Society General Meeting*, Detroit, MI, USA, 2011, pp. 1-7, doi: 10.1109/PES.2011.6039203

[18] J. Fan, S. Li, S. Liu, X. Deng and X. Zhu, “Maximum Power Point Tracking Constraint Conditions and Two Control Methods for Isolated Photovoltaic Systems.” *MPDI Processes.* 2023; vol.11, no.11:3245. https://doi.org/10.3390/pr11113245

[19] M. Patsalides, G. E. Georghiou, A. Stavrou and V. Efthymiou, "Thevenin equivalent circuit for the study of high photovoltaic penetration in distribution grids," *IEEE PES ISGT Europe 2013*, Lyngby, Denmark, 2013, pp. 1-5, doi:10.1109/ISGTEurope.2013.6695421

[20] Z. Batushansky and A. Kuperman, "Thevenin-based approach to PV arrays maximum power prediction," *2010 IEEE 26-th Convention of Electrical and Electronics Engineers in Israel*, Eilat, Israel, 2010, pp. 000598-000602, doi:10.1109/EEEI.2010.5662149

[21] M.T. Ahmed, T. Gonçalves, and M. Tlemcani, “Single diode model parameters analysis of photovoltaic cell,” *2016 IEEE International Conference on Renewable Energy Research and Applications (ICRERA),* Birmingham, UK, 2016, pp. 396-400, doi:10.1109/ICRERA.2016.7884368

[22] D.T. Cotfas et al “The methods to determine the series resistance and the ideality factor of diode for solar cells-review,” *2012 13th International Conference on Optimization of Electrical and Electronic Equipment (OPTIM),* Brasov, Romania, 2012, pp. 966-972, doi:10.1109/OPTIM.2012.6231814

[23] P.S.M. Saad, M.Y. Bin Kasbudi, and Y. Hashim, “I-V and P-V Solar Cell Characteristics Simulation for a Single Diode Photovoltaic,” *2022 IEEE International Conference in Power Engineering Application (ICPEA)*, Shah Alam, Malaysia, 2022, pp.1-5, doi:10.1109/ICPEA53519.2022.9744703

[24] C. Y. Lai, C. Xiang and T. H. Lee, "Identification and control of nonlinear systems via piecewise affine approximation," *49th IEEE Conference on Decision and Control (CDC)*, Atlanta, GA, USA, 2010, pp. 6395-6402, doi: 10.1109/CDC.2010.5717032

[25] M. Azab, “Design approach and performance analysis of trap filter for three-phase PV grid integration systems using evolutionary search algorithms,” *Journal of King Saud University - Engineering Sciences* , vol. 33, no. 7, pp. 491-506, 2021, doi:10.1016/j.jksues.2020.06.002.

[26] R.H.G. Tan, P.L.J. Tai, and H. Mok, Dv, “Solar irradiance estimation based on photovoltaic module short circuit current measurement,” *2013 IEEE International Conference on Smart Instrumentation, Measurement and Applications (ICSIMA)*, Kuala Lumpur, Malaysia, 2013, pp. 1-4, doi:10.1109/ICSIMA.2013.671794

[27] Y. J. Wang and P. C. Hsu, “Analysis of Partially Shaded PV Modules Using Piecewise Linear Parallel Branches Model. ”*International Journal of Electrical and Computer Engineering*, 2009, vol. 3, no. 12, pp. 2354- 2360.

Düzce University
Journal of Science & Technology
Research Article

Assessment of Rapid Urbanization Effects on Land Use Dynamics: A Google Earth and GIS Approach in Kemalöz Neighborhood, Uşak, Türkiye - An Earth Science Perspective

Umit YILDIZ[a,*]

[a] *Black Hills Natural Science Field Station, Geology and Geological Engineering, South Dakota School of Mines, Rapid City, SD, United States*
** Corresponding author's e-mail address: umit.yildiz@sdsmt.edu*
DOI: 10.29130/dubited.1462304

ABSTRACT

As urbanization continues to increase, the concerns about sustainable land use and management are also growing. Thus, there has been an increasing number of scientific research studies conducted on this phenomenon. In many cases, these studies have been performed using expensive remote sensing software with free but lower-resolution Landsat imagery (>30m). In contrast, Google Earth provides high-resolution imagery, offering a more detailed analysis of land use changes. On the other hand, Google Earth Pro imageries have a geometric resolution of 1.5 meters to 2 meters for most of the covered areas in the world. The objective of this study is to investigate changes in land use in the Kemalöz neighborhood of Uşak, Türkiye, which is the fastest-growing district, by utilizing Google Earth Pro and GIS for rapid assessment of land use change between 2005 and 2024, offering an alternative to remote sensing software and low-resolution Landsat imagery. The study also aims to evaluate the relative benefits of integrating geoscience to analyze land-use changes to provide insights to policymakers and local officials to make informed decisions about the most effective way to manage land to mitigate the negative effects of urbanization. The findings of this study indicated that the build-up land use has increased from 1,734 to 2,755 km^2 from 2005 to 2024. Vegetation land use has increased from 1,081 to 1,392 km^2 between 2005 and 2024. Agricultural land use has decreased from 1,781 to 1,149 km^2 between 2005 and 2024. Barren land use has decreased from 1,803 to 1,103 km^2. This suggests significant urban development or infrastructure expansion occurred in the study area over the 19 years.

Keywords: *Urbanization, Land Use, Google Earth, Earth Science*

Hızlı Kentselleşmenin Arazi Kullanım Dinamikleri Üzerindeki Değerlendirmesi: Kemalöz Mahallesi, Uşak, Türkiye'de Bir Google Earth ve CBS Yaklaşımı - Bir Yer Bilimleri Perspektifi

ÖZET

Kentselleşmenin artmasıyla birlikte, sürdürülebilir arazi kullanımı ve yönetimine yönelik endişeler de artmaktadır. Bu nedenle, bu fenomen üzerine yapılan bilimsel araştırmaların sayısı artmaktadır. Çoğu durumda, bu çalışmalar, ücretsiz ancak daha düşük çözünürlüklü Landsat görüntüleri (>30m) ile pahalı uzaktan algılama yazılımları kullanılarak gerçekleştirilmiştir. Buna karşılık, Google Earth yüksek

Received: 31/03/2024, Revised: 01/10/2024, Accepted: 11/10/2024

çözünürlüklü görüntüler sunarak, arazi kullanımı değişikliklerinin daha detaylı bir analizini sağlamaktadır. Öte yandan, Google Earth Pro görüntüleri, dünya genelindeki çoğu alan için 1,5 metreden 2 metreye kadar geometrik çözünürlüğe sahiptir. Bu çalışmanın amacı, Türkiye'nin Uşak şehrinin en hızlı büyüyen mahallesi olan Kemalöz'ün arazi kullanımındaki değişiklikleri incelemektir. Bu inceleme, 2005 ile 2024 arasındaki arazi kullanım değişikliklerini hızlı bir şekilde değerlendirmek için Google Earth Pro ve Coğrafi Bilgi Sistemi (GIS) kullanarak, maliyetli uzaktan algılama yazılımlarına ve düşük çözünürlüklü Landsat görüntülerine alternatif sunmaktadır. Çalışma ayrıca, arazi kullanımı değişikliklerini analiz etmek için yer bilimlerini entegre etmenin göreli faydalarını değerlendirmeyi amaçlamaktadır, böylece karar vericilere ve yerel yetkililere kentselleşmenin negatif etkilerini azaltmak için araziyi en etkili şekilde yönetme konusunda bilgi vermektedir. Bu çalışmanın bulguları, inceleme alanında 19 yıl boyunca önemli bir kentsel gelişme veya altyapı genişlemesi olduğunu göstermektedir. 2005 ile 2024 arasında yapılan inceleme, yapılaşma alanının 1.734'ten 2.755 km^2'ye, bitki örtüsü kullanım alanının ise 1.081'den 1.392 km^2'ye arttığını göstermiştir. Tarım alanı kullanımının ise 2005 ile 2024 arasında 1.781'den 1.149 km^2'ye azaldığı tespit edilmiştir. Kullanılmayan arazi alanının ise 1.803'ten 1.103 km^2'ye azaldığı görülmektedir. Bu sonuçlar, inceleme alanında önemli bir kentsel gelişme veya altyapı genişlemesi olduğunu göstermektedir.

Anahtar Kelimeler: *Kentselleşme, Arazi Kullanımı, Google Earth, Yer Bilimleri*

I. INTRODUCTION

While the world's population growth is on, urbanization is one of the most significant problems to date. The latest World Urbanization Prospects of 2018 states that more than half of the world's population which is equal to 4.2 billion people already live in urban areas [1]. This figure is expected to be higher by 5.2 billion in 2030, according to the UN's estimate [1]. Thus, the trend of the rural population leaving the countryside to the city for the sake of gaining better jobs, health care, as well as educational opportunities, is observed. Urbanization can bring both positive effects and negative impacts. The possibilities include implanted infrastructures that are more innovative and sustainable, improved health care and education services, increased economic growth, cultural diversity, and cultural exchange, and the chance for the improvement of social connections and community development. However, the rapid growth of a town's population is a major problem, and this leads to an over-exploitation of resources and facilities, which eventually leads to socio-economic issues, environmental pollution, noise pollution, and traffic jams [2,3,4]. Sustainable policies targeted at controlling the expansion of urban areas and raising the standard of living of all residents can be crafted only with an appreciation of the complex processes of urbanization. Urbanization is a process in which there is a net outflow of people from the rural areas to the urban areas. This phenomenon especially takes place in developing countries [5,6,7]. Thus, the policymakers have to take the appropriate steps to reduce the size of the negative impact of the growing population in the cities. One of these steps in tackling the urbanization challenges is the proper management of the uses. The interrelation between people and the place they live in has been significantly affected by urbanization, which is causing momentous changes in this relationship. The evolutionary process of urban land use occurs through a gradual increase in the complexity of urban land use where smaller and less complicated ones are converted into larger and more complex ones [8,9,10]. The spatial structure of urban land use, therefore, also plays a key role when the relationship between the land and the people in the urbanization process is analyzed [10,11,12]. Moreover, precise and updated land cover and land-use change data are also an important factor for urban planning and management, and all kinds of environmental monitoring activities [13,14,15].

As concerns about correct land management in the current urbanization have grown, there has been an increasing number of scientific research studies conducted. In many cases, these studies have been performed using expensive remote sensing software with free but lower-resolution Landsat imagery (>30m). In contrast, Google Earth provides high-resolution imagery, offering a more detailed analysis of land use changes [16,17,18,19]. Fu and Weng [20] conducted a historical reconstruction of land-use

and urban area changes from 1984 to 2011 by analyzing 507 Landsat images that were taken from 1984 to 2011 in order to understand the effect of land-use and urban area changes that were caused by human activities. Ha et al. [21] performed a 20-year land-use land-cover change in Vietnam using the Random Forest algorithm and Landsat imagery. Another urban land-use tracking study was carried out by Frimpong and Molkenthin [22] across the Random Forest algorithm and Landsat image data from 1986, 2013, and 2015. Many examples could be cited to illustrate the use of Landsat imagery in land use research. All of these studies have one thing in common: this very functionality is achieved by the Landsat dataset, which is often separated from other remote sensing datasets due to its low resolution when compared to the imagery provided by Google Earth [23, 24, 25]. The Global Landcover Facility (GLCF) provides free access to satellite data as a support of remote sensing research and is the source of satellite imagery in several studies [26]. However, there are drawbacks to the GLCF; images from sensors such as the Landsat Multispectral Scanner (e.g. Landsat 7) typically have lower to medium spatial resolutions, from 30 to 80 meters. In addition, a large financial commitment is often needed to obtain more recent and high-resolution imagery, which poses budgetary issues for any studies. On the other hand, Google Earth Pro imageries have a geometric resolution of 1.5 meters to 2 meters for most of the covered areas in the world (Figure 1). At these resolutions, Google Earth imagery makes it simple for human viewers to distinguish between the primary categories of natural land cover and to identify different components of the man-made landscape, including individual houses, industrial complexes, and road networks [27]. Numerous scholars have already begun to employ Google Earth Engine which is a rapidly expanding and openly accessible satellite imagery source [28,29,30,31,32]. Semiconductor devices such as sensors and transistors play a critical role in remote sensing technology by enhancing the accuracy and efficiency of data collection and processing [12,22].

Figure 1*. The satellite imageries illustrate the different resolution levels of Google Earth Pro (a), Landsat 7 (b), and Landsat OLI (c) over the Changqi River Bay, China. (Modified from [33]).*

The objective of this study is to investigate changes in land use in the Kemalöz neighborhood of Uşak, Türkiye, which is the fastest-growing district, by utilizing Google Earth Pro and ArcGIS for rapid assessment of land use change, offering an alternative to remote sensing software and low-resolution Landsat imagery. The study also aims to evaluate the relative benefits of using higher-resolution Google Earth imagery over Landsat imagery to analyze land-use changes to provide insights to policymakers and local officials to make informed decisions about the most effective way to manage land in order to mitigate the negative effects of urbanization. This research will also contribute to the growing body of research on the use of Google Earth Engine as an openly accessible satellite imagery source for land use and urban planning studies. It will offer insights specific to the Kemalöz neighborhood in Uşak, Türkiye, addressing the need for localized studies in rapidly growing urban areas.

II. STUDY AREA

The research area is located in the city center of Uşak province in the inner-western Anatolian region of the Aegean Region in Türkiye. It is a frontier between the Aegean and Central Anatolian regions, positioned at 38°40'24.64"N - 29° 24'20.88"E. The area of the province is about 5,341 square kilometers and the total population is around 377,000 according to the 2024 census. According to the Köppen-Geiger system, Uşak's climate is broadly classified as Csa, with warm temperatures and hot, dry summers [34]. The average annual temperature in Uşak is 12°C with annual precipitation ranging between 430 mm and 700 mm [17].

Kemalöz neighborhood, which is located in Uşak province, Türkiye, is one of the rapidly urbanizing districts in the region, thus offering an excellent research area to investigate urban growth processes. Kuyucak and Hacikadem villages, where the agricultural activities are intensive, form the southern and western borders of the Kemalöz neighborhood. The local administration of the Central Municipality in Uşak agreed to annex the villages of Kuyucak and Hacikadem to its municipal body in 2015. Therefore, the southern and western borders of Kemalöz neighborhood extended to the south and west, encompassing large agricultural fields. The study area, which covers an approximate area of 6.5 square km, has experienced evident population growth during the past years (Figure 2). Its population grew from 17,836 in 2005 to 40,007 by 2023 (Figure 3). This consistent population increase since 2005 is an intriguing case study of fast urbanization. Notably, the population density of the Kemalöz neighborhood is extremely high, with 6,154 people per square kilometer. This figure contrasts considerably with the global average population density of 59.22 people per square kilometer, highlighting the significant level of urbanization in this region. Such a dense city framework presents novel difficulties and opportunities for urban planners and policymakers, needing a solid understanding of land use dynamics and their implications for sustainable urban planning and development. The population growth in the Kemalöz district from 17,836 in 2005 to 40,007 by 2023 can be attributed to both urbanization and the administrative expansion that occurred when Kuyucak and Hacikadem villages were annexed to the Central Municipality of Uşak in 2015. While a portion of the population increase is undoubtedly linked to the physical growth of urban infrastructure and housing developments, the annexation of these villages also contributed to the overall population rise. However, the population density figures calculated in this study specifically pertain to the urban core of Kemalöz, excluding the impact of the villages' total population. Therefore, while the expansion of administrative borders increased the total land area, much of the observed growth is still indicative of significant urbanization within the original boundaries of the district.

The study area lies on the geologic Asartepe Formation [35]. It is a multicolored, generally red and orange, occasionally white, loosely lime, tuff, clay cemented, laminated with coal seams, semi-rounded pebbly conglomerate-sandstone succession. This formation sometimes contains thin marly calcareous beds and is thought to be formed in a fluvial environment. The Lower Quaternary Asartepe Formation unconformably overlays the Ulubey Formation, and it is underlain by Quaternary alluvium [35]. The maximum thickness is 200 m. It crops out in large areas in the western part of Uşak city where the study area is situated.

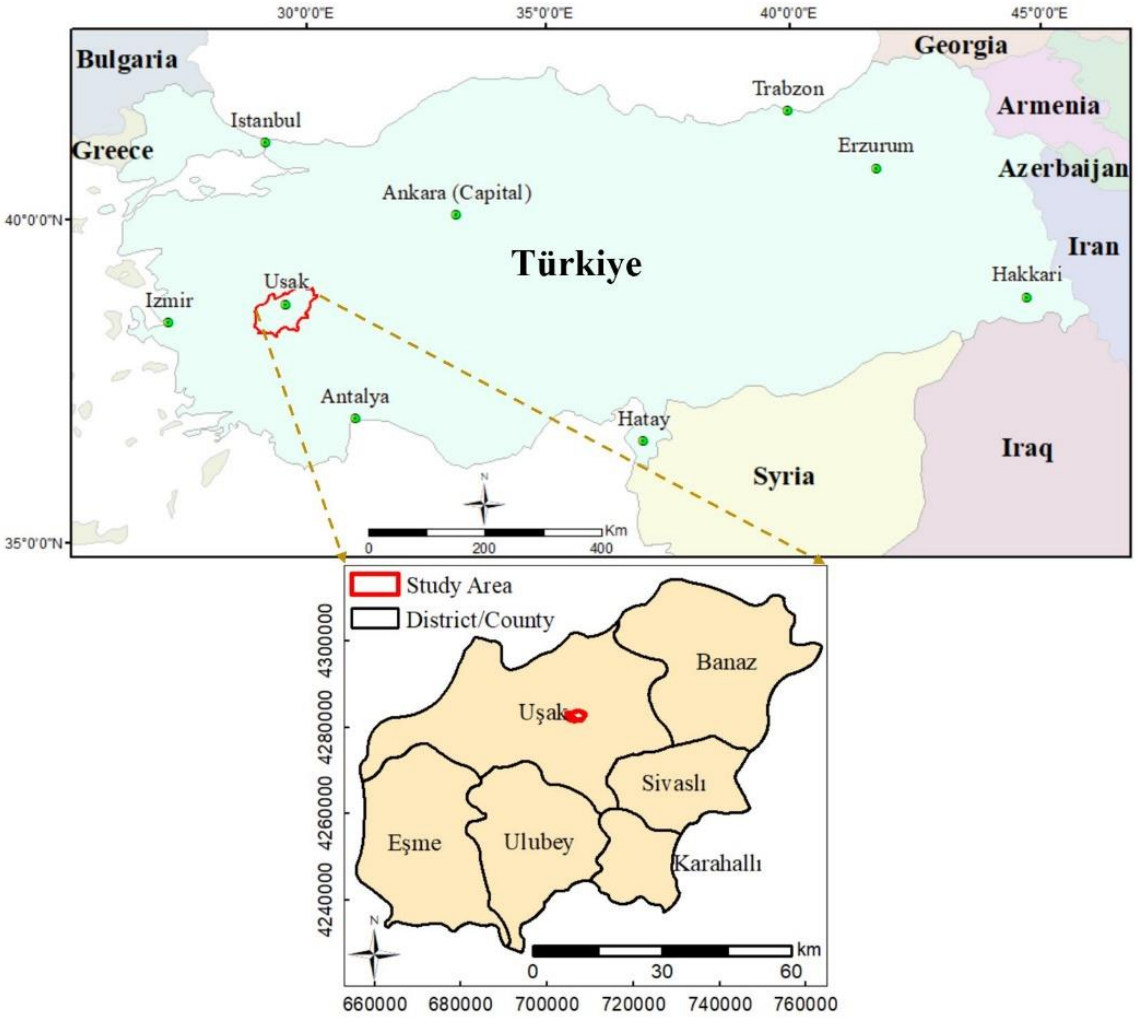

Figure 2*. Maps illustrating the study area's location. The map at the top is based on a Geographic Coordinate System (GCS), while the one at the bottom utilizes a Universal Transverse Mercator (UTM) Zone 35N projection, with the European Datum of 1950 (ED1950).*

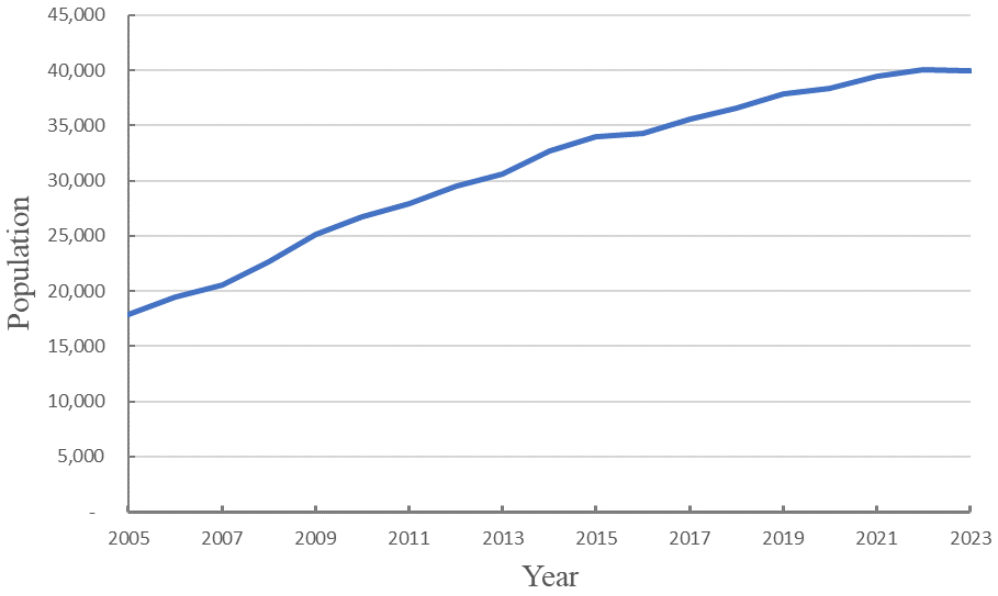

Figure 3. *The chart illustrates the population changes over time in Kemalöz neighborhood , Uşak, Türkiye.*

III. METHODS

A. DATA COLLECTION

Firstly, the boundary of the Kemalöz neighborhood was obtained from the General Directorate of Land Registry and Cadastre then it was digitized and converted into a shapefile in ArcGIS 10.7 [36]. Subsequently, 12 control points encompassing the boundaries of the Kemalöz neighborhood were marked in Google Earth 7.3.6. [23]. Historical satellite images from 5/18/2005 and 4/30/2024 were selected and downloaded to the computer, ensuring that the chosen images were cloud-free and clear. These imageries were then georeferenced and transformed from the geographic coordinate system to a projected coordinate system using the Universal Transverse Mercator (UTM) projection with European Datum 1950 in ArcGIS 10.7. Afterward, the images encompassing the district boundary were clipped using the digitized district boundary shapefile in ArcGIS 10.7.1. The following land use classes were evaluated in the current study: built-up areas, vegetation, agricultural areas, and barren/open terrain. There were no water bodies in the study area, hence the waterbody class was ignored.

The built-up area encompasses all urbanized regions and associated infrastructure like buildings and roads, while barren/open land encompasses vacant areas, rocky terrain, scrubland, and agricultural zones where crops and fruits are cultivated. Vegetation includes all non-agricultural forests and woodlands (Figure 4). Subclasses were not further categorized into specific uses since the study aims to analyze the overall extent of urbanization without focusing on specific subclass uses such as residential, commercial, industrial, institutional, and recreational land uses.

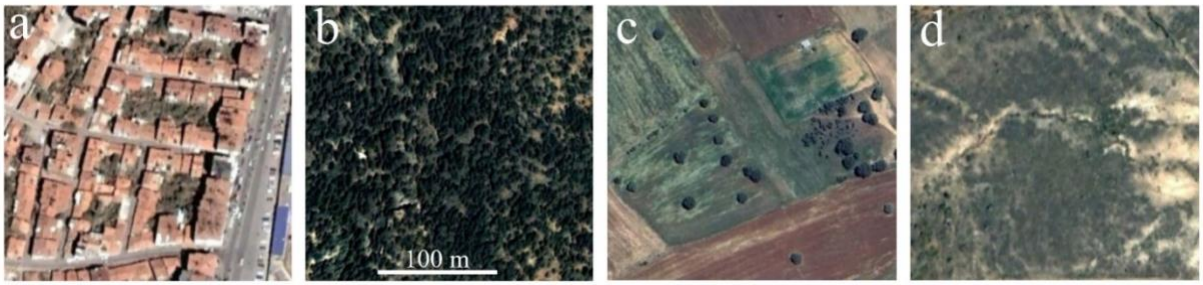

Figure 4. *Training image samples of high-resolution Google Earth imageries of different land use classes (a- built-up; b- vegetation; c- agricultural; d- open/barren). The white scale bar applies to all images and is 100 meters long.*

B. DATA ANALYSIS TECHNIQUES

The land use analyses were performed in ArcGIS 10.7.1, by utilizing the classification tool. Previously clipped imageries were selected in this tool, and the circle or polygon option was selected to create training samples on the imageries, and training sample signatures were saved to be used in the subsequent operations. Later, the Maximum Likelihood Classification (MLC) algorithm was employed to generate training samples for each class. Subsequently, appropriate colors were assigned for each class (e.g. green for vegetation, gray for built areas, etc.). The MLC algorithm is widely used in land use studies to perform a supervised classification of raster imageries into different land use classes. This tool operates on the cells within each class sample in a multi-dimensional space, taking into account that they follow a normal distribution. The tool provides this feature by picking the cell in the signature file and also considering the means and covariances of the class signatures. The assumption of normality in a class sample denotes that, a class is described by a mean vector and a covariance matrix [36]. The tool performs the classification taking into account these features for every cell value. Using them, the tool calculates the statistical probability of a class to identify the class to which the cells belong. In the context of the study, the "EQUAL" option for priory probability weighting is set into the system to get the class to which the cell has the maximum chance of belonging [36].

IV. LIMITATIONS

While the methodology employed in this study provides a detailed analysis of land use changes, several limitations must be acknowledged. Firstly, the georeferencing of historical satellite images may introduce positional inaccuracies due to variations in the original image resolution and quality. Although every effort was made to ensure precision by using control points and a standard projection system (UTM with European Datum 1950), small misalignments may still occur. Additionally, the Maximum Likelihood Classification (MLC) algorithm assumes that the spectral data within each land use class follow a normal distribution, which might not hold true for all classes, especially in heterogeneous or mixed land use areas. Furthermore, the absence of subclasses, such as differentiating between residential, commercial, or industrial zones within built-up areas, limits the granularity of the analysis. Another limitation is the reliance on satellite imagery alone, as the study does not account for other data sources such as field surveys or socio-economic factors that may influence urbanization trends. Lastly, this study assumes that land cover changes between 2005 and 2024 are solely related to urbanization and natural vegetation shifts, without considering other external drivers such as policy changes or economic factors that could affect land use dynamics.

IV. RESULTS

Maps illustrating different land-use classes in 2005 and 2024 are presented in Figures 5 and 6 respectively. The build-up land use has increased from 1,734 to 2,755 km^2 from 2005 to 2024. The total population increase in the study area is likely influenced significantly by both urbanization and the expansion of administrative borders. The significant rise in built-up areas from 1,734 km^2 in 2005 to 2,755 km^2 in 2024 also suggests that urbanization plays a major role in attracting people to the district. As urban areas expand, they often provide more housing, jobs, and services, which can lead to population growth. The annexation of Kuyucak and Hacikadem villages to the Central Municipality in 2015 expanded the district's borders. This expansion likely contributed to the population increase by incorporating additional residents from these villages into the overall population count of Kemalöz. This clearly suggests significant urban development or infrastructure expansion over the 19 years. Vegetation land use has increased from 1,081 to 1,392 km^2 between 2005 and 2024. This indicates a slight increase in green cover, possibly due to afforestation efforts or natural regrowth. Agricultural land use has decreased from 1,781 to 1,149 km^2 between 2005 and 2024. This suggests a decline in agricultural land due to urbanization or possibly changes in farming practices. Barren land use has decreased from 1,803 to 1,103 km^2. This indicates a reduction in barren or unproductive land, possibly due to reclamation efforts, afforestation, or urban development. A summary of land use between the years 2005 and 2024 is presented in Table 1.

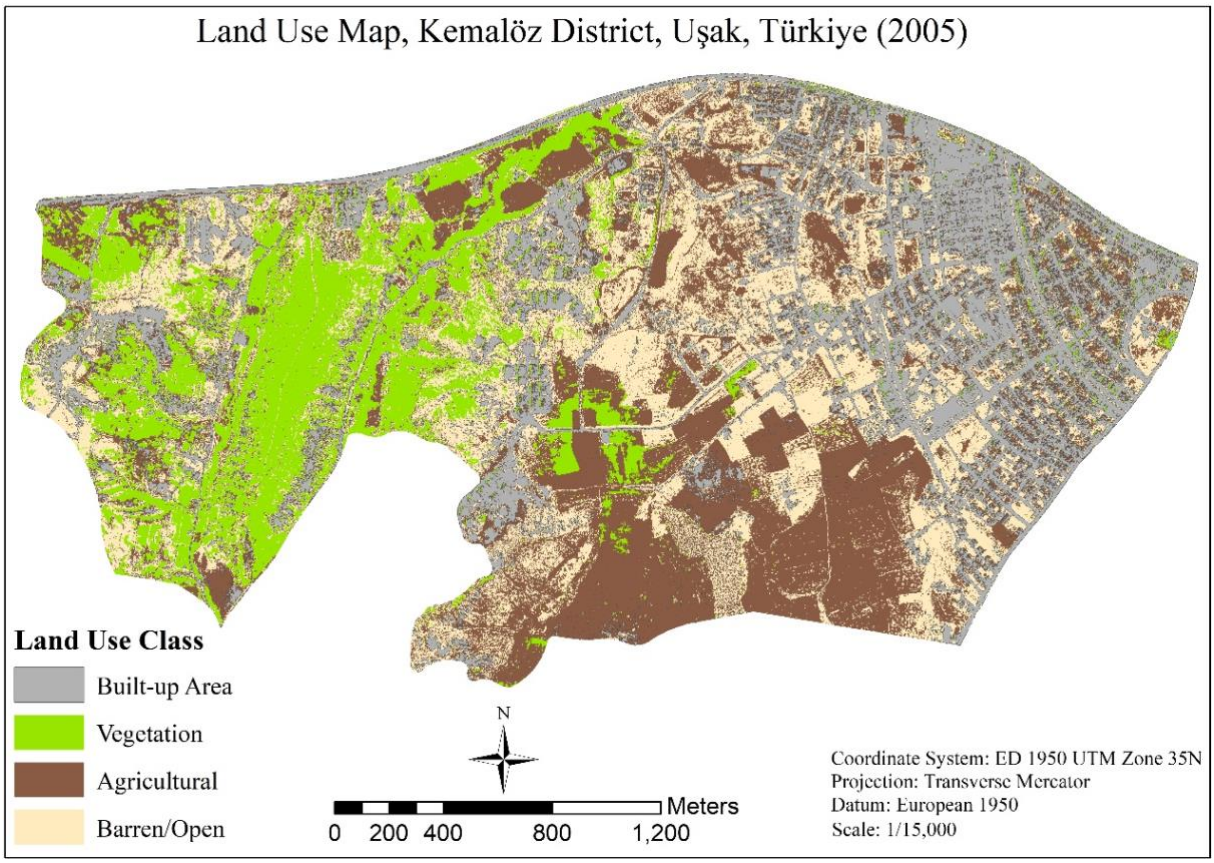

***Figure 5**. Map illustrating different land-use classes in 2005.*

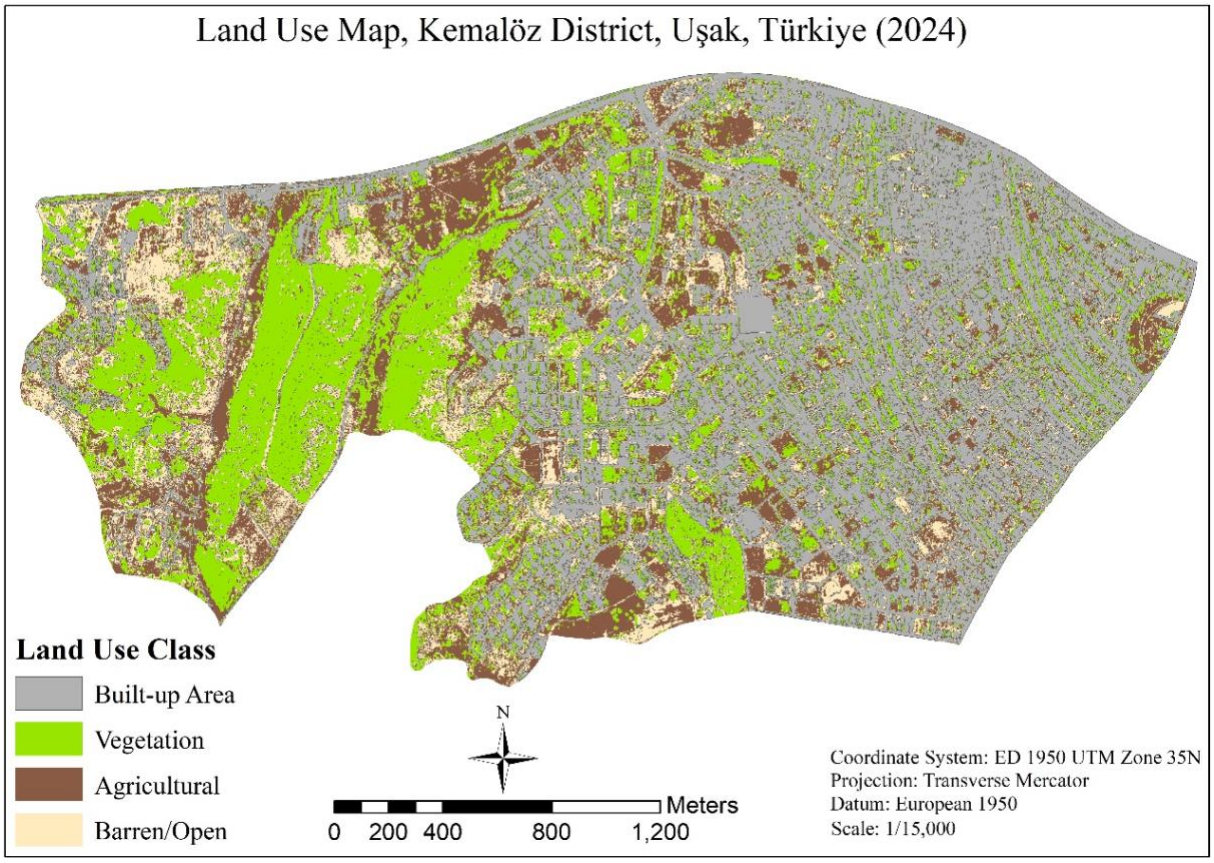

***Figure 6**. Map illustrating different land-use classes in 2024.*

Table 1. *The table presents the data for the land classes (Building, Vegetation, Agricultural, and Barren) for the years 2005 and 2024. The numbers indicate the areas, which are in km^2, covered by each land class in the respective years.*

Land Class	2005	2024
Building	1,734	2,755
Vegetation	1,081	1,392
Agricultural	1,781	1,149
Barren	1,803	1,103

The percentage distribution of various land uses across different zones is displayed in Figure 7. The study area comprises a total surface land area of 6,398 km². In 2005, the land was categorized as follows: 27% as build-up, 17% as vegetation, 28% as agricultural, and 28% as open/barren land. By contrast, in 2024, the distribution of land use shifted, with 43% designated as build-up areas, 22% as vegetation cover, 18% as agricultural land, and 17% as barren or open land (Figure 5).

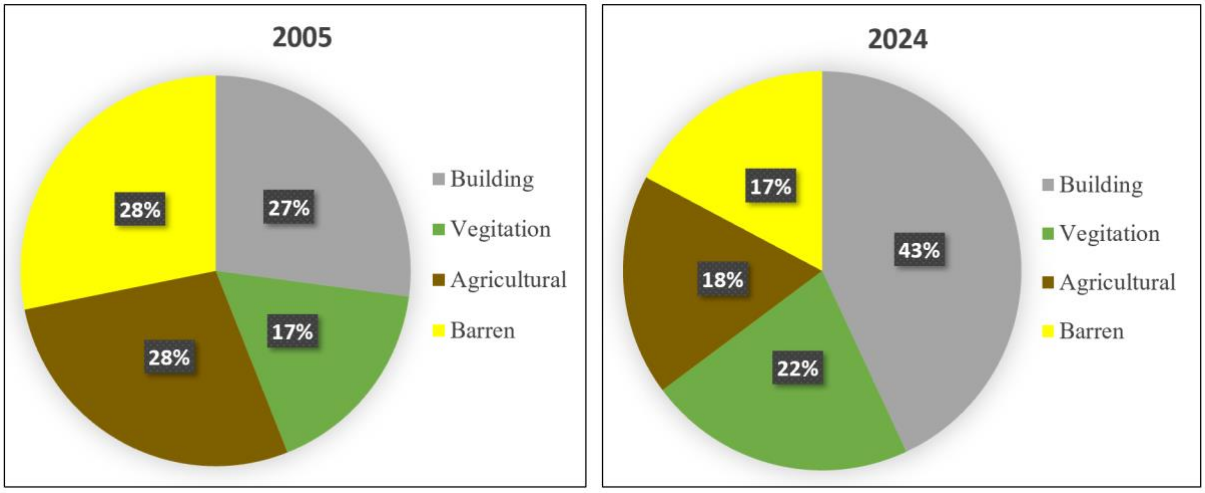

Figure 7*. Charts showing the distribution of land use classes for 2005 on the left, and 2024 on the right.*

The maps from 2005 and 2024 vividly illustrate the significant changes in land use over the span of 19 years, particularly highlighting the substantial increase in urbanization and the notable decrease in agricultural lands. In the map from 2005, the landscape is characterized by relatively smaller pockets of built-up areas amidst larger expanses of agricultural land and open/barren areas. However, in the map from 2024, the built-up areas have visibly expanded, forming extensive urban clusters that dominate the landscape. Figures 5 and 6 clearly show that the urban development and the infrastructure construction have been going at an increasing speed over the years. Moreover, the maps also show the decrease in agricultural lands from 2005 to 2024. What was a large amount of farmland in 2005 is now an urban area and the amount of farmland has been reduced by 2024. The land use change in this regard, most certainly, indicates the effects of urbanization on agricultural landscapes and it is the result of factors that include population growth, industrialization, and land use changes. Also, the maps show an increase in the vegetation range from 2005 to 2024, but this is overshadowed by the rapid growth of built-up areas. Although the measures taken for afforestation or natural regeneration are mostly helpful, the overall trend towards urbanization is the largest influence on the dynamics of land use. Visually, the maps from 2005 and 2024 confirm the counter-intuitive and impressive capacity of urbanization to manifest physically as a change in the landscape and also agricultural land use. Such changes not only demonstrate the urban area's socio-economic condition but also show the importance of sustainability in land management in the case of fast urban growth.

The geological setting comprising the entirety of the Kemalöz neighborhood, which is a part of the Lower Quaternary Asartepe Formation [35], influences the pattern of land use and urbanization

tendencies. The Asartepe Formation implies unconventional conditions for sustainable soil management. For instance, the lithological composition will determine whether there is enough fertile soil, proper drainage, and stable land, thus affecting agricultural and urban development strategies. Comprehending the geological background is fundamental in the land use planning and management process as this assists in identifying the areas that are at risk of geological hazards, including landslides and soil erosion, and regions suitable for particular land use, such as agriculture and urban development.

V. DISCUSSIONS

This research examined the land use changes in the Kemalöz neighborhood , a rapidly developing area in Uşak-Türkiye, using Google Earth Pro and GIS tools. It was demonstrated in this study that there were statistically significant changes in land use patterns from 2005 to 2024 with a rise in urban areas and a decline in agricultural areas. This indicates the significant imprint of urbanization on the landscape and calls for acceptable land use management solutions to avoid adverse effects.

Considering the rapidly growing built-up areas and infrastructures in the Kemalöz neighborhood area, it is predicted that more agricultural lands will be disappearing in the near future. This trend of rapid urbanization is consistent with the global trend of urban growth influenced by factors like an increase in population, industrialization, and change in land use types. Rapid urbanization comes with challenges such as intensified resource consumption, environmental degradation, and the social-economic inequalities among the urban dwellers which is a call for well-planned and managed land uses.

Furthermore, the study compared the use of Google Earth imagery (resolution <5 meters) with traditional Landsat imagery for land use analysis. The higher resolution of Google Earth imagery enhances the ability to accurately outline land use areas and detect the changes at different time intervals. This pilot study illustrates the ability of the freely available, high-resolution satellite imagery sources to provide a rapid assessment of changes in land use for a given study area. This may provide valuable information for urban planning and management efforts.

The continued expansion of urban areas in Kemalöz neighborhood aligns with global trends, driven by population growth and industrialization. This underscores the need for better urban planning policies, such as zoning regulations to limit urban sprawl and preserve agricultural and green spaces. Using high-resolution Google Earth imagery also proves valuable for resource-limited areas, providing a cost-effective tool for monitoring land use and informed decision-making.

Future studies could examine the socio-economic factors driving land use changes in the region and evaluate the effectiveness of current land use policies. Further research could also integrate additional remote sensing data or focus on longer-term trends to improve land use classification accuracy. Expanding this analysis to other urbanizing regions would provide comparative insights and enhance the generalizability of the findings.

VI. CONCLUSIONS

The findings of this study could be useful for understanding the land use dynamics of Kemalöz neighborhood, Uşak, Türkiye, for the last two decades. The observed phenomenon of growing built-up areas and decreasing agricultural lands illustrates the extent of the urbanization impact on the landscape of the study area. Thus, sustainable land management practices are key to mitigate the adverse effects of urban development particularly by tackling environmental degradation and social-economic inequalities.

In addition, the application of Google Earth imagery along with GIS techniques provides a quicker and cheaper approach to monitor land use changes, especially in rapidly urbanized areas. This research also

adds to the existing body of knowledge on remote sensing technologies that can be used within the field of urban planning and management, highlighting the imperative of using high-resolution satellite imagery in order to acutely and promptly assess land use changes.

In particular, this research has some direct recommendations for the authorities, urban planners, and local communities who should take a proactive attitude towards environmental protection and sustainable land use that will allow cities to develop and survive in the long run in the modern conditions of urbanization. Finally, further investigation is necessary to thoroughly evaluate the land use dynamics throughout Uşak City using the approach developed in this pilot study. This technique will allow for a complete assessment and investigation of the patterns and drivers of land use change across the entire region.

ACKNOWLEDGEMENTS: The author expresses his sincere gratitude to the South Dakota School of Mines for generously providing access to their ArcGIS license, which was instrumental in conducting this study.

VII. REFERENCES

[1] United Nations, Department of Economic and Social Affairs, and Population Division. "*World Urbanization Prospects 2018*: Highlights (ST/ESA/SER. A/421)." (2019).

[2] Fenoglio, M. S., Rossetti, M. R., & Videla, M. (2020). Negative effects of urbanization on terrestrial arthropod communities: A meta-analysis. *Global Ecology and Biogeography*, 29(8), 1412-1429.

[3] Herrero-Jáuregui, C., & Concepción, E. D. (2023). Effects of counter-urbanization on Mediterranean rural landscapes. *Landscape Ecology*, 38(12), 3695-3711.

[4] Cheng, Z., & Hu, X. (2023). The effects of urbanization and urban sprawl on CO2 emissions in China. *Environment, Development and Sustainability*, 25(2), 1792-1808.

[5] Menashe-Oren, A., & Bocquier, P. (2021). Urbanization is no longer driven by migration in low-and middle-income countries (1985–2015). *Population and Development Review*, 47(3), 639-663.

[6] Asadzadeh, A., Kötter, T., Fekete, A., Moghadas, M., Alizadeh, M., Zebardast, E., ... & Hutter, G. (2022). Urbanization, migration, and the challenges of resilience thinking in urban planning: Insights from two contrasting planning systems in Germany and Iran. *Cities*, 125, 103642.

[7] Golding, S. A., & Winkler, R. L. (2020). Tracking urbanization and exurbs: Migration across the rural–urban continuum, 1990–2016. *Population research and policy review*, 39(5), 835-859.

[8] Antrop, M. (2004). Landscape change and the urbanization process in Europe. *Landscape and Urban Planning*, 67(1-4), 9-26.

[9] Melchiorri, M., Florczyk, A. J., Freire, S., Schiavina, M., Pesaresi, M., & Kemper, T. (2018). Unveiling 25 years of planetary urbanization with remote sensing: Perspectives from the global human settlement layer. *Remote Sensing*, 10(5), 768.

[10] Song, X., Feng, Q., Xia, F., Li, X., & Scheffran, J. (2021). Impacts of changing urban land-use structure on sustainable city growth in China: A population-density dynamics perspective. *Habitat International*, 107, 102296.

[11] Haase, D., Kabisch, N., & Haase, A. (2013). Endless urban growth? On the mismatch of population, household and urban land area growth and its effects on the urban debate. *PloS One*, 8(6), e66531.

[12] Wolff, M., Haase, D., & Haase, A. (2018). Compact or spread? A quantitative spatial model of urban areas in Europe since 1990. *PloS One*, 13(2), e0192326.

[13] MohanRajan, S. N., Loganathan, A., & Manoharan, P. (2020). Survey on Land Use/Land Cover (LU/LC) change analysis in remote sensing and GIS environment: Techniques and Challenges. *Environmental Science and Pollution Research*, *27*(24), 29900-29926.

[14] Zengin, E. (2023). A Combined Assessment of Sea Level Rise (SLR) Effect on Antalya Gulf (Türkiye) and Future Predictions on Land Loss. *Journal of the Indian Society of Remote Sensing*, *51*(5), 1121-1133.

[15] Acar, R. U., & Zengin, E. (2023). Performance Assessment of Landsat 8 and Sentinel-2 Satellite Images for the Production of Time Series Land Use/Land Cover (Lulc) Maps. *Journal of Scientific Reports-A*, (053), 1-15.

[16] Yildiz, U., & Ozkul, C. (2024). Heavy metals contamination and ecological risks in agricultural soils of Uşak, western Türkiye: a geostatistical and multivariate analysis. *Environmental Geochemistry and Health*, *46*(2), 58.

[17] Yildiz, U., & Ozkul, C. (2022). Spatial distribution and ecological risk assessment of heavy metals contamination of urban soils within Uşak, western Turkiye. *International Journal of Environmental Analytical Chemistry*, 1-23.

[18] Acar, R. U., & Özkul, C. (2020). Investigation of heavy metal pollution in roadside soils and road dusts along the Kütahya–Eskişehir Highway. *Arabian Journal of Geosciences*, *13*(5), 216.

[19] Zengin, E. (2023). Inundation risk assessment of Eastern Mediterranean Coastal archaeological and historical sites of Türkiye and Greece. *Environmental Monitoring and Assessment*, *195*(8), 968.

[20] Fu, P., & Weng, Q. (2016). A time series analysis of urbanization induced land use and land cover change and its impact on land surface temperature with Landsat imagery. *Remote sensing of Environment*, 175, 205-214.

[21] Ha, T. V., Tuohy, M., Irwin, M., & Tuan, P. V. (2020). Monitoring and mapping rural urbanization and land use changes using Landsat data in the northeast subtropical region of Vietnam. *The Egyptian Journal of Remote Sensing and Space Science*, 23(1), 11-19.

[22] Frimpong, B. F., & Molkenthin, F. (2021). Tracking urban expansion using random forests for the classification of landsat imagery (1986–2015) and predicting urban/built-up areas for 2025: A Study of the Kumasi Metropolis, Ghana. *Land*, 10(1), 44.

[23] Desktop, Google Earth Pro, Release 7.3.6, Google L.L.C., Mountain View, California 94043 USA, 2022.

[24] Wu, H., Lin, A., Xing, X., Song, D., & Li, Y. (2021). Identifying core driving factors of urban land use change from global land cover products and POI data using the random forest method. *International Journal of Applied Earth Observation and Geoinformation*, *103*, 102475.

[25] Zhang, X., Liu, L., Chen, X., Gao, Y., Xie, S., & Mi, J. (2020). GLC_FCS30: Global land-cover product with fine classification system at 30 m using time-series Landsat imagery. *Earth System Science Data Discussions, 2020*, 1-31.

[26] Malarvizhi, K., Kumar, S. V., & Porchelvan, P. (2016). Use of high-resolution Google Earth satellite imagery in land-use map preparation for urban-related applications. *Procedia Technology*, 24, 1835-1842.

[27] Leachtenauer, J.C., Malila, W., Irvine, J., Colburn, L. and Salvaggio, N. (1997). General image-quality equation: GIQE. *Applied Optics*, 36(32), pp.8322-8328.

[28] Liu, C., Li, W., Zhu, G., Zhou, H., Yan, H., & Xue, P. (2020). Land use/land cover changes and their driving factors in the Northeastern Tibetan Plateau based on Geographical Detectors and Google Earth Engine: A case study in Gannan Prefecture. *Remote Sensing*, 12(19), 3139.

[29] Floreano, I. X., & de Moraes, L. A. F. (2021). Land use/land cover (LULC) analysis (2009–2019) with Google Earth Engine and 2030 prediction using Markov-CA in the Rondônia State, Brazil. *Environmental Monitoring and Assessment*, 193(4), 239.

[30] Cui, J., Zhu, M., Liang, Y., Qin, G., Li, J., & Liu, Y. (2022). Land use/land cover change and their driving factors in the Yellow River Basin of Shandong Province based on Google Earth Engine from 2000 to 2020. *ISPRS International Journal of Geo-Information*, 11(3), 163.

[31] Feizizadeh, B., Omarzadeh, D., Kazemi Garajeh, M., Lakes, T., & Blaschke, T. (2023). Machine learning data-driven approaches for land use/cover mapping and trend analysis using Google Earth Engine. *Journal of Environmental Planning and Management*, 66(3), 665-697.

[32] Zhao, Z., Islam, F., Waseem, L.A., Tariq, A., Nawaz, M., Islam, I.U., Bibi, T., Rehman, N.U., Ahmad, W., Aslam, R.W. and Raza, D., 2024. Comparison of three machine learning algorithms using Google Earth engine for land use land cover classification. *Rangeland Ecology & Management*, 92, pp.129-137.

[33] Chen, H., Li, D., Chen, Y., & Zhao, Z. (2023). Spatial-temporal evolution monitoring and ecological risk assessment of coastal wetlands on Hainan island, China. *Remote Sensing*, 15(4), 1035.

[34] Kottek, M., Grieser, J., Beck, C., Rudolf, B., & Rubel, F. (2006). World map of the Köppen-Geiger climate classification updated.

[35] Ercan, T., Dincel, A., Metin, S., Turkecan, A., & Gunay, E. (1978). Geology of Usak. *Bulletin of Geological Society of Turkiye*. 21, 97.

[36] Desktop, ESRI ArcGIS, Release 10.7. 1, Environmental Systems Research Institute, Redlands, CA, USA, 2019.

Düzce University Journal of Science & Technology

Research Article

On Gaussian Quadra Fibona-Pell Sequence and A Quaternion Sequence Formed by the Terms of This Sequence

Faruk KAPLAN [a], Arzu ÖZKOÇ ÖZTÜRK [a, *]

[a] *Department of Mathematics, Faculty of Arts and Science , Düzce University, Düzce, TURKEY*
** Corresponding author's e-mail address: arzuozkoc@duzce.edu.tr*
DOI: 10.29130/dubited.1555372

ABSTRACT

In this study, the Gaussian quadra Fibona-Pell sequence is proposed and examined. The quadra Fibona-Pell sequence is first extended to define the Gaussian quadra Fibona-Pell sequence. Then the generating function, Binet-like formula, and some identities are represented. In addition, some formulas related to the Gaussian quadra Fibona-Pell sequence and some matrices containing terms of the sequence are studied. Finally we define a quaternion sequence formed by the terms of Gaussian quadra Fibona-Pell sequence.

Keywords: *Fourth-order recurrence relation, Gaussian numbers, Quaternion, Quadra Fibona-Pell sequence.*

Gauss Quadra Fibona-Pell Dizisi ve Bu Dizinin Terimleri Tarafından Oluşturulan Bir Kuaterniyon Dizisi Üzerine

ÖZET

Bu çalışmada, Gauss quadra Fibona-Pell dizisi önerilmekte ve incelenmektedir. İlk olarak, quadra Fibona-Pell dizisi genişletilerek Gauss quadra Fibona-Pell dizisi tanımlanmıştır. Daha sonra, bu dizinin üreteç fonksiyonu, Binet-benzeri formülü ve bazı özdeşlikler sunulmuştur. Ayrıca, Gauss quadra Fibona-Pell dizisi ile ilgili bazı formüller ve dizinin terimlerini içeren bazı matrisler de incelenmiştir. Son olarak, Gauss quadra Fibona-Pell dizisinin terimlerinden oluşan bir kuaterniyon dizisi tanımlanmıştır.

Anahtar kelimeler: *Dördüncü mertebeden yineleme bağıntısı, Gauss sayıları, Kuaterniyon, Dörtlü Fibona-Pell dizisi.*

Geliş: 24/09/2024, Düzeltme: 09/10/2024, Kabul: 18/10/2024

I. INTRODUCTION

When it comes to number sequences, Fibonacci and others naturally come to mind. The Fibonacci number sequence and various sequences, such as Lucas, Pell, Jacobsthal, and Horadam similar to this number sequence, have found applications in many branches, not only in mathematics. When the literature is examined, there are many studies on number sequences. For detailed information, you review Koshy's book [1].

There are also Gaussian forms of some number sequences with recurrence relation in the literature. Here, too, the terms forming these number sequences are complex numbers. Again, many works in the literature involve Gaussian forms of number sequences. z is a Gaussian integer such that $z = a + ib$, with $i^2 = -1$, where a and b are arbitrary integers. Gauss [2], in 1832, such numbers were first published and also mentioned the properties of the set of complex integers.

Horadam [3], in 1963, introduced the concept the complex Fibonacci numbers called the Gaussian Fibonacci numbers as follows:

$GF_n = GF_{n-1} + GF_{n-2}$, for $n \geq 2$

where $GF_0 = i$ and $GF_1 = 1$ are initial values.

Note that $F_n + iF_{n-1} = GF_n$ for all $n > 0$ and $GF_{-n} = F_{-n} + iF_{-n-1}$ where F_n, $n-th$ Fibonacci number. The table below gives the first few values of Gaussian Fibonacci numbers with positive and negative subscripts.

Table 1. Gaussian Fibonacci numbers with positive and negative subscripts.

n	GF_n	GF_{-n}
0	i	i
1	1	$1-i$
2	$1+i$	$-1+2i$
3	$2+i$	$2-3i$
4	$3+2i$	$-3+5i$
5	$5+3i$	$5-8i$
6	$8+5i$	$-8+13i$
7	$13+8i$	$13-21i$
8	$21+13i$	$-21+34i$
.	.	.
.	.	.
.	.	.

And then, Jordan [4], expanded the knowledge on the subject for Fibonacci sequences. If γ and δ are the roots of the characteristic equation of the Gaussian Fibonacci sequence, Binet-like formula of the Gaussian Fibonacci sequence can be given as follows:

$$GF_n = \frac{\gamma^n - \delta^n}{\gamma - \delta} + i\frac{\gamma\delta^n - \delta\gamma^n}{\gamma - \delta}$$

where $\gamma = \frac{1+\sqrt{5}}{2}$ and $\delta = \frac{1-\sqrt{5}}{2}$. Generating function of GF_n is

$$GF(t) = \frac{i + t - it}{1 - \mathrm{t} - \mathrm{t}^2}. \tag{1.1}$$

Halıcı and Öz [5], in 2016, introduced the Gaussian Pell numbers as follow:

$GP_n = 2GP_{n-1} + GP_{n-2}$, for $n \geq 2$

where $GP_0 = i$ and $GP_1 = 1$.

Note that $GP_n = P_n + iP_{n-1}$ and $GP_{-n} = P_{-n} + iP_{-n-1}$ where P_n , $n - th$ Pell number. The table below gives the first few values of Gaussian Pell numbers with positive and negative subscripts.

Table 2. Gaussian Pell numbers with positive and negative subscripts.

n	GP_n	GP_{-n}
0	i	i
1	1	$1 - 2i$
2	$2 + i$	$-1 + 5i$
3	$5 + 2i$	$5 - 12i$
4	$12 + 5i$	$-12 + 29i$
5	$29 + 12i$	$29 - 70i$
6	$70 + 29i$	$-70 + 169i$
7	$169 + 70i$	$169 - 408i$
8	$408 + 169i$	$-408 + 985i$
.	.	.
.	.	.
.	.	.

For this new sequence, [5] has the following. If Ψ and Ω are the roots of the characteristic equation of the Gaussian Pell sequence, the Binet-like formula of the Gaussian Pell sequence can be given as follows:

$$GP_n = \frac{\Psi^n - \Omega^n}{\Psi - \Omega} + i\frac{\Psi\Omega^n - \Omega\Psi^n}{\Psi - \Omega}$$

where $\Psi = 1 + \sqrt{2}$ and $\Omega = 1 - \sqrt{2}$. Generating function of GP_n is

$$GP(t) = \frac{i + t - 2it}{1 - 2\mathrm{t} - \mathrm{t}^2}. \tag{1.2}$$

Looking at the literature, there are studies similar to these, such as [6–8], and more. As for the present day, in [9], the author introduced the Gaussian Mersenne numbers and also gave the matrix form and various identities. The same author, in [10], studied the Gaussian numbers for Padovan and Pell-Padovan numbers, which are integer sequences with a recurrence relation of the third order.

In [11], the author gave linear summation for the Gaussian generalized Pentanacci numbers he introduced. In [12], also the author focuses on the Gauss form of (p, q) −Jacobsthal and (p, q) −Jacobsthal Lucas numbers. Some identities are presented for the relevant new sequences. In [13], the authors obtained various identities for Gauss Leonardo numbers such as the Binet formula,

Cassini identity, and generating function. Earliest, we remind some properties of about quadra Fibona-Pell sequence. The information in this section is taken from [14]. The quadra Fibona-Pell numbers are defined by fourth-order recurrence relation as

$W_n = 3W_{n-1} - 3W_{n-3} - W_{n-4}$, for $n \geq 4$ (1.3)

with the beginning conditions $W_0 = W_1 = 0$, $W_2 = 1$, and $W_3 = 3$.

The characteristic equation of (1.3) and the roots of this equation are

$x^4 - 3x^3 + 3x + 1 = 0$

and

$\gamma = \frac{1+\sqrt{5}}{2}, \delta = \frac{1-\sqrt{5}}{2}$, $\Psi = 1 + \sqrt{2}$, and $\Omega = 1 - \sqrt{2}$.

(1.3) can be extended to negative subscripts as follows:

$W_n = 3W_{n-1} - 3W_{n-3} - W_{n-4}$, for all $n \geq 4$.

Note that for convenience throughout the paper, we use the abbreviation qFP for quadra Fibona-Pell. The first few qFP numbers with positive subscripts and negative subscript are given in the table below:

Table 3. qFP numbers with positive and negative subscripts.

n	W_n	W_{-n}
0	0	0
1	0	0
2	1	-1
3	3	3
4	9	-9
5	24	24
6	62	-62
7	156	156
8	387	-387
.	.	.
.	.	.
.	.	.

One of the different applications of the qFP sequence can be seen in the article [15].

II. GAUSSIAN QUADRA FIBONA-PELL NUMBERS

In this part of the study, inspired by some of the works mentioned in the references, we introduce the iteration relation of the Gaussian qFP sequence, which is used to construct the Binet formula and derive some identities, etc.

Definition 2.1. Gaussian qFP numbers can define GW_n recursively:

$$\mathrm{GW}_n = 3\mathrm{GW}_{n-1} - 3G\mathrm{W}_{n-3} - \mathrm{GW}_{n-4},\ n \geq 4 \tag{2.1}$$

with the initial conditions

$$\mathrm{GW}_0 = 0$$

$$\mathrm{GW}_1 = 0$$

$$\mathrm{GW}_2 = 1$$

$$\mathrm{GW}_3 = 3 + i.$$

Moreover, take note of that

$$\mathrm{GW}_n = \mathrm{W}_n + i\mathrm{W}_{n-1}.$$

The first few Gaussian qFP numbers with positive subscripts and negative subscript are given in the table below:

Table 4. Gaussian qFP numbers with positive and negative subscripts.

$\boldsymbol{n}$	$\boldsymbol{GW_n}$	$\boldsymbol{GW_{-n}}$
0	0	0
1	0	$-i$
2	1	$-1+3i$
3	$3+i$	$3-9i$
4	$9+3i$	$-9+24i$
5	$24+9i$	$24-62i$
6	$62+24i$	$-62+156i$
7	$156+62i$	$156-387i$
8	$387+156i$	$-387+951i$
.	.	.
.	.	.
.	.	.

The characteristic equation of (2.1) is

$$x^4 - 3x^3 + 3x + 1 = 0. \tag{2.2}$$

Then, the roots of (2.2) are

$$\Omega = 1 - \sqrt{2}, \Psi = 1 + \sqrt{2}, \gamma = \frac{1+\sqrt{5}}{2}, \delta = \frac{1-\sqrt{5}}{2}. \tag{2.3}$$

Immediately note that γ and δ belongs to the Gaussian Fibonacci numbers also Ψ and Ω belongs to the Gaussian Pell numbers for the characteristic equations. Our next result is the generating function of the sequence in our focus.

Theorem 2.1. The generating function of Gaussian quadra Fibona-Pell sequence GW_n is as follow:

$$GW(t) = \frac{\mathrm{t}^2 + i\mathrm{t}^3}{\mathrm{t}^4 + 3\mathrm{t}^3 - 3\mathrm{t} + 1}.$$

Proof. The generating function of the related sequence is a function such that whose formal power series expansion at $t = 0$ has the form

$$GW(t) = \sum_{r=0}^{\infty} GW_r\ t^r = GW_0\ + GW_1\ t + GW_2\ t^2 + GW_3\ t^3 + GW_4\, t^4 + \cdots$$

Therefore, from the power series,

$$GW(t) = \sum_{r=0}^{\infty} GW_r\ t^r = GW_0\ + GW_1\ t + GW_2\ t^2 + GW_3\ t^3 + GW_4\, t^4 + \cdots$$

$$-3tGW(t) = -3t\sum_{r=0}^{\infty} GW_r\ t^r = -3GW_0\ t - 3GW_1\ t^2 - 3GW_2\ t^3 - 3GW_3\ t^4 - 3GW_4\, t^5 + \cdots$$

$$3t^3GW(t) = 3t^3\sum_{r=0}^{\infty} GW_r\ t^r = 3GW_0\ t^3 + 3GW_1\ t^4 + 3GW_2\ t^5 + 3GW_3\ t^6 + 3GW_4\, t^7 + \cdots$$

$$t^4GW(t) = t^4\sum_{r=0}^{\infty} GW_r\ t^r = GW_0\ t^4 + GW_1\ t^5 + GW_2\ t^6 + GW_3\ t^7 + GW_4\, t^8 + \cdots.$$

If both sides of the equation are added together

$$GW(t) - 3tGW(t) + 3t^3GW(t) + t^4GW(t) = GW_0\ + GW_1\ t + GW_2\ t^2 + GW_3\ t^3 + (-3GW_0\ t - 3GW_1\ t^2 - 3GW_2\ t^3) + 3GW_0\ t^3.$$

Hence, if necessary arrangements are made, we have

$$GW(t) = \frac{GW_0\ + t(GW_1\ - 3GW_0\,) + t^2(GW_2\ - 3GW_1\,) + t^3(GW_3\ - 3GW_2\ + 3GW_0}{1 - 3t + 3t^3 + t^4}.$$

Here, when the initial conditions are written, we have

$$GW(t) = \frac{\mathrm{t}^2 + i\mathrm{t}^3}{\mathrm{t}^4 + 3\mathrm{t}^3 - 3\mathrm{t} + 1}. \tag{2.4}$$

The present result gives the Binet formula for Gaussian qFP sequence.

Theorem 2.2. For $\mathrm{n} \geq 0$, the Binet formula for a related sequence is

$$GW_n = \left(\frac{\Psi^n - \Omega^n}{\Psi - \Omega} + i\frac{\Psi\Omega^n - \Omega\Psi^n}{\Psi - \Omega}\right) - \left(\frac{\gamma^n - \delta^n}{\gamma - \delta} + i\frac{\gamma\delta^n - \delta\gamma^n}{\gamma - \delta}\right). \tag{2.5}$$

Proof. We know that from (2.4)

$$GW(t) = \frac{\mathrm{t}^2 + i\mathrm{t}^3}{\mathrm{t}^4 + 3\mathrm{t}^3 - 3\mathrm{t} + 1}.$$

Adjust this a bit, we have

$$GW(t) = \frac{i + t - it}{1 - \mathrm{t} - \mathrm{t}^2} - \frac{i + t - 2it}{1 - 2\mathrm{t} - \mathrm{t}^2}.$$

If the generating functions of Gaussian Pell and Gaussian Fibonacci sequences are taken into consideration, that is, it follows that from (1.1) and (1.2)

$$GW(t) = GP(t) - GF(t).$$

The following result gives the sum of the first n terms of $G\mathrm{W}_n$.

Theorem 2.3. The sum of the first n terms of $G\mathrm{W}_n$ is

$$\sum_{r=1}^{n} GW_r = \frac{GW_n + 4GW_{n-1} + 4GW_{n-2} + GW_{n-3} + i + 1}{2}$$

for n $\geq$ 3.

Proof. We know that the recurrence relation of the relevant sequence is

$$GW_n = 3GW_{n-1} - 3GW_{n-3} - GW_{n-4}$$

$$GW_{n-3} + GW_{n-4} = 3GW_{n-1} - 2GW_{n-3} - GW_n$$

If we make a little edit and write open for n, we have

$$GW_1 + GW_0 = 3GW_3 - 2GW_1 - GW_4$$

$$GW_2 + GW_1 = 3GW_4 - 2GW_2 - GW_5$$

$$GW_3 + GW_2 = 3GW_5 - 2GW_3 - GW_6$$

$$GW_{n-4} + GW_{n-5} = 3GW_{n-2} - 2GW_{n-4} - GW_{n-1}$$

. .

. .

. .

$$GW_{n-3} + GW_{n-4} = 3GW_{n-1} - 2GW_{n-3} - GW_n$$

Here, if the collection is done, both of side

$$\begin{aligned} GW_{n-3} + GW_0 + 2(GW_1 + GW_2 + \cdots + GW_{n-4} &= 3(GW_3 + GW_4 + \cdots GW_n) \\ &\quad -2(GW_1 + GW_2 + \cdots GW_{n-3}) \\ &\quad -(GW_4 + GW_5 + \cdots GW_n). \end{aligned}$$

The two results for the relevant sequence are as follows:

Theorem 2.4. For n $\geq$ 0, the following recurrence relations are valid:

$$\boldsymbol{a}.\ \mathrm{GW}_{2n} = 9\mathrm{GW}_{2n-2} - 20\mathrm{GW}_{2n-4} + 9\mathrm{GW}_{2n-6} - \mathrm{GW}_{2n-8}.$$

$$\boldsymbol{b}.\ \mathrm{GW}_{2n+1} = 9\mathrm{GW}_{2n-1} - 20\mathrm{GW}_{2n-3} + 95 - \mathrm{GW}_{2n-7}.$$

Proof. ***a***. In the proof, we start from the recurrence relation, $GW_n = 3GW_{n-1} - 3GW_{n-3} - GW_{n-4}$.

Here, if we put *n* instead of $2n$ and use (1.3), then

$$\begin{aligned}\mathrm{GW}_{2n} = 3\mathrm{GW}_{2n-1} - 3\mathrm{GW}_{2n-3} - \mathrm{GW}_{2n-4} &= 3(3\mathrm{GW}_{2n-2} - 3\mathrm{GW}_{2n-4} - 9\mathrm{GW}_{2n-5}\\ &\quad -3(3\mathrm{GW}_{2n-4} - 3\mathrm{GW}_{2n-6} - \mathrm{GW}_{2n-7})\\ &\quad -3(3\mathrm{GW}_{2n-5} - 3\mathrm{GW}_{2n-7} - \mathrm{GW}_{2n-8})\\ &= 9\mathrm{GW}_{2n-2} - 18\mathrm{GW}_{2n-4} - 6\mathrm{GW}_{2n-5} + \mathrm{GW}_{2n-6}\\ &\quad +6\mathrm{GW}_{2n-7} + \mathrm{GW}_{2n-8}\\ &= 9\mathrm{GW}_{2n-2} - 20\mathrm{GW}_{2n-4} + 9\mathrm{GW}_{2n-6} - \mathrm{GW}_{2n-8}.\end{aligned}$$

***b*.** The proof here is done by following the previous proof steps.

The exponential generating function for $G\mathrm{W}_n$ is below.

Theorem 2.5. Exponential generating function for the $G\mathrm{W}_n$ is

$$\sum_{n=0}^{\infty} G\mathrm{W}_n \frac{x^n}{n!} = \left(\frac{\mathrm{e}^{\Psi x} - \mathrm{e}^{\Omega x}}{\Psi - \Omega} + i\frac{\Psi\mathrm{e}^{\Omega x} - \Omega\mathrm{e}^{\Psi x}}{\Psi - \Omega}\right) - \left(\frac{\mathrm{e}^{\gamma x} - \mathrm{e}^{\delta x}}{\gamma - \delta} + i\frac{\gamma\mathrm{e}^{\delta x} - \delta\mathrm{e}^{\gamma x}}{\gamma - \delta}\right)$$

for $\geq$ 0 .

Proof Motivating from related Binet formula

$$\sum_{n=0}^{\infty} G\mathrm{W}_n \frac{x^n}{n!} = \sum_{n=0}^{\infty}\left[\left(\frac{\Psi^n - \Omega^n}{\Psi - \Omega} + i\frac{\Psi\Omega^n - \Omega\Psi^n}{\Psi - \Omega}\right) - \left(\frac{\gamma^n - \delta^n}{\gamma - \delta} + i\frac{\gamma\delta^n - \delta\gamma^n}{\gamma - \delta}\right)\right]\frac{x^n}{n!}$$

$$= \sum_{n=0}^{\infty}\left[\frac{1}{\Psi - \Omega}\left((\Psi^n - \Omega^n) + i(\Psi\Omega^n - \Omega\Psi^n)\right) - \frac{1}{\gamma - \delta}\quad\left((1 - i\delta)\gamma^n - i(1 - i\gamma)\delta^n\right.\right.$$

$$= \frac{1}{\Psi - \Omega}\left[\sum_{n=0}^{\infty}\frac{(\Psi x)^n}{n!} - \sum_{n=0}^{\infty}\frac{(\Omega x)^n}{n!} + i\left(\Psi\sum_{n=0}^{\infty}\frac{(\Omega x)^n}{n!} - \Omega\sum_{n=0}^{\infty}\frac{(\Psi x)^n}{n!} - \right)\right]$$

$$-\frac{1}{\gamma-\delta}\left[(1-i\delta)\sum_{n=0}^{\infty}\frac{(\gamma x)^n}{n!}-(1-i\gamma)\sum_{n=0}^{\infty}\frac{(\delta x)^n}{n!}\right].$$

We derive the matrix representation for GW_n below.

III. MATRIX REPRESENTED OF GAUSSIAN QUADRA FIBONA-PELL NUMBERS

Matrices and matrix representations find a place in many fields and can also be associated with the recurrence relation. For $n \geq 0$.

$$\begin{pmatrix} GW_{n+4} \\ GW_{n+3} \\ GW_{n+2} \\ GW_{n+1} \end{pmatrix} = \begin{pmatrix} 3 & 0 & -3 & -1 \\ 1 & 0 & 0 & 0 \\ 0 & 1 & 0 & 0 \\ 0 & 0 & 1 & 0 \end{pmatrix} \begin{pmatrix} GW_{n+4} \\ GW_{n+3} \\ GW_{n+2} \\ GW_{n+1} \end{pmatrix}$$

where the square matrix S of order 4 is;

$$S = \begin{pmatrix} 3 & 0 & -3 & -1 \\ 1 & 0 & 0 & 0 \\ 0 & 1 & 0 & 0 \\ 0 & 0 & 1 & 0 \end{pmatrix}.$$

Theorem 3.1. Let $n \geq 0$ be integer . Then

$$\begin{pmatrix} GW_{n+4} \\ GW_{n+3} \\ GW_{n+2} \\ GW_{n+1} \end{pmatrix} = \begin{pmatrix} 3 & 0 & -3 & -1 \\ 1 & 0 & 0 & 0 \\ 0 & 1 & 0 & 0 \\ 0 & 0 & 1 & 0 \end{pmatrix}^n \begin{pmatrix} GW_3 \\ GW_2 \\ GW_1 \\ GW_0 \end{pmatrix}.$$

Proof It can be proven using mathematical induction. If $n \geq 0$, the result is clear. Suppose that the statement is true for $n = m - 1$. Then,

$$\begin{pmatrix} GW_{m+3} \\ GW_{m+2} \\ GW_{m+1} \\ GW_m \end{pmatrix} = \begin{pmatrix} 3 & 0 & -3 & -1 \\ 1 & 0 & 0 & 0 \\ 0 & 1 & 0 & 0 \\ 0 & 0 & 1 & 0 \end{pmatrix}^{m-1} \begin{pmatrix} GW_3 \\ GW_2 \\ GW_1 \\ GW_0 \end{pmatrix}.$$

We want to show that this is true for $n = m$. This means that

$$\begin{pmatrix} 3 & 0 & -3 & -1 \\ 1 & 0 & 0 & 0 \\ 0 & 1 & 0 & 0 \\ 0 & 0 & 1 & 0 \end{pmatrix}^{m} \begin{pmatrix} GW_3 \\ GW_2 \\ GW_1 \\ GW_0 \end{pmatrix} = \begin{pmatrix} 3 & 0 & -3 & -1 \\ 1 & 0 & 0 & 0 \\ 0 & 1 & 0 & 0 \\ 0 & 0 & 1 & 0 \end{pmatrix} \begin{pmatrix} 3 & 0 & -3 & -1 \\ 1 & 0 & 0 & 0 \\ 0 & 1 & 0 & 0 \\ 0 & 0 & 1 & 0 \end{pmatrix}^{m-1} \begin{pmatrix} GW_3 \\ GW_2 \\ GW_1 \\ GW_0 \end{pmatrix}$$

$$= \begin{pmatrix} 3 & 0 & -3 & -1 \\ 1 & 0 & 0 & 0 \\ 0 & 1 & 0 & 0 \\ 0 & 0 & 1 & 0 \end{pmatrix} \begin{pmatrix} GW_{m+3} \\ GW_{m+2} \\ GW_{m+1} \\ GW_m \end{pmatrix}$$

$$= \begin{pmatrix} GW_{m+4} \\ GW_{m+3} \\ GW_{m+2} \\ GW_{m+1} \end{pmatrix}$$

Thus the proof is concluded.

IV. ON GAUSSIAN QUADRA FIBONA-PELL QUATERNIONS

The quaternion structure, discovered by Hamilton in 1843, attracted much attention in mathematics. A quaternion is represented in mathematics in the form:

$\mathbb{H} = \{q = a_0\, 1 + a_1\, i + a_2\, j + a_3\, k : a_0\,, a_1\,, a_2\,, a_3 \in \mathbb{R}\}$.

which satisfies the following multiplication rules:

$$i^2 = j^2 = k^2 = -1 \tag{4.1}$$

$$jik = -1$$

$$ij = k$$

$$jk = i.$$

Point out that $\{1, i, j, k\}$ does not provide the commutative property in the products between the base elements, but the set $\mathbb{H}$ holds the associative property of multiplication. In the literature, the symbol $\mathbb{H}$ was adopted for the set of quaternions based on Hamilton. Here are some basic arithmetic operations provided by the set $\mathbb{H}$. A quaternion can also be written as

$$q = a_0\, 1 + a_1\, i + a_2\, j + a_3\, k$$

where q can be written separately as the scalar part of the quaternion:

$$S_q = a_0\, 1$$

and as the vector part

$$V_q = a_1\, i + a_2\, j + a_3\, k.$$

Therefore, the quaternion q can be expressed both scalar and vector as

$$q = S_q + V_q = a_1\, i + a_2\, j + a_3\, k.$$

Searching the literature for quaternions and number sequences, we realize that the author at [3] introduced the Fibonacci quaternion and presented recurrence relation for relevant sequence. Since then, the growing interest in this field is evident from the existence of many works [16–19]. For example, in [20], the authors worked on sequences of quaternions with polynomial coefficients. Also in [21] the authors combined quaternion-type structures with different integer sequences. An example of an octonion, which is a quaternion formed using eight bases, can be found in [22]. In [23], the same authors studied the binomial transform of Horadam quaternions. In [24], the authors introduced quaternions whose coefficients are Gaussian Fibonacci numbers and presented various identities. In [25], authors worked on quaternions whose coefficients are Gaussian Lucas numbers. It is seen from many similar studies such as [26–28] that the interest in this field has not decreased. Especially, one of the interesting points of quaternion-Gaussian numbers is that quaternion-Gaussian numbers are used to investigate graphical models in [29]. Motivated by these studies, we identify quaternions with qFP coefficients and examine some identities.

Describe the quaternions with Gaussian quadra Fibona-Pell coefficients as:

$$QGW_n = GW_n + GW_{n+1}\, i + GW_{n+2}\, j + GW_{n+3}\, k \tag{4.2}$$

where initial conditions of (4.2) as follows:

$$QGW_0 = 3k$$

$QGW_1 = i + 10k$

$QGW_2 = 3i + 27k$

$QGW_3 = 10i + 71k.$

We can write the following recurrence relation with Gaussian quadra Fibona-Pell sequence

$QGW_n = 3QGW_{n-1} - 3QGW_{n-3} - QGW_{n-4}$, for $n \geq 0$ (4.3)

The characteristic equation of (4.3) is

$x^4 - 3x^3 + 3x + 1 = 0.$ (4.4)

The roots of the characteristic equation of (4.4) are $\Psi = 1 + \sqrt{2},\ \Omega = 1 - \sqrt{2},\ \gamma = \frac{1+\sqrt{5}}{2},\ \delta = \frac{1-\sqrt{5}}{2}.$

First, start by finding the generating function of the sequence.

Theorem 4.1. The generating function of QGW_n is

$$QGW(t) = \frac{QGW_0 + t(QGW_1 - 3QGW_0) + t^2(QGW_2 - 3QGW_1) + t^3(QGW_3 - 3QGW_2 + 3QGW_0)}{1 - 3t + 3t^3 + t^4}$$

where $QGW_0 = 3k, QGW_1 = i + 10k, QGW_2 = 3i + 27k,$ and $QGW_3 = 10i + 71k.$

Proof In the following equation, where formal power series expansion for QGW_r is given, all the information necessary for the generating function is obtained.

$$QGW(t) = \sum_{r=0}^{\infty} QGW_r\ t^r = QGW_0 + QGW_1\ t + QGW_2\ t^2 + QGW_3\ t^3 + \cdots + QGW_r + \cdots.$$

Therefore, from the power series,

$$QGW(t) = \sum_{r=0}^{\infty} QGW_r\ t^r = QGW_0\ + QGW_1\ t + QGW_2\ t^2 + QGW_3\ t^3 + QGW_4\, t^4 + \cdots$$

$$-3tQGW(t) = -3t \sum_{r=0}^{\infty} QGW_r\ t^r = -3QGW_0\ t - 3QGW_1\ t^2 - 3QGW_2\ t^3 - 3QGW_3\ t^4 + \cdots$$

$$3t^3 QGW(t) = 3t^3 \sum_{r=0}^{\infty} QGW_r\ t^r = 3QGW_0\ t^3 + 3QGW_1\ t^4 + 3QGW_2\ t^5 + 3QGW_3\ t^6 + \cdots$$

$$t^4 QGW(t) = t^4 \sum_{r=0}^{\infty} QGW_r\ t^r = QGW_0\ t^4 + QGW_1\ t^5 + QGW_2\ t^6 + QGW_3\ t^7 + QGW_4\, t^8 + \cdots.$$

Hence, if necessary arrangements are made, we get

$$QGW(t) = \frac{QGW_0\ + t(QGW_1\ - 3QGW_0\,) + \mathrm{t}^2(QGW_2\ - 3QGW_1\,) + \mathrm{t}^3(QGW_3 - 3QGW_2 + 3QGW_0\,)}{1 - 3\mathrm{t} + 3\mathrm{t}^3 + \mathrm{t}^4}$$

so desired is achieved.

Theorem 4.2. The Binet formula for the relevant quaternion sequence QGW_n is

$$QGW_n\ = \frac{1}{\Psi - \Omega}(\Psi^n A - \Omega^n \mathrm{B} + \Psi\Omega^n C - \Omega\Psi^n D) - \frac{1}{\gamma - \delta}\quad (\gamma^n E - \delta^n \mathrm{F} + \gamma\delta^n G - \delta\gamma^n H)$$

where $\mathrm{A}\ = 1 + \Psi i + \Psi^2 j + \Psi^3 k,\ \mathrm{B}\ =\ 1 + \Omega i + \Omega^2 j + \Omega^3 k,\ C = i - \Omega + \Omega^2 k - \Omega^3 j,$

$D = i - \Psi + \Psi^2 k - \Psi^3 j, E = 1 + \gamma i + \gamma^2 j + \gamma^3 k, F = 1 + \delta i + \delta^2 j + \delta k,$

$G = i - \delta + \delta^2 k - \delta^3 j, H = i - \gamma + \gamma^2 k - \gamma^3 j.$

Proof. Binet's formula for the Gaussian quadra Fibona-Pell number sequence in (2.5) was also derived. If we substitute this formula into the quadra Fibona-Pell quaternion, we have

$$QGW_n = GW_n + GW_{n+1}\, i + GW_{n+2}\, j + GW_{n+3}\, k$$

$$= \left(\frac{\Psi^n - \Omega^n}{\Psi - \Omega} + i\frac{\Psi\Omega^n - \Omega\Psi^n}{\Psi - \Omega}\right) - \left(\frac{\gamma^n - \delta^n}{\gamma - \delta} + i\frac{\gamma\delta^n - \delta\gamma^n}{\gamma - \delta}\right)$$

$$+ \left(\frac{\Psi^{n+1} - \Omega^{n+1}}{\Psi - \Omega} + i\frac{\Psi\Omega^{n+1} - \Omega\Psi^{n+1}}{\Psi - \Omega}\right) i - \left(\frac{\gamma^{n+1} - \delta^{n+1}}{\gamma - \delta} + i\frac{\gamma\delta^{n+1} - \delta\gamma^{n+1}}{\gamma - \delta}\right) j$$

$$+ \left(\frac{\Psi^{n+2} - \Omega^{n+2}}{\Psi - \Omega} + i\frac{\Psi\Omega^{n+2} - \Omega\Psi^{n+2}}{\Psi - \Omega}\right) j - \left(\frac{\gamma^{n+2} - \delta^{n+2}}{\gamma - \delta} + i\frac{\gamma\delta^{n+2} - \delta\gamma^{n+2}}{\gamma - \delta}\right) j$$

$$+ \left(\frac{\Psi^{n+3} - \Omega^{n+3}}{\Psi - \Omega} + i\frac{\Psi\Omega^{n+3} - \Omega\Psi^{n+3}}{\Psi - \Omega}\right) j - \left(\frac{\gamma^{n+3} - \delta^{n+3}}{\gamma - \delta} + i\frac{\gamma\delta^{n+3} - \delta\gamma^{n+3}}{\gamma - \delta}\right) j$$

$$= \frac{\Psi^n(1 + \Psi i + \Psi^2 j + \Psi^3 k) - \Omega^n(1 + \Omega i + \Omega^2 j + \Omega^3 k)}{\Psi - \Omega}$$

$$+ \frac{\Psi\Omega^n(i - \Omega + \Omega^2 k - \Omega^3 j) - \Omega\Psi^n(i - \Psi + \Psi^2 k - \Psi^3 j)}{\Psi - \Omega}$$

$$- \frac{\gamma^n(1 + \gamma i + \gamma^2 j + \gamma^3 k) - \delta^n(1 + \delta i + \delta^2 j + \delta k)}{\gamma - \delta}$$

$$+ \frac{\gamma\delta^n(i - \delta + \delta^2 k - \delta^3 j) - \delta\gamma^n(i - \gamma + \gamma^2 k - \gamma^3 j)}{\gamma - \delta}$$

where $A = 1 + \Psi i + \Psi^2 j + \Psi^3 k$, $B = 1 + \Omega i + \Omega^2 j + \Omega^3 k$, $C = i - \Omega + \Omega^2 k - \Omega^3 j$,

$D = i - \Psi + \Psi^2 k - \Psi^3 j$, $E = 1 + \gamma i + \gamma^2 j + \gamma^3 k$, $F = 1 + \delta i + \delta^2 j + \delta k$

$G = i - \delta + \delta^2 k - \delta^3 j, H = i - \gamma + \gamma^2 k - \gamma^3 j.$

The $QG W_n^*$ used in the next theorem is the conjugate of QGW_n .

Theorem 4.3. The quaternions with Gaussian qFP coefficients satisfy:

a. $QGW_{n+1} = 3QGW_n - 3QGW_{n-2} - QGW_{n-3}$ for $n \geq 3$.

b. $QGW_n + QG W_n^* = 2GW_n$.

Proof. Start from the right side equation and use (4.3), we have

a. For n ≥ 3,

$3QGW_n - 3QGW_{n-2} - QGW_{n-3}$

$= 3(GW_n + GW_{n+1}\, i + GW_{n+2}\, j + GW_{n+3}\, k)$

$-3(GW_{n-2} + GW_{n-1}\, i + GW_n\, j + GW_{n+1}\, k)$

$-(GW_{n-3}\, 1 + GW_{n-2}\, i + GW_{n-1}\, j + GW_n\, k)$

$= (\, 3GW_n - 3GW_{n-2} - GW_{n-3}\,)$

$+(3GW_{n+1} - 3GW_{n-1} - GW_{n-2}\,)i$

$+(3GW_{n+2} - 3GW_n - GW_{n-1}\,)j$

$$+(3GW_{n+3} - 3GW_{n+1} - GW_n)k$$

$$= GW_{n+1} + GW_{n+2}\, i + GW_{n+3}\, j + GW_{n+4}\, k$$

$$= QGW_{n+1}\ .$$

b. From (4.3) and quaternion conjugate, we get

$$QGW_n + QG\,W_n^* = GW_n + GW_{n+1}\, i + GW_{n+2}\, j + GW_{n+3}\, k$$

$$+GW_n - GW_{n+1}\, i - GW_{n+2}\, j - GW_{n+3}\, k$$

$$= 2GW_n$$

V. CONCLUSION

Since quaternions find serious areas of study in many fields, from physics (such as quantum physics) to mathematics (graphical modelling), in this article, it was considered to examine quaternions in terms of the Gaussian qFP integer coefficient sequence.

Firstly, after giving detailed preliminary information and literature about the quadra Fibonacci-Pell sequence, the Gaussian Fibona-Pell sequence was introduced in the second part. Sum formulas, recurrence relation, Binet formula, some identities, and generating functions were introduced for the related new sequence. The matrix representation for the relevant sequence was presented in the third part. In the last part, the quadra Fibona-Pell quaternion sequence, which is the focus of our attention, was introduced. Therefore, in our future paper, we idea to present some known identities, such as Cassini, Catalan, and d'Ocagne, and create a binomial transform for quaternion sequences and their key characteristics.

VII. REFERENCES

[1] T. Koshy, "*Fibonacci and Lucas numbers with applications*, " John Wiley and Sons, vol. 1, 2018.

[2] C. Gauss, "*Theoria residuorum biquadraticorum*," Commentatio prima, Typis Dieterichchianis, 1832.

[3] A. F. Horadam, "Complex Fibonacci numbers and Fibonacci quaternions," *American Mathematical Monthly*, vol. 70, pp. 289-291, 1963.

[4] J. H. Jordan, "Gaussian Fibonacci and Lucas numbers," *The Fibonacci Quarterly*, vol. 3, pp. 315-318, 1965.

[5] S. Halıcı and S. Öz, "On some Gaussian Pell and Pell–Lucas numbers," *Ordu University Journal of Science and Technology*, vol. 6, no.1, pp. 8-18, 2016.

[6] G. Berzsenyi, "Gaussian Fibonacci numbers*," The Fibonacci Quarterly*, vol. 15, no. 3, pp. 233-236, 1997.

[7] C. J. Harman, "Complex Fibonacci numbers," *The Fibonacci Quarterly*, vol. 19, no.1, 82-86, 1981.

[8] S. Pethe and A. F. Horadam, "Generalised Gaussian Fibonacci numbers," *Bulletin of the Australian Mathematical Society*, vol. 33, no. 1, pp. 37-48, 1986.

[9] D. Taşcı, "On Gaussian Mersenne numbers," *Journal of Science and Arts*, vol. 57, no. 4, pp. 1021-1028, 2021.

[10] D. Taşcı, "Gaussian Padovan and Gaussian Pell-Padovan Sequences," *Communications Faculty of Sciences University of Ankara Series A1: Mathematics and Statistics*, vol. 67, no. 2, pp. 82-88, 2018.

[11] Y. Soykan, "Linear summing formulas of generalised pentanacci and Gaussian generalised pentanacci numbers," *Journal of Advances in Mathematics and Computer Science*, vol. 33, no. 3, pp. 1-14, 2022.

[12] N. Saba and A. Boussayoud, "Gaussian (*p,q*)-Jacobsthal and Gaussian (*p,q*)-Jacobsthal Lucas numbers and their some interesting properties," *Journal of Mathematical Physics*, vol. 63, no. 11, pp. 1-17, 2022.

[13] K. Prasad, R. Mohanty, M. Kumari, and H. Mahato, "Some new families of generalized *k*-Leonardo and Gaussian Leonardo numbers," *Communication in Combinatorics and Optimization*, vol. 3, no. 9, pp. 539-553, 2024.

[14] A. Özkoç, "Some algebraic identities on quadra Fibona- Pell integer sequence," *Advances in Difference Equation*, vol. 2015, no. 148, pp. 1-10, 2015.

[15] A. Özkoç Öztürk and E. Gündüz, "Binomial transform for Quadra Fibona-Pell sequence and Quadra Fibona-Pell quaternion," *Universal Journal of Mathematics and Applications*, vol. 5, no. 4, pp. 145-155, 2022.

[16] S. Halıcı, "On Fibonacci quaternions," *Advances in Applied Clifford Algebras*, vol. 22, pp. 321-327, 2012.

[17] E. Polatlı, “A generalization of Fibonacci and Lucas quaternions,” *Advances in Applied Clifford Algebras*, vol. 26, no. 2, pp. 719-730, 2016.

[18] S. Halıcı and A. Karataş, “On a generalization for Fibonacci quaternions,” *Chaos, Solitons and Fractals*, vol. 98, pp. 178-182, 2017.

[19] E. Ozkan and M. Uysal, “O*n* quaternions with higher order Jacobsthal numbers components,” *Gazi University Journal of Science*, vol. 36, no. 1, pp. 336-347, 2023.

[20] A. Özkoç Öztürk and F. Kaplan, “Some properties of bivariate Fibonacci and Lucas quaternion polynomials,” *Facta Universitatis, Series: Mathematics and Informatics*, vol. 35, no. 1, pp. 073-087, 2020.

[21] E. Polatlı, “On Certain Properties of Quadrapell Quaternions,” *Karaelmas Fen ve Mühendislik Dergisi*, vol. 8, no. 1, pp. 305-308, 2018.

[22] C. Kızılateş and E. Polatlı, “New families of Fibonacci and Lucas octonions with q-integer components,” *Indian Journal of Pure and Applied Mathematics*, vol. 52, no. 1, pp. 231-240, 2021.

[23] F. Kaplan and A. Özkoç Öztürk, “On the binomial transforms of the Horadam quaternion sequence,” *Mathematical Methods in the Applied Sciences* , vol. 45, no. 8, pp. 12009-12022, 2022.

[24] S. Halıcı and G. Cerda Morales, “On quaternion-Gaussian Fibonacci numbers and their properties,” Analele Stiintifice ale Universitatii Ovidius Constanta, vol. 29, no. 1, pp. 71-81, 2021.

[25] S. Halıcı, “On quaternion-Gaussian Lucas numbers,” Mathematical Methods in the Applied Sciences, vol. 44, no. 9, pp. 7601-7606, 2021.

[26] H. Arslan, “Gaussian Pell and Gaussian Pell-Lucas quaternions,” *Filomat*, vol. 35, no. 5, pp. 1609-1617, 2021.

[27] A. Z. Azak, “Pauli Gaussian Fibonacci and Pauli Gaussian Lucas quaternions,” *Mathematics*, vol. 10, no. 24, pp. 4655, 2022.

[28] A. Ertaş and F. Yılmaz, “On quaternions with Gaussian Oresme coefficients,” *Turkish Journal of Mathematics and Computer Science*, vol. 15, no. 1, pp. 192-202, 2023.

[29] A. Sloin and A. Wiesel, “Proper quaternion Gaussian graphical models,” *IEEE Transactions on Signal Processing*, vol. 62, no. 20, pp. 5487-5496, 2014.

Düzce University
Journal of Science & Technology

Research Article

Study on Drug Repurposing for ALS Treatment Using Pre-trained Knowledge Graph Embeddings: Methods and Findings

Selcan YALKIZIMI [a,*], Ümit ŞENTÜRK [b]

[a] *Department of Computer Engineering, Faculty of Engineering, Bolu Abant İzzet Baysal University, Bolu, TURKEY*
[b] *Department of Computer Engineering, Faculty of Engineering, Bolu Abant İzzet Baysal University, Bolu, TURKEY*
** Corresponding author's e-mail address: 2210711001@ogrenci.ibu.edu.tr*
DOI: 10.29130/dubited.1507832

ABSTRACT

In this study, research has been conducted using pre-trained knowledge graph embedding for drug repurposing in treating ALS (Amyotrophic Lateral Sclerosis), and its results have been presented. Drug repurposing studies for ALS have been carried out through two main methods: disease-drug relationship and genes-drug relationship. Drug repurposing recommendations for ALS have been provided by predicting connections between disease and drug entities on the DRKG (Drug Repurposing Knowledge Graph). The findings obtained from the study have been evaluated by comparing them with the list of clinical trial drugs obtained from DrugBank. DRKG has been utilized as a comprehensive biological knowledge graph containing genes, compounds, diseases, biological processes, side effects, and symptoms. This graph has proven to be an effective resource for extracting information related to ALS disease. In drug repurposing studies, drugs obtained through disease-drug relationships have been compared with the list of clinical trial drugs associated with ALS, yielding significant results. Additionally, interactions between genes associated with ALS and drugs related to these genes have been examined in studies conducted through gene-drug relationships. The results obtained from the study demonstrate that DRKG is an effective resource for identifying drugs with potential therapeutic effects in the treatment of ALS. The findings suggest that drug repurposing studies could offer new and effective solutions for the treatment of ALS, marking a significant step forward in this regard.

Keywords: *Drug repurposing, ALS (Amyotrophic Lateral Sclerosis), Pre-trained knowledge graph embedding, Clinical trial drugs*

Önceden Eğitilmiş Bilgi Grafik Gömme Yöntemleri Kullanılarak ALS Tedavisi için İlaç Yeniden Kullanımı Üzerine Bir Çalışma: Yöntemler ve Bulgular

ÖZ

Bu çalışmada, ALS hastalığının tedavisinde ilaç yeniden kullanımı amacıyla önceden eğitilmiş bilgi grafik yerleştirmesi kullanılarak bir çalışma yapılmış ve sonuçları sunulmuştur. İki ana yöntemle, yani hastalık ve ilaç ilişkisi ile genler ve ilaçlar üzerinden, ALS için ilaç yeniden kullanımı çalışmaları gerçekleştirilmiştir. DRKG (Drug Repurposing Knowledge Graph) üzerinde hastalık ve ilaç varlıkları arasındaki bağlantılar tahmin edilerek ALS için ilaç yeniden kullanımı önerileri sunulmuştur. Çalışma sonucunda elde edilen bulgular, DrugBank üzerinden elde edilen klinik deneme ilaçları listesi ile karşılaştırılarak değerlendirilmiştir. DRKG, genleri, bileşikleri, hastalıkları, biyolojik süreçleri, yan etkileri ve semptomları içeren geniş kapsamlı bir biyolojik bilgi

Received: 03/07/2024, Revised: 01/10/2024, Accepted: 20/10/2024

grafiği olarak kullanılmıştır. Bu grafik, ALS hastalığı ile ilgili bilgilerin çıkarılmasında etkili bir kaynak olmuştur. İlaç yeniden kullanımı çalışmalarında, hastalık-ilaç ilişkisi üzerinden elde edilen ilaçlar, ALS ile ilişkilendirilmiş klinik deneme ilaçları listesiyle karşılaştırılmış ve önemli sonuçlar elde edilmiştir. Ayrıca, gen- ilaç ilişkisi üzerinden yapılan çalışmalarda, ALS ile ilişkilendirilmiş genler ve bu genlerle ilişkilendirilmiş ilaçlar arasındaki etkileşimler incelenmiştir. Çalışmanın elde ettiği sonuçlar, DRKG' nin ALS tedavisinde potansiyel terapötik etkilere sahip ilaçları belirlemede etkili bir kaynak olduğunu göstermektedir. Elde edilen bulgular, ilaç yeniden kullanımı çalışmalarının ALS hastalığının tedavisinde yeni ve etkili çözümler sunabileceği konusunda önemli bir adım olarak değerlendirilebilir.

Anahtar Kelimeler: *İlaç yeniden kullanımı, ALS (Amyotrofik lateral skleroz), Önceden eğitilmiş bilgi grafik gömme, Klinik deneme ilaçları*

I. INTRODUCTION

Amyotrophic Lateral Sclerosis (ALS), first described by Charcot in the nineteenth century, is defined as a progressive neurodegenerative disease with a survival of three to five years. This disease, the treatment and etiology of which are unknown, is characterized by permanent loss of function of upper and lower motor neurons. ALS, which is diagnosed in 1500 to 4500 people every year in our country, is known as a fatal disease characterized by progressive loss of muscle function. Although many symptomatic and therapeutic drug researches continue, only FDA-approved riluzole and edaravone are included in the treatment protocol [1]. There is currently no treatment that will completely cure the disease in motor neuron disease. Symptomatic and supportive therapies help to improve the quality of life and life span of patients [2]. The prognosis of the disease is not good. Patients die 2-5 years after diagnosis [3]. The effect of Riluzole, which is paid for by the Social Security Institution (SGK) in Türkiye and used for the treatment of ALS patients, is also controversial. Although it is claimed that this drug slows down the progression of the disease, it has been observed that some patients who took Riluzole regularly did not stop the progression of the disease and could not prevent the worsening of the prognosis [3]. Although the etiology of ALS is not known exactly, it is suggested that many different factors play a role in its pathogenesis. Genetics, oxidative stress, glutamate excitotoxicity, mitochondrial dysfunction, axonal transport disorder, neuroinflammation, and RNA disorders are the main factors [4]. Familial ALS cases constitute approximately 10% of all ALS cases and are phenotypically and genetically heterogeneous [5]. It is usually inherited as Autosomal Dominant (OD; inheritance pattern in which one copy of a gene causes the disease). The association with a mutation in Superoxide Dismutase 1 (SOD-1; an enzyme that neutralizes free radicals) was first proposed in 1993. Subsequent developments have shown that some genes cause ALS, while others increase the risk of ALS or may affect the disease process [4].

Drug repurposing is an innovative approach to exploring new therapeutic uses for existing drugs. It focuses on research to understand how existing drugs can effectively treat different diseases beyond the purposes for which they were originally designed. It is based on identifying new interactions between biological entities such as genes and compounds. Traditional approaches to do this rely on costly and time-consuming experimental methodologies. As a result, several approaches have been developed that aim to leverage the various types of information that already exist about drugs, their targets, and diseases to reduce cost and accelerate drug reuse. Among these, approaches that represent existing knowledge in the form of a knowledge graph and utilize graph-based machine learning techniques based on graph neural networks and knowledge graph embedding models have gained popularity [6].

The drug discovery process ranges from reading and analyzing already existing literature to testing the ways in which potential drugs interact with targets. The preclinical development phase of drug discovery involves testing potential drug targets in animal models. Using artificial intelligence at this stage can help trials run smoothly [7]. It can enable researchers to more quickly and successfully predict how a drug might interact with an animal model. After going through the preclinical development phase and receiving approval from the United States Food and Drug Administration (FDA or USFDA), researchers began testing the drug with human participants. In general, this is a four-step process and is generally

considered to be the longest and most expensive stage of the manufacturing journey [7]. A representative drug discovery step is schematized in Figure 1. The drug discovery process comprises several major steps that include identifying compounds by screening compound collections via primary assays, such as high through-put screening in vitro, and secondary assays that include counter-screens and ADMET (absorption, distribution, metabolism, excretion, and toxicity) studies. Structure–activity relationship (SAR) and in silico studies in combination with cellular functional tests are used in an iterative cycle to improve the functional properties of the drug candidates. New drug candidates with desired characteristics are synthesized via organic synthesis. The selected drug candidate which has now passed all preclinical tests successfully is given to human patients in a clinical trial [8].

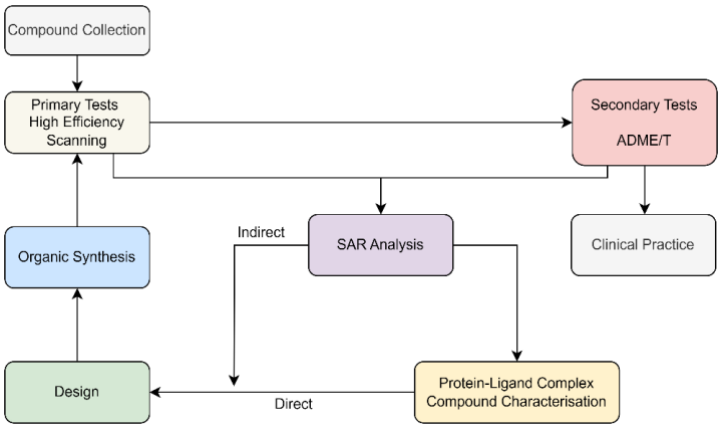

Figure 1. *A representative diagram highlighting the steps and cyclical nature of the drug discovery process [8].*

Most drugs that enter clinical trials fail, often due to a poor understanding of the mechanisms governing drug response. Machine learning techniques hold tremendous promise for better drug response predictions, but most have not reached clinical application due to their lack of interpretability and focus on monotherapies [9]. The methods to be used for the rapid screening of drug molecules are the HTS(High-Throughput Screening) method and the virtual screening method. In the HTS method, thousands of molecules are rapidly screened whether they show activity against a specific receptor or enzyme. In virtual screening, drug molecules can be rapidly classified or ranked in activity order by using machine learning methods. For this purpose, machine learning methods such as support vector machines (SVM) and random forest (RF) are frequently used in the literature for the detection of active molecules. However, these algorithms do not perform well in unbalanced datasets. For this reason, the data sets in the literature where these algorithms are used are mostly composed of balanced datasets[10]. The enormous amount of PubChem bioassay data, PubChem, which is updated daily, constitutes a publicly available big data resource for compounds with various target response information, including most drugs and drug candidates. Similar to PubChem, ChEMBL is a database containing binding, functional, ADME, and toxicity data for a large number of compounds. Compared to PubChem, ChEMBL contains a large amount of manually compiled data from the literature. DrugBank [11], one of the data sources designed specifically for drugs and drug candidates, is a publicly available database containing all approved drugs with their mechanisms, interactions, and relevant targets [12].

With the increase in the data size in the associated databases, it has become necessary to use new methods for virtual screening. In recent years, deep neural networks (DNNs) have shown very good performances in many areas and have surpassed the performances of machine learning methods such as SVM and RF [10]. In a 2014 study, Gramatica et al. presented a new methodology for directing existing drugs to diseases that were not initially targeted using biomedical knowledge. This methodology involves graphically representing and automatically analyzing knowledge using computational linguistics and graph theory [13]. In 2016, Udrescu et al. presented a new approach based on complex network science techniques, starting from the assumption that the analysis of drug-drug interactions can lead to the development of new drug discovery tools. In this study, they revealed functional drug categories and relationships, linked network clusters to relevant pharmacological properties, and

validated 85% of predicted properties by cross-checking with various databases [14]. In 2020, Zhou et al. published a study presenting powerful network-based methodologies for the rapid identification of candidate reusable drugs and potential drug combinations targeting 2019-nCoV/SARS-CoV-2 [15]. In 2020, Ioannidis et al. proposed an RGCN(Relational Graph Convolutional Network) model that greatly outperforms GCN(Graph Convolutional Network) and state-of-the-art KGE (Knowledge Graph Embedding) models on low-connected learning tasks using effective deep graph learning (DGL) methods and confirmed the identification of several drugs used in clinical trials as possible drug candidates [16]. In addition, in 2020, Ioannidis et al. constructed a comprehensive biological knowledge graph between genes, compounds, diseases, biological processes, side effects, and symptoms to assist such machine learning techniques, and this graph was named Drug Repurposing Knowledge Graph (DRKG) [6]. In 2022, Xiangxiang Zeng and his team developed an artificial intelligence model called ImageMol, which was pretrained on 10 million unlabeled molecules. This model successfully predicted molecular targets, as well as properties such as drug metabolism, toxicity, and brain permeability, and identified anti-SARS-CoV-2 candidate molecules. It has been demonstrated that this system could be effective in accelerating the drug discovery process for neurodegenerative diseases like Alzheimer's and diseases like COVID-19 [17]. In the same year, Wang and his team introduced new methods for molecular property prediction and drug discovery using graph and sequence-based neural networks. These methods demonstrated significant improvements in ROC-AUC and PRC-AUC metrics in COVID-19 drug discovery tasks during the AI Cures open challenge [18]. In 2023, Kang-Lin Hsieh and colleagues conducted a study on drug repurposing for Alzheimer's disease using DRKG, showing that molecular profiles integrated into a knowledge graph could systematically identify potentially reusable drugs [19]. Similarly, in 2024, Yunguang Qiu and Feixiong Cheng summarized artificial intelligence-supported drug discovery methodologies focused on the complex molecular structure of Alzheimer's disease, emphasizing the importance of AI-based drug repurposing strategies in identifying new indications for Alzheimer's disease [20].

In contrast to approaches in the existing literature, this study addresses drug reuse for ALS disease through a bidirectional analysis examining both disease-drug and gene-drug associations. DRKG's extensive network of biological knowledge underpins the methods used, enabling a more comprehensive assessment of the potential therapeutic implications of gene-drug and disease-drug linkages in ALS. One of the main contributions of the study is that this two-pronged approach enables a broader perspective of potential drug candidates for ALS. While the literature often focuses on a single type of association, the analysis here of both disease-drug and gene-drug associations provides an opportunity to more accurately determine the therapeutic effects of drugs. The use of DRKG and advanced analysis methods enables prediction of associations between disease and drug entities with higher accuracy through pre-trained knowledge graph overlays and provides drug reuse recommendations. The identification of new treatment strategies for ALS by evaluating gene-drug associations reflects an innovative approach. Furthermore, the comparison of the results with ALS-associated clinical trial drugs provides an important contribution in assessing the clinical relevance of the findings. These contributions draw attention to the development of new approaches to drug reuse in ALS treatment and the importance of knowledge graphs in this process.

In the remaining sections of this study, Chapter 2 provides a detailed explanation of the dataset and methods used in the project, while Chapter 3 presents the findings of research on drug repurposing for ALS disease. Chapter 4 extracts drug repurposing results for ALS disease using DRKG embeddings and summarizes the findings of the study. Subsequently, Chapters 5 and 6 will present a discussion on the overall outline of the study and potential future research directions. Additionally, an evaluation will be conducted on how the findings could contribute to clinical applications and the implications of these findings on ALS treatment. This evaluation may play an important role in shaping future research aimed at developing new therapeutic strategies for the treatment of ALS disease.

II. METHODS

In this section, the dataset and methods used in the paper are described in detail. Using the pre-trained knowledge graph embedding of the dataset DRKG (Drug Reuse Knowledge Graph), a drug reuse study was performed to provide a recommendation for the treatment of ALS disease. Drug reutilisation is studied in two ways: through disease and drug associations and through genes and drugs interactions. By predicting the links between disease entities and drug entities in the DRKG, a drug reuse recommendation for ALS is presented. Firstly, a list of ALS-related diseases was extracted from the DRKG. Diseases are coded with identification numbers on the DRKG. This was done by scanning the identification code of ALS disease on DRKG. A list of drugs on Drugbank was used as candidate drugs in our study. There are 8104 drugs in this drug list. In order to evaluate the drugs for reuse, they were compared with the list of clinical trial drugs associated with ALS disease collected from Drugbank. Figure 2 provides a Graphical Summary of the Data Set and Methods of the Drug Reuse Study for ALS Disease.

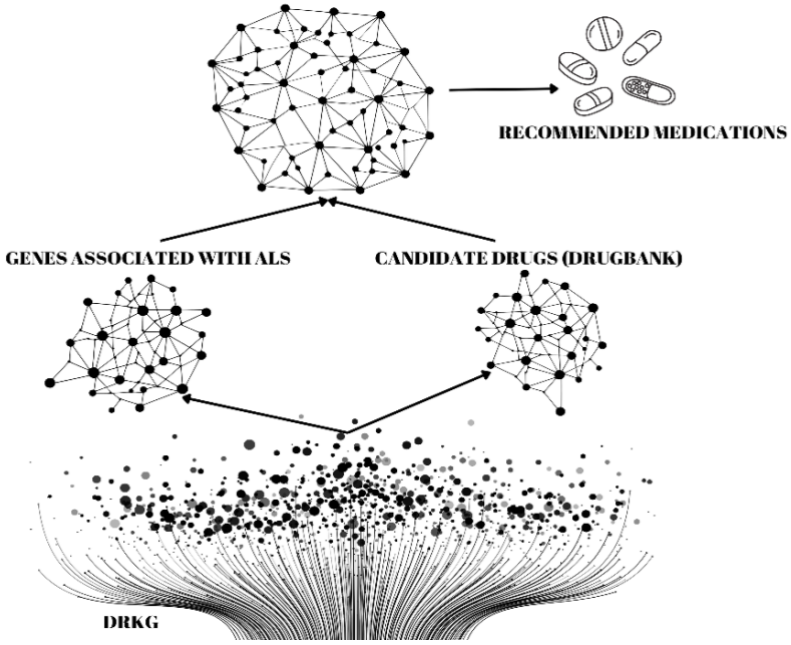

Figure 2. *Drug Reuse Study for ALS Disease: Graphical Summary of Data Set and Methods*

A. DATASET

DRKG is a comprehensive biological knowledge graph that associates genes, compounds, diseases, biological processes, side effects, and symptoms. Figure 3 visualizes the possible interactions between entity type pairs in the DRKG.

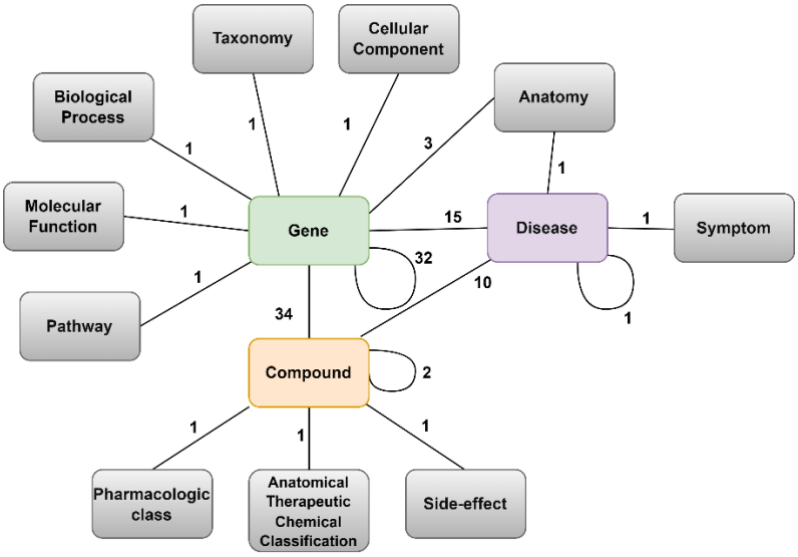

Figure 3. *Representation of the DRKG. The number next to an edge indicates the number of relationship types between the corresponding entity types in the DRKG [21].*

It contains information from six existing databases, including DRKG, DrugBank, Hetionet, GNBR, String, IntAct, and DGIdb, as well as data collected from recent publications specifically related to COVID-19. This database contains 97,238 entities belonging to 13 entity types and 5,874,261 triples belonging to 107 edge types. These 107 edge types represent a type of interaction between one of the 17 entity type pairs, as shown in Table 1 (more than one type of interaction is possible between the same pair of entities)[21]. The type-wise distribution of entities in DRKG and the original data sources are shown in Table 1.

Table 1. *Number of nodes per node type in the data sources in the DRKG [21].*

Entity type	Drugbank	GNBR	Hetionet	STRING	IntAct	DGIdb	Bibliography	Total Entities
Anatomy	-	-	400	-	-	-	-	400
Atc	4,048	-	-	-	-	-	-	4,048
Biological Process	-	-	11,381	-	-	-	-	11,381
Cellular Component	-	-	1,391	-	-	-	-	1,391
Compound	9,708	11,961	1,538	-	153	6,348	6,25	24,313
Disease	1,182	4,746	257	-	-	-	33	5,103
Gene	4,973	27,111	19,145	18,316	16,321	2,551	3,181	39,22
Molecular Function	-	-	2,884	-	-	-	-	2,884
Pathway	-	-	1,822	-	-	-	-	1,822
Pharmacologic Class	-	-	345	-	-	-	-	345
Side Effect	-	-	5,701	-	-	-	-	5,701
Symptom	-	-	415	-	-	-	-	415
Tax	-	215	-	-	-	-	-	215
Total	19,911	44,033	45,279	18,316	16,474	8,899	9,464	97,238

Table 2 shows examples of the number of triples between different pairs of entity types in DRKG for DRKG and various data sources.

Table 2. *Some of the numbers of interactions in DRKG and in data sources [21].*

Entity-type pair	Drugbank	GNBR	Hetionet	STRING	IntAct	DGIdb	Bibliography	Total interactions
(Gene, Gene)	-	66,722	474,526	1,496,708	254,346	-	58,629	2,350,931
(Compound, Gene)	24,801	80,803	51,429	-	1,805	26,29	25,666	210,794

(Disease, Gene)	-	95,399	27,977	-	-	-	461	123,837
(Compound, Compound)	1,379,271	-	6,486	-	-	-	-	1,385,757
(Compound, Disease)	4,968	77,782	1,145	-	-	-	-	83,895

DRKG is available in its final form on Git Hub. An image created by selecting samples from the data on the DRKG database is shown in Table 3.

Table 3. *Sample DRKG database file image.*

Gene::2157	bioarx::HumGenHumGen:Gene:Gene	Gene::2157
Compound::DB09080	bioarx::DrugHumGen:Compound:Gene	Gene::154
Compound::DB00669	DRUGBANK::ddi-interactor-in::Compound:Compound	Compound::DB13064
Gene::10959	GNBR::Te::Gene:Disease	Disease::MESH:D006509
Gene::2742	Hetionet::GpBP::Gene:Biological Process	Biological Process::GO:0006821
Gene::6202	Hetionet::GiG::Gene:Gene	Gene::26156
Anatomy::UBERON:0000057	Hetionet::AuG::Anatomy:Gene	Gene::113791
Compound::DB01115	Hetionet::CcSE::Compound:Side Effect	Side Effect::C0344232
Gene::3007	Hetionet::GpPW::Gene:Pathway	Pathway::PC7_2529

In the DRKG study, data from the DrugBank, Hetionet, GNBR, String, IntAct, and DGIdb databases were filtered and a list of triples (head-entity, relationship type, tail-entity) of data from each dataset was first extracted. In this process, an entity type was associated with an identifier of the entity followed by an identification number that makes it unique. For example Gen::229475. In the representation of relationships, the database name, the relationship name, and the types of head and tail entities were used. Example: DGIDB::INHIBITOR::Gene:Compound. Different ids can be used to represent entities such as genes, compounds, and diseases from different data sources, these ids are mapped to a common ID to remove the incompatibility here. Finally, relations with less than 50 edges were excluded by removing relations with insufficient data [21].

B. GRAPH NEURAL NETWORK(GNN)

Graph neural network (GNN) is a deep learning method that belongs to the artificial neural network (ANN) family and performs information extraction from graphs. It was first used in 2008 and its development started in 2014 and after [22]. GNNs, which were developed in response to the failure of convolutional neural networks (CNNs) to meet the expected performance on visuals, are used in many fields such as physics, chemistry, biology, and cyber security [22]. Graphs are a type of data structure that models a set of objects (nodes) and their relationships (edges). Recently, research on analyzing graphs with machine learning has received increasing attention due to the great expressive power of graphs [23]. A graph G = (V, E) consists of two sets: V the set of nodes (also called vertices), and E the set of edges (also called arcs). Each edge connects a pair of nodes, indicating a relationship between them [6]. Graph analysis, a unique non-euclidean data structure for machine learning, focuses on tasks such as node classification, link prediction, and clustering. Graph neural networks (GNNs) are deep learning-based methods that operate on the graph domain. Due to its convincing performance, GNN has recently become a widely applied graph analysis method [23]. Studies in this field are increasing day by day in Türkiye, and graph-based methods such as GNN are used in many national theses and research projects. However, this type of network is still developing in our country compared to global applications.

In general, the GNN model structure consists of four steps:
1- Finding the structure of the graph,
2- Determining the graph type and scale,
3- Determine the design loss function,
4- Building the model using computational modules [23].

III. FINDINGS

In this section, the findings from the research on drug repurposing for amyotrophic lateral sclerosis (ALS) are presented. The study conducted two separate analyses based on disease-drug and gene-drug relationships to obtain results for both approaches. First, using the **mesh code** for ALS, the connections between disease and drug entities in the DRKG database were predicted. In this process, scores representing the disease-drug relationship were calculated, and drugs with the highest scores were identified. These drugs were then compared with a list of 158 clinical trial drugs related to ALS obtained from DrugBank to derive results. Secondly, gene-drug relationships were examined by assessing the connections between disease-related genes and drugs. Similar formulas and algorithms were employed to determine the relationships between genes and drugs. The findings from both methods were completed by comparing the repurposed drugs with the clinical trial drugs related to ALS.

Mesh code (Medical Subject Headings) is a frequently used indexing term in medical literature. Mesh terms are a standard list of terms used to categorize and index medical subjects. Mesh codes are a unique identifier of each Mesh term and are used to categorize and index research in medical literature. These codes are used in scientific papers, references in medical literature, and databases. Here, we aimed to access all ALS disease entity links in our database by using the mesh code "D000690", which is the mesh code of ALS disease.

$$d = \gamma - \|h + r - t\|_2 \quad (1)$$

$$score = \log\left(\frac{1}{1 + \exp(-d)}\right) \quad (2)$$

In the formula provided in Equation 1[6]:
d: is a score representing the drug-disease relationship.
γ: is a constant coefficient (which may depend on a specific dataset or model parameter).
h: is a vector representing the disease.
r: is a vector representing the relationship between the drug and the disease.
t: is a vector representing the drugs.
‖h + r - t‖_2: This term represents the L2 norm of the vectorial difference between the disease and the drug, which measures how close the drug and the disease are.
This equation measures the similarity between the drug and the disease in vector space and determines how strong the treatment effect is.

In the formula for Log-Sigmoid Score Calculation provided in Equation 2[6]:
score: is defined as the final score of the relationship between the drug and the disease.
log-sigmoid function: brings the score into a specific range, making all scores negative. This function is the logarithm of the sigmoid function, which ensures that the scores remain within a more manageable range.
This equation normalizes the relationship score calculated by d (the value obtained from the first equation) through a logarithmic sigmoid function. The log-sigmoid function compresses the scores into a range between 0 and 1, thus producing a score that represents the strength of the relationship. At the same time, this function is used to bring all scores into a range below 0.

In our study, the ['Hetionet::CtD::Compound:Disease','GNBR::T::Compound:Disease'] connection was used as the edge connection type for the drug-disease relationship. This connection represents the treatment relationship between a specific drug and a disease. When repurposing drugs, only treatment-related edge connections should be used. The formulas provided in Equation 1 and Equation 2 are used to calculate the edge score. Here, the log-sigmoid function must be used to ensure all scores are < 0 [6]. After calculating the edge scores, a list of the drugs with the highest scores, i.e., those most associated

with the disease, was generated. These drugs were then compared with the list of 158 clinical trial drugs related to ALS collected from DrugBank, and a result list was obtained.

In the study conducted through gene-drug relationships, drug repurposing for ALS was investigated by predicting the connections between host gene entities related to the disease and drug entities in DRKG. The connection relationships of target gene entities associated with the disease were listed in a file, and for the drugs, a list entirely obtained from DrugBank was used. The edge connection types 'GNBR::N::Compound:Gene', 'DRUGBANK::target::Compound:Gene, DGIDB::INHIBITOR::Gene:Compound' were used in separate trials. The formulas given in Equation 1 and Equation 2 for calculating the edge scores and the pathway followed in the disease-drug relationship were also applied here. Equation 1 was used to calculate the relationship score between the gene and the drug, thereby measuring the vectorial distance between the genes and drugs to determine the connection strength. Equation 2 used the log-sigmoid function to normalize this score and obtain the edge score. This score was used to identify and rank the relationship between genes and drugs. After calculating the edge scores, the repurposed drugs were compared with clinical trial drugs related to ALS, and a list was created.

IV. RESULTS

In this section, we obtain drug repurposing results for ALS disease by using pretrained DRKG embeddings. In the study based on disease-drug relationships, drug repurposing for ALS was conducted by predicting the connections between disease entities and drug entities in DRKG. In the study based on gene-drug relationships, trials were carried out using inhibitory connections between genes and drugs. Separate results were obtained from the drug repurposing analysis conducted with both methods.

A. DRUG REPURPOSING THROUGH THE DISEASE-DRUG LINK

Among the first 100 drugs found for the treatment of ALS disease based on the disease-drug relationship, 18 drugs, which are also on the drugbank clinical drug trial list, are listed in Table 4 starting from the most related one according to the edge score.

Table 4. *The 18 drugs and their scores are also included in the Drugbank clinical drug trial list.*

Order No	Drug Name	Edge Score
[0]	Trehalose	-0.1777
[1]	Arimoclomol	-0.1847
[3]	Pridopidine	-0.2015
[6]	Testosterone	-0.2211
[8]	Mecobalamin	-0.2360
[13]	Sirolimus	-0.2563
[23]	Minocycline	-0.2878
[25]	Quinidine	-0.2961
[26]	Mycophenolate mofetil	-0.2963
[28]	Ubidecarenone	-0.2986
[31]	Colchicine	-0.3003
[56]	Methylprednisolone	-0.3561
[59]	Cimetidine	-0.3604
[62]	Tamoxifen	-0.3657
[66]	Tretinoin	-0.3686
[68]	Thalidomide	-0.3704
[73]	Capsaicin	-0.3746
[91]	Ceftriaxone	-0.3956

The first 10 of the first 100 drugs listed for the treatment of ALS disease, regardless of whether they were used in clinical trials on the disease-drug relationship, are listed in Table 5 in order of relationship priority.

Table 5. *The top 10 drugs are listed regardless of whether they have been used in clinical trials.*

Order No	Drug Name	Identity Code	Edge Score
1	Trehalose	DB12310	-0.1777
2	Arimoclomol	DB05025	-0.1847
3	Glutathione	DB00143	-0.1869
4	Pridopidine	DB11947	-0.2015
5	Melatonin	DB01065	-0.2073
6	Cholesterol	DB04540	-0.2127
7	Testosterone	DB00624	-0.2211
8	Dexamethasone	DB01234	-0.2328
9	Mecobalamin	DB03614	-0.2360
10	Estradiol	DB00783	-0.2475

When evaluating drugs associated with ALS, the reason for considering not only the drugs used in clinical studies but also those that have not yet been implemented in clinical practice is that some drugs, despite being insufficiently researched, may provide potential benefits and pave the way for future studies. Furthermore, the evaluation of these drugs can contribute to innovative approaches in the management of ALS, offering a broader treatment perspective.

When comparing the drugs listed in Table 5, which we obtained as output, with the clinical trial list related to ALS collected from DrugBank in Table 4, it is observed that the five drugs (Trehalose, Arimoclomol, Pridopidine, Testosterone, Mecobalamin) that have the highest edge scores and are most associated with the disease are common in the clinical trial list.

B. DRUG REPURPOSING THROUGH GENE-DRUG LINKAGE

In this section, experiments were performed by selecting inhibitory association links appearing in three data sources: 'GNBR::N::Compound:Gene', 'DRUGBANK::target::Compound:Gene' and 'DGIDB::INHIBITOR::Gene:Compound'. In the study for the gene-drug association for ALS disease treatment, in order to predict the links between genes and drugs to act as inhibitors, a list of biological gene entities associated with ALS disease was taken on DRKG and it is seen that there are 550 associated genes. Then, using the pre-trained knowledge graph placements and the equation used to calculate the edge score, we found the 100 drugs with the highest score and ranked these drugs per target gene. Thus, according to the type of inhibitory relationship we chose, the gene with the highest drug-gene association and the drugs associated with it were found. Then, in order to evaluate the connection of our prediction with the clinical drugs used in treatment, the overlap and the number of hits between these 100 predicted drugs and the drugs used in clinical trials for treatment were checked. Here, the number of hits is related to determining how many of the total number of genes the predicted drug is associated with. If a drug is associated with all genes, the number to be seen here will be equal to the total number of genes we found associated with ALS, i.e. 550. The same study was repeated for the three types of association mentioned above.

Within the scope of the 'GNBR::N::Compound::Gene' relationship, when we listed the genes associated with ALS disease in the list of genes associated with this disease, Gene::627 and Gene::9217 genes associated with 16 drugs were determined as the genes with the most drug associations. Among the drugs associated with these genes, those with the most drug associations are listed first and these associations can be seen in Table 6.

Table 6. *List of drugs Gene::627 and Gene::9217 related to 16 drugs by 'GNBR::N::Compound:Gene' relationship.*

Gene::627	16	Gene::9217	16
[9]	Tretinoin	[5]	Sirolimus
[12]	Capsaicin	[21]	Ubidecarenone
[17]	Testosterone	[24]	Quinidine
[32]	Sirolimus	[30]	Tamoxifen
[33]	Tamoxifen	[32]	Capsaicin
[44]	Methylprednisolone	[53]	Bosutinib
[50]	Scopolamine	[56]	Thalidomide
[59]	Thalidomide	[59]	Methylprednisolone
[69]	Dextromethorphan	[60]	Tretinoin
[79]	Trazodone	[65]	Prednisone
[81]	Minocycline	[67]	Cimetidine
[83]	Dronabinol	[77]	Minocycline
[84]	Prednisone	[81]	Colchicine
[87]	Pimozide	[93]	Testosterone
[89]	Atropine	[97]	Mycophenolate mofetil
[91]	Midazolam	[99]	Atropine

Table 7 shows the top 10 of the 100 drugs with the highest score listed according to the 'GNBR::N::Compound:Gene' relationship and the top 10 drugs that overlap with the list of ALS clinical trial drugs and how many genes these drugs are associated with, that is, the number of hits. For example, the drug named Sirolimus coded with the id ‘DB00877’, which is also included in the clinical trial list related to ALS Disease, is associated with 538 genes related to ALS disease and ranks first, while the drug named Tretinoin coded with the id ‘DB00755’ is associated with 522 genes and ranks second. The drug named Tamoxifen with the ID code ‘DB00675’ is in the 3rd place with 478 hits.

Table 7. *The top 100 highest-scoring drugs listed by 'GNBR::N::Compound:Gene' association overlap with the list of ALS clinical trial drugs and the number of genes with which these drugs are associated.*

Identity Code	Drug Name	Hit Count
DB00877	Sirolimus	538
DB00755	Tretinoin	522
DB00675	Tamoxifen	478
DB00624	Testosterone	398
DB01041	Thalidomide	360
DB00908	Quinidine	307
DB06616	Bosutinib	257
DB06774	Capsaicin	256
DB00635	Prednisone	198
DB01394	Colchicine	179

Within the scope of the 'DRUGBANK::target::Compound::Gene' relationship, Gene::283, Gene::5551, and Gene::6647 genes, which were found to be associated with 13 drugs, were identified as the genes with the most drug associations in the list of genes associated with ALS disease. Among the drugs associated with these genes, those with the most drug associations were ranked first and these associations can be seen in Table 8. When the drugs associated with three different genes that ALS disease interacts within the current association type are analyzed, it is seen that there are common drugs in all three gene types.

Table 8. *List of drugs Gene::5551 and Gene::283 related to 13 drugs by association with 'DRUGBANK::target::Compound:Gene'.*

Gene::283	**13**	**Gene::5551**	**13**	**Gene::6647**	**13**
[8]	Bosutinib	[7]	Sirolimus	[0]	Arimoclomol
[11]	Capsaicin	[11]	Prednisone	[7]	Cannabidiol
[19]	Colchicine	[13]	Tretinoin	[23]	Medical Cannabis
[26]	Cannabidiol	[16]	Thalidomide	[30]	Bosutinib
[36]	Tretinoin	[22]	Minocycline	[33]	Sirolimus
[49]	Trametinib	[36]	Methylprednisolone	[51]	Dolutegravir
[54]	Sirolimus	[39]	Mycophenolate mofetil	[69]	Minocycline
[60]	Tenofovir alafenamide	[44]	Colchicine	[70]	Colchicine
[66]	Tamoxifen	[56]	Dextromethorphan	[77]	Tretinoin
[80]	Testosterone	[68]	Quinidine	[78]	Mycophenolate mofetil
[81]	Medical Cannabis	[89]	Bosutinib	[81]	Quinidine
[91]	Thalidomide	[91]	Testosterone	[83]	Tauroursodeoxycholic acid
[95]	Dolutegravir	[94]	Tacrolimus	[84]	Capsaicin

Table 9 shows the top 10 of the 100 drugs with the highest score listed according to the 'DRUGBANK::target::Compound::Gene' relationship and the top 10 drugs that overlap with the ALS clinical trial drugs list and how many genes these drugs are associated with, that is, the number of hits. Here, it was revealed that the drug named Bosutinib coded with the ID code ‘DB06616’, which is also included in the clinical trial list related to ALS Disease, ranked first with 446 genes related to ALS disease, the drug named Dolutegravir coded with the id code ‘DB08930’ ranked second with 379 genes, and the drug named Sirolimus coded with the id code ‘DB00877’ ranked third with 360 genes.

Table 9. *The top 100 highest-scoring drugs listed by 'DRUGBANK::target::Compound::Gene' are associated with the list of ALS clinical trial drugs and the number of genes with which these drugs are associated.*

Identity Code	**Drug Name**	**Hit Count**
DB06616	Bosutinib	446
DB08930	Dolutegravir	379
DB00877	Sirolimus	360
DB00755	Tretinoin	320
DB00908	Quinidine	218
DB09061	Cannabidiol	211
DB06774	Capsaicin	187
DB00624	Testosterone	152
DB08911	Trametinib	152
DB00675	Tamoxifen	120

Within the scope of the 'DGIDB::INHIBITOR::Gene::Compound' relationship, when we list the genes associated with ALS disease in the list of genes associated with this disease, Gene::4283, which is associated with 14 drugs, was determined as the gene with the most drug associations. Among the drugs associated with this gene, those with the most drug associations are listed first and these relationships can be seen in Table 10.

Table 10. *List of drugs related to Gene::4283 which is related to 14 drugs by association with 'DGIDB::INHIBITOR::Gene:Compound'.*

Gene::4283	14
[7]	Olanzapine
[12]	Methylprednisolone
[33]	Prednisone
[46]	Ciprofloxacin
[57]	Sirolimus
[61]	Corticotropin
[64]	Tretinoin
[68]	Tacrolimus
[73]	Fingolimod
[76]	Testosterone
[85]	Pimozide
[93]	Thalidomide
[94]	Atropine
[98]	Trazodone

Table 11 shows the top 10 of the 100 drugs with the highest score listed according to the 'DGIDB::INHIBITOR::Gene::Compound' relationship and the top 10 drugs that overlap with the ALS clinical trial drugs list and how many genes these drugs are associated with, that is, the number of hits. It was revealed that the drug named Tretinoin coded with the ID code 'DB00755', which is also included in the clinical trial list related to ALS Disease, ranked first in relation to 455 genes related to ALS disease, the drug named Sirolimus coded with the id code 'DB00877' ranked second in relation to 445 genes and the drug named Bosutinib coded with the id code 'DB06616' ranked third in relation to 425 genes.

Table 11. *The top 100 highest-scoring drugs listed by 'DGIDB::INHIBITOR::Gene:Compound' association overlap with the list of ALS clinical trial drugs and the number of genes with which these drugs are associated.*

Identity Code	Drug Name	Hit Count
DB00755	Tretinoin	455
DB00877	Sirolimus	445
DB06616	Bosutinib	425
DB00864	Tacrolimus	314
DB00908	Quinidine	291
DB00624	Testosterone	266
DB08911	Trametinib	230
DB01041	Thalidomide	194
DB00688	Mycophenolate mofetil	150
DB00675	Tamoxifen	144

In this study, drug reuse studies were performed separately on the disease-drug relationship and gene-drug relationship and separate results were obtained for both studies. A list of 158 drugs in clinical trials related to ALS disease from clinical drug studies on Drugbank was compiled and the results were compared with this list.

Among the first 100 drugs found through the disease-drug relationship for the treatment of ALS disease, 18 drugs that are also on the drugbank clinical drug trial list were found and listed. When we compared the clinical trial list compiled from DrugBank with the first 10 drugs selected among the top 100 drugs with the highest edge score, i.e. the most associated with the disease, which we obtained regardless of whether they were used in clinical studies on disease-drug association for the treatment of ALS disease, it was seen that the 5 drugs with the highest edge score in the clinical trial list (Trehalose, Arimoclomol, Pridopidine, Testosterone, Mecobalamin) were the same.

In the study conducted for the gene-drug association, 550 gene information was collected on ALS-related DRKG, and using the inhibitory links between these genes and drugs, a drug reuse study was

performed separately according to each selected inhibitory linkage type associated with ALS disease, and the 100 drugs with the highest score were found and these drugs were ranked per target gene. As a result, the gene with the most drug-gene connections and the drugs associated with it were listed according to the type of inhibitory linkage we selected. In addition, we listed the 100 drugs with the highest scores that overlapped with the list of ALS clinical trial drugs, that is, how many drugs are currently registered as trial drugs for ALS disease on the Drugbank and how many genes these drugs are associated with (number of hits). The same study was repeated for three different inhibitory association types and separate results were obtained. According to these results, the prominent findings for each association type are as follows; According to the 'GNBR::N::Compound::Gene' Association, the genes associated with the most drugs are Gene::627 and Gene::9217 and these genes are associated with 16 drugs. According to this association type, Sirolimus (DB00877) is associated with 538 genes, Tretinoin (DB00755) is associated with 522 genes, and Tamoxifen (DB00675) associated with 478 genes are among the prominent drugs overlapping with the clinical trial drug list. According to the 'DRUGBANK::target::Compound::Gene' Association, the genes associated with the most drugs are Gene::283, Gene::5551, and Gene::6647, which are associated with 13 drugs. Drugs that stand out by overlapping with the clinical trial drug list according to this association type include Bosutinib (DB06616), which is associated with 446 genes, Dolutegravir (DB08930), which is associated with 379 genes, and Sirolimus (DB00877), which is associated with 360 genes. According to the 'DGIDB::INHIBITOR::Gene::Compound' association, Gene::4283 is the gene associated with the most drugs, and this gene is associated with 14 drugs. The prominent drugs that overlap with the clinical trial drug list according to this association type are Tretinoin (DB00755), which is associated with 455 genes, Sirolimus (DB00877), which is associated with 445 genes, and Bosutinib (DB06616), which is associated with 425 genes. These results show interactions between ALS disease-associated genes and their associated drugs for all three types of associations. The drug Tretinoin (DB00755) shows interactions with ALS disease-associated genes under both the 'GNBR::N::Compound:Gene' association and the 'DGIDB::INHIBITOR::Gene:Compound' association. Bosutinib (DB06616) stands out by showing interaction with ALS disease-associated genes under 'DRUGBANK::target::Compound::Gene' and 'DGIDB::INHIBITOR::Gene::Compound' association types. In addition, Sirolimus (DB00877) interacts with genes associated with ALS disease under all three association types. These common drugs were associated with genes associated with ALS disease under different association types in the gene-drug association study. On the other hand, Sirolimus (DB00877) was prominent both in the gene-drug association study and in the disease-drug association study. These results indicate that these drugs may have potential therapeutic effects on ALS and may influence the prioritization of these drugs in relevant studies. However, as stated at the beginning of the study, although the FDA-approved drugs riluzole and edaravone, which are included in the current treatment protocol for ALS disease, were included in our clinical trial drug list, they were not listed as recommendations as a result of our training. However, the results of this study show that many drugs used in clinical trials were discovered as possible drug candidates. This study by no means recommends specific drugs but provides a deep learning methodology to prioritize some of the available drugs for research.

V. DISCUSSION

The results of this study represent an important step in the discovery of potential ALS treatment candidates through disease-drug and gene-drug linkages. In the disease-drug association study, when the drugs with the highest scores were identified, they were found to be in common with some clinical trial drugs. This suggests that the disease-drug association approach may be effective in identifying the potential reuse of drugs currently being trialed in clinical trials.

On the other hand, the gene-drug association study examined the interactions between genes associated with ALS disease and drugs associated with these genes using different types of inhibitory relationships. This study highlights the potential of a gene-drug association-based treatment strategy for ALS disease. In particular, the identified partner drugs were associated with ALS disease-associated genes under different association types, suggesting that these drugs may have potential therapeutic effects on ALS.

The results of this study may contribute to the development of new approaches for the discovery of potential treatment candidates for ALS. However, the limitations of this study should also be considered. For example, the lack of data sources used, or the limited datasets may affect the generalisability of the results. Therefore, it is important for further research to confirm and extend these findings.

VI. CONCLUSION

In this study, we focused on the identification of potential therapeutic drugs for the treatment of ALS disease. For this purpose, separate studies on disease-drug association and gene-drug association were carried out. In addition, drugs in the clinical trial phase in the DrugBank database were also analyzed and compared with the results obtained.

Firstly, in the study on the disease-drug association, drug reuse studies for ALS disease were performed using data to estimate the links between disease and drug entities in DRKG. Using the mesh code 'D000690', access to all entity links for ALS disease was provided. Then, the drugs with the highest scores on the disease-drug association were identified and these drugs were compared with ALS disease-related clinical trial drugs collected from drugbank. Similarly, in the gene-drug association study, the links between genes and drugs for ALS disease were predicted. Separate trials were conducted for three different relationship types and the drugs with the highest scores were identified. Finally, the results obtained through disease-drug association and gene-drug association may play an important role in identifying potential treatment candidates for ALS disease.

VII. REFERENCES

[1] Z. Yildirim, D. N. Toktaş, Ö. Demir, G. Zülfiye, and B. Ş. Utsukarçi, "Amyotrofik Lateral Skleroz Patofizyolojisi ve Tedavi Yaklaşımları," *Hacettepe University Journal of the Faculty of Pharmacy,* vol. 43, no. 1, pp. 50-69, 2023.

[2] F. Kamel, D. M. Umbach, L. Stallone, M. Richards, H. Hu, and D. P. Sandler, "Association of lead exposure with survival in amyotrophic lateral sclerosis," *Environmental Health Perspectives,* vol. 116, no. 7, pp. 943-947, 2008.

[3] F. Özcan, A. Kaya, and M. E. Yayla, "Amyotrofik lateral skleroz hastalığı ve aile hekiminin rolü," *Celal Bayar Üniversitesi Sağlık Bilimleri Enstitüsü Dergisi,* vol. 3, no. 3, pp. 431-435, 2016.

[4] A. D. Marangoz and Ç. Erdoğan, "Amyotrofik lateral skleroz (ALS) hastalığının patogenezi," *Pamukkale Medical Journal,* vol. 13, no. 2, pp. 477-484, 2020.

[5] S. Byrne *et al.*, "Rate of familial amyotrophic lateral sclerosis: a systematic review and meta-analysis," *Journal of Neurology, Neurosurgery & Psychiatry,* 2010.

[6] V. N. Ioannidis *et al.*, "Drkg-drug repurposing knowledge graph for covid-19," *arXiv preprint arXiv:2010.09600,* 2020. [Online]. Available: https://github.com/gnn4dr/DRKG/tree/master?tab=readme-ov-file#drkg-dataset.

[7] İ. N. Çelik, F. K. Arslan, R. Tunç, and İ. Yıldız, "İlaç Keşfi ve Geliştirilmesinde Yapay Zekâ," *Journal of Faculty of Pharmacy of Ankara University,* vol. 45, no. 2, pp. 400-427, 2021.

[8] H. S. Chan, H. Shan, T. Dahoun, H. Vogel, and S. Yuan, "Advancing drug discovery via artificial intelligence," *Trends in pharmacological sciences,* vol. 40, no. 8, pp. 592-604, 2019.

[9] B. M. Kuenzi *et al.,* "Predicting drug response and synergy using a deep learning model of human cancer cells," *Cancer cell,* vol. 38, no. 5, pp. 672-684. e6, 2020.

[10] H. Kanberiz, "Derin öğrenme ile ilaç moleküllerinin aktivitelerinin sınıflandırılması," Sağlık Bilimleri Enstitüsü.

[11] DrugBank. "DrugBank Online." https://go.drugbank.com (accessed 27 January 2024, 2024).

[12] H. Zhu, "Big data and artificial intelligence modeling for drug discovery," *Annual review of pharmacology and toxicology,* vol. 60, pp. 573-589, 2020.

[13] R. Gramatica, T. Di Matteo, S. Giorgetti, M. Barbiani, D. Bevec, and T. Aste, "Graph theory enables drug repurposing–how a mathematical model can drive the discovery of hidden mechanisms of action," *PloS one,* vol. 9, no. 1, p. e84912, 2014.

[14] L. Udrescu *et al.,* "Clustering drug-drug interaction networks with energy model layouts: community analysis and drug repurposing," *Scientific reports,* vol. 6, no. 1, p. 32745, 2016.

[15] Y. Zhou, Y. Hou, J. Shen, Y. Huang, W. Martin, and F. Cheng, "Network-based drug repurposing for novel coronavirus 2019-nCoV/SARS-CoV-2," *Cell discovery,* vol. 6, no. 1, p. 14, 2020.

[16] V. N. Ioannidis, D. Zheng, and G. Karypis, "Few-shot link prediction via graph neural networks for covid-19 drug-repurposing," *arXiv preprint arXiv:2007.10261,* 2020.

[17] X. Zeng *et al.,* "Accurate prediction of molecular properties and drug targets using a self-supervised image representation learning framework," *Nature Machine Intelligence,* vol. 4, no. 11, pp. 1004-1016, 2022/11/01 2022, doi: 10.1038/s42256-022-00557-6.

[18] Z. Wang *et al.,* "Advanced graph and sequence neural networks for molecular property prediction and drug discovery," *Bioinformatics,* vol. 38, no. 9, pp. 2579-2586, 2022, doi: 10.1093/bioinformatics/btac112.

[19] K.-L. Hsieh, G. Plascencia-Villa, K.-H. Lin, G. Perry, X. Jiang, and Y. Kim, "Synthesize heterogeneous biological knowledge via representation learning for Alzheimer's disease drug repurposing," *Iscience,* vol. 26, no. 1, 2023.

[20] Y. Qiu and F. Cheng, "Artificial intelligence for drug discovery and development in Alzheimer's disease," *Current Opinion in Structural Biology,* vol. 85, p. 102776, 2024.

[21] V. N. a. S. Ioannidis, Xiang and Manchanda, Saurav and Li, Mufei and Pan, Xiaoqin and Zheng, Da and Ning, Xia and Zeng, Xiangxiang and Karypis, George. "DRKG - Drug Repurposing Knowledge Graph for Covid-19." https://github.com/gnn4dr/DRKG/ (accessed 15 January 2024, 2024).

[22] H. T. Gümüş and C. Eyüpoğlu, "Grafik Sinir Ağlarına Genel Bir Bakış," *EMO Bilimsel Dergi,* vol. 13, no. 2, pp. 39-56, 2023.

[23] J. Zhou *et al.,* "Graph neural networks: A review of methods and applications," *AI open,* vol. 1, pp. 57-81, 2020.

Düzce University
Journal of Science & Technology

Research Article

Investigation of The Architectural Features of Traditional Houses: Samsun-Havza Case

Eda Nur KURT [a], Alper BİDECİ [b,*]

[a] *Department of Architecture, Institute of Graduate Studies, Düzce University, Düzce, TÜRKİYE*
[b] *Department of Architecture, Faculty of Art Design and Architecture, Düzce University, Düzce, TÜRKİYE*
** Corresponding author's e-mail address: alperbideci@duzce.edu.tr*
DOI: 10.29130/dubited.1560145

ABSTRACT

The Havza district of Samsun province is home to rare settlements that have preserved their cultural, socioeconomic, and architectural heritage through to the present day. The characteristics of these settlements are considered cultural heritage and should be preserved to guide future generations. In this context, the study was conducted on 10 traditional houses located in Bahçelievler and Ilıca neighborhoods. Five houses were selected from each neighborhood that are representative of unique construction techniques and material usage. Recent reinforced concrete structures were excluded from this study. The physical assessments of the settlements were conducted through on-site inspections and photographic documentation. The traditional houses were analyzed in terms of construction techniques, materials, and structural conditions. The study concluded that preserving the existing architectural fabric and improving current conditions through traditional construction techniques is essential.

Keywords: *Traditional house, Architectural features, Samsun-Havza, Construction techniques*

Geleneksel Evlerin Mimari Özelliklerinin İncelenmesi: Samsun-Havza Örneği

ÖZ

Samsun ilinin Havza ilçesi kültürel, sosyo-ekonomik ve mimari mirasını günümüze kadar koruyan ender yerleşim yerlerine ev sahipliği yapmaktadır. Bu yerleşim yerlerinin özellikleri kültürel miras olarak kabul edilmekte ve gelecek nesillere yol gösterici olması için korunması gerekmektedir. Bu kapsamda Bahçelievler ve Ilıca mahallelerinde yer alan 10 geleneksel ev üzerinde, her mahalleden kendine özgü yapım teknikleri ve malzeme kullanımını temsil eden beş ev seçilerek bir çalışma yapılmıştır. Son dönemdeki betonarme yapılar bu çalışmanın dışında tutulmuştur. Yerleşimlerin fiziki değerlendirmeleri yerinde incelemeler ve fotografik dokümantasyon yoluyla gerçekleştirilmiştir. Geleneksel evler, yapım teknikleri, malzemeleri ve yapısal koşulları açısından analiz edildi. Çalışmada mevcut mimari dokunun korunması ve geleneksel inşaat teknikleriyle mevcut koşulların iyileştirilmesinin önemli olduğu sonucuna varılmıştır.

Anahtar Kelimeler: *Geleneksel Ev, Mimari Özellikler, Samsun-Havza, Yapım Teknikleri*

Received: 02/10/2024, Revised: 21/10/2024, Accepted: 21/10/2024

I. INTRODUCTION

The unique and characteristic structures, materials, and construction techniques of traditional architecture hold significant cultural heritage and value. However, changing conditions brought about by urbanization, economic factors, and technological advancements have not only hindered the construction of such structures under contemporary conditions but also led to the disuse and eventual disappearance of existing buildings constructed with traditional techniques [1]. Various studies have emphasized the importance of traditional architecture in maintaining cultural identity and continuity [2, 3]. Yet, the challenges posed by modern development trends often result in a loss of these historically significant buildings.

In shaping architectural structures, various factors such as climate, geographical location, building materials, and beliefs play a critical role. These factors are particularly influential in determining the facade and plan layout of residential buildings [4]. Traditional houses exhibit distinct plan types and structural elements depending on the region they are located in. Studies on traditional Turkish houses suggest that spatial organization and design are closely related to the cultural and environmental context [5].

The term "Turkish House" used today primarily refers to examples from the Ottoman Empire, specifically those dating back to the 17th century. Due to changes in usage, construction materials, and various other factors over time, many examples of civil architecture, particularly traditional houses, have not been preserved [6]. In Turkish houses, the concept of creating spaces at a human scale is predominant. Based on this idea, the functional living space is defined by an upper limit. Elements such as cupboards, doors, and windows are placed below this limit, while features like shelves can extend beyond it [7].

In the context where traditional architecture developed in Anatolia, the accumulated knowledge in material traditions played a significant role in shaping new architectural traditions. Particularly in terms of building materials and technology, wood and stone reached widely accepted standards. The spaces, tools, and products developed and enriched with these materials offer a remarkably rich heritage [8, 9]. The integration of local materials and construction techniques in traditional buildings has been recognized as a crucial factor in the preservation of architectural authenticity and sustainability [10]. For example, Rapoport [11] emphasizes the role of vernacular architecture in adapting to environmental conditions and cultural practices, while Oliver [12] highlights how traditional building techniques can provide insights for sustainable architecture.

As in other provinces of the Black Sea region, wood is widely used in Samsun due to the abundance of forested areas. However, due to major fires in the history of Samsun, not many wooden structures in the city center have survived to the present day. Nevertheless, the majority of traditional architecture consists of wooden buildings [13]. The residential architecture in the Samsun region has developed under the influence of both the Eastern Black Sea and Central Anatolia regions. In the villages, square-plan houses elevated with rubble stone to protect from ground moisture are common. The northern facades of these structures often feature wooden railings and balconies. In the interior regions, such as Ladik district, traditional Anatolian architecture is represented by houses made of adobe, rubble stone, and lath-and-plaster. In Havza and Vezirköprü districts, wooden structures are prevalent [14]. Typically, these buildings are two stories above ground level. The facades are constructed of rubble brick, with interior partitions made using lath-and-plaster. The second floors often include projections, sometimes supported by two wooden columns, while in other cases, they are reinforced with iron rods. The hipped roofs, covered with traditional Turkish tiles, have wooden eaves. Inside, a central hall, or "sofa," is present, with other rooms opening onto this space. Wood is commonly used in both flooring and ceilings [15].

In this study, a total of 10 houses were examined, with five selected from each of the two neighborhoods, Bahçelievler and Ilıca, surrounding Havza district in Samsun province. The construction techniques,

materials, and structural conditions of these buildings, which were constructed using traditional methods, were thoroughly investigated to document their current state and highlight the importance of their preservation.

II. FIELD STUDY

A. SAMSUN PROVINCE AND HAVZA DISTRICT

Samsun is located in the central part of the Black Sea region, along the middle stretch of the Black Sea coast. It is bordered by Sinop to the west, Ordu to the east, and Tokat and Amasya to the south. The relatively lower elevation of the Black Sea Mountains in Central Black Sea region facilitates easy land and rail connections between Samsun and the Central Anatolia region, enhancing the city's significance. The name "Samsun" is believed to have originated from the Greek word "Amisos," although it is also suggested that the name has pre-Greek origins. Similar to neighboring Amasya, it is understood to be of Anatolian origin. The current name "Samsun" is derived from the Turkish dominance of the 7th and 8th centuries. In Western sources, the city's name appears as "Sampson." During the Ottoman period, the city was referred to as Samsun, while the district was named Canik. In the late 19th century, Samsun was administered as a subprovince within the Trabzon Vilayet. After the establishment of the Republic, it became a province bearing its own name and has since become a symbol of the War of Independence. [8].

Havza is a district in the Samsun Province. It features a terrain that is partly flat and partly mountainous. The district center is situated in a valley surrounded by mountains on three sides. Havza is located on a major road and railway that connects the coastal provinces of the Central and Eastern Black Sea regions with the Central Anatolia, Western Anatolia, and Marmara regions. To the east, it is bordered by Kavak and Ladik; to the west, by Vezirköprü; to the north, by Bafra; and to the south, by Merzifon and Suluova districts of Amasya [9].

Today, Havza has 98 neighborhoods. In Havza and its surroundings, 8 neighborhoods were selected for analysis, focusing on 5 traditional houses in each neighborhood in terms of construction techniques. The neighborhoods examined were chosen to encircle the Havza district, and they are as follows: Bahçelievler, and Ilıca. Samsun Province is seen in Figure 1 (a), and Samsun Province Havza District can be seen in Figure 1 (b).

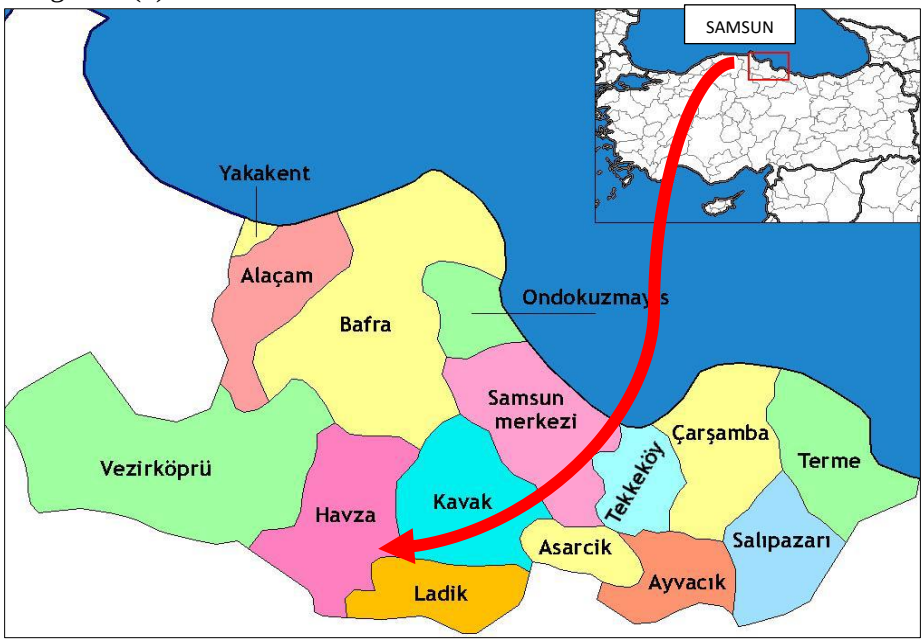

Figure 1*.Location of Samsun Province on the map of Türkiye and Location of Havza in Samsun Province*

A. 1. Neighborhoods in the Study Area

Construction technique, material and structural condition analyzes of the selected houses in Bahçelievler, and Ilıca neighborhoods located within the borders of Havza district were made.

A. 1. 1. Bahçelievler District

In Bahçelievler District, five traditional houses were examined according to construction techniques (Figure 2). It was observed that the construction techniques used in the examined houses were created with a brick or adobe filling material system inside a wooden frame.

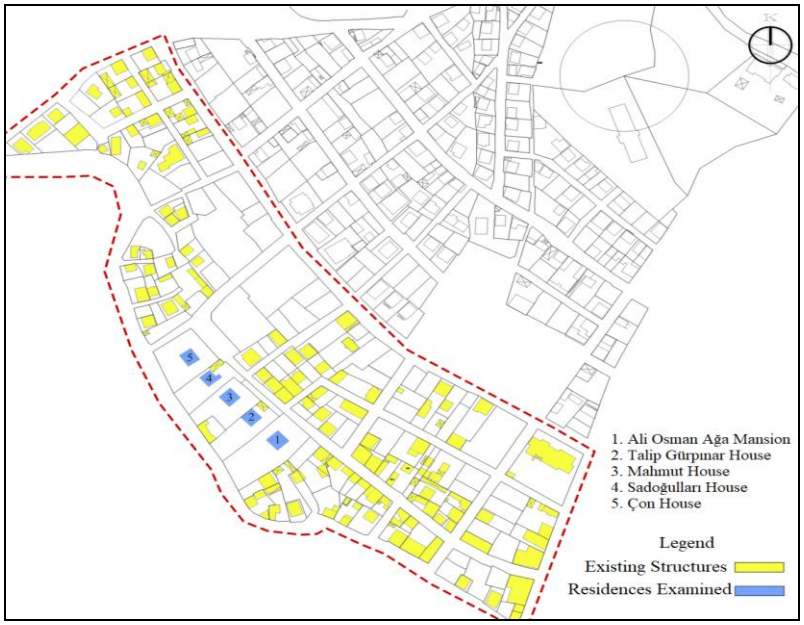

Figure 2. *Locations of the Houses Examined in Bahçelievler Neighborhood*

Ali Osman Ağa Mansion

The structure was built on a raised masonry stone base, with fired brick and adobe infill used between the wooden frame on the ground and first floors (Figure 3). Fired bricks were arranged in various patterns, such as herringbone and straight, creating an aesthetic and unique facade. The building has plaster that was applied while preserving the wooden skeleton frame, but over time, parts of the plaster have fallen off. The house has two external doors. The main entrance door is located approximately 80 cm above the ground, beneath the bay window of the structure. This entrance door is a wooden double-leaf door with an original design. The rear facade entrance door is also elevated from the ground and is a single-leaf wooden door. On both sides of the entrance door, there are symmetrical wooden sash windows. Wooden sash windows are repeated throughout most of the building. All windows in the building feature window head decorations. The windows in the bay window differ from the other windows of the building; they are more decorative and taller. The wall ornamentation above the bay window indicates that the structure was built with aesthetic concerns in mind. The windows of the building are symmetrical and aesthetic. The wooden sash window on the rear facade has been replaced with a single-leaf PVC window (Figure 4). The roof of the rectangular-shaped structure is a hip roof covered with traditional Turkish tiles.

***Figure 3**. Ali Osman Ağa Mansion*

***Figure 4**. Ali Osman Ağa Mansion window and window top ornament examples*

Talip Gürpınar House

The Talip Gürpınar House was built on a raised masonry stone base, with fired brick and adobe infill used between the wooden frame on the ground and first floors (Figure 5). The fired bricks and adobe were arranged in various patterns, such as herringbone and straight, creating a unique facade. The building features plaster applied while preserving the wooden skeleton frame; however, over time, some parts of the plaster have peeled off. The house has two external doors. The main entrance door is at ground level, located beneath a bay window. It is a double-leaf wooden door with a horizontal window above it. On the other side of the facade with the main entrance, there is a wooden double-leaf door beneath a wooden porch, which is believed to have been added later and is located 10 steps above the ground, covered with traditional Turkish tiles. The building has two bay windows. Beneath the bay window on the left side facade, there is a flat window. Throughout most of the building, wooden sash windows are repeated (Figure 6). On the ground floor, there are flat windows in addition to sash windows. The windows on the first floor feature window head decorations. The middle window decoration of the bay window above the entrance door differs from the other window decorations of the building; it is more decorative and taller. The area above the bay window was constructed using a wooden masonry method without the use of wall infill material. The windows of the building are symmetrical and aesthetic. The roof of the rectangular-shaped structure is a hip roof covered with traditional Turkish tiles.

Figure 5. *Talip Gürpınar House*

Figure 6. *Talip Gürpınar house guillotine window examples*

Mahmut House

The Mahmut House was constructed on a masonry stone foundation, with stone, adobe, and brick infill within a wooden frame on the ground floor and fired brick and adobe infill between the wooden framework on the first floor. The building has plaster applied while preserving the wooden skeleton frame; however, over time, some parts of the plaster have deteriorated. The house has one external door. The main entrance door is at ground level and located beneath a bay window. It is a double-leaf wooden door. On the rear facade of the entrance, the wooden frame structure is visible in the middle of the first floor; however, due to the considerable damage to the building, it is thought that the wooden framework system continues in the damaged area on the first floor.

Most of the windows in the building are repeated wooden sash windows. The window levels on the ground floor vary. The windows on the first floor are symmetrical and feature window head decorations, although these have been damaged over time. The middle window decoration in the bay window above the entrance door differs from the other window decorations of the building; it is more decorative and taller. Above the bay window, a triangular wooden masonry method was employed without the use of wall infill material. The roof of the rectangular-shaped structure is significantly damaged but is a hip roof. The roof is covered with traditional Turkish tiles.

Figure 7*. Mahmut House*

Sadoğulları House

The Sadoğulları House was built on a masonry stone foundation, with the ground and first floors constructed using the wooden "Bağdadi" method within a wooden framework. In the section believed to have been added later, the ground floor was built with solid brick masonry, while the first floor was constructed with fired brick infill within a wooden framework. The building features plaster applied while preserving the wooden skeleton frame, but over time, some of the plaster has deteriorated. The house has two external doors. The main entrance door is 12 steps above the ground, located under a balcony covered by a metal porch on the first floor. The entrance door is a double-leaf wooden door. There is also a single-leaf wooden door on the first floor that is exposed and cannot be accessed from outside. A horizontal window is located above the entrance door. On the front facade where the entrance is located, there are two symmetrical windows beneath the ground floor level, indicating the presence of a basement. Since entry into the building was not possible, the use of the basement area is unknown. On the rear facade of the entrance, there is a single-leaf entrance door located 7 steps above the ground. Next to the rear entrance door is a veranda under a metal porch accessible from the interior. Most of the windows in the building are paired wooden sash windows that repeat throughout. Due to numerous additions on the rear facade, this side does not appear symmetrical or decorative. In the section of the building that was added (where solid brick masonry is used on the ground floor and fired brick infill within a wooden framework is used on the first floor), the windows are flat. Generally, the windows of the building are symmetrical. The roof of the structure is a hip roof, covered with traditional Turkish tiles (Figure 7).

Figure 7*. Sadoğulları House*

Çon House

The structure was built using fired brick and adobe as infill materials between the wooden frame on both the ground and first floors. The fired bricks were arranged in different patterns, such as herringbone and straight, to create an aesthetically pleasing and unique façade. The building has two entrances. Due to the recent commencement and subsequent suspension of restoration efforts, the doors are currently missing. Both entrance doors are at ground level. The entire building features repeating wooden sash windows that are symmetrical, with decorative elements above each window. The window above the main entrance door opening is taller and serves as a distinguishing feature of the entrance. On the side façade, there is an area thought to have been a bathhouse. Additionally, a modern brick extension has been added to the continuation of the side façade. The rectangular building has a hipped roof, covered with traditional Turkish tiles (Figure 8).

Figure 8. *Çon House*

A. 1. 2. Cevizlik District

Five traditional houses in Cevizlik District have been examined according to their construction techniques (Figure 9). It was observed that the construction techniques used in these houses were timber frame and timber masonry methods.

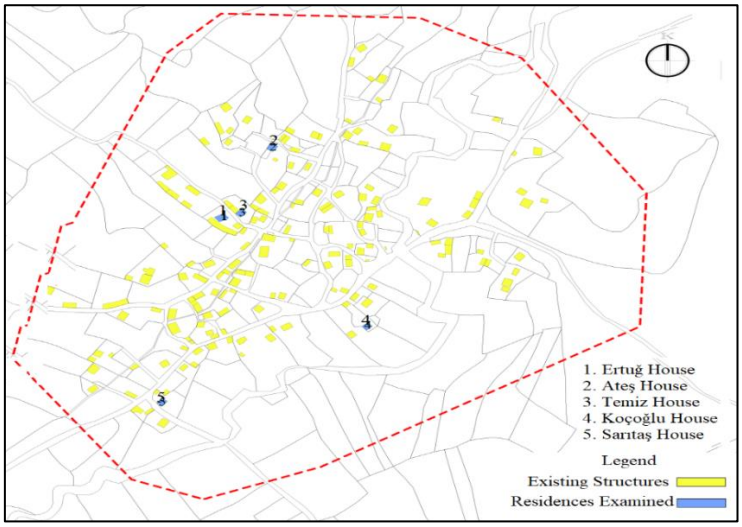

Figure 9. *Locations of the Houses Examined in Cevizlik Neighborhood*

Ertuğ House

Ertuğ house was built with a rubble stone system on the ground floor and a timber frame filled with fire brick material on the first floor. On the ground floor front façade, a hybrid construction technique was employed by using fire brick material within a timber frame instead of the rubble stone system. The fire bricks were arranged in a herringbone pattern to create an aesthetic and unique façade. The front façade of the ground floor is plastered. On the left side of the building, the ground floor beams have been extended to form a cantilevered projection on the first floor. The house has one external door. The main entrance door is three steps above the ground level and is located under the bay window. The entrance door is a double-leaf wooden door, with a square window above it. On the ground floor front façade, there is a flat wooden window. On the first floor, the wooden sash windows are aligned and symmetrical. The roof of the rectangular-shaped building is a hipped roof. The roofing material used is Turkish-style tiles (Figure 10).

Figure 10. *Ertuğ House*

Ateş House

Ateş house was constructed with a rubble stone system on the ground floor and a timber frame filled with fire brick material on the first floor. The fire bricks were arranged in a herringbone pattern, creating an aesthetic and unique façade. The front façade of the ground floor is plastered. The house has a single external door. The veranda is elevated three steps above ground level, while the main entrance door is at the same level as the ground. It is located beneath the bay window, which is supported by brackets. Above the entrance door, there is a sheet metal canopy elevated by wooden posts, which is inconsistent with the original structure. The entrance door is a single-leaf wooden door, with single-leaf wooden windows on either side. A flat wooden window is used on the front façade of the ground floor. The windows on the first floor have been replaced with PVC windows, which are inconsistent with the original structure. The rectangular-shaped building has a hipped roof, and the roofing material used is Marseille tiles (Figure 11).

Figure 11. *Ateş House*

Temiz House

Temiz house was constructed with a rubble stone system on the ground floor and a timber frame filled with fire brick material on the first floor. A hybrid construction technique was chosen for the front façade of the ground floor, using fire brick infill within a timber frame instead of the rubble stone system. The fire bricks were arranged in a herringbone pattern, resulting in an aesthetic and unique façade. The front façade of the ground floor is plastered. The house has a single external door. The main entrance door is three steps above the ground level and is located beneath the bay window. The entrance door is a double-leaf wooden door, with a small rectangular window beside it. Flat wooden windows were used on both the ground floor and the first floor. The windows are aligned and symmetrical. The rectangular-shaped building has a hipped roof, covered with traditional Turkish tiles (Figure 12).

Figure 12. *Temiz House*

Koçoğlu House

The building features a masonry stone system on the ground floor, while the first floor is constructed using a timber frame filled with wooden masonry materials. The entire structure is covered with plaster, though over time, some sections have deteriorated and peeled off. The house has three exterior doors. In addition to the main entrance, there are two single-leaf wooden doors on the first floor, opening onto a balcony made of wooden projections. The main entrance door is at ground level and is a double-leaf wooden door. The first floor features wooden sash windows. The roof, which is rectangular in shape, is a hipped roof covered with traditional Turkish tiles (Figure 13).

Figure 13. *Koçoğlu house left side facade and guillotine window*

Sarıtaş House

The building was constructed with a masonry stone system on the ground floor and a timber frame filled with fire bricks on the first floor. On the front façade of the ground floor, instead of the masonry stone system, a hybrid construction technique using fire bricks within a timber frame was preferred. The fire bricks were arranged in a herringbone pattern, creating an aesthetically unique façade. The building lacks plaster. There are two exterior doors. Due to the sloped terrain, the structure appears as two stories from the front façade and as a single story from the rear façade, with ground-level entrances on both sides. The main entrance door, a double-leaf wooden door, is located beneath a cantilevered bay window supported by brackets. The rear entrance is a single-leaf wooden door. A veranda, supported by wooden posts, was created under the alaturka tile roof at the rear, just below the roofline. In some parts of the building, damage was repaired with bricks, which are inconsistent with the original structure. Wooden casement windows are used on both the ground and first floors, aligned symmetrically. The roof of the rectangular building is a hipped roof, covered with traditional Turkish tiles (Figure 14).

Figure 14. *Sarıtaş house*

III. RESULTS AND DISCUSSIONS

The examination of traditional houses in the Samsun-Havza region revealed significant insights into their construction techniques, material use, and overall structural integrity. As expected, the majority of houses investigated were constructed using a timber frame system with a mixture of adobe, brick, and stone infill, consistent with traditional Black Sea architectural practices. The analysis was conducted on 40 houses in total, with Bahçelievler and Ilıca neighborhoods being the primary focus.

The houses in both neighborhoods exhibit a wide range of construction materials, particularly a combination of stone and timber, which aligns with the geographical characteristics of the region. It was observed that in many cases, the first floors were elevated using rubble stone to protect the wooden frames from ground moisture, a common practice in areas prone to dampness. The timber frames were filled with fire bricks arranged in aesthetically pleasing patterns, such as the herringbone design, which not only served a structural purpose but also enhanced the visual appeal of the façades. However, damage to the materials over time, particularly to the wooden elements, has been a significant concern, with improper repairs (e.g., using modern brick) altering the original design.

One of the most prominent architectural features identified was the use of bay windows, which were supported by wooden brackets. These projections, coupled with wooden sash windows, added to the aesthetic complexity of the structures. Symmetry was a key aspect of the window arrangement, contributing to the overall harmony of the façades. However, in some cases, the replacement of original

wooden windows with PVC or modern materials has disrupted the visual coherence and historical authenticity of the buildings.

The roofing materials predominantly consisted of alaturka tiles, typical of Turkish vernacular architecture, and were laid over hipped roofs. Despite their durability, several roofs showed signs of damage due to weathering and lack of maintenance, particularly in structures that had not undergone recent restoration efforts.

The study identified numerous instances where traditional construction techniques had been compromised due to unsympathetic restoration or neglect. For instance, some houses featured modern interventions that did not align with the original design principles, such as the use of brick in areas originally constructed with timber. These alterations not only impact the visual integrity of the houses but also present structural challenges, as the modern materials are often incompatible with the traditional construction methods.

IV. CONCLUSION

This study has explored the architectural features, construction techniques, and material usage of traditional houses in Bahçelievler and Ilıca neighborhoods of Samsun's Havza district. The findings highlight the significance of traditional timber frame construction and the aesthetic patterns achieved with infill materials such as brick and adobe. The careful use of local resources, combined with techniques like stone elevations to protect wooden frames from ground moisture, underscores the adaptation of architectural practices to the regional climate and geographical conditions.

The research reveals that the original structural integrity and aesthetic quality of these houses have been altered over time due to various factors, including unsympathetic restorations and the replacement of original materials with modern alternatives. Such interventions have compromised the authenticity and historical value of the traditional buildings, posing challenges for their preservation.

To maintain the cultural and architectural heritage of the region, it is recommended that restoration efforts prioritize the use of traditional materials and methods. Establishing guidelines for interventions and encouraging local participation in preservation initiatives can help safeguard these structures for future generations. The study not only contributes to the documentation and analysis of the Havza district’s traditional architecture but also offers a framework for future conservation strategies that respect the historical and cultural context of the area.

V. REFERENCES

[1] Kurt, E.N., “Investigation of Construction Techniques of Traditional Residences in Havza District of Samsun Province,” Master’s Thesis, Department of Architecture, Institute of Graduate Studies, Düzce University, Düzce, Türkiye, 2024.

[2] Ürer, H., “Geleneksel Türk Evi Ölçeğinde Eski Gediz Evlerinin Cephe Düzenlemeleri,” *Sanat Tarihi Dergisi,* c. 22, s. 2, ss.189–230, 2013.

[3] Küçükerman, Ö., *Kendi Mekanının Arayışı İçinde Türk Evi,* 2. baskı, İstanbul, Türkiye: Türkiye Turing ve Otomobil Kurumu Yayını, 1985, böl. 1, ss. 87–89.

[4] Küçükerman, Ö., *Anadolu Mirasında Türk Evleri*, 1.baskı, Ankara, Türkiye, T.C. Kültür Bakanlığı yayını, 1995, böl. 1, ss. 34–38.

[5] Duymaz, A.Ş., *19. Yüzyılda Samsun'un Kentsel Gelişimine Dair Birkaç Mimari Örnek*, 1.baskı, Samsun, Türkiye, Samsun:Kültür Yayınları, 2013, böl. 1, ss. 34–38.

[6] Aydın, M., *Samsun'da Sivil Mimarlık*, 1.baskı, İstanbul, Türkiye, Yapı Endüstri Merkezi Yayınları, 1997, böl. 1, ss. 25–29.

[7] Yiğitpaşa, N.T., and Funda, U., "A Group House Architecture in Century Samsun*", Journal of International Amisos*, vol:1, no:1, pp. 22-43, 2016.

[8] Samsun İl Özel İdaresi, *Samsun Kültür ve Turizm Envanteri*, 1. Baskı, Samsun, Türkiye, Samsun Valiliği Yayınları, 2003, böl. 1, ss. 10–12.

[9] T.C. Samsun Valiliği Kültür Müdürlüğü, *Geçmişten Günümüze Kültür Değerleriyle Samsun*, 1. Baskı, Samsun, Türkiye, Samsun Kültür Müdürlüğü Yayınları, 1997, böl. 1, ss. 21–25.

[10] Kuban, D., *Türk Hayatlı Evi: Anlamı ve İlgası*, 1. Baskı, İstanbul, Türkiye, Eren Yayıncılık, 1995, böl. 1, ss. 15–17.

[11] Rapoport, A., *House Form and Culture*, 1st ed., vol. 1, London, UK: Pearson Publisher, 1969, pp. 12-17.

[12] Oliver, P., *Built to Meet Needs: Cultural Issues in Vernacular Architecture*. 1st ed., vol. 1, Oxford, UK: Elsevier Publisher, 2006, pp. 55-69.

[13] Küçükerman, Ö., *Türk Evi: Osmanlı Dönemi Geleneksel Sivil Mimarlığı*, 1.baskı, İstanbul, Türkiye, Türkiye Turing ve Otomobil Kurumu Yayınları, 1978, böl. 1, ss. 11–13.

[14] Akın, G., "Anadolu'da Geleneksel Ev Mimarisi ve Korunması Üzerine Bir Değerlendirme." *Türk Sanatı ve Kültürü Araştırmaları Dergisi*, c. 7, s. 1, ss. 34-48, 2001.

[15] Sönmez, N., *Anadolu'da Geleneksel Ahşap Yapılar*, 1.baskı, Ankara, Türkiye, Atatürk Kültür, Dil ve Tarih Yüksek Kurumu Yayınları, 1998, böl. 1, ss. 21–23.

Düzce University
Journal of Science & Technology

Research Article

Modeling and Control of a Novel Permanent Magnet Linear Motor

Uğur HASIRCI [a,*], Ziya DEMİRKOL [b]

[a] *Department of Electrical and Electronics Eng., Düzce University, Düzce, TURKEY*
[b] *Department of Electronics and Automation, Kastamonu University, Kastamonu, TURKEY*
** Corresponding author's e-mail address: ugurhasirci@duzce.edu.tr*
DOI: 10.29130/dubited.1548730

ABSTRACT

This paper concerns on modeling and linear controller design of a novel permanent magnet DC linear motor. The paper first introduces the novelty of designed and implemented motor, and then presents its dynamical model. By using the developed model, a linear controller has been designed and the results of the numerical simulation of the designed controller have been presented to show the effectiveness and stability of the designed controller. Some future prospects for the designed and simulated controller have also been provided.

Keywords: *Permanent Magnet DC Linear Motors, Controller Design, Simulation*

Yeni Bir Kalıcı Mıknatıslı Lineer Moturun Modellenmesi ve Kontrolü

ÖZ

Bu çalışma, yeni bir kalıcı mıknatıslı DC lineer motorun modellenmesi ve bu motor için lineer kontrolör tasarımı üzerinedir. Makalede ilk önce, tasarlanan ve üretilen yeni motor tanıtılmış ve motorun dinamik modeli elde edilmiştir. Geliştirilen bu model üzerinden bir lineer kontrolör tasarlanmıştır ve daha sonra tasarlanan kontrolörün etkinliğini ve kararlılığını göstermek amacıyla nümerik simülasyon sonuçları sunulmuştur. Son olarak da bu kontrolör bazı gelecek önerileri sunulmuştur.

Anahtar Kelimeler: *Kalıcı Mıknatıslı DC Lineer Motorlar, Kontrolör Tasarımı, Simülasyon*

Received: 11/09/2024, Revised: 23/10/2024, Accepted: 24/10/2024

I. INTRODUCTION

Electric motors convert electrical energy into mechanical motion. Conventional rotary motors produce rotary motion. If linear motion is needed, then there are two basic options; either using some equipment like gears and belts to convert rotary motion into linear motion, or using directly a linear motor. Either options have some advantages and disadvantages, for example, the gears and belts bring mechanical losses and extra costs while the linear motors bring stroke limitations. Less force/current ratio compared to the conventional rotary motors is another disadvantage of the linear motors. To contribute overcoming such limitations, a completely new linear motor has been proposed [1] and patented [2]. It has no stroke limitations and also high force/current ratio. To clearly reveal the advantages this motor offers, a useful review of the pertinent available literature on the linear motors have been provided below.

Linear motors are widely used in industry. Some areas of applications are 3D printers [3], maglev trains [4], elevators [5], CNC systems [6], and automatic doors [7]. Just like the rotary motors, the linear motors can be classified as DC Linear Motor, AC Linear Motors, and Synchronous Linear Motors. First DC Linear Motor is proposed in 1964 [8]. But there were wounds on both rotor and stator in this motor, i.e., no permanent magnets had been used. Starting from 1970's, permanent magnets have been widely used in the linear motors since they reduce motor volume, increase the motor efficiency, and lead to less cost for fixed force value. Figure 1 shows a basic sketch of a moving-magnet DC Linear Motor, which is called a single-sided DC Linear Motor, since permanent magnets are placed on only one side of the stator, the stationary part [1]. If another group of the permanent magnets are placed on the other side of the stator to produce higher force, this configuration is called double-sided. The configuration in Figure 1 is also called flat, since it is geometry is flat, but if both stator and rotor is produced in a tubular geometry to produce higher force, this is called a permanent magnet tubular DC Linear Motor.

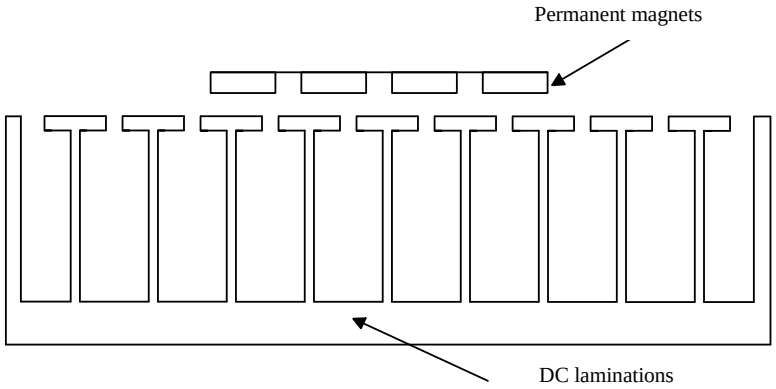

Figure 1. *A sketch of a permanent magnet DC linear motor*

The principal benefit that a linear motor offers is the elimination of the extra equipment to convert rotary motion into linear motion. But, on the other hand, there are some disadvantages of this type of motors. Besides the some other disadvantages, historical development of the DC linear motors dictates two basic disadvantages; (1) low force-current ratio, (2) limitation on motor stroke (length of the stator). The first permanent magnet DC Linear Motor has been proposed by Basak in 1975 [9]. This motor has a length of 45 cm, and produces 1.5 N force per 1 A. These two values are especially important to explain both improvements in permanent magnet DC linear motor technology and the benefit of the motor to be controlled in this study. It is especially because that these values are quite low and many researchers have focused on the design and implementation of novel DC Linear Motors to improve these values. To contribute these improvement efforts, several motors of same type used in this study have been proposed and their force/current ratios have been reported. For example, for 1 A current, the developed force is 2.67 N in [10], 27 N in [11], 1 N in [12], 7.8 N in [13], 1 N [14], and 24 N in [15]. A very recent study [16] reports generation of 27 N force per ampere. Reported experimental results clearly show that there

is still a need to improve force/current ratio for this type of motor to be able use them for some special applications like electromagnetic launchers.
In 2023, a completely novel permanent magnet DC linear motor has been designed, implemented and tested [1-2]. This motor has a tubular geometry, as shown in Figure 2. Moving unit, armature or rotor, has two parts; upper shaft and lower shaft, both made by using 1010 mild steel material, and includes Neodymium-Ferro-Boron permanent magnets. The armature is moving through 4 cylindrical bar via linear bearings. Stationary part, stator, again made by using 1010 mild steel material, and includes wounds. Terminals of each coil are connected to the collector, also called commutator, to carry the current flowing through coils by using brushes.

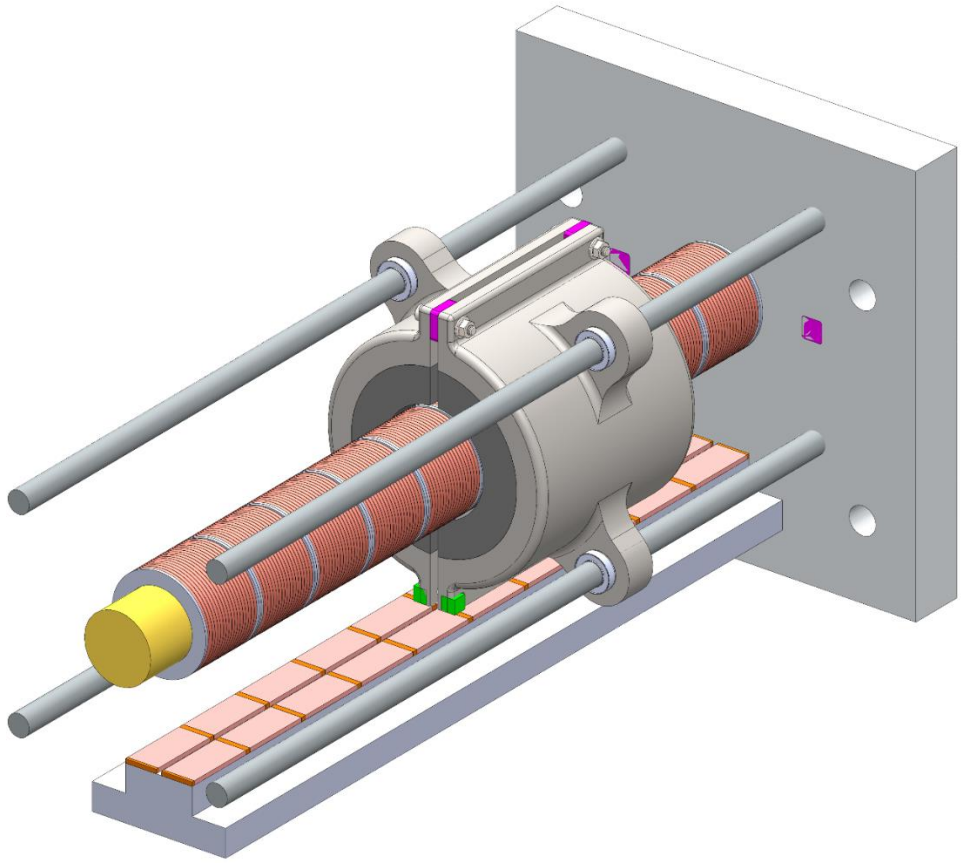

Figure 2. *A 3D sketch of a novel permanent magnet DC linear motor*

Experimental test results reported in [1] shows that the motor introduced above develops 195 N force per 1 A. Such a force/current ratio makes this motor an inspring solution to the problem of high-force need for some types of special applications. Another benefit this motor offers is drive mechanism simplicity, i.e., there is no need to complex drive circuit if the stator is fabricated longer. When more coils are used at the stator to get more stroke, only need is more collector cell instead of using complex power electronics circuits. So the introduced motor produces a solution to two basic problems of permanent magnet DC linear motors, i.e., the motor produces high force/current ratio and eliminates the complex drive mechanism to get longer stroke. More analytical, magnetic, and thermal analysis results and experimental data can be found in [17] for this motor.

Figure 3 shows an implemented form of the motor. This figure also shows the components of the test systems of the motor. The motor is supplied by a DC power source via a drive system and all the measurement results have been assigned to variable defined in MATLAB/Simulink environment. Position of the motor has been measured by a linear potentiometer, developed force has been measured by a Loadcell, and, current flowing through the armature wounds has been measured by a proper current sensor. By using the setup introduced in Figure 3, time variations of the developed force, armature

current, and armature position have been recorded. Figure 4, for example, shows the developed static force versus position.

Figure 3. *Test setup*

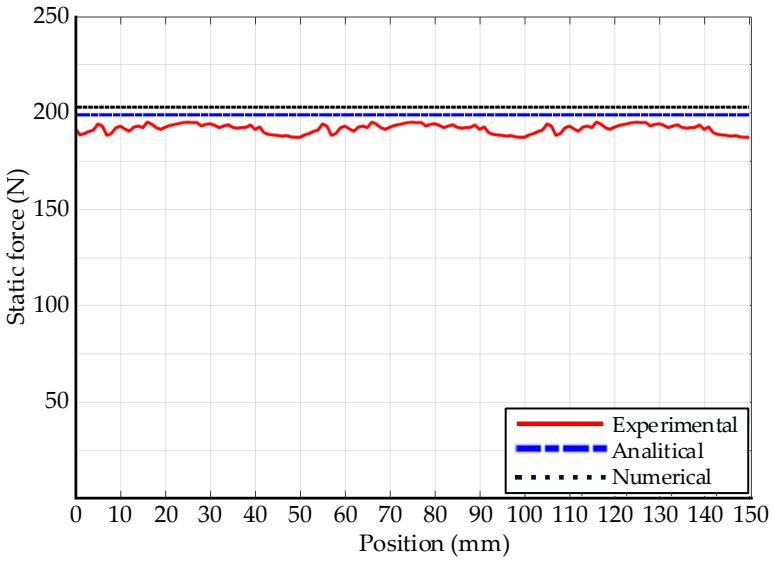

Figure 4. *Developed force with respect to position*

Figure 4 shows that numerical, analytical, and experimental results are in good compliance. The figure also shows that the developed force hits 195 N experimentally. Control of this novel motor is the main focus of this paper. Position, speed, current, and force control of the motor have potential for proving feasibility of the motor for some type of special applications. Even if there are many studies on the brushless DC linear motor control [18-23], there are only a few studies on control of brushed DC linear motor since brush mechanism brings fault risk and maintenance requirements. But, on the other hand, some special applications especially needs brushed motor. For example, DC electromagnetic launchers need a brush mechanism since the energy can not be transferred from the stationary part to moving part via induction, that is, a physical contact between two parts is a must in DC electromagnetic launchers. For this reason, brushed DC linear motors need more effort on control of position, speed, current, and force to prove the performance and feasibility of this type of motors for some special applications like DC electromagnetic launchers.

The rest of the paper is organized as follows: Chapter II defines the control problem by introducing the system model. It is important to point out that only linear control design by using a linear model of the system will be used in this study. Nonlinear control of the motor is out of scope of this study. Chapter III presents a controller design by using a linear model. Chapter IV provides an observer design. Numerical simulation results of the designed controller and observer are given in Chapter V. The last section concludes all the results with some future prospect.

II. CONTROL PROBLEM DEFINITION

Dynamical state-space model of a permanent magnet brushed DC linear motor can be expressed as [17]

$$\frac{di_a(t)}{dt} = -\frac{R}{L}i_a(t) - \frac{K}{L}v(t) - \frac{1}{L}e(t) \quad (1)$$

$$\frac{dv(t)}{dt} = \frac{K}{M}i_a(t) - \frac{\alpha}{M}v(t) \quad (2)$$

where $i_a(t)$, armature current (A), and $v(t)$, armature speed (m/sec), are the state variables, $e(t)$, armature voltage (V), is the control input signal. The parameters are R, coils resistance (Ω), L, coil inductance (H), α, viscous friction coeeficient, K, force coefficient (N/A), and M, mass of the moving part (kg). In vector-matrix form, the system model can also be expressed as

$$\begin{bmatrix} \frac{di_a(t)}{dt} \\ \frac{dv(t)}{dt} \end{bmatrix} = \begin{bmatrix} -\frac{R}{L} & -\frac{K}{L} \\ \frac{K}{M} & -\frac{\alpha}{M} \end{bmatrix} \begin{bmatrix} i_a(t) \\ v(t) \end{bmatrix} + \begin{bmatrix} -\frac{1}{L} \\ 0 \end{bmatrix} e(t) \quad (3)$$

$$y = [0 \quad 1] \begin{bmatrix} i_a(t) \\ v(t) \end{bmatrix} \quad (4)$$

where linear model is considered under no-load condition. An experimental study to determine the exact values of the parameters in the dynamical model given above has been presented in [24]. Due to lack of space, details of the determination process have not been presented here. By using the experimental values given in [24], the model given above can be represented as

$$\begin{bmatrix} \frac{di_a(t)}{dt} \\ \frac{dv(t)}{dt} \end{bmatrix} = \begin{bmatrix} -391.11 & -4444.44 \\ 12.60 & -4.46 \end{bmatrix} \begin{bmatrix} i_a(t) \\ v(t) \end{bmatrix} + \begin{bmatrix} -22.22 \\ 0 \end{bmatrix} e(t) \quad (5)$$

$$y = [0 \quad 1] \begin{bmatrix} i_a(t) \\ v(t) \end{bmatrix} \quad (6)$$

since the parameter values are R=17.6 Ω, L=45 mH, K=200 N/A, M=15.88 kg, =200 N/A, and α=70.91. The eigenvalues of the system matrix given in Eq. (5) are $\lambda_{1,2}$=−2±j1.36. This necessarily means that the system is inherently stable since its eigenvalues have negative reals parts. Even so, the system should be controlled to ensure that the system satisfies a predefined performance specifications. So the first control problem can be defined as "*for the system given in Eqs. 5&6, design the control input signal, $e(t)$, to ensure that the system has 0.1 second settling time and 10% percent overshoot for step input*".

Note that one of the state variables is the speed of the motor. Generally speaking, speed of a DC motor is measured by taking the time derivative of position information taking by using a position sensor. But numerical derivation adds noise to the system. This may lead chattering, one of the most important problems in electromechanical system. For this reason, after presenting the design of a controller for the problem defined above, an observer design for the estimation of the speed of the motor to avoid chattering problem is also presented. Instead of defining it as a control problem, an observation problem can be defined as follows: "*for the system given in Eqs. 5&6, design an observer with observation performance of 0.02 second settling time and %20 percent overshoot for step input".* In the observer design, it will be assumed that the both state variables are not available for measurement. The following chapter provides a control design algorithm step-by-step for the defined control problem. Full state feedback is used in the controller design. Chapter IV shows the design of a Luenberger Observer for the

observation problem defined above. Simulation results of the controller and observer have also been provided to show the performance and feasiblity of the designed controller and observer.

III. CONTROLLER DESIGN

To be able to design a state-feedback controller for the system given in Eqs. 5&6, first the controllability of the system must be checked. The controllability matrix,

$$\boldsymbol{P_C} = [\boldsymbol{B}\ \boldsymbol{AB}] = \begin{bmatrix} -22.22 & 8690.5 \\ 0 & -279.97 \end{bmatrix} \tag{7}$$

is full rank since its determinant equals 6221. So the system is controllable and a state-feedback controller can be designed for it. Since the system order is 2, then the state feedback controller will have the form

$$e(t) = u(t) = -\boldsymbol{K}\boldsymbol{x}(\boldsymbol{t}) = [K_1 \quad K_2]\begin{bmatrix} x_1(t) \\ x_2(t) \end{bmatrix} = -K_1 x_1(t) - K_2 x_2(t) = -K_1 i_a(t) - K_2 v(t) \tag{8}$$

where $u(t)$ is the control input signal, and $\boldsymbol{K} = [K_1 \quad K_2]$ is the controller gain vector. To find the values of the control gains, K_1 and K_2, a standard derivation for the linear time-invariant systems can be used. Consider the general form of the state equation for a linear time-invariant system:

$$\dot{\boldsymbol{x}} = \boldsymbol{A}\boldsymbol{x} + \boldsymbol{B}u \tag{9}$$

If the control input signal, $u(t)$, is designed as in Eq. (8), i.e., $u(t) = -\boldsymbol{K}\boldsymbol{x}(\boldsymbol{t})$**,** then the final form of the state equation will be

$$\dot{\boldsymbol{x}} = (\boldsymbol{A} - \boldsymbol{BK})\boldsymbol{x} \tag{10}$$

To be able to say that the vector differential equation given in Eq. (10) is bounded, i.e., stable, the necessary and sufficient condition is the eigenvalues of the newly-formed system matrix, $(\boldsymbol{A} - \boldsymbol{BK})$, must have negative real parts [25]. Investigating this matrix yields

$$\boldsymbol{A} - \boldsymbol{BK} = \begin{bmatrix} 22.22K_1 - 391.11 & 22.22K_2 - 4444.44 \\ 12.6 & -4.46 \end{bmatrix} \tag{11}$$

and its eigenvalues are

$$\det(s\boldsymbol{I} - (\boldsymbol{A} - \boldsymbol{BK})) = s^2 + (395.57 - 22.22K_1)s + (57744 - 280K_2 - 99K_1) \tag{12}$$

To design the control gains, the general form of the characteristic equation of second-order systems with pre-defined control objective given in Chapter II can be used. "*0.1 second settling time and 10% percent overshoot"* yields a damping ratio of $\varphi = 0.591$ and a natural frequency of $\omega_n = 67.68$ rad/sec. So the characteristic equaiton will be

$$s^2 + 2\varphi\omega_n s + \omega_n^2 = s^2 + 80s + 4578.40 \tag{13}$$

By considering Eqs. (12) and (13) together, the values of the control gains are found as $K_1 = 14.2$ and $K_2 = 184.84$. So the control gain matrix will be in the form of

$$\boldsymbol{K} = [K_1 \quad K_2] = [14.2 \quad 184.84] \tag{14}$$

and the control input signal, which is the voltage to be applied to the motor, will be in the form of

$$e(t) = -K_1 i_a(t) - K_2 v(t) = -14.20 i_a(t) - 184.84 v(t) \tag{15}$$

Numerical simulation of the designed controller will be given in Section V.

IV. OBSERVER DESIGN

For some type of applications, the state variables may not be available for measurements, or, even if they are available for measurement, measuring some state variable may add considerable noise to the system. This noise may lead to chattering, which is one of the most important problems in electromechanical systems. For the system considered in this study, one of the state variables is speed of the moving part, the armature. The easiest way to measure it is to measure the position of the armature by using some sensors and then taking time derivative of position information. But numerical derivation generally adds noise to the system. This may lead to fluctuation in control input signal, which is the voltage to be applied to the motor. So an observer to estimate the dynamic values of the state variables may be needed. In this study, a full-state uncertainty will be considered and a Luenberger Observer [25] will be designed to estimate the state variables.

To be able to design an observer for the system given in Eqs. 5&6, first the observability of the system must be checked. The observability matrix,

$$P_o = [\boldsymbol{C}\ \boldsymbol{CA}]^T = \begin{bmatrix} 0 & 1 \\ -12.60 & -4.46 \end{bmatrix} \tag{16}$$

is full rank since its determinant equals -12.60. So the system is observable and an observer can be designed for it. General form of the Luenberger Observer for linear time-invariant systems is

$$\frac{d}{dt}\hat{\boldsymbol{x}} = \boldsymbol{A}\hat{\boldsymbol{x}} + \boldsymbol{B}u + \boldsymbol{L}(\boldsymbol{y} - \boldsymbol{C}\hat{\boldsymbol{x}}) \tag{17}$$

where $\hat{\boldsymbol{x}}$ is estimation of state vector, $\boldsymbol{x}$, and $\boldsymbol{L}$ is the observer gain matrix in the form of $\boldsymbol{L} = [L_1 \quad L_2]^T$ since the system is second-order. To quantify the observation performance of the observer to be designed, an observation error signal can be defined as

$$\boldsymbol{e} = \boldsymbol{x} - \hat{\boldsymbol{x}} \tag{18}$$

Note that if the error signal given in Eq. (18) goes to zero, this necessarily means that $\hat{\boldsymbol{x}} \to \boldsymbol{x}$, i.e., estimated values of the state variables go to their real values. To ensure that it goes to zero, its dynamics can be investigated as

$$\dot{\boldsymbol{e}} = \dot{\boldsymbol{x}} - \frac{d}{dt}\hat{\boldsymbol{x}} \tag{19}$$

and if Eq. (17) is substituted into Eq. (18), it results in

$$\dot{\boldsymbol{e}} = (\boldsymbol{A} - \boldsymbol{LC})\boldsymbol{e} \tag{20}$$

where the output equation of a single-input single-output system, $y = \boldsymbol{Cx}$, has been subtituted into Eq. (19) also. To be able to say that the vector differential equation given in Eq. (19) is bounded, i.e., stable, the necessary and sufficient condition is the eigenvalues of the newly-formed system matrix, $(\boldsymbol{A} - \boldsymbol{LC})$, must have negative real parts [25]. Investigating this matrix yields

$$\boldsymbol{A} - \boldsymbol{LC} = \begin{bmatrix} -391.11 & -L_1 - 4444.44 \\ 12.6 & -L_2 - 4.46 \end{bmatrix} \tag{21}$$

and its eigenvalues are

$$\det(s\boldsymbol{I} - (\boldsymbol{A} - \boldsymbol{LC})) = s^2 + (395.57 + L_2)s + (57744 + 391.11L_2 + 4.46L_1) \tag{22}$$

To design the observer gains, the general form of the characteristic equation of second-order systems with pre-defined control objective given in Chapter II can be used. "*0.02 second settling time and %20 percent overshoot"* yields a damping ratio of $\varphi = 0.455$ and a natural frequency of $\omega_n = 438.64$ rad/sec. So the characteristic equaiton will be

$$s^2 + 2\varphi\omega_n s + \omega_n^2 = s^2 + 400s + 192410 \tag{23}$$

By considering Eqs. (22) and (23) together, the values of the observer gains are found as $L_1 = 29985$ and $L_2 = 4.43$. So the observer gain matrix will be in the form of

$$\boldsymbol{L} = [L_1 \quad L_2]^T = [29985 \quad 4.43]^T \tag{24}$$

Numerical simulation of the designed observer will be given in Section V.

V. NUMERICAL SIMULATION

All the numerical simulations are done by using MATLAB/Simulink environment. Values of the controller and observser gains are set to the values found in Sections III and IV, respectively. All the system parameter values are set to the values as in [24], also given in Section II. Figure 5 shows the step response of the designed closed-loop system. As shown in the figure, percent overshoot is 10%, as predescribed, and settling time is 0.0876, less than predescribed 0.1, due to rounding errors.

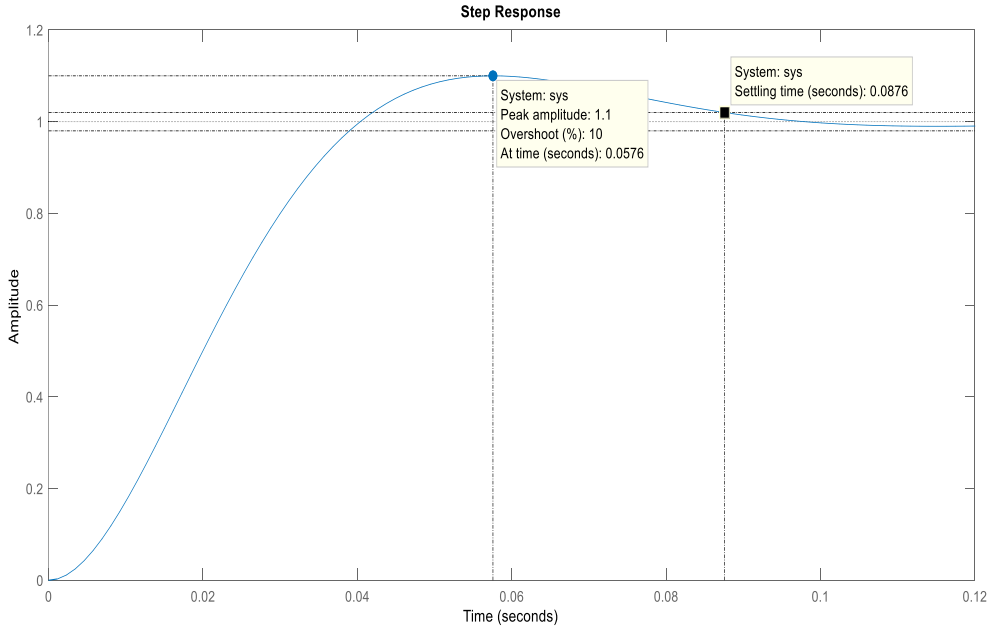

Figure 5. *Step response of the designed closed-loop system*

Figure 6 shows the step response of the designed observer dynamics. As designed, the percent overshoot is 20%. Settling time is 0.019, less than predescribed 0.02 due to rounding errors. Note that its final value is 1, which means the designed observer guarantees that it estimates the unmeasurable state variables with zero observation error while time goes to infinity, with a settling time of 0.019 second and a percent overshoot of 20%. It is worthy to point out that these performance criterion, percent overshoot of 20% and settling time of 0.02 second, is quite forcing values for an electromechanical

system, which leads high observer gain values. One can also choose performance values as less forcing values, which leads smaller observer gain values.

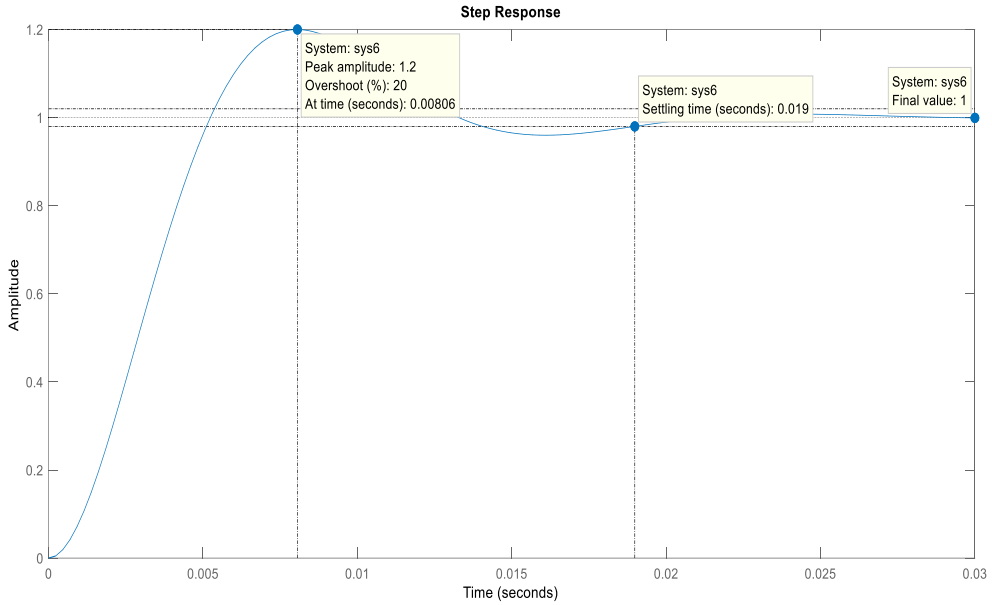

Figure 6. *Step response of the designed closed-loop observer*

VI. CONCLUSION

A state-feedback controller and full-state observer have been designed for a novel permanent magnet DC linear motor. Designed state-feedback controller guarantees that the closed-loop system has specifications of 0.1 second settling time and 10% percent overshoot. In addition, the designed observer guarantees that observation error will converge to zero while time goes to infinity. In this way, a controller design will be possible even if the state variables are not available for measurement. The designed Luenberger Observer also has performance specifications of 0.02 settling time and 20% percent overshoot, which are very challenging and leads to large values of observer gains. Numerical simulation results obtained by using MATLAB/Simulink environment proves the performance and feasibility of both the controller and observer.

Some future prospects should also be worthy to point out. Designed and simulated controller can be implemented by using a proper software and hardware combination. Such an experiment will add value to the proof of performance and feasibility of the controller designed in this study. Some other types of feedback or feedforward control methods could also be considered.

In addition, the observer design can also be implemented to show the real-time performance and feasibility of the estimation scheme introduced in this study. Even if the Luenberger Observer is the most common and well-known observer type for a second-order system, some alternative observation schemes could also be considered.

Note that the dynamical model given in Eqs. (1) and (2) is linear. Nonlinear model of the permanent magnet DC linear motor introduced in this study can also be used to design some nonlinear controllers with better performance. Design of such a nonlinear controller is the authors' current interest. This will also lead to need of designing a nonlinear state observer for this system. So the nonlinear observer design and implementation is another future prospect.

V. REFERENCES

[1] Z. Demirkol, U. Hasirci, and R. Demirci, "Design, implementation and test of a novel cylindrical permanent magnet DC linear motor," *Energies*, vol. 16, no. 8, pp. 1-17, 2023.

[2] Z. Demirkol, U. Hasirci, and R. Demirci, Bir Doğrusal Motor, Patent, 2023.

[3] F. Tarak, "Doğrusal (Lineer) motorlu endüstriyel sistemin 3 boyutlu yazıcıya dönüştürülmesi", Yüksek Lisans Tezi, Mekatronik Mühendisliği Bölümü, İstanbul Teknik Üniversitesi, İstanbul, Türkiye, 2021.

[4] U. Hasirci, A. Balikci, Z. Zabar, and L. Birenbaum, "A novel magnetic levitation system: design, implementation, and nonlinear control," *IEEE Transactions on Plasma Sciences*, vol. 39, no. 1, pp. 492–497, 2011.

[5] O. O. Oruç ve F. Dikmen, "Lineer motorlu engelli asansör tasarımı," *Kocaeli Üniversitesi Fen Bilimleri Dergisi*, c. 3, s. 1, ss. 110-113, 2020.

[6] S. Gordon, and M. T. Hillery, "Linear motor based high speed CNC milling machine," *33rd International MATADOR Conference*, 2000, pp 519–524.

[7] M. Ekmekçi, "Otomatik açılıp kapanan kapılar için tüp tipi indüksiyon motor tasarımı", Yüksek Lisans Tezi, Elektrik Eğitimi Bölümü, Gazi Üniversitesi, Ankara, Türkiye, 2006.

[8] R. Demirci, "Adaptive control of DC linear motors", PhD dissertation, Electrical Engineering Department, University of Cardiff, Cardiff, United Kingdom, 1998.

[9] A. Basak, "An investigation of DC linear motor.", PhD dissertation, Electrical Engineering Department, Wales University, Brighton, United Kingdom, 1975.

[10] H. Yajima, H. Wakiwaka, S. Senoh, H. Yamada, and J. Oda, "Optimum design of a long stroke thin linear DC motor," *Electrical Engineering in Japan*, vol. 118, no. 1, pp. 84–93, 1997.

[11] H. Yajima, H. Wakiwaka, K. Minegishi, N. Fujiwara, and K. Tamara, "Design of linear DC motor for high-speed positioning," *Elsevier Sensors and Actuators*, vol.81, no. 1, pp. 281–284, 2000.

[12] R. C. Okonkwo, "Design and performance of permanent-magnet DC linear motors," *IEEE Transactions on Magnetics*, vol. 42, no. 9, pp. 2179–2183, 2006.

[13] R. Demirci, and M. Dursun, "Adaptive position controller for double armature brushless dc linear motor," *International Conference on Electrical Machines*, 2000, pp. 1-6.

[14] A. Basak, and A.F.F. Filho, "The design and analysis of a novel brushless DC linear motor," *Journal of Magnetism and Magnetic Materials*, vol. 133, no. 3, pp. 640–643, 1994.

[15] J. Wang, W. Wang, and K. Atallah, "A linear permanent-magnet motor for active vehicle suspension," *IEEE Transactions on Vehicle Technologies*, vol. 60, no. 1, pp. 55–63, 2011.

[16] A. Farhadi, H. Yousefi, Y. Norollahi, and A. Hajinezhad, "A comprehensive analysis on a novel DC-excited flux-switching linear motor as a new linear vehicle for transportation systems," *IET Electric Power Applications*, vol 17, no. 1, pp. 36–46, 2023.

[17] Z. Demirkol. "Tübüler DC lineer motor tasarımı ve denetimi," Doktora Tezi, Elektrik-Elektronik ve Bilgisayar Mühendisliği Bölümü, Düzce Üniversitesi, Düzce, Türkiye, 2023.

[18] I. Davoudkhani, and M. Akbari, “Adaptive speed control of brushless DC (BLDC) motor based on interval type-2 fuzzy logic,” *24th Iranian Conference on Electrical Engineering (ICEE)*, 2016, pp. 1119-1124.

[19] Y. Zheng, W. Jiang, and Z. Zhang, “Characteristic model-based speed adaptive control design of permanent magnet brushless DC motor,” *IEEE 5th International Conference on Power, Intelligent Computing and Systems (ICPICS)*, 2023, pp. 1-6.

[20] A. V. Stepanov, and V. N. Enin, “Sensorless control of low-power brushless DC motor based on the use of back-emf,” *International Ural Conference on Electrical Power Engineering (UralCon)*, 2019, pp. 1-5.

[21] N. N. Baharudin, and S. M. Ayob, “Brushless DC motor drive control using Single Input Fuzzy PI Controller (SIFPIC),” *IEEE Conference on Energy Conversion (CENCON)*, 2015, pp. 13-18.

[22] W. Han, B. Gao, and H. Guo, “Finite time synchronization of fractional-order brushless DC motor systems by soft variable structure control,” *33rd Chinese Control and Decision Conference (CCDC)*, 2021, pp. 218-223.

[23] N. Zhang, and G. Chen, “Speed tracking of brushless DC motors with load disturbance,” *15th International Conference on Control, Automation, Robotics and Vision (ICARCV)*, 2019, pp. 779-782.

[24] Z. Demirkol ve U. Hasirci, “Sürekli Mıknatıslı Tübüler DC Lineer Motor Parametrelerinin Belirlenmesi,” *Selçuk 9. Uluslararası Uygulamalı Bilimler Kongresi*, Konya, Türkiye, 2023, ss. 370-377.

[25] N. S. Nise, *Control Systems Engineering*, 4th ed., New Jersey, USA: John Wiley & Sons, 2024, pp. 471-473.

Düzce University
Journal of Science & Technology

Research Article

The Role of Self-Assembly Monolayers (SAM) on Schottky Diode Performance

Adem MUTLU [a,*], Cem TOZLU [b], Mustafa CAN [b]

[a] *Solar Energy Institute, Ege University, İzmir, TÜRKİYE*
[b] *Graphene Application and Research Center, İzmir Katip Celebi University, İzmir, TÜRKİYE*
** Corresponding author's e-mail address: adem.mutlu@ege.edu.tr*
DOI: 10.29130/dubited.1530876

ABSTRACT

This study investigates the electrical and charge transport properties of Schottky diodes with a p-Si/TiO_2/SAM/Al structure, incorporating the self-assembly monolayers (SAMs) 4", 4""-[biphenyl-4,4"-diylbis(phenylimino)]dibiphenyl-4-carboxylic acid (MZ187) onto a titanium dioxide (TiO_2) layer synthesized via the sol-gel method. The impact of the MZ187 molecule on diode performance was evaluated based on parameters such as the barrier height ($Ø_b$), ideality factor (n), and series resistance (R_s). Experimental results reveal that the MZ187 monolayers on TiO_2 substantially enhanced diode performance, reducing the n from 3.7 for the control diode to 2.7 for the MZ187-modified diode. The R_s was also significantly reduced, while the $Ø_b$ increased. The rectification ratio increased from $1.3x10^2$ for the control diode to $2.2x10^3$ for the MZ187 modified diode. These improvements are attributed to the ability of MZ187 molecules to minimize interface states (N_{ss}) and improve surface quality. These findings underscore the critical role of SAMs in optimizing Schottky diode performance and demonstrate how the MZ187 molecule enhances diode efficiency by altering interface properties. The effectiveness of SAM coatings in enhancing Schottky diode performance makes a significant contribution to the field of nanoelectronics. This research paves the way for future studies on the use of SAMs in various nano electronic applications and offers promising potential for improving the performance and reliability of these technologies.

Keywords: *Schottky diode, sol-gel TiO_2, self-assembly monolayer, electrical characterization, interfaces, surface modification*

Kendiliğinden Organize Olan Tek Tabaka Moleküllerin (SAM) Schottky Diyot Performansı Üzerindeki Rolü

ÖZ

Bu çalışma, p-Si/TiO_2/SAM/Al yapısına sahip Schottky diyotlarının elektriksel ve yük taşıma özelliklerini incelemektedir. Schottky diyotları, sol-jel yöntemiyle sentezlenen titanyum dioksit (TiO_2) tabakasına, kendiliğinden organize olan monolayer (SAM) molekülü olan 4",4" "-[bifenil-4,4" -diylbis(fenilimino)]dibifenil-4-karboksilik asit (MZ187) uygulanarak üretilmiştir. MZ187 molekülünün diyot performansı üzerindeki etkisi, idealite faktörü (n), seri direnci (R_s) ve bariyer yüksekliği ($Ø_b$) gibi parametreler üzerinden değerlendirilmiştir. Deneysel sonuçlar, TiO_2 üzerinde monolayer MZ187 kaplamasının diyot performansını önemli ölçüde iyileştirdiğini göstermektedir. Kontrol diyot için 3.7

Received: 13/08/2024, Revised: 23/10/2024, Accepted: 30/10/2024

olan *n*, MZ187 modifiye diyot için 2.7'ye düşmüştür. R_s, MZ187 nedeniyle azalmış ve $\emptyset_b$ artmıştır. Doğrultma oranı, kontrol diyot için $1.3x10^2$'den MZ187 modifiye diyot için $2.2x10^3$'e yükselmiştir.
Bu iyileşmeler, MZ187 moleküllerinin arayüzey durumlarını (N_{ss}) minimize etme ve yüzey özelliklerini geliştirme yeteneğine atfedilmektedir. Bu çalışma, SAM'ların Schottky diyot performansını optimize etmedeki kritik rolünü vurgulamakta ve MZ187 molekülünün arayüzey özelliklerini değiştirerek diyot verimliliğini nasıl iyileştirdiğini göstermektedir. SAM kaplamalarının Schottky diyot performansını artırmadaki etkinliği, nanoelektronik alanına önemli katkılar sağlamaktadır. Bu araştırma, SAM'ların çeşitli nanoelektronik uygulamalarda kullanımına yönelik gelecekteki çalışmalara temel oluşturmakta ve bu teknolojilerin performansını ve güvenilirliğini artırmada umut verici etkiler sunmaktadır.

Anahtar Kelimeler: *Schottky diyot, sol-gel TiO_2, kendiliğinden organize olan tek tabaka, elektriksel karakterizasyon, arayüzeyler, yüzey modifikasyonu*

I. INTRODUCTION

Metal/insulator/semiconductor (MIS) contacts play a crucial role in semiconductor device technology and significantly influence the stability and performance of these devices. The behavior of these devices is determined by the characteristics of the semiconductor/metal interface. The insulating interface layer in MIS structures plays a critical role in enhancing device performance by affecting the barrier height ($\emptyset_b$) and diode parameters [1-4]. The performance of MIS Schottky diodes is influenced by various parameters such as the interface states at the insulator/metal and insulator/semiconductor interfaces, the $\emptyset_b$, the ideality factor (n), and the series resistance (R_s). Both the interface layer and R_s are critical parameters for MIS Schottky diodes because the total voltage applied to the diode is shared among the R_s, interface layer and the depletion layer. The magnitude of this voltage depends on the structure of the interface layer and thickness as well as R_s. Therefore, since the effectiveness and reliability of these devices are closely linked to both the R_s and the quality of the interface layer, it is imperative to meticulously account for R_s to achieve an accurate and reliable assessment of their electrical characteristics [5-9].

Titanium dioxide (TiO_2) is a widely studied material due to its impressive properties, such as a high dielectric constant, thermal stability, wide bandgap, high refractive index, and low leakage current density [10,11]. Considering its general properties, TiO_2 exhibits high transparency across a wide range of wavelengths due to the combination of Ti 3d and O 2p orbitals. Although TiO_2 has three different crystal phases—anatase, rutile, and brookite—all phases have the same chemical formula. However, differences in bond lengths and crystal structures among the phases lead to variations in density and electronic properties. The band gaps are 3.2 eV, 3.0 eV, and 3.3 eV for anatase, rutile and brookite respectively, resulting in distinct electronic properties for each phase [12]. While the anatase and rutile phases have similar valence band positions, brookite has a lower band position. The band positions vary among the phases, with brookite having the highest conduction band position. Anatase and rutile phases possess a tetragonal crystal system, whereas brookite has an orthorhombic structure. The surface properties also differ; anatase and rutile are more hydrophobic compared to brookite. The stability and efficiency of TiO_2 phases depend on nanoparticle size and synthesis method. Anatase is preferred for smaller nanoparticles, while rutile and brookite are stable at larger sizes [12-14]. The versatile nature of TiO_2 makes it promising for a wide range of applications, including catalysis, sensors, anti-reflective coatings, solar cells, and Schottky diodes. TiO_2 can be produced using various methods such as sol-gel technique, atomic layer deposition (ALD) and chemical vapor deposition, sputtering [15]. Among these techniques, the sol-gel method offers high control over the solution, ensuring control of composition and homogeneity. It also provides advantages over other coating approaches, particularly in situations where cost is a significant concern [16].
In 2008, Altındal et al. coated p-Si with TiO_2 prepared with the sol-gel method and coated with a dip-coating technique. They achieved n of 1.51 at room temperature and observed a significant decrease in the zero-bias barrier height ($\emptyset_{b0}$) along with an increase in the n value over the temperature range of 80-300 K [17]. Barış et al. used the DC magnetron sputtering technique to produce Au/TiO_2 (rutile) and

Au/TiO_2 (anatase) structures. They observed that as the temperature increased, the $\emptyset_b$ increased from 0.57 to 0.82 eV for rutile and increased from 0.74 to 0.85 eV for anatase [18,19]. In 2014, Aydın et al. achieved n of 1.8 and $\emptyset_b$ of 0.66 eV from Al/TiO_2/p-Si diodes prepared using the ALD [20]. In 2015, Altındal et al. reported $\emptyset_b$ of 1.068 eV at 100 kHz and 0.347 eV at 1 MHz in Au/TiO_2/n-4H-SiC diode structures prepared using the ALD [21]. In 2018, Yılmaz et al. achieved $\emptyset_b$ of 0.92 eV and n of 2.39 at room temperature from Ag/TiO_2 nanotube/Ti electrode structures containing TiO_2 nanotubes produced using the electrochemical anodization method [22]. In 2021, Taşdemir et al. reported n of 2.39 for Al/Zr-doped TiO_2/p-Si structures synthesized using sol-gel and drop-casting methods [23]. In 2022, Bilgili et al. achieved n of 1.39 and a $\emptyset_b$ of 0.52 eV for thin TiO_2 films, and n of 1.41 and $\emptyset_b$ of 0.50 eV for thick TiO_2 films in Ag/TiO_2/n-InP diode structures prepared using the sputtering method [24]. Tsui et al. demonstrated that coating the metal/4H-SiC interface with a 5 nm TiO_2 layer reduced the $\emptyset_b$ from 0.9 eV to 0.63 eV [25]. In 2023, Taşyürek coated TiO_2 nanotubes, produced using the anodization method, with DC magnetron sputtering to create Pt/TiO_2 nanotube/Ti diodes, achieving n of 1.25 and $\emptyset_b$ of 0.91 eV [26].

Surface states (N_{ss}) on semiconductor surfaces arise from defects, doped bonds, oxygen vacancies, structural changes due to metallization, doping atom levels, and natural or deposited interface layers at the metal/semiconductor interface. These conditions significantly impact the electrical parameters and conduction mechanisms of semiconductor devices. Reducing these conditions is critical for high-performance devices. TiO_2 is a commonly used insulating layer in Schottky diodes, as noted in many studies, and it contains surface defects that require passivation. While various methods exist to passivate defects in TiO_2, employing self-assembly monolayers (SAMs) provides a simpler and more cost-efficient approach to addressing surface defects [27-31].

SAMs are composed of three main components: head groups, alkyl chains, and functional groups. These structures chemically bond to surface atoms and arrange themselves in a two-dimensional pattern, improving surface morphology. This can lead to higher current densities and luminescence values in applications such as LEDs [32]. SAMs are widely used in various fields, including organic thin-film transistors (OTFTs), OLEDs, solar cells and nano sensors. They can also be used to reduce trap states caused by hydroxyl groups on SiO_2 substrates in silicon-based metal oxide semiconductors. Increasing the alkyl chain length reduces surface energy and imparts hydrophobic properties to the surface. Additionally, it lowers the threshold voltage by reducing trap states in oxide layers and increases carrier mobility. SAM materials contribute to aligning the energy difference between the work function of the metal oxide buffer layer and the highest-occupied molecular orbital (HOMO) or lowest-unoccupied molecular orbital (LUMO) energy levels of the organic material. However, to our knowledge, comprehensive analyses of the diode parameters and charge transport characteristics of metal/SAMs/TiO_2-based Schottky diodes are rare in literature. Although there exists research focused on modulating the Schottky barrier by incorporating SAMs at the Pt/TiO_2 interface, detailed investigations into these aspects are limited [33-37]. To enhance the performance of next-generation Schottky diodes, a detailed investigation of the effects of SAM molecules is required. In the study conducted by Can and Havare (2022), the MZ187 molecule demonstrated excellent electronic properties due to its strong π-conjugation, making it a promising candidate for organic semiconductor applications. When employed as a SAM in OLED devices, MZ187 was found to enhance charge transport and reduce interface trap states. This capability has inspired its integration into Schottky diode structures, where its role in modifying the interface properties can lead to improved diode performance, particularly in terms of reducing R_s and increasing $\emptyset_b$ [38].

This study explores the influence of SAMs on the electrical properties and charge transport behavior of Schottky diodes in an Al/SAM/TiO_2/p-Si structure. Our research reveals the impact of SAMs on key parameters such as n, R_s, and $\emptyset_b$. We demonstrated how SAMs enhance the performance of Schottky diodes, contributing to the advancement of nano electronic devices.

II. EXPERIMENTAL SECTION

A. Materials: Ammonium hydroxide (NH_4OH), hydrogen peroxide (H_2O_2), hydrofluoric acid (HF), titanium (IV) isopropoxide ($Ti(OC_3H_7)_4$), trimethylamine (C_3H_9N), acetic acid (CH_3COOH), acetonitrile (CH_3CN), and ethanol (C_2H_5OH) obtained from Sigma-Aldrich.

B. Sol-gel TiO_2 preparation: The TiO_2 solution was prepared using the sol-gel method, following the steps detailed in our previous research [39]. Titanium (IV) isopropoxide was gradually added to ethanol and mixed at room temperature for one hour to initiate hydrolysis and condensation reactions. Subsequently, acetic acid and trimethylamine were added to the solution in ethanol to adjust the pH and control the nucleation and growth of TiO_2 particles. The solution was then mixed for three hours to ensure thorough mixing and homogeneity of the components. The solution was left to age overnight, allowing further condensation reactions to occur and improving the homogeneity and stability of the resulting TiO_2 solution.

C. 4", 4""-[biphenyl-4,4" -diylbis(phenylimino)]dibiphenyl-4-carboxylic acid (MZ187) Synthesis: The synthesis steps of the molecule are detailed in the OLED study by Can and Havare [38].

D. Schottky Diode Fabrication: The diode in the Al/SAMs/TiO_2/p-Si configuration was produced on the p-type silicon substrate with a resistivity of 5-10 Ωcm. The front surface of the silicon substrates was cleaned using the RCA cleaning procedure, which includes oxide removal, organic cleaning, and ionic cleaning steps [40]. Initially, the substrates were subjected to an NH_4OH:H_2O_2:H_2O (1:1:6) solution to eliminate organic impurities and followed by a 10 minutes heating period. Subsequently, a 30 second treatment with HF:10H_2O was employed to remove the SiO_2 layer. The substrates were then immersed in an HCl + H_2O_2 + 6H_2O solution for 10 minutes. After each step, the Si substrates were dried with N_2 gas. Before the TiO_2 deposition, a 1200 Å layer of aluminum (Al) with 99.999% purity was thermally evaporated onto the back side of the Si substrate in a 10^{-6} Torr vacuum environment. The substrates were subjected to annealing at 570°C for 5 minutes in a nitrogen atmosphere to form an ohmic back contact with low resistance. This step was crucial for optimizing the electrical contact between the metal and the semiconductor, ensuring effective charge carrier transport and reducing contact resistance. The TiO_2 layer was applied to the substrates by spin coating at 2000 rpm for 30 seconds and then annealed at 450°C for 1 hour to obtain a thin TiO_2 film in anatase phase [41,42]. The TiO_2-coated substrates were immersed for 24 hours in a solution of MZ187 prepared by dissolving in acetonitrile at a concentration of 1 mM at room temperature. Finally, using a shadow mask, a 100 nm Al metal was deposited onto the top surface of the MZ187 molecules under high vacuum conditions (10^{-6} Torr).

E. Characterization: The electrical characteristics of the Schottky diodes were evaluated by performing the current-voltage (*I–V)* measurements with a Keithley 2400 source meter across a voltage range of -2 to 2 V. These measurements were carried out at ambient temperature and under dark conditions. The TiO_2 film thickness was measured via the Ambios P7 profilometer. Capacitance-voltage (*C-V*) measurements were carried out using a Keithley 4200 system, measuring the device capacitance across an applied voltage sweep from -2 V to 2 V.

III. RESULTS AND DISCUSSION

The *I-V* characteristics of Schottky diodes with/without MZ187 are presented on a semi-logarithmic scale in Figure 1a. The device architecture is shown in Figure 1b. As expected, the diodes exhibited good rectifying behavior, with current increasing linearly with voltage at low forward bias voltages. However, at higher voltages, this linear relationship was disrupted due to the presence of R_s and interface layers, leading to the formation of interface states. The deviation from linearity at elevated voltages is primarily due to the increasing influence of R_s and interface layers within the device. These resistance components become more pronounced under higher applied voltages, resulting in the emergence of

interface states and adversely affecting the device performance [43]. Understanding these mechanisms is crucial for developing high-performance Schottky diodes, as it highlights the limitations imposed by interface effects and resistance losses. The current flow in these devices is influenced by various factors. These include the temperature variations, semiconductor fabrication parameters, applied forward bias, and the presence of insulating layers. Different theoretical models, such as thermionic emission (TE), Cheung-Cheung, and Norde functions, have been proposed to explain the charge transport mechanisms of Schottky diodes. According to TE theory, the *I-V* characteristics of MIS contacts are described by the relationship between the current and the applied forward bias, as given by Equation 1 [3,44,45].

$$I = I_0 \left(\exp\left(\frac{qV}{nkT}\right) - 1 \right) \quad (1)$$

$$I_0 = AA^*T^2 \exp\left(-\frac{q\emptyset_{b0}}{kT}\right) \quad (2)$$

Here, I_0 is the reverse saturation current, q is the electron charge, k is the Boltzmann constant, n is the ideality factor indicating how close the diode is to ideal behavior (n=1), A is the rectifying contact area (7.85×10^{-3} cm^2), T is the temperature, and A^* is the effective Richardson constant (32 A/cm^{2}K^2 for p-Si). Additionally, $\emptyset_{b0}$: the barrier height at zero forward bias, and the relationship is given by:

$$\emptyset_{b0} = \frac{kT}{q} \ln\left(\frac{AA^*T^2}{I_0}\right) \quad (3)$$

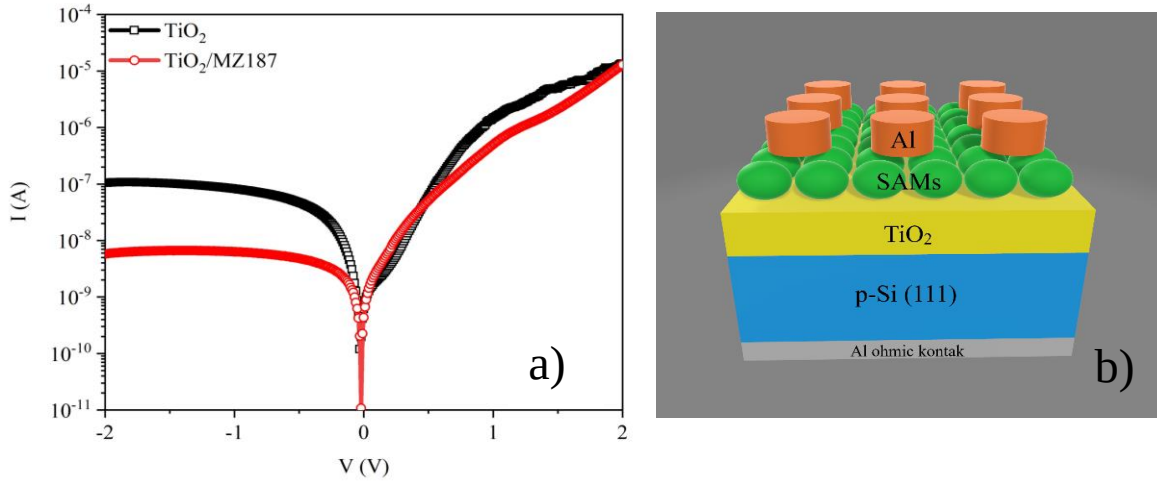

Figure 1. (a) *I-V characteristics of the Schottky diodes, and* ***(b)*** *the diode configuration fabricated with MZ187.*

The n can be derived from the following Equation 4, which considers the slope of the *lnI-V* in the forward bias region (for V>3kT/q):

$$n = \frac{q}{kT} \frac{\mathrm{d}V}{\mathrm{d}(\ln I)} \quad (4)$$

The n values calculated from the *lnI-V* graphs for the control and MZ187-modified TiO_2-based diodes are 3.7 and 2.7 at room temperature, respectively. This indicates that the MZ187-modified diodes exhibit a more ideal diode behavior. Deviations from ideality can be attributed to factors such as R_s, N_{ss}, and interface insulation layers. The rectification ratios (IF/IR) derived from the *I-V* in the range of +2V to -2V are 1.3×10^2 for the control diode and 2.2×10^3 for the MZ187-modified diode, demonstrating an improvement in the rectification ratio with MZ187 compared to the control diode.

To calculate the Schottky barrier height $\emptyset_{b0}$, the reverse saturation current I_0 can be used. First, the I_0 are obtained from the intersection of the *lnI-V*' curves under zero forward bias conditions, which are

$3.5x10^{-9}$ A for the control diode and $1.2x10^{-9}$ A for the MZ187-based diode. This indicates that MZ187 reduces the reverse saturation current, resulting in lower leakage current. Subsequently, $\emptyset_{b0}$ can be determined by substituting I_0 into Equation 3. The values of $\emptyset_{b0}$ for the control and MZ187-based diodes are obtained to be 0.76 eV and 0.79 eV, respectively. These results show that MZ187 enhances the barrier height, thereby improving the overall performance of the device [27,46,47].

As known, the forward *I-V* characteristics of Schottky diodes can exhibit significant non-ideal behavior at high voltage regions due to factors such as R_s. The R_s is influenced by the presence of the semiconductor/metal interface and leads to non-ideal diode characteristics. The method developed by Cheung-Cheung is highly effective in determining R_s, and this method can be used to find the Schottky diode parameters $\emptyset_b$ and n. The Cheung-Cheung functions are as follows:[48]

$$I = I_0 \exp\left(\frac{q(V-IR_s)}{nkT}\right) \tag{5}$$

$$\frac{\mathrm{d}V}{\mathrm{d}(lnI)} = IR_s + n\left(\frac{kT}{q}\right) \tag{6}$$

$$H(I) = V - n\frac{kT}{q}\ln\left(\frac{I}{AA^*T^2}\right) \tag{7}$$

$$H(I) = IR_s + n\emptyset_B \tag{8}$$

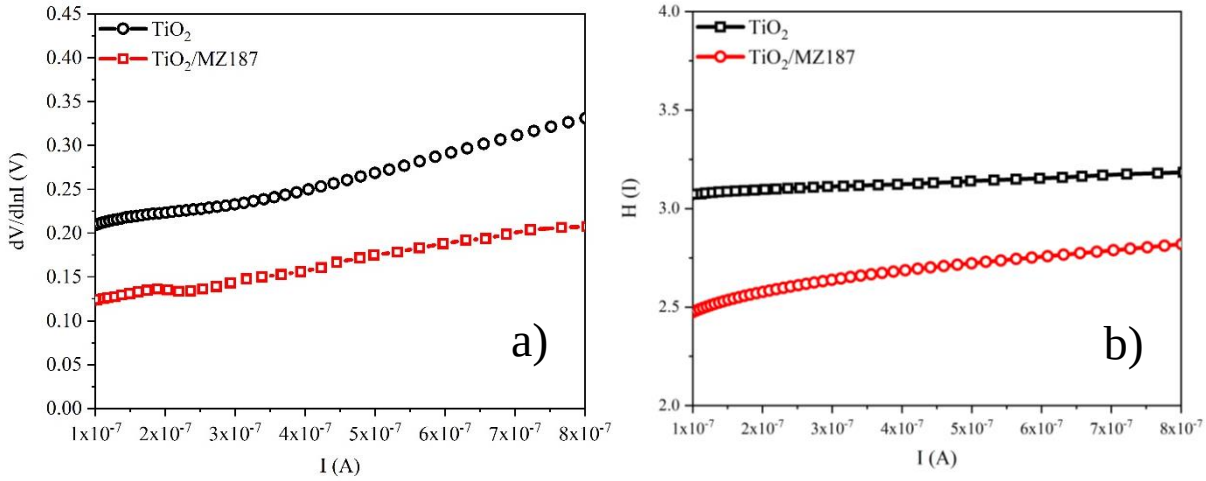

Figure 2. (a) *dV/dLnI(V)-I (A) and* ***(b)*** *H(I)-I graphs of Schottky diodes.*

The *n* values derived from Equation 6 for the control and the MZ187-modified TiO_2 diode at room temperature are 4.4 and 2.8, respectively. The slope of the linear graph obtained from Equation 6 allows us to calculate R_s. The calculated R_s values for the control and MZ187-based diodes are 168.3 kΩ and 129.2 kΩ, respectively. The decrease in R_s with the MZ187 molecule indicates that passivation has occurred at the Al/TiO_2 interface. From the linear fit of the *H(I)-I* graph, plotted using Equation 8, the y-intercept provides the $\emptyset_b$ value, while the slope gives R_s. The R_s calculated from the *H(I)-I* graph for the control and MZ187-based diodes are 90.3 kΩ and 76.1 kΩ, respectively, demonstrating that MZ187 reduces the series resistance and improves the device performance. The $\emptyset_b$ values are 0.80 eV for the control diode and 0.82 eV for the MZ187-based diode (Figure 2). These findings indicate that MZ187 not only decreases the series resistance but also increases the barrier height, thereby enhancing the overall performance of the Schottky diodes [49,50].

Another important method for calculating $\emptyset_b$ and R_s is the Norde method. The Norde functions expressed based on *I-V* measurements are as follows:[51]

$$F(V) = \frac{V}{\gamma} - \frac{kT}{q}\ln\left(\frac{I}{AA^*T^2}\right) \quad (9)$$

$$\emptyset_b = F(V_0) + \frac{V_0}{\gamma} - \frac{kT}{q} \quad (10)$$

$$R_s = \frac{kT(\gamma - n)}{qI_{min(V_0)}} \quad (11)$$

Here, γ is a random integer greater than n. V is the voltage and I represent the current obtained from the I-V measurements. After determining the γ values as 4 for the control and 3 for the MZ187-based diodes, the $F(V)$-V plot can be constructed. From the $F(V)$-V plot in Figure 3, the diode barrier heights $\emptyset_b$ can be calculated by substituting the values corresponding to the minimum $F(V_0)$ at the lowest voltage V_0 into the equation. The $\emptyset_b$ values calculated from Equation 10 are 0.78 eV for the control and 0.80 eV for the MZ187-based diodes. The R_s values calculated from Equation 11 are 5.5 MΩ for the control and 3.5 MΩ for the MZ187-based diodes. Both analytical methods demonstrate that the MZ187 molecule effectively improves the performance of Schottky diodes. The decrease in R_s values for MZ187-based diodes indicates surface passivation, resulting in reduced resistance to current conduction. Additionally, the increase in $\emptyset_b$ values suggests that these diodes offer a higher barrier height and consequently lower leakage current [52].

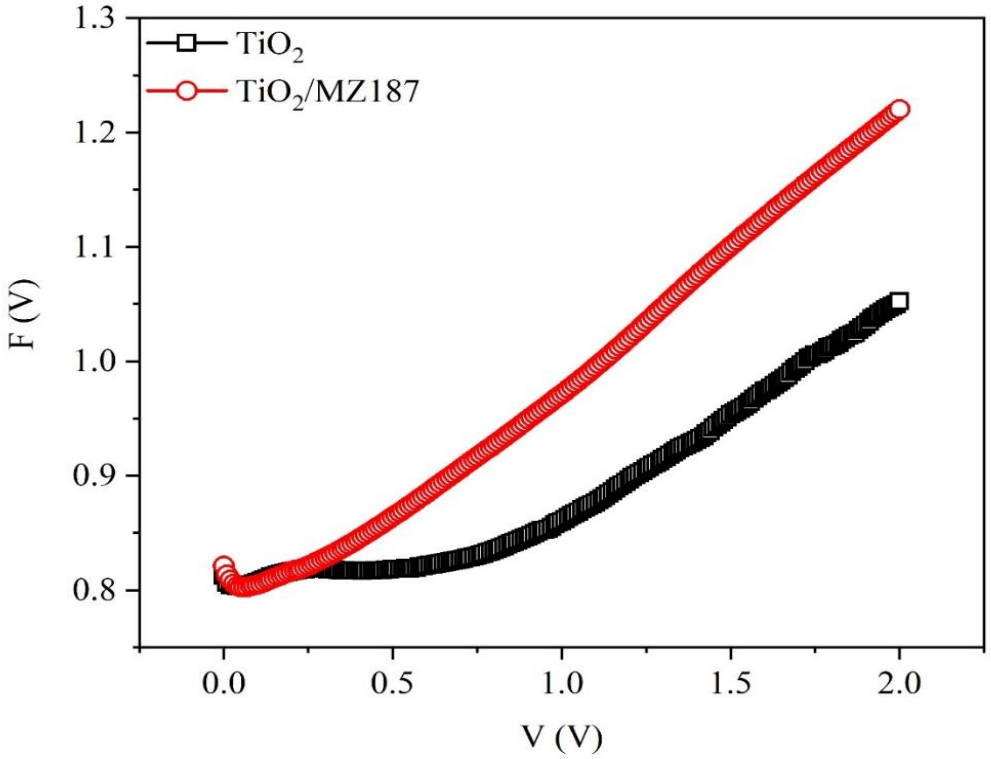

Figure 3. *F(V)-V plots of Schottky diodes.*

It is evident that the Schottky diode parameters obtained using the three different methods vary significantly from one another. The Norde method assumes an ideal metal/semiconductor contact and typically considers the ideality factor n=1. This method collects data from the linear region of the I-V, where the current changes exponentially. As a result, R_s values calculated using the Norde method are 5.5 MΩ for the control and 3.5 MΩ for the MZ187-based diodes. In contrast, the Cheung-Cheung method uses data from the nonlinear regions of the I-V, accounting for R_s and determining $\emptyset_b$ values. This method considers interface effects and free carriers but may yield different results due to the indirect evaluation of these effects. For the Cheung-Cheung method, R_s values are calculated as 168.3 kΩ for the control and 129.2 kΩ for the MZ187-based diodes. The $\emptyset_b$ values are 0.78 eV and 0.80 eV for the Norde method and 0.80 eV and 0.82 eV for the Cheung-Cheung method, respectively. These

differences arise from the different regions of the *lnI-V* graph from which each method collects data. As shown in Table 1, there are significant variations in the R_s obtained using the three methods. The R_s values obtained from the Norde method may differ from those obtained using the Cheung-Cheung and *I-V* technique. Furthermore, difficulties in accurately identifying the minimum points of the *F(V)-V* curves can introduce error margins. The Norde method, which derives the R_s from the linear region of the *lnI-V* characteristics, and accurately identifying the turning points of the graph is critical for calculating R_s correctly. Consequently, the differences between methods are due to the regions of data analysis and the assumptions used [3,53,54].

Table 1. *Electrical parameters of Schottky diodes obtained using different methods.*

Device parameters	**TiO_2**	**TiO_2/MZ187**
n *(I-V)*	3.7	2.7
n *(dV/dln(I)) (kΩ)*	4.4	2.8
I_0 (A)	$3.5x10^{-9}$	$1.2x10^{-9}$
Ø (I-V) eV	0.76	0.79
Ø (H-V) eV	0.80	0.82
Ø (F-V) eV	0.78	0.80
R_s *(dV/dln(I)) (kΩ)*	168.3	129.2
R_s *(H(I)-I) (kΩ)*	90.3	76.1
R_s *(F(V)-V) (MΩ)*	5.5	3.5
Rectification ratio	$1.3x10^2$	$2.2x10^3$

The experimental findings presented in this study are in good agreement with the electrical parameters observed in similar Schottky diode structures reported in Table 2. The calculated parameters such as ideality factor and series resistance exhibit comparable trends, strengthening the consistency of the results obtained with the results obtained from previous studies on TiO_2-based Schottky diodes fabricated with different deposition techniques.

Table 2*. Comparison of electrical parameters in Schottky diodes with TiO_2 fabricated using various deposition techniques.*

Deposition Method	**Structure**	**T *(K)***	**n**	**$Ø_b$ *(eV)***	**Ref.**
ALD	Au/TiO_2/n-4H-SiC	300	-	1.068 (100 kHz), 0.347 (1 MHz)	[21]
ALD	TiO_2 Interlayer/4H-SiC	300	-	0.63-0.90	[25]
ALD	Al/TiO_2/p-Si	300	1.8	0.66	[20]
DC Magnetron Sputtering	Au/TiO_2 (rutile)/n-Si	200-380	3.50-1.9	0.57-0.82	[18]
DC Magnetron Sputtering	Au/TiO_2 (anatase)/n-Si	340-400	2.47-2.24	0.74-0.85	[19]
DC Magnetron Sputtering	Ag/TiO_2/n-InP	300	1.39 (60 Å), 1.41 (120 Å)	0.50-0.52	[24]
Electrochemical Anodization	Ag/TiO_2 nanotube/Ti	300	2.39	0.92	[22]
Electrochemical Anodization	Pt/TiO_2 nanotubes/Ti	300	1.25	0.91	[26]
Sol-Gel/Drop Casting	Al/Zr-doped TiO_2/p-Si	300	2.39	-	[23]
Sol-Gel/Spin coating	**Al/SAMs/TiO_2/p-Si**	**300**	**2.7**	**0.79**	**this work**

The electrical properties of Schottky barrier diodes can vary significantly based on the interaction between the interfacial layer's thickness and the N_{ss} at the metal-semiconductor junction. N_{ss} is a critical factor that directly influences the diode's overall performance and quality, particularly affecting the n and $\emptyset_b$. The distribution of N_{ss} can be derived from the forward-bias *I-V* of the diode. The voltage dependence of N_{ss} can be mathematically described using the following Equation 12:[9,55,56]

$$N_{ss}(V) = \frac{1}{q}\left[\frac{\varepsilon_i}{d}(n(V)-1) - \frac{\varepsilon_s}{W_d}\right] \quad (12)$$

Here, N_{ss} represents the density of surface states at equilibrium with the semiconductor, W_d denotes the width of the depletion region, ε_s is the permittivity of the semiconductor, ε_i is the permittivity of the interfacial layer, n is the ideality factor, d is the thickness of the insulating layer. The TiO_2 thin film's thickness was measured at 53 nm using a profilometer. The expression for W_d can be written as:[40]

$$W_D = \left[\frac{2\varepsilon_0\varepsilon_s V_0}{qN_A}\right]^{\frac{1}{2}} \quad (13)$$

where ε_s=11.8ε_0, and V_0 represents the built-in potential, which is determined by extrapolating the *1/C²–V* curve onto the voltage axis as shown in Figure 4. Analysis of the *1/C²–V* characteristic at 500 kHz yields a slope that corresponds to an acceptor density (N_A) of 2.7x10^{17} cm^{-3} within the semiconductor. The calculated W_d is 63 nm. Extrapolation of this curve on the voltage axis allows for the determination of the V_0. This capacitance relation is represented by:[45]

$$C^{-2} = \frac{2(V_0+V)}{\varepsilon_0\varepsilon_s q A^2 N_A} \quad (14)$$

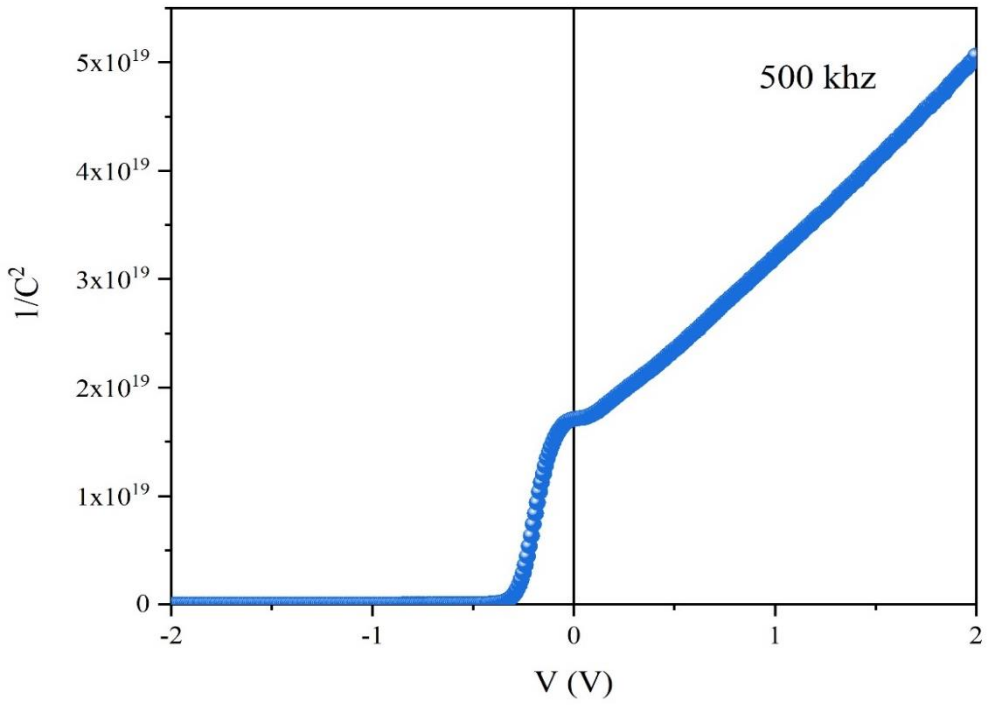

Figure 4. *1/C²–V characteristics of the Schottky diode with MZ187 at 500 kHz.*

For p-type semiconductors, the energy of the surface states (E_{ss}) with respect to the valence band maximum of the semiconductor is given by:

$$\emptyset_e = \emptyset_{bo} + \beta(V - IR_s) = \emptyset_{bo} + \left(\frac{1}{1-n(V)}\right)(V - IR_s) \quad (15)$$

$$E_{ss} - E_v = q[\emptyset_e - (V - IR_s)] \quad (16)$$

Here, V represents the applied voltage drop, $\emptyset_e$ is the effective barrier height. Using Equation (12), N_{ss} as a function of voltage can be determined. As shown in Figure 5, N_{ss} decreases as $E_v - E_{ss}$ increases. Clearly, the use of the MZ187 molecule has led to a reduction in N_{ss}. The observed decrease in N_{ss} indicates a reduction in trap states at the Al/TiO_2 interface in the MZ187-modified diodes [9,57]. The reduction of trap states enhances the device's performance and stability, as trap states can negatively impact electrical parameters and lead to carrier recombination [58,59]. These results highlight the potential of SAMs to improve interface quality and enhance the electrical properties of Schottky barrier diodes.

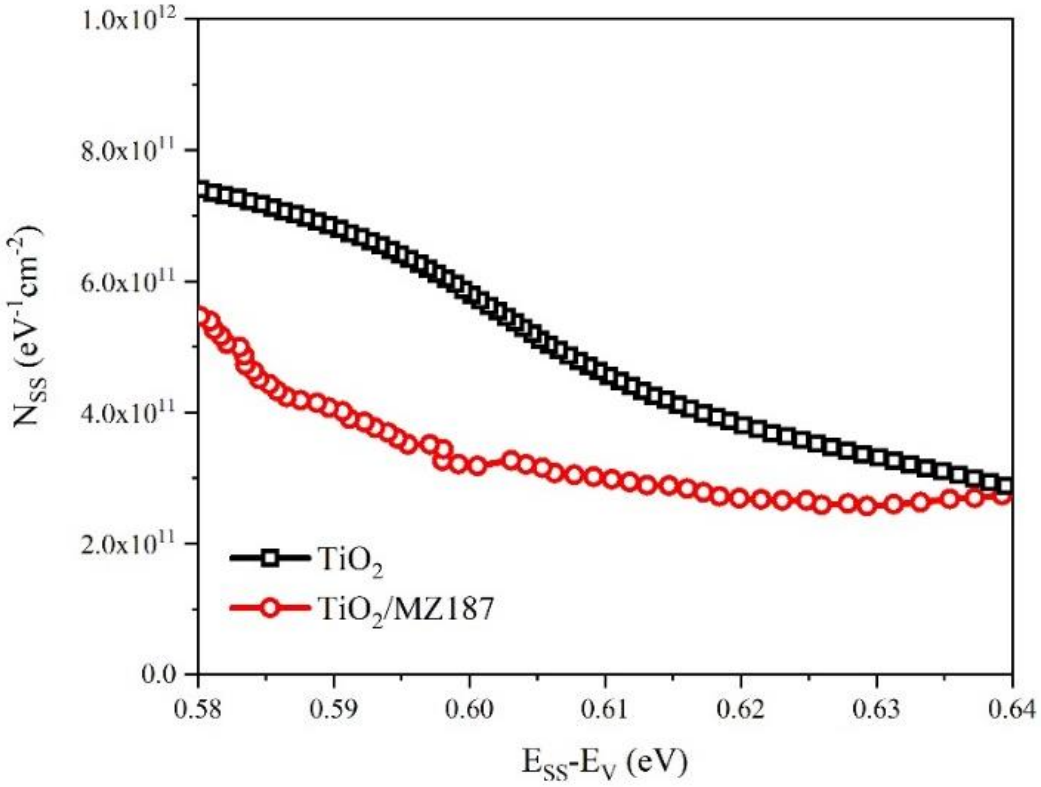

***Figure 5**. N_{ss} as a function of E_{ss}-E_v for the Schottky diodes at room temperature.*

III. CONCLUSION

In this study, the electrical properties and charge transport mechanisms of Schottky barrier diodes fabricated using the MZ187 molecule were examined. The results demonstrate that the MZ187 molecules enhance the Schottky diode performance. Compared to the control diode, the n values for MZ187-based diode decreased from 3.7 to 2.7. The R_s values, calculated using various methods, significantly decreased in the MZ187-modified diode, indicating that the MZ187 molecules improves surface quality. The application of the MZ187 molecule resulted in an increase in $\emptyset_b$. The rectification ratio of the control diode was $1.3x10^2$, while for the MZ187-coated diode, this ratio increased to $2.2x10^3$. This improvement was achieved by reducing localized interface states at the metal/semiconductor interfaces due to MZ187 molecules. The findings of this study indicate that SAM coatings are an effective method for improving Schottky diode performance. The use of SAM molecules holds potential for enhancing the efficiency and stability of nano-electronic devices. Our research contributes to the development of nano-electronic devices by revealing the effects of SAMs on key parameters such as rectification ratios, R_s, n, and $\emptyset_b$. Additionally, exploring the combinations of SAM molecules with

different metal oxides and semiconductors will be a crucial step towards developing higher performance and more stable devices.

IV. REFERENCES

[1] A. J. King, A. Z. Weber, and A. T. Bell, "Theory and simulation of metal-insulator-semiconductor (MIS) photoelectrodes," *ACS Appl Mater Interfaces*, vol. 15, no. 19, pp. 23024–23039, 2023.

[2] S. Zeyrek, "The effect of interface states and series resistance on current-voltage characteristics in (MIS) schottky diodes," *Afyon Kocatepe University Journal of Sciences and Engineering*, vol. 15, no. 2, pp. 1–9, 2015.

[3] S. M. Sze and Kwok K. Ng, *Physics of Semiconductor Devices Third Edition*, New Jersey, USA, John Wiley & Sons, Inc., 2007, pp. 90-96.

[4] Ç. Ş. Güçlü, "A comparison electronic specifications of the ms & mps type Schottky diodes (SDS) via utilizing voltage-current (V-I) characteristics," *Gazi University Journal of Science Part A: Engineering and Innovation*, vol. 10, no. 1, pp. 62–69, 2023.

[5] M. Soylu, I. S. Yahia, F. Yakuphanoglu, and W. A. Farooq, "Modification of electrical properties of al/p-si Schottky barrier device based on 2′-7′-dichlorofluorescein," *J Appl Phys*, vol. 110, no. 7, pp. 074514, 2011.

[6] S. S. Fouad, G. B. Sakr, I. S. Yahia, D. M. Abdel-Basset, and F. Yakuphanoglu, "Capacitance and conductance characterization of nano-ZnGa 2Te4/n-si diode," *Mater Res Bull*, vol. 49, no. 1, pp. 369–383, 2014.

[7] Ö. Vural, Y. Şafak, A. Türüt, and Ş. Altindal, "Temperature dependent negative capacitance behavior of Al/rhodamine-101/n- GaAs Schottky barrier diodes and R s effects on the C-V and G/ω-V characteristics," *J Alloys Compd*, vol. 513, pp. 107–111, 2012.

[8] K. Shili, M. Ben Karoui, R. Gharbi, M. Abdelkrim, M. Fathallah, and S. Ferrero, "Series resistance study of Schottky diodes developed on 4H-SiC wafers using a contact of titanium or molybdenum," *Microelectron Eng*, vol. 106, pp. 43–47, 2013.

[9] O. Pakma, N. Serin, T. Serin, and Ş. Altndal, "On the energy distribution profile of interface states obtained by taking into account of series resistance in Al/TiO2/pSi (MIS) structures," *Physica B Condens Matter*, vol. 406, no. 4, pp. 771–776, 2011.

[10] Gyanan, S. Mondal, and A. Kumar, "Tunable dielectric properties of TiO2 thin film based MOS systems for application in microelectronics," *Superlattices Microstructures*, vol. 100, pp. 876–885, 2016.

[11] G. Zerjav, K. Zizek, J. Zavasnik, and A. Pintar, "Brookite vs. rutile vs. anatase: What's behind their various photocatalytic activities?," *J Environ Chem Eng*, vol. 10, no. 3, pp. 107722, 2022.

[12] R. Agarwal, Himanshu, S. L. Patel, S. Chander, C. Ameta, and M. S. Dhaka, "Understanding the physical properties of thin TiO2 films treated in different thermal atmospheric conditions," *Vacuum*, vol. 177, pp. 109347, 2020.

[13] J. Buckeridge *et al.*, "Polymorph engineering of Tio2: demonstrating how absolute reference potentials are determined by local coordination," *Chemistry of Materials*, vol. 27, no. 11, pp. 3844–3851, 2015.

[14] S.-D. Mo and W. Y. Ching, "Electronic and optical properties of three phases of titanium dioxide: Rutile, anatase, and brookite," *Physical Review B*, Vol. 51, no. 19, pp. 13023-13032, 1994.

[15] W. Promnopas *et al.*, "Crystalline phases and optical properties of titanium dioxide films deposited on glass substrates by microwave method," *Surf Coat Technol*, vol. 306, pp. 69–74, 2016.

[16] D. Bokov *et al.*, "Nanomaterial by sol-gel method: synthesis and application," *Advances in Materials Science and Engineering*, Vol. 2021, Issue 1, pp. 5102014, 2021.

[17] O. Pakma, N. Serin, T. Serin, and Ş. Altindal, "The double Gaussian distribution of barrier heights in Al/ TiO 2/p-Si (metal-insulator-semiconductor) structures at low temperatures," *J Appl Phys*, vol. 104, no. 1, pp. 014501, 2008.

[18] B. Kinaci, S. Şebnem Çetin, A. Bengi, and S. Özçelik, "The temperature dependent analysis of Au/TiO2 (rutile)/n-Si (MIS) SBDs using current-voltage-temperature (I-V-T) characteristics," *Mater Sci Semicond Process*, vol. 15, no. 5, pp. 531–535, 2012.

[19] B. Kinaci, T. Asar, Y. Özen, and S. Özçelik, "The analysis of Au/Ti02/n-Si Schottky barrier diode at high temperatures using I-V characteristics," O*ptoelectronics and Advanced Materials-rapid Communications*, vol. 5, no. 4, pp. 434–437, 2011.

[20] S. B. K Aydin, I. E. Yildiz, and I. Kanbur Çavu, "ALD TiO 2 thin film as dielectric for Al/p-Si Schottky diode,"*Bulletin of Materials Science*, Vol. 37, pp. 1563-1568, 2014.

[21] E. E. Tanrikulu, D. E. Yildiz, A. Günen, and Altindal, "Frequency and voltage dependence of electric and dielectric properties of Au/TiO2/n-4H-SiC (metal-insulator-semiconductor) type Schottky barrier diodes," *Phys Scr*, vol. 90, no. 9, pp. 095801, 2015.

[22] M. Yilmaz, B. B. Cirak, S. Aydogan, M. L. Grilli, and M. Biber, "Facile electrochemical-assisted synthesis of TiO2 nanotubes and their role in Schottky barrier diode applications," *Superlattices Microstructures*, vol. 113, pp. 310–318, 2018.

[23] İ. H. Taşdemir, Ö. Vural, and İ. Dökme, "Electrical characteristics of p-Si/TiO2/Al and p-Si/TiO2-Zr/Al Schottky devices," *Philosophical Magazine*, vol. 96, no. 16, pp. 1684–1693, 2016.

[24] A. Kürşat Bilgili, R. Çağatay, M. K. Öztürk, and M. Özer, "Investigation of electrical and structural properties of Ag/TiO 2 /n-InP/Au Schottky diodes with different thickness TiO 2 interface", *Silicon,* Vol. 14, pp. 3013-3018, 2022.

[25] B. Y. Tsui, J. C. Cheng, L. S. Lee, C. Y. Lee, and M. J. Tsai, "Schottky barrier height modification of metal/4H-SiC contact using ultrathin TiO2 insertion method," *Japanese Journal of Applied Physics,* Vol. 53, pp. 04EP10, 2014.

[26] L. B. Taşyürek, "Synthesis of TiO2 nanotubes and photodiode performance," *Türk Doğa ve Fen Dergisi*, vol. 12, no. 3, pp. 72–77, 2023.

[27] A. M. Nawar, M. Abd-Elsalam, A. M. El-Mahalawy, and M. M. El-Nahass, "Analyzed electrical performance and induced interface passivation of fabricated Al/NTCDA/p-Si MIS–Schottky heterojunction," *Appl Phys A Mater Sci Process*, vol. 126, no. 113, 2020.

[28] F. Yakuphanoglu, S. Okur, and H. Özgener, "Modification of metal/semiconductor junctions by self-assembled monolayer organic films," *Microelectron Eng*, vol. 86, no. 11, pp. 2358–2363, 2009.

[29] Z. Çaldıran, "Modification of Schottky barrier height using an inorganic compound interface layer for various contact metals in the metal/p-Si device structure," *J Alloys Compd*, vol. 865, pp. 158856, 2021.

[30] G. Güler, Ö. Güllü, Ş. Karataş, and Ö. F. Bakkalolu, "Analysis of the series resistance and interface state densities in metal semiconductor structures," *J Phys Conf Ser*, vol. 153, pp. 012054, 2009.

[31] I. M. Afandiyeva, S. Altındal, L. K. Abdullayeva, and A. I. Bayramova, "Self-assembled patches in PtSi/n-Si (111) diodes," *Journal of Semiconductors*, vol. 39, no. 5, pp. 054002, 2018.

[32] M. Can *et al.*, "Electrical properties of SAM-modified ITO surface using aromatic small molecules with double bond carboxylic acid groups for OLED applications," *Appl Surf Sci*, vol. 314, pp. 1082–1086, 2014.

[33] S. Kim and H. Yoo, "Self-assembled monolayers: Versatile uses in electronic devices from gate dielectrics, dopants, and biosensing linkers," *Micromachines,* Vol. 12 (5), pp. 565, 2021.

[34] Z. R. Lan, J. Y. Shao, and Y. W. Zhong, "Self-assembled monolayers as hole-transporting materials for inverted perovskite solar cells," *Mol. Syst. Des. Eng.*, Vol. 8, pp. 1440-1455, 2023.

[35] S. H. Hsiao, J. X. Wu, and H. I. Chen, "High-selectivity NOx sensors based on an Au/InGaP Schottky diode functionalized with self-assembled monolayer of alkanedithiols," *Sens Actuators B Chem*, vol. 305, pp. 127269, 2020.

[36] B. De Boer, A. Hadipour, M. M. Mandoc, T. Van Woudenbergh, and P. W. M. Blom, "Tuning of metal work functions with self-assembled monolayers," *Advanced Materials*, vol. 17, no. 5, pp. 621–625, 2005.

[37] Y. Liu, D. Ji, and W. Hu, "Recent progress of interface self-assembled monolayers engineering organic optoelectronic devices," *DeCarbon*, vol. 3, p. 100035, 2024.

[38] M. Can and A. K. Havare, "OLED application of π-conjugated phenylimino carboxylic acid organic semiconductor material," *EPJ Applied Physics*, vol. 97, no. 33, pp.8, 2022.

[39] C. Tozlu, A. Mutlu, M. Can, A. K. Havare, S. Demic, and S. Icli, "Effect of TiO 2 modification with amino-based self-assembled monolayer on inverted organic solar cell," *Appl Surf Sci*, vol. 422, pp. 1129–1138, 2017.

[40] Western Kern, *Handbook of Semiconductor Wafer Cleaning Technology*, New Jersey, USA, pp. 253-256, 1993.

[41] H. Noh, S. G. Oh, and S. S. Im, "Preparation of anatase TiO 2 thin film by low temperature annealing as an electron transport layer in inverted polymer solar cells," *Appl Surf Sci*, vol. 333, pp. 157–162, 2015.

[42] M. Shahiduzzaman *et al.*, "Low-temperature treated anatase TiO2 nanophotonic-structured contact design for efficient triple-cation perovskite solar cells," *Chemical Engineering Journal*, vol. 426, pp. 131831, 2021.

[43] O. Pakma, N. Serin, T. Serin, and Ş. Altındal, "On the energy distribution profile of interface states obtained by taking into account of series resistance in Al/TiO2/pSi (MIS) structures," *Physica B Condens Matter*, vol. 406, no. 4, pp. 771–776, 2011.

[44] E. H. Rhoderick and R. H. Williams, *Metal-Semiconductor Contacts Second Edition*, Clarendon Press, Oxford, pp. 89-109, 1988.

[45] B. Akın, M. Ulusoy, and S. Altındal Yerişkin, "Investigation of the interface state characteristics of the Al/Al2O3/Ge/p-Si heterostructure over a wide frequency range by capacitance and conductance measurements," *Mater Sci Semicond Process*, vol. 170, pp. 107951, 2024.

[46] H. J. Lee, W. A. Anderson, H. Hardtdegen, and H. Lilth, "Barrier height enhancement of Schottky diodes on n- In0.53Ga0.47As by cryogenic processing," *Appl. Phys. Lett.*, Vol. 63, 1939–1941, 1993.

[47] A. D. Marwick, M. O. Aboelfotoh, and R. Casparis, "Increase in Schottky barrier height in the CoSi 2 /Si (100) interface caused by hydrogen." *Mrs Online Proceeding Library*, Vol. 281, pp. 629-634, 1992.

[48] S. K. Cheung and N. W. Cheung, "Extraction of Schottky diode parameters from forward current-voltage characteristics," *Appl Phys Lett*, vol. 49, no. 2, pp. 85–87, 1986.

[49] S. Y. Yu, D. C. Huang, Y. L. Chen, K. Y. Wu, and Y. T. Tao, "Approaching charge balance in organic light-emitting diodes by tuning charge injection barriers with mixed monolayers," *Langmuir*, vol. 28, no. 1, pp. 424–430, 2012.

[50] G. S. Kim, S. H. Kim, J. Park, K. H. Han, J. Kim, and H. Y. Yu, "Schottky barrier height engineering for electrical contacts of multilayered MoS2 transistors with reduction of metal-induced gap states," *ACS Nano*, vol. 12, no. 6, pp. 6292–6300, 2018.

[51] H. Norde, "A modified forward I-V plot for Schottky diodes with high series resistance," *J Appl Phys*, vol. 50, no. 7, pp. 5052–5053, 1979.

[52] G. Çankaya and N. Uçar, "Schottky barrier height dependence on the metal work function for p-type si Schottky diodes," *Z. Naturforsch*., Vol. 59a, pp. 795-798, 2004.

[53] D. A. Aldemir, A. Kökce, and A. F. Özdemir, "Schottky diyot parametrelerini belirlemede kullanılan metotların geniş bir sıcaklık aralığı için kıyaslanması," *SAÜ Fen Bilimleri Enstitüsü Dergisi*, Vol. 21, Issue 6, pp. 1286-1292, 2017.

[54] S. Hameed, Ö. Berkün, and S. Altındal Yerişkin, "On the voltage dependent series resistance, interface traps, and conduction mechanisms in the Al/(Ti-doped dlc)/p-si/Au Schottky barrier diodes (SBDs)," *Gazi University Journal of Science Part A: Engineering and Innovation*, vol. 11, no. 1, pp. 235–244, 2024.

[55] H. C. Card and E. H. Rhoderick, "Studies of tunnel MOS diodes I. Interface effects in silicon Schottky diodes," *J. Phys. D: Appl. Phys*., Vol. 4, pp. 1589, 1971.

[56] S. ALTINDAL YERİŞKİN, "Effects of (0.01Ni-PVA) interlayer, interface traps (Dit), and series resistance (Rs) on the conduction mechanisms(CMs) in the Au/n-Si (MS) structures at room temperature," *Iğdır Üniversitesi Fen Bilimleri Enstitüsü Dergisi*, vol. 9, no. 2, pp. 835–846, 2019.

[57] D. E. Yildiz, Ş. Altindal, Z. Tekeli, and M. Özer, "The effects of surface states and series resistance on the performance of Au/SnO2/n-Si and Al/SnO2/p-Si (MIS) Schottky barrier diodes," *Mater Sci Semicond Process*, vol. 13, no. 1, pp. 34–40, 2010.

[58] I. Taşçıoğlu, G. Pirgholi-Givi, S. A. Yerişkin, and Y. Azizian-Kalandaragh, "Examination on the current conduction mechanisms of Au/n-Si diodes with ZnO–PVP and ZnO/Ag2WO4 –PVP interfacial layers," *J Solgel Sci Technol*, vol. 107, no. 3, pp. 536–547, 2023.

[59] Ç. Ş. Güçlü, "On the impact of pure PVC and (PVC: Ti) interlayer on the conduction mechanisms and physical parameters of classic metal-semiconductor (MS) Schottky diodes (SDs)," *Physica B: Condensed Matter*, Vol. 689, pp. 416173, 2024.

Düzce University
Journal of Science & Technology

Research Article

Investigation of Corrosion Fatigue Crack Growth in Aluminium Alloy-Based Metal Matrix Composites: A Comparative Study

Ilyas UYGUR[a*], Husnu GERENGI[a]

[a] *Duzce University, Faculty of Engineering, Department of Mechanical Eng. 81620, DUZCE, TURKEY*
** Corresponding author's e-mail address: ilyasuygur@duzce.edu.tr*
DOI: 10.29130/dubited.1562991

ABSTRACT

The need for high-strength alloys that can withstand the harsh conditions of saline environments is a common challenge in engineering applications. These materials must maintain their structural integrity under corrosive conditions. Corrosion fatigue of aluminium-based composites is an important consideration in the design and use of these materials, as it can significantly reduce the strength and service life of the composite. Corrosion fatigue occurs when a material is repeatedly exposed to a corrosive environment and cyclic loading, leading to the formation of cracks and eventual failure. The susceptibility of aluminium-based composites to corrosion fatigue depends on several factors, including the type and amount of reinforcement used, the composition of the matrix and the specific corrosive environment. It is therefore important that these factors are carefully considered and appropriate testing carried out to ensure the longevity and reliability of the composite in its intended application. In this study, fatigue crack growth tests were carried out at four different stress ratios on 2124-T4 +25% SiCp/Al composites at room temperature and in a 3.5% salt solution environment. It was found that the influence of the salt solution at low stress ratios was significant on the fatigue crack growth rates. However, the effect of the saline environment on the fatigue response diminished at high stress ratios.

Keywords: *Corrosion fatigue, fatigue crack propagation, Al-alloy composites, salt solution, hydrogen embrittlement*

Alüminyum Alaşımlı Metal Matris Kompozitlerde Korozyon Yorulma Çatlak Büyümesinin İncelenmesi: Karşılaştırmalı Bir Çalışma

ÖZ

Tuzlu ortamların zorlu koşullarına dayanabilecek yüksek mukavemetli alaşımlara duyulan ihtiyaç, mühendislik uygulamalarında yaygın bir zorluktur. Bu malzemeler korozif koşullar altında yapısal bütünlüklerini korumalıdır. Alüminyum bazlı kompozitlerin korozyon yorgunluğu, kompozitin mukavemetini ve hizmet ömrünü önemli ölçüde azaltabileceğinden, bu malzemelerin tasarımında ve kullanımında önemli bir husustur. Korozyon yorgunluğu, bir malzeme tekrar tekrar korozif bir ortama ve döngüsel yüklemeye maruz kaldığında ortaya çıkar ve çatlak oluşumuna ve nihayetinde malzemenin hasar görmesine yol açar. Alüminyum bazlı kompozitlerin korozyon yorgunluğuna karşı duyarlılığı, kullanılan takviye tipi ve miktarı, matrisin bileşimi ve spesifik aşındırıcı ortam gibi çeşitli faktörlere bağlıdır. Bu nedenle, kompozitin amaçlanan uygulamada uzun ömürlü ve güvenilir olmasını sağlamak için bu faktörlerin dikkatlice değerlendirilmesi ve uygun testlerin yapılması önemlidir. Bu çalışmada,

Received: 07/10/2024, Revised: 30/10/2024, Accepted: 30/10/2024

2124-T4 +%25 SiCp/Al kompozitler üzerinde oda sıcaklığında ve %3.5 tuz çözeltisi ortamında dört farklı gerilme oranında yorulma çatlağı büyüme testleri gerçekleştirilmiştir. Düşük gerilme oranlarında tuz çözeltisinin etkisinin yorulma çatlak büyüme oranları üzerinde önemli olduğu bulunmuştur. Bununla birlikte, tuzlu ortamın yorulma tepkisi üzerindeki etkisi yüksek gerilme oranlarında azalmıştır.

Anahtar Kelimeler: *Korozyon yorulması, yorulma çatlak ilerlemesi, Al-alaşım kompozitler, tuz çözeltisi, hidrojen gevrekleşmesi*

I. INTRODUCTION

The exceptional properties of high strength-to-weight ratio, good wear resistance, fatigue resistance and toughness make aluminium-based metal matrix composites a popular choice for advanced engineering applications [1]. In particular, 2124 aluminium alloy is a heat treatable alloy that belongs to the 2000 series of aluminium alloys. It consists mainly of aluminium, copper and magnesium. This alloy is known for its strength and durability, making it a popular choice for aerospace and aircraft applications, as well as highly stressed structural components. Aluminium alloy 2124 is also widely used in automotive and marine applications and in the manufacture of high strength aluminium products such as armour plate and pressure vessels. The high strength-to-weight ratio of the alloy makes it a good choice for applications where weight reduction is a priority. In the petroleum industry, corrosion fatigue is a particular concern for equipment used in the production, transportation and storage of crude oil and natural gas. This equipment is often exposed to harsh environments such as salt water or high temperatures, which can accelerate the corrosion fatigue process. In addition, the fluids used in the petroleum industry are often highly corrosive, which can exacerbate the problem. Mitigating corrosion fatigue is important to ensure the safety and reliability of equipment used in the petroleum industry and to prevent unplanned downtime and costly equipment failures. The addition of particles to aluminium alloys has shown significant improvements in both tensile and fatigue properties. This is particularly evident when the alloys are produced using a powder metallurgical process optimised to achieve uniform particle distribution, refined matrix microstructure and minimal matrix strengthening reaction [2].

Corrosion fatigue is a phenomenon that occurs when a material experiences a combination of corrosion and cyclic loading, such as bending or twisting. This can lead to premature failure of the material, even at loads that would not cause failure through the tensile stress alone. The corrosion fatigue process begins with the formation of small cracks on the surface of the material, which grow over time due to the combined effects of corrosion and cyclic loading. Earlier studies have suggested that fatigue cracks tend to initiate earlier and propagate at a faster rate in corrosive environments compared to those in air. This phenomenon can result in premature failure of metallic materials [3]. To address this issue, engineers and scientists in the various industry use a variety of techniques to evaluate the susceptibility of equipment to corrosion fatigue, and to design equipment that is more resistant to this phenomenon. These techniques include laboratory testing, computer simulations, and field testing of equipment in simulated or actual service environments. Additionally, corrosion inhibitors, corrosion protection coatings and coatings with corrosion resistant alloys are used to reduce the material degradation by corrosion [4]. In our previous works, the effects of stress ratio, particle sizes, notch behaviour and volume fraction of particulate SiC (SiCp)/Al composites on fatigue lives have been studied in detail [5], [6]. The fatigue lives and ductility of the materials corresponded to the strain or stress ratios. Also microstructural observations showed that the density and length of slip bands increased with the increasing strain or stress ratio at the given strain or stress amplitude, and so did the volume fraction and size of coarse constituents or particles, which were responsible for the reduction of fatigue life and ductility of the material [7], [8]. Although there is a significant amount of literature on the fatigue properties of 2000 series aluminum alloys, the impact of stress ratio on the growth rates of corrosion fatigue cracks (FCGR) has not been extensively explored. Therefore, this study aims to investigate the FCGR of 2124-T4 +25% SiCp /Al composites under four different stress ratios in both room temperature and a 3.5% salt solution environment. The primary objective of this research is to provide a more

comprehensive understanding of the corrosion fatigue behavior of 2124-T4 +25% SiCp /Al composite and to demonstrate how stress ratios affect it.

The fatigue life and ductility of the materials corresponded to the strain or stress ratios. Microstructural observations also showed that the density and length of slip bands increased with increasing strain or stress ratio at a given strain or stress amplitude, as did the volume fraction and size of coarse constituents or particles, which were responsible for the reduction in fatigue life and ductility of the material [7], [8]. Although there is a considerable amount of literature on the fatigue properties of 2000 series aluminium alloys, the effect of stress ratio on corrosion fatigue crack growth rates (FCGR) has not been extensively investigated. Therefore, this study aims to investigate the FCGR of 2124-T4 +25% SiCp /Al composites under four different stress ratios both at room temperature and in a 3.5% salt solution environment. The primary objective of this research is to provide a more comprehensive understanding of the corrosion fatigue behaviour of 2124-T4 +25% SiCp /Al composite and to demonstrate how stress ratios affect it.

II. MATERIAL AND METHOD

The materials were 2124 (Al-Cu-Mg-Mn) Al alloys with 25 vol% SiCp MMCs. All materials were manufactured by Aerospace Composite Materials (UK) and were designated as AMC225 (25 vol% 2-3 μm SiCp). Prior to machining, solution annealing was carried out at 505 oC for 1 hour, followed by cold water quenching and then natural ageing (T4) at room temperature. The alloy composition, particle size determination and distribution, and tensile response of these composites have been extensively investigated and discussed elsewhere [9]. For the evaluation of fatigue crack propagation, a 5x5 mm 'corner crack' (CC) specimen was adopted. A crack was initiated from a 0.25 mm deep edge slit. Pulsed direct current potential drop (DCPD) systems were used to monitor crack growth. At pre-determined stages of the test, a constant DC power supply delivered a 50A, two pulse to the specimen for 2 s while the fatigue cycles were held at 75% of the peak load.

During this period, the potential drop across the crack was measured. The potential drop data were converted to length and the FCGR was evaluated as a function of the applied stress intensity range ΔK [10]. The effects of cyclic frequency (55Hz), stress (R) ratios R=0.1, R=0.3, R=0.5 and R=0.9 and 1 Hz sinusoidal waveform were applied to all specimens. All tests were performed under constant amplitude load control test conditions using the Ampsler Vibraphore testing machine. All tests were carried out in air and 3.5% saline solution. A typical specimen and the DCPD wires are shown in Figure 1. The fracture surfaces of the specimens were observed in a Jeol 35c SEM to determine the dominant fracture modes and to characterize the fine scale topography of the fatigue fracture surfaces.

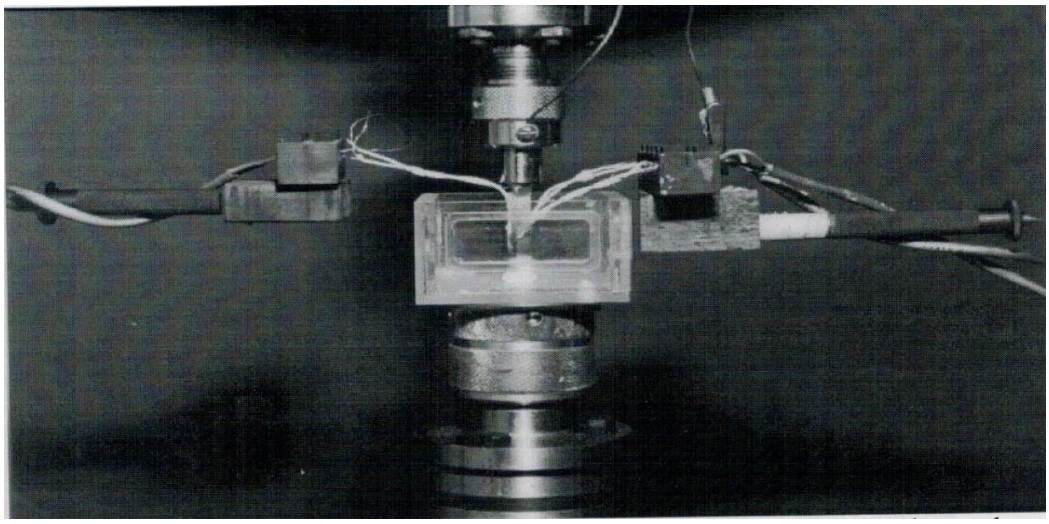

Figure 1. *Vibraphore tester with salt solution environmental chamber and AC PD wire connection*

III. RESULTS AND DISCUSSION

Comparisons of crack growth rates in air and salt solution environments at various R-ratios are shown in Figure 2-4 for the MMC material AMC225. It is clear that there is a strong environmental enhancement of the crack growth rates. In particular, the FCGR increased by a factor of 4 in the aggressive environment at R=0.1 (see Figure 2). However, the effect of the hostile environment on crack growth rates decreased as the R ratio increased (see Fig. 3 and Fig. 4). The effect of the saline solution on the FCGR is shown in Figure 5 for the AMC200 base alloy. For an equivalent ΔK, the FCGR increased rapidly in salt solution compared to air. However, unlike the MMC, there is no reduction in the FCGR of the base material as the R ratio increases. It can be said that as ΔK values and general growth rates increase, the effect of the environment on FCGR decreases due to the dominant role of static fracture modes and the relatively reduced time available for any interaction to occur.
Figure 6 summarizes the effects of environment on crack growth for AMC225 MMC material in terms of crack length versus cycles. It can clearly be seen that the life to failure is 5 times longer in air than in the 3.5% salt solution environment at R=0.1. However, the difference between the two environments decreased as the R ratio in salt solution increased. For example, at R=0.9, the life differences between air and saline environments were only 17%. The largest effect of the environment was observed at R=0.1 for AMC225. It is well known that corrosion fatigue is a time-dependent phenomenon. The acceleration of FCGR and the reduction of the threshold stress intensity range ΔKth in salt solution have been reported previously for Al alloys [10]-[12].

Three main mechanisms have been proposed to explain the detrimental effects of the environment on fatigue in Al-alloys [13]. i. electrochemical dissolution of film rupture, ii. crack surface film effect and iii. hydrogen embrittlement (HE). Based on the circumstantial evidence, HE is often cited as the primary damage mechanism for environmental fatigue crack propagation [14]. The presence of hydrogen in the metal lattice is thought to increase dislocation mobility at low stress levels. This results in a loss of ductility and tensile strength. Consequently, hydrogen induced embrittlement is associated with very high crack velocity in the hostile environment. At the frequencies provided by the Vibrophore test facility, most of the corrosion fatigue tests in this study lasted only 3 to 6 hours (see Figure 6). This is unlikely to be sufficient time for the alternative electrochemical dissolution and surface film cracking (O2 related) process to act as a controlling mechanism. However, H2 is extremely mobile and can act quickly by influencing dislocation motion. Therefore, HE is likely to be the dominant mechanism during the present study.

The effect of salt solution on FCGR is generally attributed to the HE mechanism in a wide range of materials including Al alloys [14], [15]. For Al-alloy MMC in an aggressive environment, corrosion fatigue models developed to describe crack growth should address the following factors: i: microstructural properties (grain size, volume fraction, particle size), ii: stress-strain behaviour [6]-[8], iii: fracture toughness, iv: the effect of O_2, H_2 and Cl^- on FCGR in an aggressive environment [2] and v: dislocation kinetics in composites.

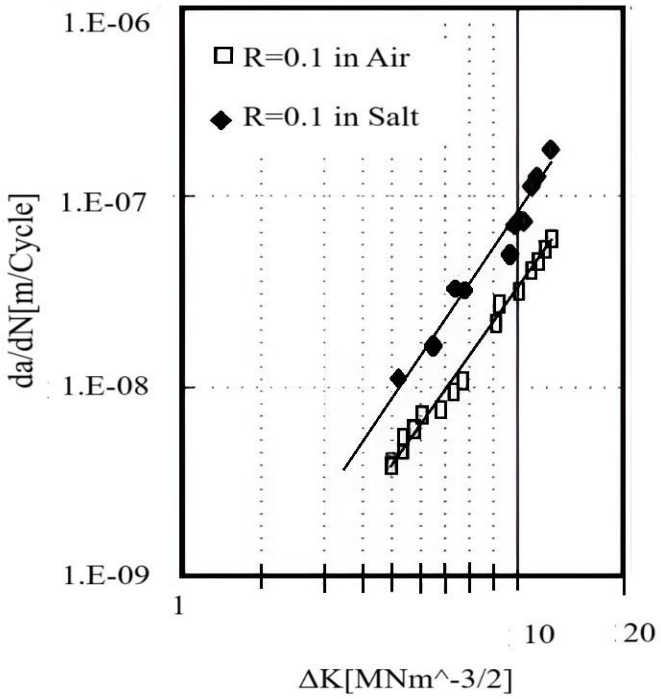

Figure 2. *The effect of 3.5% NaCl solution on the FCGR at R=0.1 for AMC225-T4*

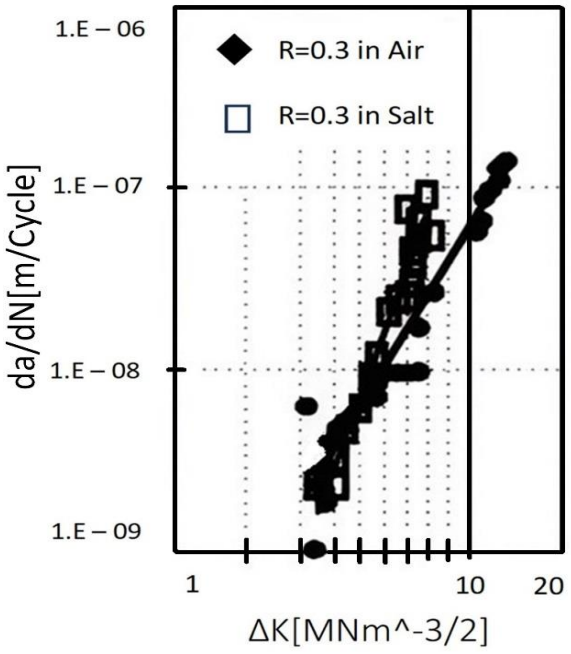

Figure 3. *The effect of 3.5% NaCl solution on the FCGR at R=0.3 for AMC225-T4*

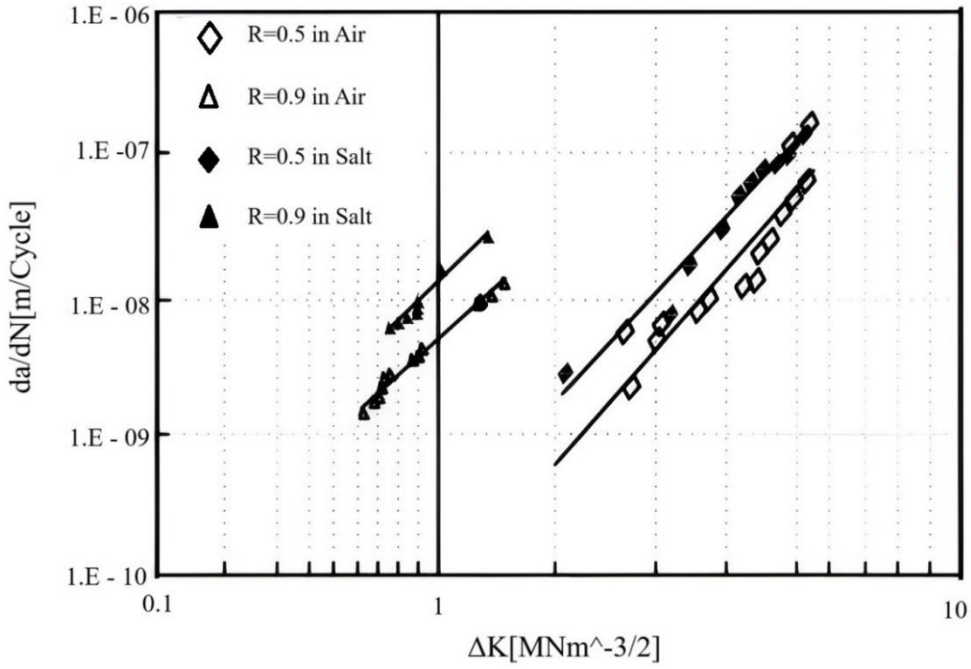

Figure 4. *The effect of 3.5% NaCl solution on the FCGR at R=0.5 and R=0.9 for AMC225-T4*

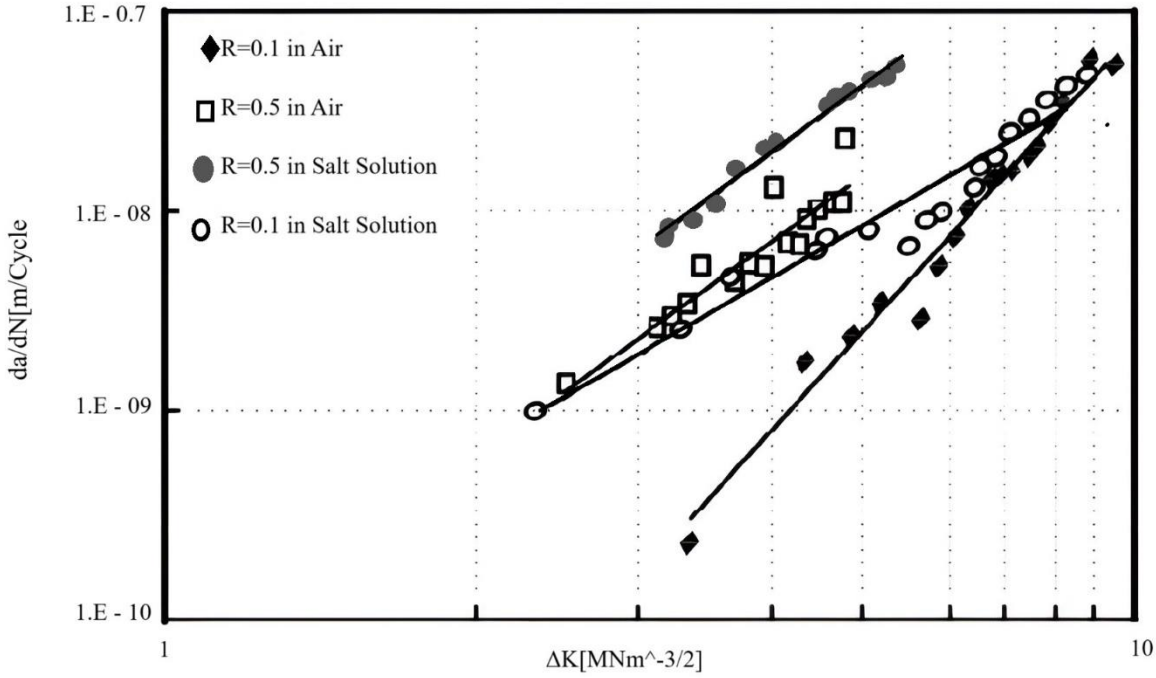

Figure 5. *The effect of 3.5% NaCl solution on the FCGR at R=0.1 and R=0.5 for AMC225-T4 for AMC200-T4 unreinforced base material at a maximum applied stress of 150 Mpa*

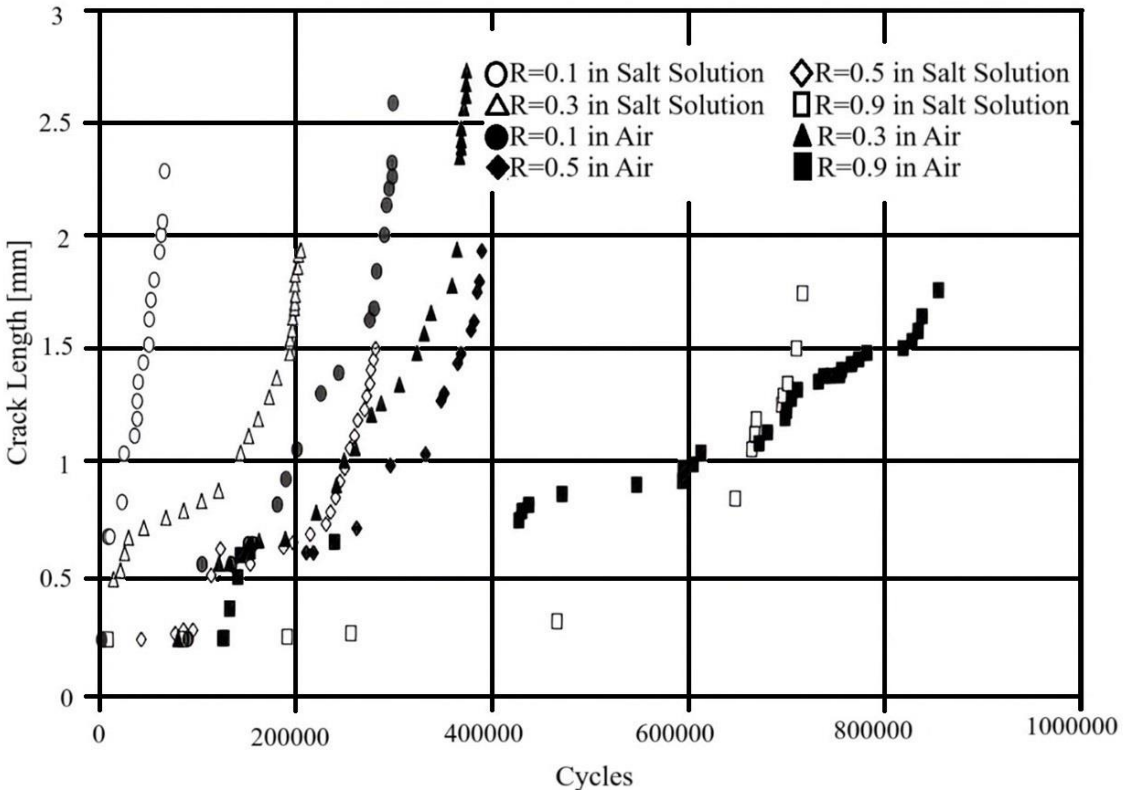

Figure 6. *The effect of environments on crack length of AMC225-T4 MMC material with various stress ratios*

The fracture behaviour of the specimens was investigated using the SEM. The specimens examined were tested at the same stress level (150 MPa). The fracture behaviour of all materials is compared in Figures 7 to 9 at magnifications of 17x and 3500x. In the composite material the crack was perpendicular to the applied tensile stress. All composite samples failed in a similar manner in air or salt solution and at the various stress ratios. It can be seen that the crack started from a 0.5 mm slit and grew in a quarter circular fashion to a length of 5 mm2 when fast fracture occurred in air (see Fig.8.a). A typical high magnification SEM image of the composite is shown in Fig.8.b. At the low ΔK values, the fracture surfaces were featureless and very flat. However, at stress intensities of 6MPa$\sqrt{m}$ the appearance of the fracture surface changed (see Fig.8.b). The fracture surface was quite rough with many peaks and valleys. Extensive deformation was observed around the SiC particles. The SiCp were associated with large ductile pits and the Cu2 Mn3 Al20 precipitate particles with small pits. Typical SEM images of the composite in a salt solution environment are shown in Figure 9.a and b.

Comparison with room temperature fracture surfaces showed that there was no major difference in fracture mode and crack growth mechanism. However, typical differences in fracture surface appearance were observed; i: the semicircular slow crack growth region was 2 mm2 in salt solution, which is significantly smaller than in air (5 mm2), ii: corrosion products occurred on the fracture surface. EDX analysis of the dark areas showed that these were composed mainly of Cl and Na residues. iii: Crack growth fracture surfaces were rougher than in air (see Fig.8.b and Fig.9.b). iv: Many individual microcracks were observed in the stage II growth region in salt solution. v: Fracture particles were more prominent in salt solution than in air. The alloys investigated exhibited brittle fracture behaviour in both environments, as evidenced by the presence of cleavage facets and quasi-cleavage areas on the fracture surfaces. However, the more hostile environment resulted in a flatter fracture surface, enhanced particle interface cleavage and particle cracking, and promoted corrosion pits on the fracture surface (Figure 9.b). In general, in saline environments, freely initiated corrosion fatigue cracks often originated from pits caused by exposure to the hostile environment [16], [17].

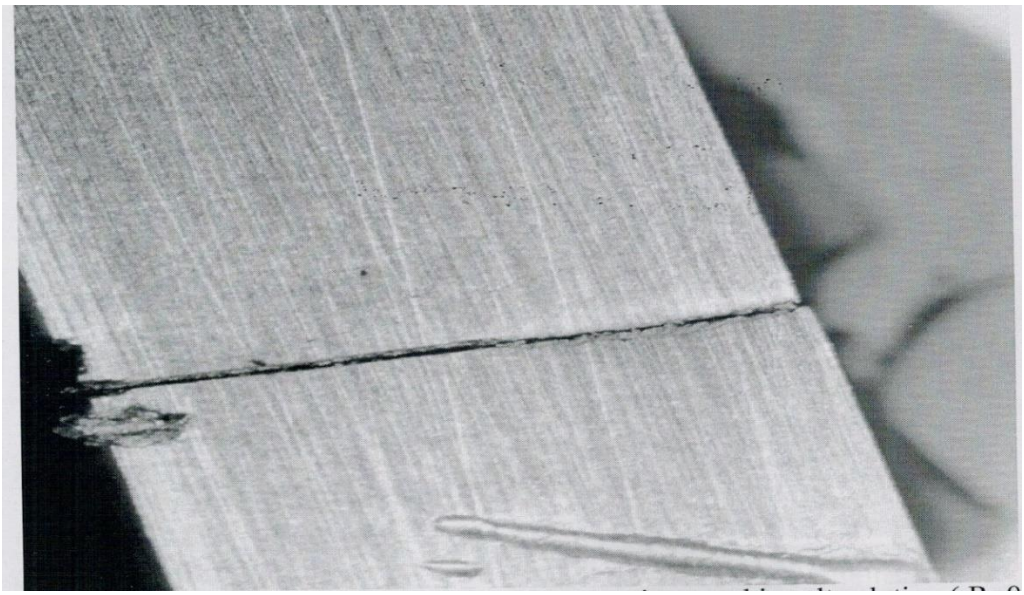

Figure 7. *Fatigue crack path of AMC 225 composite tested in salt solution (R=0.5, σmax = 175 MPa, Nf =265000cycles)*

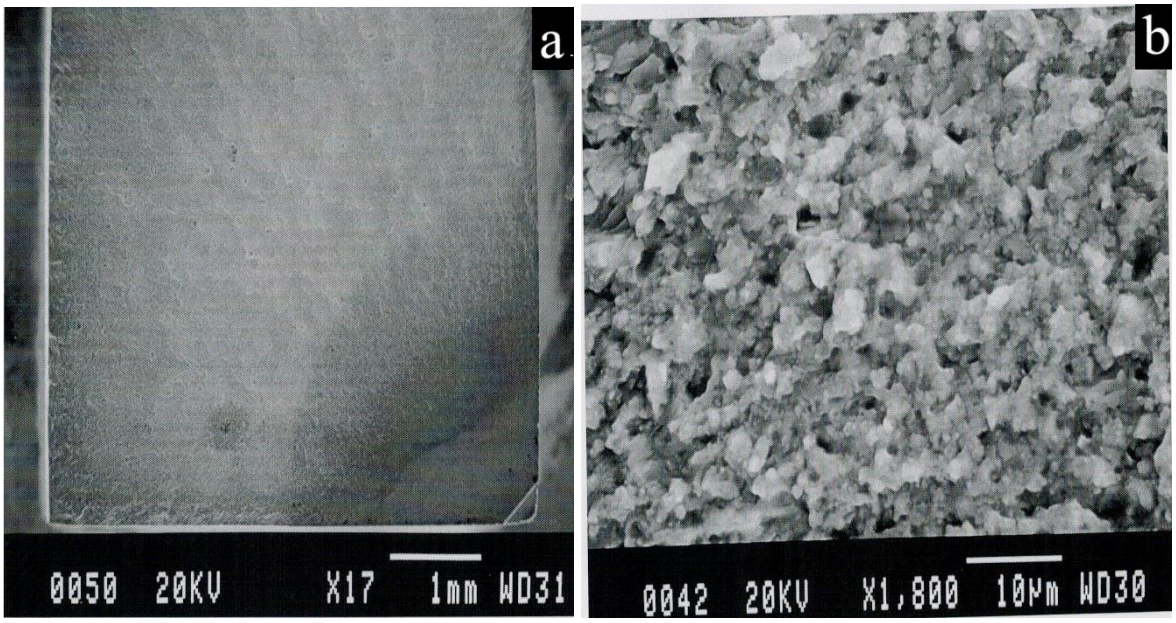

Figure 8. a) *Fracture surface of AMC225 in air* ***b)*** *Fracture surface of the same MMC in the overload region. The fatigue crack has propagated from left to right*

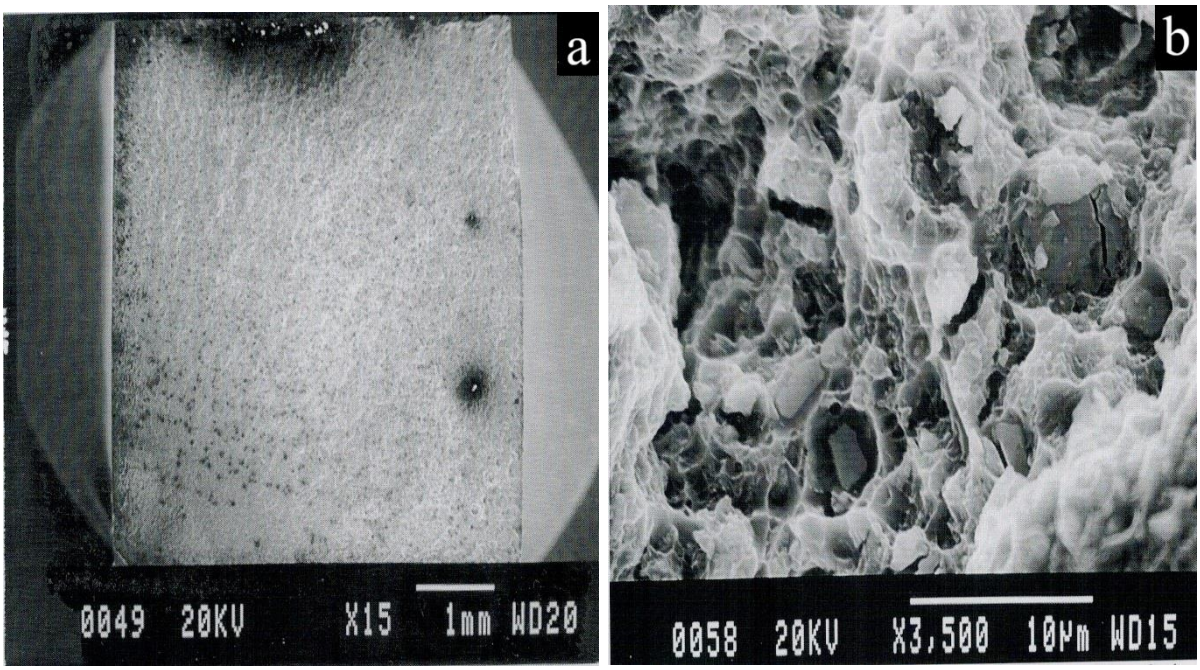

Figure 9. a) *Fracture surface of AMC 225 in salt solution* ***b)*** *Fracture surface of the same MMC in the overload region. The crack propagates from left to right*

IV. CONCLUSION

This study investigated the influence of an aggressive environment on the fatigue crack propagation rates of 2124/SiCp composites under naturally aged (T4) conditions. The main conclusions can be summarised as follows:

1. The influence of the salt solution was significant at low stress ratios on the fatigue crack growth behavior of AMC225 MMC and the unreinforced alloy AMC200. However, the effect of the saline environment on the fatigue crack growth rate (FCGR) decreased at higher stress ratios.
2. The AMC225 composite exhibited superior crack growth resistance at high stress ratios in both air and saline environments. In particular, the FCGR increased by a factor of 4 in the aggressive environment at R=0.1. Unlike the MMC, the FCGR of the AMC200 base material did not decrease with increasing R-ratios.
3. Hydrogen embrittlement is likely to be the dominant mechanism contributing to crack growth in the aggressive environment.
4. The fracture behavior of the AMC225 composite was brittle, showing features such as cleavage facets and quasi-cleavage areas on the fracture surfaces in both environments. The more hostile environment resulted in a flatter fracture surface, increased particle-interface cleavage and particle cracking, and promoted corrosion pits at the fracture sites.
5. Future research should explore the fatigue crack growth behavior of these composites under different environmental conditions, such as high temperatures or exposure to various corrosive agents.

ACKNOWLEDGEMENTS: This scientific study was conducted at the Department of Materials Engineering, University of Wales, Swansea. The author extends sincere gratitude to Prof. Dr. W. J. Evans and Prof. Dr. Martin Bache for their invaluable help and support. Special thanks are also extended to the "Young Corrosion Team" of Duzce University Corrosion Research Laboratory for their invaluable assistance in drawing the figures.

V. REFERENCES

[1] S.K. Pasha, A. Sharma, and P. Tambe, "Mechanical properties and tribological behavior of Al7075 metal matrix composites: A review," *Materials Today: Proceedings*, vol. 56, no. 3, pp. 1513–1521, 2022.

[2] I. Uygur, "Environmentally assisted fatigue response of Al-Cu-Mg-Mn with SiC particulate metal matrix composites," Ph.D. thesis, University of Wales, SWANSEA, U.K., 1999.

[3] O. Karpenko, S. Oterkus, and E. Oterkus, "Titanium alloy corrosion fatigue crack growth rates prediction: Peridynamics based numerical approach," *International Journal of Fatigue*, vol. 162, p. 107023, 2022.

[4] B. Güney, Y. Dilay, M.M. Solomon, H. Gerengi, A. Özkan, M. Yıldız, "Corrosion characteristics of plasma spray, arc spray, high velocity oxygen fuel, and diamond jet coated 30MnB5 boron alloyed steel in 3.5 wt.% NaCl solution," *Corrosion Reviews*, vol. 40, no. 1, pp. 51-63, 2022.

[5] I. Uygur, A. Cicek, E. Toku, R. Kara, and S. Saridemir, "Fatigue life predictions of metal matrix composites using artificial neural networks," *Archives of Metallurgy and Materials*, vol. 59, no. 1, pp. 97-103, 2014.

[6] I. Uygur, "Notch behavior and fatigue life predictions of discontinuously reinforced MMCs," *Archives of Metallurgy and Materials*, vol. 56, no. 1, pp. 109-115, 2011.

[7] H. Hao, D. Ye, and C. Chen, "Strain ratio effects on low-cycle fatigue behavior and deformation microstructure of 2124-T851 Aluminum alloy," *Materials Science & Engineering A*, vol. 605, pp. 151–159, 2014.

[8] I. Uygur, W.J. Evans, M. Bache, and B. Gulenc, "Fatigue behaviour of SiCp reinforced 2124 Aluminium matrix composites," *Metallofizika i Noveishie Tekhnologii*, vol. 26, no. 7, pp. 927-939, 2004.

[9] I. Uygur, "Tensile behaviour of P/M processed (Al-Cu-Mg-Mn) / SiCp composites," *Iranian Journal of Science and Technology*, vol. B28, no. B2, pp. 239-248, 2004.

[10] Z.J. Lu, "Environmetally assisted small crack propagation in an Al-Zn-Mg Alloy" University of Wales, SWANSEA, U.K., 1995.

[11] J. Llorca, J. Ruiz, J.C. Healy, M. Elices, and C.J. Beevers, "Fatigue crack propagation in salt water, air and high vacuum in a spray-formed particulate-reinforced metal matrix composite," *Materials Science & Engineering A*, vol. 185, pp. 1–15, 1994.

[12] J. Schijve, "Fatigue of structures and materials in the 20th century and the state of the art," *International Journal of Fatigue*, vol. 25, pp. 679-702, 2003.

[13] R.P. Gangloff, R.S. Piascık, D.L. Dicus, and J.C. Newman, "Fatigue crack propagation in aerospace Al- alloys," *Journal of Aircraft*, vol. 31, no. 3, pp. 720-725, 1994.

[14] E.R. De Los Rios, Z.Y. Sun, K.J. Miller, “A theoretical and experimental study of environmental hydrogen-assisted short fatigue crack growth in an Al-Li alloy,” *Fatigue and Fracture of Engineering Materials and Structures*, vol. 17, no. 12, pp. 1459-1464, 1994.

[15] R.P. Gangloff, *Environmental effect on fatigue crack propagation in Metals Handbook*, 9th edt. vol. 8, ASM Ohio, USA, 1985.

[16] A. Bag, W. Zhou, “Tensile and fatigue behaviour of AZ91D Mg-alloy,” *Journal of Materials Science Letters*, vol. 20, pp. 457-459, 2001.

[17] N.E. Co, J.T. Burns, “Effects of micro-scale corrosion damage features and local microstructure on fatigue crack initiation location,” *International Journal of Fatigue*, vol. 150, p. 106301, 2021.

Düzce University
Journal of Science & Technology

Research Article

The Impact of Artificial Intelligence Enhanced No-Code Software Development Platforms on Software Processes: A Literature Review

Osman KOÇ [a,*], İbrahim YÜCEDAĞ [b], Ümit ŞENTÜRK [c]

[a] *Department of Electrical-Electronics and Computer Engineering, Institute of Science and Technology, Düzce University, Düzce, TURKEY*
[b] *Department of Computer Engineering, Faculty of Engineering, Düzce University, Düzce, TURKEY*
[c] *Department of Computer Engineering, Faculty of Engineering, Abant Izzet Baysal University, Bolu, TURKEY*
** Corresponding author's e-mail address: info@osmkoc.com*
DOI: 10.29130/dubited.1554356

ABSTRACT

This literature review examines the impact of artificial intelligence-based (AI-based) no-code software development platforms on software processes. The study primarily focuses on accelerating software development processes, reducing costs, and optimizing business operations. Existing studies in the literature demonstrate how these types of platforms facilitate complex application development even for non-technical users and enhance time-cost optimization. This review highlights how no-code platforms have become more effective and efficient with AI-supported tools, transforming the current software development ecosystem. The article discusses the potential benefits and challenges of AI-based no-code platforms, emphasizing their promising future in the software industry.

Keywords: *No-Code, Low-Code, AI, Web development, Software development cost*

Yapay Zeka Tabanlı No-Code Platformlarının Yazılım Geliştirme Süreçlerine Etkisi: Literatür Taraması

Öz

Bu literatür taraması, yapay zeka (artificial intelligence – AI) tabanlı kodsuz (no-code – NC) yazılım geliştirme platformlarının yazılım süreçlerine olan etkilerini inceler. Çalışma, özellikle yazılım geliştirme süreçlerinin hızlanması, maliyetlerin azaltılması ve iş süreçlerinin optimizasyonu üzerinde durmaktadır. Literatürde yer alan mevcut çalışmalar, bu tür platformların teknik olmayan kullanıcıların bile karmaşık uygulamalar geliştirmelerini nasıl kolaylaştırdığını ve zaman-maliyet optimizasyonunu nasıl daha iyi hale getirdiğini göstermektedir. Bu inceleme, NC platformlarının, AI destekli araçlarla nasıl daha etkin ve verimli hale geldiğini, bu entegrasyonların mevcut yazılım geliştirme ekosistemini nasıl dönüştürdüğünü ortaya koymaktadır. Makale, AI tabanlı NC platformların potansiyel faydalarını ve karşılaşılabilecek zorlukları tartışarak, bu teknolojilerin yazılım endüstrisindeki gelecek vaatlerini vurgulamaktadır.

Anahtar Kelimeler: *Kodsuz, Az kodlu, Yapay zeka, Web geliştirme, Yazılım geliştirme maliyeti*

Received: 22/09/2024, Revised: 20/10/2024, Accepted: 31/10/2024

I. INTRODUCTION

The world of software development, as a constantly evolving and transforming ecosystem, has become an inevitable necessity in every sector of today's business world. Especially digital transformation processes are rapidly increasing the software needs of businesses. Proportional to this need, the software industry reached a size of 565 billion dollars in 2019 and continues to grow exponentially. The growth graph is shown in Figure 1 [1]. Factors such as the widespread adoption of cloud computing infrastructures and the ability to reach cross-border customers through marketplaces have also triggered this growth in recent years.

The rapid growth of the sector and its contribution to many areas led to a significant increase in software costs. Many expense items such as resource requirements, license fees, development, support, and maintenance costs of software have become a major financial burden, especially for small and medium-sized enterprises (SMEs). In this context, no-code (NC) and low-code (LC) platforms have emerged as a great advantage, especially for Small and Medium-sized Enterprises (SMEs). By allowing users to develop applications with minimal technical knowledge, they significantly reduce software costs.

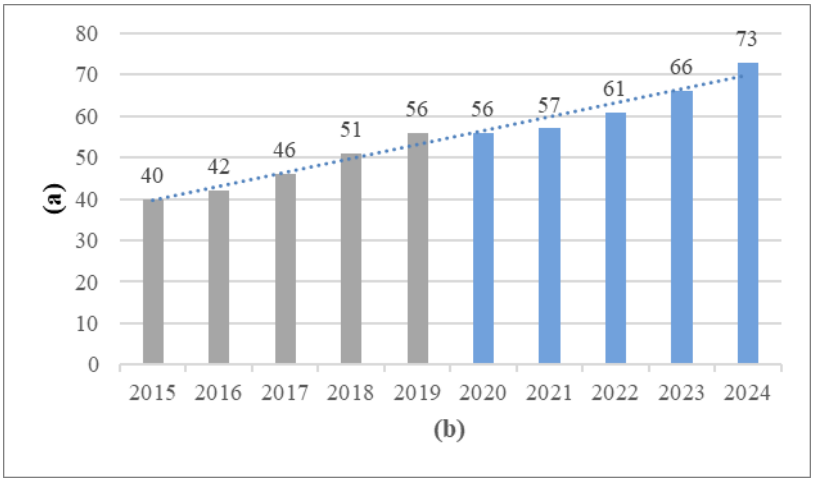

Figure 1. (a) *Market size in billion dollars and* ***(b)*** *Years for Software Industry Market Size, World Total, 2015-2024.*

According to Gartner's 2022 and 2023 reports, the usage rate of NC and LC platforms worldwide increased by 19.6% in 2022, and it is observed that the use of these platforms exceeded 20% by 2023. Moreover, according to Gartner's 2024 report, it is predicted that the low-code application development technologies market will reach 26.9 billion dollars [2].

The use of advanced technologies such as Artificial Intelligence (AI) and Natural Language Processing (NLP) in these platforms can further accelerate software development processes and significantly reduce costs. AI-based no-code/low-code (NCLC) platforms have the ability to understand commands given by users in natural language and generate code accordingly. In this study, the effects of NCLC platforms and AI support on software development processes, performance and cost benefits are examined in detail.

This paper makes several key contributions to the current literature. First, it provides a comparative analysis of AI-powered no-code/low-code platforms against traditional software development methods, focusing on their impact on efficiency, accessibility, and cost reduction. Second, it highlights the challenges of scalability, security, and sustainability in AI-enhanced platforms, offering guidance for businesses navigating digital transformation. Lastly, it identifies gaps in the existing research and suggests future directions for optimizing the integration of AI into no-code platforms, contributing to the ongoing development of this rapidly evolving field.

II. LITERATURE REVIEW

The literature review includes a comparative analysis of AI-based NCLC platforms with traditional software development methodologies and classical NC platforms. El Kamouchi et al (2023) conducted a systematic literature review on low-code/no-code development, providing an extensive analysis of its advantages and challenges in software processes [3]. This analysis reveals how AI support transforms software development processes and how these processes improve in terms of cost, time, and accessibility.

A. LARGE LANGUAGE MODELS (LLM)

Language models are used in natural language processing by predicting the probability distributions of word sequences. When a sequence of words of any length (m) is given to the language model, it assigns a probability to the entire sequence. Its representation is shown in formula (1) [4].

$$P(w_1, \dots, w_m) \tag{1}$$

NLP is used in many artificial intelligence applications such as machine translation and text-to-speech conversion. Language models can be both parametric and non-parametric. While practical language models use an artificial neural network with a predetermined number of parameters, non-parametric language models have an undetermined number of parameters [5]. LLM is used to increase language understanding and generation capabilities using developing deep learning techniques, large datasets, and powerful computing resources. The main feature of these models is that they use a large text dataset as training data. These datasets can include millions of text documents collected from the internet or books, which helps the model develop a deep understanding of language [6]. Since 2010, large language models such as GPT (Generative Pre-trained Transformer) and BERT (Bidirectional Encoder Representations from Transformers) have revolutionized the field of natural language processing. They greatly improved language understanding and generation capabilities. By the 2020s, models like GPT-3 and GPT-4 became popular with their ability to generate large-scale language and began to be used in many fields.

B. GENERATIVE AI (GENAI)

Generative AI refers to artificial intelligence language models that generate/create content. It has become possible to produce content in many areas such as text, image, and music using these models. It has achieved great success especially in natural language processing (NLP) and image processing fields [7]. Generative AI encompasses language models trained using very large data and can then create new data by analyzing this data. It fundamentally uses deep learning techniques. Using deep learning techniques along with artificial neural networks, very complex relationships are learned and patterns between data are discovered. This ability of artificial neural networks allows computers to understand what is in a photo or what happens in a story. Deep learning techniques come into play in this process. Deep learning helps computers find patterns between data. Thus, artificial intelligence models gain the ability to learn and produce new data [8]. These models generally consist of two points: encoder and decoder. The encoder has the task of examining and understanding the data and representing it in a special way. The decoder, on the other hand, can create new data from this representation information.

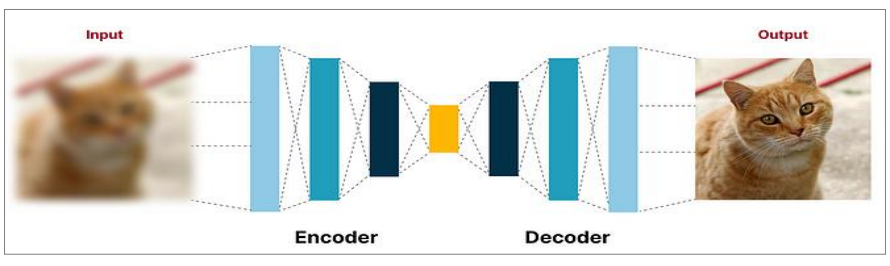

Figure 2. *Example of encoder and decoder of Generative AI language models*

As seen in Figure 2 [9], a cat photo and the information that this image belongs to a cat are given as input to the encoder. The encoder learns how the cat looks from this input. Later, it can create a new cat image (output) through the decoder with what it has learned. With this method, language model training is performed.

C. SOFTWARE CODE GENERATION WITH LLM

It was mentioned that LLM produces new data/outputs by feeding on millions of data. This data also includes software codes. The language model, which acquires technical knowledge from open-source codes on the internet and articles, documents, and books written in the field of software, can produce code from an input made in natural language. On this subject, OpenAI Company [10] took the first step with its artificial intelligence called ChatGPT [11], and then products such as GitHub Copilot and Microsoft Copilot were also introduced by other companies. In this area where interest is increasing, different artificial intelligence products are being released every day. These use large language models such as GPT-3 (Generative Pre-trained Transformer 3) and GPT-4 (Generative Pre-trained Transformer 4). OpenAI Company is an artificial intelligence research and development laboratory aimed at benefiting humanity. Founded in 2015, it is considered a rival to DeepMind [12]. OpenAI first developed the GPT-3 language model and gained great interest by releasing ChatGPT, an artificial intelligence chatbot using this model, on November 30, 2022 [13]. After this interest and success, Microsoft invested 1 billion USD in OpenAI. GPT-3 is a third-generation autoregressive language model that uses deep learning to produce human-like text. In simpler terms, it is a computational system designed to generate sequences of words, code, or other data starting from a source input called a prompt [14]. It can respond in the same language to prompts entered in many languages. Its only disadvantage is that since it has data up to September 2021, the answers it gives are also shaped accordingly. As a result of these developments, OpenAI released its new model GPT-4 on March 14, 2023 [15]. GPT-4, which has up-to-date information, can understand more complex inputs compared to GPT-3. Unlike GPT-3, which only responds to textual inputs in the same way; GPT-4 can process other data such as images and videos. Finally, on May 13, 2024, OpenAI released a more capable model with GPT-4o, combining artificial intelligence's image processing and audio data generation capabilities, allowing real-time video and voice conversations with artificial intelligence. The ChatGPT mobile application using the GPT-4o model can recognize any object shown on the camera during video calls and play long conversations or games. By integrating this model into smart glasses, there are many different usage possibilities such as being able to intervene urgently to an injured person. The model can understand the image received from the glasses and tell you what to do both verbally and through the image on the glasses. Since the data in the language models also includes software information, it is possible to use these abilities to produce software codes as well. Their ability to give software code in an explanatory way in response to a prompt made in natural language allowed language models to be used for different purposes.

D. AI APPLICATIONS SKILLED IN CODE GENERATION

It was mentioned that large language models can produce software code due to the data they contain. By using artificial intelligence applications supported by large language models, developer productivity and efficiency can be increased; code generation, debugging, refactoring, and creating test scenarios can be handled faster and more easily. In this regard, GitHub Copilot [16] and Microsoft Copilot [17] artificial intelligence stand out in corporate software development, while artificial intelligence products such as CodeQwen1.5 [18], Llama3 [19], and Claude 3 Opus [20] can be seen in individual uses. Although Microsoft Copilot and OpenAI ChatGPT artificial intelligence products are capable in many areas, products such as GitHub Copilot, CodeQwen1.5, and Claude 3 Opus can produce better results in code generation [21]. You can see the comparison of these and similar artificial intelligence applications that are widely used in terms of quality, speed, and cost in Figure 3, Figure 4, and Figure 5 below.

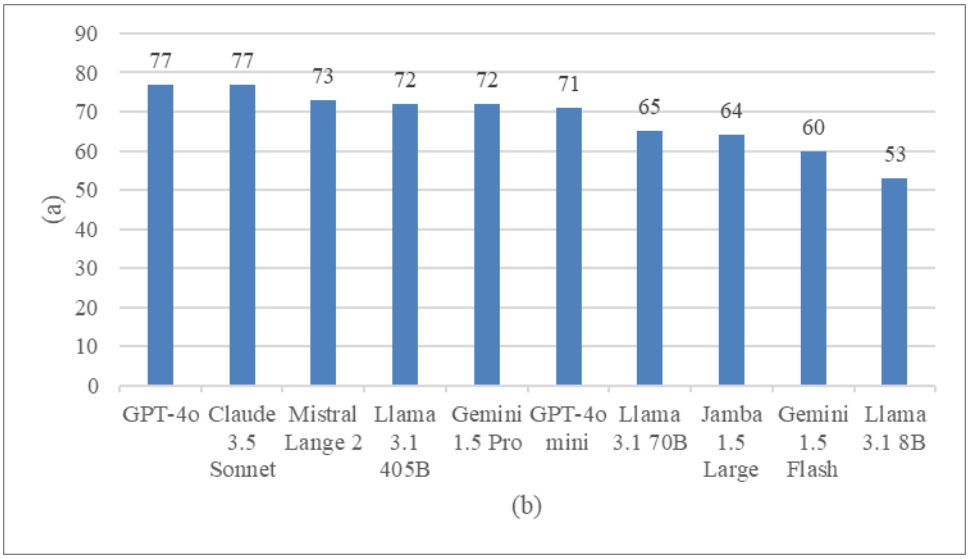

Figure 3. (a) *AI Quality Index values and* ***(b)*** *AI platforms*

Figure 3 shows the quality index of artificial intelligence models [22]. Here, higher values represent better performance. According to this index, GPT-4o and Claude 3.5 Sonnet receive the highest quality value with 77 points, while Mistral Lange 2, Llama 3.1 405B, and Gemini 1.5 Pro follow this order with close values.

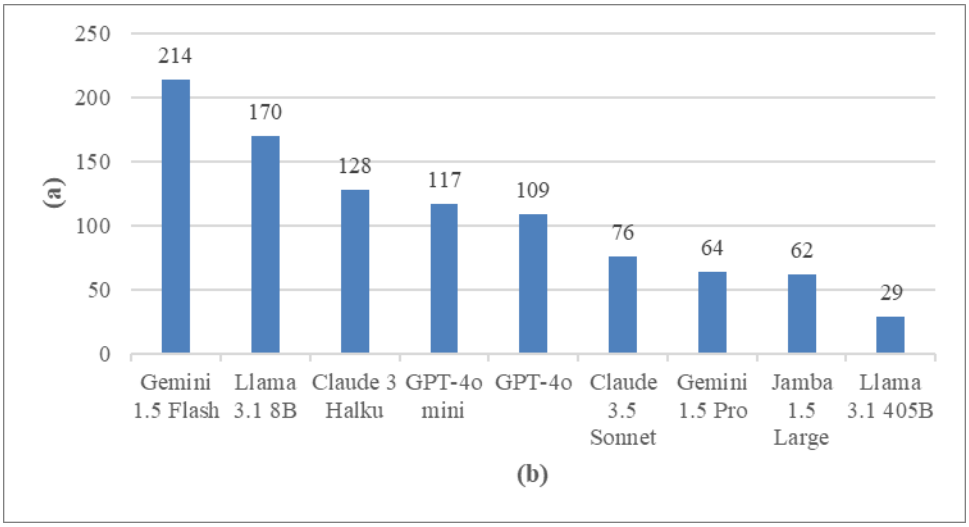

Figure 4. (a) *Output speed per second and* ***(b)*** *AI platforms*

Figure 4 [22] shows the number of output tokens produced per second per model. The higher this number, the faster the model works. Here, Gemini 1.5 Flash has the highest value with 214 tokens, 44 tokens ahead of its closest rival, the Llama 3.1 8B model.

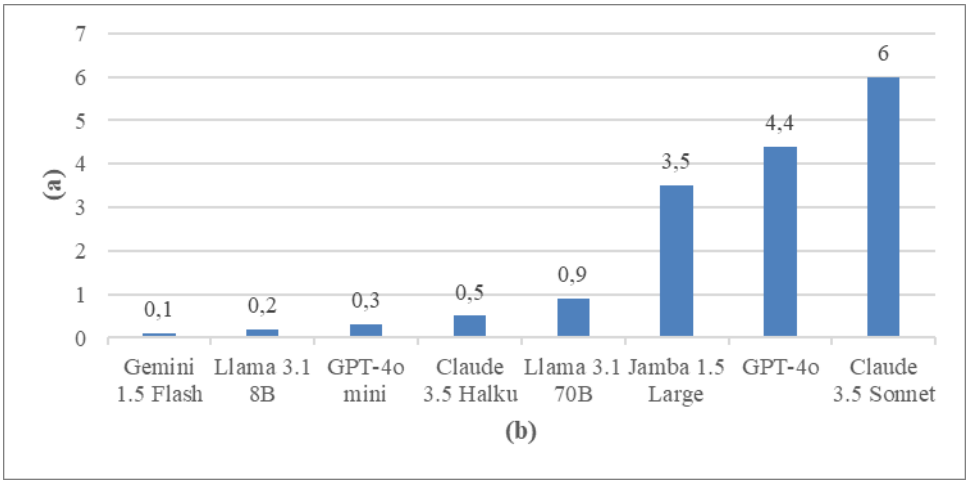

Figure 5. (a) *US dollars spent per 1 million tokens and* ***(b)*** *AI platforms*

Figure 5 [22] shows the cost of models in US dollars for every million tokens. Lower values in this graph indicate less cost. The Gemini 1.5 Flash model shows the best performance in terms of cost efficiency with 0.1 USD. These three graphs visually explain how artificial intelligence models are compared in different dimensions such as cost, speed, and quality. The graphs are prepared according to the latest analysis data as of August 2024. According to these values, it is not very accurate to say that this is the best artificial intelligence, but the best one can vary depending on what you will use artificial intelligence for and what your constraints will be.

E. NO-CODE AND LOW-CODE PLATFORMS (NCLC)

No-Code and Low-Code (NCLC) platforms allow users to develop applications with minimal technical knowledge. Using these platforms designed with drag-and-drop method, it is possible to develop applications or interfaces easily and practically without writing any code or with very little code addition. While providing a faster development process for those who know code, for those who do not know or know little, just learning to use the platform is enough to develop applications. On this subject, GitHub CEO Chris Wanstrath stated, "The future of coding is no coding at all." [23].

Many studies are being conducted in this field, both academically and experimentally. Moskal (2021) discusses the importance of NCLC technology in the digitalization process and how this technology can be used in businesses. Liu et al. (2024) detail the design and implementation of a universal NCLC web design tool, showing how such tools can increase efficiency in digital monitoring systems. Van Lunteren (2023) addresses the use of NCLC platforms to train and deploy customized object detection models [8], [9], [24].

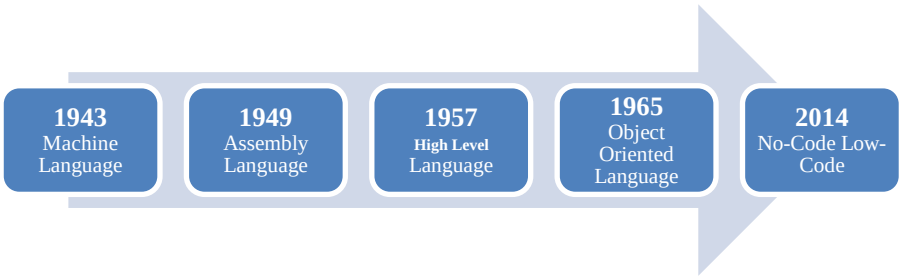

Figure 6. *Evolution of algorithms from machine code to NCLC structure*

The evolution from machine language to NCLC platforms is shown in Figure 6 [23]. There are many platforms or software products that provide NCLC development opportunities. The most popular ones for 2024 can be listed as; Mendix, Xano, Zoho Creator, Webflow, Google AppSheet, ServiceNow App

Engine, Zeroqode, Glide, Thunkable, Adalo, Blockly, and Logotec App Studio. Sample views from Blockly and Mendix interfaces can be seen in Figure 7 [25], Figure 8 [26], and Figure 9 [27], [28].

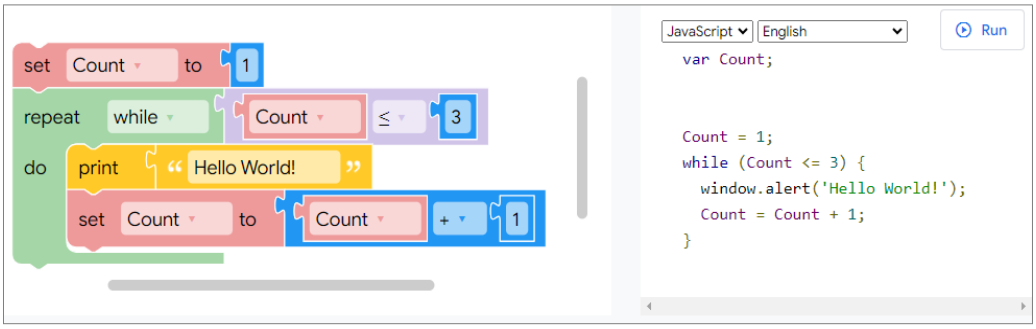

Figure 7. *Blockly Interface – Drag and drop elements to write code*

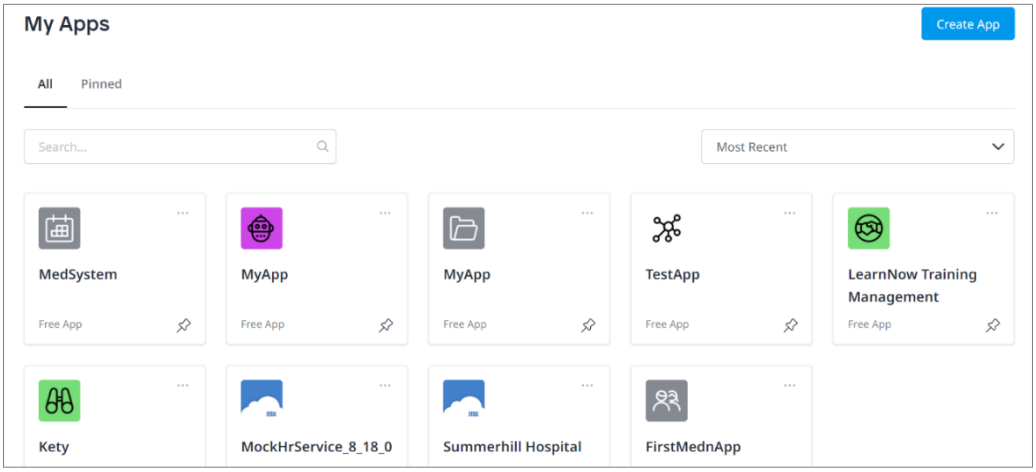

Figure 8. *Mendix Interface – My applications page*

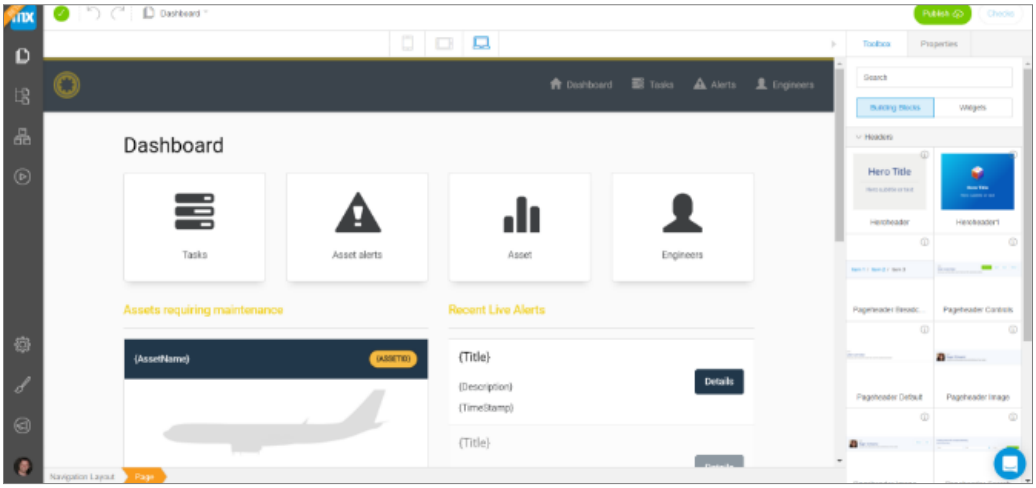

Figure 9. *Mendix Interface – Application development page*

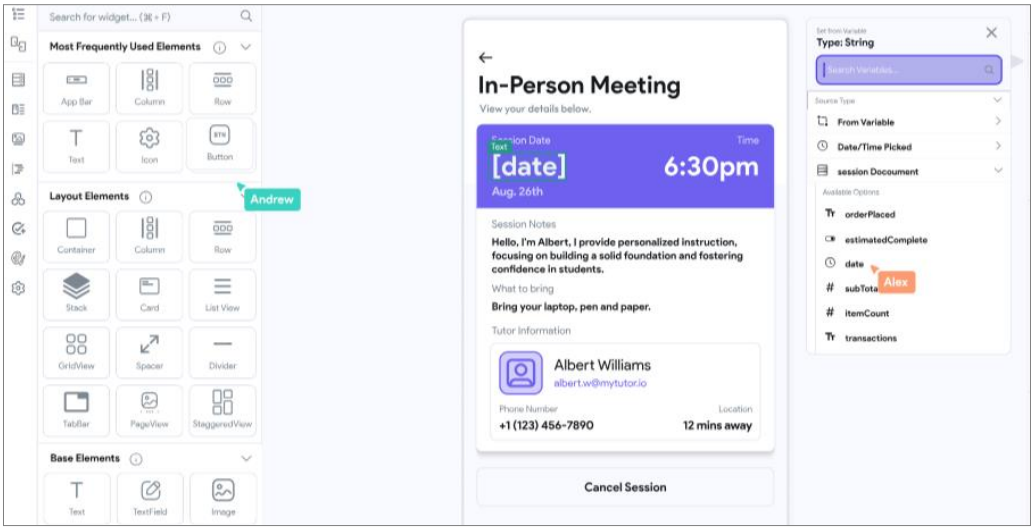

Figure 10. *FlutterFlow Interface – Mobile application development with drag and drop method*

A screenshot from the FlutterFlow platform for mobile application development can be seen in Figure 10 [29]. It is possible to publish the mobile application developed here for Android or iOS operating systems. Also, there is the opportunity to work together with other people who are allowed to work. The sole purpose of all these platforms is to enable companies of all sizes to easily create custom web and mobile applications. Apart from the drag-and-drop development opportunity, they have the chance to use applications that many companies need without the effort of development with the ready-made modules they contain.

F. AI-BASED NCLC PLATFORMS

Platforms that provide NCLC development opportunities were mentioned. Although these platforms have greatly simplified traditional software development processes, they have fallen behind advanced artificial intelligence and large language models. For this reason, AI-based NCLC platforms have started to be seen. Amazon CEO Andy Jassy, in a post he shared in August 2024, talks about the importance of AI-based code development. Andy mentions in his post that using Amazon Q, which they developed as a software development assistant, they converted an application to Java 17 in a few hours, but if they did it with the traditional software development method, it would be done with the daily effort of 50 developers. Accordingly, he emphasized that they saved as much as the daily work cost of 4500 developers per year with the AI-supported software development assistant [30]. While NCLC platforms are seen to benefit small and medium-sized enterprises, AI support is seen to provide high benefits in large-scale enterprises like in this example. Amazon Q does not currently offer a platform in NCLC structure. But it is possible to show Amazon SageMaker product similar to NCLC structure. As examples of other AI-based NCLC platforms, many platforms such as Buildfire AI, Akkio, DataRobot, Obviously AI, Google Teachable Machine, Lobe AI, Nanonets, Levity AI, Causaly AI, PredictNow AI, Invideo, AI Squared, E42, Flagright, and CallFluent AI can be listed [31].

BuildFire AI [32] is an AI-powered NCLC platform that allows everyone to develop mobile applications without coding knowledge. Thanks to AI support, the platform offers the opportunity to develop applications much faster compared to other NCLC-based platforms. The application needed is automatically created by AI with answers given to some questions about the business. It even uses the logo and colors on the company's website for the application to be in harmony with the company brand. Thus, instead of struggling for weeks just for design, it is possible to handle this in seconds with AI and

no-code structure. It offers the opportunity to publish the developed mobile application on iOS and Android operating systems.

Akkio [33] allows creating an AI-powered chatbot. While many tasks can be easily done using this chatbot, it is possible to customize the chatbot according to yourself using the NCLC structure. In addition, it can create some reports and graphs in seconds without writing code. For example, it can create detailed graphs with simple commands such as "create a graph about monthly sales".

DataRobot [34] uses generative AI and predictive workflows to improve business results. The platform is used in a wide range of industries including banking, fintech, healthcare, insurance, manufacturing and aviation. For example, it can be used with hospitals and health applications to predict which patients are more likely to be admitted. This way, doctors can proactively take steps to improve their health. An insurance company can use it to predict which products are most likely to be successful when cross-selling to specific customers. Warehouses can predict traffic to optimize resource planning. DataRobot simplifies many complex tasks without requiring code.

Google, which has many products in every field, did not hold back in this area either and offered Google Teachable Machine [35] solution. This platform uses Tensorflow, a machine learning library for model training and production. Using Teachable Machine, you can easily create datasets from images taken from the camera and file uploads. Then it offers the opportunity to produce and use models without any coding with this dataset. For example, it will create a dataset and model from a face scanned from the camera at different angles. There is the possibility to edit the codes of the model it creates with the LC method. It stands out as a facilitating platform for people working in machine learning fields.

Lobe AI [36], developed by Microsoft, is very similar to the Google Teachable Machine platform and can be considered as a competitor. As of August 2024, it only works using image classification; images are labeled to train the model, but it is known that object detection and data classification models will be available in the future. Also, Lobe AI has project templates that automatically select the best machine learning architecture for the project.

Amazon SageMaker [37], [38] is a cloud-based, AI-powered NCLC platform designed for enterprise companies. This platform provides data scientists, engineers, and developers with the ability to easily process data, create models, train models, and deploy [37]. While users without technical knowledge can work in machine learning fields with NC development capability, users with technical knowledge can make improvements or customizations by editing the codes created by the platform with the LC feature. The platform is similar to Google's Teachable Machine and Microsoft's LobeAI products in terms of service and usage. One of the biggest advantages of SageMaker is the ability to deploy your model that you developed on the platform. Thus, you can share this over the web or use it in your applications.

LevityAI [39] is an NC workflow automation platform that allows creating artificial intelligence and machine learning models using the uploaded dataset [40]. Users can create an AI-powered model with LevityAI to complete common tasks based on specific triggers. You can connect to systems already in use such as CRM databases, email providers, and management systems, and create workflows by creating AI blocks. Thus, it is possible to easily make an automation application for continuous tasks.

CausalyAI [41] is designed for biomedical scientific research and development. It is used to eliminate human bias during scientific research and studies. CausalyAI has all published biomedical literature and can produce answers to questions asked in this direction. These answers, which can be accessed by doing literature review for weeks, can be found in seconds with CausalyAI. It is possible to develop a wide

variety of useful applications by integrating this artificial intelligence into no-code/low-code development environments. For example, it can help identify biomarkers in drug development programs and regulate success rates. It can also verify and characterize biomarkers in these studies. This capability can be customized using the low-code method and can be integrated into existing applications or made to work together. As of August 2024, there is no NCLC platform within CausalyAI yet, but it can be added to existing NCLC platforms with API support.

AI Squared [42] uses both predictive and generative AI models to support web-based applications. The platform can be applied on the web application already in use. It allows quick editing and development of the existing web application using AI-powered LC method on AI Squared. In this respect, it is different from many other artificial intelligence platforms.

CallFluent AI [43] is a platform that can create an AI-powered voice call representative in 1 minute without writing code. These created representatives can make communication smoother and more efficient by managing tasks such as answering customer questions or scheduling appointments. The platform has a flexible structure, allowing businesses to make additional developments according to their own special needs. It can be used in many areas where time will be saved to automate daily tasks. All these possibilities are very important for reducing costs in businesses [44].

III. COMPARATIVE ANALYSIS

To fully understand the effects of AI-based NCLC platforms on software development processes, it is necessary to compare these platforms both with traditional NCLC platforms and among themselves. In this section, we will discuss the advantages offered by AI-based platforms compared to traditional platforms, the differences between different AI-based applications, and how these platforms are evaluated according to various usage areas.

AI-based NCLC platforms offer significant advantages compared to traditional platforms. While traditional platforms allow users to develop simple applications with limited technical knowledge, AI-based platforms make complex functions possible. For example, AI-powered platforms such as LobeAI and Amazon SageMaker make it possible to integrate and automate machine learning models, while traditional NCLC platforms generally do not offer such features. In addition, the user interface of AI-powered platforms is more intuitive and user-friendly; this accelerates the development process and reduces costs.

Table 1. *Comparison Table of AI-Powered and Traditional NCLC Platforms*

Feature	**AI-Powered NCLC Platforms**	**Traditional NCLC Platforms**
Ease of use	Easier to use with natural language commands.	Drag-and-drop interface, easy to use but has a learning process.
Customization ability	High – AI can understand complex and custom needs.	Fast – Requires manual component selection and configuration.
Development speed	Very Fast – AI quickly converts requests into code.	Moderate – May require some manual interventions.

Table 1 (cont). *Comparison Table of AI-Powered and Traditional NCLC Platforms*

Automation level	High – Routine tasks are performed automatically.	Medium – May require some manual interventions.
Code quality	Medium – AI applies best practices and current standards. But there is a possibility of writing erroneous code.	Variable – Depends on platform and user skills.
Learning curve	Low – Quick adaptation thanks to natural language use.	Medium – Need to learn platform features.
Cost	High initially, low in the long term.	Generally lower initial cost.
Scalability	High – AI easily provides integration to needs.	Medium – May require manual scaling.
Integration capabilities	Wide – AI provides easy integration with various systems.	Limited – Limited to predefined integrations.
Debugging and troubleshooting	Advanced – AI can detect and correct errors.	Manual – User needs to find and correct errors.
Data security	Medium – AI use may require additional security measures.	High -- Less complex, easier to provide security.
Updates and maintenance	Automatic – AI provides continuous learning and improvement.	Manual – Requires periodic updates and maintenance.

The comparison between AI-powered and traditional NCLC platforms extends beyond mere technological capabilities, encompassing a wide range of factors that significantly impact the software development lifecycle. These factors include ease of use, development speed, customization abilities, long-term cost implications, and scalability. Understanding these differences is crucial for organizations as they navigate the complex landscape of modern software development tools. While AI-powered platforms promise enhanced automation and potentially more sophisticated outputs, they also introduce new challenges in terms of data security and initial implementation costs. Traditional NCLC platforms, on the other hand, often offer simplicity and a lower barrier to entry, but may lack the advanced features necessary for more complex projects. The choice between these two types of platforms can have far-reaching implications for an organization's digital strategy, affecting not only the immediate development process but also long-term maintenance and scalability of applications. Moreover, the rapid pace of technological advancement in AI means that the capabilities gap between these platform types is likely to evolve, adding another layer of complexity to the decision-making process. As organizations strive to balance innovation with practicality, a thorough understanding of these platforms' strengths and limitations becomes indispensable. The following table provides a comprehensive overview of these differences, highlighting key aspects that organizations should consider when choosing between AI-powered and traditional NCLC platforms, and offering insights into how these choices may shape their software development capabilities in the years to come [45], [46].

Table 2. *Comparison Table of AI-Powered NCLC Platforms*

Platform	Main Focus	Key Feature	Target Audience	Usage Areas
Amazon Q	General AI assistant	Natural language processing, data analysis, code generation	Businesses, developers	Business intelligence, software development
BuildFire AI	Mobile app development	Automatic code generation, design suggestions	SMEs, entrepreneurs	Mobile app creation
Akkio	Predictive analytics	Automatic code generation, data visualization	Data analysts, businesses	Customer analysis, risk assessment
DataRobot	Enterprise AI platform	Automatic machine learning, model deployment	Large enterprises	Predictive modeling, data science
Obviously AI	Predictive analytics	Natural language queries, fast model creation	SMEs, data analysts	Sales prediction, customer segmentation
Google Teachable Machine	Image classification	Easy model training, web-based interface	Educators, students	Educational projects, simple AI applications
Lobe AI	Image classification	Drag-and-drop model training, easy export	Developers, designers	Visual recognition applications
Causaly AI	Biomedical research	Causal inference, literature analysis	Researchers, pharmaceutical companies	Drug discovery, disease research
AI Squared	AI integration	Adding AI to existing applications, model management	Developers, businesses	Application development, AI integration

The table above shows the fundamental differences between AI-powered NCLC platforms and traditional NCLC platforms. AI-powered platforms offer easier use, faster development process, and higher customization possibilities thanks to their natural language processing capabilities. Also, they can be more efficient in the long term with automatic debugging and continuous learning features. However, traditional NC platforms continue to be an attractive option especially for small-scale projects with lower initial costs and a simpler structure. Both approaches have their own advantages and usage areas. Businesses should choose the most suitable platform according to their own needs, technical capabilities, and budgets. In the future, with the development of artificial intelligence technologies, more advanced hybrid platforms that combine these two approaches can be expected to emerge [45], [46].

Platforms such as BuildFireAI, Akkio, and DataRobot offer different functionalities. These platforms are optimized for various usage scenarios. For example, BuildFire AI is designed specifically for mobile application development, while Akkio is optimized for data analytics and business intelligence

solutions. DataRobot, on the other hand, is strong in automatic machine learning modeling and has the capacity to process large datasets. Some feature comparisons by platforms are shown in Table 2.

These various AI-powered NC platforms demonstrate how technology can be integrated into different sectors and business processes. Each platform stands out with its unique strengths and areas of expertise. Users should choose the platform that best suits their specific needs, technical competencies, budgets, and long-term goals. For example, a corporate company may prefer Amazon Q for business intelligence and code generation, while an entrepreneur may use Buildfire AI to quickly develop mobile applications. On the other hand, a business that wants to add artificial intelligence capabilities to its existing applications may prefer AI Squared. When making a choice, factors such as the scalability of the platform, integration capabilities, user-friendliness, and support services offered should also be considered. Also, in this period when artificial intelligence technology is developing rapidly, it is an important criterion that the chosen platform is continuously updated and open to innovations. As a result, the most efficient artificial intelligence platform will be the one that can meet the user's current requirements as well as support future growth and change potential.

A. EVALUATION ACCORDING TO USAGE AREAS

A comprehensive analysis of how different AI-powered NCLC platforms are used in various sectors reveals the wide impact area of this technology. As seen in Table 2, these platforms offer solutions in a wide variety of fields. In the healthcare sector, AI-powered no-code platforms provide great benefits not only in patient data management and analysis but also in more advanced applications. For example, platforms like CausalyAI accelerate drug discovery and disease research by making causal inference and literature analysis in biomedical research. This contributes to the development of treatment methods by enabling more effective use of medical knowledge. In the finance sector, these platforms go beyond analyzing customer data and making predictions. While PredictNowAI offers time series analysis for stock market prediction and risk management, Flagright provides real-time risk monitoring and behavioral analysis in fraud detection and KYC (Know Your Customer) [47] processes. These tools help optimize investment strategies while increasing financial security [48].

In the business world, general AI assistants like Amazon Q are used in business intelligence and software development processes, increasing efficiency. Buildfire AI simplifies the mobile application development process especially for SMEs and entrepreneurs. E42, on the other hand, offers virtual AI agents and business process automation to optimize the internal operations of large enterprises. In the education sector, platforms like Google Teachable Machine provide educators and students with the opportunity to develop simple AI applications, making AI education more accessible [49]. This ensures that future generations are familiar with AI technologies, encouraging long-term technological innovation. In the field of marketing and content production, platforms like Invideo enable the rapid and effective creation of social media videos and advertisements with AI-powered video editing and template libraries. This allows small businesses and content producers to produce professional quality content. In the field of customer services, solutions like CallFluent AI increase the quality of customer interactions and support staff training by performing speech and emotion analysis. This improves customer satisfaction while also improving operational efficiency. Each sector and usage area has its own unique needs and requirements; this determines which platform is most suitable. For example, while platforms like Lobe AI or Google Teachable Machine for image classification may be ideal for a startup that wants to do rapid prototyping, more advanced analytical platforms like DataRobot or Akkio may be more suitable for a corporate company that needs to do comprehensive data analysis. This diversity shows how NCLC platforms can play a transformative role in different sectors and business processes. As technology evolves and these platforms become more sophisticated, it is expected that usage areas will expand further and boundaries between sectors will blur.

IV. DISCUSSION

The benefits provided by AI-based NCLC platforms to software development processes are quite extensive. However, it should not be forgotten that these technologies also have some challenges and limitations. In this section, we will examine in detail the advantages offered by AI-based NCLC platforms, potential challenges that may be encountered, and problems that may arise in the future.

AI-based NCLC platforms offer various advantages such as accelerating software development processes, reducing costs, and increasing flexibility. For example, while traditional software development processes can take weeks or even months, it is possible to develop complex applications within a few days thanks to these platforms. In addition, artificial intelligence algorithms can analyze large amounts of data to better understand users' needs and offer appropriate solutions. This provides a significant advantage in terms of both time and cost. Although AI-based NCLC platforms offer many advantages, there are also some challenges and limitations. First, these platforms may increase concerns about data privacy and security. The lack of transparency in artificial intelligence's decision-making processes can make it difficult for users to fully understand the results. Also, despite the complex structures of these platforms, there may be situations that require users to have technical knowledge. Such challenges may prevent the widespread adoption of AI-based platforms. With technological developments, potential problems that AI-based NCLC platforms may encounter will also emerge. For example, as artificial intelligence becomes increasingly complex, it will lead to questioning the ethical dimensions and usage limits of these technologies. Also, issues such as data integrity and security will become even more important during the development and management of these platforms. Developers and users will need to plan carefully for these issues.

A comprehensive analysis of the findings obtained from the literature review provides a deep understanding of the effects of these findings on software development processes. In this section, a general evaluation of the findings in the literature will be made, the theoretical and practical contributions of these findings will be discussed, and future research directions will be discussed. The literature review evaluated the effects of AI-based NCLC platforms on software development processes from various aspects. The current literature suggests that the use of these platforms significantly accelerates software development processes, reduces costs, and increases software quality. However, some studies also emphasize the technical limitations of these platforms and the difficulties in user adaptation. These findings indicate that these technologies are open to development and will be better in the future.

This review offers important contributions from both theoretical and practical perspectives. Theoretically, it provides a deeper understanding of the effects of AI-based NCLC platforms on software development processes. From a practical point of view, it offers suggestions on how these platforms can be used more effectively in software development processes. This article can be a useful resource for both academic researchers and software developers. Future research in this field should focus on further optimization of AI-based NCLC platforms and expansion of their usage areas. In particular, studies examining the applications and usage scenarios of these platforms in different industries should be conducted. It is also important to investigate the long-term effects of integrating artificial intelligence into these platforms. Such research can shape the future development of this technology.

V. CONCLUSION

In this section, the effects of AI-based NCLC platforms on software development processes will be evaluated in general, and suggestions will be presented for organizations that want to increase the use of these technologies. These suggestions aim to make the best use of the advantages offered by the platforms and overcome potential challenges.

The effects of AI-based NCLC platforms on software development processes have been extensively addressed in the literature, and it has been revealed that this technology offers multifaceted advantages. These platforms make significant contributions to accelerating development processes, reducing costs, and empowering non-technical users. While platforms such as Amazon Q and DataRobot offer groundbreaking solutions in corporate-level AI integration and data analytics, platforms such as Buildfire AI and Invideo are revolutionizing specific areas (mobile application development and video content production). Google Teachable Machine and Lobe AI democratize AI education, enabling a wider user base to benefit from these technologies. However, the challenges and limitations encountered during the use of these platforms should not be ignored. Data security and privacy are critical, especially in platforms like Flagright and PredictNow AI that process sensitive financial data. Also, the transparency and explainability of AI decisions is a significant concern, especially in systems like Causaly AI that perform complex analysis. This article provides a comprehensive framework for evaluating the current state and future potential of AI-based NCLC platforms. Given the rapid development of technology, trends and innovations in this field need to be constantly monitored.

For companies aiming to optimize the use of AI-based NCLC platforms in their software development processes, a comprehensive strategy is essential. This strategy should begin with a thorough evaluation to select the most suitable platform for their specific needs. For instance, while Amazon Q might be the go-to choice for general-purpose solutions, specialized platforms like Nanonets or Levity AI could be more appropriate for niche requirements. Once a platform is chosen, implementing robust security measures becomes paramount, particularly for those handling sensitive data like Flagright and E42. Regular security audits and state-of-the-art encryption methods should be standard practice.

The success of implementing these platforms heavily relies on proper training and skill development. Organizations should invest in comprehensive training programs for their employees, tailoring the content to the specific platforms in use. For example, users of Google Teachable Machine would benefit from foundational machine learning concept training. Alongside technical training, it's crucial to establish clear guidelines for ethical AI usage. This includes developing policies that ensure AI decision transparency and explicability, which is especially critical for platforms like PredictNow AI that deal with financial forecasting.

As organizations grow and evolve, so too should their technological infrastructure. Therefore, it's vital to select platforms that offer scalability to meet expanding needs. Platforms like AI Squared, which allow for seamless AI integration into existing systems, can be particularly valuable in this regard. To ensure ongoing effectiveness, continuous monitoring and optimization of these platforms is necessary. Analytical tools such as Akkio and Obviously AI can be instrumental in this ongoing assessment process. The integration of NCLC platforms often necessitates a reimagining of existing business processes. For instance, CallFluent AI could drive a complete overhaul of customer service processes. This technological shift should be accompanied by a cultural transformation within the organization, fostering an environment that embraces AI and NCLC platforms. User-friendly platforms like Lobe AI can be catalysts for this cultural shift.

Legal and regulatory compliance cannot be overlooked, especially when dealing with sensitive domains. Platforms like Causaly AI, which operate in the biomedical research space, must adhere strictly to relevant legal and regulatory frameworks. Finally, the journey towards effective NCLC platform utilization should not be a solitary one. Collaborating with other organizations and academic institutions to share best practices and develop joint solutions can accelerate progress and innovation in this rapidly evolving field. By adopting this holistic approach, organizations can harness the full potential of AI-based NCLC platforms, driving their digital transformation efforts and positioning themselves at the forefront of technological innovation. The key to success lies in staying agile, continuously adapting to new developments, and maintaining a strategic focus on leveraging these powerful tools to gain a competitive edge in the market.

In conclusion, AI-based NCLC platforms stand out as effective tools with the potential to make software development processes more accessible and optimize them. These technologies accelerate development

processes while reducing costs and allow users with limited technical expertise to create complex applications. However, the effective use of these platforms requires careful planning, continuous training, and adoption of ethical principles. Organizations should consider potential challenges while evaluating the opportunities offered by these technologies. When implemented with a strategic approach, AI-powered NCLC platforms have the potential to play an important role in businesses' digital transformation processes and lead future innovation initiatives. Continuous monitoring and adaptation to developments in this field will be critical for organizations to gain competitive advantage and be at the forefront of technological advancements.

VI. REFERENCES

[1] TÜSİAD Yazılım Çalışma Grubu et al., "Türkiye'de Yazılım Ekosisteminin Geleceği," Deloitte, Jan. 2021.

[2] M. R. DeLisi and C. Howley, "Gartner Forecasts Worldwide Low-Code Development Technologies Market to Grow 20% in 2023," Gartner. Accessed: Aug. 01, 2024. [Online]. Available: https://www.gartner.com/en/newsroom/press-releases/2022-12-13-gartner-forecasts-worldwide-low-code-development-technologies-market-to-grow-20-percent-in-2023

[3] H. El Kamouchi, M. Kissi, and O. El Beggar, "Low-code/No-code Development : A systematic literature review," in Proceedings - SITA 2023: 2023 14th International Conference on Intelligent Systems: Theories and Applications, Institute of Electrical and Electronics Engineers Inc., 2023. doi: 10.1109/SITA60746.2023.10373712.

[4] Z. Jiang, F. F. Xu, J. Araki, and G. Neubig, "How Can We Know What Language Models Know?", doi: 10.1162/tacl.

[5] D. Jurafsky and J. H. Martin, "Speech and Language Processing An Introduction to Natural Language Processing, Computational Linguistics, and Speech Recognition with Language Models Third Edition draft Summary of Contents."

[6] B. Akbulut, "Büyük Dil Modelleri: Dilin Evrimi ve Yapay Zekâ (Bölüm 2)," Medium. Accessed: Jul. 25, 2024. [Online]. Available: https://medium.com/kodluyoruz/büyük-dil-modelleri-dilin-evrimi-ve-yapay-zekâ-bölüm-2-458ddea54f09

[7] B. Akbulut, "Generative AI: Yapay Zekâ Dünyasının Yaratıcı Gücü ~ Bölüm 1," Medium. Accessed: Jul. 25, 2024. [Online]. Available: https://medium.com/kodluyoruz/%C3%BCretken-yapay-zek%C3%A2-yapay-zek%C3%A2-d%C3%BCnyas%C4%B1n%C4%B1n-yarat%C4%B1c%C4%B1-g%C3%BCc%C3%BC-b%C3%B6l%C3%BCm-1-a7fc1ad65dd6

[8] P. van Lunteren, "EcoAssist: A no-code platform to train and deploy custom YOLOv5 object detection models," J Open Source Softw, vol. 8, no. 88, p. 5581, Aug. 2023, doi: 10.21105/joss.05581.

[9] M. Moskal, "No-Code Application Development on the Example of Logotec App Studio Platform," Informatyka, Automatyka, Pomiary w Gospodarce i Ochronie Srodowiska, vol. 11, no. 1, pp. 54–57, 2021, doi: 10.35784/IAPGOS.2429.

[10] T. Nur and F. □1, "ELT FORUM 12(1) (2023) Journal of English Language Teaching Artificial intelligence (AI) technology in OpenAI ChatGPT application: A review of ChatGPT in writing English essay," Journal of English Language Teaching, vol. 6, no. 1, 2017, [Online]. Available: http://journal.unnes.ac.id/sju/index.php/elt

[11] Ö. Aydin and E. Karaarslan, "OpenAI ChatGPT Generated Literature Review: Digital Twin in Healthcare." [Online]. Available: https://ssrn.com/abstract=4308687

[12] L. Floridi and M. Chiriatti, "GPT-3: Its Nature, Scope, Limits, and Consequences," Dec. 01, 2020, Springer Science and Business Media B.V. doi: 10.1007/s11023-020-09548-1.

[13] J. Liu, C. Liu, P. Zhou, R. Lv, K. Zhou, and Y. Zhang, “Is ChatGPT a Good Recommender? A Preliminary Study,” Oct. 2023.

[14] P. Dhoke and P. Lokulwar, “Evaluating the Impact of No-Code/Low-Code Backend Services on API Development and Implementation: A Case Study Approach,” in 2023 14th International Conference on Computing Communication and Networking Technologies, ICCCNT 2023, Institute of Electrical and Electronics Engineers Inc., 2023. doi: 10.1109/ICCCNT56998.2023.10306945.

[15] OpenAI et al., “GPT-4 Technical Report,” Mar. 2023, [Online]. Available: http://arxiv.org/abs/2303.08774

[16] M. Wermelinger, “Using GitHub Copilot to Solve Simple Programming Problems,” in SIGCSE 2023 - Proceedings of the 54th ACM Technical Symposium on Computer Science Education, Association for Computing Machinery, Inc, Mar. 2023, pp. 172–178. doi: 10.1145/3545945.3569830.

[17] M. Kytö, “Copilot for Microsoft 365: A Comprehensive End-user Training Plan for Organizations.”

[18] B. Hui et al., “Qwen2.5-Coder Technical Report,” Sep. 2024, [Online]. Available: http://arxiv.org/abs/2409.12186

[19] A. Grattafiori et al., “The Llama 3 Herd of Models,” Jul. 2024, [Online]. Available: http://arxiv.org/abs/2407.21783

[20] Y. Sonoda et al., “Diagnostic performances of GPT-4o, Claude 3 Opus, and Gemini 1.5 Pro in ‘Diagnosis Please’ cases,” Jpn J Radiol, Nov. 2024, doi: 10.1007/s11604-024-01619-y.

[21] “Kodlama için en iyi 5 büyük dil modeli,” Innova. Accessed: Aug. 13, 2024. [Online]. Available: https://www.innova.com.tr/blog/kodlama-icin-en-iyi-5-buyuk-dil-modeli

[22] “Comparison of Models: Quality, Performance & Price Analysis,” Artificial Analysis. Accessed: Dec. 28, 2024. [Online]. Available: https://artificialanalysis.ai/models

[23] A. Verma, “‘The Future Of Coding Is No Coding At All’ — Did GitHub CEO Predict Traditional Programming’s Death?,” Fossbytes, Oct. 13, 2017. Accessed: Nov. 20, 2024. [Online]. Available: https://fossbytes.com/coding-automation-programming-github-ceo/

[24] H. Liu, C. Zhang, S. Sun, H. Zhou, Y. Xie, and T. Jiang, “Universal No-code Web Design Tool for Substation Digital Monitoring System,” in IMCEC 2024 - IEEE 6th Advanced Information Management, Communicates, Electronic and Automation Control Conference, Institute of Electrical and Electronics Engineers Inc., 2024, pp. 1391–1394. doi: 10.1109/IMCEC59810.2024.10575868.

[25] F. Sufi, “Algorithms in Low-Code-No-Code for Research Applications: A Practical Review,” Feb. 01, 2023, MDPI. doi: 10.3390/a16020108.

[26] N. Fraser, Ten Things We’ve Learned from Blockly. IEEE, 2015.

[27] H. Marc and P. Mileff, “Introduction to Mendix,” Production Systems and Information Engineering, vol. 11, no. 3, p. 64, doi: 10.32968/psaie.2023.3.5.

[28] “User Interfaces - Software Development Life Cycle,” Mendix. Accessed: Aug. 21, 2024. [Online]. Available: https://www.mendix.com/evaluation-guide/app-lifecycle/develop/ux-multi-channel-apps/user-interfaces/

[29] M. Fadaee, “Building The Foundation for an AI-Integrated Career Coaching Application with FlutterFlow,” Bachelor’s Thesis, HAMK, 2024.

[30] A. Jassy, “One of the most tedious but critical tasks activity.. – Amazon Q,” Linkedin. Accessed: Aug. 29, 2024. [Online]. Available: https://www.linkedin.com/posts/andy-jassy-8b1615_one-of-the-most-tedious-but-critical-tasks-activity-7232374162185461760-AdSz/

[31] W. Filipek, “Top No-Code AI Tools of 2024: In-Depth Guide,” Buildfire. Accessed: Aug. 28, 2024. [Online]. Available: https://buildfire.com/no-code-ai-tools/

[32] “BuildFire App Builder Web Site.” Accessed: Aug. 28, 2024. [Online]. Available: https://buildfire.com/

[33] M. Annamalai et al., Sharding the Shards: Managing Datastore Locality at Scale with Akkio. Usenix, 2018. [Online]. Available: https://www.usenix.org/conference/osdi18/presentation/annamalai

[34] E. Huovila, “USE OF MACHINE LEARNING IN SUPPLY CHAIN MANAGEMENT-CASE STUDY WITH DATAROBOT.”

[35] D. Agustian, P. P. G. P. Pertama, P. N. Crisnapati, and P. D. Novayanti, “Implementation of Machine Learning Using Google’s Teachable Machine Based on Android,” in 3rd International Conference on Cybernetics and Intelligent Systems, ICORIS 2021, Institute of Electrical and Electronics Engineers Inc., 2021. doi: 10.1109/ICORIS52787.2021.9649528.

[36] “Lobe AI GitHub Page,” Lobe. Accessed: Aug. 28, 2024. [Online]. Available: https://www.lobe.ai/

[37] T. Özdoğan, “SageMaker nedir?,” Linkedin. Accessed: Aug. 29, 2024. [Online]. Available: https://www.linkedin.com/pulse/sagemaker-nedir-tunahan-%C3%B6zdo%C4%9Fan/

[38] D. Nigenda et al., “Amazon SageMaker Model Monitor: A System for Real-Time Insights into Deployed Machine Learning Models,” in Proceedings of the ACM SIGKDD International Conference on Knowledge Discovery and Data Mining, Association for Computing Machinery, Aug. 2022, pp. 3671–3681. doi: 10.1145/3534678.3539145.

[39] “Levity AI Web Site.” Accessed: Aug. 29, 2024. [Online]. Available: https://levity.ai/

[40] K. Sukhanova, “Create No-Code Models with Levity,” TechAcute, Oct. 25, 2022. Accessed: Dec. 29, 2024. [Online]. Available: https://techacute.com/no-code-models-levity/

[41] “Causaly AI Web Site,” Causaly. Accessed: Aug. 28, 2024. [Online]. Available: https://www.causaly.com/

[42] “AI Squared Web Site,” AI Squared. Accessed: Aug. 28, 2024. [Online]. Available: https://squared.ai/

[43] “CallFluent AI Web Site,” CallFluent AI. Accessed: Aug. 28, 2024. [Online]. Available: https://callfluent.com/

[44] B. Yalçıner et al., “Yazılım Kalite Maliyetlerinin Kontrol Altında Tutulması Yoluyla Proje Geliştirme Maliyetlerinin Düşürülmesi: Literatüre bir bakış.”

[45] S. Martínez-Fernández et al., “Software Engineering for AI-Based Systems: A Survey,” ACM Transactions on Software Engineering and Methodology, vol. 31, no. 2, Apr. 2022, doi: 10.1145/3487043.

[46] A. N. Duc, I. Sundbø, E. Nascimento, A. Nguyen-Duc, and T. Conte, “Software engineering for artificial intelligence and machine learning software: A systematic literature review”, doi: 10.48550/arXiv.2011.03751.

[47] V. U. Rajput, “Research on Know Your Customer (KYC),” 2013. [Online]. Available: www.ijsrp.org

[48] D. Kecerdasan Buatan, M. Hidayat, S. Yulia Defitri, H. Hilman STIE Persada Bunda, and U. Mahaputra Muhammad Yamin, “The Impact of Artificial Intelligence (AI) on Financial Management,” 2024. [Online]. Available: https://journal.ppipbr.com/index.php/productivity/index

[49] N. Goksel and A. Bozkurt, “Artificial Intelligence in Education,” 2019, pp. 224–236. doi: 10.4018/978-1-5225-8431-5.ch014.

Düzce University
Journal of Science & Technology

Research Article

THE EFFECT OF GRAPHENE NANOPARTICLES ON THE MECHANICAL PROPERTIES OF WOVEN ARAMID/EPOXY COMPOSITES

Ömer ŞEN [a], Musa YILDIRIM [b*]

[a] *Department of Industrial Design Eng. Karabük University Technology Faculty, KARABÜK TURKEY*
[b] *Department of Mechanical Eng. Karabük University Engineering Faculty, KARABÜK TURKEY*
* *Corresponding author's e-mail address: musayildirim@karabuk.edu.tr*
DOI: 10.29130/dubited.1542336

ABSTRACT

In this study, the effect of the amount of graphene added to aramid fiber/epoxy composites on the mechanical properties of these composites was investigated. In the study, graphene nanoparticles were added to the epoxy matrix at four different rates and mixed by mechanical methods, and then 5-layer aramid epoxy graphene composite plates were obtained using hand lay-up and vacuum infusion methods. Samples were cut from these composite plates according to ASTM 790 for bending test and ASTM D3039 for tensile test and three-point bending and tensile tests were performed. Microstructure examinations were carried out under a macro microscope. After the studies, it was observed that agglomeration occurred in the microstructures of the produced composites. It was determined that graphene added to the aramid epoxy composite increased the bending strength and bending modulus, the highest bending stress was observed in the samples with 1% graphene added. The flexural strength, which compared to the undoped composite, increased about 64 % in this sample. In addition, the highest tensile strength was measured in the undoped sample, and after the 0.25% graphene addition, the tensile strength decreased due to the agglomeration of graphene that occurred in the structure.

Keywords: *Graphene nanoparticles, Mechanical properties, Aramid fibers, Epoxy composites*

Grafen Nanopartiküllerinin Dokuma Aramid/Epoksi Kompozitlerinin Mekanik Özelliklerine Etkisi

Öz

Bu çalışmada aramid fiber /epoksi kompozitlere ilave edilen grafen miktarının bu kompozitlerin mekanik özelliklerine etkisi incelenmiştir. Çalışmada epoksi matris içerisine dört farklı oranda grafen nanopartiküller ilave edilerek mekanik yöntemle karıştırıldıktan sonra el yatırma ve vakum infüzyon yöntemleri kullanılarak 5 katlı aramid epoksi grafen kompozit plakalar elde edilmiştir. Elde edilen bu kompozit plakalardan eğme testi için ASTM 790 ve çekme testi için ASTM D3039 standartlara göre numuneler kesilerek üç nokta eğme ve çekme testleri yapılmıştır. Mikro yapı incelemeleri makro mikroskop altında yapılmıştır. Yapılan çalışmalar sonrasında üretilen kompozitlerin mikro yapılarında aglomerasyonun oluştuğu gözlemlenmiştir. Aramid epoksi kompozite ilave edilen grafenin eğilme

Received: 02/09/2024, Revised: 28/10/2024, Accepted: 31/10/2024

dayanımı ve eğilme modülünü arttırdığı %1 grafen ilave edilen numunelerde en yüksek eğilme gerilmesi gözlenmiştir. Katkısız numunelere göre bu numunede eğilme mukavemeti yaklaşık %64 oranında artmıştır. Ayrıca çekme testleri sonrasında en yüksek çekme dayanımının katkısız numunelerde olduğu, %0.25 den daha fazla grafen ilave edilen numunelerde ise grafenin yapıda oluşturduğu aglomerasyona bağlı olarak çekme dayanımının düştüğü tespit edilmiştir.

Anahtar Kelimeler: *Grafen nanopartikülleri, Mekanik özellikler, Aramid lifler, Epoksi kompozitler*

I. INTRODUCTION

Polymer matrix composites are of great interest today due to the need for high strength and light materials. Fiber-reinforced polymer matrix composites are used in many areas such as the aerospace industry, the defense industry, and the automotive industry due to their low density, high mechanical properties, and high corrosion resistance [1-3]. Epoxy resin is one of the widely used matrix materials in fiber-reinforced polymer composites due to its chemical corrosion resistance and low shrinkage during curing, as well as its low weight and high adhesion properties. Glass fiber, carbon fiber, and aramid fibers are used to reinforce this matrix material [4-6]. Aramid fiber is a type of synthetic fiber that contains at least 85% amide bonds between two aromatic rings. Kevlar, Twaron, and Teijinconex are the most common commercially known aramid fibers. In general, aramid fiber is divided into two groups: meta-aramids and para-aramids. In para-aramids the bonds are aligned in the fiber direction, while in meta-aramids the bonds are formed in a zigzag pattern. Para aramids have higher strength due to different bond direction and type. Aramid fibers are used commercially in the form of yarn and woven fabrics [7-8]. Aramid fiber is a preferred reinforcement element in polymer matrix composites due to its many superior properties such as low density (1.44 g/cm3), high rigidity, high strength (3620 MPa tensile strength), and high specific module. These polymer matrix composites, which are formed by combining with various resins, are used in applications requiring high performance such as ballistic armors in airplanes and helicopters [9-10]. However, composites manufactured using strong fiber and the appropriate matrix may not always exhibit high mechanical properties. A significant parameter affecting the mechanical properties in fiber-reinforced composites is the interfacial properties between the matrix and the fiber. With the high interfacial adhesion between the matrix and the fiber, the load transfer from the matrix to the fiber is easier, thus increasing the strength of the composite [11, 12]. Since aramid fibers have chemical inertia, high crystallinity, and smooth surface properties, the interfacial bond between the matrix and the fiber is weak. To improve this bond, the properties of composites are being enhanced with carbon-based nanofillers such as carbon nanotubes and graphene. Graphene is considered one of the most effective fillers for improving bonding at the fiber/matrix interface among all carbon allotropes [13- 15].

Graphene is one of today's most popular materials, consisting of carbon atoms arranged in a hexagonal lattice to form a 2D layer, large surface area (2630 m2/g), an elastic modulus of 1.1 TPa, and high fracture toughness (125GPa) as well as high thermal and electrical conductivity. Due to these superior properties, it is used as a filler material in fiber-reinforced polymer matrix composites [9, 16, 17]. AF Ávila et al., [18] examined the bending properties of the carbon fiber/epoxy composite by adding graphene at different rates and found that graphene affected the bending strength, the highest bending strength was obtained with the addition of 0.5% graphene and emphasized that the graphene added at higher rates could not be homogeneously distributed in the structure and causes agglomeration. Namdev et al., [16] examined the mechanical properties of the composites produced by adding graphene at different rates into carbon fiber/epoxy composites and reported that the added graphene increased the tensile bending strength but after 0.5%, the graphene nanoparticles agglomerated in the structure and reduced the strength. Wu et al., (9) stated that the composites produced by adding graphene oxide at different rates into aramid/epoxy composites increased the bending strength and bending modulus and strengthened the interfacial bond between the matrix and the aramid fiber. Alsaadi et al., [19] examined

the effect of graphene added in epoxy/kevlar composites and epoxy/carbon/kevlar composites on mechanical properties and emphasized that they improved tensile, bending and impact properties.

Various studies are carried out in this regard. However, many issues need to be clarified about the effects of nano-filling materials added in woven aramid fiber epoxy composites on mechanical properties. In this study, the mechanical properties of woven aramid fabric/epoxy composites produced by adding graphene nanoparticles to the epoxy resin at 4 different rates were examined.

II. MATERIALS AND METHOD

In this study, Hexion brand epoxy (MGS Lamination L160), commercially available from Dost Kimya (Istanbul), was used as the matrix material and MGS H160 as the hardener for the curing of this resin. As a reinforcement element, basket type aramid (Twaron® 1680 dtex Type 2040) fiber woven fabrics supplied commercially from the same company were used. Graphene nanoparticles with 99.9% purity, 5 nm diameter, and a surface area of 170 m2/g, commercially available from Nanokar (Istanbul) company, were used as filler material.

After the resin weight is adjusted to be twice the woven aramid fabric to be used, 0.25%, 0.5%, 1%, and 2% graphene was weighed on a precision scale and added to the epoxy resin and mixed in a mechanical mixer for 15 minutes. After the mixing process, the basket type which was cut in 135 mm X 345 mm dimensions, was laid in a plexi mold in 5 layers, and the resin fiber cloth was spread with the help of a roller by hand layup method. After the hand layup process, the vacuum bagging method was applied to obtain equal thickness in each region and to remove the air. The produced composite plates were kept at room temperature for 24 hours for curing. The production phase of composite plates is shown schematically in Figure 1.

The specimens of the obtained composite plates were cut using a water jet according to the standards for the bending (ASTM 790) and tensile tests (ASTM D3039).

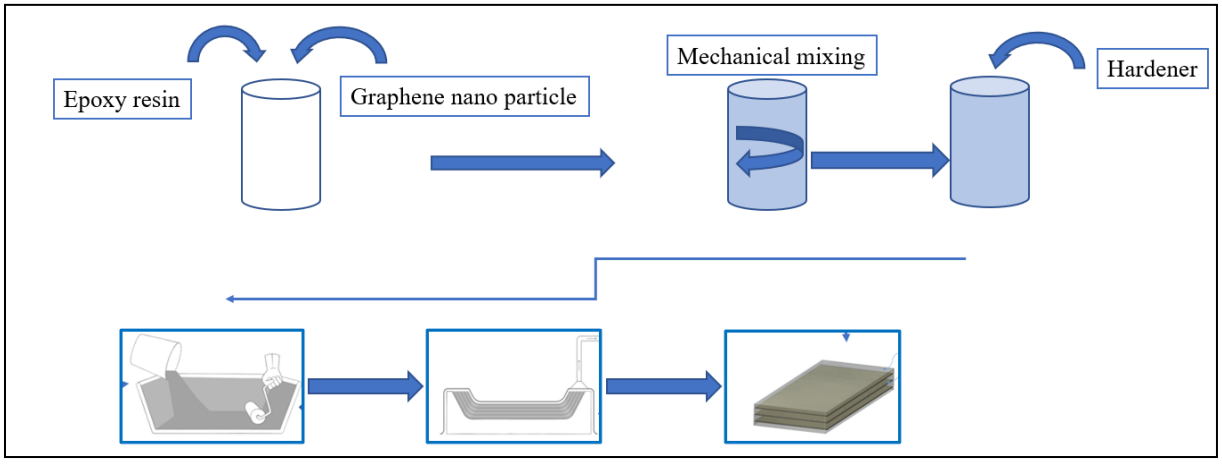

Figure 1. *The schematic view of the production of composites plates*

Stereo microscope was used to observe the microstructures of the produced composites.

A. Three-Point Flexural Test

Flexural tests of the composites produced by adding graphene at different rates and the images and dimensions of which are given in Figure 2 were carried out in Zwick/Roell Z600 brand device at room temperature at 1 mm/min jaw progression speed with 50 mm distance between supports. By using the data obtained after the experiment and the equations given below, Flexural stress (Equation 1), Flexural strain (Equation 2), and Flexural modulus (Equation 3) were calculated, respectively.

$$\sigma L = \frac{3\mathrm{P} \times \mathrm{L}}{2b \times d^2} \quad (1)$$

Here; σL = Flexural stress (MPa), P = Flexural load (N), L = distance between support points (mm), b = Specimens width (mm), d = Specimens Thickness (mm)

$$\varepsilon L = \frac{6\delta \times \mathrm{d}}{L^2} \quad (2)$$

Here; εL = Flexural strain (mm/mm), δ = Deflection of sample (mm), L = distance between support points (mm), d = Specimens Thickness (mm). The constant equivalent of δ is taken as P = 300 N in the equation.

$$EL = \frac{L^3 \times \mathrm{m}}{4\mathrm{b} \times d^3} \quad (3)$$

Here; EL = Flexural elastic modulus (MPa), L = distance between support points (mm), b = Specimens width (mm), d = Specimens thickness (mm), m = tangent angle of the deflection curve.

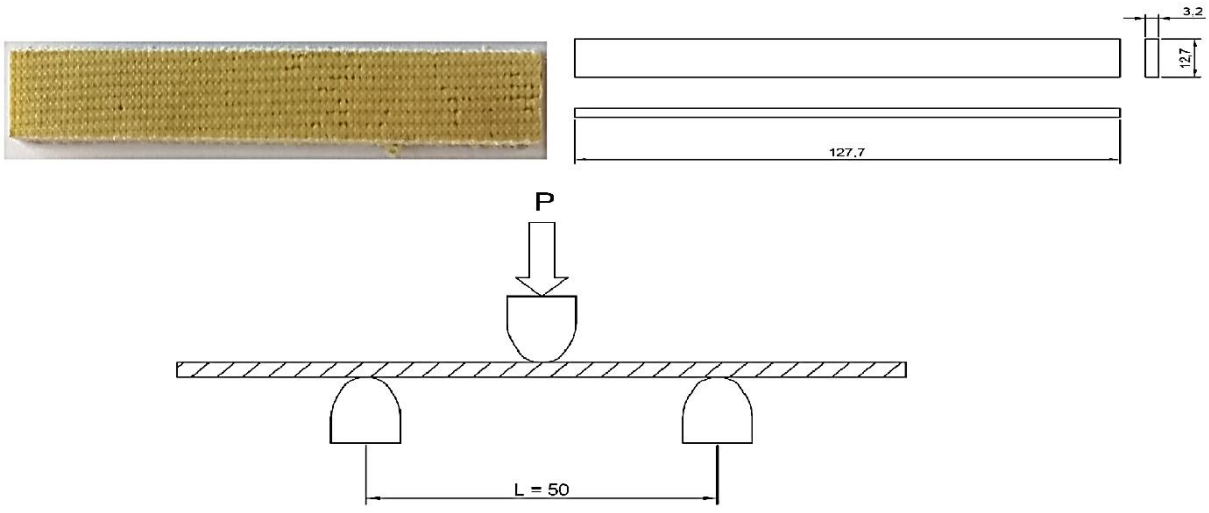

Figure 2. *The images of flexural test samples and dimensions*

A. 1. Tensile Testing

The tensile tests of the composites produced by adding graphene at different rates and the images and dimensions of which are given in Figure 3 were carried out at room temperature at a tensile speed of 2 mm/min in a 100kN capacity MTS Landmark servohydraulic universal tensile device.

Figure 3. *Tensile test samples and dimensions*

III. RESULTS AND DISCUSSION

B. Microstructure Examination

Figure 4 shows the stereomicroscope images of the composites obtained by adding 0%, 0.25%, 0.5%, 1%, and 2% graphene nanoparticles into aramid fiber woven fabric epoxy, respectively.

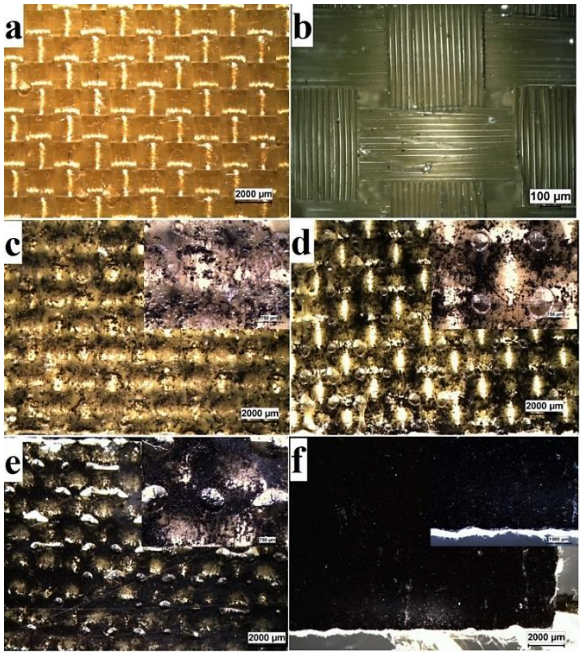

Figure 4. *Stereomicroscope images of the composites with different amount of graphene;* ***(a)*** *epoxy/aramid 0% graphene* ***(b)*** *epoxy/aramid 0% graphene (high magnification)* ***(c)*** *epoxy/aramid*

*0.25% graphene **(d)** epoxy/aramid 0.5% graphene **(e)** epoxy/aramid 1% graphene f) epoxy/aramid 2% graphene*

As can be seen in the microstructure images given above, the aramid fabric is basket type (a = undoped), and the matrix completely covers the aramid fabric. When the microstructure images of the composites produced by adding graphene at different rates to the epoxy aramid composite were examined, it was determined that the added graphene was collected in certain regions of the composite layer and agglomerated in these regions. In the composite to which 2% graphene was added (Figure.2f), the color of the epoxy matrix became completely black and caused it to agglomerate in all regions. The most significant problem seen in nanocomposites is that the added nanoparticles tend to agglomerate due to the high surface energy and the strong Van der Waals bond. The presence of agglomeration causes the supplemented element not to be distributed homogeneously in the structure. This adversely affects the mechanical properties of nanocomposites [19, 20].

B. 1.Three-Point Flexural Test

The load-deformation graphs of the composites obtained by adding 0%, 0.25%, 0.5%, 1%, and 2% graphene nanoparticles to Aramid fiber woven fabric epoxy are given in Figure 5.

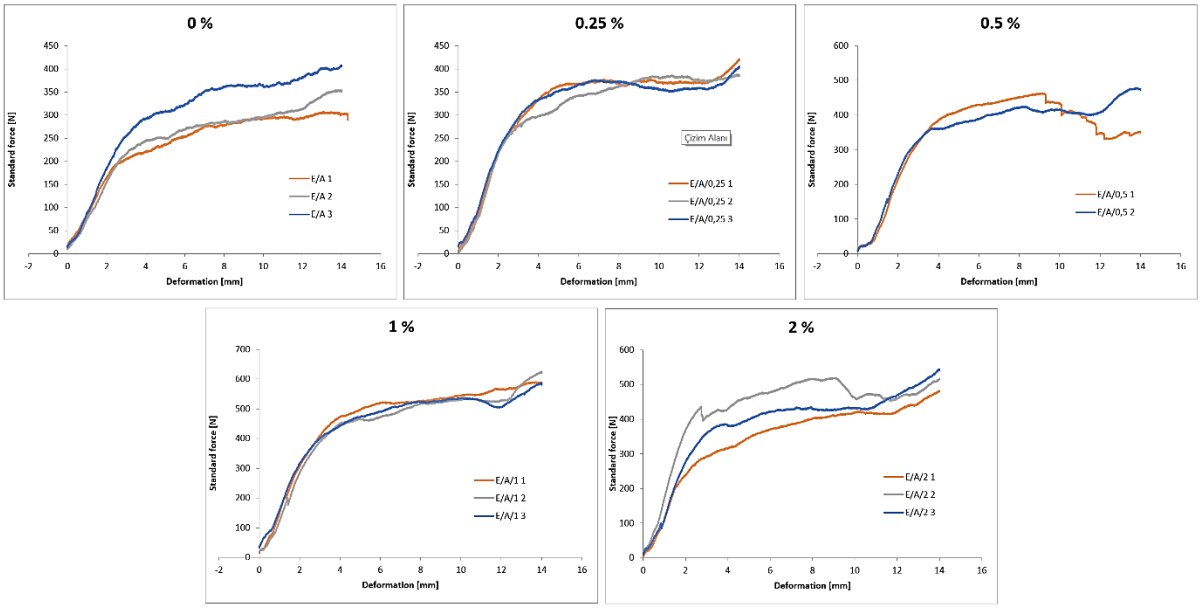

***Figure 5.** The load-deformation graphs of the composites with different amount graphene*

The flexural strength, flexural elongation, and flexural modulus values calculated using these values according to equation 1, equation 2, and equation 3 are given in Table 1. The flexural strength and flexural modulus graph created by using these values are given in Figure 6.

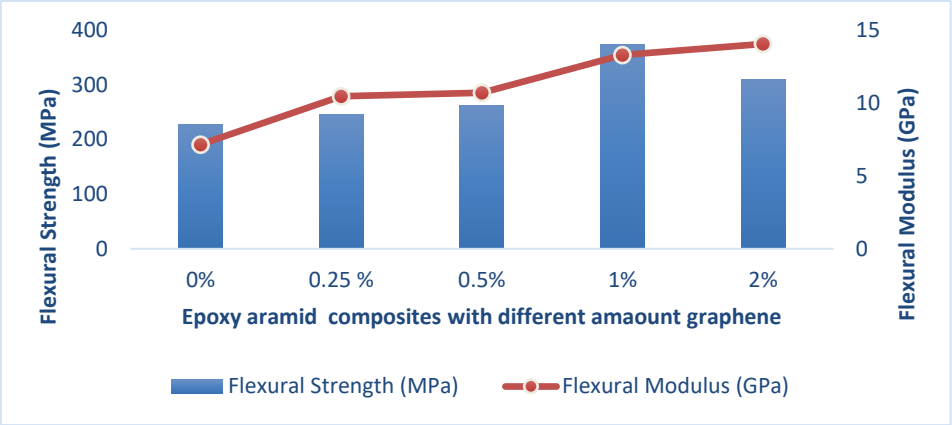

Figure 6. *The flexural strength and flexural modulus graph*

Table 1 *The Flexural properties of produced composites with different amount graphene*

Composite	Flexural Strength (MPa)	Flexural strain(mm/mm)	Flexural Modulus (MPa)
Epoxy/ Aramid	228,47	0,015296	7163,16
Epoxy/Aramid/ 0.25% Graphene	246,04	0,003844	10468,30
Epoxy/Aramid/ 0.5% Graphene	263,12	0,003198	10726,06
Epoxy/Aramid/ 1% Graphene	373,35	0,002409	13317,77
Epoxy/Aramid/ 2% Graphene	310,60	0,002164	14068,11

As can be seen in Figure 6, while the maximum flexural strength of the undoped aramid/epoxy composite was 228 MPa, the flexural strength is 246 MPa in the composite with 0.25% graphene, 263 MPa in the composite with 0.5% graphene, 373 MPa in the composite with 1% graphene, and 310 MPa in the composite with 2% graphene. The highest flexural strength was achieved in the composite with 1% graphene. This rate increased by about 64% compared to the undoped composite. It was determined that the flexural strength increases with the graphene added. The main reason for this increase is that the added graphene increases the interfacial bond between epoxy, which is the matrix, and aramid, which is the reinforcing element. Previous studies emphasized that the nano-sized fillers increased the interfacial bond between the matrix and the fiber, thus facilitating the load transfer from the matrix to the fiber and increasing the strength [9, 19, 20]. The flexural strength of the 2% added composite decreased. As can be seen from the microstructure pictures given in Figure 4, the reason for this decrease is that the added graphene agglomerates in certain regions and reduces the mechanical properties.

B. 2. Tensile Testing

The stress-strain graph and ultimate tensile results of the composites produced by adding graphene nanoparticles at the rates of 0%, 0.25%, 0.5%, 1%, and 2% into the aramid fiber woven fabric epoxy is given in Figure 7.

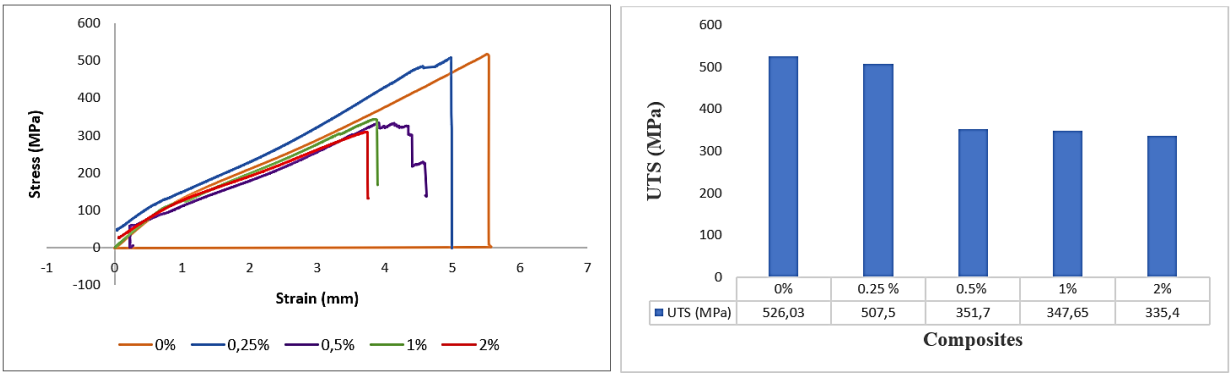

Figure 7 *Stress-Strain and Ultimate tensile results of composites with different amount graphene*

While the highest tensile strength was obtained in the composite without graphene added, this value decreases slightly in the composite with 0.25% graphene added. However, in composites with 0.5% and above graphene added, tensile strength decreases significantly. The added graphene ratio is expected to increase tensile strength. However, since the graphene added during production is concentrated in certain regions and agglomerated in these regions, it reduces the tensile strength. The fact that the specimen is subjected to compressive stress in the load-applied region and tensile stress on the outer surface of the specimen in the bending test while it is exposed to vertical stress in the tensile test is considered the reason for this decrease in tensile strength while there is an increase in flexural strength.

IV. CONCLUSION

The results of this study, in which the mechanical properties of the composites produced by adding graphene nanoparticles at the rates of 0%, 0.25%, 0.5%, 1%, and 2%, into the aramid fiber woven fabric epoxy were examined are summarized. In microstructure examinations, it was observed that as the amount of graphene added to the aramid/epoxy composite increased, graphene was agglomerated in certain regions. It was determined that graphene added to the Aramid/Epoxy composite at different rates affects the flexural properties of the composite. As the amount of added graphene increased, the flexural strength and flexural modulus increased compared to the undoped composite. The highest flexural strength was measured in the composite with 1% graphene added. It was determined that the undoped composite had the highest tensile strength, agglomeration occurred in the structure with the increase in the amount of added graphene, and the tensile strength decreased after this agglomeration.

ACKNOWLEDGEMENTS: The authors are thanks to the financial support for this study from Karabuk University Scientific Research Projects Department (KBÜBAP-21-YL-010)

V. REFERENCES

[1] I. Taraghi, A. Fereidoon, and A. Mohyeddin, "The effect of Mwcnts on the mechanical properties of woven kevlar/epoxy composites," *Steel and Composite Structures,* vol. 17, no. 6, pp. 825-834, 2014. doi:10.12989/scs.2014.17.6.825.

[2] S.A. Mirsalehi, A.-A. Youzbashi, and A. Sazgar, "Enhancement of out-of-plane mechanical properties of carbon fiber reinforced epoxy resin composite by incorporating the multi-walled carbon nanotubes," *SN Applied Sciences,* vol. 3, no. 6, pp. 1-12, 2021. doi:10.1007/s42452-021-04624-2.

[3] T. Topkaya, Y.H. Çelik, and E. Kilickap, "Mechanical properties of fiber/graphene epoxy hybrid composites," *Journal of Mechanical Science and Technology,* vol. 34, no. 11, pp. 4589-4595, 2020. doi:10.1007/s12206-020-1016-4.

[4] T.P. Sathishkumar, S. Satheeshkumar, and J. Naveen, "Glass fiber-reinforced polymer composites–A review," *Journal of Reinforced Plastics and Composites,* vol. 33, no. 13, pp. 1258-1275, 2014. doi:10.1177/0731684414530790.

[5] T.K. Das, P. Ghosh, and N.-C. Das, "Preparation, development, outcomes, and application versatility of carbon fiber-based polymer composites: A review," *Advanced Composites and Hybrid Materials,* vol. 2, no. 2, pp. 214-233, 2019. doi:10.1007/s42114-018-0072-z.

[6] B. Zhang, L. Jia, M. Tian, N. Ning, L. Zhang, and W. Wang, "Surface and interface modification of aramid fiber and its reinforcement for polymer composites: A review," *European Polymer Journal,* vol. 147, p. 110352, 2021. doi:10.1016/j.eurpolymj.2021.110352.

[7] G. Mittal, K.Y. Rhee, V. Mišković-Stanković, and D. Hui, "Reinforcements in multi-scale polymer composites: Processing, properties, and applications," *Composites Part B: Engineering,* vol. 138, pp. 122-139, 2018. doi:10.1016/j.compositesb.2017.11.028.

[8] S. Prashanth, K.M. Subbaya, K. Nithin, and S. Sachhidananda, "Fiber Reinforced Composites–A review," *Journal of Material Science and Engineering,* vol. 6, no. 3, pp. 2-6, 2017. doi:10.4172/2169-0022.1000341.

[9] Y. Wu, B. Tang, K. Liu, X. Zeng, J. Lu, T. Zhang, and X. Shen, "Enhanced flexural properties of aramid fiber/epoxy composites by graphene oxide," *Nanotechnology Reviews,* vol. 8, no. 1, pp. 484-492, 2019. doi:10.1515/ntrev-2019-0043.

[10] S. Kumar, D.S. Gupta, I. Singh, and A. Sharma, "Behavior of kevlar/epoxy composite plates under ballistic impact," *Journal of Reinforced Plastics and Composites,* vol. 29, no. 13, pp. 2048-2064, 2010. doi:10.1177/0731684409343727.

[11] M.E. Islam, T.H. Mahdi, M.V. Hosur, and S. Jeelani, "Characterization of carbon fiber reinforced epoxy composites modified with nanoclay and carbon nanotubes," *Procedia Engineering,* vol. 105, pp. 821-828, 2015. doi:10.1016/j.proeng.2015.05.078.

[12] M.S. Tareq, S. Zainuddin, E. Woodside, and F. Syed, "Investigation of the flexural and thermomechanical properties of nanoclay/graphene reinforced carbon fiber epoxy composites," *Journal of Materials Research,* vol. 34, no. 21, pp. 3678-3687, 2019. doi:10.1557/jmr.2019.302.

[13] A.H.I. Mourad, N. Cherupurakal, F. Hafeez, I. Barsoum, F.A. Genena, M.S. Al Mansoori, and L.-A. Al Marzooqi, "Impact strengthening of laminated kevlar/epoxy composites by nanoparticle reinforcement," *Polymers,* vol. 12, no. 12, p. 2814, 2020. doi:10.3390/polym12122814.

[14] S. Sharma, A.K. Pathak, V.N. Singh, S. Teotia, S.R. Dhakate, and B.P. Singh, "Excellent mechanical properties of long multiwalled carbon nanotube bridged kevlar fabric," *Carbon,* vol. 137, pp. 104-117, 2018. doi:10.1016/j.carbon.2018.05.017.

[15] V.G.S. Veerakumar, B.P. Shanmugavel, and S. Harish, "On the influence of the functionalization of graphene nanoplatelets and glass fiber on the mechanical properties of GFRP composites," *Applied Composite Materials,* vol. 28, no. 4, pp. 1127-1152, 2021. doi:10.1007/s10443-021-09908-9.

[16] A. Namdev, A. Telang, and R. Purohit, "Effect of graphene nano platelets on mechanical and physical properties of carbon fibre/epoxy hybrid composites," *Advanced Materials and Processing Technologies,* vol. 8, pp. 1168-1181, 2022. doi:10.1080/2374068X.2021.1939557.

[17] A. Kumar, K. Sharma, and A.R. Dixit, "Effects of various functional groups in graphene on the tensile and flexural properties of epoxy nanocomposites: A comparative study," *Fullerenes, Nanotubes and Carbon Nanostructures,* vol. 30, no. 11, pp. 1123-1133, 2022. doi:10.1080/1536383X.2022.2077332.

[18] A.F. Ávila, L.D.O. Peixoto, A. S. Neto, J.D. Ávila Junior, and M.G.R. Carvalho, "Bending investigation on carbon fiber/epoxy composites nano-modified by graphene," *Journal of the Brazilian Society of Mechanical Sciences and Engineering,* vol. 34, pp. 269-275, 2012.

[19] M. Alsaadi, B. Younus, A. Erklig, M. Bulut, O. Bozkurt, and B. Sulaiman, "Effect of Graphene Nano-Platelets on Mechanical and Impact Characteristics of Carbon/Kevlar Reinforced Epoxy Hybrid Nanocomposites," *Proceedings of the Institution of Mechanical Engineers, Part C: Journal of Mechanical Engineering Science,* vol. 235, no. 23, pp. 7139-7151, 2012. doi:10.1177/09544062211016883.

[20] S. Fu, Z. Sun, P. Huang, Y. Li, and N. Hu, "Some basic aspects of polymer nanocomposites: A critical review," *Nano Materials Science,* vol. 1, no. 1, pp. 2-30, 2019. doi:10.1016/j.nanoms.02.006.

Düzce University
Journal of Science & Technology

Research Article

Analysis And Improvement of Poor Bearing Capacity Soils in Düzce Province by Jet grouting Method

Ali ATEŞ [a], Burak YEŞİL [b,*], Şükrü ÇİMEN [c], Serdal ALEMDAR [d]

[a] *Faculty of Engineering, Civil Engineering Department, Bolu Abant İzzet Baysal University, Bolu, TURKEY, (ORCID:0000-0001-6297-85-71)*
[b] *Construction Technology, Düzce Vocational School, Düzce University, Düzce, TURKEY (ORCID: 0000-0001-5320-9359)*
[c,d] *Ministry of Environment, Urbanisation and Climate Change, Düzce Provincial Directorate, Branch Directorate Responsible for Building Inspection and Building Materials, Düzce, TURKEY*
* *Corresponding author's e-mail address: burakyesil@duzce.edu.tr*
DOI: 10.29130/dubited.1548995

ABSTRACT

Turkey is situated in an earthquake-prone zone, and due to its geographic location, Düzce is among the most hazardous regions in the country and the world. The seismic risk in Düzce province is significantly influenced by the North Anatolian Fault (NAF), which is characterized by an active tectonic structure. This area has experienced earthquakes of varying magnitudes both before and after the instrumental recording period. Especially, two significant earthquakes occurred in 1999: on August 17, an earthquake with a moment magnitude of Mw = 7.4 struck the Adapazarı-İzmit region. Shortly after, on November 12, 1999, another earthquake with a moment magnitude of M_w=7.1 hit Düzce area at approximately 18:57, lasting for about 30 seconds. During the August 17 earthquake, the eastern section of the Düzce fault, measuring 43 km, was activated. The November 12 earthquake is considered to have been triggered by the previously unbroken eastern section of the Düzce fault as a result of the initial faulting. In the city center, the soil composition mainly consists of fine gravel and sandy gravel in certain areas. Previous earthquakes have resulted in structural damages primarily due to bearing capacity issues, and liquefaction phenomena have also been observed in some locations. In this study, the soil beneath a planned three-story building in Düzce, an area identified having a liquefaction risk, was improved using the jet grout method.

Keywords: *Bearing capacity, Jet groud, Ground improvement, Geotechnical*

Düzce İlinde, Taşma Gücü Zayıf Zeminlerin Jet grout Yöntemi ile Analizi ve İyileştirilmesi

ÖZ

Türkiye bir deprem kuşağı üzerinde bulunmaktadır. Ülkemizin üzerinde bulunduğu kuşak itibari, Düzce ile Dünyanın ve ülkemizin en riskli bir bölgesinde bulunmaktadır. Düzce ilinin depremsellik riski Kuzey Anadolu Fayı (KAF) etkisinde bulunmaktadır. Bu bölge aktif bir tektonik yapıya sahiptir. Aletsel dönem öncesinde ve sonrasında değişik zamanlarda farklı büyüklükte depremlere maruz kalmıştır. Son dönemde 1999 yılında iki farklı deprem meydana gelmiştir; 17 Ağustos 1999 tarihinde Adapazarı İzmit bölgesinde deprem moment büyüklüğü M_w=7,4 büyüklüğünde bir deprem meydana gelmiştir. 12 Kasım 1999 tarihinde akşam saatlerinde yaklaşık 18.57'de Düzce'de deprem moment büyüklüğü M_w=7,1 olan bir deprem kaydedilmiş ve 30 s sürmüştür. 17 Ağustos 1999 depreminde Düzce fayın 43 km uzunluğundaki doğu bölümü kırılmıştır. 12 Kasım 1999 depremi ise, 17 Ağustos 1999'daki faylanmanın Düzce fayının kırılmayan doğu bölümünün tetiklemesi sonucu meydana geldiği düşünülmektedir. Şehir içi yer yer ince çakıl ve kumlu çakıl şeklinde bir semin formasyonuna

Received: 13/09/2024, Revised: 28/10/2024, Accepted: 31/10/2024

sahiptir. Önceki depremlerde daha çok taşıma gücüne bağlı olarak yapı hasarları meydana gelmişse de yer yer sıvılaşma olgularına da rastlanılmıştır. Bu çalışmada Düzce ilinde sıvılaşma riski olan alanda yapılması düşünülen üç katlı yapının üzerine oturacağı zemin iyileştirme yöntemlerinden Jet grout yöntemi kullanılarak iyileştirilmiştir.

Anahtar Kelimeler: *Taşıma gücü, Jet groud, Zemin İyileştirme, Geoteknik*

I. INTRODUCTION

Jet grouting is a versatile and widely adopted soil improvement method. It involves injecting a high-pressure grout mixture into the ground to form soil-cement columns, which improve the mechanical properties of the soil. The technique is particularly effective in weak and soft soils, enhancing load-bearing capacity and mitigating settlement issues. In recent years, several studies have focused on optimizing jet grout applications through numerical modeling, experimental research, and the integration of advanced computational methods such as artificial neural networks (ANNs).

The impact of jet grout columns on soil settlement have been explored in many studies. A study is conducted at Sakarya University used Plaxis 2D and 3D software to analyze the effects of jet grout columns with varying geometrical parameters on soil settlement. It was concluded that jet grout columns significantly reduced settlement, with reductions of up to 22% depending on the column length, spacing, and diameter. It was also noted that increasing the diameter could lead to group effects, which might reduce efficiency.

A similar study by Wang et al. examined the lateral displacement caused by jet grouting in clayey soils and found that the method substantially improved soil stability, particularly in reducing horizontal displacement [1]. Furthermore, Shen et al. highlighted the potential of jet grouting in enhancing bearing capacity and minimizing settlement, especially in liquefaction-prone soils [2].

Jet grouting has also proven the effective in reducing liquefaction potential in earthquake-prone areas. Shen et al. showed that jet grout columns significantly improved the stability of liquefiable soils by increasing their bearing capacity and reducing pore water pressure. The ability of jet grout columns to enhance soil cohesion and mitigate liquefaction risks makes this method highly valuable for projects in seismic regions [2].

Jet grouting has also been extensively studied for its applications in organic and peat soils, which are characterized by low shear strength and high compressibility. Yalçın et al. investigated the use of jet grout columns in undisturbed peat soils and found that the bearing capacity increased by four times for square foundations and 4.5 times for strip foundations [3].

Wong et al. similarly evaluated jet grout applications in soft marine clays, demonstrating that large-diameter columns effectively improved soil stability. Their work underlines the importance of column diameter and length optimization for achieving maximum ground improvement [4].
In a related study, Güllü utilized genetic programming to predict the rheological properties of jet grout mixtures, improving the overall efficiency and performance of jet grout applications. The integration of ANN and other machine learning techniques presents a valuable opportunity for optimizing jet grouting in various soil conditions [5].

One of the critical challenges in jet grouting applications is predicting soil displacement under various loading conditions. In a study carried out in Konya, Turkey, ANN models were used to predict settlement and displacements in a site where 3,351 jet grout columns were installed. The models used input parameters such as grout column length, diameter, and applied loads, achieving highly accurate displacement predictions [6].

Jet grouting is widely applied in a range of geotechnical projects, including foundation strengthening, tunnel construction, and slope stabilization. Lenard et al. emphasized the importance of optimizing column geometries and grout compositions to achieve the desired performance in various soil conditions [7].

Recent studies have also highlighted the need for continued research into jet grouting optimization, particularly through the use of advanced numerical modeling techniques. Vu and Le discussed the effectiveness of large soil-cement columns in improving soil characteristics and emphasized the need for further studies on grout distribution and column arrangement in challenging soil types [8].

Turkey is situated in the Alpine-Himalayan earthquake zone, leading to frequent seismic activity throughout the country. Both historical and instrumental records indicate that Turkey has experienced various earthquakes, resulting in significant loss of life and property. Given the persistent earthquake risk, it is imperative to construct earthquake-resistant structures to coexist with this natural threat.
Düzce province lies along the North Anatolian Fault (NAF) system, where losses in bearing capacity are commonly observed during earthquakes. Past seismic events have revealed structural failures primarily attributed to bearing capacity issues in the superstructure.

Soil-related failures, including those caused by liquefaction, have also impacted infrastructure. Bearing capacity failures typically occur in soft and weak soils. In sandy and alluvial soils, the presence of groundwater can lead to liquefaction under the shear forces generated by an earthquake. Areas with liquefaction potential often experience significant loss of bearing capacity, resulting in damage to structures situated on these compromised soils.

Düzce province features alluvial and fine-grained sandy gravel soils, which pose challenges for construction. Therefore, any structures built on weak soils or those with a risk of liquefaction must undergo ground improvement before construction [9]. In this context, the soil beneath a planned approximately 1,000 m² building with a basement, ground floor, and three additional stories set to be constructed by the Düzce Provincial Directorate of the Ministry of Family and Social Policies on a 1,918.84 m² parcel (No. 535) in Kiremitocağı Neighborhood, Central District has been reinforced to enhance its earthquake resistance.

Table 1. *Symblos and explanations*

Symbol	Explanation	Symbol	Explanation
a_{max}	Maximum horizontal ground acceleration	A_{JG}	Area Relocation Rate
σ_{vo}	Total vertical stress (kN/m^2)	D_a	Average diameter
$\sigma_{vo'}$	Effective vertical stress (kN/m^2),	K_o	Coefficient of ground pressure at rest
τ_{ave}	Average cyclic stress resistance (kN/m^2)	K_s	Soil pressure coefficient
r_d	Strain reduction coefficient	$P_{ul(grup)}$	Load-bearing capacity of the jet grout column group
$\sigma_{V'}$	Effective vertical stress with unit (kPa)	Q_b	Terminal unit carrying capacity at depth H
δ	Friction angle between ground and column	$Q_{12(ort)}$	Average lateral friction value at depth h_2
α	Reduction factor for adhesion	$Q_{11(ort)}$	Average lateral friction value at depth h_1
c_u	Sliding resistance undrainage	$(N_1)_{60}$	Corrected hit count
ζ	Reduction factor for ultimate load capacity	$(N_{1.60})_{cs}$	Number of SPT strokes corrected for fines.
ν	Poisson's ratio	c	Cohesion
γ	Unit weight of the soil.	f	Internal friction angle

Table 1 (cont). *Symblos and explanations*

ρ	Density based on longitudinal ground shear wave velocity given by Telford 1976	**g**	Gravitational acceleration
A_b	Column base area	**G_{JG}**	Shear Modulus (MPa)
N_{q*}	Load-bearing capacity coefficient for deep foundations	**R**	The diameter of the column to be constructed under the foundation after the excavation of the foundation.
σ_{vo}	Vertical soil pressure	**z**	Depth (m)
β	Reduction factor	**C_N**	Load correction factor
CRR	Cyclic resistance ratio	**C_R**	Drill rod length coefficient
CSR	Cyclic stress ratio	**C_S**	Sheath coefficient
B	Block width	**C_B**	Drilling diameter coefficient
L	Block length	**C_E**	Energy correction coefficient
$L=B_x$	Foundation long side	**G_r**	Ratio to shear modulus
$B=B_y$	Foundation short side	**G_s**	Maximum shear modulus of soil
Bk_x, Bk_y	Distance to the nearest column's foundation corner	**H**	Layer depth (m)
D_f	Foundation excavation	**I**	Structure importance coefficient
FC	Fine grain ratio of the soil	**F**	A correction factor depending on the ground type
M_v	Volumetric compression coefficient	**h_1**	Thickness of the soft layer at which negative surface friction can be produced
M_w	Earthquake moment magnitude	**h_2**	The carrier layer in which the column is well embedded
P_u	Colony bearing capacity	**a_r**	Area displacement rate
P_{base}	Colony endpoint bearing capacity	**n**	Number of rows in the horizontal direction
P_{lat}	Column lateral bearing capacity	**m**	Number of rows in the vertical direction
$P_{ul(column)}$	The load-bearing capacity of a single jet grout column	**FS**	Factor of safety
S_y, S_x	Distance between columns	**A**	Unit cell area
		V_s	Ground shear wave speed (m/s)

II. MATERIAL AND METHOD

A. STUDY AREA

The site under consideration is a 1,000 m² building comprising a basement, ground floor, and three additional stories. This project is being planned by the Düzce Provincial Directorate of the Ministry of Family and Social Policies on parcel 535, which measures 1,918.84 m², located in the Kiremitocağı Quarter of the Central District in Düzce province (Figure 1). Since this structure is located is soft soil, the soil needs to be improved and is shown in the figure 1. Also the ground water level is high in the area. The mentioned area is under the effect of Duzce fault that is the ability of potential earthquake occurance.

Figure 1. *Jet grout soil improvement study area*

A. 1. Field Studies

The site for a building with a basement, ground floor, and three additional stories, covering approximately 1,000 m², is planned to be constructed by the Düzce Provincial Directorate of the Ministry of Family and Social Policies on a 1,918.84 m² parcel (No. 535) in the Kiremitocağı Quarter of the Central District. This location is situated in an earthquake zone, specifically along the North Anatolian Fault System (NAF). Three borings, each measuring 12.50 m (sk1-sk2-sk3), were conducted on the site. A simplified geological cross-section has been provided based on the land application and drilling studies carried out in the field (Figure 2).

Figure 2. *Land drilling locations*

Some index parameters related to the soil were obtained in the drilling works carried out in the area where soil improvement is considered. According to the revised zoning plan approved on 11.03.2005, it is located in Precautionary Area 2 (PA-2), where construction is not allowed without precautions. Soil group 'D' and local soil class 'Z4', T_A:0,20 sec, T_B:0,90 sec was determined for the parcel. The

geological unit in the study area is Qal (alluvial fan) unit (clay, silt sand) of Plio-Quaternary age and soil type is (ML-MH-SM-SC-GM) according to TS 1500 [20] (Table 1).

Table 2. *Simplified Geological Sil Section Values*

SK1			SK-2		SK-3	
Depth (m)	**Soil Type**	**Ground Water Table (m)**	**Depth (m)**	**Soil Type**	**Depth**	**Soil Type**
1,5	CL		1,5	CL	1,5	CL
3	CH		3	CH	3	CH
4,5	CH	4	4,5	CH	4,5	CH
6	CL		6	CL	6	CL
7,5	CL		7,5	CL	7,5	CL
9	SM	9	9	SM	9	SM
10,5	SC		10,5	SC	10,5	SC
12	GM		12	GM	12	SM

B. METHOD

B.1. Criteria for Determination of Liquefaction Potential

The method proposed by Seed and Idriss, known as the "simplified method," is commonly used in liquefaction analyses [10]. Liquefaction calculations can be performed using Standard Penetration Test (SPT) field data obtained from boreholes in the study area. In this method, two basic parameters must be estimated to determine the potential for liquefaction.

The first is the ratio of the dynamic or cyclic stress ratio (CSR), which represents the earthquake energy potential in the soil layers and characterizes the strength of the seismic waves generated by the earthquake. This ratio compares the response of the soil to horizontal shear stress, providing a safety factor that indicates the condition of the soil (Eq. 1).

$$FS = CRR/CSR \quad (1)$$

If the liquefaction safety factor obtained from this equation is less than 1, it indicates a liquefaction hazard at the site. Conversely, if the safety factor is greater than 1, it suggests that the site is not risky for liquefaction.

Also referred to as the simplified approach, the value of the cyclic stress ratio generated by earthquake forces during seismic events can be calculated using Eq. 2 [10].

$$CSR=0{,}65\ (a_{max}/g)\ (\sigma_v/\sigma'_v)r_d \quad (2)$$

The effective stress reduction coefficient can be determined according to Liao and Whitman [11] as follows (Eq.3, Eq.4);

$$r_d = 1 - 0{,}00765z \qquad z \leq 9.15\ m \quad (3)$$

$$r_d = 1.174 - 0.0267 \qquad 9.15 < z \leq 23 \quad (4)$$

This area is seismically active and lies within the North Anatolian Fault system (NAF). Historical and instrumental records confirm that this region experiences significant seismic activity. In previous years, two major earthquakes occurred along the Düzce Fault, with magnitudes of 7.40 and 7.20 on

August 17, 1999, and November 12, 1999, respectively. According to the literature, it is estimated that the fault may rupture along one-third of its length [12].

In the event of an earthquake occurring in the study area, the moment magnitude is expected to be 7.2, with a maximum horizontal ground acceleration expected to reach 0.51 g [13][14]. To assess the liquefaction potential of the study area, the $(N_1)_{60}$ value was derived from the Standard Penetration Test (SPT) data obtained through drilling in the site.

Estimating the cyclic resistance ratio, the corrected SPT blow count can be calculated using the following equation (Eq. 5), which takes into account factors such as cover load, drill rod length, casing, borehole diameter, and energy correction coefficients. In this context, $(N_1)_{60}$ is defined as follows:

$$(N_{1.60})_{CS}=N_{land}\ CS.C_E.C_N.C_B.C_R \tag{5}$$

The overburden correction factor can be found by Eq. 6 proposed by Liao and Whitman. [11]

$$C_N = \frac{1.7}{0.7+0.01*\sigma_{V'}} \tag{6}$$

It was proposed to correct the SPT numbers according to the fine grain ratio by considering the effect of the fine grain ratio of the soil with the following equation (Eq.7-Eq.11) [15].

$$(N_{1.60})_{CS} =\alpha+\beta N_{1,60} \tag{7}$$

FC≤%5 için α=0 ve β=1 (8)

%5<FC<%35 için $\alpha=\exp\left(1.76-\frac{190}{(FC)^2}\right)$ (9)

$$\beta=\left[0.99+\left(\frac{FC}{1000}\right)^{1.5}\right] \tag{10}$$

FC≥%35 için α=1 ve β=1,2 (11)

For an earthquake with a moment magnitude of M_w = 7.5, Seed and Idriss proposed a cyclic resistance ratio (CRR) based on the $(N_1)_{60,CS}$ values, as expressed in Equation (Eq. 12). This equation illustrates the response of soils in relation to their liquefaction behavior [10].

$$CRR=\frac{1}{34-(N_1)_{60,CS}}+\frac{(N_1)_{60,CS}}{135}+\frac{50}{\left[10(N_1)_{60,CS}+45\right]^2}-\frac{1}{200} \tag{12}$$

Here, the Idriss correction coefficients given by C_E are 0.75 for a safe ram type for this effective energy development deployment, and 0.75, 0.85, 0.95 and 1.00 for the correction in the length of the rod, depending on the length of the rod, with a temperature correction of 1.0 for the standard bit copy receiver. In addition, according to the literature of A. W. Skempton, it is understood that the borehole diameter correction is also 1.0 [16].

B.2. Bearing Strength of Jet grout Columns

The jet grout method is a ground improvement technique with a wide range of applications, suitable for nearly all types of soil. This technique involves cutting the ground with a high-pressure water or water-air mixture, and then injecting cement grout at high pressure to fill the resulting voids.

Jet grouting technology can be categorized into three types based on the systems used: single-fluid, double-fluid, and triple-fluid. Generally, two different methods are employed to calculate the bearing capacity of existing jet grouting columns. The first method treats the jet grouting column as a distinct structural element, while the second method applies principles similar to those used for pile bearing capacity.

Due to its production method, the jet grout column is blended with the surrounding natural soil through direct contact. Additionally, the cross-section of the jet grout column can be regularized, featuring either a recessed or rough structure. As a result, the interaction between the natural soil and the jet grouting column is typically more effective than that achieved through driving or pre-piling, even in fine or coarse-grained soils.

A jet grouting expert should regard the technique as a form of soil stabilization, and the bearing capacity of jet grouting columns should be considered as group bearing capacity. Consequently, the bearing capacity of a group of jet grouting columns is accepted as block bearing capacity in design calculations. Block bearing capacity can be utilized in two different ways in programming: the primary method focuses on the bearing resistance of the jet-grouted pavement, while the broader method is presented without controlling ground settlements. In this project, it was decided to extend the design according to the first approach.

To determine how effectively the jet grout columns can transfer structural loads to the ground in the field, a thorough calculation is necessary. There are various methods available for these computations. In this study, the two main dimensions and earthquake parameters presented in table 2,3 are analysed.:

Table 3. *Limit values used for column design in granular soils.*

	Long side (m)	**Short side (m)**	**Excavation depth (m)**	**Nearest column distance from the foundation corner (m)**	**Number of columns in the x direction**	**Number of columns in the y direction**	**Column length after excavation (m)**	**Column diameter**	**Distance between columns (m)**	**Groundwater level after excavation (m)**
Larger foundation	36.78	26.79	3.70	0.5	12	9	12	0.8	3.18 and 2.79	0.3
Smaller foundation	16.8	4.8	3.70	0.5	6	2	12	0.8	3.00 and 3.00	0.3

Table 4. *Groundwater and Earthquake Parameters*

Description	**Value**
Unit Weight of Water (kN/M^3)	10
Water Level (m)	0,3
Magnitude of Earthquake	7.2
Short Period and Short Period Design Spectral Acceleration coefficient	0,414

Additional parameters are detailed in the appendix. The summary of the jet grouting results, including 12 columns, totals 120 columns (108+12), and is illustrated in Tables 4 to 6.

Table 5. *Land drilling locations*

Parameters	**Foundation 1**	**Foundation 2**
x coordinate	0	10,15
y coordinate	0	27,10
S_x	3,18 m	3 m

Table 5 (cont). *Land drilling locations*

S_y	2,94 m	3 m
Number of columns (x)	12	6
Number of columns (y)	9	2
Total number of columns	108	12
Bk_x	0,5 m	0,5 m
Bk_y	0,5 m	0,5 m
B_x	36,78 m	16,80 m
B_y	26,79 m	4,80 m

Table 6. *Soil parameters*

Parameters	**Values**
Unit volume weight	18,33 kN/m^3
Internal friction angle	3^o
Cohesion	32 kN/m^2
Adhesion reduction factor	0,45
Modulus of elasticity	552200 kN/m^2
Poisson ratio	0,46
Water saturated unit volume weight	19,00 kN/m^3
Horizontal restitution coefficient	1
Unimproved soil safety stress	81 kN/m^2
Free compressive strength	100 kPa
Factors related to ground conditions	1
SPT N	26
Fine content	%95
Correction factor depending on soil type	1,029

Table 7. *Column Parameters*

Parameters	**Values**
Jet-groud diameter	0,80 m
Unit volume weight	18,33 kN/m^3
Free compressive strength	6 MPa
Material safety factor	2
Reduction factor for jet-groud column end bearing capacity	1

B.3. Jet grout Columns Bearing Strength Methods

If the Jet grout column is considered as a separate structural element in itself, the bearing capacity of the Jet grout column is calculated as the pile bearing capacity as Eq.13 [17].

$$P_u = P_{base} + P_{lat} \tag{13}$$

For cohesionless (sandy) soils, Eq.14;

$$P_u = A_b\, q_b + \Pi D_a \int_{l_1}^{l_2} \gamma z\, K_s tang\delta d_z \tag{14}$$

Eq.15 for cohesive soils;

$$P_u = A_b\, q_b + \Pi D_a \int_{l_1}^{l_2} \alpha\, c_u d_z \quad (15)$$

Cohesionless, i.e. coarse-grained soils;
The end resistance of the arm can be found with Eq.16;

$$q_b = \frac{1+2K_o}{2}\, \sigma_{vo} N_q^* \xi \quad (16)$$

For cohesive soils, i.e. fine-grained soils, Eq. 17;

$$qb = 9c_u \quad (17)$$

Jet grout columns are vibrated with the jet grout column together with the compaction process on the ground. The studies carried out, it is seen that the cross-sectional part of the Jet grout column is wavy and rough and thus does not form a smooth structure. This is since the communication between the natural soil and the jet grout column is much more intense in clay or cohesionless soils compared to driven or pre-piles. (Figure 3-4).

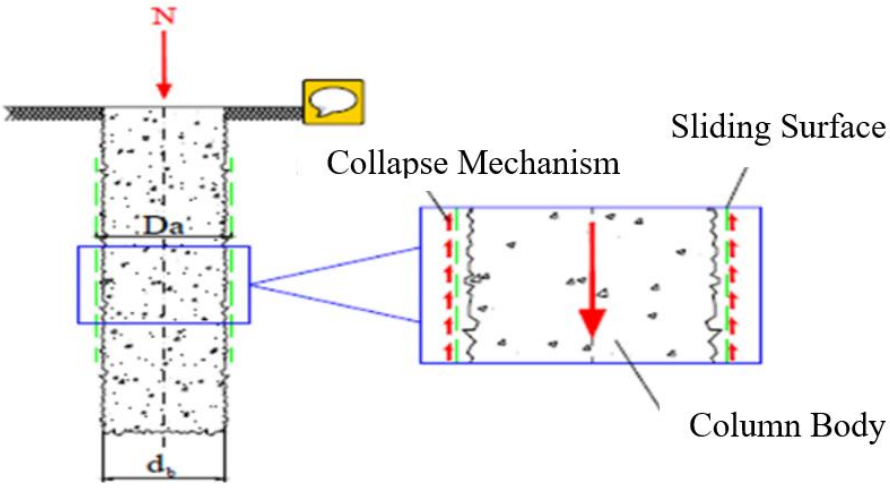

Figure 3. *Behaviour of the Jet grout column [10].*

Adhesion reduction factor in relation to the slip surface that may occur around the production perimeter of the Jet grouting column:

In cohesive, i.e. fine-grained soils;
α = 1 for normally consolidated soils
α = 0.45 in over consolidated soils
K_s > 1 in granular soils

The choice of column diameter is very important here. The average column diameter to be used in the design should be designed to be on the safe side of the diameter to be made in the field.

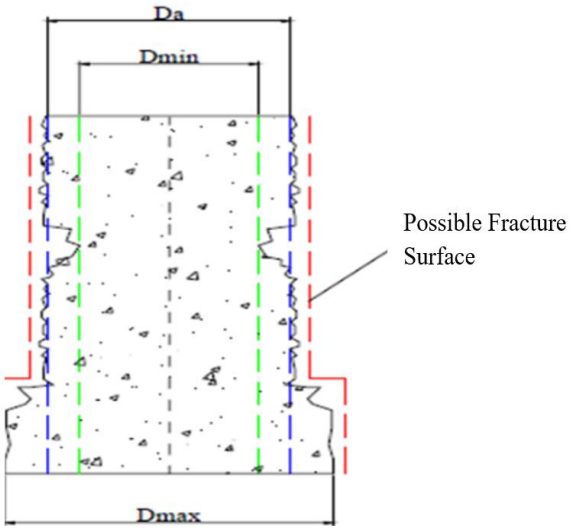

Figure 4. *Possible slip surface in the Jet grout column manufactured in the ground [10].*

Accurate determination of the column diameter and the adjustment of the reinforcement factor, either 0.45 or 1, are crucial when considering the effects that jet-grout columns experience during installation in granular soils, with soil pressure temperatures ranging from 1 to 1.4 [17].

Before theoretically assessing the bearing capacity of bored piles, it is also important to evaluate the potential negative environmental impacts associated with jet-grout columns. The strength of solidified clay can reach values as high as 4 MPa, while sandy gravels can achieve strengths of up to 12 MPa. For this analysis, a representative value of 6 MPa was selected.

The parameters of the jet grout columns demonstrate full mobility, typically resulting in minimal settlement. The amount of settlement required to achieve full mobilization of the end bearing capacity is also quite small [17]. Data presented in Tables 7 and 8 were compiled by Garassino.

Table 8. *Limit values used for column design in granular soils [17].*

Pile Type	**Creep Force Reduction Factor**		**Limit Values for Unit Wall Friction**	**Tip Power reduction Factor**
	δ/φ	**Ks**	**τ** (kPa)	**ξ**
Bored Pile	0,6	0,5-0,65	100-200	0,33-0,5
Drive Pile (Open End)	2/3	0,65-0,95	120	0,7-0,8
Drive Pile (Closed End)	0,75	1,0-1,5	120-180	1,0
Jet Grout Column	1	1,0-2	≥180	1,0

Table 9. *Limit values used for Jet grout column design in cohesive, i.e. fine-grained soils [17].*

Pile Type	**Creep Force Reduction Factor**		**Limit Values for Unit Wall Friction**	**Tip Power reduction Factor**
	α (Normal Consolidated)	**α (Over Consolidated)**	**τ** (kPa)	**ξ**
Bored Pile	0,9	0,35	275	0,66

Table 9 (cont). *Limit values used for Jet grout column design in cohesive, i.e. fine-grained soils [17].*

Drive Pile (Open End e: outside, i: inside)	0,95e 0,80i	0,40e 0,35i	200	0,7
Drive Pile (Closed End)	0,95	0,45	200	0,8
Jet Grout Column	1	0,45	280	1

C. GROUND IMPROVEMENT WITH COLUMNS FORMED IN THE GROUND

Soil consolidation refers to the process of altering the behavior of a soil mass through various production techniques [17]. The calculations for consolidation can be performed using two distinct methods: the first involves calculating the bearing capacity, while the second focuses on block analysis, which is based on limiting settlements.
The bearing capacity calculation technique is further divided into two components: group bearing capacity and block analysis. These methods help assess the overall performance and stability of the soil under applied loads.

C.1. Group Bearing Capacity Calculation of Load-Bearing Elements

The bearing capacity of the whole group is the sum of the bearing capacity of the Jet grouting columns within the group (Eq.18).

$$P_{ul(grup)} = \beta\ n\ m\ P_{ul(column)} \tag{18}$$

C.2. Block Analysis Method

The bearing capacity of the block considers the group of jet grouting columns as a cohesive unit. In this approach, the bearing capacity is determined by the friction force acting on the side surfaces and the bearing force on the bottom surface of the prism formed by the group (Eq. 19) (see Figure 5). This method allows for a comprehensive assessment of the group's performance under load.

$$P_{ul(grup)} = B.L.Q_b + 2(B+L).(h_2.Q_{12(ort)} - h_1.Q_{11(ort)}) \tag{19}$$

If there is no negative surface friction, h1 0 and h2 H should be accepted.

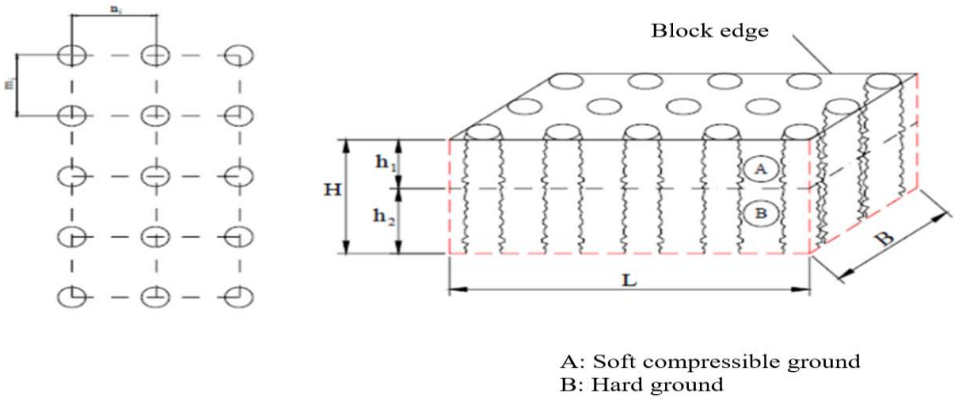

Figure 5. *Total/block bearing capacity of the soil improved with jet grout columns [17]*

III. CALCULATION METHOD

A. DETERMINATION OF MAXIMUM SHEAR MODULUS OF SOIL

The initial step in calculating columns with high shear strength achieved through the mixing of cement and soil is to determine the maximum shear modulus of the soil and to estimate the earthquake magnitudes.

To accomplish this, it is essential to establish the soil shear wave velocity profile. This can be done directly using methods such as Down-Hole or Suspension PS Logging, or indirectly through field test results, including SPT, CPT, and PMT. For this purpose, the shear wave velocity can be calculated using the following equation (Eq. 20) [18][19]:

$$V_s=62{,}14.\ N^{0{,}219}.\ H^{0{,}230}.\ F \quad (20)$$

The correction factor shall be 1.000 for clay soils, 1.091 for fine sands, 1.029 for medium grained sands, 1.073 for coarse grained sands, 1.151 for sand and gravel and 1.485 for gravelly soils.

B. UNIT AREA RATIO METHOD AND DETERMINATION OF SHEAR STRESSES

If the liquefaction analysis needs to be adjusted, guidelines for selecting methods that minimize liquefaction damage will initiate a process to determine the most suitable ground treatment for the site. In this context, Hayden and Baez outline the procedural steps for stone column applications.

The first step involves selecting an appropriate column diameter and spacing, followed by an iterative process for the columns composed of a soil mixture with a high shear modulus. The shear moduli of these columns will be defined based on the uniaxial cylindrical compressive test strengths (fJG) from columns located on sites with similar conditions, which may result from varying field application studies or initial contractor assessments. This information must be validated through practical experience during the construction phase.

Specimens obtained from the core samples of the jet grout columns will be subjected to uniaxial cylindrical tests, allowing for the calculation of the moduli of elasticity (E_{JG}) and shear (G_{JG}) based on a Poisson's ratio of 0.5 under the specified temperature conditions (see Eq. 21 - Eq. 25).

Elastic Shear Modulus (Eq.20):

$$E_{JG}=4730\sqrt{f_{JG}}\ (\text{MPa}) \quad (21)$$

Shear Modulus (Eq.21):

$$G_{JG}=\frac{E_{JG}}{2(1+v)} \quad (22)$$

Area Relocation Rate (Equation 22 and Equation 23):

$$ar=\frac{A_{JG}}{A} \quad (23)$$

$$as=\frac{A_S}{A}=1-ar \quad (24)$$

Shear Modulus of Shear Velocity (Eq.24):

$$G_s=\rho V_S^{\,2} \quad (25)$$

In the later stages of the analysis, the fundamental principles of calculation rely on the distribution of shear stresses among the columns that are uniformly arranged over the earthquake-resistant unit area, as well as the interaction between these columns and the surrounding soil, determined by the ratio of their shear moduli.

It is recognized that in alluvial soils with potential for liquefaction, the shear wave velocity typically remains below 200 m/s. Consequently, the ratio of the shear modulus of the mixture produced from the jet grouting process to the soil's shear modulus is generally maintained between 15 and 160 times that of the columns. This ratio emphasizes the impact of the chosen application diameter and size range, leading to more pronounced effects on the performance of the columns. since the shear wave velocity will be low in soft soils, it will attract horizontal earthquake forces. The soil beneath the structure mentioned was strengthened and its strength increased with the jet grout method related with figure 6.

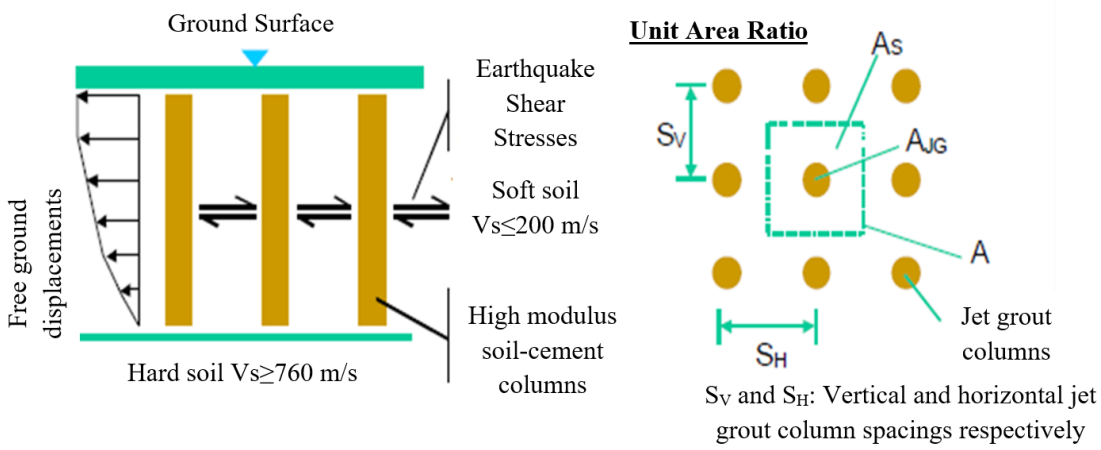

Figure 6. *Dispersion model of earthquake shear waves and definition of unit cell*

C. STRUCTURAL CONTROLS

To mitigate the risk of liquefaction in the ground between the columns, it is essential that the columns possess a high shear modulus and sufficient resistance to the shear forces acting upon them. To ensure the adequacy of the column cross-section against the shear force V_{JG}, the following equation (Eq. 26) is referenced. In this equation, the cement mix is evaluated under specific design conditions, with the reinforcing components of the columns treated as low-decay elements:

$$V_{JG}=0{,}3\sqrt{f_{JG}}\,A_{jG} \tag{26}$$

If similar results are found here with the help of similar results obtained by experience from previously obtained data, they should be applied to a safety coefficient value of 2 under minimum conditions (f_{JG}). The results should be checked with in-situ core equivalent samples carried out during the production phase.

D. FINDING

D. 1. Field Findings

For the foundation excavation of 3.70m and foundation depth of 3.20m, the soil safety stress was 0.81kg/cm² and the soil bearing capacity was 2.43 kg/cm². According to the drilling data, the vertical bedding coefficient was calculated as 750-1250ton/m³ and it was recommended to be taken between

these values. The groundwater level was measured at 4 m and it was stated that it may change up and down by 1m depending on the seasons. It is recommended to take a structure importance coefficient of 1.4. There is no potential risk of liquefaction.

Geotechnical parameters (unit volume weights, cohesion, internal friction angle and volumetric compression coefficients, fine grain ratio) according to the laboratory data obtained from 3 12.50 m (sk1-sk2-sk3) borings in the field; for SK1 (3.50-4.0m); 18.74 KN/m³, cohesion 30.96 kN/m², internal friction angle 2o and volumetric compaction coefficient 0.0475cm²/kgf, for SK2 (2.50-3.0m); unit volume weight 18.45Kn/m³, cohesion 34. 40 kN/m², internal friction angle 3o and M_v=0,0338cm²/kgf, for SK3 (3.0-3.50m); 18.14Kn/m³, c=42.99 kN/m², internal friction angle 3o and volumetric compaction coefficient 0,0286 cm²/kgf. As a result of the sieve analysis, the average percentage (%) of those passing through the sieve numbered 200 was 95 and the SPT (N) averages were reduced by 1/2 and taken as 26.

According to the average of the geophysical data, the average thickness of the 1st layer is 4.25m, and since the excavation depth was determined as 3.70m, the 2nd layer data (after 4.25m) were taken into consideration. Accordingly, the average shear wave velocity for the 2nd layer is 315m/sec, the average Poisson's ratio is 0.45, the average modulus of elasticity is 552200 kN/m², and the average ground dominant vibration period is 0.68 sec.

D. 2. Bearing Capacity of Jet grout Column Group

P_{ugrup} was calculated as 78172.878 kN, large foundation as +8685.875 kN and small foundation as 86858.753 kN. In addition, the bearing capacity values obtained for large foundations and small foundations are given below (Table 9).

Table 10. *Bearing capacity values obtained for foundations*

No	A_c (m^2)	σ_{vo} (kN/m^2)	σ'_{VO} (kN/m^2)	N_q	K_O	q_b (kN/m^2)	P_{base} (kN)	P_{lat} (kN)	P_u (kN)	σ_{Ult} (kN/m^2)
1	0,503	5,499	5,499	1,122	0,948	288	144,76	10,857	155,622	89,024
1	0,503	219,96	114,66	1,122	0,948	288	144,76	423,436	568,201	135,421

D. 3. Soil Liquefaction Values

According to the data obtained from the ground improvement site, liquefaction analysis results were performed before ground improvement and no liquefaction was observed at the end of the calculation (Table 10).

Table 11. *Soil Liquefaction Values*

No	z	σ_{vo} (kN/m^2)	σ'_{VO} (kN/m^2)	SPN	C_n	N60	α	β	$N_{1,60}$	C_m	CSR 7,5	τ (kPa)	r_d	τ_{av}	FS	Result
1	0,3	5,499	5,499	26	1,7	45	5	1,2	33	1,11	0,238	1,45	0,998	0,591	2,46	Sufficient
2	12	219,96	114,66	26	0,913	27	5	1,2	18	1,11	0,386	43,055	0,854	20,21	2,13	Sufficient

IV. CONCLUSION

The site investigation study has been prepared for the planned construction of a 1,000 m² building with a basement, ground floor, and three additional stories by the Düzce Provincial Directorate of the Ministry of Family and Social Policies on a 1,918.84 m² parcel (No. 535) in the Kiremitocağı Neighborhood, Central District, Treasury of Finance. According to this study, the area is situated in a

1st degree earthquake zone. The revised zoning plan approved on March 11, 2005, designates this site as within Precautionary Area 2 (PA-2), where construction is prohibited without appropriate measures.

Although the liquefaction analysis indicates that there is no risk of liquefaction, improvement of the site is necessary due to its location within the North Anatolian Fault zone system. For the existing building load of 7,606 tons, with a foundation excavation depth of 3.70 m and a foundation depth of 3.20 m, the soil safety stress is determined to be 0.81 kg/cm², while the soil bearing capacity is assessed at 2.43 kg/cm². Drilling data suggest a vertical bedding coefficient of 750-1,250 t/m³, and it is recommended that this value be adopted within that range. The groundwater level in the area is measured at 4 m, with potential seasonal fluctuations of ±1 m.

For the large foundations, with a long side of 36.78 m and a short side of 26.79 m, the foundation excavation is 3.70 m. The nearest column is located 0.5 m from the foundation corner, with 12 columns in the x-direction and 9 columns in the y-direction. The columns will extend to a length of 12 m and have a diameter of 0.8 m, with spacing between columns of 3.18 m and 2.94 m. The groundwater level after foundation excavation is anticipated to be 0.3 m.

The small foundations consist of 108 columns, with a long side of 16.8 m and a short side of 4.8 m, also featuring a foundation excavation of 3.70 m. The distance from the nearest column to the foundation corner is again 0.5 m, with 6 columns in the x-direction and 2 in the y-direction. These columns will also be 12 m long with a diameter of 0.8 m and spaced 3.00 m apart. The groundwater level after foundation excavation for these foundations is also projected to be 0.3 m. In total, there will be 120 columns, including both large and small foundations.

Based on the data, soil improvement was executed using the jet grouting method, yielding the following results: the safety stress of the improved ground is 1.33 kg/cm², the improved vertical soil bearing coefficient (k_0) is 1,596 t/m³, and the load-bearing capacity of the jet grout column group is 86,858.753 kN. The expected settlement following the improvement is 0.22 mm. The ground classification after improvement is designated as "C," and the local soil class is classified as "Z4," indicating that the improvements have been considered as appropriate.

Finally, since the shear wave velocity will be low in soft soils, it will attract horizontal earthquake forces. The soil beneath the structure mentioned was strengthened and its strength increased with the jet grout method and mentioned in above.

ACKNOWLEDGEMENTS: We thank the Düzce Provincial Directorate of Environment and Urbanization for their contributions to the work.

V. REFERENCES

[1] Z. F. Wang, S. L. Shen, and W. C. Cheng, "Lateral Displacement Induced by Jet Grouting in Clayey Soils," *Géotechnique*, vol. 67, no. 7, pp. 621–630, 2017.

[2] S. L. Shen, Z. F. Wang, and W. C. Cheng, "Estimation of Liquefaction Prevention Using Jet Grouting," *Geotechnical Engineering*, vol. 67, no. 7, pp. 621–630, 2017.

[3] H. Yalçın, Z. Kaya, C. C. Çadır, E. Uncuoğlu, A. Erol, and M. Akın, "Improvement of an Undisturbed Peat Soil with Jet Grout Columns: Physical and Numerical Modeling," *Arabian Journal for Science and Engineering*, vol. 48, no. 1, pp. 105–115, 2023.

[4] R. K. N. Wong, Yee Foo Weng, Gan Kok Leong and Shih-Hao Cheng "A Case Study of Effectiveness of Large Diameter Jet Grout for Soil Improvement Works in Soft Marine Clay," in *Geotechnics for Sustainable Infrastructure Development*, Springer vol. 62, no. 1, pp. 649–655, 2019.

[5] H. Güllü, "Prediction of Rheological Characteristics of Jet Grout Mixtures Using Genetic Programming," *Neural Computing and Applications*, vol. 29, no. 1, pp. 251-260, 2017.

[6] G. Mısır, "Jet Grout Yöntemi İle Zemin İyileştirme ve Deplasman Tahmini: Vaka Analizi," *Avrupa Bilim ve Teknoloji Dergisi*, c. 18, ss. 290-299, 2020.

[7] M. J. Lenard, P. Alam, and G. R. Madey, "The Application of Neural Networks and a Qualitative Response Model to the Auditor's Going Concern Uncertainty Decision," *Decision Science*, vol. 26, no. 2, pp. 209–227, 1995.

[8] M. N. Vu and Q. H. Le, "Large Soil-Cement Columns in Vietnam," in *Geotechnics for Sustainable Infrastructure Development*, Springer, vol. 62, no. 1, pp. 555–562, 2019.

[9] A. Ateş, "Yozgat (Şefaatli) İlçesi Adalet Sarayı Temel Zemininin Sıvılaşma Potansiyelinin Araştırılması ve Zemin İyileştirilmesi: Vaka Analizi," *Düzce Üniversitesi Bilim ve Teknoloji Dergisi*, c. 5, ss. 258-272, 2017.

[10] H. B. Seed and I. M. Idriss, "Title of the Paper," *Journal of Soil Mechanics & Foundations Div.*, vol. 97, no. 9, pp. 1249-1273, 1971.

[11] S. S. C. Liao and R. V. Whitman, "Overburden Correction Factors for SPT in Sand," *Journal of Geotechnical Engineering*, ASCE, vol. 112, no. 3, pp. 373-377, 1986.

[12] M. R. K., "Application of Linear Statistical Model of Earthquake Magnitude Versus Fault Length in Estimating Maximum Expectable Earthquakes," *Geology*, vol. 5, pp. 464-466, 1977.

[13] D. L. Wells and K. J. Coppersmith, "New Empirical Relationships Among Magnitude, Rupture Length, Rupture Width, Rupture Area, and Surface Displacement," Bull. Seismol. Soc. Am., vol. 84, pp. 974-1002, 1994.

[14] R. Ulusay, E. Tuncay, H. Sonmez, and C. Gokceoglu, "An Attenuation Relationship Based on Turkish Strong Motion Data and Iso-acceleration Map of Turkey," *Engineering Geology*, vol. 74, pp. 265-291, 2004.

[15] T. L. Youd et al., "Liquefaction Resistance of Soils: Summary Report from the 1996 NCEER and 1998 NCEER/NSF Workshops on Evaluation of Liquefaction Resistance of Soils," *Journal of Geotechnical and Geoenvironmental Engineering*, vol. 127, no. 10, pp. 817-833, 2001.

[16] A. W. Skempton, "Standard Penetration Test Procedures and the Effects in Sands of Overburden Pressure, Relative Density, Particle Size, Aging, and Overconsolidation," *Geotechnique*, vol. 36, no. 3, pp. 425-447, 1986.

[17] L. A. Grassino, "Design Procedures for Jet-Grouting," *in Seminar on Jet Grouting*, Singapore, Apr. 7, 1997.

[18] Y. Ohta and N. Goto, "Empirical Shear Wave Velocity Equations in Terms of Characteristic Soil Indexes," *Earthquake Engineering & Structural Dynamics*, vol. 6, no. 2, pp. 167-187, 1978.

[19] A. Özyanki, H. Dindar, and A. Ekinci, "Killi Zeminlerde Çok Kanallı Yüzey Dalgası Analizi Yöntemi ile Elde Edilen Kayma Dalga Hızı ile Plastisite İndisi ve Standart Penetrasyon Sayısı Korelasyonu," *Avrupa Bilim ve Teknoloji Dergisi*, c. 20, ss. 490-497, 2020.

[20] *İnşaat Mühendisliğinde Zeminlerin Sınıflandırılması,* Türk Standartları Enstitüsü TS 1500, 2000.

Düzce University
Journal of Science & Technology

Research Article

Synthesis of Plant-Based Ester for Metalworking Fluids and Tribological Performance

Ertuğrul KAYA [a,*]

[a] *3-S Engineering and Consulting Company, R&D Center, Düzce, TURKEY*
* *Corresponding author's e-mail address:* ekaya@3-s.com.tr
DOI: 10.29130/dubited.1501022

ABSTRACT

Lubricants derived from plant-based raw materials offer great potential for the development of environmentally friendly and renewable esters due to their easier and faster biodegradability, reducing dependence on petrochemical raw materials and creating new synthesis processes. The increasing burden of environmental regulations and the depletion of petroleum-derived raw materials have prompted many industries to opt for products based on natural raw materials. Due to these positive effects, vegetable oil-based esters have recently been considered as potential candidates for industrial use. In this context, ester synthesis from cottonseed oil, a natural biodegradable raw material source, was carried out by transesterification with isopropyl alcohol. The structure of the synthesized ester was elucidated by GC-FID and FTIR and important physical parameters such as acid number, saponification number, viscosity and density of the ester were investigated. The synthesized isopropyl cottonseed oil ester was used to formulate a synthetic metalworking fluid at concentrations of 2%, 4% and 6%. The tribological properties of the formulated metalworking fluid were evaluated using the Reichert test and the chip corrosion test. It was found that the addition of 6% isopropyl cottonseed oil ester to the synthetic metalworking fluid exhibited the best tribological properties.

Keywords: *Cottonseed oil, Metalworking fluid, Transesterification, Tribology.*

Metal İşleme Sıvısında Kullanılan Bitkisel Yağ Bazlı Ester Sentezi ve Tribolojik Performansı

ÖZ

Bitkisel bazlı hammaddelerden elde edilen yağlayıcılar, daha kolay ve daha hızlı biyolojik olarak parçalanabilmeleri, petrokimyasal hammaddelere bağımlılığı azaltmaları ve yeni sentez süreçleri yaratmaları nedeniyle çevre dostu ve yenilenebilir esterlerin geliştirilmesi için büyük bir potansiyel sunmaktadır. Çevresel düzenlemelerin artan yükü ve petrol türevi hammaddelerin tükenmesi, birçok endüstriyi doğal hammaddelere dayalı ürünleri tercih etmeye yöneltmiştir. Bu olumlu etkiler nedeniyle, bitkisel yağ bazlı esterler son zamanlarda endüstriyel kullanım için potansiyel adaylar olarak değerlendirilmektedir. Bu bağlamda, biyolojik olarak parçalanabilen doğal bir hammadde kaynağı olan pamuk tohumu yağından ester sentezi, izopropil alkol ile transesterifikasyon yoluyla gerçekleştirilmiştir. Sentezlenen esterin yapısı GC-FID ve FTIR ile aydınlatılmış ve esterin asit sayısı, sabunlaşma sayısı, viskozitesi ve yoğunluğu gibi önemli fiziksel parametreleri incelenmiştir. Sentezlenen izopropil pamuk tohumu yağı esteri, %2, %4 ve %6 konsantrasyonlarında sentetik bir metal işleme sıvısı formüle etmek için kullanılmıştır. Formüle edilen metal işleme sıvısının tribolojik özellikleri Reichert testi ve talaşlı korozyon testi kullanılarak değerlendirilmiştir. Sentetik metal işleme sıvısına %6 izopropil pamuk tohumu yağı esteri ilavesinin en iyi tribolojik özellikleri sergilediği bulunmuştur.

Received: 13/06/2024, Revised:30/10/2024, Accepted:02/11/2024

Anahtar Kelimeler: *Pamuk yağı, Metal işleme sıvısı, Transesterifikasyon, Triboloji.*

I. INTRODUCTION

In recent years, vegetable oils have been widely used in both academic and industrial research.The components of vegetable oils have many highly reactive sites as they contain double bonds, carboxylic groups. This different structure and functionality offer a great opportunity for the creation of various reactions [1]. Vegetable oils, especially biodegradable lubricants such as rapeseed, canola, jatropha, coconut, palm, cotton, hazelnut are some of the more possible and promising alternatives as basic feedstocks for biodiesel and cutting fluids. They are easily biodegradable and less costly than synthetic base oils [2], [3]. The global production of vegetable oils is estimated at more than 100 million tons, which covers only 10% of the demand for diesel fuel [2].

Vegetable oils and their esters are also used as lubricants, corrosion inhibitors and high-pressure additives in metalworking fluids (MWF). Lubricants based on plant-based renewable raw materials offer great potential for the development of ecological and renewable esters, as they are environmentally friendly, much easier and faster to degrade, and create new synthesis processes by reducing dependence on petrochemical raw materials [4]. The increasing obligations imposed by environmental regulations and the depletion of petroleum-based raw materials have directed many industries towards products derived from natural raw materials. Vegetable oil-based esters recently been increasingly used industrially due to their advantageous properties, such as excellent lubricity, high viscosity index, and low toxicity [5].

The increasing use of metals due to technological advancements has made the process from metal processing to the final product extremely important in industry. In addition, environmental concerns that have arisen in recent years have encouraged the metal and metalworking industry to use environmentally friendly and more efficient natural raw materials in the production of final metal products [6].

In particular, the ecological nature of oils and emulsions used in metalworking has gained significant importance. The main characteristic of fluids used in metal processing is to provide excellent lubrication, enabling the easy shaping of metal. Emulsifiers, which ensure the homogeneous mixing of oil and water in oil-water emulsions, are essential components of a good MWFs. Another crucial feature of MWFs are their ability to protect against corrosion during and after metal processing [7]. Corrosion is an unavoidable natural process and all metals are subject to corrosion according to the laws of thermodynamics. Even the slightest corrosion during the shaping of metals can lead to in the complete loss of material. Therefore, methods to protect metal materials against corrosion are widely used in the metal and metalworking industries. In MWF, one of the most important components is corrosion inhibitors. The materials used in new-generation MWF fulfill not only one feature but also more than one feature [8]. El-Din et. al. produced five different hydrophilic-lipophilic balance (HLB) values (10, 9.5, 9, 8.5, 8) using environmentally friendly ingredients and castor oil in a study to produce a new MWF. Performance evaluations showed that the prepared cutting fluid (E1) reduced the cutting force from 500 N to 280 N on a dry high-speed steel sample, while the commercial cutting fluid recorded this value as 340 N [9]. He et. all, cottonseed oil (CSO) was converted into a bio-based lubricant of branched nonyl isodecyl esters (NIEs). Pour point (-47 °C), kinematic viscosity (200.3 mm^2/s) and viscosity index (141) of NIEs were superior to CSO. The oxidation onset temperature (307.21°C) and oxidation induction time (21 minutes) are also higher than CSO. The coefficient of friction (0.07), wear track diameter (132 μm) and oil film coverage (100%) are better than CSO and commercial lubricants. This bio-based lubricant has the potential to replace mineral oils, according to the study [10].

Isopropyl cottonseed oil ester was synthesized by transesterification of cottonseed oil, a vegetable oil source, with isopropyl alcohol. Various derivatives of synthesized product have been reported in the literature as lubricants in MWF [11]. In this study, the structure of the synthesized iso-propyl cottonseed

oil ester has been elucidated using FTIR spectroscopy and a GC-FID device. The acid number, saponification number, density, kinematic viscosity and flash point of the synthesized product have been measured. In the study, the synthesized ester has been added to a synthetic MWF formulation at certain ratios (2%, 4%, 6%). The lubrication performance test (Reichter Test) and the corrosion properties of MWF were examined by machining corrosion test, which is the preferred simple method for determining the corrosion rate in the industry.

II. MATERIAL AND METHOD

A. MATERIAL

The cottonseed oil used in the synthesis was supplied by the Pam Yağ Gıda ve Kimya Inc. Co., isopropyl alcohol and sodium methylate were purchased From Sigma- Aldrich and used without purification. Agilent 8890 GC instrument was used for GC-FID spectra of the synthesised esters. The PerkinElmer Spectrum Two 4000-400 cm-1 ATR instrument was used for Fourier transform infrared spectroscopy (FTIR). The BIOLAB Viscol-10A automatic kinematic viscometer was used to measure viscosity and the Normalab NCL 440 was used for flash point.

B. METHOD

B. 1. Ester Synthesis

Cottonseed oil, isopropyl alcohol and sodium methoxide (1:6.7:0.1) were mixed and placed in a 250 mL three-necked flask. The reaction was kept at a temperature of 75 °C and stopped after 3 hours. After the reaction, the excess alcohol was removed from the mixture using vacuum. The resulting product was transferred to a separatory funnel and allowed to settle. The glycerol formed during the reaction was separated from the product and the free glycerol remaining in the product was removed by washing the product three times. After removal of water and free glycerol from the reaction product, the final product was characterized by GC-FID and FTIR.

B. 2. Physical Properties for Synthesized Ester

B.2.1. Determination of acid and saponification number

The acid number of the synthesized ester was determined according to the official AOCS method Cd 3d-63 [12] , the saponification value was determined according to the official AOCS method TI 1a-64 [13].

B.2.2. Determination of kinematic viscosity, density and flash point

The kinematic viscosity of the synthesized product was measured according to ASTM D445 [14]. The density of the synthesized product was measured according to ASTM D891-18 [15] and the flash point was determined according to ASTM D1310 [16].

B.2.3. GC-FID test

Reaction products were monitored by capillary column gas chromatography, using a Agilent 8890 GC (Fig 1) equipped with a flame ionization detector (FID) according to AOCS Ce 1a-13 method [17]. CP-Sil 88 for FAMEs GC Columns has been used. The injection system was split-splitless. The carrier gas was helium at a flow rate of 1mL/minutes. The internal standard technique was used to quantify the amount of the chemical species.

Figure 1. *Agilent 8890 GC.*

B.2.4. FTIR

FTIR characterization is used to determine the changes in functional groups that occur before and after the esterification reaction. These changes can be observed by a shift in specific wave numbers or the appearance of new absorption peaks. Characteristic peaks in the FTIR spectrum of esters, especially bands such as the C=O ester group and the C-O ester group, help to determine the presence and identity of the compound. These peaks are important for assessing the accuracy and purity of the samples [18]. In addition, the peaks in the FTIR spectrum of esters enable the monitoring of chemical reactions. PerkinElmer Spectrum Two 4000-400 cm-1 ATR device has been used for FTIR spectra (Fig 2).

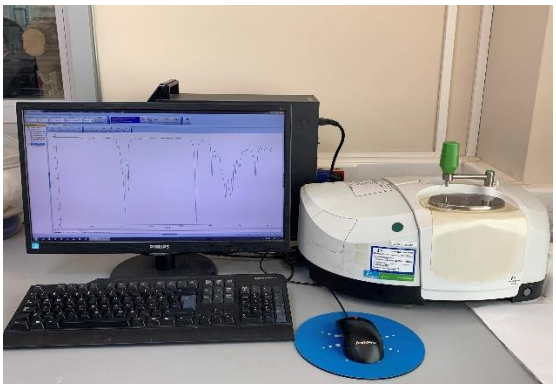

Figure 2. PerkinElmer Spectrum Two FTIR device.

B. 3. Tests on MWF

B.3.1. Lubrication performance test (Reichtert Test)

The Reichert test is used to determine the wear properties (WP) and extreme pressure properties (EP) of lubricants and additives in MWF. The effect of the synthesized ester on the lubrication performance in MWF and its quality-enhancing impact on the machined metal surface was tested using the Reichert Test device (Fig 3) [19]. The metal bearing tested is AISI 52100 steel. In the Reichert test, 25 mL of MWF is placed in the reservoir, and a rotating bearing is semi-immersed in it. An untreated roller is placed in the indentation and the test is started with a pressure of 200 Newton. The test duration is 100 seconds. Throughout the test, the rotating metal bearing is treated with the MWF, and the fluid remains between the bearing and the roller. The better the MWF protects the roller during the test, the fewer wear marks will appear on the roller. At the end of the test, the roller is removed from its position, and

the length and width of the wear mark (in millimeters) are measured and calculated according to Equality is given 1.

$$Lubrication\ performance\ test = \frac{Scar\ (length) \times Scar\ (width) * 3.14}{4} \quad (1)$$

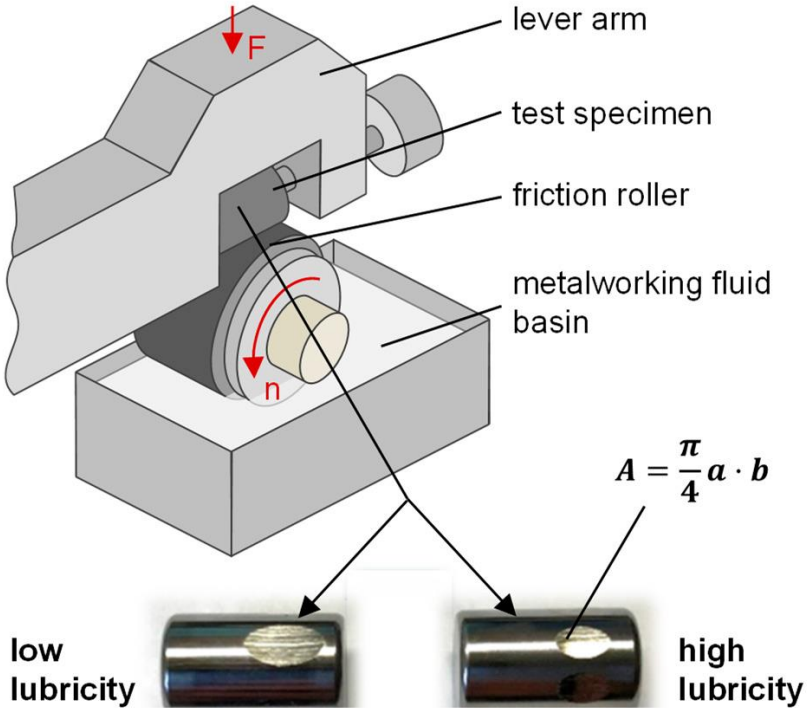

Figure 3. *Reichert tribology test [19].*

B.3.2. Corrosion test

Corrosion test of 1%, 2% and 3% emulsions of MWF was carried out according to DIN 51360-2 standard[20].

III. RESULTS AND DISCUSSION

A. ESTER CHARACTERISATION AND PHYSICAL PROPERTIES

Isopropyl cottonseed oil ester was synthesized under the specified conditions and the structure of this ester has been elucidated by GC-FID and FTIR. Cottonseed oil contains myristic acid in a range of 0.6-1%, palmitic acid in a range of 21.4-26.4%, stearic acid in a range of 2.1-3.3%, oleic acid in a range of 14.7-21.7%, and linoleic acid in a range of 46.7-58.3% [21]. Figure 4 shows the GC-FID chromatogram of the synthesized ester. When the chromatogram was analyzed, the GC chromatogram showed five different peaks with two different intensities; the peaks at retention times 16.5, 22.94 and 24.37 (Figure 4) have a lower intensity (122 to 294 pA) compared to the peaks at 19.3 and 26.85 minutes with intensities of 12.18 to 86.5 pA. The GC chromatogram of the fatty acid isopropyl ester standards shows peaks at retention times between 15 and 28 minutes.

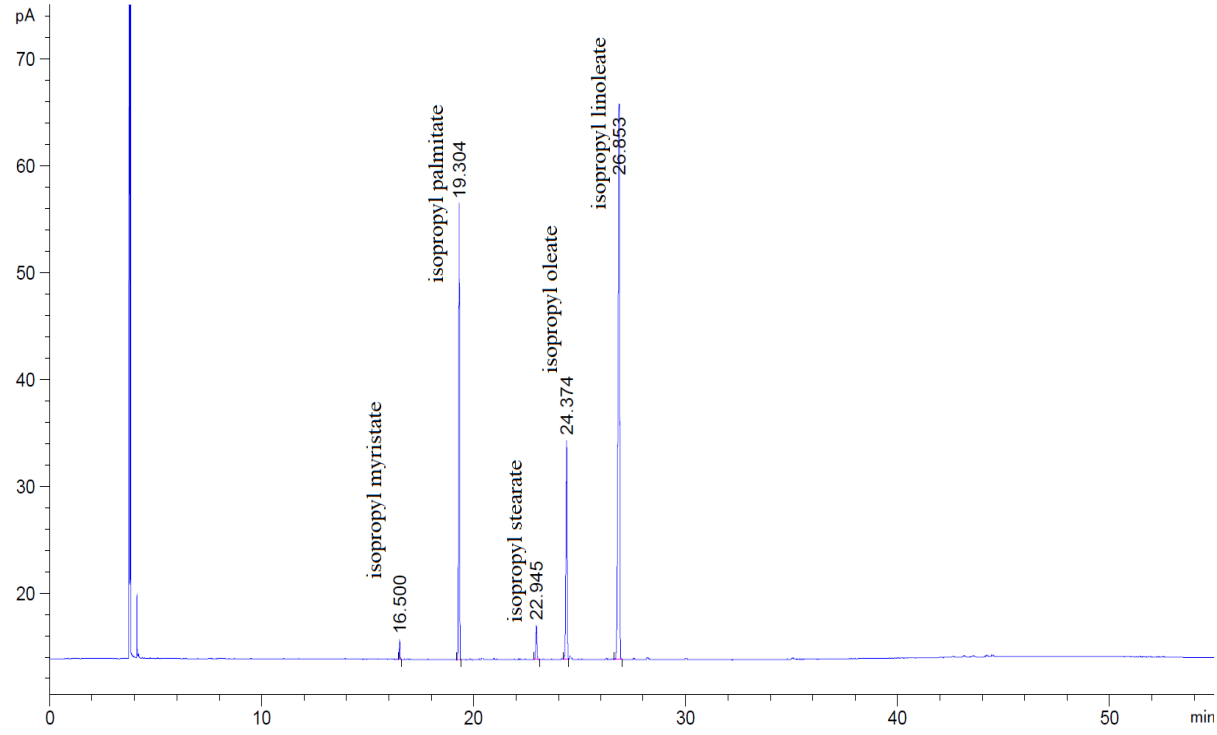

Figure 4. *GC chromatogram for Isopropyl cotton fatty acid ester.*

According to these data, the transesterification process is considered successful because the majority of the reaction product consists of the desired products. Accordingly, the peak at 16.5 belongs to isopropyl myristate, the peak at 19.3 to isopropyl palmitate, the peak at 22.94 to isopropyl stearate, the peak at 24.37 to isopropyl oleate and the peak at 26.85 to isopropyl linoleate.

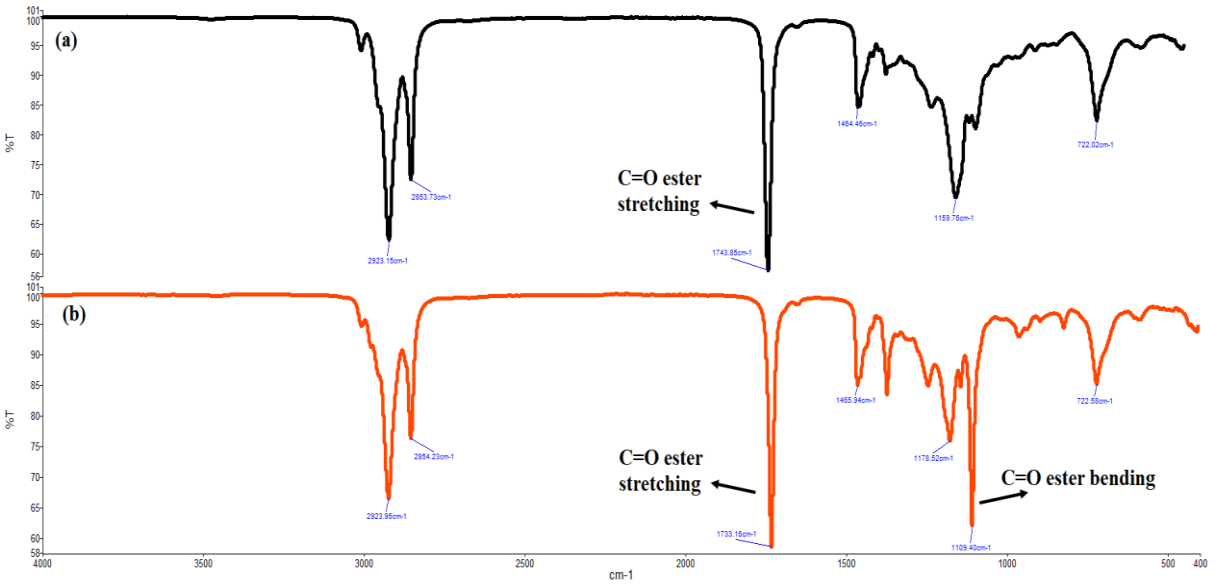

Figure 5. *Comparison between IR spectra of cottonseed oil (a) and isopropyl cottonseed oil ester (b).*

The spectra of cottonseed oil (Fig. 5(a)) and isopropyl cottonseed oil ester (Fig. 5(b)) are shown in comparison. The wavelength of the alcohol, -OH (3300-3100 cm-1) is not seen in the isopropyl cottonseed oil ester. This suggests that the OH bond in the isopropyl alcohol has completely reacted with the oil to form the ester. There is also a shift from a wavelength of 1743 cm-1 for the spectrum of cottonseed oil to a wavelength of 1733 cm-1 for the spectrum of isopropyl cottonseed oil ester. There is also a wavelength of 1109 cm-1 after transesterification, indicating the CO bond functional group as a result of the formation of the ester isopropyl cottonseed oil ester [22].

Tests such as saponification number, acid number, viscosity, density and flash point of the synthesized ester were performed and the results are given in Table 1.

Table 1. *Some parameters of the synthesized ester*

Sample	**Acid number** *(mgKOH/g)*	**Saponification number** *(mgKOH/g)*	**Viscosity** *(cSt) (40 C°)*	**Density** *(g/cm³)*	**Flash point** *(C°)*
Iso-propyl cottonseed oil ester	0,25	185,5	3,3	0,87	175

The saponification number of esters, acid number, density, viscosity and flash point are important criteria for determining the performance and stability of lubricants. These parameters are critical to understanding both the chemical and physical properties of lubricants and their suitability for the application [23]. The saponification number is used to determine the amount of the esters and triglycerides present in the oil. The saponification number of the esters is important for assessing the biodegradability and environmental impact of lubricants [24]. Acid number indicates the amount of free fatty acids in a lubricant and is used to assess the oxidation stability of the oil. The density determines the mass and volume of the lubricant. It is also a critical parameter in understanding how lubricants behave under different temperature and pressure conditions [25]. Viscosity refers to the fluid resistance of the lubricant and determines the effect of the oil on friction, wear and energy loss [26]. Flash point indicates the ignition temperature of a lubricant's vapours and is used to assess the risk of fire [27].

B. MWF PERFORMANCE TESTS

MWF contain pH regulators, lubricants, anti-wear additives, extreme pressure additives, metal passivators, metal chelating agents, antifoaming agents, boron compounds, emulsifiers, ionic and non-ionic surfactants and corrosion inhibitors[19]. Some physical properties of the original metalworking fluid and the metalworking fluid with % Isopropyl cottonseed oil ester (2%, 4%, 6%) are given in Table 2.

Table 2. *Some parameters of the MWF*

Sample	**Viscosity** *(cSt) (40 C°)*	**Density** *(g/cm³)*
Original MWF	33,5	0,84
2% Isopropyl cottonseed oil ester added MWF	33,1	0,83
4% Isopropyl cottonseed oil ester added MWF	33,3	0,84
6% Isopropyl cottonseed oil ester added MWF	33,5	0,85

Reichert Test device was used to measure the effect of the synthesized isopropyl cottonseed oil ester on the lubrication performance in metal processing fluids and the quality enhancing effect on the treated metal surface. Fewer scars caused by metal-metal friction ensures a smaller average area. For this reason, synthesized isopropyl cottonseed oil ester was used in different ratios in the metal treatment liquid and Reichert test was performed. The synthesized cotton oil ester was added as 2%, 4% and 6% in the formulation of a synthetic MWF. The scar width and length measurements caused by metal-metal friction in the Reichert test device are given in Table 3. Figures of the rollers processed in the Reichert test machine are given in Figure 6.

Table 3. *Isopropyl cottonseed oil ester Reichert test result.*

Sample, %	**Scar**		**Average area** *(mm^2)*
	Height *(mm)*	**Width** *(mm)*	
0	7,3	3,8	21,77
2	7,3	3,7	21,20
4	7,0	3,2	17,58
6	7,0	3,1	17,03

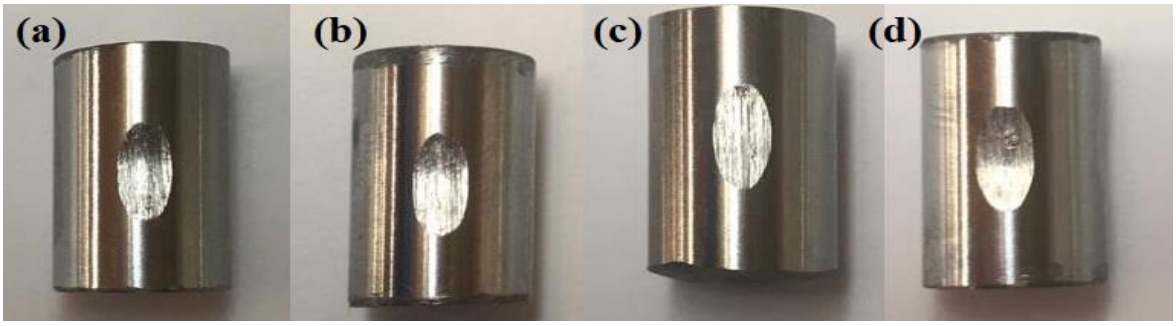

Figure 6. *Roller result from the Reichert test of isopropyl cottonseed oil ester with (a) without ester, (b) 2.0% ester, (c) 4.0%, (d) 6.0% ester.*

The Reichter test results in Table 3 show that when the synthesized isopropyl cottonseed oil ester was added to the MWF formulation, the area of the scars on the test rollers decreased. The best utilization rate of the synthesized ester in the developed synthetic MWF is 6%. It is known in the literature that vegetable oils and esters derived from them are more homogeneous than mineral oils [1], [5], [8], [28], [29], [30], [31]. Vegetable oil and ester derivatives have higher boiling point and larger molecular weight, which leads to increased stability in metalworking fluids and less product loss due to evaporation [29]. In addition, lubricating and wear properties of vegetable oils and vegetable oil-based esters are also known to be better than mineral oils [29]. Vegetable oil-based esters are generally obtained from unsaturated long-chain fatty acids and have a high lubricity due to this structure. Fox and Stachowiak reported in a study that vegetable oil-based esters enable energy savings by reducing friction between metal and metal and allowing operation at lower temperatures [32]. The polar groups of plant-based esters bind to metal surfaces and form a protective film. This film layer offers high abrasion resistance and extends the service life of the devices. In a study on these properties, it was shown that the anti-wear protection performance of esters from palm and sunflower oil is superior to that of esters from mineral oils [33]. In the Reichert test, the synthesized product added instead of a petroleum-derived mineral oil in the original formulation gave better results due to its good lubricity and anti-wear properties. The increase in the amount of the synthesized product was proportional to the decrease in wear in the Reichert test. With the increase of vegetable oil based ester in the metal working fluid, the metal surface was less abraded. This indicates that the synthesized ester has good lubricity and anti-wear properties. According to Reichert's test results, unsaturated long-chain fatty acids and polar groups in cottonseed oil improve the lubricity and anti-wear properties of the metalworking fluid.

Pour 4 g of corrosion chips onto the filter paper placed in the Petri dish using a precision balance. After pouring 5 ml of emulsion from 1%, 2% and 3% emulsion mixture of the prepared full synthetic MWF onto the corrosion sawdust with the help of a pipette, the petri dish was closed and kept in the laboratory environment. After 24 hours, the results of the corrosion stains formed on the filter paper were recorded. A corrosion cips test was performed on the product developed from the synthesized product with 6% full synthetic MWF formulation. The result of this process is shown in Figure 6.

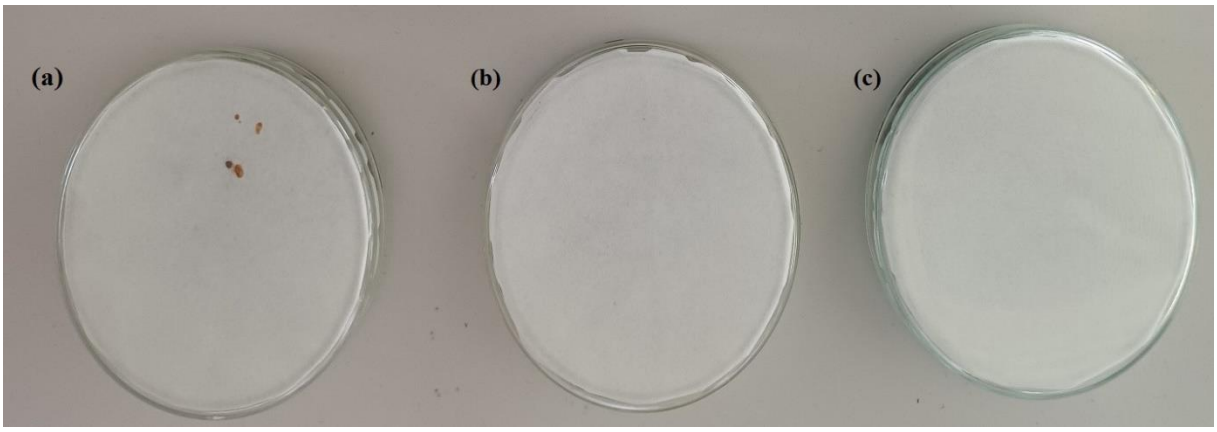

Figure 7. *Corrosion cips test results of 1% (a), 2% (b) and 3% (c) emulsions of prepared synthetic MWF.*

When testing the machining corrosion of the product developed from the synthesized product with a 6% MWF formulation (Figure 7), a corrosion unit is observed in the 1% emulsion of the synthetic MWF. No corrosion is observed in the 2% and 3% emulsions after 24 hours. This shows that the synthesized product has both an anticorrosive effect and lubricant properties.

IV. CONCLUSION

In this study, a high value-added ester was synthesized from cottonseed oil, a vegetable raw material. The structure of the ester synthesized by the transesterification method was elucidated by FTIR and GC-FID. Physical parameters such as acid number, viscosity and saponification number of this synthesized ester were also performed and reported in the literature. The synthesized ester was used to develop a synthetic MWF formulation that is used in the metalworking industry. The tribological properties of the MWFs developed by using the synthesized ester at different ratios (2%, 4% and 6%) were analyzed by Reichtert test and corrosion properties were also investigated. The results showed that the isopropyl cotton oil ester used at 6% in synthetic MWF had the best tribological properties. In the Reichtert test of the metalworking fluid containing mineral oil, 21.77 mm^2 of the roller surface was worn. In the metalworking fluid with synthesized isopropyl cottonseed oil ester additives (2%, 4%, 6%), the wear decreased to 21.2 mm^2, 17.58 mm^2 and 17.03 mm^2 respectively. This shows that vegetable-based fatty esters have good lubricants and anti-wear properties. At the same time, the results of the machining corrosion test show that vegetable oil-based esters protect the metal surface better than mineral based oils. The performance of vegetable oil-based esters can change depending on the workpiece and machining process, so the work can be extended to different workpiece materials and machining processes, which will expand the scope of the work in the future. In conclusion, further studies need to be conducted to obtain more conclusive results. Nevertheless, the data from this study can be used as a basis for further formulation studies using isopropyl cottonseed oil esters and other vegetable oil esters.

ACKNOWLEDGEMENTS: This work is supported by 3-S Engineering R&D Department (Project no: PTZ-10 and PTZ-15).

V. REFERENCES

[1] S. Miao, P. Wang, Z. Su, and S. Zhang, "Vegetable-oil-based polymers as future polymeric biomaterials," *Acta Biomaterialia*, vol. 10, no. 4, pp. 1692–1704, 2014.

[2] L. Isom and M. Hanna, "Biodiesel current and future perspectives," in *Handbook of Plant-Based Biofuels*, LCC, USA: CRC Press, 2008, pp. 177–181.

[3] Y. X. Xu and M. A. Hanna, "Synthesis and characterization of hazelnut oil-based biodiesel," *Industrial Crops and Products*, vol. 29, no. 2–3, pp. 473–479, 2009.

[4] G. Salinas-Solano, J. Porcayo-Calderon, L. M. Martinez, J. Canto, M. Casales, O. Sotelo-Mazon, J. Hanao and L. Martinez-Gomez, "Development and evaluation of a green corrosion inhibitor based on rice bran oil obtained from agro-industrial waste," *Industrial Crops and Products*, vol. 119, pp. 111–124,2018.

[5] B. Kamya, H. Wang, T. Razipour, D. W. Chambers, A. S. Bassi and C. Xu, “Production of high-end bio-lubricant products via epoxidation of canola oil trimethylolpropane (COTMP) esters,” *Industrial Crops and Products*, vol. 222, no. 3, pp. 119-127, 2024.

[6] R. Sankaranarayanan, N. R. J. Hynes, J. S. Kumar and G. M. Krolczyk, “A comprehensive review on research developments of vegetable-oil based cutting fluids for sustainable machining challenges,” *Journal of Manufacturing Processes*, vol. 67, pp. 286–313, 2021.

[7] D. F. Silva-Alvarez, I. Dominguez-Lopez, M. A. Vidales Hurtado, C. Gutierrez-Antonio, K. A. Flores-Garay, and A. L. Garcia-Garcia, “A review on the menagerie of green fluids and nanoparticles to develop sustainable biolubricant technologies,” *Environmental Technology & Innovation Journal*, vol. 33, pp. 103-115, 2024.

[8] S. A. Lawal, I. A. Choudhury, and Y. Nukman, “Evaluation of vegetable and mineral oil-in-water emulsion cutting fluids in turning AISI 4340 steel with coated carbide tools,” *Journal of Cleaner Production*, vol. 66, pp. 610–618, 2014.

[9] M. R. Noor El-Din, M. R. Mishrif, S. V. Kailas, and J. K. Mannekote, “Studying the lubricity of new eco-friendly cutting oil formulation in metal working fluid,” *Industrial Lubrication and Tribology*, vol. 70, no. 9, pp. 1569–1579, 2018.

[10] C. He, Y. Yan, S. Li, L. Zhang, X. Zhao, Z. Deng and X. Zhang, “Modification of cottonseed oil with lipases and ionic liquid catalysts to prepare highly branched lubricant with low pour point and high viscosity,” *Biochemical Engineering Journal*, vol. 192, p. 108-118, 2023.

[11] S. Patil, K. Rajurkar, S. Patil and A. Pratap, “Synthesis of guerbet esters and its application in drilling and grinding oil” *Tribology International*, vol. 177, pp. 107-119, 2023.

[12] *Acid Value of Fats and Oils*, AOCS Official Method Cd 3d-63, 2017.

[13] *Saponification Value of Industrial Oils and Derivatives*, AOCS Official Method Tl 1a-64, 2022.

[14] *Standard Test Method for Kinematic Viscosity of Transparent and Opaque Liquids*, ASTM D445, 2024.

[15] *Standard Test Methods for Specific Gravity, Apparent, of Liquid Industrial Chemicals*, ASTM D891, 2016.

[16] *Standard Test Method for Flash Point and Fire Point of Liquids by Tag Open-Cup Apparatus*, ASTM D1310, 2018.

[17] *Fatty Acid in Edible Oils and Fats by Capillary GLC*, AOCS Official MEthod Ce 1a-13, 2017.

[18] G. Pipuš, I. Plazl, and T. Koloini, “Esterification of benzoic acid with 2-ethylhexanol in a microwave stirred-tank reactor,” *Industrial & Engineering Chemistry Research*, vol. 41, no. 5, pp. 1129–1134, 2002.

[19] B. Seidel and D. Meyer, “Investigation of the influence of aging on the lubricity of metalworking fluids by means of design of experiment,” *Lubricants*, vol. 7, no. 11, p. 94, 2019.

[20] *Testing of cooling lubricants; determination of corrosion preventing characteristics of cooling lubricants mixed with water; chip/filter paper method*, European Standarts DIN 51360-2, 1981.

[21] M. A. Zia, S. H. Shah, S. Shoukat, Z. Hussain, S. U. Khan, and N. Shafqat, “Physicochemical features, functional characteristics, and health benefits of cottonseed oil: a review,” *Brazilian Journal of Biology*, vol. 82, pp.1-15, 2022.

[22] P. Dubey, P. Sharma, and V. Kumar, “FTIR and GC–MS spectral datasets of wax from Pinus roxburghii Sarg. needles biomass,” *Data Brief*, vol. 15, pp. 615–622, 2017.

[23] R. Padmini, P. V. Krishna and G. K. Rao, “Effectiveness of vegetable oil based nanofluids as potential cutting fluids in turning AISI 1040 steel,” *Tribology International,* vol. 94, pp. 490-501, 2016.

[24] S. M. Alves, B. S. Barros, M. F. Trajano, K. S. B. Ribeiro and E. Moura, “Tribological behavior of vegetable oil-based lubricants with nanoparticles of oxides in boundary lubrication conditions” *Tribology International,* vol. 65, pp. 28-36, 2013.

[25] S. Gill and A. Rowntree, “Liquid lubricants for spacecraft applications,” in *Chemistry and Technology of Lubricants*, Dordrecht, Netherlands: Springer, 2009, pp. 375–387.

[26] R. L. Stambaugh and B. G. Kinker, “Viscosity index improvers and thickeners,” in *Chemistry and Technology of Lubricants*, Dordrecht, Netherlands: Springer, 2009, pp. 153–187.

[27] E. Brinksmeier, D. Meyer, A. G. Huesmann-Cordes and C. Herrmann, "Metalworking fluids mechanisms and performance," *CIRP Annals*, vol. 64, no. 2, pp. 605-628, 2015.

[28] B. Kamyab, H. Wang, C. Xu, D. W. Chambers, and A. S. Bassi, “Preparing vegetable oils-based metalworking fluids by a hydrolysis-esterification two-step process,” *Biomass Bioenergy*, vol. 183, pp. 167-175, 2024.

[29] I. S. Afonso, G. Nobrega, R. Lima, J. R. Gomes, and J. E. Ribeiro, “Conventional and recent advances of vegetable oils as metalworking fluids: a review,” *Lubricants*, vol. 11, no. 4, pp. 160-178, 2023.

[30] A. Adhvaryu, S. Z. Erhan, and J. M. Perez, “Tribological studies of thermally and chemically modified vegetable oils for use as environmentally friendly lubricants,” *Wear*, vol. 257, no. 3–4, pp. 359–367, 2004.

[31] B. Podgornik, S. Jacobson, and S. Hogmark, “Influence of EP and AW additives on the tribological behaviour of hard low friction coatings,” *Surface and Coatings Technology*, vol. 165, no. 2, pp. 168–175, 2003.

[32] N. J. Fox and G. W. Stachowiak, “Vegetable oil-based lubricants—A review of oxidation,” *Tribology International*, vol. 40, no. 7, pp. 1035–1046, 2007.

[33] S. Soni and M. Agarwal, “Lubricants from renewable energy sources – a review,” *Green Chemistry Letters and Reviews*, vol. 7, no. 4, pp. 359–382, 2014.

Düzce University
Journal of Science & Technology

Research Article

Determination of Excavation Volume Using UAV-Based PPK Method in Open Mining Sites Tatlıdere Forests in Düzce

Yılmaz TÜRK [a,*], Berkan BALABAN [b]

[a] *Department of Forest Engineering, Faculty of Forestry, Düzce University, Düzce, TURKEY*
[b] *Institute of Postgraduate Education, Düzce University, Düzce, TURKEY*
** Corresponding author's e-mail address: yilmazturk@duzce.edu.tr*
DOI: 10.29130/dubited.1515664

ABSTRACT

Remote sensing technologies have the potential to provide cost-effective, fast, and easy solutions for the determination of surface changes (material volume) after quarrying (open-pit mine) activities. In areas where the topography is rugged and difficult to access, the use of ground measurement techniques causes difficulties. In such cases, the use of remote sensing techniques is indispensable. The Post Processing Kinematic (PPK) measurement technique provides an alternative solution to other photogrammetry methods in areas whose topography is not suitable for satellite-based positioning. This study investigates the applicability of the UAV-based PPK method for the calculation of cut volume in quarry operations. The study area was selected as a quarry located within the boundaries of Tatlıdere Forestry Operation Chief in Düzce province and operated by a legal entity. Using a DJI Phantom 4 RTK unmanned aerial vehicle (UAV) with a PPK application module, a total of two flights in PPK flight mode were performed at the quarry on 30 September 2021 and 19 May 2022 (covering a period of approximately 7 months). The material volume, which is important for quarry operation, was calculated and the excavation volume in the two flight time intervals was found to be 104.170 m^3 and the cut area was found to be 44.348 m^2. According to the results obtained, UAV systems should be used in quarry management in terms of time and work safety in obtaining data.

Keywords: *Cut volume, UAV, PPK method, Quarry, Düzce*

Düzce Tatlıdere Ormanları Açık Maden Sahalarında İHA-Tabanlı PPK Yöntemi Kullanılarak Kazı Hacminin Belirlenmesi

Öz

Taş ocaklarında yapılan faaliyetler sonrası meydana gelen yüzey değişimlerinin (materyal hacmi) belirlenmesinde uzaktan algılama teknolojileri, maliyet-etkin, hızlı ve kolay çözümler sunma potansiyeli taşımaktadır. Topografyanın engebeli ve ulaşılması güç olduğu alanlarda yersel ölçüm tekniklerini kullanmak zorluklara neden olmaktadır. Bu gibi durumlarda uzaktan algılama tekniklerinin kullanımını olmazsa olmaz kılmaktadır. Coğrafi yapısı, uydu bazlı konumlamaya müsait olmayan alanlarda ölçü sonrası veri değerlendirme (Post Processing Kinematic-PPK) ölçüm tekniği diğer fotogrametri yöntemlerine alternatif çözüm sağlamaktadır. Bu çalışmada İHA-tabanlı PPK yönteminin taş ocağı işletmeciliğindeki kazı hacminin hesaplanmasında kullanılabilirliği incelenmiştir. Çalışma alanı olarak, işletmesi tüzel kişiliğe ait Tatlıdere (Düzce) Orman İşletme Şefliği'ndeki taş ocağı seçilmiştir. Çalışmada DJI Phantom 4 RTK marka ve PPK uygulama modülü sahip insansız hava aracı (İHA) kullanılarak, taş ocağında 30 Eylül 2021 ve 19 Mayıs 2022 tarihlerinde (yaklaşık 7 aylık süreci kapsayan) PPK uçuş modunda toplam iki uçuş gerçekleştirilmiştir. Taş ocağı işletmeciliği için önemli olan materyal hacmi hesaplanmış, iki uçuş zaman aralığındaki kazı miktarı 104,170 m^3 ve kazı alanı ise 44,348 m^2 bulunmuştur. Elde

Received:13/07/2024, Revised: 07/10/2024, Accepted: 04/11/2024

edilen sonuçlar doğrultusunda taş ocağı işletmeciliğinde İHA sistemleri veri elde etmede zaman ve iş güvenliği açısından kullanmalıdır.

Anahtar Kelimeler: *Kazı hacmi, İHA, PPK metot, Taş ocağı, Düzce*

I. INTRODUCTION

With the increase in the world population, the use of natural resources has also increased. The management and utilisation of natural resources requires periodic observations and measurements. Geographic Information Systems (GIS) and remote sensing (RS) techniques are often favoured in all natural resource management science related research. In recent years, Unmanned Aerial Vehicles (UAVs) have been used to produce high resolution and accurate digital elevation models (DEMs) of spatial data. With UAV, workload is reduced, time is saved and more precise data is obtained.

The minerals that are offered and used for the benefit of humanity are generally obtained through surface mining activities in natural habitats considered as forests. Many geotechnical applications, including civil works, are carried out in mining areas for the purpose of operation, and the natural soil structure and soil cover are changed [1]. In mountainous areas with difficult terrain conditions, obtaining data with traditional surveying techniques is very labour intensive and tiring. Today, UA methods are more preferred instead of traditional ground surveying techniques which are costly. With the development of technology, ground, aerial and satellite-based data collection methods provide great advantages in terms of speed and cost. The data collected with modern methods and tools are quickly analysed and made available to applied disciplines [2].

Robotic systems developed in recent years provide researchers with different measurement techniques, saving time and economy. Among these techniques, which are gaining momentum rapidly, are UAV systems, which are evaluated within the scope of close-up photogrammetry and divided into various classes [3]. These systems are preferred for measurement and evaluation studies covering sciences such as forestry, agriculture, mining and construction due to their temporal flexibility and ability to produce precise data [4-7].

New generation image processing techniques have a significant impact on the widespread use of UAV systems. The increasing use of the Structure-from-motion (SfM) algorithm, which is described as the return of photogrammetry, in the digital environment has a large share in the development of UAVs and systems [8]. UAVs and their systems are equipped with global navigation satellite system (GNSS) receivers, Inertial Measurement Unit (IMU) and many other sensors. The knowledge of these systems and sensors is effective in converting the block images obtained from the 2D plane into 3D with the SfM technique. High resolution digital elevation models (DEMs) and orthophotos can be easily created with many commercial or open source software working with SfM logic [9, 10].

In models requiring high precision and accuracy, the position information obtained from the GNSS-GPS module on the UAV is insufficient. Different GNSS techniques are used to ensure that the position parameters of the UAV have centimetre accuracy [11]. This high precision includes direct georeferencing, real-time kinematics (RTK) and post-process kinematics (PPK) technologies [12]. PPK measurement technique provides an alternative solution to the RTK method in areas where the topographical structure and coverage limits of the stations providing data are not suitable for satellite-based positioning [13].

In the volume calculation of the material quarried in the quarry, the volume calculation was previously made by counting the loaded transport vehicles and entering them into the weighbridge. In addition, the

material volume was also determined with devices such as takeometer, level etc. Nowadays, with the developing technology, material volume can be found by photogrammetric measurements. Cors-GPS is also used for monitoring open mine sites and determining the volume of material. The material volume is calculated with the boundaries of the permit area and the DEM created. However, since the open mine sites are generally located in mountainous areas, the topography is rugged and difficult to access, and the field measurement methods are more difficult and time-consuming in terms of occupational safety. In addition to UAV technology, automated data collection technologies include imaging of the land surface by photography, video or digitisation and the calculation of material volume using different remote sensors (non-contact) (laser, acoustic and infrared) [14]. The disadvantages of these methods are that remote sensing sensors are more expensive than existing UAV sensors. In addition, other methods are more difficult and time-consuming in terms of occupational safety since data will be obtained by walking around in the field. In addition to these, nowadays, local laser scanners, handheld and smart device compatible 3D devices (viDoc RTK, Handheld Lidar), GPS integrated cameras have the ability to be used in open mine sites. These methods are also disadvantageous compared to UAV systems since data is collected by walking in the field.

Open pit mining, or in other words surface mining, is a form of production applied in areas where the ore is located close to the surface of the ground in order to economically extract the cover layer on the mine when necessary [14] (Figure 1). The spread and size of the ore close to the surface has enabled open pit mining to diversify within itself. Today, three different methods for surface mining find their place in practice. These can be exemplified as lignite and coal quarries with horizontal ore deposits, metallic quarries with sloping or steeply dipping ore deposits, and industrial raw material and natural stone quarries with ore deposits formed on the slope close to the surface [15].

In this study, UAV-based PPK method was used to monitor the quarry performing surface mining activities with UAV and the volume of material extracted was calculated for the quarry operator. Therefore, this study aims to answer the question of whether the quarry material volume can be calculated without data loss with the UAV-based PPK method.

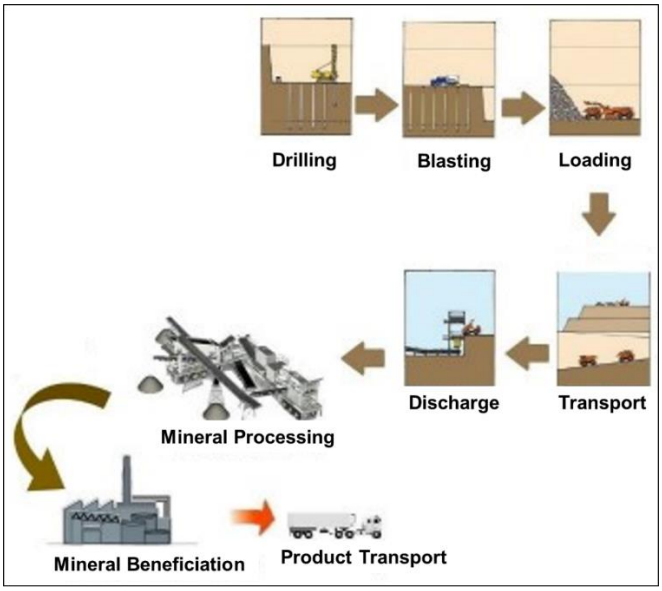

Figure 1. *Operation of open pit mining sites [14]*

II. MATERIAL AND METHOD

A. MATERIAL

A. 1. Study Area

The quarry, which is located within the boundaries of Tatlıdere Forest Management Chiefdom (FMC) within Düzce Forest Management Directorate, located in the southwest of the Western Black Sea Region, was selected as the study area (Figure 2). The quarry, which is 16 km away from the centre of Düzce, has an average elevation of 430 m above the sea and is a II-A Limestone site. The quarry permit area is approximately 112237 m² and the works were started in 2012 and production is still continuing. In the study area, UAV flights were carried out in two different time periods and the quarry was monitored for approximately 7 months. Bolu Regional Directorate of Forestry Permit Easement Branch Directorate, to which the study area is affiliated, has a total of 45 open pit mining permits operating in Düzce province as of 2024 [16].

The total area of Tatlıdere FMC is 4428 ha, of which 4090 ha is forested and 338 ha is non-forested. The study area is under the influence of both the Black Sea Climate Zone and the Central Anatolian Climate Zone. The differences in the climatic characteristics of the region have led to the formation of a rich range of plant diversity. The forests of the plan unit are generally leafy forests. The main tree species of Tatlıdere Forest Management Directorate are Oriental Beech (*Fagus orientalis*), European Hornbeam (*Carpinus betulus*), Sessile Oak (*Quercus petraea*), Scotch Pine (*Pinus sylvestris*), Austrian Pine (*Pinus nigra*) [17].

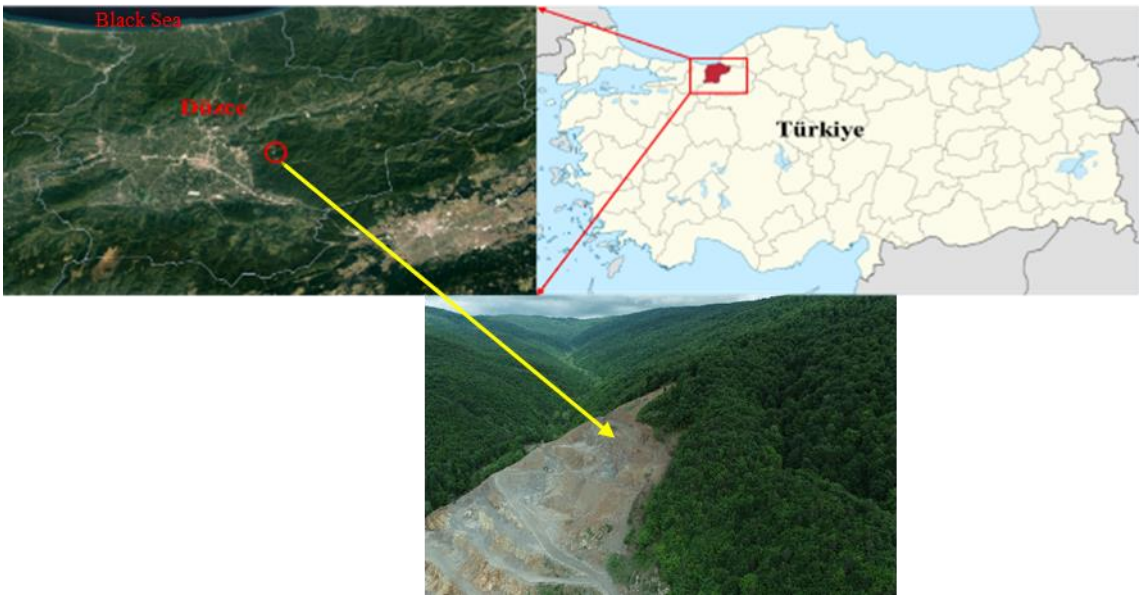

Figure 2. *Study area and its surroundings*

A. 2. Tools and Equipment Used

In the study, the first flight was performed on 30 September 2021 and the second flight was performed on 19 May 2022 with the DJI Phantom 4 RTK UAV platform. CHCN X91 GNSS receiver was used for coordinate acquisition (Figure 3). The UAV system used has a 20-megapixel camera capable of taking photos in the visible range (RGB) defined by the manufacturer. The UAV system is equipped with a multi-frequency RTK/PPK GNSS module that provides high position accuracy [18]. Intel ® Xeon ® CPU E5-1650 v3 @ 3.50GHz 48 GB processor model and 4 GB AMD FirePro W5100 graphics card workstation were used for data processing, visualisation and analysis. PPK method was used in the

study. PPK method offers higher accuracy than RTK method. However, the PPK method has limitations such as extra time, equipment (GNSS receiver) and software. Although rare, a potential source of error in this method is the inability to collect static data with the GNSS receiver.

Figure 3. a) *UAV DJI Phantom 4 RTK System,* ***b)*** *CHCN X91 GNSS receiver*

B. METHOD

B. 1. Acquisition of Digital Images with UAV System

The basic steps of image acquisition by UAV are pre-field preparation (preparation of flight plans and field work), flight realisation and post-flight operations. In the pre-field preparation phase, some necessary preliminary information such as weather conditions and topography of the relevant area should be obtained before travelling to the field. The optimum weather conditions for UAV flight are stated as a cloudy sky without wind and precipitation [19, 20].

The flight planning process was created with the DJI GS RTK application from the control of the DJI Phantom 4 RTK system. In this context, firstly, DEM data was obtained in Global Mapper software for the study area. The DEM data of the site and a vector data (in KML format) covering the boundaries of the flight area were transferred to the controller via SD card and a flight plan was prepared (Figure 4). Then, using these data, the time was taken into account depending on the size of the area and the battery capacity of the UAV, and finally, planning was carried out to perform adaptive flight.

Figure 4. *Creation of DEM data and preparation of flight plan*

Using the DJI Phantom 4 RTK UAV system with PPK application module, two flights were carried out in PPK mode in the quarry, which is an open mining area, on 30 September 2021 and 19 May 2022. The

photographs taken within this scope have 60% front and 70% side overlap ratios and the flight height is planned as 150 m. The flights were carried out in weather conditions without wind and precipitation. CHCN X91 GNSS receiver was used as a solution for PPK static measurement positioning. In PPK mode, when the UAV is in the air, the rover observation file "Rinex.obs" (RINEX observation data) is saved directly to the SD memory card. The GNSS receiver is installed on a tripod at a location with known coordinates and the measurement was started in static mode at an antenna height of 200 cm. Since RINEX observation data should cover the entire flight, static data acquisition was carried out before and after the UAV flight for 15 minutes each. The static data is stored in the internal memory of the GNSS receiver in a special file format ".HCN".

B. 2. Processing of Digital Images Taken by UAV

After the flights were completed, Agisoft Metashape Professional Version 1.5.2 software was used to process the images taken by the UAV and produce point cloud, DEM and orthophoto images with high resolution and accuracy [21] (Figure 5). Agisoft Metashape is a stand-alone software product that performs photogrammetric processing of digital images and generates 3D spatial data to be used in GIS applications, cultural heritage documentation, and visual effects production as well as for indirect measurements of objects of various scales [21]. The software ran on Windows 10 64-bit operating system. The accuracy level of the image registration process was set as medium, and the quality settings were selected as high for the other depth maps and dense cloud generation stages. The outputs produced as a result of photogrammetric analysis of the images are DEM and orthomosaics in “tiff” format.

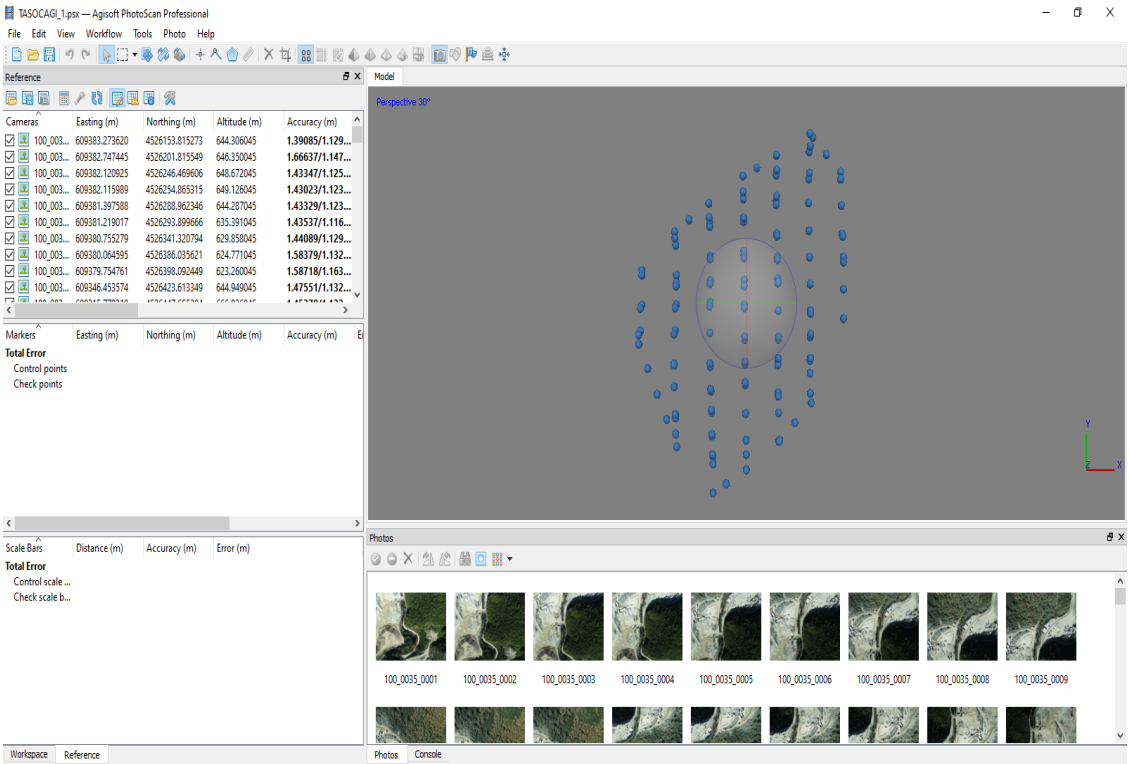

Figure 5. *Data processing in Agisoft Photscan Professional version 1.5.2*

Correction of camera positions for images taken in PPK mode was made using CHC Geomatics Office 2 software (Figure 6). The software is a powerful office software solution, designed for engineers as an integrated platform to make a link between field and office workflow from multiple sensors and generating rich deliverables. It supports 4 modules: GNSS, RTK, road and UAV, which allows for processing massive fieldwork data in one software. “PPKRAW” files for the rover and base observation files, “HCN” files for the GNSS base station were transferred to the software, and the corrected camera positions after the process were saved as a CSV file.

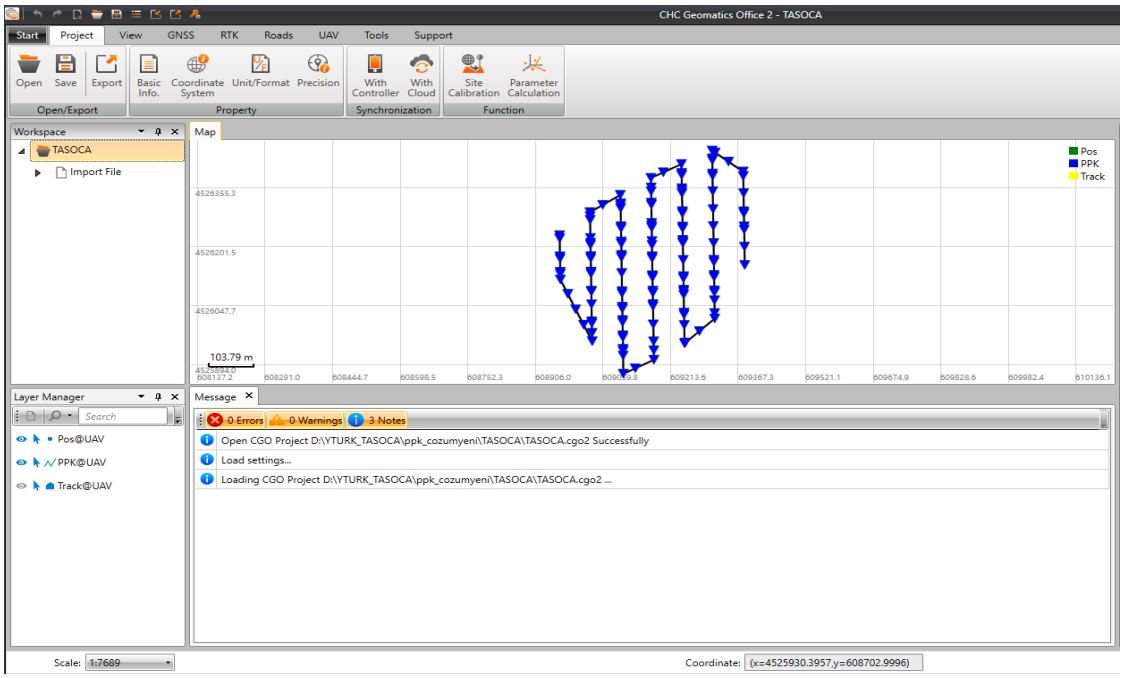

Figure 6. *Correcting photo positions in CHC Geomatics Office 2 PPK balancing software*

The corrected camera positions recorded as CSV were replaced with uncorrected camera positions in the Agisoft Metashape software, and the PPK data was analyzed and balanced and orthomosaic and DEM were produced (Figure 7).

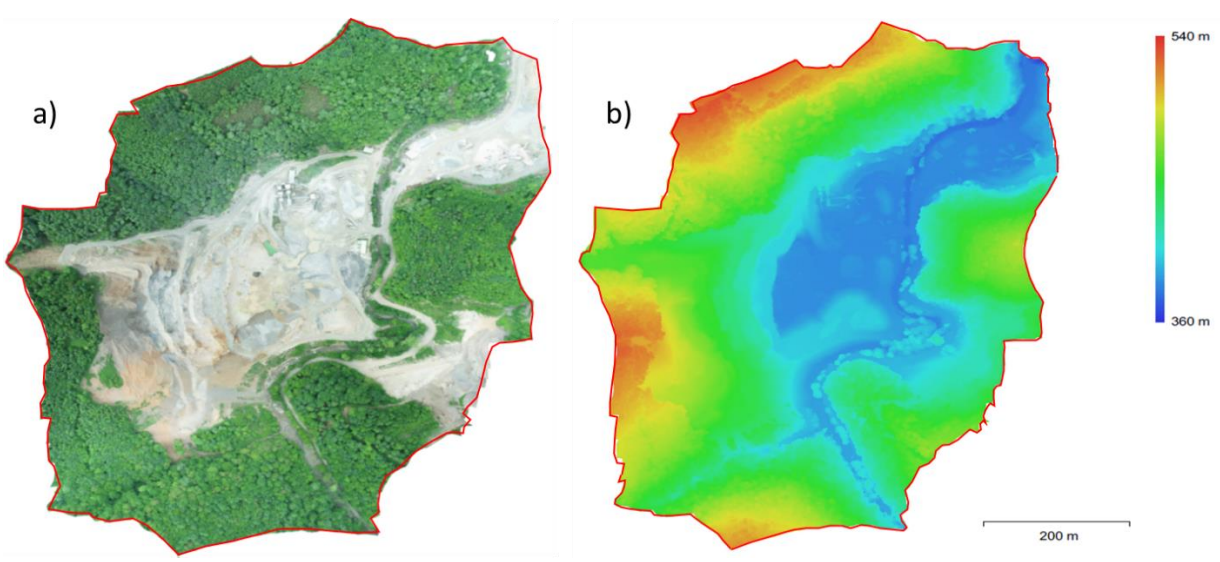

Figure 7. *Reconstructed:* ***a)*** *orthophoto image,* ***b)*** *digital elevation model*

During the photo alignment and optimization process, the root average square error rates for X, Y, Z, XY and total error of the calculated camera positions of the PPK data were calculated [21].

The average error was found by the following formula;

$$\text{Total Error} = \frac{\sqrt{\sum_{i=1}^{n}[(X_{i,t}-X_{i,g})^2+(Y_{i,t}-Y_{i,g})^2+(Z_{i,t}-Z_{i,g})^2]}}{n} \quad (1)$$

In the formula, "g" is the input value for camera position i and "t" is the estimated value for camera position i.

B. 3. Determination of Cut Volume

In the study, the DEM difference method was used to determine the quarry excavation volume. In this process, DEM is applied by subtracting the value of each pixel that constitutes the DEM data produced in raster format (in DEM, this value is the height above sea level) from the value of the overlapping pixel in the other DEM in the time series (Figure 8-a). DEM differences were removed from the second flight based on the first flight data (Figure 8-b). The study area boundaries were cut out from the difference DEM data produced. Then, the material cut volume and area were determined. To determine the volume and area, an add-on in the form of a toolbox is designed into the ArcGIS software ArcMap module using the Python programming language [22] (Figure 8-c). As shown in Figure 8-d from the Algorithm difference data produced, all pixels with positive difference values give the filling volume and area, and negative difference values give the cut volume and area. The algorithm records the volume and area information as a text file (with .txt extension) in the location defined as the workspace. In the text file, the lower (0 m) and upper limit (30 m) values were determined according to the field measurement results (Figure 8-e).

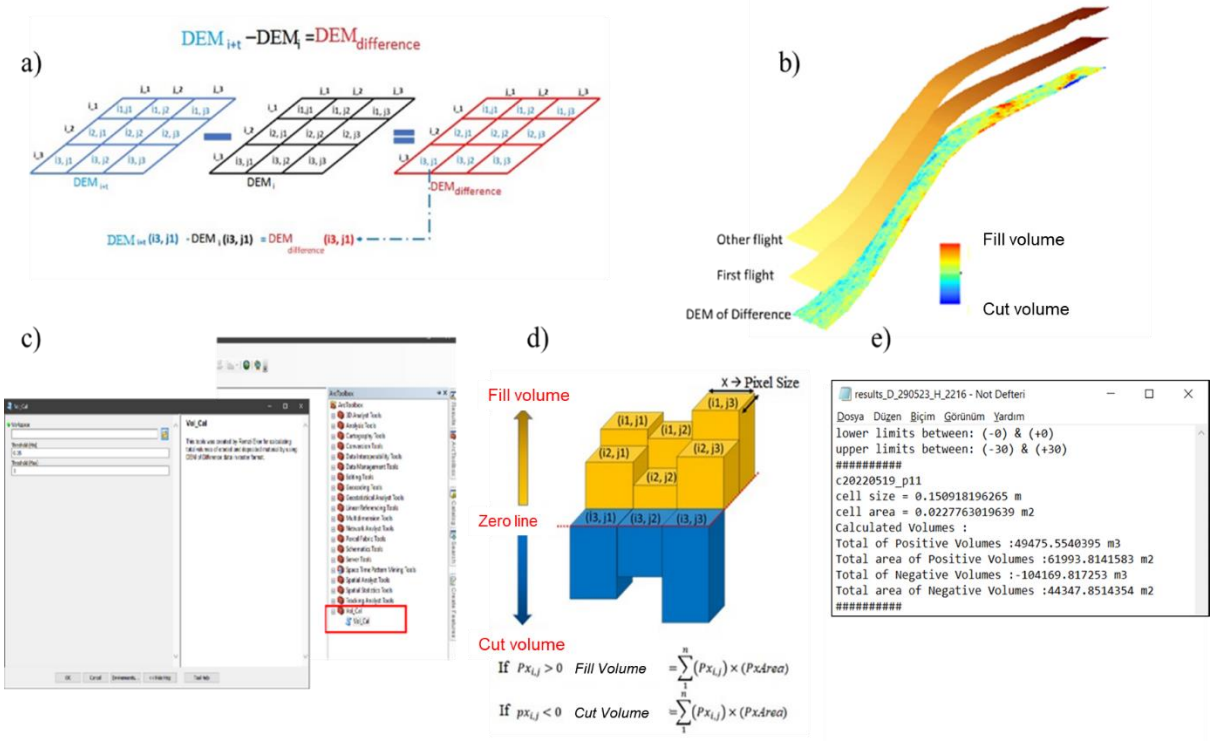

Figure 8. *Analyses for the determination of cut and fill volume*

III. RESULTS AND DISCUSSIONS

Photogrammetric products (orthophoto and DEM) that evaluate both horizontal (X and Y) and vertical (Z) position accuracy were created with the images obtained from PPK flights. When the location error estimates of all cameras in the orthophoto images created as a result of the PPK method were examined, the total average camera position error was found to be 47.41 cm before the balancing solution in the PPK method (GNSS), while it was calculated as 0.68 cm after the balancing solution.

According to the results calculated from the difference between the first flight and second flight data with the UAV; the excavation amount in the quarry is calculated as 104.170 m³ and the cut area is 44.348 m^2. Volumetric cut map is given in Figure 9 and areal cut classes map is given in Figure 10. There are a limited number of studies on determining the amount of material with UAV [6, 23, 24]. [25] They evaluated the soil pile volume measurements with UAV and found a volume of 38.56 m³ as a result of the study, and stated that the difference with the Total Station was 1.94 m³ (98.95% compatible). In his study [26], he compared UAV and Total Station volume data and found that the values found as a result of both methods were 99.33% compatible with each other in terms of precision. In addition, other studies [6, 21, 27, 28, 29] have examined the usability of UAV in determining cut and fill volumes in the construction of forest roads. In these studies, they stated that UAV technology is effective in forest road volume calculations and can be used to accurately calculate the cut and fill volume.

In another study [30], UAV and close range photogrammetry were used to determine soil losses on forest road excavation slopes in semi-arid mountainous areas, and the results of the two methods were found to be close to each other. [31, 32], in their studies, concluded that laser scanning and terrestrial photogrammetry methods can be used for volume calculations. When these studies are analysed; it is revealed that UAV systems can also be used in volume calculations. The use of UAV systems for open pit quarry operations will contribute in terms of fast access to data, accuracy and occupational safety. In UAV applications, it is very difficult or impossible to obtain positional information with RTK-CORS network in hard-to-reach areas such as quarries and mostly close to mountainous areas (forestry, national parks, etc.) [13]. Therefore, more precise and reliable results can be obtained with the UAV-PPK method without data loss.

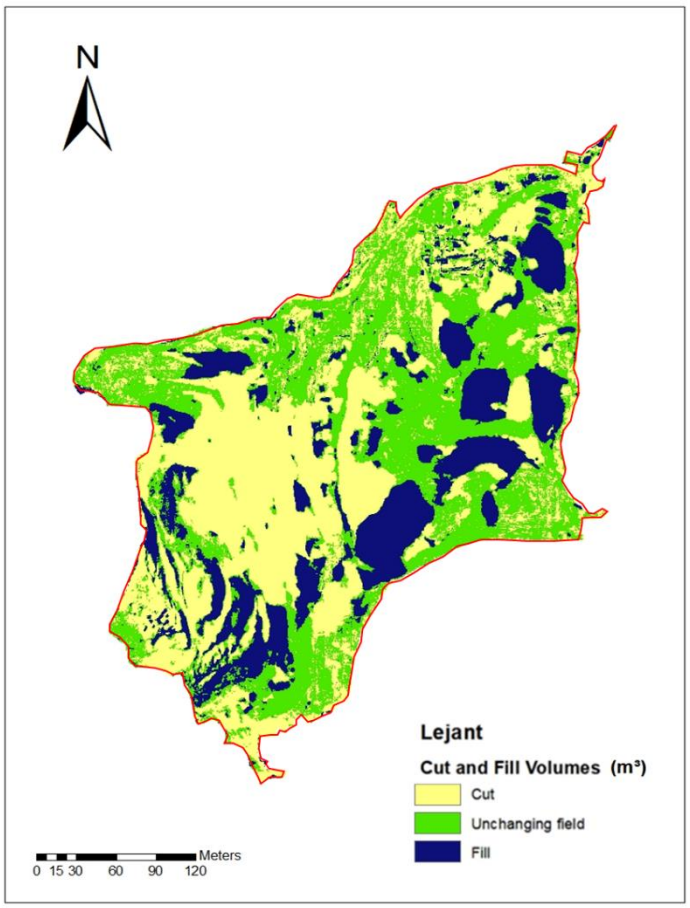

Figure 9. *Volumetric cut and fill map*

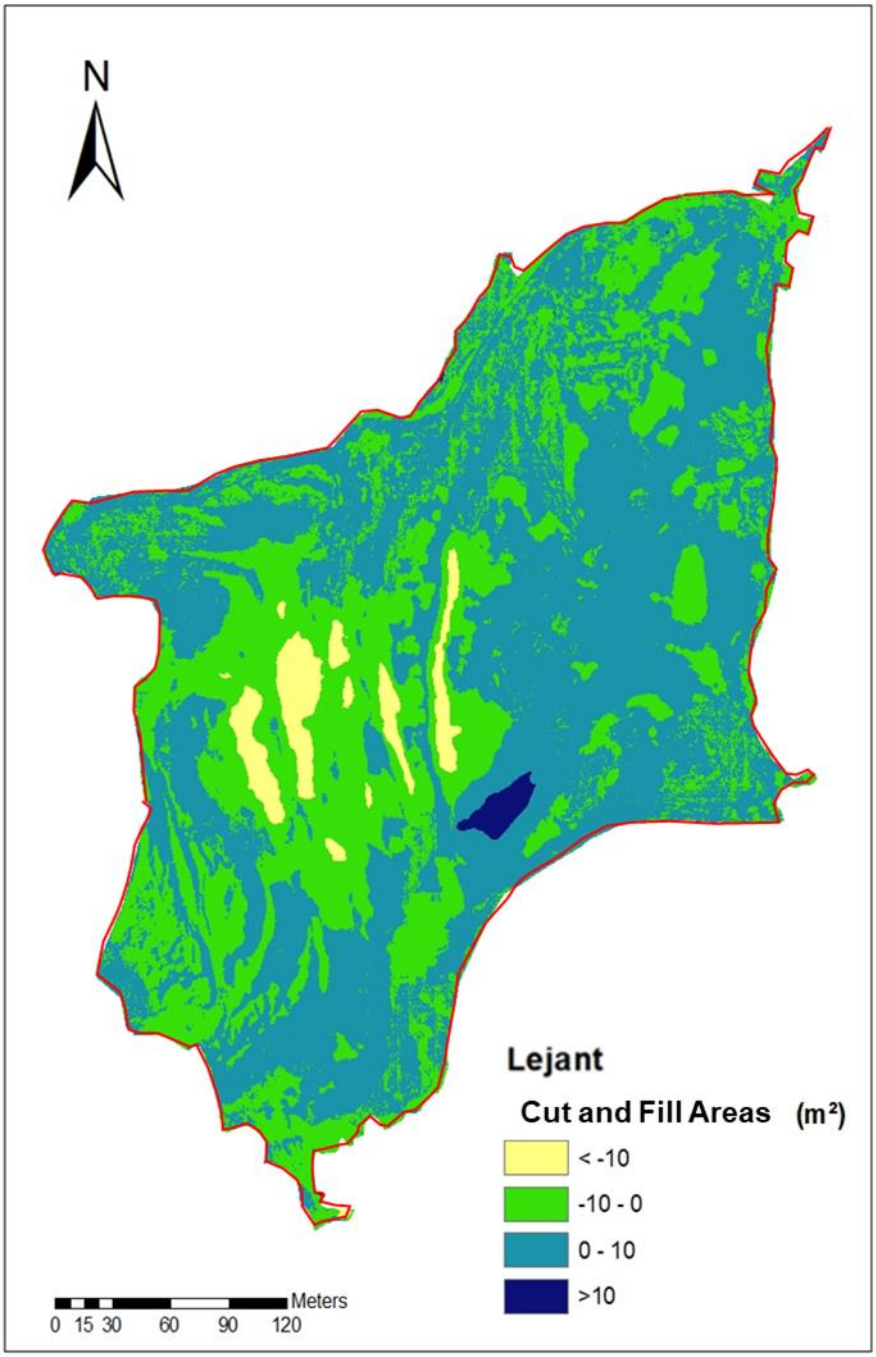

Figure 10. *Areal cut and fill classes map*

IV. CONCLUSION

In this study, the use of the UAV-based PPK method in monitoring ground change after cut in open-pit mining sites (quarries) was examined. The volume of material important for quarry operation was calculated, the cut amount was found to be 104.170 m^3 and the cut area was 44.348 m^2. The quarry operator's use of UAV also provides advantages in terms of workforce, occupational safety, time and controls. In addition, thanks to the flights made in shorter periods, how much material is produced between each flight and the total production will be calculated and border violations will be possible easily. Absolutely direct positioning method in UAV applications; The PPK method is more useful in

terms of positional accuracy in areas that are difficult to reach and mostly close to forested areas, such as quarries, and therefore it is appropriate to use it in such areas. The General Directorate of Forestry can also use UAVs to control permit-easement areas, thus providing significant advantages in terms of workforce, occupational safety, time and control. Since the calculations and controls to be made with UAV are easier and faster than traditional methods, permit areas can be checked more frequently in shorter periods and make it easier to determine the amount of material produced. In addition, the use of the PPK method in studies carried out with UAV allows more precise results to be obtained.

ACKNOWLEDGEMENTS: Authors thank the editor and the anonymous reviewers for their constructive comments that helped us improve the manuscript.

Data Availability The entire dataset was presented in the manuscript.

Declarations

Ethical approval This article does not contain any studies with human participants or animals.

Conflict of interest The authors declare no competing interests.

V. REFERENCES

[1] E.S. Festin, M. Tigabu, M.N. Chileshe, S. Syampungani and P.C. Ode´n, "Progresses in restoration of post-mining landscape in Africa," *J. For. Res*., vol. 30, pp. 381–396, 2019.

[2] A. Kabadayı and M. Uysal, "Extractıon of buıldıngs from data obtaıned by unmanned aerıal vehıcle," *Turkish Journal of Unmanned Aerial Vehicles*, vol. 1, no. 1, pp. 08–14, 2019.

[3] A.C. Watts, V.G. Ambrosia and E.A. Hinkley, "Unmanned aircraft systems in remote sensing and scientific research: classification and considerations of use," *Remote Sensing*, vol. 4, no. 6, pp. 1671–1692, 2012.

[4] M. Akgül, H. Yurtseven, M. Demir, A.E. Akay, S. Gülci and T. Öztürk, "Usage opportunities of generating digital elevation model with unmanned aerial vehicles on forestry," *Journal of The Faculty of Forestry Istanbul University*, vol. 66, no. 1, pp. 104–118, 2016.

[5] E. Tercan, "Use of unmanned aerial vehicles in roadway measurements: Okurcalar city center example," *Nigde Ömer Halisdemir University Journal of Engineering Sciences*, vol. 7, no. 2, pp. 649–660, 2018.

[6] E. Buğday, "Capabilities of using UAVs in forest road construction activities," *European Journal of Forest Engineering*, vol. 4, no. 2, pp. 56–62, 2018.

[7] I. Colomina and P. Molina, "Unmanned aerial systems for photogrammetry and remote sensing: A review," *Journal of Photogrammetry and Remote Sensing*, vol. 92, pp. 79–97, 2014.

[8] S. Gülci, H. Yurtseven and M. Akgül, "Assessment of pre-flight block plannıng for lowcost unmanned air vehicles," *Turkish Journal of Forest Science*, vol. 5, no. 1, pp.114–126, 2021.

[9] K. Shervais. (2023, July 27). *Structure from motion: introductory guide* [Online]. Available: https://www.unavco.org/education/resources/educational-resources/lesson/field-geodesy/module-materials/sfm-intro-guide.pdf

[10] L. Wallace, A. Lucieer, Z. Malenovský, D. Turner and P. Vopěnka, "Assessment of forest structure using two UAV techniques: A comparison of airborne laser scanning and structure from motion (SfM) point clouds," *Forests*, vol. 7, no. 3, pp. 1–16, 2016.

[11] M. Rehak, R. Mabillard and J. Skaloud, "A microUAV with the capability of direct georeferencing. *The International Archives of the Photogrammetry Remote Sensing and Spatial Information Sciences*, vol. 40, no. 1, pp. 317–323, 2013.

[12] Y. Taddia, F. Stecchi, A. Pellegrinelli, "Coastal mapping using DJI phantom 4 RTK in post-processing kinematic mode," *Drones*, vol. 4, no. 2, pp. 1–19, 2020.

[13] R. Eker, E. Alkan and A. Aydın, "A comparative analysis of uav-rtk and uav-ppk methods in mapping different surface types," *European Journal of Forest Engineering*, vol. 7, no. 1, pp. 12–25, 2021.

[14] K.H. McGhee, *Automated pavement distress collection techniques*, vol. 334, Washington, USA, 2004, pp. 1–85.

[15] MEUCC, "Ministry of Environment, Urbanisation and Climate Change, project to facilitate the implementation of the identification and mitigation of air pollution from industry, mining activities," Sectoral Application, Dokuz Eylül University, İzmir, Türkiye, Jan. 1, 2020.

[16] BRDF, "Permit Easement Branch Office Report," Bolu Regional Directorate of Forestry, Bolu, Türkiye, May. 26, 2024.

[17] GDF, "Tatlıdere Forest Management Chiefdom Functional Forest Management Report," General Directorate of Forestry, Düzce, Türkiye, Dec. 12, 2018.

[18] DJI. (2022, Februbary 20). *DJI Phantom 4 Introduction* [Online]. Available: https://providyo.com/dji-p4-multispectral

[19] G. Lindner, K. Schraml, R. Mansberger and J. Hübl, "UAV monitoring and documentation of a large landslide," *Applied Geomatics*, vol. 8, no. 1, pp. 1–11, 2016.

[20] R. Eker, A. Aydın and J. Hübl, "Unmanned aerial vehicle (UAV)-based monitoring of a landslide: Gallenzerkogel landslide (Ybbs-Lower Austria) case study," *Environmental Monitoring And Assessment*, vol. 190, pp. 1–14, 2018.

[21] AGISOFT. (2023, May 27). *Agisoft metashape user manual: professional edition, version 1.7* [Online]. Available: https://www.agisoft.com/pdf/metashape_1_7_en.pdf

[22] Y. Türk, H. Canyurt, E. Remzi and A. Aydın, "Determination of forest road cut and fill volumes by using unmanned aerial vehicle: A case study in the Bolu-Taşlıyayla," *Turkish Journal of Forestry Research*, vol. 9, no. special issue, pp. 97–104, 2022.

[23] M. Akgül, H.Yurtseven, S. Akburak, M. Demir, H.K. Cigizooğlu, T. Öztürk, M. Ekşi and A.O. Akay, "Short term monitoring of forest road pavement degradation using terrestrial laser scanning," *Measurement*, vol. 103, pp. 283–293, 2017.

[24] W. Anurogo, M.Z. Lubis, H. Khoirunnisa, D.S.P.A. Hanafi, F. Rizki, G. Surya and N.A. Dewanti, "A simple aerial photogrammetric mapping system overview and image acquisition using unmanned aerial vehicles (UAVs)," *Geospatial Information*, vol. 1, no. 1, pp.11–18, 2017.

[25] S. Gülci and G. Kılınç, "Assessment of drone-assısted soıl stockpile volume measurement,"

presented at International Academic Research Congress, 2018, Antalya, Türkiye, 2018.

[26] A. Ulvi, "Analysis of the utility of the unmanned aerıal vehıcle (UAV) in volume calculation by using photogrammetric techniques," *International Journal of Engineering and Geosciences*, vol. 3, no. 2, 43–49, 2018.

[27] M.G. Ciritcioğlu and E. Buğday, "Assessment of unmanned aerial vehicle use opportunities in forest road project (Düzce Sample)," *Journal of Bartın Faculty of Forestry*, vol. 24, no. 2, pp. 247–257, 2022.

[28] M. Kınalı and E. Çalışkan, "Use of unmanned aerial vehicles in forest road projects," *Journal of Bartın Faculty of Forestry*, vol. 24, no. 3, pp. 530–541, 2022.

[29] H. Hasegawa, A.A. Sujaswara, T. Kanemoto and K. Tsubota, "Possibilities of using UAV for estimating earthwork volumes during process of repairing a small-scale forest road, case study from Kyoto Prefecture, Japan," *Forests*, vol. 14, no. 4, pp. 1–11, 2023.

[30] Y. Türk, V. Özçelik and E. Akduman, "Capabilities of using UAVs and close range photogrammetry to determine short-term soil losses in forest road cut slopes in semi-arid mountainous areas," *Environ. Monit. Assess*., vol., 196, pp. 1–18, 2024.

[31] R. Eker, "Comparative use of PPK-integrated close-range terrestrial photogrammetry and a handheld mobile laser scanner in the measurement of forest road surface deformation", *Measurement*, vol., 206, pp. 1–12, 2023.

[32] M. Yakar, H.M. Yılmaz and H.M. Mutluoğlu, "Using Laser Scanning and Local Photogrammetry in Volume Calculations," presented at 12th Turkish Map Scientific and Technical Congress, Ankara, 2009.

Düzce University
Journal of Science & Technology

Review Article

Developing Countries' Challenges in Cultivating Salt-Tolerant Fodder Peas for Animal Feed

Nilay KAYIN [a,*], Alev AKPINAR BORAZAN [b], Ferzat TURAN [c]

[a] *Bilecik Seyh Edebali University, Graduate School of Education, Department of Biotechnology, Bilecik, TÜRKİYE*
[b] *Bilecik Şeyh Edebali University, Faculty of Engineering, Department of Chemical Engineering, Bilecik, TÜRKİYE*
[c] *Sakarya University of Applied Sciences, Faculty of Agriculture, Department of Field Crops, Sakarya, TÜRKİYE*
** Corresponding author's e-mail address: nilay.kayin@bilecik.edu.tr*
DOI: 10.29130/dubited.1532300

ABSTRACT

As a result of the rapid increase in the world population, the problem of balanced and adequate nutrition has emerged, and the importance of animal production has increased even more. In this respect, to ensure sufficient and balanced nutrition of existing animals, there is a need to increase the cultivation areas of fodder crops and proper management of pastures and breeding studies. For this reason, fodder pea (*Pisum sativum* L.), which has high nutritional value and is preferred for animal consumption, is a vital fodder plant to meet this need. Fodder peas are suitable for consumption as animal feed because they contain high levels of carbohydrates and digestible substances. However, salinity, one of the abiotic stress factors, is an essential problem for fodder peas. Salinity significantly limits the development of the plant and leads to yield losses. Although the consequences of climate change vary in many parts of the world, it is predicted that the frequency and severity of conditions such as decreased precipitation, increased temperatures, floods, droughts, and increased saline areas will increase with climate change in developing countries. In addition, salt stress also affects the photosynthetic mechanism in plants and causes changes in chlorophyll, carotenoid, phenolic, and antioxidant concentrations. Since the reclamation of saline farmland is expensive and complex, it is more appropriate to grow salinity-resistant plants. Therefore, gene studies to improve the salinity tolerance of plants have gained momentum in recent years. In this review, studies conducted in the last 20 years are discussed. Salt tolerance in gene-transferred and non-transferred peas, as well as plant growth in a saline environment, were assessed by comparing proline, chlorophyll, total phenolic, and antioxidant levels. In summary, this study seeks to highlight the issues of drought, aridity, and salinity, all of which are expected to worsen as climate change progresses.

Keywords: *Abiotic stress, Secondary metabolite, Salinity, Fodder pea*

Gelişmekte Olan Ülkelerin Hayvan Beslenmesinde Tuza Toleranslı Yem Bezelyesi Yetiştirmede Karşılaştıkları Zorluklar

ÖZ

Dünya nüfusunun hızla artması sonucu dengeli ve yeterli beslenme sorunu ortaya çıkmış ve bu noktada hayvansal üretimin önemi daha da artmıştır. Bu açıdan mevcut hayvanların yeterli ve dengeli beslenmeleri için meraların doğru yönetimi ve ıslah çalışmalarının yanında yem bitkileri ekim alanlarının artırılmasına da ihtiyaç vardır. Bu nedenle beslenme değeri yüksek ve hayvanlar tarafından tüketimi tercih edilen yem bezelyesi (*Pisum sativum* L.) bu ihtiyacı gidermek için önemli bir yem bitkisidir. Yem bezelyesi, yüksek düzeyde karbonhidrat ve sindirilebilir

Received: 30/07/2024, Revised: 12/11/2024, Accepted: 12/11/2024

maddeler içermesi nedeniyle hayvan yemi olarak tüketime uygundur. Fakat yem bezelyesi için abiyotik stres faktörlerinden tuzluluk, önemli bir problemdir. Tuzluluk, bitkinin gelişimini önemli ölçüde sınırlamakta ve verim kayıplarına yol açmaktadır. İklim değişikliğinin ortaya çıkaracağı sonuçlar dünyanın birçok yerinde farklılık göstermekle birlikte, gelişmekte olan ülkelerde de, iklim değişikliği ile birlikte, yağışların azalacağı, sıcaklıkların artacağı, sel, kuraklık, tuzlu alanların artışı gibi durumların sıklığının ve şiddetinin artacağı tahmin edilmektedir. Ayrıca tuz stresi bitkilerde fotosentetik mekanizmayı da etkileyerek klorofil, karotenoid, fenolik ve antioksidan konsantrasyonunda da değişikliğe sebep olmaktadır. Tuzlu tarım arazilerinin ıslahı pahalı ve zor olduğu için tuzluluğa dayanıklı bitkilerin yetiştirilmesi daha uygundur. Bu nedenle, son yıllarda bitkilerin tuzluluk toleranslarını geliştirmeye yönelik gen çalışmaları hız kazanmıştır. Bu derlemede, son 20 yıldır yapılan çalışmalar ele alınmıştır. Gen aktarılmış bezelyeler ve aktarılmamış bezelyelerin tuz toleransı, bitkilerin tuzlu ortamda gelişimleri prolin, klorofil, toplam fenolik ve antioksidan madde içeriği kıyaslanarak değerlendirilmiştir. Özet olarak, özellikle iklim değişikliği ile birlikte artacağı öngörülen kuraklık, çoraklık ve tuzluluk problemlerini ortaya koyulması amaçlanmaktadır. Böylece, yem bezelyesinin yetiştirilme alanlarının artırılması ve kaba yem ihtiyacı giderilmesi ve marjinal alanların üretimine kazandırılması konusuna ışık tutacaktır.

Anahtar Kelimeler: *Abiyotik stres, Sekonder metabolit, Tuzluluk, Yem bezelyesi*

I. INTRODUCTION

As a result of the rapid increase in the world population, the problem of balanced and adequate nutrition has emerged, which has further increased the importance of agricultural land and animal production. The development of people's eating habits and the continuous progress in the direction of health and safety have led to an increase in the global demand for food products of animal origin, including meat, eggs and milk [1]. These demands and challenges have further increased the importance of the forage crops market for farmers, especially to produce better quality animal products and improve animal productivity [2]. In addition, the importance of food safety has increased as a result of the "Mad Cow Disease" in Europe in 1989, the "*Salmonella*" cases in the USA in 1993 and 2008, and the "Tainted Milk Powder" incident in China in 2008. These events have also increased awareness of animal production. [1]. Forage crop agriculture is the most important way of producing continuous and safe forage. Quality roughage has a special place in ruminant nutrition. In animal nutrition, quality roughages should be a must for being an economic source, rich in protein, cellulose, fat, vitamins and minerals, increasing meat and milk yield, preventing metabolic diseases related to feeding and obtaining high quality animal products [3], [4]. Livestock breeding is also very important for the development of developing countries, increasing export potential, supplying raw materials to industry, preventing unemployment in rural areas and providing new employment [5], [6], [7], [8]. In addition, it is the best insurance against drought, famine and other natural disasters [5].

In countries with developed livestock breeding, the proportion of forage crops cultivated constitutes 25% of the total agricultural land in the UK, 30% in Italy, 31% in the Netherlands, 36% in Germany, 71% in Brazil and 13% in Turkey [9], [10], [11]. According to FAO and national statistical sources, there are approximately 137 million hectares of forage crop cultivated area in Latin America and the Caribbean region, followed by 12 million hectares in South and Southeast Asia, 6.5 million hectares in Central-West Asia and North Africa, and 14.6 hectares in Turkey [10], [12], [13].

Among fodder crops, fodder pea *Pisum sativum* L. is a legume rich in protein, vitamins, minerals and bioactive compounds used for both human and animal nutrition [14], [15]. The country with the highest production in the world is Canada, followed by China, Russia and India [15].

When the growing conditions of forage crops are evaluated, biotic and abiotic stress factors significantly limit plant growth and cause great yield losses in agriculture [16], [17]. Especially abiotic stress factors prevent the survival of plants. Due to global climate change, the majority of agricultural land is exposed to stress conditions and abiotic stress reduces agricultural yields by up to 60% [18], [19], [20]. Among abiotic stressors, salinity is the primary factor that will directly affect crop yields today and in the future [16], [21], [22], [23]. Today, more than 6% of the world's land area and 20% of the world's irrigated

land is affected by salinity. Even in well-watered soils, salinity causes water deficit by reducing the osmotic potential of solutes in the soil, thus making it difficult for roots to draw water from the surrounding environment (soil solution) [24], [25]. According to the Food and Agriculture Organization of the United Nations (FAO, 2018), the area of saline soils in the world continues to increase steadily, suggesting that 50% will face salinity problems by 2050 [14], [21], [26].

The objective of this paper is to review and evaluate the current evidence on the extent of forage crops and forage peas cultivated in the world and the abiotic stressors of salt stress. This study is organized in 2 parts; (i) to determine the current area and production characteristics of forage crops cultivated in the world and (ii) to determine the extent of *Pisum sativum* L., a globally important forage crop, and to review the available evidence on salt stress in forage crops, especially forage peas. Our geographical focus covers all of Latin America and the Caribbean except the southern cone countries of South America (Argentina, Chile, Paraguay and Uruguay), developing countries in Asia except China, Mongolia and North Korea, Africa and Turkey.

II. FEED PLANTS

Livestock production is socioeconomically very important for developing countries and the continuous increase in per capita income leads to an increase in the demand for livestock products [27]. At this point, since feed production is of primary importance for livestock/poultry productivity, it is very important to examine agricultural production for developing countries [28]. At this point, when forage crop cultivation is evaluated, forage crops in developing countries include many species. These include tropical grasses such as *Brachiaria spp.* and *Panicum maximum* as well as legumes such as *Stylosanthes spp*., *Leucaena leucocephala* and *Vigna unguiculata*. *Brachiaria spp.* of African origin is the most widely cultivated forage species and accounts for a significant proportion of the area in Latin America. *Trifolium alexandrinum* is the dominant species in Egypt and *Medicago sativa* is widely used in North Africa. Today, more than 600 grass species are used for grazing and animal feeding [10].

In Brazil, 80 percent of cultivated pastures (80 million hectares) are covered by *Brachiaria spp.* and it is estimated that *B. brizantha cv. marandu* alone covers 40 million hectares. *Brachiaria spp.* are native to East and Central Africa, where they are an important component of the pioneer species of open grasslands (*B. decumbens*), humid savannas (*B. humidicola*), stream banks (*B. mutica*) and cleared rainforests (*B. ruziziensis*) [29], [30].

African grasslands represent the most important source of genetic material for grasses such as *Brachiaria*, *Pennisetum* and *Panicum*, while Latin America represents the most important source of genetic material for forage legumes and shrubs such as *Stylosanthes spp., Arachis pintoi, Leucaena leucocephala, Gliricidia sepium* and *Cratylia argentea* [30].

Annual clovers (*Medicago spp*.) and subterranean clover (*Trifolium subterraneum*) from the Mediterranean basin are common in Mediterranean-type climate zones such as South Africa. Several tropical pasture grasses grown on a fairly large scale are propagated vegetatively, usually in areas with reliable rainfall. These are usually stoloniferous and the most important are Giant Star Grass *Cynodon aethiopicus, Cynodon nlemfuensis*, Pangola Grass *Digitaria eriantha subsp. pentzii*, formerly *D. decumbens* and *Pará Grass Brachiaria mutica*. These African grasses have been widely used in Latin America for many years [30], [31].

Forage cereals include oats (*Avena sativa* and *A. strigosa*), maize (*Zea mays*), sorghum (*Sorghum bicolor*), pearl millet (*Pennisetum americanum*), barley (*Hordeum sativum*), rye (*Secale cereale*), proso millet (*Panicum miliaceum*) and finger millet (*Eleusine coracana*). *Saccharum officinarum* is also used as feed. Federizzi and Mundstock (2004) reported that in 2003, more than two million hectares of fodder oats were grown in Argentina and Uruguay and more than three million hectares in Brazil [30].

Table 1. *Fodder crop varieties and cultivation areas in developing countries according to the International Agricultural Research Advisory Group [3], [10].*

Country or region	Feed types	Cultivation areas between 2010-2015 (hectares)
Brazil	*Brachiaria spp.*	5.000
Andean Countries	*Brachiaria spp.*	3.357
Central America	*Brachiaria spp.*	1.560
India	*Stylosanthes*	250
Thailand	*Stylosanthes*	300
West Africa	*Stylosanthes*	36
West Africa	*Vigna ungiculata*	1.615
East Africa	*Calliandra spp.*	186
Turkey	*Pisum sativum spp.*	24.319
Turkey	*Medicago sativa*	662.888

In Turkey, *Medicago sativa* has the highest share in the cultivation area with 662,888 hectares. In Thailand and India, *Stylosanthes* cultivation areas are 300 and 250 hectares, respectively. *Brachiaria spp.* in Central America and *Vigna ungiculata* in West Africa have an area of 1,560 and 1,615 hectares, respectively (Table 1).

Forage crops are generally divided into two groups as cool season wheatgrass and cool season legume forage crops according to their climate requirements (Table 2).

Table 2. *Cool season wheatgrass and legume forage crops [32], [33].*

Cool Season Forage Crops	
Wheatgrass Group	Legume Group
Lolium perenne L.	*Vicia pannonica* L.
Lolium multiflorum L.	*Lotus corniculatus* L.
Phalaris aquatica L.	*Lotus pedunculatus* L.
Cynodon dactylon	
Agropyron elongatum L.	*Lathyrus saivus* L.
Bromus inermis L.	*Pisum sativum* L.
Dactylis glomerata L.	*Trifolium alexandrinum* L.
Festuca arundinacea L.	*Trifolium meneghinianum* L.
Elytrigia elongata	*Trifolium resupinatum* L.
Puccinellia ciliata	*Medicago* sp.

Cool season forage crops are generally resistant to hot and arid climates. Especially *Agropyron elongatum* L. and *Festuca arundinacea* L. have high salt tolerance. In addition, *Festuca arundinacea* L. has a high tolerance to extreme temperatures.

Cool season legume forage crops are also very cold tolerant. *Vicia pannonica* L. can withstand temperatures down to -16°C, especially in conditions without snow cover. *Lathyrus saivus* L. and *Trifolium meneghinianum* L. are among the most drought tolerant forage crops. At the same time, *Trifolium meneghinianum* L. and *Lotus corniculatus* L. have high salt tolerance while *Pisum sativum* L. has low salt tolerance [32].

A summary of forage plant researches and analyses on protein sources, which is one of the most important nutrients in animal nutrition, is presented in Table 3.

Table 3. *Some nutritional value ratios of some forage crops (%)*

Forage crops	**Nutrient content**	**Rate (%)**	**Reference**
Medicago sativa	Protein	8.034-8.042	[34]
	Fiber	5.883	
Medicago sativa	Protein	32	[35]
Medicago sativa	Protein	8,7-13,9	[36]
	NDF	39,6-54,3	
	ADF	30,6-41,8	
Trifolium alexandrinum L.	Protein	3.102-3.105	[34]
	Fiber	4.867	
Avena sativa L.	Protein	4.114-4.116	[34]
	Fiber	12.35	
Zea mays L.	Protein	5.13-5.19	[34]
	Fiber	4.867	
Zea mays L.	Protein	6.5-6.9	[37]
	NDF	49.1-50.0	
	ADF	29.4-29.6	
Sorgum L.	Protein	3.90-5.64	[38]
Lolium perenne	Protein	6-34	[35]
	NDF	34-62	
	ADF	4-42	
	Dry matter	11-37	
Lolium multiflorum	Protein	6-28	[35]
	ADF	2-35	
Trifolium repens	Protein	32	[35]
Agropyron cristatum	Protein	8-36	[35]
Leucaena leucocephala	Dry matter	24-93	[35]
Panicum maximum	Dry matter	22-91	[35]

Table 3 (cont). *Some nutritional value ratios of some forage crops (%)*

Cynodon nlemfuensis	Dry matter	97	[35]
Pisum sativum L.	Protein	17.6-21.2	[39]
Pisum sativum L.	Protein	17.73-27.17	[40]
Pisum sativum L.	Protein	16.25-18.69	[41]
	NDF	38.40-42.82	
	ADF	28.5	
Pisum sativum L.	Protein	16,8-19,9	[42]
	NDF	38,6-42,8	
	ADF	29,0-34,4	
Pisum sativum L.	Protein	18,1-23,9	[43]
	NDF	33,2-38,3	
	ADF	27,9-30,2	
Vicia sativa L.	Protein	8.1-12.4	[44]
	NDF	42.0-51.4	
	ADF	29.5-37.3	
Vicia sativa L.	Protein	5.1-15.4	[45]
	NDF	37.4-48.1	
	ADF	28,1-31.2	

In order to reveal the nutritive value of fodder plants, the protein ratio of *Medicago sativa* is 8-32%, Lolium perenne 6-34%, *Agropyron cristatum* 8-36%. The protein ratio of *Pisum sativum* L. varies between 16-27% (Table 3). When these ratios are evaluated, *Pisum sativum* L. fodder peas show less variation in protein ratio in different growing areas. This situation makes fodder peas valuable in terms of nutrition.

A. FORAGE PEA (*Pisum sativum L.)*

Our geographical focus covers all of Latin America and the Caribbean except the southern cone countries of South America (Argentina, Chile, Paraguay and Uruguay), developing countries in Asia except China, Mongolia and North Korea, Africa and Turkey.

Pisum sativum L. is one of the important grain legume crops grown worldwide. In many developing countries such as Latin America, Africa and Turkey, it is also used for feeding ruminants in the form of fresh feed, feed dry matter, feed meal, silage and hay [46]. Legumes account for about 30% of the world's agricultural production. Legume residues provide soil organic matter balance. In years of

irregular rainfall distribution (temperate climates) or rainfall deficiency (Southern European climatic conditions), when mineral nitrogen uptake is poor, legumes have a particularly positive effect on the soil. The decomposition of *Fabaceae* plant residues in soil provides forms of nitrogen to both successional plants and soil microorganisms through biological nitrogen sorption [47], [48]. Accordingly, the "European Green Deal" policy aims to reduce fertilizer consumption by at least 20% by 2030 while maintaining soil fertility. In order to achieve these targets, peas are important for providing nitrogen to the soil in the process of nitrogen fixation. Increasing pea cultivation will reduce the use of nitrogen from mineral fertilizers and maximize biological nitrogen use [49].

In addition, the inclusion of legumes in crop rotation has an important place in global agriculture as it contributes to the reduction of weed, pest and disease populations [47], [48]. When cereals and legumes are grown in rotation, they increase soil fertility by altering physical and chemical properties and counteracting soil erosion. Thanks to the well-developed root systems of legumes, they also provide soil aeration. Another important feature of legumes is that they positively affect sustainable agriculture by eliminating the need for fertilizer by binding atmospheric nitrogen to the soil as a result of symbiotic effect with *Rhizobium* spp. bacteria [48]. Pea, one of the most important plants in the *Fabaceae* family, has a protein content of 21-32%. It is rich in lysine, an essential amino acid important for nutrition, and low in sulfur-containing amino acids. It also has low allergenicity [47], [48].

Forage pea (*Pisum sativum* L.) is one of the high quality forage resources from the legume forage crops group. In terms of nutrient composition, forage peas contain proportionally higher crude protein (21-25%), starch from carbohydrates and dietary fiber from digestible substances (86-87%) than other roughages and have high antioxidant activity [4], [44], [47], [50], [51]. Forage peas, which are important in terms of containing essential amino acids, are used in the nutrition of slaughter, dairy and laying animals without affecting production and fattening performance. In many countries of the world, forage pea cultivation is given importance in terms of replacing high-cost soybean meal in terms of protein value [39], [47], [48]. For this reason, forage pea (*Pisum sativum* L.), which has high nutritional value and is preferred for consumption by animals, is an important fodder plant in terms of closing the roughage deficit. Fodder pea, whose grains, green and dry grass are used as forage plant, is preferred both as a pasture plant and as a green fertilizer plant [14], [32], [52]. In addition, forage peas grown as silage for animal nutrition have high nutritional value and taste preferred by animals [53]. In addition to minerals such as phosphorus and calcium, it also contains vitamins A and D [50], [52], [54]. In addition to these advantages, since it is affected by biotic-abiotic stress conditions, the cultivation rate is relatively low [48].

III. SALT STRESS

Agricultural areas in developing countries face salt stress [24]. For example, in Turkey, 32 million hectares of the approximately 1.5 million hectares of agricultural land are under salinity stress. Of the 230 million hectares of irrigated land, 45 million hectares are affected by salt stress. Salt problems of this magnitude are thought to cause great economic losses in parallel with the loss in crop yield and quality [22], [55]. Salinity occurs naturally in arid and semi-arid climatic zones, and insufficient rainfall and high evaporation, poor drainage, improper agricultural practices and soil characteristics increase the salinity problem [26], [56], [57]. When salt tolerance is evaluated in terms of forage crops, they are classified as partially sensitive, partially resistant and resistant to salinity (Table 4).

Table 4. *Classification of forage crops in terms of salinity tolerance [19].*

Partially Sensitive to Salinity	**Partially Resistant to Salinity**	**Resistant to Salinity**
Medicago sativa	*Lolium perenne* L.	*Agropyron cristatum*
Vicia sativa	*Lolium multiflorum* L.	*Elymus junceus*
Pisum sativum L.	*Sorghum*	*Cynodon dactylon*
Trifolium repens	*Agropyron intermedium*	*Agropyron elongatum*
Trifolium pratense	*Lotus corniculatus*	
Phleum pratense	*Melilotus albus*	
Trifolium alexandrinum	*Melilotus officinalis*	
Zea mays		

Salinity is one of the most serious environmental factors limiting the productivity of forage crops due to the high concentrations of salinity-sensitive Agricultural plants show a range of responses to salt stress. Salinity reduces the agricultural production of most crops and also affects the physicochemical properties of the soil and the ecology-based balance of the region. Average yields for all major crops are only one-quarter to one-half of record yields; some of these losses are due to soil salinity [58].

High salinity causes both ionic and osmotic stresses, leading to secondary stresses such as oxidative stress and nutritional disorders. Furthermore, with increasing salt concentration in the soil, plant water uptake becomes difficult and plant growth slows down due to deterioration of soil structure [19], [22]. Orcan and Orcan (2024) examined the effect of different types of salts on *Oryza sativa* L. plant. Plant seeds were exposed to different concentrations of NaCl, $CaCl_2$ and $MgCl_2$ salts (0, 30 mM, 90 mM) in hormone-free and salt-free MS medium. As a result, a reduction in nutrients was observed for all three salt types [59]. Nedjimi et al. (2020) determined the salinity tolerance index of different salts (NaCl, Na_2SO_4, $CaCl_2$ and $MgCl_2$) on *M. vulgare* plants at four salinity levels (0, 50, 100 and 150 mM) as Na2SO4 < MgCl2 < CaCl2 < NaCl [60].

Exposure of plants to high salt conditions results in changes in gene expression and transcription factors. These genes and transcription factors are grouped as follows: (I) ion transport or homeostasis (e.g. *SOS*, *NHX1*, *HKT1* and *H+- ATPase* genes), (II) senescence-related genes (e.g. *SAG*), (III) molecular chaperone proteins (e.g. *HSP*) and (IV) dehydration-related genes (e.g. *DREB*). The expression of these genes increases or decreases according to stress conditions [22], [61], [62].

Krasensky and Jonak (2012) examined the expression patterns of stress-related genes under drought, high temperature and salinity conditions. They stated that changes in the expression of genes involved in plant signaling associated with environmental stresses such as salicylic acid, jasmonic acid, abscisic acid and calcium ion at initial, final and intermediate times provide information about the growth status of a plant under stress. Research on the expression information of a gene in different tissues under different environmental conditions and developmental stages reveals that it provides information about the growth status of a plant under stress at the molecular level [63].

SOS (salt overly sensitive) gene contributes to the development of salt stress tolerance in plants by controlling the flow of Na^+ ion in the cytosol [26]. Liu et al. (2015) revealed that salt stress is also controlled with the increase in the expression of *SOS1* gene [64]. *SOS (Salt Overly Sensitive)* genes regulate the *SOS* signaling pathway and control the Na^+ and K^+ ion balance [65]. *SOS* signaling pathway is activated as a result of an increase in the amount of Na^+. In terms of molecular structure of *SOS* genes, *SOS3* gene encodes a calcium binding protein, *SOS2* gene encodes a serine/threonine protein kinase, *SOS1* gene encodes a plasma membrane Na^+ /H^+ antiporter. *SOS1*, *SOS2* and *SOS3* function linearly [61]. *SOS3* interacts with *SOS2* and activates it. *SOS2* and *SOS3* activate *SOS1* and control the expression level of *SOS1*. As a result, activation of *SOS1* ensures ion balance and salt tolerance under salinity conditions [66].

Dehydration-related gene products such as *LEA* (*late embryogenesis abundant*) and *DREB* (*dehydration response element binding*) also elicit a response to salt stress and regulate signal transduction, protecting cellular structures and promoting salt tolerance [67]. *LEA* proteins are located in the cytoplasm and protect cellular structures during stress. Under stress conditions, hydrophilic and soluble *LEA* proteins are expressed by *LEA* genes and bind water. In this way, they play a role in protecting cellular membrane and protein/enzyme structures from water deficiency during salt stress [66]. In addition, the expression of *DREB* genes also increased under abiotic stress conditions. The expression of genes such as *AtDREB1*, *DREB2A*, *DREB2B*, *AtDREB2A*, *OsDREB2A* also increases rapidly under high salinity conditions. The expression of a large number of genes during salt stress suggests that these genes can be used to develop salt tolerant plants [26], [66].

It has been revealed that the expression of *Osmyb4* gene isolated from *Oryza sativa* activates cold-induced promoters such as PAL2, ScD9, SAD and COR15a. As a result of overexpression of this gene, it is reported that more than 250 genes are activated, a significant portion of which are also associated with abiotic and biotic stress [17]. Aydın et al. (2014) obtained transgenic potato plants expressing *Osmyb4* gene in a study they conducted. It was revealed that these potato plants in which *Osmyb4* gene was transferred showed better development compared to those in which the gene was not transferred [68]. Vannini et al. (2006) showed that 50% of the *Arabidopsis* plants in which *Osmyb4* gene was transferred survived after 300 mM NaCl treatment, whereas *Arabidopsis* plants in which the gene was not transferred completely disappeared [69]. On the other hand, plants increase intracellular osmotic pressure by producing osmoregulatory proteins such as proline in their cells against the stress caused by high salt concentration. Because most of the eukaryotic cells cannot tolerate salts such as NaCl because they disrupt the structure of enzymes. In plants, in order to prevent this situation, the cell produces many osmoregulatory substances such as proline proteins that do not disrupt the structure of enzymes [23], [70], [71]. There are also different plant mechanisms against salt stress such as osmotic effect, ion excretion and tissue tolerance. Osmotic effect decreases the water availability of plants as a result of increased salt concentration in the soil. The ion excretion mechanism reduces the accumulation of toxic salt in the leaves. Tissue tolerance is the growth retardation observed in plants in the face of salt stress [19], [26], [56].

Salt stress negatively affects the photosynthetic mechanism, which is one of the most important metabolic processes in plants, causing stomatal closure and changes in chlorophyll structure [57], [72]. Taffouo et al. (2010) reported that the total chlorophyll concentration of tomato (*Lycopersicum esculentum* L.) leaves under salt stress decreased significantly [73]. Shahid et al. (2011) reported that chlorophyll content decreased in different pea genotypes under salt stress [74]. Taibi et al. (2016) revealed that photosynthetic pigments of *Phaseolus vulgaris* L. decreased in the face of increasing salt concentration [75]. Kaymak and Acar (2020) determined that the amount of chlorophyll a, chlorophyll b and carotenoid in the leaves of forest clover (*Bituminaria bituminosa* L.) decreased with increasing salt concentration [76]. Loudari et al. (2020) revealed a significant decrease in chlorophyll content of tomato plants (*Lycopersicum esculentum* L.) as a result of salt application [72].

Plants produce secondary metabolites as a defense mechanism against pathogens and insects. The formation of these metabolites is also possible under different environmental stress conditions (e.g. salinity) and it is this group of metabolites that constitutes the majority of plant antioxidants. Phenolic compounds are one of the secondary metabolites produced in plant tissues to scavenge free radicals and/or inhibit their production through hydroperoxide decomposition [16], [77]. Many studies have revealed that peroxidase and polyphenoloxidase enzymes involved in the synthesis of phenolic compounds increase under biotic and abiotic stress conditions [78]. Kıpçak et al. (2019) found that the total phenolic matter content in the green parts of bean genotypes treated with different concentrations of salt decreased significantly compared to control plants [79]. In addition, reactive oxygen species are formed in plants under oxidative stress in saline conditions. These reactive oxygen species cause serious problems in plants such as inactivation of proteins and enzymes, injury to plant metabolism, change in the structure of photosynthetic components, and lipid peroxidation [80]. Phenolic compounds neutralize these reactive oxygen species thanks to their antioxidant activities [79]. Boughalleb et al. (2020)

revealed that the total phenolic and antioxidant content of Polygonum equisetiforme plants under different salt concentrations increased especially up to 300 mM salt concentration [77].

Since reclamation of saline agricultural lands is expensive and difficult, it is more appropriate to grow salinity-tolerant plants to increase yields in these areas. Therefore, studies to improve the salinity tolerance of plants have gained momentum in recent years [14]. In this context, studies in the field of molecular biology, biotechnology and genetic engineering have increased in recent years to overcome yield problems in agricultural fields. The productivity achieved through classical breeding studies, especially in the agricultural field, cannot meet the food needs of the growing world population due to the limitations in arable land.

IV. CONCLUSION

Especially for developing countries, it is very important to increase forage crops cultivation areas with proper management of pastures and breeding studies in order to ensure adequate and balanced nutrition of existing animals. For this reason, the forage pea (*Pisum sativum* L.), which has high nutritional value and is preferred by animals, is an important fodder plant in animal nutrition. However, salinity is an important problem, especially for forage peas. Among abiotic stress factors, salinity is the primary factor that will directly affect crop yields today and in the future. As a result of exposure of plants to salt, changes in gene expression and transcription factors occur. With gene studies, salinity genes in the plant are found, characterized, isolated and transferred to the target cell to obtain transgenic plants. The aim here is to provide salinity tolerance as a deficiency in the plant. This also contributes to plant breeding methods. Today, crops are grown in this way on 3.7% of the world's agricultural land, and according to statistics from the International Service for the Acquisition of Agricultural Biotechnology Applications (ISAAA), global biotech crop coverage reaches 170.3 million hectares. Since 2014, transgenic crops have been grown in the US, Brazil, Argentina, India and Canada. This study shows that the usable agricultural areas can be increased in the future with the suggestions put forward by the researchers for the elimination of the salinity problem in feed crops, which is an important problem for livestock in developing countries.

V. REFERENCES

[1] W. Wang, Y. Liang, Z. Ru, H. Guo, and B. Zhao, " World forage import market: competitive structure and market forces," *Agriculture*, vol. 13, no. 9, pp. 1-18, 2023.

[2] Anonim. (2024, February 22). *Morgor Intelligence*. Forage Feed Market Trends: https://www.mordorintelligence.com/industry-reports/forage-feed-market/market-trends adresinden alındı.

[3] M. Tan, and H. Yolcu, "Current status of forage crops cultivation and strategies for the future in Turkey: a review," *Journal of Agricultural Sciences*, vol. 27, no. 2, pp. 114 - 121, 2021.

[4] Ö. Canbolat, K. C. Akbay, and A. Kamalak, " Possibilities of use of molasses as carbohydrate source in pea silages," *KSU Journal Of Agriculture and Nature,* vol. 22, no. 1, pp. 122-130, 2019.

[5] A. K. Verma, R. Singh, and P. Kumar, "Review on the role of animal husbandry in rural development," *Journal of Rural Advancement*, vol. 1, no. 1, pp. 62-69, 2012.

[6] Y. D. Saygı, and Ö. F. Alarslan, " Effects of roughage support practices on dairy cattle breeding in Yozgat region ," *Journal of Veterinary Medicine,* vol. 83, no. 2, ss. 25-35, 2012.

[7] E. Ateş, and A. S. Tekeli, " The effect of different based fertilizer applications on herbage yield and quality of fodder pea (*pisum arvense* L.), " *KSU Journal Nature Science,* vol. 20, pp. 13-16, 2017.

[8] O. Öztürk, C. Şen, and B. Aydın, " Comparative analysis of forage crops cultivation and pasture utilization habits of livestock enterprises," *Journal of Field Crops Central Research Institute,* vol. 28, no. 1, pp. 29-38, 2019.

[9] U. Özkan, " Comparative overview and evaluation of forage crops agriculture in Turkey," *Turkish Journal of Agricultural Engineering Research,* vol. 1, no. 1, pp. 29-43, 2020.

[10] K. Fuglie, M. Peters, and S. Burkart, "The extent and economic significance of cultivated forage crops in developing countries," *Frontiers in Sustainable Food Systems,* vol. 5, no. 712136, pp. 1-8, 2021.

[11] R. M. Simeao, D. D. Silva, F. C. Santos, L. Vilela, M. T. Silveira, A. C. Resende, and P. P. Albuquerque, "Adaptation and indication of forage crops for agricultural production in sandy soils in Western Bakia State, Brazil," *Acta Scientiarum Agronomy,* vol. 45, no. e56144, pp. 1-11, 2021.

[12] TÜİK. (2023, 05 20). *Crop production statistics*. Data Portal for Türkiye Statistics: https://biruni.tuik.gov.tr/medas/?locale=tr adresinden alındı

[13] E. Koçak, "A review of the current status of forage crops cultivation and evaluation in Türkiye," *Turkish Journal of Range and Forage Science,* vol. 4, no. 2, pp. 59-65, 2023.

[14] G. Demirkol, N. Yılmaz, and Ö. Önal Aşcı, "Effects of salt stress on germination and seedling development in selected genotypes of fodder pea (*pisum sativum ssp. arvense* L.)," *KSU Journal Of Agriculture and Nature,* vol. 22, no. 3, pp. 354-359, 2019.

[15] D. T. Wu, W. X. Li, J. W. Wan, Y. C. Hu, R. Y. Gan, and L. Zou, "A comprehensive review of pea *(pisum sativum* L.) : chemical composition, processing, health benefits, and food applications," *Foods,* vol. 12, no. 2527, pp. 1-40, 2023.

[16] A. A. Mohamed, and A. A. Aly, "Alterations of some secondary metabolites and enzymes activity by using exogenus antioxidant compound in onion plants grown under sea water stress," *American- Eurasion Journal of Scientific Research,* vol. 3, no. 2, pp. 139-146, 2008.

[17] G. Aydın, "Effect of *Osmyb4* gene expression on salinity tolerance of potato transformed with oryza sativa Osmyb4 gene," *Anadolu Journal of Agricultural Sciences,* vol. *35*, pp. 115-123, 2020.

[18] T. Hirayama, and K. Shinozaki, "Research on plant abiotic stress responses in the past genome era: past, present and future", *The Plant Journal,* vol. 61, pp. 1041-1052, 2010.

[19] M. Arslan, S. Çetin, and C. Erdurmuş, " Negative effects of salt stress on plant growth and salinity tolerance of some forage crops," *Journal of Agricultural Engineering,* vol. 360, pp. 32-39, 2013.

[20] R. Kopecka, M. Kameniarova, M. Cerny, B. Brzobohaty, and J. Novak, "Abiotic stress in crop production," *International Journal of Molecular Sciences,* vol. 24, no. 6603, pp. 1-47, 2023.

[21] J. Kang, W. Xie, Y. Sun, Q. Yang, and M. Wu, "Identification of genes induced by salt stress from *medicago truncatula* L. seedlings," *African Journal of Biotechnology,* vol. 9, no. 45, pp. 7589-7594, 2010.

[22] Y. Bu, J. Kou, B. Sun, T. Takano, and S. Liu, "Adverse effect of urease on salt stress during seed germination in *Arabidopsis thaliana*," *FEBS Letters,* vol. 589, pp. 1308-1313, 2015.

[23] H. Korkmaz, and A. Durmaz, "Responses of plants to abiotic stress factors ", *Gümüşhane University Journal of Science and Technology,* vol. 7, no. 2, pp. 192-207, 2017.

[24] D. Rhodes, and P. J. Rich, "Preliminary genetic studies of the phenotype of betaine deficieny in *Lea mays* L.," *Plant Physiology,* vol. 88, pp. 102-108, 1988.

[25] M. H. Izadi, J. Rabbani, Y. Emam, A. Tahmasebi, and M. Pessarakli, "Effect of salinity stress on physiological performance of various wheat and barley cultivars," *Journal of Plant Nutrition,* vol. 37, pp. 520-531, 2014.

[26] İ. Tiryaki, "Adaptation mechanisms of some field crops to salt stress, " *KSU Journal Of Agriculture and Nature*, vol. 21, no. 5, pp. 800-808, 2018.

[27] K. M. Singh, R. P. Singh, A. K. Jha, and A. Kumar, "Understanding the fodder markets for sustainable development of livestock sector in bihar-a rapid appraisal approach." New Delhi, 2012.

[28] S. Mizanbekova, A. Umbetaliev, A. Aitzhanova, and R. Aklybaev, "Priorities of mixed fodder production development in emerging countries: the case of Kazakhstan," *Revista ESPACIOS 38* vol. 42, pp. 1-13, 2017.

[29] F. J. Carvalho, R. B. Elias, A. A. Silva, and T. S. Campos, "Sources and dosages of nitrogen applied with urea coated with polymers in marandu palisade grass", *Revista Agrogeoambiental, vol. 10, no. 3*, pp. 135-143, 2018.

[30] FAO. (2024, 04 01). *Food and Agriculture Organization of the United Nations*. Plant Genetic Resources of Forage Crops Pasture and Rangelands: , https://www.fao.org/agriculture/crops/thematic-sitemap/theme/seeds-pgr/sow/sow2/tbs/en/ adresinden alındı.

[31] S. Amritkar, J. Chavan, A. Kakad, and M. Shaikh, "Phytochemical and pharmacological review of cynodon dactylon grass with its potential effects," *Journal of Pharmaceutical and Biological Sciences,* vol. 11, no. 2, pp. 112-116, 2023.

[32] E. Açıkgöz, "Forage Crops," 3rd ed., vol. 182, Bursa: Uludag University Foundation Publishing House, 2001, pp. 584.

[33] M. A. Carmona, M. M. Oliveira, J. C. Martins, M. L. Cabral, J. A. Passarinho, M. L. Fernandes, . . . D. Crespo, "Avalıaçao da tolerancıa a salınıdade de especıes forrageıras," *Pastagens e Forragens,* vol. 24, no. 25, pp. 85-96, 2003.

[34] S. Rehman, S. Nizam, S. Rubab, S. Bahadur, and X. Wei, "Evaluation of protein content in some fodder crops," *Hamdard Medicus,* vol. 66, no. 1, pp. 1-14, 2023.

[35] M. A. Lee, "A global comparison of the nutritive values of forage plants grown in contrasting environments," *Journal of Plant Research*, vol. 131, pp. 641-654, 2018.

[36] E. Çaçan, and K. Kökten, " Comparison of some alfalfa genotypes (*medicago sativa* L.) in terms of straw yiled and straw quality," *Euroasia Journal of Mathematics, Engineering, Natural & Medical Sciences International Indexed & Refereed*, vol. 8, no. 9, pp. 266-272, 2020.

[37] E. Çaçan, and S. İpekeşen, "Variation of some quality characteristics in silage corn according to different sowing times," *International Journal of Food, Agriculture and Animal Sciences,* vol. 1, no. 1, pp. 37-45, 2021.

[38] I. Inal, C. Yücel, D. Yücel, and R. Hatipoğlu, "Nutritive value and fodder potential of different sweet sorghum genotypes under mediterranean conditions," *Turkish Journal of Field Crops*, vol. 26, no. 1, pp. 1-7, 2021.

[39] S. Walter, J. Zehring, K. Mink, U. Quendt, K. Zocher, and S. Rohn, "Protein content of peas (*pisum sativum*) and beans (*vicia faba*)-influence of cultivation conditions," *Journal of Food Composition and Analysis, vol. 105, no. 104257*, pp. 1-9, 2022.

[40] R. Karayel, and H. Bozoğlu, "Tryptophane and raw protein contents of local pea (*pisum sativum* L.) lines for different sowing dates," *Journal of Agricultural Science*, vol. 21, pp. 337-345, 2015.

[41] S. Temel, B. Keskin, R. Tosun, and S. Çakmakçı, " Determination of herbage yield and quality performances in forage pea varieties sown as spring," *Turkish Journal of Agricultural and Natural Sciences*, vol. 8, c.2, pp. 411–419, 2021.

[42] F. Alatürk, Ç. Çınar, and A. Gökkuş, " Effects of different row spacings on yield and quality of some field pea cultivars," *Turkish Journal of Agricultural and Natural Sciences*, vol. 8, no. 1, pp. 53–57, 2021.

[43] H. Okkaoğlu, E. Ay, C. Büyükkileci, M. Akça Pelen, and H. Özpınar, " Effects of cutting times on dry matter yield and quality of field pea (*pisum sativum spp. arvense* L.), " *ANADOLU Journal of Aegean Agricultural Research Institute*, vol. 32, no. 2, pp. 253-263, 2022.

[44] E. Çaçan, M. Kaplan, K. Kökten and H. Tutar, "Evaluation of some forage pea (*pisum sativum ssp. arvense* L.) lines and cultivars in term of seed yield and straw quality", *Journal of the Institute of Science and Technology*, vol. 8, no. 2, pp. 275-284, 2018.

[45] A. Bakoğlu, K. Kökten, and Ö. Kılıç, "Yield and nutritive value of common vetch (*vicia sativa* L.) lines and varieties," *Turkish Journal of Agricultural and Natural Sciences*, vol. 3, no. 1, pp. 33-37, 2016.

[46] V. Mihailovic, and A. Mikic, "Ideotypes of forage pea (*pisum sativum*) cultivars," *Quantitative Traits Breeding for Multifunctional Grasslands and Turf*, pp. 183-186, 2014.

[47] A. Kotlarz, A. Sujak, W. Strobel, and W. Grzesiak, "Chemical composition and nutritive value of protein of the pea seeds effect of harvesting year and variety," *Vegetable Crops Research Bulletin*, vol. 75, pp. 57-69, 2011.

[48] P. Hara, M. Piekutowska, and G. Niedbala, "Prediction of protein content in pea (*pisum sativum* L.) seeds using artificial neural networks," *Agriculture*, vol. 13, no. 29, pp. 1-21, 2022.

[49] D. Janusauskaite, "Productivity of three pea (*pisum sativum* L.) varieties as influenced by nutrient supply and meteorological conditions in boreal environmental zone," *Plants*, vol. 12, no. 1938, pp. 1-14, 2023.

[50] L. Ouafi, F. Alane, H. Rahal Bouziane, and A. Abdelguerfi, "Agro-morphological diversity within field pea (*pisum sativum* L.) genotypes," *African Journal of Agricultural Research*, vol. 11, no. 40, pp. 4039-4047, 2016.

[51] B. Yazıcılar, M. Şimşek, İ. Bezirganoğlu, and D. İlhan, "DNA and protein content variations of Turkish pea (*pisum sativum* L.) genotypes," *Journal of Agriculture, Food, Environment and Animal Sciences*, vol. 2, no. 2, pp. 77-89, 2021.

[52] A. S. Tekeli, and E. Ateş, "Yield and its components in field pea (*pisum arvense* L.) lines", *Journal of Central European Agriculture*, vol. 4, no. 4, pp. 313-317, 2003.

[53] T. Yavuz, " The effects of different cutting stages on forage yield and quality in pea (*pisum sativum* L.) and oat (*avena sativa* L.) mixtures," *Journal of Field Crops Central Research Institute*, vol. 26, no. 1, pp. 67-74, 2017.

[54] A. Uzun, E. Açıkgöz, and H. Gün, "Yield and quality characteristics of some pea (*pisum sativum* L.) varieties harvested at different growing stages," *Journal of Agricultural Faculty of Uludag University*, vol. 26, no. 1, pp. 27-38, 2012.

[55] A. Doğru, and S. Canavar, " Physiological and biochemical components of salt tolerance in plants," *Academic Platform Journal of Engineering and Science*, vol. 8, no. 1, pp. 155-174, 2020.

[56] S. J. Roy, S. Negrao, and M. Tester, "Salt resistant crop plants," *Current Opinion in Biotechnology*, vol. 26, pp. 115-124, 2014.

[57] H. Zambi, and Ö. Önal Aşcı, " Effect of NaCl stress on chlorophyll and mineral content of forage pea," *International Journal of Agriculture and Wildlife Science*, vol. 6, no. 3, pp. 562-569, 2020.

[58] H. Upadhyay, A. Juneja, H. Turabieh, S. Malik, A. Gupta, Z. K. Bitsue and C. Upadhyay, "Exploration of crucial factors involved in plants development using the fuzzy AHP method," *Hindawi*, pp. 1-9, 2022.

[59] M. Y. Orcan, and P. Orcan, "Effect of Na, Mg, Ca chloride salts on mineral element, proline and total protein content in rice (*oryza sativa* L.) grown in vitro," *International Journal of Secondary Metabolite*, vol. 11, no. 1, pp. 144-156, 2024.

[60] B. Nedjimi, Z. E. Souissi, B. Guit, and Y. Daoud, "Differential effects of soluble salts on seed germination of *Marrubium vulgare* L." *Journal of Applied Research on Medicinal and Aromatic Plants*, vol. 17, no. *100250*, pp. 1-6, 2020.

[61] O. Borsani, V. Valpuesta, and M. A. Botella, "Developing salt tolerant plants in a new century: a molecular biology approach," *Plant Cell Tissue and Organ Culture*, pp. 101-115, 2003.

[62] H. Kuduğ, " DNA applications in agricultural biotechnology, " *Journal of Gaziosmanpasa Scientific Research*, c. 8, s. 2, ss. 1-10, 2019.

[63] J. Krasensky, and C. Jonak, "Drought, salt and temperature stres induced metabolic rearrangements and regulatory networks", *Journal of Experimental Botany*, vol. 63, no. 4, pp. 1593-1608, 2012.

[64] M. Liu, T. Z. Wang, and W. H. Zhang, "Sodium extrusion associated with enhanced expression of *SOS1* underlines different salt tolerance between *Medicago falcata* and *Medicago truncatula* seedlings," *Environmental and Experimental Botany*, pp. 46-55, 2015.

[65] S. Yokoi, R. A. Bressan, and P. M. Hasegawa, "Salt stress tolerance of plants", *JIRCAS Working Report*, pp. 25-33, 2002.

[66] E. Yılmaz, A. L. Tuna, and B. Bürün, "Tolerance strategies developed by plants to the effects of salt stress," *C.B.U. Journal of Science*, vol. 7, no. 1, pp. 47-66, 2011.

[67] S. Romo, E. Labrador, and B. Dopico, "Water stress regulated gene expression in *Cicer arietinum* seedlings and plants," *Plant Physiology and Biochemistry*, pp. 1017-1026, 2001.

[68] G. Aydın, M. Yücel, M. T. Chan, and H. A. Öktem, "Evaluation of abiotic stress tolerance and physiological characteristics of potato (*solanum tuberosum* L. cv. *Kennebec*) that heterologously expresses the rice *Osmyb4* gene," *Plant Biotechnology Reports*, pp. 295-304, 2014.

[69] C. Vannini, M. Iriti, M. Bracale, F. Locatelli, F. Faoro, P. Croce, . . . A. Genga, The ectopic expression of the rice *Osmyb4* gene in *Arabidopsis* increases tolerance to abiotic, environmental and biotic stresses," *Physiological and Molecular Plant Pathology*, vol. 69, no. 1-3, pp. 26-42, 2006.

[70] A. Sakamoto, and N. Murata, "The role of glycine betaine in the protection of plants from stress: clues from transgenic plants," *Plant, Cell and Environment* vol. 25, pp. 163–171, 2002.

[71] Ö. Çelik, and S. G. Ünsal, "Expression analysis of proline metabolism-related genes in salt-tolerant soybean mutant plants," *Plant Omics Journal* vol. 6, no. 5, pp. 364-370, 2013.

[72] A. Loudari, C. Benadis, R. Naciri, A. Soulaimani, Y. Zeroual, M. E. Gharous, . . . A. Oukarroum, "Salt stress affects mineral nutrition in shoots and roots and chlorophyll a fluorescence of tomato plants grown in hydroponic culture," *Journal of Plant Interactions,* vol. 15, no. 1, pp. 398–405, 2020.

[73] V. D. Taffouo, A. H. Nouck, S. D. Dibong, and A. Amougou, "Effects of salinity stress on seedlings growth, mineral nutrients and total chlorophyll of some tomato (*lycopersicum esculentum* L.) cultivars", *African Journal of Biotechnology*, vol. 9, no. 33, pp. 5366-5372, 2010.

[74] M. A. Shahid, M. A. Pervez, R. M. Ballal, C. M. Ayyub, M. Ghazanfar, T. , Abbas, . . . A. Akram, "Effect of salt stress on growth, gas exchange attributes and chlorophyll contents of pea (*pisum sativum*)," *African Journal of Agricultural Research,* vol. 6, no. 27, pp.5808-5816, 2011.

[75] K. Taïbi, F. Taïbi, L. A. Abderrahim, A. Ennajah, M. Belkhodja, and J. M. Mulet, "Effect of salt stress on growth, chlorophyll content, lipid peroxidation and antioxidant defence systems in *phaseolus vulgaris* L.," *South African Journal of Botany*, vol. 105, pp. 306–312, 2016.

[76] G. Kaymak, and Z. Acar, "Determination of salinity tolerance levels of tedera (*bituminaria bituminosa* L.) genotypes," *Anadolu Journal of Agricultural Sciences*, vol. 35, pp. 51-58, 2020.

[77] F. Boughalleb, R. Abdellaout, M. Mahmoudi, and E. Backhshandeh, "Changes in phenolic profile, soluble sugar, proline, and antioxidant enzyme activities of *polygonum equisetiforme* in response to salinity," *Turkish Journal of Botany*, vol. 44, pp. 25-35, 2020.

[78] J. M. Ruiz, R. M. Rivero, I. Lo´pez-Cantarero, and L. Romero, "Role of Ca in the metabolism of phenolic compounds in tobacco leaves (*nicotiana tabacum* L.)," *Plant Growth Regulation*, vol. 41, pp. 173-177, 2003.

[79] S. Kıpçak, A. Ekincialp, Ç. Erdinç, E. Kabay, and S. Şensoy, " Effects of salt stress on some nutrient content and total antioxidant and total phenol content in different bean genotypes," *Yuzuncu Yıl University Journal of Agricultural Sciences*, vol. 29, no.1, pp. 136-144, 2019.

[80] M. R. Amirjani, "Effect of salinity stress on growth, mineral composition, proline content, antioxidant enzymes of soybean," *American Journal of Plant Physiology* vol. 5, no. 6, pp. 350-360, 2020.

Düzce University
Journal of Science & Technology

Research Article

The Microstructure, Hardness and Density Investigation of Mg Composites Reinforced with Nanoclay

Mikail ASLAN[a,*]

[a] *Department of Metallurgical and Material Science Engineering , Faculty of Engineering, Gaziantep University, Gaziantep, TURKEY*
** Corresponding author's e-mail address: aslanm@gantep.edu.tr*
DOI: 10.29130/dubited.1525745

ABSTRACT

Magnesium (Mg) stands out as a prevalent material in engineering, finding essential utility as a biomaterial due to its unique combination of low density, stiffness, high damping capacity, superior bending resistance, and impressive specific strength. Despite its high reactivity and somewhat inadequate mechanical properties for rigorous engineering applications, the incorporation of reinforcing nanoparticles has shown significant potential in enhancing the performance of magnesium-based composites. This study investigates the microstructure evaluation, hardness, and density of magnesium composites reinforced with nanoclay using a powder metallurgy approach. Nanoclay was preferred as a reinforcement element at weight percentages of 1%, 3%, 5%, and 7%. The densities of the composites were measured using the Archimedean principle, revealing that the addition of nanoclay generally increases the density of the composites due to the higher density of nanoclay compared to pure magnesium. However, the composite with 5% nanoclay exhibited a lower density than the one with 3% nanoclay, likely due to agglomerations leading to increased internal voids. Surface preparation for Vickers hardness testing involved sanding with 600, 1000, and 2000 mesh sanders, followed by polishing with 6µ and 3µ diamond suspensions. Hardness measurements, conducted using an AOB Vickers microhardness tester, indicated that the highest hardness value was observed in the composite with a 7% weight percentage of nanoclay, demonstrating that nanoclay addition enhances hardness. However, the composite with 3% nanoclay showed lower hardness compared to other reinforced composites. Optical images of the structures revealed metallographic spots indicative of contamination. These findings contribute to the understanding of the structural and mechanical behavior of nanoclay-reinforced magnesium composites, highlighting the potential for optimizing such materials for various applications in automotive, aerospace, and medical fields.

Keywords: *Nanoclay, Mg composites, Hardness, Microstructure and density measurement*

Nanokil ile Takviye Edilmiş Mg Kompozitlerin Mikroyapılarının Sertliklerinin ve Yoğunluklarının Araştırılması

ÖZ

Magnezyum (Mg), mühendislikte yaygın bir malzeme olarak öne çıkmakta ve düşük yoğunluk, sertlik, yüksek sönüm kapasitesi, üstün eğilme direnci ve etkileyici spesifik mukavemet gibi benzersiz kombinasyonu nedeniyle biyomalzeme olarak hayati bir işlev görmektedir. Yüksek reaktivitesine ve zorlu mühendislik uygulamaları için mekanik özelliklerinin yetersiz olmasına rağmen, güçlendirici nanoparçacıkların eklenmesi, magnezyum bazlı kompozitlerin performansını artırma potansiyeli göstermiştir. Bu çalışma, toz metalurjisi yaklaşımı kullanılarak nanokil ile güçlendirilmiş magnezyum kompozitlerinin mikro yapı değerlendirmesi, sertlik ve yoğunluğunu araştırmaktadır. Nanokil, ağırlık yüzdeleri olarak %1, %3, %5 ve %7 oranlarında bir güçlendirme elemanı olarak tercih edilmiştir. Kompozitlerin yoğunlukları, Archimedes prensibi kullanılarak ölçülmüştür ve nanokilin

Received: 31/07/2024, Revised: 06/11/2024, Accepted: 13/11/2024

eklenmesinin genellikle kompozitlerin yoğunluğunu artırdığı, çünkü nanokilin saf magnezyumdan daha yüksek bir yoğunluğa sahip olduğu görülmüştür. Ancak, %5 nanokil içeren kompozit, %3 nanokil içeren kompozitten daha düşük yoğunluk göstermiştir, bu durum aglomerasyonların iç boşlukları artırması ile ilişkilendirilebilir. Vickers sertlik testi için, numune 600, 1000 ve 2000 mesh zımpara ile zımparalandı ve ardından 6µ ve 3µ elmas süspansiyonları ile parlatıldı. AOB Vickers Mikrosertlik testi kullanılarak yapılan sertlik ölçümleri, en yüksek sertlik değerinin %7 ağırlık yüzdesine sahip nanokil içeren kompozitte gözlemlendiğini ve nanokil eklemenin sertliği artırdığını göstermiştir. Ancak, %3 nanokil içeren kompozit diğer güçlendirilmiş kompozitlere göre daha düşük sertlik göstermiştir. Yapıların optik görüntüleri, kontaminasyonu belirten metalografik noktaları ortaya çıkarmıştır. Bu bulgular, nanokil ile güçlendirilmiş magnezyum kompozitlerinin yapısal ve mekanik davranışlarının anlaşılmasına katkıda bulunur ve bu tür malzemelerin otomotiv, havacılık ve tıp alanlarındaki çeşitli uygulamalar için optimize edilme potansiyelini gösterir.

Anahtar Kelimeler: *Nanokil, Mg kompozit, Sertlik, Mikroyapı ve yoğunluk*

I. INTRODUCTION

Metal matrix composites (MMCs) have garnered significant attention for their promising reinforcement properties[1]. Especially, magnesium (Mg) composite stands out as a prevalent material in engineering and finds essential utility as a biomaterial [2]. The potential of Mg-based metal matrix composites extends across diverse sectors, including automotive, aerospace, and medical fields [3]. MMC Mg systems, at their core, exhibit remarkable high strain rate capabilities [4]. This makes them pivotal in the pursuit of weight reduction and the attainment of optimal mechanical properties crucial for aerospace and automotive components [5].

Recently, there has been a remarkable surge in the application of Mg as a structural material. Mg boasts dimensional stability and excellent machinability [6]. As the 8th most abundant element on Earth, Mg also exhibits high thermal conductivity. The allure of Mg lies in its unique combination of attributes: low density, stiffness, high damping capacity, superior bending resistance, and impressive specific strength [7].

The high reactivity of pure magnesium and its somewhat inadequate mechanical properties for rigorous engineering applications have led to the prevalent use of magnesium with reinforcing nanoparticles in such contexts[8-10]. Researchers have focused their efforts on developing magnesium matrix composites with diverse reinforcements [11-20]. In these studies, various particles are used to enhance mechanical properties of the Mg composites. Nie et al.[21] studied SiC nanoparticle reinforced Mg matrix composite fabricated by ultrasonic vibration squeeze casting method. At the interface, composites featuring 10 μm SiC particles exhibit notably high dislocation density, whereas those with 60 nm SiC particles show fewer dislocations near the interface between the particles and the matrix. Additionally, a significant number of dislocations are generated due to thermal mismatch, constituting thermodynamically unstable crystal defects that render materials with high energy levels unstable. Another study conducted by Reddy et al. [22] is related to the titanium oxide reinforced magnesium composites. The findings unveil that the incorporation of nano reinforcement particles results in a reduction in the density of the dendritic pattern, along with a uniform dispersion of nano reinforcement particles within the magnesium phase. Various properties including hardness (18.24%), tensile strength (22.12%), compressive strength (24.32%), and wear resistance (26.52%) were improved. Lastly, Kumar et al.[23] examine nanoclay reinforced aleminium metal matrix composite produced by semi-solid state casting method. Results indicates that nanoclay led to increase from 74 BHN to 82 BHN .

In this study, the microstructure evaluation, hardness, and density of magnesium composites reinforced with nanoclay were investigated using a powder metallurgy approach. The impact of varying nanoclay ratios on the resulting magnesium metal matrix composites was also explored.

II. MATERIALS AND METHODS

In the production of the nanoclay-reinforced magnesium composites, both magnesium and nanoclay were procured from Nanografi and Grafene Chemical Industries, respectively. Raw form of SEM of nanoclay particles is given in Figure 1.

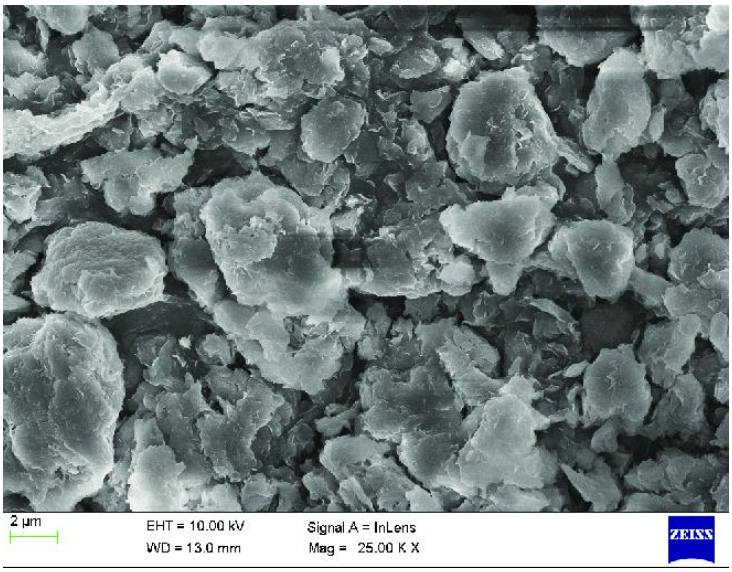

Figure 1. *The SEM of nanoclay particles*

Samples weighing 10 g each were carefully measured. Four different weight percentages of nanoclay (1%, 3%, 5%, and 7%) were selected. Subsequently, the materials were blended in a beaker and thoroughly mixed using a magnetic stirrer operating at 800 rpm for thirty minutes to achieve homogeneity. After the powder attained a uniform distribution, it was cold-pressed in a steel die at 200 MPa to yield bulk samples. The procedure of producing nanoclay reinforced Mg composites is given in Figure 2.

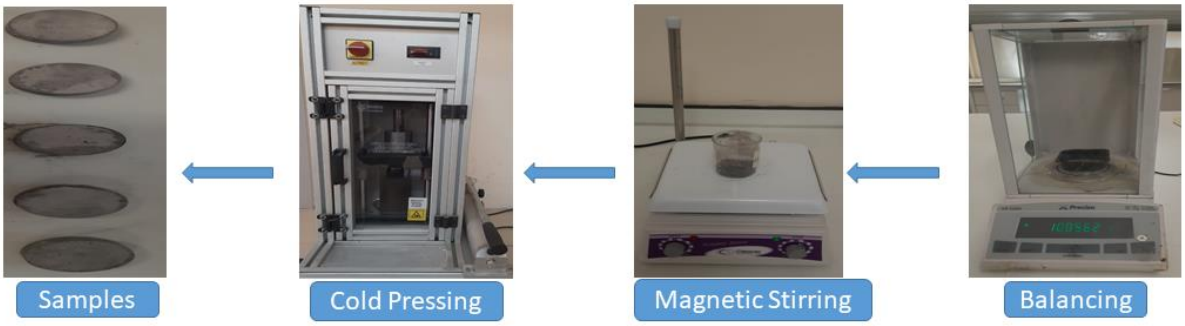

Figure 2. *The procedure of fabricating of the given composites*

III. RESULTS AND DISCUSSION

Nanoclay was preferred as reinforcement elements at weight percentages of 1%, 3%, 5%, and 7%. The densities of the studied materials were measured via the Archimedean principle. Figure 3 indicates the measured densities of the composites at various nanoclay ratios. Except for the sample with 1% nanoclay, nanoclay addition leads to increase in density values. This is consistent because the density of nanoclay is higher than the density of pure magnesium. However, the density of the sample having with 5% nanoclay is lower density than the sample having 3% nanoclay. Agglomerations in this composite lead to increased internal voids, reducing the composite's density since the presence of these

agglomerates can lead to the formation of internal voids or gaps within the composite. These voids arise because the clustered nanoparticles occupy a larger volume than if they were uniformly distributed. The existence of voids reduces the overall packing density of the composite material. Since density is defined as mass per unit volume, the presence of internal voids decreases the mass that contributes to the composite's total volume, leading to a lower overall density.

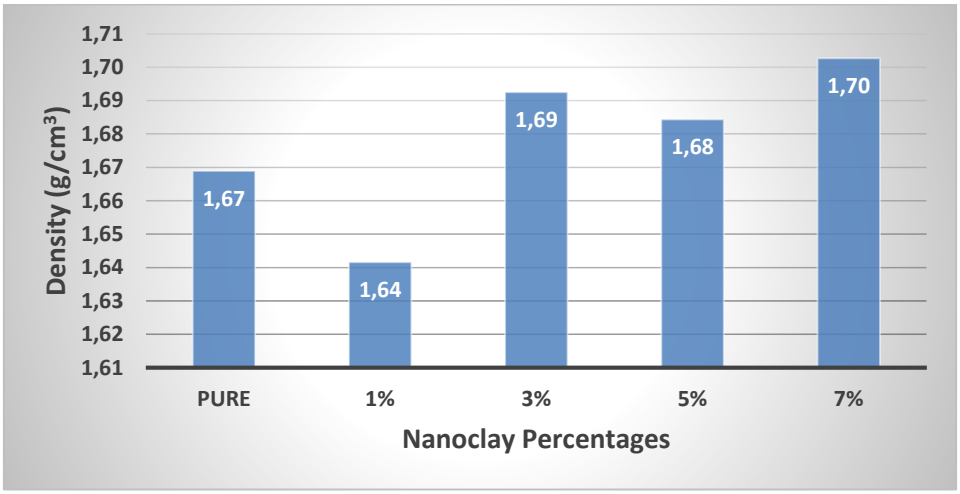

Figure 3. *Density measurements of the given composites*

Sanding and polishing were implemented to prepare the surface for the vickers hardness. 600, 1000 and 2000 mesh sanders were used for metallographic sanding process. Then, for polished better quality surfaces, the samples were polished with 6µ and 3µ diamond suspensions respectively. Hardnesss measurements were conducted using an AOB Vickers Microhardness tester with a load of 0.1 kgf and a dwell time of 5 seconds. 10 measurements were taken for each measurements and then the average values were calculated. Figure 4 illustrates the Vickers hardness values of the given samples. The highest hardness value was seen in the composite with a 7% weight percentage of nanoclay. This indicated that the addition of the nanoclay led to increase in the hardness values. However, the composite having 3% weight percentage of nanoclay is lower value than the other reinforced composites. It may be related to the slightly higher number of spots on the surface in this sample, which reduces the hardness values. The standard errors for the samples with 0%, 1%, 3%, 5%, and 7% reinforcements are 1.61, 2.30, 1.59, 1.57, and 2.18, respectively. The minimal standard variations in the hardness values indicate that the nanoclay particles were homogeneously distributed within the Mg matrix to an acceptable degree. Notably, the highest standard error was recorded in the 1% sample, which corresponds with the density values.

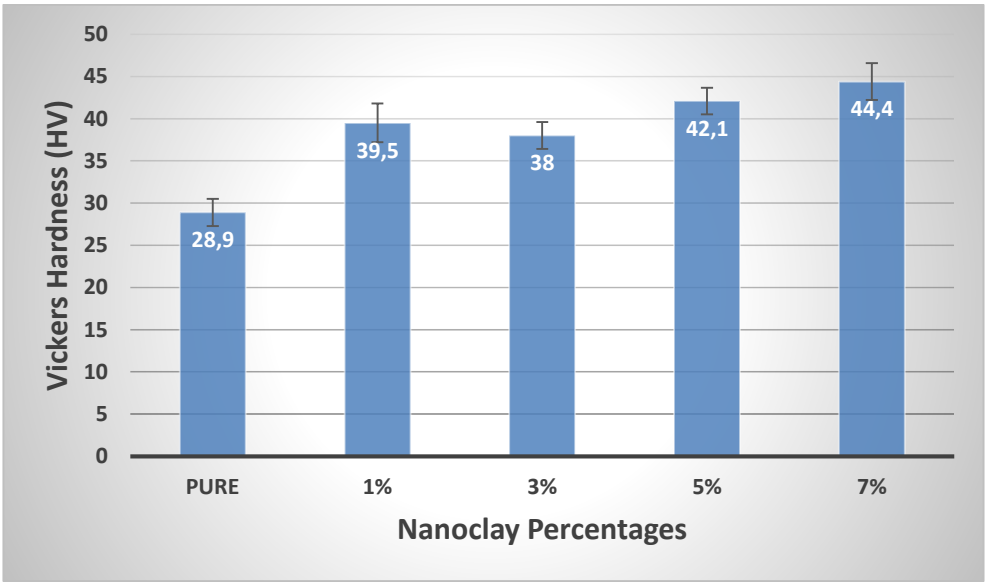

Figure 4. *Vickers hardness of the given composites.*

Figure 5 displays optical microscope images of the given structures, within which metallographic spots are visible, indicative of contamination. Grain boundaries are visible in all structures, but there is no clear evidence to suggest that the addition of nanoclay alters grain size of the composites.

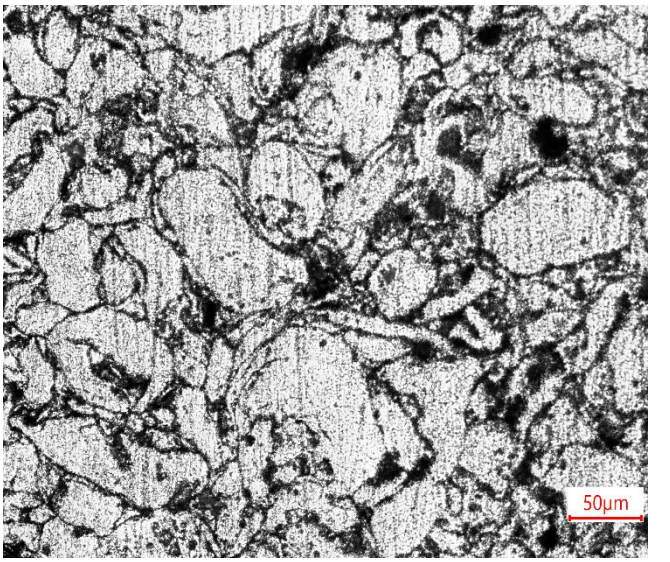

Pure Magnesium

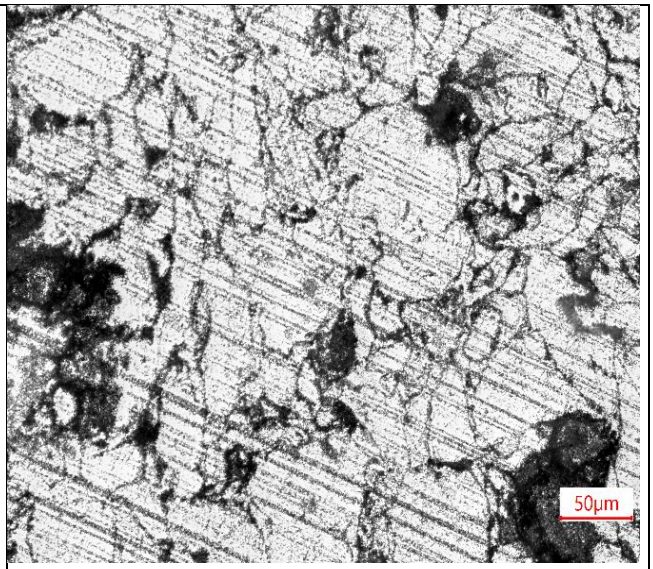

%1 Nanoclay

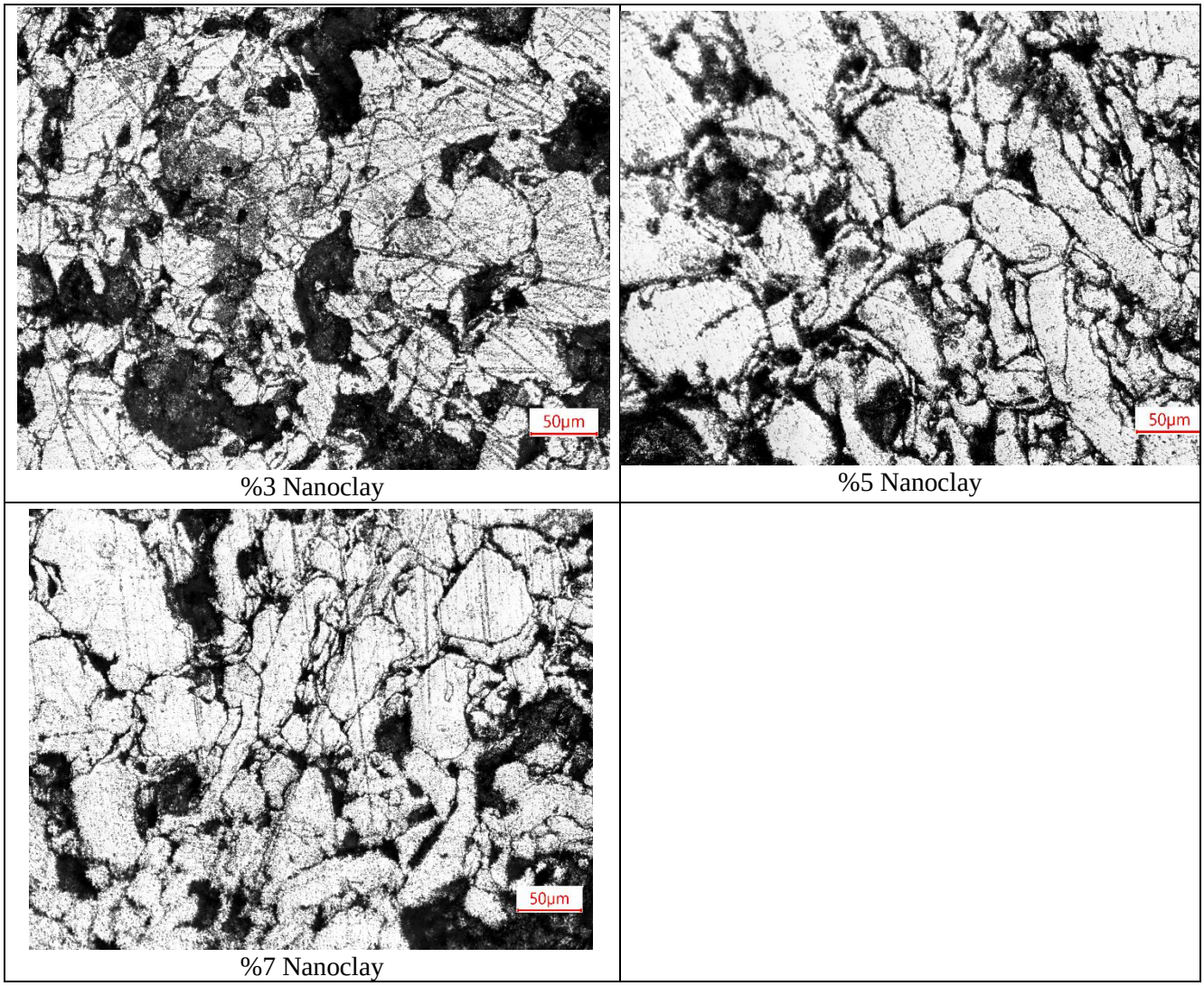

Figure 5. *Optical microscope image of the given composites.*

IV. CONCLUSION

This study successfully investigated the microstructure, hardness, and density of magnesium composites reinforced with varying percentages of nanoclay using a powder metallurgy approach. Key findings include:

1. **Density Measurements**: The addition of nanoclay generally increased the density of the composites, consistent with the higher density of nanoclay compared to pure magnesium. However, the composite with 5% nanoclay exhibited a lower density than the one with 3% nanoclay, likely due to agglomerations that increased internal voids.

2. **Hardness Testing**: Vickers hardness measurements revealed that the composite with a 7% weight percentage of nanoclay had the highest hardness value, indicating that nanoclay addition enhances hardness. Conversely, the composite with 3% nanoclay showed lower hardness than the other reinforced composites.

3. **Microstructure Analysis**: Optical images showed metallographic spots indicative of contamination across all samples. Grain boundaries were visible in all structures, but there was no clear evidence suggesting that nanoclay addition alters the grain size of the composites.

Overall, the incorporation of nanoclay into magnesium composites can significantly enhance their density and hardness, although care must be taken to manage agglomerations that can affect these properties negatively. These insights are valuable for optimizing magnesium-based composites for applications in automotive, aerospace, and medical fields, where mechanical strength and material stability are critical. Future research should focus on refining the dispersion techniques to minimize agglomeration and further enhance the composite properties. Additionally, future research could explore the use of various nanoparticles or hybrid nanoparticles to enhance mechanical properties of magnesium composites for applications in automotive, aerospace, and medical fields.

V. REFERENCES

[1] E. Tekoğlu *et al.*, "Metal matrix composite with superior ductility at 800° C: 3D printed In718+ ZrB2 by laser powder bed fusion," *Composites Part B: Engineering,* vol. 268, p. 111052, 2024.

[2] J. Wu, X. Cheng, J. Wu, J. Chen, and X. Pei, "The development of magnesium-based biomaterials in bone tissue engineering: A review," *Journal of Biomedical Materials Research Part B: Applied Biomaterials,* vol. 112, no. 1, p. e35326, 2024.

[3] F. Aydın, "Recent advances in mechanical properties of Mg matrix composites: a review," *Materials Science and Technology,* vol. 40, no. 5, pp. 339-376, 2024.

[4] M. Güden, O. Akil, A. Tasdemirci, M. Ciftcioglu, and I. W. Hall, "Effect of strain rate on the compressive mechanical behavior of a continuous alumina fiber reinforced ZE41A magnesium alloy based composite," *Materials Science and Engineering: A,* vol. 425, no. 1-2, pp. 145-155, 2006.

[5] W. Zhang and J. Xu, "Advanced lightweight materials for Automobiles: A review," *Materials & Design,* vol. 221, p. 110994, 2022.

[6] S. V. S. Prasad, S. B. Prasad, K. Verma, R. K. Mishra, V. Kumar, and S. Singh, "The role and significance of Magnesium in modern day research-A review," *Journal of Magnesium and alloys,* vol. 10, no. 1, pp. 1-61, 2022.

[7] Y. Yang, X. Xiong, J. Chen, X. Peng, D. Chen, and F. Pan, "Research advances in magnesium and magnesium alloys worldwide in 2020," *Journal of Magnesium and Alloys,* vol. 9, no. 3, pp. 705-747, 2021.

[8] S. Sambasivam *et al.*, "Significance of reinforcement in Mg-based MMCs for various applications: a review," *Materials Today: Proceedings,* vol. 416, no. 1-2, pp. 155-165, 2023.

[9] A. Ercetin *et al.*, "Microstructural and Mechanical Behavior Investigations of Nb-Reinforced Mg–Sn–Al–Zn–Mn Matrix Magnesium Composites," *Metals,* vol. 13, no. 6, p. 1097, 2023.

[10] L. K. Pillari, K. Lessoway, and L. Bichler, "Carbon nanotube and graphene reinforced magnesium matrix composites: a state-of-the-art review," *Journal of Magnesium and Alloys,* vol. 11, no. 6, p. 1825-1905, 2023.

[11] P. Monish, K. K. L. Hari, and K. Rajkumar, "Manufacturing and characterisation of magnesium composites reinforced by nanoparticles: a review," *Materials Science and Technology,* vol. 39, no. 15, pp. 1858-1876, 2023.

[12] X. Zhou, D. Su, C. Wu, and L. Liu, "Tensile mechanical properties and strengthening mechanism of hybrid carbon nanotube and silicon carbide nanoparticle-reinforced magnesium alloy composites," *Journal of Nanomaterials,* vol. 2012, pp. 83-83, 2012.

[13] F. Zeng *et al.*, "Fabrication and mechanical properties of mesoporous silica nanoparticles reinforced magnesium matrix composite," *Journal of Alloys and Compounds,* vol. 728, pp. 413-423, 2017.

[14] M. Subramani, S.-J. Huang, and K. Borodianskiy, "Effect of SiC nanoparticles on AZ31 magnesium alloy," *Materials,* vol. 15, no. 3, p. 1004, 2022.

[15] K. B. Nie, X. J. Wang, L. Xu, K. Wu, X. S. Hu, and M. Y. Zheng, "Effect of hot extrusion on microstructures and mechanical properties of SiC nanoparticles reinforced magnesium matrix composite," *Journal of Alloys and Compounds,* vol. 512, no. 1, pp. 355-360, 2012.

[16] S. C. Tjong, "Novel nanoparticle-reinforced metal matrix composites with enhanced mechanical properties," *Advanced engineering materials,* vol. 9, no. 8, pp. 639-652, 2007.

[17] J. Lan, Y. Yang, and X. Li, "Microstructure and microhardness of SiC nanoparticles reinforced magnesium composites fabricated by ultrasonic method," *Materials Science and Engineering: A,* vol. 386, no. 1-2, pp. 284-290, 2004.

[18] Y.-X. Luo *et al.*, "Research progress on nanoparticles reinforced magnesium alloys," *Journal of Materials Research and Technology,* vol. 30, no. 2, pp. 5166-5191, 2024.

[19] K. B. Nie, X. J. Wang, K. K. Deng, X. S. Hu, and K. Wu, "Magnesium matrix composite reinforced by nanoparticles–a review," *Journal of magnesium and alloys,* vol. 9, no. 1, pp. 57-77, 2021.

[20] H. Dieringa, "Properties of magnesium alloys reinforced with nanoparticles and carbon nanotubes: a review," *Journal of Materials Science,* vol. 46, pp. 289-306, 2011.

[21] K. Nie, K. Deng, X. Wang, and K. Wu, "Characterization and strengthening mechanism of SiC nanoparticles reinforced magnesium matrix composite fabricated by ultrasonic vibration assisted squeeze casting," *Journal of Materials Research,* vol. 32, no. 13, pp. 2609-2620, 2017.

[22] D. A. K. Reddy *et al.*, "Investigating the mechanical properties of titanium dioxide reinforced magnesium composites," *Materials Today: Proceedings,* vol. 11, no. 6, pp. 1619-1632, 2023.

[23] P. S. R. Kumar, D. R. Smart, and S. J. Alexis, "Evaluation of mechanical properties of MWCNT/nanoclay reinforced aluminium alloy metal matrix composite," in *IOP Conference Series: Materials Science and Engineering*, 2018, vol. 346, no. 1, p. 012013: IOP Publishing.

Düzce University
Journal of Science & Technology

Research Article

Van der Pol Oscillator, its Control Theoretical Analysis Using Dissipative Canonical Equations and its Lyapunov Function

Cem CİVELEK[a,*], Bedri SEVİNÇ[b]

[a] *Department of Electrical & Electronics Engineering, Faculty of Engineering, Turkish-German University, Istanbul, TURKIYE*
[b] *Milas Vocational School, Muğla Sıtkı Koçman University, Muğla, TURKIYE*
** Corresponding author's e-mail address:* cenkcivel@gmail.com
DOI: 10.29130/dubited.1448747

ABSTRACT

In this research paper, beginning with the Lagrangian and generalized velocity proportional (Rayleigh) dissipation function of a physical/engineering system, the Lagrange-dissipative model ({L,D}-model briefly) of the system is initially developed. Upon satisfying the prerequisite condition for a Legendre transform, the Hamiltonian function can be obtained. With the Hamiltonian function and the generalized velocity proportional (Rayleigh) dissipation function, dissipative canonical equations can be derived. Using these dissipative canonical equations as the state-space equations of the system allows for the investigation of observability, controllability, and stability properties. In addition to the equilibrium (or critical or fixed) points of the system, stability properties can also be verified through a Lyapunov function as a residual energy function (REF). Since the proposed method is valid for both linear and nonlinear systems, it has been applied to the Van der Pol oscillator/equation.

Keywords: *Observability, Controllability and stability of Van der Pol oscillator/equation, Lyapunov function for stability of Van der Pol oscillator/equation.*

Van der Pol Osilatörü, Yitimli Kanonik Denklemler Kullanarak Kontrol Teorik Analizi ve Lyapunov Fonksiyonu

ÖZ

Bu araştırma makalesinde, bir fiziksel/mühendislik sisteminin Lagrangian ve genelleştirilmiş hız orantılı (Rayleigh) yitim fonksiyonu ile başlayarak, öncelikle bu sistemin Lagrange-dissipatif modeli (kısaca {L,D}-modeli) oluşturulmuştur. Legendre dönüşümü için gerekli koşulunun sağlanmasıyla Hamilton fonksiyonu elde edilebilir. Hamilton fonksiyonu ve genelleştirilmiş hız orantılı (Rayleigh) yitim fonksiyonuyla, yitimli kanonik denklemler elde edilebilir. Yitimli kanonik denklemlerin sistemin durum uzayı denklemleri olarak kullanılması; gözlemlenebilirlik, kontrol edilebilirlik ve kararlılık özelliklerinin araştırılması için kullanılır. Sistemin denge (veya kritik veya sabit) noktalarının yanı sıra, sistemin kararlılık özellikleri, artık enerji fonksiyonu (REF) olarak bir Lyapunov fonksiyonu aracılığıyla da doğrulanabilir. Önerilen yöntem doğrusal ve doğrusal olmayan sistemler için de geçerli olduğundan, yöntem Van der Pol osilatörüne/denklemine uygulanmıştır.

Anahtar Kelimeler : *Van der Pol denklemi, Gözlemlenebilirlik, Denetlenebilirlik, Kararlılık, Van der Pol denklemi kararlılığı için Lyapunov fonksiyonu*.

Received: 08/03/2024, Revised: 11/11/2024, Accepted: 15/11/2024

I. INTRODUCTION

A non-conservative oscillator with a nonlinear damping was examined by Balthasar van der Pol in 1920, where the related equation and oscillation are called as Van der Pol equation and Van der Pol oscillation respectively.

Dynamical systems described by Van der Pol equations occur in various fields of physical and engineering sciences. These cover also biological and geological/geophysical sciences.

Some of the first articles on Van der Pol equation/oscillator are [1-2-3-4]. Also, different books available on nonlinear dynamics and chaos include Van der Pol equation/oscillator like [5-6-7-8]. The equation/oscillator has different applications in different sciences. The equation was also used even in seismology to model the two plates in a geological fault as in [9].

Physical and mathematical foundations of Lagrangians and Hamiltonians are contained in [10-11-12], where [12] is a very rare source including conditions for a Legendre transform. Modelling a physical or an engineering dynamical system by means of a Lagrangian L, a generalized velocity proportional (Rayleigh) dissipation function D and a Hamiltonian H depending on tensorial variables in contravariant and covariant forms was shown in [13], which also includes the dissipative canonical equations. In different tensorial forms, the extended Hamiltonians to obtain canonical equations in case of dissipative systems directly are given in [14] which contains also higher order {L,D}-models. Therefore, higher order Lagrangians, dissipation functions and nonconservative Hamiltonians are introduced in this study. The method to obtain a Lyapunovfunction as residual energy function in a systematic way was introduced in the reference [15].

In general, observability and controllability of nonlinear systems are given in [16]. Mathematically, Lie derivatives for observability and Lie brackets for controllability for linear and nonlinear systems are explained in [17] in detail. And the approaches convert to the usual linear case of observability and controllability matrices if the system is a linear one.

Physical system analysis related to observability, controllability and stability using its equations of generalized motion and canonical equations both in dissipative forms are studied in [18]. In the article[19], Duffing oscillator/equation was analyzed related the concepts given using equations of generalized motion including dissipation which can also be applied here.

This time, dissipative canonical equations will rather be used in this study. But observability and controllability analysis of Van der Pol oscillator/equation in general lacks in the literature. And this analyze is performed first time using classical mechanical approach including dissipation with statespace method as far as known by us. Moreover, Lyapunov's direct (or second) method is applied as residual energy function, and this is not considered for Van der Pol oscillator/equation in any other literature before which provides more precise results from the point of physics.

Lagrange-dissipative model of the Van der Pol oscillator/equation was derived here firstly. Provided that the condition for a Legendre transform is fulfilled, the Hamiltonian of the system and the dissipative canonical equations can be obtained which differs than the usual approaches with no dissipation. In this context, the method proposed is explained in detail. As far as we know, Van der Pol oscillator is analyzed for the first time by means of observability, controllability using the method and stability using Lyapunov function which is valid for linear and nonlinear cases. Lyapunov function as a residual energy function obtained as sum of Hamiltonian and negative form of dissipative energy will be used for the stability analysis. Finally, the conclusions which were established was stated.

II.OBTAINING THE {L,D}-MODEL AND THE EQUATIONS OF GENERALIZED MOTION

The Lagrangian in its most general form is

$$L(\dot{q},q,t) = T(\dot{q},t) - U(\dot{q},q,t) \tag{1}$$

$T(\dot{q},t)$ is the kinetic and $U(\dot{q},q,t)$is the potential energy parts of the Lagrangian. And the generalized velocity proportional (Rayleigh) dissipation function has the following form:

$$\frac{\partial D}{\partial \dot{q}_k} = R_k \dot{q}_k \Rightarrow D(\dot{q}_k) = \frac{R_k}{2}\dot{q}_k^2 \;;\; R_k = const.|_{\dot{q}_k} \tag{2}$$

where k presents the degree of freedom. The extended Euler-Lagrange differential equation is

$$\frac{d}{dt}\frac{\partial L}{\partial \dot{q}_k} - \frac{\partial L}{\partial q_k} + \frac{\partial D}{\partial \dot{q}_k} = F_k \;;\; k = 1,\cdots,\mathrm{f} \tag{3}$$

The external generalized force F_k may be included in the generalized velocity proportional (Rayleigh) dissipation function $D(\dot{q}_k)$ in form $-\dot{q}_k F_k$ as negative loss or in the Lagrangian as negative potential in form of $-q_k F_k$ to obtain the equations of generalized motion using extended Euler-Lagrange differential equation.

The second-degree differential equation of the generalized motion obtained through extended Euler-Lagrange differential equation has the most general form given below:

$$M_k\ddot{q}_k + R_k\dot{q}_k + K_k q_k + C_k = F_k \Rightarrow \ddot{q}_k + \frac{R_k}{M_k}\dot{q}_k + \frac{K_k}{M_k}q_k + \frac{C_k}{M_k} = \frac{F_k}{M_k} \;;\; M_k \neq 0 \tag{4}$$

where M_k is the generalized mass, R_k is the generalized resistive and K_k is the generalized capacitive elements respectively, C_k is the constant when available.

Equations of generalized motion can be written in state space form to analyze the generalized motion related to observability, controllability, and stability. But we here, will prefer to analyze the system related the concepts using state space form of dissipative canonical equations since the Hamiltonian is needed to construct a Lyapunov function in form of a residual energy function.

III.LEGENDRE TRANSFORM, HAMILTONIAN H AND OBTAINING DISSIPATIVE CANONICAL EQUATIONS

Prerequisite that the condition for a Legendre transform given as

$$\left|\frac{\partial^2 L}{\partial \dot{q}_r \partial \dot{q}_k}\right| = \left|\frac{\partial p_r}{\partial \dot{q}_k}\right| \neq 0 \;;\; r,k = 1,\cdots,\mathrm{f} \tag{5}$$

İs fulfilled, one can obtain the Hamiltonian *H* related to the Lagrangian *L* given as

$$H(p_k, q_k, t) = \sum_{k=1}^{f} p_k \dot{q}_k - L(\dot{q}_k, q_k, t) \tag{6}$$

The canonical equations are:

$$\dot{q}_k = \frac{\partial H}{\partial p_k} \ , \ \dot{p}_k = -\frac{\partial H}{\partial q_k} \tag{7}$$

The dissipative canonical equations are in what follows:

$$\dot{q}_k = \frac{\partial H}{\partial p_k} \ , \ \dot{q}_k = \frac{\partial H}{\partial p_k} \ ; \ \dot{p}_k = -\frac{\partial H}{\partial q_k} - \frac{\partial D}{\partial \dot{q}_k} \tag{8}$$

Prerequisite that the external generalized force(s) are not included in any potential or dissipation function in any form, the dissipative canonical equations in general can be written in matrix form as below:

$$\underbrace{\frac{d}{dt}\begin{bmatrix} q_k \\ p_k \end{bmatrix}}_{\dot{\boldsymbol{x}}} = \underbrace{\begin{bmatrix} \frac{\partial H}{\partial p_k} \\ -\frac{\partial H}{\partial q_k} - \frac{\partial D}{\partial \dot{q}_k} \end{bmatrix}}_{\boldsymbol{f(q)}} + \underbrace{\begin{bmatrix} 0 \\ 1 \end{bmatrix} F_k}_{\boldsymbol{g(q)u}} \ ; \ \underbrace{y = q_k}_{\boldsymbol{h(q)}} \tag{9}$$

IV. OBSERVABILITY USING THE DISSIPATIVE CANONICAL EQUATIONS

For a physical system, observability is proven using Lie derivatives of $\boldsymbol{h}$ with respect to $\boldsymbol{f}$

$$L_f^0 \boldsymbol{h} = \boldsymbol{h}(\boldsymbol{q}) \ ; \ L_f^1 \boldsymbol{h} = \nabla \boldsymbol{h}(\boldsymbol{q}).\boldsymbol{f}(\boldsymbol{q}) \tag{10}$$

where the first Lie derivative is as follows:

$$L_f^1 \boldsymbol{h} = \underbrace{\begin{bmatrix} \frac{\partial h}{\partial p_k} & \frac{\partial h}{\partial q_k} \end{bmatrix}}_{\nabla \boldsymbol{h}(\boldsymbol{q})} \underbrace{\begin{bmatrix} f_1(p_k, q_k) \\ f_2(p_k, q_k) \end{bmatrix}}_{\boldsymbol{f}(\boldsymbol{q})} \tag{11}$$

The related vector of all Lie derivatives $\boldsymbol{G}$ and the observability matrix $\boldsymbol{O}$ that is the multiplication of the matrix **O** with the operator ∇ have the forms given below:

$$\boldsymbol{G} = \begin{bmatrix} L_f^0 \boldsymbol{h} \\ L_f^1 \boldsymbol{h} \end{bmatrix} \Rightarrow \boldsymbol{O} = \nabla \boldsymbol{G} = \begin{bmatrix} \frac{\partial L_f^0 \boldsymbol{h}}{\partial p_k} & \frac{\partial L_f^0 \boldsymbol{h}}{\partial q_k} \\ \frac{\partial L_f^1 \boldsymbol{h}}{\partial p_k} & \frac{\partial L_f^1 \boldsymbol{h}}{\partial q_k} \end{bmatrix} \tag{12}$$

For such a physical system to be observable (locally, if the system is a nonlinear one) at a point q_0, the rank of the observability matrix $\boldsymbol{O}$ must be $n = 2$.

V. CONTROLLABILITY USING THE DISSIPATIVE CANONICAL EQUATIONS

With the Lie bracket given below

$$[\boldsymbol{f},\boldsymbol{g}] = \left[\frac{\partial \boldsymbol{g}}{\partial p_k} \quad \frac{\partial \boldsymbol{g}}{\partial q_k}\right]\boldsymbol{f} - \left[\frac{\partial \boldsymbol{f}}{\partial p_k} \quad \frac{\partial \boldsymbol{f}}{\partial q_k}\right]\boldsymbol{g} \tag{13}$$

controllability of a physical system modelled by the Hamiltonian *H* together with dissipation function *D*) can be proven, if the controllability matrix $\boldsymbol{Q} = [\boldsymbol{g},[\boldsymbol{f},\boldsymbol{g}]]$has the rank $n = 2$.

VI. EQUILIBRIUM POINTS AND THE STABILITY USING THE EIGENVALUES AND THE LYAPUNOV FUNCTION IN FORM OF A RESIDUAL ENERGY FUNCTION

Equilibrium points for dissipative Hamiltonian systems are obtained using the term below:

$$(\dot{q}_k;\, \dot{p}_k\,) = \left(\frac{\partial H}{\partial p_k}; -\frac{\partial H}{\partial q_k} - \frac{\partial D}{\partial \dot{q}_k}\right) = (0\,;0) \tag{14}$$

The Hamiltonian leads to a system of 2f differential equations of order one compared to the f differential equations of order two obtained through extended Euler-Lagrange differential equations. Its state space form is given in the following:

$$\underbrace{\frac{d}{dt}\begin{bmatrix} q_k \\ p_k \end{bmatrix}}_{\dot{\boldsymbol{x}}} = \underbrace{\begin{bmatrix} 0 & \frac{1}{M_k} \\ -\frac{\partial H}{\partial q_k}\frac{1}{q_k} & -\frac{\partial D}{\partial \dot{q}_k}\frac{1}{p_k} \end{bmatrix}}_{[J]}\underbrace{\begin{bmatrix} q_k \\ p_k \end{bmatrix}}_{\boldsymbol{x}} + \underbrace{\begin{bmatrix} 0 \\ 1 \end{bmatrix}F_k}_{\boldsymbol{g(q)u}}\,;\, M_k, q_k, p_k \neq 0 \quad ;\quad \underbrace{y = q_k}_{\boldsymbol{h(q)}} \tag{15}$$

where $x = [q_k, p_k]^T$ is the vector of the canonical variables, *T* stands for transpose and $[J]$ is the Jacobian of the matrix $[f(q)]$. This is valid for linear and also, for nonlinear systems if the nonlinear terms are linearized in the matrix $[f(q)]$ and written in form of a Jacobian matrix. And the eigenvalues of characteristic equation of the Jacobian matrix are given by the equation

$$c_k(\lambda) = |\lambda[I] - [J]| = \begin{vmatrix} \lambda & -\frac{1}{M_k} \\ \frac{\partial H}{\partial q_k}\frac{1}{q_k} & \lambda + \frac{\partial D}{\partial \dot{q}_k}\frac{1}{p_k} \end{vmatrix} = \lambda^2 + \lambda\frac{\partial D}{\partial \dot{q}_k}\frac{1}{p_k} + \frac{1}{M_k}\frac{\partial H}{\partial q_k}\frac{1}{q_k} = 0 \tag{16}$$

The system is (asymptotically) stable if

$$\left.\begin{aligned} \lambda_1.\lambda_2 &= \frac{1}{M_k}\frac{\partial H}{\partial q_k}\frac{1}{q_k} > 0 \Rightarrow \frac{\partial H}{\partial q_k} > 0 \\ \lambda_1 + \lambda_2 &= -\frac{\partial D}{\partial \dot{q}_k}\frac{1}{p_k} < 0 \Rightarrow -\frac{\partial D}{\partial \dot{q}_k} < 0 \end{aligned}\right\} \Rightarrow \lambda_1 < 0,\ \lambda_2 < 0; \lambda_1 \neq \lambda_2 \tag{17}$$

and marginally stable in case of a lossless system, when the roots are in complex conjugate form:

$$\frac{\partial D}{\partial \dot{q}_k} = 0\,;\ \frac{1}{M_k}\frac{\partial H}{\partial q_k}\frac{1}{q_k} > 0 \Rightarrow \frac{\partial H}{\partial q_k} > 0 \Rightarrow \lambda_{1,2} = \pm j\sqrt{\frac{1}{M_k}\frac{\partial H}{\partial q_k}\frac{1}{q_k}} \tag{18}$$

When the Hamiltonian $H(p_k, q_k)$ together with the generalized velocity proportional (Rayleigh) dissipation function $D(\dot{q}_k)$ is known, then the system can be analyzed for observability, controllability and stability.

If the Jacobian matrix $[J]$covers nonlinear terms through which the eigenvalues can not be found, the Lyapunov function in form of residual energy function can be used for stability.

Since the REF is defined as

$$\mathrm{H} = H - \int \left[\sum_{k=1}^{f} \frac{\partial D(\dot{q}_1, \dot{q}_2, \ldots, \dot{q}_f)}{\partial \dot{q}_k}\dot{q}_k\right] dt \quad ; \quad 0 < \mathrm{H} < \infty\ \forall\, t \in \mathbb{R}_0^+ \tag{19}$$

and the first-time derivative of the REF, is total power, which reads

$$\frac{d\mathrm{H}}{dt} = -\sum_{k=1}^{f} \frac{\partial D(\dot{q}_1, \dot{q}_2, \ldots, \dot{q}_f)}{\partial \dot{q}_k}\dot{q}_k \quad ; \quad 0 < \mathrm{H} < \infty\ \forall\, t \in \mathbb{R}_0^+ \tag{20}$$

VII. OBSERVABILITY, CONTROLLABILITY AND STABILITY ANALYSIS OF VAN DER POL OSCILLATOR USING THE DISSIPATIVE CANONICAL EQUATIONS

A. OBTAINING the {L,D}-MODEL and the EQUATIONS of GENERALIZED MOTION of VAN DER POL OSCILLATOR

In its most general form, the Van der Pol oscillator with a nonlinear damping is a non-conservative dynamical system and the dynamics of the system is governed by the differential equation:

$$\ddot{q} + \mu(q^2 - 1)\dot{q} + q = F \tag{21}$$

which is an important special case of the *Liénard equation*, where the variable q is the time dependent generalized coordinate, F is the external generalized force and the scalar μ is the parameter indicating nonlinearity and also the strength of the damping. Accordingly, if $\mu = 0$, that is no damping, then the case converts to harmonic oscillator which is always conservative. Other cases are:

$$\begin{aligned} \mu > 0 &\Rightarrow \begin{cases} q^2 - 1 > 0 \Rightarrow |q| > 1 : damping\ is\ positive \\ q^2 - 1 < 0 \Rightarrow |q| < 1 : damping\ is\ negative \end{cases} \\ \mu < 0 &\Rightarrow \begin{cases} q^2 - 1 > 0 \Rightarrow |q| > 1 : damping\ is\ negative \\ q^2 - 1 < 0 \Rightarrow |q| < 1 : damping\ is\ positive \end{cases} \end{aligned} \tag{22}$$

Here, we will be interested of positive damping factor μ which will deliver positive or negative damping depending on $|q| > 1$ or $|q| < 1$, where $\mu = 0$ means the non-dissipative case.

In our case, through comparing one obtains

$$\left.\begin{matrix}\ddot{q}+\mu(q^2-1)\dot{q}+q=F\\ \ddot{q}+\frac{R}{M}\dot{q}+\frac{K}{M}q+\frac{C}{M}=\frac{F}{M}\end{matrix}\right\}\begin{cases}\frac{F}{M}=F\Rightarrow M=1\,;\frac{R}{M}=R=\mu(q^2-1)\\ \frac{C}{M}=0\Rightarrow C=0\,;\frac{K}{M}=1\Rightarrow K=M=1\end{cases} \tag{23}$$

The generalized velocity proportional (Rayleigh) dissipation function in this case is:

$$\frac{\partial D(\dot{q},q)}{\partial\dot{q}}=\mu(q^2-1)\dot{q}\Rightarrow D(\dot{q},q)=\frac{\mu(q^2-1)}{2}\dot{q}^2 \tag{24}$$

The related {*L*,*D*}-model with an autonomous Lagrangian L and the related momentum is

$$\{L,D\}=\begin{cases}L=\underbrace{\frac{\dot{q}^2}{2}}_{T(\dot{q})}-\underbrace{\frac{q^2}{2}}_{U(q)}\Rightarrow p=\dot{q}\\ D(q,\dot{q})=\frac{\mu(q^2-1)}{2}\dot{q}^2\end{cases} \tag{25}$$

Here, the generalized velocity proportional (Rayleigh) dissipation function D does not only depend on generalized velocity $\dot{q}$ in form of $D=D(\dot{q})$ but also generalized coordinate in form of $D=D(\dot{q},q)$.

B. LEGENDRE TRANSFORM, HAMILTONIAN H, the EXTENDED HAMILTONIAN H OBTAINING DISSIPATIVE CANONICAL EQUATIONS of VAN DER POL OSCILLATOR and THEIR MATRIX EQUATION FORM

The condition for a Legendre transform is already fulfilled since:

$$\left|\frac{\partial^2 L}{\partial\dot{q}_r\partial\dot{q}_k}\right|=\left|\frac{\partial p_r}{\partial\dot{q}_k}\right|=1\neq 0\ \ ;\ r,k=1 \tag{26}$$

Thus, the related Hamiltonian reads:

$$H(p,q)=\underbrace{\frac{p^2}{2}}_{T(p)}+\underbrace{\frac{q^2}{2}}_{U(q)} \tag{27}$$

The extended Hamiltonian cannot be used here to obtain the dissipative canonical equations directly as the generalized velocity proportional (Rayleigh) dissipation function has the form of $D=D(\dot{q},q)$ and not $D=D(\dot{q})$. And the dissipative canonical equations for this system are

$$\begin{aligned}\dot{q}&=\frac{\partial H}{\partial p}=p\\ \dot{p}&=-\frac{\partial H}{\partial q}-\frac{\partial D}{\partial\dot{q}}=-q-\mu\dot{q}(q^2-1)=-q-\mu p(q^2-1)\end{aligned} \tag{28}$$

The dissipative canonical equations in state space form for Van der Pol oscillator can be rewritten in form of a matrix equation including generalized external force as follows:

$$\underbrace{\frac{d}{dt}\begin{bmatrix}q\\p\end{bmatrix}}_{\dot{\boldsymbol{x}}} = \underbrace{\begin{bmatrix}p\\-q-\mu p(q^2-1)\end{bmatrix}}_{\boldsymbol{f}(\boldsymbol{q})} + \underbrace{\begin{bmatrix}0\\1\end{bmatrix}F}_{\boldsymbol{g}(\boldsymbol{q})\boldsymbol{u}} \; ; \; \underbrace{y=q}_{\boldsymbol{h}(\boldsymbol{q})} \tag{29}$$

C. OBSERVABILITY USING the DISSIPATIVE CANONICAL EQUATIONS of the VAN DER POL OSCILLATOR

The Lie derivatives of $\boldsymbol{h}$ with respect to $\boldsymbol{f}$ are

$$L_{\boldsymbol{f}}^{0}\boldsymbol{h} = \boldsymbol{h}(\boldsymbol{q}) = q \; ; \; \boldsymbol{\nabla h}(\boldsymbol{q}) = [0 \quad 1] \tag{30}$$

Accordingly;

$$L_{\boldsymbol{f}}^{1}\boldsymbol{h} = [0 \quad 1]\begin{bmatrix}p\\-q-\mu p(q^2-1)\end{bmatrix} = -q-\mu p(q^2-1) \tag{31}$$

The vector of all Lie derivatives and its multiplication with $\boldsymbol{\nabla}$ are for the case is

$$\boldsymbol{G} = \begin{bmatrix}L_{\boldsymbol{f}}^{0}\boldsymbol{h} & L_{\boldsymbol{f}}^{1}\boldsymbol{h}\end{bmatrix} \Rightarrow \boldsymbol{\nabla G} = \begin{bmatrix}0 & 1\\-\mu(q^2-1) & -1-2\mu pq\end{bmatrix} \tag{32}$$

And the determinant of which has rank two, when

$$\mu(q^2-1) \neq 0 \Rightarrow q \neq \pm 1 \tag{33}$$

i.e. the system is (locally) observable everywhere except the points $|q| = 1$.

D. CONTROLLABDLDTY USING THE DISSIPATIVE CANONICAL EQUATIONS of the VAN DER POL OSCILLATOR

Calculating the Lie brackets yields here:

$$[\boldsymbol{f},\boldsymbol{g}] = [0 \quad 0]\begin{bmatrix}p\\-q-\mu p(q^2-1)\end{bmatrix} - \begin{bmatrix}1 & 0\\-\mu(q^2-1) & -1-2\mu pq\end{bmatrix}\begin{bmatrix}0\\1\end{bmatrix} = \begin{bmatrix}0\\1+2\mu pq\end{bmatrix} \tag{34}$$

Hence the controllability matrix $\boldsymbol{Q}$ is in the form

$$\boldsymbol{Q} = [\boldsymbol{g},[\boldsymbol{f},\boldsymbol{g}]] = \begin{bmatrix}0 & 0\\1 & 1+2\mu pq\end{bmatrix} \tag{35}$$

$\boldsymbol{Q}$ has rank zero, implying that, this system is not controllable.

E. EQUILIBRIUM POINTS and the STABILITY USING the EIGENVALUES of the VAN DER POL OSCILLATOR and its LYAPUNOV FUNCTION in FORM of a RESIDUAL ENERGY FUNCTION

Equilibria condition for such a dissipative Hamiltonian system in general is

$$(\dot{q};\dot{p}) = \left(\frac{\partial H}{\partial p}; -\frac{\partial H}{\partial q} - \frac{\partial D}{\partial \dot{q}}\right) = (0\,;0) \tag{36}$$

Therefore, equilibrium points are:

$$\begin{aligned} &\dot{q} = 0 \Rightarrow p = 0 \\ &\dot{p} = -q - \mu p(q^2 - 1) = 0 \Rightarrow p = -\frac{q}{\mu(q^2 - 1)} = 0 \Rightarrow q = 0 \end{aligned} \tag{37}$$

The state space equation related the dissipative canonical equations of Van der Pol equation can be written as:

$$\underbrace{\frac{d}{dt}\begin{bmatrix} q \\ p \end{bmatrix}}_{\dot{x}} = \underbrace{\begin{bmatrix} 0 & 1 \\ -1 & -\mu(q^2 - 1) \end{bmatrix}}_{[J]} \underbrace{\begin{bmatrix} q \\ p \end{bmatrix}}_{x} + \begin{bmatrix} 0 \\ 1 \end{bmatrix} F \quad ; \quad \underbrace{y = q}_{h(q)} \tag{38}$$

Using Jacobian matrix $[J]$ of the system and its eigenvalues, stability of the equilibrium points can be understood better. With the characteristic equation, results can be obtained as follows:

$$|\lambda[\mathrm{I}] - [J]| = \begin{vmatrix} \lambda & -1 \\ 1 & \lambda + \mu(q^2 - 1) \end{vmatrix} = \lambda^2 + \lambda\mu(q^2 - 1) + 1 = 0 \tag{39}$$

The (asymptotic) stability is proven when

$$\left.\begin{aligned} &\lambda_1\lambda_2 = 1 \\ &\lambda_1 + \lambda_2 = -\mu(q^2 - 1) < 0 \Rightarrow |q| > 1 \end{aligned}\right\} \Rightarrow \lambda_1 < 0 \; ; \; \lambda_2 < 0 \tag{40}$$

The characteristic equation for the equilibrium point $q = 0$ is

$$\lambda^2 + \lambda\mu(q^2 - 1) + 1|_{q=0} = \lambda^2 - \lambda\mu + 1 = 0 \Rightarrow \left\{\begin{matrix} \lambda_1\lambda_2 = 1 \\ \lambda_1 + \lambda_2 = \mu \end{matrix}\right\} \Rightarrow \lambda_1 > 0 \; ; \; \lambda_2 > 0 \tag{41}$$

Thus, the equilibrium point $q = 0$ is unstable.
Lyapunov function in form of a residual energy function, that must be positive definite, is

$$\mathrm{H} = \frac{p^2}{2} + \frac{q^2}{2} - \int \mu(q^2 - 1)\dot{q}^2 \, dt \tag{42}$$

with the first-time derivative

$$\dot{\mathrm{H}}(p_k, q^k) = -\mu(q^2 - 1)\dot{q}^2 \tag{43}$$

which must be in negative semidefinite form to ensure stability and fulfill the following condition:

$$-\mu(q^2 - 1)\dot{q}^2 \leq 0 \tag{44}$$

where equality means marginal while less means asymptotic stability. Accordingly, one obtains the result satisfying the Eq.(44)

$$\dot{q} \in \mathbb{R} \Rightarrow \dot{q}^2 \geq 0 \quad ; \quad q^2 - 1 \geq 0 \Rightarrow |q| \geq 1 \tag{45}$$

And as such the regions with border lines $|q| \geq 1$ in phase space are stable regions while the region $|q| < 1$ is unstable.

VIII. CONCLUSIONS

It was demonstrated that for a Van der Pol oscillator/equation as a nonlinear system, when {L,D}-model and thus Hamiltonian are known, then the system can be analyzed by means of observability, controllability and stability using the approach which was performed for the first time in order to Van der pol oscillator/equation in general here. Moreover, stability analysis can also be performed using Lyapunov function as residual energy function. As can be seen that this kind of Lyapunov function is constructed using Hamiltonian and dissipative function together for linear and also nonlinear systems. This kind of analysis method is valid for every linear and nonlinear system where kinetic, potential energies and (generalized velocity proportional) Rayleigh dissipation functions are involved. It can also be applied specially to coupled engineering/physical systems, where different physical quantities are available, with no need to convert the physical quantities to the other.

IX. REFERENCES

[1] Van der Pol, B., "A theory of the amplitude of free and forced triode vibrations," *Radio Review (later Wireless World)*, 1, pp. 701–710, 1920.

[2] Van der Pol, B., "Relaxation-oscillations," *The London, Edinburgh, and Dublin Philosophical Magazine and Journal of Science* 2.11, pp. 978–992, 1926.

[3] Van der Pol, B., Van Der Mark, J., "Frequency demultiplicationi" *Nature* 120.3019,pp. 363-364, 1927.

[4] Cartwbight, M. L., "Balthazar van der Pol*," Journal of the London Mathematical Society*, s1-35 (3): 367–376, 1989.

[5] Guckenheimer, J., Holmes, P., *Nonlinear oscillations, dynamical systems, and bifurcations of vector fields*, Springer Book Archive-Mathematics, 1997.

[6] Thompson, J. M. T., Stewart, H. B., *Nonlinear Dynamics and Chaos*, John Wiley, 2002.

[7] Ott, E., *Chaos in dynamical systems*, Cambridge university press, 2002.

[8] Wiggins, S., *Introduction to Applied Nonlinear Dynamical Systems and Chaos*, 2nd ed., Springer, 2003.

[9] Cartwright, J.H.E., Eguíluz V.M., Hernández-García E., Piro O.," Dynamics of Elastic Excitable Media," *International Journal of Bifurcation and Chaos*, 9.11:2197–2202, 1999.

[10] Arnold, V. I., *Mathematical methods of classical mechanics*,Graduate texts in mathematics, Springer,1989.

[11] Goldstein, H., *Classical Mechanics*, Addision-Wesley, pp. 11-16, 1980.

[12] Heil, M., Kitzka, F., *Grundkurs Theoretische Mechanik*, 1984.

[13] Suesse, R., Civelek, C., "Analysis of engineering systems by means of Lagrange and Hamilton formalisms depending on contravariant, covariant tensorial variables," *Forschung im Ingenieurwesen-Engineering Research*, 68, pp. 63-74, 2003.

[14] Suesse, R., Civelek, C., "Analysis of coupled dissipative dynamic systems of engineering using extended Hamiltonian for classical and nonconservative Hamiltonian H∗ n for higher order Lagrangian systems," *Forschung im Ingenieurwesen* 77.1-2, pp. 1-11, 2013.

[15] Civelek, C.,"Stability analysis of engineering/physical dynamic systems using residual energy function," *Archives of Control Sciences*, 2018.

[16] Huijberts, H., Nijmeijer, H., *Controllability and observability of nonlinear systems."Control Systems, Robotics, and Automation*, by Unbehauen, H. - Vol. XII –Encyclopedia of Life Support Systems, Eolss Publishers, Oxford, 2009.

[17] Hedrick, J.K., Girard, A. (2015, December 23). *Control of Nonlinear Dynamic Systems*, [Online]. Available: https://www.researchgate.net/publication/290128700_Control_of_nonlinear_dynamic_systems_theory and_applications

[18] Civelek, C., Suesse, R., "Physical system analysis related to observability, controllability and stability using its equations of generalized motion and canonical equations both in dissipative forms," *Journal of the Brazilian Society of Mechanical Sciences and Engineering* 44.7, pp.302, 2022.

[19] Civelek, C., "Observability, controllability and stability of a nonlinear RLC circuit in form of a Duffing oscillator by means of theoretical mechanical approach," *Journal of Electrical Engineering* 73.2, pp. 140-145, 2022.

Düzce University
Journal of Science & Technology

Review Article

Foam Concrete And Surfactants

Nuri IŞILDAR [a,*]

[a] *Natural and Industrial Building Materials R&A Center,Suleyman Demirel University, Isparta, TURKEY*
* *Corresponding author's e-mail address: nuriisildar@sdu.edu.tr*
DOI: 10.29130/dubited.1513320

ABSTRACT

Lightweight concrete types have gained attention today due to their diverse range of applications. Cellular concretes such as aerated concrete and foam concrete hold a significant place in the construction sector due to their sustainability and recyclability. These materials stand out for their high efficiency, offering properties such as thermal insulation and fire resistance. In particular, pore size and distribution in foam concrete are among the most critical factors determining the mechanical strength and insulation performance of the material. In this context, understanding the chemical composition and properties of the foaming agent in detail is essential for achieving the desired performance. Surface-active agents, known as surfactants, are important components widely used in foam concrete production. The correct selection and application methods of surfactant types are crucial for ensuring that the concrete achieves its targeted properties. This study aims to examine the characteristics of various surfactants and contribute to meeting the desired performance criteria in foam concrete production.

Keywords: *Foam concrete, Foaming agent, Surfactant*

Köpük Beton ve Surfaktanlar

ÖZ

Hafif beton türleri, günümüzde çeşitli kullanım alanlarıyla dikkat çekmektedir. Gaz beton ve köpük beton gibi hücresel betonlar, sürdürülebilirlik ve geri dönüştürülebilirlik özellikleriyle yapı sektöründe önemli bir yere sahiptir. Bu malzemeler, ısı yalıtımı ve yanmazlık gibi yüksek verimlilik sunan özellikleriyle öne çıkmaktadır. Özellikle köpük betonda, gözenek boyutu ve dağılımı, betonun mekanik dayanımı ve yalıtım performansını belirleyen en kritik faktörler arasında yer almaktadır. Bu bağlamda, kullanılan köpük ajanının kimyasal yapısı ve özelliklerinin ayrıntılı olarak bilinmesi, istenilen performansın elde edilmesi için zorunludur. Yüzey aktif maddeler, diğer adıyla surfaktanlar, köpük beton üretiminde yaygın olarak kullanılan önemli bileşenlerdir. Surfaktan türlerinin doğru seçimi ve uygulama yöntemleri, betonun hedeflenen nitelikleri kazanması açısından büyük öneme sahiptir. Bu araştırmada, farklı surfaktanların özellikleri ele alınarak, köpük betonun arzu edilen performans kriterlerini sağlamasına yönelik katkılar sunulması hedeflenmiştir.

Anahtar Kelimeler: *Köpük beton, Köpük ajanı, Yüzey aktif madde*

Received: 09/07/2024, Revised: 16/11/2024, Accepted: 17/11/2024

I. INTRODUCTION

In the context of enhancing the insulation properties of lightweight concrete, the use of different components and methods is quite common. Minor differences in the components and curing methods can have significant effects on strength and insulation. One of the essential components of cellular concrete is foaming agents, primarily used to achieve porosity. Accordingly, there are numerous studies that involve the use of foaming agents with different origins and other specific properties [1], [2], [3], [4].

Comparative studies on the effects of foaming agents on foam concrete properties are extremely limited. In these studies, the foaming agents are mostly identified only by their commercial names, whether they are synthetic or natural, their usage amounts, and sometimes their densities. Therefore, there are challenges in comparing and evaluating the effectiveness of different foaming agents whose compositions and properties are not fully known. Sahu and Gandhi highlight that different foam formers lead to variations in the void structure of concrete, and they emphasize that there are fundamentally opposing results regarding the effects of natural and synthetic surfactants on foam stability, pore size, and compressive strength [5].

The primary materials used as foaming agents in foam concrete are surfactants, also known as surface-active agents. Therefore, recognizing surfactants and understanding their mechanisms of action on foam concrete properties are considered essential.

II. SURFACTANTS

Surfactants are surface-active agents composed of special types of molecules that reduce the surface tension (interfacial tension) between two liquids or between a liquid and a solid/gas, containing both lyophilic and lyophobic groups. Surfactants have a wide range of applications; they are used in products like shampoos, detergents, and other cleaning agents, as well as in cosmetic products such as creams, lotions, and perfumes. Additionally, they find use in lightweight concrete, paint, paper, ink, plastics, fibers, agricultural chemicals, food, and especially the oil industry, among other areas.

In conditions where the fluid is mostly water, the terms hydrophilic and hydrophobic are used instead of lyophilic and lyophobic for the polar head group and the tail parts of the molecule that prefer the non-polar environment, respectively. The primary classification of surfactants depends on the charge state of their hydrophilic groups and includes anionic, cationic, zwitterionic (amphoteric), and non-ionic surfactants [6]. Ionic surfactants with cationic (positively charged head group) characteristics often contain functional groups with nitrogen, such as amines and quaternary ammonium salts, while anionic (negatively charged head group) surfactants contain functional groups like carboxylate, sulfate, sulfonate, and phosphate. Zwitterionic surfactants, often referred to as amphoteric or ampholytic, typically have a positively charged ammonium or imidazolium group and a negatively charged carboxylate, sulfonate, sulfate, or phosphate group [7]. Non-ionic surfactants, which have little or no electrical interaction between the head groups, usually have hydrophilic groups made up of polyoxyethylene, glycerol, and sorbitol [8].

In aqueous solutions, surfactants can exist in monomolecular or supramolecular structures depending on their concentration [8]. The formation and shapes of supramolecular micelles are closely related to the type of surfactant, its concentration, and the chemical properties of the solution [10].

According to Porter, the chain length of hydrophobic groups is a determining factor for the solubility, adsorption, and surface-active efficiency of surfactants in water [11]. Surfactants with a chain length of 10-18 carbons exhibit low solubility and maximum surface-active properties, while those with a chain length of less than 8 carbons show increased solubility but weaker surface-active properties. In contrast, those with a chain length greater than 18 carbons demonstrate these properties at a minimum level [12].

Surfactants are classified as natural or synthetic based on their sources. According to Hayes and Smith, the main components of biologically derived surfactants include fatty acyl groups (derived from oilseeds, animal fats, and derivatives like fatty alcohols and amines), carbohydrates, proteins, extractive substances, and some biorefinery by-products [13]. The breakdown of proteins from animal sources (such as casein, blood, keratin, fish scales, and other animal carcass waste) into smaller hydrophobic molecules through peptide bond cleavage leads to decreased surface tension, interfacial formation, and the development of hydrogen bonds between molecular groups and air bubbles [14]. Boruah and Gogoi have listed common natural plant-based surfactant sources, including soapbark (Quillaja saponaria), chickpeas (Cicer arientinum), alfalfa (Medicago sativa), oats (Avena sativa), pepper (Piper nigrum), tea (Camellia assamica), spinach (Spinacia oleracea), and yucca (Yucca schidigera), attributing their surface-active properties to the presence of saponins [15].

A. SURFACTANTS AS FOAMING AGENTS

Foam is a structure in which bubbles of gas are separated by membranes in a liquid environment. Foam agents are additives that promote the formation of more foam bubbles by reducing surface tension [16]. The increase in surface viscosity due to the adsorption of the surfactant at the air-liquid interface weakens the drainage between the bubbles, contributing to the thinning of the bubble film and thus reducing bubble coalescence. In foam concrete studies, the most commonly used foam agents are synthetic and protein-based [17], [18], [19], [20], [21], [2], [22], [23], [24], although composite [25], [12], aluminum powder, hydrogen peroxide, detergents, adhesive resins, and saponins [26] have also been observed to be used (Table 1).

The evaluation of surfactants as potential foaming agents depends on their foam capacity, density, stability, dilution ratio, production pressure, and cost-effectiveness. For determining the required foam volume for the desired foam concrete density, it is necessary to know the foam capacity, which is the volumetric foam amount that can be produced per unit amount of surfactant, and the foam density. Foam stability is determined by the time it takes for the foam to revert to its original liquid and gas phases, or in other words, the drainage time [27]. Processes such as gravity-liquid flow, capillarity-liquid suction, gas-liquid interface shear stresses, and coalescence and expansion, which can occur simultaneously, affect foam drainage [28].

B. SURFACTANTS AND THEIR EFFECTS ON FOAM CONCRETE

It has been observed that certain properties such as CMC (Critical Micelle Concentration) and viscosity, which are highly influential on the properties of foam concrete, are provided very limitedly in Table 1 regarding foam agents.

Table 1. *Foaming Agents Used in Some Studies on Foam Concrete Production and Their Characteristics*

Foaming Agents	**Origins**	**Dilution Rate**	**Foam Density**	**Density**	**pH**	**Viscosity**	**CMC**	
AYDOS-LİGHTCON 25-28	Synthetic			+	+			[67]
FOAMCRETE 10K	Synthetic							[68]
İKSA FOAM–AD	Synthetic			+	+			[69]
MİLOFOAM	Plant							[70]
Biosaponeks	Saponin							[71]
NANO	Plant							[72]
ROGEN	Polymer							[73]
GENFİL	Organic		+	+				
GENOCELL	Organic			+				[74]
BETAFOAM CLC	Protein							
Dodecyl trimethyl ammonium bromide		+	+					[44]
Hexadecyl trimethyl ammonium bromide							+	[33]

Table 1 (cont). *Foaming Agents Used in Some Studies on Foam Concrete Production and Their Characteristics*

Trimethyl tetradecyl ammonium bromide							+	
Cetyl trimethyl ammonium bromide		+						[57]
Octylphenol ethoxylate		+						
Lauryl alcohol ethoxylate					+		+	[75]
Sodium Lauryl Sulfate	Synthetic	+						[17]
								[76], [27],[1]
		+			+			[48]
		+					+	[29]
Sodium Laureth Sulfate	Synthetic							[1], [55]
					+			[20]
		+	+	+	+			[77],[78]
		+			+			[48]
Sodium dodecyl sulphate	Synthetic	+	+					[18]
								[4],[20],[79]
					+		+	[75]
		+						[57]
		+					+	[31]
Sodium dodecyl benzene sulfanate	Synthetic							[80],[4],[81],[1]
Sodium alcohol ether sulphate		+			+			[48]
		+	+					[44]
Sodium alpha-olefin sulfanate	Synthetic				+			[54],[82],[16]
								[4]
				+			+	[20]
								[21]
		+			+			[48]
							+	[33]
BENOTEH PB-C	Synthetic							[2],[83]
PİONEER PG	Synthetic							[2]
PENTA SURFACTANT 430A	Synthetic						+	[36]
PENOSTROM	Synthetic			+	+		+	
H_2O_2								[84],[81],[85], [86]
MİCROAİR	PEG Faty acid							[80]
								[4]
PB-LUKS	Synthetic			+	+			[87]
FOAMTEK	Synthetic	+	+	+	+			[77],[78]
	Synthetic	+	+					[88]
SY-F30 (Plant + Animal-Based)	Composite	+						[3]
LASTON	Protein							[2]
FOAMSEM	Protein			+	+	+		[23]
PİONEER BIO	Protein							[2]
FOAMİN	Protein	+	+	+	+			[77], [78]
NORAITE PA-1	Protein	+	+					[89],[90],[91], [92],[93]
TEGO Betain F 50)	Organic Coconut Oil							[94]
Vinsol Resin	Organic Pine Tree							[80]
Kokodietanolamid	Coconut Oil							[1]
Cocoamidopromil betaine		+						[44]
FA-1		+		+	+			[95]

Table 1 (cont). *Foaming Agents Used in Some Studies on Foam Concrete Production and Their Characteristics*

Micro Air 210 (Alkyl Ether Sulphate)								[76]
Nonyl Phenol Ethoxylate		+						[17]
Alkyl Ethoxy Sulphate					+			[16], [82]
Rosin Malate					+			[54]
BİOPORE							+	[36]
Pb-2000							+	
Oleic Acid								[76]
EABASSOC		+	+	+	+			[96],[97]
		+	+					[98]
AREKOM							+	[36]
Polyurethane			+					[99]
	Protein		+					[22]
	Protein	+						[57]
	Protein							[100]
	Protein	+	+					[101]
	Protein		+					[102]
	Protein Hemoglobin							[103]
	Protein Enzymatic							[104]
	Protein Collagen				+			[51]
	Protein Antibacterial Enzyme			+				[24]
	Protein	+	+	+	+	+		[19]
	Protein	+	+					[105]
	Organic	+	+					[106]
	Organic	+	+					[107]
	Synthetic		+					[56]
	Synthetic							[108]
				+	+			[45]
	Detergent							[95]
	Plant Soap			+	+			[16], [82]
	Fe-protein			+	+			[54],[16],[82]
		+						[109]
	Natural							[108]
	Plant		+					[56]
	Animal-Based		+					
	Synthetic	+	+	+	+			[19]

B.1. Critical Micelle Concentration (CMC)

The critical micelle concentration (CMC) of a surfactant corresponds to the concentration above which there is insufficient space for adsorption due to monomolecular adsorption being completed, leading to the formation of multiple micelles. If surfactants are above their CMC in solution, they may enter the dispersed phase in limited quantities or migrate to the water-air interface, and excess surfactant molecules will form micelles [29].

Surfactant effectiveness, which is a function of the interface concentration causing a decrease in surface tension, is influenced by factors such as the chemical structure of the surfactant, solution ionic strength and ion types, particles, the ratio of CMC to C20 (the concentration required to reduce the surface tension of the solution by 20 mN/m), pH, temperature, and others. Generally, an increase in surfactant concentration improves foaming until reaching CMC, beyond which further increases do not contribute to foam production. Furthermore, an increase in surfactant hydrophobicity enhances adsorption at the interface, thereby improving foaming, but excessively high hydrophobicity can lead to a surfactant film

that is too rigid or insoluble, thereby reducing foaming [30]. Indeed, Johnson et al. reported that sodium dodecyl sulfate with the same CMC as a commercial dishwashing surfactant required 10 times the CMC for optimal foam formation, and further increases resulted in a decrease in foam mass [31].

Feneuil et al. noted that higher yield stress values in cement paste increase foam stabilization; in the context of the adsorption of most surfactants on cement particles and their concentration-dependent effects on the yield stress of cement paste, an increase in interparticle hydrophobic attractive forces increases yield stress, which rapidly weakens beyond the threshold concentration, leading to a significant decrease in yield stress [32]. CMC is generally indicated as an appropriate concentration for foam stability [33]. However, Kuzielová et al. mentioned that surfactant concentration is also among the factors affecting foam stability, with different opinions on whether it should be lower or higher than the critical micelle concentration (CMC) for optimal concentration [34]. In a study where they used a protein-based surfactant at normal and low (1.4% and 0.7% w/w, respectively) concentrations, they evaluated that the low concentration surfactant increased foam stability and accelerated hydration without significant differences compared to normal concentration, which was much higher than CMC.

Tran et al. emphasize that selecting a concentration equal to or below the CMC value is crucial for foam stability [35]. In a study where concentrations of 300, 600, 1000, and 2000 ppm of sodium dodecyl sulfate were used below the CMC value (~2500 ppm), it was shown that at higher concentrations of surfactant (2000 ppm), the increased coalescence and agglomeration were due to the hardening of cell walls resisting drainage and increasing the curvature of intermediate films with smaller bubble sizes. On the other hand, in another study where different foam agents were used at mass ratios of 0.5-5% (Biopore, PB-2000, Arekom, Penta Surfactant 430A, and Penostrom), it was noted that Penta Surfactant 430A and Penostrom caused a greater decrease in surface tension compared to others, thereby improving micelle formation conditions. Additionally, considering foam concrete strength, Penta Surfactant 430A at 2.6% of CMC was deemed appropriate [36].

B.2. Viscosity

Viscosity resulting from the collision of particles flowing at different velocities within a liquid increases as the particle count increases [37]. The addition of high viscosity achieved through the inclusion of surfactants used in foam creation or certain additives reduces system drainage, leading to higher internal pressure in bubbles and thus formation of smaller, stable bubbles [12], [5], [38]. This enhances the performance of foam concrete [39]. Recent studies frequently encounter materials such as nano-silica and hydroxypropyl methylcellulose [40], nano-alumina [41], starch [42], carboxymethyl cellulose [43], nano-silica and nano-calcium carbonate [44], and xanthan gum [45], [46], used as foam stabilizers, each with varying mechanisms of action.

In a study optimizing the extraction process of surfactants from two different natural sources (protein-based sesame seeds and saponin-based hingot fruit), research focused on fundamental properties such as initial foam density, foam stability, bubble size, and surfactant viscosity. Increasing the heating temperature from 50°C to 100°C and extending the duration from 3 hours to 10 hours resulted in increases of 45% and 29%, respectively, in surfactant viscosity, while causing decreases in initial foam density, foam drainage, and bubble size. It was noted that the concentration of NaOH used for protein hydrolysis in sesame seeds had little effect on the examined properties [47].

In another study investigating the effects of xanthan gum on the properties and stability of different surfactants (Hingot- natural saponin-based and Nonylphenol ethoxylate- nonionic synthetic) and the resulting changes in foam concrete's setting behavior, compressive strength, and thermal conductivity [46], it was found that xanthan gum caused a tenfold increase in viscosity for both surfactants but did not lead to significant changes in surface tension. The increase in viscosity was evaluated to decrease bubble size and increase lamellar thickness, indicating the effectiveness of the xanthan gum-Hingot combination, which resulted in a 51% increase in compressive strength. Decreases in thermal conductivity were attributed to reductions in pore size caused by xanthan gum.

A study on nano-silica and nano-calcium carbonate, with an average particle size of 50 nm, investigated their effects on foam properties and stabilization mechanisms with anionic (sodium alcohol ether sulfate), cationic (dodecyl trimethyl ammonium bromide), and amphoteric (liquid cocoamidopropyl betaine) surfactants, as well as their impacts on foam concrete properties. The study concluded that increasing nanoparticle content led to increased foam density for all surfactants, while reducing foam formation times and water release amounts. Positively charged nanoparticles could bind to anionic and amphoteric molecules at the gas-liquid interface, reducing gas-liquid contact area and internal gas flow, thereby stabilizing foams. Nano-calcium carbonate was found more effective in reducing fluidity and increasing foam concrete viscosity, thereby enhancing foam concrete strength. It was also observed that nanoparticles dispersed in the foam liquid film altered the Ca and Si content of foam concrete pore wall surfaces, affecting hydration product formation and surface microstructure.

This research highlights the diverse effects of different additives and surfactants on foam properties and the performance of foam concrete.

B.3. pH

The type and charge of surfactants, as well as the pH of the foam solution, play a crucial role in foam stability. It is known that the attachment of positively or negatively charged ionic surfactants to the surface of air bubbles increases foam stability due to electrostatic repulsion [29]. It has been reported that zwitterionic surfactants exhibit optimal foaming properties at alkaline pH levels [12], while in another study using anionic surfactants (sodium lauryl sulfate, alpha olefin sulfonate, sodium lauryl ether sulfate, and sodium alcohol ether sulfate) with pH values of 6.7, 6.6, 6.7, and 6.8 respectively, alpha olefin sulfonate provided better gains in mechanical, transport, and microstructural properties of anionic lightweight concrete. Additionally, it was noted that the scope of the study was not sufficient for evaluations related to potential effects of non-ionic or mixed surfactants [48].

Composite protein surfactants have been found to be more effective than other used rosins, dodecyl, and lauric acids in reducing surface tension or increasing bubble film strength, thereby achieving more stable bubbles. For pH values of 7.9, 8.2, 8.0, and 8.1, composite protein, resin, dodecyl, and lauric acid exhibited foaming rates of 22.1%, 29.6%, 33.3%, and 42.5%, bubble film resistances of 682.5, 340.8, 321.6, and 305.4 Pa, and minimum stable bubble radii of 0.17, 0.21, 0.21, and 0.27 mm, respectively [49]. On the other hand, in a study examining foam stability by adjusting the pH of composite foam-forming agents (sodium α-alkenyl sulfonate, sodium dodecyl sulfate, coconut oil, liquid resin with foam stabilizers hydroxypropyl methylcellulose ether, xanthan gum, and sucrose) to a range of 11-14 using diluted NaOH solution, a foaming coefficient of 41, settlement distance of 1 hour, and zero bleeding rate were determined, with the foam maintaining stability for 2 hours but beginning to deteriorate once the pH exceeded 12.4 [39]. Another study compared nano-alumina modified surfactants and $Ca(OH)_2$ as foam stabilizers adjusted to pH 9, 11, and 12.5 with deionized water applications. For deionized water and the mentioned pH levels, viscosities were determined as 0.248, 0.263, 0.235, and 0.200 PaS, and bubble wall thicknesses were 39.25, 49.52, 33.30, and 26.05 μm, respectively. It was noted that the reaction of alumina-$Ca(OH)_2$ on the surface delayed bubble disproportionation and fusion, thereby preventing drainage and enhancing foam stability, ultimately achieving a finer and more homogeneous pore structure for improved performance of foam concrete [50].

The relationship between foam yield and pH in protein-based surfactants is quite specific. The highest foam yield is typically obtained near the isoelectric point pH, varying across a wide pH range for different surfactants. Generally, an increase in pH enhances foaming [51]. However, under very high alkaline conditions, the reduced solubility of protein particles in water makes them less suitable for foaming [52]. In cementitious mixtures, the foaming behaviors of 13 proteins were examined in deionized water and a synthetic pore solution (0.1062 M KOH, 0.0489 M Na_2SO_4, 0.037 M K_2SO_4, and 0.0212 M $Ca(OH)_2$ - pH ~13.6). It was evaluated that the high pH of the pore solution increased foaming, bubble film roughness, and thickness, indicating improved foam stability [53].

B.4. Foam Shape and Size Distribution

In foamed concrete, pore sizes are generally classified into three size ranges based on different standards and methods: gel pores (<10 nm), capillary pores (10-10,000 nm), and macro pores (10,000-100,000 nm, including entrained and entrapped air pores). The foam bubbles obtained with foaming agents are mostly spherical, and the pores of the foamed concrete used exhibit spherical or nearly spherical, ellipsoidal, or irregular structures. The high concentration of foaming agent increases the number and distribution of bubbles. Additionally, the properties of the liquid film separating the bubbles vary depending on the type of surfactant. Bubble size is related to bubble stability and shape.

Spherical, small-diameter bubbles with good distribution enhance foam stability. Due to the inverse proportionality of the pressure difference between the inside and outside of the bubble to the bubble radius and direct proportionality to surface tension, smaller bubbles have a higher curvature radius than larger bubbles [54]. Differences in curvature radius between adjacent air bubbles lead to pressure differences, which disrupt bubbles if they exceed the surface tension of the cement paste [55].

Studies on the effects of different types of surfactants on foam bubble size and foam concrete porosity are actively ongoing. Microstructure analysis using X-CT and bubble analysis apparatus has shown that synthetic surfactants lead to smaller pore sizes, a narrower range of pore sizes, and smaller pore connections [56]. In a study using sodium dodecyl sulfate (anionic), cetyltrimethyl ammonium bromide (cationic), octyl phenol ethoxylate (nonionic), and protein-based (amphoteric) surfactants, it was found that the size distribution of bubbles in foams larger than 300 μm undergoes a complex change over time, initially increasing and then decreasing. It was also reported that the type of charge of the surfactant affects adsorption and stabilizes the foam due to decreased gas transfer, and as particles harden, the process of pore formation occurs [57].

Some studies also observe the use of composite surfactants or certain additives. A combination of anionic and non-ionic (neutral) surfactants was found to reduce the maximum pore diameter from 1.84 mm to 1.49 mm and increase strength by 25%, compared to using only anionic surfactants. It was evaluated that most anionic surfactants are adsorbed onto positively charged areas of cement particles, leading to excessive migration from the air-liquid interface and compromising foam stability [58]. In another study evaluating the performance of foam produced using sodium lauryl sulfate and nonylphenol ethoxylate surfactants with the additive sodium carboxymethyl cellulose, it was noted that increasing surfactant and additive concentrations led to the formation of smaller foam bubbles, resulting in a 24-44% decrease in average air void diameter and a 29-37% increase in compressive strength of concrete [5]. Xiong et al. used nano-Al_2O_3 to adjust viscosity for stabilizing foam and methyl cellulose to enhance foam stability for a synthetic surfactant containing CH_3 as a hydrophobic group and -COOH as a hydrophilic group [59]. In another study, foam concrete with different densities (398, 460, 580, and 759 kg/m^3) was produced using a polymer composite foam agent, and pore sizes and distributions from nanometer to micron levels were determined using nuclear magnetic resonance. It was evaluated that increasing density reduced micro-pore sizes and increased compressive strength and thermal conductivity [60].

B.5. Density

Foam density plays a critical role in calculating the necessary foam volume required to achieve the desired density of foam concrete [27]. According to ASTM C796/C796M standard, the recommended unit volume mass for foam concrete ranges from 30 to 65 kg/m³ [61]. This range can be adjusted based on recommendations from manufacturers depending on the foaming agent used, chemical additives, and foam generator. Additionally, it is emphasized that foam density depends on various factors such as the type of surfactant [62], surfactant concentration [27], additives [17], lamellar thickness [63], foam production pressure [1], and viscosity of the foam solution.

The bubbles within the foam are surrounded by a liquid layer called lamellae. The thickness of these lamellae and the properties of the liquid within them significantly influence the overall properties of the foam [12]. Generally, high-density foams have thicker lamellar layers compared to low-density foams. Therefore, as the thickness of the lamellar film around the bubbles increases, the stability of the foam also increases. Researchers argue that synthetic foaming agents tend to expand more compared to protein-based foaming agents, resulting in lower density [64].

Therefore, when using low-density foams in foam concrete production, it is recommended to add foam thickening agents to increase foam density. Researchers have added various additives such as carboxymethyl cellulose [17], sodium hydroxide, sodium carbonate, and sodium chloride to increase the viscosity of the foam solution and thereby improve foam density and concrete properties [12].

It has been found that starch nanoparticles modified with hydrophobicity through citric acid, in combination with synthetic surfactants containing hydrophilic and hydrophobic groups, increased foam density from 21 kg/m^3 to 69 kg/m^3 and viscosity from 0.135 to 0.189 PaS. Additionally, the compressive strength after 28 days of curing increased from 2.35 MPa to 2.77 MPa. These changes were attributed to the uniform adsorption of hydrophobic starch nanoparticles on foam surfaces and their use in filling inter-pore spaces between foam-cement matrix [42]. A similar approach was demonstrated by Xiong et al., aiming to prepare ultra-stable foam using thionyl chloride ($SOCl_2$) treatment and nano-alumina (NA) modification, utilizing vegetable (PS) and animal protein (AS) based and synthetic surfactants (SS) with similar functional groups [41]. Indeed, the addition of nano-alumina increased foam densities for vegetable, animal, and synthetic surfactants from 18, 21, and 19 kg/m^3 to 22, 24, and 76 kg/m^3 respectively. The differences in drainage reductions of 4%, 5%, and 11% respectively in 5 minutes were attributed to the homogeneous and discrete distribution of nano-alumina, where homogeneous distribution increased interfacial resistance and consequently delayed drainage further. On the other hand, the hydration product of $Ca(OH)_2$ - nano-alumina pozzolanic reaction was evaluated to fill cell wall pores, thereby enhancing the performance (mechanical strength, drying shrinkage, and homogeneity) of foam concrete.

III. CONCLUSION

In studies on foam concrete, the limited provision of foam agent characteristics such as only commercial names, whether they are synthetic or natural, their usage amounts, and densities makes it difficult to evaluate the findings obtained [65]. Furthermore, even when the same foam agent is used, variations in dilution ratio, shaping process, air pressure, addition to mortar, and mixing process can lead to changes in the properties of foam concrete. Therefore, this situation underscores the key role of foam quality in foam concrete properties.

Natural surfactants are reported to be 60-70% cheaper than synthetic surfactants, and their high medical values, along with antimicrobial and antibacterial properties against microorganisms, have made them an indispensable part of human life [15]. Yang et al., evaluated a foam agent (SJ-2) derived from fruits of certain natural plants such as Chinese soapberry, whose main chemical component is triterpenoid saponin. They examined its effects on the workability, permeability, air bubbles, strength, freeze/thaw resistance, etc., of fresh and hardened concrete, comparing it with Vinsol resin and abietic soap concrete. The agent was considered a high-quality air-entraining agent based on these evaluations [66].

In related studies, it is suggested that instead of synthetic surfactants, whose exact contents are often undisclosed and widely used, there would be benefit in exploring the comparative use of natural surfactants as part of sustainability efforts.

IV. REFERENCES

[1] Ranjani, I. S., Ramamurthy, K.. "Relative assessment of density and stability of foam produced with four synthetic surfactants," *Materials and structures*, 4310, 1317-1325, 2010.

[2] Prishepa, I.A. Shangin, S.N. KurmangalievIn, R.M. "Vliyaniye Modifitsiruyushchikh Dobavok Na Svoystva Penoobrazovateley Tsementnykh Kompozitsiy", *Ix Mezhdunarodnaya Konferentsiya Studentov I Molodykh Uchenykh*, Perspektivy Razvitiya Fundamental'nykh Nauk. 2012

[3] Xingjun, L., Mingli, C., Yan, L., Xin, L., Qian, L., Rong, T., Yuping, D., "A new absorbing foam concrete: preparation and microwave absorbing properties," *Advances in concrete construction*, vol. 3, no. 2, pp. 103-111, 2015.

[4] Gao, L., "Experimental study of the effect of chemical additives on mechanical properties of foamed concrete," *Functional materials*, vol. 26, no. 4, pp. 802-806, 2019.

[5] Sahu, S. S., and Gandhi, I. S. R., "Studies on influence of characteristics of surfactant and foam on foam concrete behaviour," *Journal of Building Engineering*, vol. 40, pp. 1-16, 2021.

[6] Kronberg, B., Holmberg, K., and Lindman, B., "Types of surfactants, their synthesis, and applications," *Surface Chemistry of Surfactants and Polymers*, pp. 1-47, 2014.

[7] Gerola, A. P., Costa, P. F., Quina, F. H., Fiedler, H. D., and Nome, F., "Zwitterionic surfactants in ion binding and catalysis," *Current opinion in colloid & interface science*, vol. 32, pp. 39-47, 2017.

[8] Nakama, Y., *Cosmetic Science and Technology Theoretical Principles and Applications*. Kanagawa, Japan, Elsevier, 2017, Chapter 15 - Surfactants, pp. 231-244.

[9] Mokaya, R. (Robert A. Meyers (Ed)), *Encyclopedia of Physical Science and Technology*, Third Edition, California, U.S., Academic Press Inc., 2003, Mesoporous Materials Synthesis and Properties, pp. 369-381.

[10] Middleton, J. M., Siefert, R. L., Markie'Sha, H. J., Schrand, A. M., and Kolel-Veetil, M. K., "Micelle formation, structures, and metrology of functional metal nanoparticle compositions," *AIMS Materials Science*, vol. 8, no. 4, pp. 560-586, 2021.

[11] Porter, M.R., *Handbook of Surfactants*. Cardiff, UK, Springer, 2013, pp. IX-227.

[12] Sahu, S. S., Gandhi, I. S. R., Khwairakpam, S., "State-of-the-art review on the characteristics of surfactants and foam from foam concrete perspective," *Journal of The Institution of Engineers* India: Series A, vol. 99, pp. 391-405, 2018.

[13] Hayes, D. G., and Smith, G. A.. *Biobased surfactants*, Champaign, USA, Aocs Press, 2019, ch. 1, pp. 3-38.

[14] Panesar, D. K., "Cellular concrete properties and the effect of synthetic and protein foaming agents", *Construction and building materials*, vol. 44, pp. 575-584, 2013.

[15] Bulbul Boruah, B. B., and Minti Gogoi, M. G., "Plant based natural surfactants". *Asian Journal of Home Science*, vol. 8, no. 2, pp. 759-762, 2013.

[16] Kim, J. M., Jeong, J. Y., "Influence of foaming agents on the properties of foamed concretes having various densities," *한국건축시공학회지*, vol.12, no. 1, pp. 22-30, 2012.

[17] Colak, A., "Density and strength characteristics of foamed gypsum," *Cement and Concrete Composites*, vol.22, no. 3, pp.193-200, 2000.

[18] Hajimohammadi, A., Ngo, T., Mendis, P., Kashani, A., and van Deventer, J. S., "Alkali activated slag foams: the effect of the alkali reaction on foam characteristics," *Journal Of Cleaner Production*, vol. 147, pp. 330-339, 2017.

[19] Ghorbani, S., Sharifi, S., de Brito, J., Ghorbani, S., Jalayer, M. A., and Tavakkolizadeh, M., "Using statistical analysis and laboratory testing to evaluate the effect of magnetized water on the stability of foaming agents and foam concrete," *Construction and Building Materials*, vol. 207, pp. 28-40, 2019.

[20] He, J., Gao, Q., Song, X., Bu, X., He, J. "Effect of foaming agent on physical and mechanical properties of alkali-activated slag foamed concrete," *Construction and Building Materials*, vol. 226, pp. 280-287, 2019.

[21] Senff, L., Novais, R. M., Carvalheiras, J., Labrincha, J. A., "Eco-friendly approach to enhance the mechanical performance of geopolymer foams: Using glass fibre waste coming from wind blade production,"*Construction and Building Materials*, vol. 239, pp. 1-11, 2020.

[22] Davraz, M., Kilinçarslan, Ş., Koru, M., Tuzlak, F., "Investigation of relationships between ultrasonic pulse velocity and thermal conductivity coefficient in foam concretes," *Acta Physica Polonica* A, vol. 130 no. 1, pp. 469-470, 2016.

[23] Mestnikov, A., Semenov, S., Strokova, V., Nelubova, V., "Autoclave Foam Concrete: Structure and Properties," *In Aıp Conference Proceedings*, vol. 1698, no. 1, pp. 1-6, 2016.

[24] Oren, O. H., Gholampour, A., Gencel, O., Ozbakkaloglu, T., "Physical and mechanical properties of foam concretes containing granulated blast furnace slag as fine aggregate," *Construction and Building Materials*, vol. 238, pp. 1-9, 2020.

[25] Ai, L., "Construction method of the new thermal insulation material foam concrete," 6th *International Conference on Management, Education, Information and Control*, 2016, pp. 408-412.

[26] Chica, L., Alzate, A., "Cellular concrete review: New trends for application in construction," *Construction and Building Materials*, vol. 200, pp. 637-647, 2019.

[27] Ranjani, G., Ramamurthy, K.,"Analysis of the foam generated using surfactant sodium lauryl sulfate," *International Journal of Concrete Structures and Materials*, vol. 4, no.1, pp. 55-62, 2010.

[28] Lioumbas, J. S., Georgiou, E., Kostoglou, M., and Karapantsios, T. D., "Foam free drainage and bubbles size for surfactant concentrations below the CMC," *Colloids and Surfaces A: Physicochemical and Engineering Aspects*, vol. 487, pp. 92-103, 2015.

[29] Souza, M. T., Maykot, C. K., Araújo, A. C. Z., Raupp-Pereira, F., and de Oliveira, A. N., "Electrolytes' influence on foamability and foam stability of cement suspensions," *Construction and Building Materials*, vol 157, pp. 363-371, 2017.

[30] Tunstall, L. E., Ley, M. T., and Scherer, G. W., "Air entraining admixtures: Mechanisms, evaluations, and interactions," *Cement and Concrete Research*, vol. 150, pp. 1-25, 2021.

[31] Johnson, P., Vaccaro, M., Starov, V., and Trybala, A., "Foam formation and interaction with porous media," *Coatings*, vol. 10, pp. 1-16, 2020.

[32] Feneuil, B., Pitois, O., and Roussel, N., "Effect of surfactants on the yield stress of cement paste," *Cement and Concrete Research*, vol. 100, pp. 32-39, 2017.

[33] Mortada, N., Phelipot-Mardele, A., & Lanos, C. "Effects of surfactants on aqueous foams properties: a step towards mineral foams". *European Journal of Environmental and Civil Engineering*, vol. 26, no. 14, pp. 7307-7318, 2022.

[34] Kuzielová, E., Pach, L., and Palou, M., "Effect of activated foaming agent on the foam concrete properties," *Construction and Building Materials*, vol. 125, pp. 998-1004, 2016.

[35] Tran, N. P., Nguyen, T. N., Ngo, T. D., Le, P. K., and Le, T. A., "Strategic progress in foam stabilisation towards high-performance foam concrete for building sustainability: A state-of-the-art review," *Journal of Cleaner Production*, vol. 375, pp. 1-27. 2022.

[36] Gorbach, P., Shcherbin, S., and Savenkov, A., "The method of selecting a foaming agent and its concentration in the production of non-autoclaved hard cellular concrete", In *MATEC Web of Conferences*, vol. 212, no. 01004, pp. 1-5, 2018.

[37] Boddepalli, U., Gandhi, I. S. R., and Panda, B., "Stability of three-dimensional printable foam concrete as function of surfactant characteristics," *Frontiers of Structural and Civil Engineering*, vol. 17, no. 6, pp. 935-947, 2023.

[38] Falliano, D., Restuccia, L., and Gugliandolo, E., "A simple optimized foam generator and a study on peculiar aspects concerning foams and foamed concrete". *Construction and Building Materials*, vol. 268, pp.1-16, 2021.

[39] He, J., Liu, G., Sang, G., He, J., and Wu, Y., "Investigation on foam stability of multi-component composite foaming agent," *Construction and Building Materials*, vol. 391, pp. 1-15, 2023.

[40] She, W., Du, Y., Miao, C., Liu, J., Zhao, G., Jiang, J., and Zhang, Y., "Application of organic- and nanoparticle-modified foams in foamed concrete: Reinforcement and stabilization mechanisms," *Cement and Concrete Research*, vol. 106, pp. 12-22, 2018.

[41] Xiong, Y., Zhu, Y., Chen, C., and Zhang, Y., "Effect of nano-alumina modified foaming agents on properties of foamed concrete," *Construction and Building Materials*, vol. 267, pp. 1-13, 2021.

[42] Song, N., Li, Z., Yi, W., and Wang, S., "Properties of foam concrete with hydrophobic starch nanoparticles as foam stabilizer," *Journal of Building Engineering*, vol. 56, pp. 1-12, 2022.

[43] Sahu, S. S., Ranjani Gandhi, I. S., Kumar, A., and Garg, S., "Evaluation of suitability of carboxymethyl cellulose in performance improvement of sodium lauryl sulfate foam and compressive strength of foam concrete," *Advances in Civil Engineering Materials*, vol. 10, no. 1, pp. 74-92, 2021.

[44] Jiang, L., Wang, Z., Gao, X., Cui, M., Yang, Q., and Qin, J., "Effect of nanoparticles and surfactants on properties and microstructures of foam and foamed concrete," *Construction and Building Materials*, vol. 411, pp.1-12, 2024.

[45] Zhu, H., Chen, L., Xu, J., and Han, Q., "Experimental study on performance improvement of anionic surfactant foaming agent by xanthan gum," *Construction and Building Materials*, vol. 230, pp. 1-8, 2020.

[46] Wagh, C. D., and Gandhi, I. S. R., "Investigations on the performance of xanthan gum as a foam stabilizer and assessment of economic and environmental impacts of foam concrete production," *Journal of Building Engineering*, vol. 82, pp. 1-23, 2024.

[47] Khwairakpam, S., Gandhi, I. S. R., and Wagh, C., "Investigations on Optimization of Extraction Process of Surfactant from Hingot Fruit (Balanites aegyptiaca) and Sesame Seed (Sesamum indicum) and Its Suitability in Foam Concrete Production," *Arabian Journal for Science and Engineering*, vol. 48, no. 10, pp. 14119-14152, 2023.

[48] Maglad, A. M., Mydin, M. A. O., Datta, S. D., Abbood, I. S., and Tayeh, B. A., "Impact of anionic surfactant-based foaming agents on the properties of lightweight foamed concrete," *Construction and Building Materials*, vol. 438, pp. 1-16, 2024.

[49] Xiao, M., Li, F., Yang, P., Li, B., Wei, J., and Yu, Q. "Influence of slurry characteristics on the bubble stability in foamed concrete," *Journal of Building Engineering*, vol. 71, pp. 1-12, 2023.

[50] Yuanliang, X., Baoliang, L., Chun, C., and Yamei, Z., "Properties of foamed concrete with Ca (OH)2 as foam stabilizer". *Cement and Concrete Composites*, vol. 118, pp. 1-11, 2021.

[51] Montayev, S. A., Shakeshev, B. T., Ryskaliyev, M. Z., Adilova, N. B., Narikov, K. A., "Collagen agent technology for foam concrete production," *ARPN J. Eng. Appl. Sci*, vol. 12, no. 5, pp. 1674-1678, 2017.

[52] Cai, J., Zhang, G., Xie, Z., Zhu, Y. "Preparation of foaming agent from photosynthetic bacteria liquid by direct thermal alkaline treatment," *Construction and Building Materials*, vol. 238, pp. 1-8, 2020.

[53] Masoule, M. S. T., Baffoe, E., and Ghahremaninezhad, A., "On the physicochemical properties and foaming characteristics of proteins in cement environment," *Construction and Building Materials*, vol. 366, pp. 1-17, 2023.

[54] Kim, J. M., Kwak, E. G., Oh, K. C., Kang, C.,"Properties of bubble according to types and concentrations of concrete foaming agent," *Journal of the Korea concrete institute*, vol. 232, pp. 151-158, 2011.

[55] Sang, G., Zhu, Y., Yang, G., Zhang, H., "Preparation and characterization of high porosity cement-based foam materia," *Construction and Building Materials*, vol. 91, pp. 133-137, 2015.

[56] Sun, C., Zhu, Y., Guo, J., Zhang, Y., Sun, G., "Effects of foaming agent type on the workability, drying shrinkage, frost resistance and pore distribution of foamed concrete," *Construction and Building Materials*, vol. 186, pp. 833-839, 2018.

[57] Zhang, M., Li, J., Bian, P., Gao, P., Guo, B., Zhan, B., and Yu, Q., "Investigation of the evolutionary behavior and stabilization mechanism of foams with different properties in cement paste," *Construction and Building Materials*, vol. 426, pp. 1-13, 2024.

[58] Kashani, A., Ngo, T. D., Nguyen, T. N., Hajimohammadi, A., Sinaie, S., and Mendis, P., "The effects of surfactants on properties of lightweight concrete foam," *Magazine of concrete research*, vol. 72, no. 4, pp.163-172, 2020.

[59] Xiong, Y., Hu, Z., Jia, Z., Liu, C., Ma, L., and Liu, Z., "Effect of formic acid as an accelerator on foam-stability, compressive strength, and pore size distribution of foam concrete," *Journal of Building Engineering*, vol. 66, pp. 1-11, 2023.

[60] Bie, Y., Ba, S., and Chen, S., "Studies on foamed concrete micropores and their effects on stress distribution and heat conduction," *Journal of Building Engineering*, vol. 87, pp. 1-11, 2024.

[61] Standard Test Method for Foaming Agents for Use in Producing Cellular Concrete Using Preformed Foam, ASTM C796/C796M, 2019.

[62] Hamad, A. J., "Materials, production, properties and application of aerated lightweight concrete," *International journal of materials science and engineering*, vol.2, no. 2, pp. 152-157, 2014.

[63] M. Krzan, "Rheology of the wet surfactant foams and biofoams-a review," *Tech. Trans. Chem*. 1-Ch, pp. 9–27, 2013.

[64] Amran, Y., Farzadnia, N., Ali, A., "Properties and applications of foamed concrete; a review," *Constr. Build. Mater*. vol. 101, pp. 990–1005, 2015.

[65] Brady, K. C., Watts, G. R. A., and Jones, M. R., "Specification for foamed concrete," Crowthorne, UK: TRL Limited, 2001, pp. 1-78.

[66] Yang, Q., Zhu, P., Wu, X., Huang, S., "Properties of concrete with a new type of saponin air-entraining agent," *Cement and Concrete Research*, vol. 308, pp. 1313-1317, 2000.

[67] Aydos Chemical Industry and Trade Inc. (Jul. 10, 2023), *Köpük Ajanı* [Online]. Available: https://www.aydos.com.tr/tr/urunler/kopuk-ajani.

[68] Draco. (Jul. 10, 2023). *Foam Concrete*, [Online]. Available: https://www.draco.com.tr/FOAMCRETE-i354.

[69] Iksa Constructıon Addıtıves Industry and Trade Inc. (2022). Accessed: Oct. 03, 2022 [Online]. Available: http://www.iksa.com.tr/pdf/bkk1.pdf.

[70] Milonga Inc. (2022) Accessed: Oct. 03, 2022 [Online]. Available: https://milohafifbeton.com/?gclid=EAIaIQobChMIvMnpzN7gIVESwYCh3glQjeEAAYASAAEgKhdvD_BwE.

[71] Biosaponeks. (Jun. 10, 2024), *Uygulamalar*. [Online]. Available: https://biosaponeks.com.tr/tr/ uygulamalar.html.

[72] Nanohb. (Mar. 05, 2024) *Köpük Ajanı.* [Online].https://www.nanohbt.com/kopuk-ajani.html.

[73] Artra Construction. Landscape Plastic Inc. (Oct. 10, 2022) [Online]. Available: http://www.artrainsaat.com.

[74] Fatsa Chemical Industry and Trade Inc. (Oct. 10, 2022). *Hafif Köpük Beton Ajanı* [Online]. Available: https://www.fatsakimya.com/kategori/hafif-kopuk-beton-ajani/

[75] Emami, H., Ayatizadeh Tanha, A., Khaksar Manshad, A., and Mohammadi, A. H., "Experimental investigation of foam flooding using anionic and nonionic surfactants: A screening scenario to assess the effects of salinity and ph on foam stability and foam height," *ACS omega*, vol. 7, no. 17, pp. 14832-14847, 2022.

[76] Esmaily, H., Nuranian, H., "Non-autoclaved high strength cellular concrete from alkali activated slag," *Construction and Building Materials*, vol. 26, no. 1, pp. 200-206, 2012.

[77] Falliano, D., De Domenico, D., Ricciardi, G., Gugliandolo, E., "Key factors affecting the compressive strength of foamed concrete," In *IOP Conference Series: Materials Science and Engineering*, vol. 431, no. 6, pp. 1-8, 2018.

[78] Falliano, D., De Domenico, D., Ricciardi, G., Gugliandolo, E., "Experimental investigation on the compressive strength of foamed concrete: Effect of curing conditions, cement type, foaming agent and dry density," *Construction and Building Materials*, vol. 165, pp. 735-749, 2018.

[79] Wang, X., Huang, J., Dai, S., Ma, B., Jiang, Q., "Investigation of silica fume as foam cell stabilizer for foamed concrete," *Construction and Building Materials*, vol. 237, pp. 1-12, 2020.

[80] Stencel, J. M., Song, H., Cangialosi, F., "Automated foam index test: Quantifying air entraining agent addition and interactions with fly ash–cement admixtures," *Cement and Concrete Research*, vol. 39, no. 4, pp. 362-370, 2009.

[81] Pan, Z., Li, H., Liu, W., "Preparation and characterization of super low density foamed concrete from Portland cement and admixtures," *Construction and Building Materials*, vol. 72, pp. 256-261, 2014.

[82] Kim, J. M., Jeong, J. Y., Hwang, E. H., Shin, S. C., "Properties of foamed concrete according to types and concentrations of foam agent," *Journal of the Korea concrete institute*, vol. 24, no. 1, pp. 61-70, 2012.

[83] Kudyakov, A. I., Kopanitsa, N. O., Sarkisov, J. S., Kasatkina, A. V., Prischepa, I. A., "Foam concrete of increased strength with the thermomodified peat additives," In *IOP Conference Series: Materials Science and Engineering*, vol. 71, no. 1, pp. 1-7, 2015.

[84] Liu, R., Ouyang, P., Yang, Y., Qi, W., "Relationship Between FreezeThaw Resistance and AirVoid Characteristics of Foam Concrete with Hydrogen Peroxide as Foaming Agent," *Journal of The Chinese Ceramic Society*, vol. 428, no. 8, pp. 1055-1063, 2014.

[85] Łach, M., Korniejenko, K., Mikuła, J., "Thermal insulation and thermally resistant materials made of geopolymer foams," *Procedia Eng*, vol. 151, pp. 410-416, 2016.

[86] Samson, G., Cyr, M., "Porous structure optimisation of flash-calcined metakaolin/fly ash geopolymer foam concrete," *European Journal of Environmental and Civil Engineering*, vol. 22, no. 12, pp.1482-1498, 2018.

[87] Steshenko, A., Kudyakov, A., Konusheva, V., Syrkin, O., "Structure formation control of foam concrete," In *AIP Conference Proceedings* vol. 1800, no. 1, pp. 1-8, 2017.

[88] Batool, F., Bindiganavile, V., "Fresh properties of fiber reinforced cement-based foam with Pozzolans," *Iranian Journal of Science and Technology*, Transactions of Civil Engineering, vol. 44, pp 253-264, 2020.

[89] Othuman, M. A., Wang, Y. C., "Elevated-temperature thermal properties of lightweight foamed concrete," *Construction and Building Materials*, vol. 25, no. 2, pp. 705-716, 2011.

[90] Awang, H., Mydin, M. A. O., Roslan, A. F., "Effect of additives on mechanical and thermal properties of lightweight foamed concrete," *Advances in applied science research*, vol. 3, no. 5, pp. 3326-3338, 2012.

[91] Awang, H., Mydin, M. A. O., Roslan, A. F., "Mıcrostructural ınvestıgatıon of lıghtweıght foamed concrete ıncorporatıng varıous addıtıves," *International Journal of Academic Research*, vol. 4, no. 2, pp. 196-200, 2012.

[92] Mydin, M. A. O., Wang, Y. C., "Mechanical properties of foamed concrete exposed to high temperatures," *Construction and Building Materials*, vol. 26, no. 1, pp. 638-654, 2012.

[93] Roslan, A. F., Awang, H., Mydin, M. A. O., " Effects of various additives on drying shrinkage, compressive and flexural strength of lightweight foamed concrete LFC," *In Advanced Materials Research*, vol. 626, pp. 594-604. 2013.

[94] Krämer, C., Schauerte, M., Kowald, T. L., Trettin, R. H., "Three-phase-foams for foam concrete application," *Materials Characterization*, vol. 102, pp. 173-179, 2015.

[95] Waheed, A., Arshid, M. U., Mehboob, S., Ahmed, A., Sultan, T., "Preparation of Low-Cost Foam Concrete Using Detergent," *Technical Journal*, vol. 24, no. 4, pp. 1-7, 2019.

[96] Hilal, A. A., Thom, N. H., Dawson, A. R., "On void structure and strength of foamed concrete made without/with additives," *Construction and Building Materials*, vol. 85, pp. 157-164, 2015.

[97] Hilal, A. A., Thom, N. H., Dawson, A. R., "On entrained pore size distribution of foamed concrete," *Construction and Building Materials*, vol. 75, pp. 227-233, 2015.

[98] Van, L. T., Kim, D. V., Xuan, H. N., Tho, V. D., Bulgakov, B. I., Alexandrova, O. V., "Modelling of the effect of the water-cement ratios on properties foam concrete," *In Journal of Physics: Conference Series* Vol. 1425, No. 1, pp. 1-9, 2019.

[99] Harith, I. K., " Study on polyurethane foamed concrete for use in structural applications," *Case studies in construction materials*, vol. 8, pp. 79-86, 2018.

[100] Long, W. W., Wang, J. S., "Study on compressive strength and moisture content of different grades density of foam concrete," In *2015 International Conference on Material Science and Applications (ICMSA-15)*, 2014, pp. 167-172 .

[101] Bing, C., Zhen, W., Ning, L., "Experimental research on properties of high-strength foamed concrete," *Journal of materials in civil engineering*, vol. 24, no. 1, pp. 113-118, 2012.

[102] Wei, S., Yiqiang, C., Yunsheng, Z., Jones, M. R., "Characterization and simulation of microstructure and thermal properties of foamed concrete," *Construction and building materials*, vol. 47, pp. 1278-1291, 2013.

[103] Remadnia, A., Dheilly, R. M., Laidoudi, B., Quéneudec, M., "Use of animal proteins as foaming agent in cementitious concrete composites manufactured with recycled PET aggregates," *Construction and Building Materials*, vol. 23, no. 10, pp. 3118-3123, 2009.

[104] Yang, K. H., Lee, K. H., Song, J. K., Gong, M. H., "Properties and sustainability of alkali-activated slag foamed concrete," *Journal of Cleaner Production*, vol. 68, pp. 226-233, 2014.

[105] Kilincarslan, Ş., Davraz, M., Akça, M., "The effect of pumice as aggregate on the mechanical and thermal properties of foam concrete", *Arabian Journal of Geosciences*, vol. 11, no. 289, 2018.

[106] Nambiar, E. K., Ramamurthy, K., "Shrinkage behavior of foam concrete," *Journal of materials in civil engineering*, vol. 21, no. 11, pp. 631-636. 2009.

[107] Dayalan, J., "Experimental Study on Properties of Light Weight Foam Concrete," *International Research Journal of Engineering and Technology IRJET*, vol.06, no. 5, 2019.

[108] Varghese, S., Ashok, A. M., Joseph, A. K., Emmanuel, S., Swathylekshmi, O. V., "A study on properties of foamed concrete with natural and synthetic foaming agent,"*International Research Journal of Engineering and Technology*, vol. 4, no. 3, pp. 2009-2011, 2017.

[109] Akthar, F. K., Evans, J. R. G., " High porosity (> 90%) cementitious foams", *Cement and Concrete Research*, vol. 40, no. 2, pp. 352-358, 2010.

Düzce University
Journal of Science & Technology

Research Article

Visible Digital Image Watermarking Using Single Candidate Optimizer

Harun AKBULUT [a,*]

[a] *Department of Computer Engineering, Faculty of Engineering and Architecture, Nevsehir Haci Bektas Veli University, Nevşehir, TURKIYE*
** Corresponding author's e-mail address: harun.akbulut@nevsehir.edu.tr*
DOI: 10.29130/dubited.1532300

ABSTRACT

With the advent of internet technologies, accessing information has become remarkably facile, while concurrently precipitating copyright conundrums. This predicament can be ameliorated by embedding copyright information within digital images, a methodology termed digital image watermarking. Artificial intelligence optimization algorithms are extensively employed in myriad problem-solving scenarios, yielding efficacious outcomes. This study proposes a visible digital image watermarking method utilizing the Single Candidate Optimizer (SCO). Contrary to many prevalent metaheuristic optimization algorithms, SCO, introduced in 2024, is not population-based. The fitness function of SCO is designed to maximize the resemblance between the watermarked image and both the host and watermark images. Experiments were conducted on images commonly utilized in image processing, and the results were evaluated using eight quality metrics. Additionally, the obtained numerical results were juxtaposed with those from well-known and widely-used genetic algorithms, differential evolution algorithms, and artificial bee colony optimization algorithms. The findings demonstrate that SCO outperforms the others in visible digital image watermarking. Furthermore, due to its non-population-based nature, SCO is significantly faster compared to its counterparts.

Keywords: *Single candidate optimizer, Digital image watermarking, Metaheuristic optimization algorithms*

Tek Aday Optimizasyon Algoritması Kullanarak Görünür Dijital Resim Damgalama

ÖZ

İnternet teknolojilerinin gelişmesiyle birlikte bilgiye erişim çok kolay hale gelirken diğer taraftan telif hakkı problemini ortaya çıkarmıştır. Bu problem dijital resimlerin içerisine telif hakkı ile ilgili bilgi gömerek çözülebilmektedir. Bu yöntemlere dijital resim damgalama denir. Yapay zeka optimizasyon algoritmaları bir çok problem çözümünde kullanılmakta ve etkili sonuçlar vermektedir. Bu çalışmada Single candidate optimizer (SCO) kullanarak görünür dijital görüntü damgalama yöntemi önerilir. 2024 yılında önerilen SCO, bir çok yaygın meta-sezgisel optimizasyon algoritmasının aksine popülasyon tabanlı değildir. SCO'nun amaç fonksiyonu olarak damgalanmış görüntünün hem barındırıcı hem de damga görüntüsü ile benzerliğini maksimize eden fonksiyon kullanılır. Deneyler görüntü işlemede yaygın kullanılan görüntülere uygulanmış ve sekiz adet kalite metriği kullanılarak sonuçlar değerlendirilmiştir. Ayrıca elde edilen sayısal sonuçlar iyi bilinen ve yaygın kullanılan genetik algoritma, diferansiyel gelişim algoritması ve yapay arı kolonisi optimizasyon algoritmaları ile karşılaştırılmıştır. Elde edilen bulgular SCO'nun görünür dijital görüntü damgalama için diğerlerinden daha iyi sonuç verdiğini göstermiştir. Ayrıca SCO'nun popülasyon tabanlı olmadığı için diğerlerine göre çok daha hızlı sonuç verdiği görülmüştür.

Received: 12/08/2024, Revised: 07/10/2024, Accepted: 20/11/2024

Anahtar Kelimeler: *Tek aday optimizasyon algoritması, dijital resim damgalama, meta-sezgisel optimizasyon algoritmaları*

I. INTRODUCTION

With the rapid advancement of information technologies, digital images, films, audio, and multimedia applications have become inextricable constituents of our quotidian existence, concomitantly engendering copyright dilemmas due to facile access to digital data. In recent years, scholars have devised digital watermarking techniques to ameliorate the copyright conundrums associated with digital content. Digital watermarking can be delineated as a method for embedding copyright data within the structure of digital content without compromising its integrity. This technique is prevalently employed for safeguarding the copyright of digital images. The process of embedding data within digital images can be executed either at the pixel level or in the frequency domain via various transformation methods. Moreover, digital watermarking can be classified into visible and invisible categories, contingent upon whether the embedded data is perceptible or not. Visible digital watermarking is characterized by the amalgamation of the host image and the watermark, necessitating that the watermark not only encapsulates maximal information from the host image but also retains its clarity while exhibiting robustness against potential attacks [1].

Scholars have propounded an array of watermarking-based methodologies to address challenges such as security, perceptibility, capacity, intricacy, and resilience. These methodologies can be fundamentally categorized into two distinct classes: spatial domain and frequency domain. In the former, the watermarked image is generated through a series of operations performed on individual pixels or pixel groups. In contrast, the latter approach involves manipulating the frequencies obtained within the transformation domain to produce the watermarked image. While the first method is characterized by its low computational cost and considerable robustness, the latter entails a higher computational burden. Moreover, in the second method, any error introduced during the manipulation of the combination coefficients during watermarking can propagate across the entire image, potentially resulting in an artificial watermarked image [1-2].

Single-domain approaches often fail to achieve satisfactory performance, necessitating the integration of multiple digital watermarking techniques to enhance efficacy. Anand et al. [3] introduced a dual watermarking method to bolster the security of COVID-19 patients, embedding both a logo and patient information to reinforce the integrity and authenticity of CT images. Roy et al. [4] developed a DCT-SVD hybrid watermarking technique aimed at copyright protection, wherein the scrambled watermark is embedded within DCT coefficient blocks, demonstrating superior robustness and high imperceptibility in simulations. Abdulrahman et al. [5] devised a color image watermarking system utilizing a DCT-DWT hybrid to ensure copyright protection. Additionally, an efficient block-based color image watermarking method embeds the watermark logo into the principal component to mitigate the false positive problem.

Numerous meta-heuristic algorithms have been extensively utilized in the literature to ascertain the optimal value of the multiple embedding factors. Darwish et al. [6] proposed a GA-based approach to integrate both sequential and segmented watermarking, utilizing the GA to identify suitable locations within the cover image. The dual watermarks are embedded into the YCbCr color channel via the Walsh-Hadamard Transform (WHT), significantly enhancing watermarking capacity and rendering the technique impervious to image manipulation attacks. Mittal et al. [7] employed an exponential k-best GSA (eKGSA) to determine optimal thresholds for multi-level image segmentation. Wang et al. [8] implemented a hierarchical gravity search algorithm to mitigate premature convergence and enhance search capacity. Rawal et al. [9] devised a fast convergent GSA, accelerating convergence and exploitation through a sigmoidal function and exponential step size. Additionally, Mittal et al. [10] introduced an advanced GSA, known as Intelligent GSA (IGSA), to improve convergence precision.

Aslantaş et al. [11] proposed a novel robust image watermarking technique based on the Discrete Cosine Transform (DCT) utilizing the Genetic Algorithm (GA). The GA was employed to optimize the mid-band frequency coefficients, and the proposed method demonstrated commendable efficacy. Zhang et al. [12] presented a watermarking method based on Curvelet and Arnold transforms, employing GA for optimizing threshold values to enhance the resilience of the watermarked image. Jagadeesh, and associates [13] developed an improved image watermarking technique grounded in Singular Value Decomposition (SVD) using GA. The GA was utilized to optimize the quantization step size, and the proposed method was shown to be more secure and robust against attacks such as low-pass filtering, median filtering, image compression, and resizing.

As previously mentioned, artificial intelligence optimization algorithms are employed in image watermarking methods and in solving a multitude of problems [14-17], yielding effective results. In this study, a visible digital image watermarking method is proposed utilizing the SCO, a non-population-based approach, in contrast to other meta-heuristic optimization algorithms suggested in 2024. The contributions of this work to the literature can be delineated as follows:

- The implementation of SCO, a relatively novel technique for visible digital image watermarking.
- The objective quality assessment of the watermarked images is conducted using eight quality metrics that are prevalently employed in the literature.
- The evaluation of the watermarked images also incorporates subjective assessment.
- A comparative analysis is undertaken with widely recognized and utilized meta-heuristic optimization algorithms, namely, Genetic Algorithm (GA), Differential Evolution (DE), and Artificial Bee Colony (ABC).

II. OPTIMIZED DIGITAL IMAGE WATERMARKING

A. SINGLE CANDIDATE OPTIMIZER (SCO)

The Single Candidate Optimizer (SCO) [18], proposed by Shami et al. in 2024, eschews the population-based method of traditional metaheuristic optimization algorithms, opting instead for a solitary candidate approach. This method updates the position of a single candidate, resulting in markedly accelerated solutions compared to its population-based counterparts. SCO employs a biphasic strategy to balance exploration and exploitation. In the initial phase, candidate solution positions are updated using Equation 1.

$$x_j = \begin{Bmatrix} gbest_j + (w|gbest_j|)\ if\ r_1 < 0.5 \\ gbest_j - (w|gbest_j|)\ otherwise \end{Bmatrix} \quad (1)$$

Here, r_1 is a randomly generated value between [0, 1].
In the second phase, SCO explores the vicinity of the best position obtained in the first phase, thereby identifying superior positions via Equation 2.

$$x_j = \begin{Bmatrix} gbest_j + ((r_2 w(ub_j - lb_j))\ if\ r_2 < 0.5 \\ gbest_j - ((r_2 w(ub_j - lb_j))\ otherwise \end{Bmatrix} \quad (2)$$

Here, r_2 is randomly generated value between [0, 1]. ub_j and lb_j denote the upper and lower bounds, respectively. w is the parameter that provides the balance between exploration and exploitation. w is obtained using Equation 3.

$$w^t = exp^{-\left(\frac{bt}{T}\right)^b} \quad (3)$$

Here, b is a constant, t is the current iteration number, and T is the maximum iteration number.

A principal challenge in metaheuristic optimization algorithms is their propensity to become ensnared in local optimum. To mitigate this issue, SCO leverages Equation 4.

$$x_j = \begin{Bmatrix} gbest_j + ((r_3(ub_j - lb_j))\ if\ r_3 < 0.5 \\ gbest_j - ((r_3(ub_j - lb_j))\ otherwise \end{Bmatrix} \quad (4)$$

Here, r_3 is randomly generated value between [0, 1].

Occasionally, problem boundaries may be transgressed, necessitating the application of normalization via Equation 5.

$$x_j = \begin{Bmatrix} gbest_j\ if x_j > ub_j \\ gbest_j\ if x_j < lb_j \end{Bmatrix} \quad (5)$$

SCO initiates the problem-solving process by generating a random solution, then iteratively updates the candidate's positions to converge upon an optimal solution. The initial candidate solution generation in SCO is calculated using Equation 6.

$$x_j = lb_j + r_4(ub_j - lb_j) \quad (6)$$

Subsequently, position updates are performed throughout the iterations using Equations 1 and 2. The newly obtained position is evaluated using the fitness function, and if it surpasses the known best solution, it is updated as the new optimal position. This process persists until the maximum iteration count, T, is reached. The fundamental steps of SCO are delineated in Algorithm 1.

Algorithm 1 Pseudo Code of SCO

```
Set c=0, p=0 and define the values of a and m
Generate the initial candidate solution using Eq (6) and calculate  fitness f(gbest)
while t<T do
    if t<a then
        Update position Eq (1)
    else
        if p=0 then
            c=c+1
        end if
        if c=m then
            c=0
            Update position Eq(4)
        else
            Update position Eq(2)
        end if
    end if
Calculate fitness f(x)
if f(x) is better than f(gbest) then
   gbest=x
   f(gbest)=f(x)
   p=1
else
   p=0
end if
t=t+1
end while
return gbest
```

B. VISIBLE DIGITAL IMAGE WATERMARKING USING SINGLE CANDIDATE OPTIMIZER

In the proposed methodology, an initial candidate solution is stochastically generated by the SCO algorithm with the lower bound set to 0 and the upper bound set to 1, employing Equation (6). Subsequently, utilizing this amalgamation coefficient, the host and watermark images are integrated via Equation (7).

$$WI = w * H + (1 - w) * W \tag{7}$$

Here, WI denotes the watermarked image, while w represents the amalgamation coefficient engendered by the SCO algorithm. H signifies the host image, and W denotes the watermark image, respectively.

The watermarked image is thus procured using Equation (7). Thereafter, the fitness function value of the watermarked image is ascertained using Equation (8). Throughout each iteration, the amalgamation coefficient is iteratively refined employing Equation (1), (2), and (4) to ascertain the optimal amalgamation coefficient.

$$Fitness = C(H, WI) + C(EW, W) \tag{8}$$

Here, H represents host image, WI represents watermarked image, W represents watermark image, EW represents extrapolated watermark image, $C(H, WI)$ represents the correlation coefficient between the H and WI and, $C(EW, W)$ represents the correlation coefficient between the EW and W. $C(H, WI)$ is calculated using equation 9. The block diagram of the proposed methodology is delineated in Figure 1.

$$C(H, WI) = \frac{\sum_m \sum_n (H_{mn} - \bar{H})(WI_{mn} - \overline{WI})}{\sqrt{(\sum_m \sum_n (H_{mn} - \bar{H})^2)((WI_{mn} - \overline{WI})^2)}} \tag{8}$$

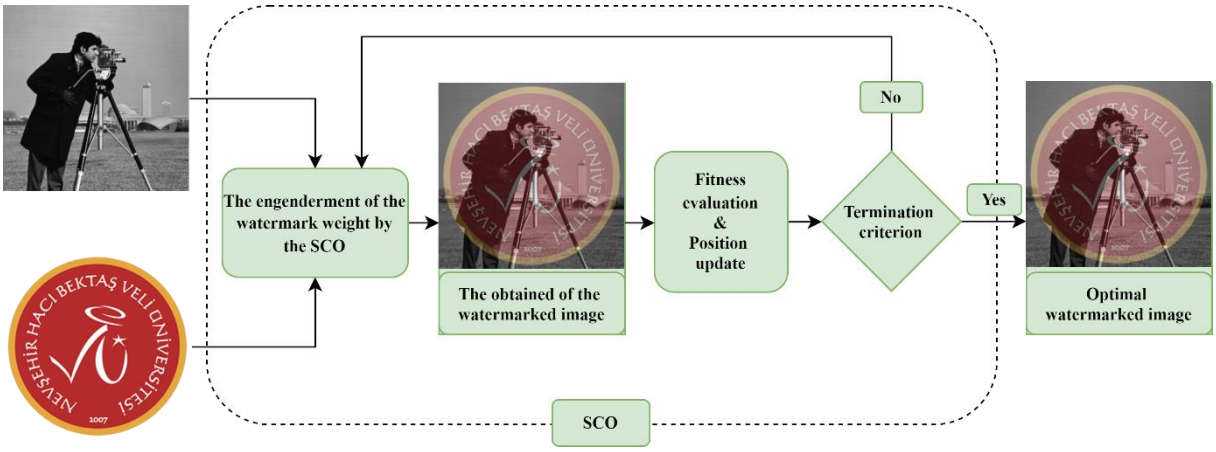

Figure 1. *A block diagram of visible image watermarking utilizing SVO*

C. THE OPTIMIZATION ALGORITHMS USED FOR COMPARISON

This section elucidates the metaheuristic optimization algorithms that are prevalently utilized and well-established in optimization problems, particularly in comparison with SCO. The metaheuristic optimization algorithms selected for comparison encompass the Genetic Algorithm (GA), which serves as a progenitor of population-based metaheuristic optimization algorithms inspired by evolutionary principles; the Differential Evolution Algorithm (DE),

which is a forerunner of deterministic population-based metaheuristic optimization algorithms; and the Artificial Bee Colony Optimization Algorithm, which is a pioneering representative of swarm intelligence-based metaheuristic optimization algorithms.

C. 1. Genetic Algorithm

The genetic algorithm (GA) [19], founded on natural selection and genetic principles, was developed by John Holland and his students in the 1960s. It is an efficacious tool for solving optimization problems. GA is a population-based algorithm that commences with a randomly generated initial population. The quality of solutions is assessed using a predefined objective function. Population size is a critical control parameter; an excessively large population increases computational cost, especially problematic in online applications, while a very small population diminishes the algorithm's ability to explore the search space and achieve global optimization.

GA employs genetic operators such as selection, crossover, and mutation. The selection operator favors high-quality individuals, enhancing their representation in subsequent generations, thereby progressing toward optimal solutions. The crossover operator combines two randomly chosen individuals from the solution pool to produce a new, high-quality individual, aiding in reaching the optimal solution and avoiding local optima. The mutation operator introduces random changes to a selected solution, fostering the discovery of previously unexplored high-quality individuals in the solution space.

C. 2. Differential Evolution Algorithms

The differential evolution algorithm (DE) [20] is a population-based, expeditious, and robust stochastic direct search optimization algorithm. DE can be employed to ascertain optimal solutions for nonlinear, non-differentiable, and multi-modal continuous space functions comprised of real parameters. Despite utilizing a heuristic algorithm structure, DE distinguishes itself through unique mechanisms for generating new solutions and its ‘greedy’ selection process. Similar to other evolutionary algorithms, DE employs operators such as initial population generation, crossover, mutation, and selection. The fundamental steps of DE include the formation of the initial population, evaluation of population individuals, mutation, crossover, and selection. These operators are sequentially and iteratively applied until a predetermined termination criterion, such as reaching the maximum number of iterations per generation, is satisfied

C. 3. Artificial Bee Colony Optimization Algorithms

The Artificial Bee Colony (ABC) [21] algorithm, developed by Karaboğa, is a recently advanced optimization algorithm based on swarm intelligence, modeling the intelligent foraging behaviors of honeybees for numerical problem optimization. In the ABC algorithm, food source regions represent potential solution values for the problem to be solved. The nectar amounts in food sources identified by scout bees correspond to the quality values of potential solutions. Worker bees are dispatched to the food sources detected by scout bees. These worker bees evaluate the quality of the food source they are working on and its neighboring sources, tending towards the source with better solution quality. When a worker bee returns to the hive with information about the current solution and the new position, it communicates this data to the onlooker bees through a dance. The higher the quality of the solution proposed by the worker bee, the greater the likelihood it will be selected by the onlooker bees. Once the food amount at

a source is depleted, indicated by reaching the threshold value set by the ABC algorithm's limit parameter, the worker bee becomes a scout bee and resumes exploration.

D. QUALITY METRICS

The appraisal of watermarked images' quality presents a challenge for researchers. Given the unique attributes of each watermarked image, a singular objective quality metric capable of evaluating all such images has yet to be devised. Consequently, it is imperative to assess the quality of a watermarked image using multiple metrics. In this study, eight widely recognized objective quality metrics from the literature have been employed. These quality metrics and their formulated representations are delineated in Table 1. The first column of Table 1 enumerates the name of the quality metric, followed by its abbreviation used in this paper, and the final column presents its formulated expression.

Table 1. *Quality metrics used for objective evaluation.*

Abbr	Name	Formulas
M_1	Variance [22]	$M_1(F) = \frac{1}{mxn}\sum_{(i,j)}(F(i,j)-\mu)^2$
M_2	Entropy [23]	$M_2(F) = -\sum_{i=0}^{L} h_f(i) log_2 h_f(i)$
M_3	Spatial frequency [24]	$M_3 = \sqrt{R^2 + C^2}$ $R = \sqrt{\frac{1}{mxn}\sum_i\sum_j [f(i,j)-f(i-1,j)]^2}$ $C = \sqrt{\frac{1}{mxn}\sum_i\sum_j [f(i,j)-f(i,j-1)]^2}$
M_4	Standard deviation [25]	$M_4(F) = \sqrt{\sum_{i=0}^{L}(i-\bar{\imath})^2 log_2 h_f(i)}$
M_5	Edge based quality metric [26]	$M_5(F) = \frac{\sum_{n=1}^{N}\sum_{m=1}^{M} Q^{AF}(n,m)w^A(n,m) + Q^{BF}(n,m)w^B(n,m)}{\sum_{n=1}^{N}\sum_{m=1}^{M}(w^A(n,m)+w^B(n,m))}$
M_6	Chen-Blum quality metric [27]	$M_6(F) = Sm_A(x,y)Q_{AF}(x,y) + Sm_B(x,y)Q_{BF}(x,y)$ Here $Sm_A(x,y)$ denotes global quality map.

Table 1 (cont). *Quality metrics used for objective evaluation.*

M_7	Nonlinear correlation information entropy [28]	$H^r(X) = -\sum_{i=1}^{b} \frac{n_{ij}}{N} log_b\left(\frac{n_{ij}}{N}\right)$ $M_7(X,Y) = H^r(X) + H^r(Y) - H^r(X,Y)$
M_9	Sum of the correlations of differences [29]	$M_9(F) = c(D_A, F) + c(D_B, F)$

III. EXPERIMENTAL RESULTS

In this section, an objective quality assessment for digital image watermarking using SCO is presented based on various quality metrics. The experiments were conducted on a system running Windows 7, equipped with an i5 2.3 GHz processor, 16 GB RAM, and utilizing Matlab software. The watermarking process was performed using the watermark image depicted in Figure 2 on images commonly employed in image processing, as shown in Figure 2. The resultant numerical outcomes are provided in a comparative analysis with GA, DE, and ABC optimization algorithms. To ensure a fair evaluation, common parameter values were uniformly selected. For the unique parameters of each optimization algorithm, recommended values were employed. The parameter values used for the optimization algorithms are detailed in Table 2. The first column of the table lists the optimization algorithm, followed by the parameter values used in the experiments. Preliminary trials established the maximum number of iterations as 500 for each algorithm, with a population size of 10 for all algorithms except SCO. Due to the probabilistic nature of the optimization algorithms, each was executed independently thirty times. The maximum, mean, and corresponding standard deviation values obtained from these executions are presented in the tables.

Table 2. *The parameter values of the optimization algorithms used in the experiments.*

Algorithms	**Parameter Values**
SCO	m=5, alpha=1000, b=2.4
GA	pc=0.7 mu=0.1
DE	beta_min=0.2, beta_max=0.8, pCR=0.2
ABC	nOnlooker=nPop, L=round(.6*nVar*nPop), a=1

Figure 2. *The image set utilized for the experiments.*

Tables 3-7 present the numerical results obtained from the experiments conducted for digital image watermarking. The first column of the respective tables denotes the name of the optimization algorithms (Alg.). Following this, the maximum (M), average (A), and standard deviation (S) values obtained for each quality metric are provided. Subsequently, the numerical results obtained for each quality metric are listed sequentially. After each quality metric value, the rank (R) of the algorithm in the corresponding quality metric is specified. The final column furnishes the total ranking values (T_R) to facilitate a more straightforward objective evaluation for the readers. The T_R value is calculated by summing the scores each optimization algorithm achieves in descending order of their rank values across all quality metrics. Namely, an optimization algorithm receives a score of 4 when ranked first in any quality metric and a score of 1 when ranked last. Upon examining the pertinent tables, it is observed that the S values are exceedingly low, approaching zero. This indicates that the method exhibits stability in digital image watermarking.

Table 3. *The numerical results obtained for Experiment Image 1.*

Alg.		M_1		M_2		M_3		M_4		M_5		M_6		M_7		M_8		
		Value	R	Value	R	Value	R	Value	R	Value	R	Value	R	Value	R	Value	R	T_R
SCO	M	1331,260		6,973		4,426		36,486		0,429		0,410		0,817		1,103		
	A	1331,185	1	6,971	3	4,423	4	36,485	1	0,429	1	0,410	1	0,817	4	1,103	1	1
	S	0,064		3E-04		5E-04		0,0009		9E-06		2E-05		6E-06		0,0002		
ABC	M	1331,260		6,971		4,424		36,486		0,429		0,410		0,817		1,103		
	A	1331,148	4	6,971	1	4,424	1	36,485	4	0,429	4	0,410	4	0,817	1	1,103	4	4
	S	0,030		6E-05		1E-04		0,0004		2E-06		3E-06		3E-06		8E-05		
DE	M	1331,260		6,971		4,424		36,486		0,429		0,410		0,817		1,103		
	A	1331,164	2	6,971	4	4,423	3	36,485	2	0,429	2	0,410	2	0,817	3	1,103	2	2
	S	0,049		1E-04		2E-04		0,0007		3E-06		5E-06		5E-06		0,0001		
GA	M	1331,260		6,971		4,424		36,486		0,429		0,410		0,817		1,103		
	A	1331,156	3	6,971	2	4,423	2	36,485	3	0,429	3	0,410	3	0,817	2	1,103	3	3
	S	0,042		8E-05		2E-04		0,0006		2E-06		4E-06		4E-06		0,0001		

Table 3 delineates the numerical results acquired for Experiment Set 1 using optimization algorithms, evaluated across various quality metrics. For Image 1, SCO achieved the optimal outcome in five quality metrics, whereas it registered the worst values in M_3 and M_7. Consequently, it is evident that for Image 1, SCO demonstrated the superior performance, followed sequentially by DE, GA, and ABC.

Table 4. *The numerical results obtained for Experiment Image 2.*

Alg.		M_1		M_2		M_3		M_4		M_5		M_6		M_7		M_8		
		Value	**R**	**Value**	**R**	**Value**	**R**	**Value**	**R**	**Value**	**R**	**Value**	**R**	**Value**	**R**	**Value**	**R**	**T_R**
SCO	**M**	2273,255		7,295		4,348		47,679		0,410		0,344		0,822		1,208		
	A	2273,255	1	7,295	1	4,348	3	47,679	1	0,410	1	0,344	1	0,822	1	1,208	1	1
	S	0,000		4E-15		2E-15		2E-14		2E-16		1E-16		3E-16		5E-16		
ABC	**M**	2273,255		7,295		4,351		47,679		0,410		0,344		0,822		1,208		
	A	2272,436	4	7,294	4	4,349	1	47,670	4	0,410	3	0,344	4	0,822	4	1,208	3	4
	S	1,058		8E-04		0,001		0,0111		2E-05		9E-05		8E-05		0,0001		
DE	**M**	2273,255		7,295		4,348		47,679		0,410		0,344		0,822		1,208		
	A	2273,255	1	7,295	1	4,348	3	47,679	1	0,410	1	0,344	1	0,822	1	1,208	1	1
	S	0,000		4E-15		2E-15		2E-14		2E-16		1E-16		3E-16		5E-16		
GA	**M**	2273,255		7,295		4,355		47,679		0,410		0,344		0,822		1,208		
	A	2273,005	3	7,295	3	4,348	2	47,676	3	0,410	4	0,344	3	0,822	3	1,208	4	3
	S	0,696		3E-04		0,001		0,0073		4E-05		0,0002		9E-05		0,0007		

Table 4 delineates the numerical outcomes obtained for Experiment Set 2 using optimization algorithms, assessed based on various quality metrics. For Image 2, SCO exhibited the preeminent performance across all quality metrics except M_3, wherein DE matched SCO's performance. Consequently, for Image 2, it can be inferred that SCO and DE demonstrated equivalent performance, followed by GA and ABC exhibiting relatively superior performance in that order.

Table 5. *The numerical results obtained for Experiment Image 3.*

Alg.		M_1		M_2		M_3		M_4		M_5		M_6		M_7		M_8		
		Value	**R**	**Value**	**R**	**Value**	**R**	**Value**	**R**	**Value**	**R**	**Value**	**R**	**Value**	**R**	**Value**	**R**	**T_R**
SCO	**M**	2978,976		7,619		4,410		54,580		0,415		0,438		0,818		1,378		
	A	2978,183	3	7,619	2	4,409	3	54,573	3	0,415	3	0,438	2	0,818	4	1,378	3	3
	S	0,348		2E-04		3E-04		0,0032		2E-05		4E-05		6E-06		4E-05		
ABC	**M**	2981,680		7,620		4,417		54,605		0,416		0,438		0,818		1,378		
	A	2979,453	1	7,619	4	4,410	1	54,584	1	0,416	1	0,438	4	0,818	1	1,378	1	1
	S	1,170		5E-04		0,002		0,0107		0,0003		0,0001		3E-05		0,0002		
DE	**M**	2978,976		7,619		4,410		54,580		0,415		0,438		0,818		1,378		
	A	2978,111	4	7,619	1	4,409	4	54,572	4	0,415	4	0,438	1	0,818	3	1,378	4	4
	S	0,345		2E-04		3E-04		0,0032		5E-06		1E-05		8E-06		4E-05		
GA	**M**	2981,302		7,619		4,417		54,601		0,416		0,438		0,818		1,378		
	A	2978,611	2	7,619	3	4,410	2	54,577	2	0,415	2	0,438	3	0,818	2	1,378	2	2
	S	0,959		3E-04		0,002		0,0088		0,0002		8E-05		2E-05		0,0001		

Table 5 presents the numerical results obtained for Experiment Set 3 using optimization algorithms, assessed across various quality metrics. For Image 3, the ABC algorithm exhibited superior performance across all quality metrics except M2 and M6. Therefore, for digital image watermarking of Image 3, the

ranking of performance is as follows: ABC, GA, SCO, and DE. It can be inferred that SCO did not demonstrate commendable performance for this image.

Table 6. *The numerical results obtained for Experiment Image 4.*

Alg.		M_1		M_2		M_3		M_4		M_5		M_6		M_7		M_8		
		Value	R	Value	R	Value	R	Value	R	Value	R	Value	R	Value	R	Value	R	T_R
SCO	M	2343,499		7,534		6,987		48,410		0,494		0,437		0,817		1,319		
	A	2343,012	3	7,534	3	6,986	4	48,405	3	0,494	3	0,437	1	0,817	2	1,319	2	2
	S	0,775		2E-04		2E-04		0,008		1E-05		4E-05		9E-06		0,0002		
ABC	M	2351,873		7,542		6,990		48,496		0,494		0,437		0,817		1,320		
	A	2343,025	2	7,535	1	6,987	1	48,405	2	0,494	4	0,437	4	0,817	4	1,319	4	3
	S	1,916		0,001		0,001		0,0198		0,0001		0,0002		8E-05		0,0003		
DE	M	2343,499		7,534		6,987		48,410		0,494		0,437		0,817		1,319		
	A	2343,434	1	7,534	4	6,987	2	48,409	1	0,494	2	0,437	3	0,817	1	1,319	1	1
	S	0,196		2E-04		4E-05		0,002		5E-08		1E-06		2E-06		6E-05		
GA	M	2343,499		7,535		6,989		48,410		0,494		0,437		0,817		1,319		
	A	2342,985	4	7,534	2	6,987	3	48,404	4	0,494	1	0,437	2	0,817	3	1,319	3	3
	S	0,704		3E-04		5E-04		0,0073		2E-05		8E-05		1E-05		0,0002		

Table 6 delineates the numerical results obtained for Experiment Set 4 utilizing optimization algorithms, evaluated based on various quality metrics. For Image 4, it can be posited that DE demonstrated superior performance relative to the others, while GA and ABC exhibited equally performance, trailing SCO.

Table 7. *The numerical results obtained for Experiment Image 5.*

Alg.		M_1		M_2		M_3		M_4		M_5		M_6		M_7		M_8		
		Value	R	Value	R	Value	R	Value	R	Value	R	Value	R	Value	R	Value	R	T_R
SCO	M	2607,305		7,440		4,655		51,062		0,434		0,388		0,819		1,152		
	A	2607,231	2	7,440	1	4,655	1	51,061	2	0,434	1	0,388	4	0,819	2	1,152	1	1
	S	0,053		3E-05		2E-04		0,0005		6E-06		2E-05		2E-06		2E-05		
ABC	M	2607,305		7,440		4,655		51,062		0,434		0,388		0,819		1,152		
	A	2606,953	3	7,440	2	4,655	3	51,058	3	0,434	3	0,388	2	0,819	3	1,152	2	3
	S	0,600		6E-04		9E-04		0,0059		3E-05		0,0001		1E-05		0,0003		
DE	M	2611,984		7,440		4,655		51,108		0,434		0,388		0,819		1,152		
	A	2607,276	1	7,440	3	4,655	2	51,061	1	0,434	4	0,388	3	0,819	1	1,152	3	2
	S	1,010		9E-04		0,002		0,0099		0,0002		0,0001		2E-05		0,0004		
GA	M	2607,305		7,440		4,655		51,062		0,434		0,388		0,819		1,152		
	A	2606,800	4	7,440	4	4,654	4	51,057	4	0,434	2	0,388	1	0,819	4	1,151	4	4
	S	0,667		7E-04		0,001		0,0065		2E-05		0,0002		1E-05		0,0004		

Table 7 provides the numerical results obtained for Experiment Set 5 using optimization algorithms, evaluated across various quality metrics. For Image 5, it can be asserted that SCO demonstrated the best performance in four quality metrics and the second-best performance in three other metrics. Conversely, it is evident that GA exhibited the poorest performance. Thus, for digital watermarking of Image 5, the algorithms' performance can be ranked in the following order: SCO, DE, ABC, and GA.

In Table 8, the computational cost of the optimization algorithms is delineated. The table's initial column enumerates the algorithms subjected to comparison, followed by the stamping time for each individual image. Upon scrutinizing the table, it can be discerned that the SCO algorithm demonstrates a markedly superior computational speed relative to its counterparts. It is further observable that DE succeeds SCO, trailed by ABC, and ultimately by GA, in terms of computational duration. Thus, it may be posited that, for digital image watermarking, SCO exhibits a computational efficiency that surpasses the other algorithms included in the comparison.

Table 8. *Comparative evaluation of algorithmic computation times*

	Image Set				
	1	**2**	**3**	**4**	**5**
SCO	0.843273	0.832979	0.822952	0.827584	0.813185
GA	2.956.302	2.184.961	2.286.389	2.267.131	2.232.963
DE	2.042.678	1.942.010	1.972.971	1.924.230	1.955.935
ABC	2.197.032	2.155.925	2.181.180	2.242.619	2.240.701

In the evaluation of watermarked images, a single quality metric proves inadequate, and solely relying on objective assessment also falls short. Alongside objective evaluation, subjective assessment is essential. Figure 3 illustrates the watermarked images obtained from the conducted experiments. Due to the proximity of the numerical results and the similarity among the watermarked images, there is no discernible visual difference, which precludes the possibility of conducting a subjective evaluation.

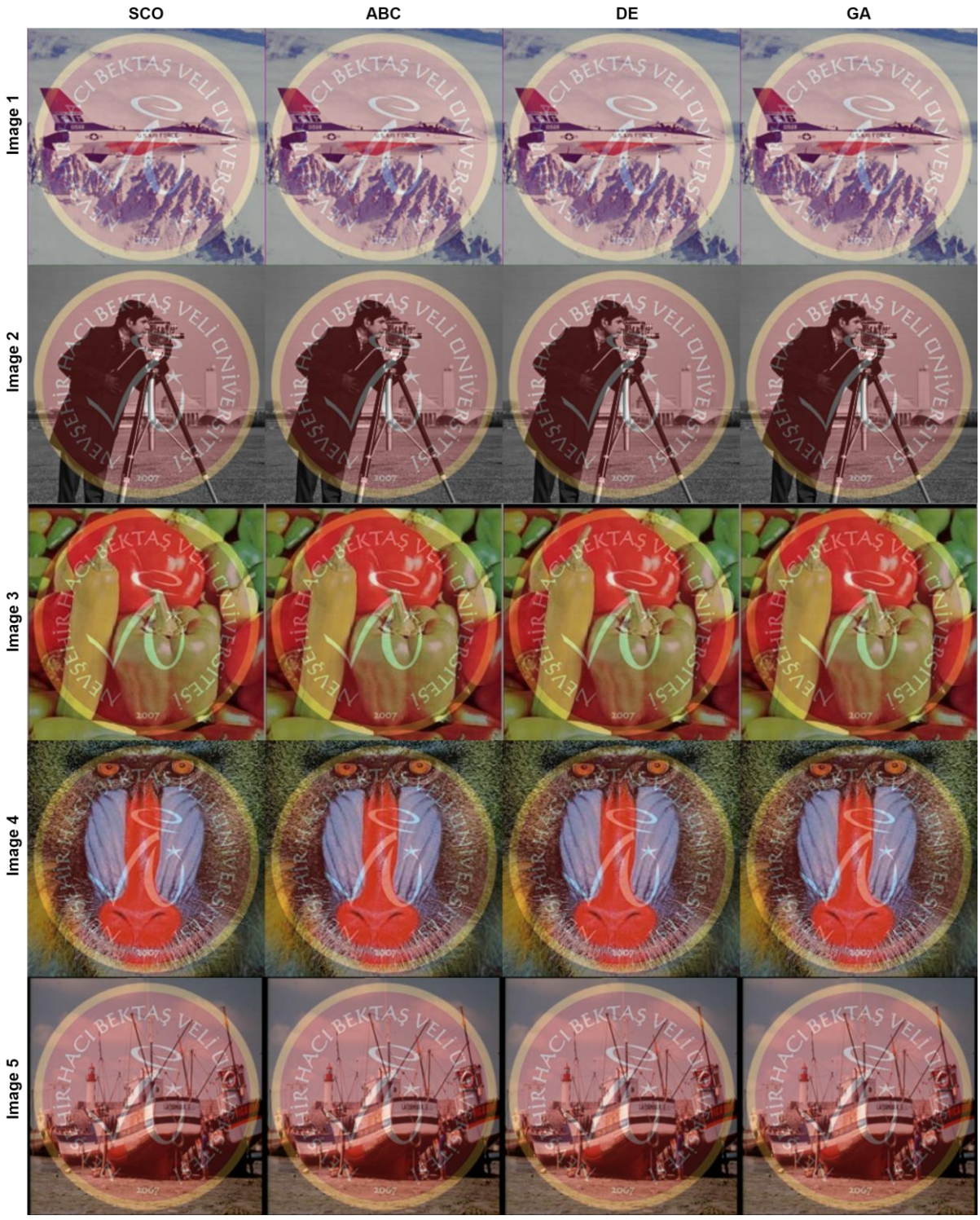

Figure 3. *The obtained watermarked images*

As illustrated in Figure 3, although the numerical results of the optimization algorithms vary across all image sets, there is no discernible visual distinction among the resulting watermarked images. Thus, it can be inferred that the optimization algorithms employed in this study yield comparable results in terms of subjective evaluation for visible digital watermarking.

IV. CONCLUSION

In summation, the advent of digital image watermarking, particularly through the employment of the Single Candidate Optimizer (SCO), proffers a significant advancement in the realm of copyright protection amidst the burgeoning ease of information accessibility afforded by internet technologies. This study elucidates the efficacy of SCO, a non-population-based algorithm, in optimizing the congruence between watermarked images and their respective host and watermark counterparts. Numerical evaluations, conducted on standard image processing datasets and assessed via an octet of quality metrics, substantiate the superiority of SCO over traditional metaheuristic algorithms such as genetic algorithm, differential evolution, and artificial bee colony optimization. The preeminence of SCO is further accentuated by its expeditious performance, attributable to its non-population-based framework. Consequently, SCO emerges as a paramount technique for visible digital image watermarking, offering enhanced fidelity and computational efficiency.

In this study, the host image is considered in its entirety, and an optimal fusion coefficient is accordingly derived. Given that natural images do not encompass homogeneous information, the uniform application of the derived fusion coefficient across the entire image may engender undesirable artifacts in the watermarked image. To obviate this issue, methodologies could be devised whereby the host image is partitioned into blocks, with distinct fusion coefficients ascertained for each block. Furthermore, methods that optimize the commonly employed block size in image fusion could be implemented to evaluate the results.

ACKNOWLEDGEMENTS: The author declares no conflict of interest.
AUTHOR CONTRIBUTIONS (COMPULSORY): This article is submitted by a single author.

V. REFERENCES

[1] H. Akbulut, V. Aslantas, and H. Ulutaş, "Visible Image Watermarking Based on Image Fusion with Shearlet Transform Using Genetic Algorithm," *Electronic Letters on Science and Engineering*, vol. 13, no. 3, pp. 1-9, 2017.

[2] Singh, R. et al. "From classical to soft computing based watermarking techniques: A comprehensive review", *Future Generation Computer Systems*, vol. 141, pp. 738–754, 2023.

[3] A. Anand and A. K. Singh, "Dual Watermarking for Security of COVID-19 Patient Record," *IEEE Transactions on Dependable and Secure Computing*, vol. 20, no. 1, pp. 859–866, Jan. 2023

[4] S. Roy and A. K. Pal, "An indirect watermark hiding in discrete cosine transform–singular value decomposition domain for copyright protection," *Royal Society Open Science*, vol. 4, no. 6, p. 170326, Jun. 2017

[5] A. K. Abdulrahman and S. Ozturk, "A novel hybrid DCT and DWT based robust watermarking algorithm for color images," *Multimedia Tools and Applications*, vol. 78, no. 12, pp. 17027–17049, Jan. 2019

[6] S. M. Darwish and L. D. S. Al-Khafaji, "Dual Watermarking for Color Images: A New Image Copyright Protection Model based on the Fusion of Successive and Segmented Watermarking," *Multimedia Tools and Applications*, vol. 79, no. 9–10, pp. 6503–6530, Dec. 2019

[7] H. Mittal and M. Saraswat, "An optimum multi-level image thresholding segmentation using non-local means 2D histogram and exponential Kbest gravitational search algorithm," *Engineering Applications of Artificial Intelligence*, vol. 71, pp. 226–235, May 2018

[8] Y. Wang, Y. Yu, S. Gao, H. Pan, and G. Yang, “A hierarchical gravitational search algorithm with an effective gravitational constant,” *Swarm and evolutionary computation*, vol. 46, pp. 118–139, May 2019

[9] P. Rawal, H. Sharma, and N. Sharma, “Fast Convergent Gravitational Search Algorithm,” in *Algorithms for intelligent systems*, 2020, pp. 1–12

[10] H. Mittal and M. Saraswat, “An automatic nuclei segmentation method using intelligent gravitational search algorithm based superpixel clustering,” *Swarm and Evolutionary Computation*, vol. 45, pp. 15–32, Mar. 2019

[11] V. Aslantas, S. Ozer and S. Ozturk, "A novel image watermarking method based on Discrete Cosine Transform using Genetic Algorithm," *2009 IEEE 17th Signal Processing and Communications Applications Conference*, Antalya, Turkey, 2009, pp. 285-288

[12] C. Zhang and M. Hu, "Curvelet Image Watermarking Using Genetic Algorithms," *2008 Congress on Image and Signal Processing*, Sanya, China, 2008, pp. 486-490

[13] B. Jagadeesh, S. S. Kumar and K. R. Rajeswari, "Image Watermarking Scheme Using Singular Value Decomposition, Quantization and Genetic Algorithm," *2010 International Conference on Signal Acquisition and Processing*, Bangalore, India, 2010, pp. 120-124

[14] R. Çolak, T. Yiğit, “Üniversite Ders Çizelgeleme Probleminin Genetik Algoritma ile Optimizasyonu”, *Düzce Üniversitesi Bilim ve Teknoloji Dergisi*, c. 9, s. 6, ss. 150-166, 2021

[15] T. Timuçin, S. Biroğul, “Hibrit Genetik Algoritma Kullanarak Ameliyat Odası Çizelgeleme”, *Düzce Üniversitesi Bilim ve Teknoloji Dergisi*, c. 10, s. 1, ss. 255-274, 2022

[16] M. N. Demir, Y. Altun, “Otonom Araçla Genetik Algoritma Kullanılarak Haritalama ve Lokasyon”, *Düzce Üniversitesi Bilim ve Teknoloji Dergisi*, c. 8, s. 1, ss. 654-666, 2020

[17] R. Özdemir, M. Taşyürek, and V. Aslantaş, “Improved Marine Predators Algorithm and Extreme Gradient Boosting (XGBoost) for shipment status time prediction,” *Knowledge-Based Systems*, vol. 294, p. 111775, Apr. 2024

[18] T. M. Shami, D. Grace, A. Burr, and P. D. Mitchell, “Single candidate optimizer: a novel optimization algorithm,” *Evolutionary Intelligence*, Aug. 2022

[19] J. H. Holland, Adaptation in natural and artificial systems: an introductory analysis with applications to biology, *control and artificial intelligence*. Ann Arbor, Mich, 1975.

[20] R. Storn and K. Price, “Differential Evolution – A Simple and Efficient Heuristic for global Optimization over Continuous Spaces,” *Journal of Global Optimization*, vol. 11, no. 4, pp. 341–359, Jan. 1997

[21] D. Karaboga and B. Basturk, “A powerful and efficient algorithm for numerical function optimization: artificial bee colony (ABC) algorithm,” *Journal of Global Optimization*, vol. 39, no. 3, pp. 459–471, Apr. 2007

[22] V. Aslantas and R. Kurban, “A comparison of criterion functions for fusion of multi-focus noisy images,” *Optics Communications*, vol. 282, no. 16, pp. 3231–3242, Aug. 2009

[23] K. Ma, Kai Zeng, and Zhou Wang, “Perceptual Quality Assessment for Multi-Exposure Image Fusion,” *IEEE Transactions on Image Processing*, vol. 24, no. 11, pp. 3345–3356, Nov. 2015

[24] A. M. Eskicioglu and P. S. Fisher, “Image quality measures and their performance,” *IEEE Transactions on Communications*, vol. 43, no. 12, pp. 2959–2965, 1995

[25] Y. Liu, S. Liu, and Z. Wang, “A general framework for image fusion based on multi-scale transform and sparse representation,” *Information Fusion*, vol. 24, pp. 147–164, Jul. 2015

[26] C. S. Xydeas and PetrovićV., “Objective image fusion performance measure,” *Electronics Letters*, vol. 36, no. 4, p. 308, 2000

[27] Y. Chen and R. S. Blum, “A new automated quality assessment algorithm for image fusion,” *Image and Vision Computing*, vol. 27, no. 10, pp. 1421–1432, Sep. 2009

[28] H. Wang and X. Yao, “Objective reduction based on nonlinear correlation information entropy,” *Soft Computing*, vol. 20, no. 6, pp. 2393–2407, Mar. 2015

[29] V. Aslantas and E. Bendes, “A new image quality metric for image fusion: The sum of the correlations of differences,” *AEU - International Journal of Electronics and Communications*, vol. 69, no. 12, pp. 1890–1896, Dec. 2015

Düzce University
Journal of Science & Technology

Research Article

Landscape Design Proposal in Public Spaces: A Case of Düzce Uzun Mustafa Neighborhood

Özlem ÖZKAN ÖNÜR [a], Eda KAYA,[b] Özgür YERLİ [b,*]

[a] *Department of Architecture, Faculty of Engineering and Architecture, İstanbul Niişantaşı University, İstanbul, TURKEY*
[b]*Department of Landscape Architecture, Faculty of Forestry, Düzce University, Düzce, TURKEY*
** Corresponding author's e-mail address: ozguryerli@duzce.edu.tr*
DOI: 10.29130/dubited.1522861

ABSTRACT

Public spaces are considered a critical process that determines the initial spatial perception of an individual in their environment and shapes their experiences and memories. These spaces include public buildings, open areas, and locations that are in constant interaction with the surroundings. The analysis of the landscape features of the physical environment aims to create an interaction between different uses in urban landscape design and to transform a busy street into a livable area. The surroundings of public buildings such as the Düzce Governorship Meteorology Directorate, Düzce Vocational School, and library in the Uzun Mustafa neighborhood of Düzce have passive urban open and green areas. In this study, the mentioned areas were evaluated, the landscape features of the physical environment were analyzed, and revision proposals related to urban landscape design were made. By utilizing the satellite image and zoning plan of the study area, it was aimed to eliminate elements that cause confusion in human psychology according to urban and landscape features. In the method of the study, internal and external factors were considered based on the project design processes of the area, and a SWOT analysis was conducted to minimize the impact of weaknesses and elements that pose threats in the area. As a result, this study aimed to create a more livable space that meets the needs of users in areas with passive, unused or undesigned surroundings of public buildings and to contribute more effectively to the daily life of the community in spaces with different functions.

Keywords: *Düzce, Environment, Landscape design, Public spaces, Urban.*

Düzce Uzun Mustafa Mahallesi: Kamusal Alanları Yeniden Canlandırma İçin Peyzaj Tasarım Önerileri

ÖZ

Kamusal alanlar, bireyin yaşadığı çevredeki ilk mekân algısını belirleyen ve deneyimlerini, anılarını şekillendiren kritik bir süreç olarak kabul edilir. Kamu binaları, açık alanlar ve çevre ile sürekli etkileşim halinde olan mekanlar bu alanları oluşturur. Fiziksel çevrenin peyzaj özelliklerinin analizi, kentsel peyzaj tasarımında farklı kullanımlar arasında bir etkileşim yaratmayı ve yoğun bir caddeyi yaşanabilir bir alan haline getirmeyi hedefler. Düzce Uzun Mustafa mahallesindeki Düzce Valiliği Meteoroloji Müdürlüğü, Düzce Meslek Yüksek Okulu ve kütüphane gibi kamu binalarının çevreleri pasif kentsel açık ve yeşil alanlara sahiptir. Bu çalışmada, bahsi geçen alanların değerlendirme çalışmaları yapılarak fiziksel çevrenin peyzaj özellikleri analiz edilip kentsel peyzaj tasarımına ilişkin revizyon önerilerinde bulunulmuştur. Çalışma alanının uydu görüntüsü ve imar planından yararlanılarak kentsel ve peyzaj özelliklerine göre insan psikolojisinde karmaşaya sebep olan unsurların giderilmesi amaçlanmıştır. Çalışmanın yönteminde, alanın proje tasarım süreçlerine dayanarak iç ve dış faktörler göz önünde

Received: 26/07/2024, Revised: 18/10/2024, Accepted: 25/11/2024

bulundurulmuş, zayıf yönler ve alanda tehdit oluşturacak unsurların etkisini minimalize etmek için SWOT analizi yapılmıştır. Sonuç olarak bu çalışma ile mevcutta pasif, kullanılmayan ya da çevresi tasarlanmamış kamu yapılarının bulunduğu alanlar için kullanıcı ihtiyaçlarına yönelik daha yaşanabilir bir mekan oluşturulmuş, farklı işlevlere sahip mekanlarda toplumun günlük hayatına daha etkili bir şekilde katkı sağlanması hedeflenmiştir.

Anahtar Kelimeler: *Düzce, Çevre, Peyzaj tasarım, Kamusal alan, Kent.*

I. INTRODUCTION

The term "public" generally means "open to general use", so it refers to public spaces, urban areas that everyone can access and use [1]. The concept of public space is used to help develop the design, management, and usage of spaces [2]. Public spaces are areas where the lifestyles of communities are determined and where social interaction is central. The streets, squares, and parks of a city shape social life and at the same time create common living spaces through play and relaxation areas. These spaces are formed through places where people can meet their recreational needs and interact. Therefore, it is expected that landscape design studies in these areas will have the capacity to meet the needs of users from all segments of society [3]. While emphasizing the importance of public spaces, public welfare, visual enhancement, environmental health, and economic development are identified as the most important goals [2]. In this context, the planning and management of public spaces aim to create a sustainable and livable public living space, not only by organizing physical spaces but also by organizing the social and cultural fabric of society. This perspective requires a more comprehensive understanding to be adopted in the design and management of public spaces [4]. The creation of perceptible and aesthetic spaces is realized with the designer's foresight. In the outdoor design of public institutions and organizations; it is necessary to take into account the preservation of environmental character, the provision of inside-outside space relationship, the continuity of urban fabric, accessibility, symbol creation, formality, perceptibility, visuality, and aesthetics [5].

When landscape design is done in public buildings and their surroundings, the diversity of users, the wide age range, and economic reasons restrict the design [6-7]. The more the complexity of the structure to be designed and its context increases, the challenges faced by the designer also grow proportionally. This complexity is not only related to the functions of the structures or the environmental factors designed, but also to the complexity of urban scale designs. Urban design is a process that shapes the physical features of a certain environment and expands the physical list of structures [8]. The site selection of the area chosen for design, examination of ecological features, determination of the traditional architectural approach, creation of the needs program, design of floor plans and facades, walls, windows, decorations, and landscape arrangement principles can be evaluated as a whole [9]. The designer also needs to consider the factors affecting the physical qualities of a certain environment on a broader scale. Public buildings and their surroundings are seen as common areas that not only meet people's daily needs but also carry out cultural activities and bring society together [10]. Public spaces, an environment where unique human phenomena such as values, culture, language are brought to life; are subjects that bring together in a common denominator in an economic, political and social context [11]. Humanity has strived for years with the desire to beautify, improve, and make the space they live in more livable. Landscape architecture studies aim to create more livable environments for people, adhering to this philosophy. Historical developments have shown that humans have gone through many changes and development processes to reach different goals. Landscape architecture is a discipline that plays a critical role in shaping the design in terms of the space and purpose of the area to be designed. This discipline conducts various studies in rural and urban areas [12]. Urban areas are largely defined by buildings but are regions that extend beyond buildings. These areas emerge as a result of collective living and include different types of spaces [6].

The El Raval district of Barcelona, once synonymous with crime and poverty at the end of the 20th century, has transformed into a cultural hub through the local government's urban regeneration projects. El Raval, revitalized by the restoration of historic buildings, the opening of art galleries, the

establishment of museums, and the presence of universities, has become an attractive destination for both tourists and locals. Projects such as Park Güell and the Barcelona Pavilion have also contributed to this transformation by emphasizing the importance of public spaces [27]. Urban regeneration refers to planned interventions aimed at halting physical, social, and economic decline in cities and revitalizing urban life. This process particularly targets rejuvenating outdated or dysfunctional urban areas, improving environmental quality, and strengthening social structures. Urban regeneration repurposes urban spaces while preserving historical fabric, restores economic vitality, and enhances societal benefits.

Successful urban revitalization examples from around the world demonstrate the multifaceted nature of this concept:

- The Edinburgh Design Guidance has provided a revitalization that respects cultural heritage by focusing on new development areas in the city. By prioritizing local context and urban character in design processes, it aimed to improve public spaces to meet user needs.
- The Bath Pattern Books managed the revitalization process by preserving the historical and architectural heritage of public spaces, focusing on creating sustainable, accessible, and livable spaces. In this process, the cultural fabric of the city was preserved while being enriched with modern design principles [28].
- The Blyth Urban Design Guide developed a revitalization strategy that made the city more attractive by preserving the visual and functional characteristics of the historic city center. This process, carried out in collaboration with local people, also improved the social and economic structure of the city [29].
- The Tonsley Urban Design Protocol presented an approach aimed at increasing the active use of urban space. Making public spaces more accessible and vibrant for social and cultural interaction was one of the main goals of this revitalization process.
- The Hong Kong Urban Design Guidelines developed a revitalization process aimed at increasing pedestrian mobility and the sustainability of public spaces. This process demonstrated how public space quality can be improved in a high-density city.
- The Cambridge Urban Design Guide presented a heritage-sensitive urban revitalization strategy by focusing on historic buildings and streetscapes. This guide developed proposals that increase the functionality of public spaces while preserving the city's identity.
- The San Francisco Urban Design Guide aimed to create a more livable environment that meets user needs by improving the urban fabric and public spaces. In the revitalization process, it was aimed to establish strong connections between indoor activities and public spaces.

These examples demonstrate that urban revitalization is a comprehensive process that encompasses not only physical but also social, cultural, and economic dimensions [30]. The more complex the structure to be designed and its contexts, the greater the challenges faced by the designer. This complexity is related not only to the functions of the structures or the designed environmental factors, but also to the complexity of urban-scale designs. Urban design, in particular, is a process that challenges the physical characteristics of a specific environment and is not limited to merely expanding the physical list of structures. This, when expressed in academic terms, requires the designer to address the factors affecting the physical qualities of a specific environment in a broader scope. For example, the Rector's Residence Design Process and Architectural Project at Bartın University Campus was approached holistically. In this process, fundamental stages such as site selection, examination of ecological features, determination of the traditional architectural approach, and creation of the needs program were completed [8]. Additionally, the design of floor plans and facades, walls, windows, decorations, and landscaping principles were considered as important parts of this whole [9]. In the study titled "Evaluation of the Front Garden Landscape Design Study of Erzurum Metropolitan Municipality Building in the Context of Design Principles", data collection, examination, and on-site observation studies were carried out following the literature review. After the current situation and analysis studies, evaluations were made within the framework of design criteria, emphasizing the importance of creating identity in urban design and designing areas suitable for the city [3]. In the examination study of the design process of the

pedestrian zone located in Düzce University Campus; steps such as identifying problems, collecting and analyzing the current situation and data, evaluating and correlating these analyses, creating stain diagrams in line with the main design principles, and finally producing preliminary, implementation, and detail projects were followed [13]. In studies evaluated within the context of Landscape Design Principles, after the literature review, data collection, examination, and on-site observation studies are carried out. After the current situation and analysis studies, evaluations are made within the framework of design criteria [3]. Steps such as identifying the problems, collecting and analyzing the current situation and data, evaluating these analyses and associating them with each other, creating stain diagrams in line with the design main principles, and finally producing field application and detail projects are followed. This process emphasizes the importance of creating identity in urban design and designing suitable areas for the city [13]. Advancements in transportation and communication technologies have left significant impacts on social structure and urban space with the evolution of the global economic order. However, these developments have led to the fragmentation of public life and increased physical distance between individuals. Social media platforms have accelerated this process by creating virtual gathering spaces and moved individuals' social interactions to the virtual environment. This situation has contributed to the increase of closed residential areas and social segregation. Additionally, the Covid-19 pandemic confined people to their homes last year and this situation has made the need of society for quality public spaces more evident. Therefore, the importance of public spaces and the contribution they provide to social unity has gained more importance with the new normals. It emphasizes the need for cities to consider these changes and needs when designing public spaces. Detailed proposals and evaluations related to this subject have been determined by the authors and presented in Table 1.

Table 1. *Landscape design suggestions and principles in public building environments [14],[15].*

	Principles	**Landscape Design Proposal in Public Building Environments**
1	Land Use Planning	Planning of general land use, creating balanced housing, commerce and green spaces
2	Accessibility	Enhance accessibility to public spaces by adding wheelchair-friendly paths, ramps, and seating areas
3	Green Spaces	Creating extensive green areas that include various plant species, trees, and grass areas, encourages the public to become intertwined with nature
4	Ecological Balanced Design	Use of landscape elements that are respectful to natural ecosystems, support biodiversity, and are compatible with local flora
5	Reducing Carbon Footprint	Strategies that include afforestation projects, carbon emission reducing design elements, and sustainable transportation alternatives
6	Social Participation	Strengthening social ties by creating multi-purpose public spaces that can meet the needs of various communities
7	Sustainable Material Use	The preference of recyclable materials and the use of environmentally friendly building materials
8	Active and Passive Fields	Designing active usage areas such as sports fields, walking paths, and passive usage areas such as rest and seating areas in a balanced way.

Table 1 (cont). *Landscape design suggestions and principles in public building environments [14],[15].*

9	Child-Friendly Design	The addition of landscape elements that encourage the participation of children, with playgrounds, entertainment, and education elements
10	Health	The creation of areas that encourage physical activity, such as outdoor sports fields, health tracks, and yoga areas
11	Healthy Nutrition and Agriculture	Creating small agricultural areas within the neighborhood to provide access to healthy food and agricultural products
12	Security	Providing security measures, lighting systems, and safe walking areas in public spaces
13	First Aid Points	To ensure quick intervention in emergencies, it is necessary to identify and equip first aid points within the neighborhood
14	Disaster Preparedness and Safe Shelters	Planning of safe shelters to ensure they are prepared for disaster situations
15	Public Hygiene and Cleaning	Provision of public toilets, garbage bins, and regular cleaning services

This table states the fundamental principles that influence landscape design proposals around public buildings. In land use, strategies such as promoting mixed uses and focusing on access to public transport are highlighted. In public spaces, the importance of social interactions, accessible housing, tolerance, and dialogue are emphasized. In transportation, factors such as encouraging the use of public transport, walking and cycling, healthy living design, and traffic safety are prioritized. In the health category, protecting public health is important. In safety, the protection of fundamental rights and freedoms and the provision of general security are emphasized. In the design category, respect for local culture, aesthetic values, and the transfer of traditional architectural styles to future generations gain importance. In the field of education and culture, a broad perspective is offered, such as preserving traditions and involving children in urban planning processes. The combination of these principles ensures that cities are sustainable, diverse, and human-centered.

In this study, landscape design suggestions for the public buildings surrounding the Uzun Mustafa neighborhood in Düzce City (Turkey) have been made. These suggestions aim to enhance the quality of life for the residents of the neighborhood, increase social interaction, and create a public space that can meet various needs. It also focuses on organizing green spaces, social activity centers, transportation facilities, safe routes, and various public services by supporting the sustainability of the neighborhood. It aims to improve the safety, health, and living standards of the neighborhood residents by emphasizing the importance of critical issues like health, safety, and land use. With the implementation of these suggestions, it is expected that the Uzun Mustafa neighborhood of Düzce City will become a livable environment and provide a public space that can meet the various needs of its residents.

A detailed analysis of the current situation has been conducted for the revitalization of public spaces in Düzce Uzun Mustafa Neighborhood. During this process, elements such as the physical infrastructure of the neighborhood, its social structure, economic situation, and the use of public spaces have been examined. It is emphasized that the area needs revitalization due to the decrease in its attractiveness, the dysfunctionality of public spaces, and infrastructure problems. Proposals for the neighborhood include increasing green spaces, strengthening infrastructure, and implementing economic and social revitalization projects. Taking into account the views of local residents during this process is also of great importance.

Lynch Analysis is a method used in urban design to make cities more legible and understandable. It is based on Kevin Lynch's five key concepts: Edges, Districts, Paths, Nodes, and Landmarks.

- Edges: These are boundaries that separate different areas. Clarifying these boundaries in design facilitates wayfinding.
- Districts: These are urban areas with similar characteristics. In design, the identity of these areas is strengthened.
- Paths: These are the main lines along which people move. They are organized to improve transportation and accessibility.
- Nodes: These are important points where paths intersect. These areas are significant for social interaction and wayfinding.
- Landmarks: These are distinct structures that define the city and aid in wayfinding. They are emphasized in design.

Lynch Analysis contributes to making spaces more functional and user-friendly in urban design by using these elements. As shown in Figure 1, the relationship of Kevin Lynch analysis to the field of study is given.

Figure 1. *Relating Kevin Lynch analysis to the field of study*

II. MATERIAL AND METHOD

A. PHYSICAL STRUCTURE OF DÜZCE PROVINCE

The province of Düzce, located between two metropolitan cities, is surrounded by the provinces of Bolu in the east, Sakarya in the west, and Zonguldak in the northeast. The boundaries of Düzce province are formed by Hendek district in the west, Kocaali district in the northwest, Alaplı district in the northeast, the Black Sea in the north, and the Elmacık Mountains in the south, and it is surrounded by mountain masses. Its total area is 2492.44 km², located between 40°50' north latitude and 31°40' longitude. Its coastline to the Black Sea is approximately 30 km. Kaplandede Mountain is located in the north, Orhan Mountain in the northeast, Bolu Mountains in the east, Elmacık Mountains in the south, Çamdağ in the west, and Muhapdede Mountain in the southwest. The elevation of the hills located here reaches up to

1830 meters at most. The highest point of the field is Kardüz Peak (1830 m) located on the Elmacık Mountains that form the southern border, and the lowest point is Efteni Lake (109 m) located in the southwest [16]. The map provided in Figure 2 illustrates Düzce's location in Turkey and its borders with neighboring provinces.

Figure 2. *Location of Düzce province [17].*

B. UZUN MUSTAFA NEIGHBORHOOD

According to the 2022 ADNKS (Address Based Population Registration System) population census results, the population of Uzun Mustafa neighborhood in the central district of Düzce province is 5,901. Of this population, 2,801 are male, and 3,100 are female. Uzun Mustafa neighborhood is located in Düzce province, in the Aziziye (Günlü) district connected to the center of Düzce. The location of the neighborhood map has ‘‘40° 50' 37.8996’’ North and ‘‘31° 8' 52.2528’’ East GPS coordinates.

The distance from Uzun Mustafa neighborhood to the city center of Düzce is approximately 1 kilometer. As shown in Figure 3, the location of Düzce/Uzun Mustafa neighborhood, the satellite images of the neighborhood in Figure 4, and photographs from Uzun Mustafa neighborhood can be seen in Figure 5.

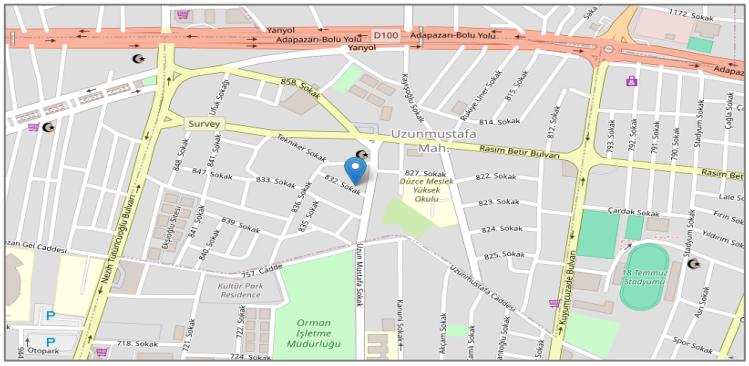

Figure 3. *The location of Düzce/Uzun Mustafa neighborhood in Düzce province [19].*

Figure 4. *Satellite images of Düzce/Uzun Mustafa neighborhood in Düzce province [18].*

Figure 5.*Views of Düzce/Uzun Mustafa neighborhood in Düzce province.*

The material of the study includes landscape design suggestions for the Düzce Governorship Meteorology Directorate building, High School and library building located in Uzun Mustafa neighborhood of central district of Düzce province. After a literature review, data collection, review and on-site observation studies were conducted, photographs of the area were taken and evaluations were made. Based on the data obtained from the relevant institutions and organizations, and the results of on-site observations obtained during field studies, the determination, interpretation and application of the functional approach criteria considered in the landscape design process of these structures were examined. Aesthetic criteria considered

in the design of the area, public space design principles and basic design principles were evaluated.

A landscape design for the working area has been created using AutoCAD. This design was developed taking into account the topography of the area, existing vegetation, and environmental factors. Additionally, SketchUp software was used to provide a three-dimensional visualization of the project and enable a more realistic presentation of the buildings.

The study was carried out in five stages:

- In the first stage, data related to the research topic was obtained by scanning the literature.
- In the second stage, a land survey was conducted to examine the current situation of the research area and its surroundings, and it was evaluated within the framework of landscape design principles.
- In the third stage, the image map of the area was prepared based on the criteria used in Lynch's visual analysis.
- In the fourth stage, the strengths and weaknesses of the area, as well as threats and opportunities, have been identified through a SWOT analysis.
- In the fifth and final stage, proposals have been presented that will improve socio-cultural life and ensure cultural continuity based on urban landscape design principles.

Firstly, literature data related to the subject and field were evaluated using various resources. In parallel with literature studies and field observations based on on-site detection; the current situation analysis has been made regarding the fill-gap analysis, floor heights analysis, urban equipment areas analysis, building material analysis, transportation analysis, focus points analysis, and landmark analysis for the sample area. A need program has been created together with the analysis of the current situation and problems. After the concept study, a design idea supported by various drawings and visuals was determined.

The analyses have guided the design by revealing the problems in the study area. In this context, urban foci, green spaces, pedestrian axes, and design axes have been examined and the elements guiding the project have been determined. The findings of these analyses are included in the conclusion section of the study. Within the scope of the findings obtained, a SWOT Analysis was conducted to identify the strengths and weaknesses, as well as opportunities and threats related to the field. SWOT analysis is a method used to analyze internal and external factors on a subject related to a region or institution and to reveal its current situation [20],[21]. These factors are classified into four groups as strengths, weaknesses, opportunities, and threats.

In similar studies serving as examples for this study, the same method was used, field analyses were conducted to evaluate the data, existing problems were identified, suggestion ideas (concepts) were developed, and the creation of field diagrams, pre-project and application projects were realized [3],[9],[22], [23].
The stages of the method followed for the revision of urban landscape design in this study are listed below.

- In the first stage of the study, after the literature review on urban landscape design, on-site examination and detection studies of the Long Mustafa neighborhood were carried out and photographs of the area were taken. Later, the zoning plan for the study area was obtained from Düzce Municipality.
- In the second stage, a SWOT analysis was conducted with the aim of putting forward suggestions for the revision of the landscape design of the Uzun Mustafa neighborhood.
- In the final stage of the study, problems related to public buildings and their surroundings in the neighborhood of Uzun Mustafa were identified, and evaluations were made by bringing suggestions in the context of appropriate landscape design.

II. FINDINGS AND DISCUSSION

A. SWOT ANALYSIS RESULTS

A SWOT analysis has been conducted considering the internal and external factors of the workspace, to minimize the impact of the weaknesses in the area and the elements that will pose a threat in the field. SWOT analysis is an analysis made to increase the strong aspects and opportunities provided by the field [24]. The data belonging to Uzun Mustafa neighborhood has been synthesized and the SWOT analysis has been carried out by the study team.

Strong sides (S);

- The work area being located in the city center in terms of location
- Having training areas in the workspace for the region
- Being a convenient area in terms of transportation
- The natural landscape and green areas of Uzun Mustafa neighborhood
- Active participation of neighborhood residents can increase the likelihood of success for joint projects and initiatives.

Weak points (W);

- Due to the high human circulation in the regional workspace, there is noise pollution.
- Solutions can be focused on problems such as inadequate infrastructure, roads, water and energy, in addition to frequently experienced water and energy outages.

Opportunities (O);

- The presence of shopping points in the immediate vicinity of the workspace for the region
- Having health centers in the workspace
- Being in an area open to projects and initiatives compatible with environmental and social sustainability principles
- Opportunities to organize local workshops, activities, and programs to address educational and cultural deficiencies in the neighborhood can be evaluated.

Threats (T);

- Being an earthquake risk area
- Vulnerability to climate change, floods and other natural disasters
- Rapid urban expansion and housing constructions can threaten natural areas.

As a result of the SWOT analysis, it has identified the strengths and weaknesses, opportunities and threats of the study area according to its urban and landscape features. Especially among the strengths, the presence of green spaces and natural landscape features occupy an important place; among the weaknesses, however, traffic intensity and inadequate green infrastructure stand out. The analysis results will allow for the development of revision suggestions that are appropriate to aesthetic, functional, social, cultural, and psychological demands in urban landscape design.

The area designated as Uzun Mustafa neighborhood is one of the largest and most important neighborhoods of Düzce province. The area is located in the city center, but because the area has not been given the necessary importance, the presence of many factors causing visual pollution has revealed that the area is not in good condition. When the steps in the specified method are followed, gathering areas suitable for the area, community center, sports area, park for children, facade design suggestions for public buildings such as Düzce Governorship Meteorology Directorate and Düzce Vocational High School and library building have been presented. A design plan has been created for landscaping works for public building environments in a way that will meet the needs of the users. This plan aims to provide a healthy and safe living space and to create a sustainable environment with sufficient social facilities. Also, the design of landscape structural elements such as garbage containers to be suitable for the

environment, and the visual pollution will not be caused by such as taking electric boxes underground will provide visual aesthetics to the region. In order to design it in accordance with the surroundings of the region, firstly, the green area analysis and road analysis studies of the working area Düzce / Uzun Mustafa neighborhood were carried out. Figure 6. The road and green area analyses of the Study Area Düzce / Uzun Mustafa neighborhood are given.

Figure 6. *Road and green area analysis of the working area Düzce/Uzun Mustafa neighborhood*

Green spaces are a comprehensive system that controls the development of the city in the urban fabric, takes on unifying and distinguishing functions, ensures the integrity of the city in general, and adds value to the city in ecological, aesthetic, recreational and economic aspects. Green spaces, which are a basic need for cities, should be provided in accordance with the principle of integrity and continuity. The findings of this study are in line with definition of roads as one of the elements that form the image of a city [25]. According to Lynch, the definitive characteristics of certain roads can strengthen the city's image or sometimes gain importance for structural reasons. In addition, identifiable and continuous paths are considered as a functional necessity. The outputs of this study meet the requirements and functions mentioned by Lynch. The study area is an important part that ensures the integrity of the open-green area system in its immediate vicinity. In accordance with this approach, the aim of the landscaping of the area is to create gaps that will support structural elements by preserving existing plant structures and to meet the need for shaded areas. This plant tissue aims to meet user needs by integrating with large hard grounds created in the field of urban landscape design. Along with mass green areas, clean grass areas are also included in the plant design. By bringing a landscape design proposal over the existing situation plan, the new situation plan of the area has been created as shown in Figure 7.

Figure 7. *Landscape design proposal plan views for the study area Düzce/Uzun Mustafa neighborhood*

The study area is located in Düzce/Uzun Mustafa neighborhood, where the rebuilt library building currently has no landscaping. Therefore, suggestions such as seating areas have been made as landscape building elements for the back garden of the building aimed at students and reading areas. As shown in Figure 8, views of the library and its surroundings, and in Figure 9, a landscape design proposal plan is given for the location of the library and its surroundings.

Figure 8. *Views of the library and its surroundings located in the Uzun Mustafa neighborhood in the workplace in Düzce*

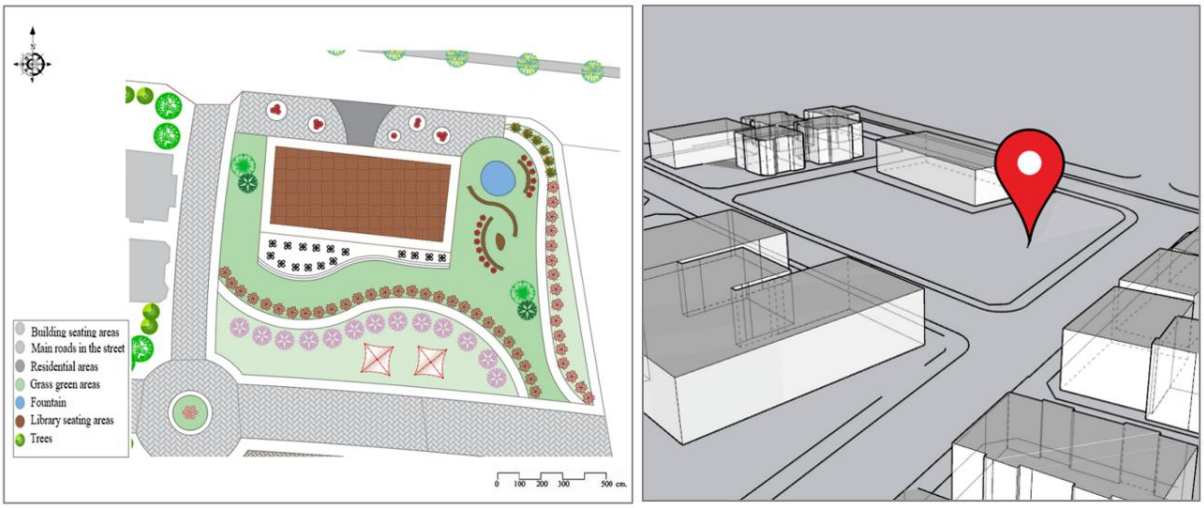

Figure 9. *Landscape design proposal for the location and surroundings of the library located in the working area Düzce/Uzun Mustafa neighborhood*

As presented in detail in Table 2, the various uses and specific growth characteristics of coniferous and deciduous ornamental plants native to Düzce province have been comprehensively addressed. In light of this information, it can be recommended to plan and position these plants in the study area in the most strategically and aesthetically appropriate manner. This planning process can be carried out by considering factors such as the plants' natural habitats, their adaptation to climate conditions, visual effects, and contributions to landscape design. Thus, a landscape arrangement that is compatible with Düzce's local ecosystem, sustainable, and visually attractive can be achieved.

Table 2. *Düzce ornamental plants and their features*

Leafy	*Prunus cerasifera pissardii nigra*		Garden, park, landscape	Medium height, wide crown
	Liquidambar orientalis		Landscape, decorative shade	Medium-large size
	Prunus serrulata		Garden, ornamental plant	Medium height, flowering
	Lagerstromia indica		City gardens, parks	Small tree, colorful flowers

Table 2 (cont). *Düzce ornamental plants and their features*

	Cornus alba		Hedge plant, landscape	Bush form, durable
	Buxus sempervirens		Shaping, hedge plant	Slow growing, compact
	Chaenomeles japonica		Decorative garden plant	Small size, flowering
	Lavandula officinalis		Ornamental plant, scented	Low-stature, bushy
	Syringa vulgaris		Decorative, flowering plant	Medium height, abundant flowers
Needle	*Picea pungens glauca*		Landscape, ornamental plant	Large, pyramidal
	Cedrus deodora		Landscaping, large gardens	Fast growing, large size
	Pinus mugo		Rock gardens, hedge plant	Small size, compact
	Berberis thunbergii		Landscape, hedge plant	Small, colorful leaves

The Düzce Vocational High School located in the study area has an incongruous appearance both in terms of facade appearance and its surroundings. Therefore, a landscape design plan has been proposed by performing facade renovation on the structure and adding a parking lot, seating areas, and landscaping to its surroundings. The appearances of the Düzce Vocational High School building and its surroundings are shown in Figure 10, the location of the structure and the facade design are given in Figure 11, and a landscape design proposal plan for its surroundings is given in Figure 12.

Figure 10. *Views of Düzce Vocational High School and its surroundings located in the working area Düzce/Uzun Mustafa neighborhood*

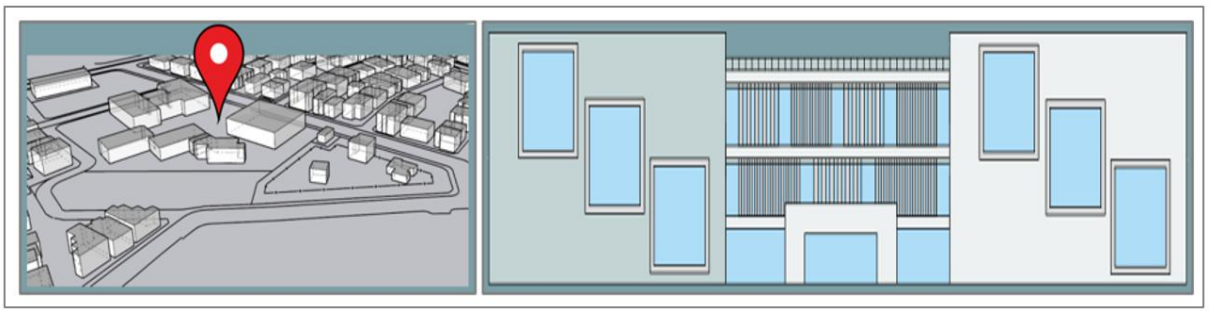

Figure 11. *The location of Düzce Vocational High School located in the working area Duzce/Uzun Mustafa neighborhood and views of its surroundings*

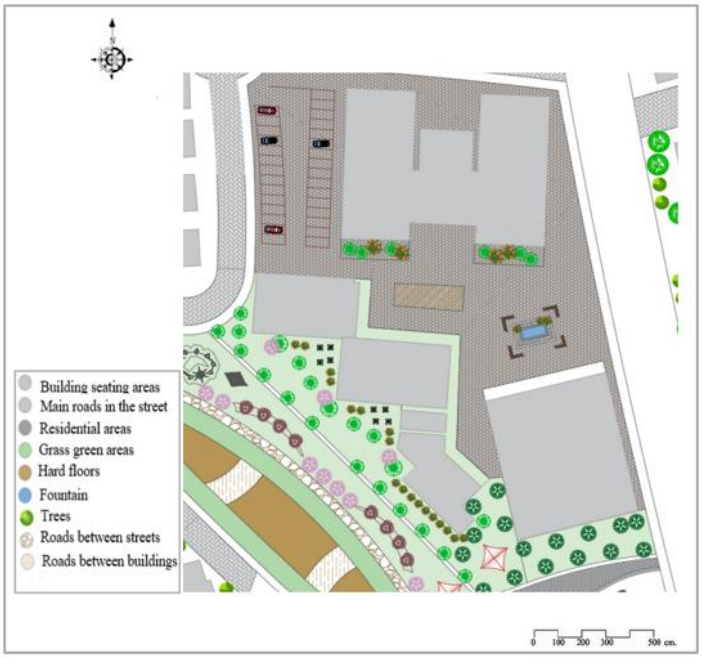

Figure 12. *Landscape design suggestion for Düzce Vocational High School located in the Uzun Mustafa neighborhood, the study area in Düzce*

The building of the Düzce Governorship Meteorology Directorate, located in the work area, has an inconsistent appearance both in terms of facade appearance and its surroundings. Improvements have been made on the facade of the building and it has been handled together with its surroundings. For this

area, a landscape design proposal plan has been created by making a parking lot, seating areas, and landscaping. As shown in Figure 13, the building of the Düzce Governorship Meteorology Directorate, located in the Düzce/Uzun Mustafa neighborhood, the facade design proposal of the building and its location, in Figure 14 the plan appearance of the landscape design proposal for the surroundings of the building has been given.

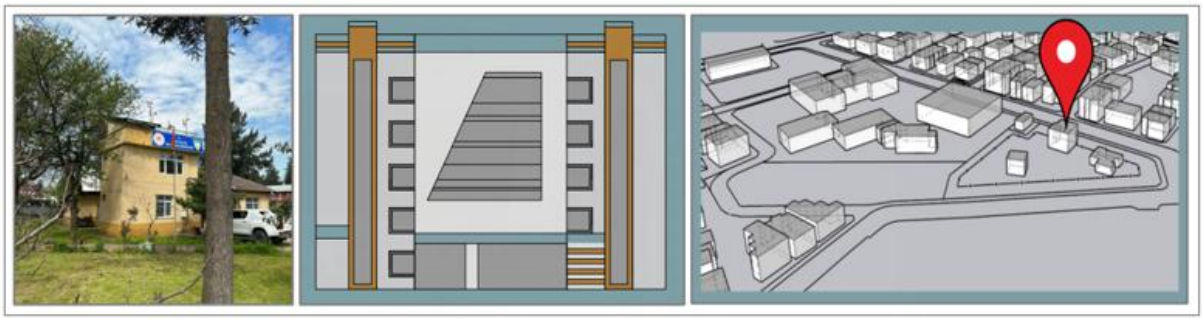

Figure 13. *The building of Düzce Governorship Meteorology Directorate, located in the Uzun Mustafa neighborhood of the study area Düzce, the facade design proposal of the building and its location*

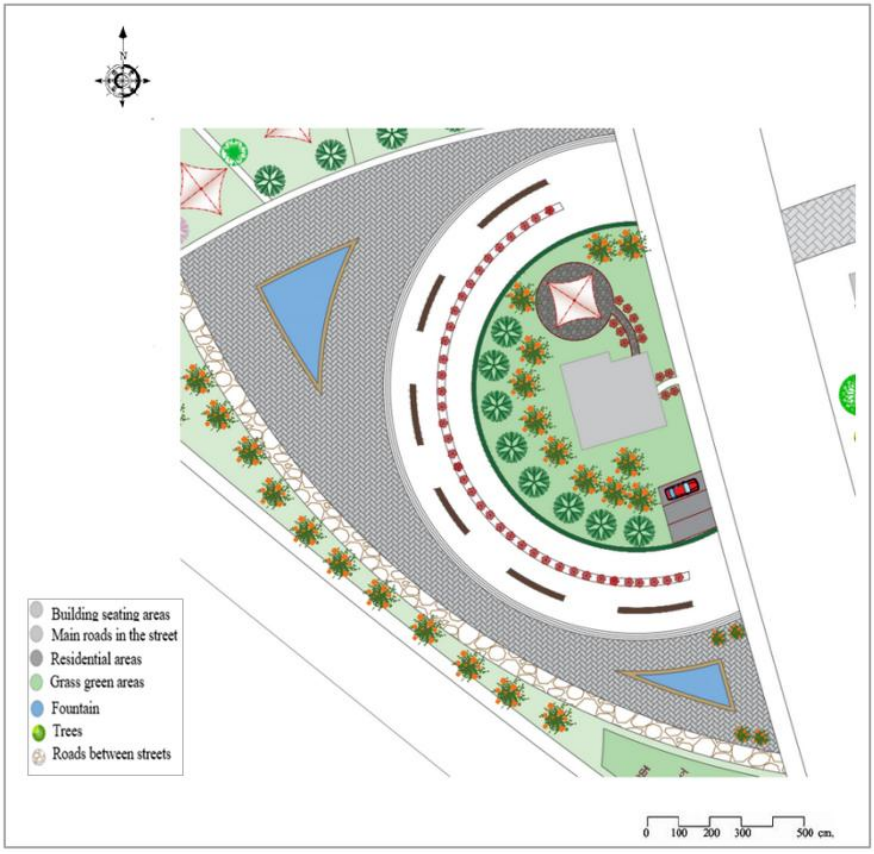

Figure 14. *The plan view of the landscape design proposal for the area around the Düzce Governorship Meteorology Directorate, located in the Uzun Mustafa neighborhood of the study area Düzce*

It is proposed to use the vacant spaces of the working area Düzce/Uzun Mustafa neighborhood and establish a community center where shops, playgrounds, sports areas, parks, and cafes are all together, aiming to bring people together. Considering it next to the Vocational High School and the library will also provide a positive development for students. The facade appearance of the community center designed for Düzce/Uzun Mustafa neighborhood in the work area is shown in Figure 15. The location of the community center and the plan view of the landscape design proposal are given in Figure 16.

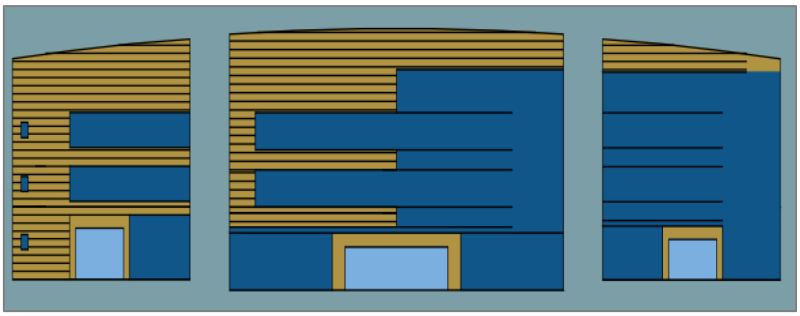

Figure 15. *The facade view of the community center designed for the work area Düzce/Uzun Mustafa neighborhood*

Figure 16. *Location and landscape design proposal plan view of the community center designed for the working area Düzce/Uzun Mustafa neighborhood*

Safe park areas have been designed for children living in the region to play comfortably, and these areas are shown in Figure 17. The plan view of the children's park designed for the work area Düzce/Uzun Mustafa neighborhood is given.

Figure 17. *Plan view of the children's park designed for the work area Düzce/Uzun Mustafa neighborhood*

Due to the earthquake risk of this area within the boundaries of Düzce/Uzun Mustafa neighborhood, assembly areas have been designed for the local people to ensure their safety. As shown in Figure 18, the location and plan view of the gathering areas designed for the Düzce/Uzun Mustafa neighborhood and the plan view of the gathering areas are given in Figure 19.

Figure 18. *The location of the assembly areas designed for the workspace in Düzce/Uzun Mustafa neighborhood*

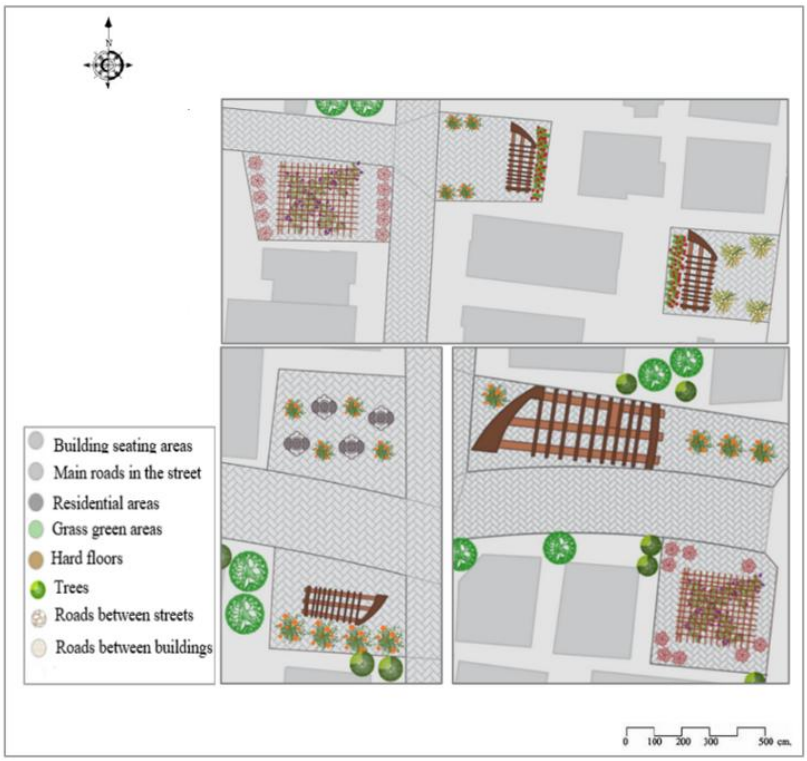

Figure 19. *Plan views of the assembly areas designed for the working area Düzce/Uzun Mustafa neighborhood*

In the workspace, seating areas have been created to meet people's relaxation needs and strengthen social bonds. These areas are arranged so that users can comfortably spend time and chat. The flower beds, which are landscaping elements, are designed to improve the overall atmosphere of the environment, adding peace, tranquility, and aesthetic beauty to the surroundings. These flower pools should offer visitors a visual feast by being adorned with colorful flowers suitable for the season and should also provide a sense of natural freshness. Thus, the workspace has been enriched both functionally and

aesthetically, becoming a place that can respond to the physical and spiritual needs of users. Figure 20 shows the flower pool and seating areas, Figure 21 shows the flower pools, and Figure 22 provides images of the seating elements.

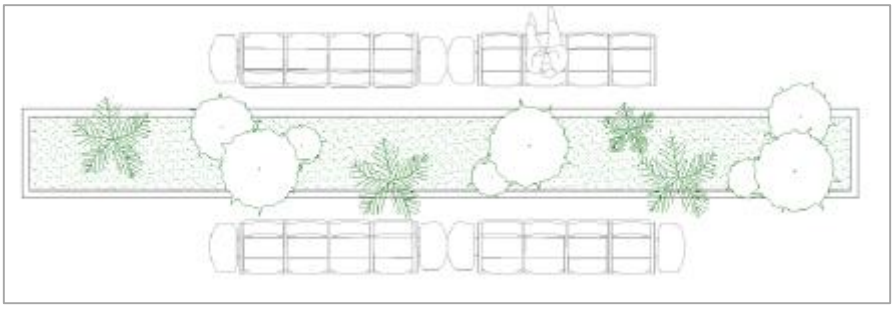

Figure 20. *Views of the designed flower pool and seating areas in the Düzce/Uzun Mustafa Neighborhood study area*

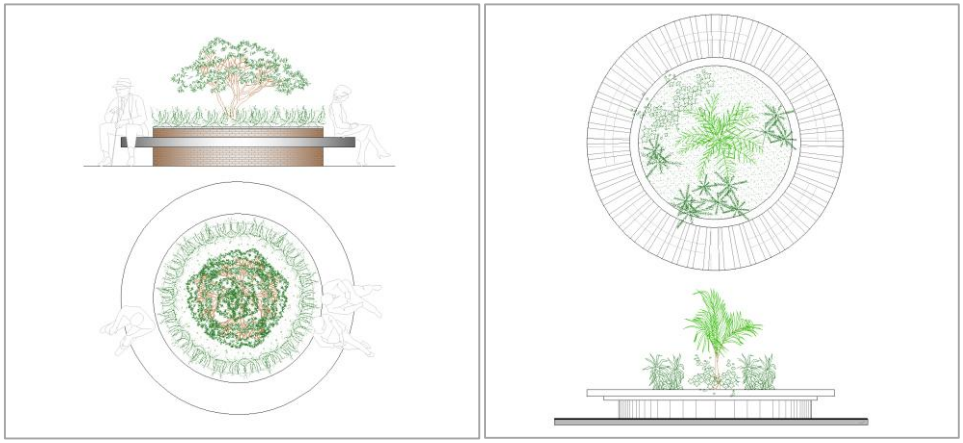

Figure 21. *Views of the designed flower pool in the Düzce/Uzun Mustafa Neighborhood study area*

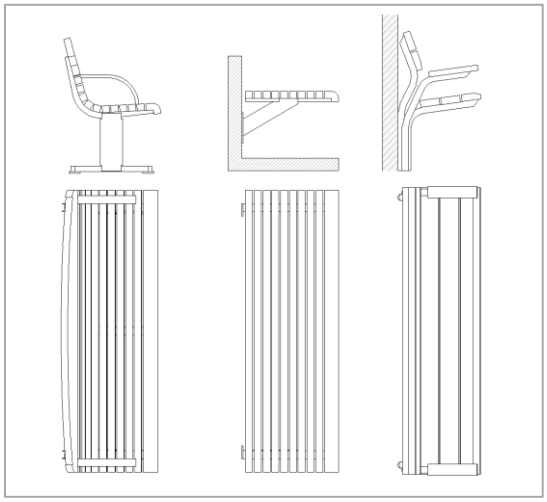

Figure 22. *Views of the designed seating areas in the Düzce/Uzun Mustafa Neighborhood study area*

Lighting used in landscape design should be applied in a way that reveals the architectural features, formation, and function of spaces. The visuals of landscape lighting elements given in Figure 23 designed to enable nighttime use and maintain the visual beauty created in spaces.

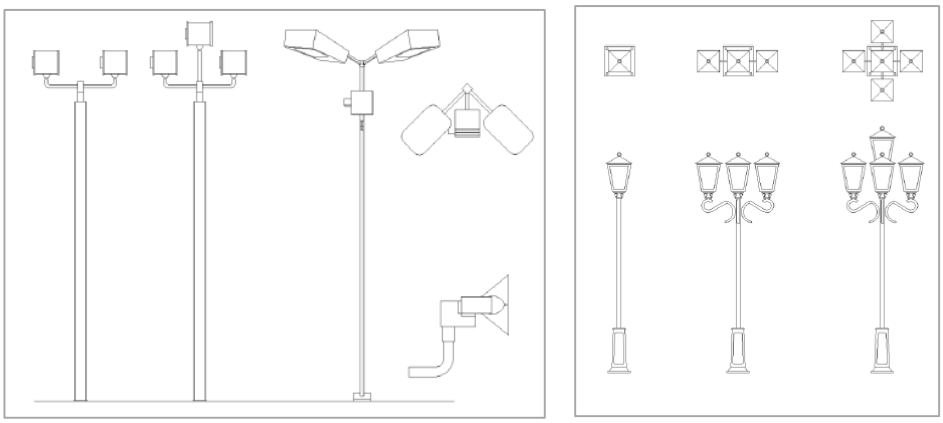

Figure 23. *Views of landscape lighting elements designed for the study area in Düzce/Uzun Mustafa study area*

New garbage containers have been suggested in order to aesthetically improve the environment with the aim of eliminating the visual pollution in this region as a work area. In Figure 24, the existing garbage containers are shown, while Figure 25 shows the appearance of the proposed new garbage containers.

a) ***b)***

Figure 24. ***a)*** *The Appearances of the garbage containers located in the working area in Düzce/Uzun Mustafa neighborhood* ***b)*** *The appearances of the proposed trash containers in the working area in Düzce/Uzun Mustafa neighborhood*

It is suggested to design the facades of electrical transformer buildings in accordance with the environment to improve the general appearance of the workspace, and to remove the electricity poles and lay them underground. The appearance of the electrical transformer buildings and electric poles causing visual pollution in the working area located in Düzce/Uzun Mustafa neighborhood are given in Figure 25.

Figure 25. *Appearances of transformer buildings located in the working area of Düzce/Uzun Mustafa neighborhood*

IV. CONCLUSION

The Uzun Mustafa neighborhood in the province of Düzce, holds an important position due to its location in the city center. However, observations and determinations show that the current situation of the neighborhood is not good, and sufficient services have not been provided to this area. The SWOT analysis conducted for Uzun Mustafa neighborhood reveals the strengths, weaknesses, opportunities, and threats of the neighborhood. This analysis forms an important and scientific basis for understanding the potentials and the challenges faced by the neighborhood this carries the potential to increase the touristic attraction of the neighborhood and strengthen social bonds among local residents. Accessibility can support economic and cultural interaction by facilitating access for neighborhood residents and potential visitors. Infrastructure deficiencies and employment issues play a significant role among the weaknesses. Infrastructure deficiencies limit the quality of life and economic development of the neighborhood. Employment issues can hinder the economic empowerment of neighborhood residents, and this situation threatens long-term sustainability goals. Opportunities include the use of renewable energy, ecotourism, and education-culture programs. Ecotourism has the potential to increase tourism revenues while preserving natural beauties. Education and cultural programs can offer opportunities to develop the skills of local residents and increase social awareness. However, urban expansion, the effects of climate change, and economic uncertainty constitute the main threats faced by the neighborhood. Rapid urban expansion can threaten natural areas, and this situation can make it difficult to preserve the culture of the neighborhood and environmental sustainability.

The future success for Uzun Mustafa neighborhood will rely on a comprehensive strategic plan that will be shaped by the participation of local residents and stakeholders. By considering the needs, expectations, and suggestions of the residents, collaborating with various sectors, and effectively utilizing local resources, it is possible to maximize the potential of the neighborhood. In addition to this work, it is thought to select urban equipment elements (trash cans, lighting elements, bands, bollards, etc.) in accordance with the design. The Uzun Mustafa neighborhood has been subjected to irregular and unplanned construction, especially it does not carry intensity in terms of its historical texture. In this area, spaces with different functions can be proposed to create a more livable space for user needs. For example, by assigning various functions such as a library, workshop, exhibition area, it can be aimed to contribute more effectively to the daily life of the community. When the neighborhood is evaluated in terms of transportation, it has been detected that transportation is easy for vehicles but creates visual pollution due to heavy vehicle traffic and poses a barrier for pedestrians. Therefore, a pedestrian priority design approach has been adopted. Firstly, it is thought to reduce the road which is double-laned to a single lane and to expand pedestrian paths. Also, a disabled track is planned on the bicycle path and pedestrian path. As part of the pedestrian-priority design, plant arrangements that will separate pedestrian and vehicle roads and create shade and aesthetic contribution have been proposed. These arrangements will both add visual appeal to the street and ensure that pedestrians move safely. In conclusion, this study can be seen as an important step to understand the current situation of the neighborhood and guide its future development.

ACKNOWLEDGMENTS: We would like to express our gratitude to Touka Alamour and Maïmouna Koné, students from the Department of Architecture at Düzce University, for their contributions to this study.

V. REFERENCES

[1] N. Gürallar, ‘‘Kamusal alan kamu – kamusal alan – kamu yapıları – Kamusal mekan: Modernite öncesi ve sonrası için bir terminoloji tartışması,’’ *Mimarlık,* c.350, 2009.

[2] S. Carr, M. Francis L. G. Rivlin and A. M. Stone, *Public Space,* Published by the Press Syndicate of University of Cambridge, pp. 400, 1992.

[3] H. Turgut, ‘‘Erzurum Büyükşehir Belediye Binası Ön Bahçe Peyzaj Tasarım Çalışmasının Tasarım İlkeleri Bağlamında Değerlendirilmesi,’’ *Artvin Çoruh Üniversitesi Orman Fakültesi Dergisi*, c.12, s. 2, ss. 185-198, 2011.

[4] H. Lefebvre, *The Production of Space, Blackwell Publishing*, Londra.1991.

[5] Ö. Atabeyoğlu, ‘‘Erzurum Kentindeki Resmi Kurum ve Lojman Bahçelerinin Peyzaj Mimarlığı Açısından İncelenmesi,’’ Atatürk Üniversitesi Fen Bilimleri Enstitüsü Yüksek Lisans tezi, Erzurum, Türkiye, 2004.

[6] D. Yıldız, ‘‘Peyzaj ile Mimarlık-Kentsel Tasarım İlişkileri ve Mimari Tasarıma Etkileri,’’ İstanbul Teknik Üniversitesi Fen Bilimleri Enstitüsü Yüksek Lisans tezi. İstanbul, Türkiye, 1996.

[7] R. V. Sağlar, ‘‘Kamusal Mekânlar ve Tasarım İlkeleri,’’ İstanbul Teknik Üniversitesi Fen Bilimleri Enstitüsü Yüksek Lisans tezi, İstanbul, Türkiye, 1998.

[8] G. A. Sargın, ‘‘Kentsel programı tasarlamak,’’ *Planlama Dergisi*, TMMOB Şehir Plancıları Odası Yayını, no. 33, ISSN: 1300-7319, 2005.

[9] Çelikyay, S. ‘‘Bartın Üniversitesi yerleşkesinde rektör konutu tasarım süreci ve mimari proje,’’ *İnönü Üniversitesi Sanat ve Tasarım Dergisi,* c. 1, s. 1, ss. 11-22, 2011.

[10] S. Kostoff, *The City Assembled, Thames and Hudson*, London,1999.

[11] Ö. Yerli, ‘‘Bir yapının kamusal açık yeşil alan şeklinde tasarlanması,’’ *TMD Uluslararası Hakemli Tasarım ve Mimarlık Dergisi,* ss. 1-13, 2016.

[12] M. Carmona and S. Tiesdell, ‘‘Urban design reader, Architectural Press,’’ *Elsevier*, 2007.

[13] Z. Demir, H. Müderrisoğlu, Ö. Yerli, S. Özdede and G.A. Kesim, *Bartın Orman Fakültesi Dergisi*, I. Ulusal Batı Karadeniz Ormancılık Kongresi Bildiriler Kitabı, s.1, ss. 232-240, 2009.

[14] L. N. Groat, *Contextual compatibility in architecture: An Issue of Personal Taste?* Cambridge University Pres, pp. 228-253, 1988.

[15] G. Uzgören, M.Y. Erdönmez, ‘‘Kamusal açık alanlarda mekân kalitesi ve kentsel mekân aktiviteleri ilişkisi üzerine karşılaştırmalı bir inceleme,’’ *Megaron*, c.12, s. 1, ss. 41- 56, 2017.

[16] E. Koçak, *Düzce ilinin Cbs ve uzaktan algılama tabanlı tarım coğrafyası*. Ankara, 2023.

[17] (2024, May 20). [Çevrimiçi]. Erişim: https://www.milliyet.com.tr/egitim/haritalar/duzce-haritasi.

[18] (2024, May 26). [Çevrimiçi]. Erişim: https://www.google.com/search?q=google+earth+d%C3%BCzce+uzun+mustafa+mah.

[19] (2024, April 9). [Çevrimiçi]. Erişim:https://www.arasikackm.com/m/uzun-mustafa-mah-duzce.

[20] C. Cengiz, P. Keçecioğlu Dağlı, ‘‘Bartın geleneksel kent dokusunda yaya konfor düzeyinin saptanmasına yönelik bir çalışma,’’ *Bartın Orman Fakültesi Dergisi*, c.19, s.1, ss.19-31, 2017.

[21] B. Acarlı, T. Kiper, A. Korkut, “Kent meydanlarının fiziksel mekan kalitesi: İstanbul Taksim Meydanı ve yakın çevresi,” *Kent Akademisi,* c. 11, s.33, ss. 29-41, 2018.

[22] H. Çınar, ‘‘XVIII. Yüzyılın İlk yarısında Ayıntab şehrinin sosyal ve ekonomik durumu,’’ *Vakıflar Dergisi,* s.7, ss.117-138, 2007.

[23] Z. Demir, H. Müderrisoğlu, Ö. Yerli, S. Özdede ve G.A. Kesim, I. Ulusal Batı Karadeniz Ormancılık Kongresi Bildiriler Kitabı, *Bartın Orman Fakültesi Dergisi,* no.1, ss. 232-240, 2009.

[24] S. G. Bozkurt, “Gürün ilçesinin ekoturizm potansiyelinin incelenmesi,’’ *Journal of the Institute of Science and Technology,* vol. 9, no. 4, ss. 2255-2265, 2019.

[25] K. Lynch, *Kent İmgesi*. Türkiye İş Bankası Yayınları. 2010.

[26] (10 September, 2024). [Çevrimiçi]. Erişim: https://www.google.com/search?sca_esv=9783522cabc36d5f&sxsrf=ADLYWIJmthpygvmzjsg6ROHkW07MW6U5dA

[27] A. H., Küçük, ‘‘Kentsel dönüşüm boyutları: Barselona'da Raval bölgesi örneği,’’ Yayınlanmamış Yüksek Lisans tezi, İstanbul Teknik Üniversitesi, Fen Bilimleri Enstitüsü, İstanbul, Türkiye, 2014.

[28] Bath & North East Somerset Council. (2015b). *Pattern book volume 2: technical and operational guidance.* [Çevrimiçi]. Erişim: https://www.bathnes.gov.uk/sites/default/files/sitedocuments/Planning-and-Building-Control/Planning-Policy/Evidence-Base/Urban-Design-Landscape-and-Heritage/bath_pattern_book_part_2.pdf

[29] Blyth Valley Borough Council. (2008). *Blyth urban design guide and public realm strategy*. [Çevrimiçi]. Erişim: https://www.northumberland.gov.uk/NorthumberlandCountyCouncil/media/Planning-and-Building/Conservation/DG-Blyth-Urban-Design-and-Public-Realm.pdf

[30] S. N., Yener Metin and S. Polat, ‘‘Kamusal mekân kalitesini yükseltmek için kentsel tasarım araçlarından nasıl faydalanabiliriz?’’ *Kent Araştırmaları Dergisi*, s.12, ss.115-145, 2021.

[31] S. N., Yener Metin and S. Polat, ‘‘Kamusal mekân kalitesini yükseltmek için kentsel tasarım araçlarından nasıl faydalanabiliriz?’’ *Kent Araştırmaları Dergisi,* s.12, ss.115-145, 2021.

Düzce University Journal of Science & Technology

Research Article

Comparison of Swelling Pressures Determined by Two Different Methods

Ömür ÇİMEN [a,*], S. Nilay KESKİN [b]

[a] *Department of Civil Engineering, Faculty of Engineering and Natural Sciences, Süleyman Demirel University, Isparta, TURKEY*
[b] *Department of Civil Engineering, Faculty of Engineering and Natural Sciences, Süleyman Demirel University, Isparta, TURKEY*
** Corresponding author's e-mail address: omurcimen@sdu.edu.tr*
DOI: 10.29130/dubited.1541087

ABSTRACT

Expansive soils are a problem affecting many parts of the world. The fact that the expenses incurred due to the damage caused by swelling soils are quite high shows that this problem cannot be ignored. In this study, swelling pressures of compacted clays are determined using two different test methods, one of which is an oedometer test equipment. Three different clay samples were used in the tests. Free and constant-volume swell tests are conducted on compacted samples prepared at various water contents and dry densities. Free swell pressure and constant-volume swell pressure tests are performed on samples with identical initial conditions using oedometer testing equipment. These tests are repeated more than two times. Regression analysis was conducted on the free and constant-volume swell pressures based on the obtained data. Then, the swelling pressures calculated using the empirical equation are compared with test results and literature data.

Keywords: *Clay soil, Free swelling pressure, Constant volume swelling pressure.*

İki Farklı Yöntemle Belirlenen Şişme Basınçlarının Karşılaştırılması

ÖZ

Şişen zeminler dünyanın birçok bölgesini etkileyen bir sorundur. Şişen zeminlerin neden olduğu hasarlar nedeniyle oluşan masrafların oldukça yüksek olması bu sorunun göz ardı edilemeyeceğini göstermektedir. Bu çalışmada, sıkıştırılmış killerin şişme basınçları ödometre test cihazı kullanılarak iki farklı deney yöntemi ile belirlenmiştir. Üç farklı kil numunesi ile deneyler yapılmıştır. Farklı su muhtevalarında ve farklı kuru birim hacim ağırlıklarda hazırlanan sıkıştırılmış numunelerde serbest şişme deneyleri ve sabit hacimli şişme deneyleri yapılmıştır. Başlangıç koşulları aynı olan numuneler üzerinde ödometre test cihazı ile serbest şişme basıncı ve sabit hacimli şişme basıncı deneyleri yapılmıştır. Bu deneyler her numune için en az iki kez yapılmıştır. Elde edilen verilerden serbest şişme basıncı ve sabit hacimli şişme basıncı için regresyon analizi yapılmıştır. Daha sonra, ampirik denklemden bulunan şişme basıncı değerleri hem deney sonuçları hem de literatür verileri ile karşılaştırılmıştır.

Anahtar Kelimeler: *Kil zemin, Serbest şişme basıncı, Sabit hacimli şişme basıncı.*

Received: 30/08/2024, Revised: 08/12/2024, Accepted: 09/12/2024

I. INTRODUCTION

Clayey soils can increase in volume by absorbing water or may exhibit excessive pressure when this volume increase is restricted, characteristics known as swelling behavior in soils. When examining the swelling properties of clay, the aim is to determine the swelling pressure and percentage. The ratio of the volume increase of a soil sample in its natural state or compressed in the laboratory until it becomes saturated with water under a certain load, to its initial volume, is called swelling potential. The pressure that prevents volume changes in swelling soil is called swelling pressure. There are many methods for determining swelling characteristics. These methods can be considered in three groups [1]: 1) Mineralogical methods: X-ray diffraction, differential thermal analysis, dye adsorption, chemical analysis, and electron microscope method, 2) Indirect methods: clay consistency limits properties, PVC method, activity method, suction pressure method, and empirical relations. Since these methods reflect the soil characteristics of certain geographical regions, it is not independently recommended for usage, 3) Direct measurement: The measurement is the most accurate method for determining the clay's swelling percentage and pressure. The most commonly used direct measurement technique is the one-dimensional consolidation method in ASTM D4546 [2]. Three methods have been proposed for direct measurement. The first method is the swell-consolidation method (CS) or swell-load method. In this test, the stress on vertical direction is subjected to the specimen and wetted under that vertical stress while the specimen is laterally confined. The second method is the constant volume (CV) or zero-swell method. The vertical stress of this second method is subjected to the specimen and the vertical strain that is confined during wetting. The last method is the swell overburden method (SO). In this test, many specimens (three or more specimens) are loaded to the different initial applied vertical loads around estimated swelling pressure, and water is added to monitor the swell until the primary swell completes or is compressed to reach equilibrium positions [2].

The swelling mechanism in soils with swelling potential is quite complex. Swelling occurs due to changes in internal forces within the clay-water system, which disrupts the balance of internal stresses. Clay grains generally have negative electrical charges on their surfaces and positive electrical charges on their edges. Negative charges are balanced by cations in the groundwater held by electrical forces on the surfaces of the clay plates. The intergranular electrical field is a function of both the electrical charges and the electrochemistry of the groundwater. Van Der Waals surface forces and adsorption forces between clay crystals and water molecules are affected by intergranular forces. This change in the electrical field between grains occurs as swelling or shrinkage. Factors affecting the swelling behavior of soil can be grouped into three main groups [1]: 1) Soil properties affected by the basic structure of the internal force field (Plasticity, dry unit volume weight, clay mineralogy, groundwater chemistry, soil absorption capacity, soil structure and fabric, initial water content, etc.), 2) Environmental factors affected by changes in the internal force system (Change of water content, groundwater chemistry, dry unit volume weight, etc.), 3) Stress state in the soil.

The swelling pressure of the soil can be determined using different test techniques in the one-dimensional oedometer test system. Changes in test techniques include the condition of the sample (undisturbed, disturbed), surcharge load (1 kPa, 7 kPa, 30 kPa or geological load on the field), water content (natural, optimum), and stress state (dead load, constant volume, etc.). The three oedometer procedures produce different swelling pressure measurements. The swelling pressure from the SC test leads to the greatest measurement, the intermediate value results in the constant volume (CV) test, and the smallest value results from the swell overburden (SO) test. The loading conditions, side friction effect, and wetting process are the factors causing different swelling pressure values [3]. When the swelling pressures obtained in the swelling tests performed by applying free swelling, constant volume swelling, and geological load are listed from largest to smallest, the following order emerges; free swelling pressure, constant volume swelling pressure, and swelling pressure found by applying geological load. It has been stated that these differences are due to differences in loading and wetting conditions in the test methods [3]. It has been implied that the swelling test with geological load applied is more suitable for field conditions, while the constant volume and free swelling tests are not

fully appropriate for field conditions [4]. It was found that the swelling pressures obtained from the triaxial pressure test were better suited to field conditions compared to those obtained from the oedometer test [5, 6, 7].

Tisot and Aboushook [8] stated that the swelling pressure obtained from free swelling experiments was three times higher than that obtained from constant volume swelling experiments. Al-Shamrani and Dhowian [9] compared the swelling pressures obtained from free and constant-volume swelling experiments on clays compacted under the same conditions indicating that the free swelling pressure was 1.4 times greater than the constant-volume swelling pressure. Liang et al. [10] first introduced the recently developed suction-controlled swelling pressure device to measure the swelling pressure of expanding soil in a wide suction range. The development of swelling pressure was closely related to the water retention characteristics. At high suction, the swelling pressure stems mainly from interlayer hydration; at low suction, however, the swelling pressure was controlled by the development of double layers, accompanied by the collapse of some macropores. The nuclear magnetic resonance (NMR) technique was introduced to determine the specific amount of adsorbed and capillary water contents, shedding new insights into the swelling behavior of compacted expansive soil during the wetting process under confined conditions. The reason that the compacted expansive soils show nonmonotonic swelling behavior can be attributed to the fact that the compacted expansive soils include pores of different types and sizes, such as the intra-aggregate pores and the inter-aggregate pores [11].

Microlevel properties such as mineralogical and chemical compositions greatly control the macro behavior of expansive soils. In the study, 46 different samples of expansive-type soil were collected from various locations across India. The mineralogical and chemical contents of the soil samples were analyzed to investigate their combined impact on swelling property. The results are unique and significant for field engineers, as they can predict swelling behavior based on measured chemical and mineral parameters [12]. Taherdangkoo et al. [13] present a dataset comprising maximum swelling pressure values from 759 compacted soil samples, compiled from 16 articles published between 1994 and 2022. The dataset is classified into two main groups: 463 samples of natural clays and 296 samples of bentonite and bentonite mixtures, providing data on various types of soils and their properties. Different swelling test methods, including zero swelling, swell consolidation, restrained swell, double oedometer, free swelling, constant volume oedometer, UPC isochoric cell, isochoric oedometer, and consolidometer, were employed to measure the maximum swelling pressure. The comprehensive nature of the dataset enhances its applicability for geotechnical projects. The dataset is a vital resource for understanding the intricate interactions between soil properties and swelling behavior, which enhances advancements in soil mechanics and geotechnical engineering.

Numerous studies indicate that swelling pressure can be estimated using various soil properties. In a study, the swelling stress of soils collected from 15 locations in 5 sites across South Africa has been predicted by using the artificial neural network (ANN), genetic programming (GP), and evolutionary polynomial regression (EPR)-based intelligent techniques [14]. Neuronet models relating the potential expansiveness to some geotechnical properties are derived to overcome the need to perform lengthy swelling pressure determination experiments [15]. In another study, different independent scenarios of explanatory features' combinations that influence soil behavior in swelling were investigated. Preliminary results indicated Bayesian linear regression (BLR) as possessing the highest amount of deviation from the predictor variable (the actual swell-strain) [16]. The activity, water content, dry unit weight, liquid limit, plastic limit, plasticity index, and clay content were considered as the input parameters of the models as they are commonly measured during the experimental testing of soil behavior. The results show that the feed-forward neural network trained with the Levenberg–Marquardt algorithm is the most accurate model for the prediction task. The model performance is satisfactory, showing an acceptable agreement with experimental data. The developed model showed substantial improvements over previous empirical and semi-empirical correlations in determining the swelling potentials of both natural and artificial soils [17].

In this study, the constant-volume swelling pressures and free swelling pressures of compacted clays were compared under the same initial conditions. Correlations between free swelling pressure and

constant volume swelling pressure have been made and an empirical relationship has been proposed. The free swelling pressure values obtained from the experiments were compared with the calculated free swelling pressure values obtained from the empirical relationship. The proposed empirical relationship was compared using experimental data from the literature obtained under identical experimental conditions. It is shown that the proposed relationship can be used to pre-estimate the free swell pressure.

II. MATERIAL AND METHOD

A. DEFINITION OF SAMPLES

Experiments were conducted on disturbed clay samples with high plasticity taken from various regions in the study. Sample 1 was taken from Istanbul-Türkiye, and samples 2 and 3 were taken from Antalya-Türkiye. Soil classes were determined using sieve analysis and consistency limit tests on the samples according to the Unified Soil Classification System. Optimum water contents and maximum dry unit volume weights were determined by performing standard compaction tests. The results obtained from the experiments are given in Table 1.

Table 1. *Properties of the samples used in the experiments [18]*

Properties	Sample 1	Sample 2	Sample 3
Liquid limit (%)	75	73	66
Plastic limit (%)	21	26	28
Plastisity index (%)	54	47	38
Grain unit volume weight (kN/m^3)	27.4	27.7	28.1
Max. dry unit volume weight (kN/m^3)	16.1	16.0	15.2
Optimum water content (%)	23	23	27
Gravel (%)	1	1	0
Sand (%)	6	3	2
Silt + Clay (%)	93	96	98
Soil Class	CH	CH	CH

Since the mineralogy of the soil samples influences swelling behavior, it was determined. The X-ray diffraction method is widely used to determine the mineralogy of the clay samples. XRD analyses were conducted on both the clay portion and the entire sample. XRD analyses were performed separately on the oriented and unoriented samples where the clays were air-dried, swollen with ethylene glycol, and heated at 550 °C. The resulting diffraction curves are given in Figures 1-3. The X-ray analyses were carried out in two parts: whole rock analysis and clay size analysis. In whole rock analyses, smectite, chlorite, quartz, feldspar, calcite, and illite minerals are present in the samples. Besides, only the clay part of the samples was separated and clay fraction analyses were performed on it. The clay sample was saturated with ethylene glycol to determine the clay mineral type, followed by an X-ray analysis. Samples subjected to ethylene glycol treatment were heat treated at 550ºC and X-ray images were taken. The minerals obtained from the analyses were determined in order of abundance and are given in the third section.

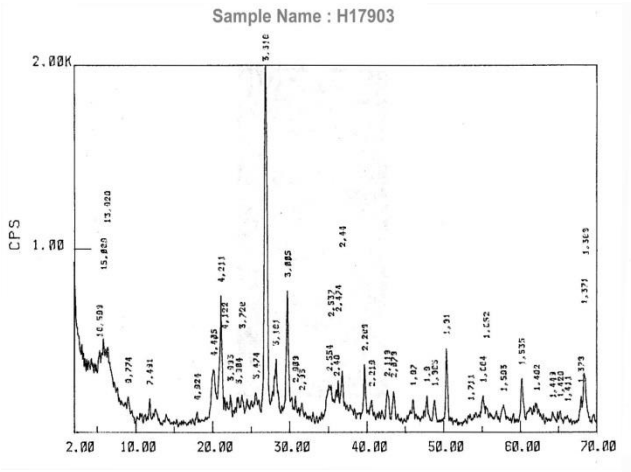

a) Whole rock analysis

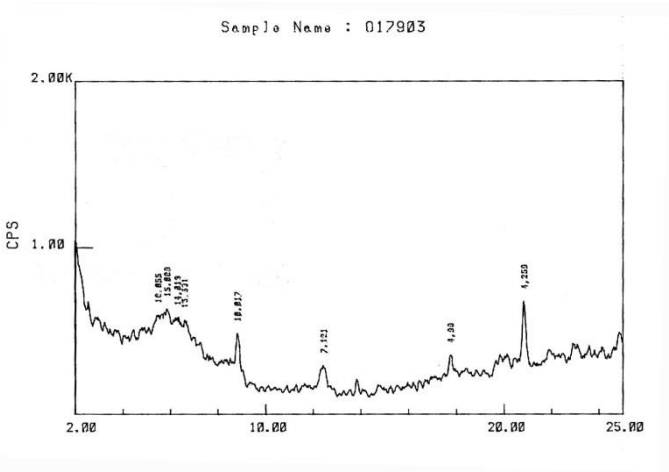

b) Orientation

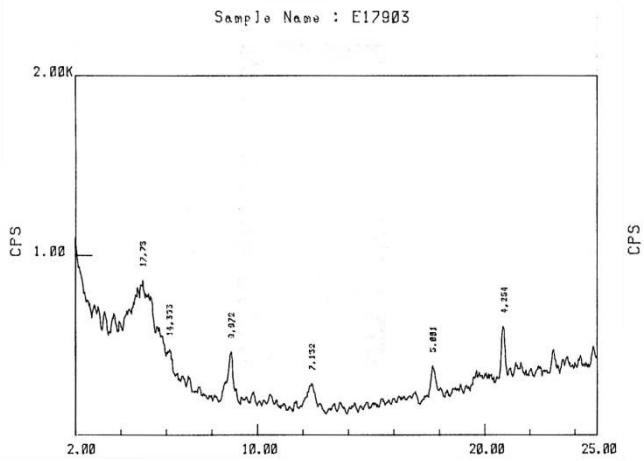

c) Analysis with ethylene glycol

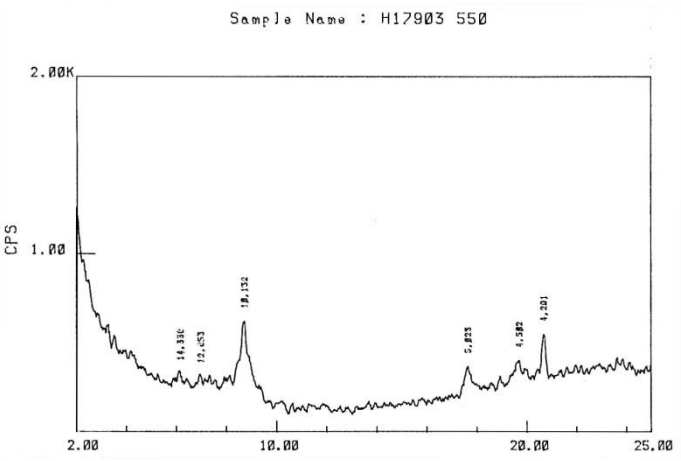

d) Analysis subjected to heat at 550 °/1 hour

Figure 1. *X-ray diffraction curves of sample 1 [18]*

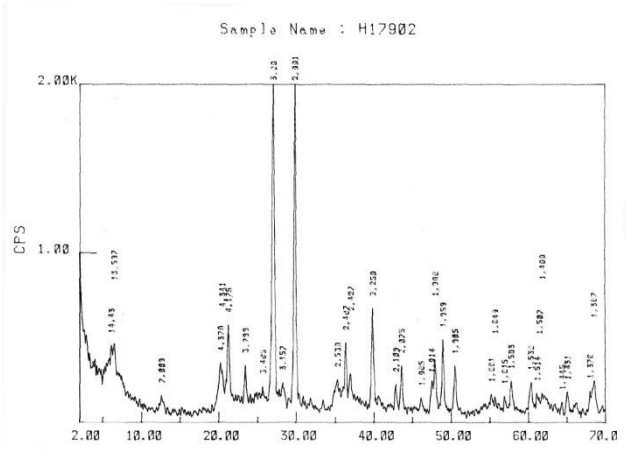

a) Whole rock analysis

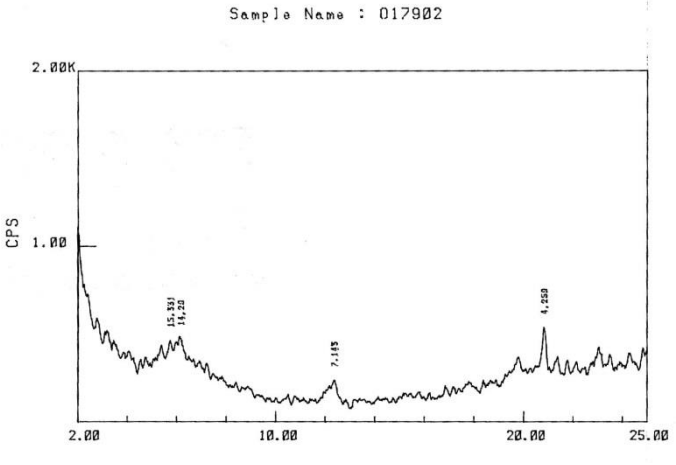

b) Orientation

Figure 2. *X-ray diffraction curves of sample 2 [18]*

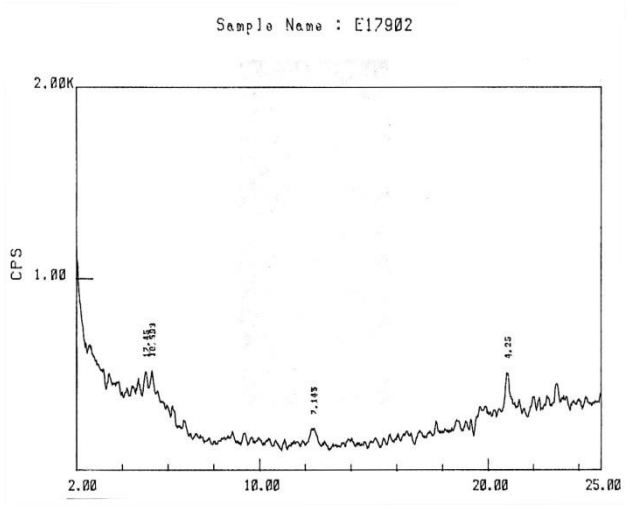

c) Analysis with ethylene glycol

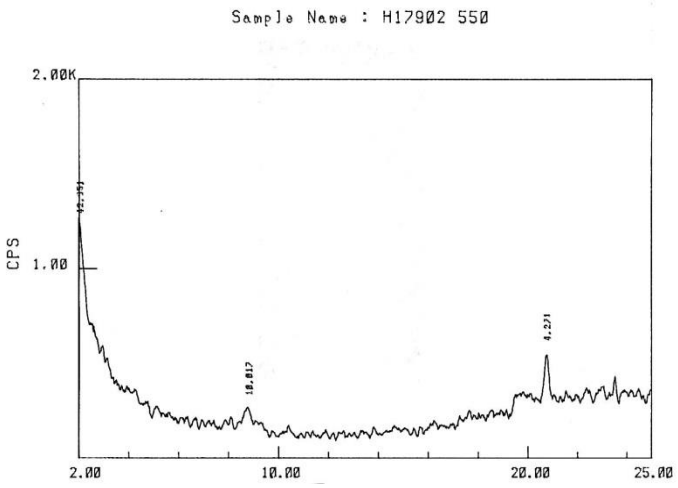

d) Analysis subjected to heat at 550 °/1 hour

Figure 2 (cont). *X-ray diffraction curves of sample 2 [18]*

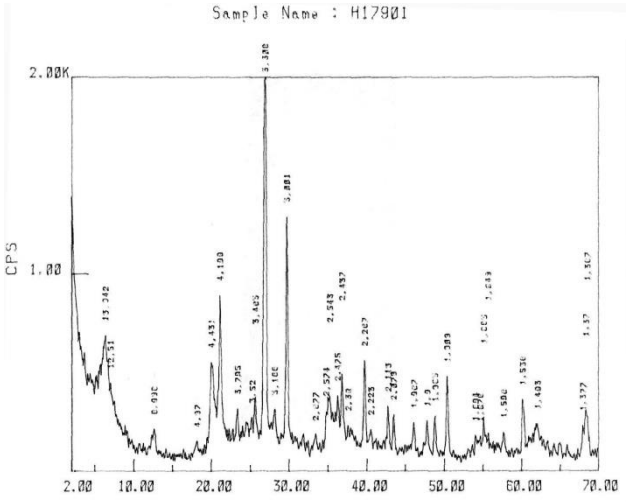

a) Whole rock analysis

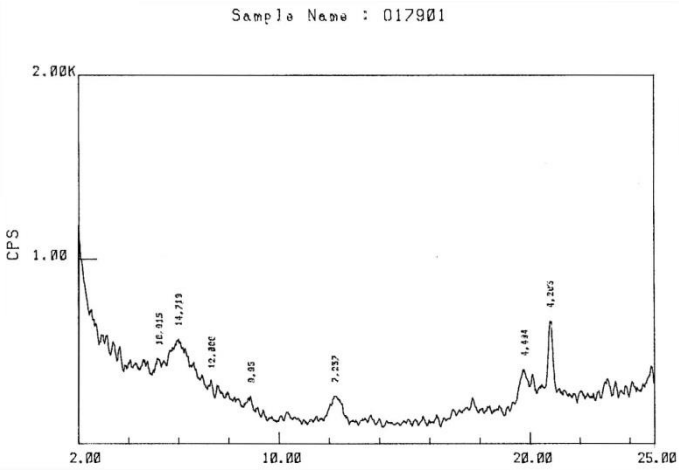

b) Orientation

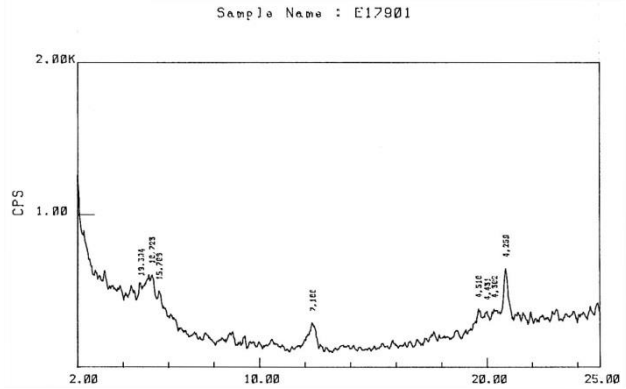

c) Analysis with ethylene glycol

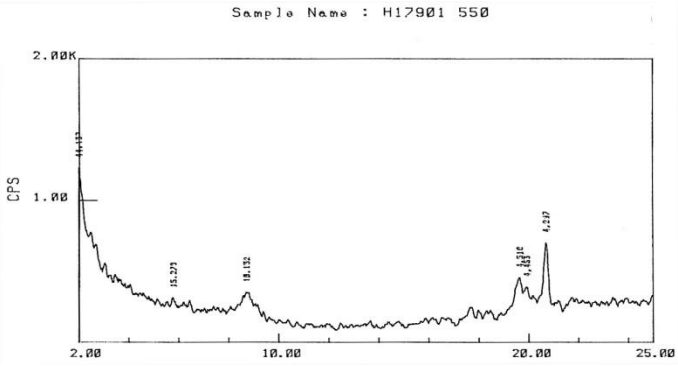

d) Analysis subjected to heat at 550 °/1 hour

Figure 3. *X-ray diffraction curves of sample 3 [18]*

A. 1. Determination of Swelling Pressures by Oedometer Method

The free swelling method specified as Method A and the constant volume swelling method specified as Method C, which is among the ASTM D4546 [2] test methods, are selected to determine the swelling pressures. Samples under the No.40 sieve were prepared by mixing at different

predetermined initial water contents (15%, 20%, 25%, 30%, 35%, 40%) to be on the dry and wet side of the optimum water content. The optimum water content of the samples was used to determine these initial water contents. Distilled water was used in every stage of the experiments performed on the samples.

Samples prepared at different water contents were compacted with standard compaction at different dry unit volume weights (11.5 kN/m^3, 13.0 kN/m^3, 14.0 kN/m^3, 15.0 kN/m^3, 16.0 kN/m^3, 17.0 kN/m^3). An oedometer ring was immersed in these prepared samples and the sample was placed in the ring. Experiments were primarily carried out on samples prepared at the same dry unit volume weight and different initial water contents. Then, it was carried out for samples prepared at the same water content and different dry unit volume weights. During compaction, care was taken to maintain consistent water content and achieve homogeneous compaction.

The soil samples placed in the oedometer cell were allowed to absorb water via capillary under a surcharge load of 1 kPa. The swelling amount of the soil samples allowed to swell in this way was determined from the vertical deformation meter. After waiting until the final swelling of the soil samples was completed, that is, after the value read on the deformation clock was fixed, the oedometer cell was filled with water and waited for 24 hours. At the end of this period, it was observed that the final swelling value of the sample did not change. After the swelling of the sample was completed, load was applied to the sample in small steps. At least 24 hours were waited at each load level. The pressure required to reset the total swelling amount was determined and thus the swelling pressure of the ground was determined. This pressure was taken as the pressure at which the hand of the clock measuring the vertical deformation returned to its starting point (zero). This pressure value was recorded as free swelling pressure.

In the second series of studies, the samples were prepared under the same initial conditions and allowed to absorb water via the capillary method, and this time they were subjected to a constant volume swelling test. In these experiments, continuous loading was applied to ensure that the deformation clock on the oedometer cell remained at zero while the sample was receiving water. The pressure applied to the sample was constantly increased to prevent swelling and the needle of the vertical deformation clock was kept constant at zero. Then, the cell was filled with water and the pressure value obtained after waiting 24 hours was recorded. The pressure at which inflation was inhibited is the constant volume inflation pressure. The results obtained from the experiments were correlated.

III. RESULTS AND DISCUSSION

This study aims to compare swelling pressures and investigate the relationship between them by using results from free swelling and constant volume swelling experiments conducted with three different soil samples. Firstly, the mineral structure of the samples was determined by X-ray analysis. The analyses identified the dominant clay minerals and others in the samples in order of their abundance. Accordingly, the minerals identified in the samples were:
Sample 1: smectite + chlorite, quartz, calcite, feldspar, illite.
Sample 2: smectite + chlorite, quartz, feldspar, calcite.
Sample 3: smectite + chlorite, calcite, illite, quartz.

The mineral structure of the samples used in the experiments suggests a high potential for swelling. The clay minerals that exhibit greater expansion belong to the 2:1 group of clay minerals, characterized by layers of tetrahedrons and octahedrons where cations and water molecules are held in the interlayer spaces. As can be seen in Table 2, the swelling clay exhibits greater interlayer spacing than non-swelling clay. Different clay minerals exhibit different swelling potentials due to changes in their structure and interlayer bonding. Smectites and vermiculites undergo significant volume changes

when wet and dry [20]. Regarding swelling, clay type is a more important factor than clay percentage and the amount of smectite is also effective in the swelling potential measured in the laboratory [21].

Table 2. *Basal spacing of different types of clay minerals based on swelling potential [19]*

Clay Mineral	Type	Basal Spacing(A)	Swelling Potential
Kaolinite	1:1	7.2	Almost none
Montmorillonite	2:1	9.8-20	High
Vermiculite	2:1	10-15	High
Mica	2:1	10	Low
Chlorite	2:1:1	14	None

The results obtained from the swelling experiments are presented in Table 3. The table shows P_s the constant volume swelling pressure and P_s' the free swelling pressure. The results obtained from the swelling experiments are presented in Table 3. The table indicates that at a constant dry unit volume weight, swelling pressure decreases as the initial water content increases. The swelling pressure increases as the dry unit volume weight rises at a constant initial water content. At the same time, it can be seen that the free swelling pressure is higher than the constant-volume swelling pressure. The sample is subjected to a low surcharge pressure in the free swelling pressure tests. The low pressure applied facilitates the entry of the water into the clay having high swelling properties. In constant volume swelling pressure experiments, the applied pressure reduces water ingress.

Table 3. *Initial conditions and swelling pressure values of the samples [18]*

		Sample 1		Sample 2		Sample 3	
γ_k (kN/m^3)	w_o(%)	P_s (kPa)	P_s' (kPa)	P_s (kPa)	P_s' (kPa)	P_s (kPa)	P_s' (kPa)
11.5	15	126	208	79	163	42	86
	20	98	161	65	128	33	75
	25	86	157	50	103	24	52
	30	53	112	26	63	18	41
	35	33	69	19	48	10	22
	40	26	42	8	20	4	10
13.0	15	152	321	90	202	51	110
	20	135	260	80	187	43	96
	25	98	202	59	128	39	88
	30	63	130	38	92	22	71
	35	51	100	26	68	10	24
	40	32	48	12	32	6	15
14.0	15	281	509	120	340	68	203
	20	198	300	100	271	54	126
	25	132	281	71	152	42	98
	30	78	173	48	102	31	85
	35	61	103	26	58	15	48
	40	37	68	18	43	9	22
15.0	15	345	640	143	376	74	217
	20	296	410	112	250	65	183
	25	170	290	85	186	51	122
	30	94	145	56	122	40	94
16.0	15	405	680	171	398	82	250
	20	289	478	129	282	66	204
	25	186	292	98	210	49	132
17.0	15	483	848	189	482	88	260
	20	312	526	150	326	72	218

As an example of the swelling pressure values in Table 3, the relationship between constant volume swelling pressure and different water contents, when the dry unit weight is 13 kN/m^3, is given in Figure 4. The relationship between free swelling pressure and different water contents is presented in Figure 5. It is seen that swelling pressures decrease as water content increases at constant dry unit weight from Figures 4 and 5.

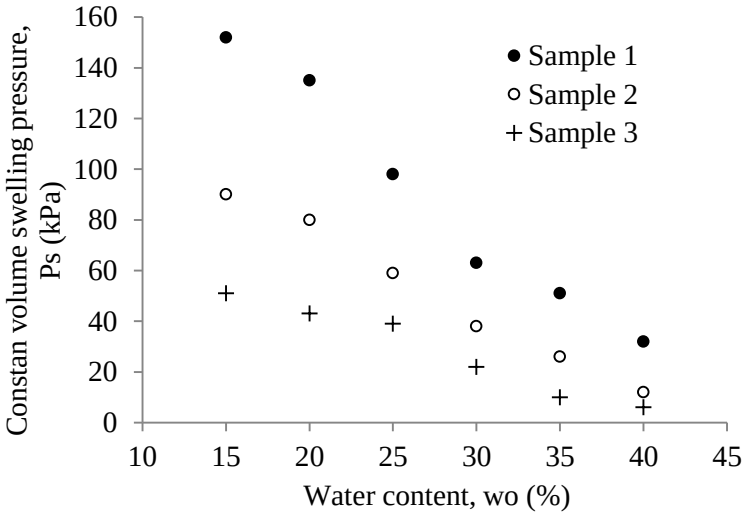

Figure 4. *Relation between water content and constant volume swelling pressure for* $\gamma_k = 13.0\ kN/m^3$

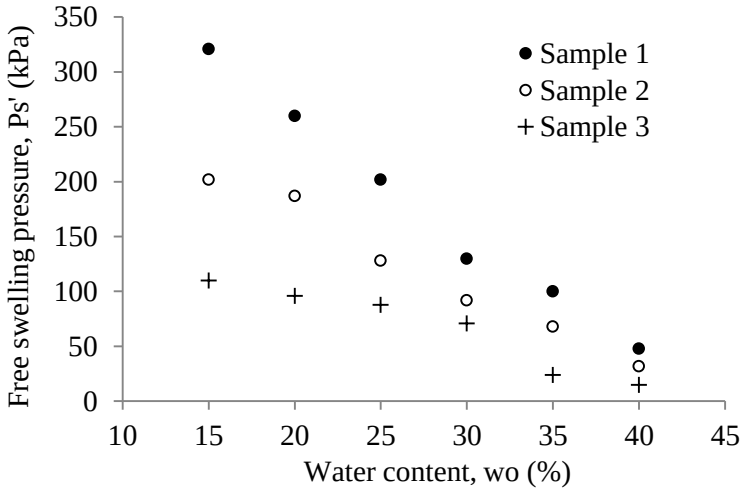

Figure 5. *Relation between water content and free swelling pressure for* $\gamma_k = 13.0\ kN/m^3$

The relationship between the free swelling pressures determined from swelling experiments in which volume change is not prevented and the swelling pressure values obtained from swelling experiments in which volume change is prevented is given in Figure 6. This relationship was obtained by comparing the constant-volume and free swelling pressures on samples prepared under the same initial conditions. It can be seen that free swelling pressures are higher than fixed volume swelling pressures. Equation (1) was obtained from the regression analysis between the results obtained from the two groups of swelling test results.

$$P'_{s,c} = 3.111 P_s^{0.9149} \quad (1)$$

In this relation, the term $P'_{s,c}$ is the free swelling pressure calculated according to Equation 1, and P_s (kPa) is the constant-volume swelling pressure. The coefficient of determination (R^2) for this relationship was 0.964.

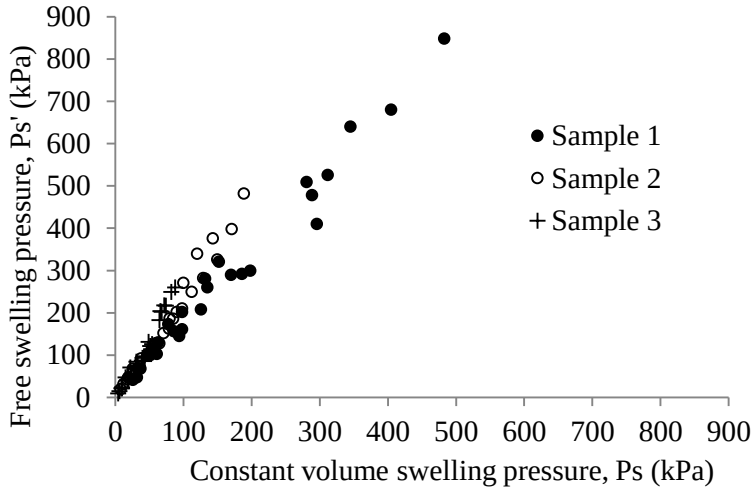

Figure 6. *Relationship between constant volume swelling pressure and free swelling pressure [18]*

The comparison of the free swelling pressure value determined with the help of this equation and the free swelling pressures obtained from the experiments can be seen in Figure 7. Based on the error calculations between the free swelling pressures from the experiments and those derived from Equation (1), the average error was -0.015, while the average absolute error was 0.132. It can be implied according to the error values that free swelling pressures can be estimated from the constant volume swelling pressure values using Equation (1) developed in this study.

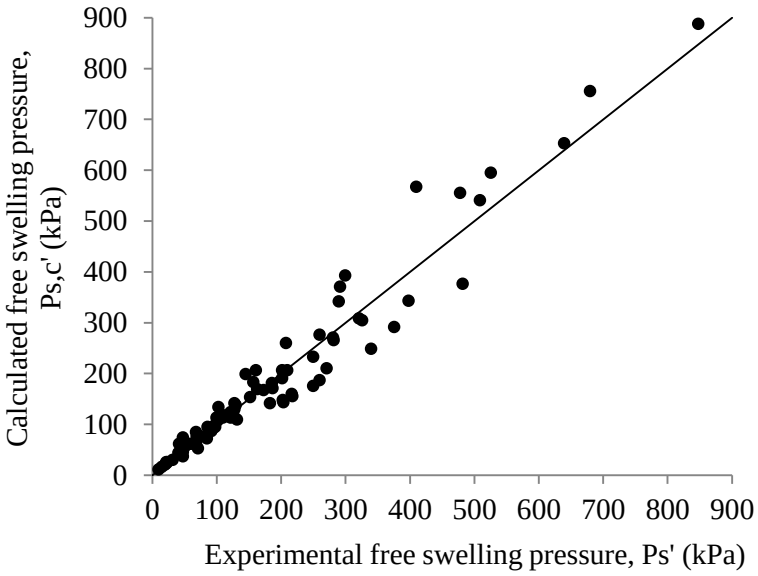

Figure 7. *Comparison of free swelling pressures obtained from experiments and Equation 1 [22]*

Free and constant volume swelling pressure test results in the literature were used to test the proposed relationship. Table 4 has been prepared for this purpose. When this table is examined, it is seen that the calculated free swelling pressure values are in good agreement with the experimental free swelling pressure values in the sources. It is stated that Equation 1 can be used as a preliminary idea to estimate the free swelling pressure. However, the importance of mineralogical structure, grain settlement, climatic conditions, external loads, and stress conditions in the field should not be forgotten.

Table 4. *Comparison of the values obtained from Equation (1) with literature data [22]*

Literature	P_s (kPa)	P_s' (kPa)	$P_{s,c}'$ (kPa)
Keskin [23]	50	125	112
Abduljauwad and Sulaimani [7]	560	3100	1017
	480	1390	883
	420	1340	781
	380	1200	713
Abduljauwad et al. [24]	800	3100	1409
	520	1820	950
Al- Muhaidib [3]	70	230	152
	18	60	44
Al-Shamrani and Dhowian [9]	960	1700	1665
	586	829	1060

IV. CONCLUSION

The swelling pressures of clays with high swelling potential containing smectite minerals were investigated in the study. This mineral increases its volume when in contact with water, significantly increasing the swelling pressure. Chlorite generally has a lower swelling capacity but can increase the swelling effect when present with smectite. All three samples contain smectite and chlorite, which are significant components of the swelling pressure. Quartz is a mineral with no swelling capacity and is present in all three samples. Calcite is a carbonate mineral that does not directly influence swelling potential. However, it can affect the compressibility properties of the soil and indirectly reduce the swelling pressure. Calcite is present in all three samples, suggesting that this mineral may help stabilize swelling. Illite is a clay mineral with a lower swelling capacity than smectite. In samples containing illite (Sample 1 and Sample 3), the swelling potential of smectite may be somewhat balanced. Feldspar minerals are generally chemically stable and do not contribute directly to the swelling pressure. Feldspar is present in samples 1 and 2. Swelling pressure test results performed on three different high-plasticity clay soil samples using two different methods with the help of an oedometer test set are included. Test samples were prepared with standard compaction at various initial water contents and different dry unit volume weights. The relationship between free swelling and constant volume swelling pressure was obtained. The constant-volume swelling test gives results in a shorter time. With the proposed equation, the free swelling pressure can be determined by knowing the constant volume swelling pressure in compressed soils. It is important to note that the correlation obtained was based on a limited dataset and that various factors significantly influence swelling.

ACKNOWLEDGEMENTS: This study was produced from project number 310 titled “Fuzzy Logic Approach in Determining Swelling and Suction Properties of Clayey Soils”. The authors would like to thank Süleyman Demirel University Scientific Research Projects Coordination Unit for their support.

V. REFERENCES

[1] Nelson, J.D., and Miller, D.J., *Expansive Soils Problem and Practice in Foundation and Pavement Engineering,* John Wiley & Sons, 253 p.,1992.

[2] Astm, D4546, “Standart test methods for one dimensional swell or settlement potential of cohesive soils,” *Annual Book of ASTM Standarts*, vol.4, no.8, pp.992-1100, 1986.

[3] Al-Muhaidib, A.I., “Swelling behaviour of expansive shales from the middle region of Saudi Arabia,” *Geotechnical Geol. Eng.*, vol.16, no.4, pp.291-307, 1998.

[4] El-Sayed, S.T., and Rabbaa, S.A., "Factors affecting behavior of expansive soils in the laboratory and field," *Geotechnical Engineering*, vol.17, pp.89-107, 1986.

[5] Erol, A.O., "In-situ and laboratory measured suction parameters for predictions of swelling," *In Proceeding of the Seventh International Conference on Expansive Soils*, Dallas, TX, 2-30, 1992.

[6] Al-Shamrani, M.A., and Al- Mhaidib, A.I., "Swelling behavior under oedometric and triaxial loading conditions," In: shackelford, C.D., Houston, S.L., Chang, N.Y., (Eds.), *Advances in Unsaturated Geotechnics, Geotechnical Special Publication*, vol.99, pp.344-360, 2000.

[7] Abduljauwad, S.N., and Al-Sulaimani, G.J., "Determination of swell potential of Al-Qatif clay," *Geotechnical Testing Journal*, vol.16, no.4, pp.469-484, 1993.

[8] Tisot, J.P., and Aboushook, M.I., "Triaxial study of the swelling characteristic," *Proc. of the Asian Regional Conference on Soil Mechanics and Foundation Engineering*, Haifa, 94-97, 1983.

[9] Al- Shamrani, M.A., and Dhowian, A.W., "Experimental study of lateral restraint effects on the potential heave of expansive soil," *Engineering Geology*, vol.69, pp.63-81, 2003.

[10] Liang, W., Yan, R., Xu, H., Zhang, O., Tian, H., and Wei, C., "Swelling pressure of compacted expansive soil over a wide suction range," *Applied Clay Science*, vol.203, 106018, 2021.

[11] Delage, P., "Some microstructure effects on the behaviour of compacted swelling clays used for engineered barriers," *Chinese Journal of Rock Mechanics and Engineering*, 25. Science Press, 16 Donghuangchenggen North St, Beijing, pp. 721–732. 100717, China, 2006.

[12] Hanumantha, R., Reddy, P.S., Mohanty, B., and Reddy, K.R., "Combined effect of mineralogical and chemical parameters on swelling behaviour of expansive soils," *Scientific Reports*, vol.11, pp.16562, 2021.

[13] Taherdangkoo, R., Shehab, M.,Ardejani, F.D., and Butscher, C., "Experimental Data on Maximum Swelling Pressure of Clayey Soils and Related Soil Properties," *MDPI*, vol. 9, no.4, pp.57, , 2024.

[14] Aneke, F., Onyelowe, K.C., and Ebid, A.M., "AI-Based estimation of swelling stress for soils in South Africa," *Transportation Infrastructure Geotechnology*, vol.11, pp.1049-1072, 2024.

[15] Prabhakara Rao, V.V.N., "Swelling pressure of soil using a predictive tool," *International Journal of Computer Applications*, vol.63, no.19, pp. 27-32, 2013.

[16] Eyo, E.U., Abbey, S.J. Lawrance, T.T., and Tetteh, F.K., "Improved prediction of clay soil expansion using machine learning algorithms and meta-heuristic dichotomous ensemble classifiers," *Geoscience Frontiers*, vol.13, no.1, pp.101296, 2022.

[17] Narmandakh, D., Butcher, C. ,Ardejani, F.D. ,Yang, H., Nagel, T., and Taherdangkoo, R., "The use of feed-forward and cascade-forward neural networks to determine swelling potential of clayey soils," *Computers and Geotechnics*, vol.157, pp.105319, 2023.

[18] Çimen, Ö., "Determination of swelling and suction properties of clay soils with fuzzy logic," PhD thesis, Süleyman Demirel University, Isparta, Turkey, (in Turkish), 2002.

[19] Kumari, N., and Mohan, C., "Basics of Clay Minerals and Their Characteristic Properties," DOI: 10.5772/intechopen.97672, 2021.

[20] Ohri, M.L., "Swelling pressure of clays and its control," *International Conference on Poblematic Soils,* Nottingham, United Kingdom, vol. 2, pp. 427- 433, 2003.

[21] Karathanasis, A.D., and Hajek, B.F., "Shrink– swell potential of montmorillonitic soils in udic moisture regimes," *Soil Sci. Soc. Am. J*., vol. 49, pp. 159 – 166, 1985.

[22] Çimen, Ö., and Keskin, S.N., "Relationship of free and constant volüme swelling pressure tests at compacted clays," *Eleventh National Congress of Soil Mechanics and Foundation Engineering*, 7-8 September 2006, Karadeniz Technical University, 514-524, (in Turkish), 2006.

[23] Keskin, S.N., "İstanbul neojen kilinin şişme davranışına ön konsolidasyonun, minerolojik özelliklerin ve çevresel faktörlerin etkisi," PhD thesis, ITU Institute of Science, Istanbul, Turkey, 155p., (in Turkish), 1993.

[24] Abduljauwad, S.N., Al-Sulaımanı, G.J., Basunbul, I.A., and Al-Buraim, I., "Laboratory and field studies of response of structures to heave of expansive clay," *Geotechnique*, vol.48, no.1, pp.103-121, 1998.

Düzce University
Journal of Science & Technology

Research Article

A Comparative Analysis of Vision Transformers and Transfer Learning for Brain Tumor Classification

Ahmet SOLAK [a,*]

[a] *Department of Electrical and Electronics Engineering, Faculty of Engineering and Natural Sciences, Konya Technical University, Konya, TURKEY*
** asolak@ktun.edu.tr*
DOI: 10.29130/dubited.1521340

ABSTRACT

Accurate brain tumor classification is crucial in neuro-oncology for guiding treatment plans and improving patient outcomes. Leveraging the potential of Vision Transformers (ViTs), this study investigates their efficacy in binary classification of brain tumors using magnetic resonance (MR) images, comparing them to CNN-based models such as VGG16, VGG19, and ResNet50. Comprehensive evaluation using accuracy, precision, recall, and F1-score reveals ViTs' superior performance, achieving 92.59% accuracy, surpassing VGG16 (85.19%), VGG19 (74.04%), and ResNet50 (88.89%). These findings highlight ViTs as a transformative tool for clinical adoption, enhancing diagnostic accuracy and patient care in neuro-oncology.

Keywords: *Brain tumor classification, Vision transformers, Deep learning, Transfer learning, Medical imaging*

Beyin Tümörü Sınıflandırması için Görü Dönüştürücü ve Transfer Öğrenmenin Karşılaştırmalı Analizi

ÖZ

Beyin tümörlerinin doğru sınıflandırılması, nöro-onkolojide tedavi planlarını yönlendirmek ve hasta sonuçlarını iyileştirmek için kritik öneme sahiptir. Bu çalışmada, Manyetik Rezonans (MR) görüntüleri kullanılarak Vision Transformers (ViTs) yönteminin beyin tümörlerinin ikili sınıflandırmasındaki etkinliği araştırılmış ve VGG16, VGG19 ve ResNet50 gibi CNN tabanlı modellerle karşılaştırılmıştır. Doğruluk, kesinlik, duyarlılık ve F1-skoru gibi kapsamlı değerlendirme metrikleri, ViTs'in üstün performansını ortaya koymuştur; ViTs, %92,59 doğrulukla VGG16 (%85,19), VGG19 (%74,04) ve ResNet50'yi (%88,89) geride bırakmıştır. Bu bulgular, ViTs'in nöro-onkolojide tanısal doğruluğu artıran ve hasta bakımını iyileştiren dönüştürücü bir araç olarak klinik uygulamalara entegrasyonu için umut vadeden bir yöntem olduğunu göstermektedir.

Anahtar Kelimeler: *Beyin tümörü sınıflandırması, Görü dönüştürücü, Derin öğrenme, Transfer öğrenme, Tıbbi görüntüleme*

Received: 24/07/2024, Revised: 28/11/2024, Accepted: 09/12/2024

I. INTRODUCTION

Brain tumors represent a significant challenge in contemporary medicine, encompassing a heterogeneous group of neoplasms that arise within the central nervous system. These neoplasms are classified as either primary, originating from intrinsic brain tissue, or secondary, resulting from metastatic spread of extracerebral malignancies [1]. The clinical impact of brain tumors is profound and multifaceted, often manifesting as neurological deficits, cognitive impairment, and potentially life-threatening sequelae. The complex nature of these tumors, coupled with their location in critical neuroanatomical structures, presents unique diagnostic and therapeutic challenges that necessitate a multidisciplinary approach to patient care [2].

Timely and accurate diagnosis of brain tumors is of paramount importance in the fields of neurology and oncology, as it significantly influences treatment strategies, prognostic outcomes, and overall patient management. Advanced neuroimaging modalities, including high-resolution magnetic resonance imaging (MRI) with various sequences and multimodal computed tomography (CT), play a pivotal role in the initial detection and characterization of intracranial lesions. However, definitive diagnosis frequently requires histopathological examination of tumor tissue obtained through stereotactic biopsy or surgical resection. This diagnostic process is further augmented by molecular profiling and genetic analysis, which provide crucial information for tumor classification, prognostication, and the development of targeted therapeutic approaches. The integration of these diagnostic modalities not only guides clinical decision-making but also facilitates personalized treatment paradigms, potentially improving survival rates and preserving neurological function in patients with brain tumors.

In recent years, the application of artificial intelligence (AI) to brain tumor classification has emerged as a promising frontier in neuro-oncology, offering potential improvements in diagnostic accuracy, efficiency, and prognostic assessment. Machine learning algorithms, particularly deep learning neural networks, have demonstrated remarkable capabilities in analyzing complex medical imaging data, including MRI and CT scans [3-5]. These AI-driven systems can be trained on large datasets of annotated images to recognize subtle patterns and features that may elude human observers, potentially enhancing the detection and classification of brain tumors.

Convolutional Neural Networks (CNNs) have been widely adopted for brain tumor classification due to their capacity to extract hierarchical features from medical imaging data [6-8]. CNNs excel at capturing local spatial patterns through convolutional layers, making them particularly suitable for analyzing the intricate structural characteristics of brain tumors in MRI and CT scans. These networks have demonstrated high accuracy in tasks such as tumor detection, segmentation, and grading. However, CNNs have certain limitations in this context. They may struggle with capturing long-range dependencies within images, which can be crucial for understanding the global context of tumor appearance and spread. Additionally, CNNs typically require large, annotated datasets for training, which can be challenging to obtain in medical imaging due to privacy concerns and the scarcity of expert-labeled data. The fixed receptive field of CNNs may also limit their ability to adapt to variations in tumor size and shape across different patients.

Vision Transformers (ViTs) have emerged as a promising alternative to CNNs for brain tumor classification, offering several potential advantages [9]. Unlike CNNs, ViTs process images as sequences of patches, employing self-attention mechanisms to capture global relationships within the image. This approach allows ViTs to model long-range dependencies more effectively, potentially improving the understanding of tumor context and spatial relationships. ViTs have shown impressive performance on various computer vision tasks, often surpassing CNNs, and this success is beginning to translate to medical imaging applications. The self-attention mechanism in ViTs provides a more flexible approach to feature extraction, potentially adapting better to the heterogeneous nature of brain tumors. Furthermore, ViTs may require less extensive data augmentation compared to CNNs, which could be beneficial given the limited availability of medical imaging datasets. However, it is important to note that ViTs are computationally intensive and may require larger datasets for optimal performance.

The field of applying ViTs to brain tumor classification is still evolving, and further research is needed to fully elucidate their advantages and potential limitations in clinical settings.

This study presents a comprehensive investigation into the classification of brain tumors using MR imaging, employing both CNN-based transfer learning models and ViT. The research focuses on distinguishing between MR images with and without brain tumors, aiming to evaluate and compare the performance of these advanced deep learning architectures on the given dataset. The methodology encompasses the application of pre-trained CNN models, leveraging transfer learning techniques to adapt these networks to the specific task of brain tumor classification. Concurrently, the study implements ViT, a more recent approach in computer vision, to assess its efficacy in this medical imaging context. The performance of these models is rigorously examined, considering metrics such as accuracy, precision, recall and F1-score. This comparative analysis seeks to elucidate the strengths and limitations of each approach, potentially informing future directions in the application of artificial intelligence to neuroradiological diagnosis.

II. RELATED WORKS

Artificial intelligence-based applications for brain tumor classification and segmentation have proliferated in recent years. This study focuses specifically on binary brain tumor classification, limiting the scope of relevant literature review to studies addressing this aspect. Charfi et al. proposed a hybrid artificial intelligence system for the automatic detection of brain tumors using a dataset comprising 80 MR images, categorized into tumorous and non-tumorous samples. Their approach integrates computational methods including histogram-based thresholding, discrete wavelet transforms, principal component analysis, and backpropagation neural networks, achieving an accuracy rate of 90% [10]. Nazir et al. employed an artificial neural network for classifying tumors as malignant or benign. Their methodology encompasses three stages: preprocessing, feature extraction, and classification. The preprocessing stage utilizes filters for noise reduction, while the feature extraction phase extracts color moments from MR images, which are subsequently fed into a simple artificial neural network. The study, conducted on a dataset of 25 normal and 45 abnormal images, achieved an overall accuracy of 91.8% [11]. Vani et al. focused on the Support Vector Machine (SVM) algorithm for image classification. They developed a Simulink model for tumor classification, presenting a prototype for SVM-based object detection that classifies images and evaluates whether the classified image is cancerous. Their approach yielded an accuracy of 82% [12]. Gupta et al. evaluated the potential of machine learning in the accurate and rapid diagnosis of cerebral tumors using MRI. In a study involving 200 subjects, images were acquired using volumetric Fluid Attenuated Inversion Recovery (FLAIR) acquisition and normalized to 12 useful sections for classification. Discrete Wavelet Transform (DWT) was utilized for feature extraction, and Principal Component Analysis (PCA) for feature selection. Various classifiers (SVM, k-NN, CART, and Random Forest) were tested, with linear SVM yielding the best results: 84% sensitivity, 92% specificity, and 88% accuracy [13]. Asif et al. conducted a classification study using popular deep learning models including Xception[14], NasNet Large [15], DenseNet121 [16], and InceptionResNetV2 [17] on two different brain MR datasets, one binary and one multiclass. The images in the dataset were cropped, preprocessed, and augmented. Transfer learning models were trained and tested using ADAM [18], SGD [19], and RMSprop optimization algorithms. Performance was evaluated based on criteria such as accuracy, sensitivity, precision, specificity, and F1-score. Experimental results indicated that the proposed CNN model, the Xception architecture, outperformed other models. On the binary dataset, the Xception model demonstrated an accuracy of 91.94%, precision of 87.50%, recall of 96.55%, and an F1 score of 91.8% [20]. Shilaskar et al. propose a system for brain tumor detection and classification using machine learning models on MRI data. Their approach employs Histogram of Oriented Gradients (HOG) for feature extraction and evaluates various classifiers, including SVM, Logistic Regression, Gradient Boost, K-Nearest Neighbors (KNN), and XGBoost. Among these, the XGBoost classifier achieves the highest accuracy of 92.02%, outperforming other models such as Logistic Regression (77.62%) and SVM (74.19%). This highlights XGBoost's potential for precise medical diagnostics, although limitations in dataset size are noted. The

authors emphasize future research on larger datasets and deep learning techniques for better generalization and accuracy [21]. Pilaoon et al. use pretrained deep convolutional neural networks, specifically GoogLeNet and AlexNet, to classify Glioblastoma Multiforme (GBM) brain tumors using MRI images from the REMBRANDT database. Their transfer learning approach eliminates manual segmentation and feature extraction, reducing human error. AlexNet achieves a higher accuracy of 93.62%, while GoogLeNet achieves 80.85%. The study highlights the potential of automated deep learning methods to support medical staff in diagnosing brain tumors and improving patient survival rates [22]. Dhaniya et al. propose a hybrid CNN-LSTM model for classifying brain tumors from MRI images. Their approach involves preprocessing with a Wiener filter, data augmentation (including rotation, cropping, and CLAHE), and segmentation using the Adaptive Particle Swarm Optimization (APSO) algorithm. The CNN extracts features, and LSTM handles the classification. The model achieves an accuracy of 92.03%, outperforming standalone methods such as SVM (87.06%) and LSTM (88.5%), demonstrating its effectiveness for automated tumor detection [23]. These studies collectively demonstrate the evolving landscape of AI-based approaches in brain tumor classification, highlighting the potential for improved diagnostic accuracy and efficiency in clinical settings.

III. MATERIALS AND METHODS

A. DATASET

In this study, a publicly available dataset comprising 253 MRI images, 155 of which were tumorous and 98 of which were non-tumorous, was examined [24]. Figure 1 illustrates representative examples of the images included in the dataset. Given the variability in image dimensions across the dataset, a standardization process was employed to ensure consistency. This involved resizing the images to a fixed size of 128x128 pixels. Subsequently, data augmentation was conducted due to the limited number of images in the dataset. In this study, a variety of data augmentation techniques, including random horizontal flipping, small rotations (±2%), and random zooming (up to 20%), were employed. These augmentations were applied dynamically during the training process, meaning that the dataset size remained 253 images (155 tumorous and 98 non-tumorous). However, the model was exposed to different variations of each image across epochs, effectively enhancing its ability to generalize to unseen data. After, the data were employed for the purpose of training the classification network. Figure 2 illustrates the framework of the study.

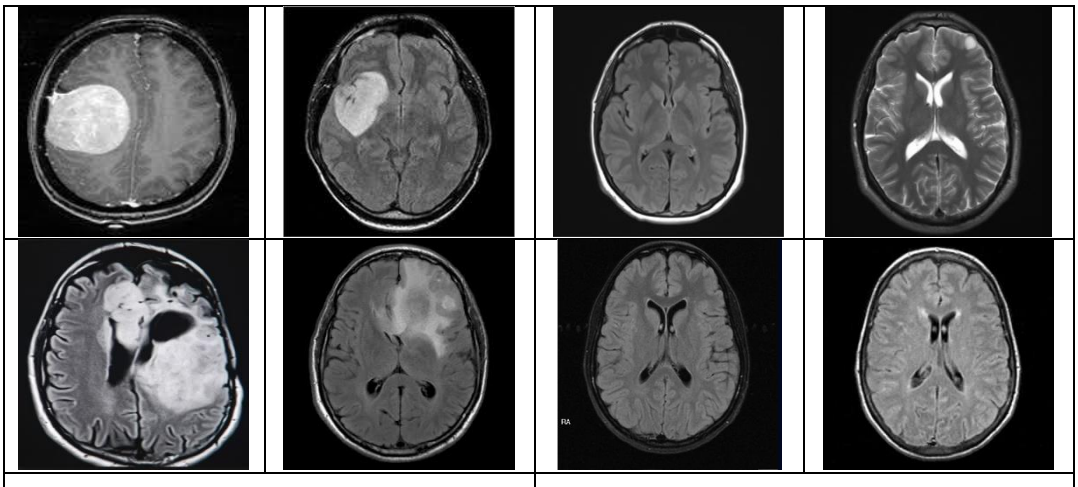

Figure 1. *Sample images from the data set.* ***(a)*** *MR images with tumor and* ***(b)*** *MR images without tumor*

Figure 2. *Flowchart of the study*

B. MODELS

B. 1. Transfer Learning Models

Transfer learning is a machine learning technique that employs the knowledge acquired from solving one problem to address a distinct but analogous problem. In the context of deep learning and computer vision, transfer learning typically involves the utilization of a neural network that has undergone pre-training on a substantial dataset (e.g., ImageNet [25]) as a foundation for a novel task with a comparatively limited dataset. This approach is particularly advantageous when the target task has limited labeled data, as it enables the model to leverage general features learned from the source domain. Transfer learning can be implemented through a variety of strategies, including feature extraction, in which the pre-trained network is utilized as a fixed feature extractor, and fine-tuning, in which some or all layers of the pre-trained network are further trained on the target dataset.

The VGG-16 architecture, introduced by Simonyan and Zisserman [26], is a convolutional neural network that is notable for its simplicity and depth. The network comprises 16 weight layers, including 13 convolutional layers and 3 fully connected layers. The convolutional layers utilize small 1-step 3x3 filters, interspersed with a 2x2 maximum pooling layer. The network maintains a uniform structure throughout, with the number of filters doubling after each maximum pooling layer, beginning with 64 and increasing to 512. The final layers comprise two fully connected layers, each comprising 4096 units, followed by a softmax output layer. The depth and uniform architecture of VGG-16 contributed to its success in image classification tasks, thereby establishing it as a popular choice for transfer learning in various computer vision applications.

VGG-19 represents an extension of the VGG-16 model, incorporating three additional convolutional layers, resulting in a total of 19 weight layers (16 convolutional and 3 fully connected) [26]. The overall structure is analogous to that of VGG-16, with additional depth provided by the incorporation of 3x3 convolutional layers in the subsequent stages of the network. Similarly to its predecessor, VGG-19 employs the use of small 3x3 filters throughout the network, in conjunction with a maximum of 2x2 pooling for the purpose of spatial minimization. The augmented depth of VGG-19 enables the acquisition of more intricate features, which may ultimately result in enhanced performance on specific tasks. However, the additional layers also result in increased computational requirements and a greater number of parameters, which may render the model more susceptible to overfitting in the context of smaller datasets.

ResNet-50, a component of the Residual Network family as outlined by He et al. [27], addresses the issue of degradation in exceedingly deep neural networks through the introduction of residual connections, representing a novel approach to network design. The network comprises 50 layers, including convolutional layers, batch normalization, rectified linear unit (ReLU) activations, and jump connections. The network is divided into stages, with each stage comprising multiple residual blocks.

These blocks facilitate the activation of shortcut connections that circumvent one or more layers, thereby enabling the network to learn residual functions with reference to layer inputs. This architectural design mitigates the vanishing gradient problem, thereby enabling the training of networks with considerably greater depth. ResNet-50 commences with a 7x7 convolutional layer, followed by a maximum pooling layer, and then progresses through four stages of residual blocks, concluding with a global average pooling layer and a fully connected layer. The incorporation of residual connections enables ResNet-50 to attain state-of-the-art performance on a diverse array of image classification tasks while maintaining a relatively modest number of parameters.

These architectures (VGG-16, VGG-19 and ResNet-50) have proven to be effective for transfer learning on many computer vision tasks, including medical image analysis. Their pre-trained weights on large-scale datasets such as ImageNet provide a valuable starting point for fine-tuning on specific tasks such as brain tumor classification, often leading to better performance and faster convergence compared to training from scratch.

B. 2. Vision Transformers

Advancements in artificial intelligence and deep learning have significantly enhanced researchers' capabilities in medical image classification. The literature abounds with studies leveraging CNNs, widely regarded as the foundation of deep learning, yielding remarkably successful outcomes. While CNNs excel in extracting local features such as color, texture, edges, and corners, they may exhibit limitations in capturing global features, including object shapes, sizes, and relationships. This distinction is particularly crucial in the analysis of medical images, where global context can be as important as local details. Consequently, this study endeavors to compare the performance of CNN-based deep learning networks with the more recently developed Vision Transformer (ViT) model [9], which offers potential advantages in capturing both local and global image characteristics.

The ViT represents a novel approach to image classification, drawing inspiration from transformer architectures that have demonstrated exceptional performance in natural language processing tasks. The general structure of the ViT model is illustrated in Figure 3. The ViT architecture comprises several key components:

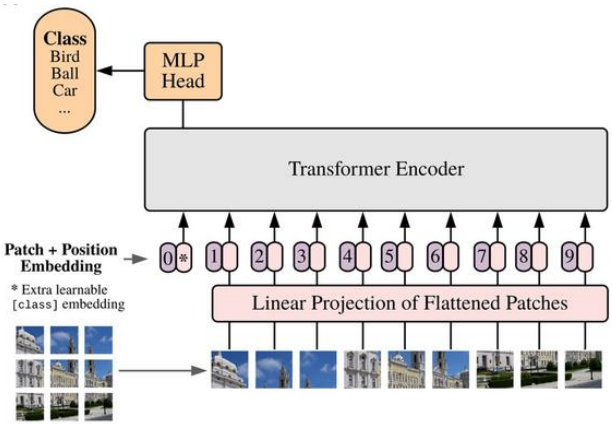

Figure 3. *ViT Architecture [9]*

B.2.1. Patch Embedding

The input image is segmented into fixed-size, non-overlapping patches. For an image of dimensions *HxW (Height x Width)*, divided into patches of size *PxP*, *N* patches are generated, where $N = \frac{HW}{P^2}$. Figure 4 illustrates the patch extraction process from a sample image in the dataset. Subsequently, each patch is flattened into a one-dimensional vector, as demonstrated in Figure 5. These flattened patches are then projected onto a higher-dimensional space through trainable linear transformations.

B.2.2. Position Embedding

To preserve the spatial information of the patches, positional embeddings are added to the patch embeddings. This process enables the model to maintain awareness of the original spatial arrangement of image fragments. Additionally, a specialized class token is prepended to the sequence of patch embeddings to facilitate image classification.

B.2.3. Transformer Encoder

This component forms the core of the ViT architecture and consists of two primary layers:

a) Multi-Head Self-Attention: This mechanism allows the model to weigh the importance of each patch relative to all others, enabling the capture of long-range dependencies and global context within the image.

b) Feed-Forward Neural Network (FFN) or Multi-Layer Perceptron (MLP): Each sub-layer is followed by Layer Normalization (LN) and residual connections. The FFN is applied uniformly to each position, processing the output of the self-attention mechanism.

Layer Normalization is applied before and after both the multi-head self-attention and FFN layers to stabilize training. Residual connections are incorporated around each sub-layer to facilitate gradient flow during the training process.

B.2.4. MLP Head

The final classification layer comprises one or more fully connected layers followed by a softmax activation. This component processes the output from the transformer encoder to determine the image's class membership.

This architecture enables the ViT model to potentially capture both fine-grained local features and broader global contexts, making it a promising candidate for medical image analysis tasks such as brain tumor classification.

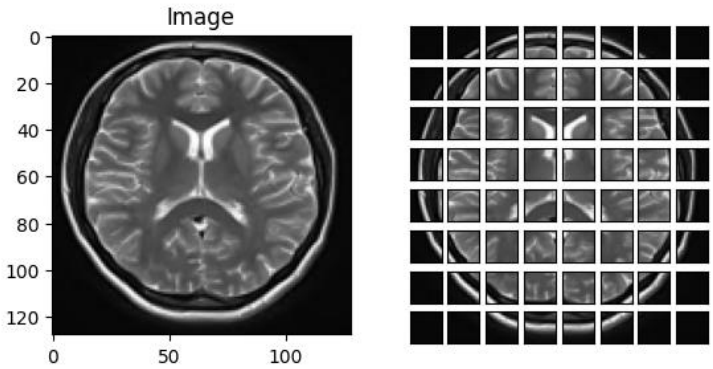

Figure 4. *Sample of Image Patches*

Figure 5. *Flattened Patches*

The selection of hyperparameters for the ViT model was a meticulous process designed to achieve a balance between performance and computational efficiency for brain tumor classification, particularly when dealing with potentially larger images. To accommodate the increased image size of 128x128 (*Height (H)* × *Width (W)*) pixels, the batch size was prudently reduced to 32. Furthermore, the patch size was correspondingly increased to 16x16 (*HxW*) pixels, resulting in 64 patches per image. To ensure training stability with these larger images, the learning rate was modestly adjusted to 0.0003, and weight

decay was set to 0.00003. In an effort to capture potentially more intricate patterns within the data, the number of training epochs was extended to 100.

Beyond hyperparameter selection, the architectural parameters were also fine-tuned to enhance the model's capacity for brain tumor classification. The number of Transformer encoder layers was strategically increased to 12, facilitating a deeper exploration of image features. The projection dimension was set to 128 to create a higher-dimensional representation of the image data. To enable a greater number of parallel attention mechanisms within the model, the number of attention heads was augmented to eight. The Transformer hidden units were meticulously adjusted to correspond with the new projection size, while the MLP head units were maintained for optimal performance. Finally, a dropout rate of 0.1 was implemented in both the attention and MLP layers to mitigate overfitting during training. In conclusion, these deliberate hyperparameter and architectural choices aimed to achieve a well-balanced ViT model, capable of efficient and accurate brain tumor classification.

C. EVALUATION METRICS

The assessment of a machine learning model's performance holds significant importance in understanding its effectiveness and facilitating comparisons across different methodologies. This section provides a comprehensive overview of the metrics utilized to evaluate model performance specifically within the domain of brain tumor classification.
In the realm of image classification, "accuracy" refers to the percentage of correctly classified images by a given model. It is computed as the ratio of correctly classified images to the total number of images, as defined in 1. Here, TP denotes true positives, TN represents true negatives, FP stands for false positives, and FN indicates false negatives. While achieving high accuracy is typically desirable, its interpretation can be misleading in scenarios where dataset classes are imbalanced, with one class (e.g., healthy images) significantly outnumbering others (e.g., tumor images).

$$Accuracy = \frac{TP+TN}{TP+TN+FP+FN} \quad (1)$$

Precision, a critical metric in classification tasks, quantifies the accuracy of positive predictions made by the model. It measures the proportion of true positives (correctly identified tumors) among all instances predicted as positive. Mathematically, precision is expressed as 2. A high precision value signifies that the model effectively identifies tumors while minimizing false positives. This metric is essential in evaluating the reliability of the model's positive predictions in clinical contexts and other applications where accurate identification is paramount.

$$Precision = \frac{TP}{TP+FP} \quad (2)$$

The recall metric quantifies the proportion of correctly identified true positive instances (tumors) out of all actual positive cases in the dataset. It is calculated using 3. A high recall value signifies that the model effectively detects a significant portion of the true tumor instances present in the dataset, indicating its ability to minimize false negatives and capture most actual positives.

$$Recall = \frac{TP}{TP+FN} \quad (3)$$

The F1 score represents a composite metric that integrates precision and recall, offering a balanced assessment of the model's effectiveness. It is computed using the harmonic mean of precision and recall, as defined by 4.

$$F1 - Score = \frac{2*Precision*Recall}{Precision+Recall} \quad (4)$$

The confusion matrix provides a detailed and structured overview of the model's predictive performance by displaying the counts of TP, TN, FP, and FN across each class. This matrix serves as a visual aid that effectively illustrates how well the model distinguishes between classes and where potential errors arise. In a binary classification scenario, the structure of the confusion matrix is delineated as Table 1.

Table 1. *Confusion Matrix*

Actual/Predicted	Positive	Negative
Positive	TP	FN
Negative	FP	TN

IV. EXPERIMENTATION AND RESULTS

The training environment for this study was configured using Google Colab, which provides access to the Tesla T4 GPU and utilizes TensorFlow 2.15 as the primary deep learning framework. The Tesla T4 GPU, comprising 320 Turing Tensor Cores and 16 GB of GDDR6 VRAM, provided substantial computational capability, facilitating effective model training and inference. TensorFlow 2.15's extensive capabilities in deep learning enabled the implementation of complex neural network architectures and optimization algorithms that were necessary for achieving the study's objectives. This configuration not only guaranteed robust performance but also facilitated reproducibility and collaboration by Colab's cloud-based infrastructure.

The study employed a data partitioning strategy of 80:10:10 for training, validation, and testing sets, respectively, across all models. To enhance model generalization, data augmentation techniques were applied to the training set. Each model underwent independent training sessions, with subsequent performance evaluations conducted on the designated test data.

The training protocol adhered to the following parameters: input images were standardized to 128x128x3 dimensions, with a batch size of 32. The AdamW optimizer [28] was employed, utilizing a modestly adjusted learning rate of 0.0003 and a weight decay of 0.00003. Training proceeded for 100 epochs, incorporating a dropout rate of 0.1 to mitigate overfitting. Binary cross-entropy served as the loss function for all models.

The training processes for all models were executed sequentially. Figure 7 presents confusion matrices illustrating the classification performance of each model on the test set. In Figure 7 (a), the VGG-16 model erroneously classified 4 out of 27 tumor-positive images as tumor-free. Figure 7 (b) depicts the VGG-19 model's performance, which misclassified a total of 7 images: 4 tumor-positive images were incorrectly labeled as tumor-free, while 3 tumor-free images were mistakenly classified as tumor-positive. Figure 7 (c) shows the ResNet50 model's results, where 3 tumor-positive images were misclassified as tumor-free. Finally, Figure 7 (d) illustrates the ViT model's performance, which misclassified only 2 tumor-positive images as tumor-free.

Comparative analysis of model performance reveals that the ViT model achieved superior results, while the VGG-19 model demonstrated the least accurate performance. It is noteworthy that in the context of brain tumor classification, where even a single misclassification can have profound implications for patient care, the ViT model's superior performance is particularly significant. This underscores the potential of transformer-based architectures in medical image analysis, especially in applications where accuracy is paramount for patient outcomes.

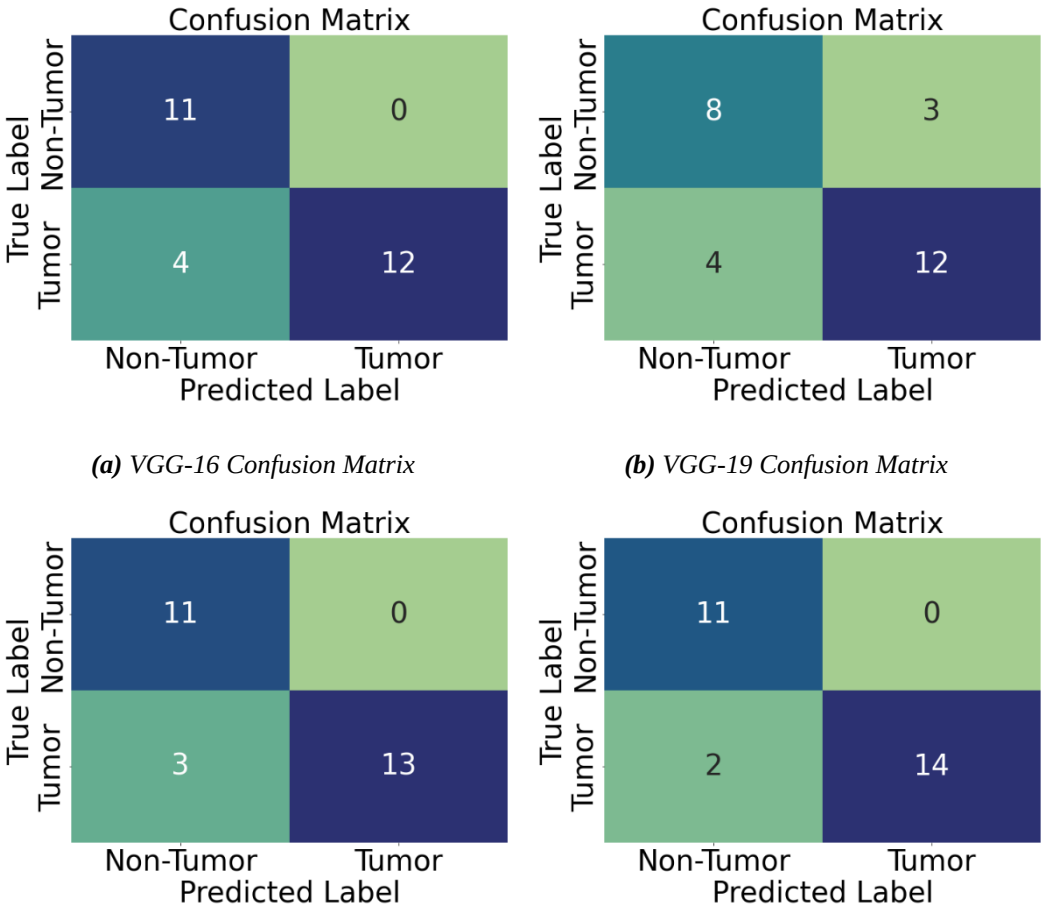

(a) *VGG-16 Confusion Matrix*

(b) *VGG-19 Confusion Matrix*

(c) *ResNet50 Confusion Matrix*

(d) *ViT Confusion Matrix*

Figure 7. *Confusion matrices for all models*

Comparing the performance of different models using evaluation metrics is essential for enhancing the reliability and robustness of the study. Table 2 presents the accuracy, precision, recall, and F1-score values for each trained model on the test images. According to the table, the VGG-16 model achieved 85.19% accuracy, 86.67% precision, 87.50% recall, and an 85.16% F1-score. Conversely, the VGG-19 model attained 74.04% accuracy, 73.33% precision, 73.86% recall, and a 73.49% F1-score. The ResNet50 model demonstrated superior performance with 88.89% accuracy, 89.29% precision, 90.62% recall, and an 88.83% F1-score. Lastly, the ViT model outperformed the others, achieving 92.59% accuracy, 92.30% precision, 93.75% recall, and a 93.01% F1-score. Upon examining the evaluation metrics and performances, it is evident that the ViT model delivers the most successful results.

Table 2. *Test Results on Evaluation Metrics*

Models	**Accuracy**	**Precision**	**Recall**	**F1-Score**	**Training Time (mins)**	**Test Time (secs)**
VGG16	% 85.19	% 86.67	% 87.50	% 85.16	52.52	1.09
VGG19	% 74.04	% 73.33	% 73.86	% 73.49	51.51	0.91
ResNet50	% 88.89	% 89.29	% 90.62	% 88.83	20.89	0.38
ViT	% 92.59	% 92.30	% 93.75	% 93.01	16.49	0.52

In the evaluations conducted on the test images, the ViT model demonstrated the most successful results. To illustrate the model's performance on the test images, Figure 8 presents examples of the images and the corresponding predictions made by the model. As noted from the confusion matrix, only two images

were misclassified by the ViT model. Figure 8 includes an example of one such misclassification, providing further insight into the model's predictive behavior.

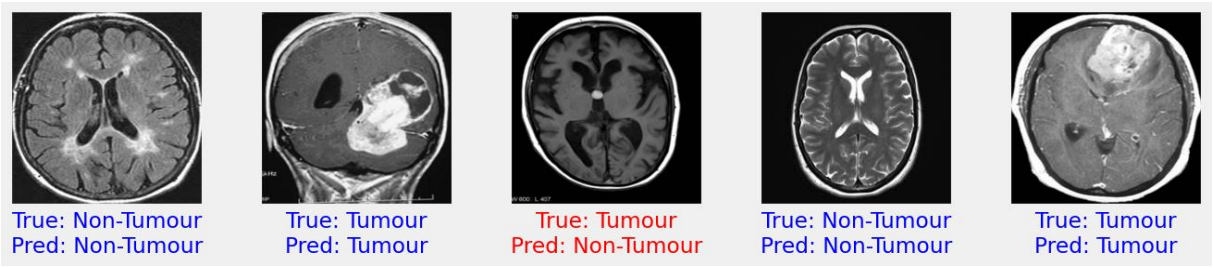

Figure 8. *Sample Test Images and Predictions of the ViT Model*

V. DISCUSSION

This study investigated the effectiveness of the ViT model for brain tumor classification using MR images. The results suggest that ViT may outperform traditional CNN-based transfer learning approaches, including VGG-16, VGG-19, and ResNet50. ViT achieved superior accuracy and performance across multiple image evaluation metrics, such as precision, recall, and F1-score.

The superior performance of the ViT model can potentially be attributed to its ability to capture long-range dependencies within the image data. This capability is particularly advantageous in the domain of medical imaging, where spatial relationships between image features hold significant importance for accurate diagnosis. Unlike CNNs that primarily rely on local feature extraction through convolutional filters, the ViT model leverages an attention mechanism. This mechanism allows the model to selectively focus on the most relevant regions of the image, potentially leading to enhanced classification accuracy in tasks like brain tumor classification.

Table 3. *Comparison with previous studies*

	Model	**Accuracy**	**Precision**	**Recall**	**F1-score**
[10]	ANN	% 90	----------	% 82	----------
[11]	Normal densities based linear classifier	%73.03	----------	----------	----------
	Naive Bayes Classifier	% 76.92	----------	----------	----------
	SVM	% 88.46	----------	----------	----------
	ANN	% 91.8	----------	----------	----------
[12]	SVM	% 82	----------	----------	----------
[13]	Linear SVM	% 88	----------	% 84	----------
	k-NN	% 82	----------	% 80	----------
	Random Forest	% 86	----------	% 88	----------
	CART	% 76	----------	% 64	----------
[20]	Xception	% 91.94	% 87.50	% 96.55	% 91.80
	NasNet Large	% 91.74	% 90.00	% 93.10	% 91.53
	DenseNet121	% 90.32	% 89.66	% 89.66	% 89.86
	InceptionResNetV2	% 90.32	% 96.00	% 82.76	% 88.89
[21]	Gradient Boost	% 67.53	% 70.64	% 66.97	% 67.51
	KNN	% 68.52	% 95.15	% 68.19	% 77.85
	SVM	% 74.19	% 77.08	% 75.40	% 75.83
	Logistic Regression	% 77.62	% 94.99	% 76.40	% 84.24
	XG Boost	% 92.02	% 92.07	% 91.82	% 91.85

Table 3 (cont). *Comparison with previous studies*

[22]	Google Net	% 80.85	----------	% 93.94	----------
	Alex Net	% 93.52	----------	%96.97	----------
[23]	ANN	% 85.7	%86.7	% 87.8	% 88.6
	SVM	% 87.06	% 88.06	% 89.06	% 89.4
	LSTM	% 88.5	% 89.5	% 89.39	% 90.2
	CNN-LSTM	% 92.03	% 92.93	% 92.36	% 94.3
This Study	VGG16	% 85.19	% 86.67	% 87.50	% 85.16
	VGG19	% 74.04	% 73.33	% 73.86	% 73.49
	ResNet50	% 88.89	% 89.29	% 90.62	% 88.83
	ViT	**% 92.59**	**% 92.30**	**% 93.75**	**% 93.01**

It is also of great importance to compare the study with previous studies in the literature in terms of its reliability and robustness. In this regard, a comparison of this study with different studies is included in Table 3. Although the data sets may not be common to all studies, all compared studies belong to binary brain tumor classification studies. On the other hand, the study numbered [20] used the same data set as in this study in terms of the data set used. This is especially important in terms of comparison. As a result of the comparison with both machine learning-based models and deep learning-based models, it is clearly seen in Table 3 that the study conducted with ViT gives the most successful results.

The integration of ViT models into clinical workflows holds promise for significantly improving the accuracy and efficacy of brain tumor diagnosis. This advancement could translate to better patient outcomes. ViT-powered systems could potentially offer radiologists a valuable tool for automated second opinions, potentially leading to a reduction in misdiagnoses and more optimized treatment plans. The encouraging results obtained in this study warrant further investigation while acknowledging inherent limitations. The employed dataset, while valuable, may not comprehensively capture the entire spectrum of brain tumor presentations. This limitation highlights the need for future research to utilize even larger and more diverse datasets for model validation. Additionally, the computational resources required for training the ViT models are substantial, potentially hindering their real-world implementation in resource-constrained settings. Future research efforts should prioritize the optimization of these models for efficient training with lower computational resources. This would facilitate broader adoption and enhance the clinical applicability of ViT-based brain tumor classification techniques.

This study evaluates the performance of Vision Transformers (ViTs) in comparison to CNN-based transfer learning models (VGG-16, VGG-19, and ResNet50) for brain tumor classification. The ViT model achieved the highest accuracy (92.59%), precision (92.30%), recall (93.75%), and F1-score (93.01%), outperforming its counterparts.

Specifically, the ViT model misclassified only 2 tumor-positive images as tumor-free, demonstrating superior robustness compared to the VGG-16 (4 misclassifications) and VGG-19 (7 misclassifications). ResNet50, while showing competitive performance (88.89% accuracy), lagged slightly behind the ViT in precision and recall, underscoring the advantages of the transformer-based architecture in capturing global image features.

Remarks:

- **Superior Modeling of Global Features**: The ViT model's ability to process images as sequences of patches and leverage self-attention mechanisms likely contributed to its superior

classification accuracy. This highlights its potential for analyzing complex medical images where global spatial relationships are critical.

- **Clinical Implications**: The minimal misclassification rate of the ViT model emphasizes its potential for reducing diagnostic errors in clinical settings, particularly in tasks where false negatives (tumor-free classifications of tumor-positive images) could have serious consequences for patient care.
- **Model Efficiency**: While the ViT model demonstrates superior performance, its computational intensity remains a limitation. Future efforts could focus on optimizing transformer architectures for resource-constrained environments.

VI. CONCLUSION

This study presents a comprehensive investigation into the application of deep learning methodologies for the classification of MR images, specifically distinguishing between tumorous and non-tumorous brain scans. Our research focused on evaluating the performance of the Vision Transformer (ViT), a relatively novel architecture, in comparison to established CNN-based transfer learning models. The results unequivocally demonstrate the superiority of the ViT model in this classification task, consistently outperforming its CNN-based counterparts across multiple evaluation metrics.

Furthermore, our findings were benchmarked against previous studies in the literature, revealing that our ViT implementation achieved state-of-the-art performance in brain tumor classification from MR images. This outcome not only validates the efficacy of transformer-based architectures in medical image analysis but also underscores the potential for significant advancements in automated diagnostic tools for neuro-oncology.

Future Work

While the ViT model has shown remarkable promise, further research is warranted to enhance its robustness and clinical applicability. Future work could include:

- **Utilizing larger and more diverse datasets**: Expanding the dataset to include varied tumor types, multi-class classification tasks, and data from multiple imaging modalities will improve the generalizability of the model.
- **Exploring multimodal approaches**: Combining MR imaging with additional clinical data, such as patient history or genomic information, to develop a more holistic diagnostic model.
- **Optimizing model efficiency**: Reducing computational requirements of ViT models through techniques like pruning, quantization, or lightweight transformer architectures to facilitate deployment in resource-constrained clinical environments.
- **Validation in real-world settings**: Collaborating with healthcare providers to test the ViT model in live clinical workflows and gather feedback on its performance and usability.
- **Extending ViT applications**: Investigating the potential of ViTs for other medical imaging tasks, such as early detection of other cancers or organ-specific imaging challenges.

In conclusion, this study contributes valuable insights to the field of medical image analysis, particularly in brain tumor classification. The demonstrated efficacy of the ViT model suggests a promising direction for the development of more accurate and reliable diagnostic support systems in clinical settings. By addressing these future directions, the ViT framework can continue to evolve, offering significant advancements in early detection and diagnosis, ultimately leading to improved patient outcomes in neuro-oncology.

VII. REFERENCES

[1] L. M. DeAngelis, "Brain tumors," *New England journal of medicine,* vol. 344, no. 2, pp. 114-123, 2001.

[2] J. H. Sampson, M. D. Gunn, P. E. Fecci, and D. M. Ashley, "Brain immunology and immunotherapy in brain tumours," *Nature Reviews Cancer,* vol. 20, no. 1, pp. 12-25, 2020.

[3] G. S. Tandel, A. Balestrieri, T. Jujaray, N. N. Khanna, L. Saba, and J. S. Suri, "Multiclass magnetic resonance imaging brain tumor classification using artificial intelligence paradigm," *Computers in Biology and Medicine,* vol. 122, p. 103804, 2020.

[4] R. Mehrotra, M. Ansari, R. Agrawal, and R. Anand, "A transfer learning approach for AI-based classification of brain tumors," *Machine Learning with Applications,* vol. 2, p. 100003, 2020.

[5] R. Ranjbarzadeh, A. Caputo, E. B. Tirkolaee, S. J. Ghoushchi, and M. Bendechache, "Brain tumor segmentation of MRI images: A comprehensive review on the application of artificial intelligence tools," *Computers in biology and medicine,* vol. 152, p. 106405, 2023.

[6] W. Ayadi, W. Elhamzi, I. Charfi, and M. Atri, "Deep CNN for brain tumor classification," *Neural processing letters,* vol. 53, pp. 671-700, 2021.

[7] Ş. Öztürk and U. Özkaya, "Skin lesion segmentation with improved convolutional neural network," *Journal of digital imaging,* vol. 33, pp. 958-970, 2020.

[8] O. Dikmen, "Deep Learning Models for the Detection and Classification of COVID-19 and Associated Lung Diseases Using X-Ray Images," *Artificial Intelligence Theory and Applications,* vol. 4, no. 2, pp. 121-142, 2024.

[9] A. Dosovitskiy *et al.*, "An image is worth 16x16 words: Transformers for image recognition at scale," *arXiv preprint arXiv:2010.11929,* 2020.

[10] S. Charfi, R. Lahmyed, and L. Rangarajan, "A novel approach for brain tumor detection using neural network," *International Journal of Research in Engineering and Technology,* vol. 2, no. 7, pp. 93-104, 2014.

[11] M. Nazir, F. Wahid, and S. Ali Khan, "A simple and intelligent approach for brain MRI classification," *Journal of Intelligent & Fuzzy Systems,* vol. 28, no. 3, pp. 1127-1135, 2015.

[12] N. Vani, A. Sowmya, and N. Jayamma, "Brain tumor classification using support vector machine," *International Research Journal of Engineering and Technology (IRJET),* vol. 4, no. 7, pp. 792-796, 2017.

[13] T. Gupta, T. K. Gandhi, R. Gupta, and B. K. Panigrahi, "Classification of patients with tumor using MR FLAIR images," *Pattern Recognition Letters,* vol. 139, pp. 112-117, 2020.

[14] F. Chollet, "Xception: Deep learning with depthwise separable convolutions," in *Proceedings of the IEEE conference on computer vision and pattern recognition*, 2017, pp. 1251-1258.

[15] B. Zoph, V. Vasudevan, J. Shlens, and Q. V. Le, "Learning transferable architectures for scalable image recognition," in *Proceedings of the IEEE conference on computer vision and pattern recognition*, 2018, pp. 8697-8710.

[16] G. Huang, Z. Liu, L. Van Der Maaten, and K. Q. Weinberger, "Densely connected convolutional networks," in *Proceedings of the IEEE conference on computer vision and pattern recognition*, 2017, pp. 4700-4708.

[17] C. Szegedy, S. Ioffe, V. Vanhoucke, and A. A. Alemi, "Inception-v4, inception-resnet and the impact of residual connections on learning," in *Thirty-First AAAI Conference on Artificial Intelligence*, 2017.

[18] D. P. Kingma and J. Ba, "Adam: A method for stochastic optimization," *arXiv preprint arXiv:1412.6980*, 2014.

[19] S. Ruder, "An overview of gradient descent optimization algorithms," *arXiv preprint arXiv:1609.04747*, 2016.

[20] S. Asif, W. Yi, Q. U. Ain, J. Hou, T. Yi, and J. Si, "Improving effectiveness of different deep transfer learning-based models for detecting brain tumors from MR images," *IEEE Access*, vol. 10, pp. 34716-34730, 2022.

[21] S. Shilaskar, T. Mahajan, S. Bhatlawande, S. Chaudhari, R. Mahajan, and K. Junnare, "Machine Learning Based Brain Tumor Detection and Classification using HOG Feature Descriptor," in *2023 International Conference on Sustainable Computing and Smart Systems (ICSCSS)*, 2023, pp. 67-75: IEEE.

[22] P. Pilaoon, N. Maneerat, A. Nakthewan, R. Varakulsiripunth, and K. Hamamoto, "Brain Tumor Classification using Pretrained Deep Convolutional Neural Network," in *2023 9th International Conference on Engineering, Applied Sciences, and Technology (ICEAST)*, 2023, pp. 84-88: IEEE.

[23] R. Dhaniya and K. Umamaheswari, "CNN-LSTM: A Novel Hybrid Deep Neural Network Model for Brain Tumor Classification," *Intelligent Automation & Soft Computing*, vol. 37, no. 1, 2023.

[24] N. Chakrabarty. (2019). *Brain MRI Images Dataset for Brain Tumor Detection* [Online]. Available: https://www.kaggle.com/datasets/navoneel/brain-mri-images-for-brain-tumor-detection

[25] J. Deng, W. Dong, R. Socher, L.-J. Li, K. Li, and L. Fei-Fei, "Imagenet: A large-scale hierarchical image database," in *2009 IEEE conference on computer vision and pattern recognition*, 2009, pp. 248-255: Ieee.

[26] K. Simonyan and A. Zisserman, "Very deep convolutional networks for large-scale image recognition," *arXiv preprint arXiv:1409.1556*, 2014.

[27] K. He, X. Zhang, S. Ren, and J. Sun, "Deep residual learning for image recognition," in *Proceedings of the IEEE conference on computer vision and pattern recognition*, 2016, pp. 770-778.

[28] I. Loshchilov and F. Hutter, "Decoupled weight decay regularization," *arXiv preprint arXiv:1711.05101*, 2017.

Düzce University
Journal of Science & Technology

Research Article

The Production of Hydrochar from Hazelnut Waste and its Use in the Removal of Pb (II) and Cr (III)

Buğra DİKBASAN [a], Sami DURSUN [a,*]

[a]*Department of Metallurgical and Materials Engineering, Konya Technical University, Konya, TÜRKİYE*
** Corresponding author's e-mail address: samidursun@ktun.edu.tr*
DOI: 10.29130/dubited.1584464

ABSTRACT

Heavy metals (HMs) are causing an increasing amount of harm to the environment and living organisms. A variety of studies is being conducted to eliminate or diminish such pollutants. In this study, hydrochar was produced from hazelnut waste (HW), and Pb and Cr ion removal research was conducted with this adsorbent. In this way, both the evaluation of HW was provided and the removal of HMs, which are very harmful for the environment. The structural and morphological properties of the produced hydrochars were characterized by thermogravimetric analysis (TGA), differential scanning calorimetry (DSC), field emission scanning electron microscopy (FE-SEM), Fourier transform infrared (FT-IR), and EDX analyses. The effects of many parameters, such as initial concentration, temperature, adsorbent dosages, contact time, and pH on adsorption were discussed. In the studies executed in different parameter environments, it was determined that hydrochar removed 76% and 67% of Pb and Cr ions, respectively. Also, Langmuir and Freundlich isotherm models, pseudo-first-order and pseudo-second-order kinetic models, and thermodynamic parameters like Gibbs free energy were investigated in order to gain a better understanding of the adsorption system of the generated hydrochar. Furthermore, the hydrochar's reusability as an adsorbent was investigated, and it was demonstrated that the material continued to function effectively even after four cycles.

Keywords: *Adsorption, Hydrochar, Heavy metal, Hazelnut waste*

Fındık Atıklarından Hidrokömür Üretimi ve Pb (II) ve Cr (III) Gideriminde Kullanımı

ÖZ

Ağır metaller çevreye ve canlı organizmalara her geçen gün daha çok zarar vermektedir. Bu tür kirleticileri ortadan kaldırmak veya azaltmak için çok sayıda çalışma yapılmıştır ve yapılmaya da devam etmektedir. Bu çalışmada fındık atığından (HW) hidrokömür üretilmiş ve üretilen bu adsorbanla Pb ve Cr iyonlarının giderim çalışmaları yapılmıştır. Bu şekilde hem HW'nin değerlendirilmesi sağlanmış hem de çevre için çok zararlı olan ağır metallerin giderimi sağlanmıştır. Üretilen hidrokömürlerin yapısal ve morfolojik özellikleri TGA, DSC, FE-SEM, FT-IR ve EDX analizleri ile karakterize edilmiştir. Başlangıç konsantrasyonu, sıcaklık, adsorban dozajları, temas süresi ve pH gibi birçok parametrenin adsorpsiyon üzerindeki etkileri tartışılmıştır. Farklı parametre ortamlarında yapılan çalışmalarda hidrokömürün, Pb ve Cr iyonlarının sırasıyla %76'sını ve %67'sini giderdiği belirlenmiştir. Ayrıca, üretilen hidrokömürün adsorpsiyon sistemini daha iyi anlamak için Langmuir ve Freundlich izoterm modelleri, pseudo-birinci mertebe ve pseudo-ikinci mertebe kinetik modelleri ve Gibbs serbest enerjisi gibi termodinamik parametreler araştırıldı. Ayrıca, hidrokömürün bir adsorban olarak yeniden kullanılabilirliği araştırıldı ve malzemenin dört döngüden sonra bile etkili bir şekilde çalışmaya devam ettiği gözlemlendi.

Anahtar Kelimeler: *Adsorpsiyon, Hidrokarbon, Ağır metal, Fındık atığı*

Received: 14/11/2024, Revised: 10/12/2024, Accepted: 11/12/2024

I. INTRODUCTION

Unconscious consumer society, along with industrial and agricultural operations, are the primary causes of the daily rise in pollution in water resources [1]. The reason for pollution is not only this, but also some natural events can cause this situation [2]. For example, water passing through mineral deposits can produce high concentrations of HMs through erosion or dissolution [3]. Studies have demonstrated that this pollution will worsen daily if preventative measures are not implemented. [4]. To prevent or reduce this pollution, methods including chemical precipitation, ion exchange, membrane filtration, evaporation, and adsorption are used [2, 5]. One of these techniques is adsorption, which uses adsorbents with a high adsorption capacity, a big surface area, and the right pore size [6]. Materials used in the adsorption process include fly ashes, coals, zeolites, metal oxides, and silica gels. Hydrochar utilization has grown significantly in importance recently as a result of the expensive cost of some adsorbent materials [7, 8].

One method for using biomass energy is hydrothermal carbonization, which produces hydrochars [9]. This technology's high conversion efficiency and very moderate reaction conditions provide it significant advantages over other methods like roasting and pyrolysis [10-12]. The hydrochar process is used in several research studies in the literature, and the hydrochars that are produced are used in numerous ways. Yang et al. produced hydrochars from bamboo using the hydrothermal carbonization method. The analyses performed showed that the hydrochar produced from bamboo can improve fuel properties and combustion behavior [13]. Nizamuddin et al. converted palm bark into hydrochar by the hydrothermal carbonization method and examined the chemical, structural, and dielectric properties of the hydrochar [11]. Many hydrochar productions using various wastes, such as corn stalks, fish waste, and pine, can also be given in addition to these studies [14-16].

Türkiye is the country that produces the most hazelnuts in the world and, accordingly, produces the most HW annually [17, 18]. These waste materials are typically used to contaminate or fuel the environment, and there is little evaluation of them. In addition, these biomasses consist mostly of hemicellulose, cellulose, and lignin, which are also cheap. Consequently, it is crucial to turn agricultural wastes like HW into hydrochar. Studies on this topic are growing daily, and these hydrochars play a significant part in eliminating both organic and inorganic contaminants from water. In this way, both local wastes are evaluated, and a method with lower costs compared to other methods is used [19].

In this study, hydrochar production was carried out from agricultural HW, and the obtained hydrochars were used as adsorbents. The chemical, thermal, and morphological properties of the obtained hydrochars were investigated using different analysis techniques such as FT-IR, TGA and DSC analyses, FE-SEM, and elemental analyses. In addition, the effects of contact time, pH, and temperature on the adsorption of Pb and Cr metals by hydrochars were investigated. Additionally, kinetic, adsorption isotherm and thermodynamic research was done to learn more about the adsorption system. Moreover, the reusability of the generated hydrochar was also examined by recycle testing.

II. MATERIAL VE METOD

A. MATERIALS

HW were supplied from the northwestern part of Türkiye (Düzce). The chemicals Lead nitrate ($Pb(NO_3)_2$, purity 99.95%) for Pb ions and Chromium (III) nitrate nonahydrate ($Cr(NO_3)_3.9H_2O$, purity 99%) for Cr ion to be used in adsorption studies were supplied by Sigma-Aldrich.

B. METHOD

HW were supplied from the northwestern part of Türkiye (Düzce). The chemicals $Pb(NO_3)_2$ for Pb ions and $Cr(NO_3)_3.9H_2O$ for Cr ion to be utilized in research on adsorption were supplied by Sigma-Aldrich.

B. 1. Preparation of Metal Ion Solutions

The sources of the tested HMs, $Cr(NO_3)_3.9H_2O$ and $Pb(NO_3)_2$, were dissolved in 1000 mg/L of deionized water to create stock solutions. The appropriate working solution was prepared by diluting this stock solution to appropriate volumes.

B. 2. Preparation of Adsorbent Materials

Tap water was used to clean HWs initially, followed by distilled water. They were then dried for 12 h at 70°C in an oven. The cleaned and dried HW was crushed into smaller particles. These particles were transferred to a hydrothermal reactor with deionized water. Then, the reactor's temperature was adjusted to 220°C and maintained there for 180 min. The reactor was let to cool to room temperature once the reaction ended.

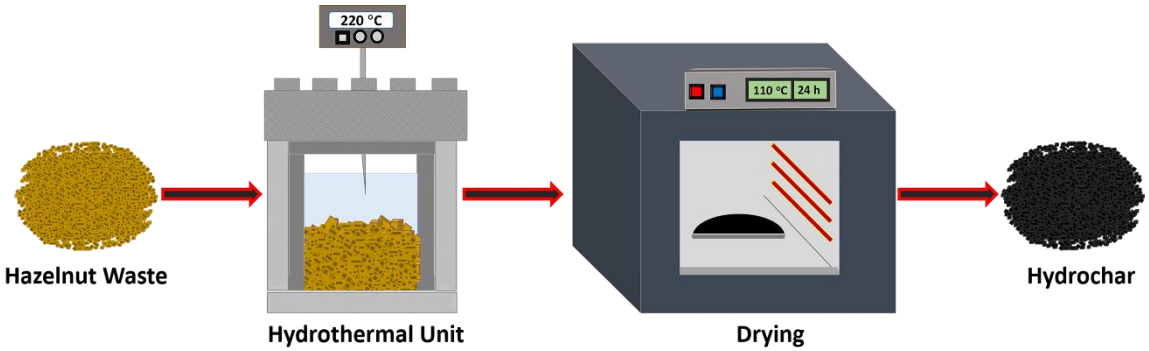

Figure 1. *Schematic diagram of hydrochar production from hazelnut waste*

The obtained hydrochar was filtered with a filter. It was preserved for use in adsorption research after being dried for 24 h at 110°C in an oven. The schematic diagram regarding the production of the hydrochar used as an adsorbent is given in Figure 1.

B. 3. Adsorption Studies of Heavy Metals Ions

In each adsorption study, adsorption experiments were conducted using only one of Pb^{2+} and Cr^{3+}. Experiments with varying parameters were performed to investigate the effects of various environmental conditions on adsorption. In pH effect studies, initial HM concentration was determined as 50 mg/L, hydrochar amount as 50 mg, and shaking time as 240 min. To examine the impact of pH, adsorption tests were realized at pH = 2, 4, 6, 8, and 10. Here, pH adjustments were made using HCl or NaOH solutions. In addition to temperature effect tests conducted at 25°C, 35°C, 45°C, and 55°C, contact time studies were conducted in the range of 0-240 min. In each experiment, 50 mg of hydrochar was put into 100 mL of HM solution (50 mg/L). After each contact time, the concentration was controlled with a UV-visible spectrophotometer (VWR 3100-PC).

C. CHARACTERIZATION

The chemical structures of the hydrochars produced by the hydrothermal system were looked into using FT-IR (Vertex-70 Bruker) spectroscopy. The thermal behavior of the HW and the resulting hydrochar was examined using TGA and DSC studies. The analysis was executed under N_2 atmosphere (25–800

°C temperature range, 20 °C/min heating rate) with a Mettler Toledo brand device. The microstructures and morphologies of the hydrochars used for adsorption prior to and following adsorption studies were examined using a Zeiss Gemini 500 brand FE-SEM. A UV-visible spectrophotometer of the VWR 3100-PC brand was used to control the solution concentration in order to determine the adsorbents' adsorption capability.

D. DATA ANALYSIS

The adsorption capacity of the generated hydrochar and the percentages of HM removal were calculated with the use of Equations 1 and 2.

$$q_e = \frac{C_0 - C_e}{M} \times V \quad (1)$$

$$\%\,Removal = \frac{C_0 - C_e}{C_0} \times 100 \quad (2)$$

C_0 (mg/L) and C_e (mg/L), respectively, represent the starting and equilibrium concentrations of HM ions in the solution. The weight of the adsorbent is represented by M (g), the volume of the solution used in the tests by V (L), and the quantity of HM ions adsorbed by qe (mg/g).
In the study, adsorption isotherm studies were executed to design an optimum adsorption system. Equilibrium isotherm data were assessed through utilization of the most preferred Langmuir and Freundlich adsorption isotherms. Equation 3 represents the Langmuir adsorption isotherm.

$$\frac{C_e}{q_e} = \frac{1}{q_{max} K_L} + \frac{C_e}{q_{max}} \quad (3)$$

In this equation, q_{max} (mg/g) defines the maximum adsorption capacity, while K_L (l/mg) defines the Langmuir constant. The equation of another isotherm, the Freundlich adsorption isotherm, is given in Equation 4.

$$ln\ q_e = ln K_F + \frac{1}{n} ln C_e \quad (4)$$

K_F (mg/g) and n in the equation represent the Freundlich constant and heterogeneity factor.
We investigated the adsorption kinetics of hydrochar using pseudo-first- and second-order kinetic models. Equations 5 and 6 provide the equations for these two models, respectively.

$$ln\ (q_e - q_t) = ln q_e - K_1 t \quad (5)$$

The pseudo-first-order rate constant in this equation is denoted as K_1. q_e and q_t represent the amounts of HMs adsorbed on the adsorbent at equilibrium and at any given period.

$$\frac{t}{q_t} = \frac{1}{K_2 q_e^2} + \frac{t}{q_e} \quad (6)$$

K_2 is the pseudo-second-order rate constant in this equation. The amounts of HMs adsorbed on the adsorbent at any given time are indicated by q_e and q_t, as previously mentioned.
The thermodynamic parameters related to adsorption were determined by the equations given below (Equations 7 and 8). Following the calculation of ΔS^0 and ΔH^0 values from the graph's slope and intercept using the provided data, Eq. 10 was employed to ascertain the Gibbs free energy value.

$$ln K_L = \frac{\Delta S^o}{R} - \frac{\Delta H^o}{RT} \quad (7)$$

$$\Delta G = \Delta H - T\Delta S^o \quad (8)$$

where K_L (mL/g), R and T (K) represent the distribution coefficient, gas constant, and temperature of the solution, respectively.

III. RESULTS AND DISSCUSSION

A. FT-IR ANALYSIS

FT-IR tests were executed to learn more about the chemical makeup of the generated hydrochars and to have an idea about the changes that occurred in the hydrochar after HM adsorption studies. FTIR spectra of HW and hydrochar before hydrochar production are given in Figure 2a. When the spectrum of HW was examined, a peak was observed at 3415 cm^{-1}, and it was determined that this peak belonged to the OH stretching vibration, which is commonly found in the cellulose, lignin, and hemicellulose found in HW [20, 21]. The C-H vibration band describes the peak at 2914 cm^{-1}. The peaks belonging to the C=O vibration and C-O stretching of the carboxyl group are located at 1546 and 1454 cm^{-1}, respectively [22]. The vibration of C-N bonds can be related to the peak at 1247 cm^{-1}. The peaks observed at 1071 and 924 cm^{-1} refer to the C-O bond of alcohols and carboxylic acids, respectively [4].
When the spectrum related to hydrochar is examined, a significant change and peak formation are observed compared to the pre-hydrothermal treatment due to hydrolysis. It is seen that the peak belonging to the O-H band is not in the spectrum belonging to hydrochar due to dehydration. Because dehydration is a reaction that usually occurs after macromolecules are hydrolyzed. As a result of hydrothermal removal of hydrophilic hydroxyl groups, hydrophobicity increases, and the peak that is rarely seen in HW at 1600 cm^{-1} is observed more in the hydrochar spectrum. In addition, dehydration and decarboxylation following hydrolysis fragmentation make the carboxylic acid O-H band at 1305 cm^{-1} more apparent [23]. Additionally, the peaks corresponding to the C=C and C–H bonds forming the hydrochar are present at 1463 cm^{-1} and 832 cm^{-1}, respectively [24].

Figure 2b shows the FT-IR curve with the spectra before and after the Pb and Cr ions were adsorbed. The hydrochar's spectrum is presented once again to highlight the differences between its pre- and post-adsorption Pb and Cr ion spectra. The interaction of the Pb and Cr ions with the hydrochar caused a shift in the peaks' positions. The presence of peaks with very low wave numbers is evidenced by the existence of Pb and Cr-hydrochar bonds [25-27].

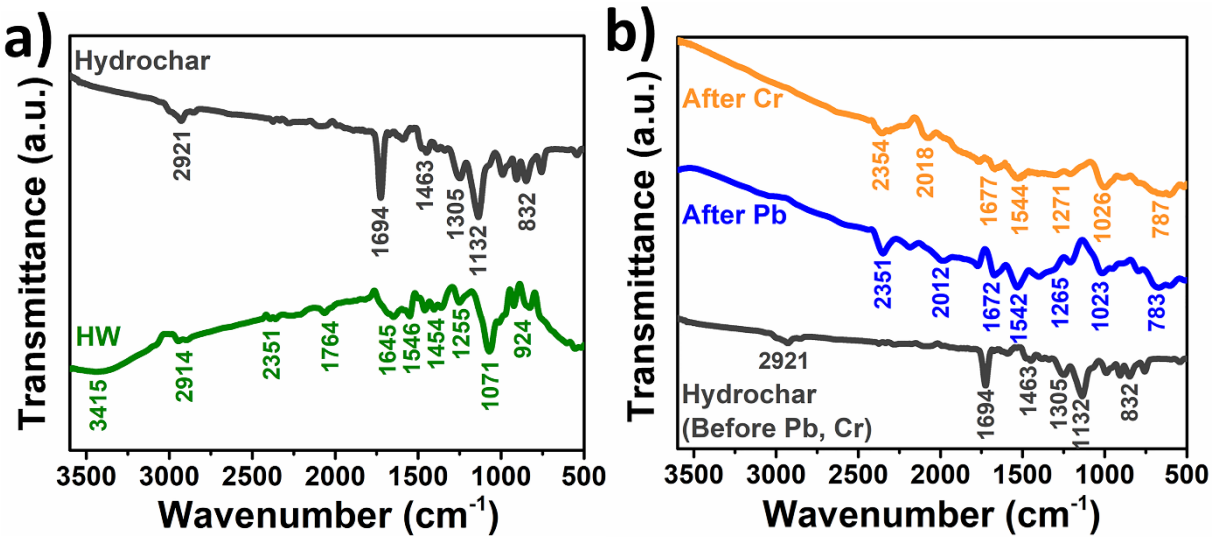

Figure 2. (a) *FT-IR spectra of hazelnut waste and hydrochar* ***(b)*** *before and after adsorption of Pb and Cr ions*

B. TGA AND DSC ANALYSES

The thermal behavior of HW and hydrochar samples resulting from HW was examined using TGA-DSC analyses; the findings are displayed in Figures 3a and b. With a heating rate of 20 °C/min, analyses were fulfilled in the temperature range of 25 to 800 °C. As demonstrated in the HW spectrum in the TGA graph, no appreciable mass decrease was noted in the material up to 200 °C. This shows that the HW has very low internal moisture. The breakdown of cellulose and lignin in the HW's structure explains the 64% mass drop that was observed between 200 and 560 °C [21, 28]. Examining the hydrochar sample reveals that, up to nearly 700 °C, the volume of sample does not diminish. The fact that the weight loss starts around 700 °C indicates that the hydrochar has high thermal stability [29].

When temperatures exceed 700 °C, only a 21% decrease in mass was detected. While the mass loss in the HW sample started at 200 °C, this loss was observed in hydrochars at temperatures above 700 °C. This shows that the thermal stability of the hydrochar is quite high compared to the HW. The other graph supporting this result is the DSC graph, and the HW spectrum in the DSC curve shows that the cellulose and lignin in the HW structure are resistant to degradation and that the material has good thermal stability [30].

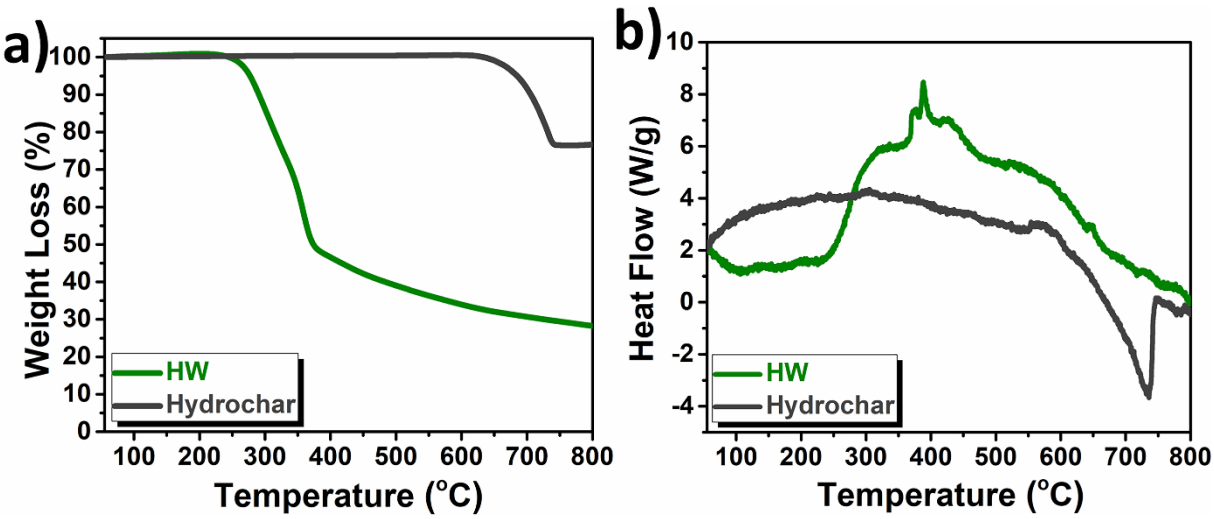

Figure 3. (a) *TGA and,* ***(b)*** *DSC graphs of hazelnut waste and hydrochar*

C. FE-SEM AND EDX ANALYSES BEFORE AND AFTER ADSORPTION

The microstructures and surface morphologies of hydrochars before and after HM adsorption studies were investigated using the FE-SEM imaging technique. The FE-SEM images of hydrochars before adsorption, hydrochars following Pb adsorption, and hydrochars following Cr adsorption are shown in Figures a, c, and e, respectively. The images given in Figures b, d, and f are the EDX and elemental mapping analysis results of hydrochars before adsorption and hydrochars after Pb and Cr adsorption, respectively.

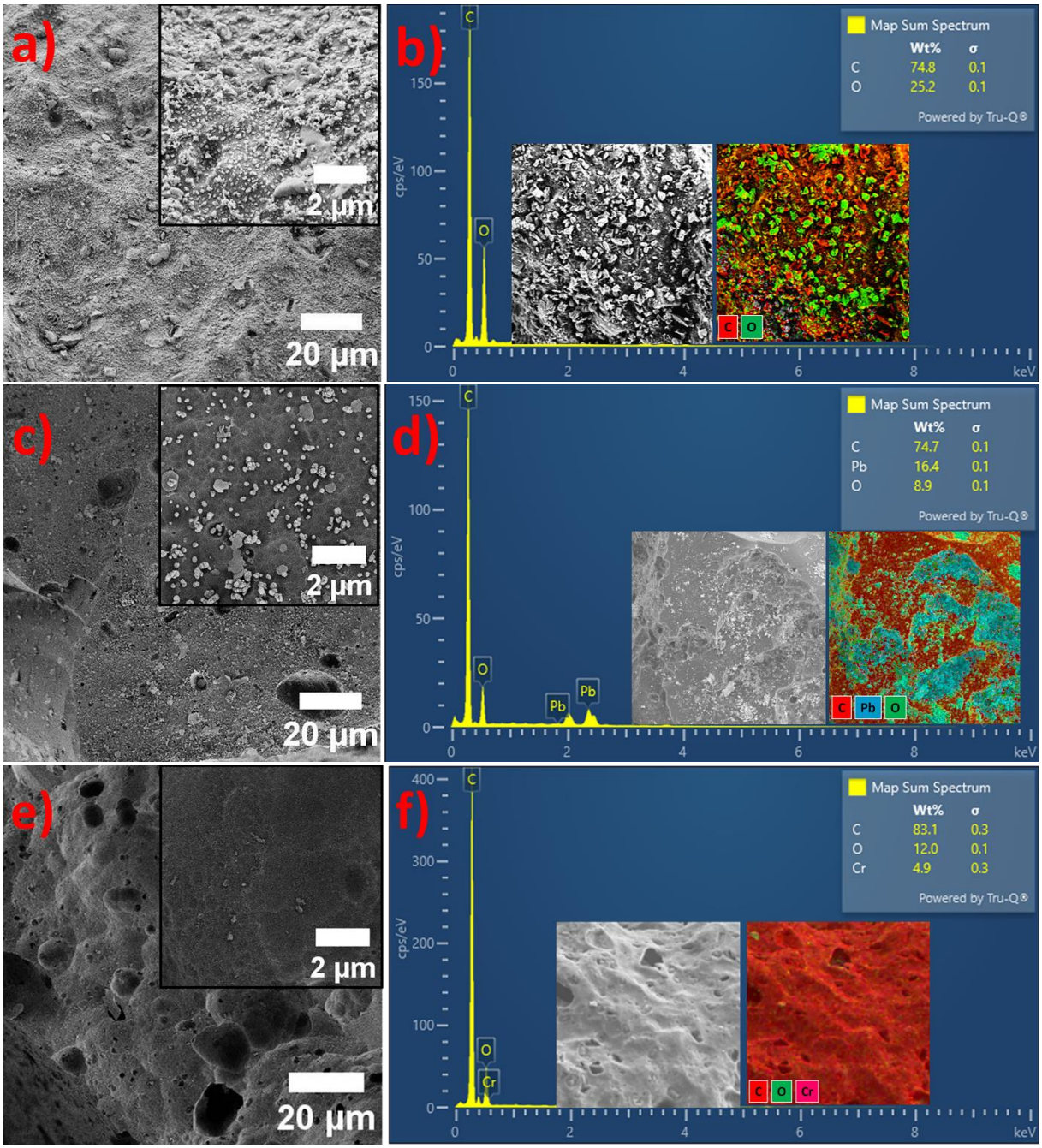

Figure 4. *FE-SEM images of* ***(a)*** *before adsorption,* ***(c)*** *after Pb and* ***(e)*** *Cr adsorption and EDX and elemental mapping analyses of* ***(b)*** *before adsorption,* ***(d)*** *after Pb and,* ***(f)*** *Cr adsorption*

In order to better understand this situation, both before and after adsorption, EDX and elemental analysis measurements were performed. These analyses show that HM were successfully adsorbed by the hydrochar. While only C and O elements are observed in the elemental analysis graph given in Figure 4b, in addition to these, Pb is clearly observed in Figure 4d and Cr is clearly observed in Figure 4f. In addition to these results, elemental mapping measurements also support this result. When the other mapping images are examined compared to the mapping belonging to the hydrochar, the presence of Pb in Figure 4d and Cr in Figure 4f is clearly seen.

D. HEAVY METAL ADSORPTION STUDIES

The initial pH of the medium is very important for the adsorption process. Considering this situation, the effect of pH on Pb and Cr removal was examined and given in Figure 5a. As the pH rose from 2 to 10, it was found in the trials that the elimination of Pb and Cr both reduced. The impact of pH on the interaction between HM ions and hydrochar surface charges describes this circumstance. According to the research, HW biocarbon's zeta potential was 3.81 [32]. According to a different study, the forms of Cr (VI) ions vary depending on the pH of the solution; at pH values below 6.1, $HCrO_4$ is the predominant form of Cr (VI) [33]. The removal of HMs is further promoted at low pH levels by the electrostatic interaction between the positively charged hydrochar and the negatively charged Cr (VI) ions. Furthermore, in an alkaline environment, OH competition might also stop Pb and Cr ions from migrating to the hydrochar surface, which might diminish the effectiveness of HM removal at higher pH levels [34].

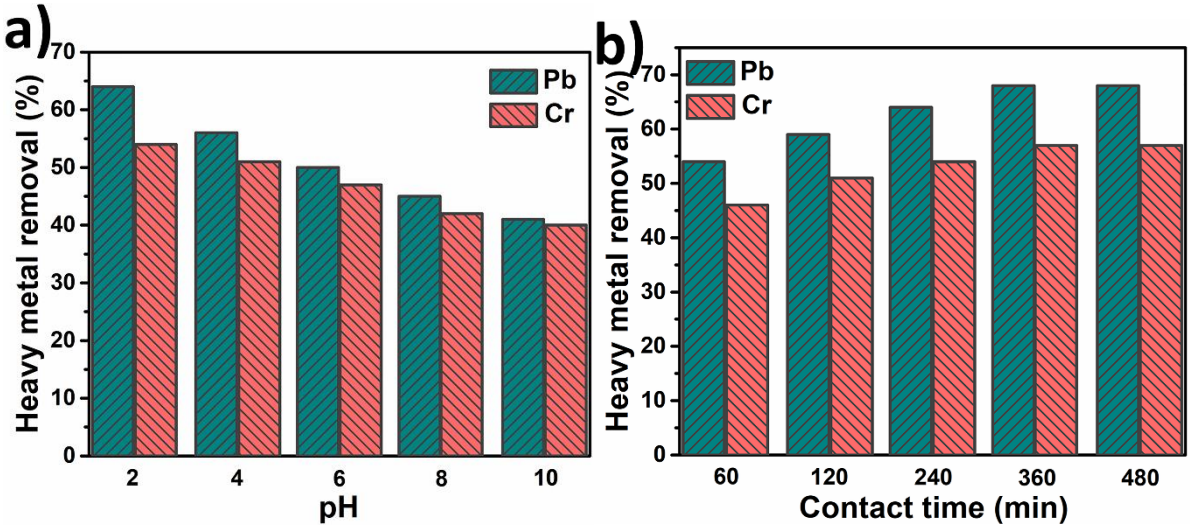

Figure 5. *Effect of* ***(a)*** *initial pH and,* ***(b)*** *adsorption time on heavy metal removal*

Since another important parameter in adsorption is the contact time, studies on the contact time were conducted, and the results are presented in Figure 5b. Although HM ion removal was fast at first, it partially decreased as time progressed. While an increase in removal efficiency was observed up to 360 min, it was determined that the system reached equilibrium at the 360th min. After equilibrium, the adsorption process was continued for another 120 min, but no change was observed in HM removal. This circumstance can be ascribed to the reality that first there were a lot of active sites needed for adsorption on the adsorbent surface, but over time, the number of binding sites on the surface decreased, and after equilibrium, the adsorbent surface's active sites were saturated [35].

Adsorbent dosage and HM initial concentration are the other two parameters affecting the adsorption capacity. Adsorbents of various weights were first added, the medium's pH was brought down to 2, and 240 min of HM removal experiments were conducted. The results are shown in Figure 6a. The graph demonstrates that as the amount of adsorbent grows, so does the effectiveness of HM removal. In the

studies conducted using 20 mg hydrochar, 44% Pb and 40% Cr ions were removed, respectively, while this value reached 64% and 54% in the use of 50 mg hydrochar.

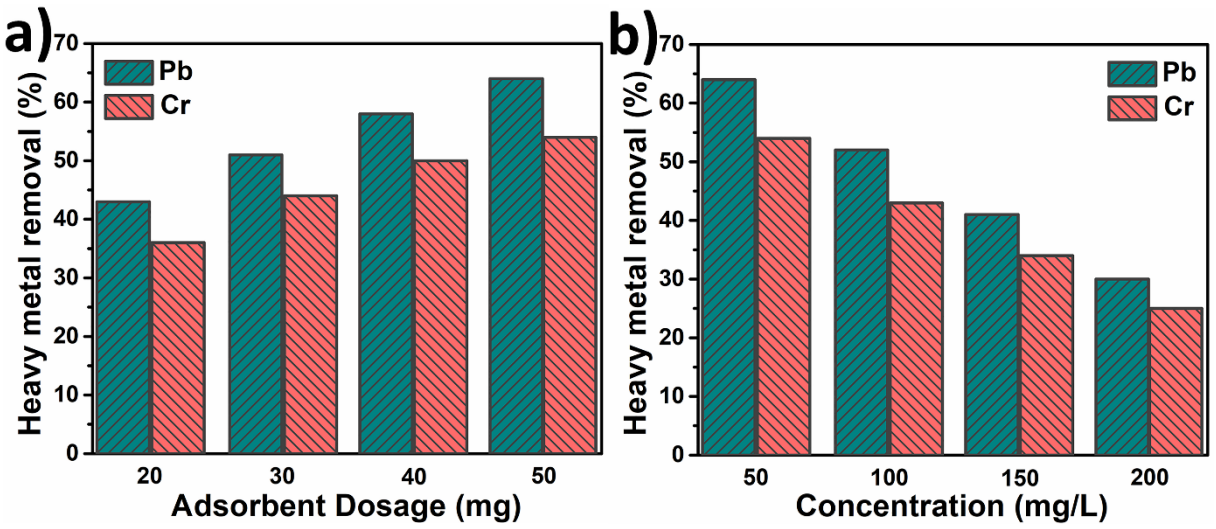

Figure 6. *Effect of* ***(a)*** *adsorbent dosage and,* ***(b)*** *heavy metal initial concentration on heavy metal removal*

The impact of the starting concentration on HM removal was examined using Pb and Cr ions at varying concentrations. These studies were carried out using 50 mg of adsorbent. The graph showing the change in HM removal percentage with HM concentration is given in Figure 6b. According to what the graph indicates, increasing both Pb and Cr concentrations causes a decrease in the removal values of these metals. When Pb and Cr with 50 mg/L concentration are used, the %removal value is 64% and 54%, respectively, while when Pb and Cr with 200 mg/L concentration are used, this value decreases to 30% and 26%. This circumstance results from metal ions' increased ability to engage with the adsorbent's binding sites at low concentrations. However, as the concentration of these HM ions increases, the necessary active sites for adsorption begin to saturate, and the adsorbent cannot remove more HMs [21].

When it comes to adsorption capacity, the effect of both adsorbent dosage and HM initial concentration on metal removal efficiency can generally be related to the active surface area. When the adsorbent dosage is high, there will be more active areas, but since there will not be enough HM, there may not be enough interaction. This causes a decrease in adsorption capacity. The temperature parameter is very important for the removal of HMs. Thereby, the effect of temperature on adsorption was looked into in this phase of the study. Figure 7a presents the study's findings. According to the outcomes, an increase in the removal of both Pb and Cr was detected as the temperature increased. While 64% and 54% of Pb and Cr were removed in the adsorption experiments executed at room temperature, these values were determined to be 75% and 66% in the experiments executed at 55 ºC. The increase in HM removal as the temperature increased means that the process was chemical. The increase in temperature decreased the activation energy that had to be overcome for adsorption to occur and increased the exchange between HM ions and the hydrochar adsorbent [36]. Furthermore, an endothermic adsorption process is indicated by the rise in adsorption capacity with temperature. The studies and results related to the effect of temperature will be utilized in the section on the investigation of thermodynamic properties.

It is critical that materials employed as adsorbents be reusable. For this reason, reusability tests are generally performed, and information can be obtained about how suitable the material used is for use as an adsorbent. Figure 7b displays the findings from the test of the adsorbent's reusability in this study part. Within the parameters of this experiment, four cycles were conducted. After the second, third, and fourth cycles, a decrease of 6.2, 7.0, and 5.3% was observed in HM removal, respectively. According to these findings, the adsorbent continues to play a significant role in the removal of HMs even after four cycles.

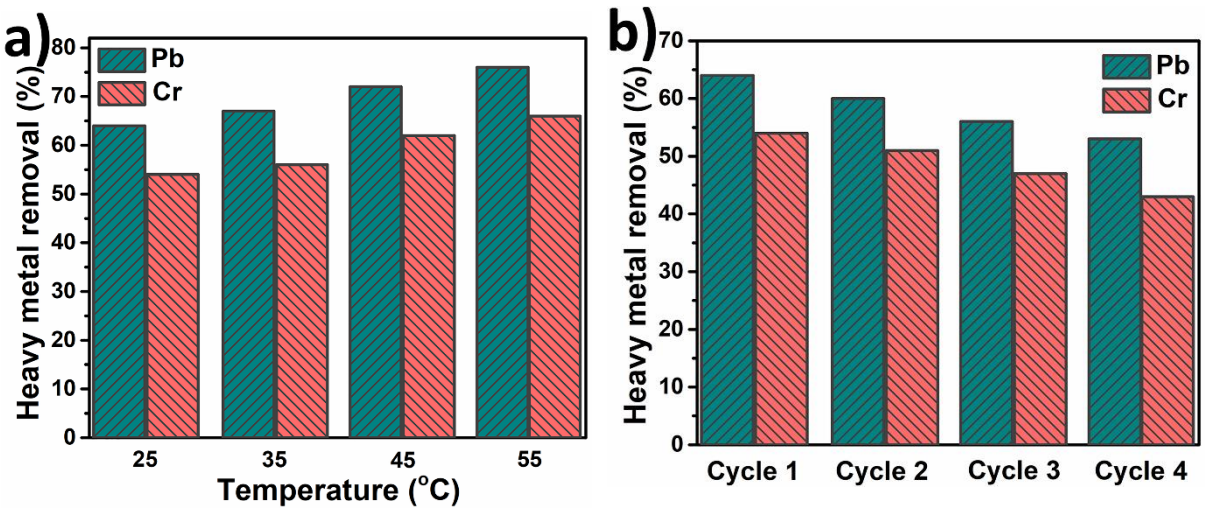

Figure 7. (a) *Effect of temperature on heavy metal removal and* ***(b)*** *hydrochar reusability studies*

E. ADSORPTION ISOTHERM, KINETIC AND THERMODYNAMIC STUDIES

In this section of the research, the isotherm, kinetics and thermodynamics of adsorption are discussed respectively.

E. 1. Adsorption Isotherms

First, the adsorption isotherm is focused on to determine adsorption efficiency. For this purpose, Langmuir and Freundlich isotherms, which come to mind first when the adsorption isotherm is mentioned, were used. To briefly mention both isotherms, the Langmuir isotherm mentions that molecules attached to the surface are attached in a single layer, while the Freundlich isotherm mentions multilayer heterogeneous surfaces [37].

Table 1. *Langmuir and Freundlich isotherm constants.*

	Langmuir			***Freundlich***		
	q_{max} *(mg/g)*	K_1	R^2	K_f *(mg/g)*	***n***	R^2
Pb	*39.308*	*0.038*	*0.997*	*6.121*	*2.833*	*0.962*
Cr	*35.198*	*0.027*	*0.999*	*4.152*	*2.487*	*0.976*

In this section, measurements were first executed using different concentrations of each metal ion for both Pb and Cr (Figure 6b). 100 mL of medium solution, 50 mg of adsorbent, and pH = 2 are the other parameters in the experiments. The title of data analysis gives a thorough explanation of the equations utilized in the computations. Table 1 displays the findings of the computations performed on the experimental data. In the study executed in the presence of Pb ions, the R_2 (correlation coefficients) values of Langmuir and Freundlich isotherms were established as 0.997 and 0.962, respectively. In the presence of Cr ions, these values for the Langmuir and Freundlich isotherms were 0.999 and 0.976, respectively. It is clear that the Langmuir isotherm model has a higher correlation coefficient compared to the Freundlich isotherm model for both HMs. This result shows that the active sites of the hydrochar with equal affinity share the metal ions and that single-layer adsorption is active. In addition, when the calculated n values in the adsorption of both metals are examined, the results being between 1 and 10 indicate that these metals have undergone a suitable adsorption process [38].

E. 2. Kinetic Studies

Adsorption kinetic studies were executed to get an idea about the adsorption mechanism. The kinetic experiments were conducted using pseudo-first- and pseudo-second-order kinetic models. The equations related to both models are given in detail in the data analysis section. Table 2 presents the outcomes derived from the equations utilizing the experimental data. The table shows that when Pb metal is present, the pseudo-second order kinetic model's correlation value (0.997) is higher than the pseudo-first order kinetic model's correlation value (0.915) and approaches 1. The same remains true for Cr (the pseudo-first order kinetic model's correlation value is 0.909, and the pseudo-second order kinetic model's correlation value is 0.998). These findings indicate that the pseudo-second-order kinetic model may account for the adsorption of both metal ions with hydrochars [39].

Table 2. *Adsorption rate constants of pseudo- first-order and second-order kinetic model.*

	Pseudo-first-order			**Pseudo-second-order**		
	$\mathbf{K_1}$ *(1/min)*	$\mathbf{q_e}$ *(mg/g)*	$\mathbf{R^2}$	$\mathbf{K_2}$ *(g/mg min)*	$\mathbf{q_e}$ *(mg/g)*	$\mathbf{R^2}$
Pb	-0.00027	78.671	0.915	0.00113	69.444	0.997
Cr	-0.00031	65.578	0.909	0.00158	58.139	0.998

E. 3. Thermodynamic Study

Thermodynamic parameters also provide ideas about the adsorption process. The equations required to determine the changes in enthalpy, Gibbs free energy, and entropy, which are among these parameters, are provided under the heading "Data Analysis". The graph in Figure 7a was used to determine the thermodynamic parameters. The results obtained through the experimental results and equations are listed in Table 3. Because of the investigation into the adsorption of both metal ions, it was determined that ΔG was negative. This shows that adsorption occurred spontaneously. In addition, the decrease in ΔG values as the temperature increased shows that adsorption continued as the temperature increased. It was observed that ΔH was positive in the adsorption of both Pb and Cr ions. This means that the process is endothermic in both metal adsorption [31, 39].

Table 3. *Thermodynamic parameters for heavy metal ions adsorption.*

	Pb			***Cr***		
T *(K)*	ΔH^o *(kJ/mol)*	ΔG^o *(kJ/mol)*	ΔS^o *(kJ/mol)*	ΔH^o *(kJ/mol)*	ΔG^o *(kJ/mol)*	ΔS^o *(kJ/mol)*
298	1.884482	-0.01834	52.27178	1.686733	-0.01532	42.96343
308		-0.03851			-0.03045	
318		-0.66444			-0.51664	
328		-1.25314			-1.16897	

IV. CONCLUSION

Since the material used in the production of adsorbent in this study is obtained from waste, it will both keep the cost of adsorbent production quite low and increase environmental cleaning as it will be used in the removal of heavy metals. Adsorbents were used to remove Pb and Cr metal ions produced using the hydrocarbon production method. First of all, the characterization of the produced hydrocarbons was carried out and as a result of the characterizations, it was seen that hydrochar was successfully produced. The appropriate conditions for adsorption were determined by considering many different parameters, from adsorbent dosage to pH, contact time to HMs concentration. It was determined that the adsorption

efficiency was higher in low pH conditions, and the highest adsorption occurred at pH=2. In the contact time study, it was observed that the adsorption efficiency increased as time passed at the beginning, and the adsorption efficiency was optimum at 360 min. In addition, as the adsorbent dosage increased, there was an increase in the adsorption of heavy metal ions, while the increase in the heavy metal ion concentration used negatively affected the adsorption. Consequently, to the experiments, the adsorption capacity for Pb and Cr ions was determined to be 39.308 and 35.198 mg/g, respectively. To learn more about the adsorption system, the adsorbent's kinetic, isotherm, and thermodynamic features were investigated. First of all, the adsorption isotherm was focused on to determine the adsorption efficiency, and it was determined that Langmuir was the most suitable isotherm model. Adsorption kinetic studies were performed to get an idea about the adsorption mechanism, and it was pointed out that the second-order kinetic model was noted to be more suitable for adsorption. In addition, thermodynamic properties were investigated to gain more information about the process of adsorption and discovered that the Gibbs free energy values of the adsorption studies for both HM ions were negative, meaning that the adsorption tended to occur spontaneously. Furthermore, experiments were conducted on the reusability of the hydrochar adsorbent in the presence of both Pb and Cr ions, and it was noticed that the adsorbent still played an active role even after four cycles. These results showed that the adsorption capacity of the material selected as adsorbent was sufficient compared to similar materials. In addition, as a result of the recycle studies, it was observed that the produced adsorbent material was quite durable and usable.

ACKNOWLEDGEMENTS: The Konya Technical University Scientific Research Projects (BAP) Fund provided funding for this study under grant number 241019045.

V. REFERENCES

[1] V. Parlak, "Classification of Pollution and Their Entry Rotues into Aquatic Ecosystems," in *Aquatic Toxicology in Freshwater: The Multiple Biomarker Approach*: Springer, 2024, pp. 123-137.

[2] M. Zbair, H. A. Ahsaine, Z. Anfar, and A. Slassi, "Carbon microspheres derived from walnut shell: Rapid and remarkable uptake of heavy metal ions, molecular computational study and surface modeling," *Chemosphere*, vol. 231, pp. 140-150, 2019.

[3] P. Quevauviller, O. Thomas, and A. V. Derbeken, *Wastewater quality monitoring and treatment*. Wiley Online Library, 2006.

[4] M. A. Al-Ajji and M. A. Al-Ghouti, "Novel insights into the nanoadsorption mechanisms of crystal violet using nano-hazelnut shell from aqueous solution," *Journal of Water Process Engineering*, vol. 44, p. 102354, 2021.

[5] G. Argun, G. Çalık, and H. K. Alpoğuz, "Cr (VI) Metal Katyonunun Elektromembran Ekstraksiyonu ile Uzaklaştırılması ve Kinetik Olarak İncelenmesi," *Düzce Üniversitesi Bilim ve Teknoloji Dergisi,* vol. 12, no. 3, pp. 1267-1278, 2024.

[6] Y. Altunkaynak, M. Canpolat, and Ö. Yavuz, "Sulu Çözeltilerden Pb^{2+} İyonlarının Uzaklaştırılmasında Atık Portakal Kabuklarının Kullanılması: Kinetik ve Termodinamik Çalışmalar," *Düzce Üniversitesi Bilim ve Teknoloji Dergisi,* vol. 11, no. 2, pp. 1105-1120, 2023.

[7] G. Crini, "Non-conventional low-cost adsorbents for dye removal: a review," *Bioresource technology*, vol. 97, no. 9, pp. 1061-1085, 2006.

[8] F. Fan, Z. Yang, H. Li, Z. Shi, and H. Kan, "Preparation and properties of hydrochars from macadamia nut shell via hydrothermal carbonization," *Royal society open science*, vol. 5, no. 10, p. 181126, 2018.

[9] F. Fan *et al.*, "Preparation and characterization of biochars from waste Camellia oleifera shells by different thermochemical processes," *Energy & Fuels,* vol. 31, no. 8, pp. 8146-8151, 2017.

[10] J. Zhang, J. Liu, and R. Liu, "Effects of pyrolysis temperature and heating time on biochar obtained from the pyrolysis of straw and lignosulfonate," *Bioresource Technology,* vol. 176, pp. 288-291, 2015.

[11] S. Nizamuddin, N. Mubarak, M. Tiripathi, N. Jayakumar, J. Sahu, and P. Ganesan, "Chemical, dielectric and structural characterization of optimized hydrochar produced from hydrothermal carbonization of palm shell," *Fuel,* vol. 163, pp. 88-97, 2016.

[12] T. Wang *et al.*, "Acetic acid and sodium hydroxide-aided hydrothermal carbonization of woody biomass for enhanced pelletization and fuel properties," *Energy & fuels,* vol. 31, no. 11, pp. 12200-12208, 2017.

[13] W. Yang, H. Wang, M. Zhang, J. Zhu, J. Zhou, and S. Wu, "Fuel properties and combustion kinetics of hydrochar prepared by hydrothermal carbonization of bamboo," *Bioresource technology,* vol. 205, pp. 199-204, 2016.

[14] S. Guo, X. Dong, T. Wu, F. Shi, and C. Zhu, "Characteristic evolution of hydrochar from hydrothermal carbonization of corn stalk," *Journal of analytical and applied pyrolysis,* vol. 116, pp. 1-9, 2015.

[15] S. Kannan, Y. Gariepy, and G. V. Raghavan, "Optimization and characterization of hydrochar produced from microwave hydrothermal carbonization of fish waste," *Waste management,* vol. 65, pp. 159-168, 2017.

[16] Q. Wu *et al.*, "Characterization of products from hydrothermal carbonization of pine," *Bioresource technology,* vol. 244, pp. 78-83, 2017.

[17] E. Demirkaya, O. Dal, and A. Yüksel, "Liquefaction of waste hazelnut shell by using sub-and supercritical solvents as a reaction medium," *The Journal of Supercritical Fluids,* vol. 150, pp. 11-20, 2019.

[18] L. Perez-Armada, S. Rivas, B. González, and A. Moure, "Extraction of phenolic compounds from hazelnut shells by green processes," *Journal of Food Engineering,* vol. 255, pp. 1-8, 2019.

[19] H. A. Alhashimi and C. B. Aktas, "Life cycle environmental and economic performance of biochar compared with activated carbon: a meta-analysis," *Resources, Conservation and Recycling,* vol. 118, pp. 13-26, 2017.

[20] T. H. Tran *et al.*, "Adsorption isotherms and kinetic modeling of methylene blue dye onto a carbonaceous hydrochar adsorbent derived from coffee husk waste," *Science of the Total Environment,* vol. 725, p. 138325, 2020.

[21] S. Dursun, "Production of novel hazelnut shell-based semi-IPN biocomposite absorbents and their use in removing heavy metal ions from water," *Environmental Science and Pollution Research,* vol. 30, no. 15, pp. 44276-44291, 2023.

[22] E. Pehlivan, T. Altun, S. Cetin, and M. I. Bhanger, "Lead sorption by waste biomass of hazelnut and almond shell," *Journal of hazardous materials,* vol. 167, no. 1-3, pp. 1203-1208, 2009.

[23] A. Funke and F. Ziegler, "Hydrothermal carbonization of biomass: A summary and discussion of chemical mechanisms for process engineering," *Biofuels, Bioproducts and Biorefining,* vol. 4, no. 2, pp. 160-177, 2010.

[24] M. T. Reza *et al.*, "Hydrothermal carbonization of biomass for energy and crop production," *Appl. Bioenergy,* vol. 1, no. 1, pp. 11-29, 2014.

[25] P. Wang *et al.*, "Synthesis and application of iron and zinc doped biochar for removal of p-nitrophenol in wastewater and assessment of the influence of co-existed Pb (II)," *Applied Surface Science,* vol. 392, pp. 391-401, 2017.

[26] A. Mandal, N. Singh, and T. Purakayastha, "Characterization of pesticide sorption behaviour of slow pyrolysis biochars as low cost adsorbent for atrazine and imidacloprid removal," *Science of the Total Environment,* vol. 577, pp. 376-385, 2017.

[27] D. Kołodyńska, J. Bąk, M. Kozioł, and L. Pylychuk, "Investigations of heavy metal ion sorption using nanocomposites of iron-modified biochar," *Nanoscale Research Letters,* vol. 12, pp. 1-13, 2017.

[28] M. A. Mahmood and S. Ceylan, "Insights into reaction modeling and product characterization of hazelnut shell pyrolysis," *BioEnergy Research,* pp. 1-11, 2021.

[29] L. K. Palniandy, L. W. Yoon, W. Y. Wong, S.-T. Yong, and M. M. Pang, "Application of biochar derived from different types of biomass and treatment methods as a fuel source for direct carbon fuel cells," *Energies,* vol. 12, no. 13, p. 2477, 2019.

[30] H. Siddiqi, M. Bal, U. Kumari, and B. Meikap, "In-depth physiochemical characterization and detailed thermo-kinetic study of biomass wastes to analyze its energy potential," *Renewable Energy,* vol. 148, pp. 756-771, 2020.

[31] N. Kaya and Z. Yildiz Uzun, "Investigation of effectiveness of pyrolysis products on removal of alizarin yellow GG from aqueous solution: a comparative study with commercial activated carbon," *Water Science and Technology,* vol. 81, no. 6, pp. 1191-1208, 2020.

[32] Y. Zhang, Y. Tang, R. Yan, J. Li, C. Li, and S. Liang, "Removal performance and mechanisms of aqueous Cr (VI) by biochar derived from waste hazelnut shell," *Environmental Science and Pollution Research,* vol. 30, no. 43, pp. 97310-97318, 2023.

[33] S. Rha and H. Y. Jo, "Waste foundry dust (WFD) as a reactive material for removing As (III) and Cr (VI) from aqueous solutions," *Journal of hazardous materials,* vol. 412, p. 125290, 2021.

[34] L. Liu, X. Liu, D. Wang, H. Lin, and L. Huang, "Removal and reduction of Cr (VI) in simulated wastewater using magnetic biochar prepared by co-pyrolysis of nano-zero-valent iron and sewage sludge," *Journal of Cleaner Production,* vol. 257, p. 120562, 2020.

[35] M. Changmai, P. Banerjee, K. Nahar, and M. K. Purkait, "A novel adsorbent from carrot, tomato and polyethylene terephthalate waste as a potential adsorbent for Co (II) from aqueous solution: Kinetic and equilibrium studies," *Journal of Environmental Chemical Engineering,* vol. 6, no. 1, pp. 246-257, 2018.

[36] V. Jonasi, K. Matina, and U. Guyo, "Removal of Pb (II) and Cd (II) from aqueous solution using alkaline-modified pumice stone powder (PSP): equilibrium, kinetic, and thermodynamic studies," *Turkish Journal of Chemistry,* vol. 41, no. 5, pp. 748-759, 2017.

[37] K. V. Kumar *et al.*, "Characterization of the adsorption site energies and heterogeneous surfaces of porous materials," *Journal of materials chemistry A,* vol. 7, no. 17, pp. 10104-10137, 2019.

[38] M. B. Gholivand, Y. Yamini, M. Dayeni, S. Seidi, and E. Tahmasebi, "Adsorptive removal of alizarin red-S and alizarin yellow GG from aqueous solutions using polypyrrole-coated magnetic nanoparticles," *Journal of Environmental Chemical Engineering,* vol. 3, no. 1, pp. 529-540, 2015.

[39] G. Torğut and K. Demirelli, "Comparative adsorption of different dyes from aqueous solutions onto polymer prepared by ROP: kinetic, equilibrium and thermodynamic studies," *Arabian Journal for Science and Engineering,* vol. 43, pp. 3503-3514, 2018.

Düzce University
Journal of Science & Technology

Research Article

Diagnosis of the Skin Cancer by Vision Transformers

Uğur DEMİROĞLU [a,*]

[a] *Department of Software Engineering, Faculty of Engineering, Architecture and Design, Kahramanmaraş İstiklal University, Kahramanmaraş, TÜRKİYE*
** Corresponding author's e-mail address: ugur.demiroglu@istiklal.edu.tr*
DOI: 10.29130/dubited.1572317

ABSTRACT

Skin cancer, one of the most frequent cancers, requires early identification for efficient treatment and better survival. Early diagnosis relies on precise and quick skin lesion categorization into benign and malignant categories. This work uses Vision Transformers (ViTs) to classify skin cancer photos by modeling long-range relationships and capturing complicated visual patterns. ViTs, originally created for natural language processing, have showed great potential in picture classification tasks because to their self-attention processes, outperforming CNNs. A public collection of 270 skin lesion images—240 malignant and 30 benign—was used in this study. Preprocessing included scaling and normalizing the dataset to 384x384x3 and splitting it into 80% training and 20% testing sets. Transfer learning optimised a pre-trained ViT model for this job. To improve accuracy and avoid overfitting, hyperparameters were carefully selected for network training. Parallel computing accelerated training to 30 minutes and 20 seconds. Vision Transformers classify medical images well, according to the study. The ViT model outperformed numerous other methods with 98.15% accuracy on the test set. A confusion matrix analysis showed great sensitivity in detecting malignant lesions and low misclassification of benign patients. These findings show that ViTs can capture detailed medical picture aspects, making them useful for dermatological diagnoses. This study shows that Vision Transformers can improve diagnosis accuracy and lays the groundwork for their use in other medical imaging fields. In the battle against skin cancer and other illnesses that need early diagnosis, ViTs' scalability, efficiency, and precision are important. Future research might integrate ViTs with other deep learning architectures to improve robustness and flexibility. This study adds to the data supporting sophisticated AI in medical diagnostics and lays the groundwork for automated, reliable, and efficient healthcare solutions.

Keywords: *Skin cancer, Categorized images, Malignant and benign classes, Classification, Vision transformers*

Vision Transformers ile Cilt Kanseri Tanısı

ÖZ

En sık görülen kanserlerden biri olan cilt kanseri, etkili tedavi ve daha iyi sağ kalım için erken teşhis gerektirir. Erken teşhis, cilt lezyonlarının iyi huylu ve kötü huylu kategorilere hassas ve hızlı bir şekilde sınıflandırılmasına dayanır. Bu çalışma, uzun menzilli ilişkileri modelleyerek ve karmaşık görsel desenleri yakalayarak cilt kanseri fotoğraflarını sınıflandırmak için Görüntü Dönüştürücülerini (ViT'ler) kullanır. Başlangıçta doğal dil işleme için oluşturulan ViT'ler, kendi kendine dikkat süreçleri sayesinde CNN'leri geride bırakarak resim sınıflandırma görevlerinde büyük potansiyel göstermiştir. Bu çalışmada 240 kötü huylu ve 30 iyi huylu olmak üzere 270 cilt lezyonu görüntüsünün genel koleksiyonu kullanılmıştır. Ön işleme, veri kümesinin 384x384x3'e ölçeklenmesini ve normalleştirilmesini ve %80 eğitim ve %20 test kümelerine bölünmesini içeriyordu. Transfer öğrenme, bu iş için önceden eğitilmiş bir ViT modelini optimize etti. Doğruluğu artırmak ve aşırı uyumu önlemek için, ağ eğitimi için hiperparametreler dikkatlice seçildi. Paralel hesaplama, eğitimi 30 dakika 20 saniyeye hızlandırdı. Çalışmaya göre, Görüntü Dönüştürücüler tıbbi görüntüleri iyi sınıflandırıyor. ViT modeli, test setinde %98,15 doğrulukla diğer birçok yöntemi geride bıraktı. Bir karışıklık matrisi analizi, kötü huylu lezyonları tespit etmede büyük

Geliş: 23/10/2024, Düzeltme: 07/12/2024, Kabul: 12/12/2024

hassasiyet ve iyi huylu hastaların düşük yanlış sınıflandırılması gösterdi. Bu bulgular, ViT'lerin ayrıntılı tıbbi resim yönlerini yakalayabildiğini ve bu sayede dermatolojik teşhisler için yararlı hale geldiğini gösteriyor. Bu çalışma, Görüntü Dönüştürücülerin teşhis doğruluğunu artırabileceğini ve diğer tıbbi görüntüleme alanlarında kullanımları için temel oluşturduğunu gösteriyor. Cilt kanseri ve erken teşhis gerektiren diğer hastalıklarla mücadelede, ViT'lerin ölçeklenebilirliği, verimliliği ve hassasiyeti önemlidir. Gelecekteki araştırmalar, sağlamlığı ve esnekliği artırmak için ViT'leri diğer derin öğrenme mimarileriyle entegre edebilir. Bu çalışma, tıbbi teşhislerde sofistike yapay zekayı destekleyen verilere katkıda bulunuyor ve otomatik, güvenilir ve verimli sağlık çözümleri için temel oluşturuyor.

Anahtar Kelimeler: *Cilt kanseri, Kategorize edilmiş görüntüler, Kötü huylu ve iyi huylu sınıflar, Sınıflandırma, Vision transformers*

I. INTRODUCTION

Cancer is a disease characterized by the uncontrolled proliferation and spread of aberrant cells. [1] These aberrant cells can develop tumors, which can infiltrate adjacent tissues or spread throughout the body via the bloodstream or lymphatic system. There are numerous varieties of cancer, each with its own distinct features and treatment choices. The causes of cancer are diverse and vary by type. The majority of malignancies are thought to be caused by a combination of hereditary and environmental causes. Skin cancer is one of the most prevalent types of cancer. It occurs when abnormal skin cells multiply uncontrollably. There are three forms of skin cancer: basal cell carcinoma, squamous cell carcinoma, and melanoma. Basal cell carcinoma and squamous cell carcinoma are commonly known as non-melanoma skin malignancies. They are typically curable, but if neglected, they can spread to other parts of the body. Melanoma is the most deadly form of skin cancer and can be fatal if not diagnosed and treated promptly. It is caused by the unregulated proliferation of melanocytes, which create melanin, the pigment that gives skin its color [2].

Early detection of cancer is critical for successful treatment and better results. Detecting cancer in its early stages allows for more effective treatment options, which frequently result in improved survival rates. Early detection may also lessen the need for severe therapies such as surgery, chemotherapy, or radiation therapy. Furthermore, early discovery can help prevent cancer from spreading to other parts of the body, considerably increasing the likelihood of a complete cure. As a result, regular screenings and checkups are critical for early cancer identification and improved general health. For the diagnosis of the diseases from medical images, computerized techniques have gained much attention recently.

Classification systems for medical images serve an important role in healthcare since they allow for accurate and efficient diagnosis and treatment. These strategies use algorithms to classify medical images based on their visual qualities. For example, they can be used to distinguish between benign and malignant tumors, identify different types of diseases, and track disease progression over time. By automating the classification process, medical personnel can save time while improving diagnostic accuracy, resulting in better patient outcomes. Furthermore, classification approaches can be used to help with treatment planning and monitoring, ensuring that patients receive appropriate care. This paper uses the Vision Transformers (ViT) approach for classification [3]. ViT has had a considerable impact on the field of computer vision, namely picture classification. Unlike typical convolutional neural networks (CNNs), ViT employs transformers, a sequence-to-sequence modeling architecture initially designed for natural language processing. ViT divides images into patches, flattens them into vectors, and then feeds them via a transformer encoder. This method enables ViT to handle photos of varying sizes and resolutions efficiently. Furthermore, ViT has shown competitive performance with CNNs, particularly on large-scale datasets. Their scalability, flexibility, and solid theoretical underpinning make them an appealing option for a variety of computer vision tasks, including medical picture processing and distant sensing. Additional information regarding the approach can be found in the following sections.

Based on the evidence presented above, computerized techniques are extremely important in the early detection of cancers. This hypothesis has piqued the interest of experts, leading to useful studies on the subject. It would be useful to give a brief literature survey. Subba and Sunaniya used an attention-based GoogLeNet-style CNN to improve brain tumor classification in [4] and Elbedoui et al. investigated deep learning methods for dermoscopic image-based skin cancer detection in [5]. More specifically, valuable studies focused on skin cancer detection implementing the Vision Transformers method are listed in Table 1, briefly.

This study significantly advances the domain of medical image analysis by investigating the use of Vision Transformers (ViTs) for classifying skin cancer pictures. The study clearly illustrates that ViTs, through their self-attention mechanism, can capture intricate patterns in high-dimensional picture data, exceeding the accuracy and computing efficiency of typical Convolutional Neural Networks (CNNs). The authors get a remarkable classification accuracy of 98.15% using a publicly accessible skin cancer dataset, underscoring the model's efficacy in differentiating between benign and malignant tumors. The approach of the work include dataset preparation, training the ViT model with optimal hyperparameters, and utilizing parallel computing to improve the training process. The research presents ViTs as a scalable and adaptable option for medical imaging applications, highlighting their capacity to enhance diagnostic precision and enable early skin cancer diagnosis. This study situates its findings within the wider context of deep learning progress, citing relevant research that combines Vision Transformers with other designs to improve performance. The research highlights the transformational potential of ViTs in dermatological diagnostics and sets the stage for future advancements in automated, AI-driven healthcare solutions.

This study is organized in the following way. Section 2 gives information about the used dataset including the images. Section 3 recalls the Vision Transformers which is the main method used in this study. A case study is given in Section 4 presenting the results obtained and the last section has the conclusions.

Table 1. *Studies focused on skin cancer detection using the vision transformers*

Study	Year	Classifying Method
Elbedoui et al [5]	2024	Efficient andaccurate pre-trained models, EfficientNet-B0-V2 and Vision Transformers ViT-b16
Mejri et al [6]	2024	VGG-16(Visual Geometry Group) and ResNet-50 model (ResidualNetwork)
Hameed et al [7]	2024	Vision Transformers
Kumar et al [8]	2024	Combines the MobileNetV2and Vision Transformer (ViT) architectures
Dagnaw et al [9]	2024	Two pretrained ViTs, three Swin transformers, five pretrained CNNs, and three visual-based explainable artificial intelligence (XAI) models.The ViT-base, ViT-large, Swin-tiny, Swin-base, and Swin-small transformer models and VGG19, ResNet18,ResNet50, MobileNetV2, and DenseNet201 pretrained CNN models
Yang et al [10]	2024	Inception ResNet, ViT-Base
Remya et al [11]	2024	Vision Transformer model with transfer learning, channel attention mechanism, and ROI for the accurate detection

Table 1 (cont). *Studies focused on skin cancer detection using the vision transformers*

Abou et al [12]	2024	Pre-trained ImageNet architectures and Vision Transformer models
Ashfaq et al [13]	2023	Various deep neural networks (DNN), Vision Transformer (ViT)
Islam et al [14]	2023	Combines DenseNet121 and Xception, two cutting-edge pretrained CNNs, to extract useful features
Desale et al [15]	2024	A combination of techniques such as piecewise linear bottom hat filtering, adaptive median filtering, Gaussian filtering, and an enhanced gradient intensity method is used for pre-processing
Kusumastuti et al [16]	2023	Convolutional Neural Networks (CNN),EfficientNet, and Vision Transformer (VIT) methods

II. THE SKIN CANCER DATASET

The dataset used in this study is a skin cancer dataset, categorized into malignant and benign images, and was downloaded from Kaggle [17]. This dataset contains images of skin lesions classified into two categories: malignant and benign. It is organized into two folders:

- *Malignant:* This folder contains images of skin lesions diagnosed as malignant, indicating the presence of skin cancer. These images can be used to train models that detect and differentiate malignant skin conditions.
- *Benign:* This folder contains images of non-cancerous skin lesions that are not immediately life-threatening. These images are essential for training models to accurately distinguish between harmful and harmless skin conditions.

This dataset can be used for tasks such as image classification, deep learning model training, and medical image analysis. Researchers and practitioners can leverage this dataset to develop models that assist in the early detection and diagnosis of skin cancer. The dataset consists of 270 images, with 30 benign and 240 malignant cases, totaling 7MB in size. The images have a resolution of 96 DPI, with a 24-bit depth, and all images have a width and height of at least 200 pixels. The image format is JPG, and the benign/malignant status is used to label cancer types.

The dataset, which is under a public license, is widely used in medical, cancer, and computer vision research fields. It is freely accessible for download and continuous use in these areas. Fig. 1 shows sample images from benign and malignant cases. The dataset used in this study was chosen due to its suitability for the research objective: classifying skin cancer images into benign and malignant categories. This publicly available dataset, sourced from Kaggle, provides a reliable and diverse set of skin lesion images specifically categorized to facilitate machine learning tasks in medical diagnostics. It includes 270 images, with 240 malignant and 30 benign samples, ensuring a clear representation of both classes required for training and testing classification models. The dataset's organization into well-defined categories aligns with the goals of this study, enabling the Vision Transformer (ViT) model to effectively learn the distinctions between malignant and benign lesions. Additionally, the dataset’s manageable size (7MB) and standardized image resolution (minimum 200 pixels in width and height, with 24-bit depth) make it computationally efficient for model training without requiring extensive preprocessing. Its public license further promotes reproducibility and accessibility, ensuring that findings from this research can be validated and extended by other researchers. These characteristics collectively make the dataset an ideal choice for exploring the potential of ViTs in skin cancer diagnosis.

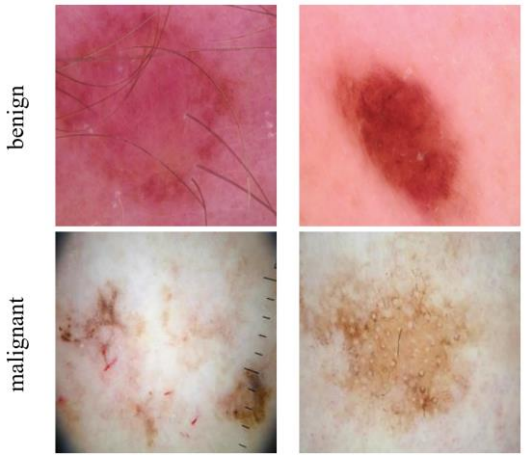

Figure 1. *Sample images from the dataset.*

III. THE VISION TRANSFORMERS

The ViT is a deep learning architecture originally developed for Natural Language Processing (NLP), designed to overcome the limitations of Recurrent Neural Networks (RNNs) in learning long-range dependencies. The Transformer can directly model the relationships between all words in an input sequence using the self-attention mechanism. As a result, Transformer models can achieve faster and more accurate results compared to RNNs. The Transformer architecture is composed of the following components.

ViT, or Vision Transformer, is a model for image classification that uses a Transformer-like architecture on image patches. An image is divided into fixed-size patches, each of which is then linearly embedded, position embeddings are added, and the resulting sequence of vectors is fed into a standard Transformer encoder. To perform classification, the standard approach of adding an extra learnable "classification token" to the sequence is used. The ViT architecture is given in Fig. 2 [18].

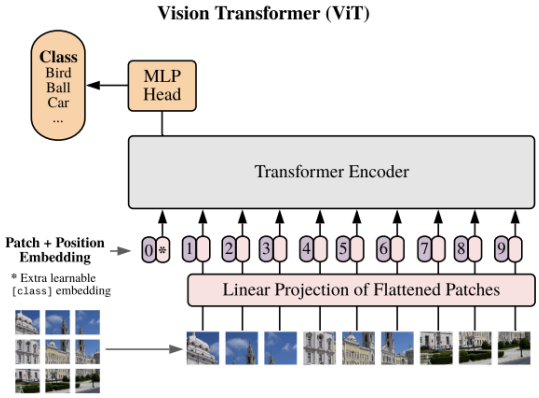

Figure 2. *The ViT architecture.*

Since their introduction in NLP, transformers have gained significant attention, achieving highly successful results and often replacing models like Long Short-Term Memories (LSTMs). The most notable feature of transformers is the self-attention mechanism, which analyzes relationships between all words in a sequence. This mechanism allows the model to treat the input as a whole. In contrast, convolutional layers in Convolutional Neural Networks (CNNs) process information based on the filter size, which is referred to as locality in the literature. This locality limits CNNs from capturing global semantic features, whereas transformers, by processing the entire input holistically, can extract strong global semantic features.

Unlike traditional CNNs, which eliminate the need for manually crafted features, the Vision Transformer (ViT) differentiates itself by leveraging a self-attention mechanism to gather global contextual information from the entire image. This approach divides an input image into fixed-size patches, embeds each patch into high-dimensional vectors, and processes these vectors using a transformer encoder. This methodology enhances ViT's ability to capture complex long-term dependencies and subtle relationships between different regions of the image.

In this study, a pre-trained Vision Transformer (ViT) neural network will be used for the classification of brain MRI images. ViT is a neural network model that employs a transformer architecture to encode image inputs into feature vectors. The network consists of two main components: the backbone and the head. The backbone is responsible for the encoding step, where it takes input images and extracts feature vectors. The head is responsible for making predictions by mapping the encoded feature vectors to prediction scores. In this study, the pre-trained ViT network has already learned strong feature representations for images. Using transfer learning, the model can be fine-tuned for better performance on specific tasks. The block diagram of the ViT network can be found in Fig. 3 [19].

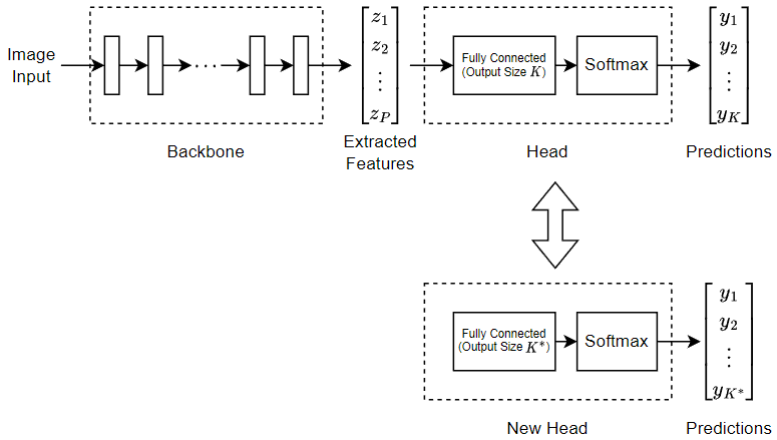

Figure 3. *Block diagram of the ViT network.*

This diagram outlines the architecture of a ViT network that makes predictions for K classes and illustrates how the network is structured to enable transfer learning for a new dataset with K classes. The diagram highlights the process of adapting the pre-trained ViT model to the specific task by fine-tuning the network for the new dataset. The backbone of the ViT extracts feature representations from the input images, while the classification head is modified to output predictions for the new K classes. This adjustment enables the network to learn and generalize effectively on the new dataset while leveraging the pre-trained knowledge.

IV. APPLICATION

80% of the dataset is used for training, with the remaining 20% reserved for non-training test data. The images were scaled and normalized to 384x384x3 and processed as color images for both training and testing. The training parameters are set at Mini Batch Size = 16, Maximum Epochs = 5, Iterations Per Epoch = 13, and Validation Frequency = 3. The network was trained using Stochastic Gradient Descent with Momentum (SGDM) as the optimizer, which was combined with a stochastic solver. It would be useful to describe these terms. The training of the Vision Transformer (ViT) model in this study was optimized using carefully selected parameters to balance performance and computational efficiency. A mini-batch size of 16 was employed, allowing for the processing of smaller subsets of the data at a time, which facilitates more frequent weight updates and effective utilization of computational resources. Training was conducted over 5 epochs, with each epoch comprising 13 iterations, and a validation frequency of 3 iterations was set to monitor performance and detect overfitting. The learning rate was initialized at 1e-4 to ensure stable and gradual convergence, while shuffling the data at each epoch

improved the model's ability to generalize by preventing it from memorizing the data order. Training was accelerated using parallel computing with 16 workers on a high-performance system featuring an NVIDIA RTX A4000 GPU. The optimization algorithm used was Stochastic Gradient Descent with Momentum (SGDM), which enhanced convergence by incorporating a momentum term. SGDM updates the model's weights iteratively based on the gradient of the loss function while adding a fraction of the previous weight update to the current step. This approach reduces oscillations, accelerates convergence, and helps navigate the loss landscape effectively, particularly in regions with small gradients. Together, these parameters and the SGDM algorithm enabled the ViT model to achieve efficient training and impressive classification accuracy of 98.15%, underscoring its capability in diagnosing skin cancer images accurately.

The use of an 80/20 train-test split instead of cross-validation in this study was mainly influenced by the dataset's particular attributes and the computing efficiency needed for training Vision Transformers (ViTs). Although cross-validation offers a more reliable assessment of a model's generalizability through the utilization of multiple training and testing folds, this methodology can be computationally intensive, especially when applied to deep learning models such as Vision Transformers, which demand considerable time and resources for training. This study utilized a dataset of 270 photos, with an 80/20 split allocating 216 images for training, therefore enabling the ViT model to discern significant patterns. The remaining 54 photos were allocated for testing, enabling an objective assessment of the model's performance. Conversely, cross-validation would have subdivided the dataset into smaller training and validation subsets, thus restricting the data available for training in each fold, which might negatively impact the performance of a data-intensive model such as ViTs. The computing burden of cross-validation is substantial. Given constrained computer resources, repeatedly training the ViT model over many folds would have considerably augmented training duration and resource expenditure without guaranteeing commensurate insights. The 80/20 division, coupled with meticulous validation throughout training (e.g., via validation frequency), facilitated a compromise between efficiency and thorough assessment of the model. Although cross-validation may provide a little more dependable assessment of generalizability, the 80/20 split was used as a pragmatic and efficient method for this investigation. Future research may integrate cross-validation should bigger datasets or enhanced computational resources be accessible, enabling a more thorough examination of the ViT model's performance resilience.

Table 2. *Specifications of the computer used in the experiment.*

Processor	12th Gen Intel(R) Core(TM) i9-12900F 2.40 GHz
Cores, Processors	16, 24
Installed RAM	64.0 GB (63.7 GB usable)
GPU	NVIDIA RTX A4000
DirectX version	12 (FL 12.1)
GPU Memory	47.9 GB (16.0 GB Dedicated, 31.9 GB Shared)
SSD Capacity	477 GB

Training was completed in 30 minutes and 20 seconds. Training accuracy was attained at 0.9815. Fig. 4 depicts the confusion matrix that was obtained.

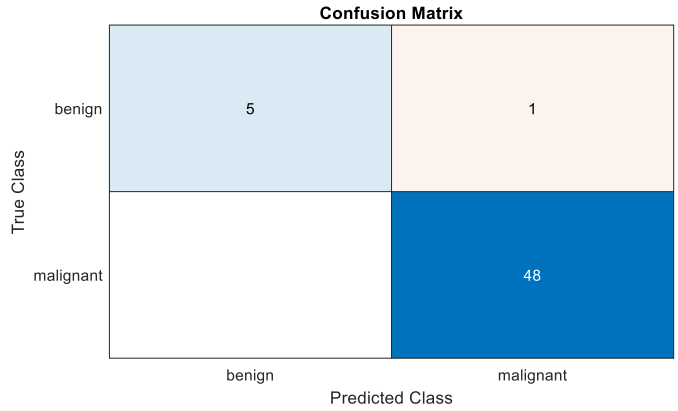

Fiure 4. *The confusion matrix.*

Upon examining the Confusion Matrix, it is observed that out of 54 test samples, 6 are benign and 48 are malignant images. Among the benign images, 5 were correctly predicted, while 1 was misclassified. Similarly, all 48 malignant images were correctly predicted. The progress of training iterations, iteration time, mini-batch performance, test performance, and errors are presented in Table 3. This detailed breakdown provides insights into the model's performance during training and testing, showing how well it generalizes across different data points.

Table 3. *Training iterations.*

Epoch	Iteration	Time Elapsed (hh:mm:ss)	Mini-batch Accuracy	Validation Accuracy	Mini-batch Loss	Validation Loss
1	1	00:00:36	43.75%	90.74%	1.8579	0.3866
1	3	00:01:40	81.25%	88.89%	1.4480	0.9417
1	6	00:02:57	100.00%	88.89%	0.0013	1.0018
1	9	00:04:23	87.50%	88.89%	0.6754	0.5734
1	12	00:05:49	93.75%	98.15%	0.1009	0.1070
2	15	00:07:09	68.75%	96.30%	1.0546	0.1256
2	18	00:08:33	75.00%	92.59%	0.9555	0.2944
2	21	00:09:54	87.50%	94.44%	0.4395	0.2519
2	24	00:11:20	87.50%	96.30%	0.2401	0.1465
3	27	00:12:45	93.75%	98.15%	0.0954	0.0846
3	30	00:14:06	93.75%	98.15%	0.0842	0.0959
3	33	00:15:29	100.00%	98.15%	0.0029	0.1047
3	36	00:16:52	81.25%	98.15%	0.4746	0.0795
3	39	00:18:16	100.00%	98.15%	0.0046	0.0520
4	42	00:19:40	100.00%	96.30%	0.0020	0.0456
4	45	00:21:03	87.50%	98.15%	0.4422	0.0501
4	48	00:22:24	100.00%	98.15%	0.0002	0.1098
4	50	00:23:18	100.00%		0.0302	
4	51	00:23:47	87.50%	96.30%	0.6107	0.1627
5	54	00:25:11	93.75%	98.15%	0.0553	0.1036
5	57	00:26:34	100.00%	98.15%	0.0050	0.0773
5	60	00:27:55	100.00%	98.15%	0.0042	0.0613
5	63	00:29:20	100.00%	98.15%	0.0041	0.0572
5	65	00:30:19	100.00%	98.15%	0.0015	0.0454

Fig. 5 shows the training and error graphics. As shown in the figure, the test accuracy of the training process utilizing the ViT network was 98.15%. This shows the effectiveness of the method.

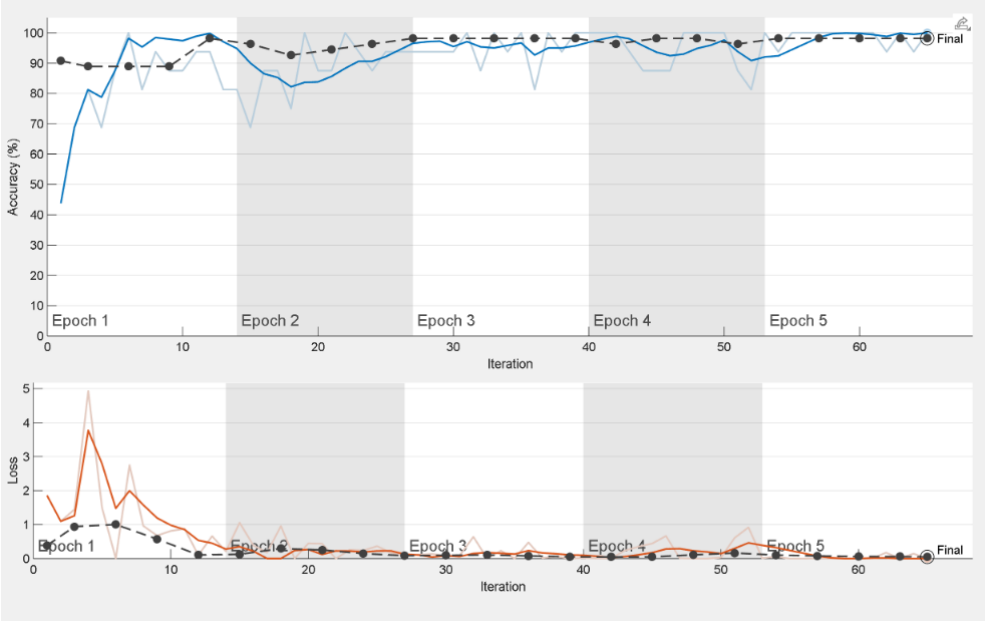

Figure 5. *Training and loss visualization.*

The selection of a modest dataset including 270 photos for this investigation was determined by the accessibility of publically available, pre-categorized skin lesion photographs. Although the dataset size may seem limited, it was adequate to illustrate the efficacy of Vision Transformers (ViTs) in differentiating between benign and malignant skin lesions. The main objective of this work was to assess the independent performance of ViTs on a realistic dataset instead of attaining optimal results by considerable dataset augmentation. Nonetheless, it is recognized that an expanded dataset frequently improves model generalizability and robustness. Techniques such as data augmentation (e.g., rotation, flipping, and scaling) or sophisticated methods like Generative Adversarial Networks (GANs) may be utilized to artificially expand the dataset size. These strategies may provide more diversity into the training data, potentially enhancing the model's capacity to generalize to unfamiliar pictures. For example, augmentation can present the model with various orientations and lighting conditions, but GANs can produce wholly new yet realistic samples that replicate the original data's underlying distribution. The choice to exclude augmentation or GANs in this investigation was intentional, concentrating on evaluating the baseline performance of the ViT model on a conventional, unaltered dataset. This method guarantees that the outcomes are only ascribed to the model's design and training regimen, rather than being affected by supplemented input. Future study may investigate the influence of these strategies on categorization accuracy. Combining ViTs with enriched datasets or GAN-generated pictures is expected to sustain or maybe improve the existing accuracy of 98.15%, hence further substantiating the model's relevance in dermatological diagnoses.

IV. CONCLUSION

This study demonstrates the efficacy of Vision Transformers (ViTs) in categorizing skin cancer photos, with an accuracy of 98.15%. This study distinguishes itself from previous research by concentrating on the usage of Vision Transformers (ViTs) as an independent methodology, rather than employing hybrid approaches that integrate ViTs with other architectures. Kumar et al. used ViTs with MobileNetV2 to augment performance, whilst Desale et al. employed intricate preprocessing methods, such as gradient-based intensity modifications, to increase classification results. This work illustrates that Vision Transformers (ViTs), when fine-tuned and trained with optimum parameters, may achieve competitive outcomes independently, without the need for substantial preprocessing or hybrid designs. This study diverges from Mejri et al., who employed pretrained CNNs such as VGG-16 and ResNet-50, and Hameed et al., who integrated several CNN and transformer models for improved segmentation and classification. This work demonstrates the practicality of a pre-trained ViT model by simplifying the

architecture and training procedure, particularly on smaller datasets. The dataset employed herein comprises 270 photos, somewhat less than those utilized in other comparative research; yet, the findings obtained are comparable to or superior to those from studies employing bigger datasets, such as the ISIC dataset utilized by Hameed et al. A further critical distinction pertains to computational efficiency. This work maximized training by parallel computing and simple preprocessing, in contrast to others that need substantial resources for training intricate hybrid models or doing complicated data augmentation. The training was accomplished in approximately 30 minutes and 20 seconds, underscoring the efficacy of ViTs in contrast to CNN-based approaches, which often need extended training durations owing to their dependence on localized feature extraction. This research highlights the independent capability of Vision Transformers as a scalable, efficient, and extremely precise instrument for skin cancer diagnostics. It distinguishes itself by attaining superior performance with less computer resources and dataset prerequisites, demonstrating the wider use of ViTs in medical imaging. Future research may examine comparisons on more extensive datasets and explore the incorporation of explainable AI methodologies to better substantiate ViTs in therapeutic applications.

V. REFERENCES

[1] B. Banushi, S. R. Joseph, B. Lum, J. J. Lee, and F. Simpson. "Endocytosis in cancer and cancer therapy," *Nature Reviews Cancer*, *23*(7), 450-473, 2023.

[2] M. Naqvi, S. Q. Gilani, T. Syed, O. Marques, and H. C. Kim. "Skin cancer detection using deep learning—a review," *Diagnostics*, 13(11), 1911, 2023.

[3] K. Han, Y. Wang, H. Chen, X. Chen, J. Guo, Z. Liu, and D. Tao. "A survey on vision transformer," *IEEE transactions on pattern analysis and machine intelligence*, 45(1), 87-110, 2022.

[4] A. B. Subba, and A. K. Sunaniya. "Computationally optimized brain tumor classification using attention based GoogLeNet-style CNN," *Expert Systems with Applications*, 125443, 2024.

[5] K. Elbedoui, H. Mzoughi, and M. B. Slima. "Deep Learning Approaches for Dermoscopic Image-Based Skin Cancer Diagnosis. In *2024 IEEE 7th International Conference on Advanced Technologies, Signal and Image Processing (ATSIP), 2024*, Vol. 1, pp. 1-7, IEEE.

[6] S. Mejri, and A. E. Oueslati. Dermoscopic Images Classification Using Pretrained VGG-16 and ResNet-50 Models", in *2024 IEEE 7th International Conference on Advanced Technologies, Signal and Image Processing (ATSIP)*, 2024, Vol. 1, pp. 342-347, IEEE.

[7] M. Hameed, A. Zameer, and M. A. Z. Raja. "A Comprehensive Systematic Review: Advancements in Skin Cancer Classification and Segmentation Using the ISIC Dataset," *CMES-Computer Modeling in Engineering & Sciences*, 140(3), 2024.

[8] M. R. Kumar, S. Priyanga, J. S. Anusha, V. Chatiyode, J. Santiago, and P. Revath. "Synergistic Skin Cancer Classification: Vision Transformer alongside MobileNetV2," in *2023 4th International Conference on Intelligent Technologies (CONIT), 2024*, pp. 1-7, IEEE.

[9] G. H. Dagnaw, M. El Mouhtadi, and M. Mustapha. "Skin cancer classification using vision transformers and explainable artificial intelligence," *Journal of Medical Artificial Intelligence*, 2024.

[10] G. Yang, S. Luo, and J. Li. "Advancing skin cancer classification across multiple scales with attention-weighted transformers," in *Fourth Symposium on Pattern Recognition and Applications (SPRA 2023)* (Vol. 13162, pp. 30-35). SPIE, 2024.

[11] S. Remya, T. Anjali, and V. Sugumaran. “A Novel Transfer Learning Framework for Multimodal Skin Lesion Analysis,” *IEEE Access*, 2024.

[12] M. Abou Ali, F. Dornaika, I. Arganda-Carreras, H. Ali, and M. Karaouni. “Naturalize Revolution: Unprecedented AI-Driven Precision in Skin Cancer Classification Using Deep Learning,” *BioMedInformatics*, 4(1), 638-660, 2024.

[13] M. Ashfaq, and A. Ahmad. “Skin Cancer Classification with Convolutional Deep Neural Networks and Vision Transformers Using Transfer Learning. In Advances in Deep Generative Models for Medical Artificial Intelligence (pp. 151-176),” *Cham: Springer Nature* Switzerland, 2023.

[14] N. Islam, J. T. Raya., M. T. Maisha, and D. M. Farid. “Feature Fusion with Attention Mechanism for Skin Cancer Classification,” in *2023 6th International Conference on Electrical Information and Communication Technology (EICT)*, 2023, pp. 1-6, IEEE.

[15] R. P. Desale, and P. S. Patil. “An efficient multi-class classification of skin cancer using optimized vision transformer,” *Medical & Biological Engineering & Computing*, 62(3), 773-789, 2024.

[16] R. Kusumastuti, and A. Sunyoto. “Skin Cancer Classification Using EfficientNetV2 and ViT B16,” in *2023 6th International Conference on Information and Communications Technology (ICOIACT)*, 2023, pp. 395-400, IEEE.

[17] C. Kaggle. (2024, Oct 20). *Dataset* [Online]. Available: https://www.kaggle.com/datasets/shashanks1202/skin-cancer-dataset

[18] C. Paperswithcode. (2024, Oct 20). *Method* [Online]. Available: https://paperswithcode.com/method/vision-transformer

[19] C. Mathworks. (2024, Oct 20). *Matlab* [Online]. Available: https://www.mathworks.com/help/deeplearning/ug/train-vision-transformer-network-for-image-classification.html

Düzce University
Journal of Science & Technology

Research Article

Thermodynamic, Economic and Environmental Assessment of Vapor Compression Refrigeration System Using Mono and Binary Nanolubricants (TiO_2-B)

Gökhan YILDIZ [a,*]

[a] *Department of Electronics and Automation, Düzce Vocational School, Düzce University, Düzce, TURKEY.*
** Corresponding author's e-mail address: gokhanyildiz@duzce.edu.tr*
DOI: 10.29130/dubited.1601461

ABSTRACT

Nowadays, the need for energy is gaining significant importance. However, energy consumption in developed countries is quite high. Almost 40% of this energy consumption comes from heating, refrigeration, and air conditioning systems in buildings. Hence, even a minor enhancement in refrigeration systems will lead to energy savings on a global scale. Many studies are being conducted for this circumstance. One of these is the addition of nanoparticles to refrigerants and lubricants. In this study, the effects of mono and binary nanolubricants obtained from different nanoparticles (TiO_2 and Boron) used at different concentrations (3.5 g/L and 7 g/L) in the vapor compression refrigeration system were evaluated in terms of energy, exergy, environment, and economy. As a result, a 16.47% increase in COP value was obtained in 7 g/L TiO_2-B binary nanolubricant compared to pure POE. The energy consumption of the compressor in the system reduced by 13.06% in the 7 g/L TiO_2-B binary nanolubricant compared to POE. A 35.20% decrease in total exergy destruction was detected in 7 g/L TiO_2-B binary nanolubricant compared to POE. 43.44% increase in exergy efficiency occurred in 7 g/L TiO_2-B binary nanolubricant compared to POE in the system. When the system was examined from an economic perspective, a 35.84% improvement was observed in the 7 g/L TiO_2 binary nanolubricant compared to POE. When the system was examined environmentally, an 11.90% reduction was achieved in 7 g/L TiO_2-B binary nanolubricant compared to POE. As a result, it is seen that significant improvements occur in the system as the concentration increases when mono and binary nanolubricants are used compared to POE.

Keywords: *Energy, Environment, Exergy, Binary nanofluid, Vapor compression refrigeration system.*

Mono ve İkili Nanoyalayıcı (TiO_2-B) Kullanılan Buhar Sıkıştırmalı Soğutma Sisteminin Termodinamik, Ekonomik ve Çevresel Değerlendirmesi

ÖZ

Enerji her geçen gün önemli bir hal almaktadır. Ancak, gelişmiş ülkelerdeki enerji tüketimi oldukça fazladır. Bu enerji tüketiminin neredeyse %40 binalardaki ısıtma, soğutma ve iklimlendirme sistemlerinden kaynaklıdır. Bu nedenle, bu sistemlerde yapılacak olan küçük bir iyileştirme bile küresel boyutta enerji tasarrufuna yol açacaktır. Bu durum için birçok çalışma yapılmaktadır. Bunlardan bir tanesi de soğutucu akışkanlara ve yağlayıcılara nanoparçacık ilave edilmesidir. Bu çalışmada, buhar sıkıştırmalı soğutma sisteminde farklı konsantrasyonlarda (3,5 g/L ve 7 g/L) kullanılan farklı nanoparçacıklardan (TiO2 ve Boron) elde edilen mono ve ikili nanoyağlayıcıların sistem üzerindeki etkileri enerji, ekserji, çevresel ve ekonomik açıdan değerlendirilmiştir. Sonuç olarak, COP değerinde saf POE'ye göre 7 g/L TiO2-B ikili nanoyağlayıcıda %16,47'lik artış elde edilmiştir. Sistemdeki kompresörün enerji tüketiminde saf POE'ye göre 7 g/L TiO2-B ikili nanoyağlayıcıda

Received: 14/12/2024, Revised: 13/01/2025, Accepted: 15/01/2025

%13,06'lık azalma meydana gelmiştir. Toplam ekserji yıkımında saf POE'ye göre 7 g/L TiO2-B ikili nanoyağlayıcıda %35,20'lik azalma tespit edilmiştir. Sisteminde ekserji veriminde saf POE'ye göre 7 g/L TiO2-B ikili nanoyağlayıcıda %43,44'lük artış meydana gelmiştir. Sistem ekonomik açıdan incelendiğinde saf POE'ye göre 7 g/L TiO2 ikili nanoyağlayıcıda %35,84'lük iyileşme gözlenmiştir. Sistem çevresel olarak incelendiğinde saf POE'ye göre 7 g/L TiO2-B ikili nanoyağlayıcıda %11,90'lık azalma gerçekleşmiştir. Sonuç olarak, saf POE'ye göre mono ve ikili nanoyağlayıcılar kullanıldığında konsantrasyon arttıkça sistem üzerinde önemli iyileşmeler meydana geldiği görülmektedir.

Anahtar Kelimeler: *Enerji, Çevre, Ekserji, İkili nanoakışkan, Buhar sıkıştırmalı soğutma sistemi*

I. INTRODUCTION

Today, in industrialized countries, a portion of electricity consumption is used in cooling applications. The market volume of the heating, ventilation, and air conditioning (HVAC) sector is expected to reach 241.8 billion dollars in 2025 [1]. HVAC systems account for a large portion of energy consumption in buildings. For example, it is known that more than 50% of total building energy consumption in the United States comes from HVAC applications [2]. In Australia, it has been determined that HVAC applications are responsible for 20-50% of the total energy used in buildings. In household refrigeration systems, it is generally used for the preservation of food products and air conditioning of spaces. It is estimated that approximately 1.5 billion household refrigerators are used in the world. Commercial refrigeration devices are used in various industrial applications, especially in the storage of foods. According to the World Refrigeration Organization, it is estimated that there are 90 million commercial refrigeration devices in operation worldwide [3]. In China, 1% of the population had air conditioning in 1990, while 100% of the population had air conditioning in 2009 [4]. Approximately 17% of electricity in the world is used in refrigeration applications and 45% of this is used in buildings [5]. The International Energy Agency's 2050 technology roadmap recommends using more efficient systems that will simultaneously produce heating, cooling, and hot water for buildings.

The usage of nanofluids has become widespread with the development of nanotechnology to increase efficiency in cooling and heating systems in recent years. To increase performance in cooling systems, nanoparticles are added to refrigerants and lubricants and used as nanorefrigerants and nanolubricants. Nanolubricants are obtained by adding nanoparticles to the lubricant. The resulting nanolubricant is then placed into the compressor. Nano refrigerants are obtained by directly mixing conventional refrigerants and nanoparticles. The most important reason for adding nanoparticles to liquids is that solid-phase materials have higher thermal properties than lubricants and refrigerants. This will increase the thermal properties of the liquids used in the cooling system [6, 7]. As a result, it improves the thermal performance of most systems requiring high heat transfer [8, 9].

Zawawi et al. studied the performance of Al_2O_3-SiO_2/PAG binary nanolubricants at a 60:40 composition ratio at different concentrations (0.005-0.06% by volume) on automotive air conditioning system. The experiments were carried out with a charge of 95-155 g R134a and different compressor speeds between 900-2100 rpm [10]. Chauhan performed performance analysis in an ice machine using R134a as refrigerant, PAG46 as lubricant, and binary nanoparticles (Al_2O_3-SiO_2) with concentrations ranging from 0.02% to 0.1%. The lowest compressor power and highest COP were observed at 0.08% concentration. Compressor power consumption was 6.8% and 3.5% higher for binary nanolubricants than for mono nanolubricants, Al_2O_3, and SiO_2, respectively. It was determined that the COP value of binary nanolubricants at 0.08% volume concentration was 10.89% and 5.3% higher than Al_2O_3 and SiO_2 mono nanolubricants, respectively [11]. Wanatasanappan et al. studied the thermophysical performances of Al_2O_3-CuO binary nanolubricants at different mixing ratios (20:80, 40:60, 50:50, and 60:40) at 1% concentration. Thermal conductivity and viscosity measurements were carried out between 30 and 70 °C. The highest thermal conductivity for Al_2O_3-CuO nanofluid was obtained in the 60:40 mixture with a 12.33% increase compared to the reference fluid. Additionally, the viscosity of

the hybrid nanofluid showed a decreasing trend with increasing temperature [12]. Zawawi et al. studied the thermophysical properties of Al_2O_3-SiO_2/PAG binary nanolubricants at concentrations of 0.02 to 0.1 vol. C between temperatures of 303 and 353 K. These nanolubricants used in the experiments behaved as Newtonian fluids in these temperature ranges. The highest thermal conductivity increase was obtained as 2.41% at 0.1% concentration and 303 K temperature. The viscosity value was observed to improve by 9.71% at 0.1% concentration and 333 K temperature [13]. Asokan et al. studied the thermophysical properties such as thermal conductivity, viscosity, density, and specific heat capacity of low-concentration hybrid nanofluids. These thermophysical properties were compared in low-concentration mono and hybrid nanofluids. Mono and hybrid nanofluids were prepared at concentrations of 0.02%, 0.04%, and 0.06%. The results obtained showed that the thermal conductivities of hybrid nanofluids were higher than those of mono nanofluids. The thermal conductivity of Al_2O_3-CuO nanofluid increased by 2.3% compared to CuO and 3.6% compared to Al_2O_3 [14]. Senthilkumar et al. performed performance evaluation in a vapor compression refrigeration system (VCRS) using 40 and 60 g of R600a refrigerant with Al_2O_3-SiO_2 nanolubricant at concentrations of 0.4 g/L and 0.6 g/L. As a result of the experiments, a 30% increase in performance, a 25% increase in cooling capacity, and an 80 W decrease in power consumption were achieved [15]. Senthilkumar et al. performed performance analysis in a VCRS using binary nanolubricant consisting of CuO and SiO_2 nanoparticles at concentrations of 0.2 g/L and 0.4 g/L and 40 and 60 g of R600a refrigerant. CuO-SiO_2 binary nanolubricants resulted in a 35% reduction in COP, 18% in cooling capacity, and 75 W in compressor energy consumption [16]. Kumar and Rajput investigated the performance of a VCRS using different concentrations (0.1, 0.2, 0.3, and 0.4 g/L) of TiO_2-SiO_2/MO nanolubricant and different amounts (80, 100 and 120 g) of R600a. Under optimum conditions, a 37.83% improvement in the COP value of the refrigeration system with 80 g R600a was detected. A 13.46% reduction in compressor energy consumption was observed in the system using 80 g R600a. The highest value of exergy efficiency and the lowest value of exergy loss were obtained with 77% and 96.90 W values, respectively, at a concentration of 0.2 g/L in the system using 100 g R600a [17]. Akhtar and Rajput performed performance evaluation in a VCRS using multi-walled carbon nanotube (MWCNT)-Graphene sheets (GN) nanolubricant and 200 g R134a at different concentrations (0.3, 0.5, 0.7 and 0.9 g/L). Hybrid nanolubricant was prepared in the ratio of 50:50. Experimental results showed that compressor power consumption and pressure ratio decreased by 16.09% and 5.68%, respectively. An increase of 11.29% was determined in the COP value of 0.7 g/L hybrid nanolubricant compared to pure POE [18]. Govindasamy et al. investigated the performance of refrigeration systems with normal and microchannel condensers with and without nanoparticles. Experiments were carried out using CeO_2-ZnO hybrid nanolubricants prepared at different ratios (0.5:1.5, 1:1, and 1.5:0.5) and R134a refrigerant. As a result of the experiments, a 33.3% increase in the COP value of the refrigeration system containing a 1:1 binary nanolubricant microchannel condenser was achieved [19].

Approximately 35-40% of the world's energy consumption comes from heating, cooling, and air conditioning systems in buildings. Nowadays, since energy has become very important, it has become necessary to increase energy efficiency in these systems. The best solution to solve this circumstance is to make improvements that will reduce the energy consumption of the system. Studies show that the compressor plays the biggest role in energy consumption in refrigeration and heating systems. Therefore, improvements that can decrease the compressor's energy consumption will specify meaningful energy savings, considering that this circumstance is implemented worldwide. This study focuses on the effects of using TiO_2 and Boron (B) mono and binary nanolubricants at different concentrations (3.5 g/L and 7 g/L) in a VCRS on system performance. In this study, TiO_2 was chosen as the nanoparticle because it was mentioned in the literature that it gave good performance, and the B nanoparticle was chosen because it showed good performance in thermal systems but was determined to be used less in refrigeration systems. The results of energy, exergy, enviroeconomic, and thermoeconomic analyses of TiO_2-B mono and binary nanolubricants at different concentrations in the VCRS were compared with the base fluid.

II. MATERIAL and METHODS

This section includes theoretical explanations and equations of the first and second laws of thermodynamics, environmental analysis, and economic analysis used to evaluate the performance of the VCRS. Additionally, the preparation and thermophysical properties of mono and binary nanolubricants to be utilized in the VCRS are given. In addition, the schematic representation of the VCRS used in the experiments, its technical specifications, and the preparation of the experiments are generally mentioned.

A. NANOFLUID PREPARATION

POE, TiO_2, and B nanoparticles were utilized to obtain mono and binary nanolubricants in this study. The nanoparticles utilized in the experiments were supplied by Nanografi Co, Türkiye. Some technical properties of these nanoparticles are shown in Table 1.

Table 1. *Some technical properties of nanoparticles (taken by supplier).*

Nanoparticle	Purity, %	Density, g/cm^3	Average Particle Size, nm	Morphology	Thermal Conductivity, W/m.K
TiO_2	+99.5	4.5	45	Nearly Spherical	8
B	+99.5	3.58	100	Nearly Spherical	27

As given in Table 1, the shapes of the nanoparticles used in the experiments are close to spherical and their sizes vary between 45 and 100 nm. SEM images are given in Figure 1 to see the chemical structures of the nanoparticles. SEM images were taken at 1 μm size from the FEI brand Quanta FEG 250 model device located at Düzce University laboratories.

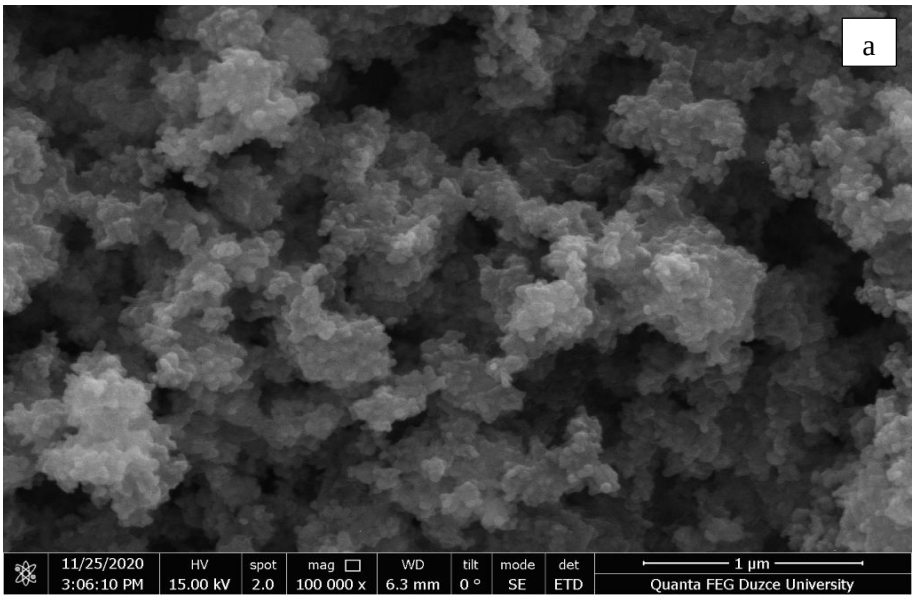

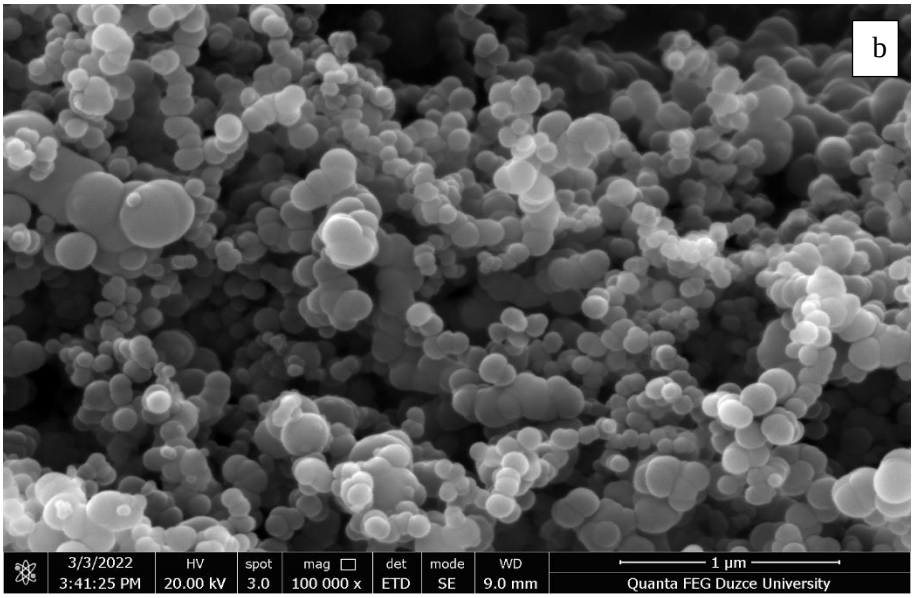

Figure 1. *SEM photos of nanoparticles a) TiO_2, and b) B.*

A precision balance was utilized to measure the masses of POE and nanoparticles. POE, mono, and binary nanoparticles were blended with a mechanical stirrer at 25 ℃ for 2 h. They were subjected to ultrasonic bath treatment at 50 Hz frequency and 250 W power for 2.5 hours under laboratory conditions to ensure homogeneous distribution of nanoparticles in the POE base fluid. All steps in the preparation of mono and binary nanolubricants are shown in Figure 2.

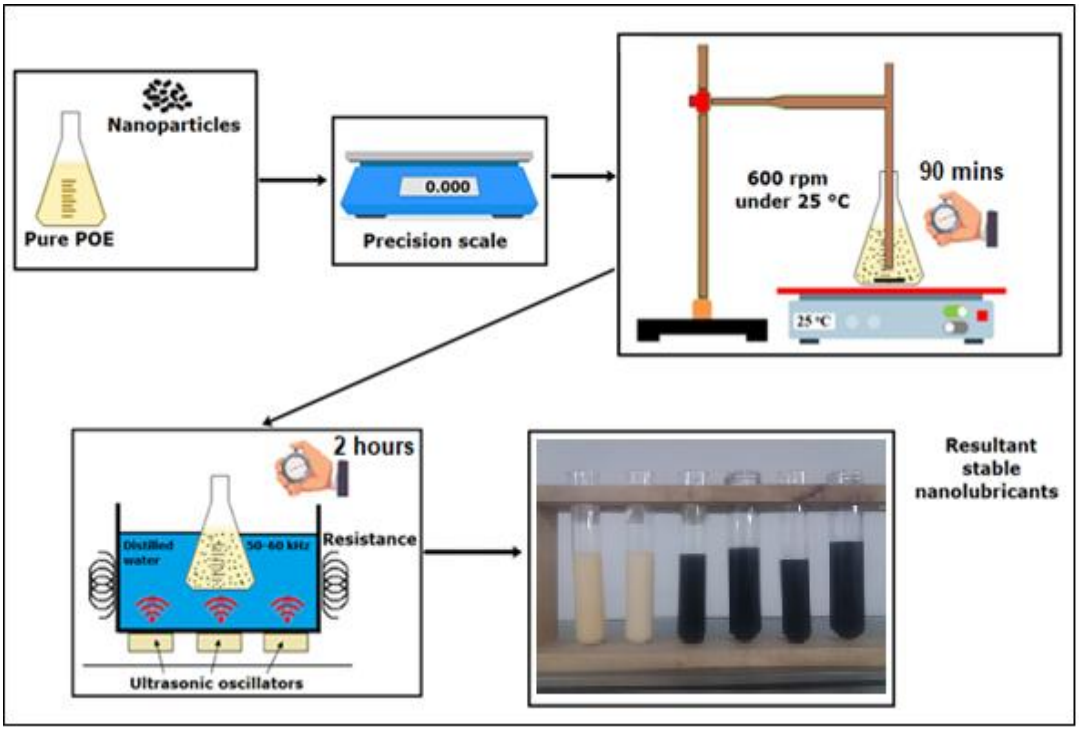

Figure 2. *Steps of preparation of mono and binary nanolubricants.*

B. EXPERIMENTAL SETUP

VCRSs are the most commonly utilized refrigeration systems in practical applications. The mechanical VCRS consists of four main components: compressor, condenser, expansion valve, and

evaporator. In VCRSs, refrigerants are utilized to complete the cycle. In this study, R134a, used in refrigeration applications, was utilized as the refrigerant. The schematic representation of the test rig is given in Figure 3.

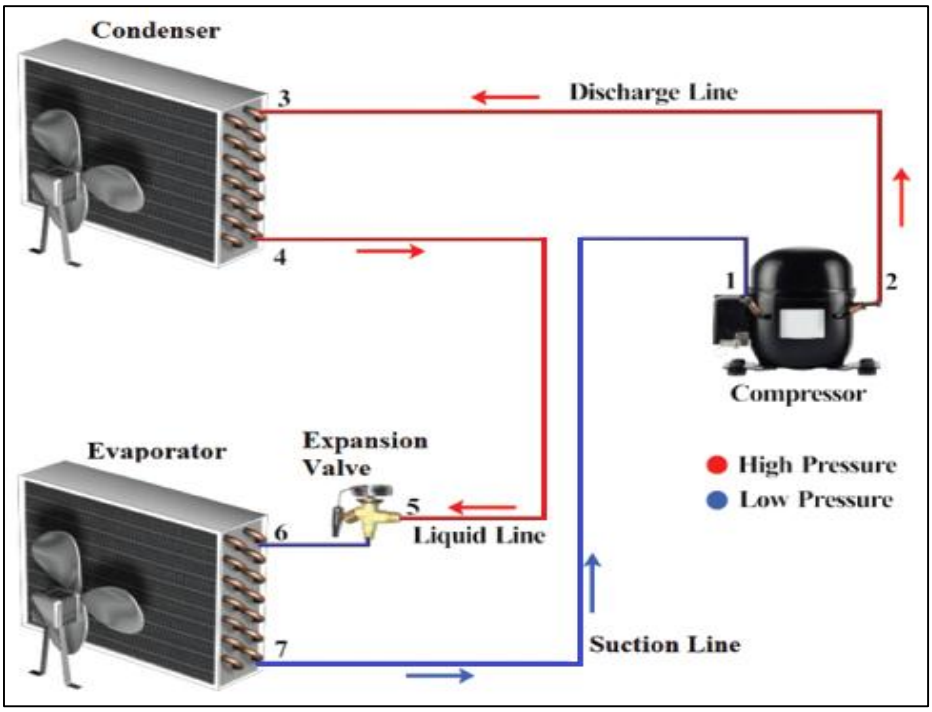

Figure 3. *Schematic view of VCRS*

Before starting the experiments on the VCRS, leak tests were performed. N_2 was charged to the VCRS at 18 bar pressure to determine if there was a leak. To make the leak test more effective, the system was left at this pressure for 1 day. It was determined that there was no change in the pressure values in the system after 1 day. After determining that there were no leaks, 170 g of R134a and 200 mL of POE were added to the VCRS. After the specified amount of POE and refrigerant were charged into the system, the system was operated until it reached equilibrium conditions. When the system reached equilibrium conditions, data were taken at 10-minute intervals for 1 hour. The same methods were applied for other mono and binary nanolubricants (3.5 g/L TiO_2, 7 g/L TiO_2, 3.5 g/L B, 7 g/L B, 3.5 g/L TiO_2-B and 7 g/L TiO_2-B). The tests were carried out at an average of 60% relative humidity and 22 °C ambient temperature conditions. While changing the nanolubricant, the refrigerant was discharged and recharged. Even if the refrigerant is thoroughly drained from the system, there is a possibility that refrigerant may remain in some areas within the system. Therefore, the system was purged with N_2 for approximately 2-3 minutes before refrigerant charging. Refrigerant charging was carried out after this procedure. The experiments were repeated three times for reliability. The technical properties of the VCRS utilized in the experiments are shown in Table 2.

Table 2. *Technical specifications of VCRS*

Components	Specifications
Compressor	Displacement: 4.05-9.09 cm^3 Cooling capacity: 325-970 W
Evaporator	Capacity: 1 kW
Condenser	Capacity: 1.4 kW

Table 2 (cont). *Technical specifications of VCRS*

Thermostatic expansion valve	Temperature range: -40/10 °C Static superheat: 4 °C
Filter drier	Temperature range: -40/70 °C Net volume: 0.464 L

C. THERMODYNAMIC ANALYSIS

In this study, thermodynamic analyses were applied to investigate the performance of mono and binary nanolubricants utilized in the VCRS. Various energy and exergy methods were considered while applying thermodynamic analyses. Thermal equilibrium equations were applied for each system component.

The amount of heat transferred per unit of time from the evaporator ($\dot{Q}_{evap}$) in the VCRS is calculated in Equation 1.

$$\dot{Q}_{evap} = \dot{m}_r(h_7 - h_6) \tag{1}$$

The amount of heat released from the condenser ($\dot{Q}_{cond}$) in the refrigeration system per unit time is calculated in Equation 2.

$$\dot{Q}_{cond} = \dot{m}_r(h_4 - h_3) \tag{2}$$

Depending on the mechanical and electrical efficiency, the compressor capacity and compressor electrical power are given in Equation 3 and Equation 4.

$$\dot{W}_{comp} = \dot{m}_r(h_2 - h_1) \tag{3}$$

$$\dot{W}_{comp,el} = \frac{\dot{W}_{comp}}{\eta_{mech} \times \eta_{el}} \tag{4}$$

COP represents the electrical power consumed by the compressor. It corresponds to the heat transferred from the evaporator per unit of time. COP is calculated as in Equation 5.

$$COP = \frac{\dot{Q}_{evap}}{\dot{W}_{comp,el}} \tag{5}$$

It is important to determine the energy availability in VCRSs. Therefore, exergy analysis is necessary. The exergy for the steady flow control volume is given in Equation 7. $E_{x,dest}$ in the equation represents exergy destruction. The first two terms in the equation express the flow exergy, the next term expresses the heat transfer exergy, and the last two terms express the work exergy. In the equations, subscripts represent the input and output conditions.

$$E_{x,dest} = \sum \dot{E}_{x,in} - \sum \dot{E}_{x,out} + \sum \left[\dot{Q}\left(1 - \frac{T_0}{T}\right)\right]_{in} - \sum \left[\dot{Q}\left(1 - \frac{T_0}{T}\right)\right]_{out} + \sum \dot{W}_{in} - \sum \dot{W}_{out} \tag{7}$$

The flow exergy for each cycle in the VCRS is given in Equation 8.

$$\dot{E}_x = \dot{m}_r[h - h_0 - T_0(s - s_0)] \tag{8}$$

The general expression of exergy destruction for the compressor is given in Equation 9 and Equation 10.

$$\dot{E}_{x,dest,comp} = \dot{E}_{x,1} - \dot{E}_{x,2} + \dot{W}_{comp,el} \quad (9)$$

$$\dot{E}_{x,dest,comp} = \dot{m}_r[(h_1 - T_0 s_1) - (h_2 - T_0 s_2)] + \dot{W}_{comp,el} \quad (10)$$

The general expression of exergy destruction for the condenser is given in Equation 11 and Equation 12.

$$\dot{E}_{x,dest,cond} = \dot{E}_{x,3} - \dot{E}_{x,4} - \left[\dot{Q}_{cond}\left(1 - \frac{T_0}{T_{cond}}\right)\right] \quad (11)$$

$$\dot{E}_{x,dest,cond} = \dot{m}_r[(h_3 - T_0 s_3) - (h_4 - T_0 s_4)] - \left[\dot{Q}_{cond}\left(1 - \frac{T_0}{T_{cond}}\right)\right] \quad (12)$$

The exergy destruction for the evaporator is given in Equation 13 and Equation 14.

$$\dot{E}_{x,dest,evap} = \dot{E}_{x,6} - \dot{E}_{x,7} + \left[\dot{Q}_{ev}\left(1 - \frac{T_0}{T_{evap}}\right)\right] \quad (13)$$

$$\dot{E}_{x,dest,evap} = \dot{m}_r[(h_6 - T_0 s_6) - (h_7 - T_0 s_7)] + \left[\dot{Q}_{evap}\left(1 - \frac{T_0}{T_{evap}}\right)\right] \quad (14)$$

The exergy destruction of the expansion valve is given in Equation 15 and Equation 16.

$$\dot{E}_{x,dest,exv} = \dot{E}_{x,5} - \dot{E}_{x,6} \quad (15)$$

$$\dot{E}_{x,dest,exv} = \dot{m}_r T_0 (s_6 - s_5) \quad (16)$$

The total exergy destruction caused by all system components is calculated in Equation 17.

$$\dot{E}_{x,dest,overall} = \dot{E}_{x,dest,comp} + \dot{E}_{x,dest,cond} + \dot{E}_{x,dest,evap} + \dot{E}_{x,dest,exv} \quad (17)$$

D. ENVIROECONOMIC ANALYSIS

Fossil fuels, which are predominantly used in energy production, increase the amount of CO_2 released into the atmosphere. Increasing amount of CO_2 in the atmosphere causes problems such as global warming and environmental pollution. Different measures are being taken to solve these problems and reduce CO_2 emissions around the world. The environmental cost analysis carried out in line with this goal is based on the CO_2 emission price. In this study, the amount of CO_2 reduction provided by the VCRS using mono and binary nanolubricants at different concentrations is given in Equation 19.

$$W_{comp,el} = \dot{W}_{comp,el}.t \quad (18)$$

$$\phi_{CO_2} = \psi_{CO_2} \times W_{comp,el} \quad (19)$$

In Equation 19, ϕ_{CO_2} is the amount of CO_2 emissions reduced by the system, and ψ_{CO_2} is the amount of CO_2 produced by the operation of coal-fired power plants. The value of ψ_{CO_2} is taken as 2.08 $kgCO_2/kWh$ [20, 21]. The environmental cost value of the system is calculated in Equation 20.

$$Z_{CO_2} = z_{CO_2}.\varphi_{CO_2} \quad (20)$$

In Equation 20, z_{CO_2} represents the international carbon price and varies between 13 and 16 \$/tCO_2. The value of z_{CO_2} was taken as 14.5 \$/tCO_2 in the calculations [22].

E. ECONOMIC ANALYSIS

The economic viability of an energy system can be assessed by calculating some economic indicators such as the cost of useful products over the facility life and the payback period. In such an analysis, the costs of components and other expenses have to be estimated to find out the total revenue requirement. For simplifications, smoothed costs can be used instead of taking the cost change from year to year. Thermoeconomic analysis combines the principles of economic and thermodynamic analysis (usually exergy analysis). The analysis called exergoeconomic analysis is divided into two categories: cost accounting and optimization-based approaches.

The annual operating cost (ARC) of the system is given in Equation 21. $\dot{m}$ in the equation represents the mass flow rate of the refrigerant in the VCRS.

$$ARC = (\dot{m}\Delta P/\rho)t_{op}.CE \tag{21}$$

The present value of an annuity is the monetary value of the total annual payment at the end of a certain period if it had been invested at the beginning of the annuity with the effective interest rate. The initial investment cost recovery factor (CRF) is calculated in Equation 22 [23].

$$CRF = \frac{i(1+i)^n}{(1+i)^n-1} \tag{22}$$

In Equation 22, n is the service life of the VCRS and i is the assumed annual interest. The life of the experimental system is 20 years [24] and the assumed annual interest is 10% [25]. The first annual cost (FAC) is calculated as in Equation 23.

$$FAC = CRF \times TCI \tag{23}$$

TCI in the equation represents the initial investment cost.

$$SFF = \frac{i}{(1+i)^n-1} \tag{24}$$

In Equation 25, ASV represents the annual scrap value, SFF represents the depreciation fund factor, and SV represents the scrap value of the system.

$$ASV = SFF \times SV \tag{25}$$

$$SV = \mu \times TCI \tag{26}$$

Annual maintenance cost (AMC) was used in the calculations as 10% of the initial investment cost [26]. In the equation, AC represents the annual cost.

$$AC = FAC + AMC + ARC - ASV \tag{27}$$

$$R_{g,ex} = \frac{\dot{E}x_{out}}{AC} \tag{28}$$

F. UNCERTAINTY ANALYSIS

The method called uncertainty analysis is used for error analysis of experimental data. According to this method, let the quantity to be measured in the system be R and the n independent variables

affecting this quantity be $x_1, x_2, x_3, \dots, x_n$. In this case, $R = R(x_1, x_2, x_3, \dots, x_n)$ can be written. If the error rates for each independent variable are $w_1, w_2, w_3, \dots, w_n$ and the ratio of the R magnitude is W_R, the uncertainty analysis can be written as Equation 29. Total uncertainty is 1.21%.

$$W_R = \left[\left(\frac{dR}{dx_1}w_1\right)^2 + \left(\frac{dR}{dx_2}w_2\right)^2 + \cdots + \left(\frac{dR}{dx_n}w_n\right)^2\right]^{1/2} \quad (29)$$

Table 3. *Specifications of the measurement devices.*

No.	**Measurement Instrument**	**Range**	**Accuracy**
1	Thermocouple (K type)	(-30)-130 °C	0.5%
2	Radwag precision scales	0-220 g	0.001 g
3	Energy meter	0.1-3680 W	0.1 W
4	Pressure transmitter	0-30 bar	1 bar

III. RESULTS and DISCUSSION

In this section, the system performance of the VCRS using different concentrations of mono and binary nanolubricants was investigated and interpreted in terms of energy, exergy, environment and economy. Experimental data were taken at 10 minute intervals for 1 hour after the system reached equilibrium. Experiments were conducted at approximately 22 ℃ and 60% relative humidity.

Compressor energy consumption of mono and binary nanolubricants at different concentrations used in the VCRS is given in Figure 4. As seen in Figure 4, it was observed that the energy consumption of the compressor decreased significantly as the concentrations of mono and binary nanolubricants increased compared to pure POE. While the compressor energy consumption in pure POE was 392.97 W, the lowest energy consumption was obtained as 341.64 W in 7 g/L TiO_2-B/POE nanolubricant. This is because the nanoparticles used in the VCRS are approximately spherical in shape and exhibit a rolling effect, acting as a bearing of nanoparticles to reduce power loss [27]. Nanoparticles exhibit ball bearing behavior to reduce power loss caused by the reduction of friction between mating surfaces because of the rolling effect. Additionally, heat transfer between fluids increases due to the high thermal conductivity values of nanolubricants [28, 29]. In this case, it is a parameter that reduces the energy consumption.

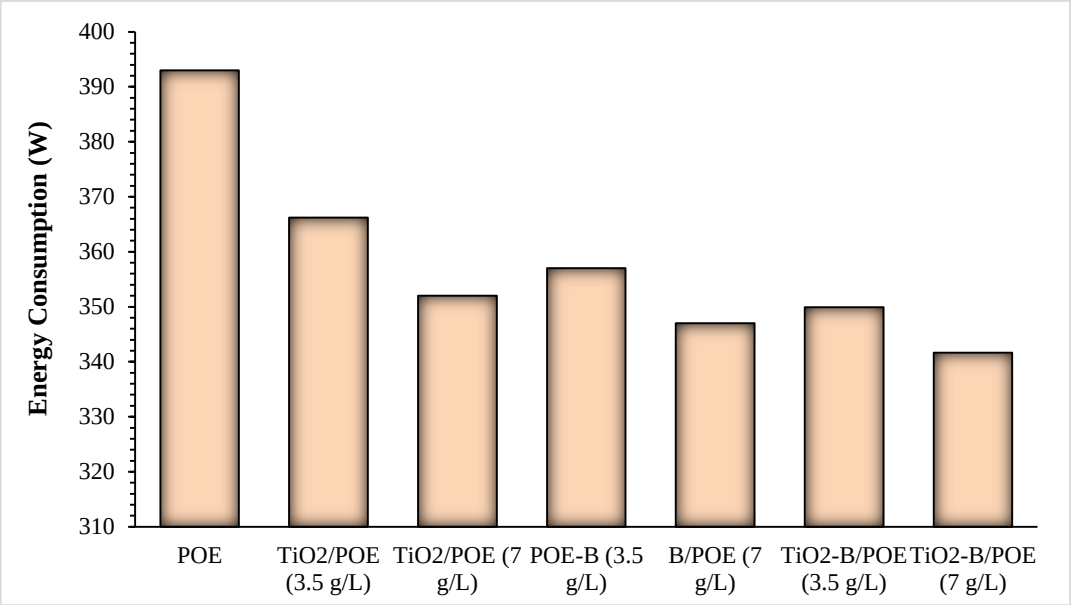

Figure 4. *Energy consumption of mono and binary nanolubricants at different concentrations*

COP changes of mono and binary nanolubricants at different concentrations used in the VCRS are given in Figure 5. There is a significant increase in the COP values of mono and binary nanolubricants compared to pure POE as the concentration increases. While the lowest COP value was 3.4 in pure POE, the highest COP value was determined in 7 g/L TiO_2-B/POE nanolubricant. One of the most important factors that cause the COP value to be higher in mono and binary nanolubricants compared to POE is low energy consumption. As seen in the COP formula, cooling capacity and energy consumption play a major role in the COP value. Therefore, due to the thermophysical properties of mono and binary nanolubricants, reducing friction in the compressor and having high thermal conductivity, the energy consumption is lower than the compressor energy consumption in the system using pure POE. In addition, the cooling capacities in mono and binary nanolubricants are higher than those in pure POE, which is another reason why the COP value is high. This result shows that increasing the fraction of binary nanolubricants used in the VCRS has higher efficiency compared to pure POE.

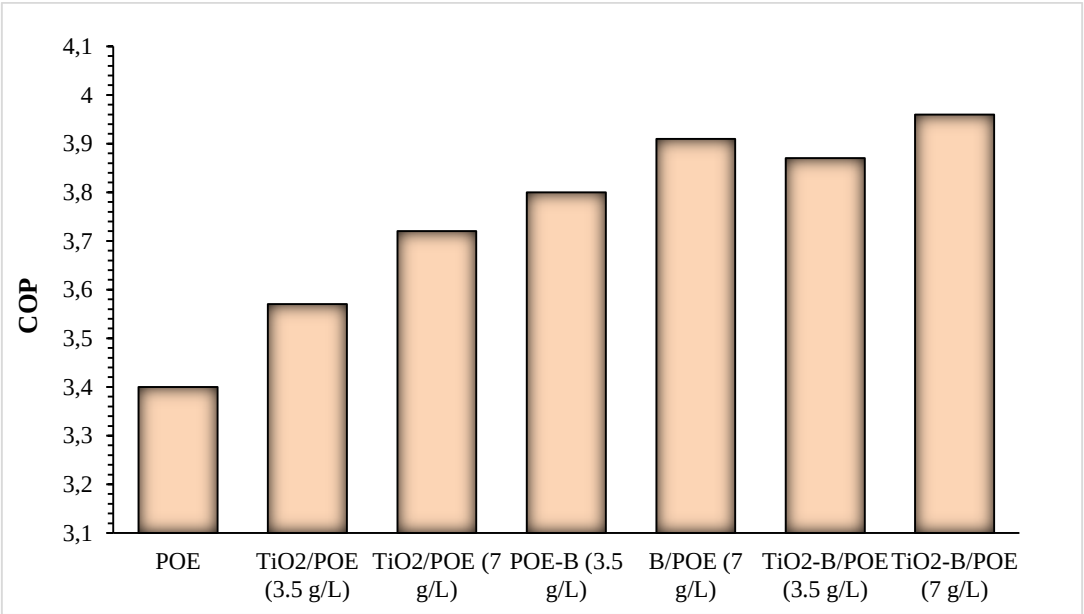

Figure 5. *COP values of mono and binary nanolubricants at different concentrations*

The total exergy destruction of pure POE, mono and binary nanolubricants at different concentrations in the VCRS is shown in Figure 6. The total exergy destruction of mono and binary nanolubricants decreases as the concentration enhances compared to pure POE. The lowest total exergy destruction was obtained as 618.696 W in pure POE, while the highest total exergy destruction was obtained as 400.924 W in 7 g/L TiO_2-B/POE. As seen in the figure, as the concentrations of mono and binary nanolubricants enhance, the type of nanolubricants in the VCRS becomes clear.

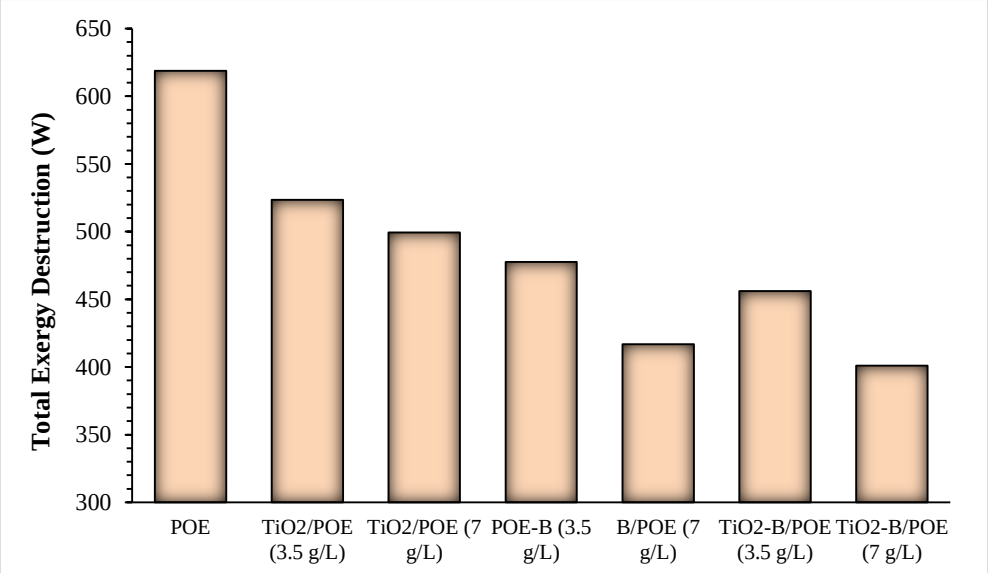

Figure 6. *Total exergy destruction of mono and binary nanolubricants at different concentrations*

The exergy efficiencies of POE, mono and binary nanolubricants at different concentrations in the VCRS are given in Figure 7. Exergy efficiency increases as the concentrations of mono and binary nanolubricants increase compared to pure POE. The lowest exergy efficiency was obtained with 34.53% in pure POE, and the highest exergy efficiency was determined with 49.53% in 7 g/L TiO_2-B/POE. As seen in Figure 5, the trend in COP changes is similar to the second law efficiency. This can be explained as the role of enhancing nanoparticle amount due to increased heat transfer with enhancing concentration. The thermal properties of nanolubricants that need to be taken into account can also be well understood at high concentrations.

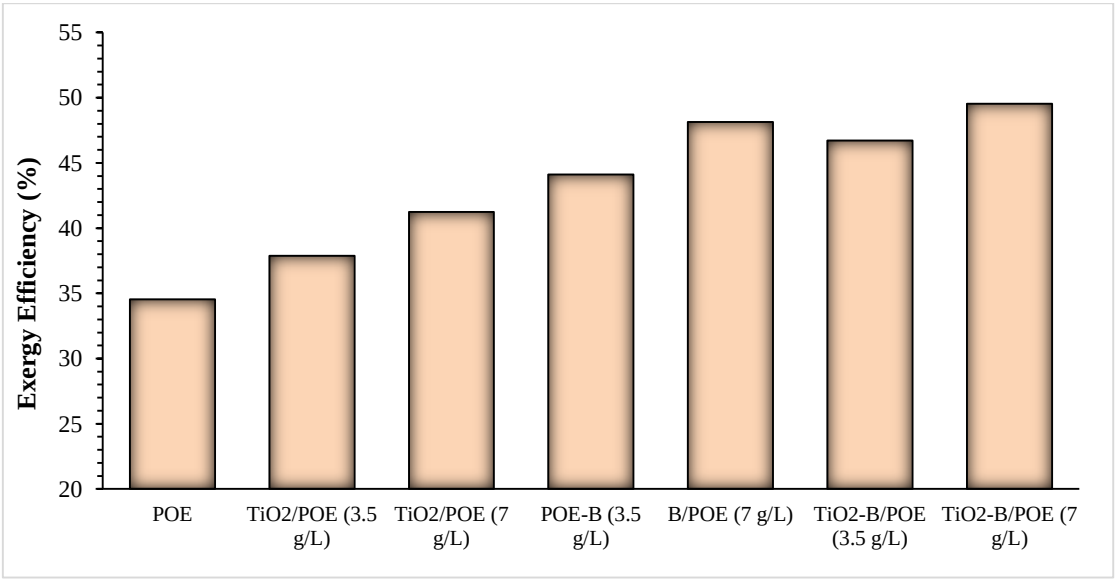

Figure 7. *Exergy efficiencies of mono and binary nanolubricants at different concentrations*

Today, the environmental potential of thermal energy systems is as important as the efficiency of the systems due to the effects of global warming. The emission pricing in the VCRS using POE, mono and binary nanolubricants to provide environmental vision is shown in Figure 8. The highest amount obtained per CO_2 emitted was 0.21 ¢/h in pure POE, while the highest amount was 0.185 ¢/h. Since this amount is calculated based on the amount of energy consumed by the system, it is parallel to the energy consumption trend in Figure 4.

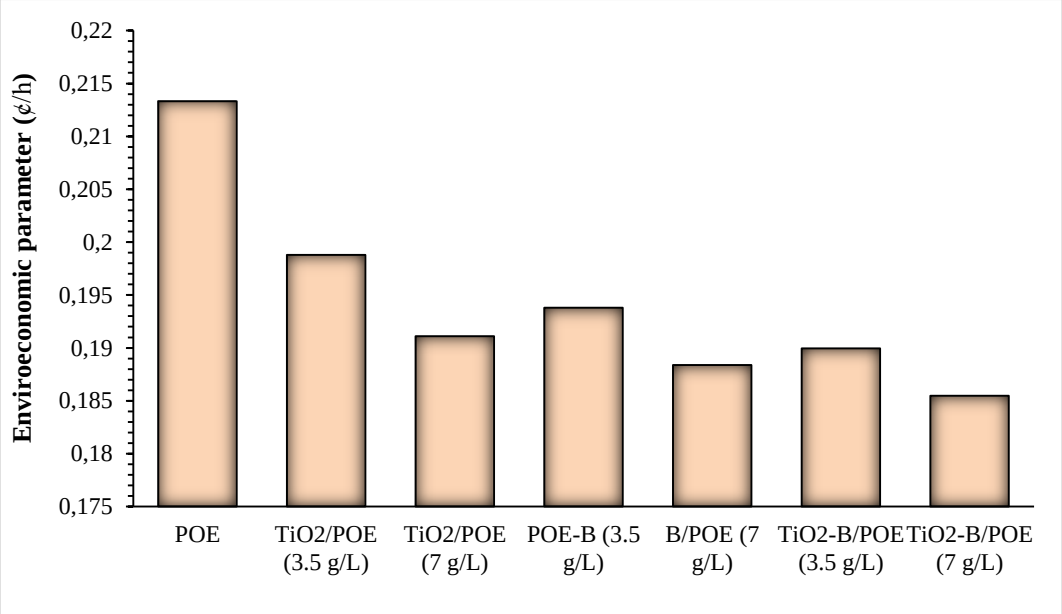

Figure 8. *Enviroeconomic values of mono and binary nanolubricants at different concentrations*

Evaluating a system in terms of economy is as important as improving the performance of the system. The economic comparison of pure POE, mono and binary nanolubricants used in VCRS is given in Figure 9. As seen in the figure, the worst economic performance was obtained with 1.409 kWh/$ in pure POE, while the best economic performance was obtained with 0.904 kWh/$ in 7 g/L TiO_2-B/POE nanolubricant. In the VCRS, energy consumption decreases as the concentrations of mono and binary nanolubricants increase compared to pure POE, and accordingly the economic cost decreases in direct proportion. According to Figure 9, the $R_{g,ex}$ values of mono and binary nanolubricants gave better results than POE. The reason for this can be explained as the increase in exergy efficiency and the decrease in exergy destruction when mono and binary nanolubricants are utilized in the VCRS.

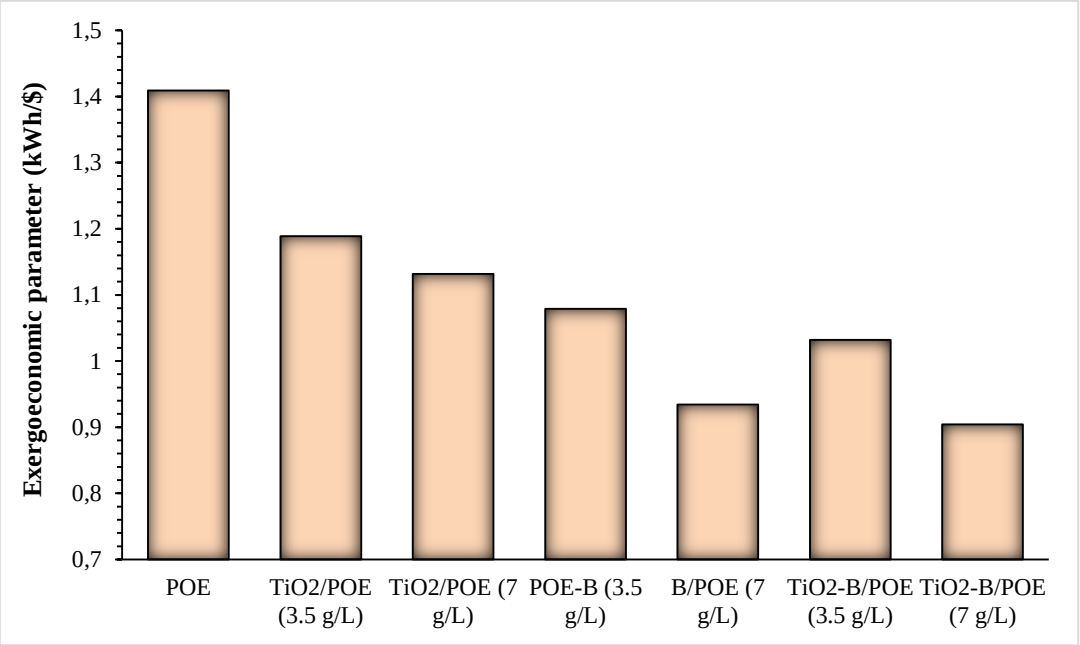

Figure 9. *Exergoeconomic values of mono and binary nanolubricants at different concentrations*

IV. CONCLUSION

In this study, different nanoparticles (TiO_2 and B) were added to the pure POE used in the VCRS at different concentrations (3.5 g/L and 7 g/L) to acquire mono and binary nanolubricants. The effects of the obtained mono and binary nanolubricants on the system performance were evaluated in terms of energy, exergy, environment and economy by comparing them with pure POE. Important details obtained as a result of the experiments are given below:

- Meaningful improvement was determined in mono and binary nanolubricants utilized in VCRS compared to POE. The highest COP increase was obtained as 16.47% in 7 g/L TiO_2-B nanolubricant compared to POE. It was determined that the COP value of the VCRS increased with the increase in the concentration of nanolubricants compared to POE.

- Mono and binary nanolubricants used in VCRSs have significantly reduced the energy consumption. Energy consumption increased by 13.06% in 7 g/L TiO_2-B binary nanolubricant compared to pure POE. This decreases the load on the compressor as nanolubricants decrease wear in the compressor and increase performance. Compressor efficiency is increased by using mono and binary nanolubricants.

- The total exergy destruction of the vapor-compression refrigeration system varies with the usage of mono and binary nanolubricants at different concentrations. As the concentration ratio enhances, the total exergy destruction of all mono and binary nanolubricants decreases while their exergy efficiency increases. Total exergy destruction decreased by 35.20% in 7 g/L TiO_2-B nanolubricant compared to POE.

- Exergy analysis in thermal energy systems is an important parameter to evaluate the usability of the system. In this way, improvements that can be made to the system can be seen. A meaningful increase in exergy efficiency was observed with the usage of mono and binary nanolubricants in the VCRS. Exergy efficiency was found to increase by 43.44% in 7 g/L TiO_2-B nanolubricant compared to pure POE.

- Exergoeconomic parameters of mono and binary nanolubricants utilized in VCRS were determined. Exergoeconomic parameter was improved by 35.84% in 7 g/L TiO_2-B binary nanolubricant compared to pure POE. Although B nanoparticle has a price 3-4 times more expensive than TiO_2 nanoparticle, it has lower economic performance because it increases system performance and causes a significant decrease in energy consumption.

- When mono and binary nanolubricants used in VCRSs were evaluated, they showed better performance than environmentally pure POE. This is because mono and binary nanolubricants reduce the energy consumption of the system, thus releasing less CO_2 into the environment. In environmental performance, 11.90% improvement was achieved in 7 g/L TiO_2-B binary nanolubricant compared to pure POE.

Nanofluids offer substantial advantages for enhancing VCRS performance. Nevertheless, there are benefits and drawbacks to nanofluids. One of the most significant drawbacks is that, after a while, nanofluids made using the one- or two-step approach sink to the bottom of the base fluid. As a result, the system cannot display the nanofluid's thermophysical characteristics. This is the main obstacle keeping the use of nanofluids in the refrigeration industry from becoming commercially viable. Furthermore, whereas binary and ternary nanofluids are used sparingly, mono nanofluids have been used extensively in previous research. Increasing the number of studies on this topic will improve the literature. Furthermore, there has been very few research on how the same sort of nanoparticles' size behave in systems. Increasing the number of these studies is critical for future research.

V. REFERENCES

[1] D. C. Savitha, P. K. Ranjith, B. Talawar, and N. Rana Pratap Reddy, "Refrigerants for sustainable environment–a literature review," *International Journal of Sustainable Energy*, vol. 41, no. 3, pp. 235-256, 2022.

[2] X. Cao, X. Dai, and J. Liu, "Building energy-consumption status worldwide and the state-of-the-art technologies for zero-energy buildings during the past decade," *Energy and Buildings*, vol. 128, pp. 198-213, 2016.

[3] B. Citarella, L. Viscito, K. Mochizuki, and A. W. Mauro, "Multi-criteria (thermo-economic) optimization and environmental analysis of a food refrigeration system working with low environmental impact refrigerants," *Energy Conversion and Management*, vol. 253, pp. 115152, 2022.

[4] A. Zendehboudi, A. Mota-Babiloni, P. Makhnatch, R. Saidur, and S. M. Sait, "Modeling and multi-objective optimization of an R450A vapor compression refrigeration system," *International Journal of Refrigeration*, vol. 100, ss. 141-155, 2019.

[5] Á. R. Gardenghi, J. F. Lacerda, C. B. Tibiriçá, and L. Cabezas-Gomez, "Numerical and experimental study of the transient behavior of a domestic vapor compression refrigeration system–Influence of refrigerant charge and ambient temperature," *Applied Thermal Engineering*, vol. 190, pp. 116728, 2021.

[6] M. W. Bhat, G. Vyas, A. J: Jaffri, and R. S. Dondapati, "Investigation on the thermophysical properties of Al_2O_3, Cu and SiC based Nano-refrigerants," *Materials Today: Proceedings*, vol. 5, no. 14, pp. 27820-27827, 2018.

[7] M. Ghazvini, H. Maddah, R. Peymanfar, M. H. Ahmadi, and R. Kumar, "Experimental evaluation and artificial neural network modeling of thermal conductivity of water based nanofluid containing magnetic copper nanoparticles," *Physica A: Statistical Mechanics and its Applications*, vol. 551, pp. 124127, 2020.

[8] A. Manoj Babu, S. Nallusamy, and K. Rajan, "Experimental analysis on vapour compression refrigeration system using nanolubricant with HFC-134a refrigerant," *Nano Hybrids*, vol. 9, pp. 33-43, 2016.

[9] K. Martin, A. Sözen, E. Çiftçi, and H. M. Ali, "An experimental investigation on aqueous Fe–CuO hybrid nanofluid usage in a plain heat pipe," *International Journal of Thermophysics*, vol. 41, pp. 1-21, 2020.

[10] M. N. M. Zawawi, W. H. Azmi, and M. F. Ghazali, "Performance of Al_2O_3-SiO_2/PAG composite nanolubricants in automotive air-conditioning system," *Applied Thermal Engineering*, vol. 204, pp. 117998, 2022.

[11] S. S. Chauhan, "Performance evaluation of ice plant operating on R134a blended with varied concentration of Al_2O_3-SiO_2/PAG composite nanolubricant by experimental approach," *International Journal of Refrigeration*, vol. 113, pp. 196-205, 2020.

[12] V. V. Wanatasanappan, M. Z. Abdullah, and P. Gunnasegaran, "Thermophysical properties of Al_2O_3-CuO hybrid nanofluid at different nanoparticle mixture ratio: An experimental approach," *Journal of Molecular Liquids*, vol. 313, pp. 113458, 2020.

[13] N. N. M. Zawawi, W. H. Azmi, A. A. M. Redhwan, M. Z. Sharif, and K. V. Sharma, "Thermo-physical properties of Al_2O_3-SiO_2/PAG composite nanolubricant for refrigeration system," *International Journal of Refrigeration*, vol. 80, pp. 1-10, 2017.

[14] N. Asokan, P. Gunnasegaran, and V. V. Wanatasanappan, "Experimental investigation on the thermal performance of compact heat exchanger and the rheological properties of low concentration mono and hybrid nanofluids containing Al_2O_3 and CuO nanoparticles," *Thermal Science and Engineering Progress*, vol. 20, pp. 100727, 2020.

[15] A. Senthilkumar, E. P. Abhijith, and C. A. A. Jawhar, "Experimental investigation of Al_2O_3/SiO_2 hybrid nanolubriant in R600a vapour compression refrigeration system," *Materials Today: Proceedings*, vol. 45, pp. 5921-5924, 2021.

[16] A. Senthilkumar, P. V. Abhishek, M. Adithyan, and A. Arjun, "Experimental investigation of CuO/SiO_2 hybrid nano-lubricant in R600a vapour compression refrigeration system," *Materials Today: Proceedings*, vol. 45, pp. 6083-6086, 2021.

[17] A. Kumar and S. P. S. Rajput, "Energetic and exergetic analysis of a Vapour compression refrigeration test rig in varying concentrations of (TiO_2-SiO_2/MO) hybrid nano-lubricants and R600a refrigerant charges," *Energy Sources, Part A: Recovery, Utilization, and Environmental Effects*, vol. 45, no. 3, pp. 9118-9132, 2023.

[18] M. J. Akhtar and S. P. S. Rajput, "Energy and exergy analysis of vapour compression test rig using R134a blended with GN-MWCNT/POE hybrid nano-lubricants," *Energy Sources, Part A: Recovery, Utilization, and Environmental Effects*, vol. 46, no. 1, pp. 188-208, 2024.

[19] S. Govindasamy, M. Kaliyannan, S. Sadhasivam, and R. Kadasari, "Experimental analysis of domestic refrigeration system using nanorefrigerant [CeO_2+ ZnO+ R134a]," *Thermal Science*, vol. 26, no. (2 Part A), pp. 969-974, 2022.

[20] R. Tripathi, G. N. Tiwari, and V. K. Dwivedi, "Overall energy, exergy and carbon credit analysis of N partially covered photovoltaic thermal (PVT) concentrating collector connected in series," *Solar Energy*, vol. 136, pp. 260-267, 2016.

[21] Y. Su, Y. Zhang, and L. Shu, “Experimental study of using phase change material cooling in a solar tracking concentrated photovoltaic-thermal system,” *Solar Energy*, vol. 159, pp. 777-785, 2018.

[22] A. D. Tuncer, A. Khanlari, A. Sözen, E. Y. Gürbüz, C. Şirin, and A. Gungor, “Energy-exergy and enviro-economic survey of solar air heaters with various air channel modifications,” *Renewable Energy*, vol. 160, pp. 67-85, 2020.

[23] A. Kumar and A. Layek, “Energetic and exergetic performance evaluation of solar air heater with twisted rib roughness on absorber plate,” *Journal of Cleaner Production*, vol. 232, pp. 617-628, 2019.

[24] H. Hassan, M. S. Yousef, and S. Abo-Elfadl, “Energy, exergy, economic and environmental assessment of double pass V-corrugated-perforated finned solar air heater at different air mass ratios,” *Sustainable Energy Technologies and Assessments*, vol. 43, pp. 100936, 2021.

[25] A. R. Abd Elbar, M. S. Yousef, and H. Hassan, “Energy, exergy, exergoeconomic and enviroeconomic (4E) evaluation of a new integration of solar still with photovoltaic panel,” *Journal of Cleaner Production*, vol. 233, pp. 665-680, 2019.

[26] P. T. Saravanakumar, D. Somasundaram, and M. M. Matheswaran, “Exergetic investigation and optimization of arc shaped rib roughened solar air heater integrated with fins and baffles,” *Applied Thermal Engineering*, vol. 175, pp. 115316, 2020.

[27] S. S. Sanukrishna, M. Shafi, M. Murukan, and M. J. Prakash, “Effect of SiO_2 nanoparticles on the heat transfer characteristics of refrigerant and tribological behaviour of lubricant,” *Powder Technology*, vol. 356, pp. 39-49, 2019.

[28] S. S. Rawat, A. P. Harsha, and A. P. Deepak, “Tribological performance of paraffin grease with silica nanoparticles as an additive,” *Applied Nanoscience*, vol. 9, pp. 305-315, 2019.

[29] A. Singh, P. Chauhan, and T. G. Mamatha, “A review on tribological performance of lubricants with nanoparticles additives,” *Materials Today: Proceedings*, vol. 25, pp. 586-591, 2020.